

Chemical Reaction Engineering—II

Hugh M. Hulburt, *Editor*

The Third International Symposium
on Chemical Reaction Engineering
co-sponsored by the American
Chemical Society, the American
Institute of Chemical Engineers,
the Canadian Society for Chemical
Engineering, and the European
Federation of Chemical Engineering,
held at Northwestern University,
Evanston, Ill., Aug. 27–29, 1974.

ADVANCES IN CHEMISTRY SERIES

133

AMERICAN CHEMICAL SOCIETY

WASHINGTON, D. C. 1974

**American Chemical
Society Library**

1155 16th St. N. W.

Washington, D. C. 20036

In Chemical Reaction Engineering—II; Hulburt, H.;
Advances in Chemistry; American Chemical Society: Washington, DC, 1975.



ADCSAJ 133 1-698 (1974)

Copyright © 1974

American Chemical Society

All Rights Reserved

Library of Congress Catalog Card 74-82952

ISBN 8412-0200-1

PRINTED IN THE UNITED STATES OF AMERICA

Advances in Chemistry Series

Robert F. Gould, *Editor*

Advisory Board

Kenneth B. Bischoff

Bernard D. Blaustein

Ellis K. Fields

Edith M. Flanigen

Jesse C. H. Hwa

Phillip C. Kearney

Egon Matijević

Thomas J. Murphy

Robert W. Parry

FOREWORD

ADVANCES IN CHEMISTRY SERIES was founded in 1949 by the American Chemical Society as an outlet for symposia and collections of data in special areas of topical interest that could not be accommodated in the Society's journals. It provides a medium for symposia that would otherwise be fragmented, their papers distributed among several journals or not published at all. Papers are refereed critically according to ACS editorial standards and receive the careful attention and processing characteristic of ACS publications. Papers published in ADVANCES IN CHEMISTRY SERIES are original contributions not published elsewhere in whole or major part and include reports of research as well as reviews since symposia may embrace both types of presentation.

PREFACE

The International Symposia on Chemical Reaction Engineering, of which this is the third, have afforded a biennial occasion to survey the state of the art and science. This third symposium shows two major differences from earlier meetings. The first is the number of papers concerned with direct process applications—roughly one third—a distinct increase over previous symposia. One could wish for greater participation by industrial organizations, but it is significant that the academic institutions have submitted a substantial number of the studies on specific applications.

The second major difference is the ever widening geographical scope of the symposium. Papers are presented from 13 countries, with authors from four continents (including one co-author now in Africa and with Japan and Azerbaidjan contending for representation of Asia). There are 27 papers from Europe, 19 from North America, and 5 from Australia and Japan. Reaction engineering is a truly international endeavor.

Earlier symposia have stressed the logical structure of chemical reaction engineering and reactor types. The present one is organized around functional aspects which may appear in many types of reactors. Three sessions are devoted to explicit applications, though many of the other papers might also be classified as applications. Attention has shifted from concentration on fundamental principles and theoretical analysis of model systems to specific current processes and reaction types in the light of those principles. Not that all the fundamentals are now clear for much remains to be done; however, they are becoming clear enough to be useful in everyday reaction engineering problems. By considering these problems the art of engineering is refined, and the science is sharpened in its effectiveness.

This volume contains the contributed papers presented at the symposium. A second volume will contain invited reviews of each of the areas treated in the nine sessions.

HUGH M. HULBURT

Evanston, Ill.
May 1974

Organizing Committee
for the
Third International Symposium on
Chemical Reaction Engineering

H. M. Hulburt, *Chairman*
J. B. Butt, *Co-Chairman*

D. S. Hacker, *Local Arrangements and Events*
W. F. Stevens, *Session Staff and Facilities*
G. M. Brown, *Treasurer*

Members: K. B. Bischoff (AIChE)
D. Thoenes (EFChE)
V. W. Weekman, Jr. (ACS)
J. M. H. Fortuin (EFChE)
I. G. Dalla Lana (CSCHE)

A Vibration Mixed Reactor for Chemical Kinetics in Gas/Solid Catalyzed Reactions

P. SUNDERLAND

Department of Chemical Engineering, University of Leeds, England

E. M. A. EL KANZI

University of Khartoum, Sudan

An experimental reactor was designed in which a piston reciprocating at high speed provided the mixing needed to minimize the diffusional effects that frequently obscure the intrinsic chemical kinetics of gas/solid catalyzed reactions. Residence time distribution measurements for non-reacting mixtures showed that macromixing was invariably good. The rate of oxidation of o-xylene over a supported vanadium pentoxide catalyst shows that even under unfavorable conditions, temperature and concentration gradients in the reactor are small. The reactor has considerable potential for studying gas/solid catalyzed reactions.

Often a reactor is needed which can provide intrinsic chemical reaction rate data for gas/solid catalyzed reactions. In such a reactor, interphase temperature and concentration gradients must be made as small as possible by using vigorous turbulent mixing. The temperature and concentration of reactants at the catalyst surface then approach the values in the bulk gas phase. Good design should eliminate regions where serious bypassing or stagnation of the gaseous reactants can occur.

The contribution of homogeneous reactions to overall rate must be considered. However, since the heterogeneous reaction is the one of interest, it is desirable to minimize homogeneous reactions by keeping the ratio of voids to volume occupied by catalyst as small as possible.

The catalyst should be mounted in the reactor so that all catalyst surface is equally accessible to reactants. The effects of intraparticle temperature and concentration gradients can be eliminated by using low surface area catalysts. If the reactor can also be cheaply made and operated, a further advantage is gained.

For fast, complex, exothermic reactions, some form of differential reactor has proved to be the most useful for obtaining rate data. The once-through tubular fixed bed differential reactor operating at low conversion is good, but there are problems with the detection and analysis of small concentration

changes. The recycle reactor proposed by Boreskov (1) and Perkins and Rase (2) and used by others (3, 4, 5, 6, 7, 8), does not have these analytical problems, and at sufficiently high recycle rate (4) it behaves as a well-mixed differential stirred tank reactor. A major disadvantage for many reactions, however, is the need for a recycle pump capable of operating at elevated temperatures.

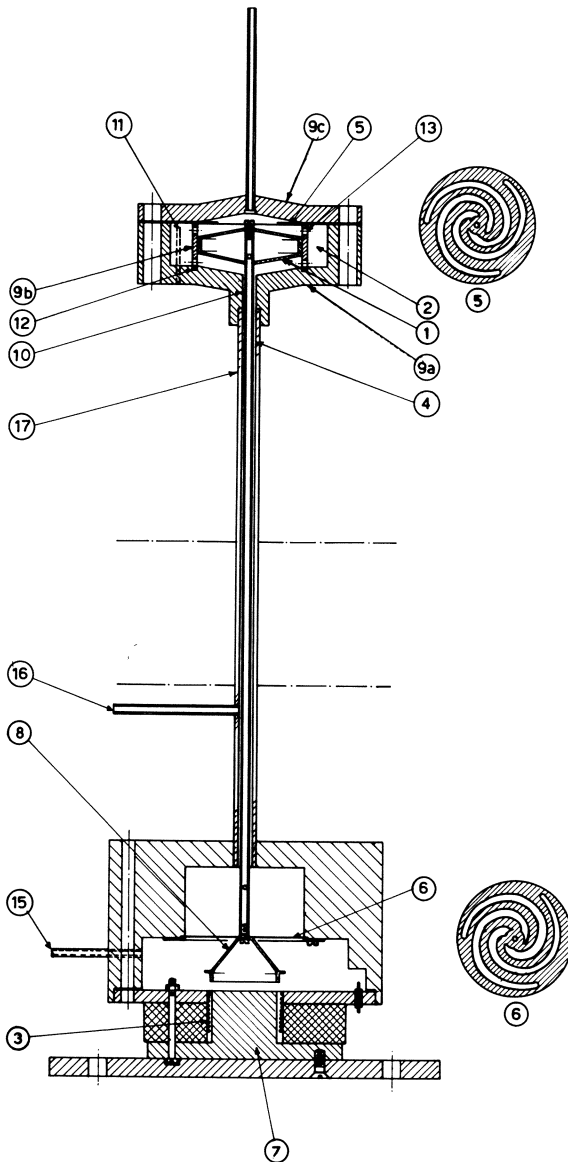


Figure 1. The reactor

A continuous flow stirred tank gas/solid catalyst reactor with "internal" rather than external recycle can possess almost all the desirable characteristics. The design of such a reactor has been attempted by many workers. A stirred tank reactor in which catalyst was mounted in the vanes of a high speed rotor was first proposed (9) and later used by Carberry (10). A similar rotating basket reactor was developed by Brisk *et al.* (11) and used by Calderbank *et al.* (12). A more recent version is that of Choudhary and Doraiswamy (13). An alternative form of stirred tank reactor in which gaseous reactants are forced through a stationary catalyst bed by a high speed impeller has been proposed (13, 14, 15). Garanin *et al.* (16) and later Brown and Bennett (17) designed stirred-tank reactors with directed flow of gaseous reactants through a fixed bed of catalyst.

In all the reactors, good mixing in the absence of reaction was undoubtedly achieved, but the effectiveness in minimizing concentration and temperature gradients if a fast exothermic reaction were taking place is uncertain. The vibration mixed reactor was designed to eliminate some objections to these earlier reactors.

Vibration Mixed Reactor (VMR)

The reactor is shown in Figure 1; Table I is the key to Figure 1. The design is unusual in that mixing within the reactor (Figure 1.9) is done by a piston (1) reciprocating at high speed rather than the more normal rotary devices. The frequency and amplitude of reciprocation can be varied over a wide range, but 50 cps with an amplitude of 0.6 cm provided adequate mixing in our experiments. It can be argued that this mode of agitation where the catalyst bed is swept and the direction of flow is altered for each stroke provides better mixing than a system in which the flow is always in the same direction.

Drive Unit. The piston was driven through a piston rod (4) by means of a coil (3) oscillating at 50 cps in the annulus of a powerful pot magnet (7). Varying the applied voltage altered the amplitude of vibration and hence the

Table I. Key to Figure 1

Item	Name	Composition
1	Piston	18/8 stainless steel
2	Catalyst bed	
3	Moving coil ^a	
4	Piston rod	18/8 stainless steel
5	Upper spring	Nimonic 75
6	Lower spring	Be/Cu alloy
7	Pot magnet ^a	soft iron
8	Connecting cone	aluminium
9a	Main body of reactor	18/8 stainless steel
9b	Piston sleeve	18/8 stainless steel
9c	Upper portion of reactor	18/8 stainless steel
10	Space between piston rod and sheath	
11	Thermocouple well	
12	Grooves to hold piston sleeve	
13	Holes to allow free movement of gases	
14	Reactant inlet	18/8 stainless steel
15	Reactant inlet	18/8 stainless steel
16	Piston rod sheath	18/8 stainless steel

^a Moving coil and magnet supplied by Rank-Wharfedale Ltd., Idle, England.

degree of mixing. Operation with amplitudes > 0.6 cm is possible using either a more powerful moving coil and magnet assembly or a less bulky piston and rod. Frequencies other than 50 cps are possible if the drive unit is coupled to a frequency oscillator and power amplifier.

For minimum power requirements and efficient operation, it was necessary to center the coil, piston, and rod and then balance all the vibrating parts dynamically. This was done by flat Archimedian type spiral springs at top (5) and bottom (6). Since the top spring had to withstand the hot corrosive reactor environment, it was made from Nimonic 75, a 80/20 nickel/chromium alloy; the bottom spring, in a less demanding environment, was a beryllium/copper alloy. By varying the thickness of the springs, the vibrating parts could be tuned to any desired frequency.

Because the piston was magnetically driven, it was relatively easy to make the drive unit and reactor leakproof and suitable for operation at elevated pressure. The coil and magnet were outside the constant temperature bath and far enough from the bath not to require any cooling. The unit was silent in operation.

Reactor. The reactor was made from 18/8 stainless steel in three parts (Figure 1.9 a, b, c). The piston and rod were made from the same type of steel, hollowed to reduce their mass.

The main body of the reactor (9a) was shaped to take the piston at maximum displacement and yet keep the total free space to a minimum. Reactor inlet was at the base (15); a thermocouple well (11) at the top allowed measurement of the gas temperature. There were eight holes (13), slightly larger than 0.635 cm in diameter, drilled at regular intervals into the body of the reactor around its perimeter, each hole able to admit two 0.635-cm diameter catalyst spheres. The loosely mounted spheres allowed free access of gaseous reactants to all the available surface area. Because of the shallowness of the catalyst bed (2) and the loose packing, resistance to gas passage through the bed was minimal. This nullified any tendency for gases to leak past the piston or to be merely compressed and decompressed rather than to pass through the catalyst bed. Temperature control was good, partly because of turbulent mixing and partly because of the proximity of the catalyst spheres to the surrounding constant temperature bath. For low conversions, some of the spheres can be replaced by dummy spheres to give the desired conversion without increasing the volume of free space.

The piston ring or sleeve (Figure 1.9 b) slotted into grooves (12) in the base of the reactor and was rigid when the reactor was bolted together. Holes in the ring at top and bottom corresponded with the holes drilled in the main body of the reactor to allow gas to pass through the catalyst bed. The inside of the ring and the piston itself were carefully machined to ensure good fit so that leakage past the piston was minimized with no danger of seizure during operation. The upper portion of the reactor (9c) was shaped to accommodate the piston at maximum amplitude and keep free space to a minimum. It contained the exit port for the gaseous effluent.

Constant Temperature Bath. A constant temperature environment for the reactor was provided by a commercial gas chromatograph oven. For highly exothermic reactions, better control could be achieved by a liquid heat transfer medium.

Flow Through the Reactor. Premixed feed can be introduced *via* the lower entry port (Figure 1.15), in which case the space (10) between piston rod and sheath (16) surrounding the rod acts as a preheater. If a reactant would attack the coil insulation, provision was made to introduce reactants separately. Another inlet port (14) allowed a reactant to be introduced directly into the sheath surrounding the piston rod. Here the space between piston rod and sheath acts both as premix and final preheat.

Macromixing Characteristics of the Reactor

Two types of ideal flow are limiting forms for fluid flow through a reactor. These are the so-called plug or piston flow and the perfectly mixed or back mix flow. Between the two extremes lie flow patterns found in actual reactors. For non-reacting processes the application of population balance models to determine approach to ideality was formally organized by Danckwerts (18); he defined distribution functions for the residence times of fluid elements in a process vessel. Injection of a pulse of tracer into the inlet fluid stream produces an outlet concentration/time curve which records the age fraction of fluid elements. For a perfectly mixed reactor,

$$C(\theta) = E(\theta) = \exp(-\theta) \quad (1)$$

When the perfect mixing model is unsatisfactory, a stirred tank reactor with dead space may be represented by Equation 2. A stirred tank with bypassing can be represented by Equation 3.

$$E(\theta) = \exp\left(\frac{-\theta}{a_1}\right) \quad (2)$$

$$E(\theta) = a_2 \exp(-a_2\theta) \quad (3)$$

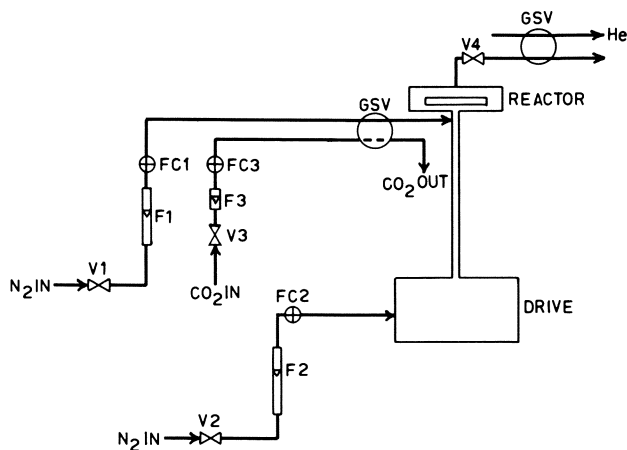


Figure 2. Flow diagram for macromixing tests: flow indicator (F), flow controller (FC), gas sampling valve (GSV), and valve (V)

Visual examination of the $E(\theta)$ vs θ curve is often sufficient to indicate non-ideality if there is serious bypassing or large pockets of stagnant fluid in the reactor. For less clearcut non-ideality, mathematical models were developed (19, 20) to determine the deviation from ideality. A schematic of the apparatus used in this work is given in Figure 2. Carbon dioxide used as a tracer was introduced into the main stream of nitrogen *via* the gas sample valve. The frequency of reciprocation was kept constant at 50 cps. Flow rates were varied

within the range 60–180 cm³/min NTP, and piston amplitude was varied from zero to 0.6 cm. Most of the tests were carried out under ambient conditions although some results were obtained at 473°K. Effluent composition was monitored by taking samples at frequent intervals for chromatographic analysis.

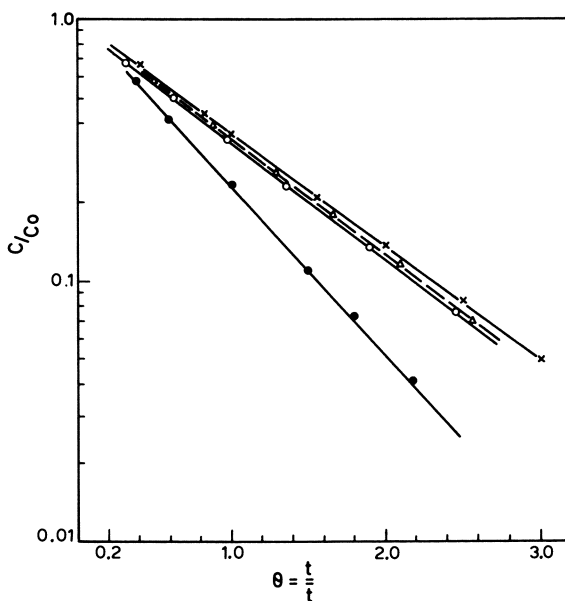


Figure 3. Effect of piston amplitude on macromixing: \times = 2.8 mm amplitude, Δ = 1.9 mm amplitude, \circ = 1.5 mm amplitude, and \bullet = 0.0 mm amplitude

For a perfectly mixed reactor, a plot of $\log_e E(\theta)$ vs. θ should yield a straight line of slope -1 . The results of a typical series of runs in which amplitude is varied at constant speed of reciprocation and flow rate are illustrated in Figure 3. Only for amplitudes approaching zero were the macromixing characteristics of the reactor non-ideal.

Effectiveness of the Reactor in Minimizing Heat and Mass Transfer Effects

Certain methods can be used to predict the onset of heat and mass transfer limitations for gas/solid catalyzed reactions. They usually involve an estimation of the magnitude of the heat and mass transfer coefficients which can then be used in the steady-state mass and energy balance equations to indicate the size of temperature and concentration gradients across the boundary layer surrounding the catalyst particle. Yang and Hougen (21, 22) prepared dimensionless charts for estimating partial pressure and temperature changes across a boundary layer in terms of a Reynold's number for a range of operating conditions. More recently, Mears (23) and Hudgins (24) derived analytical criteria to predict the onset of heat and mass transfer limitation using the perturbation approach (25, 26). Mears assumed that the reaction rate depends exponentially on temperature, and he accounts for the temperature gradient across the boun-

dary layer but neglected the concentration gradient. Thus, if the observed rate were to differ by not more than 5% from the true rate, he was able to propose the criterion:

$$\frac{(-\Delta H) R d_p}{h T_o} < 0.3 \frac{R_g T_o}{E} \quad (4)$$

For mass transfer in fixed beds Yang and Hougen (22) derived:

$$j_D = 2.44 \text{Re}^{-0.5} \text{ for } \text{Re} < 620 \quad (5)$$

and

$$j_D = 1.25 \text{Re}^{-0.41} \text{ for } \text{Re} > 620 \quad (6)$$

Similar relationships have been proposed by Chilton and Colburn and Petrovic and Thodos (27) with some modifications at low Reynold's numbers. For heat transfer in packed beds De Acetis and Thodos (28) reported a ratio of 1.51 for j_H/j_D , later revised (29) to 1.076. Satterfield and Resnick (30) preferred 1.37.

Diagnostic tests, which usually involve studying the effect of varying flow rate past the catalyst pellets, have also been used. When increasing flow rate no longer increases the reaction rate, then chemical reaction is said to be controlling. Chambers and Boudert (31) noted the need for care with this test because of its lack of sensitivity especially at low Reynold's numbers. Experimental measurements of h and k (11) and interphase gradients have been attempted (32, 33).

Oxidation of *o*-Xylene. To explore the micromixing characteristics of the reactor, *o*-xylene was oxidized over a vanadium pentoxide catalyst on a low surface area alumina support (9). Data available (34, 35, 36, 37, 38, 39, 40, 41, 42, 43) indicated that this reaction was appropriate.

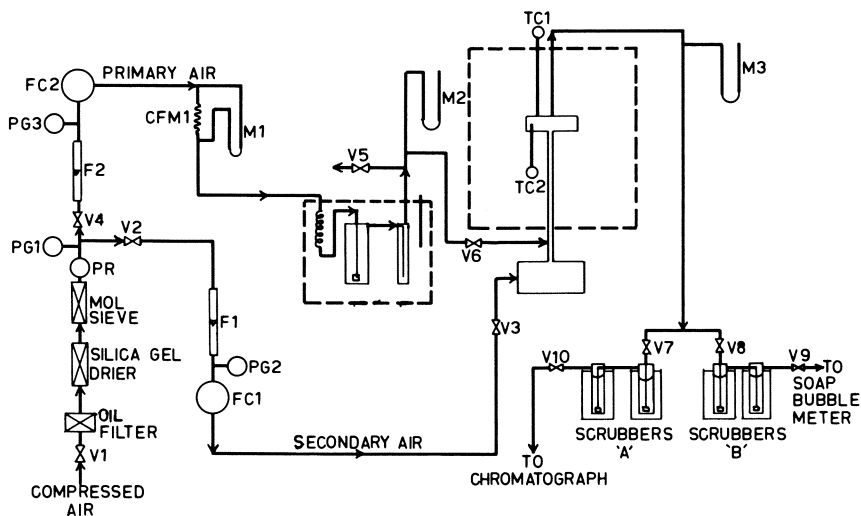


Figure 4. Flow diagram for *o*-xylene oxidation: capillary flowmeter (CFM), flow indicator (F), flow controller (FC), manometer (M), pressure gage (PG), pressure regulator (PR), thermocouple (TC), and valve (V)

A steady-state heat and mass balance yields Equations 7 and 8 which can be used to determine temperature and concentration gradients:

$$\Delta T = \frac{r(-\Delta H)}{h a} \quad (7)$$

$$\Delta C = \frac{r}{k a} \quad (8)$$

In the early stages of the work, the equations were used to aid reactor design and to indicate roughly a region of operating conditions within which chemical control could be expected. For this purpose, the kinetic data of Herten and Froment (40) were used. The methods available for estimating h and k are subject to some uncertainty even when applied to fixed bed reactors where the gas passes through the bed in one direction. For the VMR, where the direction of flow changes, estimation of h and k can at best be only approximate. Nevertheless, h and k were estimated after the method of Yang and Hougen (22), the gas flow past the catalyst being a pessimistic value derived from the mean velocity of the piston during a single stroke and the reactor designed accordingly.

When the reactor was built, limited *o*-xylene oxidation experiments were done using the setup in Figure 4. The results so far seem to confirm our predictions.

Discussion

Macromixing was good within the range of conditions studied except at extremely low amplitudes of reciprocation. Results with *o*-xylene show that the reactor effectively minimized heat and mass transfer contributions to overall reaction rate but the extent of the effectiveness cannot be properly assessed until work in progress becomes available. This work is concerned with the experimental measurement of h and k for varying rates of reciprocation of the piston. In addition, the oxidation rate of *o*-xylene at higher temperatures is being studied to test the predictions of the present work. Exploring this region between chemical and diffusional control should itself provide evidence as to whether the values of h and k chosen were realistic. It has been possible to postulate a rate expression to describe accurately the rate of oxidation of *o*-xylene within a limited range of operating conditions. The results indicate that the VMR offers some advantages over most of the stirred tank type reactors developed to date.

Nomenclature

a	external surface area of the catalyst per unit mass, cm ² /gram of catalyst
a_1	fraction of active volume
a_2	fraction of active stream
C	concentration, gram-moles/liter
C_0	initial concentration, gram-moles/liter
$C(\theta)$	concentration at dimensionless time θ , moles/liter
ΔC	concentration change, gram-moles/liter
d_p	diameter of the catalyst particle, cm
E	activation energy for the oxidation of <i>o</i> -xylene, cal/gram-mole of <i>o</i> -xylene

$E(\theta)$	$C(\theta)/C_0$
h	heat transfer coefficient
ΔH	enthalpy change for <i>o</i> -xylene oxidation, cal/gram-mole of <i>o</i> -xylene reacted
i_D	j factor for mass transfer
i_H	j factor for heat transfer
k	mass transfer coefficient
r	rate of <i>o</i> -xylene consumption, gram-moles/sec gram of catalyst
R	rate of <i>o</i> -xylene consumption, gram moles/sec cm ³ of catalyst
t	time, sec
\bar{t}	mean residence time, sec
T_0	temperature at the catalyst surface, °K
ΔT	temperature change, °K
θ	t/\bar{t}
Re	Reynolds number

Literature Cited

1. Borskov, G. K., *Zh. Fiz. Khim.* (1956) **30**, 2787.
2. Perkins, T. K., Rase, H. F., *AIChE J.* (1958) **4**, 351.
3. Butt, J. B., Walker, C. A., Bliss, H., *AIChE J.* (1962) **8**, 42.
4. Gillespie, B. M., Carberry, J. J., *Ind. Eng. Chem., Fundam.* (1966) **5**, 164.
5. Langer, R. M., Walker, C. A., *Ind. Eng. Chem.* (1954) **46**, 1299.
6. Leinroth, J. P., Sherwood, T. K., *AIChE J.* (1964) **10**, 524.
7. Satterfield, C. N., Roberts, G., *AIChE J.* (1968) **14**, 159.
8. Sunderland, P., Ph.D. Thesis, University of Leeds, England, 1974.
9. Carberry, J. J., *Ind. Eng. Chem.* (1964) **56**, (ii), 39.
10. Tajbl, D. G., Simmons, J. B., Carberry, J. J., *Ind. Eng. Chem.* (1966) **5**, 171.
11. Brisk, M. L., Day, R. L., Jones, M., Warren, T. B., *Trans. Inst. Chem. Eng.* (1968) **46**, 73.
12. Calderbank, P. H., Watt, G. I., Ellis, S. N., *Proc. 5th European/2nd Intern. Symp. Chem. Reaction Eng., Amsterdam, 1972*, B2—1.
13. Choudhary, V. R., Doraiswamy, L. K., *Ind. Eng. Chem., Process Design Develop.* (1972) **11**, 420.
14. Tajbl, D. G., Feldkirchner, H. L., Lee, A. L., *ADVAN. CHEM. SER.* (1967) **69**, 1666.
15. Tajbl, D. G., *Can. J. Chem. Eng.* (1969) **47**, 154.
16. Garaniñ, V. I., Kurchi, U. M., Minachev, Kh. M., *Kinet. Katal.* (1967) **8**, 605.
17. Brown, C. E., Bennett, C. O., *AIChE J.* (1970) **16**, (5), 817.
18. Danckwerts, P. V., *Chem. Eng. Sci.* (1953) **2**, 1.
19. Cholette, A., Coultier, L., *Can. J. Chem. Eng.* (1959) **37**, 105.
20. Corrigan, T. E., Beavers, W. O., *Chem. Eng. Sci.* (1970) **23** (9), 1005.
21. Hougen, O. A., *Ind. Eng. Chem.* (1961) **53** (7), 515.
22. Yang, K. H., Hougen, O. A., *Chem. Eng. Progr.* (1950) **46**, 146.
23. Mears, D. E., *J. Catal.* (1971) **20**, 127.
24. Hudgins, R. R., *Can. J. Chem. Eng.* (1972) **50**, 427.
25. Anderson, J. B., *Chem. Eng. Sci.* (1963) **18**, 147.
26. Bowen, J. R., Acrivos, A., Oppenheim, A. K., *Chem. Eng. Sci.* (1968) **18**, 177.
27. Petrovic, L. J., Thodos, G., *Ind. Eng. Chem. Fundam.* (1968) **7**, 274.
28. De Acetis, J., Thodos, G., *Ind. Eng. Chem.* (1960) **52**, 1003.
29. Sen Gupta, A., Thodos, G., *AIChE J.* (1962) **8**, 608.
30. Satterfield, C. N., Resnick, H., *Chem. Eng. Progr.* (1954) **50**, 504.
31. Chambers, R. P., Boudert, M., *J. Catalysis* (1961) **6**, 141.
32. Hughes, R., Koh, H. P., *Chem. Eng.* (1970) **1**, 186.
33. Kehoe, J. P., Butt, J. B., *AIChE J.* (1972) **18** (2), 347.
34. Bernardini, F., Ramacci, M., *Chim. Ind.* (1966) **48** (1), 9.
35. Bhattacharya, S. K., Gulati, I. B., *Ind. Eng. Chem.* (1958) **50**, 1719.
36. Bhattacharya, S. K., Krishnamarthy, J., *Appl. Chem. (London)* (1963) **13** (12), 547.
37. Calderbank, P. H., Caldwell, L., Watts, G. I., *Symp. Chem. Reaction Eng., Univ. Leeds, April 1971*.

38. Costa Novella, E., Escardino, E., *An. Real Soc. Espan. Fis. Quim. Ser. B* (1963) (11), 66.
39. Froment, G. I., *Ind. Eng. Chem.* (1967) **59** (2), 18.
40. Herten, J., Froment, G. I., *Ind. Eng. Chem., Process Design Develop.* (1968) **7** (4), 516.
41. Jusola, J. A., Mann, R. F., Downie, J., *J. Catalysis* (1970) **17**, 106.
42. Mann, R. F., Downie, J., *Can. J. Chem. Eng.* (1968) **46** (1), 71.
43. Simard, G. L., Steger, J. F., Arnott, R. J., Seigel, L. A., *Ind. Eng. Chem.* (1955) **47**, 1424.

RECEIVED January 2, 1974.

Experimental Simulation of a Continuous Stirred Tank Reactor for Teaching Reactor Design and Control

MICHAEL L. BRISK

Department of Chemical Engineering, University of Sydney, Sydney, Australia

A novel application of on-line simulation was developed to provide flexible, realistic, safe student experiments to illustrate multiple steady states and dynamic instabilities in the design and control of stirred chemical reactors. An exothermic reaction is simulated in a small CSTR using only steam and water. Heat generation in the reactor, produced by live steam injection, is controlled as a dynamic function of reactor temperature by an on-line analog computer which provides the reaction kinetics and reaction rate-temperature relationships. The reactor exhibits three steady states and under closed-loop temperature control demonstrates limit cycle phenomena. It has been a valuable teaching tool, and with the addition of direct digital computer control its application is extending to research into reactor control algorithms.

The concepts of steady state and dynamic instabilities in continuous stirred tank reactors (CSTR's) are important topics in chemical engineering courses on reactor design and process control. They are also difficult concepts requiring fairly advanced analytical methods for their mathematical treatment, and the student's understanding of them is aided if he can experiment with these phenomena in the laboratory. However, the design and operation of experimental reactors which allow this is awkward. There can be difficulties with materials of construction, and there are problems in providing and handling reasonable quantities of the necessary chemicals. For example, in one of the few published experimental studies of CSTR stability, it was necessary to run quite a small reactor (0.6 ft³) as a batch reactor to conserve chemicals (1). Once a reaction system has been chosen the equipment tends to be rather inflexible, and it is not simple to vary operating parameters over much of a range. There is, too, an uncomfortable safety problem associated with student operation of a reactor at an unstable state.

One solution to this is to write a mathematical model for a selected reaction system and simulate the reactor with associated control loops on a general purpose analog computer. Until recently this approach has been used by the

author to allow students to observe the characteristics of reactor behavior. Although it offers flexibility, this method just does not provide the same experience and "feel" for the system that is obtained by operation of a real reactor. This was noticeably true of undergraduates with no plant experience, who found it very difficult to visualize and believe in the actual system they were modeling if they could not test their model. In particular, the time scale of the analog simulation was much faster than a real system. This is normally exploited as an advantage in simulation, but it removed a further element of reality from the student's experimental study, particularly when dealing with controller responses.

The novel system described in this paper has been developed in an attempt to overcome these various problems and provide students with realistic but safe laboratory experiments in reactor stability and reactor control, with emphasis on: (a) observation of stable and unstable steady states; (b) observation of dynamic behavior and the use of standard control hardware to control the reactor; (c) use of DDC by an on-line digital computer for startup and control of the reactor.

Experimental Simulation

In an early experimental study of CSTR dynamics (2) a synthetic reactor was described in which an exothermic reaction could be carried out using only steam and water. Heat was generated in the reactor by injecting live steam at a rate proportional to the temperature, using a conventional proportional controller to manipulate the steam valve. This early attempt could represent only a locally linearized model of a zero-order reaction.

In the present work this concept has been adapted by replacing the proportional controller by an on-line analog computer which is used to control the rate of steam injection to a small CSTR. The computer generates both the steady state Arrhenius reaction rate-temperature relationship and the dynamics of the reaction kinetics. The hardware reactor plus on-line computer together simulate a real reactor with an exothermic chemical reaction. The combination has been christened an "experimental simulation" of a CSTR.

Equipment

The complete system is shown in Figure 1. Cold water, representing a reactant, is metered into a 0.4 ft³ stirred, insulated vessel where it is heated by live steam. The steam valve is manipulated by an on-line analog computer which measures the temperature in the reactor by thermocouple and solves the kinetic equations for the heat generation rate. The computer used is a superseded 100 V, 10 amplifier valve machine which had been withdrawn from teaching use several years ago but was kept in working order.

The thermocouple signal, compensated for cold junction variation, is pre-amplified by a factor of 1000 with a low-drift dc amplifier, the output of which provides the computer input signal. This input is further amplified (10×) and filtered (0.5 sec time constant) by the first operational amplifier in the computer circuit (Figure 2) to give a working signal of 0.4 V/°C. The computer output (scaled to 0 to 5 V dc) drives an electropneumatic converter with output in the range 3 to 15 psig. This in turn manipulates a ½-inch steam valve through a pneumatic valve positioner which reduces valve hysteresis to a negligible level, simplifying the inclusion of the valve characteristic in the computer calculation.

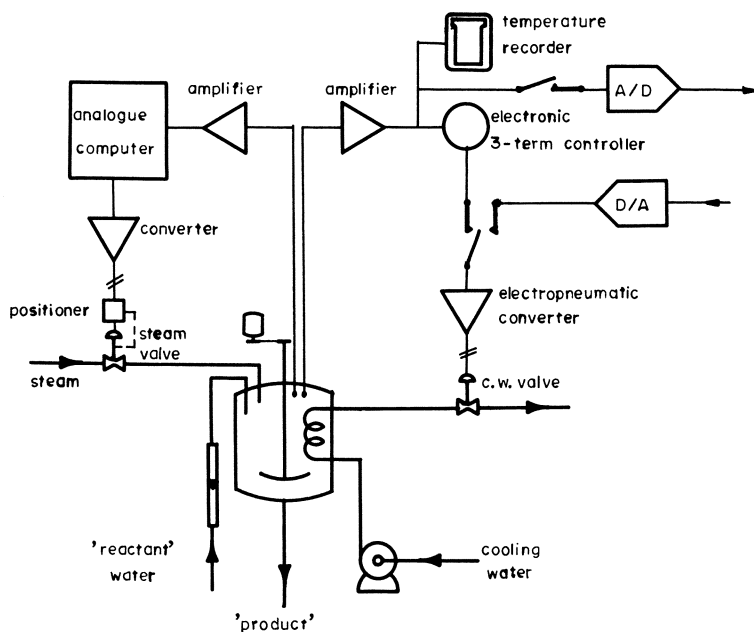


Figure 1. Reactor system

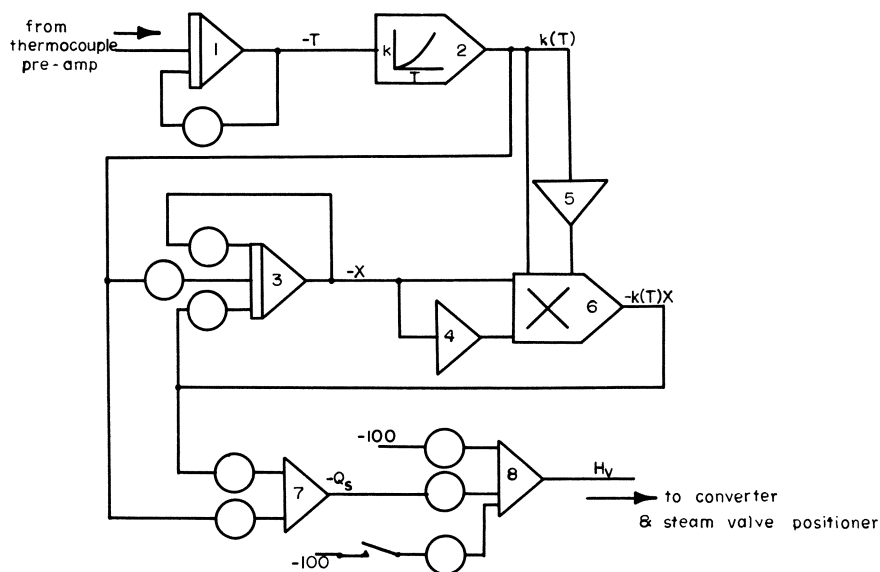


Figure 2. Analog computer circuit

Reactor temperature can be controlled either by conventional control hardware or direct digital control (DDC) by an on-line digital computer. A separate thermocouple in the reactor actuates a three-term electronic controller.

The controller output ultimately operates a $\frac{1}{2}$ -inch pneumatic valve varying cooling water flow through a coil providing 3.9 ft² of heat transfer area inside the vessel. This coolant valve is not fitted with a positioner. The controller input signal can also be supplied to an analog-to-digital converter from which it can be sampled as many as 10 times a second by a time-shared PDP-11 digital computer. The DDC algorithm output, after analog-to-digital conversion, can drive the cooling water valve directly through an electropneumatic converter.

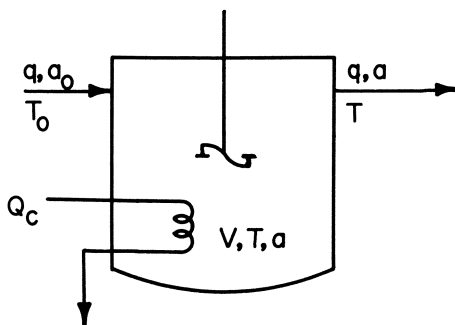


Figure 3. Stirred reactor

Simulation Model

Suppose an irreversible exothermic reaction is carried out in the CSTR of Figure 3. Dynamic mass and heat balances can be written in terms of fractional conversion:

$$\frac{dX}{dt} = -\frac{q}{V}X + \frac{r(X, T)}{a_0} \quad (1)$$

$$V\rho c \frac{dT}{dt} = -q\rho c(T - T_0) + (-\Delta H)Vr(X, T) - U \quad (2)$$

where it has been assumed: (a) the reactor is well mixed; (b) there is no volume change on reaction; (c) the average specific heats and densities of reactants and products are the same and do not vary with temperature; (d) the stirrer adds no heat to the system, and there are negligible heat losses through the vessel walls.

It is also assumed that the reaction rate is given by simple first-order kinetics:

$$r(X, T) = k(T)a_0(1 - X) \quad (3)$$

where

$$k(T) = Ae^{-E/RT} \quad (4)$$

This restriction to first-order kinetics is dictated by the limited analog computer hardware available and is not a general restriction.

A dynamic heat balance on the steam injection vessel of Figure 1 can be written:

$$V\rho c \frac{dT}{dt} = -Q\rho c(T - T_0) - Q_s c(T - T_r) + Q_s H_s - U \quad (5)$$

The second two terms on the right side of Equation 5 can be combined:

$$Q_s (H_s - c(T - T_r)) = Q_s H'_s \quad (6)$$

because the sensible heat content of the condensed steam does not vary significantly for small changes in temperature, and is only about 7% of H_s at the levels involved. Equation 5 then becomes:

$$V \rho c \frac{dT}{dt} = -Q \rho c (T - T_o) + Q_s H'_s - U \quad (7)$$

Equations 2 and 7 are now alike provided

$$Q_s H'_s = (-\Delta H) V r(X, T)$$

Because the maximum heat generation rate from the reaction (at complete conversion) is

$$H_{\max} = q a_o (-\Delta H)$$

it follows that

$$Q_s = \frac{H_{\max}}{H'_s} \frac{V}{q a_o} r(X, T) \quad (8)$$

In particular, for a first-order reaction

$$Q_s = \frac{H_{\max}}{H'_s} \frac{V}{q} k(T) (1 - X) \quad (9)$$

The relationship between steam flow rate and computer output voltage is the steam valve characteristic. With a valve fitted with a positioner this characteristic is linear over the entire operating range with no hysteresis. It is represented by the equation:

$$Q_s = 55.6 H_v - 30.5 \quad (10)$$

Thus an on-line analog computer measuring the steam vessel temperature can simulate a true chemical reaction by solving Equations 1, 4, 8, and 10 simultaneously in real time. The appropriate rate expression for first-order kinetics comes from Equation 3. A more complex kinetic expression could be handled easily given the necessary computer hardware. The voltage proportional to steam rate, H_v , is then used to manipulate the steam valve to admit the correct steam flow rate to the reactor.

For first-order reaction kinetics, the analog circuit required to solve Equations 1, 3, 4, 9, and 10 (omitting the details of magnitude scaling of the equations) is shown in Figure 2. The Arrhenius-type temperature dependence of the rate constant (Equation 4) is represented by a 24-segment, variable diode function generator. The product of rate constant and conversion is generated by a time division function multiplier. The remaining computing components are standard linear summers, integrators, and coefficient potentiometers.

To select suitable reaction parameters for the simulation, heat generation and removal rates were calculated as functions of temperature over the range 65° to 200°F using values of E/R in Equation 4 from 14000° to 20000°R. It was found that $E/R = 16000^\circ\text{R}$ was the most suitable choice to remain within the linear region of both steam and cooling water valves and provide con-

venient steady-state operating temperatures. The parameters finally selected for simulation and the corresponding steam reactor values are listed in Table I.

Table I. Reaction and Reactor Parameters

Parameter	Value
Pre-exponential factor	$1.515e^{26.6}\text{min}^{-1}$
Activation energy	31800 Btu (lb mole) ⁻¹
Heat of reaction	-2920 Btu (lb mole) ⁻¹
Molecular weight (water)	18 lb (lb mole) ⁻¹
Reactor volume	0.385 ft ³
Reactant water rate	1080 lb/hr
Coolant rate (steady state)	450 lb/hr
Steam flow for 100% conversion, 60 psig saturated steam	150 lb/hr
Nominal inlet reactant and coolant temperature	68°F

Operating Experience with the System

Steady-State Behavior Without Control. If Equations 1 and 2 are solved simultaneously with both the left hand sides set to zero, the steady-state of the reactor can be predicted. To do this, a value for the heat removed by the coolant, U , is needed. A series of tests on the steam reactor established that heat transfer to the cooling coil was such that under all relevant operating conditions the exit cooling water temperature approached the reactor temperature to $0.5 \pm 0.1^\circ\text{F}$. U was therefore evaluated using the empirical relationship:

$$U = Q_c(T - T_c - 0.5) \quad (11)$$

The parameters of Table I then give predicted steady states at 76°, 129°, and 167°F (solid lines in Figure 4). The steady state at 129°F is of course unstable, and any small disturbance to the reactor temperature at this point should cause the uncontrolled reactor to drive to the upper or lower stable steady state.

The open-loop behavior of the steam reactor demonstrates this phenomenon well. When the correct cooling water rate is set and steam is supplied to the cold reactor, the temperature settles to a lower steady state of 75° to 80°F according to inlet water temperature which varies somewhat with ambient conditions. The reactor temperature can be artificially raised by increasing the computer output voltage, H_v , with the adjustable switched potentiometer shown in Figure 2. This applies a bias voltage to increase the opening of the steam valve. When this bias voltage is removed with the reactor temperature below about 125°F, the temperature slowly settles back to the lower stable point. If the temperature is forced to rise above 135°F, it will climb to the upper stable point (164° to 169°F) upon removal of the bias. It is virtually impossible to adjust the manual bias to hold the reactor steady near 130°F for more than a few minutes. The reactor temperature starts to drift up or down—the direction is not readily predictable—ultimately returning to one of the stable states in the absence of the bias voltage. This behavior is typical of a real reactor and emphasizes to the student the need for control if a condition other than the extremes of high or low temperatures (and hence high or low conversions) is required.

Another useful experiment for the reactor design student is to establish the upper and lower limits for cooling water flow and hence the quench and ignition temperatures, T_Q and T_I , shown in Figure 4. If the reactor is operating

at the upper stable state and the cooling water flow rate is increased slowly enough to maintain a pseudo-steady state, the reactor temperature drops smoothly to a temperature near 146°F with a coolant flow of 510 lb/hr. A further small increase in coolant flow causes a large drop in temperature to close to the lower stable point at 76°F. The reaction has been quenched as shown by the upper dotted heat removal line in Figure 4. The reverse of this is ignition, which occurs at 93°F when the coolant rate drops below 80 lb/hr, as shown by the lower dotted line of Figure 4. These experiments are dramatic when performed on the steam reactor and strongly reinforce basic design principles.

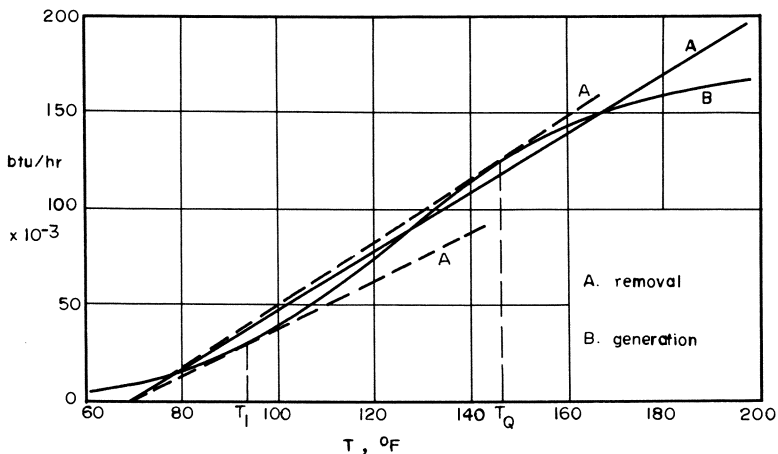


Figure 4. Heat generation and removal rates

Dynamic Operation with Analog Closed-Loop Control. The solution of the dynamic forms of Equations 1 and 2 together with the equations of closed-loop temperature control cannot be accomplished analytically but can be obtained using an analog or hybrid computer (*e.g.*, Ref. 1). Alternatively, it is possible to linearize Equations 1 and 2 about a selected operating point and apply linear control theory to predict, for example, the minimum controller gain necessary to stabilize the reactor at the unstable steady state (3). Application of the latter method about the unstable steady state at 129°F leads to a pseudo-first-order time constant of -1.76 min for the reactor temperature dynamics. The dynamic relationship between concentration and temperature is represented by a time constant of 0.70 min. After calculating these values, control students can then compute the minimum proportional gain at 129°F: 109% proportional band (p.b.) (0.061 psi/°F). The more able students are encouraged to attempt analog computer solution of the nonlinear equations, including the true non-linear control valve characteristic (but without hysteresis), using an EAI TR-48 computer. With conventional time scaling techniques a faster-than-real-time solution is possible, allowing simple trial-and-error methods to be used to find controller parameters. This nonlinear simulation predicts a minimum gain of 80% p.b. (0.083 psi/°F). This is different from the linear analysis which at best can only predict local stability in a very small region about the steady state.

All students then test their predictions on the steam reactor, attempting to control it near 129°F. Figure 5 shows typical results for startup of the cold reactor under proportional control, with the manual reset of the controller adjusted to provide 450 lb/hr of coolant for zero error at 129°F. At 100% p.b. the gain is too low to stabilize the reactor (curve A). A proportional band of 60% (gain = 1.11 psi/°F) is necessary just to hold the reactor in a stable, nonlinear oscillation (a limit cycle) about the set point (curve B). Increasing the controller gain to the maximum available (5% p.b.) reduces the cycling amplitude (curve C) but does not remove it. A still higher gain would be required fully to stabilize the operating point, but this cannot be too high if the closed loop itself is not to become unstable because of minor dynamic lags in valve, cooling coil, and thermocouple. Analog solution of the nonlinear model predicts a maximum controller gain of 0.25%. This is too high for a standard controller but can be achieved by DDC as noted below.

In general the agreement between the actual steam reactor and the analog nonlinear model is quite reasonable and builds students' confidence in mathematical modeling. However, the existence of the discrepancy between the minimum gain predicted by the nonlinear model and that required by the reactor spurred some better students to carry out a more detailed study. In particular it has been shown that some of this discrepancy is the result of cooling water valve hysteresis. This effect was noted by Ramirez and Turner (1) and

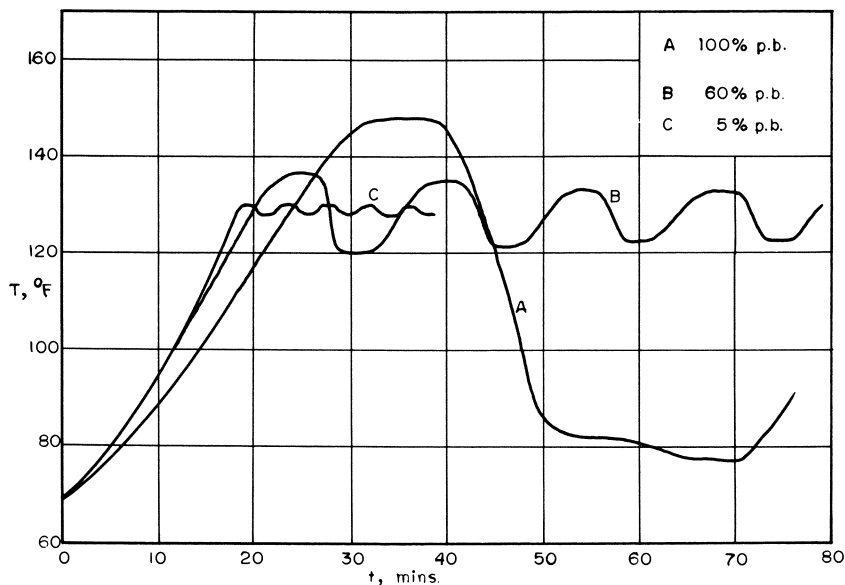


Figure 5. Transient response with proportional control

was analyzed theoretically by Hyun and Aris (4). The cooling water valve on the steam reactor has substantial hysteresis in the operating region (Figure 6). If this is included in the analog model, using the appropriate backlash circuits, the predicted minimum gain rises to 1.02 psi/°F (65% p.b.), close to the actual value of 1.11 psi/°F. The remaining difference is probably a

combination of experimental variations and the empirical representation of the cooling coil heat transfer (Equation 11).

From a control teaching point of view the reactor has another unique feature. It is easy to obtain its phase plane portrait experimentally. Such a representation, involving plots of the dynamic behavior of the reactor as concentration, or conversion *vs.* temperature trajectories (3), provides a clear

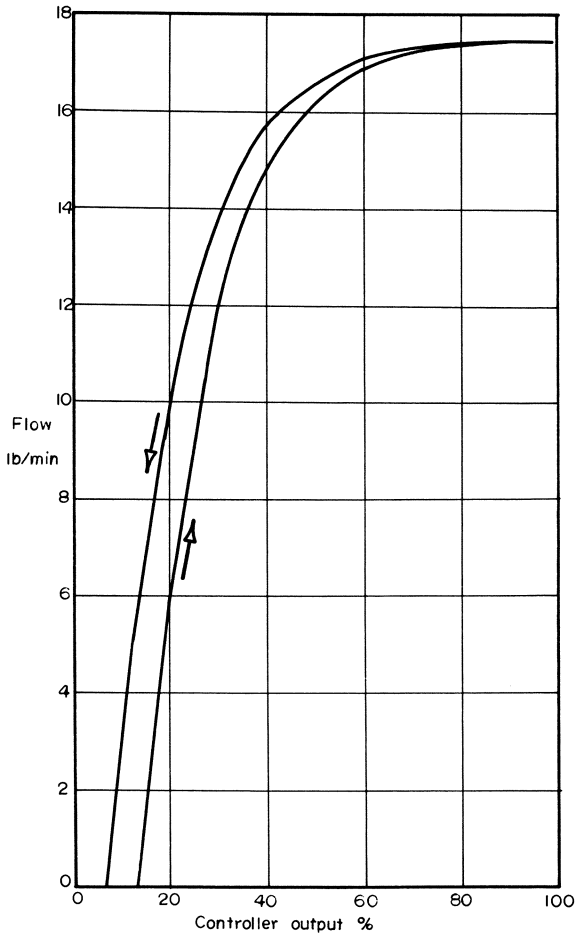


Figure 6. Coolant valve characteristic

picture of reactor stability with and without control over the whole operating region. Figures 7 and 8 are typical of the results obtained simply by connecting an X-Y recorder to the voltages proportional to conversion and temperature in the circuit of Figure 3 and disturbing the reactor by the manual steam adjustment. To obtain various starting conversions different from steady-state values, the output of integrator 3 was given various initial conditions other than zero.

Figure 7 is the phase portrait of the reactor without control. Stable nodes occur at the two stable steady-state conditions of Figure 4. The unstable steady state at 129°F is approached by some trajectories, but the reactor always drifts back to a stable node. Trajectories starting near 129°F, such as those from point A, return sometimes to the lower, sometimes to the upper node. The use of the minimum proportional gain to stabilize the system at the unstable steady state is shown in Figure 8A, which clearly reveals the limit cycle behavior noted before. The higher gain shown in Figure 8B shrinks the cycle amplitude but does not remove it.

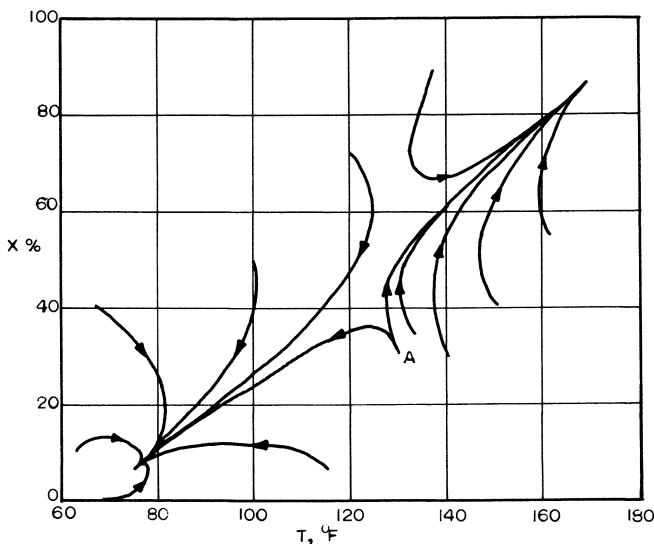


Figure 7. Phase plane for uncontrolled reactor

Dynamic Operation with Direct Digital Control. Recently DDC has been added to the steam reactor with the eventual aim of studying special purpose nonlinear algorithms for CSTR control. For undergraduate students the DDC application has been limited to providing simple experience with computer control with emphasis on the effects of sampling frequency and the use of a virtually unlimited range of controller gain. A standard three-term incremental algorithm (5) was programmed in assembler language on a PDP-11 computer, together with logging and alarm routines and a startup sequence for the reactor. Reactor operation is now merely the typing in of the desired set point and controller constants on a local teletype terminal. A routine has also been provided for on-line alteration of controller settings. The most significant result of this feature is the observation that the control loop can be made unstable if the proportional gain is increased beyond the equivalent of 0.33% p.b. when the DDC sampling interval is 0.2 sec, which is fast enough to be regarded as continuous control. This compares well with the analog model predictions mentioned above and effectively completes the student's survey of the controllability of the reactor. Postgraduate students have just started using the facility, and they will investigate the effects of other modes of control besides proportional, and alternatives to the three-term algorithm.

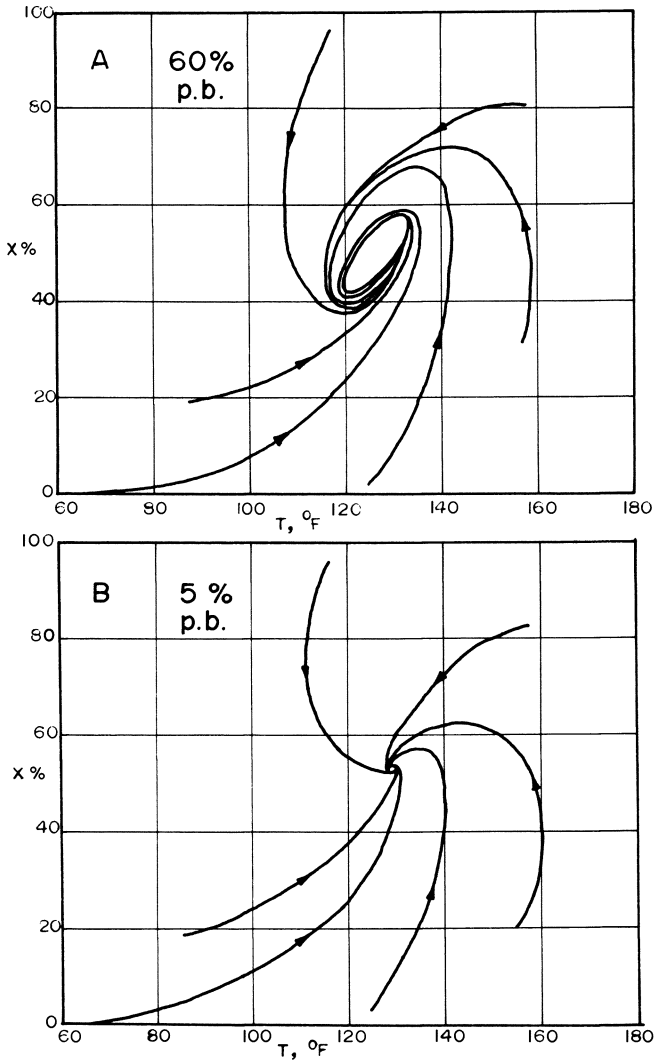


Figure 8. Phase planes with control

Nomenclature

- A pre-exponential constant, min^{-1}
- a reactant concentration, $\text{lb mole}/\text{ft}^3$
- a_0 reactant feed concentration, $\text{lb mole}/\text{ft}^3$
- c specific heat, $\text{Btu}/\text{lb}/^\circ\text{F}$
- E activation energy, $\text{Btu}/(\text{lb mole})$
- H_s steam enthalpy with respect to T_r , Btu/lb
- H'_s effective steam enthalpy, Btu/lb
- H_v voltage proportional to steam rate
- ΔH heat of reaction, $\text{Btu}/(\text{lb mole})$

k	first-order reaction rate constant, min^{-1}
Q	water flow rate, ft^3/hr
Q_c	coolant rate, lb/hr
Q_s	steam flow rate, lb/hr
q	reactant flow rate, ft^3/hr
r	reaction rate, $\text{lb mole}/\text{hr}/\text{ft}^3$
R	universal gas constant, $\text{lb mole}/\text{Btu}/^\circ\text{R}$
t	time
T	reactor temperature, $^\circ\text{F}$ or $^\circ\text{R}$
T_c	coolant inlet temperature, $^\circ\text{F}$
T_0	feed temperature, $^\circ\text{F}$
T_r	reference temperature, $^\circ\text{F}$
U	heat removal rate by coolant, Btu/hr
V	reactor volume, ft^3
X	fractional conversion
ρ	density, lb/ft^3

Literature Cited

1. Ramirez, W. F., Turner, B. A., *AIChE J.* (1969) **15**, 853.
2. Weber, T., Harriott, P., *Ind. Eng. Chem., Fundamentals* (1965) **4**, 264.
3. Aris, R., Amundson, N. R., *Chem. Eng. Sci.* (1958) **7**, 121.
4. Hyun, J. C., Aris, R., *Chem. Eng. Sci.* (1972) **27**, 1341.
5. Davies, W. D. T., *Instr. Pract.* (1967) **21**, 70.

RECEIVED January 2, 1974.

Process Parameters of Fluidized-Bed Burning of Graphite from HTGR Fuel Elements

R. BÖHNERT, G. KAISER, and E. MERZ

Institute for Chemical Technology, Kernforschungsanlage Jülich, GmbH, Jülich, Germany

The only large scale method suitable to separate the residual nuclear fuel materials from the large amounts of graphite of HTGR fuel elements during reprocessing is burning the fuel with air, oxygen-carbon dioxide mixtures, or pure oxygen. The experiments to date for burning crushed graphite fuel elements in an inert-free fluidized bed have demonstrated the technical feasibility of this process step. Combining known theoretical relationships with experiments in crushing the fuel elements, in fluidization, and in burning has led to a satisfactory means for predicting the operating points of a fluidized-bed burning process. This paper describes the studies defining the ranges of interest for the crushed particle size distribution, the gas velocities, and operating temperatures and pressures.

In commercial power-producing reactors, the fuel is generally in the reactor long enough so that fission products and neutron capture products, including bred fissile isotopes, have accumulated to where they significantly affect the economic optimization of fuel recycle. The purpose of reactor fuel reprocessing is thus to recover and purify fissile material from irradiated fuel. In general, reprocessing of spent fuels from high-temperature gas-cooled reactors (HGTR's) consists of shipping irradiated fuel elements from the reactor to a reprocessing plant, removing as much extraneous material from the fuel as possible by dissolving the fuel in nitric acid, separating and purifying the uranium and thorium by solvent extraction, disposing of the radioactive wastes, and decontaminating the gaseous radioactive effluents from the reprocessing steps.

The feature which sets HTGR fuel apart from all other reactor fuels is the large amount of carbon which is directly associated with the fertile and fissile materials. Several fuel designs have been proposed by different designers and fuel element manufacturers; the most important are the hexagonal block elements of the Gulf General Atomic Co. (U.S.) and the spherical elements of several companies in the Federal Republic of Germany. The salient feature of both concepts is that the fissionable materials are contained in pyrocarbon (PyC) coated particles containing either sintered $(U,Th)O_2$ or $(U,Th)C_2$ kernels. The coated particles are imbedded in a graphite matrix. About 95 wt % of the fuel elements is graphite. Thus, the basic problem in HTGR fuel

reprocessing is the removal of this large quantity of carbon from the relatively small amount of fuel material—*i.e.*, uranium and thorium. The preferred method for this task is burning the graphite in the so-called head-end step of reprocessing.

This method of burning was first proposed in 1964 by the Oak Ridge National Laboratory (1). At that time it was recognized that fluidized-bed burning of the crushed fuel promised advantages over fixed-bed burning because of higher specific throughputs, easier heat removal and control, lower burning temperatures (thus minimizing off-gas contamination), and a considerably easier continuous operation. Most subsequent efforts have concentrated on the fluidized-bed burning concept (2, 3, 4). In the approach being studied in the United States, the material which is fluidized is finely divided alumina particles, which acts as an efficient heat transfer medium to carry the heat of combustion from the burning carbon to the wall of the burner. However, we at KFA in Germany are pursuing an approach without using an extra added inert fluidizing heat transfer medium (5). This measure should improve overall operating simplicity and economy, particularly since the later separation of fuel ash and alumina is eliminated.

For several years we have been studying the feasibility of burning graphite in a fluidized bed, using the density difference between the heavy metal particles and the graphite to form a support and gas distribution zone for the burning bed by allowing the particles to settle out. Thus, the settled particles form the flow bottom plate, and they can be removed almost carbon-free as a free flowing product continuously or batchwise. For large reprocessing plants, carbon throughputs are of the order of tons per day. The desired throughputs should be accomplished with a minimum number of process steps and pieces of equipment.

Experimental

Fluidized-bed burning of HTGR fuel elements has the following process steps: (1) size reduction of the fuel elements by crushing and/or grinding, (2) transport of the crushed fuel to the fluidized bed burner, (3) burning of the graphite and pyrocarbon with oxygen, and (4) removal of the bare oxide particles, or ashes from the carbide particles, from the burner.

Experiments with unirradiated and irradiated fuels were done. Only spherical fuel elements of German design (*e.g.*, AVR type from the first prototype HTGR power plant) with a 60-mm diameter were used. However, no major differences are expected for the other fuel elements.

Two hammer mills and a jaw crusher were available for the crushing tests. The average crushed particle size for the hammer mills was varied by changing the sieve plate openings while the jaw crusher had an adjustable slit width. As could be shown in preliminary experiments using quartz burning tubes, the size of the crushed product must be fixed somewhere between 0.6 and 3 mm.

Three burners of different size and design were used (the results listed are mean values from all experiments):

(a) A 60-mm diameter fluidizing tube equipped with an enlarged upper section containing sintered metal filters for cold and hot runs; air-cooled water vapor; average throughput, *ca.* 4 grams C/min.

(b) An 80-mm diameter fluidizing tube equipped again with an enlarged upper section but with external cyclones and filters for cold and hot runs; cooled with a recirculating water-steam carried by air to the burner; average throughput, *ca.* 15 grams C/min (*see* Figure 1).

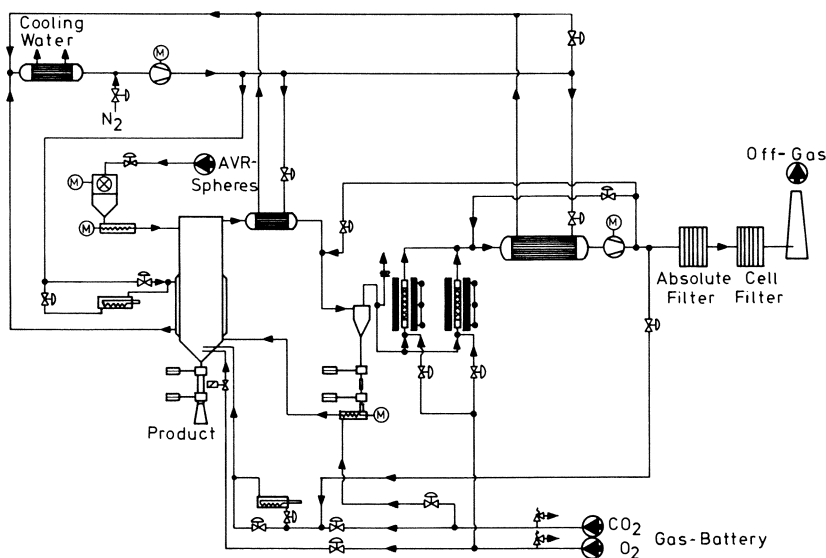


Figure 1. Schematic for hot cell burning studies with the 80-mm diameter burner

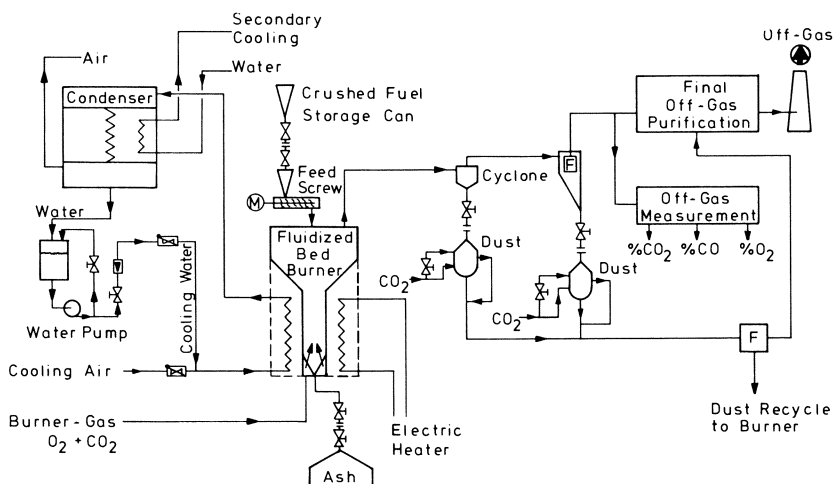


Figure 2. Generalized flowsheet for the fluidized-bed burning studies with 300-mm diameter burner. Bed temperature: $\leq 800^{\circ}\text{C}$; carbon burning rate: 3 kg C/hr + 30%; burning gas: O_2 ; off-gas composition: $\text{CO}_2:\text{CO} \approx 5:1$.

(c) A 300-mm diameter fluidizing tube for cold runs only; cooled like b; average throughput, ca. 70 grams C/min (see Figure 2).

Details of the hot cell arrangement of burner b and semitechnical arrangement with burner c are shown in Figures 1 and 2.

The burner design with internal filters (a) did not give a complete burning of the dust trapped in the upper regions of the furnace. Much better per-

formance was obtained applying external filtering devices to collect and recycle the dust carried out with the off-gas. Combustion was done for several operating conditions with pure oxygen and for O₂-CO₂ mixtures using the crushed fuel and particles as the sole content of the fluidized bed.

Crushed fuel is metered into the burner by a feed screw. The burner gas passes through a perforated entrance cone into the furnace. After the precooled off-gas has passed through the cyclone filtering device, samples are taken to determine CO₂, CO, and O₂ content prior of its release through the stack after a final purification. The burners are brought to operating temperature either by external resistance heaters or with preheated combustion gas. It is possible to recycle the CO₂ from the off-gas stream to the fluidizing gas stream. We decided to fix the operating temperature at less than 950°C to prevent ash melting or agglomeration. From fluidized-bed technology, the following parameters must be established: (a) particle size distribution of crushed fuel, (b) carbon burning rate, (c) composition of burner gas and gas velocities, and (d) average operating temperature and pressure.

Theory, Results, and Discussion

Permissible Sizes for the Crushed Fuel. The diameter of the coated fuel particles lies between 0.3 and 0.6 mm. The density of the graphite amounts to $\rho_s = 1.7$ grams/cm³. Burning with pure oxygen yields at 800°C an off-gas with a CO₂:CO ratio of approximately 5:1. The average particle size of crushed fuel, d_K , should be ≤ 2 mm to minimize particle breakage. The minimum fluidization velocity, v_L , is given by Ergun (6):

$$v_L = \frac{d_K^2 \epsilon^3 \rho_s g}{\eta [150 (1 - \epsilon) + 1.75 \text{ Re}]} \text{ for } 1 < \text{Re} < 4000$$

- Re = Reynold's number
- d_K = average spherical particle size of crushed graphite
- g = acceleration due to gravity
- ρ_s = density of the solid
- ρ_g = density of the gas
- ϵ = void fraction
- η = dynamic viscosity
- m = mass flow per hour

The maximum fluidization velocity, v_s , is given by Schytil (7):

$$v_s \leq 0.153 d_K^{1.14} (\rho_s - \rho_g)^{0.71} \times g^{0.71} \left(\frac{1}{\rho^{0.29} \times \eta^{0.43}} \right) \text{ for } 2 < \text{Re} < 500$$

Permissible ranges of particle sizes and velocities for fluidized-bed burning lie between the two lines in Figure 3. This figure shows the theoretical carbon burning rates for a fluidized bed of graphite suspensions in O₂-CO₂-CO-mixtures based on pure oxygen as the feed gas. The specific burning rate [grams C/cm² × hr] is limited by the average particle size in the steady-state fluidized bed as shown. The limits of the burning rates, to prevent fluidization of fuel kernels of various particle diameters are also indicated. A further limit to the average particle size is the design of the entrance cone and the fluid velocity in the burner. The gas concentration and velocity chosen in the burner determine the average steady-state particle size as well as the amount of graphite fines carried out of the burner with the off-gas. The maximum sized dust particle that remains with the fluidized bed may be deduced from Figure

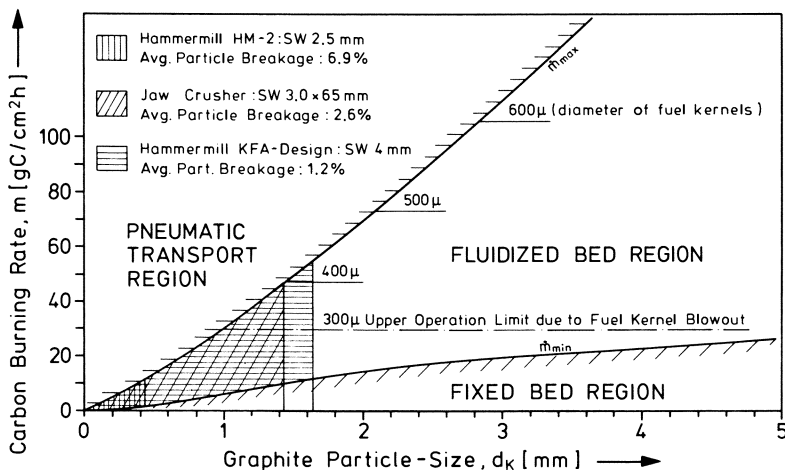


Figure 3. Theoretical carbon burning rates for a fluidized bed of graphite suspensions in O_2 - CO_2 - CO -mixtures as a function of graphite particle size and size of fuel kernels, based on pure oxygen as feed gas

Table I. Results of Crushing Studies on Fuel Spheres

Crusher Product No.	1	2	3	4	5
Crusher type	H-1	H-1	H-1	B	H-2
H $\hat{=}$ hammermill					
B $\hat{=}$ jaw crusher					
Rotation of hammers	l	q	!	—	l
l $\hat{=}$ parallel to slits					
q $\hat{=}$ perpendicular to slits					
Slit width (SW), mm	1.5	2.5	3.0	2.0	3.5
Avg. graphite particle size, d_K , μ	260	500	550	1300	1350
Tap density, ρ_s , grams/cm ³	0.82	0.93	1.01	0.87	0.96
Est. surface area, F_v , cm ² /cm ³	0.61×10^4	2.3×10^3	8.7×10^2	5.8×10^2	4.1×10^2
Type of particle dist. funct.	RRS ^a	RRS ^a	RRS ^a	RRS ^a	RRS ^a
Fines (<50 μ), %	17	9	6.5	7	4.5
Fuel particle breakage, %	26 . . . 34	6.7	7.4	2.6	1.2

^aRRS = Rosin - Rammler - Sperling.

3; however, the minimum amount of dust that is blown out is determined by the distribution of fines in the crushed fuel. The importance of minimizing the amount of fines in the crusher product cannot be overemphasized. The results of crushing study runs are given in Table I.

The crushing of the AVR fuel spheres with two hammer mills (H-1: Brand Siebtechnik, Mühlheim/Germany, type M 2; H-2: improved version designed by KFA) gave good correlations of crushed particle size distribution with the Rosin-Rammler-Sperling distribution functions. Crushed product from a jaw crusher can be approximated by a double logarithmic distribution curve. However, the jaw spacing would need to be more than 2 mm to reduce the particle breakage to approximately 1%.

Permissible Gas Velocities in the Fluidized Bed. The desired maximum graphite burning rate for a chosen average particle size at steady state in the fluidized bed specifies the minimum velocity of the entrance gas since the usable range of graphite particle size maintaining a stable fluidized-bed burning depends on the specific gravity of the particles. Pure oxygen enables one to obtain the highest possible burning rate, keeping in mind the need for maintaining a stationary particle bed. The crushed graphite particle sizes determine their surface area. They, on the other hand, influence the burning kinetics. Therefore, the relative proportions of CO_2 and CO in the off-gas depend on the burning temperature as well as on the graphite particle sizes as shown in Figure 4.

Because of the very small value of the density relationship, according to Zenz (8):

$$\frac{\rho_g}{\rho_s - \rho_g} \ll 10^{-2}$$

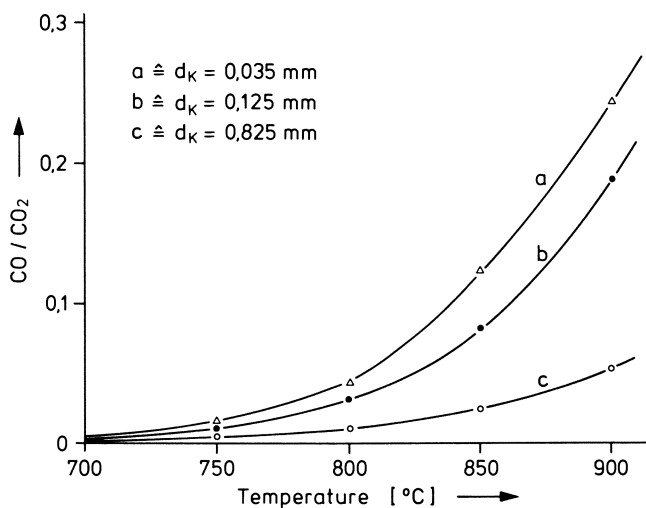


Figure 4. Experimental values of the $\text{CO}-\text{CO}_2$ ratio in the burning off-gas as a function of bed temperature and graphite particle size

as well as the measured v_s/v_L ratio, a pronounced heterogeneity in the fluidized bed must be expected. During its residence in a fluidized layer, the individual graphite particle is not completely burned because the relationship of forces weight *vs.* resistance of the flowing gas stream decreases continuously. As the particle attains the dimensions of a fluid, it follows the off-gas out of the bed into the off-gas tract. The dust will be separated from the off-gas by a cyclone and a filter and returned to the fluidized bed by a gas stream which enters the furnace just above the layer of settled kernels. The fluidized bed should be operated close to the loosening velocity not only to minimize dust recycling but to reduce the size of gas bubbles in the bed. The increase in bubble size by CO formation can be neglected.

Range of Permissible Burning Temperatures. The temperature dependence of the ratio of the maximum fluidization to minimum fluidization velocity, v_s/v_L , is very small (Figure 3). The ignition temperature for the graphite, $\geq 600^\circ\text{C}$, determines the lower limit. The upper temperature is determined by the formation of fuel particle agglomerates when the temperature exceeds 900°C . The size and strength of the agglomerates increase with increasing operating time. In other respects, however, stable operation was obtained at $650^\circ\text{--}900^\circ\text{C}$.

The temperature range chosen for the fluidized-bed burning thus is set between $650^\circ\text{C} \leq t_{\text{wall}} \leq 900^\circ\text{C}$. However, this range is also specified by two other considerations. Largely because of nuclear criticality limitations, water will be excluded from the processing hot cell. The heat will be removed by gas cooling the fluidized bed burner walls. The current high temperature steels have limited lifetimes as the operating temperatures are raised. In addition, higher operating temperatures vaporize increasingly larger amounts of volatile fission products and present increasing problems of radioactivity within the plant and removal of these materials from the large volumes of off-gas.

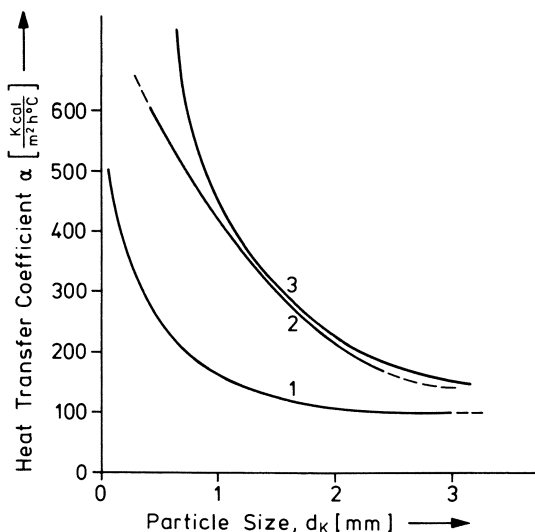


Figure 5. Heat transfer coefficient, α , bed-to-wall as a function of particle size.

Curve 1: Experimental data obtained from coal burning in a fluidized bed (11)

Curve 2: Calculated data for graphite particles applying the formula given in Ref. 12

Curve 3: Calculated data for generalized particles taken from Ref. 10

Calculation of the Fluidized-Bed Burner Dimensions. The overall reactor dimensions are minimized when the average fluidized-bed particle size at steady-state operation is as small as possible and the burning temperature is as high as possible. The heat transfer coefficient, α , from the fluidized bed to the

wall depends on the particle size, as shown in Figure 5. Assuming the specific burning rate as well as the average bed particle size, α is defined within rather narrow limits. Using the values for α determined from Figure 5, one may calculate the minimum bed height to yield a bed-to-wall temperature difference $\Delta t = 200^\circ\text{C}$ for gas cooling. Such calculations may be done by applying the calculated and experimentally measured Q values, respectively, shown in Figure 6.

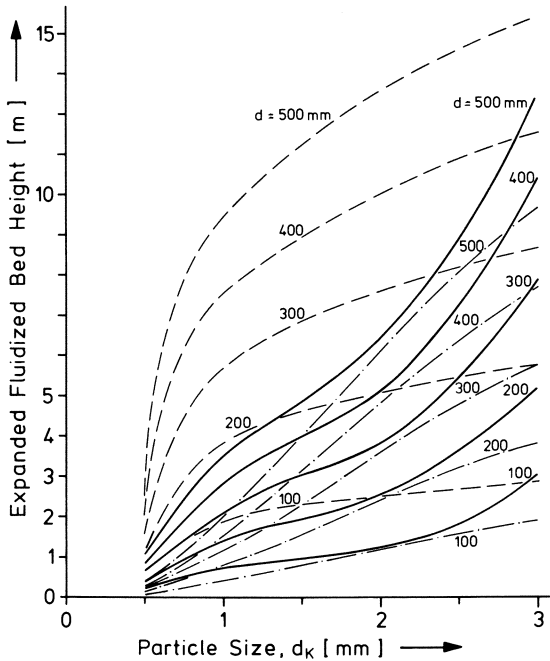


Figure 6. Minimum height of the expanded bed fluidized with $\text{CO}-\text{CO}$ at $\Delta t = 200^\circ\text{C}$ between bed and wall as a function of particle size. Bed temperature = 800°C ; d = bed diameter.

- calculated for maximum fluidization with data from Figure 5, curve 1
- calculated for minimum fluidization with data from Figure 5, curve 1
- calculated for maximum fluidization with data from Figure 5, curve 2

Figures 4 and 5 show that the minimum burner dimensions are obtained with the highest burning temperatures in combination with the smallest possible equilibrium bed particle size. The vibration criteria of Verloop (9) to test the limits of the homogeneity is predicted for the entire range of conditions of interest to the fluidized bed burning process.

Operating Pressure of the Fluidized-Bed Burner. The relationship of the specific burning rate to graphite particle size (Figure 3) holds for atmospheric

pressure. Because of the relationship between the operating pressure and the fluid velocity, one could obtain higher specific burning rates by operating the reactor under higher pressure. Maximum throughputs per burner volume are of particular interest in nuclear fuel reprocessing because of nuclear criticality limitations.

Depending on the type of fuel to be burned, one calculates that possible increases in the total carbon burning rates of factors of three to four times the normal values can be obtained by raising the pressure of burners. The uniformity of fluidization also improves because of the increasing value of the ratio,

$$\frac{\rho_R}{(\rho_s - \rho_R)}$$

with increasing pressure. This has been established in burning experiments carried out at up to 2 atm absolute pressure. The experiments have shown that total carbon burning rates can be raised (not indefinitely, however) depending on the fuel type, by at least several hundred percent by raising the operating pressure. The extra heat generated must be removed by increasing the bed height. The short length of oxygen penetration into the bed before consumption results in hot spots in burners with only a single-stage oxygen inlet. These hot spots can be avoided if one adds part of the oxygen above the settled particle bed. The advantage of more uniform fluidization obtained with higher pressure operation is somewhat offset by the increased difficulty in sealing the burner and the crushed fuel inlets. Because nuclear criticality considerations limit the diameter of circular pipe burners, higher heat removal surface areas can only be obtained with higher beds, and one can expect future burners to be relatively tall.

Literature Cited

1. Blanco, R. E. *et al.*, *Nucl. Sci. Eng.* (1964) **20**, 13.
2. Reilly, J. J. *et al.*, *U.S. Rept.—BNL No. 900* (1965).
3. Ferris, L. W., *Progr. Nucl. Energy, Ser. III* (1970) **4**, 125-128.
4. Baxter, B. J. *et al.*, *U.S. Rept. GULF-GA No. 12285* (1972).
5. Böhnert, R., Kaiser, G., Reaktortagung 1972 Hamburg, Germany, Karlsruhe: ZAED (1972) 252-255.
6. Ergun, S., *Chem. Eng. Progr.* (1952) **48** (2).
7. Schytil, F., "Wirbelschichttechnik" (Fluid Bed Technology), Springer-Verlag, Berlin, 1961.
8. Zenz, A. F. *et al.*, "Fluidization and Fluidized Particle Systems," Reinhold, New York, 1960.
9. Verloop, J., Ph.D. Thesis, University of Delft, Holland (1971).
10. Ziegler, N., "Heat and Mass Transfer to a Gas-Fluidized Bed of Solid Particles," *U.S. Rept.—ANL No. 5807* (1963).
11. Wright, S. J. *et al.*, *Brit. Chem. Eng.* (1970) **15**, 1551.
12. Beránek, J. *et al.*, "Wirbelschichttechnik," p. 187, VEB Deutscher Verlag für Grundstoffindustrie, Leipzig, DDR, 1964.

RECEIVED January 2, 1974.

The Transient Response of a Monolithic Catalyst Support

ROLAND H. HECK, JAMES WEI, and JAMES R. KATZER

Department of Chemical Engineering, University of Delaware,
Newark, Del. 19711

Performance of an automotive catalytic converter is governed by its warm-up from the time the engine is started. A wind tunnel was constructed to generate air flow at 650°F and to pass it through an initially cold monolithic support equipped with thermocouples. Temperature in the monolith was measured as a function of position and time. The thermocouples measured a temperature which is closer to the gas temperature than the solid temperature. Onsager's approximate solution agrees with the analytical solution of Schumann and can describe the transient temperature profiles. Experimental values of the average Nusselt number lie between the theoretical values based on constant wall temperature and on constant wall flux. There is a short entrance region where the local Nusselt number is higher.

The design of automobile catalytic exhaust converters requires a quantitative description of their transient temperature behavior to specified inputs. Transient temperature behavior of monoliths is very important during warm-up from a cold start and during temperature excursions which can lead to catastrophic melt-down. Theoretical models to predict transient temperature profiles have been developed, but there are essentially no data to test these theoretical results. Also a simplified model is needed that is suitable for mathematical modeling of reactor performance. In this paper we measure the transient warm-up of a number of monolithic exhaust catalyst supports and compare it with the computations from various models.

The transient heating of a monolithic catalyst support is similar to the "single blow" problem for a regenerative heat exchanger. This problem has been treated analytically by Anzelius (1), Nusselt (2), Hausen (3), and Schumann (4). Jakob has reviewed these treatments (5).

The basic equations for convective heat transfer in a monolith arise from heat balances on the solid and the gas. Non-dimensionalizing and transforming the coordinates according to Schumann gives:

$$\frac{\partial \theta_G}{\partial Y} = \theta_s - \theta_G \quad (1)$$

$$\frac{\partial \theta_s}{\partial \tau} = \theta_G - \theta_s \quad (2)$$

The assumptions involved in these equations are:

- (1) Plug flow of the gas phase
- (2) No axial conduction in the gas or solid
- (3) Constant heat transfer coefficient
- (4) No radial gradients in temperature or velocity
- (5) No heat of reaction.

In an actual catalyst warm-up the heat of reaction would also have to be considered. Boundary and initial conditions for a step change in gas temperature to a cold monolith are:

$$\theta_G = 1 \text{ at } Y = 0 \text{ for all } \tau > 0 \quad (3)$$

$$\theta_S = 0 \text{ for all } Y \text{ at } \tau < 0 \quad (4)$$

Schumann's analytical solution to Equations 1-4 involves an infinite series of Bessel functions and does not lend itself easily to computation. Kohlmayr (6) developed an analytical solution, which is more easily used but still involves an infinite series. Brinkley (7) has published values of both gas and solid temperatures for a wide range of τ and Y ; however, their use involves cumbersome nonlinear interpolation. Klinkenberg (8) and Onsager (9) derived equations which approximate the analytical solution but are easier to use. Onsager's approximations to the analytical solution are:

$$\theta_G = \frac{1}{2} [1 + \operatorname{erf}(\sqrt{\tau} - \sqrt{Y})] + \frac{Y^{1/4}}{Y^{1/4} + \tau^{1/4}} e^{-\tau-Y} (I_0(2\sqrt{\tau Y})) \quad (5)$$

$$\theta_S = \frac{1}{2} [1 + \operatorname{erf}(\sqrt{\tau} - \sqrt{Y})] - \frac{\tau^{1/4}}{Y^{1/4} + \tau^{1/4}} e^{-\tau-Y} (I_0(2\sqrt{\tau Y})) \quad (6)$$

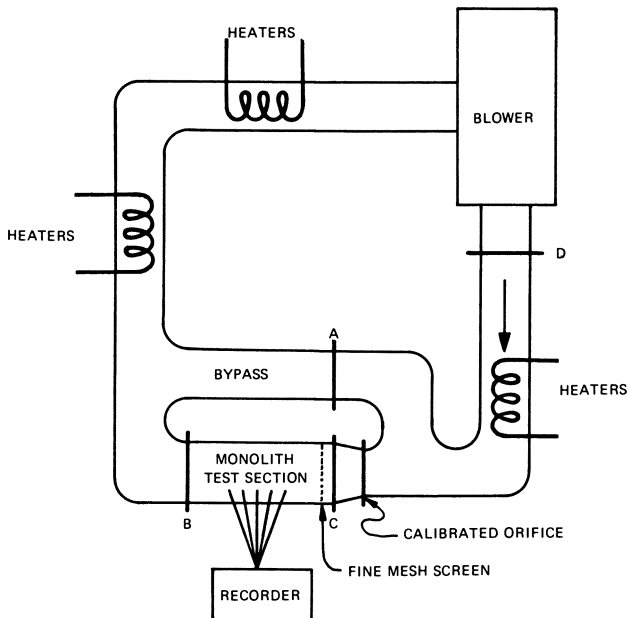


Figure 1. *Experimental apparatus*

Klinkenberg's approximations are:

$$\theta_G = \frac{1}{2} \left[1 + \operatorname{erf} \left(\sqrt{\tau} + \frac{1}{8\sqrt{\tau}} - \sqrt{Y} + \frac{1}{8\sqrt{Y}} \right) \right] \quad (7)$$

$$\theta_S = \frac{1}{2} \left[1 + \operatorname{erf} \left(\sqrt{\tau} - \frac{1}{8\sqrt{\tau}} - \sqrt{Y} - \frac{1}{8\sqrt{Y}} \right) \right] \quad (8)$$

To use either the analytical or approximate solution to Equations 1-4, a value for the heat transfer coefficient, h , is necessary. Streamline flow prevails in the monolith channels since the Reynolds number, Re , is never greater than a few hundred. The theoretical rate of heat transfer between a tube wall and the fluid entering the tube was first solved by Graetz (10). The Nusselt number, Nu , is very high at the entrance but rapidly declines to an asymptotic value a few diameters downstream. The asymptotic values for channels of various cross sections are given by Kays and London (11) and Sherony and Solbrig (12).

Experimental Methods and Materials

The apparatus consisted of a closed-loop high temperature wind tunnel into which the monolith samples were inserted (Figure 1). Air was circulated by a centrifugal blower through a loop of 4-inch diameter aluminum pipe with electric strip-heaters suspended in the flowing air. Butterfly valves A, B, and C were used to route the circulating air through either the test section or the bypass. The 5-inch diameter test section between the two butterfly valves B and C was removable, and the monolith was inserted into this section wrapped in a metal sleeve and a blown refractory (Cerafelt) blanket to prevent flow leakage by the monolith and radial heat losses. The blower and all pipes were insulated.

Table I. Properties of Monoliths

	AC	Corning Square Channel	Thermaxcomb Eight Channels/ inch	Corning Triangular Channel
Channel Geometry	square	square	sinusoidal	triangular
Overall diameter, inch	4.2	4.9	4.7	3.0
Overall length, inch, L	8.1	5.9	3.0	3.75
Volume, inch ³ , SL	112	115	52	26.5
Open area, %	65 ± 2	74 ± 2	65-70	71 ± 2
Total weight, grams	1350	868	467	230
Total superficial surface area, ft ² , EL	34	39	21	9.3
Bulk density, $\rho_s (1 - f)$, lb/ft ³	46.0	38.9	34.3	32.9
Hydraulic diameter of channel, inch, D	.060	.055	.042	.045
Holes/inch ²	182	203	275	215
Wall thickness, inch	.015	.01	.01	.01

At least seven holes of 1/16-inch diameter were drilled radially into the monolith at several axial positions. Additional holes to several radial depths at a given axial position were drilled in several monoliths. Sheathed iron-constantan thermocouples (0.01-inch diameter) were placed in the holes. Because of the hole size, wall thickness, and thermocouple size, it was not possible to locate and keep a thermocouple strictly in the wall of a channel. Thermocouple temperatures were recorded with a multipoint digital voltmeter (Doric, Digi-trend 210).

For a typical run, air was circulated through the bypass until the temperature reached 650°F. The monolith, initially at room temperature, was placed in the test section; butterfly valves B and C were opened while A was closed simultaneously. The thermocouples were scanned repeatedly, and the temperatures were recorded at the rate of two per second until all thermocouples gave constant readings. The flow rate was set with butterfly valve D and determined by measuring the pressure drop across a calibrated orifice plate.

The monolith supports studied and their properties are given in Table I. The AC monolith was provided by the AC Spark Plug Division of General Motors Corp., the Thermocomb by American Lava Co., and the Corning by Corning Glass Works.

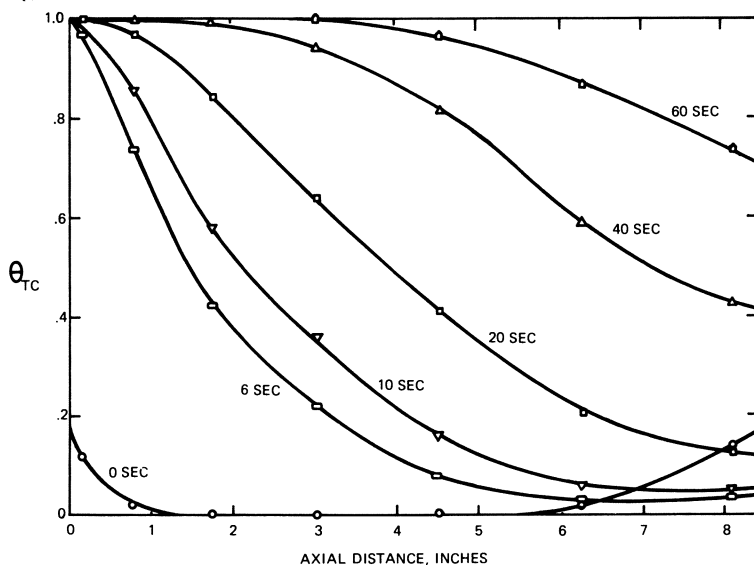


Figure 2. Transient temperature profiles in AC monolith: $Q = 41$ SCFM

Results

Data were obtained for inlet gas temperatures from 580° to 650°F and superficial flow rates of 7 to 50 SCFM. Experimental runs lasted from 30 to 180 sec. Figure 2 gives typical time-temperature profiles. The monolith temperature profile at zero time was not flat because of small leaks in the butterfly valves before the experiment was begun (Figure 2). This deviation represents less than 4% of the total heat transferred in the run. Furthermore, the deviation in the rear is almost gone after 6 sec.

Stop Flow. A stop-flow experiment was performed to determine whether the thermocouples measure the gas or solid temperature. Since the heat capacity of the solid is about a thousand times that of the gas in the monolith, the equilibrated temperature should be the solid temperature. The experiment was begun as usual, but the flow through the test monolith was stopped and diverted through the bypass after 37 sec. The measured temperature decreases sharply at the instant the flow through the test monolith was stopped (Figure 3). The observed temperature drop is between 8° and 50°F for the various axial positions measured.

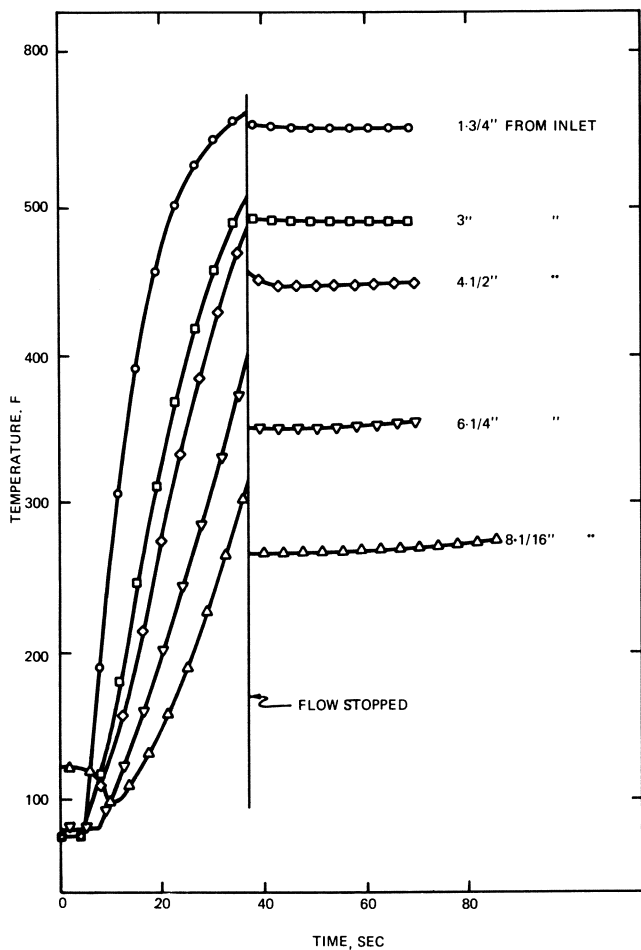


Figure 3. Results of stop-flow experiment with AC monolith:
 $Q = 46$ SCFM, inlet gas temp. = 580°F

Schumann's analytical solution predicts a maximum ($T_G - T_S$) of about 55°F for the 8-1/16 inch point for this run. This maximum should occur at the inflection point in the temperature-time curve. Our measured temperature drop for this thermocouple is about 50°F and is near the inflection point.

If it is assumed that the thermocouple has a thermal mass consisting of its sheath only and is in a free flow of air at the average velocity of the air in a channel, one obtains Equation 9:

$$T_G - T_{TC} = .08 (T_G - T_S) \quad (9)$$

The coefficient is actually larger than .08 since the mass of the thermocouple at the welded tip is in fact more than the mass of the sheath and part of its length is blocked from flow by channel walls. Analysis of several stop flow runs shows that the thermocouple temperature can be approximated by

$$T_{TC} = .8T_G + .2T_S \quad (10)$$

Axial Conduction. The importance of axial conduction in the gas and solid phase was defined in another experiment. Starting with an imposed temperature gradient in the monolith, the temperature of the monolith was allowed to equilibrate while the ends of the test section were sealed. The relaxation of the temperature was recorded. The effective thermal conductivity was calculated to be between 7 and 11 Btu inch/(hr ft² °F) at 300°F. For the temperature gradients we encountered, the rate of heat transfer by conduction is at most 1% of convection and can be ignored.

Radial Gradients. Radial gradients in velocity were minimized by placing the monolith in a metal sleeve which extended beyond the monolith face and by having just in front of the monolith an 8-inch length of straight pipe which contained a 60-mesh screen and a coarse screen. Proper positioning of the screens and the sleeve gave radially independent velocity as demonstrated by pitot tube measurements of velocity immediately behind the monolith. This minimized radial temperature gradients imposed by non-uniform flow. Temperature gradients caused by radial heat losses were minimized by insulating the monolith from the walls of the test section.

Experimental radial gradients were determined with thermocouples placed at several radial positions. Figure 4 shows that radial gradients were not significant, reaching a maximum of 30°F at the end of the run for the Corning square channel monolith. This monolith has the largest diameter of those studied and allowed room for only 0.2 inch of insulation in the test section. Hence, this is the largest radial gradient expected.

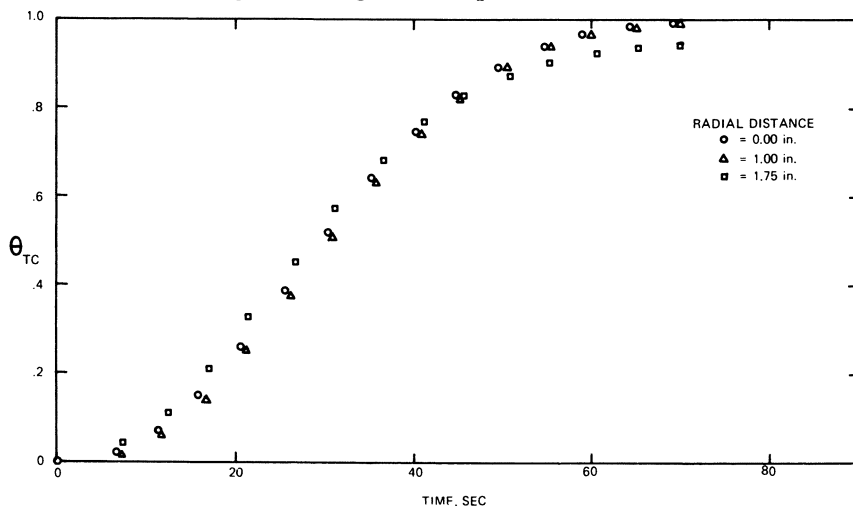


Figure 4. Radial temperature gradients in Corning square channel monolith: $Q = 20$ SCFM

Discussion

Analytical Models. Onsager's and Klinkenberg's approximate solutions, Equations 5 and 7, are compared with the analytical solution in Table II. Polynomial approximations from Abramowitz and Stegun (13) were used to evaluate the modified Bessel function of Equation 5. Both approximations are very good at high values of Y and τ ; however Onsager's is clearly better for low values of these variables. Our data has a maximum Y of about 14 and a

Table II. Comparison of Approximations with Analytical Solution

τ	Y	θ_G		
		Analytical ^a	Onsager	Klinkenberg
.5	.4	.781	.7811	.7373
.5	.8	.604	.6035	.5725
.5	1.2	.464	.4633	.4452
.5	2.0	.269	.2683	.2660
1.0	.4	.855	.8559	.8355
1.0	.8	.718	.7180	.7000
1.0	1.2	.594	.5943	.5805
1.0	2.0	.394	.3940	.3882
2.0	.4	.936	.9373	.9345
2.0	1.2	.775	.7748	.7695
2.0	2.0	.604	.6087	.5987
2.0	4.0	.270	.2703	.2693
4.0	.8	.967	.9670	.9678
4.0	2.0	.852	.8523	.8513
4.0	4.0	.572	.5717	.5702
4.0	8.0	.153	.1535	.1537
8.0	2.0	.985	.9853	.9856
8.0	6.0	.749	.7492	.7488
8.0	12.0	.216	.2161	.2161
16.0	8.0	.961	.9610	.9611
16.0	16.0	.535	.5354	.5352
16.0	18.0	.398	.3986	.3985

^a From Kays and London (11).

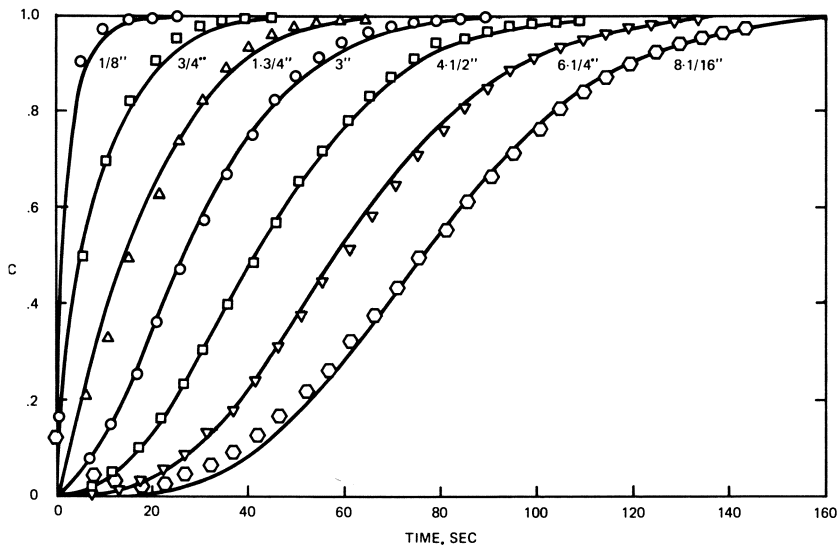


Figure 5. Comparison of data to analytical solution with constant Nu : AC monolith, $Q = 25$ SCFM, — analytical solution

maximum τ of 22. Onsager's approximation was used to generate the analytical solution used for data comparison in this work.

The experimental data are compared with the analytical solution of Equations 1-4, and an example is given in Figure 5. A Nusselt number of 3.08 in the analytical solution gives the best least-squares fit to the data and represents an average for the monolith as a whole. The root mean square deviation of the predicted curve from the data is .018 for this case.

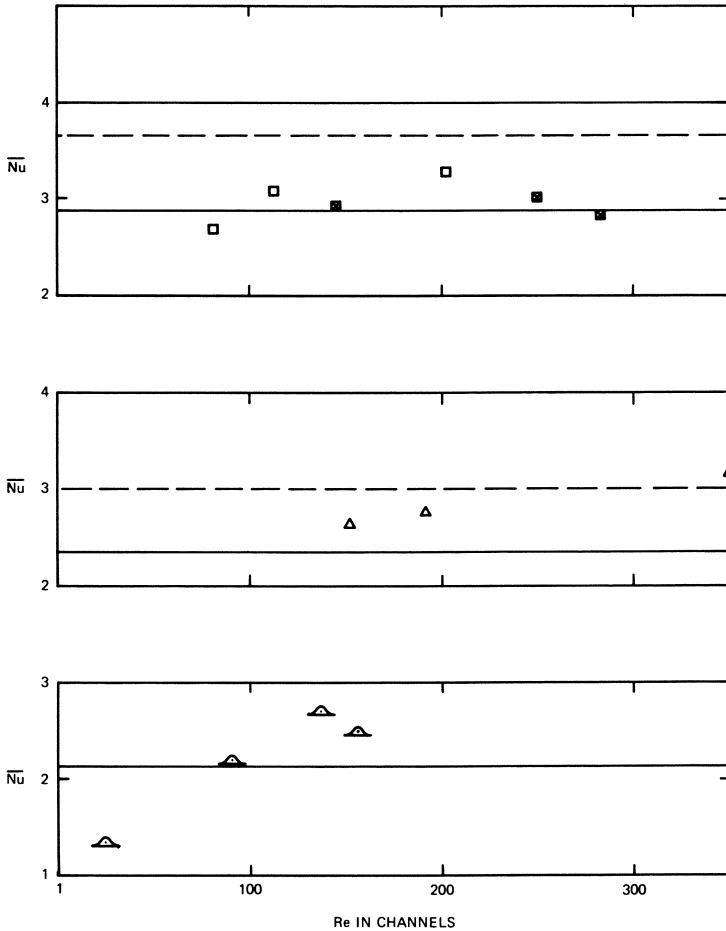


Figure 6. Average Nusselt number for heat-up of monolith: theoretical asymptotic value for constant wall flux, ---; constant wall temperature, —

- Corning square
- ⊠ AC square
- △ Corning triangular
- △ Thermocomb sinusoidal

Figure 6 is a plot of the average Nusselt number, (Nu), vs. Reynolds number, Re , in the channels for the monoliths studied. The theoretical asymptotic Nusselt numbers for fully developed flow with both constant wall temperature and constant heat flux are also given. The theoretical value for sinusoidal ducts is from Sherony and Solbrig (12), and the others are taken from Kays and London (11). The data show a somewhat higher Nu at higher Re as would be expected since the entrance region becomes longer at higher Re . The Nu for the Corning square channel monolith is slightly higher than that for the AC. The greater length of the AC monolith allows the flow to become fully developed over a larger fraction of the channel length.

If data from each thermocouple are fitted individually to determine the best mean Nusselt number, Nu_m , from the entrance to that point, one can determine the dependence of the Nusselt number on axial distance. This method of analysis permits a better fit of the experimental data than that attained in Figure 5 since the root mean square deviation from the data for this comparison is .013.

Table III compares the Nu_m determined by the last-squares fit to the theoretical values for developing thermal and hydrodynamic boundary layers. The experimentally determined values are in the range of the theoretical values; however, they seem to show a slightly stronger dependence on axial position. Sowards (14) also found a somewhat higher than theoretical dependence on length for the Sherwood number and attributed this to surface roughness. His adjustment to the theoretical equation in Table III raises the values by only 1–3%.

Table III. Observed vs. Theoretical Mean Nusselt Number as a Function of Length

x , inches	Experimental Nu_m	Theoretical ^a Nu_m
.75	3.75	3.54
1.75	3.45	3.18
3.00	3.15	3.07
4.50	2.93	3.01
6.25	2.85	2.98
8.06	2.55	2.95

^a $Nu_m = 2.89 (1 + .078 \text{ Re Pr } D/x)^{.45}$ from Hawthorn (14).

Effects on Performance. To compare the heat-up rates for monoliths with various cell geometries it is necessary to fix certain variables. If one fixes the wall thickness, percent open area, length, overall diameter, and monolith material, then for any cell geometry τ and Y are both proportional to h , as well as to Nu . Since larger τ and Y means faster heat up, the monolith with the larger Nu will heat up faster. On this basis the order of heat-up rate is squares > triangles > sinusoids. This is the same order determined by Hegedus (15) when comparing cell geometries on a mass transfer rate basis. If, however, one holds wall thickness, percent open area, total weight, pressure drop, and material of construction constant, then the order of heat-up rate becomes squares > sinusoids > triangles. For 60–70% open area the difference in NTU is no greater than 15% among these channel geometries.

Finite Element Models. Onsager's approximation gives an adequate model for Equations 1–4. However for practical application a model must be able to handle time-dependent gas inlet temperature and flow rate and any arbitrary initial temperature distribution in the solid, as well as the heat generated by chemical reaction. These are not easily handled analytically.

HOMOGENEOUS CELL MODEL. The homogeneous cell model has frequently been used to simulate packed-bed reactors (16). In this model the reactor is approximated by a series of well-mixed cells of uniform temperature. This model was considered first because of its simplicity and ease of calculation.

The solution to the cell model with boundary conditions given in Equations 3 and 4 is a cumulative sum of Poisson distributions:

$$\theta_s = \theta_G(x,t) = 1 - e^{-\lambda t} \sum_{i=0}^{m-1} \frac{(\lambda t)^i}{i!}$$

where

$$\lambda = \frac{Q \rho_G C_{pG} m}{\rho_S C_{pS} V_S}$$
$$m = \frac{nx}{L} + \frac{1}{2}$$

The heat transfer coefficient does not appear in this model, but the number of cells is chosen to fit the data. A large h corresponds to a large n . Unfortunately, n depends on the flow rate of the gas. The cell model with a fixed n predicts that the temperature profile at time t for flow rate Q must be identical to the profile at time αt for flow rate Q/α . These changes would amount to a change of Y to αY and τ to $\alpha \tau$ in the continuous model. It can be seen in Table II that a constant Y to τ ratio does not result in a constant θ .

The homogeneous cell model with a fixed n can apply only if the heat transfer coefficient is proportional to flow rate. This is more nearly true for a packed bed than a monolith.

HETEROGENEOUS CELL MODEL. Here each cell has a different temperature for the gas and the solid. The heat transfer coefficient appears in this model, and the number of cells should be very large to make the finite difference equation approach the differential equation.

A finite difference method can be used to solve Equations 1–4 with arbitrary boundary and initial conditions and with fluid and solid properties varying with both temperature and position. Brasz and Khan (17) concluded that a finite difference method can be computed more efficiently than the analytical solution of Kohlmayr (6). Harned (18) has suggested a two point central difference formula for approximating the heat-up of a packed bed. Our computations show that this model is within 5% of the analytical solution for $Y < 3$ and all values of τ , with ΔY of 1 and $\Delta \tau$ of 0.2.

Conclusion

The results of stop-flow experiments demonstrate that the temperature measured by the thermocouple is approximately 80% of the gas temperature plus 20% of the solid temperature. The effects of axial thermal conduction can be neglected. With reasonable insulation and a good deal of care to ensure uniform flow, the radial temperature gradient is negligible.

The analytical solution of the transient temperature profile in the monolith is available only for a uniform initial temperature, a sudden exposure to a gas flowing at a fixed temperature and velocity, and for a heat transfer coefficient that is independent of position. The Onsager approximation to the analytical solution is excellent and can be used easily to evaluate the parameters in the model. The experimental results agree very well with the analytical solutions, assuming an average Nusselt number. These experimental Nusselt numbers lie between the theoretical asymptotic values for constant wall temperature and for constant heat flux. As the Reynolds number increases from 50 to 250, the average Nusselt number can increase by 50%. The local Nusselt number is significantly higher at the inlet region and appears to depend more strongly on tube length than theory would predict.

The homogeneous cell model, assuming a uniform temperature in each cell, is inadequate to describe the monolith experimental results unless the number of cells used in the model is made to depend on the flow rate of gases,

thus making the model too cumbersome for use. The heterogeneous cell model, assuming separate temperatures for gas and solid in each cell, can be used to describe more varied boundary and initial conditions and must be used to model automobile exhaust reactors.

Nomenclature

C_{pG}	specific heat of gas, Btu/lb-°F
C_{pS}	specific heat of solid, Btu/lb-°F
D	hydraulic diameter, inches (4 (area/wetted perimeter))
E	superficial surface area/length, ft
f	fraction of area S open to flow
G	mass flux, lb/ft ² -sec
h	heat transfer coefficient, Btu/(min-ft ² -°F)
I_0	zeroth-order modified Bessel Function
k	thermal conductivity of gas, Btu inches/ft ² -°F-hr
L	length of monolith, inches
m	cell number
n	total number of cells
NTU	number of transfer units
Nu	Nusselt number (hD/k)
\bar{Nu}	average Nusselt number for monolith
Nu_m	mean Nusselt number from entrance
Pr	Prandtl number, $C_p\mu/k$
Q	volumetric flow rate, ft ³ /min
r	radial distance, inches
Re	Reynolds number, (DG/μ)
t	time, sec
T_G	temperature of gas, °F
T_S	temperature of solid, °F
T_{TC}	temperature of thermocouple, °F
V_S	total volume of solid, inch ³
x	distances from monolith entrance, inches
Y	dimensionless distance, ($xhE/Q\rho_G C_{pG}$)
S	total cross-sectional area of monolith, inches ²
μ	viscosity, lb/ft-sec
ρ_G	density of gas, lb/ft ³
ρ_S	density of solid, lb/ft ³
τ	dimensionless time = ($hE/(S(1-f)C_{pS}\rho_S)$) ($t - xSf/Q$)
θ_G	dimensionless gas temperature, ($T_G - T_{S_0}$)/($T_{G_0} - T_{S_0}$)
θ_S	dimensionless solid temperature, ($T_S - T_{S_0}$)/($T_{G_0} - T_{S_0}$)
θ_{TC}	dimensionless thermocouple temperature ($T_{TC} - T_{S_0}$)/($T_{G_0} - T_{S_0}$)

Acknowledgment

One of the authors (RHH) is supported by an Incentive Fellowship from the Mobil R&D Corp. This research is supported by National Science Foundation grant GK-38189 and the Unidel Foundation. The monoliths are provided by the AC Division of GM, Corning Glass Works, and the American Lava Corp., a subsidiary of the 3M Co.

Literature Cited

1. Anzelius, A., *Z. Angew. Math. Mech.* (1926) **6**, 291-4.
2. Nusselt, W., *Tech. Mech. Thermodynam.* (1930) **1**, 417-22.
3. Hausen, H., *Z. Angew. Math. Mech.* (1931) **11**, 105-14.

4. Schumann, T. E. W., *J. Franklin Inst.* (1929) **208**, 405.
5. Jakob, M., "Heat Transfer," Vol. II, Wiley, New York, 1957.
6. Kohlmayr, G. F., *AIChE J.* (1968) **14**, 499-501.
7. Brinkley, S. R., "Tables of Temperature Distribution Function for Heat Exchange Between Fluid and Porous Solid," Report, U.S. Bureau of Mines, Pittsburgh (Feb. 2, 1957).
8. Klinkenberg, A., Harmens, A., *Chem. Eng. Sci.* (1960) **11**, 260-266.
9. Thomas, H. C., *J. Amer. Chem. Soc.* (1944) **66**, 1664-6.
10. Graetz, L., *Ann. Phys.* (1883) **18**, 79-94.
11. Kays, W. M., London, A. L., "Compact Heat Exchangers," 2nd ed., McGraw-Hill, New York, 1964.
12. Sherony, D. F., Solbrig, C. W., *Int. J. Heat Mass Transfer* (1970) **13**, 145-159.
13. Abramowitz, M., Stegun, I. A., "Handbook of Mathematical Functions," Dover, New York, 1965.
14. Hawthorn, R. D., "Afterburner Catalysts . . . Effects of Heat and Mass Transfer Between Gas and Catalyst Surface," AIChE National Meeting (1972).
15. Hegedus, L. L., "Effects of Channel Geometry on the Performance of Catalytic Monoliths," Preprints of the 166th National Meeting of the American Chemical Society, Petrochemical Division (August 1973).
16. Kuo, J. C. W., Morgan, C. R., Lassen, H. G., *SAE Trans.* (1971) **80**, paper 710289.
17. Braz, J., Khan, A. V., *AIChE J.* (1972) **18**, 1274-6.
18. Harned, J. L., SAE Paper No. 720520, National Automobile Engineering Meeting, Detroit, Mich. (May 1972).

RECEIVED January 2, 1974.

Investigation of a Novel Nozzle Reactor

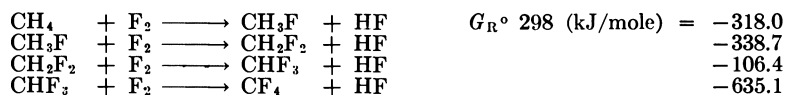
H. J. DIESNER and K. SCHUGERL

Institute für Technische Chemie, Technische Universität Hannover,
D-3000 Hannover, Callinstrasse 46, West Germany

The reaction between CH₄ and F₂ was carried out in axial symmetric turbulent supersonic jets using a concentric ring nozzle system. CH₄, inert gas, and F₂ were expanded across a central-nozzle, inner-ring-nozzle, and outer-ring-nozzle from stagnation pressures p₀ = 2-3 atm into vacuum (p₁ = 4 torr) at Re = 1.5 × 10⁵, M = 1.7-2.3 and Kn = 34-183 × 10⁻⁶. The reaction can be initiated in the first or second shock front of the supersonic jet by a solid body. Self-initiation occurs in the third shock front. The longitudinal and transversal concentration and temperature profiles were measured, and a transversal separation of the products was found in the jet. Since the reaction is restricted into a disc- and/or a ring-shaped volume at the shock front, the reaction time is short and nearly uniform; thus, the reactor can be protected from corrosion and overheating in contrast to a subsonic jet where the nozzle is destroyed within some minutes.

The reaction between F₂ and/or ClF₃ and aromatic (1, 2) and aliphatic and aromatic compounds (3, 4, 5, 6, 7, 8) has been carried out in subsonic jets. Only oxidation reactions (9, 10, 11) were investigated in supersonic jets because of the possible application of supersonic combustion ramjets for air breathing engines capable of flying at very high mach numbers.

Because of the disadvantages of the application of subsonic jets to the very exothermic four-stage reaction of F₂ with CH₄:



it was of interest to carry out this reaction in supersonic free jets. We expected that well-defined reaction volume and reaction conditions (especially reaction time) would make it possible to control this reaction better.

Experimental

Equipment and Reaction Conditions. Figure 1 shows a schematic of the equipment. F₂, He (Ar), and CH₄ were expanded separately across a nozzle system consisting of a Monel capillary of 0.3 mm diameter, an inner concentric nickel ring slit with 0.05 mm width, and an outer concentric nickel ring slit

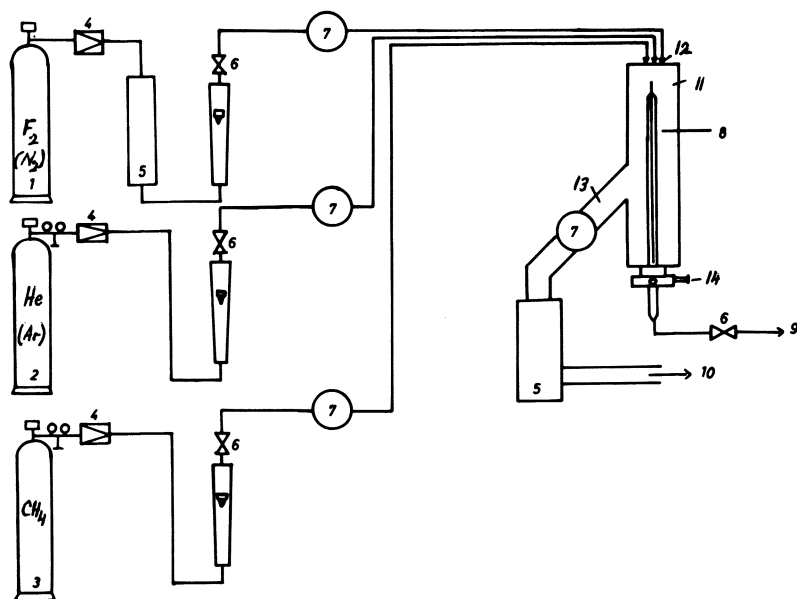


Figure 1. Apparatus. 1, 2, 3, gas flasks; 4, pressure control; 5, HF absorber; 6, valve; 7, pressure gage; 8, sampling tube; 9, to analysis; 10, vacuum pump; 11, reactor; 12, nozzle; 13, cooler; 14, 3-D manipulator.

with 0.035 mm width (Figure 2) into a copper reactor (11) (diameter: 44 mm, length: 480 mm). The reaction mixture is cooled in a heat exchanger (13); the HF is removed by NaF in a HF adsorber (5), and the rest was pumped by the mechanical vacuum pump (10) (pumping speed: 100 m³/hr). The gas samples were taken by a cooled Monel capillary (8) of 0.5 mm diameter.

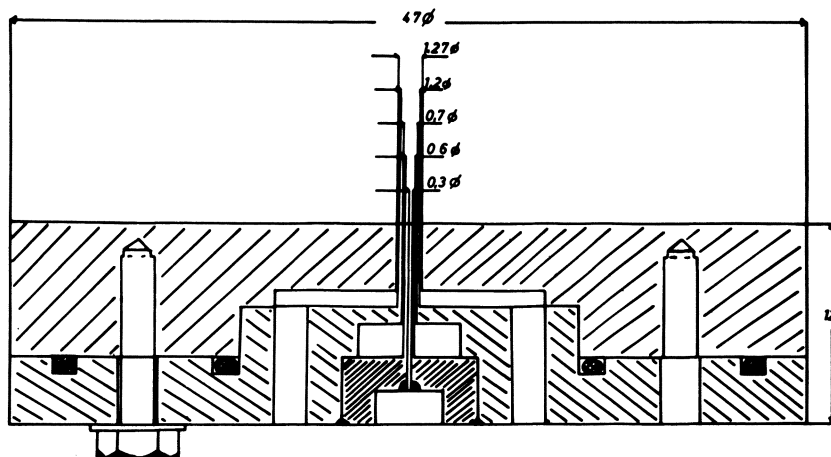


Figure 2. Nozzle (size in mm)

ter. The temperatures were measured by a nickel-chrome nickel microthermocouple which was inserted into the sampling tube (8). This tube could be moved by a precision mechanical device (14) in three dimensions. To observe

American Chemical
Society Library

the behavior of the ring-shaped reaction volume, two boron glass windows were mounted on the reactor (Figure 3).

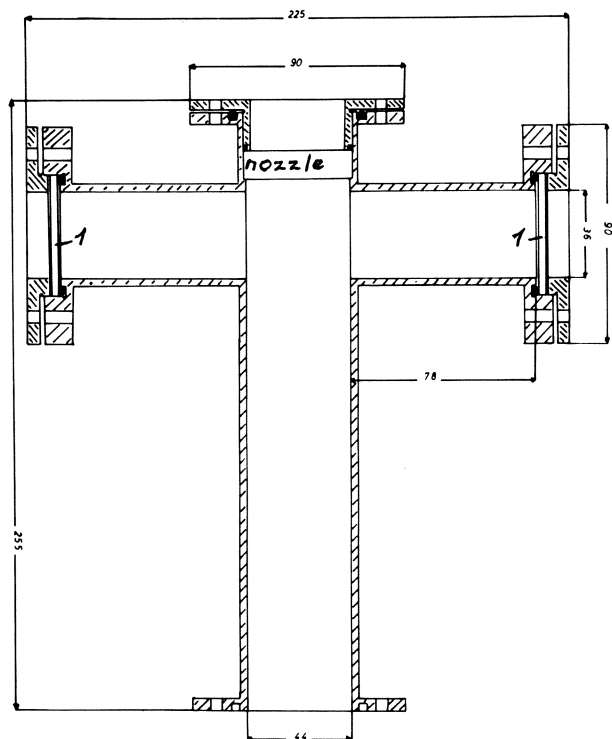


Figure 3. Reactor, boron glass windows at point 1

Longitudinal and transversal concentration and temperature profiles were measured in the reaction mixture under two different conditions (Table I).

Table I. Reaction Conditions (Static Pressure in Reactor, $p_1 = 4$ torr)

Gas	Flow Rate mmole/min	Mole %	Flow Rate Under Reaction Conditions (m/s)	Mach Number M	Reynolds Number $Re \times 10^3$	Knudsen Number $Kn \times 10^6$	Stagnation Pressure p_0 (atm)
<i>Condition I</i>							
CH ₄	99.8	36.9	975	2.3	58.2	34.3	3
F ₂	96.7	35.4	664	2.5	53.7	37.2	2.5
He	75.2	27.7	1650	1.7	10.8	183.8	2
<i>Condition II</i>							
CH ₄	99.8	40.4	975	2.3	58.2	34.3	3
F ₂	96.7	39.1	664	2.5	53.7	37.2	2.5
He	50.5	20.4	1769	1.35	7.1	119.0	1.3

Concentrations were measured by cryosorption of the reaction components from the helium gas using a charcoal column at the temperature of liquid nitrogen; the adsorbed gas was desorbed and analyzed by gas chromatography (12). To investigate the fluid dynamic behavior of the three component gas

Table II. Conditions of the Model Experiments

Gas Flow Rate m/s	Mach Number M	Reynolds Number Re $\times 10^3$	Knudsen Number Kn $\times 10^6$	Stagnation Pressure p ₀ (atm)	Static Pressure in Reactor p ₁	Type of Jet
<i>Condition III</i>						
CH ₄	975	2.3	58.2	34.3	3	4 torr
He	1658	1.7	10.9	183.8	2	4
N ₂	717	2.1	53.6	37.3	2.5	4
<i>Condition IV</i>						
CH ₄	975	2.3	58.2	34.3	3	4
Ar	492	1.6	28.5	70.1	2	4
N ₂	717	2.1	53.6	37.3	2.5	4
<i>Condition V</i>						
CH ₄	372	0.87	11.91		1.6	0.99 atm
He	580	0.60	2.48		1.3	0.99
N ₂	221	0.63	8.58		1.3	0.99
<i>Condition VI</i>						
CH ₄	372	0.87	11.9		1.6	0.99
Ar	183	0.60	6.89		1.3	0.99
N ₂	221	0.63	8.58		1.3	0.99

mixtures as a function of the properties of inert gas model mixtures consisting of CH₄, He or Ar, and N₂ (for F₂) their concentration profiles were also investigated at room temperature under four experimental conditions (Table II). The uncertainty caused by the complex interaction of the jet with the sampling tube was eliminated by careful calibration using gas mixtures with definite compositions. The concentration measurements for CH₄, N₂, Ar, and He were carried out by a four-channel mass spectrometer of type GD 150/4 of Varian MAT. Three channels were used to measure the number density of the three components, and the fourth channel was used to measure the total number density in the free jet (12).

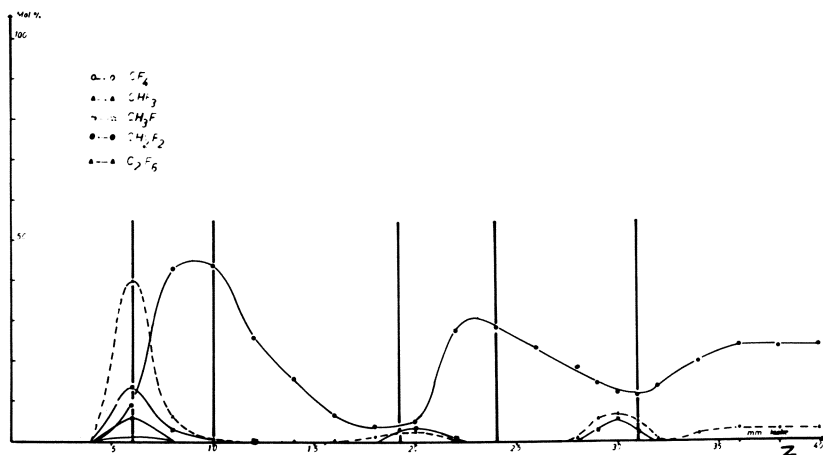


Figure 4. Longitudinal concentration profiles (He, condition I)

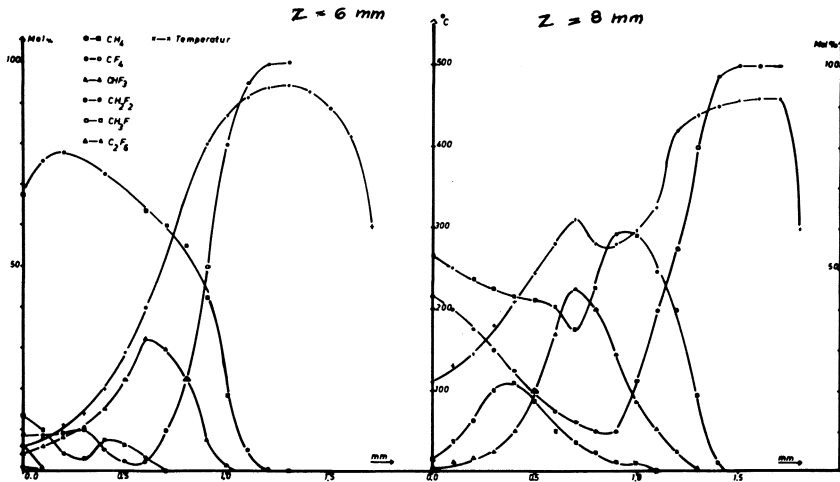


Figure 5a. Transversal temperature and concentration profiles (He, condition I)

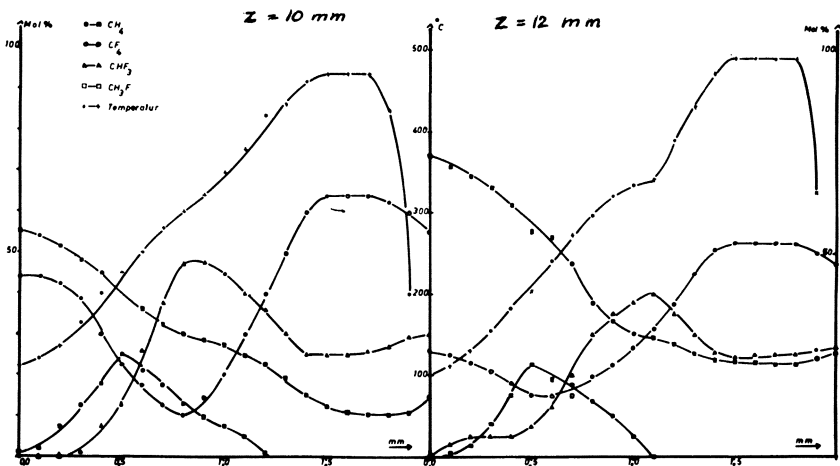


Figure 5b. Transversal temperature and concentration profiles (He, condition I)

Results

To study reaction behavior at different conditions (influence of the compositions of the jet, especially the properties and amount of the inert gas and the expansion ratio on the reaction) CH_4 and He were used in mole ratio 1:1, and the amount of F_2 was increased slowly. Initiation of the reaction could be observed at a mole ratio $\text{CH}_4:\text{F}_2$ of 1:0.5, but the reaction was not stable. At $\text{CH}_4:\text{F}_2$ of 1:1, a stable reaction with a green-blue colored flame ring at 30 mm from the nozzle was observed. By decreasing the relative amount of the ratio, He: CH_4 , to 0.3:1, the flame became yellow, and heavy soot formed. The

presence of soot on the reactor wall increases the rate of decomposition of CH_4 for mole ratios of $\text{He}:\text{CH}_4$ higher than 0.3:1. Therefore, it was necessary to clean the reactor after these runs. Application of N_2 as inert gas led to small detonations with strong soot formation. By using Ar as inert gas the location

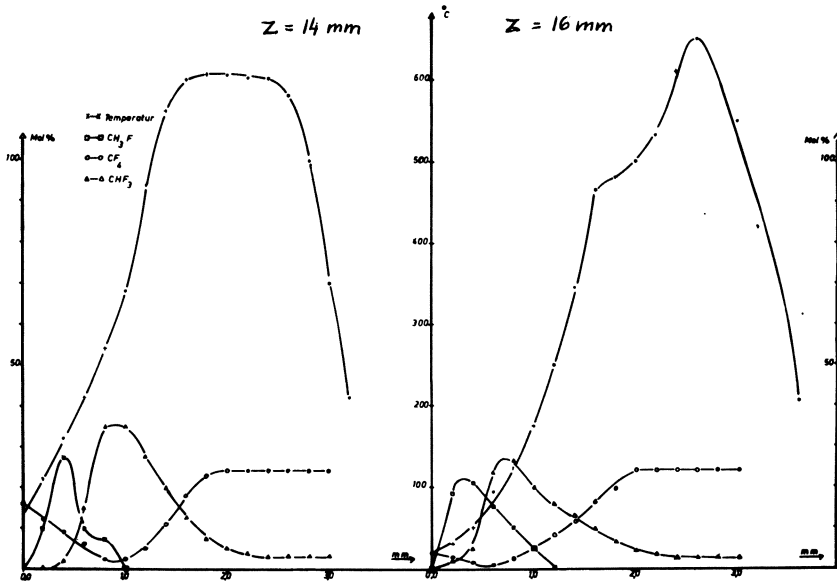


Figure 5c. Transversal temperature and concentration profiles (He, condition I)

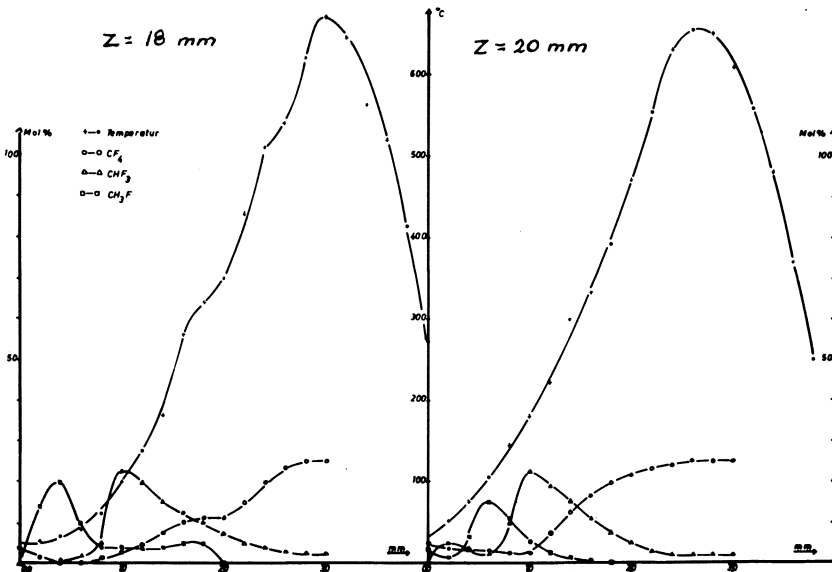


Figure 5d. Transversal temperature and concentration profiles (He, condition I)

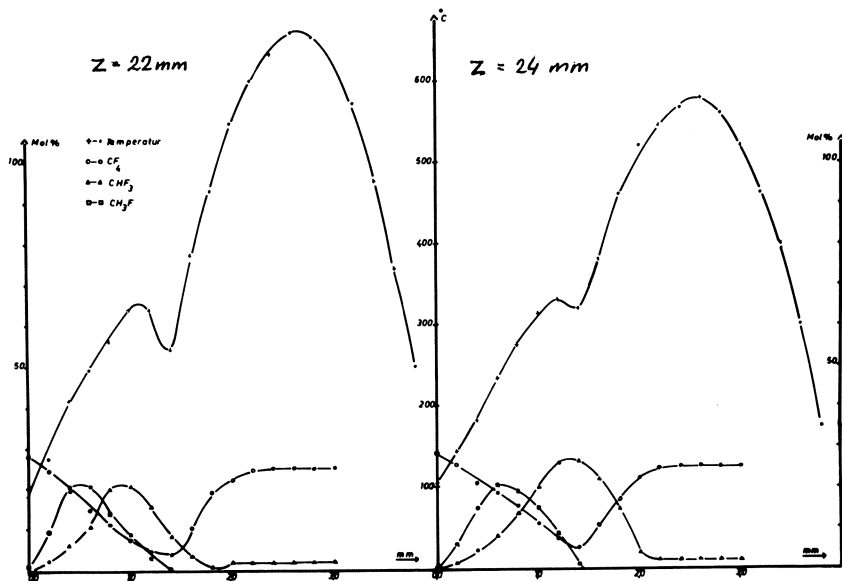


Figure 5e. Transversal temperature and concentration profiles (He, condition I)

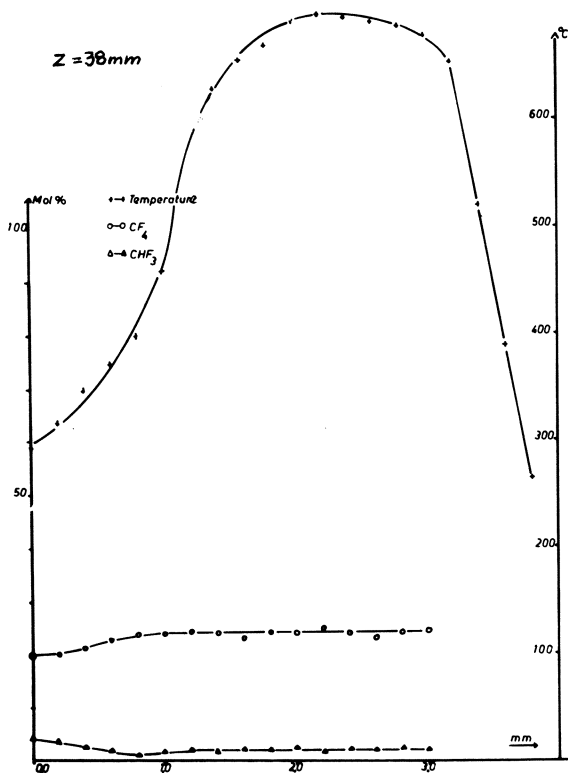


Figure 5f. Transversal temperature and concentration profiles (He, condition I)

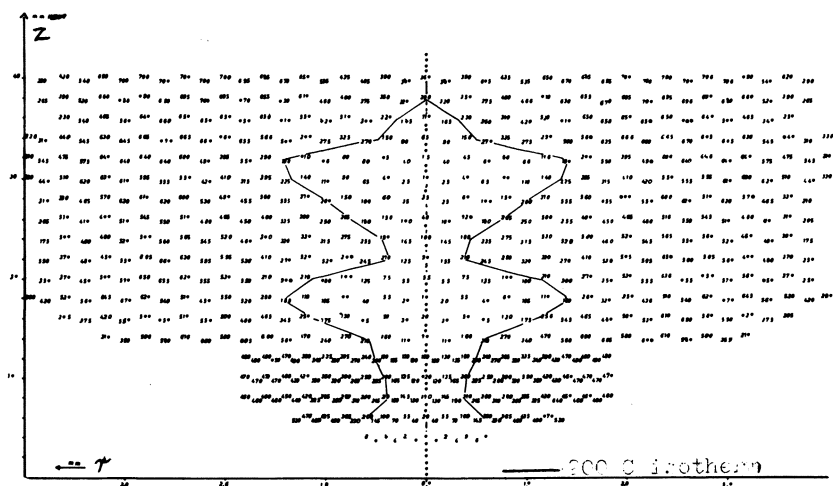


Figure 6. Temperature profiles ($^{\circ}\text{C}$) (He, condition I)

of the reaction is shifted downstream from the nozzle. The best results were achieved with He as inert gas.

Systematic investigations were carried out with two different mole ratios of He:CH₄ according to Table I. If there is no sampling tube in the supersonic jet under conditions of Table I, the location of the reaction ring is between 31 and 40 mm from the nozzle (Figure 4). If the sampling tube is shifted toward the nozzle, a new reaction ring forms, first between 19 and 23 mm, and

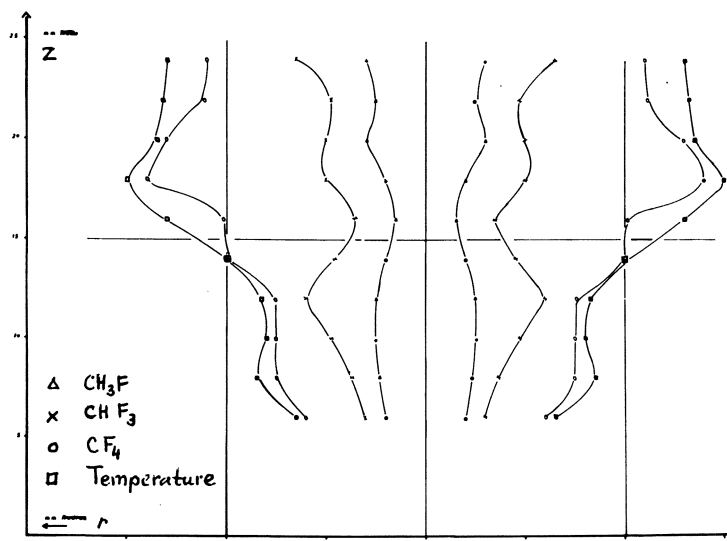


Figure 7. Longitudinal profiles of temperature and concentration maxima (He, condition I)

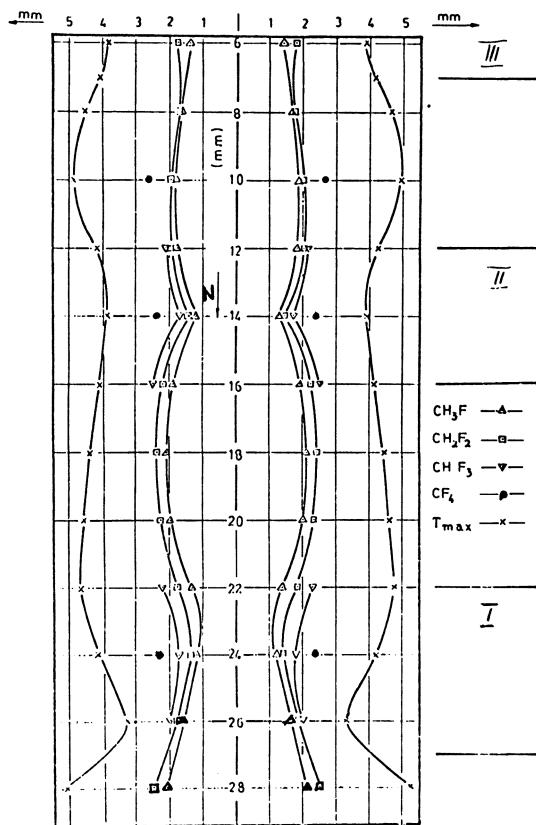


Figure 8. Longitudinal profiles of temperature and concentration maxima (He, condition II)

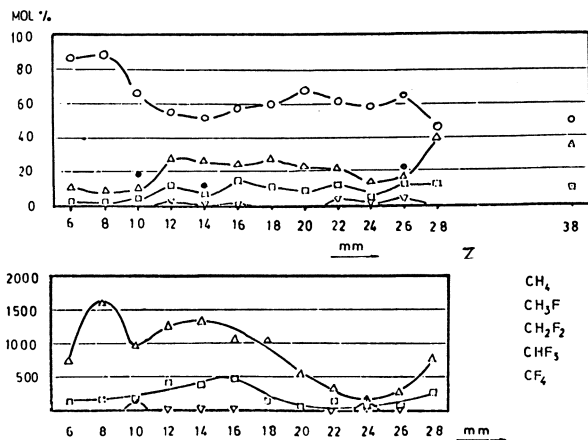


Figure 9. Top: longitudinal concentration profiles (He, condition II); bottom: number density profiles (He, condition II)

then between 6 and 10 mm from the nozzle (Figure 4). All of the temperature and concentration profiles were measured by decreasing the distance between the sampling tube and the nozzle. Typical transversal temperature and concentration profiles which were measured under condition I of Table I are plotted in Figure 5a-f. The complete temperature distribution is shown in Figure 6; the course of the transversal concentration and temperature maxima as a function of the distance from the nozzle under the same conditions is shown in Figure 7. Figure 8 shows the transversal concentration and temperature maxima as a function of the distance from the nozzle under the second condition of Table I.

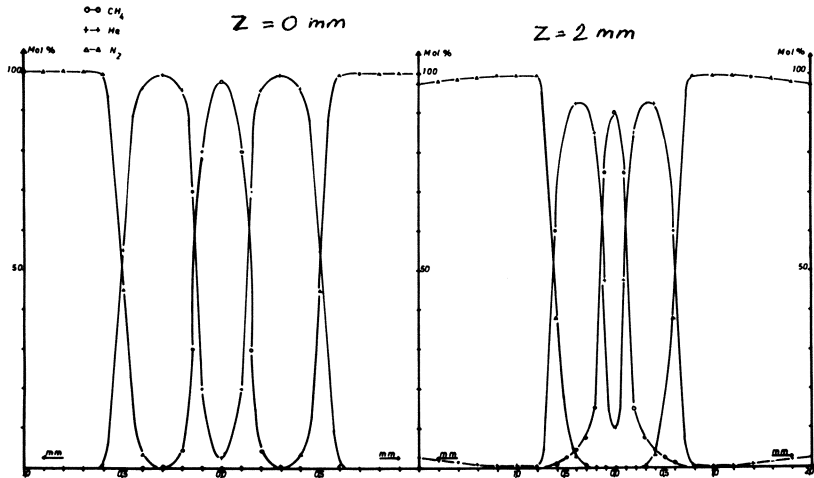


Figure 10a. Transversal concentration profiles (He, condition III)

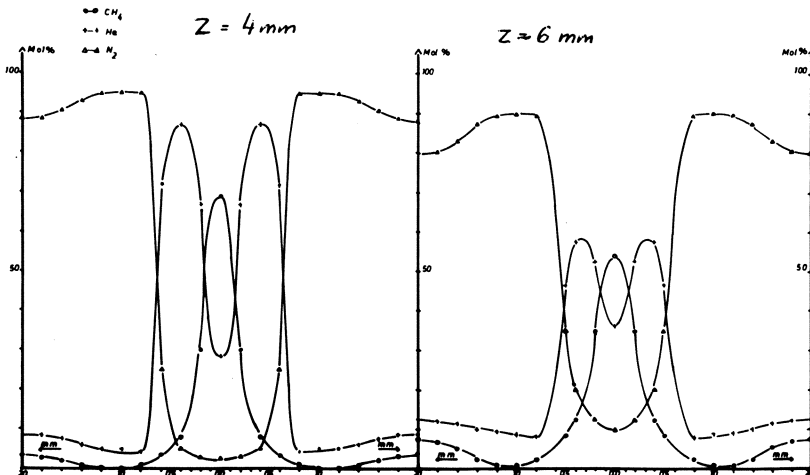


Figure 10b. Transversal concentration profiles (He, condition III)

Figure 9 shows the longitudinal product distribution (top) in mole % and the longitudinal product distribution (bottom) in number density (measured as zeroth moment of the peaks).

Since the temperature and concentration profiles in the free jet indicate that these profiles are strongly influenced by the structure of the jet, measurements were also done by model mixtures at room temperature (Table II) to study the fluid dynamic behavior of the three-component gas jet. In Figures 10a-d transversal concentration profiles of CH_4 , He, and N_2 (for F_2) are plotted for condition III of Table II. Figures 11a-d show transversal concentration profiles of CH_4 , Ar, and N_2 (for F_2) for condition IV of Table II. Figure 12

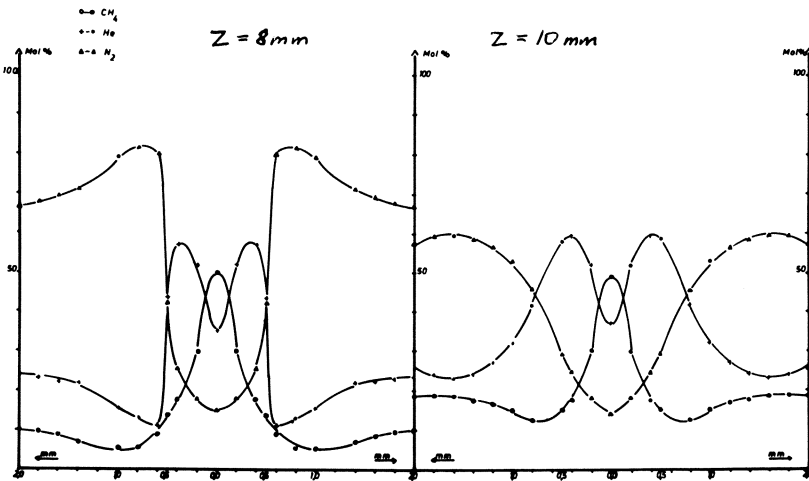


Figure 10c. Transversal concentration profiles (He, condition III)

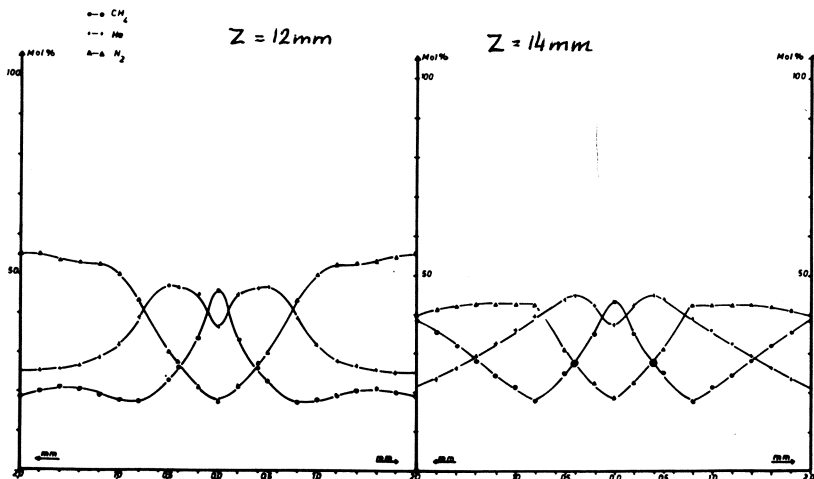


Figure 10d. Transversal concentration profiles (He, condition III)

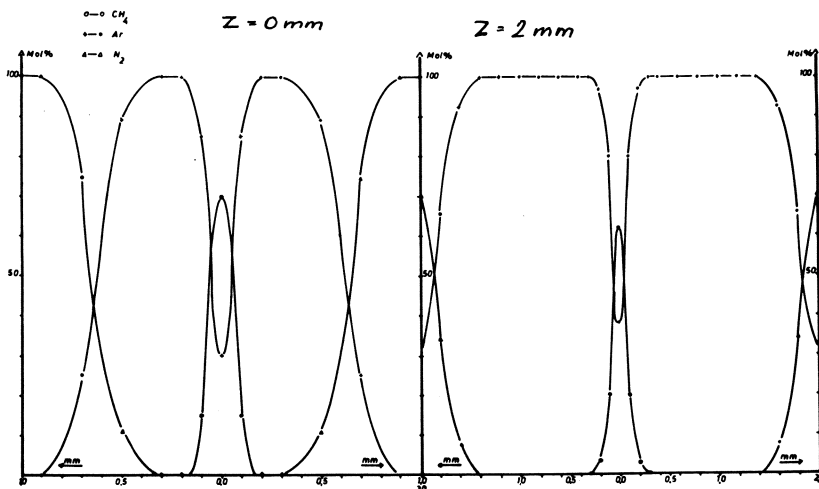


Figure 11a. Transversal concentration profiles (Ar, condition IV)

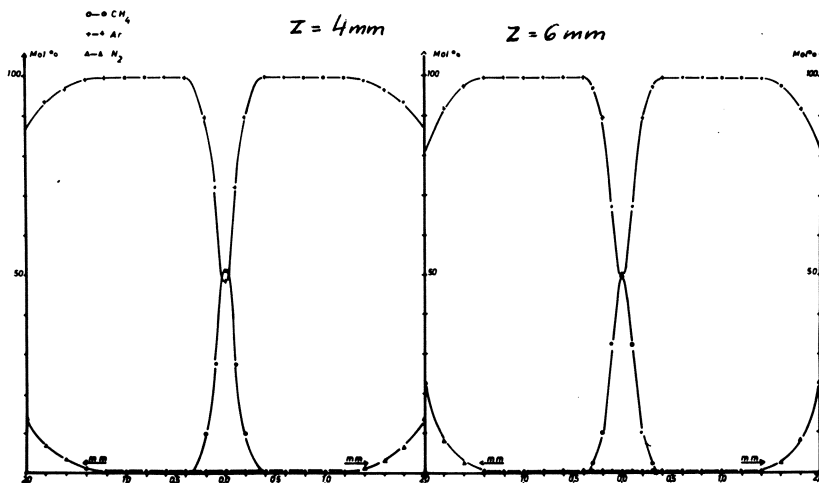


Figure 11b. Transversal concentration profiles (Ar, condition IV)

gives the course of the half-width of transversal concentration profiles of CH_4 and the maxima of the transversal concentration profiles of He and N_2 as a function of the distance from the nozzle under condition III.

Figures 13a,b and 14a,b show transversal concentrations profiles measured for model mixtures with He and Ar as inert gas in subsonic region (conditions V and VI in Table II). Reaction measurements could not be carried out in subsonic region, since the nozzle temperature became very high, the sealings were burned out, and the nozzle was destroyed within a short time.

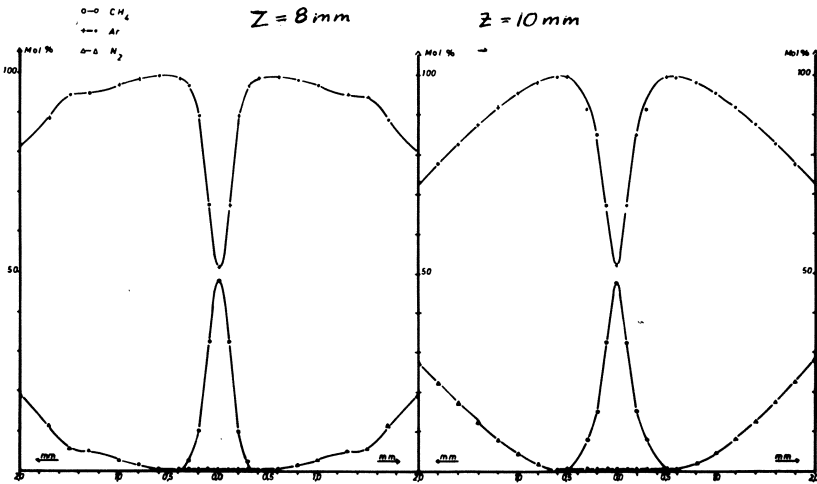


Figure 11c. Transversal concentration profiles (Ar, condition IV)

Discussion

Oscillating behavior caused by periodic ignition and extinction of the flame was observed. This behavior was especially marked (small detonations and extinctions occurred alternately) if N_2 was the inert gas. If there are no disturbances in the free jet caused by the sampling tube, a stationary disc-shaped reaction front is formed 31 mm downstream from the nozzle (Figure 4). The position of this reaction front corresponds to the constriction of the free jet caused by shock wave formation (Figure 12).

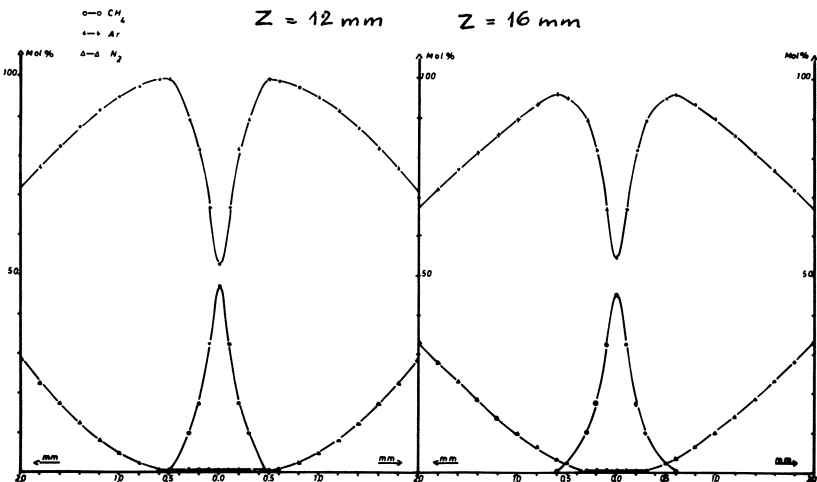


Figure 11d. Transversal concentration profiles (Ar, condition IV)

Figure 5f indicates that at this distance from the nozzle the components are nearly perfectly mixed in the jet—*i.e.*, the concentration of the components is uniform. The CH_4 is converted in this reaction front nearly completely to CF_4 (Figure 4). By reducing the distance of the sampling tube from the nozzle to less than 30 mm, the position of the reaction front suddenly changes to a distance of 20 mm from the nozzle. Figures 6, 7, and 12 indicate that at the

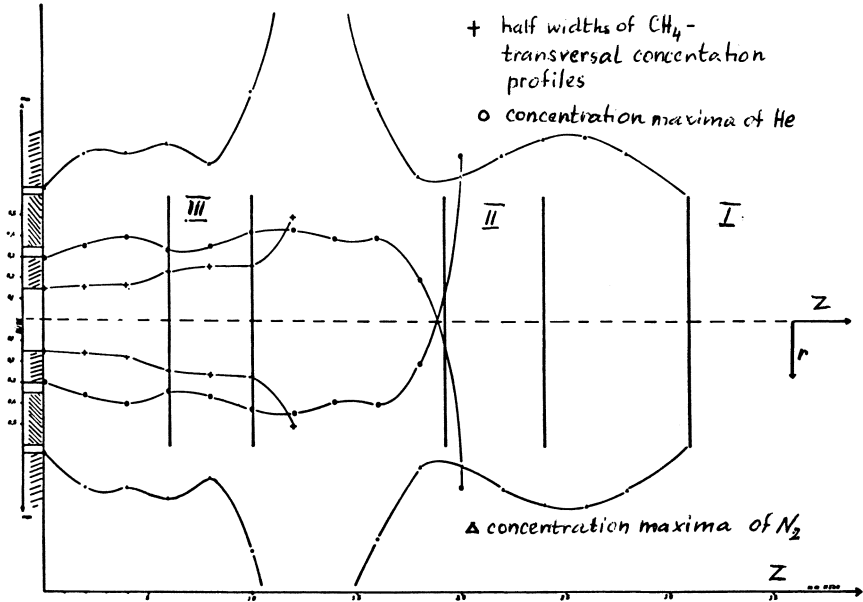


Figure 12. Longitudinal profiles of concentration half-widths and concentration maxima (He, condition III)

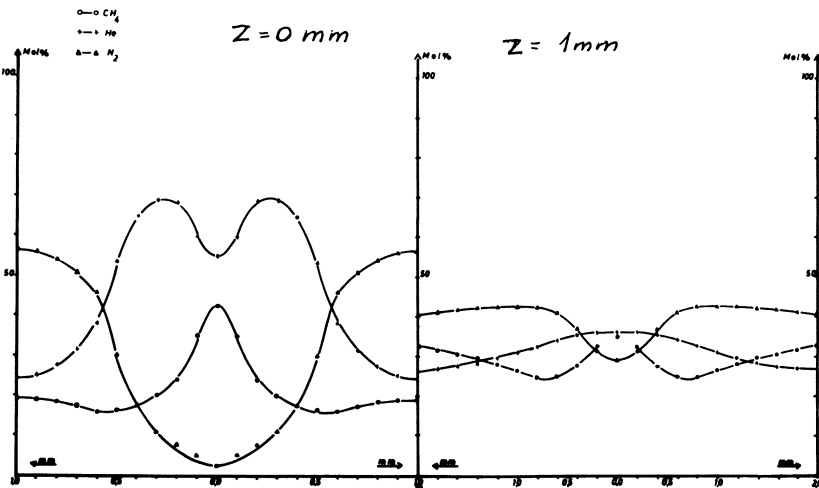


Figure 13a. Transversal concentration profiles (He, condition V)

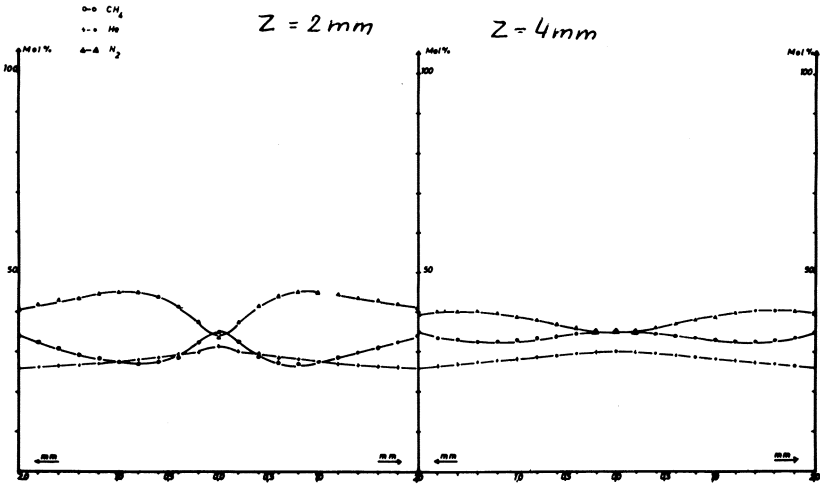


Figure 13b. Transversal concentration profiles (He, condition V)

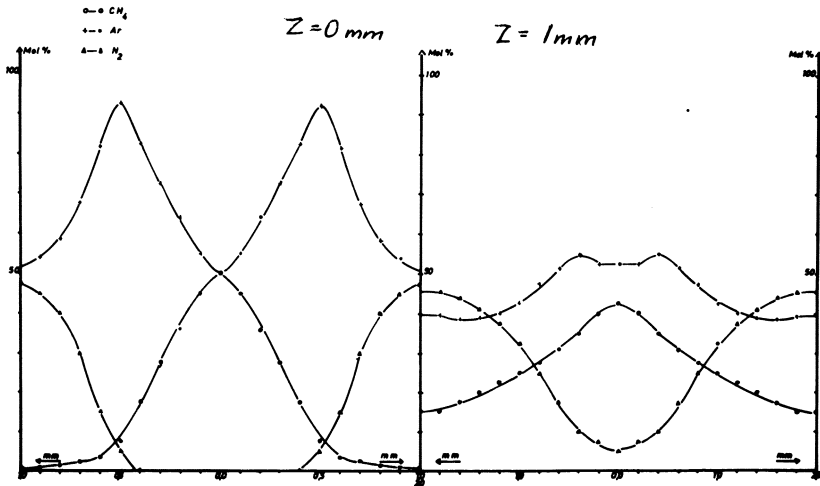


Figure 14a. Transversal concentration profiles (Ar, condition VI)

position of this reaction front (the reaction volume is ring-shaped here) the free jet is also constricted because of shock wave formation. Also in this reaction front the CH_4 is mainly converted to CF_4 and CHF_3 . By further reducing the distance of the sampling tube from the nozzle, the reaction front can be shifted to 6 mm from the nozzle. Change of position of the reaction front occurs again suddenly. The reaction volume is ring-shaped again, and its position corresponds to the constriction of the free jet caused by shock wave formation again (Figures 6, 7, and 12). From Figure 4, the abrupt increase of the

yield of CF_4 in these reaction fronts can be clearly recognized. At the point where the concentration of CF_4 begins to increase, CH_2F_2 and C_2F_6 can also be detected.

Obviously the sampling tube acts as an igniter for the chemical reaction by the shock wave formation in the free jet for reaction fronts II and III. The longitudinal temperature profiles also indicate periodic temperature variations. The positions of the temperature increase correspond to the positions of the reaction front.

Transversal temperature profiles are plotted beside the transversal product distributions in Figures 5a-f. The axisymmetric free jet consists of a low temperature core with high CH_4 concentration and three annular shells with successive concentration maxima of CH_3F , CHF_3 , and CF_4 for a mole ratio of He to CH_4 of 1:1. The temperature increases with increasing distance from the jet axis. At reaction fronts II and III the secondary temperature maximum coincides with the concentration maximum of CHF_3 . The primary temperature maximum coincides closely with the concentration maximum of CF_4 (Figures 5a-f and Figure 7).

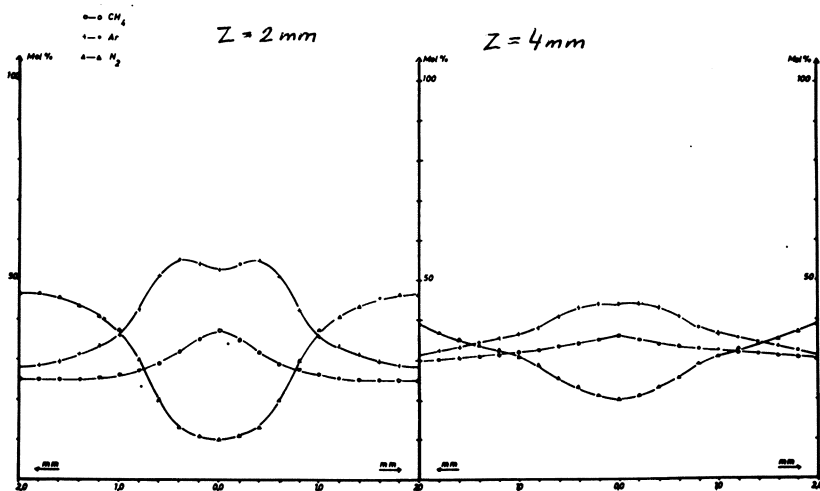


Figure 14b. Transversal concentration profiles (Ar, condition VI)

It is difficult to explain the existence of the secondary concentration maximum of CF_4 in the core of the jet at reaction fronts II and III. One can suppose that this effect is the result of the disturbance caused by the sampling tube (secondary reaction at the tube wall?). Possible back circulation of CF_4 can be discarded because the studies with the model mixtures do not indicate any back circulation (Figures 10a-d).

Reduction of the amount of the He inert gas (condition II) has a significant influence on the temperature and product distribution in the jet (Figure 8). The amount of CH_3F and CH_2F_2 products strongly increases at the expense of CHF_3 and CF_4 (e.g., Figure 15) as compared with the products under

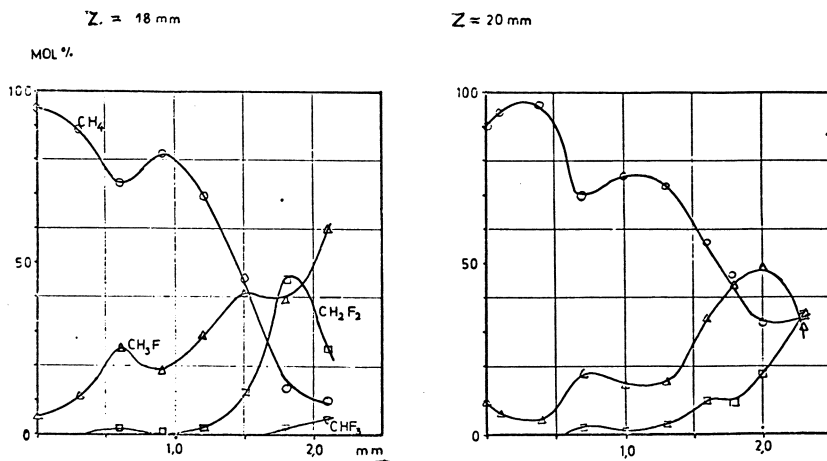
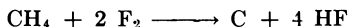


Figure 15. Transversal concentration profiles (He, condition II)

condition I. The position of the temperature maxima does not coincide with the concentration maximum of CF_4 (Figure 8) as in condition I. This shift of the temperature maximum to outer regions of the jet might be caused by the decomposition reaction:



The temperature maxima under reaction condition II are on the average 200°C higher than those under condition I. This can also be a consequence of the decomposition reaction of CH_4 .

The influence of the type of inert gas can be seen by comparing Figures 10a-d (with helium) and Figures 11a-d (with argon). With the heavier Ar as inert gas, CH_4 and F_2 mix much more slowly than with the light He gas. Thus, in the presence of Ar, the reaction front is shifted downstream in the jet.

Conditions in subsonic jets are completely different from those in supersonic jets. A comparison of Figures 10a-d (supersonic jet with helium) with Figures 13a,b, (subsonic jet with helium) and of Figures 11a-d (supersonic jet with argon) with Figures 14a,b (subsonic jet with argon) indicates that under subsonic conditions the backmixing in the reactor is extremely high in contrast to supersonic conditions. The reaction components are completely mixed at 4 mm from the nozzle. This CSTR character can be a disadvantage for consecutive reactions. The greatest disadvantage of subsonic jet systems is that reaction is not limited to a small volume but occurs in the whole volume of the reactor. Therefore the high temperature and the corrosive reaction gases destroy the reactor, especially the nozzle, within a short time.

Advantages of the Supersonic Nozzle Reactors

(1) With supersonic jets the reaction can be limited to a disc- and/or ring-shaped reaction volume which is far enough from the nozzle and the reactor wall to keep them cold and protect them from corrosion.

(2) Because of the small and well-defined reaction volume, the reaction time of the gas mixture is short and nearly uniform.

(3) The reaction products are separated in space if the reaction is induced by a solid body. With increasing distance from the jet axis, the concentration maxima of CH_3F , CH_2F_2 , CHF_3 , and CF_4 dominate. These maxima form coaxial rings in the free jet. Using a coaxial multiple skimmer a far reaching separation of the products is possible if this skimmer induces the reaction.

(4) The product distribution can be controlled easily by varying the amount of the inert gas.

(5) The disadvantage of the high price of the optimal inert gas (He) could be partly avoided by recirculating and recompressing the helium after separating the reaction components.

Nomenclature

d	nozzle diameter
Kn	$1/d$ Knudsen number
l	mean free path
M	V/V_0 Mach number
p_0	stagnation pressure in the nozzle
p_1	static pressure in the reactor
Re	Vd/ν Reynolds number
r	transversal coordinate (distance from the jet axis)
V_0	sonic velocity
V	gas velocity
z	longitudinal coordinate (distance from the nozzle)
ν	kinematic viscosity

Literature Cited

1. Tyczkowski, E. A., Bigelow, L. A., *J. Amer. Chem. Soc.* (1953) **75**, 3523.
2. Tyczkowski, E. A., Bigelow, L. A., *J. Amer. Chem. Soc.* (1955) **77**, 3007.
3. Bromme, K., Dissertation, TU Hannover (1962).
4. Cornils, B., Dissertation, TU Hannover (1964).
5. Eckermann, R., Dissertation, TU Hannover (1968).
6. Bottenberg, K., Dissertation, TU Hannover (1969).
7. Altmann, R., Dissertation, TU Hannover (1970).
8. Diesner, H. J., Diplomarbeit, TU Hannover (1970).
9. Ferri, A., Libby, P. A., Zakkai, V., "High Temperatures in Aeronautics," Turin, 1962.
10. Ferri, A., "Review of Problems in Application of Supersonic Combustion," *J. Roy. Aeronautic Soc.* (1964) **68** (645).
11. Suthrop, G., "Jahrbuch der WCCR" (1963) 366-75.
12. Diesner, H. J., Dissertation, TU Hannover (1973).

RECEIVED January 2, 1974. Work supported by Deutsche Forschungsgemeinschaft.

Ethylbenzene Dehydrogenation Kinetics in a Fixed Bed and a Continuous Stirred Gas–Solid Reactor

H. W. G. HEYNEN and H. S. VAN DER BAAN
 Department of Chemical Technology, University of Technology,
 Eindhoven, The Netherlands

For the dehydrogenation of ethylbenzene to styrene, alumina-supported uranium dioxide is a very active catalyst with a selectivity above 95% at high conversion. The kinetics of this dehydrogenation reaction can be represented by the following equation:

$$r = \frac{k(c - c_{scH}/k_{eq})}{1 + K_{FC} + K_{scS}}$$

for temperatures from 465° to 495°C. The kinetic constants in this equation have been derived from experiments in a reactor that could be operated either as a fixed bed plug flow reactor or as a continuous stirred gas–solid reactor (CSGSR). When taking into account the small deviation from ideality of the latter reactor the kinetic constants obtained could describe the results in both reactors within the experimental error.

The most important process for styrene manufacture is the dehydrogenation of ethylbenzene, usually carried out at *ca.* 600°C over metal oxide catalysts in a steam atmosphere. During dealkylation experiments of toluene (1, 2) and ethylbenzene uranium dioxide was an active and stable dehydrogenation catalyst (3), especially when used on an alumina support. Compared with data on commercial catalysts (4, 5) we found that the supported uranium dioxide catalyst showed a markedly improved selectivity even at high conversion levels. This is caused by the high activity of the catalyst which allows reaction temperatures as low as 450°C. In view of these attractive properties and because only little kinetic data on the catalytic dehydrogenation have been published (6, 7, 8), we decided to make a careful kinetic study of this reaction.

We started our study of the ethylbenzene dehydrogenation reaction over supported uranium dioxide in a plug flow fixed bed reactor. Experiments with a plug flow reactor however can be inaccurate because mass and heat transport effects may go unnoticed. Very high feed flow rates will alleviate these problems, but the resulting low conversion will introduce inaccuracies in the analysis. We therefore decided to build a continuous stirred gas–solid reactor (9)

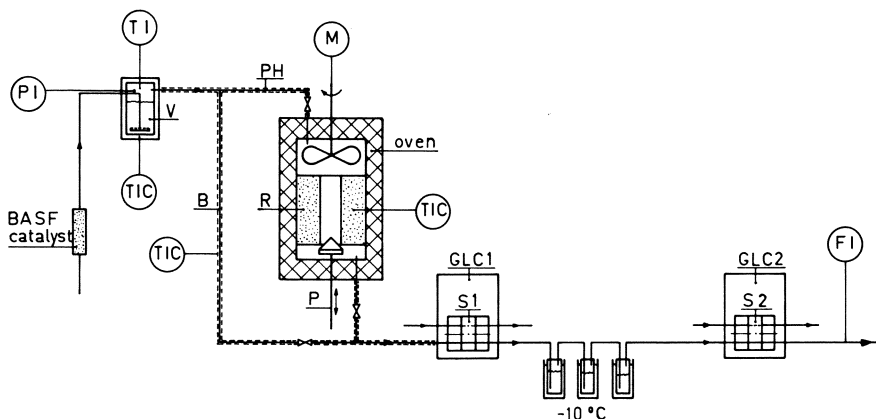


Figure 1. Apparatus

(CSGSR) where high internal flow rates could be combined with high conversion of the outside feed. We were confident that the combined information from plug flow and CSGSR experiments, as advocated by Kiperman (10), would allow us to determine the kinetic constants more accurately. Moreover, search programs for kinetic constants from CSGSR experiments are less computer time consuming than those for plug flow experiments. In our CSGSR we used forced circulation of the gas phase through a stationary bed because this allows easy measurement of the bed temperature and of the pressure drop over the bed. The latter information is especially important because from these data the flow rate through the bed can be calculated. We can thus determine how much the behavior of our CSGSR deviates from that of an ideally mixed reactor. For the forced gas circulation we used a centrifugal fan, driven by a magnetically coupled variable speed drive according to Brisk (11).

Experiments with our first CSGSR, reactor A, showed that there were discrepancies between the performance of this reactor and that of the plug flow reactor which could not be explained by the differences theoretically expected for both reactors. These discrepancies were most probably caused by differences in the history of the catalyst in the two reactors.

To ascertain that the conditions in the plug flow fixed bed and the CSGSR were fully comparable we developed a new reactor (reactor B) in which reactions under both plug flow and CSGSR conditions could be carried out on the same quantity of catalyst and that could be switched over easily from the one mode of operation to the other. Catalyst holder A could not be used for plug flow experiments because the outside gas feed causes a very low linear gas velocity in the bed. Therefore under the applied reaction conditions almost complete backmixing will occur ($D_a/uL \sim 1$).

Experimental

Preparation and Properties of the Catalyst. Uranyl acetate (20 grams $(\text{CH}_3\text{COO})_2\text{UO}_2 \cdot 2\text{H}_2\text{O}$, Merck, analytical grade) is dissolved in warm water. An excess of concentrated ammonia solution is added, and the yellow precipitate $\text{UO}_3 \cdot x\text{NH}_3 \cdot y\text{H}_2\text{O}$ is filtered off and washed with water. Aluminum nitrate, 409 grams $(\text{Al}(\text{NO}_3)_3 \cdot 9\text{H}_2\text{O}$, Merck analytical grade) is dissolved in water and poured into 300-ml concentrated ammonia solution. The precipitate is fil-

tered off and washed with water. The two precipitates are transferred to a flask, mixed with 1 liter of water and kept at 95°–100°C under vigorous stirring. After 20 hrs of stirring the solid is filtered off, washed with water and dried for 24 hrs at 135°C. Finally the product is calcined at 600°C in air for 24 hours, and the resulting catalyst is broken and sieved. The specific BET surface area, using nitrogen adsorption, was 144 m²/gram, and the average pore diameter was 46Å. Freshly prepared catalyst is reduced to UO_{2.0}/Al₂O₃, the active dehydrogenation catalyst, by ethylbenzene under reaction conditions.

Apparatus. Figure 1 shows a diagram of the apparatus. A constant flow of carrier gas (nitrogen or carbon dioxide) passes through a heated vaporizer V, filled with ethylbenzene or a mixture of ethylbenzene and styrene. The gases are carefully freed from oxygen by BASF R3-11 catalyst. The carrier gas-hydrocarbon mixture passes either *via* preheater PH through reactor R to sample valve S₁ (12) or flows directly *via* bypass B to that sampling valve. The reactor feed or the reaction products are introduced in an analysis system consisting of two gas chromatographs, GLC₁ and GLC₂ separated by cold traps. On GLC₁ benzene, toluene, ethylbenzene, and styrene can be determined; on GLC₂, hydrogen is measured. Figure 2 shows the stainless steel

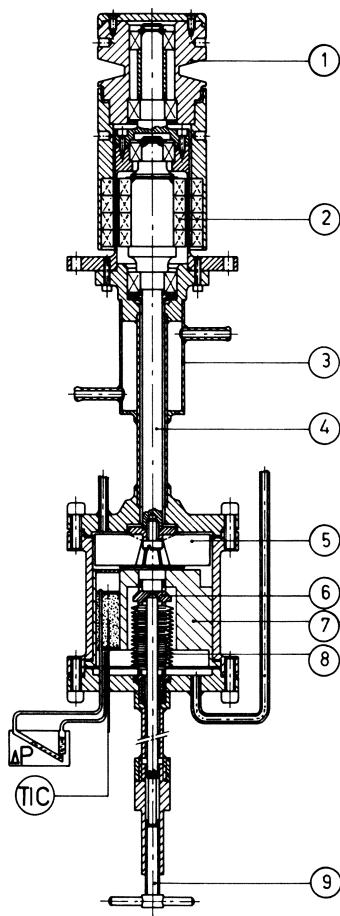


Figure 2. Continuous stirred gas solid reactor. 1. pulley, 2. magnet, 3. air cooler, 4. drive shaft, 5. fan, 6. plug, 7. catalyst holder, 8. bellows, 9. spindle.

CSGSR including the stirrer drive unit. In reactor A, which was used in the preliminary experiments, the annular catalyst holder A (Figure 3, left) was used while the final kinetic measurements were carried out in reactor B with catalyst holder B (Figure 3, right).

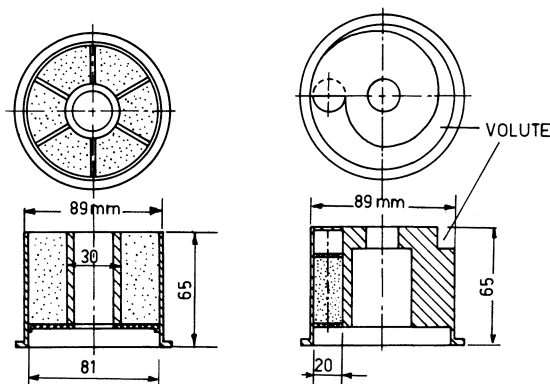


Figure 3. Catalyst holder A (left); catalyst holder B (right)

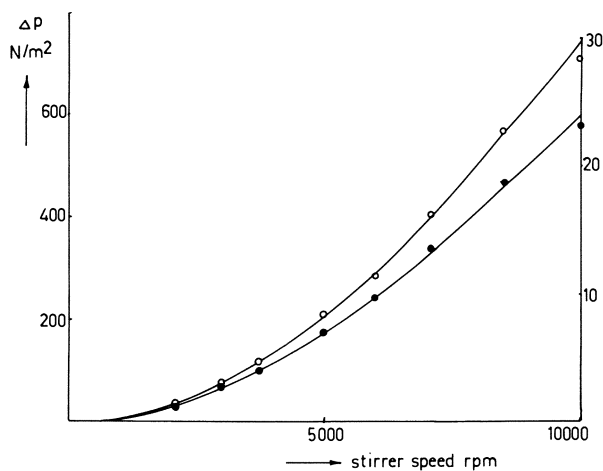


Figure 4. Internal recirculation number and pressure drop over the catalyst bed vs. stirrer speed at 500°C. Catalyst holder B filled with 8.0 grams catalyst (0.6–1 mm); cross sectional area catalyst holder, 3.1 cm²; carrier gas, carbon dioxide, 4.8 liters/hr NTP.

Results and Discussion

Reactor Characteristics. The degree of mixing in stirred gas solid reactors is usually assessed by tracer techniques. From step response measurements we concluded that reactor A can be operated as a perfect mixer under our experimental conditions. However, mixing in the catalyst bed of reactor B could not be judged accurately by the step response method because in this case the volume of the catalyst bed (8.5 cm³) is much smaller than the total free volume of the reactor (300 cm³).

Another way to check the mixing behavior is to measure the pressure drop over the catalyst bed and to calculate the gas flow through the bed by the Ergun relation. With this relation first the actual porosity of the catalyst bed was calculated from measurements of the pressure drop as a function of the feed rate through the fixed bed (central plug closed). The number of internal recirculations n is defined as:

$$n = \frac{\text{gas flow through the bed}}{\text{reactor gas feed}} - 1 \quad (1)$$

In Figure 4, for reactor B, n and the pressure drop over the catalyst bed (= discharge pressure of the fan) are given as a function of the stirrer speed.

The kinetic experiments were carried out in reactor B, which behaved as a good plug flow reactor at the reactor feed rates used during fixed bed experiments ($D_a/uL = 0.03-0.008$). By using a heavier gas (carbon dioxide instead

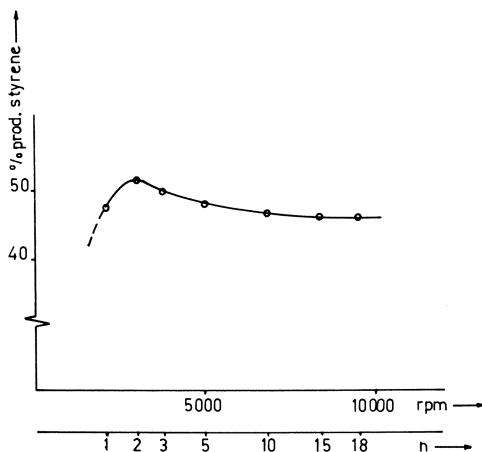


Figure 5. Styrene productivity vs. stirrer speed. Reaction conditions: reactor B filled with 8.0 grams catalyst; reaction temperature 480°C; carrier gas, 5.0 liters/hr NTP carbon dioxide; ethylbenzene feed gas concentration, $c_0 = 0.159$ mmole/liter.

of nitrogen), enough recirculations were provided at high feed rates to approach an ideally mixed reactor. Conversion experiments with varying stirrer speed confirmed this. Figure 5 shows that styrene production as a function of the stirrer speed passes through a maximum and tends to remain constant above 6000 rpm for a reactor gas feed of 5 liter/hr NTP. For the highest feed rate, 8000 rpm is required to approach this condition. At very low n the styrene production is low because bypassing through the central hole occurs while at intermediate n the reactor behaves as a plug flow reactor with a low number of recirculations.

Reaction Kinetics. Calculations according to Hougen (13) and Satterfield and Sherwood (14) have established that under the experimental conditions no limitations are to be expected by bulk gas phase or pore diffusion. This was also proved by the results of experiments which showed that a fourfold increase of the average catalyst diameter did not affect the conversion (see

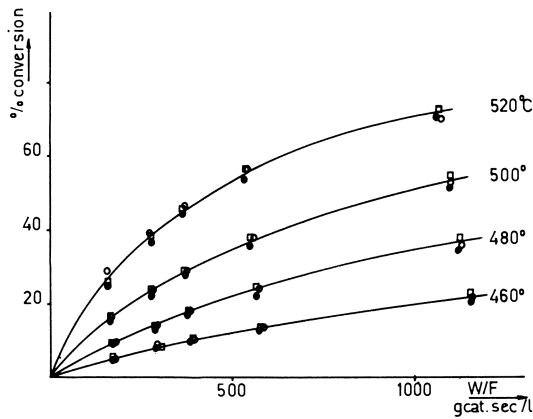


Figure 6. Ethylbenzene conversion vs. W/F at various catalyst diameters d_p :

- $0.6 < d_p < 1.0$ mm
- $0.3 < d_p < 0.42$ mm
- $0.15 < d_p < 0.30$ mm

Reaction conditions: fixed bed reactor filled with 2.0 grams catalyst; carrier gas, nitrogen; ethylbenzene vapor pressure in feed gas, 7.3 mm Hg.

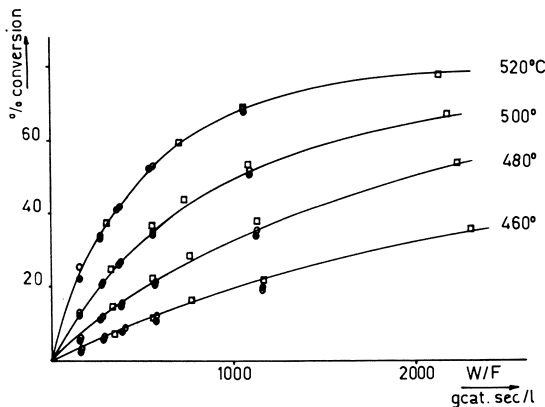


Figure 7. Ethylbenzene conversion vs. W/F for various amounts of catalyst:

- 4.0 grams catalyst
- 2.0 grams catalyst
- 2.0 grams catalyst diluted with silicon carbide

Reaction conditions: fixed bed reactor; carrier gas, nitrogen; ethylbenzene pressure in feed gas, 7.3 mm Hg.

Figure 6). Figure 7 shows that the conversion of ethylbenzene only depends on the time of contact with the catalyst—*i.e.*, equal W/F values give the same conversions when the amount of catalyst is varied. From these data follows that at constant W/F a variation of the amount of catalyst or dilution of the catalyst

with silicon carbide has no effect on the conversion. Moreover, the conversion of ethylbenzene in the empty reactor and in the reactor filled with silicon carbide (which was in some experiments used to dilute the catalyst) was shown to be negligible under our experimental conditions. A 160-hr experiment under conditions similar to the conditions of the kinetic experiments showed that no decrease in catalyst activity occurs. Therefore, either the chemical reaction at the catalyst surface or adsorption of ethylbenzene or desorption of products is rate controlling. We visualize that in the reaction step an adsorbed ethylbenzene molecule loses hydrogen, leaving an adsorbed styrene molecule on the surface, which will desorb subsequently. As far as the hydrogen is concerned two pathways are open:

(a) The hydrogen is liberated as such to the gas phase

(b) The hydrogen is first adsorbed at an adjacent site and subsequently released to the gas phase.

If the chemical reaction is rate determining, the two pathways lead to the following rate equations:

$$-\frac{dc}{dW/F} = \frac{k(c - c_{SC_H}/k_{eq})}{1 + \sum_i K_i c_i} \quad (2)$$

$$-\frac{dc}{dW/F} = \frac{k(c - c_{SC_H}/k_{eq})}{(1 + \sum_i K_i c_i)^2} \quad (3)$$

Rate expressions similar to Equation 2 were also proposed by Balandin (15) and Carrà (16).

Because of the high reaction temperatures the adsorption constants of hydrogen and carrier gas should be considerably lower than the corresponding constants for hydrocarbons and are therefore omitted in the rate equations. At an early stage of this study we found from differential measurements that of the two, only Equation 2 could describe the data.

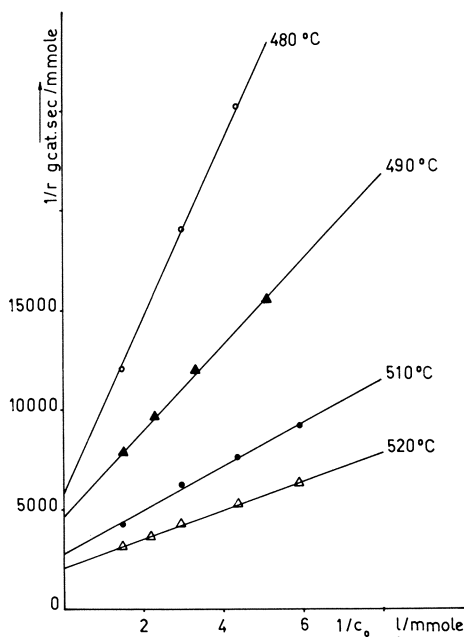


Figure 8. Differential measurements. $1/r$ vs. $1/c_0$. Reaction conditions: fixed bed reactor filled with 0.2 gram catalyst (0.15–0.3 mm); carrier gas, nitrogen.

When for differential experiments $1/r$ is plotted *vs.* $1/c_o$, straight lines are obtained if Equation 2 is valid; if Equation 3 is valid, a linear relation exists between $(c_o/r)^{1/2}$ and c_o . We carried out differential experiments in a plug flow reactor with a small amount of catalyst. The results, plotted in Figure 8, show that Equation 2 can describe the data. These experiments, however, were done with catalyst from a batch that has not been used in further studies. Therefore the kinetic constants that can be obtained from Figure 8 have not been taken into account in this study although they are comparable with those obtained later on.

Since no appreciable amounts of byproducts were found (selectivities for styrene varied from 95–99%), Equation 2 can be changed into:

$$+ \frac{dc_s}{dW/F} = \frac{k(c_o - c_s - c_s c_H/k_{eq})}{1 + K_E(c_o - c_s) + K_{scs}} \quad (2a)$$

The equilibrium constant k_{eq} was calculated from data given by Boundy (17).

For experiments with nitrogen as a carrier gas the amounts of styrene and hydrogen detected in the ethylbenzene dehydrogenation products are equal. However, as explained before, carbon dioxide was used as carrier gas in the latter experiments, and thus the amounts of styrene and hydrogen are no longer equal since hydrogen reacts with carbon dioxide. This means that to integrate Equation 2a an additional expression for c_H is required. We found that for both the fixed bed and the recirculation reactor at each reaction temperature the c_H/c_o ratio could be described by an empirical relation of the form:

Table I. Reaction Conditions for Kinetic Experiments in Fixed Bed and in CSGSR^a

Reaction Temperature, °C	Vapor Pressure in Feed Gas, mm Hg		Feed Gas Flow, liters/hr NTP
	Ethylbenzene	Styrene	
	3.0	0	5
465	7.5	0	7.5
480	8.55	6.1	10
495	14.0	0	20
	30.3	0	

^a Feed gas: carbon dioxide, purity 99.995%; catalyst: 8.00 grams, 20 wt % UO_2 on Al_2O_3 0.6–1 mm; stirrer speeds during CSGSR experiments: from 8.000 rpm at feed gas flow 5 liters/hr NTP until 10.000 rpm at feed 20 liters/hr NTP.

Table II. Results of a

Temp., °C	Feed Gas, liters/hr NTP	W/F	c_o , mmoles/liter
		$\frac{\text{grams cat sec}}{\text{liters}}$	
<i>Fixed Bed</i>			
480	20.0	560	.297
480	10.1	1102	.297
480	7.9	1410	.297
480	4.6	2424	.297
<i>CSGSR</i>			
480	20.0	565	.297
480	10.1	1114	.297
480	7.9	1413	.297
480	4.6	2418	.297

^a Vapor pressure of ethylbenzene: 14.04 mm Hg; of styrene: 0 mm Hg.

$$c_H/c_o = AW/F + B(W/F)^2$$

with a standard deviation below 0.01. We did not go into this matter further since the empirical equation was sufficiently accurate for our purpose—*i.e.*, the study of the kinetics of the dehydrogenation reaction.

For the fixed bed the concentration c_S at the outlet was calculated numerically by the Runge-Kutta method as a function of W/F , c_o , k , K_E , and K_S and the appropriate values for A and B by Equation 2b:

$$\frac{dc_S}{dW/F} = \frac{k\{c_o - c_S - c_S c_o (AW/F + B(W/F)^2)/k_{eq}\}}{1 + K_E(c_o - c_S) + K_S c_S} \quad (2b)$$

Values of k , K_E , and K_S for different reaction temperatures were determined by a numerical search procedure, minimizing the function:

$$f(k, K_E, K_S) = \sum_j \left\{ \frac{c_{S_{m,j}} - c_{S,j}}{c_o} \right\}^2 \quad (4)$$

For the CSGSR a mass balance yields:

$$\begin{aligned} rW &= Fc_S \\ \frac{W}{F} &= \frac{c_S[1 + K_E(c_o - c_S) + K_S c_S]}{k(c_o - c_S - c_S c_H/k_{eq})} \\ &= \frac{c_S[1 + K_E(c_o - c_S) + K_S c_S]}{k[c_o - c_S - c_S c_o (AW/F + B(W/F)^2)/k_{eq}]} \end{aligned} \quad (5)$$

From Equation 5 the concentration c_S could be solved as a function of W/F , c_o , k , K_E , and K_S , and the values of k , K_E , and K_S could be obtained again as described above. This approach is based on the assumption that both reactors are ideal. It is shown below that at least for the CSGSR this assumption is not completely valid. Therefore we have calculated the rate and adsorption constants with the data from the fixed bed experiments.

The experiments in both reactors were done at five different initial concentrations of ethylbenzene, each at three temperature levels and four flow rates as shown in Table I. Results of a characteristic experiment are detailed in Table II. The kinetic constants were computed from the data thus obtained. The experimental conversion data and those calculated with the computed

Characteristic Experiment^a

Productivities, %				Selectivity for Styrene, %
Benzene	Toluene	Styrene	H ₂	
0	0.5	18.3	6.8	97.4
0.1	0.6	29.1	11.8	98.0
0.2	0.8	35.7	13.4	97.4
0.6	0.9	51.9	17.6	97.2
0	0.6	15.5	6.0	96.6
0.3	0.7	26.7	10.3	96.5
0.3	0.8	30.9	11.5	96.5
0.6	1.1	42.5	16.0	96.6

Table III. Calculated Constants from Fixed Bed Experiments

Temperature, °C	$k, \times 10^{-4}$ liters/(grams cat sec)	$K_E,$ liters/mmole	$K_S,$ liters/mmole	k_{eq}^a mmoles/liter
465	3.88	1.8	2.7	.162
480	5.29	1.7	2.4	.237
495	6.99	1.9	2.1	.343

^a k_{eq} from data given by Boundy (17).

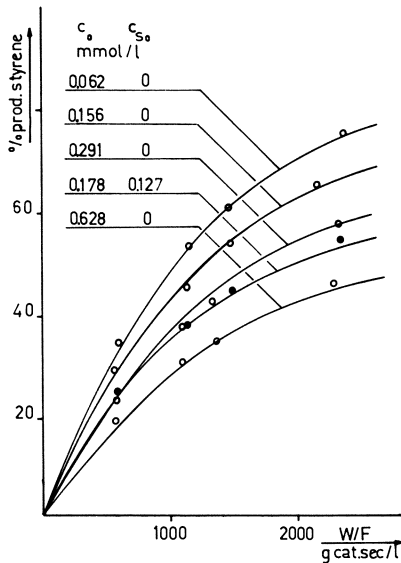


Figure 9. Fixed bed experiments at 495°C. Styrene productivity vs. W/F. Continuous lines calculated with constants from Table III.

constants were in good agreement. It appeared, however, that the styrene adsorption constant K_S could vary by a factor of 2 to 5, without influencing the sum of squares of Equation 4 very much.

To narrow the value for K_S we did experiments with a feed containing 8.55 mm ethylbenzene and 6.1 mm styrene at the same temperature levels and flow rates as chosen for the other experiments in the plug flow reactor. This resulted in the values for k , K_E , and K_S given in Table III. With these values both the fixed bed experiments with and without styrene in the feed gas and the CSGSR data could be described well, as is illustrated in Figures 9 and 10 for the experiments at 495°C. Figure 10 shows that the measured styrene productivities for the CSGSR are a little higher than those predicted from the fixed bed experiments. One reason for these deviations is that the selectivity for styrene in the CSGSR is about 1% lower than for the plug flow reactor (*see* Table II). Another reason is that at least the CSGSR is not ideal. This tends to bring the conversion curves for the plug flow reactor and the CSGSR closer. For the CSGSR the deviation from ideality can be calculated, visualizing the reactor as a recirculated plug flow reactor and obtaining the number of recirculations from the pressure drop over the bed and the feed flow rate. The data of this calculation are shown in Table IV, and the corrected conversion levels are represented in Figure 10 by dotted lines. From Figure 10 it follows that the

Table IV. Comparison of Styrene Productivities in an Ideal Plug Flow Reactor, an Ideal Mixer, and a Recirculated Plug Flow Reactor at 495°C^a

c_0 , mmoles/liter	n	W/F grams cat sec/liter	Styrene productivities, %		
			Ideal Mixer	Ideal Plug Flow	Plug Flow with n Recirculations
.062	5	600	27.1	31.1	27.7
.062	9	1200	42.3	52.2	43.2
.062	11	1800	52.0	66.5	53.2
.062	17	2400	58.8	76.1	59.8
.156	5	600	24.1	27.4	24.6
.156	9	1200	38.2	46.7	39.0
.156	11	1800	47.4	60.1	48.4
.156	17	2400	53.9	69.5	54.8
.291	5	600	20.8	23.3	21.2
.291	9	1200	33.5	40.4	34.2
.291	11	1800	42.0	52.8	42.9
.291	17	2400	48.2	61.8	49.0
.628	5	600	15.5	17.0	15.8
.628	9	1200	25.8	30.5	26.3
.628	11	1800	32.8	40.5	33.4
.628	17	2400	38.2	48.3	38.8

^a $r = \frac{6.99 \times 10^{-4}(c_0 - c_s - c_{SCH}/0.343)}{1 + 1.9(c_0 - c_s) + 2.1 c_s}$; for fixed bed: $c_H = 0.01c_0(1.58 \times 10^{-2}W/F - 3.63 \times 10^{-6}W/F^2)$; for mixer: $c_H = 0.01c_0(1.33 \times 10^{-2}W/F - 2.88 \times 10^{-6}W/F^2)$.

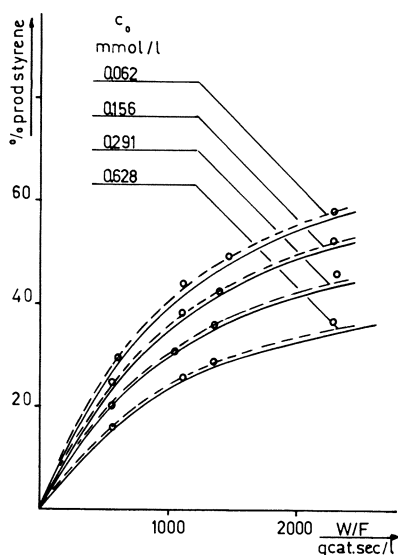


Figure 10. CSGSR experiments at 495°C. Styrene productivity vs. W/F. Continuous lines calculated with constants from Table III. Dotted lines from results of Table IV.

results in the CSGSR can be described within experimental error by using constants derived from the fixed bed experiments when the non-ideality of the CSGSR is taken into account.

Although Figure 5 implies that at 8000 rpm the reactor approaches ideality, calculations show that at 8000 rpm and higher there is still a noticeable deviation from ideal behavior. This means that tests to prove ideal behavior from conversion data as function of the stirrer speed require high accuracy.

For the rate constant k an activation energy of 22 kcal/mole is calculated. The tentative results of a statistical analysis (18) show that the confidence intervals of K_E and K_S are such that the temperature dependence of these parameters could not be determined from the data.

A final remark should be made on the validity of Equation 2b. We have assumed in our calculation that the ethylbenzene concentration is equal to $c_o - c_S$. For our experiments the selectivity was 97% with a standard deviation of 1%. Therefore the actual concentration of ethylbenzene should be $(c_o - 1.03c_S)$. This means that the k values of Table III should be increased by 1–2%.

Acknowledgments

We thank C. G. M. M. Camp, W. N. Heeren, and A. M. Jonker for carrying out most experimental work. R. Kool gave valuable advice during the computational work, and R. J. M. van der Wey designed the CSGSR.

Nomenclature

c	concentration of ethylbenzene under reaction conditions, mmole/liter
c_S, c_H	concentrations of styrene and hydrogen, mmoles/liter
c_o, c_{S_o}	concentrations of ethylbenzene and styrene under average reaction conditions before entering the catalyst bed, mmoles/liter
$c_{S_{im}}$	measured styrene concentration, mmoles/liter
c_i	concentration of component i in the reactor, mmoles/liter
D_a	axial dispersion coefficient, m^2/sec
F	total gas feed to the reactor under reaction conditions, liters/sec
k	reaction rate constant, liters/(gram cat sec)
k_{e_i}	equilibrium constant of the dehydrogenation reaction, mmoles/liter
K_i	adsorption constant of component i , liters/mmole
K_E, K_S	adsorption constant of ethylbenzene and styrene, liters/mmole
j	index number of experimental data at one reaction temperature
L	lengths of the catalyst bed, m
r	reaction rate, mmoles/(gram cat sec)
u	linear gas velocity in the catalyst bed under reaction conditions, m/sec
W	catalyst weight, grams

Literature Cited

- De Jong, J. G., Batist, Ph. A., *Rec. Trav. Chim. Pays-Bas* (1971) **90**, 749.
- Steenhof de Jong, J. G., Guffens, C. H. E., van der Baan, H. S., *J. Catalysis* (1972) **26**, 401.
- Heynen, H. W. G., van der Baan, H. S., *J. Catalysis*, in press.
- Miller, S. A., Donaldson, J. W., *Chem. Process Eng.* (Dec. 1972) **48**, 37.
- Ohlinger, H., Stadelmann, S., *Chem.-Ing.-Tech.* (1965) **37**, 361.
- Balandin, A. A., Tolstopyatova, A. A., *Zh. Obsch. Khim.* (1947) **17**, 2182.
- Carrà, S., Forni, L., *Ind. Eng. Chem., Process Design Develop.* (1965) **4**, 281.
- Wenner, R. R., Dybal, E. C., *Chem. Eng. Progr.* (1948) **44**, 275.
- Choudhary, V. R., Doraiswamy, L. K., *Ind. Eng. Chem., Process Design Develop.* (1972) **11**, 420.
- Kiperman, S. L., *Kinet. Katal.* (1972) **13**, 562.
- Brisk, M. L., Day, R. L., Jones, M., Warren, J. B., *Trans. Instn. Chem. Engrs.* (1968) **46**, T3.
- German, A. L., Heynen, H. W. G., *J. Sci. Instrum.* (1972) **5**, 413.
- Hougen, O. A., *Ind. Eng. Chem.* (1961) **53**, 509.
- Satterfield, C. N., Sherwood, T. H., "The Role of Diffusion in Catalysis," Addison-Wesley, Reading, Mass., 1963.

15. Balandin, A. A., *Advan. Catalysis* (1958) **10**, 96.
16. Carrà, S., *Chim. Ind. (Milan)* (1963) **8**, 949.
17. Boundy, R. H., Boyer, R. F., "Styrene: Its Polymers, Copolymers, and Derivatives," Reinhold, New York, 1952.
18. Heynen, H. W. G., Thesis, Eindhoven, 1974.

RECEIVED January 2, 1974.

Reaction Kinetics of the Disproportionation of Propylene over a Tungsten Oxide-Silica Catalyst

UMESH R. HATTIKUDUR and GEORGE THODOS

Northwestern University, Department of Chemical Engineering,
Evanston, Ill. 60201

The propylene disproportionation reaction was studied to establish the kinetic mechanism. Initial rate data obtained over a differential bed indicate that a dual-site mechanism is followed involving the reaction of two adjacently adsorbed propylene molecules. The actual rate-controlling step involves a Langmuir-Hinshelwood type mechanism. Reaction rate data were extended to high pressures and a range of temperatures. These relationships predict space time, W/F , for the integral bed data with an average deviation of 8.8% for 56 data points.

The catalytic disproportionation of olefins was first reported by Banks and Bailey (1) of the Phillips Petroleum Co. in 1964. In the case of propylene, the reaction may be expressed as:



This reaction has since been used industrially in the Phillips triolefin process to manufacture polymerization grade ethylene and high purity butenes. Another application of propylene disproportionation has been to increase octane rating during alkylation. Disproportionation to ethylene and butenes before alkylation is reported to improve octane ratings from 102.7 RON to 110.1. Research is opposed to direct alkylation of propylene (2).

The disproportionation of propylene was first encountered by Schneider and Frolich (3) in 1931 during the non-catalytic pyrolysis of propylene at 1386°F and 0.2 atm when 48% of the reacting propylene disproportionated. Following the work of Banks and Bailey (1), a number of investigators reported the effective use of alternative catalysts, particularly in the liquid phase using homogeneous catalysts. Such catalysts include tungsten hexachloride and *n*-butyllithium reported by Wang and Menapace (4), a combination of tungsten hexachloride, ethanol, and ethylaluminum dichloride reported by Calderon and coworkers (5), and an alkylaluminum halide-treated nitrosyl complex reported by Zuech (6).

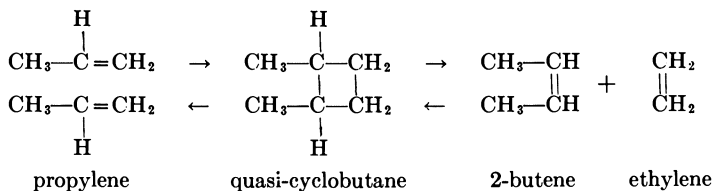
Heckelsberg *et al.* (7, 8) did an extensive study on catalysts for the disproportionation reaction. Active catalysts reported include hexacarbonyls, ox-

ides, and sulfides of molybdenum and tungsten, and oxides of rhenium, niobium, tantalum, and tellurium, supported on oxides of silicon, aluminum, thorium, and zirconium, or phosphates of aluminum, zirconium, titanium, magnesium, and calcium. The highest activity is reported to be with tungsten and molybdenum oxides on silica, alumina, or aluminum phosphate. Bailey (2) reviewed the various catalyst schemes and has included a table of catalysts and promoters found to be effective in the disproportionation reaction. Recently, Kobylinski and Swift (9) reported improved selective disproportionation with the use of thallium-treated molybdena-alumina catalysts.

Heckelsberg *et al.* (7) reported that tungsten oxide on silica was an excellent disproportionating catalyst with desirable properties. A major advantage in commercial application is the high temperature range of operation, thereby increasing resistance to poisons and reducing the time-consuming heating and cooling cycles during regeneration. Furthermore, selectivity is high, and carbon formation is limited. Water, air, acetone, carbon monoxide, hydrogen, and methanol are temporary poisons and decrease activity. However, when pure feed is introduced, the original activity is re-established.

Mechanism and Kinetics of Reaction

In 1967, Bradshaw *et al.* (10) proposed that the reaction proceeds through a "quasi-cyclobutane" intermediate as follows:



Later studies by Calderon *et al.* (5), Zuech (6), Mol *et al.* (11), Crain (12), Adams and Brandenberger (13), Woody *et al.* (14), and Banks and Bailey (15) appear to support the four-center quasi-cyclobutane intermediate formation.

The kinetic aspect of this reaction has been studied for a tungsten oxide-silica catalyst by Begley and Wilson (16) and by Luckner *et al.* (17), for a cobalt molybdate-alumina catalyst by Moffat and Clark (18) and by Lewis and Wills (19), and over a molybdenum hexacarbonyl-alumina catalyst by Davie *et al.* (20). The transient kinetic aspect involved in the break-in induction phenomena over a tungsten oxide-silica catalyst has been studied by Luckner and Wills (21).

Begley and Wilson (16) conducted a kinetic study in an integral bed reactor for pressures up to 62.25 atm and temperatures from 600° to 850°F. They concluded that their data were best represented by a Rideal type model involving a second-order interaction between adsorbed molecules and gas phase molecules. However, Moffat *et al.* (22) report experimental evidence that for the conditions involved, intraphase mass transfer is the controlling step, thereby casting doubt on the validity of the Rideal mechanism proposed by Begley and Wilson (16).

Lewis and Wills (19) used a differential bed reactor to obtain initial rates over a cobalt molybdate-alumina catalyst for pressures up to 9 atm and tem-

peratures from 250° to 400°F. Their data were best described by the Langmuir-Hinshelwood model. Moffat and Clark (18) also did experiments over a cobalt molybdate-alumina catalyst at 250° to 350°F and up to 5.5 atm to establish the validity of the Langmuir-Hinshelwood mechanism. Using this information as a basis, they could explain the rate temperature maximum observed around 400°F.

Davie *et al.* (20) investigated this reaction over a molybdenum hexacarbonyl-alumina catalyst in a static reactor for temperatures up to 171°F and pressures in the range 0.5 to 20 KNm⁻² (0.005 to 0.197 atm) and concluded that the controlling rate involved reaction between two adjacently adsorbed propylene molecules.

Luckner *et al.* (17) studied the disproportionation reaction over a tungsten oxide-silica catalyst in a differential bed reactor for temperatures of 750° to 850°F over pressures up to 9 atm. After mass transfer effects were eliminated by high flow rates and small particle sizes, their data were consistent with the Langmuir-Hinshelwood mechanism. Luckner and Wills (21) continued this work and studied the catalyst break-in phenomenon involved in the induction period. These data were correlated with both temperature and pressure and a first-order propylene partial pressure dependency.

The kinetic study of this reaction so far indicates that the actual rate-controlling step involves a Langmuir-Hinshelwood type mechanism consisting of reaction between two adjacently adsorbed molecules of propylene on the catalyst surface. The data of Begley and Wilson (16) do not seem to represent the actual reaction rate step and probably suffer from intraphase mass transfer controlling the overall reaction (22). Thus the Rideal mechanism does not seem to be valid, and the Langmuir-Hinshelwood mechanism appears to be followed for all the catalysts studied, such as cobalt molybdate-alumina, molybdenum hexacarbonyl-alumina, and tungsten oxide-silica.

This study was done to determine the contribution of the presence of reaction products along with the reactant, as observed during significant levels of conversion in an integral bed. Reaction rate data from both differential and integral bed studies were extended to high pressures and a wide range of temperatures to approach commercially used conditions.

Experimental Equipment and Procedure

The catalyst bed was accommodated in a cartridge of 5/8-inch id, 0.990-inch od, and about 3 inches in length, perforated at both ends. A 1-inch, schedule-80 (id = 0.957 inch) 316-stainless steel pipe, 45 inches in length was bored up to the middle with a 1-inch bore to form a ledge upon which the reactor cartridge rested. High pressure flanges with Teflon gaskets sealed the top and bottom of the pipe. Thermowells extended from both flange ends to the reactor cartridge and also to the middle of the sections before and after the reactor. To minimize the free space in the preheater and postheater sections, 13/16-inch stainless steel cylinders were fitted onto the 1/8-inch thermowells to form an annular space between these inserts and the pipe wall. The high heat capacity of these essentially solid inserts facilitated the maintenance of uniform temperatures. To establish a uniform flow pattern at the reactor, stainless steel screens were placed between the end of each insert and the perforated ends of the reactor cartridge. Within the reactor cartridge the catalyst bed was held between fine stainless steel screens and the dead space

above the catalyst bed was minimized with $\frac{1}{8}$ -inch stainless steel balls. Independent, manually controlled heaters were used for the preheater and post-heater sections while the reactor section temperature was maintained with a heater controlled automatically by a Leeds and Northrup Electromax controller. Two Grove back-pressure regulators for the high and low pressure range, respectively, allowed pressure control within the reactor. Pressure was measured at the upstream and downstream ends by two precision gauges calibrated with an Aminco dead weight tester. Temperatures were measured with a Leeds and Northrup compensated galvanometer that had been calibrated at convenient reference points. To confirm the validity of the reaction rates observed and to ascertain that there was no fluid bypassing the catalyst bed, a few runs were repeated in an auxiliary reactor. This reactor consisted of a 6-inch long, $\frac{1}{4}$ -inch stainless steel tube fitted at both ends with Swagelok unions and fine screen inserts. Stainless steel was used throughout in the construction. A $\frac{1}{4}$ -inch tube connected to the union at the top of the reactor served as the preheater and as the feed inlet. The bottom union was also connected to a $\frac{1}{4}$ -inch tube which ended in a Swagelok tee. The side arm of this tee was used as the reactor outlet while the straight arm was fitted with a $\frac{1}{8}$ -inch Swagelok bored through to permit the fitting of a $\frac{1}{8}$ -inch thermowell that extended up to the catalyst bed. This assembly was suspended inside the open flanged pipe which normally accommodated the reactor cartridge. While runs made in this reactor were consistent with values obtained using the reactor cartridge, maintenance of temperature was more difficult, especially at the higher temperatures and high flow rates, probably because of the lower heat capacity of this system.

Most runs were conducted with a commercial catalyst, SMR7-4520 supplied by W. R. Grace and Co., similar to the catalyst described by Luckner *et al.* (17). The catalyst was reported to have a surface area of 223 m²/gram and contained 10 wt % of tungsten oxide deposited on silica. The catalyst, obtained in the form of $\frac{1}{8}$ -inch extrusions was crushed and screened prior to use. Average particle size for the runs was 30–40 mesh. In addition, a catalyst was also prepared according to the method outlined by Heckelsberg *et al.* (8) which involved the deposition of 10.08% tungsten oxide on Davison No. 59 grade silica gel through an aqueous solution of ammonium metatungstate. The silica gel supplied by W. R. Grace and Co. was reported to have a surface area of 340 m²/gram. Results with this catalyst were consistent with those observed with the commercial catalyst.

Polymerization grade propylene (99% minimum purity) obtained from the Phillips Petroleum Co., was removed from the cylinder in the liquid state by an eductor tube, cooled in a solid CO₂ bath, and fed by a Lapp Pulsafeeder Microflow metering pump through a train consisting of De-Oxo catalyst, Drierite drying agent, and 5A Molecular Sieves into the reactor. Flow rates were measured at essentially atmospheric pressure at the downstream end, following the back-pressure regulators, by means of a Precision Wet Test Meter. While flow rates were normally measured using the reactor effluent, occasional checks were made by bypassing the reactor and thereby directly measuring feed rates. At all times, these rates agreed with each other.

Compositions were measured using a Perkin-Elmer model F11 flame ionization chromatograph in conjunction with a Leeds and Northrup Speedomax G recorder fitted with a disk integrator. The instrument was calibrated with standard mixtures of ethylene, propylene, and *cis*- and *trans*-butenes. Effluent samples were periodically introduced into the chromatograph by a sampling valve connected in line with the system.

Catalyst regeneration was effected by passing air, dried with Drierite and made carbon dioxide free with Ascarite, through the catalyst bed at 1100°F for 5 hr. During a few runs, the exhaust gases were checked for carbon dioxide and moisture content to estimate carbon deposition in the previous

run. However, values obtained for carbon deposition during the normal 8-hr period of a run were insignificant, so this procedure was later discontinued. The system was then flushed with dry, zero grade nitrogen for 1 hr at 1100°F. The temperature was then decreased to the reaction temperature while nitrogen continued to flow. Propylene was then introduced to initiate a run. Preliminary runs indicated that an induction period did not last beyond 8 hrs, and hence the flow of propylene was maintained for at least 10 hrs prior to an actual run. This steady-state period appeared to last about 12 hrs after which catalyst activity began to decline slowly. Check runs taken before and after each set of data ensured that the activity level was constant. A run consisted of setting the temperature, pressure, and flow rate desired and then analyzing effluent samples periodically until steady-state conditions were confirmed. Data were then obtained for the run.

Elimination of External and Pore Diffusion Effects

External or interphase diffusion results from the resistance of the surface film; pore diffusion relates to the diffusion of the reactants into the pores of the catalyst and diffusion of the products out of the catalyst pores to the surface. External diffusion can be minimized by increasing the flow rates; pore diffusion can be reduced by decreasing particle size of the catalyst. Experiments were conducted using 50–60 mesh catalyst of two different weights, 0.10 and 0.20 gram, and variable flow rates. Figure 1 presents the conversion, x , for these two catalyst weights vs. space time. For a given space time, the upper curve represents a flow rate twice that associated with the lower curve. The results indicate that for a catalyst weight of 0.10 gram, when W/F is maintained below 0.062, external diffusion becomes negligible. This corresponds to a flow rate of 1.61 gram-moles/hr. Thus, by maintaining a flow rate higher than this value, Reynolds numbers are sufficiently high that external diffusion becomes negligible. All runs were conducted at flow rates higher than 2.4 gram-moles/hr.

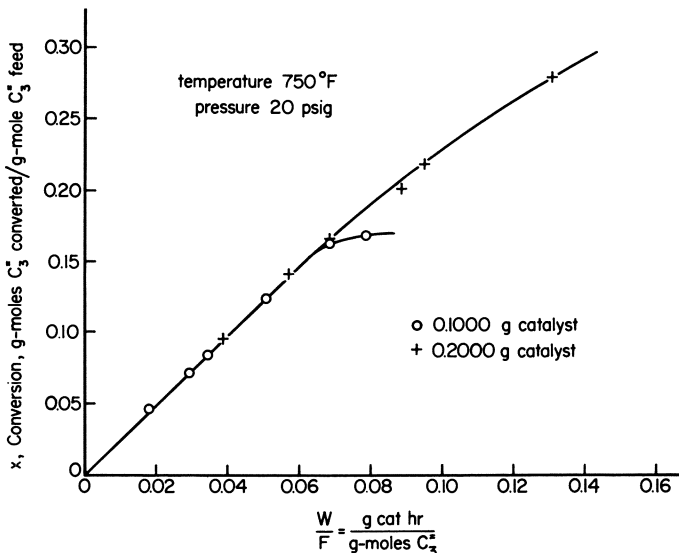


Figure 1. Conversion vs. W/F for two different catalyst charges

To eliminate the effects of pore diffusion, runs were done with five different sizes of particles, ranging from 16 to 50 mesh. The resulting reaction rate plotted *vs.* particle diameter (Figure 2) indicates that pore diffusion is negligible for particle sizes below $-20 + 30$ mesh (718 μm). Therefore, runs for the kinetic studies were conducted using $-30 + 40$ mesh particles. With the establishment of these conditions, it can be assumed that the observed reaction rate relates directly to reaction kinetics.

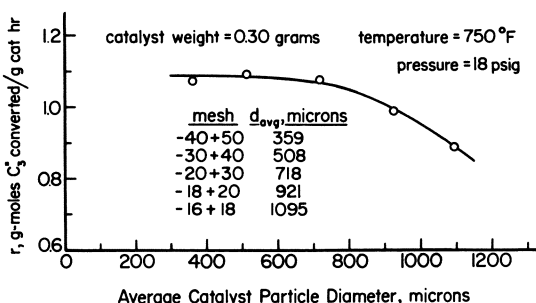


Figure 2. Experimental runs for pore diffusion effects

Table I. Anomalous Rates Observed with 0.01 Gram Catalyst

Temp., °F	Pressure, psig	Flow rate, gram- moles/hr	Conversion	Rate, gram-moles/ gram-cat. hr		Diluent
				Observed	Expected	
750	23	2.56	0.0181	4.64	2.76	quartz
750	20	3.03	0.0151	4.58	2.56	quartz
750	20	3.86	0.0118	4.56	2.57	stainless steel
750	141	3.67	0.0323	11.86	6.37	quartz
750	141	3.86	0.0310	11.97	6.36	stainless steel
800	141	3.67	0.0437	16.04	8.92	quartz
800	140	3.86	0.0420	16.38	8.91	stainless steel

Initial Rate Studies

A differential bed of catalyst was used to obtain initial rates for the disproportionation reaction. Catalyst weights used were 0.030, 0.100, and 0.300 gram. To eliminate channeling, the catalyst was mixed in all cases with crushed, screened quartz to a total bed weight of 0.600 gram. The noncatalytic nature of the quartz was confirmed experimentally in three ways. First, quartz by itself was noted to have no catalytic effect. Second, a catalyst charge of 0.300 gram alone produced similar results to catalyst diluted with quartz. Third, 0.010 gram of catalyst when diluted with quartz on one hand and with stainless steel filings on the other produced similar results.

An interesting anomaly was encountered at the extremely low catalyst weight of 0.010 gram. The reaction rates observed for this amount of catalyst were 70–90% higher than expected (*see* Table I).

Experiments were conducted at five temperatures ranging from 650° to 850°F and for pressures up to 1000 psi. At a set pressure and temperature, when steady state was achieved, three to four independent runs were conducted to minimize errors associated with chromatographic analyses and possible experimental fluctuations. The results, averaged over these runs, are reported

Table II. Initial Rate Data for the Disproportionation of Propylene^a

Pressure, psig	Catalyst, gram	x Con- version	Flow rate, gram- moles/hr	$(p_2)_{\text{avg.}}$ atm	r_0 , Initial rate		
					Exptl	Calcd	% Dev.
650°F							
18	0.3000	0.039	4.47	2.17	0.583	0.623	6.86
49	0.3000	0.060	5.97	4.19	1.190	1.411	18.57
94	0.3000	0.108	6.41	6.98	2.296	2.293	0.13
94	0.1000	0.069	3.64	7.13	2.507	2.332	6.98
129	0.0300	0.018	4.93	9.67	2.979	2.927	1.74
262	0.1000	0.067	6.14	18.18	4.130	4.126	0.10
521	0.0300	0.031	4.95	35.86	5.126	5.150	0.47
758	0.1000	0.065	8.38	50.85	5.415	5.537	2.25
979	0.1000	0.069	8.44	65.24	5.856	5.759	1.66
							4.31
700°F							
23	0.3000	0.068	6.42	2.47	1.460	1.521	4.18
48	0.1000	0.065	3.44	4.11	2.257	2.580	14.31
94	0.1000	0.077	5.55	7.10	4.247	3.937	7.30
129	0.0300	0.020	7.04	9.67	4.737	4.711	0.55
262	0.1000	0.079	7.48	18.07	5.909	6.100	3.23
521	0.0300	0.045	4.95	35.60	7.459	7.176	3.79
749	0.1000	0.080	9.02	49.86	7.221	7.548	4.53
987	0.0300	0.042	5.65	66.70	7.899	7.798	1.15
							4.88
750°F							
18	0.3000	0.105	6.87	2.09	2.400	2.300	4.17
20	0.1000	0.072	3.44	2.26	2.460	2.483	0.93
23	0.0300	0.021	3.48	2.52	2.483	2.745	10.55
49	0.1000	0.085	5.36	4.14	4.550	4.055	10.88
90	0.1000	0.061	8.73	6.89	5.302	5.410	2.04
129	0.0300	0.037	4.76	9.58	5.812	6.195	6.59
253	0.0300	0.041	5.42	17.82	7.462	7.366	1.29
510	0.0300	0.046	5.30	34.86	8.137	8.186	0.60
731	0.0300	0.046	5.65	49.55	8.602	8.468	1.56
							4.29
800°F							
18	0.1000	0.077	5.15	2.13	3.942	4.002	1.52
50	0.1000	0.076	8.49	4.22	6.476	6.348	1.98
129	0.0300	0.055	4.76	9.49	8.668	8.724	0.65
253	0.0300	0.054	5.42	17.70	9.817	9.954	1.40
510	0.0300	0.063	5.30	34.56	11.089	10.767	2.90
731	0.0300	0.058	5.65	49.24	10.885	11.042	1.44
							1.65
850°F							
17	0.1000	0.078	8.72	2.06	6.799	6.754	0.66
129	0.0300	0.072	4.76	9.41	11.386	11.441	0.48
253	0.0300	0.068	5.42	17.58	12.294	12.393	0.80
510	0.0300	0.073	5.30	34.37	12.921	12.988	0.52
731	0.0300	0.071	5.65	48.91	13.367	13.180	1.40
							0.77

x = conversion, gram-moles C_3H_6 converted/gram-mole C_3H_6 in feed; r_0 = initial rate, gram-moles C_3H_6 converted/(gram-catalyst)(hr).

in Table II. Conversions associated with these initial rate runs varied from 0.018 to 0.108.

In a differential bed, conversions are maintained sufficiently low that the reverse reaction is negligible and the rate expression becomes

$$r = \frac{\Delta x}{\Delta(W/F)} = \frac{x}{W/F} \quad (1)$$

Isothermal plots of the initial rate *vs.* total pressure are given in Figure 3. Both the single-site mechanism (Rideal) and the dual-site mechanism (Langmuir-Hinshelwood) were considered. The Hougen-Watson rate expression (23) for the Rideal single-site mechanism is

$$r = \frac{C \left[p_3^2 - \frac{p_2 p_4}{K} \right]}{1 + K_2 p_2 + K_3 p_3 + K_4 p_4} \quad (2)$$

For small conversions, the partial pressures of the products, p_2 and p_4 are sufficiently small to justify neglecting them in Equation 2. Thus, the initial rate expression for the Rideal model becomes

$$r_0 = \frac{C p_3^2}{1 + K_3 p_3} \quad (3)$$

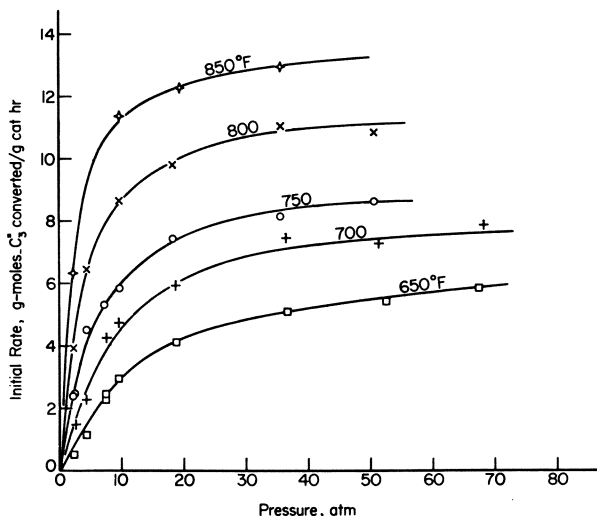


Figure 3. Isothermal relationships between initial rate and total pressure

Rearranging the terms of Equation 3

$$\frac{p_3^2}{r_0} = \frac{1}{C} + \frac{K_3}{C} p_3 \quad (4)$$

and hence a plot of p_3^2/r_0 *vs.* p_3 should be linear. Similarly, the dual-site mechanism leads to the expression

$$r = \frac{C \left[p_3^2 - \frac{p_2 p_4}{K} \right]}{[1 + K_2 p_2 + K_3 p_3 + K_4 p_4]^2} \quad (5)$$

which yields, in a similar manner,

$$r_0 = \frac{C p_3^2}{[1 + K_3 p_3]^2} \quad (6)$$

$$\frac{p_3}{\sqrt{r_0}} = \frac{1}{\sqrt{C}} + \frac{K_3}{\sqrt{C}} p_3 \quad (7)$$

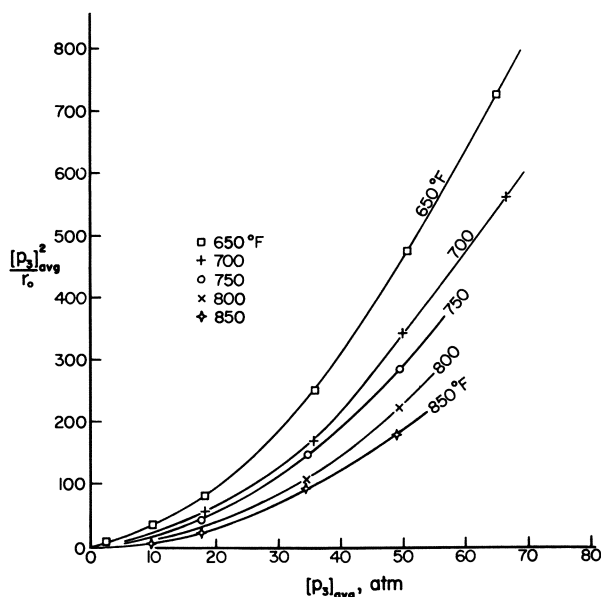


Figure 4. Test of Rideal model for experimental data

Equations 4 and 7 were tested using the experimental data. The partial pressure of propylene, p_3 , represents the average partial pressure within the catalyst bed. Plots of p_3^2/r_0 vs. p_3 and $p_3/\sqrt{r_0}$ vs. p_3 are in Figures 4 and 5, respectively. The isothermal relationships of Figure 4 are nonlinear and hence indicate that the Rideal model does not properly represent the data. Furthermore, if a straight line were forced on these relationships, the value of their intercepts, representing $1/C$, would become negative, implying that the reaction is not possible. On the other hand, the isothermal plots of Figure 5 are linear, indicating that the dual-site mechanism is possible and best represents the data. Furthermore, both the slopes and the intercepts for these relationships are positive, leading to positive values for C , the reaction rate constant, and K_3 , the propylene adsorption equilibrium constant. Accepting this behavior, we can make a nonlinear least-squares fit using Equation 6 where r_0 becomes the dependent variable rather than Equation 7 where $p_3/\sqrt{r_0}$ is the dependent variable. These values of C and K_3 along with their respective 95% confidence limits are reported in Table III. Slopes and intercepts derived from

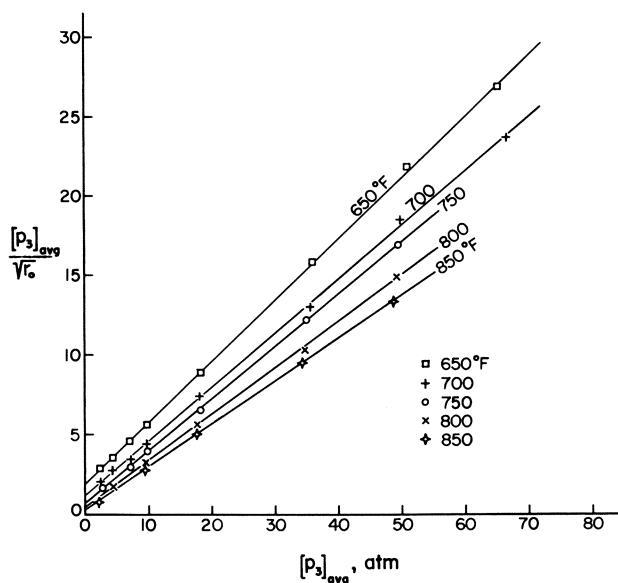


Figure 5. Test of Langmuir-Hinshelwood model for experimental data

Table III. Nonlinear Least-Square Estimates of C and K_3 with 95% Confidence Limits

Temp. °F	C , gram-moles/ (gram-cat.)(hr)(atm) ²	K_3 , 1/atm	Av. Dev., %
650	0.276 ± 0.0239	0.203 ± 0.0104	4.46
700	0.744 ± 0.1106	0.294 ± 0.0249	5.00
750	2.098 ± 0.2372	0.478 ± 0.0311	4.19
800	5.105 ± 0.5348	0.660 ± 0.0379	1.68
850	18.060 ± 1.5509	1.150 ± 0.0523	0.81

the nonlinear estimates of C and K_3 were used to produce the linear relationships of Figure 5.

From theoretical arguments, the reaction rate constant C and the propylene adsorption equilibrium constant K_3 should follow Arrhenius' rule; therefore the natural logarithm of these values was plotted vs. their reciprocal temperature ($^{\circ}\text{K}$). These plots are given in Figure 6 and indicate that this rule is followed for all but the highest temperature, 850°F , where the values of C and K_3 appear to be somewhat high. However, this behavior cannot be explained easily, because selectivity and carbon formation were similar to those encountered at the lower temperatures. Because of this deviation, the values of 850°F were given less weight and straight lines were drawn through the points of Figure 6 to produce the Arrhenius type relationships,

$$C = 1.229 \times 10^{10} e^{-30,040/RT} \quad (8)$$

and

$$K_3 = 4.082 \times 10^3 e^{-12,140/RT} \quad (9)$$

where $R = 1.987$ cal/gram-mole $^{\circ}\text{K}$ and T is the temperature ($^{\circ}\text{K}$). From

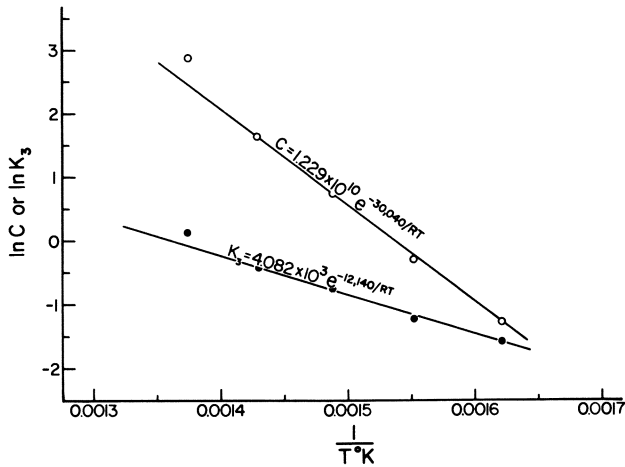


Figure 6. Arrhenius type relationships for C and K_3 .

these relationships, the activation energy for the reaction is 30,040 cal/gram-mole and that for the adsorption of propylene is 12,140 cal/gram-mole.

Integral Bed Studies

Integral bed studies were done at 650°, 750°, and 850°F for pressures up to 520 psi. These studies constituted runs in which the catalyst weight was maintained at 0.1000, 0.2000, 0.3000, 1.0000, and 2.0000 grams and in which conversions ranged from 8% up to equilibrium. To ascertain that equilibrium had been established, runs that were suspected to be at equilibrium were checked with those done at lower space velocities by either increasing the catalyst weight or by decreasing the feed flow rate. Also, the conversion associated with these equilibrium runs remained the same as pressure was varied.

Table IV. Experimental Equilibrium Conversions

	Pressure, atm	W/F	x^*
650°F	4.60	0.690	0.4531
	10.32	0.677	0.4537
	18.34	0.383	0.4533
	35.75	0.346	0.4535
			0.4534
750°F	2.21	0.342	0.4620
	2.22	0.557	0.4626
	7.58	0.194	0.4615
	7.73	0.566	0.4619
	35.69	0.367	0.4631
			0.4622
850°F	2.22	0.341	0.4682
	35.27	0.118	0.4672
	35.27	0.163	0.4676
	35.69	0.367	0.4684
			0.4679

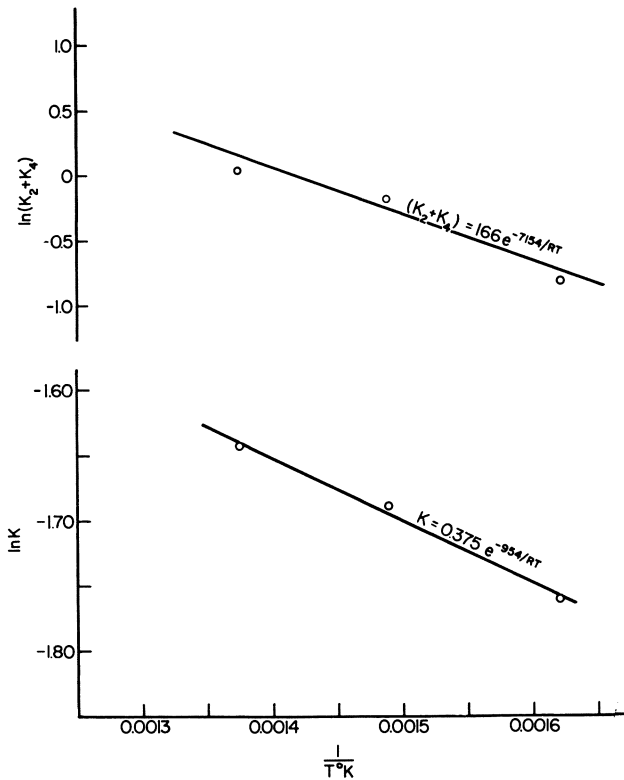


Figure 7. Arrhenius type relationships for $K_2 + K_4$ and K

When these two requirements were satisfied, the runs were considered to be at equilibrium. The results of these runs are presented in Table IV. The averaged equilibrium conversions were used to establish the equilibrium constants, $K = x^{*2}/4(1 - x^*)^2$. These constants followed an Arrhenius type relationship as depicted in Figure 7. This relationship may be expressed as

$$K = 0.375 e^{-954/RT} \quad (10)$$

where T is in degrees Kelvin.

The integral bed runs involved the use of pure propylene as feed; therefore the mole fractions of ethylene and butene, and thus their corresponding partial pressures, were essentially the same. Hence Equation 5 assumes the form

$$r = \frac{C \left[p_3^2 - \frac{p_{24}^2}{K} \right]}{[1 + K_2 p_{24} + K_3 p_3 + K_4 p_{24}]^2} \quad (11)$$

where p_{24} represents the average partial pressure of ethylene and of butene. Hence, the effect of conversion on K_2 and K_4 cannot be isolated, and the denominator takes the form $[1 + (K_2 + K_4)p_{24} + K_3 p_3]^2$. Consequently, K_2 and K_4 cannot be evaluated individually, and only the sum $(K_2 + K_4)$ can be evaluated to represent their combined contribution.

The integral bed runs, excluding the equilibrium values, are reported in Table V. For significant conversions, the simplified form of Equation 1 cannot be used, and thus the reciprocal space velocity must be represented by the integral form,

$$\frac{W}{F} = \int_0^x \frac{dx}{r} = \int_0^x \frac{[1 + (K_2 + K_4)p_{24} + K_3p_3]^2}{C \left[p_3^2 - \frac{p_{24}^2}{K} \right]} dx \quad (12)$$

Substituting the values $p_3 = \pi(1 - x)$ and $p_{24} = \pi x/2$, where π represents the total pressure and x is the conversion in Equation 12

$$\frac{W}{F} = \frac{1}{C} \int_0^x \frac{\left[\frac{1}{\pi} + (K_2 + K_4) \frac{x}{2} + K_3(1 - x) \right]^2}{(1 - x)^2 - \frac{x^2}{4K}} dx \quad (13)$$

Equation 13 can be integrated to:

$$\frac{W}{F} = \frac{1}{C} \left[\alpha^2 \int_0^x \frac{dx}{a + bx + cx^2} + 2\alpha\beta \int_0^x \frac{xdx}{a + bx + cx^2} + \beta^2 \int_0^x \frac{x^2dx}{a + bx + cx^2} \right] \quad (14)$$

where $\alpha = 1/\pi + K_3$, $\beta = (K_2 + K_4)/2 - K_3$, $a = 1$, $b = -2$, and $c = 1 - 1/4K$,

$$\int_0^x \frac{dx}{a + bx + cx^2} = \sqrt{K} \left\{ \ln \left| \frac{2cx + b - \sqrt{1/K}}{2cx + b + \sqrt{1/K}} \right| - \ln \left| \frac{b - \sqrt{1/K}}{b + \sqrt{1/K}} \right| \right\}$$

$$\int_0^x \frac{xdx}{a + bx + cx^2} = \frac{1}{2c} \left\{ \ln(a + bx + cx^2) - \ln a \right\} - \frac{b}{2c} \int_0^x \frac{dx}{a + bx + cx^2}$$

$$\text{and } \int_0^x \frac{x^2dx}{a + bx + cx^2} = \frac{x}{c} - \frac{b}{2c^2} \left\{ \ln(a + bx + cx^2) - \ln a \right\} + \frac{b^2 - 2ac}{2c^2} \int_0^x \frac{dx}{a + bx + cx^2}$$

Using the values of C , K_3 , and K obtained from Equations 8, 9, and 10, values of $(K_2 + K_4)$ were established for each run using the integral relationships expressed by Equation 14. At each temperature, an average value of $(K_2 + K_4)$ was obtained from all runs, except when these values were negative or highly deviant. These runs have been depicted in Table V. The average values of $(K_2 + K_4)$ obtained in this fashion, along with their 95% confidence limits, for all the runs are as follows:

Temp., °F	650	750	850
$K_2 + K_4$	0.444 ± 0.238	0.826 ± 0.173	1.049 ± 0.180

Values of W/F calculated from these constants and Equation 14 are included in Table V along with their associated deviations. These values of $(K_2 + K_4)$ follow an Arrhenius type relationship as depicted in Figure 7. This relationship may be expressed as

$$(K_2 + K_4) = 166 e^{-7154/RT} \quad (15)$$

where T is in degrees Kelvin.

Finally, all integral bed runs were compared with values of W/F predicted using Equation 14 and the Arrhenius relationships of Equations 8, 9,

Table V. Experimental Results for Integral Bed Runs

Pressure, atm	W, grams	F, gram- moles/hr	x	W/F		
				Exptl	Calcd	% Dev.
650°F						
2.22 ^a	2.0000	2.955	0.337	0.677	0.923	36.40 ^a
2.42	1.0000	2.826	0.191	0.354	0.337	4.85
2.42	1.0000	4.332	0.140	0.231	0.229	0.86
2.42 ^a	1.0000	8.116	0.076	0.123	0.114	7.23 ^a
4.53	1.0000	2.826	0.332	0.354	0.380	7.34
4.53	1.0000	3.811	0.275	0.262	0.270	2.82
4.32 ^a	0.3000	2.876	0.115	0.104	0.090	13.38 ^a
10.04	1.0000	2.947	0.419	0.339	0.380	11.90
10.04	1.0000	5.617	0.295	0.178	0.156	12.36
10.04	0.3000	3.396	0.193	0.088	0.083	6.55
10.04 ^a	0.3000	5.883	0.115	0.051	0.044	14.12 ^a
18.00	1.0000	5.502	0.357	0.182	0.168	7.66
18.00	0.3000	4.666	0.218	0.064	0.072	11.28
18.13	0.3000	7.563	0.146	0.040	0.042	7.06
35.75	1.0000	5.559	0.394	0.180	0.177	1.71
35.28	0.3000	4.089	0.272	0.073	0.080	9.11
35.28 ^a	0.3000	9.207	0.166	0.033	0.040	22.24 ^a
						10.40
750°F						
2.41 ^a	1.0000	6.091	0.328	0.164	0.199	21.03 ^a
2.41	1.0000	7.825	0.266	0.128	0.139	8.93
2.34 ^a	0.3000	3.196	0.221	0.094	0.109	16.29 ^a
2.34 ^a	0.3000	5.203	0.149	0.058	0.066	14.72 ^a
2.34 ^a	0.3000	11.480	0.079	0.026	0.032	23.50 ^a
2.35 ^a	0.2000	2.938	0.166	0.068	0.075	10.70 ^a
2.35 ^a	0.2000	3.516	0.140	0.057	0.061	7.98 ^a
2.35	0.2000	5.193	0.095	0.039	0.039	2.42
2.34	0.1000	2.919	0.085	0.034	0.035	1.29
4.32	1.0000	5.167	0.427	0.194	0.251	29.73
4.32	1.0000	7.710	0.329	0.130	0.124	4.57
4.38	0.3000	3.824	0.235	0.078	0.071	9.01
4.38	0.3000	6.294	0.175	0.048	0.048	1.59
4.38	0.3000	6.064	0.165	0.049	0.045	8.99
4.38 ^a	0.3000	6.640	0.146	0.045	0.039	14.53 ^a
4.38 ^a	0.3000	7.849	0.128	0.038	0.033	12.85 ^a
7.58	0.2000	2.426	0.325	0.082	0.088	7.06
7.59	0.2000	2.831	0.292	0.071	0.073	3.92
7.59 ^a	0.2000	9.603	0.140	0.021	0.027	31.36 ^a
7.59	0.2000	11.309	0.091	0.018	0.017	5.68
18.20	1.0000	6.537	0.432	0.153	0.144	5.91
18.06	0.2000	2.830	0.329	0.071	0.068	3.17
18.06	0.2000	6.537	0.265	0.049	0.047	4.08
18.06	0.2000	9.780	0.142	0.020	0.021	2.60
35.27	1.0000	8.469	0.419	0.118	0.113	4.08
35.55	0.2000	3.874	0.312	0.052	0.056	7.52
						10.13
850°F						
2.42	1.0000	8.176	0.424	0.122	0.136	11.43
2.34	0.3000	3.881	0.330	0.077	0.077	0.17
2.34	0.3000	5.949	0.255	0.050	0.052	2.35
2.34	0.3000	8.956	0.190	0.033	0.035	5.29
4.46	1.0000	9.956	0.428	0.100	0.101	0.65
4.32	0.3000	6.064	0.309	0.049	0.050	0.06
4.46	0.3000	6.692	0.283	0.045	0.043	4.82
9.83	0.3000	3.481	0.430	0.086	0.079	7.93
9.83	0.3000	5.201	0.375	0.058	0.054	5.75

Table V. Continued

Pressure, atm	W, grams	F, gram- moles/hr	x	W/F		
				Exptl	Calcd	% Dev.
9.83	0.3000	9.484	0.267	0.032	0.031	2.70
35.28	0.3000	4.493	0.432	0.067	0.068	2.24
35.28	0.3000	5.825	0.375	0.052	0.046	10.30
35.28	0.3000	9.207	0.310	0.033	0.033	0.92
						4.20

* Runs considered questionable, based on negative or highly deviant values of (k_2+k_4) , when calculated on an individual basis.

10, and 15. This comparison resulted in an average deviation of 8.8% for 56 data points. When the footnoted runs of Table V were eliminated from consideration, the average deviation decreased to a value of 5.9% for 42 runs.

Discussion of Results

The results of this study prove conclusively that the dual-site mechanism involving the reaction of two adjacently adsorbed propylene molecules is followed during the disproportionation of propylene on a tungsten oxide-silica catalyst. This result is consistent with the findings of Luckner *et al.* (17). The extension by this study to high pressures clearly indicates the failure of the Rideal model for this reaction and shows the adherence of these data to the Langmuir-Hinshelwood mechanism.

The reaction rates observed in the present study were found to be slightly higher than those reported earlier (19). These differences may be attributed to the impurities present in commercially obtained propylene. In this regard, it was noted that different batches of propylene did result in slightly different conversions. Furthermore, the use of De-Oxo in the purification train contributed to consistent reaction rates.

Nomenclature

C	overall rate constant, gram-moles C_3^{2-} converted/gram catalyst hr
F	feed rate, gram-moles C_3^{2-} /hr
K	equilibrium constant
K_2, K_3, K_4	adsorption equilibrium constants for ethylene, propylene, and butene, respectively
p_2, p_3, p_4	partial pressure of ethylene, propylene, and butene, respectively, atm
p_{24}	average partial pressure $(p_2 + p_4)/2$
r	reaction rate, gram-moles C_3^{2-} converted/gram catalyst hr
r_0	initial rate, gram-moles C_3^{2-} converted/gram catalyst hr
R	gas constant, 1.987 cal/gram-mole °K
T	absolute temperature, °K
W	weight of catalyst, grams
x	conversion, gram-moles C_3^{2-} converted/gram-mole C_3^{2-} in feed

Greek Letters

π	total pressure, atm
-------	---------------------

Literature Cited

1. Banks, R. L., Bailey, G. C., *Ind. Eng. Chem. Prod. Res. Dev.* (1964) **3**, 170.
2. Bailey, G. C., *Catalysis Rev.* (1969) **3**, 37.
3. Schneider, V., Frolich, P. K., *Ind. Eng. Chem.* (1931) **23**, 1405.
4. Wang, J., Menapace, H. R., *J. Org. Chem.* (1968) **33**, 3794.
5. Calderon, N., Ofstead, E. A., Ward, J. P., Judy, W. A., Scott, K. W., *J. Amer. Chem. Soc.* (1968) **90**, 4133.
6. Zuech, E. A., *Chem. Comm.* (1968) 1182.
7. Heckelsberg, L. F., Banks, R. L., Bailey, G. C., *Ind. Eng. Chem. Prod. Res. Dev.* (1968) **7**, 29.
8. Heckelsberg, L. F., Banks, R. L., Bailey, G. C., *Ind. Eng. Chem. Prod. Res. Dev.* (1969) **8**, 259.
9. Kobylinski, T. P., Swift, H. E., *J. Catalysis* (1972) **26**, 416.
10. Bradshaw, C. P. C., Howman, E. J., Turner, L., *J. Catalysis* (1967) **7**, 269.
11. Mol, J. C., Mouljin, J. A., Boelhouwer, C., *Chem. Comm.* (1968) 633.
12. Crain, D. L., *J. Catalysis* (1969) **13**, 110.
13. Adams, C. T., Brandenberger, S. G., *J. Catalysis* (1969) **13**, 360.
14. Woody, F. L., Lewis, M. J., Wills, G. B., *J. Catalysis* (1969) **14**, 389.
15. Banks, R. L., Bailey, G. C., *J. Catalysis* (1969) **14**, 276.
16. Begley, J. W., Wilson, R. T., *J. Catalysis* (1967) **9**, 375.
17. Luckner, R. C., McConchie, G. E., Wills, G. B., *J. Catalysis* (1973) **28**, 63.
18. Moffat, A. J., Clark, A., *J. Catalysis* (1970) **17**, 264.
19. Lewis, M. J., Wills, G. B., *J. Catalysis* (1969) **15**, 140.
20. Davie, E. S., Whan, D. A., Kemball, C., *J. Catalysis* (1972) **24**, 272.
21. Luckner, R. C., Wills, G. B., *J. Catalysis* (1973) **28**, 83.
22. Moffat, A. J., Johnson, M. M., Clark, A., *J. Catalysis* (1970) **18**, 345.
23. Hougen, O. A., Watson, K. M., "Chemical Process Principles," Vol. III, John Wiley, New York, 1947.

RECEIVED January 2, 1974.

Selectivity in the 2-Propanol Reactions over Supported Rhenium Catalysts

J. ROBERT FOWLER, JR.¹ and JAMES W. LACKSONEN

Department of Chemical Engineering, The University of Toledo,
Toledo, Ohio 43606

Rhenium-on-silica gel catalysts were prepared by standard techniques. The dehydrogenation–dehydration reactions of 2-propanol were chosen to study the selectivity exhibited by high and low rhenium concentration catalysts. High rhenium concentration catalysts behaved in a fashion typical of bulk rhenium metal—i.e., dehydrogenation predominated. On the other hand, low concentration catalysts exhibited a marked tendency to produce propylene. This tendency was most pronounced with low concentration catalysts prepared from oxygen precleaned silica gel. When various techniques were used to determine rhenium crystallite sizes, the same catalysts which had tended to catalyze the dehydration reaction failed to chemisorb hydrogen. It is proposed that strong support–metal interactions were responsible for the observed phenomena.

Metals such as platinum characteristically catalyze the dehydrogenation of secondary alcohols, and metal oxides such as alumina catalyze the dehydration reaction. Few studies, however, have reported that supported metals or metal oxides can catalyze either of these two parallel reactions in response to the amount or crystallite size of the active species. One such study was that of Rubinshtein as reported by Gil'debrand (1). He found that the selectivity between the dehydrogenation and dehydration reactions of ethanol over magnesium oxide supported on carbon black could be varied substantially depending upon "the degree of deviation of crystalline network parameters from their normal values." In another study reported by Gil'debrand, Adadurov found that the dehydration reaction of ethanol over zinc oxide supported on carbon black began to predominate as the quantity of zinc oxide was reduced. Other workers have reported that the selectivity for what they refer to as either the hydrogenation (to propane) or hydrogenolysis (to methane and ethane) of cyclopropane over nickel supported on either silica or alumina was influenced by the nature of the support (2).

Few studies of the catalytic properties of metallic rhenium have been reported. Russian workers (3) have examined both bulk and supported rhenium

¹ Present address: Diamond Shamrock Corp., 1100 Superior Ave., Cleveland, Ohio 44114.

in view of the multiplet theory. Platanov *et al.* (4) studied the reactions of 2-propanol vapor over finely divided rhenium metal prepared by a "nitric acid" method and found that acetone was formed exclusively up to 600°C.

In the present study both the size of the rhenium crystallites supported on silica gel and the nature of the support itself were varied to study the effects of these variables on a test reaction. 2-Propanol was chosen as a test reactant since only the dehydration and dehydrogenation reactions (production of acetone and hydrogen or propylene and water, respectively) should be catalyzed by rhenium over a moderate temperature range.

Experimental

Materials. The silica gel support for the rhenium catalysts was supplied by the Owens-Illinois Corp. (Toledo, Ohio) and was screened into four fractions from 100 to 325 mesh. The -100 + 140 mesh fraction was normally chosen for use. The BET surface area of the silica gel was about 536 m²/gram, the pore volume was 0.69 cm³/gram, and the average pore radius was 25 Å. This BET area did not change significantly even when the silica was heated to 500°C for 6 hrs.

Aqueous solutions of ammonium perrhenate and commercial grade hydrogen cleaned in a Deoxo unit dried in a molecular sieve water trap were used to prepare the supported rhenium catalysts. Reagent grade 2-propanol vaporized by water-pumped nitrogen (dried in the same molecular sieve trap) was the reactant. All gases used were nominally 99.99% pure, and chromatograms indicated only trace impurities.

A gas chromatograph (Varian, model 1520B) equipped with a matrix temperature programmer was used to analyze reaction products and to monitor the nitrogen desorbed during BET surface area measurements or hydrogen desorbed during rhenium surface area determinations. Details of the apparatus are given elsewhere (5); only a brief description is given here.

The 2-propanol reactions were studied in a train consisting of (1) a sparger filled with liquid 2-propanol, packed with Intalox saddles and placed in a temperature-controlled oil bath, (2) a device which maintained a constant 2-propanol level in the sparger, (3) the reactor (3-7/8 inches long, 1/2 inch od stainless steel tubing), (4) a muffle furnace enclosing the reactor, (5) a solenoid sample valve which interfaced the reaction system with the gas chromatograph but permitted continuous operation of the reactor, and (6) the chromatograph. The temperature in the packed bed of rhenium catalyst within the reactor was monitored by a shielded thermocouple inserted into the bed parallel to the center line of the reactor. A similar thermocouple was inserted into the muffle furnace which surrounded the reactor; this second thermocouple led to an on-off temperature controller. The gases exiting from the reactor were analyzed with Porapak S columns according to the matrix temperature program described elsewhere (5), and the signal from the chromatograph was integrated by an analog computer which was corrected for baseline drift and instrument noise.

BET and specific rhenium surface areas were measured by placing samples in a glass U tube connected in series with one channel of the chromatograph. For these purposes the analytical columns in the chromatograph were replaced with empty stainless steel tubes. For all analyses thermal conductivity detectors with tungsten-rhenium type WX filaments were used.

Methods. Supported rhenium catalysts were prepared by impregnating the silica support with aqueous ammonium perrhenate solutions, either 0.224M, 0.150M, or 0.0224M, followed by air drying for 6 hrs at 105°C and reduction at 500°C for 6 hrs in flowing hydrogen. Yates and Sinfelt (6) have reported

that such a reduction time fully reduces the perrhenate salt to metallic rhenium; the drying conditions are essentially those recommended by Dorling, *et al.* (7). For some catalysts the silica support was impregnated in its as-received condition; in other catalysts, it was treated with flowing oxygen for 2 hrs at 500°C and then dried by evacuation prior to impregnation. Rhenium concentrations in the various catalysts were determined spectrophotometrically with a Beckman DB-G unit using the technique of Meloche *et al.* (8) after dissolution and oxidation of the supported rhenium by the method of Malouf and White (9).

The selectivity of the various catalysts was determined in the reaction system by sparging liquid 2-propanol with nitrogen, passing this mixture over a packed bed of catalyst in the reactor, allowing sufficient time for the system to achieve steady state and then sampling the reactor off-gases. Catalyst preparation technique, reactor temperature (135°–360°C) and sparger temperature (23°–35°C) were the principal variables studied in this system. At any given set of conditions, three samples of the off-gas were taken and averaged. To minimize the influence of catalyst activity decay, each set of three samples was “bracketed” by an additional set of three samples measured at some predetermined, “standard” set of conditions as first suggested by Sinfelt (10).

To minimize longitudinal diffusional effects, the bed depth in the reactor was always such that its ratio to average particle diameter was 100 as suggested by Denbigh (11). Furthermore, the plug flow reactor was operated so that the total conversion of 2-propanol was never allowed to exceed 10–15%. For every reaction sample taken, effectiveness factors and external temperature and diffusion gradients were calculated; effectiveness factors always approached 1.0, and external gradients were negligible.

BET surface areas of both the plain silica support and various catalysts were determined with a gas chromatograph using the technique of Nelsen and Eggertson (12). The so-called three-point method was used.

Specific rhenium surface areas and crystallite sizes were measured by three methods: (1) hydrogen chemisorption at 20°C, (2) x-ray diffraction line broadening, and (3) scanning electron microscopy. The hydrogen chemisorption technique also utilized the gas chromatograph, and the method of Benesi *et al.* (13) was used. For all such measurements the catalysts were reduced *in situ* in the U tube device, the sample was cooled, and a mixture of nitrogen and hydrogen corresponding to 100-mm Hg partial pressure of hydrogen was flowed over the sample at 20°C until the sample and the gas had equilibrated. (Yates and Sinfelt (6) and Kubicka (14) have shown that a monolayer of hydrogen is formed over rhenium under these conditions). The hydrogen was desorbed from the sample by heating it to 500°C.

The x-ray diffraction studies used a Phillips diffractometer with copper $K\alpha$ radiation and a Geiger counter detector. The (101) rhenium planes were used for this diffraction study, and the average crystallite size was determined by the Scherrer Equation (15) uncorrected, in the present study, for instrumental line broadening since data for this effect were unavailable.

The last method by which an attempt was made to measure supported rhenium crystallite sizes was scanning electron microscopy. A J.S.M.-U3 S.E.M. was used. The samples were first coated with gold to a depth of about 200 Å on a glow discharge coater to render the particles electrically conductive.

Results

Catalyst Physical Properties. Table I is a representative summary of the physical properties of catalyst batches prepared from either as-received or oxygen-cleaned silica with three different strengths of ammonium perrhenate in the impregnating solutions. Although not shown, the BET surface areas averaged about 536 m²/gram for both the plain silica support (either as

received or oxygen cleaned) and for a catalyst containing the heaviest concentration of rhenium—catalyst batch 3B. The results for the specific metal surface areas, crystallite size, and dispersion are from data obtained by hydrogen chemisorption. Of course, the data from such a technique actually consist of volumes of hydrogen desorbed from the sample. The results presented in Table I are calculated from these data by using the value of 20.7 Å² for the rhenium surface area occupied by one hydrogen atom (14) and assuming that the supported crystallites were spherical.

The hydrogen chemisorption results for catalysts in Table I containing less than 2.43% rhenium are reported in parentheses. This is done because these "low concentration" catalysts produced a negative chromatogram peak as hydrogen was "desorbed" from the sample. (The peaks were opposite in polarity to those produced by direct injection of hydrogen into the front of the chromatograph by an airtight syringe). Even for catalysts containing 3.34 and 2.43% rhenium, the recorder pen at first deflected in the negative direction before the positive peak appeared. Thus, in the latter case the chromatograms resembled inverted sine waves while in the former only the first half of the inverted sine waves appeared. In both cases the recorder pen returned to the original baseline after tracing out the respective curves. The crystallite sizes indicated in Table I for these "low concentration" catalysts were approximated by using Figure 1. The data points on this figure are those for catalysts of batches 3B and 8 for which a desorbed volume of hydrogen was obtained.

The studies done with the scanning electron microscope, however, yielded some rather anomalous results. Photomicrographs of all catalysts, including those in Table I, were prepared. There were no discernible differences between photomicrographs of the plain silica support and any of the low concentration catalysts; however, photomicrographs of the high concentration catalysts revealed that catalyst particles from even the same batch of catalyst exhibited a wide range of supported rhenium particle sizes. Some particles from catalyst batch 8, for example, were identical to the plain silica support while other particles exhibited large rhenium particles on the surface of the catalyst. (These large particles were, in fact, rhenium as demonstrated conclusively by an x-ray distribution scan). Unfortunately, since the limit of resolution of the scanning electron microscope is about 100 Å, crystallites of an average size of those reported in Table I are not "visible" by this technique. Since no crystallites of about 100 Å were apparent on the surfaces of any of the catalyst particles examined and since no crystallites within the pores of the silica could be larger than the average pore diameter (about 50 Å), the technique lends credence to the approximate crystallite sizes reported in Table I.

Table I. Summary of Catalyst Physical Properties

Batch	Silica Pretreatment	% Re	Metal Surface Area, m ² /gram cat.	Crystallite Size, Å	Dispersion, %	Strength of Impregnation Solution
3B	none	3.34	2.06	46.2	27.7	0.224M
8	none	2.43	1.73	40.0	31.8	0.150M
9	O ₂ at 500°C	2.43	1.30	53.3	23.9	0.150M
4B	O ₂ at 500°C	0.423	(0.95)	(12.9)	(100)	0.0224M
10	none	0.206	(0.46)	(12.8)	(100)	0.0224M

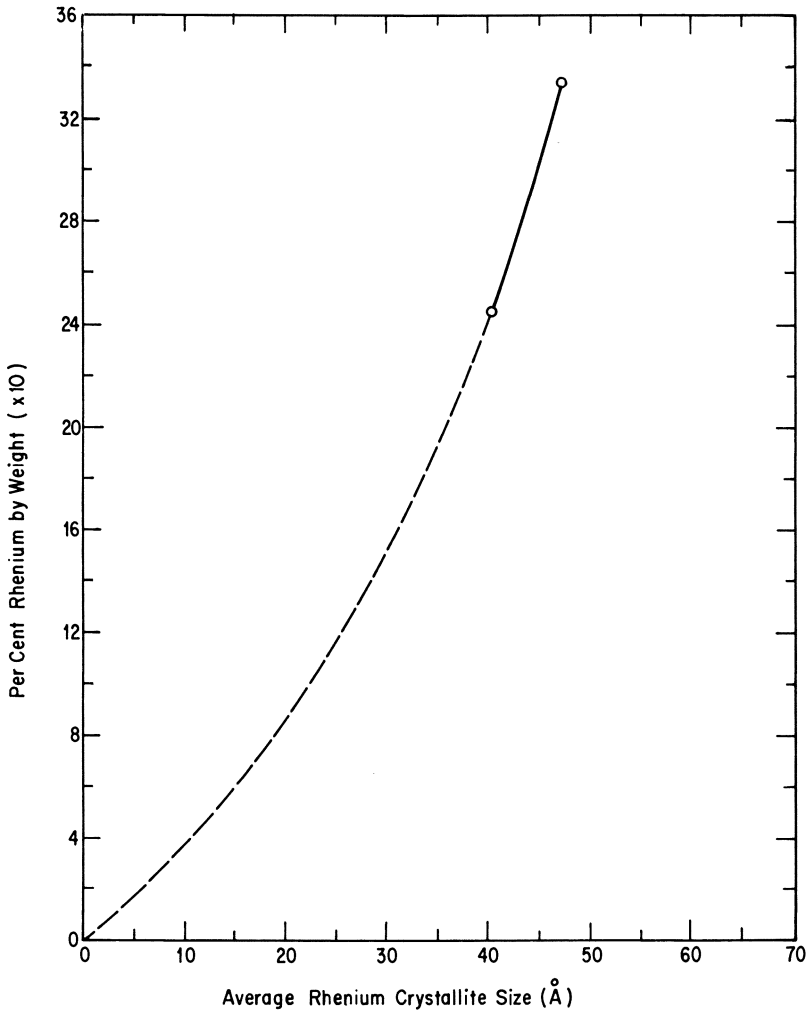


Figure 1. Estimation of crystallite sizes of rhenium on low concentration catalysts

Selectivity Studies. The results of the selectivity studies done in the reaction system are summarized in Figure 2. Here the selectivity for either dehydrogenation or dehydration is defined by the ratio of the concentration of the product of either reaction (either acetone or propylene, respectively) to the sum of the concentrations of both products. The top "band" in Figure 2 shows that the selectivity for the dehydrogenation reaction decreased as the rhenium crystallite size was decreased. This band represents results obtained with catalysts prepared from as-received silica. The second, lower band in Figure 2 indicates that the same general phenomena was exhibited by catalysts prepared from oxygen-cleaned silica. These latter catalysts, however, produced propylene (the dehydration product) almost exclusively at temperatures as low as 168°C when the rhenium crystallite size was about 13 Å. Those catalysts for which the selectivity for the dehydrogenation reaction was lowest (*i.e.*, the

low concentration catalysts) are the same catalysts which apparently failed to chemisorb hydrogen. Also note that the plain silica carrier was essentially inert over the temperature range of interest.

Other differences were shown by the catalysts prepared from as-received silica and those prepared from oxygen-cleaned silica. Catalysts from batches 8 (as-received silica) and 9 (oxygen-cleaned silica) both contained 2.43% rhenium and were used in runs 34 and 35, respectively. During each of these relatively long runs, regeneration of the catalysts was required. These regenerations, done with 2.6% oxygen in nitrogen at 400°C, were required twice as often during run 34 as during run 35. Apparently some other phenomenon rather than crystallite size variation was responsible for these latter observations.

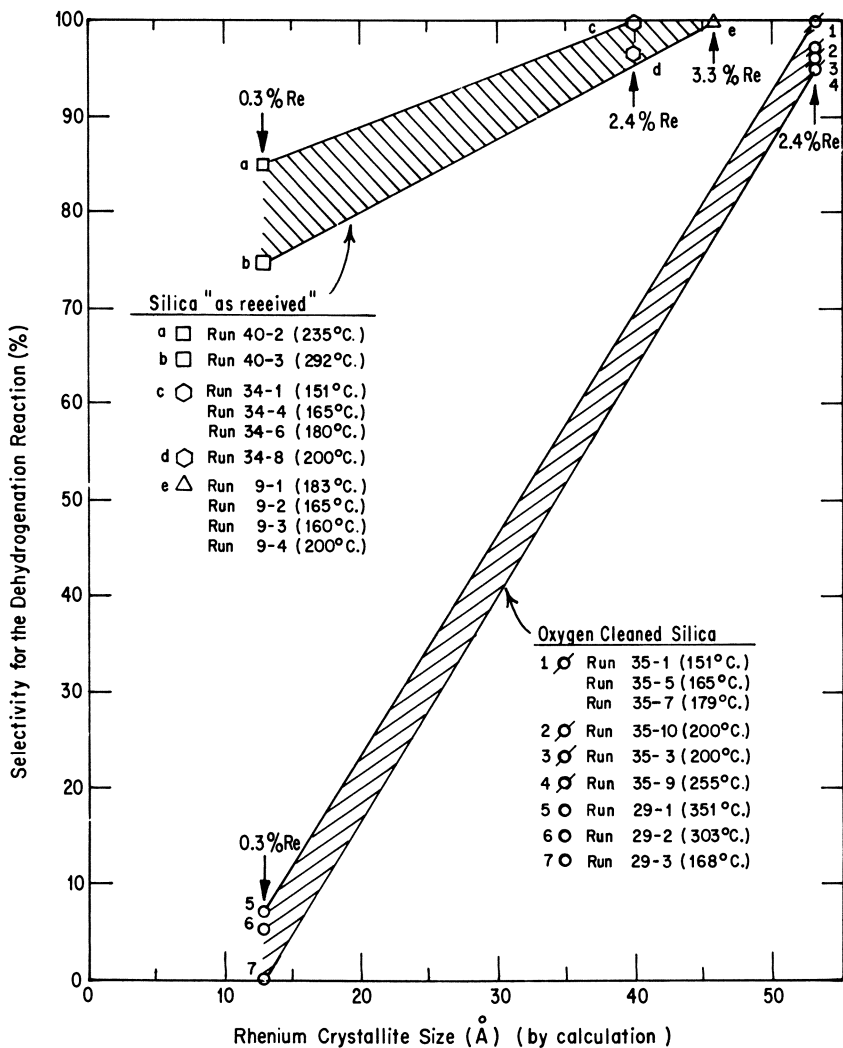


Figure 2. Dependency of selectivity upon rhenium concentration, crystallite size and pretreatment of the silica support

Discussion

The "Negative" Peak Anomaly during Hydrogen Chemisorption. During the attempted measurements of rhenium crystallite size by hydrogen chemisorption, the low concentration catalysts apparently failed to chemisorb hydrogen, and negative chromatogram peaks resulted. To explain this negative peak phenomenon, several experiments were done so that no possibilities, however remote, were neglected. First, we thought that perhaps some of the water formed during the reduction of the rhenium salt was not removed during the 6-hr hydrogen treatment of 500°C and may have been eluted from the sample as hydrogen was subsequently desorbed. If this water had passed a dry ice-acetone trap located between the sample tube and the thermal conductivity cells of the chromatograph, a negative deflection may have resulted (depending upon the relative thermal conductivities of water and the hydrogen-nitrogen mixture). Thus, liquid water was injected into the front of the chromatograph and into the same channel through which the hydrogen-nitrogen mixture was flowing. This injection resulted in a positive rather than a negative peak.

Second, we reasoned that the carrier gas (nitrogen) may have chemisorbed on the rhenium and then desorbed when the sample was heated, giving rise to a negative peak. When argon was substituted for the nitrogen, equilibrium was attained and the heating was repeated, an anomalous negative peak again appeared. The areas under the negative peaks, regardless of the nature of the carrier gas, were essentially the same. It is extremely unlikely that either carrier would chemisorb on the catalyst and that both would chemisorb to about the same extent. Third, plain silica was substituted for the low concentration catalyst, and the negative peak appeared again, regardless of the nature of the carrier gas. Fourth, the catalyst was removed from the sample tube, this device was replaced in the system, and the normal mixture of hydrogen and nitrogen was flowed through it. When steady state was achieved, the glass sample tube was heated in the usual manner to 500°C. No response to this heating occurred on the recorder. Finally, when a sample of the hydrogen-nitrogen mixture flowing over the catalyst sample was trapped in a gas-tight syringe and then injected into the front of the chromatograph, the negative peak appeared.

Any deflection of the recorder must be the result of an imbalance between the two thermal conductivity cells in the chromatograph; changes in either gas flow rate or composition through one of the cells can cause such an imbalance (18). The above elementary experiments were done to determine which of these two kinds of phenomena was responsible for the observed negative peaks. Injection of hydrogen with a gas-tight syringe had indicated that hydrogen *per se* produced a positive peak under the conditions of the experiments, so it was believed before the five experiments were conducted that either chemisorption of the carrier gas or a change in flow rate caused by the heating of the catalyst samples was most likely responsible for the observed phenomenon. (This rationale was confirmed as reasonable by another group of workers (19)).

We concluded that the most reasonable explanation of the negative peak anomaly was the rapid expulsion of the hydrogen-nitrogen mixture from the pores of the microporous catalysts as they were heated to 500°C during the chemisorption procedure. The fact that rapid expansion of the gases in the empty sample tube did not occur to any extent detectable by the chromatograph while the same effect did occur with the microporous catalysts may be reconciled by realizing that heat transfer to the gases in the microporous catalysts was undoubtedly enhanced by the presence of the catalysts themselves.

Crystallite Size Determinations. The apparent lack of hydrogen chemisorption on the small crystallites of the low concentration catalysts is intriguing. At first it might be argued that the negative peaks simply masked the positive hydrogen peak. However, this conclusion is untenable if the following calculation is made. It can be shown that the area under a chromatogram peak caused by hydrogen desorption is directly proportional to the weight fraction of the metal present in the catalyst and inversely proportional to the crystallite diameter (5). Thus, if subscript 1 refers to a catalyst which chemisorbed hydrogen and 2 refers to one which did not,

$$A_2 = \left(\frac{d_1 x_2}{d_2 x_1} \right) A_1 \quad (4)$$

where d is the crystallite diameter, x is the weight fraction, and A is the area under the positive chromatogram peak. For example, if the first entry in Table I is chosen as catalyst 1 and the fourth entry as catalyst 2,

$$A_2 = \left(\frac{46.2}{12.9} \right) \left(\frac{0.423}{3.34} \right) A_1 = 0.45 A_1.$$

Thus, the area under a chemisorption chromatogram peak for the low concentration catalysts should have been about one-half of that exhibited by the high concentration catalysts. This was not the case. In fact, the recorder pen never crossed the baseline into the positive region for any low concentration catalyst studied. For these reasons, we conclude that hydrogen did not chemisorb on the crystallites of the low concentration catalysts.

Nevertheless, the sizes of the supported rhenium crystallites determined by either direct hydrogen chemisorption or the approximation technique of Figure 1 agreed reasonably well with the results of the x-ray line broadening studies. The results of the latter study are, however, higher by a factor of about two even though it is well known (15) that x-ray line broadening often indicates a finer size of crystallites than that found from hydrogen chemisorption.

Indeed, neither method really gives an absolute value for the average size of all crystallites present. Slight differences in the calculated metal crystallite size always arise because the chemisorption technique measures the surface average diameter while x-ray line broadening measures the volume average diameter. Furthermore, the hydrogen chemisorption technique depends upon at least two parameters: a knowledge of the number of hydrogen atoms chemisorbed per surface metal atom and an assumption regarding the shape of the crystallites.

There is disagreement in the literature as to the first parameter for rhenium. This parameter must be known to calculate the average crystallite size for the following reason. Based upon the atomic radius of rhenium, the atomic densities of the three most densely packed planes of a form (the {001}, {100} and {110} planes) can be calculated easily (5). The determination of the average crystallite size from a measurement of a volume of hydrogen desorbed then depends upon the number of surface rhenium atoms which one chemisorbed atom of hydrogen occupies. Yates and Sinfelt (6) assumed a value of one hydrogen atom absorbed per metal surface atom (effective metal area of 7.6 \AA^2 associated with each rhenium surface atom) while Kubicka (14) measured a value of about three hydrogen atoms adsorbed per metal surface atom (20.7 \AA^2) by chemisorbing hydrogen on bulk rhenium of known BET area.

Kubicka's value has been used in this study. If the value of Yates and Sinfelt had been used, the results for the crystallite sizes in Table I would have been higher by a factor of about 3, and better agreement would have been found with the x-ray line broadening results. However, if this factor of 3 is invoked, the smallest crystallite sizes in Table I would have been about 39 Å while the largest would have been about 160 Å. This result would have been in better quantitative agreement with both the x-ray line broadening and scanning electron microscopy results, but would not have altered the fact that the low concentration catalysts not only failed to chemisorb hydrogen but also catalyzed a reaction which is atypical of bulk rhenium metal.

Selectivity Studies. The catalysts used in this study behaved quite differently from the powdered rhenium catalyst of Platanov *et al.* First, some of the high concentration catalysts showed a moderate degree of 2-propanol dehydration, especially above 200°C. The catalyst used in run 34, for example, was prepared from as-received silica, contained 2.43% rhenium by weight, and the average size of the rhenium crystallites was about 40 Å. It showed almost no evidence of dehydration of 2-propanol. On the other hand, the catalyst used in run 35 was prepared from oxygen-cleaned silica, again contained about 2.43% rhenium but had somewhat larger crystallites. As opposed to the catalyst in run 34, this oxygen-precleaned catalyst exhibited a somewhat greater tendency above 200°C to produce propylene (the dehydration product). Also, this latter catalyst showed a significantly longer active life than the as-received silica-rhenium catalyst used in run 34. In fact, repeated attempts to deactivate the oxygen-precleaned catalyst by exposing it to 2-propanol vapors for extended periods only slightly reduced its activity. Another catalyst, that used in run 9, was prepared from as-received silica, contained the highest percentage of rhenium of the catalysts used, and had an average crystallite size of about 46 Å. It showed no tendency whatever to form propylene.

However, this was not the case with the low concentration catalysts. The results of runs 29 and 40 are especially significant since the catalysts used in these runs (batches 7 and 10, respectively) showed a marked tendency to form propylene (as shown in Figure 2). In fact, the selectivity toward dehydration repeatedly approached 100% for the catalyst in run 29. These results were duplicated in a subsequent study (20). The catalyst for which the tendency to produce propylene was most pronounced was a low concentration catalyst prepared from oxygen-cleaned silica with an average rhenium crystallite size of about 13 Å.

Nordberg (21) has shown that organic contaminants readily adsorb on silicas exposed to the atmosphere. The treatment of some silicas in the present study with pure oxygen at 500°C no doubt removed a major part of any such contaminants. Thus, rhenium deposited on oxygen-cleaned silica may have been supported on the silica itself whereas the rhenium deposited on the as-received silica may have been at least partially supported on adsorbed organic materials. Since obvious differences existed between catalysts similar in every way except for the nature of the support, interactions between the metal and the support rather than changes in the crystallite sizes *per se* were responsible to a high degree for the differences in catalyst selectivities, and such effects were most obvious when the crystallite sizes were the smallest.

It may be argued that the so-called low-concentration catalysts may have shown the singular tendency toward 2-propanol dehydration simply because the metal oxide was insufficiently reduced so that a rhenium oxide, possibly

the dioxide (because of the grey color of the catalysts (22)), was responsible for the observed results. Additional evidence can be gained by using the dioxide itself as the active species. However, no definitive evidence for the presence of the completely reduced metal in the low concentration catalysts can be offered. A number of techniques, including hydrogen chemisorption, x-ray diffraction line broadening, and electron microscopy were used in this work to procure this evidence, but they failed. Reasonable explanations of these failures, none of which require that the oxides not be completely reduced, have been offered. Further, other workers (6) have reported that the techniques used in this study have resulted in complete reduction of the perrhenate to metal in supported catalysts.

Only on two points are we certain. First, the 2-propanol dehydration reactions were not caused by the silica support, wall effects in the equipment, or homogeneous reactions since control experiments where the reactor bed was packed with silica gel alone (both treated and untreated with oxygen) failed to demonstrate any evidence of a significant reaction of any sort over the temperature range of interest to this work. Second, it was demonstrated by hydrogen chemisorption and especially by a sharp, distinctive x-ray diffraction pattern that rhenium in this high concentration catalyst was, indeed, well reduced. Therefore, the catalysts containing a lower concentration of the perrhenate initially should have been reduced.

Acknowledgments

One of us (JRF) extends his appreciation to the National Aeronautical and Space Administration for partial support of this work through Grant No. NGT-36-010-001 and to the Owens-Illinois Corp. of Toledo, Ohio for its assistance in many ways.

Literature Cited

1. Gil'debrand, E. I., *Int. Chem. Eng.* (1966) **6**, 449.
2. Taylor, W. F., Yates, D. J. C., Sinfelt, J. H., *J. Catal.* (1965) **4**, 374.
3. Ryashentseva, M. A., Minachev, Kh. M., *Russ. Chem. Rev.* (1969) **38** (11), 944.
4. Platanov, M. S., Anissimov, S. B., Krascheninnikova, W. M., *Ber. Deut. Chem. Ges.* (1936) **69**, 1050.
5. Fowler, J. R., Ph.D. Dissertation, The University of Toledo (1972).
6. Yates, D. J. C., Sinfelt, J. H., *J. Catal.* (1969) **14**, 182.
7. Dorling, T. A., Lynch, B. W. J., Moss, R. L., *J. Catal.* (1971) **20**, 190.
8. Meloche, V. W., Martin, R. L., Webb, W. H., *Anal. Chem.* (1957) **29**, 527.
9. Malouf, E. E., White, M. G., *Anal. Chem.* (1951) **23**, 497.
10. Sinfelt, J. H., *J. Phys. Chem.* (1964) **68**, 344.
11. Denbigh, K., "Chemical Reactor Theory," Cambridge University Press, 1966.
12. Nelsen, F. M., Eggertson, F. T., *Anal. Chem.* (1958) **30**, 1386.
13. Benesi, H. A., Atkins, L. T., Mosely, R. B., *J. Catal.* (1971) **23**, 211.
14. Kubicka, H., *J. Catal.* (1968) **12**, 223.
15. Emmett, P. H., *Catalysis* (1954) **1**, 31.
16. Sinfelt, J. H., Yates, D. J. C., *J. Catal.* (1967) **8**, 82.
17. Bigelow, W. C., Halpern, J. W., *Res. News* (1972) **22** (11 and 12), Office of Research Administration, The University of Michigan, May/June.
18. McNair, H. M., Bonelli, E. J., "Basic Gas Chromatography," Consolidated Printers, Berkeley, Calif., 1968.
19. Benesi, H. A., personal communications (Oct. 4, 1972).
20. Dake, T. W., M.S. Thesis, The University of Toledo (1973).
21. Nordberg, M. E., *J. Amer. Chem. Soc.* (1944) **27**, 299.
22. Nechamkin, H., Kurtz, A. N., Hiskey, C. F., *J. Amer. Chem. Soc.* (1951) **73**, 2828.

RECEIVED January 2, 1974.

Analysis of Reactors with Immobilized Enzymes Subject to Deactivation

HARMIT S. LAMBA and MILORAD P. DUDUKOVIĆ

Chemical Engineering Department, Ohio University, Athens, Ohio 45701

The performance of the plug flow reactor (PFR) and the ideal stirred tank reactor (ISTR) for five enzyme deactivation rates coupled with four common rate expressions for enzyme catalyzed reactions is evaluated for two modes of operation. In the first, the flow rate is constant, in the second, the outlet conversion is kept constant by varying the flow rate. A mathematical technique is developed to compare efficiencies of the two reactors for an arbitrary reaction or deactivation rate. The overall performance of the two ideal reactors is mainly governed by the type of the deactivation equation, and the superiority of the plug flow reactor or the first mode of operation cannot be taken for granted.

With the advancement of technology and the development of new techniques for isolating, extracting, and purifying enzymes, large quantities of some enzymes have become available for commercial use. These highly specific and active catalysts can be used most effectively in various industrial and medical processes when the enzymes are made insoluble (immobilized) by attachment to solid support (1, 2, 3). Immobilized enzymes can be kept in a tubular reactor as a packed, moving, or fluidized bed, or they can be suspended in a stirred tank reactor. The use of immobilized enzymes eliminated the difficult and costly processes of separating the enzymes from the reaction mixture and opened a new field of reactor design which has received considerable attention in recent years (4, 5, 6).

Enzymes, particularly immobilized ones, are subject to deactivation whereby they lose some of their potency as catalysts. While catalyst deactivation has received much attention (7), little has been reported on reactors with enzyme deactivation (8, 9). This problem, however, is a major obstacle in commercial use of immobilized enzymes. In general, since immobilized enzymes are very expensive, it is important to minimize their loss by deactivation if they are ever to be used in large scale production of low value products.

This paper analyzes continuous reactors with immobilized enzymes subject to deactivation and determines the influence of flow patterns and modes of reactor operation on the performance of such systems. It is assumed that the external mass transfer resistance around particles with immobilized enzymes is negligible. Intraparticle diffusion is also neglected. A perfectly mixed ideal stirred tank reactor (ISTR) and a plug flow reactor (PFR) are the reactor

models. These ideal flow patterns represent the two extreme cases of flow through a reactor, and all real systems fall in between (10). Theoretically, the reactors within which catalytic reactions take place and in which the catalyst or enzyme is subject to deactivation can be operated in a number of ways. Three main modes of operation are of practical significance for a reactor which operates initially at a given exit fractional conversion of reactant (substrate) and at a fixed flow rate:

(1) The exit conversion is allowed to drop in time because of catalyst (enzyme) deactivation, and the reactor is shut off (for catalyst regeneration or enzyme replacement) when a predetermined final low exit conversion is reached.

(2) The flow rate through the reactor is decreased in time to compensate for the loss of catalyst (enzyme) activity and to maintain the same fixed exit fractional conversion.

(3) The temperature of the reactor (and/or pH for enzymes) is changed to compensate for decreased activity to keep the exit fractional conversion constant.

The third method has some limitations when operating reactors with immobilized enzymes because of a very narrow temperature range within which enzymes remain active. Therefore, only the first and second mode are considered here. While the first appears to be convenient since it requires almost no control, the second has attractive features since it maintains a constant quality of the product.

We wished to develop a method to compare the performance of the two ideal reactors during both modes of operation, subject to a general type of reaction and deactivation rate. In this way the right reactor type could be chosen at the early design stages. The whole profit equation was not used since it is generally cumbersome, lengthy, and specific for each case. A quantity named profit indicator, η , defined as the amount of the desired product produced per unit of enzyme lost by deactivation, is used throughout this work. Equations 1 and 2 define the profit indicator for ISTR and PFR, respectively.

$$\eta_{\text{ISTR}} = \frac{\int_0^{t_f} qS_0 x(t) dt}{E_0[1 - y(t)]V_{\text{STR}}} \quad (1)$$

$$\eta_{\text{PFR}} = \frac{\int_0^{t_f} qS_0 x(L,t) dt}{\int_0^L E_0[1 - y(Z,t)]AdZ} \quad (2)$$

where

$$AL = V_{\text{PFR}} \quad (3)$$

Profit indicator is a measure of the system's efficiency; it is considered a good criterion for comparing alternative reactor designs and modes of operation since the costs of enzyme purification, isolation, immobilization, and replacement are very high with respect to operating and capital costs. Therefore, to maximize profit, enzyme loss from deactivation must be minimized and the profit indicator maximized. To compare the two ideal reactors in an operation, it is sufficient to examine the ratio of their profit indicators. This quantity was named "profit ratio."

Reaction and Deactivation Rates

Here only single substrate reactions are considered at constant temperature and pH. Under these conditions the reaction rate can be represented as:

$$r_s = -\frac{dS}{dt} = E^m \bar{f}(S) \quad (4)$$

The rate of enzyme deactivation is an empirically evaluated expression. It was found that most deactivation data can be fitted by Equation 5:

$$r_d = -\frac{dE}{dt} = E^n \bar{g}(S) \quad (5)$$

Table I. Single

No.	Type	Mechanism
R1	Michaelis-Menten irreversible	$E + S \xrightleftharpoons[K_{-1}]{K_1} ES \xrightarrow{K} E + P$
R2	Michaelis-Menten reversible	$E + S \xrightleftharpoons[K_2]{K_1} ES \xrightleftharpoons[K_4]{K_3} E + P$
R3	substrate inhibition	$E + S \xrightleftharpoons[K_2]{K_1} ES \xrightarrow{K_3} E + P$ $ES + S \xrightleftharpoons[K_5]{K_4} ESS$
R4	product inhibition	$E + S \xrightleftharpoons[K_2]{K_1} ES \xrightarrow{K_3} E + P$ $E + P \xrightleftharpoons[K_5]{K_4} EP$

The power m was taken to be unity while a value of 1 or 0 was assigned to n . Four different rate expressions of substrate consumption, most often encountered in the literature (11, 12, 13), were chosen for analysis and are given in Table I. All of them conform to the general rate equation (Equation 4) with $m = 1$.

Five different enzyme deactivation equations were selected from the literature (8, 9, 14) (see Table II). Very little is known about the mechanism of enzyme deactivation. The rates of deactivation given in Table II seem to match best the reported qualitative and quantitative findings in the literature. They also conform to the general equation (Equation 5) with $n = 1$ or 0. Zero- and first-order deactivation were reported by many workers. Haldane (14) was the first to report that deactivation could be slowed by the presence of substrates or products, and others supported his findings (15, 16). O'Neill (8) used deactivation expressions (D2) and (D3) in his study. The complex deactivation expressions (D5) was experimentally determined for the enzyme catalase (9).

Enzymes can lose some of their efficiency to catalyze specific reactions for two main reasons—*i.e.*, inhibition and deactivation. Enzyme elution may be considered another form by which reactors with immobilized enzymes lose some of their activity. Inhibition is temporary, can generally be reversed, and can be accounted for by incorporating its effect into the rate expression for the main chemical reaction. Inhibition can be caused by substrates, products, or impurities in the feed. Inhibition effects are incorporated in rate expressions (R3) and (R4) in Table I. Deactivation involves the destruction or modification of one or more functional group of the enzyme, is more permanent, can result from excessive temperature, shear, pH, or impurities, and can be enhanced or hindered by substrates and products. Whatever the microscopic

Substrate Rate Equations

Rate Expression: $\bar{f}(S)$	Dimensionless Rate Expression: $yf(x)$
$\frac{KES}{K_m + S}$ $K_m = \frac{K + K_{-1}}{K_1}$	$y \frac{KE_oS_o(1-x)}{K_{in} + S_o(1-x)}$
$\frac{K_3ES - K_5EP}{K_m + S + K_6P}$ $K_5 = K_4K_2/K_1$ $K_m = (K_2 + K_3)/K_1$ $K_6 = K_4/K_1$	$y \frac{E_oS_o[K_3 - x(K_3 + K_5)]}{K_{in} + S_o - xS_o(1 - K_6)}$
$\frac{K_3E}{1 + \frac{K_m}{S} + \frac{S}{K_i}}$ $K_i = K_5/K_4$	$y \frac{K_iK_3E_oS_o(1-x)}{K_mK_i + K_iS_o(1-x) + S_o^2(1-x)^2}$
$\frac{KES}{S + K_m[1 + P/K_1]}$ $K = K_1K_3$	$y \frac{KK_iE_oS_o(1-x)}{K_mK_i + K_iS_o + S_o x(K_m - K_i)}$

Table II. Deactivation Rate Equations

No.	Type	Deactivation Rate: $E_m\bar{g}(S)$	Dimensionless form: $y\bar{m}g(x)$	Dimensionless Time, θ
D1	zero order	K_d	1	$\frac{K_d t}{E_o}$
D2	first order	$K_d E$	y	$K_d t$
D3	substrate protected	$\frac{K_d E}{S}$	$\frac{y}{1-x}$	$\frac{K_d t}{S_o}$
D4	product protected	$\frac{K_d E}{K' + P}$	$\frac{yS_o}{K' + S_o x}$	$\frac{K_d t}{S_o}$
D5	complex	$K_d E \left[\frac{AP}{B + P} + CP \right]$	$y \left[\frac{Ax}{B + S_o x} + Cx \right]$	$K_d t S_o$

mechanism of the deactivation process, it can be considered an additional chemical reaction that is occurring in addition to the main reaction. Deactivation effects have to be accounted for by a separate rate equation such as those in Table II.

Each substrate consumption equation has been coupled with each enzyme deactivation equation. This combination was called a reaction scheme. Twenty reaction schemes were obtained, and each has been studied for ISTR and PFR models and for two modes of reactor operation. Some kinetic parameters were varied to observe this effect on reactor performance.

To compare performance of the reactor systems and to evaluate the profit indicator, the following quantities are needed: (1) reactor size, (2) total product obtained, and (3) the enzyme lost by deactivation. These were calculated for each reaction scheme and for both modes of operation. Details of the calculations and many numerical results were represented by Lamba (17). Only the general approach taken is given here.

In most enzyme-catalyzed reactions of practical significance, deactivation is relatively slow. Its characteristic time is large compared with the mean transit time through the reactor. Therefore, the pseudo-steady-state approximation can be used—*i.e.*, a steady-state concentration profile can be assumed for any particular value of the activity profile at any moment in time.

To make the analysis comprehensive, the following dimensionless variables are used:

$$\text{Fractional conversion} \quad x = \frac{S_0 - S}{S_0} \quad (6)$$

$$\text{Fractional activity} \quad y = \frac{E}{E_0} \quad (7)$$

$$\text{Dimensionless time} \quad \theta = \frac{t}{N} \quad (8)$$

where N is a proper combination of constants for a given deactivation equation. The rate and deactivation equations in terms of dimensionless variables are given in Tables I and II, respectively.

First Mode of Reactor Operation

The initial exit conversion, x_e^1 , is chosen, and the flow rate, q , through the reactor is kept constant in this mode of reactor operation. The reactor is sized to satisfy these requirements. Since the flow rate is kept constant, the exit conversion decreases with time because of the loss of enzyme activity. Equal enzyme loading was assigned to both reactors, and the same substrate concentrations are used in the feed.

Analysis of the ISTR. According to the pseudo-steady-state assumption the equations describing an isothermal operation of the ideal stirred tank reactor (ISTR) are:

$$\tau_c = \frac{x}{yf(x)} \quad (9)$$

$$\frac{dy}{d\theta} = -y^n g(x) \quad n = 0, 1 \quad (10)$$

Equation 9 is the basic design equation for an ISTR where $yf(x)$ is the reaction rate; Equation 10 describes the deactivation process. Clearly, both

conversion and activity are functions of time only. The derivative of activity with respect to time may be evaluated by chain rule as follows:

$$\frac{dy}{d\theta} = \frac{dy}{dx} \frac{dx}{d\theta} \quad (11)$$

Evaluating dy/dx from Equation 9 and substituting this along with an expression for y obtained from Equation 9 into Equation 10 yields Equation 12 for $dx/d\theta$:

$$\frac{dx}{d\theta} = - \frac{\tau_c^{1-n} x g(x) [f(x)]^{2-n}}{f(x) - x f'(x)} \quad (12)$$

Equations 10 and 12 can now be integrated. In the simplest cases of zero- and first-order deactivation with $g(x) \equiv 1$, Equation 10 can be integrated directly (8), yielding explicitly y as a function of θ . Substituting this into Equation 9 gives an implicit relationship between x and θ . For the more complex cases considered, Equation 12 can be integrated analytically giving explicit, very lengthy relationships for θ as a function of x . Resolving Equation 9 for x , which can be readily accomplished when the resulting expression is a quadratic but becomes cumbersome for a cubic, and substituting into the above expression for $\theta = \theta(x)$ yields a relationship between θ and y . These results will be presented elsewhere (18).

We found it more useful to integrate Equations 10 and 12 numerically by a fourth-order Runge-Kutta method to obtain values for conversion and activity at equally spaced values of time, θ . These results were used to evaluate the profit indicator for various times of reactor operation, θ_t , corresponding to different final exit conversions. The profit indicator was calculated using the following formula:

$$\eta_{ST} = \left(\frac{S_o}{E_o}\right) \left(\frac{N}{\tau_c}\right) \int_0^{\theta_t} \frac{x(\theta) d\theta}{1 - y(\theta)} \quad (13)$$

Analysis of the PFR. Using the pseudo-steady-state assumption the equations describing the performance of an isothermal plug flow reactor (PFR) can be written as:

$$\frac{\partial x}{\partial z} = \tau_p y f(x) \quad (14)$$

$$\frac{\partial y}{\partial \theta} = - y^n g(x) \quad n = 0, 1 \quad (15)$$

The reactor space time, τ_p , is obtained by:

$$\tau_p = \int_0^{x(0,1)x - x_e^i} \frac{dx}{f(x)} \quad (16)$$

while z represents the dimensionless distance along the reactor. For the zero- and first-order deactivation, Equations 14 and 15 were solved analytically (10). In general, both conversion and activity are functions of time and position, and Equations 14 and 15 have to be solved simultaneously. Ozawa (19) and Bischoff (20) considered packed bed reactors with catalyst deactivation and developed analytical solutions for Equations 15 and 16 when $n = 1$ and $g(x) = f(x)$.

Lamba (17) numerically solved the general system of Equations 15 and 16 using a modification of a numerical method of Gonzales and Spencer (21). When the exit conversion, $x(\theta, 1)$, and the activity profile in the reactor are obtained, the profit indicator can be calculated as a function of reactor operating time, θ_t .

$$\eta_{FF} = \left(\frac{S_o}{E_o}\right) \left(\frac{N}{\tau_p}\right) \frac{\int_0^{\theta_t} x(\theta, 1) d\theta}{\int_0^1 [1 - y(\theta_t, z)] dz} \quad (17)$$

If it is not necessary to examine the activity profile as a function of position in the reactor and the profit indicator is the only quantity to be calculated, a new lumped variable called total activity, Y , may be defined by:

$$Y(\theta) = \int_0^1 y(\theta, z) dz \quad (18)$$

Total activity is a function of time only. The following solution can be applied to Equations 14 and 15 when $n = 1$. Equation 14 can be solved for activity, y , which is then substituted into Equation 15. Upon integrating the resulting expression along the reactor length, the following equation is obtained for total activity, Y :

$$\frac{dY}{d\theta} = -\frac{1}{\tau_p} \int_0^{x(\theta, 1)} \frac{g(x)}{f(x)} dx \quad (19)$$

Similarly, Equation 14 may be solved for y and integrated with respect to z from 0 to 1. This gives an implicit relationship for the exit conversion as a function of total activity:

$$Y(\theta) = \frac{1}{\tau_p} \int_0^{x(\theta, 1)} \frac{dx}{f(x)} \quad (20)$$

Now the chain rule can be applied to the derivative $dY/d\theta$, as used previously in the analysis of ISTR, and an ordinary differential equation for the variation of the exit conversion with time is obtained:

$$\frac{dx(\theta, 1)}{d\theta} = -f[x(\theta, 1)] \int_0^{x(\theta, 1)} \frac{g(x)}{f(x)} dx \quad (21)$$

Equation 21 can be solved analytically, resulting in very lengthy explicit relationships for operating time, θ_t , in terms of final conversion, $x(\theta_t, 1)$. Integrating the expression for dY/dx , the relationship between final total activity, $Y(\theta_t)$ and final exit conversion, $x(\theta_t, 1)$, can be obtained. These lengthy results will be presented elsewhere (18). In this work only the integrals in Equations 19 and 21 were obtained analytically. The resulting differential equations were integrated by the fourth-order Runge-Kutta method. The profit indicator can now be evaluated by:

$$\eta_{FF} = \left(\frac{S_o}{E_o}\right) \left(\frac{N}{\tau_p}\right) \frac{\int_0^{\theta_t} x(\theta, 1) d\theta}{1 - Y(\theta_t)} \quad (22)$$

Second Mode of Reactor Operation

In this mode of reactor operation the exit conversion is kept constant at all times, and the flow rate through the reactor is decreased to compensate for the loss of enzyme activity. The same enzyme loadings and same feed substrate concentrations as in the previous mode are used. The exit conversion, x_e , equal to the initial exit conversion, x_e^i , in the first mode of operation is used, and same reactor operating times are considered.

Analysis of the ISTR. The performance of an ISTR is still described by Equations 9 and 10. However, the reactor space time, τ_c , is no longer constant but varies with time while conversion x is a constant equal to the fixed exit conversion x_e . Equation 10 can now be integrated directly;

$$y(\theta) = \begin{cases} [1 - g(x_e)\theta] \left[u(\theta_t) - u\left(\theta_t - \frac{1}{g(x_e)}\right) \right] & \text{for } n = 0 \\ \exp[-(x_e)\theta g] & \text{for } n = 1 \end{cases} \quad (23)$$

A dimensionless quantity, $\lambda(\theta)$, proportional to the relative variation in flow rate can be defined as:

$$\lambda(\theta) = \frac{\tau_c^i}{\tau_c(\theta)} = y(\theta) \quad (24)$$

where τ_c^i is the initial reactor space time obtainable from Equation 9, when $y = 1$ and $x = x_e$.

The profit index can be calculated from Equation 25;

$$\eta_{ST} = \left(\frac{S_o}{E_o}\right) \left(\frac{N}{\tau_c^i}\right) x_e \int_0^{\theta_t} \frac{\lambda(\theta) d\theta}{1 - y(\theta)} \quad (25)$$

and takes the form:

$$\eta_{ST} = \left(\frac{S_o}{E_o}\right) \left(\frac{N}{\tau_c^i}\right) \frac{x_e}{g(x_e)} \left\{ \begin{cases} \left[1 - \frac{g(x_e)}{2} \theta_t \right] \left[u(\theta_t) - u\left(\theta_t - \frac{1}{g(x_e)}\right) \right] + \frac{1}{2} u\left(\theta_t - \frac{1}{g(x_e)}\right); & n = 0 \\ 1 & n = 1 \end{cases} \right. \quad (26)$$

Analysis of the PFR. The equations describing the performance of a PFR can be written (for $n = 1$) as:

$$\lambda \frac{\partial x}{\partial z} = \tau_p^i y f(x) \quad (27)$$

$$\frac{\partial y}{\partial \theta} = -y g(x) \quad (28)$$

where

$$\lambda(\theta) = \frac{\tau_p^i}{\tau_p(\theta)} \quad (29)$$

and τ_p^i , the initial reactor space time, is given by Equation 16. A numerical finite element method was developed to obtain $x(\theta, z)$, $y(\theta, z)$ and $\lambda(\theta)$ (22). The reactor was represented by N stirred tanks in series, with conversions x_i and activities y_i ($i = 2 \dots N$). The method resulted in a set of N ordinary

differential equations for the first $N - 1$ x_i 's and λ . Activity, y_i , at various locations was also obtained.

If it is not necessary to evaluate activity at different positions and if the concentration profile within the reactor is not needed, the profit indicator may be obtained in a simpler way. If total activity is defined again by Equation 18 and Equation 28 is integrated along the reactor length, after y has been substituted from Equation 27, the following ordinary differential equation is obtained:

$$\frac{dY}{d\theta} = - \frac{\lambda(\theta)}{\tau_p^i} \int_0^{x_e} \frac{g(x)}{f(x)} dx \quad (30)$$

The integral in Equation 30 is a constant since the limits of integration are independent of time owing to the fact that both entrance and exit conversions are kept constant. Integrating Equation 27 along the reactor length yields an expression for Y :

$$Y(\theta) = \frac{\lambda(\theta)}{\tau_p^i} \int_0^{x_e} \frac{dx}{f(x)} \quad (31)$$

Equation 31 establishes the relationship between λ and Y , the integral being a constant. Combining Equations 31 and 30, an ordinary differential equation for Y is obtained which can readily be solved to give;

$$Y(\theta) = \exp \left[- \left(\frac{\int_0^{x_e} \frac{g(x)}{f(x)} dx}{\int_0^{x_e} \frac{dx}{f(x)}} \right) \theta \right] \quad (32)$$

The profit indicator can now be calculated from Equation 33;

$$\eta_{PF} = \left(\frac{S_o}{E_o} \right) \left(\frac{N}{\tau_p^i} \right) x_e \int_0^{\theta_t} \frac{\lambda(\theta) d\theta}{1 - Y(\theta)} \quad (33)$$

which gives:

$$\eta_{PF} = \left(\frac{S_o}{E_o} \right) \frac{x_e}{N} \int_0^{x_e} \frac{g(x)}{f(x)} dx \quad (34)$$

For zero-order deactivation, $n = 0$, occurring in Equation D1 used in this work, no dependence on substrate and product concentrations was considered—*i.e.*, $g(x) \equiv 1$. Then:

$$\lambda(\theta) = Y(\theta) = 1 - \theta \quad (35)$$

and the profit indicator is given by Equation 36.

$$\eta_{PF} = \left(\frac{S_o}{E_o} \right) \left(\frac{N}{\tau_p^i} \right) x_e \left\{ \left[1 - \frac{\theta_t}{2} \right] [u(\theta_t) - u(\theta_t - 1)] + \frac{1}{2} u(\theta_t - 1) \right\} \quad (36)$$

Results and Discussion

When the form of the reaction and deactivation rates are given and the kinetic constants are known, profit indicator can be evaluated for each reactor

in both modes of operation above. The largest of these four numbers determines the best flow pattern and the better mode of operation.

In evaluating the profit indicator, η , in general, five quantities, independent of the kinetics, have to be chosen: (1) feed substrate concentration, (2) initial enzyme loading, (3) initial exit conversion x_e^i , (4) flow rate, and (5) reactor operating time θ_r . The first two can usually be varied within a narrow range and will depend upon a particular process. The initial exit conversion and flow rate will then determine the reactor space time, their values being bounded by the reactor cost and desired production. When these four quantities are fixed, the profit indicator for the second mode of operation is entirely determined in first-order deactivation dependence on activity [(D2), (D3), (D4), (D5)] and decreases linearly for zero-order deactivation (D1). For the first mode of operation the profit indicator depends on reactor operating time. Either a local extremum exists (minimum for some of the cases studied), or the indicator decreases (observed for most of the cases studied), or increases with the operating time. The desired value of θ_f has to be determined by considering how low a final exit conversion may be tolerated.

The profit ratio (ratio of the two profit indicators for the same mode of operation) determines which flow pattern is better in a given mode of operation. For the first mode it can be represented as:

$$p^I = \frac{\eta_{PF}}{\eta_{ST}} = \left(\frac{\tau_c}{\tau_p} \right) \left(\frac{\int_0^{\theta_f} x(\theta, 1) d\theta}{\int_0^{\theta_f} x(\theta) d\theta} \right) \left(\frac{1 - y(\theta_f)}{1 - Y(\theta_f)} \right) = (P_1)(P_2)(P_3) \quad (37)$$

where P_1 represents the ratio of ISTR and PFR volumes, P_2 is a measure of the ratio of product produced in PFR and ISTR, and P_3 is the ratio of enzyme lost in ISTR and PFR. $(P_1)(P_2)$ is the ratio of quantities of product produced per unit reactor volume for each reactor while $(P_1)(P_3)$ yields the ratio of amounts of enzyme lost per unit flow rate in the two reactors.

The profit ratio for the second mode of operation takes the following form:

$$p^{II} = \frac{\eta_{PF}}{\eta_{ST}} = \begin{cases} \left(\frac{\tau_c^i}{\tau_p^i} \right) & n = 0 \\ \frac{\tau_c^i g(x_e)}{\int_0^{x_e} \frac{g(x)}{f(x)} dx} & n = 1 \end{cases} \quad (38)$$

Lamba (17) studied the effect of various kinetic parameters on the profit indicator for all 20 reaction schemes arising from the combination of reaction rates presented in Table I and deactivation rates in Table II. Some of his results for the first mode of operation [presented in the Appendix of his M.S. Thesis (17)] show that the profit indicator can be influenced considerably by variation of kinetic parameters. However, the trends favoring one flow pattern remain the same except for the substrate inhibition rate expression (R3). Changes in activity and exit conversion with operating time θ_f for all the cases were presented graphically (17). Exit conversions and activities for two reaction schemes are presented in Figures 1 and 2. The variation of exit conversion and activity with operating time depends mainly on the deactivation equation. The activity profiles in the PFR also depend on the deactivation equation, as expected. For substrate protected deactivation (D3) the decay of activity near the entrance is much smaller than at the reactor end, for product protected

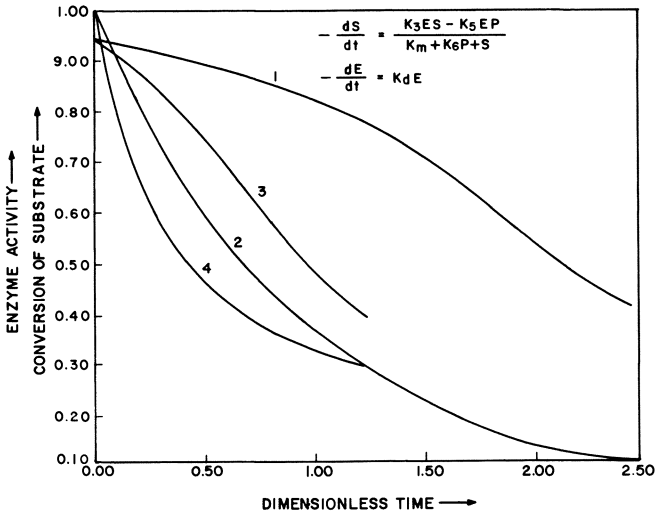


Figure 1. Conversion and activity vs. operating time for first-order deactivation and reversible Michaelis-Menten rate expression. 1. Conversion in ISTR; 2. activity in ISTR; 3. conversion in PFR; 4. activity in PFR. [Constants used: $K_s = 200$, $E_o = 5 \times 10^{-7}$, $S_o = 3 \times 10^{-4}$; $K_s = 0.01$, $K_m = 10^{-4}$; $K_e = 10^{-3}$; $K_d = 10^{-7}$.]

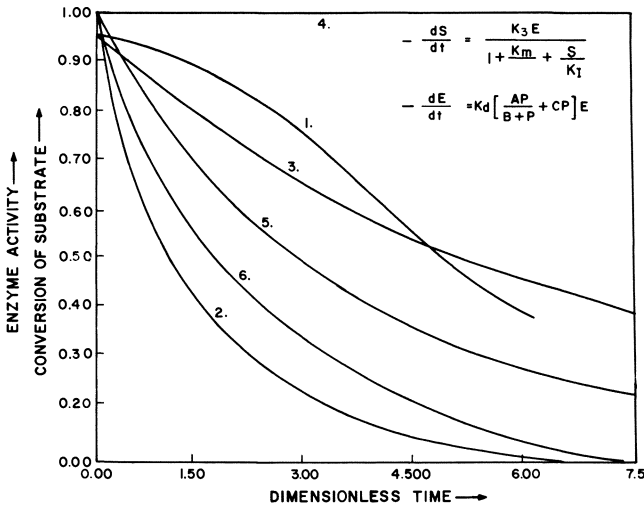


Figure 2. Conversion and activity vs. operating time for complex deactivation and substrate inhibited rate expression. 1. Conversion in ISTR; 2. activity in ISTR; 3. conversion in PFR; 4. activity in PFR at entrance; 5. activity in PFR at middle; 6. activity in PFR at exit. [Constants used: $K_s = 2 \times 10^3$; $K_i = 10^{-3}$; $S_o = 3 \times 10^{-4}$; $E_o = 5 \times 10^{-7}$; $K_m = 10^{-4}$; $K_d = 10^{-7}$; $A = 7.2 \times 10^{-2}$; $B = 1.5 \times 10^{-1}$; $C = 1.85 \times 10^{-2}$.]

deactivation (D4) the opposite is true, while the decay of activity is uniform throughout the reactor for zero (D1) and first-order deactivation (D2).

Figures 3 and 4 illustrate the change of the profit indicator (index) and the profit ratio with final exit conversion—*i.e.*, with reactor operating time. Other cases show similar behavior, the profit ratio either monotonically decreases with operating time or shows a local minimum. For a given deactivation equation only P_1 will change considerably with the type of the substrate reaction rate while P_2 and P_3 remain almost constant. For the high initial exit conversion of 0.95, values of P_1 were generally large (2 to 5) while the values of P_3 were around 1.2. P_2 values were considerably less than 1 (from 0.33 to 0.67) for product protected deactivation (D4), first-order deactivation (D2), zero-order deactivation (D1); close to 1 for the complex deactivation expression (D5), and slightly above 1 for the substrate protected deactivation (D3). For the last type of deactivation (D3) the PFR seems inherently better than the ISTR. The profit ratio is larger than 1 for most of the cases considered, indicating a better performance of the PFR. However, for zero-order deactivation (D1) and substrate inhibition (R3) the profit ratio falls to 0.65–0.91 although P_1 varies between 1.53 and 2.16. For this particular rate expression (R3) one can select such values of kinetic parameters for which P_1 is less than 1, thus possibly influencing the profit ratio for various deactivation rates. An example was constructed using the rate (R3) with first-order deactivation (D2), showing that when P_1 is low ($P_1 = 0.61$) the profit ratio favors the ISTR ($p^1 = 0.63$).

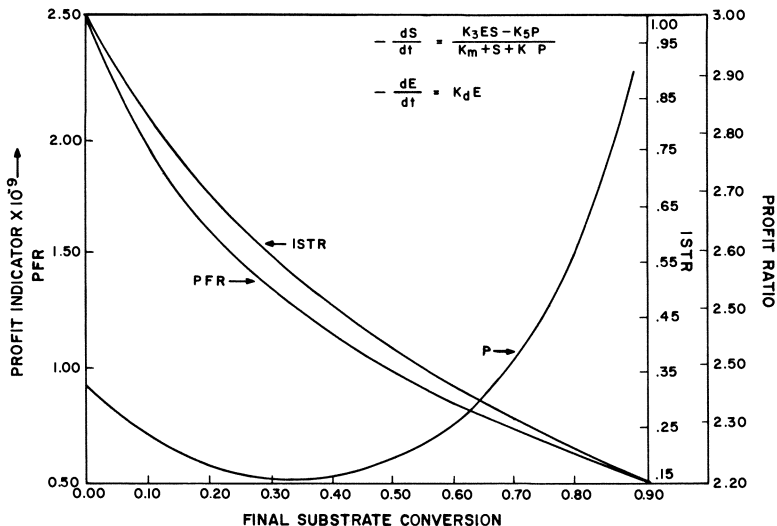


Figure 3. Profit indicators and profit ratio vs. final substrate exit conversion for first-order deactivation and reversible Michaelis-Menten rate expression

The two reactor models and two modes of operation are compared in Table III. Those values of kinetic constants were used which yield the highest profit indicators (17). The initial exit conversion was fixed at 0.95 and the final one at 0.40 for the first mode of operation. Exit conversion of 0.95 and

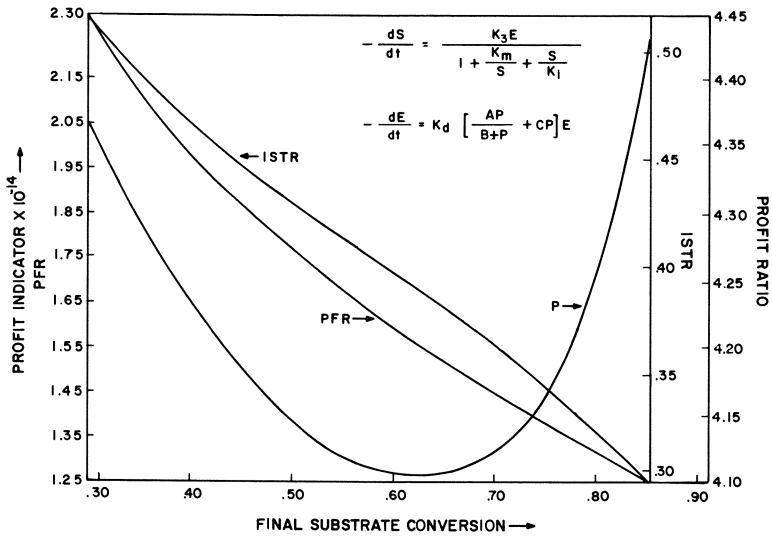


Figure 4. Profit indicators and profit ratio vs. final substrate exit conversion for complex deactivation and substrate inhibited rate expression

Table III. Comparison of the Two Modes Substrate Consumption Equation

Enzyme Deactivation Equation	Mode	KES	
		$K_m + S$	$S + K_m + K_m P / K_i$
ISTR Profit Indices			
K_d	I	2.03×10^3	9.83×10^2
	II	1.28×10^3	5.61×10^2
$K_d E$	I	8.65×10^9	4.69×10^9
	II	9.30×10^7	2.20×10^9
$K_d E / S$	I	2.72×10^6	2.99×10^6
	II	3.40×10^4	3.14×10^4
$\frac{K_d E}{K' + P}$	I	2.31×10^6	2.50×10^6
	II	1.35×10^3	1.22×10^6
$K_d E \left(\frac{AP}{B+P} + CP \right)$	I	3.91×10^{13}	4.20×10^{13}
	II	1.63×10^{13}	1.48×10^{13}
PFR Profit Indices			
K_d	I	4.96×10^3	3.46×10^3
	II	4.38×10^3	2.80×10^3
$K_d E$	I	1.51×10^{10}	1.14×10^{10}
	II	1.38×10^{10}	9.30×10^9
$K_d E / S$	I	1.18×10^6	1.67×10^6
	II	4.53×10^6	5.07×10^6
$\frac{K_d E}{K' + P}$	I	3.06×10^6	4.70×10^6
	II	2.92×10^6	4.08×10^6
$K_d E \left(\frac{AP}{B+P} + CP \right)$	I	1.46×10^{14}	2.01×10^6
	II	8.00×10^{11}	9.80×10^{12}
		$K = 2 \times 10^{-3}$	$K_m = 1 \times 10^{-4}$
		$K_m = 5 \times 10^{-5}$	$K = 2 \times 10^3$
			$K_i = 1 \times 10^{-3}$

* $S_0 = 3 \times 10^{-4}$; $E_0 = 5 \times 10^{-7}$; $K_d = 1 \times 10^{-7}$.

the operating time corresponding to the one in the first mode were used in the second mode. For a given reaction rate and deactivation equation with fixed kinetic parameters the four profit indicators in Table III provide the information about the best flow pattern and more favorable mode of operation.

Conclusions

A method is developed to compare the performance of two ideal reactors subject to enzyme deactivation. The amount of product produced per unit of enzyme lost by deactivation is chosen as a measure of reactor efficiency. This quantity, the profit indicator, is evaluated for each reactor and two different modes of operation. The ordinary differential equations describing the ISTR can be integrated directly while the partial differential equations for the PFR can be reduced to readily integrable ordinary differential equations by an integral transformation. This powerful method provides the information necessary to evaluate PFR performance. Alternative numerical techniques are developed to evaluate activity and conversion profiles within the PFR.

The ratio of two profit indicators for a fixed mode of operation may be as high as 6 (for the cases considered), and the performance of the same reactor in two modes of operation may differ by a factor of 2. Thus, the choice of a proper flow pattern and mode of operation is important for systems subject

of Reactor Operation for ISTR and PFR^a

<i>Substrate Consumption Equation</i>	
$1 + \frac{K_m}{S} + \frac{S}{K_i}$	$\frac{K_3ES - K_5EP}{S + K_m + K_3P}$
ISTR Profit Indices	
1.16×10^3	1.16×10^2
7.12×10^2	7.00×10^1
5.38×10^{10}	5.53×10^8
2.74×10^9	2.74×10^8
3.38×10^5	3.46×10^4
3.90×10^4	3.90×10^5
2.89×10^6	2.96×10^5
1.52×10^6	1.52×10^5
4.77×10^{13}	4.90×10^{12}
1.82×10^{13}	1.83×10^{12}
PFR Profit Indices	
3.48×10^3	3.78×10^3
2.98×10^3	3.15×10^9
1.08×10^{10}	1.21×10^9
9.50×10^9	1.02×10^5
1.67×10^9	1.81×10^5
5.76×10^{11}	5.94×10^4
4.40×10^6	4.95×10^5
4.08×10^{12}	4.44×10^3
2.03×10^{14}	2.19×10^{13}
1.07×10^{18}	1.12×10^{11}
$K_m = 1 \times 10^{-4}$	$K_m = 1 \times 10^{-4}$
$K_3 = 2 \times 10^3$	$K_3 = 2 \times 10^2$
$K_1 = 1 \times 10^{-3}$	$K_5 = 1 \times 10^{-2}$
	$K_6 = 1 \times 10^{-3}$

to enzyme deactivation. Although the PFR seems to be superior to the ISTR for most of the cases studied, the opposite can be true for a certain type of rate expression—*e.g.*, substrate inhibition. The superiority of the first mode when the flow rate is kept constant cannot be taken for granted either. For a given reaction rate and for the known type of enzyme deactivation the evaluation of the profit indicator will establish the superior flow pattern and the better mode of operation.

Nomenclature

A	reactor cross-sectional area; deactivation constant
B	deactivation constant
C	deactivation constant
E	enzyme concentration; enzyme activity
E_0	initial enzyme concentration
$\bar{f}(S)$	concentration dependence of the reaction rate
$f(x)$	conversion dependence of a dimensionless rate expression
$\bar{g}(S)$	concentration dependence of the deactivation rate
$g(x)$	conversion dependence of a dimensionless deactivation expression
K_d	deactivation rate constant
K'	deactivation constant
$K, K_1, K_2, K_3, K_4, K_5, K_{-1}$	reaction rate constants
K_m	Michaelis constant
L	reactor length
m	constant; power of activity in the rate expression
N	constant used to define dimensionless time
n	constant; power of activity in the deactivation expression
P_1, P_2, P_3	constants
p	profit ratio
q	flow rate
r_d	deactivation rate
r_s	reaction rate
S	substrate (reactant) concentration
S_0	substrate (reactant) concentration in the feed
t	time
t_f	reactor operating time
$u(t - a) = \begin{cases} 0 & t < a \\ 1 & t > a \end{cases}$	Heaviside's unit step function
V	reactor volume
x	fractional conversion of substrate
x_e	exit conversion
x_e^1	initial exit conversion
Y	total activity; average activity in PFR
y	activity; fractional activity
Z	distance along the reactor length
z	dimensionless distance

Greek Letters

η	profit indicator
θ	dimensionless time
θ_f	dimensionless reactor operating time
λ	dimensionless flow rate
τ	space time

Subscripts

c	ideal stirred tank reactor
p	plug flow reactor
PF	plug flow reactor
ST	ideal stirred tank reactor

Superscripts

i	initial
I	first mode of operation
II	second mode of operation

Literature Cited

1. Kay, G., *Process Biochem.* (1968) **3**(8), 36-39.
2. Silman, H. I., Katchalski, E., *Ann. Rev. Biochem.* (1968) **35**, 873-908.
3. Weetall, H. H., *Res. Develop.* (Dec. 1971) 18-22.
4. Baker, S. A., Emery, A. N., Novais, J. M., *Process Biochem.* (1973) **6**, 11-13.
5. Lilly, M. D., Dunill, P., *Process Biochem.* (1973) **6**(8), 29-35.
6. Lilly, M. D., Dunill, P., *Biotech. Bioeng. Symp. No. 3* (1972) 221-227.
7. Butt, J. B., *ADVAN. CHEM. SER.* (1972) **109**, 259-496.
8. O'Neill, S. P., *Biotech. Bioeng.* (1972) **14**, 437-491.
9. *Ibid.*, pp. 201-205.
10. Levenspiel, O., "Chemical Reaction Engineering," Wiley, New York, 1972.
11. Bernhard, S., "The Structure and Function of Enzymes," Benjamin, New York, 1968.
12. Lehninger, A. L., "Biochemistry," Worth, New York, 1972.
13. Plowman, K. M., "Enzyme Kinetics," McGraw-Hill, New York, 1972.
14. Haldane, J. B. S., "Enzymes," The M.I.T. Press, Cambridge, 1960.
15. Staub, M. C., Denes, G., *Biochem. Biophys. Acta* (1967) **139**, 519-521.
16. Scrutton, M. C., Utter, M. F., *J. Biol. Chem.* (1968) **240**, 3714-3723.
17. Lamba, H. S., M.S. Thesis, Department of Chemical Engineering, Ohio University, Athens, 1973.
18. Duduković, M. P., Lamba, H. S., unpublished data.
19. Ozawa, Y., *Chem. Eng. Sci.* (1970) **25**, 529-533.
20. Bischoff, K. B., *Ind. Eng. Chem.* (1969) **8**(4), 665-668.
21. Gonzales, L. O., Spencer, E. H., *Chem. Eng. Sci.* (1963) **18**, 753-766.
22. Duduković, M. P., Engineering Analysis, Course notes, 1973, Ohio University, Athens.

RECEIVED January 2, 1974. Work supported in part by the Ohio University Research Committee under grant OURC 443.

Description of Polymerization Dynamics by Using Population Density

D. C. TIMM and J. W. RACHOW

Department of Chemical Engineering, University of Nebraska,
Lincoln, Neb. 68508

Molecular distributions for chain-growth polymerizations are described in terms of a model based on conservation of population, a lumped parameter model. In the area of experimental analysis, theoretical relationships readily yield to graphical interpretation. Steady-state macromolecular distributions for polystyrene as functions of degree of polymerization, initiated by n-butyllithium and by 2,2-azobisisobutyronitrile, correlate. Polymerization dynamics are simulated by using the method of characteristics. Transient response surfaces for an anionic, batch polymerization of styrene are such that a single integration is required. Step responses to perturbations in residence time are simulated for a free radical polymerization of vinylidene chloride in a continuous, well mixed tank reactor.

Standard procedures for simulating molecular distributions, including number and mass fractions, as functions of degree of polymerization and time are quasi-steady-state approximation (1, 2, 3), Eigenzeit transformation (4), Z transform (5, 6, 7), generating functions (8, 9), and direct integration (10, 11). The intricacy of relationships is such that the implementation of molecular distribution data explicitly into kinetic analysis has yet to be developed. Published work (12, 13, 14) demonstrates the complexity of simulating molecular distributions given kinetic rate information *a priori*. Experimental techniques for updating kinetic mechanism subject to molar or mass distributions of resinous materials have not been reported.

The major objective of this research is to develop an alternative analysis, one which is amenable to interpretation of experimental data as well as numerical simulations. Population density analysis results in working expressions that yield to graphical interpretation, including free radical and carbanion polymerization mechanisms. Experimental verification is included. Dynamic response surfaces for batch and continuous modes of reactor operation are simulated by using the method of characteristics.

Molecular Distributions

Resinous materials are comprised of macromolecules distributed according to degree of polymerization. Traditionally, the distribution is discrete, being defined only for integer values of degree of polymerization. As shown later,

distinct advantages exist for a description in terms of a continuous independent variable. Population density is defined implicitly by the integral

$$\int_{n=j}^{n=k} A(n,t) \, dn = N(k,t) - N(j,t) \tag{1}$$

where the continuous variables $A(n,t)$ and $N(k,t)$ are the differential, molar distribution and the integral, molar distribution, respectively. Population density is defined explicitly by

$$A(n,t) = \partial N(n,t) / \partial n \tag{2}$$

Thus, population density is the slope of the continuous cumulative molar distribution, evaluated at a specific degree of polymerization and time. The physical significance of the differential distribution, Equation 2, and the cumulative distribution, Equation 1, will be exemplified in the following derivations.

A Carbanion Polymerization. Styrene will polymerize by the following carbanion mechanism (15, 16, 17) if initiated by *n*-butyllithium:

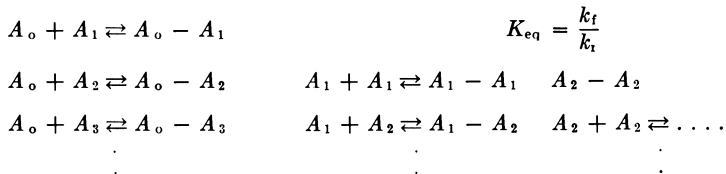
Initiation



Propagation



Association



Associated complex $A_j - A_k$ is inert toward the incorporation of monomer. The association number y has been reported to be from 2 to 7 (15, 16, 18, 19).

A method for determining rate constants subject to observations of measurable quantities, including *n*-butyllithium concentration, styrene concentration, molecular distributions, and temperature, is now demonstrated. The formulation is analogous to other particulate systems (20, 21). The basic approach will be that of a deterministic solution obtained by kinetic analysis.

Basic Conservation Equations. The first step of the analysis is to develop conservation equations for growing, unassociated molecular species having a degree of polymerization n to $n + \Delta n$, subject to stoichiometric constraints. The principle of conservation of population results in the following relationship for well mixed tank reactors:

$$\begin{aligned} \lim_{\Delta n \rightarrow 0} \left\{ \frac{\partial}{\partial t} \left[V \int_n^{n+\Delta n} A(n,t) \, dn \right] \right. &= Q \int_n^{n+\Delta n} [A_1(n,t) - A(n,t)] \, dn \\ &+ V K_p M(t) A(n,t) - V K_p M(t) A(n + \Delta n,t) \\ &\left. - V k_t \int_n^{n+\Delta n} A(n,t) \, dn \int_1^\infty A(n,t) \, dn \right\} \end{aligned}$$

$$+ V k_r \int_n^{n+\Delta n} \int_0^\infty \bar{C}(n,x,t) dx dn \} \quad ; n > 1 \quad (3)$$

To summarize, the first term is the molar rate of accumulation of unassociated polystyryl anions within the reactor, the second is their rate of change caused by bulk fluid flow, the third and fourth are flux rates across degree of polymerization boundaries resulting from propagation kinetics, and the fifth and sixth result from the rate of association and disassociation of polystyryl anions.

The kinetic mechanism implies that a flux rate across the boundaries n and $n + \Delta n$ resulting from propagating carbanions is proportional to the product of molar concentrations of carbanions at specific degrees of polymerization, $A(n,t)$ and $A(n + \Delta n,t)$, respectively, and of monomer $M(t)$. The rate of bimolecular association within the degree of polymerization interval is proportional to the molar concentration product of polystyryl anions contained within that interval, $\int_n^{n+\Delta n} A(n,t) dn$, and the total, cumulative molar concentration of unassociated ions, $\int_1^\infty A(n,t) dn$. The rate of formation of polystyryl anions of required size by dissociation is proportional to the concentration of complexes that contain a molecule of required size as one of the associated pairs. The molar concentration of these complexes is expressed by the double integral $\int_n^{n+\Delta n} \int_{x=0}^\infty \bar{C}(x,nt) dx dn$. The constraint $n > 1$ temporarily removes initiation kinetics from the analysis. In addition, rate constants are assumed to be independent of molecular size. Equation 3 is simplified to:

$$\begin{aligned} \frac{\partial}{\partial t} \{ V A(n,t) \} &= Q \{ A_i(n,t) - A(n,t) \} \\ &- \lim_{\Delta n \rightarrow 0} \left[V K_p M(t) \left\{ \frac{A(n + \Delta n,t) - A(n,t)}{\Delta n} \right\} \right] \\ &- V k_t A(n,t) \int_1^\infty A(n,t) dn + V k_r \int_0^\infty \bar{C}(n,x,t) dx \end{aligned}$$

Utilizing the definitions of a derivative and residence time and the constraint of constant volume the above expression may be simplified to

$$\begin{aligned} \frac{\partial}{\partial t} A(n,t) + K_p M(t) \frac{\partial}{\partial n} A(n,t) + \left\{ \frac{1}{\theta} + k_t A_{TOT}(t) \right\} A(n,t) \\ = \frac{1}{\theta} A_i(n,t) + k_r C(n,t) \quad ; n > 1 \end{aligned} \quad (4)$$

where $\int_1^\infty A(n,t) dn = A_{TOT}(t)$ and $\int_{x=0}^\infty \bar{C}(n,x,t) dx = C(n,t)$. Equation 4 is the desired expression relating population density of unassociated carbanions, polymerization kinetics, time, degree of polymerization, and environmental factors. A boundary condition may be obtained from the principle of conservation of population, applied at $n = 1$.

$$\begin{aligned} \lim_{\Delta n \rightarrow 0} \left\{ \frac{d}{dt} \left[V \int_1^{1+\Delta n} A(n,t) dn \right] \right\} &= Q \int_1^{1+\Delta n} [A_i(n,t) - A(n,t)] dn \\ &+ V K_I I(t) M(t) - V K_p M(t) A(1 + \Delta n,t) \\ &- V k_t A_{TOT} \int_1^{1+\Delta n} A(n,t) dn + V k_r \int_1^{1+\Delta n} C(n,t) dn \} \end{aligned}$$

In the limit,

$$A(1,t) = K_I I(t)/K_p \quad (5)$$

Molar conservation equations of monomer and initiator define these time-dependent coefficients:

$$\frac{dM(t)}{dt} = \frac{M_i(t) - M(t)}{\theta} - K_p M(t) A_{TOT}(t) \quad (6)$$

$$\frac{dI_{exp}(t)}{dt} = \frac{I_{exp,i}(t) - I_{exp}(t)}{\theta} - K_I I(t) M(t) \quad (7)$$

The total, cumulative molar concentration of unassociated polystyryl anions is derived by integrating Equation 4 with respect to degree of polymerization:

$$\begin{aligned} \int_1^{\infty} \frac{\partial A(n,t)}{\partial t} dn + K_p M(t) \int_1^{\infty} \frac{\partial A(n,t)}{\partial n} dn \\ + \left[\frac{1}{\theta} + k_f A_{TOT}(t) \right] \int_1^{\infty} A(n,t) dn \\ = \frac{1}{\theta} \int_1^{\infty} A_i(n,t) dn + k_r \int_0^{\infty} C(n,t) dn \end{aligned}$$

This equation may be simplified by applying the Leibnitz rule to the first term, integrating the second term, and subsequently utilizing Equation 5 to eliminate $A(1,t)$. For a convergent solution $A(\infty,t) = 0$. The resultant expression is

$$\begin{aligned} \frac{d}{dt} A_{TOT}(t) = K_I I(t) M(t) - \left[\frac{1}{\theta} + k_f A_{TOT}(t) \right] A_{TOT}(t) \\ + \frac{1}{\theta} \int_1^{\infty} A_i(n,t) dn + 2k_r C_{TOT}(t) \end{aligned} \quad (8)$$

The total molar concentration of all associated complexes is $C_{TOT}(t) = \frac{1}{2} \int_0^{\infty} C(n,t) dn$. The factor $\frac{1}{2}$ is necessary because this surface is symmetric, $A_j - A_k = A_k - A_j$, and unique reactions only are required.

The population density of associated polystyryl anions $C(n,t)$ which contain one molecule of specified degree of polymer may be derived by procedures analogous to that leading to Equation 4. The resultant expression is

$$\frac{\partial C(n,t)}{\partial t} + \left(\frac{1}{\theta} + k_r \right) C(n,t) = \frac{C_i(n,t)}{\theta} + k_f A_{TOT}(t) A(n,t) \quad (9)$$

In experimental investigations, the reaction is quenched with water or alcohol, resulting in the annihilation of unassociated and associated polystyryl anions. The resultant molecular distribution, determined by gel permeation chromatography, will be comprised of macromolecules originating from associated complexes and from free anions. Thus, the measured population density is

$$T(n,t) = A(n,t) + C(n,t)$$

by Equations 4 and 9

$$\frac{\partial T(n,t)}{\partial t} + K_p M(t) \frac{\partial A(n,t)}{\partial n} + \frac{1}{\theta} T(n,t) = \frac{1}{\theta} T_i(n,t)$$

If polystyryl anion association phenomenon is at equilibrium (15, 16):

$$C(n,t) = K_{\text{eq}} A_{\text{TOT}}(t) A(n,t)$$

and

$$T(n,t) = [1 + K_{\text{eq}} A_{\text{TOT}}(t)] A(n,t)$$

thus

$$T_{\text{TOT}}(t) = [1 + K_{\text{eq}} A_{\text{TOT}}(t)] A_{\text{TOT}} \quad (10)$$

and

$$\frac{\partial T(n,t)}{\partial t} + \frac{K_p M(t)}{1 + K_{\text{eq}} A_{\text{TOT}}(t)} \frac{\partial T(n,t)}{\partial n} + \frac{1}{\theta} T(n,t) = \frac{1}{\theta} T_i(n,t) \quad (11)$$

Equations 4-11 define polymerization dynamics in a well mixed tank reactor, subject to stated assumptions and constraints. The utility of the model will now be demonstrated.

STEADY STATE EVALUATION. Steady state, isothermal, continuous polymerizations were used experimentally to test proposed methodology. Only monomer, solvent, and initiator were fed to the reactor, so $T_i(n,t) = 0$. The steady state population density distribution obtained from Equation 11 is simply:

$$T(n,ss) = T(1,ss) \exp \left\{ - \frac{T_{\text{TOT}}(ss)}{\theta K_p M(ss) A_{\text{TOT}}(ss)} (n - 1) \right\} \quad (12)$$

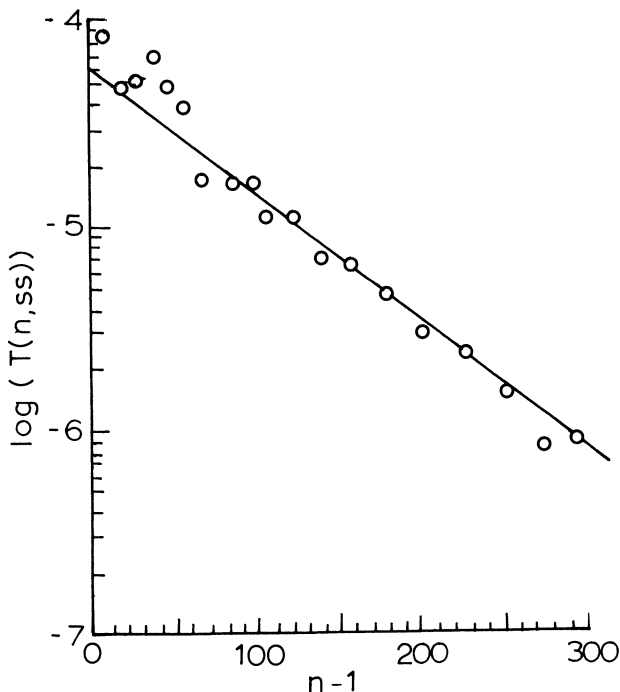


Figure 1. Steady-state molar distribution, *n*-butyllithium initiator

Figure 1 is representative of experimental distributions. Thus, there is excellent agreement between theoretical and experimental distributions. Procedures for determining population density $T(n,ss)$ and $T_{\text{TOT}}(t)$ from gel permeation

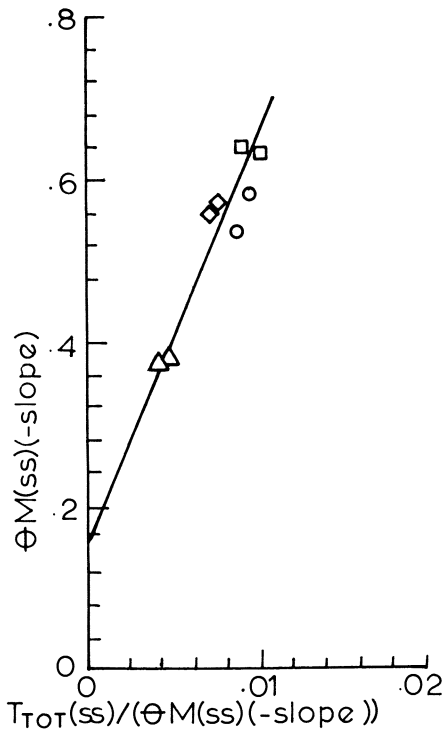


Figure 2. Determination of rate constants K_p and K_{eq}

chromatography are detailed by Rachow (22).

The rate constants associated with propagation and dimeric association, K_p and K_{eq} , respectively, may now be evaluated, utilizing $(-\text{slope}) = \frac{T_{TOT}(ss)}{\theta K_p M(ss) A_{TOT}(ss)}$. The latter may be solved explicitly for $A_{TOT}(ss)$ and substituted into Equation 10. After linearization,

$$\theta M(ss) (-\text{slope}) = \frac{1}{K_p} + \frac{K_{eq}}{K_p^2} \frac{T_{TOT}(ss)}{\theta M(ss) (-\text{slope})} \quad (13)$$

Experimental data are presented in Figure 2, substantiating the procedure.

The intercept $T(1,ss)$ and initiator concentration provide data for the evaluation of the initiation mechanism. Specifically,

$$T(1,ss) = \frac{K_I T_{TOT}(ss) I(ss)}{K_p A_{TOT}(ss)}$$

Experimentally determined *n*-butyllithium concentrations are the sum of the unassociated and associated molecules.

$$I_{exp} = y [I_y] + A_o$$

If the initiator is predominantly associated, $A_o < y [I_y]$, then

$$\frac{T(1,ss) K_p A_{TOT}(ss)}{T_{TOT}(ss)} = K_I \left[\frac{K_a}{y} \right]^{1/y} [I_{exp}]^{1/y} \quad (14)$$

Experimental data at 50°F are presented in Figure 3. The association number y is nearly 3.

Research in progress will exemplify these preliminary observations. However, they do demonstrate a practical experimental application which incorporates molecular distribution analysis into a kinetic evaluation. The simplicity of working expressions is self-evident.

BATCH REACTOR DYNAMICS. Published descriptions of differential, molar distributions are complex, nonlinear functions. The following relationship has been derived (23), utilizing a discrete, degree of polymerization model:

$$T_j(t) = \int_{\tau=0}^{\tau} \left(\frac{K_I I(\tau_1)}{(j-1)!} \exp \left(- \int_{\tau_1}^{\tau} \frac{K_p d\tau_2}{\sqrt{T_{TOT}(\tau_2) 2K_{eq}}} \right) \left(\frac{K_p}{\sqrt{2K_{eq}}} \int_{\tau_1}^{\tau} \frac{d\tau_2}{\sqrt{T_{TOT}(\tau_2)}} \right)^{j-1} \right) d\tau_1$$

where the Eigenzeit transformation is $d\tau = M(t)dt$. Thus to describe the molecular surface, numerous integrations at specific degrees of polymerization must be performed. The significance of the factorial and power can only be appreciated with the realization that the degree of polymerization j exceeds many thousands for commercial grades of polystyrene.

The population density surface, on the other hand, may be evaluated by exact solutions coupled with a single, simple integration (24). Subject to the operational constraint of a batch reactor and the Eigenzeit transformation, Equation 11 simplifies to

$$\frac{\partial T(n,\tau)}{\partial \tau} + \frac{K_p}{1 + K_{eq} A_{TOT}(\tau)} \frac{\partial T(n,\tau)}{\partial n} = 0 \quad (15)$$

The initial macromolecular distribution is $T(n,0)$. If experimental conditions yield predominately unassociated initiator, the boundary condition, Equation 5, with the aid of Equations 7 and 10 is simply

$$T(1,\tau) = \frac{K_I I(0)}{1 + K_{eq} A_{TOT}(\tau)} \exp(-K_I \tau) \quad (16)$$

Solving the partial differential equation by the method of characteristics (25, 26), the following relationships describe the population density surface:

$$\frac{d\tau}{ds} = 1 \quad (17)$$

$$\frac{dT(n,\tau)}{ds} = 0 \quad (18)$$

$$\frac{dn}{ds} = \frac{K_p}{1 + K_{eq} A_{TOT}(\tau)} \quad (19)$$

The dependent variable $A_{TOT}(\tau)$ may be evaluated in terms of $T_{TOT}(\tau)$, Equation 10. Therefore, Equation 15 is initially integrated with respect to degree of polymerization and Equation 16 is used to eliminate $T(1,\tau)$, yielding:

$$T_{TOT}(\tau) = T_{TOT}(0) + I(0) [1 - \exp(-K_I \tau)] \quad (20)$$

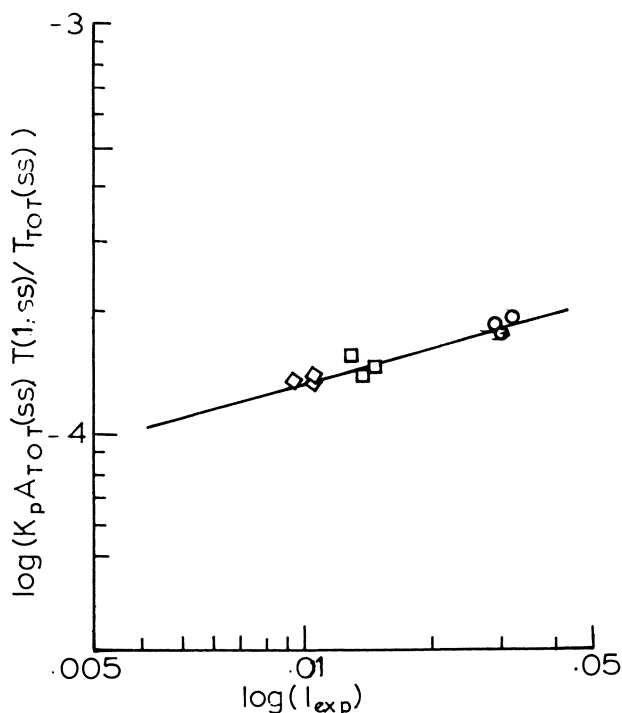


Figure 3. Determination of $K_d(K_a/y)^{1/2}$

Utilizing Equation 10:

$$A_{TOT}(\tau) = \frac{-1 + \sqrt{1 + 4K_{eq} T_{TOT}(\tau)}}{2K_{eq}} \quad (21)$$

For a characteristic emanating from the initial condition plane, suitable initial conditions for Equations 17-19 are $s = 0$, $\tau = 0$, $T(1,0)$ (see Figure 4). The characteristic equation maintains a constant magnitude $T(1,0)$; its reflection onto a constant $T(n,\tau) = 0$ plane is determined by integrating Equation 19, utilizing $d\tau = ds$.

The remainder of the surface can now be generated without additional integration by using explicit relationships. Each trajectory emanating from the initial condition plane will be of constant height (Equation 18), as specified by the initial macromolecular distribution $T(n_j,0)$. Their reflections onto the plane $T(n,\tau) = 0$ will remain a constant distance, $n(\tau) + n_j = n_j(\tau)$, from the previously generated $n(\tau)$ curve. Sufficient trajectories are rapidly generated to define that portion of the surface that results from the initial macromolecular distribution of polystyryl anions.

The population density surface resulting from initiation kinetics is generated by a similar procedure. Trajectories emanating from the boundary condition plane have magnitudes $T(1,\tau_j)$ as determined by Equation 16. Their reflections onto the plane $T(n,\tau) = 0$ will again be of constant distance from

the originally generated $n(\tau)$ curve. Sufficient trajectories to describe the surface are generated. Intermediate points may then be determined by interpolation. For the case $y \neq 1$, numerical integration will yield the boundary condition $T(1, \tau)$ and the total molar concentration $T_{TOT}(\tau)$.

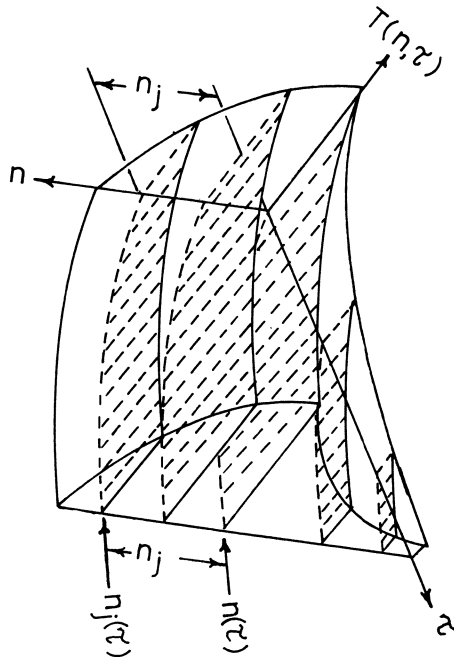


Figure 4. Response surface, living polymer

Free Radical Polymerizations

Population density will now be shown to be an effective variable for simulating and for experimental interpretation of free radical polymerizations. A representative mechanism is:

Initiation	$I \rightarrow 2A_0$	K_I
Propagation	$A_j + M \rightarrow A_{j+1}$	K_p
Transfer solvent	$A_j + S \rightarrow P_j + A_0$	K_{ts}
monomer	$A_j + M \rightarrow P_j + A_0$	K_{tm}
Termination		
disproportionation	$A_j + A_k \rightarrow P_j + P_k$	K_{td}
combination	$A_j + A_k \rightarrow P_{j+k}$	K_{tc}

The reactivity of radical fragments generated in transfer reactions is assumed to be equal to that of primary radicals formed by initiation kinetics. Through basic conservation of population laws, the following relationships may be developed:

$$\frac{\partial A(n,t)}{\partial t} + K_p M(t) \frac{\partial A(n,t)}{\partial n} + \left\{ \frac{1}{\theta} + [K_{td} + K_{tc}] A_{TOT}(t) + K_{ts} S(t) + K_{tm} M(t) \right\} A(n,t) = \frac{A_i(n,t)}{\theta} \quad (22)$$

$$A(0,t) = \frac{2K_i I(t) + \{K_{ts} S(t) + K_{tm} M(t)\} A_{TOT}(t)}{K_p M(t)} \quad (23)$$

$$\frac{dM(t)}{dt} = \frac{M_i(t) - M(t)}{\theta} - [K_p + K_{tm}] M(t) A_{TOT}(t) \quad (24)$$

$$\frac{dI(t)}{dt} = \frac{I_i(t) - I(t)}{\theta} - K_i I(t) \quad (25)$$

$$\frac{dA_{TOT}(t)}{dt} + \frac{1}{\theta} A_{TOT}(t) + [K_{tc} + K_{td}] [A_{TOT}(t)]^2 = \int_0^\infty A_i(n,t) dn + 2f K_i I(t) \quad (26)$$

$$\frac{\partial P(n,t)}{\partial t} + \frac{P(n,t)}{\theta} = \frac{P_i(n,t)}{\theta} + K_{tc} \int_{X=0}^{X=n/2} A(n-X,t) A(X,t) dX + [K_{td} A_{TOT}(t) + K_{ts} S(t) + K_{tm} M(t)] A(n,t); n \geq 0 \quad (27)$$

where the total molar concentration of free radicals is $A_{TOT}(t) = \int_0^\infty A(n,t) dn$. The term corresponding to the rate of termination by combination in Equation 27 includes all distinct, alternative reactions by which two smaller macroradicals may couple to form a single, ceased polymer molecule.

Steady State Polymerization of Styrene. Steady state distributions of macroradicals and terminated polymer molecules is readily obtained from Equations 22 and 27. If $A_i(n,t) = T_i(n,t) = 0$ for polymer-free feed, then

$$A(n,s) = A(0,ss) \exp \left\{ - \frac{\frac{1}{\theta} + [K_{td} + K_{tc}] A_{TOT}(ss) + K_{ts} S(ss) + K_{tm} M(ss)}{K_p M(ss)} n \right\} \quad (28)$$

$$\frac{P(n,ss)}{A(n,ss)} = \theta \left\{ \frac{n K_{tc} A(0,ss)}{2} + K_{td} A_{TOT}(ss) + K_{ts} S(ss) + K_{tm} M(ss) \right\} \quad (29)$$

The experimentally measured distribution will be comprised of macroradicals and terminated polymer molecules:

$$T(n,t) = A(n,t) + P(n,t) \quad (30)$$

For polystyrene initiated with 2,2-azobisisobutyronitrile, the following numbers are representative of kinetic parameters and steady-state concentrations (12).

$K_i = 1.4 \times 10^{-4}/\text{sec}$	$M(ss) = 2.4 \text{ molar}$
$K_p = 4.4 \times 10^2 \text{ liter/mole sec}$	$S(ss) = 7.4 \text{ molar}$
$K_{ts} = 2.9 \times 10^{-3} \text{ liter/mole sec}$	$I(ss) = 0.0152 \text{ molar}$
$K_{tm} = 3.2 \times 10^{-2} \text{ liter/mole sec}$	temp. = 80°C
$K_{tc} = 1.2 \times 10^8 \text{ liter/mole sec}$	$\theta = 3600 \text{ sec}$
$K_{td} = 0$	

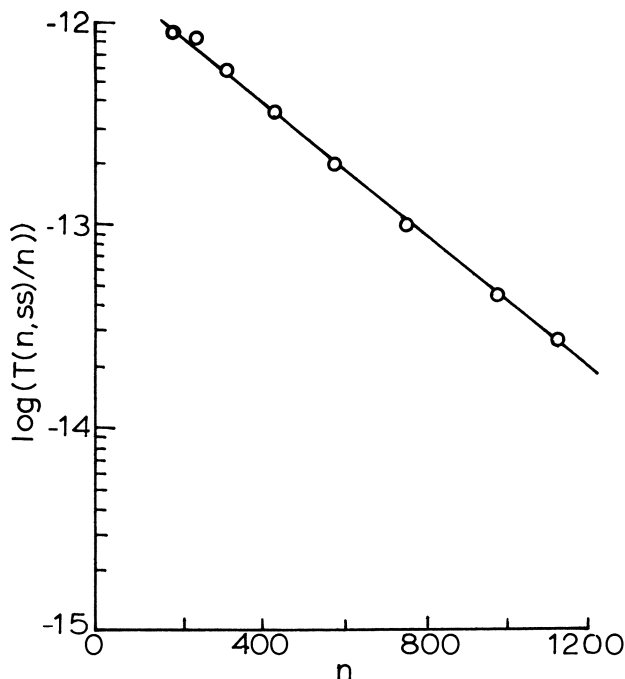


Figure 5. Molecular distribution, AIBN initiator, styrene

Therefore,

$$\frac{1}{\theta} = 0.0003; [K_{td} + K_{tc}] A_{TOT}(ss) = 15.2; K_{ts} S(ss) = 0.02;$$

$$K_{tm} M(ss) = 0.08; \text{ at } n = 10, \frac{n K_{tc} A(0,ss)}{2} = 1.1$$

Thus for $n > 10$,

$$T(n,s) = A(0,ss) \left[1 + \frac{\theta K_{tc} A(0,ss)n}{2} \right] \exp \left(- \frac{K_{tc} A_{TOT}(ss)n}{K_p M(ss)} \right)$$

A good approximation is, if $n > 10$,

$$\frac{T(n,ss)}{n} = \frac{\theta K_{tc} A^2(0,ss)}{2} \exp \left\{ - \frac{K_{tc} A_{TOT}(ss)n}{K_p M(ss)} \right\} \quad (31)$$

Thus, population density analysis provides a relationship which readily yields to graphical interpretation and which is a much simpler relationship than a Flory-Schultz description. Experimental data (27) are summarized in Figure 5, subject to the constraint of neglecting population densities of oligomers.

To evaluate kinetic constants, the additional relationships of measurable quantities are:

$$\begin{aligned} \text{Population distribution of macromolecules} \quad (-\text{slope}) &= \frac{K_{tc} A_{TOT}(ss)}{K_p M(ss)} \\ \text{intercept} &= \theta K_{tc} A^2(0,ss)/2 \end{aligned}$$

Initiation kinetics

$$A(0,ss) = \frac{2K_I I(ss)f}{K_p M(ss)}$$

Styrene concentration

$$\frac{M_{in}(ss) - M(ss)}{M(ss)\theta} = K_p A_{TOT}(ss)$$

Macroradical concentration

$$K_p M(ss) A(0,ss) = K_{tc} A_{TOT}(ss)^2$$

This set of five equations provides a means for the determination of five unknowns (three rate constants, population density of primary free radicals,

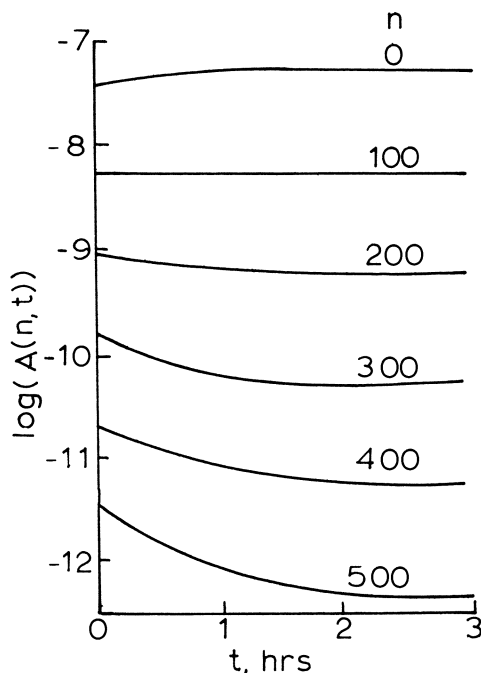


Figure 6. Free radical dynamics, AIBN initiator, polyvinylidene chloride

plus total, cumulative, molar concentration of free radicals). The rate constants can be determined graphically, similar to the procedure detailed for carbanions. Experimental research is being conducted, based on the above model.

Polyvinylidene Chloride Dynamics. Rate constants for vinylidene chloride, initiated with AIBN, are (1, 28):

$$K_i = 1.6 \times 10^{15} \exp(-15,500/T)/\text{sec}$$

$$K_p = 1.0 \times 10^{16} \exp(-12,500/T) \text{ liter/mole/sec}$$

$$K_{tc} = 1.0 \times 10^{30} \exp(-20,000/T) \text{ liter/mole/sec}$$

$$K_{td} = K_{tm} = K_{ts} = 0$$

Subject to the quasi-steady state constraint, the method of characteristics yields this set of equations for the solution of Equations 22 and 27:

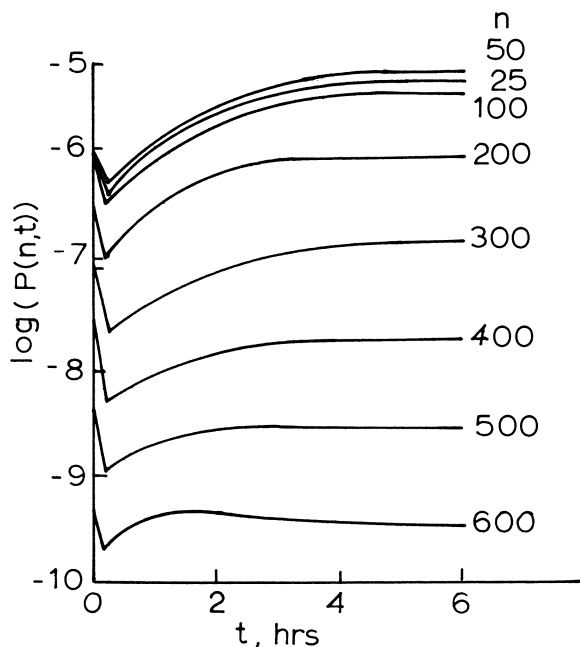


Figure 7. Cessated polymer dynamics, AIBN initiator, polyvinylidene chloride

$$dt/ds = 1.0$$

$$dn(t)/dt = K_p M(s)$$

$$dA(n,t)/dt = \frac{A_1(n,t) - A(n,t)}{\theta} - K_{tc} A(n,t) A_{TOT}(t)$$

$$dP(n_i,t)/dt = \frac{P_i(n_i,t) - P(n_i,t)}{\theta} + K_{tc} \int_{x=0}^{x=n_i/2} A(n_i - x,t) A(x,t) dx$$

Coupled with the differential equations defining monomer, initiator, and total activamer concentrations, the polymerization dynamics in Figures 6 and 7 were obtained. Initially, the system was at steady state. A step change in residence time was the forcing function. The simulation was programmed by IBM system 360 continuous system modeling program (CSMP). The simulation time was less than 1 min for a maximum degree of polymerization of 3000. The majority of this time is required simply in activating the CSMP package, an analog computer simulator.

Discussion

The principle of conservation of population yields distributed parameter equations subject to the constraint of a continuum. Solutions are readily obtained utilizing the algorithm, method of characteristics. Trajectories are exponential decays for mechanisms with termination, and time invariant for mechanisms without annihilation. Traditional descriptions, constrained by discrete molecular weight models, result in a set of lumped parameter equations.

Subsequent solutions at constant degrees of polymerization follow tortuous paths, resulting in complex mathematical descriptions (13, 14, 23).

Experimental data presented confirm theoretical descriptions. Numerical simulations demonstrate the utility of the technique. Complex, repetitive integrations have been reduced to a single integration, one that could be performed by graphical techniques.

Future developments will allow the union of sophisticated molecular analysis techniques incorporating gel permeation chromatography with a powerful simulation tool, population density analysis. Systematical study of commercial equipment will result in control systems drastically improving operation and will allow for polymerization in regions which are presently dangerous. Such will significantly increase efficiency, *i.e.*, allow greater conversion, yield products of uniform specifications, and, in some cases, make possible nonexistent but desirable new products.

Nomenclature

A_0	Free <i>n</i> -butyllithium
$A(n,t)$	Activamer population density (free radical or ionic intermediates that contain <i>n</i> styrene molecules), moles/liter
$A_i(n,t)$	Activamer population density in feed, moles/liter
$A_{TOT}(t)$	Total molar concentration of activamers, moles/liter
$C(n,t)$	Cumulative population density of associated complexes containing material of degree of polymerization <i>n</i> , moles/liter
$C(n,x,t)$	Population density of associated complexes containing a paired molecule of degree polymerization <i>n</i> , moles/liter
$C_{TOT}(t)$	Cumulative molar concentration of complexes before quenching, moles/liter
<i>f</i>	Fraction of radicals formed that produce macroradicals
I_{exp}	Experimentally measured <i>n</i> -butyllithium concentration, moles/liter
$I(t)$	Initiator concentration, moles/liter
$I_i(t)$	Initiator concentration in feed, moles/liter
<i>j, k</i>	Integer degree of polymerization, 0, 1, 2, 3 . . .
k_r, K_p	
K_{tc}, K_{td}	Bimolecular rate constants, liters/moles/sec
K_{tm}, K_{ts}	
K_i, k_r	Monomolecular rate constants, liters/sec
K_{eq}	Equilibrium rate constant, liters/moles
K_a	Equilibrium rate constant
$N(n,t)$	Cumulative molar concentration variable describing macromolecular material of degree of polymerization <i>n</i> and smaller, moles/liter
<i>n</i>	Continuous degree of polymerization
$M(t)$	Monomer concentration, moles/liter
$M_i(t)$	Monomer concentration in feed, moles/liter
$P(n,t)$	Population density of naturally terminated free radicals, moles/liter
<i>Q</i>	Solvent flow rate, liters/hr
<i>s</i>	A characteristic path
<i>ss</i>	Steady state
<i>T</i>	Temperature, °K
$T(n,t)$	Population density of polymer after quench, moles/liter
<i>t</i>	Time, hr
<i>V</i>	Volume of reactor, liters
<i>y</i>	Association number for <i>n</i> -butyllithium

Greek Symbols

Δ	Difference operator
θ	Residence time, $\theta = V/Q$, sec
τ	Eigenzeit transform, moles/liter/sec

Literature Cited

- Bamford, C. H., Barb, W. G., Jenkins, A. D., Onyon, P. F., "The Kinetics of Vinyl Polymerization by Radical Mechanisms," Butterworths, London, 1958.
- Flory, P. L., "Principles of Polymer Chemistry," Cornell University Press, New York, 1953.
- Ham, G. E., Editor, "Vinyl Polymerization," Vol. I, Part I, Marcell Dekker, New York, 1967.
- Ginell, R., Simha, R., *J. Amer. Chem. Soc.* (1943) **65**, 706, 715.
- Abraham, W. H., *Ind. Eng. Chem. Fund.* (1963) **2**, 221.
- Abraham, W. H., *Chem. Eng. Sci.* (1966) **21**, 326.
- Kilkson, H., *Ind. Eng. Chem. Fund.* (1964) **3**, 281.
- Liu, S., Amundson, N. R., *J. Chem. Rubber Technol.* (1961) **34**, 995.
- Liu, S., Amundson, N. R., *Chem. Eng. Sci.* (1962) **17**, 797.
- Denbigh, K. G., *Trans. Faraday Soc.* (1944) **40**, 352.
- Zeman, R., Amundson, N. R., *AIChE J.* (1963) **9**, 297.
- Duerksen, J. H., Hamielec, A. E., Hodging, J. W., *AIChE J.* (1967) **13**, 1081, 1087.
- Porter, R. E., unpublished M.S. Thesis, Texas A&M, 1972.
- Smith, W. F., May, J. A., Kim, C. W. W., *J. Polymer Sci.* (1966) **A2**, 365.
- Morton, M., Fetters, L. J., *J. Polymer Sci.* (1964) **A2**, 3311.
- Morton, M., Fetters, L. J., Bostick, E. E., *J. Polymer Sci.* (1963) **C1**, 311.
- Hsieh, H. L., *J. Polymer Sci.* (1965) **A3**, 153, 163, 173, 181, 191.
- Sinn, H., Hofmann, W., *Makromol. Chem.* (1962) **56**, 234.
- Worsfold, D. J., Bywater, S., *Can. J. Chem.* (1964) **42**, 2884.
- Pielou, E. C., "An Introduction to Mathematical Ecology," John Wiley and Sons, New York, 1969.
- Randolph, A. D., Larson, M. A., *AIChE J.* (1962) **8**, 639.
- Rachow, J. W., research in progress, Ph.D. Thesis, University of Nebraska, 1975.
- Edgar, T. D., Hasan, S., Anthony, R. G., *Chem. Eng. Sci.* (1970) **25**, 1463.
- Yu, F. S., unpublished M.S. Thesis, University of Nebraska, 1973.
- Aris, R., "The Optimal Design of Chemical Reactors," Academic Press, New York, 1961.
- Roberts, S. M., "Dynamic Programming in Chemical Engineering and Process Control," Academic Press, New York, 1964.
- Mody, N., unpublished M.S. Thesis, University of Nebraska, 1974.
- Bengough, W. I., Norrish, R. G. W., *Proc. Roy. Soc.* (1953) **A218**, 149.

RECEIVED January 2, 1974. Work supported by a Conoco Fellowship and by Engineering Research Center funds.

The Conjugate Dehydrogenation of Hydrocarbons

M. F. NAGIEV and T. M. NAGIEV

The Institute of Theoretical Problems of Chemical Technology,
29 Narimanov Ave., Baku-73, USSR

In the oxidative dehydrogenation of hydrocarbons by chemical induction in a chain reaction (without catalyst in a homogeneous medium) the concentration of active centers in the reaction mixture can be increased. A new method of hydrocarbon dehydrogenation—conjugate dehydrogenation—was developed where H_2O_2 is a reagent. The reaction is highly selective and gives high yields of valuable monomers from cheap, readily available raw materials. Apparatus and technology are simpler than those now used. Two overall reactions occur, one of which (dissociation of H_2O_2) induces the other (dehydrogenation of RH by H_2O_2). A new type of radical displacement reaction is proposed such that if two final products and a free radical are formed, the latter can be more active than the initial free radical.

Unsaturated hydrocarbons are produced by thermal and catalytic dehydrogenation and by catalytic oxidative dehydrogenation of the appropriate hydrocarbons. Further growth of the production of these unsaturated compounds depends on improving the efficiency of existing industrial processes and developing new, more effective processes of oxidative dehydrogenation.

Chemical reaction rates, as is well known, can be considerably increased either by creating a new chain conversion of reactants or by new, more efficient catalysts. Unfortunately, oxidative dehydrogenation of hydrocarbons *via* chain reactions—a potentially attractive method—has not yet been used on a large scale. Chemical reactions can also be considerably accelerated when one can increase the concentration of active intermediate species by other reactions. Such reactions, in which one induces the second, are called conjugate. Application of this concept, chain reaction with chemical induction, to the oxidative dehydrogenation of hydrocarbons could lead to results of great scientific and practical importance.

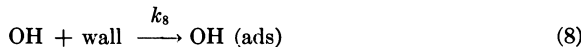
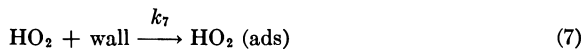
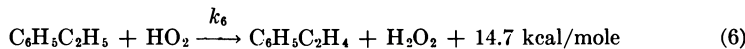
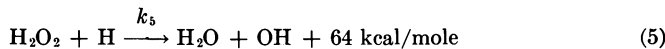
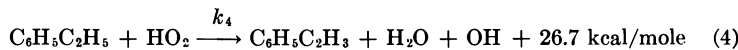
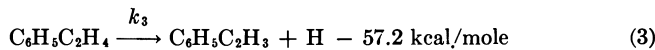
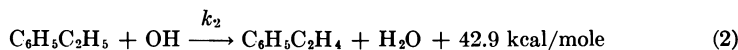
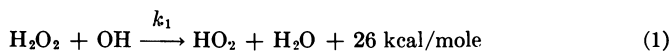
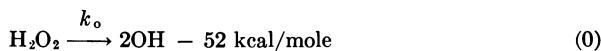
Our investigations were done to develop new heterogeneous and homogeneous processes, using hydrogen peroxide as an oxidizing agent, for producing monomers important in the chemical industry. Here we consider the production of alkenylbenzenes. Studies in this area have resulted in a basically new method of conjugate dehydrogenation of alkyl aromatic hydrocarbons in which an aqueous solution of hydrogen peroxide is used as an oxidant.

Conjugate Dehydrogenation of Ethylbenzene Using Hydrogen Peroxide

The reaction of conjugate dehydrogenation of alkylbenzenes (ethylbenzene in particular) was done in a quartz flow reactor with a reaction zone 5 cm long and a diameter of 1.6 cm (for details, see Refs. 1, 2). The principal feature of the reactor is the fact that H_2O_2 is supplied to the reaction zone as a gas without preliminary mixing with ethylbenzene. H_2O_2 did not decompose before entering the reaction zone because of a high linear rate of hydrogen peroxide aqueous solution flow in the preliminary heating. The original feed (ethylbenzene) and the reaction products were analyzed by gas-liquid chromatography in a capillary column and by gas absorption chromatography (3).

The reaction was studied over the range $450^\circ\text{--}640^\circ\text{C}$ at volumetric rates of ethylbenzene (liquid) of 0.2–0.8 ml/ml hr and volume ratios $\text{C}_6\text{H}_5\text{C}_2\text{H}_5:15\%\text{-H}_2\text{O}_2$ (aqueous solution) = 1:4 to determine the effect of S/V on the process. Under the best conditions the reaction proceeds with high conversion of ethylbenzene, with styrene yields of 40 wt % (calculated from the ethylbenzene reaction) and high selectivity of 90 wt % (i.e., the styrene yield calculated from the reacted ethylbenzene).

Kinetics and Mechanism. On the basis of the experimental data and certain theoretical considerations one may suggest a mechanism with the following elementary steps.



From this mechanism one can derive a differential equation for ethylbenzene disappearance.

$$-\frac{dN_{A1}}{dV} = K_2 C_{A1} C_{R1} + K_4 C_{A1} C_{R2} + K_6 C_{A1} C_{R2} \quad (9)$$

For the highly reactive intermediate radicals OH, HO_2 , H, and $\text{CH}_5\text{C}_2\text{H}_4$, one finds, by the quasi-steady state method,

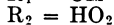
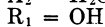
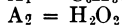
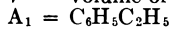
$$K_1 C_{A2} C_{R1} + K_2 C_{A1} C_{R2} - K_4 C_{A1} C_{R2} - K_5 C_{A2} C_{R8} + K_8 C_{R1} - K_0 C_{A2} = 0 \quad (10)$$

$$K_4 C_{A1} C_{R1} - K_1 C_{A2} C_{R1} + K_6 C_{A1} C_{R2} + K_7 C_{R2} = 0 \quad (11)$$

$$K_5 C_{A_2} C_{R_3} - K_3 C_{R_4} = 0 \quad (12)$$

$$K_3 C_{R_4} - K_2 C_{A_1} C_{R_1} - K_6 C_{A_1} C_{R_2} = 0 \quad (13)$$

where V = volume of the reaction zone



Kinetic rate constants of the elementary stages were estimated with our experimental data (1) and with Equations 9–13 which were derived in accordance with our theory of the reaction mechanism. Table I gives values of the pre-exponential factors and activation energies calculated from the rate constants we found for the elementary reactions. The kinetic equations derived from the assumed mechanism describe the observed process rather well, for the range of conditions studied, since the average relative deviation of N_{A1} (est) from N_{A1} (expt'l) does not exceed 7%. In addition, the probability of chain termination at the expense of the destruction of free radicals HO_2 and OH on the quartz reactor wall was determined (4):

$$K_i = \frac{\epsilon_i U_i}{d}$$

where

K_i = rate constant of termination of i free radicals

U_i = rate of thermal motion of a particle

d = vessel diameter.

Values of ϵ_i for HO_2 and OH free radicals appeared to be equal:

$$\epsilon_{HO_2} = \frac{K_8 d}{U_{HO_2}} = 0.2 \times 10^{-5} \quad \epsilon_{OH} = \frac{K_7}{U_{OH}} = 0.5 \times 10^{-6}$$

Table I. Calculated Pre-Exponential Factors and Activation Energies^a

Reaction	Pre-Exponential Factor	E, kcal/mole
0	11.0 sec ⁻¹	52.0
1	12.0 cm ³ /mole/sec	5.0
2	9.0 cm ³ /mole/sec	8.45
3	16.0 sec ⁻¹	57.2
4	9.6 cm ³ /mole/sec	11.0
5	14.0 cm ³ /mole/sec	11.0
6	9.4 cm ³ /mole/sec	12.4
7	1.0 sec ⁻¹	8.2
8	0.3 sec ⁻¹	7.0

^a Temperature = 723° – 823°C.

The definition of kinetic and diffusion regions of a heterogeneous termination reaction has been given much attention in chain reaction theory. It has been shown (4) that if the condition

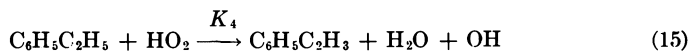
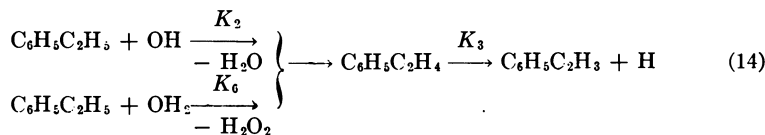
$$\frac{\epsilon_i d}{\lambda} \leq 0.5$$

is satisfied (where λ is the length of a free run of a particle), then the rate of chain termination on the surface is determined by the kinetics at the surface. Using ϵ_i values for chain termination reactions the dimensionless criteria for HO_2 and OH were calculated as:

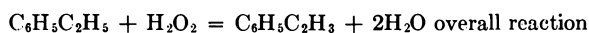
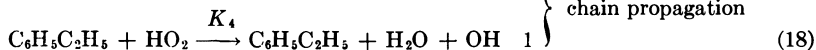
$$\frac{\varepsilon_{\text{HO}_2} d}{\lambda_{\text{HO}_2}} = 0.09 < 0.5, \quad \frac{\varepsilon_{\text{OH}} d}{\lambda_{\text{OH}}} = 0.02 < 0.5$$

Thus, the determining steps of the termination reactions are interactions on the surface, *i.e.*, chain termination takes place in the kinetic region.

According to the proposed mechanism, styrene is formed by the elementary steps:



Evaluation of the reaction velocities of these elementary steps (Table II) shows step 4 to be the fastest. On this basis, one can draw up the most probable unbranched chain mechanism, using step 4 together with steps 0 and 1, which generate the active centers for dehydrogenation in the system (HO_2).



The ratio of concentrations of the OH and HO_2 free radicals,

$$C_{\text{R}_2}/C_{\text{R}_1} \approx 10^3 \quad (21)$$

shows that chain termination involves mainly HO_2 radical destruction. On this basis, one obtains a kinetic equation for the chain reaction of conjugate dehydrogenation of ethylbenzene which proceeds *via* long chains terminated by a single dominant reaction. It is considerably simpler than Equations 9–13:

$$-\frac{dC_{\text{A}_1}}{dt} = \frac{K_0 K_4}{K_7} C_{\text{A}_1} C_{\text{A}_2} \quad (22)$$

Here the limiting step is chain propagation, Equation 18, involving HO_2 radicals.

Using Equation 22 we calculated the rate of styrene formation from 500° to 620°C at an ethylbenzene flow rate of 0.2 ml/ml hr. Table III shows that these rates agree well with those calculated by Equations 9–13. Hence, Equation 22 can be used in place of the original set for the conditions studied. From a plot of K_{eff} vs. $1/\tau$ (from Table III) the Arrhenius E_{eff} of the process is estimated to be 55.3 kcal/mole.

Table II. Reaction Velocities^a

Reaction	W, mole/liter sec
2	0.462×10^{-10}
3	0.750×10^{-7}
4	0.226×10^{-6}
5	0.742×10^{-7}

^a W values were calculated at $V_0 = 0.2$ ml/ml hr of $C_6H_5C_2H_5$ and at $600^\circ C$ at the reactor outlet.

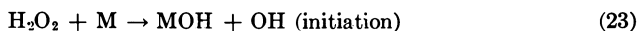
Using the equation $E = A \pm \alpha |q|$ to estimate activation energies for the chain initiation and propagation steps, together with literature data on the activation energy for the destruction of atoms or free radicals on the wall (4–12 kcal/mole), the theoretical activation energy of the overall reaction can be calculated by:

$$E_{\text{eff}} = E_0 + E_4 - E_7$$

Assuming that $E_7 = 4$, kcal/mole, one obtains $E_{\text{eff}} = 52.8$ kcal/mole (4).

The theoretical E_{eff} would agree with the experimental value if one assumes $E_7 = 2.5$ kcal/mole. This allows us to conclude that the conjugate dehydrogenation of ethylbenzene by H_2O_2 is a free radical chain reaction with the elementary steps of Equations 16, 17, 18, and 19 (5, 6, 7).

To determine the effect of the reactor walls on the process, experiments were run with the reactor filled with crushed vitreous quartz (4×4 mm). The nominal residence time in the empty reactor (based on liquid $C_6H_5C_2H_5$) at $620^\circ C$, $[C_6H_5C_2H_5] : [H_2O_2] = 1.3$, is 2.5 hrs. For the same conditions, it is 0.73 hr (based on the void volume). For equal feed rates, ethylbenzene conversion should increase sharply if the reaction is run without the packing. However, in comparing the observed data, one finds that runs with the packing gave a conversion of only 2–4 wt % less despite the large difference in contact time. This no doubt indicates catalytic action of vitreous quartz in the conjugate dehydrogenation of ethylbenzene by H_2O_2 . To explain this fact, we assumed that the rate of a free radical chain conversion of ethylbenzene is strongly influenced by the generation of OH radicals by the surface reaction



promoted by an energy gain equal to the energy of the M–OH bond (M = quartz surface).

The kinetic equation, Equation 22, can also be written

$$W = W_0 \nu \quad (24)$$

where W_0 = rate of chain initiation

$$\nu = \text{chain length} = \frac{K_4}{K_7} C_{A_2}$$

Table III. Calculated Rates of Styrene Formation^a

T, °C	K_{eff} , liters/mole sec	W_I , mole/liter sec	W_{II} , mole/liters sec	ν
500	9.1	0.94×10^{-5}	0.90×10^{-5}	16
550	32.0	0.293×10^{-4}	0.26×10^{-4}	15
600	570.0	0.264×10^{-3}	0.23×10^{-3}	27
620	750.0	0.284×10^{-3}	0.25×10^{-3}	14

^a W_I values at the reactor outlet were calculated by kinetic Equations 9–13 ($V_0 = 0.2$ ml/ml hr). W_{II} values at the reactor outlet were calculated by Equation 22.

In our case, the increased rate of ethylbenzene consumption will depend upon the effect of the surface/volume ratio (S/V factor) on the rate of initiation, W_0 .

Our experimental data in the quartz-packed reactor ($S/V = 9.3$) were treated with Equation 22. Table IV gives the initiation rate, overall reaction rate, and chain length, ν . Changing the flow rate of the feed reactant has almost no effect on the chain length in either packed and unpacked reactors. Consequently, the active species responsible for the conjugate dehydrogenation of ethylbenzene take part in the formation of the end product with approximately the same intensity at each cross section of the reactor. That is, the active centers participate in styrene formation ν times per unit time under stationary conditions.

In a flow reactor successive inflow of reagents displaces a given elementary volume of reacting substances into the next reactor section, and initial reagents are consumed along the line of flow. Thus, ν decreases along the reactor length. If the chain length, $\nu = (K_4/K_7)C_{A_2}$ (changing along the reactor length), is assumed to measure the catalytic activity of the active centers, then the catalytic activity of the active centers depends on the migration of the reacting substances through the reactor.

Table IV. Initiation Rate, Overall Reaction Rate, and Chain Length

Volume of Hydrocarbon, ml/hr	Empty Reactor ($S/V = 2.9$)			Quartz-Packed Reactor ($S/V = 9.3$)		
	W_0 (Initiation Rate), mole/cm ³ hr $\times 10^{-4}$	W (Reaction Rate), mole/cm ³ hr $\times 10^{-3}$	Chain Length, ν	W_0 , mole/cm ³ hr $\times 10^{-3}$	W , mole/cm ³ hr $\times 10^{-2}$	ν
2	0.673	0.896	13	0.408	0.556	14
4	0.676	0.910	14	0.401	0.553	14
6	0.680	0.922	14	0.412	0.566	15
8	0.685	0.940	14	0.416	0.543	13

It is also possible that the original reactants, as well as the intermediates and end products change the activity of the surface for destruction of free radicals on reactor walls or catalyst granules (quartz packing). This would be reflected in the changing rate constant for deactivation of active centers.

From Table IV it follows that the overall reaction rate in the packed reactor is two orders of magnitude higher than in the empty reactor. This is explained by the fact that the overall rate is affected mainly by the chain initiation rate according to Equation 24 since the catalytic activity (chain length) of the HO_2 radicals is nearly the same in both cases.

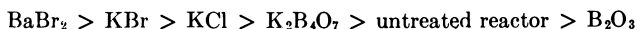
The calculated effective activation energy in the packed reactor is 49.1 kcal/mole; in the empty reactor it is 55.3 kcal/mole. The decrease of 6 kcal/mole in the presence of the quartz packing is explained by the energy gain arising from formation of the M-OH bond according to Equation 23. Thus, use of quartz packing in conjugate dehydrogenation of ethylbenzene by H_2O_2 increases the productive capacity of the reactor volume unit (8).

Conjugate Dehydrogenation of Isopropylbenzene

The object of this study is to determine the maximum efficiency of H_2O_2 in the conjugate dehydrogenation of isopropylbenzene. To obtain direct information on the process results, we have used the method of Box-Wilson in

planning experiments to determine an extremum with a minimum number of experiments. The total yield of styrene and α -methylstyrene per unit of isopropylbenzene fed was chosen as the parameter to be optimized since these monomers are chained to the same degree. By moving along the gradients, the best product yield was obtained at 56.8 wt % (styrene + α -methylstyrene) and 85 wt % selectivity. Further yield improvement along the gradient is not of practical interest since the process selectivity decreases (to 80 wt %). Thus factorial experiments show that the use of isopropylbenzene in the conjugate dehydrogenation reaction results in effective synthesis of such important industrial monomers as styrene and α -methylstyrene with high selectivity.

In the proposed mechanism, the limiting step in the chain reaction involves the HO_2 radical. Hence, the rate of the overall process depends mainly on the rate of chain termination by HO_2 radical destruction on the reactor walls. However, as reported (9), in cases where the effect of surface treatment with salts on the destruction of HO_2 radicals in formaldehyde oxidation was studied using EPR, a sequence of surface activities toward HO_2 destruction was found:



Our data indicating dependence of the overall yield of end products on the isopropylbenzene feed rate (empty reactor, $S/V = 3.5$) also show that the yield of α -methylstyrene and styrene can be increased by treating the reactor with B_2O_3 and decreased by treatment with KBr and KCl.

The surfaces treated with the salts (25) most active for HO_2 radical destruction were active in decreasing the yields of end products relative to yields in the empty reactor. This is in agreement with the EPR work.

Thus for salts used in treating the quartz reactor one can write a sequence of activity for conjugate dehydrogenation of isopropylbenzene by H_2O_2 :



Here the process selectivity remained generally high (0.91–0.98) (10, 11, 12).

Kinetic Regularities of the Conjugate Dehydrogenation of Diethylbenzene (DEB) and Vinylethylbenzene (VEB) by H_2O_2

The kinetics of the reaction were studied for a wide range of flow rates of the feed reagents, reagent ratios, temperature, and S/V ratio. The DEB and VEB had original isomeric compositions of:

<i>m</i> -DEB	53.5 wt %	<i>m</i> -VEB	71 wt %
<i>o</i> - and <i>p</i> -DEB	40.9	<i>o</i> - and <i>p</i> -VEB	29
impurities	5.6		

Figure 1 (a, b, c, d) shows that VEB accumulates as an intermediate product through the early stages of the reaction and reaches its maximum concentration at $\tau = 3.3$ hr (where $\tau = 1/v_0$, v_0 = flow rate of liquid DEB); at this point the accumulation rate becomes equal to the rate of further reaction. Further increase of τ results in a decrease in VEB concentration. For example, at 640°C, the yield of VEB isomers and the overall yield of ortho and para isomers, at $\tau = 5$ hr calculated with respect to the given initial isomer ratio, is 40.5 wt % for meta, and 25.9 wt % for ortho and para. The selectivity for meta is 70.9 wt %, and for ortho and para it is 54.6 wt %.

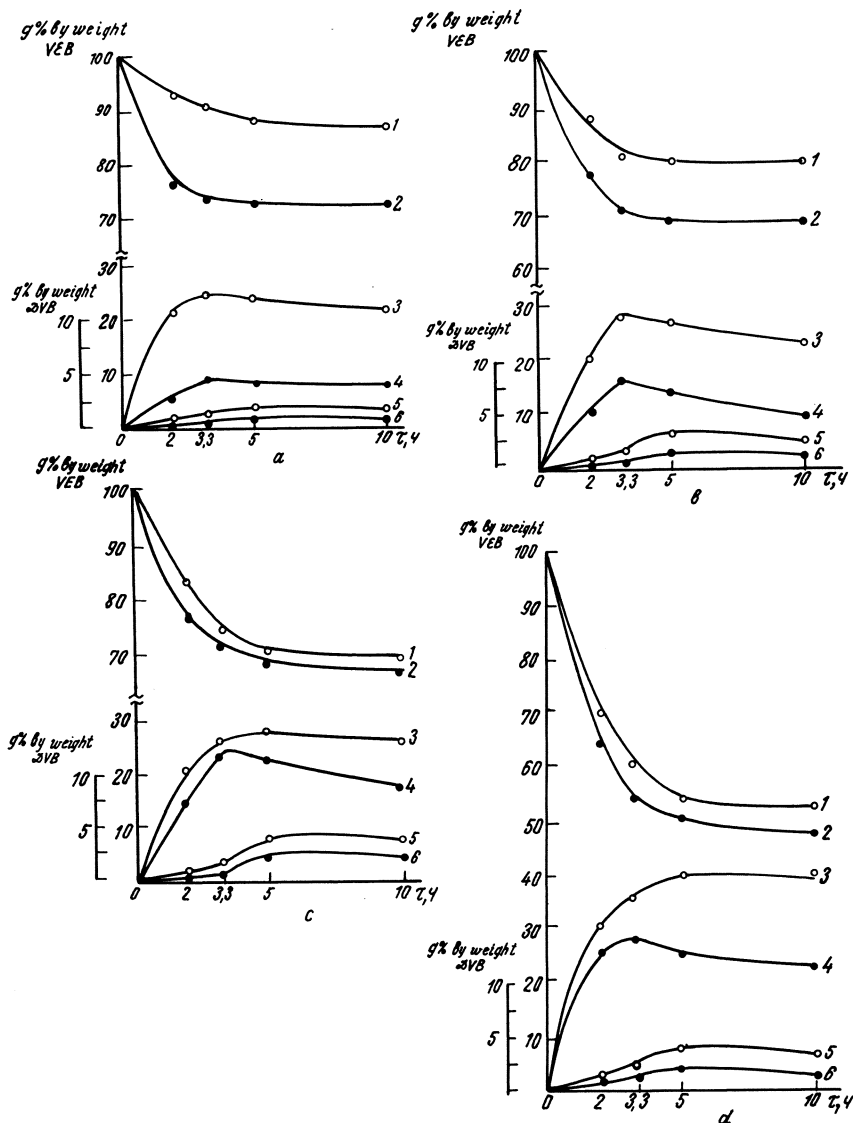


Figure 1. Kinetic regularities of conjugate dehydrogenation of diethylbenzene (DEB), using H_2O_2 , under the following conditions: H_2O_2 concentration, 20 wt %; volumetric ratio of DEB (cm^3/hr): H_2O_2 (cm^3/hr) = 1:3; plot a, at 580°C, b at 600°C, c at 620°C, and d at 640°C.

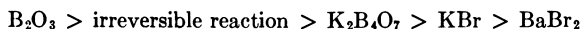
Curves:

1. Unreacted o- and p-DEB
2. Unreacted m-DEB
3. Yield of m-VEB per reacted m-DEB
4. Yield of o- and p-VEB per reacted o- and p-DEB
5. Yield of o- and p-DVB per reacted o- and p-DEB
6. Yield of m-DVB per reacted m-DEB

The rates of DVB and VEB formation grow at first with their increasing concentrations and reach a maximum at the point of inflection. However, since H_2O_2 participates in DVB formation and its concentration decreases as reaction proceeds, the point of inflection on the kinetic curve occurs below the maximum DVB concentration. As Figure 1 shows, the rate of VEB consumption falls slightly after reaching the maximum yield. This shows the deficiency of H_2O_2 concentration in the stage of DVB formation.

The kinetic curves of DVB production we obtained are S-shaped, indicating the autocatalytic character of the process, with the period of auto-acceleration extending from the origin to the point of inflection of these curves. The S curve in the region of high values of the nominal contact time shows that the DVB concentration decreases slightly. This may be explained by the fact that DVB enters into secondary reactions resulting in by-product formation.

Surface treatment in the quartz reactor (at 600°C , volume ratio $\text{DEB}:20\% \text{H}_2\text{O}_2 = 1:3$) showed that the highest yields of VEB and DVB are obtained in a reactor treated with B_2O_3 . We generated the sequence of activity of salt-treated quartz surfaces for DEB dehydrogenation with H_2O_2 as follows:



These results show that those surfaces most active toward HO_2 radical destruction are less active for conjugate dehydrogenation of diethylbenzene (4, 13).

Conclusions

A new method of conjugate dehydrogenation of hydrocarbons by H_2O_2 has been developed which allows important monomers to be obtained from cheap and available raw materials. Further investigations of the application of the conjugate dehydrogenation of hydrocarbons should permit considerably simplified technology. Hydrocarbon dehydrogenation in a homogeneous phase by a free-radical chain mechanism is free of several shortcomings typical of heterogeneous catalytic systems. In particular:

(a) Specially synthesized catalysts and the expense of their manufacture and regeneration are unnecessary.

(b) Reaction kinetics and mechanism can be studied by the well developed and clearly formulated fundamental understanding of free radical chain processes.

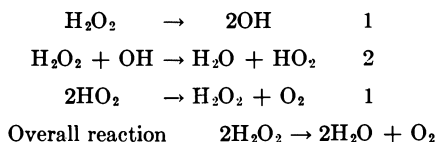
(c) Kinetic reaction models reproduce our experimental results well and hence allow rational control of both the rate and course of the reactions under study.

(d) The high selectivity of the process allows elimination of a number of engineering operations connected with separating considerable quantities of difficult-to-separate components. Moreover, increased selectivity permits more complete utilization of the process raw materials.

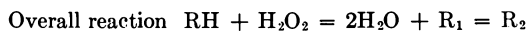
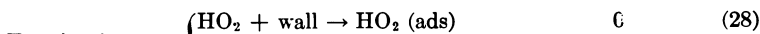
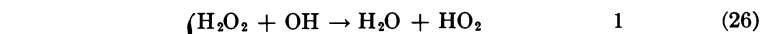
(e) The unique feature of this process is the invariance of its relative yields with respect to the productive capacity of the reactor. This is extremely important in transferring the result of laboratory investigations to industrial operation by avoiding multiple scaleup studies in pilot plants. The process model will allow laboratory data to be reproduced with great confidence on any large scale whereas heterogeneous catalytic processes for monomer production require pilot plant testing and gradual correction of the mathematical model. This requires much time and money.

Principal Results of Theoretical Importance

We suggest that the homogeneous dehydrogenation of hydrocarbons by H_2O_2 belongs to the class of conjugate reactions since there are two overall reactions in the systems studied, one of which induces the other. The primary reaction, H_2O_2 dissociation, occurs by the free radical mechanism



The secondary reaction, homogeneous dehydrogenation of hydrocarbons by H_2O_2 , follows the free radical chain reaction with the following elementary steps



Thus two overall reactions are occurring in the same reactor: dissociation of H_2O_2 induces dehydrogenation by H_2O_2 . This allows us to class the reaction as conjugate dehydrogenation.

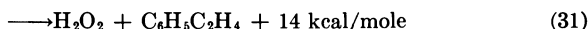
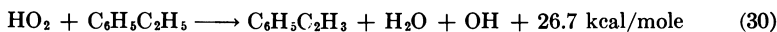
Based on the fundamental considerations in the theory of chain reactions applied to the reaction kinetics and mechanism of conjugate dehydrogenation of ethylbenzene, we introduce for the first time the following elementary step



Kinetic studies show that the chain mechanism including step 27 results not only in a kinetic equation which accounts adequately for the overall rate of disappearance of reactants but also accounts for the production of unsaturates in step 27.

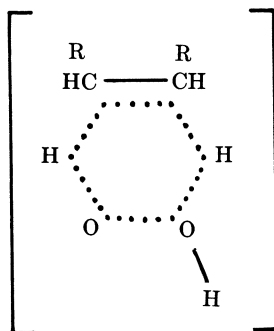
On the basis of these results, we consider it valid to extend this mechanism to the conjugate dehydrogenation of other hydrocarbons. Experimental tests confirm the validity of our proposed mechanism.

In radical substitution reactions, when the reaction of free radicals with molecules results in the transfer of an atom (usually a hydrogen atom) or radical from the molecule to a free radical, the reaction proceeds mainly in the direction by which a less active radical is formed. Thus, one should consider the competing elementary reactions



Step 30 differs from the usual radical substitution reactions (and from step 31 as well) in that a simultaneous transfer of two hydrogen atoms from adjacent

carbon atoms (in the ethylbenzene molecule) to the free radical occurs with formation of a six-centered transition state:



This decomposes in step 30 to two stable substances (styrene and water in our case) and a free radical (OH). The OH free radical is more active than the initial HO_2 . By the rule that the reaction goes mainly in the direction of less active radical formation, one should expect that step 31 would be preferable to step 30. However, the heats of reaction show that step 30 is more exothermic than step 31. Taking $E = 11.5 - 0.25 |q|$ as correct for radical substitution reactions, $E(30) = 4.8$ kcal/mole and $E(31) = 7.8$ kcal/mole (14).

Moreover, in contrast to ordinary radical substitution reactions, step 30 results in the formation of a free radical, OH, more active than the initial one but in an energetically more profitable way. Thus, the rule valid for radical substitutions where transfer of only one hydrogen atom takes place is not valid if simultaneous transfer of two hydrogen atoms from a donor occurs. Thus our studies show that if two end products and a free radical form in a radical reaction, the product free radical may be more active than the reactant radical because of energy gained in the formation of the second product.

Literature Cited

1. Nagiev, T. M., *Azerb. Chim. Zh.* (1967) (1).
2. Nagiev, T. M., Aliev, A. M., *Azerb. Neft. Choz.* (1969) (7).
3. Nagiev, T. M., Iskenderov, R. A., Medzhidov, N. D., Nagieva, Z. M., Ramzanova, Z. U., *Azerb. Neft. Choz.* (1970) (12).
4. Semenov, N. N., "On Some Problems of Chemical Kinetics and Reactivity," Nauka, Moscow, 1958.
5. Nagiev, T. M., Medzhidov, N. D., *Azerb. Chim. Zh.* (1970) (1-2).
6. Nagiev, M. F., Nagiev, T. M., *DAN SSSR* (1970) (3) 195.
7. Nagiev, T. M., Medzhidov, N. D., *Zh. Phys. Chim.* (1973) 47 (2).
8. Nagiev, T. M., *Azerb. Chim. Zh.* (1972) (3).
9. Vardanjan, P. A. *et al.*, *DAN SSSR* (1970) (1) 193.
10. Nagiev, T. M., Medzhidov, N. D., Nagizade, P. S., *Azerb. Chim. Zh.* (1971) (1).
11. Nagiev, M. F., Nagiev, T. M., Medzhidov, N. D., Iskenderov, R. A., *Azerb. Chim. Zh.* (1971) (5-6).
12. Nagiev, M. F., Nagiev, T. M., Medzhidov, N. D., *DAN SSSR* (1972) (1) 205.
13. Nagiev, T. M., Iskenderov, R. A., *Azerb. Chim. Zh.* (1972) (2).
14. Nagiev, T. M., *Azerb. Chim. Zh.* (1973) (3).

RECEIVED January 2, 1974.

American Chemical
Society Library
1155 16th St. N. W.

Wetting of Catalyst Particles under Trickle Flow Conditions

J-B. WIJFFELS,¹ J. VERLOOP² and F. J. ZUIDERWEG³

Koninklijke/Shell-Laboratorium, Amsterdam, The Netherlands

As part of a study on trickle flow reactors, packed beds of 1-, 3-, 5-, and 9.5-mm glass beads were wetted by water and cumene in trickle flow. The contacted particle fraction was measured by a direct tracer technique. The wetted fraction increased with the liquid load. Initially dry beds are poorly contacted, and contacting is considerably improved by prewetting the beds. For beds of small particles the wetted fraction increased with decreasing particle size. A model based on a minimum-energy principle was developed to account for these effects.

Packed columns and beds operated under trickle flow conditions are used as mass transfer equipment and reactors. In a trickle flow bed, liquid is distributed over the top of the bed and descends through the packing. Either concurrent or countercurrent gas flow may be applied. The performance of a trickle flow bed depends directly on the dynamic situation in the packing at the scale of the particle. Particles may or may not be contacted, area may or may not be wetted, wetted and interfacial area may or may not be effective for the process at hand. In this context we have investigated the wetting of packed beds of small-diameter glass beads by water and cumene in trickle flow.

The hydrodynamics of trickle flow beds have been extensively studied. Pressure drop, hold-ups, and residence time distribution have been measured (1, 2, 3, 4, 5). In hydrodynamic studies the results are usually expressed as overall quantities, no reference being made to the non-contacted or stagnant fraction of the bed. In connection with mass transfer processes the effective-area concept has been introduced to account for the difference in effectiveness of the bed for vaporization and gas absorption. Shulman *et al.* (6, 7, 8) and Yoshida *et al.* (9, 10) measured effective areas for different mass transfer processes. Danckwerts and Rizvi (11) determined effective interfacial areas by a chemical method described by Wesselingh and van't Hoog (12). All these methods are indirect in that the product is obtained of the effective area and the rate constant of the process used, and a number of correlations have become available (13, 14, 15). In the present study the contacted fraction of the bed

¹ Present address: Shell Internationale Chemie Maatschappij B.V., The Hague.

² Present address: Shell Internationale Petroleum Maatschappij B.V., The Hague.

³ Present address: Technological University, Delft.

was determined by a direct tracer technique. If the individual particles are completely wetted, the contacted fraction is directly related to the wetted area of the packing.

The stability of liquid flow over solid surfaces has been investigated from different points of view. Goren *et al.* (16, 17) studied the hydrodynamic stability of liquid films, and Kern (18) studied the stability of the flow of trickles on a plate. A criterion for the break-up of thin layers of liquid flowing isothermally over solid surfaces has been derived by Hartley and Murgatroyd (19) from the force balance at the upstream point of a dry patch. Wettability of the solid surface is accounted for in this force balance criterion, which has been used in several heat and mass transfer applications (20, 21, 22, 23). Here we describe the wetting of the solids by a model based on a minimum-energy principle which is closely related to the force balance criterion but provides a more general point of view.

Trickle Bed Reactor Performance

Liquid flow distribution and catalyst contacting have a pronounced influence on the performance of a trickle bed reactor (24, 25). The conversion efficiency of the system may be reduced by two effects:

- (1) Bypassing of the catalyst bed by part of the liquid flow.
- (2) Catalyst malcontacting—*i.e.*, part of the catalyst bed is not contacted by the liquid flow.

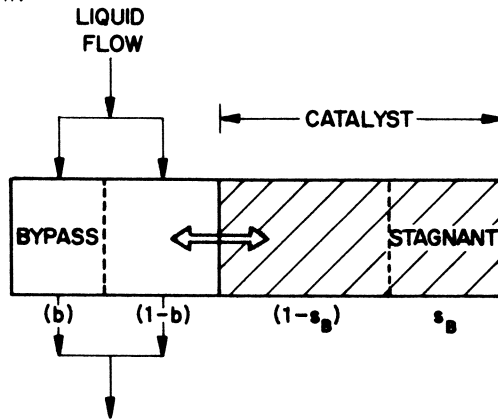


Figure 1. Schematic showing bypassing of the catalyst bed by part (b) of the liquid flow and malcontacting of part (s_B) of the catalyst bed

This situation is shown schematically in Figure 1. Let b be the fraction of the liquid flow that bypasses the catalyst bed and s_B be the non-contacted or stagnant fraction of the catalyst bed. Then, for a simple first-order process on the catalyst in contact with the liquid flow the conversion F would be:

$$F = (1 - b) \left\{ 1 - \exp \left(- \frac{1 - s_B}{1 - b} N_R \right) \right\} \quad (1)$$

where N_R would have been the number of reaction stages if the liquid moved in plug flow through the catalyst bed without bypassing or malcontacting.

The effect of bypassing can be eliminated if complete radial mixing of the liquid streams is ensured or if the reactor is subdivided into many beds with low fractional conversion and complete mixing is provided in between the beds. Then the liquid will flow through the reactor in plug flow, and all the liquid will be effectively in contact with catalyst. The conversion for the simple first-order process is then:

$$F = 1 - \exp(-(1-s_B)N_R) \quad (2)$$

Of course, the effect of catalyst malcontacting will still be present. In this paper the factors influencing the non-contacted or stagnant bed fraction are studied.

Experimental

Experiments were done with trickle flow beds to obtain:

- (a) the liquid hold-up correlation in completely contacted beds,
- (b) the non-contacted or stagnant fraction of prewetted beds,
- (c) the non-contacted fraction of initially dry beds.

The results reported pertain to beds where no gas load is applied.

Completely Contacted Beds. The liquid hold-up in packed beds depends on the degree of contacting. In the irrigated fraction of the bed it is greater than in the stagnant zones, where hold-up is zero if the particles were initially dry or equals the static hold-up if the particles were prewetted. To assess the liquid hold-up in irrigated parts of the bed we determined the hold-up of water in packed beds of glass beads, taking special measures to ensure complete contacting of the particles. The water used contained a low-foaming wetting agent; Teepol CH-53, dioctyl sodium sulfosuccinate, and cetyldimethylamine oxide were used. The glass beads were cleaned thoroughly in an alkaline solution. At the start of the experiments the beds were liquid filled. After the feed flow had been established, the beds were gradually drained, while trickle flow was developed at a steady rate. Owing to the excellent wetting power of the receding liquid film, completely contacted packed beds could be obtained at steady trickle flow conditions. This was verified by visual experiments. At the start of these experiments dye-colored water was used. After the bed had been drained—while trickling—and steady operation was reached, the feed was switched to clear water. The colored hold-up was then immediately released, and the bed became clear. The liquid hold-up was determined for glass beads of various diameters. Data for 1-, 3-, and 5-mm beads were obtained from 5-cm diameter columns, data for 9.5-mm beads from a 15-cm diameter column. The total liquid hold-up was calculated as the sum of the liquid that was drained from the bed after trickle flow had been stopped and the liquid that remained on the packing: the static hold-up, which was determined separately. The results are shown in Figure 2.

Prewetted Beds. The existence of stagnant zones, which are not contacted by the liquid flow, has been demonstrated in prewetted beds by a visual experiment. No special measures were taken to influence the degree of contacting of the particles. After saturating and draining the bed with dye-colored water, the bed remained colored long after the water percolating through it in trickle flow had become colorless. Increasing the water flow rate at this condition immediately released a part of the colored stagnant hold-up until the effluent became again entirely clear. To determine the volume of the stagnant pockets, we did experiments in a packed bed of non-porous glass beads for concurrent air/water and nitrogen/cumene trickle flow operation. The volume of stagnant pockets was measured by the following procedure.

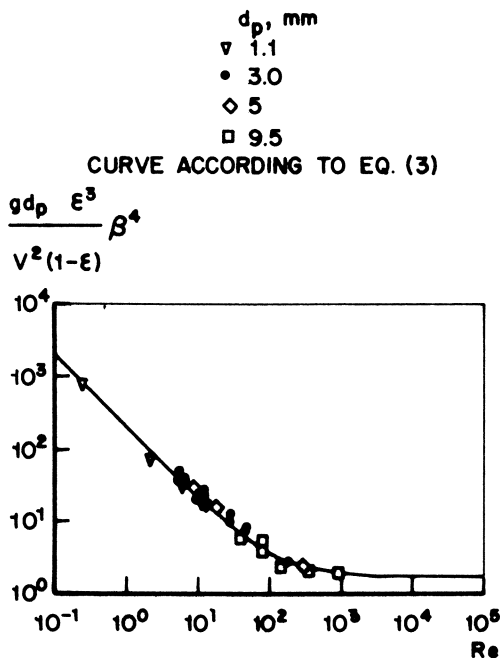


Figure 2. Total liquid hold-up vs. Reynolds number

Initially, the bed was wetted completely with a salt solution of 2 grams of ammonium chloride per liter of water or with a solution of α -methylstyrene in cumene of known concentration. After the bed had been drained, a static hold-up of the solution remained on the packing. Trickle flow operation was started with fresh tap water or fresh cumene and continued up to the point where the amount percolated was equal to about 100 times the dynamic hold-up in the bed. The duration of the trickle flow period then was about 100 times the average residence time of the liquid in the bed. It was assumed that during this period the concentration in the stagnant pockets, which are not in contact with the flowing liquid, did not change. After the bed had been drained again, a static hold-up remained on the packing which contained an amount of salt or α -methylstyrene proportional to the volume of the stagnant pockets. This amount was determined by washing the total contents of the bed with a known amount of fresh tap water or fresh cumene, respectively. The influence of the following parameters was studied.

BED DIAMETER. Experiments were done in columns of 5 and 15 cm diameter and in a 5 by 50 cm flat box, all about 1 m high. Liquid was distributed over the top of the bed by distributors with about 2000 distributing points per m^2 . Values for the stagnant hold-up found for the 5-cm columns were consistently a few per cent higher than the results with the 15-cm column and the flat box, which were about the same.

SUPERFICIAL LIQUID LOAD. The volume of the stagnant hold-up decreased greatly with increasing superficial liquid load. At values of superficial water velocity as low as 1 mm/sec nearly half the bed may not be contacted (for 3- and 5-mm particles). For superficial velocities higher than 10 mm/sec, however, the stagnant fraction is as low as about 15% or even less.

SYSTEM COMPOSITION. Stagnant hold-up was appreciably smaller in the nitrogen/cumene system than in the air/water system.

SUPERFICIAL GAS LOAD. The influence of gas load up to superficial velocities of 10 cm/sec was fairly insignificant. However, the values for the stagnant volume in beds of small particles with a large liquid hold-up were higher than those for operation without gas.

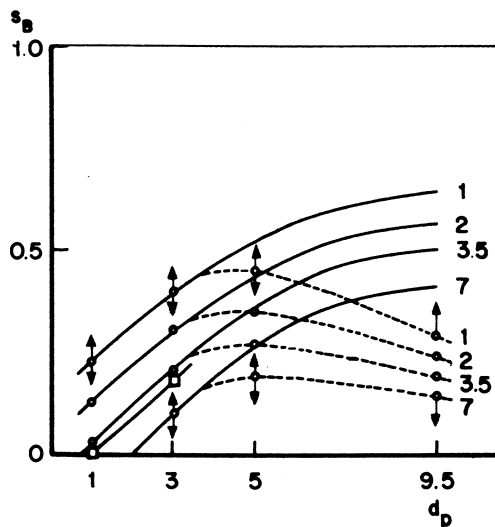


Figure 3. Non-contacted bed fraction s_B for trickle flow of water (circles) and cumene (squares) through pretwetted beds. Superficial liquid velocity is indicated in mm/sec. No gas load. Solid curves obtained from the model.

PARTICLE SIZE. Experiments were done for the nitrogen/cumene system with glass beads 1 and 3 mm in diameter and for the air/water system with glass beads 1, 3, 5, and 9.5 mm in diameter. Comparison of results for the same liquid load indicated a maximum for the stagnant hold-up with particles about 5 mm in diameter.

BED HEIGHT. A few experiments were done with air/water trickle flow over 3-mm glass beads in a bed 4 m high and 15 cm in diameter. After the trickle flow period the packing was divided into three sections, which were removed separately from the bed. The values for the stagnant hold-up for the top, middle, and bottom sections are equal to each other and to those found in a column 1 m high. The results for pretwetted beds are shown in Figure 3.

Initially Dry Beds. A few experiments were done with beds of clean initially dry glass beads of 3-mm diameter. In this case we determined the contacted or irrigated fraction of the bed. Trickle flow of salt solution of 2 grams of ammonium chloride per liter of water was supplied to the bed. The trickle flow operation was continued to the point where the amount percolated was equal to about 100 times the dynamic hold-up in the bed. After the bed had been drained, a static hold-up remained on the packing which was proportional to the irrigated bed fraction. This amount was determined by washing the total contents of the bed with a known amount of fresh tap water. The irrigated bed volume was low compared with pretwetted beds and increased greatly with superficial liquid load. The results are shown in Figure 4 together with those for pretwetted beds of 3-mm glass beads.

Interpretation of Results

The results for the total liquid hold-up for completely contacted packed beds could be correlated by a modified Ergun expression (26):

$$\frac{gd_p}{v^2} \cdot \frac{\epsilon^3}{(1-\epsilon)} \cdot \beta^4 = \frac{200}{Re} + 1.75 \quad (3)$$

where: g = acceleration from gravity
 d_p = particle diameter
 v = superficial liquid velocity
 ϵ = bed void fraction
 β = fraction of void filled with liquid

The bed Reynolds number is defined as:

$$Re = \frac{\rho v d_p}{\mu(1-\epsilon)} \quad (4)$$

in which ρ is the liquid density and μ the dynamic viscosity.

In this correlation a factor β^4 has been incorporated instead of a factor β^3 as would be expected. The additional influence of the liquid hold-up can be ascribed to various effects—*e.g.*, the tortuosity of the liquid streams depends on the liquid hold-up and the total hold-up is not completely effective for the liquid flow.

Correlation 3 is shown as the solid curve in Figure 2. By this correlation an explicit expression for the velocity can be obtained:

$$V = 38 Gr^{-1/2} (\sqrt{1 + 0.00059 Gr \beta^4} - 1) \quad (5)$$

where the superficial liquid velocity has been made non-dimensional according to:

$$V = \frac{v}{\epsilon \sqrt{g d_h}} \quad (6)$$

The hydraulic diameter d_h is defined as:

$$d_h = \frac{2\epsilon}{3(1-\epsilon)} d_p \quad (7)$$

and the Grashof number introduced is written as:

$$Gr = \frac{g d_h^3}{\nu^2} \quad (8)$$

where ν is the kinematic viscosity. By Equation 5 we can now also describe the flow in the irrigated parts of not completely contacted packed beds.

The results obtained with prewetted and initially dry beds are presented in Figures 3 and 4. They are expressed in terms of the stagnant bed fraction s_B , which for prewetted beds is defined as the volume of stagnant solution V_{stag} left in the bed after the trickle flow period divided by the volume of static solution V_{stat} present in the bed directly before the start of the trickle flow:

$$s_B = V_{stag}/V_{stat} \quad (9)$$

For initially dry beds the contacted bed fraction is defined as the volume of solution retained in the bed after irrigation during the trickle flow period,

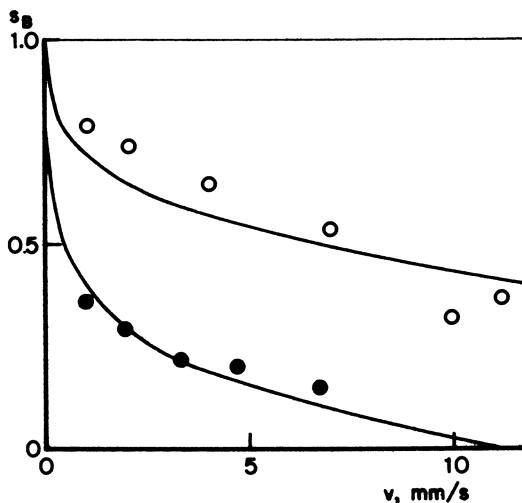


Figure 4. Non-contacted bed fraction s_B for trickle flow of water through initially dry (circles) and prewetted (dots) beds of 3-mm glass beads vs. superficial liquid velocity. No gas load. Solid curves obtained from the model.

V_{irr} , divided by the volume of static solution, V_{stat} , which would have been left in the bed if the contacting had been complete. The non-contacted bed fraction is then given by:

$$s_B = 1 - \frac{V_{irr}}{V_{stat}} \quad (10)$$

We will also introduce the fraction of the solid surface s which is not contacted by the flowing liquid. The non-contacted surface fraction s is equal to the non-contacted bed fraction if individual contacted particles are completely wetted.

The Model

We developed a model that can predict the wetting of packings in which liquid descends by gravity and the flow pattern is independent of height. We consider the steady-state operation of a trickle flow bed, and we assume that the system seeks a situation in which the energy of the system in a plane perpendicular to the direction of flow is at a minimum. [This is equivalent to the assumption that the total energy, that is the sum of kinetic, surface, potential, and internal energy of the system, is at a minimum. The total energy is conserved since the system is supposed to be adiabatic, no external work is performed on it, and the amount added by the flow is equal to the amount removed.] For a trickle flow bed this is a horizontal plane. Consider a slice of bed of infinitesimal height. For initially dry particles the energy per unit bed volume prior to the trickle flow, E_o , is given by:

$$E_o = S \sigma_{sv} \quad (11)$$

where σ_{SV} is the solid/vapor surface energy, and the specific surface area of the packing S is equal to:

$$S = \frac{6(1-\epsilon)}{d_p} \quad (12)$$

During trickle flow operation the energy per unit bed volume is given by:

$$E = sE_o + (1-s) \left\{ \epsilon\beta \frac{1}{2}\rho(u^2)_e + S\sigma_{SL} + S_{LV}\sigma \right\} \quad (13)$$

where σ_{SL} and σ denote the solid/liquid and the liquid/vapor surface energy respectively. S_{LV} is the liquid/vapor specific interfacial area. Subscript e indicates that the effective square is taken of the linear interstitial velocity u , which is related to the superficial velocity v in the irrigated zone by:

$$u = \frac{\tau v}{\epsilon\beta_e} \quad (14)$$

where τ is the tortuosity and β_e the effective liquid hold-up. The system will seek to minimize its energy:

$$\delta(E - E_o) = 0 \quad (15)$$

The minimum-energy situation is attained subject to the constraint that the overall load supplied to the top of the packing is constant:

$$v(1-s) = \text{constant} \quad (16)$$

Before solving Equation 15 some simplifying assumptions are introduced. The effective square of the interstitial velocity is written as:

$$(u^2)_e = C_e \frac{2}{\beta^2} \left(\frac{v}{\epsilon} \right)^2 \quad (17)$$

where the proportionality factor C_e is treated as a constant to avoid unnecessary detail. Furthermore, the dependence of the gas/liquid interfacial area on the hold-up is not accurately known; we assume that it is linearly proportional to the gas hold-up:

$$S_{LV} = (1-\beta)S \quad (18)$$

To simplify notation we introduce the exponent n ,

$$n = \frac{\beta}{V} \frac{dV}{d\beta} \quad (19)$$

which may be obtained from Equation 5; n varies between 2 (large particles) and 4 (small particles).

The minimum-energy condition (Equation 15) is satisfied if:

$$\left(\frac{C_e}{4} We + 1 \right) \beta = \frac{n}{n-1} (1 - \cos \theta_a) \quad (20)$$

where θ_a is the apparent angle of contact for the wetted edge. The apparent angle of contact is defined by $\sigma \cos \theta_a = \sigma_{SV} - \sigma_{SL}$. Its significance is discussed below. The Weber number is introduced,

$$\text{We} = \frac{\rho d_h}{\sigma} \left(\frac{v}{\epsilon \beta} \right)^2 \quad (21)$$

For large particles (large We) the solution is given by:

$$\frac{C_e}{4} \text{We} \beta = \frac{n}{n-1} (1 - \cos \theta_a) \quad (22)$$

and for large Re the critical hold-up and load are proportional to:

$$\beta_{\text{c:it}} : : d_h^{-2/3} \quad (23)$$

and

$$v_{\text{crit}} : : d_h^{-5/6} \quad (24)$$

The liquid flow will spread over the solid surface as long as the load and hold-up are larger than their critical values. For small particles such as investigated in this study the critical hold-up is constant and given by:

$$\beta_{\text{crit}} = \frac{n}{n-1} (1 - \cos \theta_a) \quad (25)$$

For small Re the critical load is then proportional to the hydraulic radius squared:

$$v_{\text{crit}} : : d_h^2 \quad (26)$$

Contrary to the behavior of beds of large particles, beds of small particles are wetted better as the particles get smaller.

For prewetted beds the minimum-energy condition leads to a different result. For prewetted particles the energy per unit bed volume prior to the trickle flow E_o is given by:

$$E_o = (1-f')S\sigma_{\text{SV}} + f'S\sigma_{\text{SL}} + fS\sigma \quad (27)$$

where f' is the prewetted fraction of the solid surface and f is the ratio of the gas/liquid interfacial area to the solid surface area in the prewetted bed. Although generally f' is larger than f , we will take f' equal to f since a more precise description would not be warranted in view of the crude assumption about the dependence of the liquid interfacial area on the hold-up given by Expression 18.

For prewetted beds the minimum-energy condition now leads to:

$$\left(\frac{C_e}{4} \text{We} + 1 \right) \beta = \frac{n}{n-1} (1 - f) (1 - \cos \theta_a) \quad (28)$$

and the critical hold-up in beds of small particles is given by:

$$\beta_{\text{crit}} = \frac{n}{n-1} (1 - f) (1 - \cos \theta_a) \quad (29)$$

As we discuss below, the prewetted fraction f may be taken to be about one-half. Thus, the critical load in a prewetted bed of small particles is about one-tenth that in the same bed which is initially dry.

Apparent Angle of Contact

The apparent angle of contact can be determined from capillary rise or capillary recession experiments in a packed bed. Such values are extreme.

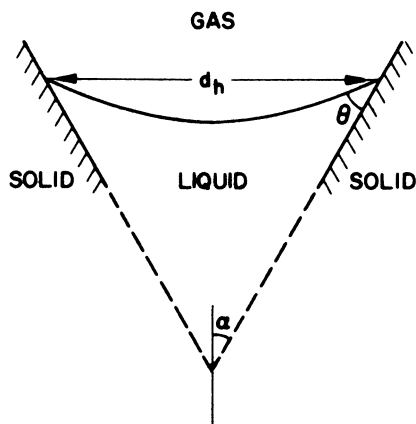


Figure 5. Spherical meniscus in a right circular cone

Capillary rise in a packed bed is halted at the most difficult passage. To model such a passage, we consider capillary rise in a right circular cone with an apex angle α with respect to the vertical (see Figure 5). Suppose the radius at the liquid interface is small enough for the interface to be approximated by a spherical surface. The interface intersects the cone at an angle of contact θ . In a packed bed the cone radius at the interface equals half the hydraulic diameter; the capillary pressure is thus:

$$\Delta p = \frac{4\sigma}{d_h} \cdot \cos(\alpha + \theta) \quad (30)$$

which balances the hydrostatic pressure ρgh , where h is the height of capillary rise in the bed. Therefore:

$$\cos \theta_a = \frac{\rho gh d_h}{4\sigma} \quad (31)$$

By this expression the apparent angle of contact θ_a in the packed bed can be obtained from the experimentally determined height of capillary rise. If the liquid is advancing, θ_a is given by:

$$\theta_a = \min(\theta + \alpha, \pi) \quad (32)$$

If the liquid is receding:

$$\theta_a = \max(\theta - \alpha, 0) \quad (33)$$

and α may be interpreted as the maximum angle of slope encountered by the liquid in the bed. Capillary rise experiments were done with beds of 1-, 3-, and 5-mm glass beads and with tap water (contact angle 30° , surface tension 0.072 N/m) and cumene (contact angle 12° , surface tension 0.030 N/m). We found that α equals about 55° for both liquids, independent of particle size. Keeping in mind that the above expression could also have been derived by minimizing the potential and surface energy and following a similar argument, the capillary rise in a prewetted bed can be described by:

$$\left\{ f + (1-f)\cos \theta_a \right\} = \frac{\rho g h d_h}{4\sigma} \quad (34)$$

Capillary rise experiments with prewetted beds of 1-, 3-, and 5-mm glass beads and with water and cumene showed that the prewetted fraction f is about one-half for these small particles.

Values for the apparent angle of contact in actual trickle flow experiments can be obtained from the experimentally determined critical hold-ups by Expressions 25 and 29. The apparent contact angle increases with the degree of contacting. The results for prewetted and initially dry beds of 3-mm particles are shown in Figure 6. The apparent contact angle can be correlated with the stagnant bed fraction according to:

$$\theta_a = \theta + (1-s_B)\alpha \quad (35)$$

Here also the maximum angle of slope α equals 55° , and the angle of contact θ of water on glass equals 30° . The prewetted fraction was assumed to be:

$$f = 0.5 \quad (36)$$

The model curves shown in the figures were computed from Equations 25 and

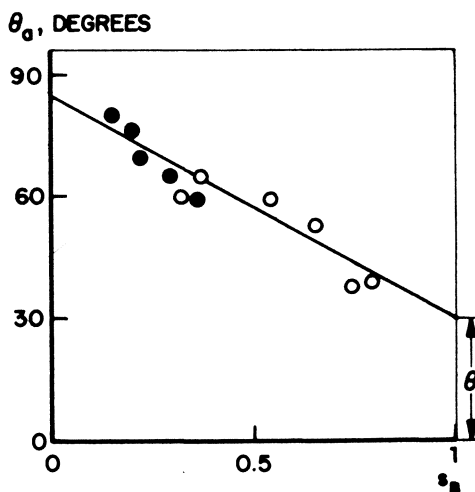


Figure 6. Apparent angle of contact for trickle flow of water through initially dry (circles) and prewetted (dots) beds of 3-mm glass beads vs. stagnant bed fraction

29, in which values for the apparent contact angle and the prewetted fraction were used as given by the above expressions. Remarkably, the model predicts larger stagnant fractions, for bed of particles with a diameter of 5 mm and larger, than were measured by our method. Remember that the contacted particle fraction is measured by the tracer method. This fraction is larger than the contacted surface fraction if each particle is not completely wetted, as is the case for particles 5 mm and larger. Comparison of hold-ups in irrigated zones with hold-ups in completely contacted beds showed that the 3-mm particles are completely wetted.

Conclusions

In the wetting of packings under trickle flow conditions the wetted fraction increases with the liquid load. Initially dry beds are poorly contacted, and the contacting is considerably improved by prewetting the beds. For beds of small particles the wetted fraction increases with decreasing particle size. A model based on a minimum-energy principle was developed which can be used to describe these experimental findings on the wetting of packings. For beds of glass beads with a diameter of 5 mm and larger the model predicts larger stagnant fractions than the non-contacted bed fractions which were actually measured because those particles, when contacted, are not completely wetted.

Nomenclature

b	fraction of liquid flow bypassing the catalyst bed
C_o	proportionality factor
d_h	hydraulic diameter, m
d_p	particle diameter, m
E	energy per unit bed volume, kg/msec ²
E_o	energy per unit bed volume prior to trickle flow, kg/msec ²
F	conversion
f	prewetted fraction
f'	prewetted fraction of solid surface
g	acceleration from gravity, m/sec ²
Gr	Grashof number
h	height of capillary rise, m
N_R	number of reaction stages
n	exponent
Re	Reynolds number
s	non-contacted surface fraction
S	specific surface area of packing, m ² /m ³
s_B	non-contacted bed fraction
S_{LV}	liquid/vapor specific interfacial area, m ² /m ³
u	interstitial velocity, m/sec
v	superficial liquid velocity in irrigated zone, m/sec
V	dimensionless velocity
V_{irr}	volume of solution after irrigation, m ³
V_{stag}	volume of stagnant solution, m ³
V_{stat}	volume of static solution, m ³
We	Weber number

Greek Letters

α	maximum angle of slope, degrees
β	fraction of void filled with liquid, kg/msec ²
Δp	capillary pressure
ϵ	bed void fraction
θ	angle of contact, degrees
θ_a	apparent angle of contact, degrees
μ	dynamic viscosity, kg/msec
ν	kinematic viscosity, m ² /sec
ρ	density, kg/m ³
σ	liquid/vapor surface energy, kg/sec ²
σ_{SL}	solid/liquid surface energy, kg/sec ²
σ_{SV}	solid/vapor surface energy, kg/sec ²
τ	tortuosity

Subscripts

crit critical value
e effective value

Literature Cited

1. Brož, Z., Kolář, V., *Coll. Czech. Chem. Commun.* (1972) **37**, 3551.
2. Charpentier, J. C., Prost, C., van Swaaij, W., Le Goff, P., *Chim. Ind.-Gén. Chim.* (1968) **99**, 803.
3. Hochman, J. M., Effron, E., *Ind. Eng. Chem., Fundamentals* (1969) **8**, 63.
4. Reiss, L. P., *Ind. Eng. Chem., Process Design Develop.* (1967) **6**, 486.
5. Turpin, J. L., Huntington, R. L., *AIChE J.* (1967) **13**, 1196.
6. Shulman, H. L., Ullrich, C. F., Wells, N., *AIChE J.* (1955) **1**, 247.
7. Shulman, H. L., Ullrich, C. F., Proulx, A. Z., Zimmerman, J. O., *AIChE J.* (1955) **1**, 253.
8. Shulman, H. L., Ullrich, C. F., Wells, N., Proulx, A. Z., *AIChE J.* (1955) **1**, 259.
9. Yoshida, F., Koyanagi, T., *Ind. Eng. Chem.* (1958) **50**, 365.
10. Yoshida, F., Koyanagi, T., *AIChE J.* (1962) **8**, 309.
11. Danckwerts, P. V., Rizvi, S. F., *Trans. Inst. Chem. Engrs.* (1971) **49**, 124.
12. Wesselingh, J. A., van't Hoog, A. C., *Trans. Inst. Chem. Engrs.* (1970) **48**, T69.
13. Jackson, G. S., Marchello, J. M., *J. Chem. Eng. Japan* (1970) **3**, 263.
14. Kataoka, T., Yoshida, H., Ueyama, K., *J. Chem. Eng. Japan* (1972) **5**, 132.
15. Onda, K., Takeuchi, H., Okumoto, Y., *J. Chem. Eng. Japan* (1968) **1**, 56.
16. Anshus, B. E., Goren, S. L., *AIChE J.* (1966) **12**, 1004.
17. Krantz, W. B., Goren, S. L., *AIChE J.* (1971) **17**, 494.
18. Kern, J., *Verfahrenstechnik* (1971) **7**, 290.
19. Hartley, D. E., Murgatroyd, W., *Int. J. Heat Mass Transfer* (1964) **7**, 1003.
20. Coulon, H., *Chem. Ing. Techn.* (1973) **45**, 362.
21. Murgatroyd, W., *Int. J. Heat Mass Transfer* (1965) **8**, 297.
22. Ponter, A. B., Davies, G. A., Ross, T. K., Thornley, P. G., *Int. J. Heat Mass Transfer* (1967) **10**, 349.
23. Zuber, N., Staub, F. W., *Int. J. Heat Mass Transfer* (1966) **9**, 897.
24. Ross, L. D., *Chem. Eng. Progr.* (1965) **61**, 77.
25. Sedriks, W., Kenney, C. N., *Chem. Eng. Sci.* (1973) **28**, 559.
26. Ergun, S., *Chem. Eng. Progr.* (1952) **48**, 89.

RECEIVED January 2, 1974.

Experimental Study of a Catalytic Trickle Bed Reactor

ALBERT H. GERMAIN, ANDRÉ G. LEFEBVRE, and
GUY A. L'HOMME

Laboratoire de Chimie Industrielle et de Génie Chimique,
Université de Liège, Rue A. Stévert, 2, B-4000, Liège, Belgique

We have used the hydrogenation of α -methylstyrene in a trickle bed reactor to understand its performance and mechanism. This study emphasizes two steady-state possibilities for such a reactor; one is predictable if we suppose that the reaction rate is limited by mass transfer in the film of liquid trickling on the uniformly wetted catalyst pellets; the other can be explained if the reaction takes place on partly wetted pellets. We also show that the role of the liquid is essential to maintain the catalyst activity by dissolving polymers. This could explain a novel experimental observation: a cyclic evolution of the catalyst activity related to the alternative operation of the pellets in gaseous and in liquid phases.

The chemical and petrochemical processes using three-phase reactors are as numerous as they are important. Among these reactors, the trickle bed is one of the most interesting. It offers several advantages over the other three-phase reaction vessels: large size apparatus is easily constructed, and the cost of operation is low compared with a stirred tank slurry reactor. For these reasons, the trickle bed reactor is frequently used in the petroleum industry, especially for hydrotreating heavy distillates (hydrocracking, hydrodesulfurization, etc.) (1). Such processes are expanding rapidly at present. On the other hand, the trickle bed reactor also presents some advantages over the fixed bed reactor operating in the vapor phase because it reduces the recirculation of great amounts of the lighter reactants (hydrogen in hydrotreating processes).

However, despite the frequent use of the trickle bed reactor in large industrial plants, little is known about its mechanisms. Since the design of such a reactor and the prediction of its performance are still extremely difficult problems for the chemical engineer, several studies have recently been done. Most of these, however, are theoretical (2, 3) or consider only the physical aspects such as pressure drop, fluid holdups, fluid residence time distributions, and hydrodynamic models. (A review of previous work has been reported by Way in 1971 (4), and by Charpentier *et al.* in 1972 (5).) Little experimental data have been published on the chemical aspects of the operation of the trickle bed reactors. Except for the studies by Satterfield and co-workers (6, 7)

and by Sedriks and Kenney (8), virtually no fundamental research has been published on this subject.

In fact, obtaining reliable measurements and the means to interpret them needs extensive experimental determinations which are time consuming and often critical. At the present state of knowledge of the three-phase systems, it is not possible to study a reaction in a trickle bed reactor without preliminary information on the reacting system. Particularly important are the knowledge of the physical properties of the fluids involved, a good characterization of the solid catalyst (including the tortuosity factor), and the determination of the intrinsic reaction rate. This information is specific for the catalytic system; it does not depend on the trickle bed reactor and can be determined independently. We have adopted such a procedure.

Selection of the Reaction System

The efficiency of such research depends greatly on the reaction system and the catalyst chosen. We have used the liquid phase hydrogenation of α -methylstyrene to cumene in the presence of a palladium-on-alumina catalyst. This reaction is apparently simple and easy to use in the laboratory; there is no secondary reaction (except a slow polymerization which does not interfere with the hydrogenation in the presence of the liquid phase); the homogeneous reaction does not take place while the heterogeneous reaction proceeds with an appreciable rate at moderate temperatures and pressures; the liquid phase can be analyzed easily and accurately by refractometry. The hydrogenation of α -methylstyrene is claimed to be nearly ideal for studying three-phase catalytic systems. Moreover, it is quite similar to the reactions in those industrial processes that involve the hydrogenation of liquids of low volatility.

Many papers report the use of the hydrogenation of α -methylstyrene to understand the mechanisms of three-phase reactors (9, 10, 11). This reaction should therefore be well known. The most interesting physical properties of the fluids have been determined experimentally. Nevertheless, it seems that only Ma (12) has tried to determine the intrinsic rate equation. His results do not seem very reliable since the reaction rates he measured are very small—much smaller than those reported by others who claim their rates were controlled by mass transfer. Ma used commercial α -methylstyrene without further purification; impurities may have therefore partly poisoned the catalyst. That is why we decided to conduct a series of experiments to obtain a reliable intrinsic rate equation for the reaction.

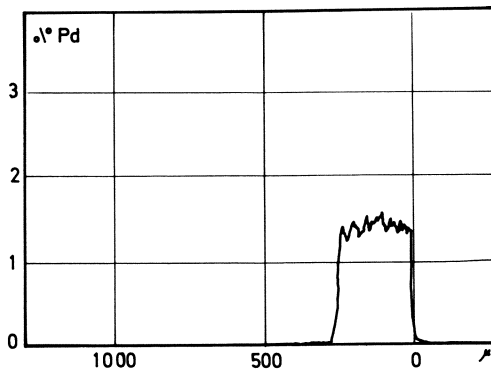
Kinetic Study of the Hydrogenation of α -Methylstyrene on Palladium-Alumina Catalyst

Characterization of the Reactants and the Catalyst. REACTANTS. All experiments reported here were done with the same quality of reactants. α -Methylstyrene, provided by Rütgerswerk A.G., was 99.5% pure. The main impurities are butylbenzene (0.4%) and cumene (0.1%). Before use, it was dried on alumina which simultaneously removed the polymerization inhibitor (*p*-tert-butylcatechol). We used 99.99% hydrogen and 99.8% nitrogen (main impurity, argon) provided by l'Air Liquide S.A. The maximum current content of oxygen in the gases was 3 ppm.

CATALYST. We used four different catalysts of palladium on porous alumina, numbered from 1 to 4. These are industrial products supplied by Engelhard Industries. In the trickle bed reactor, we used two catalysts (Nos. 3

Table I. Physical Properties of Palladium- γ -Alumina Catalysts

Property	Catalyst Number			
	1	2	3	4
Bulk form	powder	powder	cylinder	cylinder
Mean particle diameter, μ	2.5	2	—	—
Bulk dimensions, mm height			3.52	3.50
diameter			3.24	3.32
Palladium content, %	0.5	5	0.5	1
Palladium dispersion, %	20	20	37	30
Mean palladium crystallite diameter, Å	53	53	29	35
Total surface area, m^2/gram	59	57	102	202
Particle total pore volume, cm^3/gram	0.144	(0.144)	0.308	0.328
Pore volume, radius < 200 Å , cm^3/gram	0.093	(0.093)	0.190	0.220
Particle apparent density, grams/cm^3	2.44	2.39	1.74	1.69
Solid true density, grams/cm^3	3.76	3.65	(3.76)	(3.76)
Particle porosity, %	35.2	34.4	53.7	55.2

Figure 1. Palladium distribution through the pellets (\circ = external surface) (catalyst No. 3)

and 4) in the form of $\frac{1}{8} \times \frac{1}{8}$ -inch cylindrical pellets: No. 3 is a coated catalyst; No. 4 is an impregnated one. To determine the intrinsic rate equation, we used two powdered catalysts (Nos. 1 and 2) and two powders obtained by crushing the pellets of catalysts 3 and 4.

All catalysts were thoroughly characterized to enable us to interpret the experimental results on the most fundamental basis possible. All physical properties were determined experimentally (13); the most important ones are given in Table I. We think that the measurement of the palladium dispersion (defined as the fraction of the total number of metal atoms which are at the surface of the metal particles) is particularly important for studying intrinsic kinetics. This measurement was done according to the procedure of Benson *et al.* (14). On the other hand, the measurement of the palladium distribution through the pellets is absolutely essential for the kinetic study of diffusion with reaction in the liquid-filled pores of the catalyst. The results we obtained with an electronic microprobe are shown in Figures 1 and 2.

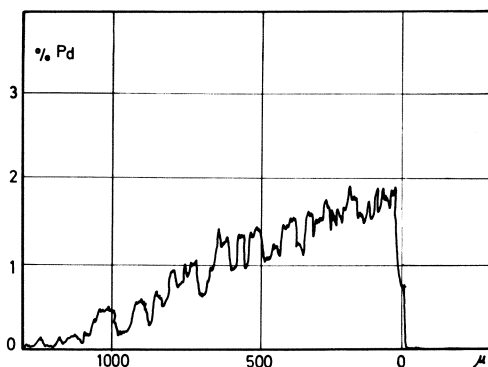


Figure 2. Palladium distribution through the pellets (o = external surface) (catalyst No. 4)

Intrinsic Rate Equation. To determine the intrinsic rate equation, the hydrogenation was carried out in a semicontinuous, stirred tank slurry reactor. Care was taken to avoid rate limitations by mass or heat transfer. The reaction rates we measured were so high that it was necessary to use very small amounts of catalyst (about 5 mg Pd/liter) to avoid concentration gradients at the gas-liquid interface. The concentration gradients at the liquid-solid interface were reduced to insignificant values by using very fine powdered catalyst ($d_p < 3 \mu$).

We assumed that the Sherwood number is 2 and calculated that the concentration of hydrogen at the outer surface of the catalyst is larger than 99.5% of its bulk liquid concentration in the most unfavorable experimental conditions ($T = 110^\circ\text{C}$, $P_{\text{H}_2} = 200$ torr). Under the same conditions, the Thiele modulus (ϕ_s) is small enough ($\phi_s = 0.528$ if $\tau = 8$, see below) to enable us to conclude that the effectiveness factor is very close to 1 and that there is no pore diffusion limitation.

This kinetic study led to important results which proved absolutely necessary for the continuation of the work:

(a) Catalyst activity depends strongly on the purity of the reactants. If the α -methylstyrene is not pure enough, the catalyst deactivates quickly. With a rigorously standardized procedure of purification, we could obtain reproducible measurements and avoid deactivation for a long time. In fact, the activity of the catalyst did not decrease until each palladium atom had converted one million molecules of α -methylstyrene to cumene.

(b) Catalyst activity is not stable during the first few hours of a run. To obtain reproducible measurements, it is necessary to measure the reaction rate after the catalyst has reached steady state activity.

(c) For the four catalysts used, the reaction rate is proportional to the exposed metallic area and does not depend on the dimensions of the palladium crystallites. The hydrogenation of α -methylstyrene appears to be "structure insensitive" (15). It is therefore easy to predict the activity of any palladium catalyst if the dispersion of the palladium is known.

(d) The best rate equation fitting our results is:

$$\tau_A = 0.05 \times \left(\frac{P_{\text{H}_2}}{1000} \right)^{0.63} \times \exp \left[\frac{10000}{R} \left(0.003 - \frac{1}{T} \right) \right] \quad (1)$$

where r_A (moles A converted/sec \times gram superficial Pd) = specific rate

A = α -methylstyrene,
 P_{H_2} (torr) = partial pressure of hydrogen,
 R (cal/mole $^{\circ}K$) = ideal gas constant,
 T ($^{\circ}K$) = absolute temperature

This equation is valid at 25 $^{\circ}$ –110 $^{\circ}C$, and at 100–2000 torr hydrogen, as far as the β -phase of the palladium-hydrogen system is stable. The reaction order with respect to α -methylstyrene is zero if its mole fraction remains greater than 0.01. It is particularly noteworthy that the reaction order with respect to hydrogen is constant and does not depend on temperature or hydrogen pressure. We found that the power law kinetic form gave the best representation of the influence of the hydrogen pressure. For example, it is not satisfactory to suppose that hydrogen adsorbs dissociatively or molecularly on the catalyst in order to formulate a Langmuir-type rate expression. Further details on the determination of the intrinsic rate equation and experimental methods are given by Germain (13).

Apparent Rate Equation. Because of the high intrinsic activity of the palladium and the rather large diameter of the catalyst pellets used in a trickle bed reactor, the effectiveness factor is small as the reaction proceeds under pore diffusion control. Unfortunately, it is not possible to calculate *a priori* the influence of diffusion on the reaction rate in the liquid-filled pores of a catalyst. In fact, to develop the theory of liquid diffusion in porous catalysts, numerous hypothesis are needed, and the experimental data are still too scarce to verify them (16, 17). Therefore we have measured experimentally the apparent reaction rate on the pelleted catalyst.

We use a stirred tank reactor similar to Carberry's (18). However, to avoid pellet crumbling, the wire basket containing the catalyst is not attached to the impeller but is substituted for a baffle. The basket is located close to the end of the impeller in a high turbulence zone which allows very high mass transfer rates at the external surface of the pellets. The reaction rate remained constant when the rotational speed was varied between 750 and 2000 rpm, which showed in this case the absence of external transport resistances. We think that this novel arrangement of the Carberry-type reactor is an important improvement for studying diffusion with reaction in the liquid-filled pores of catalyst pellets.

The results of the apparent kinetics study are summarized below.

For catalyst No. 3, the apparent rate equation is:

$$r_A = 1.10 \times 10^{-3} \left[\frac{P_{H_2}}{1000} \right]^{0.81} \exp \left[\frac{8158}{R} \left(0.003 - \frac{1}{T} \right) \right] \quad (2)$$

For catalyst No. 4, the apparent rate equation is:

$$r_A = 0.79 \times 10^{-3} \left[\frac{P_{H_2}}{1000} \right]^{0.73} \exp \left[\frac{6744}{R} \left(0.003 - \frac{1}{T} \right) \right] \quad (3)$$

The effectiveness factor of the pelleted catalysts is very low, as determined by comparing Equations 2 and 3 with Equation 1; its value is of the order of a few hundredths.

Considering the unavoidably limited accuracy of kinetic measurements, there is good agreement between the theory of diffusion with reaction in porous catalysts and our results; the theory predicts 0.815 for the apparent order with

respect to hydrogen and 7 kcal/mole for the apparent activation energy. The order with respect to α -methylstyrene remains zero for its diffusion is much easier than hydrogen because of its much greater concentration. (A more rigorous justification of this fact is given by Germain (19).)

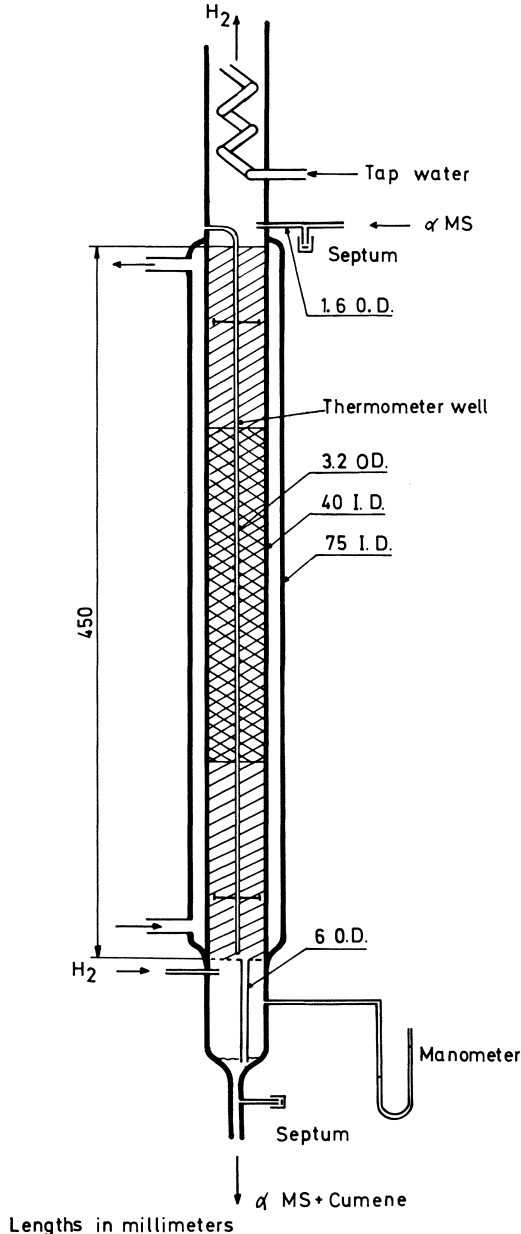


Figure 3. *Experimental trickle bed reactor*

As to the value of the pre-exponential factor, we must introduce the empirical "tortuosity factor" (τ) in computing the effective diffusion coefficient (D_{eff}) to bring theory and experiment together. D_{eff} is defined by:

$$D_{\text{eff}} = \frac{D \varepsilon}{\tau} \quad (4)$$

where D is the molecular diffusion coefficient and ε is the void fraction of the pellet. For catalyst 3, τ is equal to 9.5, and for catalyst 4, it is equal to 6.5. In theory these tortuosity factors depend on the geometry of the catalyst pores and are typical for the catalyst structure; in their computation we took into account the profile of palladium concentration in the pellets and the difference of palladium dispersion from one catalyst to the other. Further details on the determination of the apparent kinetics and comparison of our results with those of Satterfield *et al.* (6, 16) and Sedriks and Kenney (17) are given by Germain (13). With a good knowledge of the intrinsic and apparent rate equations, it is now possible to study the trickle bed reactor itself.

Experimental Apparatus and Procedure

Although commercially, cocurrent downflow is generally preferred in trickle bed reactors, we chose to study a reactor in which the gas and liquid were flowing countercurrently. Countercurrent flow can be very interesting when the reaction is limited by thermodynamic equilibrium. Nevertheless, the results we obtained are certainly valid for reactors with cocurrent downflow because, as we shall see, the gas flow rate does not seem to influence the performance of our reactor under our experimental conditions.

Our experimental trickle bed reactor is shown in Figure 3. It consists of a borosilicate glass cylinder 450 mm long and 40 mm internal diameter, jacketed with a 75-mm internal diameter borosilicate glass tube. To limit the reactor temperature rise, water at constant temperature flows through the annulus.

Hydrogen enters the reactor at the bottom and flows through a perforated stainless steel plate which supports the granular bed. Good distribution of the gas feed is ensured by the small pressure drop through this plate which is also crossed by a 4-mm id stainless steel pipe draining the liquid out of the reactor. At the top of the reactor, three 1-mm id stainless steel pipes distribute the liquid so that it trickles as uniformly as possible on the granular bed. A thermowell axially traverses the reactor. A thermocouple can be moved inside along the bed axis.

The bed comprises the catalytic section surrounded on each end by a layer of inert alumina pellets which have the same dimensions as the catalyst pellets. These alumina layers are useful for distributing the gas and the liquid feed, for bringing them into equilibrium, and for heating them as closely as possible to the temperature of the jacket.

A schematic of the reactor and of its peripheral equipment is shown in Figure 4. Liquid feed, held under constant hydrogen pressure, comes from a Mariott's bottle; it is preheated before entering the reactor. At the inlet and outlet of the reactor, liquid samples for analysis can be withdrawn through septums with a microsyringe. The gas feed is also preheated; the gas flowing out of the bed is cooled at the top of the reactor to condense the greatest part of the vapors. The experimental setup is designed to avoid any contact between the liquids and atmospheric oxygen. Hydroperoxides formed by autoxidation of hydrocarbons poison the catalyst. Throughout each run, the liquid and the gas flow rates, the temperature of the jacket, and the composition of the liquid

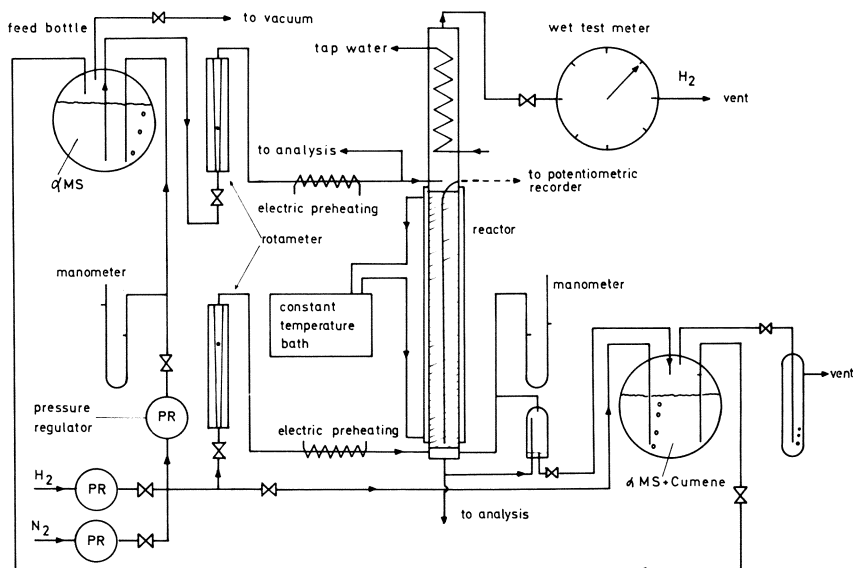


Figure 4. Experimental flow diagram

Table II. Range of Variables

Variable	Range
Total pressure	atmospheric
Temperature of the jacket	27–75°C
Liquid superficial mass flow rate	0.008–0.16 gram/cm ² sec
Gas superficial flow rate	0.16–3.34 cm ³ NTP/cm ² sec
Hydrogen partial pressure	atmospheric
α -Methylstyrene mole fraction	0.5–1

are held constant. The variation range of the main variables is given in Table II. Five different catalyst loadings were used so that five series of runs could be made. The bed parameters for each loading are given in Table III.

Before using a new bed loading, the catalyst is reduced *in situ* with hydrogen. Under a nitrogen atmosphere, cumene or α -methylstyrene enters the reactor at a flow rate high enough to flood the bed which is completely wetted. Each run lasts generally at least 10 hr, which is the time required to reach a constant conversion at the exit of the reactor. If one run does not immediately follow another, the reactor is cooled to ambient temperature, nitrogen is then substituted for hydrogen, and a small liquid flow rate is held until the next run starts.

During a run the liquid and the gas flow rates are measured by calibrated rotameters, the liquid flows are analyzed for refractive index, and the axial temperature profile is thoroughly recorded. In addition, the visual observation through the borosilicate glass wall of the reactor allows us to evaluate qualitatively pellet wetting. This last facility has been very important for explaining our results.

Since the reaction is zero order with respect to α -methylstyrene and changes in hydrogen partial pressure through the bed are negligible, the overall rate of reaction can be expressed as:

$$r = F_L (\alpha_c - \alpha_s) \text{ (moles/sec)} \quad (5)$$

where F_L = liquid molar flow rate (moles/sec); α_e , α_s = mole fraction of the α -methylstyrene, respectively, at the inlet and the exit of the reactor.

The specific rate of reaction is given by:

$$r_s = \frac{r}{w\beta} = \frac{F_L(\alpha_e - \alpha_s)}{w\beta} \quad (\text{moles/sec} \times \text{grams Pd}) \quad (6)$$

where w = weight of catalyst (gram); β = weight fraction of palladium on the catalyst.

For runs No. 1 (see Table III), the catalytic bed is not diluted with inert alumina. During these runs, we observed such high temperature gradients along the axis of the reactor that it was not possible to interpret the measurements correctly. Even when the temperature of the jacket is kept below 40°C, the temperature of the catalyst increases to 100°C or higher from the heat generated by the reaction. (The adiabatic temperature increase is close to 5.8°C for each percent conversion, as calculated by Babcock *et al.* (9).) That is why we diluted the catalytic bed with inert alumina for all further series of runs, as indicated in Table III.

Table III. Bed Parameters

Parameter	Loading No. (=Series of runs)				
	1	2	3	4	5
Height of lower alumina layer, mm	175	90	150	60	240
Height of upper alumina layer, mm	175	150	75	75	75
Catalytic bed					
height, mm	100	210	225	315	135
weight of inert granules, gram	0	120	120	180	60
weight of catalyst pellets, gram	60	30	30	30	30
palladium percentage,	0.5	0.5	1	1	1
weight of palladium, gram	0.3	0.15	0.3	0.3	0.3
Ratio of bed diameter to pellet diameter	12.5	12.5	12	12	12

Despite attempts to maintain isothermal operation, we could not avoid some temperature rise in the catalytic bed. For correlating rate data, an average value of the temperature of each run is useful. We have tried to calculate such a value from the axial temperature profile which is measured experimentally. We define a mean temperature T_m as the temperature of an hypothetical isothermal reactor in which the reaction rate should be the same as in the experimental one. This rate is expressed by:

$$\iiint_{V_R} \exp\left(-\frac{E_a}{RT}\right) dV_R = V_R \exp\left(-\frac{E_a}{RT_m}\right) \quad (7)$$

where V_R is the volume of the reactor (cm^3), and E_a is the apparent activation energy of the reaction (cal/mole). If we suppose that the temperature is uniform in each cross-section of the catalytic bed, it follows:

$$\int_0^L \exp\left(-\frac{E_a}{RT(x)}\right) dx = L \exp\left(-\frac{E_a}{RT_m}\right) \quad (8)$$

where x is the axial coordinate (cm), and L is the length of the catalytic bed (cm). Thus, we have to calculate T_m and E_a by an iterative procedure for each series of runs. The convergence is rapid; generally, three or four iterations are sufficient. Of course, the mean temperature approximation is only justified if the apparent energy of activation is constant. We shall see below that all our results were correlated rather well by a simple Arrhenius relation-

ship. We have thus, *a posteriori*, an indication of the validity of Equation 8. For the discussion of the results, it is important to note that the calculated T_m value (Equation 8) is always a little greater than the mean temperature defined in Equation 7 since the temperature on the axis of the reactor is, in theory, the maximum temperature in each cross-section for an exothermic reaction.

Results and Discussion

Wetting the Bed. With a fresh catalyst packing, complete wetting of the bed is very difficult to realize. At the beginning of a hydrogenation run, the whole packing remains dry for a long time except for some thin channels where the liquid trickles. With time, the number of wetted pellets increases slowly. According to the temperature, the bed is finally completely wetted ($T < 35^\circ\text{C}$) or not ($T > 35^\circ\text{C}$). If we substitute nitrogen for hydrogen, or pure cumene feed for pure α -methylstyrene feed, an apparently uniform wetting of the bed rapidly takes place. In fact, in such a purely physical situation, channeling exists, as can be shown by tracer experiments (20), but all the pellets are wetted according to visual observation. In the system under reaction conditions, we observe that dry areas subsist for any liquid flow rate if the temperature is high enough ($T > 35^\circ$). These areas are always located in the

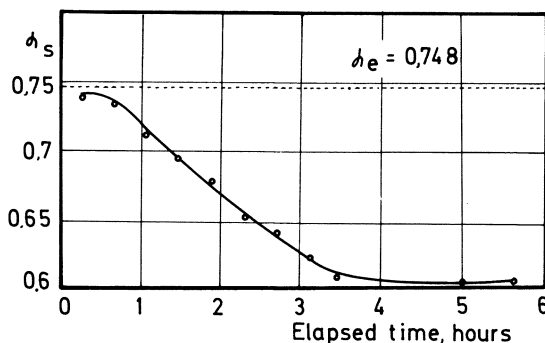


Figure 5. Equilibration of the reactor

catalytic section of the granular bed, never in the upper or lower layers of inert material. During the reaction, the dry parts of the bed are transient: some pellets may be dry at a given time, wetted a few hours later, and again dry later on. The reaction itself seems thus to have an influence upon the hydrodynamic behavior of the trickle bed. This point is important since it shows that purely hydrodynamic study should not be sufficient to characterize the liquid flow in trickle bed reactors. To be useful for designing and predicting performances of trickle bed reactors, the hydrodynamic study should be made during reaction because wetting and reaction are probably strongly connected.

Reactor Equilibration and Influence of the Liquid Flow Rate. After the beginning of a hydrogenation experiment, the overall reaction rate is changing during the first few hours of the run, as shown in Figure 5. The rate goes up or down, according to the starting procedure of the reactor. The reactor behavior at the beginning of a run is believed to be determined not only by the

catalyst activity equilibration, but mainly by the extent of wetting of the catalyst bed. If the reactor is held under nitrogen while heating to the desired temperature, the reaction rate is at first very slow when the hydrogen is fed, and then it increases slowly up to a steady state (*see* Figure 5). On the contrary, if the reactor is started under reaction conditions, it may be that the reaction rate is at first very high, and then decreases gradually to reach the steady state. Such similar behavior of a trickle bed reactor has been observed by Sedriks and Kenney (8).

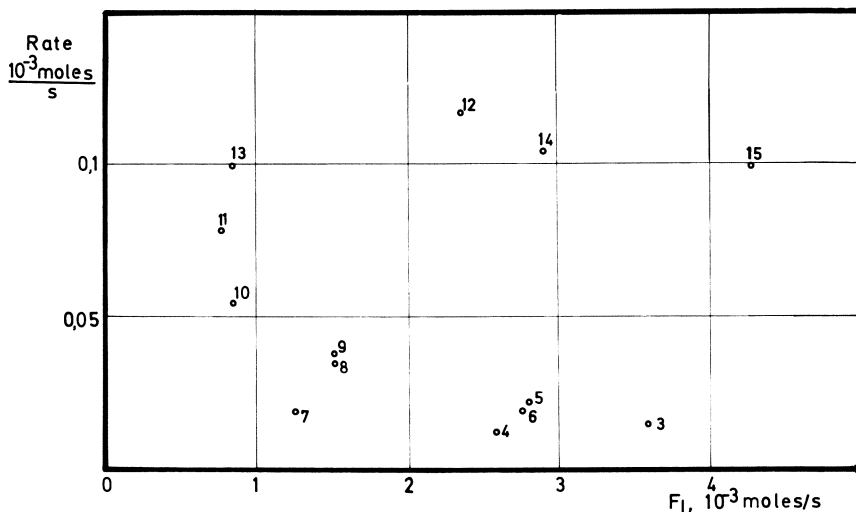


Figure 6. Liquid flow rate dependence of reaction rates (runs 203–215)

In addition, when the reactor temperature is high enough ($T > 35^{\circ}\text{C}$), we have observed at least two different steady states. Figure 6 shows reaction rates for 13 successive runs of series No. 2 (*see* Table III). The dependence of the reaction rate *vs.* the liquid flow rate is not uniform. For runs 203–210, reaction rate increases when the liquid flow rate decreases. If the liquid flow rate is increased in this sequence of runs, much higher reaction rates occur than those measured previously (runs 211–215).

These runs have been conducted at a constant jacket temperature of 55°C . The reaction rate obtained with the same catalyst pellets in the stirred tank reactor (Equation 2) at 55°C equals 0.045×10^{-3} mole/sec. This value is higher than the rates of runs 203–209 (low rate steady state) but is smaller than the rates of runs 210–215 (high rate steady state).

At first, it is quite normal that the reaction rate obtained in a trickle bed reactor is smaller than the rate prevailing in the stirred tank reactor because of the rate limitation by diffusion through the liquid film surrounding the catalyst pellets. The trickle bed reactor performance can be explained by supposing that the liquid film thickness is about 0.03 mm, which seems very likely according to the liquid holdup calculated from tracer experiments in our laboratories (20, 21) and following the equation proposed by Satterfield and Way (7).

The results obtained for runs 210–215 are, on the other hand, paradoxical. Diffusion is much easier in the stirred tank reactor, and yet we observe the

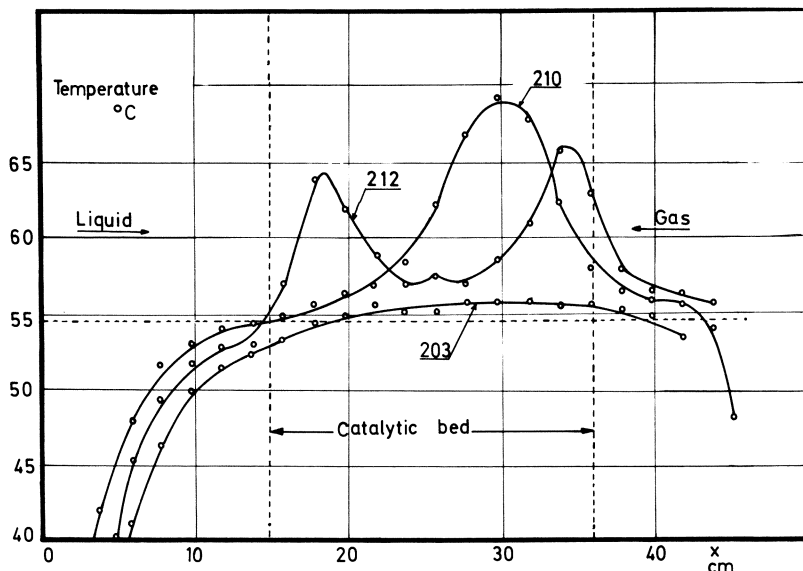


Figure 7. Axial temperature profiles

lowest reaction rates in this device. It is possible to explain at least partly this experimental fact by supposing that the catalyst temperature is much higher than the jacket temperature. We shall show however that this explanation is not completely satisfactory.

Axial Temperature Profile. The thorough measurement of the axial temperature profile is valuable in understanding the mechanisms of the trickle bed reactor. Typical measurements are shown on Figures 7 and 8. When the reaction rate is high (high rate steady state), one or more hot spots appear in the catalytic bed (runs 210 and 212 on Figure 7). When the reaction rate is low (low rate steady state), the catalytic section of the granular bed is almost isothermal (run 203 in Figure 7). During some runs, we have observed three or even four hot spots (see Figure 8), which is very difficult to explain unless the catalyst pellets and the inert pellets are not well mixed. This assumption must be ruled out. Then, why have we observed hot spots during some runs and not during others, for the same operating variables? Why are the hot spots not always at the same place for the same bed loading (runs 210 and 212 in Figure 7)? In fact, when the reaction proceeds, the warm areas move through the catalytic bed—*i.e.*, the temperature of a defined area of the bed changes continuously. The working of the bed presents some aleatory character.

Similar observations have been made above concerning the dry and wetted areas in the bed. It is also possible that the same areas are simultaneously warm and dry. Indeed we have good reasons to believe this assumption, despite the fact that we observe the dry areas near the wall of the reactor while we measure the temperature along the axis of the reactor. Given some visual observations, for example, a liquid condensation on the reactor wall just near each dry area, we may admit that the catalyst pellets are drying because they grow hot. The formation of the dry areas is not directly related to poor liquid distribution (at the wall of a packed bed, the liquid flow rate is always larger than in the bulk of the packing and should not favor dry areas)

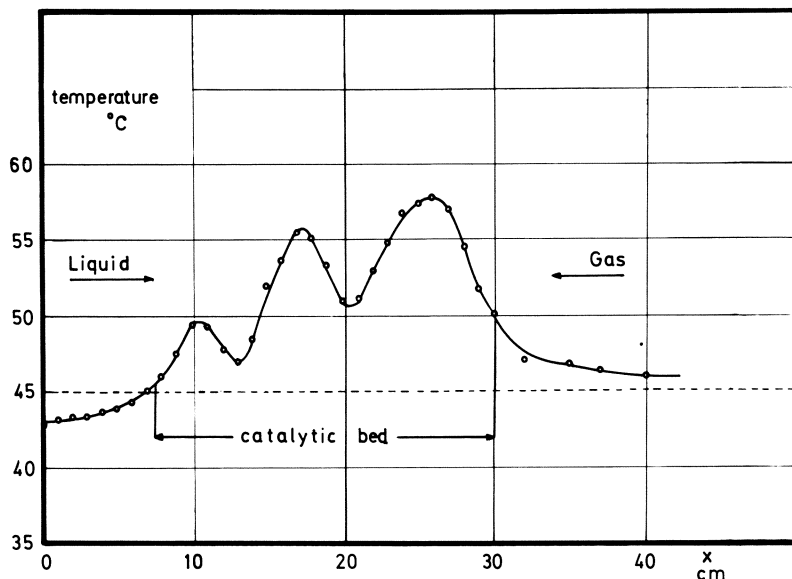


Figure 8. Axial temperature profile

but results from the heating of the catalyst. The existence of warm and dry catalyst pellets poses the question: what is the effective reaction rate at the gas-solid interface? If higher reaction rates can be obtained on dry catalyst pellets, we could explain the high rates we have observed when dry areas are present in the bed. This explanation has already been proposed by Sedriks and Kenney (22), who were studying the hydrogenation of crotonaldehyde in a trickle bed reactor.

The Hydrogenation of α -Methylstyrene in Vapor Phase. A kinetic study of the hydrogenation of α -methylstyrene vapor on palladium powdered catalyst No. 1 (see Table I) was done in our laboratory (23). Despite the difficulties in measuring very high reaction rates, this study enables us to derive useful results. The reaction order with respect to α -methylstyrene is zero, the order with respect to hydrogen partial pressure is about 0.8, and the apparent activation energy is close to 9000 cal/mole. For a fresh catalyst, the reaction rate is a little greater than the intrinsic reaction rate in the liquid phase, but the catalyst deactivation is fast; after 50 hr, the rate of reaction is negligible.

To summarize, except for deactivation, the intrinsic rate equation for the gas phase reaction is almost identical with the corresponding rate equation in the liquid phase. We arrive at the same conclusion Way (4) derived for the isomerization of cyclopropane to propylene: The reaction rates depend much more on the fugacities of the reactants, of which the partial pressures give good values, than on their concentrations.

Deactivation can be explained by catalyst poisoning by a polymer. Catalytic activity is restored by washing with benzene, cumene, α -methylstyrene, or any solvent of the α -methylstyrene polymer. This is why we do not observe any noticeable deactivation of the wetted catalyst.

Temperature Dependence of the Reaction Rate in the Trickle Bed Reactor. Because of the two steady-state possibilities, the temperature dependence of the reaction rate is not easy to establish. For the low rate steady state operation,

we do not have enough data to obtain an accurate correlation. The apparent activation energy is rather low, about 5000 cal/mole, which corroborates the assumption that the reaction rate is limited by hydrogen transfer through the liquid film surrounding the pellets. However, it is not absolutely certain that in the range of temperature and flow rates of this work the low steady state is really stable. Hereafter, we shall only consider the high rate steady state.

Figure 9 shows an Arrhenius plot of the results obtained with bed loading No. 4. The apparent activation energy is high (8100 cal/mole), even a little higher than that obtained with the same catalyst in the stirred tank. We observe also that the scattering of the experimental results is greater when the temperature is low. This is probably caused by difficulties in reaching steady-state operation. Figure 10 shows the results obtained with bed loading Nos. 3 and 5 (see Table III): the corresponding lines are c and b. Lower specific rates are obtained with the less diluted catalyst bed. Figure 10 also shows the rate obtained with the stirred tank reactor (line a). As previously pointed out, the rates in this latest case are smaller than those measured in the trickle bed reactor. This is especially surprising because the temperature used for correlating the trickle bed rate data has been a little overestimated.

Mechanisms of the Trickle Bed Reactor. The first hypothesis we considered is that the reaction proceeds with a higher rate on the dry catalyst pellets because of the easier diffusion of the reactants in the gas phase, even

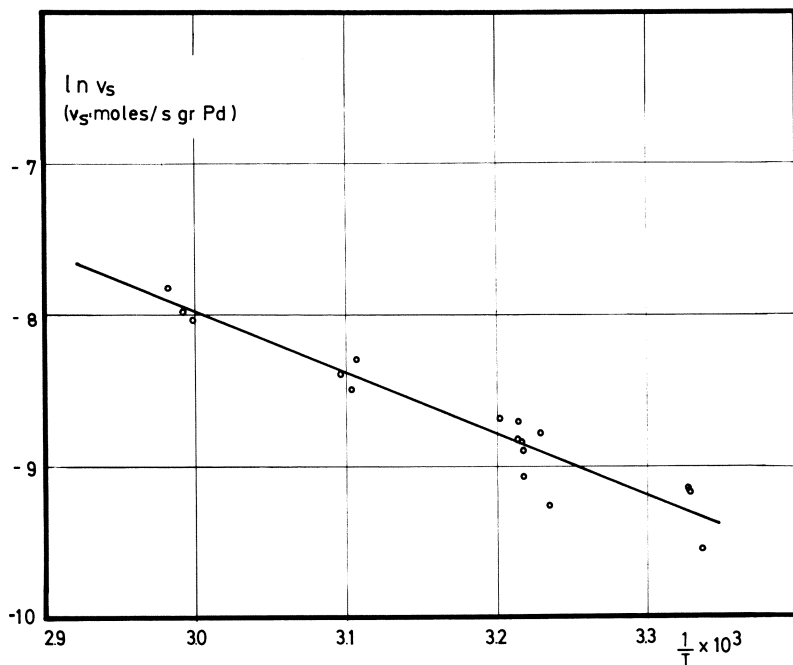


Figure 9. Temperature dependence of the reaction rates (series No. 4)

if the intrinsic reaction rate is the same in the gas phase as in the liquid phase. This hypothesis has already been formulated by Ware (24), Pelossov (25), and Sedriks and Kenney (8). It is also logical to suppose that during reaction

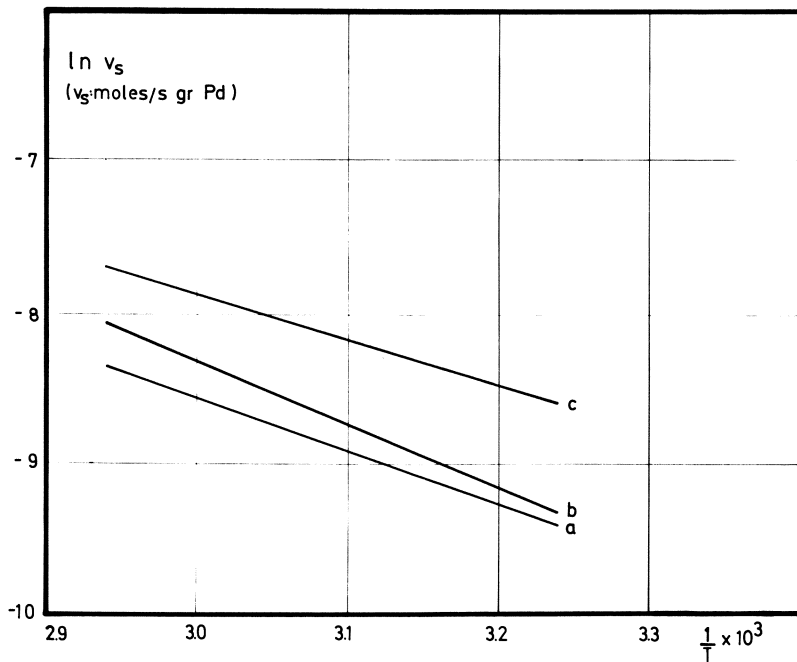


Figure 10. Temperature dependence of the reaction rates (a = stirred pellets, b = series No. 5, c = series No. 3)

the steady-state temperature of the dry pellets is higher than that of the wetted pellets.

Such a hypothesis does not hold under careful examination. If the intrinsic reaction rate in the gas phase is as high as in the liquid, the effectiveness factor of the pellets cannot be high. The apparent reaction rate obtained on dry pellets is very low. Whereas the α -methylstyrene diffuses very easily in the liquid phase, the situation is quite different in the gas phase. Because of its low volatility, the α -methylstyrene is in small concentration (at 60°C , $C = 8.7 \times 10^{-7}$ mole/cm³), and it diffuses in the slow Knudsen regime through the rather small diameter pores of the catalyst (26). In fact, the effectiveness factor of the dry catalyst pellets is so low that the effective reaction rate on these pellets (in the absence of external transfer resistances) is smaller than the rate on the wetted ones. Consequently, dry pellets cannot have a sufficiently high activity to explain the high conversion we have measured.

Therefore, the most active pellets are those which are only partly wetted. In this case, gaseous and liquid reactants diffusions are simultaneously easy in the gas-liquid interface of these pellets. Because of capillary forces, partial wetting of the pellets is enough to ensure good availability of the α -methylstyrene to the reaction sites. It is even possible that in partly wetted pellets the capillary forces create some convective mass transfer which may be more efficient than molecular diffusion. Liquid α -methylstyrene can enter a partly wetted pellet at one side, be hydrogenated to cumene near the gas-liquid interface, and reach the gaseous phase since the reaction product is more vola-

tile than the reactant. According to this mechanism, the polymer which may form cannot be dissolved and eliminated through the liquid stream.

Consequently, when the catalyst pellets are completely wetted, the apparent reaction rate is low since it is limited by the hydrogen diffusion through the liquid film surrounding the pellets and particularly by the diffusion in the liquid-filled pores of the catalyst. When dry and warm areas appear in the bed, partly wetted pellets appear at the same time on which the greatest part of the α -methylstyrene conversion proceeds. These partly wetted pellets become hot from poor heat transfer associated with their poor irrigation. As a result, their activity increases again.

As long as the reaction rate is high, the heat generated is sufficient to hold the active areas dry. However, the activity decreases gradually because of polymer formation. The pellets cool and can be wetted once again. The liquid then dissolves the polymer, and some time later catalyst activity will be restored. This explains the cyclic evolution of catalyst activity.

We can also understand why the lowest specific reaction rates are obtained in the less diluted catalyst bed. If the catalyst pellets are next to each other, large, completely dry areas may form through which the liquid has no access. Since α -methylstyrene diffusion is not easy in the gas phase, these areas, even at high temperature from the surrounding active pellets, do not contribute efficiently to the conversion of the α -methylstyrene to cumene.

Conclusions

The accurate characterization of the processes which occur in a trickle bed reactor is extremely difficult, not only because of the numerous different phenomena which exist (two-phase flow, convective and diffusive mass transfer, heat transfer, chemical reaction, and activation and deactivation of the catalyst, *etc.*), but also because all these phenomena are strongly connected; thus, it is not easy nor meaningful to study each of them independently of the others.

However, despite its complexity, the trickle bed reactor offers important advantages over the fixed bed when it operates in the gas phase. First is the possibility of feeding the reactor with approximately stoichiometric amounts of reactants, thereby avoiding expensive recirculation. A second advantage is easier temperature control. We have observed that because of the vaporization of the liquid feed, heat transfer is greatly enhanced. We could determine that the heat conductivity of the wetted bed is much higher than that of the same bed operating in the gas phase (further details are given by Saive (20)).

We also have shown another reason, quite essential, which justifies the use of the trickle bed reactor—the much more stable activity of the catalyst in the presence of a liquid. The observations concerning the hydrogenation of the α -methylstyrene are probably not specific for this reaction. In numerous industrial heterogeneous catalytic processes, heavy byproducts (tars, for example) form, settle on the catalyst, and poison it. In the presence of a liquid phase, these byproducts are dissolved, and the lifetime of the catalyst is extended.

Finally, we would emphasize how the hydrogenation of the α -methylstyrene on palladium is a good test reaction for the study of three-phase systems. It is simple to use in the laboratory but complex enough to encompass many of the problems encountered in the industrial three-phase catalytic processes.

Acknowledgment

The palladium dispersion was measured in the laboratory of M. Boudart.

Literature Cited

1. Hoog, H., "Eighth World Petroleum Congress Proceedings," Vol. 4, Applied Science Publishers, London, p. 117, 1971.
2. Schwartz, J. G., Roberts, G. W., *Ind. Eng. Chem. Process Des. Develop.* (1973) **12**, 262.
3. Sylvester, N. D., Pitayagulsarn, P., *AIChE J.* (1973) **19**, 640.
4. Way, P. F., Ph.D. Thesis, Massachusetts Institute of Technology, 1971.
5. Charpentier, J. C., Bakos, M., Le Goff, P., Société Hydrotechnique de France, XII^{mes} Journées de l'Hydraulique, Question IV, Rapport 10, Paris, 1972.
6. Satterfield, C. N., Pelossof, A. A., Sherwood, T. K., *AIChE J.* (1969) **15**, 227.
7. Satterfield, C. N., Way, P. F., *AIChE J.* (1972) **18**, 305.
8. Sedriks, W., Kenney, C. N., *ADVAN. CHEM. SER.* (1972) **109**, 251.
9. Babcock, B. D., Mejdell, G. T., Hougen, O. A., *AIChE J.* (1957) **3**, 366.
10. Sherwood, T. K., Farkas, E. J., *Chem. Eng. Sci.* (1966) **21**, 573.
11. Pruden, B. B., Weber, M. E., *Can. J. Chem. Eng.* (1970) **48**, 162.
12. Ma, Y. H., Ph.D. Thesis, Massachusetts Institute of Technology, 1966.
13. Germain, A., Collection des Publications de la Faculté des Sciences Appliquées de l'Université de Liège, No. 40, pp. 1-163, 1973.
14. Benson, J. E., Hwang, H. S., Boudart, M., *Catalysis* (1973) **30**, 146.
15. Boudart, M., Jr., Aldag, A., Benson, J. E., Dougharty, N. A., *Catalysis* (1966) **6**, 92.
16. Satterfield, C. N., Ma, Y. H., Sherwood, T. K., *Int. Chem. Eng. Symp. Ser.* (1968) **28**, 22.
17. Sedriks, W., Kenney, C. N., *Chem. Eng. Sci.* (1972) **27**, 2029.
18. Carberry, J. J., *Ind. Eng. Chem.* (1964) **56**, 39.
19. Germain, A., *op. cit.*, pp. 137-138.
20. Saive, M., travail de fin d'études, Université de Liège, Liège, Belgique, 1973.
21. Crine, M., Gosset, R., L'Homme, G., Communication No. 14, Congrès International, "Emploi des Ordinateurs en Génie Chimique," Paris, 1973.
22. Włodarczyk, J., travail de fin d'études, Université de Liège, Liège, Belgique, 1972.
24. Ware, C. H., Jr., Ph.D. Thesis, University of Pennsylvania, 1959.
25. Pelossof, A. A., Ph.D. Thesis, Massachusetts Institute of Technology, 1967.
26. Satterfield, C. N., "Mass Transfer in Heterogeneous Catalysis," M.I.T. Press, 1970, p. 41 *et seq.*

RECEIVED January 2, 1974. Study supported in part by grant from Fonds National Belge de la Recherche Scientifique.

An Experimental and Computational Study of the Hydrolysis of Methyl Formate in a Chromatographic Reactor

ROBERT G. WETHEROLD¹ and EUGENE H. WISSLER

The University of Texas, Austin, Tex. 78712

KENNETH B. BISCHOFF

Cornell University, Ithaca, N.Y. 14850

An experimental and computational study was made of the general equilibrium-limited reaction of the type $A \rightleftharpoons B + C$ occurring under chromatographic conditions. The liquid phase hydrolysis of methyl formate passed through a bed of activated charcoal was the system. This study was done to test a liquid-solid chromatographic reactor and to verify a mathematical model proposed for the system. In every experiment, conversions in excess of the equilibrium value were obtained, and complete conversion was achieved in some cases. The experimental results were compared with the results predicted by numerical solution of the mathematical model. The model was adequate if measures were taken to account for multicomponent adsorption and axial dispersion.

A chromatographic reactor involves certain fundamental principles. The column is filled with a solid adsorbent which may act also as a catalyst support, or a solid which is impregnated with a liquid (stationary phase) which may or may not be involved in the reaction. A carrier fluid (mobile phase) flows continuously through the column, and this carrier may be either an inert fluid or one of the reactants. A reactant or reaction mixture is injected into the reactor as a pulse. As the mobile phase sweeps this pulse through the column, both reaction and separation occur because the components (both reactants and products) have different affinities for the solid adsorbent or stationary phase and they will tend to separate as the pulse moves down the column. Both gas and liquid chromatographic columns can be used as chemical reactors.

One important application of these principles is in studies of chemical kinetics, adsorption, and other rate phenomena (1, 2, 3, 4, 5, 6, 7, 8). Here, a major benefit is the convenience of using standard chromatographic instrumentation in addition to the pulse separation possibilities. Of more interest to the present work are some possible industrial applications. Roginskii *et al.* (9),

¹ Present address: Mobil Chemical Co., Edison, N. J.

pointed out that in such a reactor, conditions might be created under which the reaction products separate during most or all of the time the substances are passing through the column. They suggested that some types of equilibrium-limited reactions might be forced "past" equilibrium in a chromatographic system. Matsen *et al.* (10) presented four conditions they felt were necessary for a chromatographic reactor to be advantageous: (1) the reaction must be reversible, and the equilibrium constant must be small, (2) the separation of products should limit the reaction—*i.e.*, the reaction rates should be relatively high, (3) at least two chromatographically separable products must be formed, and (4) reactants must not be separated in the reactor.

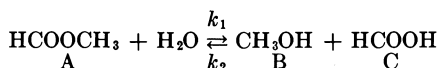
A number of experimental studies have been done of gas-phase reactions occurring under chromatographic conditions over a solid catalyst. Among these are the dehydrogenation of cyclohexane (10, 11, 12, 13, 14) and other reactions (15, 16, 17). In these cases, equilibrium yields were exceeded, in some cases by as much as an order of magnitude.

Theoretical studies were done of a reaction of the type $A \rightleftharpoons B + C$ by Magee (18), Roginskii and Rozental (19, 20), and Gore (21). Saito *et al.* (22) considered reactions having two to four components, with a maximum of two reactants. Langer *et al.* (5) defined and characterized a general "ideal chromatographic reactor" which differs from the ideal batch, plug flow, or stirred tank reactor. Most or all of these characteristics were assumed in all of the work done so far on chromatographic reactors. As defined by Langer *et al.* (5), the ideal chromatographic reactor has six basic characteristics: (1) a pulse of reactant reacts as it travels through the column, and the reaction products are instantaneously separated from the reactant and, in many cases, also from each other, (2) the mobile phase is incompressible—*i.e.*, its linear velocity is constant through the column, (3) axial dispersion and band spreading are negligible, (4) the rates of mass transfer, adsorption, and absorption are fast and not limiting—*i.e.*, the reaction rate is limiting, (5) the adsorption isotherms are linear, and (6) the column operates isothermally, and heat effects are negligible.

If the chromatographic reactor is to be industrially useful, the requirement of small, narrow pulses is very restrictive. Even though high conversions could well be obtained, total average output of products would be quite low. If the pulse is of an industrially reasonable size and duration, the reaction products can no longer be assumed to completely separate instantaneously from the reactant or from each other. For a gaseous mobile phase, the assumptions of an incompressible mobile phase and of a linear isotherm are not usually accurate. While the assumption of an incompressible mobile phase is valid for a liquid chromatographic reactor, the assumption of a linear adsorption isotherm is, generally, quite unreasonable. Axial dispersion may or may not be negligible; this needs to be determined for each individual system.

Description of System

To develop and verify a mathematical model of the process, it is not necessary that all the above conditions of Matsen *et al.* (10) be satisfied. Of the four conditions stated, only the last two, along with the requirement of a reversible reaction, are required to demonstrate the operation of a chromatographic reactor. After considerable study, the liquid-phase acid (HCl) catalyzed hydrolysis of methyl formate:



was selected. It is a reasonably fast reaction at moderate temperatures, with no significant side reactions. The reaction is reversible and equilibrium-limited, even when carried out in excess water. Activated charcoal was the adsorbent, and the reaction products of an acid and an alcohol had sufficiently different properties so that they were readily chromatographically separable.

Previous studies of the kinetics of this reaction have been done in water, aqueous acetone, and other solvents. Newling and Hinshelwood (23) found that a straightforward rate equation was satisfactory:

$$-r_A = k_1(\text{HCl}) [A] - k_2(\text{HCl}) [B] [C] \quad (1)$$

The value of $k_1 = 0.060 \text{ min}^{-1}$ at 25°C was determined, with an activation energy of 15,600 cal/mole, at 0.05 mole/liter of HCl. If the rate of hydrolysis is assumed to be proportional to the concentration of water, the value of k_1 reported by Newling and Hinshelwood can be corrected for the acetone in the reaction: 0.152 min^{-1} , which compares quite well with the value of 0.145 min^{-1} at 25°C reported by Salmi (24) for the hydrolysis done in water with HCl as a catalyst. Bell *et al.* (25) found that k_1 was a function of acid concentration. Values of k_1 obtained at 25°C ranged from 0.238 min^{-1} in 2.76N HCl to 0.420 min^{-1} in 6.41N HCl. They found the hydrolysis to be slightly endothermic, with a heat of reaction about 4.0 kcal/mole.

To get reasonably fast reaction rates, concentrations of acid in the range of 0.5–1.0N are necessary, and experimental rate data at these acid concentrations are required. Standard batch kinetic studies were performed in a 50-ml beaker (the chemical analytical details are described later). Equilibrium constants were also determined after 6–24 hr periods at $22^\circ\text{--}24^\circ\text{C}$ for acid concentrations of 0.054, 0.54, and 1.06 moles/liter. These were 9.29, 8.36, and 6.75 moles/liter, which indicates some non-ideality. These values should also be essentially the same in the presence of the activated charcoal, unless a new solute–solid complex were formed; the actual measurement of this could also be complicated by the adsorption phenomena. For the same acid catalyst concentrations, the values of k_1 , corrected to 25.0°C , were: 0.144, 0.154, and 0.176 min^{-1} . These compared well when interpolated between the literature values of Newling and Hinshelwood (23) and Salmi (24) and of Bell *et al.* (25).

Adsorption from liquids is a complicated phenomenon (26) but can often be approximately described by a Langmuir or Freundlich isotherm. Some isolated, specific studies are available; Ockrent (27), Oscik (28), and Wilson (29) have proposed a straightforward multicomponent form of the Langmuir isotherm. Data for the specific system under study were required, and were obtained using 5–15 grams of low-activity activated charcoal in an Erlenmeyer flask by classical methods, with more than 1 hr equilibration time. Binary aqueous solutions of formic acid, methyl formate, methanol, and HCl were studied, along with the ternary systems water–methanol–HCl and water–methyl formate–methanol.

The Freundlich isotherm provided the best description; the multicomponent systems could not be described by the multicomponent Langmuir isotherm of Wilson (29). Therefore, Freundlich isotherms were used to fit the binary data:

$$q_i = b_i C_i^{m_i}, \quad i = A, B, C \quad (2)$$

where q is the moles adsorbed per mass of solid. Empirical correction factors were used for the multicomponent systems. The resulting parameter values are given in Table I and provide good fits for concentrations less than 1.5 moles/liter.

Table I. Constants for Freundlich Isotherm, $q_i = b_i C_i^{m_i}$

System	No. of Data Points	Highest Solute Concn., moles/liter	b_i	m_i	% Deviation		
					Mean	Max	Standard
Formic acid-H ₂ O	12	1.631	0.00292	0.357	3.3	7.0	3.9
HCl-H ₂ O	6	1.547	0.000868	0.285	2.7	5.0	3.3
Methanol-1.03N HCl	7	1.536	0.00158	0.841	4.0	9.5	5.2
Methanol-H ₂ O	8	1.480	0.00176	0.843	3.4	9.8	4.9
Methyl formate-H ₂ O	8	1.530	0.00506	0.428	3.6	7.2	4.1

Methyl formate was adsorbed to a much greater degree than any of the other components, about twice that of formic acid; the adsorption of formic acid was roughly 50% greater than that of methanol at any given concentration; HCl was adsorbed the least. The isotherm describing the adsorption of HCl was the most nonlinear, with formic acid, methyl formate, and methanol coming next in order of decreasing nonlinearity. As shown in Table I, methanol adsorption was decreased somewhat (*ca.* 10%) by the presence of HCl in the solution. In the multicomponent systems, the main complication was that methanol adsorption was significantly reduced by the presence of methyl formate; this was handled by an empirical correction.

Mathematical Model

In developing the material balance or continuity equations for each of the components involved in the chromatographic reactor, some assumptions were made: (1) negligible axial dispersion, (2) flat velocity profile, (3) flat concentration profile (*i.e.*, plug flow), (4) constant velocity (constant fluid density), (5) constant temperature, (6) instantaneous adsorption equilibrium, (7) reaction takes place only in the liquid phase, (8) adsorption-desorption isotherms are equal (no hysteresis), (9) adsorption of one component is independent of concentration of other solutes. The final assumption that the adsorption of one component is unaffected by others in a solution is obviously invalid, but is made in the absence of any theoretical multicomponent liquid-solid isotherm. Then, the mass balance for species i is:

$$\frac{\partial C_i}{\partial t} + \frac{\rho_s}{\epsilon} \frac{\partial q_i}{\partial t} + v \frac{\partial C_i}{\partial z} = r_i \quad (3)$$

where ϵ is the total fraction of void space in the bed, ρ_s is the bulk density of packing, and v is the interstitial velocity. With the Freundlich isotherm, Equation 2, the mass balance becomes:

$$\frac{\partial C_i}{\partial t} + \frac{v}{1 + \Phi_i C_i^{e_i}} \frac{\partial C_i}{\partial z} = \frac{r_i}{1 + \Phi_i C_i^{e_i}} \quad (4)$$

where $e_i = m_i - 1$ and $\Phi_i = \rho_s m_i b_i / \varepsilon$.

Equation 4 can be made dimensionless by introducing the dimensionless time $\tau = vt/L$, length $x = z/L$, and concentrations $\eta_i = C_i/C_A^\circ$, where C_A° is the concentration of the injected reactant, component A, averaged over the width of the pulse. Then, the mass balance equations are:

$$\frac{\partial \eta_A}{\partial \tau} + \frac{1}{1 + \Phi_A(C_A^\circ)^{e_A} \eta_A^{e_A}} \frac{\partial \eta_A}{\partial x} = \left(\frac{k_1 L}{v}\right) \left(\frac{1}{1 + \Phi_A(C_A^\circ)^{e_A} \eta_A^{e_A}}\right) \left(-\eta_A + \frac{C_A^\circ}{K_e} \eta_B \eta_C\right) \quad (5)$$

$$\frac{\partial \eta_B}{\partial \tau} + \frac{1}{1 + \Phi_B(C_A^\circ)^{e_B} \eta_B^{e_B}} \frac{\partial \eta_B}{\partial x} = \left(\frac{k_1 L}{v}\right) \left(\frac{1}{1 + \Phi_B(C_A^\circ)^{e_B} \eta_B^{e_B}}\right) \left(\eta_A - \frac{C_A^{e_B} \eta_B \eta_C}{K_e}\right) \quad (6)$$

$$\frac{\partial \eta_C}{\partial \tau} + \frac{1}{1 + \Phi_C(C_A^\circ)^{e_C} \eta_C^{e_C}} \frac{\partial \eta_C}{\partial x} = \left(\frac{k_1 L}{v}\right) \left(\frac{1}{1 + \Phi_C(C_A^\circ)^{e_C} \eta_C^{e_C}}\right) \left(\eta_A - \frac{C_A^\circ}{K_e} \eta_B \eta_C\right) \quad (7)$$

These are to be solved for initial conditions of zero concentration and with boundary conditions:

$$\eta_i(0, \tau) = \eta_i^\circ(\tau), \text{ a pulse input} \quad (8)$$

Numerical procedures based on the method of characteristics (30), were suitable, but a method suggested by Coats (31) had a comparable accuracy and was simpler. In terms of Equations 5-7, the finite difference form was:

$$\frac{\eta_i(j+1, n) - \eta_i(j, n)}{\Delta \tau} + \frac{1}{1 + \bar{q}_i'} \frac{\eta_i(j, n) - \eta_i(j, n-1)}{\Delta x} = \left(\frac{k_1 L}{v}\right) \frac{r_i(j+1/2, n)}{k_1(1 + \bar{q}_i') C_A^\circ} \quad (9)$$

$i = A, B, C$

where

$$\bar{q}_i' = \frac{\rho_s}{\varepsilon} \frac{\partial q_i}{\partial C_i} \approx \frac{\rho_s}{\varepsilon} \frac{q_i(j+1, n) - q_i(j, n)}{C_i(j+1, n) - C_i(j, n)}$$

and $\tau = j\Delta\tau$, $x = n\Delta x$. The rate, r_i , is evaluated at the average of the concentrations at times j and $j+1$ for any value of n . An iterative method was thus required to obtain $\eta_i(j+1, n)$; see Ref. 32 for further details.

Even though axial dispersion was neglected in the model formulation, the numerical technique unavoidably introduces a certain amount of "numerical dispersion." For a linear isotherm, $m = 1$ or $e = 0$, an estimate of the dispersion coefficient or Peclet number is:

$$\frac{1}{Pe} = \frac{D}{vL} = \frac{1}{2N} \left(1 - \frac{1}{1 + \Phi} \frac{\Delta \tau}{\Delta x}\right), N = \frac{L}{\Delta z}$$

This value was consistent with the treatment of Hasimoto *et al.* (33) and also the more rigorous description of Chai and Hoelscher (34) and Dayan and Levenspiel (35).

Experimental

In determining the adsorption isotherms and the basic kinetics, the concentration of the formic acid in solution was found by titration. The concentrations of all components except formic acid were obtained with a gas chromatograph equipped with a thermal conductivity cell. The column gave good separation of methanol and methyl formate, although the formic acid concentration could

not be determined because it and water eluted at the same time. Operating temperature was 100°C, the carrier gas was helium; an analysis took less than 4 min. The accuracy of the analyses was estimated at $\pm 1.0\%$ at concentrations of 1.0 mole/liter or greater to $\pm 5.0\%$ at concentrations below 0.2 mole/liter.

The reactor consisted of a 4.2-inch (107 mm) length of PVC pipe, and all other reservoirs, tubing, etc., in contact with HCl were nonmetal. The various flows were measured by rotometers, and the carrier fluid driven by pressurized nitrogen. The reactant was injected with a dual infusion/withdrawal pump using hypodermic syringes. Effluent samples were taken about every 4 min and immediately injected into the chromatograph (*see* Ref. 32 for further details).

To test the assumption of instantaneous adsorption equilibration, experiments with pure methanol pulses in water and 1.03N HCl carrier solutions were performed at four different flow rates in the desired range. The leading and trailing edges were the same, indicating the absence of transport effects.

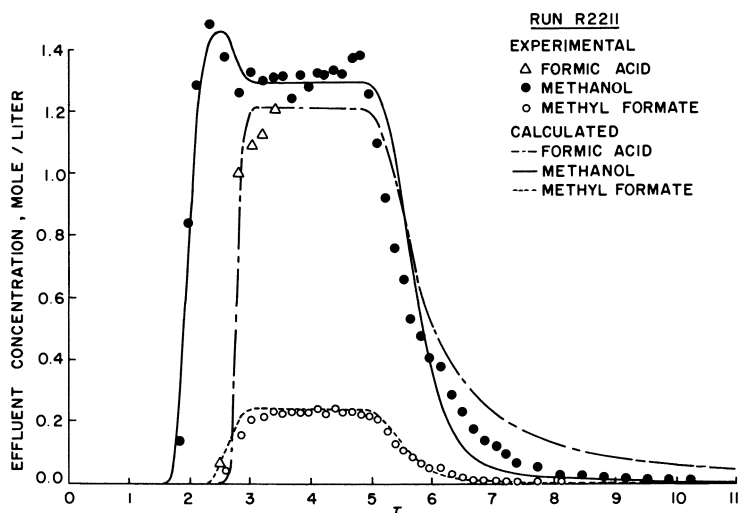


Figure 1. Effluent concentrations for run 2211—wide inlet pulse of reactant

Reaction runs were made at flow rates such that the mean residence times, L/v , were about 30 and 15 min. The inlet methyl formate concentrations, C_A^0 , were about 1.5 and 1.0 moles/liter. The inlet pulse duration was also varied. At the lower inlet concentrations, experimental conversions ranged from 100% at the shortest pulse duration of 17.5 min or 0.59 τ to 91.7% at the longest pulse duration of 200 min or 6.81 τ . The calculated equilibrium conversion for each of these four runs was 87.8%. At the higher inlet concentrations, the same trend was observed with the conversions ranging from 99.7 to 87.6% for the shortest and longest inlet pulse duration. The comparable equilibrium conversions were 83.4 to 83.8%. The shorter pulses were expected to give higher conversions because the chromatographic separation becomes more efficient as the pulses becomes shorter. However, even for the relatively long pulses of 100 to 200 min (3.8 to 6.8 τ), conversions greater than those at equilibrium were obtained. The chromatographic reactor naturally did not show a dramatic increase in conversion over the high equilibrium value, but the purpose of the study was to demonstrate models of the process rather than duplication of the previous work showing large conversion increases.

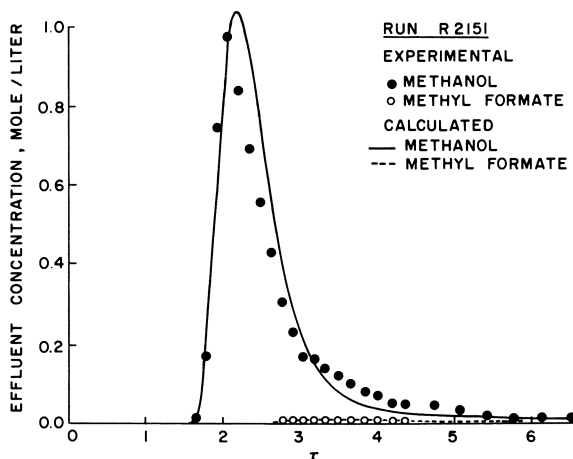


Figure 2. Effluent concentrations for run 2151—narrow inlet pulse of reactant

Comparison of Model with Experimental Results

An example of the effluent concentrations is shown for run 2211 in Figure 1. This run had a mean residence time of 28.1 min, a pulse duration of 107 min, and $C_A^\circ = 1.415$ mole/liter. The conversion was 87.6% *vs.* the equilibrium value of 83.8%. With the long inlet pulse duration, the various traveling peaks have significant overlap although the conversion still exceeds equilibrium. Figure 2 presents results for a narrow pulse duration of 18 min, with a mean residence time of 28.7 min and $C_A^\circ = 1.438$. With little peak overlap, the conversion obtained was 99.1 *vs.* 83.8%. Results with similar trends were obtained for the other run conditions.

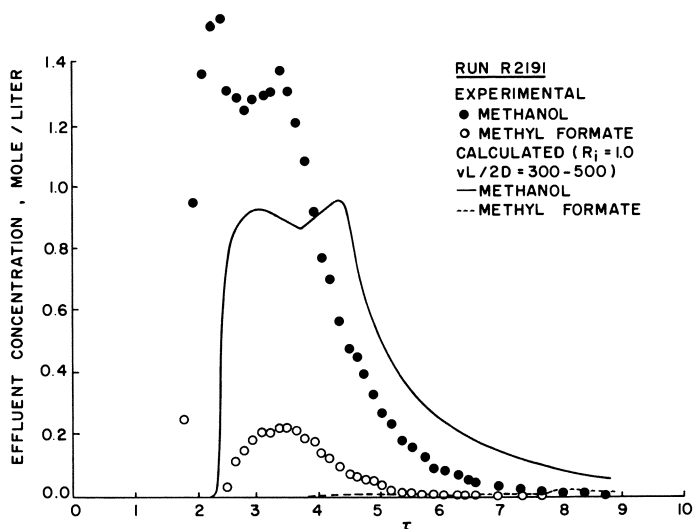


Figure 3. Comparison of experimental and model results using binary adsorption isotherms; run 2191—medium inlet pulse of reactant

Computed results using the binary adsorption isotherms gave poor results. Figure 3 shows this for run 2191 with conditions of mean residence time 28.4 min, inlet pulse duration 70 min and $C_A^\circ = 1.430$ moles/liter. To account approximately for the multicomponent nature of the adsorption system, an empirical factor was introduced into the isotherm:

$$q_i = R_i b_i C_i^{m_i}, \quad i = A, B, C \quad (10)$$

with

$$0.0 < R_i \leq 1.0.$$

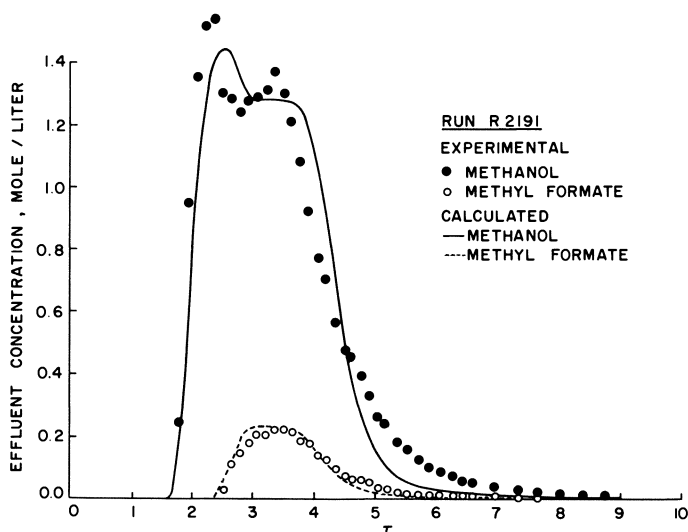


Figure 4. Improved model results with empirical multicomponent adsorption corrections; run 2191

Table II. Experimental and Theoretical Conversions

Run No.	Methyl Formate Converted, %		
	Experimental	Calculated	Equilibrium
2211	87.6	86.9	83.8
2151	99.1	97.9	83.8
2191	90.0	89.0	83.8

By empirical curve-fitting techniques, the best values for run 2211 (Figure 1) were:

$$R_A = 0.15, R_B = 0.90, R_C = 1.00$$

and these values were also used for other runs. The improvement in computed results for run 2191 is shown in Figure 4, and the calculated curves in Figures 1 and 2 were also obtained in this way. An accurate description of the adsorption is essential for the model to predict adequately the reactor results. The "numerical dispersion" effects on the leading and trailing edges of the effluent waves were also important; the length step size $N = 40$ gave reasonable agreement with the data. This corresponds to a Peclet number of $vL/D \approx 80$, which

is of the right order of magnitude for this system when compared with the results of Chao and Hoelscher (34).

With all of these factors, the overall comparisons for the runs discussed are shown in Table II.

Therefore, the model appears to do well ($< 2\%$ error) in predicting the overall conversions, even though Figures 1-4 show that all the details of the effluent waves are difficult to compute precisely. Features such as peak height and width had less than 20% discrepancy. Similar results were also found for other runs at about the same residence time, but the short residence time cases were less predictable.

A model such as that above can be used for optimum design studies for chromatographic reactors. Conversions far past equilibrium can be obtained, at least for a sufficiently short inlet pulse of reactant. However, this must be counterbalanced against the lack of throughput for short pulses. A convenient measure of the reactor usefulness is an "efficiency," defined as the amount of product produced in the chromatographic reactor over a time period, relative to the amount of product produced in a steady-state reactor with equilibrium conversion, over the same period of time. The time period could be the total elution time (to, say, 1% concentration) from the beginning to the end of pulses of all species to leave the reactor—this is a measure of the required time between pulses for essentially no overlap to occur:

$$\text{Efficiency} = \frac{\left(\frac{\text{input reactant}}{\text{pulse duration}} \right) \left(\frac{\text{chromatographic}}{\text{reactor conversion}} \right)}{\left(\frac{\text{total outlet}}{\text{elution duration}} \right) \left(\frac{\text{equilibrium}}{\text{conversion}} \right)}$$

For example, Figure 1 shows for run 2211 that the elapsed time is about $11-1.5 = 9.5 \tau$; the inlet pulse in τ units was 3.81, and so:

$$\text{Efficiency} = \frac{(3.81)(0.876)}{(9.5)(0.838)} = 42\%$$

For the narrow inlet pulse run 2151, the figure is 13.6%, and for the medium inlet pulse run 2191 it is 35.3%. These numbers give an idea of the extra reactor size required for chromatographic operation to have the same quantity output as a steady-state reactor—*e.g.*, more than twice as big for run 2211. These low numbers are based on our experimental system that was *not* chosen for its dramatic increase over equilibrium conversions. The total optimum design, however, would have to take into account such items as the extra product separation and recycle cost of the steady-state system *vs.* the high conversion and/or inherent separation of the chromatographic reactor. Obviously, each specific reaction/separation system would have to be considered in detail, although a system with adverse equilibrium limitations and/or difficult product separation would be a likely candidate where the chromatographic reactor could have advantages over the steady-state reactor.

Conclusions

(1) Conversions greater than equilibrium can be obtained in a chromatographic reactor. In some cases, almost complete conversion can be obtained.

(2) Conversion increases as inlet reactant pulse length decreases. In addition, it would be expected that the total amount injected would be impor-

tant in some situations, especially if it were large enough to approach saturation of the adsorbent.

(3) A mathematical model can be constructed to represent adequately the experimental results. However, the description of the multicomponent, competitive adsorption must be rather complete, and/or empirical correction factors used, to obtain reasonable results.

(4) The overall conversions can be readily predicted, but the details of the elution curves require careful attention to such matters as dispersion and numerical techniques.

(5) Design simulations can be performed and indicate that a chromatographic reactor may be most advantageous for reaction systems with adverse equilibrium conversions and/or difficult separations.

Literature Cited

1. Bassett, D. W., Habgood, H. W., *J. Phys. Chem.* (1960) **64**, 769.
2. Blanton, W. A., Byers, C. H., Merrill, R. P., *Ind. Eng. Chem., Fundamentals* (1968) **7**, 611.
3. Collins, C. G., Deans, H. A., *AIChE J.* (1968) **14**, 25.
4. Deans, H. A., Horn, F. J. M., Klausner, G., *AIChE J.* (1970) **16**, 426.
5. Langer, S. H., Yurchak, J. Y., *Ind. Eng. Chem.* (1969) **61**(4), 11.
6. Paratella, A., Orefice, V., Girdano, N., *Chem. Eng. Sci.* (1968) **23**, 373.
7. Roginskii, S. Z., Rozentel, A. L., *Kinet. Katal.* (1964) **5**, 104.
8. Schwab, G. M., Watson, A. M., *J. Catalysis* (1965) **4**, 570.
9. Roginskii, S. Z., Yanovskii, M. I., Gaziev, A. G., *Dokl. Akad. Nauk SSSR* (1961) **140**(5), 1125.
10. Matsen, J. M., Harding, J. W., Magee, E. M., *J. Phys. Chem.* (1965) **69**, 522.
11. Filinovskii, V. Yu., Gaziev, G. A., Yanovskii, M. I., *Dokl. Akad. Nauk SSSR* (1966) **167**, 143.
12. Gaziev, G. A., Filinovskii, V. Yu., Yanovskii, M. I., *Kinet. Katal.* (1963) **4**, 688.
13. Roginskii, S. Z., Yanovskii, M. I., Gaziev, G. A., *Kinet. Katal.* (1962) **3**, 529.
14. Roginskii, S. Z., Yanovskii, M. I., Gaziev, G. A., *Gaz. Khromatogr. Akad. Nauk SSSR, Tr. Vtoroi Vses. Konf., Moscow, 1962* (1964), 27-36.
15. Aliev, R. R., Berman, A. D., *Azerb. Khim. Zh.* (1968), 26.
16. Roginskii, S. Z., Semenenko, E. I., Yanovskii, M. I., *Dokl. Akad. Nauk SSSR* (1963) **153**, 383.
17. Semenenko, E. I., Roginskii, S. Z., Yanovskii, M. I., *Kinet. Katal.* (1964) **5**, 490.
18. Magee, E. M., *Ind. Eng. Chem., Fundamentals* (1963) **2**, 32.
19. Roginskii, S. Z., Rozentel, A. L., *Dokl. Akad. Nauk SSSR* (1965a) **162**, 621.
20. Roginskii, S. Z., Rozentel, A. L., *Dokl. Akad. Nauk SSSR* (1965b) **162**.
21. Gore, F. A., *Ind. Eng. Chem. Process Des. Develop.* (1967) **6**, 10.
22. Saito, H., Murakami, Y., Hattori, T., *Kagaku Kogaku* (1965) **29**, 585.
23. Newling, W. B. S., Hinshelwood, C. N., *J. Chem. Soc.* (1936) 1357.
24. Salmi, E. J., *Berichte* (1939) **72B**, 1767.
25. Bell, R. P., Dowding, A. L., Noble, J. A., *J. Chem. Soc.* (1955) 3106.
26. Kipling, J. J., "Adsorption from Solutions of Non-Electrolytes," Academic Press, New York, London, 1965.
27. Ockrent, C., *J. Chem. Soc.* (1932) 613.
28. Oscik, J., Szczypa, B., *Przem. Chem.* (1964) **43** (3), 145.
29. Wilson, J. N., *J. Amer. Chem. Soc.* (1940) **62**, 1583.
30. Ames, W. F., "Nonlinear Partial Differential Equations in Engineering," Academic Press, New York, London, 1965.
31. Coats, K. H., private communication, 1968.
32. Wetherold, R. G., Ph.D. Dissertation, University of Texas, Austin (1970).
33. Hashimoto, I., Deshpande, K. B., Thomas, H. C., *Ind. Eng. Chem., Fundamentals* (1964) **3**, 213.
34. Chao, R., Hoelscher, H. E., *AIChE J.* (1966) **12**, 271.
35. Dayan, J., Levenspiel, O., *Chem. Eng. Sci.* (1968) **23**, 1327.

RECEIVED January 2, 1974.

Countercurrent Moving Bed Chromatographic Reactors

S. VISWANATHAN and R. ARIS

Department of Chemical Engineering and Materials Science,
University of Minnesota, Minneapolis, Minn. 55455

The behavior of a moving bed catalytic reactor is studied for the case in which a reactant A is adsorbed on the countercurrently moving solid catalyst and the products of the reaction are rapidly desorbed. In the ideal case of no diffusion and instantaneous attainment of adsorption equilibrium, the reaction can be driven to completion in a finite length of bed. The categories of steady state and their transient approaches are described, and the effects on the steady state of diffusion and finite adsorption rates are examined.

It has been known for some time that an equilibrium reaction can be forced to completion in a pulse or chromatographic reactor (1, 2). Reactions of the type $A \rightleftharpoons B + C$ have been studied because the chromatographic separation of the products inhibits the back reaction (3). Similar ideas for simultaneous reaction and separation problems have been discussed in connection with distillation problems (4, 5, 6), and the chromatographic analog would be a moving bed adsorber. However, as Rhee has shown (7) there are some delicate questions as to the development of discontinuities or shock layers in such systems, and it seemed worthwhile to approach the subject more carefully by first considering the reaction $A \rightarrow B$. This is done for an isothermal system when B is not adsorbed to an appreciable extent; the relationship between the idealized case, in which adsorption equilibrium is maintained and there is no longitudinal diffusion, and the more realistic cases in which these effects are present is discussed. This system can produce a product stream of pure B under suitable circumstances.

Moving Bed Reactor with Adsorption Equilibrium and No Diffusion

Conservation Equations. In the idealized case it is assumed that A reacts irreversibly at a rate proportional to its adsorbed concentration on the solid phase. This solid phase moves downward with constant velocity v through a fluid phase moving upward in plug flow with velocity u . These velocities and the fraction of fluid phase, ϵ , are constant, as is the temperature, and there is no diffusion or longitudinal mixing. Moreover it is assumed that adsorption equilibrium of A between the fluid and solid phases is maintained and that B is desorbed as it is formed. Such a model is a first approximation to certain

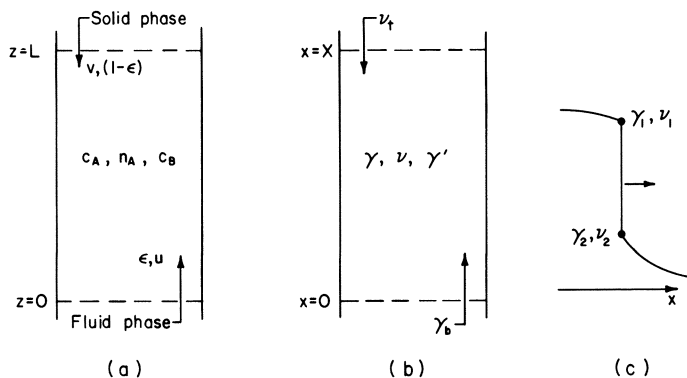


Figure 1. (a) and (b), schematic of a moving bed reactor; (c) notation for a discontinuity

hydrogenations. The system is shown in Figure 1, and the main features of the notation are illustrated there and listed in the Nomenclature section.

Mass balances over a differential element give the equations

$$\frac{\partial}{\partial t} [\epsilon c_A + (1 - \epsilon)n_A] + \frac{\partial}{\partial z} [u\epsilon c_A - v(1 - \epsilon)n_A] + k_r n_A = 0 \quad (1)$$

$$\epsilon \left[\frac{\partial c_B}{\partial t} + u \frac{\partial c_B}{\partial z} \right] = k_r n_A \quad (2)$$

If a Langmuir adsorption isotherm is considered,

$$n_A = NK_{AC_A}/(1 + K_{AC_A}) \quad (3)$$

this immediately suggests dimensionless forms of the variables:

$$\begin{aligned} \gamma &= K_{AC_A}, \gamma' = K_{AC_B}, v = n_A/N \\ x &= k_r z/\epsilon u, X = k_r L/\epsilon u, y = k_r t/\epsilon \end{aligned} \quad (4)$$

and shows that there are three important parameters

$$\mu = NK_A, \alpha = \mu(1 - \epsilon)/\epsilon, \sigma = v \alpha/u \quad (5)$$

involved in the equations

$$\left[1 + \frac{\alpha}{(1 + \gamma)^2} \right] \frac{\partial \gamma}{\partial y} + \left[1 - \frac{\sigma}{(1 + \gamma)^2} \right] \frac{\partial \gamma}{\partial x} + \mu \frac{\gamma}{1 + \gamma} = 0 \quad (6)$$

$$\frac{\partial \gamma'}{\partial y} + \frac{\partial \gamma'}{\partial x} = \mu \frac{\gamma}{1 + \gamma} \quad (7)$$

We note that γ' is not involved in Equation 6 and that this can first be solved and Equation 7 can subsequently be integrated along a characteristic.

Initial and Boundary Conditions. We confine our attention to the so-called Riemann problem for which the boundary and initial conditions are piecewise constant and take

$$\gamma(x, 0) = \gamma_0, 0 < x < X \quad (8)$$

Since the fluid is fed at the bottom and the solid at the top, we can specify

$$\gamma(0_-, y) = \gamma_b y \geq 0 \quad (9)$$

$$v(X_+, y) = v_t y \geq 0 \quad (10)$$

The notations 0_- and X_+ denote the values just outside the contacting region where these quantities can be specified; they are not necessarily the same just inside the reactor at $x = 0_+$ and $x = X_-$. When there is a discontinuity at the boundary a , mass balances about the planes $x = 0$ and/or $x = X$ give

$$\frac{\gamma_b - \gamma_{0+}}{v_b - v_{0+}} = \frac{[\gamma]_b}{[v]_b} = \sigma \quad (11)$$

$$\frac{\gamma_{X-} - \gamma_t}{v_{X-} - v_t} = \frac{[\gamma]_t}{[v]_t} = \sigma \quad (12)$$

where $[]$ is a convenient notation for the magnitude of the discontinuity in any quantity. In these relations γ_b and v_t are specified, v_b and γ_t are the concentrations in the outgoing streams and are not known; the concentrations just inside the reactor are unknown but are linked by the equilibrium relation

$$v = \gamma/(1 + \gamma) \quad (13)$$

The conditions on γ' are

$$\gamma'(x, 0) = \gamma'_o, 0 < x < X \quad (14)$$

and

$$\gamma'(0, y) = \gamma'_b, y \geq 0$$

Thus if $\gamma(x, y)$ has been determined and $\Gamma(x, y)$ denotes $\mu\gamma/(1 + \gamma)$, the solution of Equations 7 and 14 is

$$\gamma'(x, y) = \gamma'_o + \int_{x-y}^x \Gamma(x', x' - x + y) dx' \quad \text{if } y < x$$

(15)

and

$$\gamma'(x, y) = \gamma'_b + \int_0^x \Gamma(x', x' + y - x) dx' \quad \text{if } y \geq x$$

Discontinuities. If a discontinuity in γ (often referred to as a shock) moves through the reactor, we can find its speed by insisting that there is no accumulation of matter in the plane of the shock. The notation is shown in Figure 1c, and shock speed is given by

$$w_{12} = \left(\frac{dx}{dy}\right)_s = \frac{1 - \sigma[v]/[\gamma]}{1 + \alpha[v]/[\gamma]} = \frac{(1 + \gamma_1)(1 + \gamma_2) - \sigma}{(1 + \gamma_1)(1 + \gamma_2) + \alpha} = \frac{1 - \sigma(1 - v_1)(1 - v_2)}{1 + \alpha(1 - v_1)(1 - v_2)} \quad (16)$$

where $[v] = v_1 - v_2$, etc. The entropy condition shows that $\gamma_1 > \gamma_2$, but the shock can clearly move in either direction according as $(1 + \gamma_1)(1 + \gamma_2)$ is greater or less than σ . However, since the concentrations cannot be negative, a shock can be stationary or move with negative speed only if $\sigma > 1$.

Continuous Steady States. By definition a steady state satisfies

$$\left[1 - \frac{\sigma}{(1 + \gamma)^2}\right] \frac{\partial \gamma}{\partial x} + \mu \frac{\gamma}{1 + \gamma} = 0 \quad (17)$$

and hence a continuous part of its solution which has the value γ_0 at x_0 is given implicitly by

$$\mu(x - x_0) = (1 - \sigma) \ln \frac{\gamma_0}{\gamma} + \sigma \ln \frac{1 + \gamma_0}{1 + \gamma} + \gamma_0 - \gamma \quad (18)$$

Yet us define a function of one variable γ and two parameters β, α by

$$\chi(\gamma; \beta, \alpha) = (1 + \alpha) \ln \frac{\beta}{\gamma} - \alpha \ln \frac{1 + \beta}{1 + \gamma} + \beta - \gamma \quad (19)$$

so that

$$\mu(x - x_0) = \chi(\gamma; \gamma_0, -\sigma) \quad (20)$$

We note that $\chi(\beta; \beta, \alpha) = 0$ and that if $\alpha > -1$, χ decreases monotonically as γ increases. If $\alpha < -1$, it has a maximum at $\gamma = \sqrt{-\alpha} - 1$ and tends to $-\infty$ both as $\gamma \rightarrow 0$ and as γ becomes large. When the solution is known to be continuous throughout $0 < x < X$ and the value of either γ_{0+} or γ_{X-} is known, then the complete profile is given either by

$$\mu x = \chi(\gamma; \gamma_{0+}, -\sigma) \quad (21)$$

or by

$$\mu(X - x) = -\chi(\gamma; \gamma_{X-}, -\sigma) \quad (22)$$

If $\sigma > 1$, this solution does not hold if

$$\mu X > \chi(\sigma^{1/2} - 1; \gamma_{0+}, -\sigma) \quad (23)$$

because it would give two possible values for sufficiently small values of x and none at all for x near X .

Characteristic Curves. Equation 6 is a quasi-linear first-order equation in two independent variables, and its solution can be constructed by the method of characteristics with the insertion of shocks where these tend to overlap (*see, for example, Aris and Amundson (8)*). The method of characteristics allows us to discuss the solution for any inlet and initial conditions; it is only for convenience that we limit our consideration to the Riemann problem with its constant conditions. If s is a parameter along a characteristic curve

$$\frac{dx}{ds} = 1 - \frac{\sigma}{(1 + \gamma)^2}, \quad \frac{dy}{ds} = 1 + \frac{\alpha}{(1 + \gamma)^2}, \quad \frac{d\gamma}{ds} = -\frac{\mu\gamma}{1 + \gamma} \quad (24)$$

In contrast to the purely chromatographic moving bed ($\mu = 0$) these characteristics are not straight lines but curves along which γ decreases and whose tangents turn counterclockwise. The characteristic through (x_0, y_0, γ_0) is given implicitly by

$$\mu s = \ln(\gamma_0/\gamma) + (\gamma_0 - \gamma) \quad (25)$$

$$\mu(x - x_0) = \chi(\gamma; \gamma_0, -\sigma) \quad (26)$$

$$\mu(y - y_0) = \chi(\gamma; \gamma_0, \alpha) \quad (27)$$

The velocity of a point of concentration γ is

$$w = \left(\frac{dx}{dy} \right) = \frac{(1 + \gamma)^2 - \sigma}{(1 + \gamma)^2 + \alpha} \quad (28)$$

and if $\sigma > 1$, this can be either positive or negative according as γ is greater or less than $\sigma^{1/2} - 1$. Because γ decreases monotonically along a characteristic, it will eventually have a negative slope if x does not exceed X . It is asymptotic to the line

$$(\sigma - 1)(y - y'_o) + (1 + \alpha)(x - x'_o) = 0 \tag{29}$$

where

$$x'_o = x_o + \chi_o(\gamma_o, -\sigma)/\mu \tag{30}$$

$$y'_o = y_o + \chi_o(\gamma_o, \alpha)/\mu$$

and

$$\chi_o(\beta, \alpha) = (1 + \alpha) \ln \beta - \alpha \ln (1 + \beta) + \beta \tag{31}$$

The characteristics for $\gamma = 0$ are thus straight lines of the form of Equation 29. The various possible forms of the characteristic are shown in Figure 2. If $\sigma < 1$, the slope of the characteristics is always positive.

Finally, note that the flux of A can be positive or negative. Expressed dimensionlessly it is

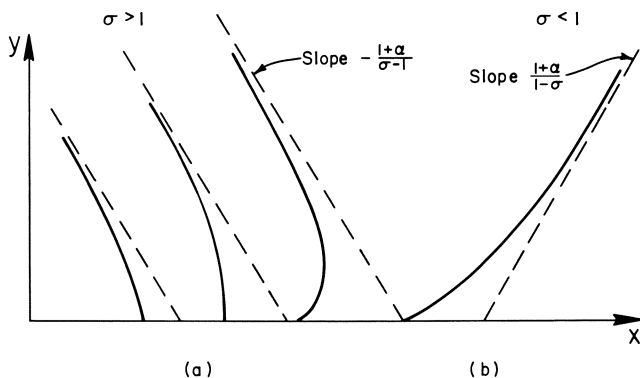


Figure 2. The various possible forms of a characteristic line: ———, characteristic; --- asymptote

$$F = \gamma - \frac{\sigma\gamma}{1 + \gamma} \tag{32}$$

and is positive or negative as γ is greater or less than $\sigma - 1$. The greatest magnitude of negative flux is $(\sigma^{1/2} - 1)^2$ attained when $\gamma = \sigma^{1/2} - 1$ and the characteristic velocity is zero. If $\sigma - 1 > \gamma > \sigma^{1/2} - 1$, then the flux is negative even though the characteristic velocity is positive.

Behavior at the Boundaries. In the Riemann problem about to be discussed there may be an initial discontinuity at one or both ends of the reactor. At $x = 0$ the discontinuity will move into the reactor if $\gamma_b > \gamma_o$ and $(1 + \gamma_b)(1 + \gamma_o) > \sigma$. This is always the case when $\sigma \leq 1$, but when $\sigma > 1$, it implies that γ_b must be sufficiently greater than γ_o . When the shock moves into the bed, the conditions at the boundary are continuous and $\gamma_{o+} = \gamma_b$, $v_b = \gamma_b / (1 + \gamma_b)$ for $y > 0$. When the discontinuity does not move into the bed, the values of y_{o+} will be determined by characteristics arriving at the axis $x = 0$, and Equation 11 determines

$$v_b = \frac{\gamma_{c+}}{1 + \gamma_{o+}} + \frac{\gamma_b - \gamma_{o+}}{\sigma} \tag{33}$$

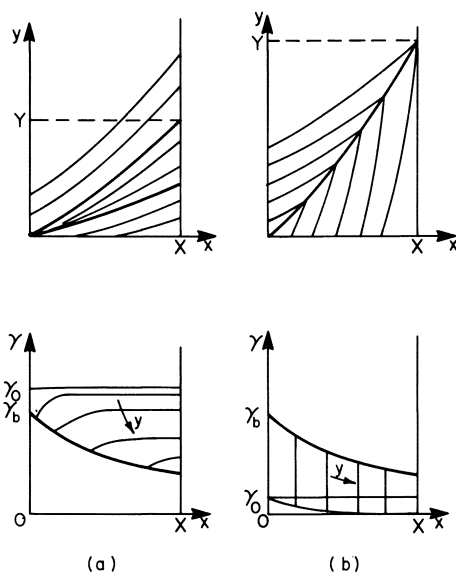


Figure 3. Physical plane portrait and concentration profiles for $\sigma < 1$. (a), $\gamma_b < \gamma_o$; (b), $\gamma_b > \gamma_o$.

Similarly at $x = X$ there is a discontinuity between v_t and $v_o = \gamma_o / (1 + \gamma_o)$, which will move into the reactor if $v_t < 1 - (1 + \gamma_o) / \sigma$. This is never the case when $\sigma \leq 1$ and requires γ_o and v_t to be sufficiently small when $\sigma > 1$. When the discontinuity moves into the reactor $v_{x-} = v_t$ and $\gamma_{x-} = v_t / (1 - v_t) = \gamma_t$. When the discontinuity does not move into the reactor, γ_{0+} is given by the characteristics arriving at $x = X$ and Equation 12 determines

$$\gamma_t = \gamma_{x-} \left\{ 1 - \frac{\sigma}{1 + \gamma_{x-}} \right\} + \sigma v_t \quad (34)$$

Categories of Reactor Behavior in the Ideal Case

When $\sigma = 0$, the system is a fixed rather than a moving bed, but the characteristics of the system are essentially unchanged for any value of $\sigma \leq 1$. This is because all characteristics have positive slope, and if there is a bottom discontinuity, it moves into and through the bed; if there is a discontinuity at the top of the bed, it remains there (Figure 3). If $\gamma_b \leq \gamma_o$, then the characteristics corresponding to concentrations in the interval (γ_b, γ_o) all fan out from the origin without overlapping. Thus the steady-state profile develops as shown in the lower part of Figure 3a; it is fully established at time $y = Y$, where Y is determined by solving

$$\mu X = \ln(\gamma_b / \gamma_{x-}) + (\gamma_b - \gamma_{x-}) - \sigma \ln \frac{\gamma_b(1 + \gamma_{x-})}{\gamma_{x-}(1 + \gamma_b)} \quad (35)$$

for γ_{x-} and substituting this value in

$$\mu Y = \ln(\gamma_b / \gamma_{x-}) + (\gamma_b - \gamma_{x-}) + \alpha \ln \frac{\gamma_b(1 + \gamma_{x-})}{\gamma_{x-}(1 + \gamma_b)} \quad (36)$$

If $\gamma_b > \gamma_o$, the profile takes somewhat longer to become established since the initial discontinuity at the inlet moves through the bed according to Equation 16 where γ_1 is borne to the back of the wave by a characteristic from the y axis and γ_2 to the front by a characteristic from the x axis. Thus if the point (x_s, y_s) is on the shock

$$\mu x_s = \ln(\gamma_b/\gamma_1) + (\gamma_b - \gamma_1) - \sigma \ln \frac{\gamma_b(1 + \gamma_1)}{\gamma_1(1 + \gamma_b)} \quad (37)$$

and

$$\mu y_s = \ln(\gamma_o/\gamma_2) + (\gamma_o - \gamma_2) + \alpha \ln \frac{\gamma_o(1 + \gamma_2)}{\gamma_2(1 + \gamma_o)} \quad (38)$$

By solving these equations for γ_1 and γ_2 , respectively, and substituting in

$$\frac{dx_s}{dy_s} = w_{12} \quad (39)$$

this differential equation can be solved for the path of the shock, and $Y^* = y_s(X)$ can be determined. The development of this profile is shown in Figure 3b. The steady-state profile is independent of γ_o although the time taken to establish it does depend on γ_o . The boundary condition at the top of the reactor does not affect the steady state, but it does affect the concentration of A in the emerging stream according to Equation 34. It is in this sense that the moving bed with $\sigma \leq 1$ is not qualitatively different from a fixed bed.

We shall not consider all possible types of behavior when $\sigma > 1$ because this belongs more properly to a mathematical study of the equations (*cf.* Viswanathan and Aris (9)). Instead we consider three of the more practical sets of conditions and solutions, comparing them later with the solutions for non-ideal cases. Since the objective is to form product B, it is reasonable to feed reactant A only at $x = 0$ and to start from a bed devoid of any of the reacting species. On the other hand, the solids entering the reactor at the top may have been recycled and hence bring reactant into the system. We thus consider the following cases:

	γ_o	γ_b	ν	X
I	0	1	0	0.75
II	0	1	0.1	1.0
III	0	1	0.5	1.0

In all cases the parameters are $\alpha = \mu = 1$, $\sigma = 1.5$.

The problem is that of following the development of the shock wave at $x = 0$ for $(1 + \gamma_o)(1 + \gamma_b) = 2 > \sigma = 1.5$. In the first case the characteristics emanating from the x axis and the line $x = X$ are all lines of slope $(1 + \alpha)/(1 - \sigma)$ and have the value $\gamma = \nu = 0$. Hence the shock is between γ_1 at the back of the discontinuity and zero at the front. If (x_s, y_s) lies on the shock path

$$\frac{dx_s}{dy_s} = \frac{1 + \gamma_1 - \sigma}{1 + \gamma_1 + \alpha} = \frac{\gamma_1^{-0.5}}{2 + \gamma_1} \quad (40)$$

while x_s and γ_1 are related by Equation 37,

$$x_s = \frac{3}{2} \ln \frac{2}{1 + \gamma_1} - \frac{1}{2} \ln \frac{1}{\gamma_1} + 1 - \gamma_1 \quad (41)$$

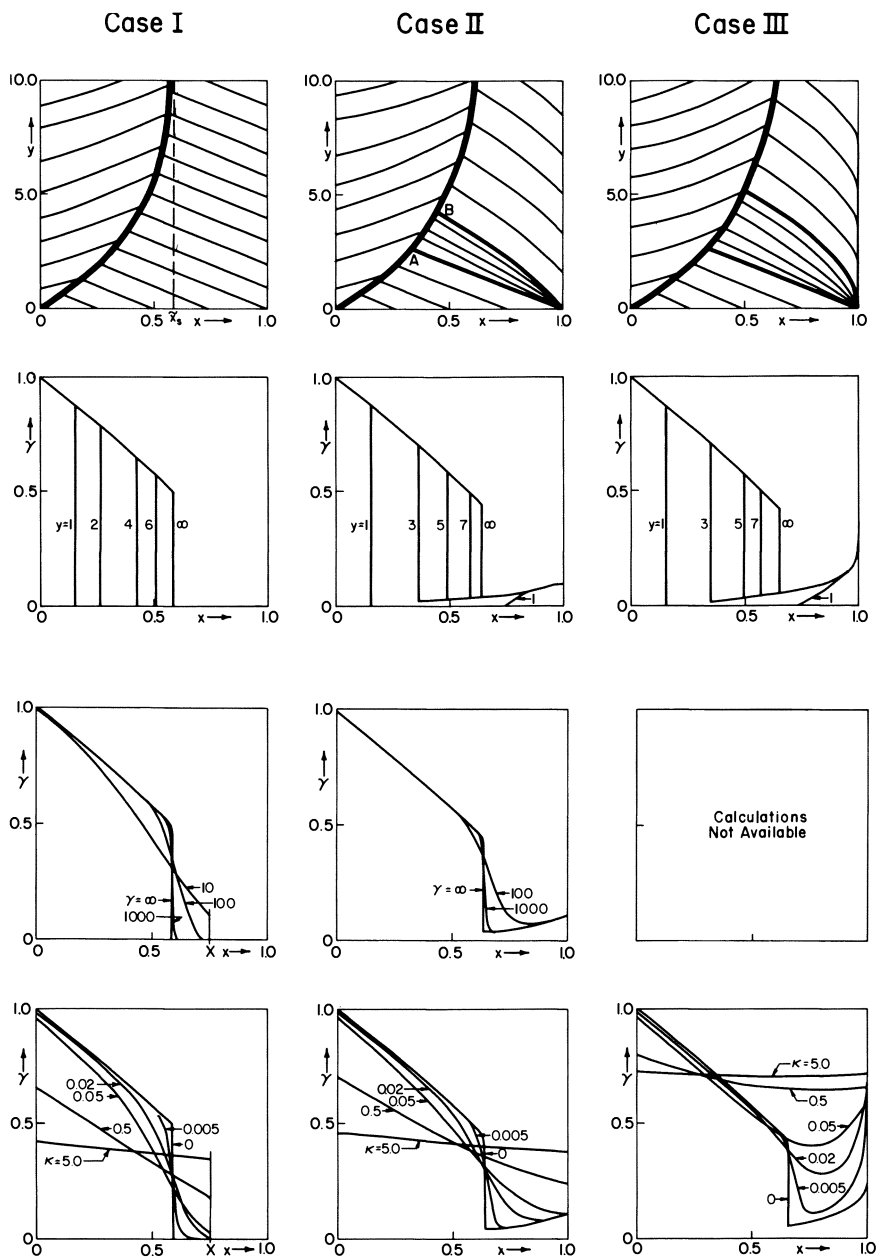


Figure 4. 1st row: shock trajectory. 2nd row: development of the steady-state concentration profile for the ideal reactor. 3rd row: steady-state concentration profiles for a reactor with finite rates of adsorption and desorption. 4th row: steady-state concentration profiles for a reactor affected by diffusion in the fluid phase.

The first column of Figure 4 shows the path of the shock as determined by these two conditions. The shock becomes stationary when $\gamma_1 = \sigma - 1 = 0.5$, and it has then reached $\tilde{x}_s = 0.585$.

In general with $\gamma_b > \sigma - 1$, $\gamma_0 = v_t = 0$, a shock will always move inward, ultimately reaching a magnitude of $[\gamma] = \sigma - 1$ and be found at

$$\mu \tilde{x}_s = \sigma \ln \frac{1 + \gamma_b}{\sigma} - (\sigma - 1) \ln \frac{\gamma_b}{\sigma - 1} + \gamma_b + 1 - \sigma \tag{42}$$

If $X > \tilde{x}_s$, this shock will stay within the bed, and the product stream will be pure B. The reaction has thus been driven to completion by the influence of the countercurrent adsorptive solid stream.

In case II the progress of this shock is influenced by the simple wave induced by the discontinuity at $x = X$ (second column of Figure 4). The concentration $v_t / (1 - v_t) = 0.111$ which is in equilibrium with $v_t = 0.1$ is less than $\sigma^{1/2} - 1 = 0.225$; therefore, the characteristics from the line $x = X = 1$ have negative slopes and no shock is formed. The characteristics corresponding to $0 < \gamma < 0.111$ fan out from $x = X, y = 0$, forming a centered simple wave. The progress of the shock is given exactly as before from 0 to A because it encounters only characteristics emanating from $y = 0$, and thus $\gamma_2 = 0$. However, between A and B, γ_2 rises from zero, and the path of the shock is given by

$$\frac{dx_s}{dy_s} = \frac{(1 + \gamma_1)(1 + \gamma_2) - \sigma}{(1 + \gamma_1)(1 + \gamma_2) + \sigma} \tag{43}$$

where γ_1 is again given by Equation 41, but γ_2 is given by

$$\begin{aligned} \mu(X - x_s) &= -\chi(\gamma_2; \gamma', -1.5) \\ \mu y_s &= \chi(\gamma_2; \gamma', 1) \end{aligned}$$

where γ' is in the interval (0, 0.111). Beyond point B the characteristics meeting at the shock both come from the vertical boundaries so that

$$\mu x_s = \chi(\gamma_1; \gamma_b, -\sigma) \tag{44}$$

and

$$\mu(X - x_s) = -\chi(\gamma_2; v_t / (1 - v_t), -\sigma)$$

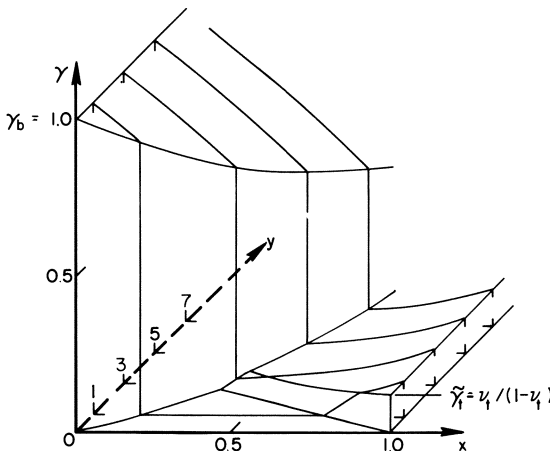


Figure 5. Isometric view of the development of the steady state for case II

The shock becomes stationary when

$$(1 + \gamma_1)(1 + \gamma_2) = \sigma \quad (45)$$

so that its asymptotic position \tilde{x}_s is given by eliminating γ_1 and γ_2 from Equations 44 and 45 and solving for x_s . Formally this can be done by solving

$$\mu X = \chi(\gamma_1; \gamma_b, -\sigma) - \chi\left(\frac{\sigma}{1 + \gamma_1} - 1; \frac{\nu_t}{1 - \nu_t}, -\sigma\right) \quad (46)$$

for γ_1 and substituting in the first of Equations 44. In case II the solution gives $\tilde{x}_s = 0.642$.

In case III the value of γ in equilibrium with $\nu_t = 0.5$ is $\gamma = 1 > \sigma^{1/2} - 1 = 0.225$. Hence in the fan of characteristics centered on $(X, 0)$ there is one which has a vertical tangent—namely, that corresponding to $\gamma = \sigma^{1/2} - 1$. The top of the reactor is thus forced to maintain a composition $\gamma_{X_t} = \sigma^{1/2} - 1$, $\nu_{X_t} = 1 - \sigma^{-1/2}$, and this is done by a discontinuity which makes

$$\gamma_t = \sigma \nu_t - (\sigma^{1/2} - 1)^2 \quad (47)$$

The asymptotic position of the shock is thus given by

$$\begin{aligned} (1 + \gamma_1)(1 + \gamma_2) &= \sigma \\ \mu \tilde{x}_s &= \chi(\gamma_1; \gamma_b, -\sigma) \\ \mu(X - \tilde{x}_s) &= \chi(\gamma_2; \sigma^{1/2} - 1, -\sigma) \end{aligned} \quad (48)$$

The solution to these equations for case III is approximately $x_s = 0.667$, and the results are shown in the third column of Figure 4. The position and magnitude of the final shock depend on the total length of the reactor in cases II and III; in case II it also depends on ν_t whereas it is independent of ν_t in the last case. Figure 5 shows an isometric view of the development of the steady state.

If $\gamma_b < \sigma - 1$, the initial discontinuity moves out of the reactor, and the solution within $(0, X)$ is $\gamma = \nu \equiv 0$. Because σ represents the ratio of the carrying capacity of the solid and fluid streams, the situation when $\sigma > 1 + \gamma_b$ may be expressed by saying that the carrying capacity of the downcoming solids is so great and the feed concentration of reactant at the bottom so poor that it is swept out of the reactor by adsorption before it has a chance to establish a reaction.

Effect of Finite Rates of Adsorption and Desorption

In the finite rates of adsorption and desorption are taken into account, the mass balances are

$$\epsilon \frac{\partial c_A}{\partial t} + \epsilon u \frac{\partial c_A}{\partial z} = -k_a(N - n_A)c_A + k_d n_A \quad (49)$$

$$(1 - \epsilon) \frac{\partial n_A}{\partial t} - (1 - \epsilon)v \frac{\partial n_A}{\partial z} = k_a(N - n_A)c_A - (k_d + k_r)n_A \quad (50)$$

$$\epsilon \frac{\partial c_B}{\partial t} + \epsilon u \frac{\partial c_B}{\partial z} = k_r n_A \quad (51)$$

where k_a and k_d are the adsorption and desorption rate constants and $k_a/k_d = K_A$. Using the same dimensionless quantities as before with the additional parameter

$$\lambda = Nk_a/k_r \quad (52)$$

we have

$$\frac{\partial \gamma}{\partial y} + \frac{\partial \gamma}{\partial x} = -\lambda\{(1 - \nu)\gamma - \nu\} \quad (53)$$

$$\alpha \frac{\partial \nu}{\partial y} - \sigma \frac{\partial \nu}{\partial x} = \lambda\{(1 - \nu)\gamma - \nu\} - \mu\nu \quad (54)$$

$$\frac{\partial \gamma'}{\partial y} + \frac{\partial \gamma'}{\partial x} = \mu\nu \quad (55)$$

Equations 53 and 54 are not reducible but since they have constant coefficients, they have fixed characteristic directions 1 and $-\alpha/\sigma$. If ξ and η are parameters along these characteristics.

$$\begin{aligned} y\xi - x\xi &= 0 \\ \sigma y\eta + \alpha x\eta &= 0 \end{aligned} \quad (56)$$

$$\begin{aligned} \gamma\xi - \lambda\{(1 - \nu)\gamma - \nu\}x\xi &= 0 \\ \sigma\nu\eta + [\lambda\{(1 - \nu)\gamma - \nu\} - \mu\nu]x\eta &= 0 \end{aligned}$$

This can be made the basis for an efficient finite differencing scheme in which it is clear that the appropriate boundary and initial conditions are

$$\gamma(x, 0) = \gamma_o(x), \nu(x, 0) = \nu_o(x) \quad (57)$$

$$\gamma(0, y) = \gamma_b(y), \nu(X, y) = \nu_t(y)$$

We concern ourselves with the steady state which will be ultimately established. This will satisfy the pair of ordinary differential equations

$$\frac{d\gamma}{dx} = -\lambda\{(1 - \nu)\gamma - \nu\} \quad (58)$$

$$-\sigma \frac{d\nu}{dx} = \lambda\{(1 - \nu)\gamma - \nu\} - \mu\nu \quad (59)$$

and is thus amenable to representation in the plane of γ and ν . In fact the trajectories in the plane of the dependent variables satisfy

$$\frac{d\nu}{d\gamma} = \frac{1}{\sigma} - \frac{\mu}{\sigma\lambda} \frac{\nu}{(1 - \nu)\gamma - \nu} \quad (60)$$

and the isoclines are the curves

$$\nu = \frac{\gamma/\Lambda}{1 + \gamma/\Lambda}, \Lambda = 1 + \frac{\mu}{\lambda} \left(1 - \sigma \frac{d\nu}{d\gamma}\right) \quad (61)$$

Thus the trajectories must fall into three types as shown in Figure 6: the monotonic decreasing (such as AB), the monotonic increasing (as CD), and the non-monotonic (as EFG). These classes are separated by the trajectories OR and OS through the saddle point at 0. In the steady state, γ_b and ν_t are independent of y , and we seek a path joining a point on $\gamma = \gamma_b$, such as L , with one on $\nu = \nu_t$, such as M , for which

$$\int_L^M \frac{d\gamma}{\nu(\gamma)\{1 + \gamma\} - \gamma} = \lambda X \quad (62)$$

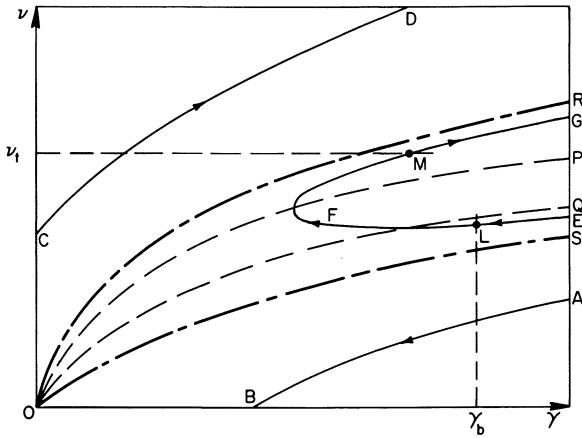


Figure 6. Concentration trajectories: — — —, separatrix; — — —, isocline; — — —, trajectory

The pair of isoclines OP and OQ , corresponding respectively to $dv/d\gamma = \infty$ and 0 , play a key role; it can be shown that the trajectories of each class correspond to increasing values of X the closer they come to the origin. The various possible trajectories are shown in Figure 7, and they depend on the position of the point of intersection of the vertical $\gamma = \gamma_b$ and the horizontal $v = v_t$ relative to the separatrices OR and OS . If $v_t = 0$, the only possibility is a trajectory such as α' with γ and v both monotonically decreasing. If (γ_b, v_t) lies below the lower separatrix, monotonically decreasing profiles are possible (β') in sufficiently short reactors, but in longer reactors non-monotonic profiles will be found (γ'). If (γ_b, v_t) lies between the separatrices, the non-monotonic profile is the only possibility (δ') while if it lies above the second separatrix, the profile can be non-monotonic (ζ') or monotonically increasing (ϵ') except when $\gamma_b = 0$; in this case it is bound to be increasing (η'). In each circumstance a solution is guaranteed because the value of X calculated from Equation 62 ranges from zero when the path vanishes at the intersection to infinity when the path approaches one or both separatrices. In the third part of Figure 4 some calculated trajectories for several values of λ are given, corresponding to the discontinuous steady state of the limiting case above it. The larger the value of λ , the sharper is the discontinuity, and in the limit $\lambda \rightarrow \infty$ the equilibrium solution is attained. The details of this limiting process are instinctive but belong to a more mathematical treatment of the subject (9).

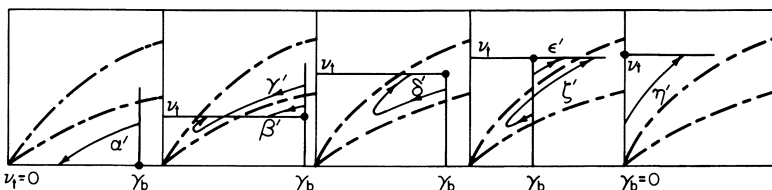


Figure 7. Concentration trajectories for various γ_b and v_t values: — — —, separatrix; — — —, trajectory

Effect of Diffusion in the Fluid Phase

Another form of nonideality that should be considered is diffusion in the fluid phase. We assume adsorption equilibrium and introduce a Fickian diffusion coefficient augmenting the convective flux of A to give a total flux of

$$- D\varepsilon \frac{\partial c_A}{\partial z} + u\varepsilon c_A - v(1 - \varepsilon)n_A$$

Then going to the dimensionless form of the equations we have

$$\left\{ 1 + \frac{\alpha}{(1 + \gamma)^2} \right\} \frac{\partial \gamma}{\partial y} = \kappa \frac{\partial^2 \gamma}{\partial x^2} - \left\{ 1 - \frac{\sigma}{(1 + \gamma)^2} \right\} \frac{\partial \gamma}{\partial x} - \mu \frac{\gamma}{1 + \gamma} \quad (63)$$

and

$$\frac{\partial \gamma'}{\partial y} = \kappa' \frac{\partial^2 \gamma'}{\partial x^2} - \frac{\partial \gamma'}{\partial x} + \mu \frac{\gamma}{1 + \gamma} \quad (64)$$

where κ and κ' are the dimensionless forms of the diffusion coefficients

$$\kappa = \frac{D_A k_r}{u^2 \varepsilon}, \quad \kappa' = \frac{D' k_r}{u^2 \varepsilon} \quad (65)$$

Again the differential equation for γ can be solved by itself first and then for γ' subsequently. The boundary conditions on γ are

$$\gamma - \kappa \frac{\partial \gamma}{\partial x} = \gamma_b \text{ at } x = 0 \quad (66)$$

$$\frac{\gamma}{1 + \gamma} + \frac{\kappa}{\sigma} \frac{\partial \gamma}{\partial x} = \nu_t \text{ at } x = X$$

It can be shown that the profile of γ in the steady state cannot have an internal maximum and that the internal minimum of γ is less than both γ_b and $\nu_t/(1 - \nu_t)$. These and various other mathematical properties will not be established here.

The numerical integration of the steady-state form of Equations 63 and 66 is not altogether trivial, but the following method of McGinnis (10) was successful. With $\gamma = \gamma_o$, $\partial \gamma / \partial x = (\gamma_o - \gamma_b) / \kappa$ at $x = 0$, Equation 63 can be integrated forward to $x = X$ where the residual

$$R(\gamma_o) = \frac{\kappa}{\sigma} \frac{\partial \gamma}{\partial x} + \frac{\gamma}{1 + \gamma} - \nu_t$$

can be calculated. Its derivative can also be calculated by simultaneously integrating the first variational equation of Equation 63; hence the root $R(\gamma_o) = 0$ can be found by Newton-Raphson. When κ is small, it is better to start at the minimum of γ or at the inflection point, and it is there that the general properties of the solution prove their value. In the lowest row of graphs in Figure 4 the effect on the steady state of a variation of κ can be seen.

Nomenclature

A, B, C	chemical species
c_A, c_B	concentration of A, B in the fluid phase
D	diffusion coefficient
F	dimensionless flux of A
k_a, k_d	adsorption and desorption rate constants

k_r	reaction rate constant
K_A	Langmuir isotherm parameter of A
n_A	concentration of A in the solid phase
N	limiting concentration of adsorbed solute
s	characteristic parameter
t	time
u	interstitial fluid velocity
v	speed of solid phase
w	speed of propagation
x	dimensionless distance
y	dimensionless time
z	distance

Greek Letters

α	$\mu(1 - \varepsilon)/\varepsilon$, a parameter in Equations 19 and 31
β	a parameter in Equations 19 and 31
γ	dimensionless concentration of A in the fluid phase
γ'	dimensionless concentration of B in the fluid phase
Γ	$\mu\gamma/(1 + \gamma)$
ε	void fraction of solid phase
η	characteristic parameter
κ, κ'	dimensionless forms of diffusion coefficients of A and B
λ	Nk_a/k_r
Λ	$1 + \frac{\mu}{\lambda} \left/ \left(1 - \sigma \frac{dv}{dy} \right) \right.$
μ	NK_A
ν	dimensionless concentration of A in the solid phase
ξ	characteristic parameter
σ	$v\alpha/u$
χ	a function, defined by Equation 19
\bar{X}	dimensionless reactor length

Subscripts

b	entrance of fluid phase
s	shock
t	entrance of solid phase
o	initial value
0+	inside of the boundary at $x = 0$
X ₋	inside of the boundary at $x = X$
1, 2	left-hand and right-hand side of shock

Literature Cited

1. Roginskii, S. Z., Yanovskii, M. I., Gaziev, G. A., *Dokl. Akad. Nauk USSR* (1961) **140**, 1125.
2. Magee, E. M., *Ind. Eng. Chem. Fund.* (1963) **2**, 32.
3. Matsen, J. M., Harding, J. W., Magee, E. M., *J. Phys. Chem.* (1965) **69**, 522.
4. Hofmann, H., *Chem. Eng. Sci.* (1958) **8**, 113.
5. Schoenemann, K., *Chem. Eng. Sci.* (1958) **8**, 161.
6. Geelen, H., Wijffels, J. B., *Proc. European Symp. Chem. Reaction Eng.*, 3rd, 1964, 125.
7. Rhee, H., Aris, R., Amundson, N. R., *Phil. Trans. Roy. Soc. London* (1971) **A269**, 187.
8. Aris, R., Amundson, N. R., "Mathematical Methods in Chemical Engineering," Vol. 2, Prentice-Hall, Englewood Cliffs, N.J., 1973.
9. Viswanathan, S., Aris, R., *AMS Meetg.*, April 1974; (to be published in *Proc. Symp. App. Mater. AMS*, 1975).
10. McGinnis, P., Jr., *Chem. Eng. Prog. Symp. Ser.* (1965) **61**(55), 2.

RECEIVED January 2, 1974. Some research reported here was done under the National Science Foundation Grant No. GK 1367.

Application of Gas Chromatography to Measurements of Diffusion in Zeolites

PHANINDRA N. SARMA¹ and HENRY W. HAYNES, JR.

Department of Chemical Engineering, University of Mississippi,
University, Miss. 38677

The authors have recently presented a theory of mass transport in gas chromatograph columns of bidisperse structured catalysts, i.e., catalysts characterized by a bimodal distribution of pore sizes. In this report experimental determinations of the effective diffusivity in pillared zeolites are presented. Agreement between theory and experiment is excellent. Time domain solutions are presented for the special case in which the diffusion is characterized by a strong molecule-pore wall interaction. Examples are presented in which the model parameters are determined from a moments analysis and a time-domain fit of the experimental residence time distribution curve.

The first detailed mathematical description of a gas chromatographic (GC) column was developed by van Deemter, Zuiderweg, and Klinkenberg in a classic paper (1). One of the parameters in the model was the effective diffusion coefficient of the pulsed gas within the pores of the column packing. A number of early investigators—*e.g.*, Habgood and Hanlan (2) and Davis and Scott (3, 4), were successful in utilizing the plate theory of van Deemter *et al.* in measurements of diffusion in porous catalysts. More recently, the theory of Kubin (5, 6) and Kucera (7) has rendered gas chromatography an extremely versatile tool for measuring rate parameters in fixed beds. Smith and co-workers (8) have refined and extended the moments theory of Kubin and Kucera and have used it in measuring axial dispersion coefficients (9), chemisorption rates, intraparticle diffusivities, adsorption equilibrium constants (10), and surface diffusivities (11). Smith's development is generally considered to be more exact and more complete than the earlier van Deemter model. However, both models are applicable only to particles characterized by a unimodal distribution of pore sizes.

Recent articles by Hashimoto and Smith (12), Ma and Mancel (13), and the present authors (14, 15) present equations applicable to bidisperse structured catalysts. This development is important because most pillared or extruded catalysts are bidisperse structured. The literature contains numerous examples in which the original equations have been incorrectly applied to such situations.

¹ Present address: E. I. du Pont de Nemours & Co., Inc., Chattanooga, Tenn. 37401.

We believe that the GC effective diffusivity technique will gain widespread acceptance now that a model applicable to bidisperse structured catalysts is available. However a necessary prerequisite is the establishment of a firm experimental basis supporting the model. In this study we have investigated the ability of the proposed model to describe diffusion in pillared zeolites.

Theoretical

We measured the response of the bed of bidisperse particles to an impulse input of diffusing component. According to the macro-micro pore model developed earlier (14), the mean and variance of the concentration-time curve at the bed exit are related to the model parameters by the following equations:

$$\mu = \frac{L}{v} [\theta_z + (1 - \theta_z) \theta_y + (1 - \theta_z) (1 - \theta_y) \theta_x (1 + K_a)] \quad (1)$$

and

$$\begin{aligned} \sigma^2 = & \frac{2LD_z^2}{v^3} [\theta_z + (1 - \theta_z) \theta_y + (1 - \theta_z) (1 - \theta_y) \theta_x (1 + K_a)]^2 \\ & + \frac{2L(1 - \theta_z) [\theta_y + (1 - \theta_y) \theta_x (1 + K_a)]^2 R_y}{3vk_t} \\ & + \frac{2L(1 - \theta_z) [\theta_y + (1 - \theta_y) \theta_x (1 + K_a)]^2 R_y^2}{15vD_y} \\ & + \frac{2L(1 - \theta_z) (1 - \theta_y) \theta_x^2 (1 + K_a)^2 R_x^2}{15vD_x} \end{aligned} \quad (2)$$

where:

$$K_a = \frac{\rho S_x}{\theta_x (1 - \theta_y)} \frac{C_a}{C_x} \quad (3)$$

is a dimensionless adsorption equilibrium constant. In many situations K_a can be calculated from the experimental mean, μ , using Equation 1. Similarly the mass transfer parameters, D_z , k_t , D_y , and D_x can be obtained from the experimental variance, σ^2 , using Equation 2 and appropriate operating conditions.

However, the moments from the chromatogram are sometimes difficult or impossible to evaluate. In particular, when the peak is characterized by a large degree of tailing, the evaluation of higher moments becomes impractical. A slight drift in the recorder baseline will lead to large errors. In some cases we have observed such severe tailing that errors in determining μ were not insignificant. Under such circumstances the evaluation of the model parameters should be conducted in the time domain.

Our model predicts that tailing will be severe for the special case in which diffusion in the microparticles is characterized by strong molecule-pore wall interactions—a phenomenon frequent in studies of diffusion in zeolites. In this case D_x is very small, and the micropore term in Equation 2 far overshadows the terms from D_y , k_t , and D_z . The transformed exit concentration can be obtained from Equation 52 of our previous publication (15) by evaluating the limit as $D_z \rightarrow 0$, $k_t \rightarrow \infty$ and $D_y \rightarrow \infty$. The result is:

$$\tilde{C}_L = C_0 \exp(C_2 - C_1 s) \tilde{F}(s) \quad (4)$$

where

$$\tilde{F}(s) = \exp(-C_2 C_3 s^{1/2} \coth C_3 s^{1/2}) \quad (5)$$

$$C_1 = \left(\frac{\theta_x + (1 - \theta_x) \theta_y}{v} \right) L \quad (6)$$

$$C_2 = \frac{3(1 - \theta_x)(1 - \theta_y) D_x L}{v R_x^2} \quad (7)$$

$$C_3 = R_x \sqrt{\frac{\theta_x}{D_x} (1 + K_a)} \quad (8)$$

The constant, C_0 , is a normalization factor equal to the peak area. As the Laplace transform, Equation 5, contains an infinite number of essential singularities in the left half of the complex plane, inversion by the method of residues is impractical. However, since all singularities lie to the left of the imaginary axis, the inversion integral can be applied with the path of integration conveniently chosen along the imaginary axis. Thus:

$$F(t) = \frac{1}{2\pi i} \int_{-i\infty}^{+i\infty} e^{st} \tilde{F}(s) ds \quad (9)$$

Upon substituting from Equation 4 and making a change of variables, Equation 9 becomes:

$$F(t) = \frac{4}{\pi C_3^2} \int_0^\infty \exp(-C_2 H_1) \cos\left(\frac{2\lambda^2 t}{C_3^2} - C_2 H_2\right) \lambda d\lambda \quad (10)$$

where

$$H_1 = \lambda \left(\frac{\sinh 2\lambda + \sin 2\lambda}{\cosh 2\lambda - \cos 2\lambda} \right) \quad (11)$$

$$H_2 = \lambda \left(\frac{\sinh 2\lambda - \sin 2\lambda}{\cosh 2\lambda - \cos 2\lambda} \right) \quad (12)$$

This inversion technique is the same as that used by Rosen (16) in a related problem. Upon taking the inverse of Equation 4 with aid of the first shifting theorem one obtains:

$$E = \frac{4 \exp(C_2)}{\pi C_3^2} \int_0^\infty \exp(-C_2 H_1) \cos(C_2 t^* \lambda^2 - C_2 H_2) \lambda d\lambda \quad (13)$$

where $E = C_L/C_0$ is the residence time distribution of the diffusing component exiting the column. The quantity t^* is a dimensionless time variable defined by Equation 14:

$$t^* = \frac{2(t - C_1)}{C_2^2 C_3^2} \quad (14)$$

At the parameter values of interest in this study the integrand of Equation 13 oscillates wildly, thus making a numerical evaluation of the integral quite time consuming. An approximation to Equation 13 can be obtained by using the fact that both H_1 and H_2 are numerically equal to λ for $\lambda > 5$. When the exponential term in the integrand decays slowly (small C_2), this substitution can be made with little loss of accuracy. Then:

$$E \cong \frac{4e^{C_2}}{\pi C_2^2 C_3^2} I \quad (15)$$

where

$$I = \int_0^{\infty} e^{-x} \cos(t^*x^2 - x) x dx \quad (16)$$

Oscillations at large values of t^* do lead to difficulties in evaluating I ; however, the only parameter in the integration is t^* . This integral has been evaluated numerically by dividing the interval of integration into subintervals and applying the Gauss-Legendre quadrature formula with an appropriate number of points to each subinterval. For large values of t^* the subintervals were taken as the distance between zeros—*i.e.*, the distance between points corresponding to the argument of the cosine being numerically equal to $(4n - 1)\pi/2$ for $n = 1, 2, 3, \dots$. The results of this integration, accurate to three significant figures, are presented in Table I. Comparison of the numerical integrations of Equations 13 and 15 reveals that the error associated with the approximate solution is less than 1% for $t^* \leq 20$ and $C_2 \leq 0.15$. For parameter values outside this range Equation 13 should be used.

Table I. Results of Numerical Integration of Equation 16

t^*	I	t^*	I	t^*	I
0.04	2.92×10^{-4}	0.6	0.586	2.6	0.1231
0.06	0.0102	0.8	0.469	2.8	0.1117
0.08	0.0535	1.0	0.380	3.0	0.1019
0.10	0.1335	1.2	0.314	3.5	0.0828
0.15	0.386	1.4	0.265	4.0	0.0689
0.20	0.575	1.6	0.226	4.5	0.0586
0.25	0.680	1.8	0.1964	5.0	0.0505
0.30	0.720	2.0	0.1724	10.0	0.0187
0.40	0.710	2.2	0.1528	15.0	0.0103
0.50	0.652	2.4	0.1367	20.0	6.74×10^{-3}

Experimental

A simplified flow diagram of the equipment is shown in Figure 1. Basically, the apparatus is a simple gas chromatograph with a thermal conductivity detector. The carrier and the pulse gases were dried before use by passing through dryers containing 8-20 mesh activated silica gel. The carrier gas flow rate was measured by Rotameter R1 maintained at a pressure of 50 psi by pressure regulator PR1. A Carle microsample valve, model 2014, with two interchangeable and demountable loops was used in all experiments. The connection between the sample valve and the column was by 1/8 inch od standard wall copper tubing. Pressure drop considerations precluded the use of smaller tubing. To keep extra-column dispersion to a minimum, the length of all pulse-carrying tubing was kept as small as possible. The effluent from the column was split into two streams by a tee at the column exit. One stream passed through a 1/16 inch od tube to the sample side of the thermal conductivity detector, TCD. The other line of 1/4 inch od tubing terminated in a pressure equalizer (PE) which was essentially a closed cylindrical tank (45 cm long by 5.8 cm id) supplied with a stream of carrier gas through pressure regulator PR3 and maintained at a constant pressure of 5 psig. The tank was constantly vented through Rotameter R2 at such a rate that a positive flow of carrier gas to the tank was ensured—*i.e.*, the venting rate was higher than the rate of inflow from the splitting tee. The reference side of the detector was supplied from the downstream of pressure regulator PR3. The purpose of the tank was to eliminate fluctuations in the column outlet pressure and to ensure equality

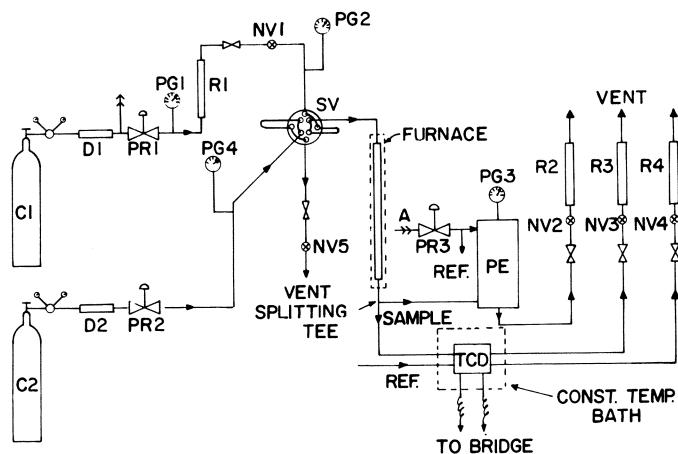


Figure 1. Simplified flow diagram

of pressure on the sample and reference sides of the detector—a requirement vital for drift-free operation.

The detector was a Gow Mac model 10-939 nano katherometer with 1/16 inch od connections. Peaks were recorded either by a Honeywell Visicorder oscillograph model 2106 (with chart speeds of up to 100 cm/sec and recording capability of up to 200 cycles/sec) or a Sargent Welch model DSRG two-pen recorder. The point of injection of the pulse was marked accurately on the recorded chart by an event marker switch actuated by the sample valve.

The column was located inside a well-insulated tubular furnace (183 cm long by 4.2 cm id). A flat temperature profile (maximum variation $\pm 3^\circ\text{C}$ at 318°C) was obtained by using a temperature controller in conjunction with four autotransformers. Heaters were provided at both ends to eliminate end effects. Thermocouples located at 20-cm intervals on the outside of the column monitored temperatures constantly. Heat transfer computations indicated that the length of the connecting tubing enclosed in the furnace was enough to preheat the carrier gas to the column temperature.

Helium and argon used in the experiments were of high purity grade (99.995 and 99.996%, respectively, according to manufacturer's specifications). The molecular sieves (Linde Division, Union Carbide Corp.), were crushed and separated into different size-fractions. Prior to a run the sieves in the column were degassed by heating to 340°C and purging with helium for 12–18 hours. The column porosities were computed from the weight of the bed and the apparent density of the zeolite particles. For measurements of axial dispersion the molecular sieves were simulated by 4-mm glass beads and 2.2-mm lead shots.

Pressure drop in the column was measured by a mercury manometer and was less than 5% of the inlet pressure at the highest velocities reported. The manometer was disconnected during an actual pulse-dispersion measurement to minimize extra-column dead volume. A correction to the first moment for holdup in the connecting lines was determined by replacing the column with a 1/8 inch union and noting the time required for the pulse to emerge. In subsequent runs with bed in place, the holdup time in the connecting tubing was subtracted from the observed mean. Contribution of the connecting tubing to the second moment was computed from correlations given by Levenspiel (17). Even with nonporous particles this contribution was much less than 1% of the observed σ^2 and was ignored.

Physical properties of the samples investigated are given in Table II. The pellet porosities are nominal values supplied by the manufacturer. The micro-particle radius, R_x , was not measured. The value in Table II was used by Hashimoto and Smith (12) in calculations with Linde 5A molecular sieve. Ruthven and Loughlin reported similar values (18). Actually it is the quantity D_x/R_x^2 that is determined experimentally, and the value chosen for R_x affects only the magnitude of D_x .

Table II. Properties of Samples Investigated^a

Sample	R_y (cm)	R_x (microns)	θ_x	θ_y	θ_z
3A	0.195	1.86	0.42	0.32	0.406
4A	0.110	1.86	0.42	0.32	0.428
4A	0.195	1.86	0.42	0.32	0.412
5A	0.102	1.86	0.42	0.32	0.421
5A	0.195	1.86	0.42	0.32	0.410

^a Bed length = 152.4 cm; bed inner diameter = 1.09 cm.

Results

Diffusion of argon in a helium carrier was studied over Linde type 3A, 4A, and 5A molecular sieves. Temperature was varied over a range from ambient to 318°C, and pressure was maintained at 5 psig for all experiments.

Effect of Pulse Concentration. Two assumptions inherent in the model seem quite restrictive. First, it is assumed that the adsorption isotherm is linear. This is only valid at very low concentrations where the extent of surface coverage amounts to a few percent of a monolayer. At higher concentrations a Langmuir type adsorption is usually observed. The second questionable point is the validity of Fick's diffusion equation. In particular, Ruthven and Loughlin (19) and Barrer (20) report Fickian diffusivities of gases in zeolites to be highly concentration dependent. These difficulties can be avoided by injecting a diluted sample into the bed entrance or in some other manner ensuring that the system is perturbed only slightly from its steady-state concentration.

Figure 2 gives the results of experiments aimed at evaluating the effect of inlet pulse concentration. Essentially identical results were obtained when pulses containing 20, 50, and 100% argon in helium were used. Our system is characterized by a small sample injection volume (0.05 cc) and a long bed length (152 cm); it is apparent from this figure that dilution of the pulse in the column is sufficiently rapid that nonlinearities in the system do not affect the results. In the remainder of the experiments the injection pulses consisted of pure argon. The values of the model parameters reported here should be considered "infinite dilution" values.

Effect of Micropore Size. The effect of the diameter of the micropore opening is well illustrated by our results with 3A, 4A, and 5A molecular sieves. According to the manufacturer, the principal factor that distinguishes between these 3 sieves is the exchangeable cation present in the matrix. The micropore opening is altered by varying the cation, but properties external to the zeolite crystal are essentially identical for the different sieves. Thus the distinctive behavior exhibited by the different sieve types as illustrated in Figure 2 is due primarily to differences in micropore opening.

The experimental E-curves change dramatically as micropore size is varied from 3A to 5A. Both the mean and the variance (a measure of peak width) are smallest for 3A molecular sieve. The mean for 4A is substantially larger than that observed with 3A but less than that observed with 5A. The variance

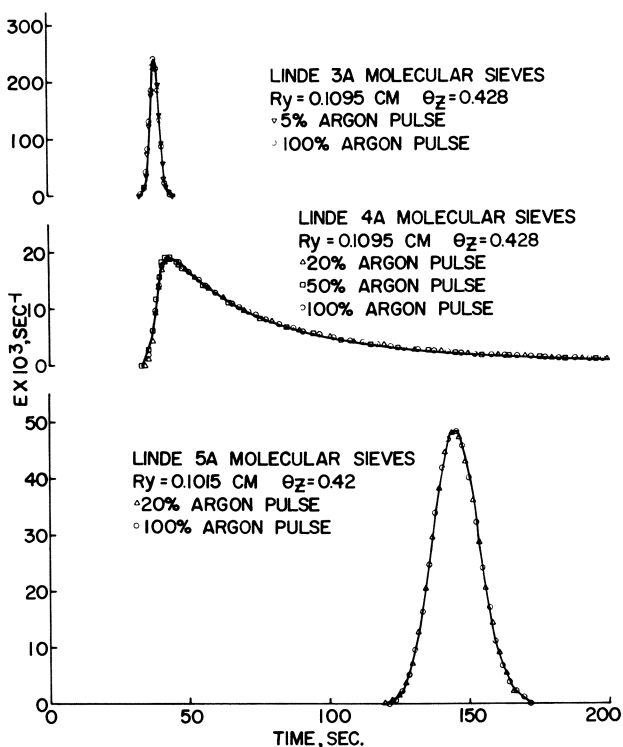


Figure 2. Effect of pulse concentration and micropore opening on R.T.D. ($v = 2.74 \text{ cm/sec}$)

is greater for 4A, but the most outstanding observation with this sample is the high degree of tailing in the E curve. This suggests that the theory developed in the previous section may be applicable to this sample. With 5A the mean is greatest, and the variance is intermediate between the results for 3A and 4A.

The behavior exhibited in Figure 2 is completely consistent with the predictions of our model. Since argon (critical diameter = 3.84 Å, Norton Chemical Products Division, Bulletin A-50) fails to penetrate the 3A crystallites, the results should correspond to the model predictions with $\theta_x = 0$. In such a situation the micropore contribution to Equations 1 and 2 would be negligible, and minimum values of μ and σ^2 would be predicted. If we postulate that argon penetrates the 4A crystallites, but only with great difficulty, then the micropore term of Equation 2 far overshadows the other terms and the tailing predicted by Equation 13 would be observed. Finally, the 5A crystallites are readily accessible to argon, the micropore term in Equation 2 is small, and a decrease in peak width is expected relative to that observed with 4A. At the same time Equation 1 predicts a significant increase in the mean as a result of penetration and adsorption in the micropores.

Evaluation of Model Parameters. According to Equation 1 a plot of the experimental first moment, μ , vs. $1/v$ should result in a straight line through the origin. First-moment plots for 3A and 5A sieves are given in Figures 3 and 4 respectively for several temperatures. If the micropores in 3A are not pene-

trated by argon molecules as already suggested, then the slopes of these plots depends only upon the porosities and bed length, and temperature should have no effect. The results in Figure 3 support this contention. On the other hand,

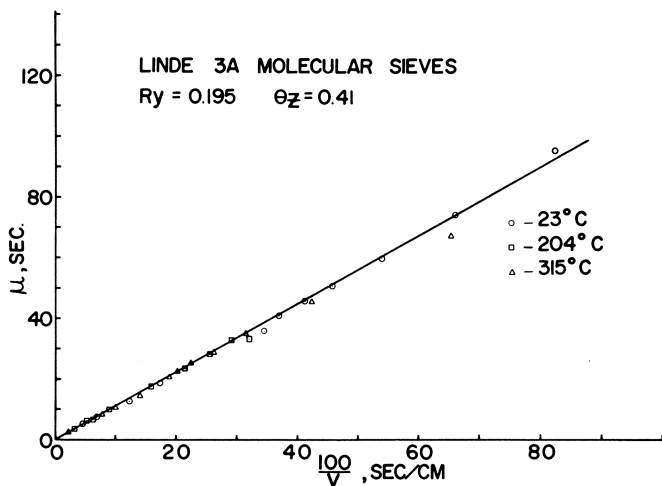


Figure 3. First-moment plot for 3A

a strong temperature effect is evident in Figure 4. Values of the adsorption equilibrium constant K_a , were determined from the slopes of these plots using Equation 1, and the results are presented in Table III. The heat of adsorption is -2.59 kcal/mole.

According to Equation 2 the experimental variance is equal to the sum of four separate contributions from axial dispersion, D_z ; external mass transfer, k_f ; macropore diffusion, D_y ; and micropore diffusion, D_x . Since our objective

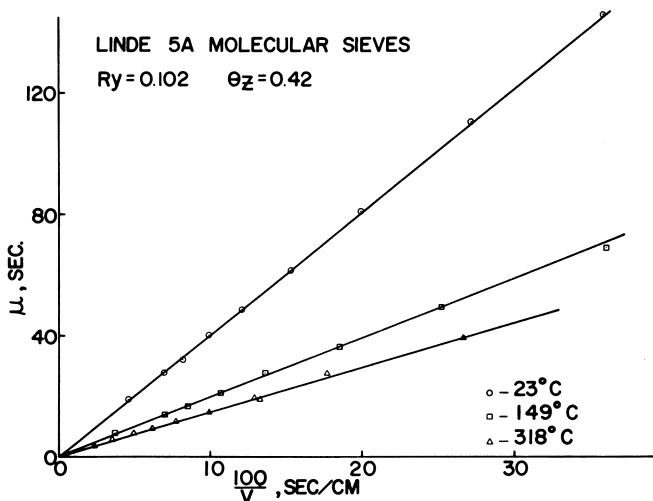


Figure 4. First-moment plot for 5A

Table III. Calculated Model Parameters for Argon in 5A Molecular Sieve

T ($^{\circ}\text{C}$)	D_x (cm^2/s)	D_y (cm^2/s)	K_a
23	2.47×10^{-7}	3.80×10^{-2}	11.41
149	6.52×10^{-7}	5.20×10^{-2}	3.09
318 ^a	3.98×10^{-7}	7.40×10^{-2}	1.19

$\Delta H_a = -2.59$ kcal/mole $E_x^b = 1.92$ kcal/mole $E_y^b = 0.58$ kcal/mole

^a Corrections for axial dispersion and external mass transfer amounted to 50–80% of the observed variance for $R_y = 0.102$ cm and 35–75% for $R_y = 0.195$ cm. The values of D_x and D_y at 318 $^{\circ}\text{C}$ are therefore felt to be unreliable.

^b Computed from low temperature runs.

is to determine the particle diffusivities, it is necessary to operate at conditions which minimize the contributions of the first two terms. High velocities are desirable, but eventually a point is reached where the pressure drop through the bed is excessive, or the response of the thermal conductivity cell is too slow to define accurately the exiting concentration–time curve. Large particle sizes enhance the macropore contribution. Our procedure was therefore to operate at velocities as high as allowed by pressure drop and cell response considerations, and to utilize large particle sizes when possible. Even at these conditions the contributions from axial dispersion and external mass transfer were significant for the 3A and 5A sieves.

The published correlations available for estimating D_z and k_t in packed beds are applicable only to situations in which the bed diameter is many multiples of the particle diameter. Because of the desirability of utilizing large particle sizes, our experiments are frequently conducted in columns comparable in diameter with the particle diameter. Nevertheless, we did use the correlation of Wakao *et al.* [Hashimoto and Smith (12)] to estimate k_t . Our justification is that the external mass transfer term, while significant in many cases, is a relatively small factor (less than 5%) compared with the sum of the total observed variance. The axial dispersion term was evaluated experimentally during “blank” runs on nonporous particles of approximately the same size as the molecular sieve samples. The experimental variance was then corrected for axial dispersion and external mass transfer by subtracting the first two terms on the right of Equation 2 computed from the estimates of k_t and D_z . In situations where these terms account for a large percentage of the observed variance, the values of the computed diffusivities must be regarded as questionable. Details of these calculations can be found elsewhere (21).

The corrected variance, σ_{xy}^2 , then depends only upon contributions from the particle diffusivities, and according to the model a plot of σ_{xy}^2 vs. $1/v$ should be a straight line passing through the origin. An illustrative plot for 5A sieve is presented in Figure 5. If macropore diffusion is a factor, the slope should vary with varying particle size; such behavior is indicated in Figure 5. From the slopes of these plots the macropore and micropore contributions can be separated and the respective diffusivities, D_y and D_x , evaluated. These results are also reported in Table III for 5A. The macropore and micropore activation energies are 0.58 and 1.92 kcal/gram mole. These computations indicate that argon can diffuse through both pore systems of 5A with relative ease. The analogous results for 3A were not calculated. With this sample the correction for axial dispersion was such a large percentage of the total variance (35–75%) that the corrected variance was not reliable. Similar problems were encountered with 5A at high temperatures.

Because of tailing in the experimental E curve for the 4A sample it was not possible to evaluate the moments with high accuracy. With this sample we determined the values of K_a and D_x which minimized the sum of squares of

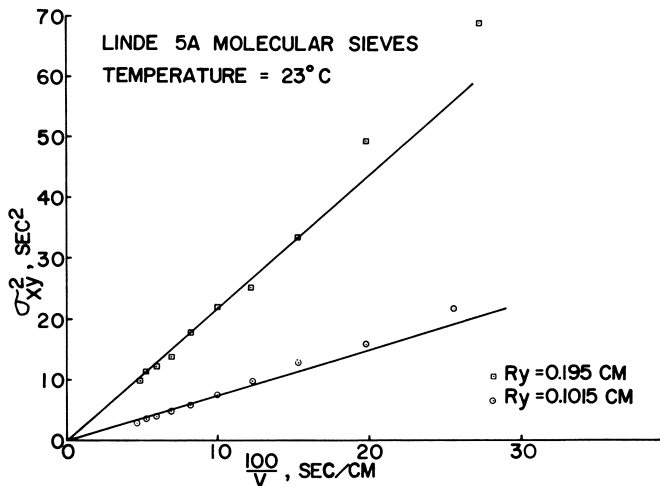


Figure 5. Corrected second-moment plot for 5A

deviations between the experimental E curve and the model predictions (Equations 13 or 15). The four-point Lagrangian interpolating polynomial was used to interpolate between the values in Table I. The regression program used the Taylor series linearization method to find the optimum parameter values. Figure 6 shows the type of fit that was obtained by this procedure. The excel-

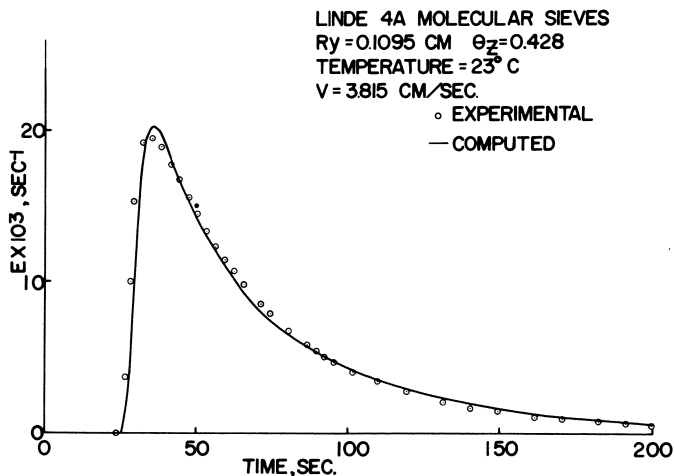


Figure 6. Comparison between experimental and calculated R.T.D. curve for 4A

lent agreement between the theoretical and experimental curves strongly supports usage of the macro-micro pore model for evaluating zeolite diffusivities by the gas chromatography method. These results do not corroborate the contention of previous workers (12) that the gas chromatograph method is not suited for measurement of micropore diffusivities.

Table IV. Calculated Model Parameters for Argon in 4A Molecular Sieve^a

R_p (cm)	θ_s	Temp. °C	v (cm/sec)	$D_x \times 10^{10}$ (cm ² /sec)	K_a
0.1095	0.428	23	3.82	3.71	7.15
0.1095	0.428	23	5.06	3.71	6.84
0.1095	0.428	23	6.42	2.96	7.38
0.1095	0.428	23	10.13	3.58	7.26
0.195	0.412	22	3.83	3.67	6.13
0.195	0.412	22	6.59	3.39	5.32
0.195	0.412	22	10.09	2.43	8.03
0.1095	0.428	149	3.90	15.72	1.96
0.1095	0.428	149	7.21	20.25	2.14
0.1095	0.428	149	9.36	20.38	1.99
0.195	0.412	149	5.48	16.40	2.04
0.195	0.412	149	7.20	18.90	2.29
0.195	0.412	149	10.36	20.84	2.17
0.195	0.412	149	11.73	21.37	2.15
0.1095	0.428	318	6.43	53.03	0.84
0.1095	0.428	318	8.74	61.19	0.82
0.1095	0.428	318	11.47	61.53	0.81
0.195	0.412	318	7.53	49.76	0.88
0.195	0.412	318	9.91	57.93	0.94
0.195	0.412	318	12.99	59.6	0.92

^a $E_x = 3.43$ kcal/mole; $\Delta H_a = -2.45$ kcal/mole.

Experimental values of K_a and D_x for 4A molecular sieve are presented in Table IV for various temperatures, velocities, and particle sizes. While the data are somewhat scattered, there is no apparent effect of particle size or velocity on the model parameters. The activation energies for diffusion and heat of adsorption computed from averaged values of D_x and K_a are respectively 3.43 and -2.45 kcal/gram mole. Thus the heats of adsorption obtained for argon on 4A and 5A molecular sieves are practically identical. Activation energy for micropore diffusion in 4A is significantly greater than that obtained with 5A, and the 4A diffusivity is smaller than the 5A diffusivity by approximately three orders of magnitude. The results indicate a strong molecule-pore wall interaction as argon diffuses in 4A molecular sieve.

We compared the results obtained by the GC technique with previous measurements based upon other methods. Walker *et al.* (22) reported diffusivities of argon in 3A molecular sieve obtained by a transient constant volume technique. It was necessary to carry out the measurement at temperatures $> 320^\circ\text{C}$ to obtain measurable rates. The diffusion was characterized by a large activation energy, 12.6 kcal/mole, and the intracrystalline diffusivity at 20°C is estimated to be of the order of 10^{-17} cm²/sec by extrapolating their results. This agrees with the present results since diffusivities of this magnitude would not be measured by the present technique. Measurements of argon diffusion in 4A and 5A have not been reported. Habgood (23) measured diffusivities of nitrogen (critical diameter = 3.0 Å) and methane (critical diameter = 4.0 Å) in powdered 4A using a constant pressure method. At 23°C the zero coverage diffusivities are calculated from their results to be 2.3×10^{-12} and 1.9×10^{-13} cm²/sec for nitrogen and methane, respectively. The corresponding activation energies were 4.07 and 7.42 kcal/mole. The results in Table IV indicate that argon diffuses more rapidly in 4A than Habgood's results seem to suggest. Heats of adsorption for argon in 4A and 5A have been reported by Breck *et al.* (24) and Breuer *et al.* (25). Breck's results were derived from adsorption isotherms which were determined gravimetrically. At

an adsorption capacity of 4 cc/gram the heats of adsorption were -3.0 and -4.5 kcal/mole, respectively, for 4A and 5A. Breuer and co-workers reported a heat of adsorption of -3.1 kcal/mole for argon in 4A at zero coverage and 228°K. No details of their experimental method were provided. These reported heats of adsorption are all greater than the values of -2.5 and -2.6 kcal/mole found here for the 4A and 5A samples.

Discussion

A special case arises when the GC effective diffusivity technique is applied to diffusion in pillared zeolites. If the intracrystalline diffusion is characterized by a strong molecule-pore mouth interaction, a large asymmetric peak results. Such behavior was observed experimentally for argon diffusing in 4A molecular sieve. For this special case a time domain solution is presented in the form of a definite integral, and a numerical approximation to this integral is developed and tabulated. Because of the large degree of tailing in these situations, it is impractical to evaluate the higher moments. A least squares regression of the model in the time domain produced an excellent fit of the experimental argon-4A residence time distribution. When the diffusing molecules have ready access to both the macropores and micropores, as was observed with argon diffusing in 5A, then both pore structures contribute to the dispersion. Tailing is not observed in this situation, and the moments can be evaluated. Contributions from macropore and micropore terms can be separated by varying particle size.

The importance of conducting measurements on blank (nonporous) samples needs to be emphasized. With the 3A sample only the macropore term contributed to the dispersion, and in some cases the experimental peak width was not significantly greater than that observed with the blank. This situation can be improved by using large catalyst particle sizes.

Nomenclature

C	gas phase concentration of diffusing species, gram mole/cc
C_a	concentration of adsorbed species, gram mole/cm ²
C_o	peak normalization factor, gram mole-sec/cc
C_1	quantity defined by Equation 6
C_2	quantity defined by Equation 7
C_3	quantity defined by Equation 8
D	diffusion or dispersion coefficient based on total area, cm ² /sec
E	residence time distribution function, sec ⁻¹
H_1	function defined by Equation 11
H_2	function defined by Equation 12
I	definite integral, Equation 16
k_f	external film mass transfer coefficient, cm/sec
K_a	adsorption equilibrium constant, Equation 3
L	column length, cm
R	particle or microparticle radius, cm
s	Laplace transform variable
S_x	surface area in micropores, cm ² /g
t	time, sec
t^*	dimensionless time, Equation 14
v	superficial velocity, cm/sec
x	dummy variable of integration
λ	dummy variable of integration
θ_x	micropore porosity, cc micropores/cc microparticle

θ_y	macropore porosity, cc macropores/cc pellet
θ_z	bed porosity, cc bed voids/cc bed
μ	mean of residence time distribution function, sec
ρ	catalyst particle density, grams/cc particle
σ^2	variance of residence time distribution function, sec ²

Subscripts

x	microparticle quantity
y	macroparticle quantity
z	bed quantity
L	quantity at column exit

Literature Cited

1. van Deemter, J. J., Zuiderweg, F. J., Klinkenberg, A., *Chem. Eng. Sci.* (1956) **5**, 271.
2. Habgood, H. W., Hanlan, J. F., *Can. J. Chem.* (1959) **37**, 843.
3. Davis, B. F., Scott, D. S., *Preprint 48d, 58th Ann. Meetg. AIChE, Philadelphia, 1965*.
4. Davis, B. R., Scott, D. S., *Preprint 13, Symp. III, 4th Intern. Congr. Catalysis, Moscow, 1968*.
5. Kubin, M., *Collect. Czech. Chem. Commun.* (1965) **30**, 1104.
6. Kubin, M., *Collect. Czech. Chem. Commun.* (1965) **30**, 2900.
7. Kucera, E., *J. Chromatogr.* (1965) **19**, 237.
8. Suzuki, M., Smith, J. M., *Chem. Eng. Sci.* (1971) **26**, 221.
9. Suzuki, M., Smith, J. M., *Chem. Eng. (London)* (1972) **3**, 256.
10. Padberg, G., Smith, J. M., *J. Catal.* (1968) **12**, 172.
11. Schneider, P., Smith, J. M., *AIChE J.* (1968) **14**, 886.
12. Hashimoto, N., Smith, J. M., *Ind. Eng. Chem., Fundamentals* (1973) **12**, 353.
13. Ma, Y. H., Mancel, C., *ADVAN. CHEM. SER.* (1973) **121**, 392.
14. Haynes, H. W., Jr., Sarma, P. N., *AIChE J.* (1973) **19**, 1043.
15. Haynes, H. W., Jr., Sarma, P. N., *NAPS Document No. 02092*, Microfiche Publications, New York, 1973.
16. Rosen, J. B., *J. Chem. Phys.* (1952) **20**, 387.
17. Levenspiel, O., "Chemical Reaction Engineering," 2nd ed., p. 284, Wiley, New York, 1972.
18. Ruthven, D. M., Loughlin, K. F., *Preprint 16c, 68th Natl. Meetg. AIChE, Houston, 1971*.
19. Ruthven, D. M., Loughlin, K. F., *Trans. Faraday Soc.* (1971) **67**, 1661.
20. Barrer, R. M., *ADVAN. CHEM. SER.* (1971) **102**, 1.
21. Sarma, P. N., Ph.D. Dissertation, University of Mississippi (1974).
22. Walker, P. L., Sr., Austin, L. G., Nandi, S. P., *Chem. Phys. Carbon* (1966) **2**, 257.
23. Habgood, H. W., *Can. J. Chem.* (1958) **36**, 1384.
24. Breck, D. W., Eversole, W. G., Milton, R. M., Reed, T. B., Thomas, T. L., *J. Amer. Chem. Soc.* (1956) **78**, 5963.
25. Breuer, P., Kiselev, A. V., Lesnik, E. A., Lopatkin, A. A., *Zh. Fiz. Khim.* (1969) **43**, 1519.

RECEIVED January 2, 1974. Work supported by a grant from the Committee on Faculty Research, University of Mississippi. The support of one of the authors (P.N.S.) was provided by the University of Mississippi Engineering Experiment Station.

The Role of Liquid Holdup and Effective Wetting in the Performance of Trickle-Bed Reactors

DAVID E. MEARS

Union Oil Company of California, Union Research Center, Brea, Calif. 92621

This paper questions the role of liquid holdup in trickle-bed catalytic reactors. The empirical dependence of the Henry and Gilbert conversion model on the 1/3-power of velocity does not agree with the exponent of 0.75 suggested by the literature for dynamic holdup in packed beds. It is, however, consistent with reported exponents of about 1/3 for the velocity dependence of the effectively wetted area. New models are derived on this basis and the implications for interpretation and scaleup of pilot plant data are discussed. An alternative derivation reveals that liquid holdup does not affect the author's criterion for freedom from significant axial dispersion effects.

Henry and Gilbert (1) recently proposed that catalyst utilization in trickle-bed hydroprocessing reactors is a direct function of the liquid holdup in their catalyst beds. A model was derived relating reactor performance to superficial mass velocity, liquid space velocity, liquid viscosity, catalyst bed length, and catalyst size. Impressive agreement was shown with pilot plant data for hydrocracking, desulfurization, denitrogenation, and aromatics saturation reactions. If correct, the model would have important practical implications for the scaleup of trickle-bed reactors, suggesting that scaleup on the basis of constant space velocity is too conservative. The present paper re-examines the role of holdup in both the conversion model and in earlier axial dispersion models.

Conversion Model Based on Holdup

Following Ross (2) and Nakamura *et al.* (3), Henry and Gilbert based their trickle-bed model on a differential material balance involving the dynamic liquid holdup:

$$F_{A0}dX_A = (-r_A) H dV \quad (1)$$

in which F_{A0} is the molar flow rate of reactant into the differential element, dX_A is the differential conversion of reactant, and dV is the differential volume

of reactor in the element. The reaction rate r_A was expressed as moles A reacting/(time) (volume of fluid in element), and the holdup H as the volume of fluid in the element/volume of the element. The molar flow rate and total catalyst volume were then related to the liquid hourly space velocity by:

$$VC_{A_0}/F_{A_0} = 1/LHSV \text{ or } G = (LHSV) \rho L \quad (2)$$

in which C_{A_0} is the initial concentration of reactant in the liquid feedstock, G is the mass velocity based on superficial bed cross section, ρ is the density of the liquid, and L is the length of the undiluted catalyst bed. Integration for a first-order reaction gave:

$$\frac{H}{LHSV} = \frac{1}{k} \ln \left[\frac{1 - X_{A_0}}{1 - X_{A_p}} \right] = \frac{1}{k} \ln \frac{C_{A_0}}{C_{A_p}} \quad (3)$$

The left side of Equation 3 was termed the space time for the reaction. In the absence of experimental holdup data for the reaction systems under consideration, they next introduced the dynamic holdup correlation of Satterfield *et al.* (4):

$$H = K \text{Re}^{1/3} \text{Ga}^{-1/3} \quad (4)$$

in which K is a proportionality constant. The Reynolds and Galileo numbers are defined in the Nomenclature. Substitution of Equation 4 in Equation 3 led to the simplified model:

$$\log \frac{C_{A_0}}{C_{A_p}} \propto (L)^{1/3} (LHSV)^{-2/3} (d_p)^{-2/3} (\nu)^{1/3} \quad (5)$$

Here d_p is the catalyst particle diameter and ν is the kinematic viscosity of the liquid. For presumed first-order reactions, this model gave linear semilog plots with several sets of pilot plant data which otherwise gave nonlinear plots. Their paper concluded that greater liquid holdup (*i.e.*, longer space time) in the catalyst bed appears to be the key to the increased catalyst utilization at higher mass velocities. While the agreement with the data is certainly good, the basis of the derivation is questionable.

The model could be criticized on several counts. First, the correlation of Satterfield *et al.*, and its exponent of 1/3 on velocity, applies to holdup of liquid on a vertical string of glass beads and a special definition of Reynolds number appropriate to this system. In packed beds the dynamic holdup is evidently proportional to a power close to 0.75 at $\text{Re} > 1$, as shown by the reported values in Table I. Second, the model suggests unrealistic conversion improvement for large reactor scaleups. For a scaleup from 3 to 60 ft, Equation 5 predicts that a conversion of 90% would increase to 99.87%, which is equivalent to a 2.72-fold increase in activity. To be fair, Henry and Gilbert warn that the model will apply only over the region where holdup increases according to Equation 4, but its stated range of $10 < \text{Re} < 600$ would cover almost all scaleups. If the more realistic 0.75 exponent were used, this criticism would be more serious.

Nevertheless, the demonstrated linear relation between $\log (C_{A_0}/C_{A_p})$ and $L^{1/3}(LHSV)^{-2/3}$ cannot be disregarded. In view of the above comments, however, this finding must be described as an empirical demonstration that reactor performance is proportional to the 1/3 power of liquid velocity. Further support for this exponent is provided by Skripek and Ballard (5), who obtained 0.30 ± 0.11 for VGO desulfurization at $90 < G < 300$ lb/hr ft².

Table I. Dependence of Dynamic Holdup in Packed Beds on Velocity

Investigators	Packing type	Reynolds No. Range	Exponent on Liquid Velocity
Buchanan (21)	raschig rings	0.05-1 10-10 ³	1/3 1.0
Gelbe (22)	various rings	10 ⁻³ -1 1-10 ²	1/3 5/11
Hochman and Effron (14)	spheres	8-70	0.76
Mohunta and Laddha (23)	rings and spheres		0.75
Michell and Furzer (19)	various packing	10-500	0.80
Otake and Okada (20)	raschig rings		0.68
Sater and Levenspiel (24)	rings and saddles	15-400	0.68 ^a
van Swaaij <i>et al.</i> (15)	raschig rings	10-200	0.68 ^a

^a Obtained by fitting data to correlation of Otake and Okada rather than by independently determining exponent.

Conversion Model Based on Effective Wetting

Effective catalyst wetting merits consideration as an alternative explanation for the dependence of reactor performance on velocity. Satterfield and Ozel (6) provided visual evidence indicating ineffective wetting in laboratory trickle-bed reactors. Careful observations

during and in the absence of reaction showed that the liquid flowed downwards in rivulets which tended to maintain their positions with time. Some catalyst pellets were thus covered with a trickling liquid film while others, although wet, were without a liquid film on the surface . . . Non-uniformity of the liquid flow in trickle-bed reactors has been reported previously, but it is worth noting that this occurred here at liquid Reynolds numbers as high as 55 [2400 lb/hr ft²] and in spite of the extreme measures taken to provide initial uniform distribution of liquid.

Considering this evidence, it seems reasonable to assume that reaction rate is proportional to the fraction of external catalyst surface which is effectively (freshly) wetted by the flowing liquid. The observed dependence of reaction rate on *ca.* the 1/3 power of velocity is strikingly close to the 0.32 power velocity dependence of the wetted area correlation of Puranik and Vogelpohl (7). This recent correlation of published data from packed columns can be written:

$$\frac{a_w}{a_t} = 1.05 \text{Re}^{0.047} \text{We}^{0.135} (\sigma_c/\sigma)^{0.206} \quad (6)$$

where σ is the surface tension of the liquid, and σ_c is the critical value of the surface tension for the given packing. At this critical value the contact angle is zero—*i.e.*, the liquid spreads for values of σ below σ_c . The Weber number (defined in the Nomenclature) is a measure of the ratio of inertial force to surface tension force and is proportional to liquid mass velocity squared.

If Equation 6 and the effectiveness factor $\eta(d_p)$ are introduced instead of holdup in Equation 1, the resulting simplified conversion model is:

$$\log \frac{C_{Ao}}{C_{Ap}} \propto (L)^{0.32} (LHSV)^{-0.68} (d_p)^{0.18} (v)^{-0.06} (\sigma_c/\sigma)^{0.21} \eta(d_p) \quad (7)$$

While similar in form to Equation 5, this model differs in its dependence on d_p , v , and σ . The prediction of this equation that conversion should decrease with increasing viscosity is more reasonable than the prediction of Equation 5

that it should increase. For practical application with a given feedstock the last three terms can be factored into the proportionality.

Tests of Conversion Models

The various predictions of the conversion models can be checked with available pilot plant data. Henry and Gilbert provide data on hydrotreating heavy feedstocks which verify the $(LHSV)^{-2/3}$ dependence of both Equations 5 and 7. Their data for hydrocracking West Texas vacuum gas oil agree with the $L^{1/3}$ dependence over a three-fold variation in reactor length (from 3.75 to 10.2 ft).

Henry and Gilbert also show data for the saturation of aromatics in white oils which are consistent with the Equation 5 prediction of a $-2/3$ power dependence on catalyst diameter. Thus they suggest that the hydrogenation process was not affected to a major degree by pore-diffusion limitations. However, a dependence of close to the $-2/3$ power on particle diameter could also result if Equation 7 applied and the reaction was severely influenced by diffusion due to the inverse dependence of the effectiveness factor on particle diameter. This explanation seems more likely, but insufficient information is available to decide this point independently by using an intraparticle transport criterion.

The models differ moderately in their predictions of the effects of viscosity and surface tension. These predictions could perhaps be checked by comparing the reactivity of a test reactant added to severely hydrotreated solvents of different viscosity and surface tension. Severe hydrotreating is necessary to minimize competitive adsorption effects such as found by Satterfield and Way (8).

Vapor Phase Reaction and Heat Transport Effects

The above development assumed that catalyst pellets not effectively wetted contribute little to the overall rate. With reactants of low molecular weight, vapor-phase reaction on unwetted pellets can occasionally be important during startup as shown by Sedriks and Kenney (10) for the hydrogenation of cronton-aldehyde over 3/16-inch Pd/Al₂O₃ pellets. However, the pores of unwetted catalyst pellets gradually filled with liquid because of capillary condensation, and the contribution of vapor-phase reaction decreased. The reaction rate also decreased with increased liquid loading. Detailed interpretation of their study is clouded by the intrusion of significant heat transfer effects for vapor-phase reaction and intraparticle mass transfer effects for liquid-phase reaction.

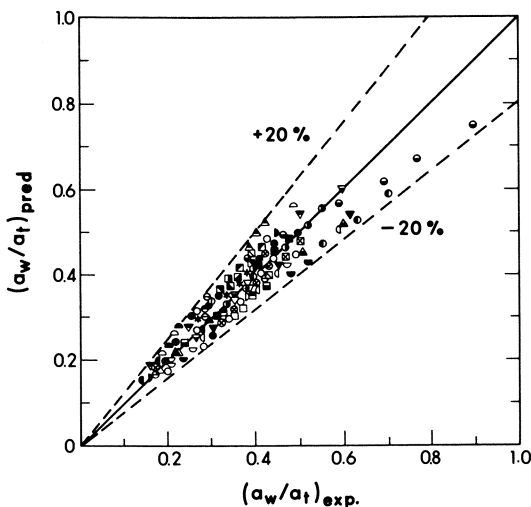
Similarly, Satterfield and Ozel (6) found that benzene hydrogenation at 76°C, four degrees below the boiling point, decreased with increasing liquid flow rate. Here the catalyst was 2% Pt/Al₂O₃ in the form of 1/4-inch spheres. Calculations indicated that interphase and intraparticle mass transfer limitations were substantial. Comparison of transport criteria of Mears (11) indicates that significant interphase heat transport effects can also be expected for particles not effectively wetted. Thus improved heat transfer at higher flow rates could have caused catalyst particles to operate at lower temperatures and thus decreased the reaction rate.

In typical hydroprocessing reactions vapor-phase transport of reactant molecules is poor owing to their relatively high molecular weight and low vapor pressure. The improvement in reactor performance usually observed

as liquid contacting increases suggests that vapor-phase reaction is not important for the class of hydroprocessing reactions in question here.

Implications for Interpretation and Scaleup of Data

The new model should be useful in testing pilot plant data for falsification of the true kinetics caused by incomplete wetting. This effect may cause first-order kinetics to appear as higher order, leading to an incorrect interpretation of the kinetics and space velocities lower than necessary.



Chemical Engineering Science

Figure 1. Parity plot of wetted area correlation (after Puranik and Vogelpohl (7))

Since the model presented is based on pilot plant data and a wetting correlation, a question arises concerning its applicability to scaleup. Nearly complete wetting of catalyst particles should be obtained as mass velocities typical of commercial reactors are approached. At a_w/a_t ratios above 0.6 the experimental data on Figure 1 tend to fall below the correlation line, suggesting an asymptotic approach to complete wetting. Therefore Equation 7 cannot be recommended as a precise basis for scaleup above mass velocities of say 1000 lb/hr ft². For scaleup, a model could be based on the form of the correlation on Onda *et al.* (8) which can be expressed as:

$$\frac{a_w}{a_t} = 1 - \exp \left\{ -1.36 Ga^{0.05} We^{0.2} \left(\frac{\sigma_c}{\sigma} \right)^{0.75} \right\} \quad (8)$$

The predictions of this correlation are quite close to those of Equation 6 over the range $100 < G < 1000$ lb/hr ft². Because We is proportional to G^2 , Equation 6 shows that the fraction wetted will asymptotically approach unity at high mass velocities. The correlation provides the basis for a scaleup model with only two adjustable coefficients:

$$\log \frac{C_{Ao}}{C_{Ap}} = \frac{k\eta}{LHSV} [1 - \exp \{-K(L)^{0.4} (LHSV)^{0.4}\}] \quad (9)$$

in which the dependences on viscosity, surface tension, density, and particle diameter have been factored into the coefficient K .

The fraction effectively wetted will also be a function of the initial distribution of liquid in the reactor and its length-to-diameter ratio, particularly in the case of commercial reactors (2, 12). The development given here assumes that a uniform initial distribution is provided.

Trickle-Bed Axial Dispersion Model

In evaluating kinetic data from trickle-bed pilot plants, it is also necessary to consider axial dispersion effects. These effects keep a reactor from achieving the ideal plug-flow conversion. To estimate when these effects are important, Mears (13) gave a criterion for freedom from significant dispersion effects. An alternative derivation is now given to show explicitly the role of liquid holdup.

The differential equation for axial dispersion for the flowing liquid is:

$$E_{ai} \frac{d^2c}{dx^2} - v_i \frac{dc}{dx} - \frac{k_n c^n \eta_s}{H} = 0 \quad (10)$$

in which E_{ai} , the axial dispersion coefficient, and v_i , the linear liquid flow velocity, are each referred to the cross section of the flowing liquid. In the third term, k_n is the reaction rate constant per bulk volume of catalyst, n is the order of the reaction, and η_s is a global effectiveness factor, defined as the product of the interphase-intraparticle effectiveness factor and the ratio a_w/a_t . The global effectiveness factor can be taken as essentially constant over the narrow range of reactor length in which dispersion effects become significant. The reaction rate is expressed per unit volume of liquid by introducing the liquid holdup in the denominator. As before thermal effects are assumed negligible. Upon multiplying through by H the equation becomes:

$$H E_{ai} \frac{d^2c}{dx^2} - H v_i \frac{dc}{dx} - k_n c^n \eta_s = 0 \quad (11)$$

Because the liquid holdup also represents the ratio of the cross section of the liquid stream to the cross section of the bed, the products HE_{ai} and Hv_i may be taken, respectively, as the dispersion coefficient E_a and mean velocity \bar{v} referred to the empty bed cross section. This puts the equation into the form originally presented.

When the equation is made dimensionless, the holdup cancels from the Peclet number based on particle diameter:

$$Pe_m = \frac{\bar{v} d_p}{E_a} = \frac{v_i d_p}{E_{ai}} \quad (12)$$

The rest of the development follows as given before.

If axial dispersion effects are to increase reactor length by less than 5% over the minimum length required with plug flow, the criterion to be met is:

$$\frac{L}{d_p} > \frac{20 n}{Pe_m} \ln \frac{C_o}{C_f} \quad (13)$$

The minimum reactor length thus increases with the order of reaction and with conversion and is independent of the holdup.

The Peclet number was estimated through the correlations of Hochman and Effron (14), van Swaaij *et al.* (15), and Furzer and Michell (16). Gen-

erally at $Re \sim 10$, the Peclet number is about 0.2. In contrast the Peclet number for gases is about 2 for $Re > 1$. Thus the minimum reactor length for freedom from significant effects could be an order-of-magnitude greater than required for vapor-phase reaction to the same conversion level.

Evaluation of Dispersion Effects

Henry and Gilbert used the above criterion and the correlation of Hochman and Effron to estimate a minimum reactor length of 14 inches for 1/16-inch catalyst particles, a Reynolds number of 10, and a conversion of 90%. It was implied that this minimum length applies for all the pilot-plant studies given as examples. In fact, the criterion requires a minimum length of 28 inches for 99% conversion. The semilog plots of Flinn *et al.* (17), which are linear at lower conversions, show curvature in the 95–99.9% conversion range. These data were obtained with 1/15-inch catalyst particles in a 10-inch bed according to Larson (18). Thus axial dispersion effects are clearly indicated as an important cause of the curvature in this case.

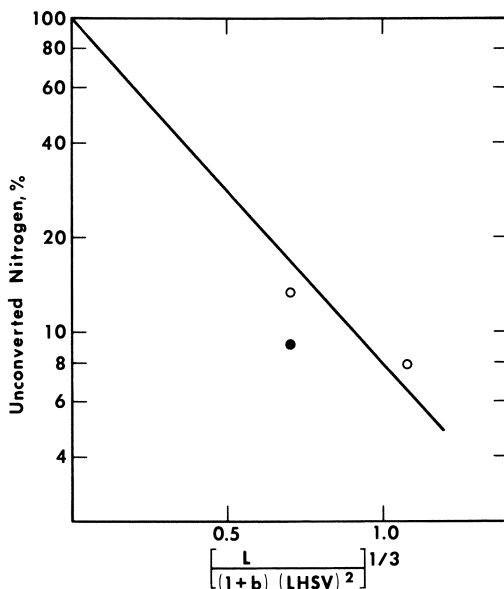


Figure 2. Semilog plot of Mears (13) denitrogenation data to trickle-bed reactor model. Filled point is for diluted bed.

Similarly for the denitrogenation data of Mears (13), the criterion required a minimum reactor length of about 33 inches arising from the larger effective particle size and conversions over 90%. Since the shortest of the three beds was 13 inches, significant axial dispersion effects were indicated for this bed length. Nevertheless, Henry and Gilbert applied their model to this data and found reasonable agreement for two of the three data points given in the original work. The third, unplotted point was obtained with the same amount of catalyst and feed rate as in the shortest bed length case, but the catalyst was diluted with an equal amount of inert diluent to lengthen

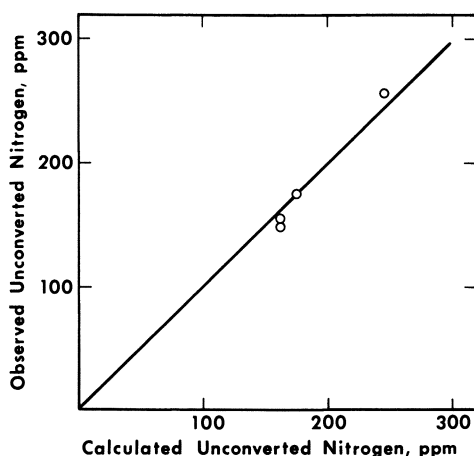


Figure 3. Parity plot of axial dispersion model predictions vs. experimental results for Mears (13) denitrogenation data

the bed and minimize the dispersion effect. When this point is added to the plot, the agreement is much poorer, as shown in Figure 2. In contrast, the predictions of the axial dispersion plot agree quite well with the observed values, as shown by the parity plot of Figure 3.

Conclusions

When axial dispersion and heat transport can be neglected, a conversion model based on the $1/3$ power of liquid velocity closely describes the dependence of trickle-bed hydroprocessing data on space velocity and bed length. Effective wetting provides a more rational basis than liquid holdup, as indicated by the agreement in velocity dependence. The new models derived on this basis should be useful in interpreting kinetic data from small pilot plants. Additional data obtained over a greater range of mass velocity, viscosity, and surface tension are needed to confirm and extend the models for scaleup.

Acknowledgment

The author acknowledges the helpful comments of T. K. Sherwood and C. N. Satterfield. O. A. Larson also graciously provided additional information on experimental conditions used in his study.

Nomenclature

- a_t external area of catalyst or packing per unit volume of bed,
 $= 6(1 - \epsilon)/d_p$, cm^2/cm^3
 a_w freshly wetted external area per unit volume of bed, cm^2/cm^3
 b dilution ratio, cm^3 of inert particles/ cm^3 of catalyst
 C concentration, mole/cm^3

d_p	diameter of catalyst particle, cm
E_a	axial dispersion coefficient referred to empty bed cross section, cm^2/sec
E_{ai}	axial dispersion coefficient referred to interstitial liquid cross section, cm^2/sec
F	volumetric flow rate, cm^3/sec
F_{Ao}	molar flow rate of reactant A, moles/hr
g	acceleration caused by gravity, cm/sec^2
G	mass velocity, $\text{grams}/(\text{cm}^2)(\text{hr})$
H	dynamic holdup, $\text{cm}^3 \text{ liquid}/\text{cm}^3 \text{ bed}$
k	reactor rate constant, hr^{-1} for first-order reaction
L	catalyst bed length, cm
$LHSV$	liquid hourly space velocity, $\text{cm}^3/(\text{hr})(\text{cm}^3 \text{ catalyst})$
n	order of reaction
\bar{v}	superficial (empty tube) velocity of liquid, cm/sec
v_i	linear velocity of interstitial liquid, cm/sec
V	catalyst bed volume, cm^3
X	conversion of limiting reactant

Dimensionless Groups

Ga	Galileo number, $= d_p^3 g \rho^2 / \mu^2$
Pe	Peclet number, $= \bar{v} d_p / E_a$
Re	Reynolds number, $= G d_p / \mu$ for packed bed $= F \rho \pi / d_p \mu$ for string of glass beads
Re_i	Reynolds number based on interstitial velocity, $= v_i \rho d_p / \mu$
We	Weber number, $= G^2 d_p / \sigma \rho$

Greek Letters

ϵ	void fraction of packed bed
μ	viscosity, $\text{grams}/(\text{cm})(\text{sec})$
ρ	density, grams/cm^3
σ	surface tension of liquid, $\text{grams}/\text{sec}^2$
σ_c	critical value of surface tension for a given packing, $\text{grams}/\text{sec}^2$
ν	kinematic viscosity, $= \mu / \rho$, cm^2/sec

Subscripts

a	axial
i	interstitial liquid
o	initial or feed property
p	final or product property
w	wetted

Literature Cited

- Henry, H. C., Gilbert, J. B., *Ind. Eng. Chem., Process Design Develop.* (1973) **12**, 328-334.
- Ross, L. D., *Chem. Eng. Progr.* (1965) **61** (10), 77-82.
- Nakamura, H., Satori, H., Tabuchi, K., Nishizaki, S., Kurita, S., Watanabe, T., Sakuma, J., *Sekiyu Gakkai Shi* (1969) **12** (10), 778-782; *Int. Chem. Eng.* (1970) **10**, 506-512.
- Satterfield, C. N., Pelosof, A. A., Sherwood, T. K., *AIChE J.* (1969) **15**, 226-234.
- Skripek, M., Ballard, J., Union Oil Co., private communication, 1973.
- Satterfield, C. N., Ozel, F., *AIChE J.* (1973) **19**, 1259-1261.
- Puranik, S. S., Vogelpohl, A., *Chem. Eng. Sci.* (1974) **29**, 501-507.
- Satterfield, C. N., Way, P. F., *AIChE J.* (1972) **18**, 305-312.
- Onda, K., Takeuchi, H., Koyama, Y., *Kagaku Kogaku* (1967) **31**, 126-134; *cf.*, Onda, K., *Mem. Fac. Eng. Nagoya Univ.* (1972) **24** (2), 165-215.
- Sedriks, W., Kenney, C. N., *Chem. Eng. Sci.* (1973) **28**, 559-568.
- Mears, D. E., *J. Catalysis* (1973) **30**, 283-287.

12. Murphree, E. V., Voorhies, A., Mayer, F. X., *Ind. Eng. Chem., Process Design Develop.* (1964) **3**, 381-386.
13. Mears, D. E., *Chem. Eng. Sci.* (1971) **26**, 1361-1366.
14. Hochman, J. M., Efron, E., *Ind. Eng. Chem., Fundamentals* (1969) **8**, 63-71.
15. van Swaaij, W. P. M., Charpentier, J. C., Villermaux, J., *Chem. Eng. Sci.* (1969) **24**, 1083-1095.
16. Furzer, I. A., Michell, R. W., *AIChE J.* (1970) **16**, 380-385.
17. Flinn, R. A., Larson, O. A., Buether, H., *Hydrocarbon Proc. Petrol. Refiner* (1963) **42** (9), 129-132.
18. Larson, O. A., Gulf Research & Development Co., Pittsburgh, Pa., private communication, 1973.
19. Michell, R. W., Furzer, I. A., *Chem. Eng. J.* (1972) **4**, 53-63.
20. Otake, T., Okada, K., *Kagaku Kogaku* (1953) **17** (5), 176-184.
21. Buchanan, J. E., *Ind. Eng. Chem., Fundamentals* (1967) **6**, 400-407.
22. Gelbe, H., *Chem. Eng. Sci.* (1968) **23**, 1401-1403.
23. Mohunta, D. M., Laddha, G. S., *Chem. Eng. Sci.* (1965) **20**, 1069-1072.
24. Sater, V. E., Levenspiel, O., *Ind. Eng. Chem., Fundamentals* (1966) **5**, 88-92.

RECEIVED January 2, 1974.

Velocity and Direction of Liquid Phase in Bubble Columns

EIICHI KOJIMA, TAKASHI AKEHATA, and TAKASHI SHIRAI

Research Laboratory of Resources Utilization, Tokyo Institute of Technology, O-Okayama, Meguro-Ku, Tokyo 152, Japan

Liquid velocity and direction were measured in bubble columns 8 and 15 cm in diameter with a newly developed probe. Three microelectrodes, at which a diffusion-controlled electrode reaction occurs, form a triangle. The direction and velocity were calculated from the cross-correlation function of voltage fluctuations of the three microelectrodes. The direction and velocity of the liquid phase varied continuously with time. In the central region of the column the liquid flow was mainly upward. Near the wall, both upward and downward flow were measured, although the ratio of the period of upward flow to the data-acquiring time was less than in the central core region. Radial flow was observed over the entire column cross-section. These results are considered to be closely related to the performance of bubble-column reactors, such as mixing, conversion, and selectivity.

It has been reported that a relatively steady stream of liquid exists in a bubble column even in batch operations. Pavlov (1), using a Pitot tube, measured the circulating velocity of the liquid phase in a batch-type bubble column 17 cm in diameter with a gas superficial velocity of 5–100 cm/sec. Yoshitome and Shirai (2) used a spherical float to measure the velocity of gas-liquid mixture in bubble columns 15 and 28 cm in diameter and showed that the liquid movement was upward in the central region but downward over the rest of the annular section. De Nevers (3) observed that when a vertical baffle was introduced in a bubble column, gas-liquid flow showed a stable circulation, but without the vertical baffle the flow became irregular and unstable. Kunugitga *et al.* (4) investigated the behavior of the liquid phase of a bubble column 5 cm in diameter and 100 cm in height by taking photographs continuously of a suspended tracer particle. They found that over the entire cross section, the observed instantaneous axial liquid velocities were both upward and downward, and the mean axial velocity was nearly zero.

A few models for circulatory flows in bubble columns have been proposed. Freedman and Davidson (5) calculated the circulation velocity by assuming that the flow in bubble columns is inviscid and compared the predictions with experimental flow patterns for low gas velocities. Rietema and Ottengraf (6) assumed that the flow is laminar and calculated the circulating velocity by

solving the equations of momentum and material balance, and compared the estimation with experimental values obtained in a glycerine-aqueous solution-air system. Miyauchi and Shyu (7) defined a turbulent viscosity of gas-liquid two-phase flow, determined it experimentally, and proposed a method for calculating steady-state circulation velocity distribution in a batch bubble column. These three models assume fixed and axisymmetrical flow patterns.

Figure 1 shows how flow patterns in bubble columns vary with time. Flow patterns were visualized by tracer particles lighted in the black background. The experimental conditions were: column diameter 15 cm, superficial gas velocity 1 cm/sec, and liquid height 45 cm. Although these three photographs were taken at the same gas flow rate, the flow patterns differ from each other. In Figure 1A, the liquid flows upward in the left part and downward in the right. In Figure 1C, the direction of flow is contrary to that in Figure 1A. In Figure 1B, the flow is axisymmetrical, upward in the central part and downward near the wall. These photographs show that at a point in a bubble column, the direction of liquid flow is not always fixed.

From the above observations, it should be pointed out that, although in previous work the flow pattern is considered to be fixed and axisymmetrical and the radial flow is not taken into account, the liquid flow in a bubble column is much more complicated, and therefore detailed measurements should be made to clarify the above observations quantitatively. In this investigation, a probe which can detect the flow direction and measure the velocity is developed and applied to the gas-liquid two-phase flow in bubble columns.

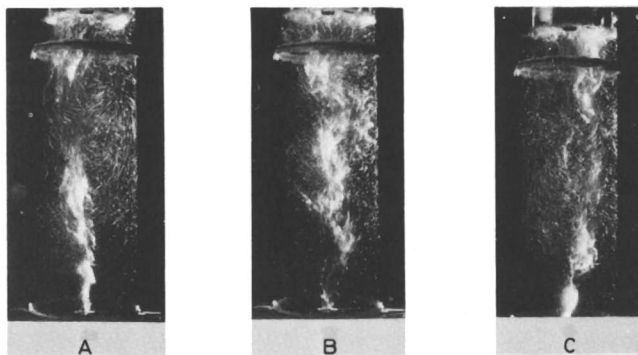


Figure 1. Liquid flow patterns

Measurement of Velocity and Direction

Probe. In a complex flow field such as in a bubble column, the usual one-pointed, direction-detecting probes are not suitable because these can be used satisfactorily only in a steady flow. In the present study a three-micro-electrode probe is developed by which the velocity and direction of unsteady flow is calculated from the cross-correlation function of three signals obtained by the probe.

The probe is shown in Figure 2. Its components are three platinum micro cathodes 0.6 mm in diameter which form a triangle 6.0 mm on each side, and three corresponding platinum rectangular anodes 3×5 cm. These electrodes utilize the electrochemical reaction of ferricyanide ion—*viz.*,

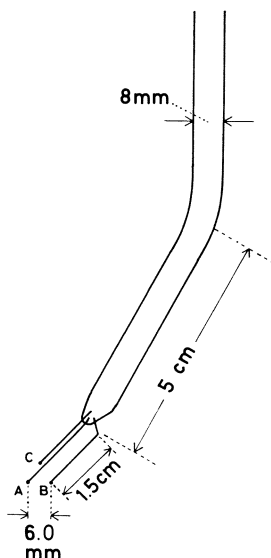
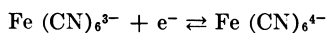


Figure 2. The probe



The electrolyte was $3 \times 10^{-3}M$ potassium ferricyanide and potassium ferrocyanide and $1M$ sodium chloride. The electric circuit is shown in Figure 3. By applying an appropriate voltage across the anode and cathode, measurements were carried out so that the electrode reaction was controlled by the mass transfer rate.

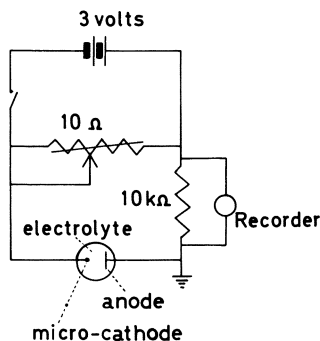


Figure 3. Electric circuit

Before each run, the probe was pretreated. The electrodes were immersed in a 5% aqueous solution of sodium hydroxide and 5 v direct current was applied for 20 min.

Principle of Measurements. The method of calculating and detecting the velocity and direction of the flow is illustrated in Figure 4. It is assumed that the liquid phase moves at a mean velocity u with some characteristic turbulent

fluctuating component on it. If the liquid flow that passes over the triangle of the three electrodes shows the same velocity fluctuation along the line perpendicular to the direction of bulk flow, and the shape of the fluctuating wave does not change substantially during the period necessary for the flow to pass over the triangle, then the same pattern of velocity fluctuation will be observed at any two electrodes, although in the downstream the signal lags in phase.

Let the velocity fluctuations be $V_A(t)$ and $V_B(t)$ observed at the electrodes A and B, respectively, and calculate the cross-correlation function $C_{AB}(\tau)$

$$C_{AB}(\tau) = E \{V_A(t - \tau)V_B(t)\} \quad (1)$$

and let the value of τ at which the function $C_{AB}(\tau)$ takes the maximum be τ_{OAB} . Then τ_{OAB} corresponds to the time required for the liquid flow to move from electrode A to electrode B. If the side AB makes an angle θ with the bulk flow, u is related to θ by the following equation

$$\cos \theta = u\tau_{OAB}/l \quad (2)$$

where l is the length of the side AB.

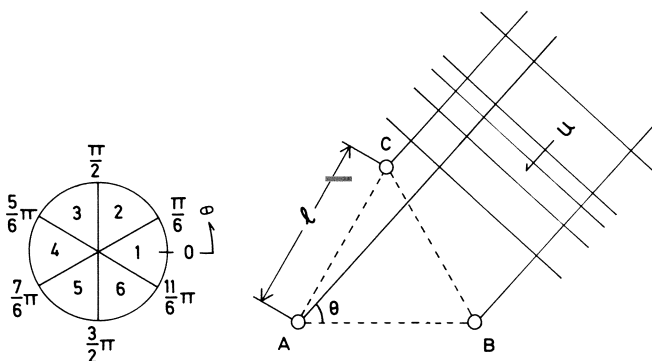


Figure 4. Principle of measurement

Table I. Direction of Liquid Flow

Range	1	2	3	4	5	6
θ	$0 \sim \frac{1}{6} \pi$	$\frac{1}{6} \pi \sim \frac{1}{2} \pi$	$\frac{1}{2} \pi \sim \frac{5}{6} \pi$	$\frac{5}{6} \pi \sim \frac{7}{6} \pi$	$\frac{7}{6} \pi \sim \frac{3}{2} \pi$	$\frac{3}{2} \pi \sim \frac{11}{6} \pi$
	$\frac{11}{6} \pi \sim 2\pi$					
τ_{OAB}	—	—	+	+	+	—
τ_{OBC}	+	—	—	—	+	+
τ_{OCA}	+	+	+	—	—	—

When the three values of τ_{OAB} , τ_{OBC} , and τ_{OCA} are obtained, the values of θ and u are calculated as follows:

(1) Find the signs of τ_{OAB} , τ_{OBC} and τ_{OCA} , and locate the range of θ . As shown in Table I, by the combination of the signs of τ_{OAB} , τ_{OBC} , and τ_{OCA} , the range of θ is determined as one of the six equally divided ranges. For example,

I				A	1	748	590	583
I		CB		A	2	738	592	580
I		CB		A	3	739	590	575
I		C		A	4	738	595	586
I		C		A	5	719	603	573
I		C	B	A	6	718	603	573
I		C	B	A	7	707	607	571
I		C	B	A	8	698	607	566
I		C	B	A	9	708	617	566
I		C	B	A	10	692	595	566
I		C	B	A	11	690	595	559
I		C	B	A	12	700	603	559
I		C	B	A	13	695	601	559
I		C	B	A	14	696	593	554
I		C	B	A	15	700	599	560
I		C	B	A	16	693	599	564
I		C	B	A	17	700	590	562
I		C	B	A	18	689	582	562
I		C	B	A	19	688	585	563
I		CB		A	20	680	580	568
I		CB		A	21	683	586	566
I		C	B	A	22	674	584	546
I		C	B	A	23	690	583	551
I		C	B	A	24	678	598	545
I		C	B	A	25	676	605	543
I		C	B	A	26	670	607	530
I		C	B	A	27	660	618	523
I		C	B	A	28	659	620	521
I		C	B	A	29	654	625	512
I		C	B	A	30	644	624	507
I		C	BA		31	641	626	507
I		C	BA		32	636	629	498
I		C	B		33	633	630	497
I		C	AB		34	628	638	496
I		C	B		35	627	631	492
I		C	AB		36	621	631	482
I		C	A	H	37	614	627	480
I		C	A	B	38	610	631	473
I		C	A	B	39	613	639	463
I		C	A	B	40	598	638	463
I		C	A	B	41	593	638	452
I		C	A	B	42	593	633	442
I		C	A	B	43	596	631	455
I		C	A	B	44	586	639	440
I		C	A	B	45	594	627	434
I		C	A	B	46	582	627	424
I		C	A	B	47	577	623	426
I		C	A	B	48	571	619	423
I		C	A	B	49	571	618	414
I		C	A	B	50	564	619	419
I		C	A	B	51	562	615	417
I		C	A	B	52	555	616	406
I		C	A	B	53	555	622	410
I		C	A	B	54	540	617	406
I		C	A	B	55	539	608	405
I		C	A	B	56	541	608	399
I		C	A	B	57	540	608	396
I		C	A	B	58	534	611	395
I		C	A	B	59	530	613	400
I		C	A	B	60	523	620	390

Figure 5. Digitalized data

in Figure 4, the signs of τ_{OAB} , τ_{OBC} , and τ_{OCA} are $-$, $-$, and $+$, respectively, that is, θ belongs to the range between $\pi/6$ and $\pi/2$.

(2) In the θ -range obtained above, solve a pair of simultaneous equations, corresponding to Equation 2, that contain any given two τ_0 's, for example, τ_{OAB} and τ_{OBC} ; then the unknown values of θ and u are determined.

Data Processing. Data processing is done as follows: The signals from the three micro-electrodes are first tape-recorded by a data recorder (TEAC R351F) and processed by an analog-to-digital (A-D) converter (FACOM 6382B), and then the cross-correlation function, the angle of flow, and the velocity are calculated by a digital computer (FACOM 270-20). An example

of digitalized data is shown in Figure 5. When an air bubble happened to envelope the micro-cathode and a characteristic square pulse signal was obtained, the digitalized data corresponding to the pulse were replaced by the data of a line connecting the feet of the pulse. In Figure 6 an example of the calculated cross-correlation function is given. For one experimental run, data-acquiring time was 40-70 sec. The frequency of A-D conversion was 1600/3 Hz. The number of data for each calculation were 800, which was determined by the consideration for the statistical errors in the computation of cross-correlation function. Thus the velocity and direction was calculated as an average value for every 1.5 sec ($= 800/533.3$ sec).

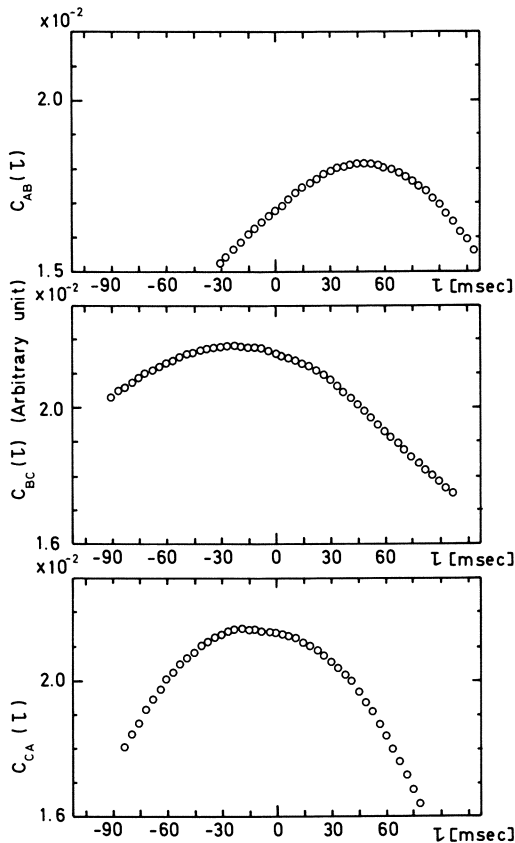


Figure 6. Cross-correlation function

Velocity and Direction of Liquid Phase in Bubble Columns

Experimental. Velocity and direction were measured in two columns, 15 cm in diameter with a single nozzle as a gas distributor in batch operation, and 8 cm in diameter with a perforated-plate gas distributor in continuous operation. The liquid employed was the electrolyte solution described in the previous section. In the continuous operation, the liquid was fed at the bottom and drained at the top of the column. Air was introduced at the bottom. The height of the column was 120 cm, and measurements were done at 90 cm from

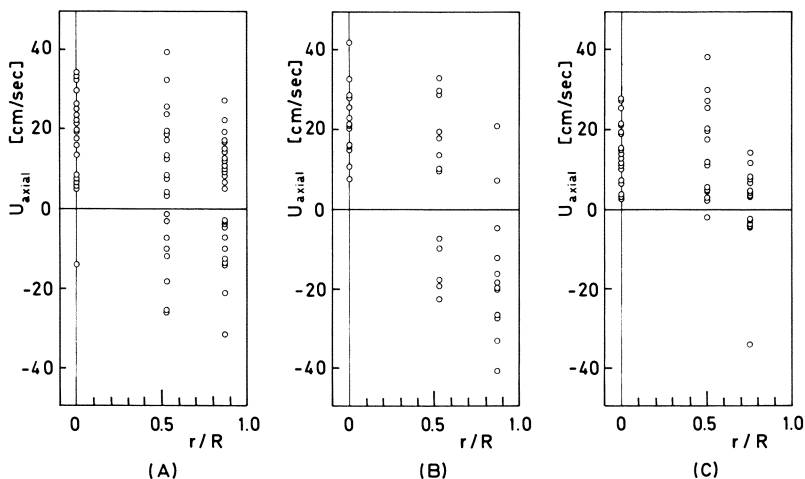


Figure 7. Distribution of the axial velocity component: (A) $u_g = 0.5$ cm/sec, batch; (B) $u_g = 1.5$ cm/sec, batch; (C) $u_g = 1.1$ cm/sec, $u_l = 1.0$ cm/sec

the bottom where there was no end effect of gas distributor and the radial distribution of gas void fraction was fully developed to an equilibrium (8).

The probe was placed so that the triangle of the three microelectrodes was in the plane that contained the axis of the column, and the base of the triangle (the side AB) was perpendicular to the axis. The three rectangular plate anodes were fixed on the wall underneath the liquid surface of the column.

Results. The axial components of the instantaneous velocities for batch systems are shown in Figures 7A and 7B. Here the instantaneous velocity means the value averaged for every 1.5 sec as described in the section on data processing. Since the axial velocities are widely scattered, the liquid flow is complicated. From these figures it is clear that the upward flow is dominant in the central region, while in the neighborhood of the wall the upward flow decreases.

Figure 7C shows the instantaneous axial velocities for continuous systems. Here the liquid flows both upward and downward, and not simply at a uniform superficial liquid velocity as assumed in previous work.

The frequency distributions of flow direction in batch operations are shown in Figures 8 and 10. The flow direction is measured by setting the side AB of the three-electrode triangle ABC horizontally as previously described. The

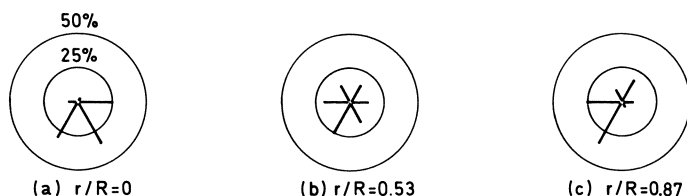


Figure 8. Local frequency distribution of flow direction ($u_g = 0.5$ cm/sec, $D_r = 15$ cm, $L/D_r = 8$, $z = 90$ cm, batch)

angle of flow θ then means that measured counterclockwise from the baseline AB. In these figures the location of bars represents the midpoint of the class interval, the angle of which is chosen as $\pi/3$, and the length of the bars represents the relative frequency—*i.e.*, the ratio of the period that the flow is observed in one of the six ranges in Table I to the data-acquiring time. They are illustrated as if the wall is on the right. Thus, for example, Figure 8a shows that on the axis of the column the ratio of upward flow is 30% (range 5) +

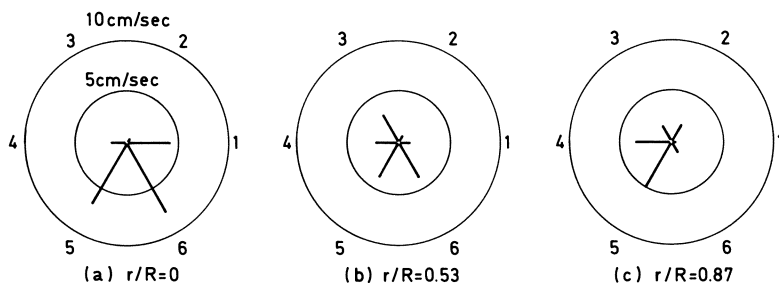


Figure 9. Time-averaged local velocity ($u_0 = 0.5$ cm/sec, $D_T = 15$ cm, $L/D_T = 8$, $z = 90$ cm, batch)

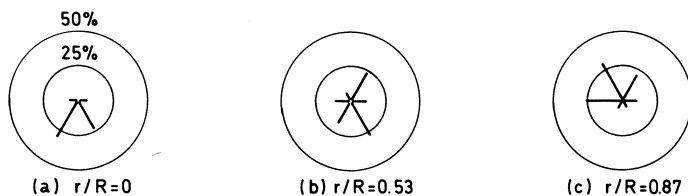


Figure 10. Local frequency distribution of flow direction ($u_0 = 1.5$ cm/sec, $D_T = 15$ cm, $L/D_T = 8$, $z = 90$ cm, batch)

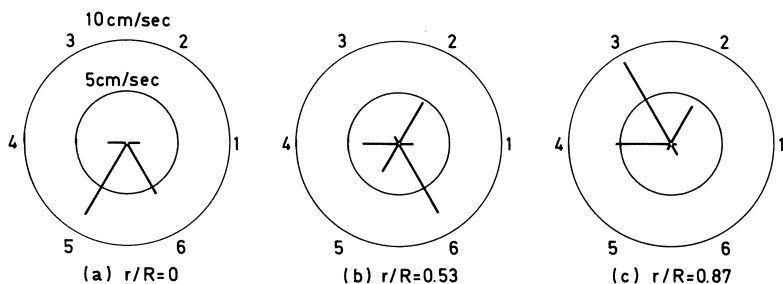


Figure 11. Time-averaged local velocity ($u_0 = 1.5$ cm/sec, $D_T = 15$ cm, $L/D_T = 8$, $z = 90$ cm, batch)

35% (range 6), that of horizontal flow from the right (from the wall) and the left is 25% (range 1) and 8% (range 4), respectively, and that of downward flow is 3% (range 2) + 0% (range 3). The time-averaged velocity, where the averaging time was 40-70 sec, is illustrated in Figures 9 and 11. Again the length of the bars represents the time-averaged velocity, and their location, the midpoint of the class interval.

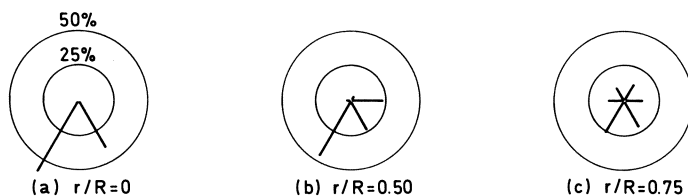


Figure 12. Local frequency distribution of flow direction for continuous system ($u_g = 1.1$ cm/sec, $u_l = 1.0$ cm/sec, $D_r = 8$ cm)

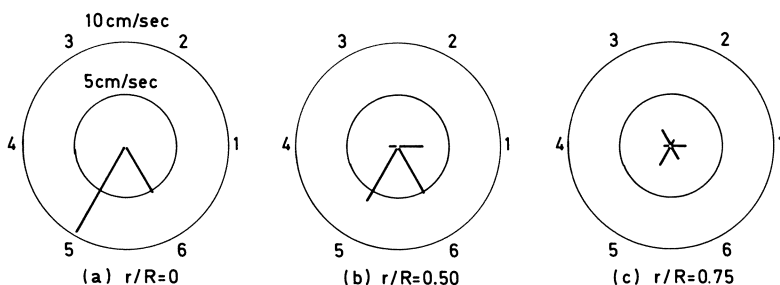


Figure 13. Time-averaged local velocity for continuous system ($u_g = 1.1$ cm/sec, $u_l = 1.0$ cm/sec, $D_r = 8$ cm)

These figures show that the characteristic pattern of liquid flow in batch-type bubble columns is as described below.

In the central part of the column ($r/R = 0$), the liquid flow was mostly upward. Near the wall ($r/R = 0.87$) both downward and upward flows were observed although the ratio of the period of upward flow to the data-acquiring time was less than that in the central core region. At $r/R = 0.53$, an intermediate nature of the above two regions appeared. Further, over the entire cross-section of the column, radial flow was observed in a considerable amount.

In the continuous system in which liquid was fed and drained continuously, the frequency distribution of flow direction and the time-averaged velocity are shown in Figures 12 and 13, respectively. The liquid does not flow uniformly at the superficial liquid velocity, but the flow pattern changes from time to time as in the batch system. In the center of the column only upward flow is observed, but near the wall ($r/R = 0.75$) downward flow exists, and the horizontal flows are observed except at the center.

Discussions

A physical picture of liquid flow in bubble columns may be drawn in the following manner. In contrast to the simple and stable flow patterns proposed by the previous investigators, the liquid flow in bubble columns was demonstrated to be complicated. In both batch and continuous systems, liquid flow is mainly upward in the central part, but in other parts both upward and downward flows are observed, although nearer to the wall the ratio of the

period of downward flow is increased. And radial flow is present across the entire cross-section.

These complicated flow patterns are considered to arise from the pumping effect of the wakes of bubble swarms. The radial distribution of the void fraction is maximum at the axis, where the ratio of the period of the upward flow is also maximum. In the batch system, a certain amount of the liquid is pumped up by the wakes of the bubbles, and the downward flow should result. In the continuous system as well, when the volume of liquid pumped per unit time by the wakes of bubbles is greater than that of liquid fed to the system, downward flow should occur. Thus by the interaction between the upward and downward flows, the radial liquid flow will appear, and the liquid flow pattern will become complicated as observed here. Usually bubble columns are operated under conditions of superficial liquid velocities up to a few centimeters per second. These conditions correspond to the situation described above. Such flows are closely related to the liquid mixing in bubble columns, and evidently they have a significant influence on the concentration distributions of reactants and intermediates, hence on the reaction yield. Finally, difficulties in this approach of measurement are briefly discussed below.

(1) By using the probe developed here, the velocity and direction in the plane that contains the three microelectrodes can be detected. However, if a flow that goes through the plane is present, the velocity calculated will be larger than the true value. A four-microelectrode probe may be used without this defect, but additional precautions will be essential so that the signals will not be disturbed by the stems of the probe. Further studies are necessary on this point.

(2) In this experiment the distance between microelectrodes was fixed at 6 mm. If the distance is too short, the disturbance created by an upstream microelectrode will superimpose on the turbulence originally present in the liquid flow and the disturbance must affect the calculated results. Conversely, if the distance is too large, the correlation of the signals of the two electrodes will disappear. The reason for this is that an eddy, observed at the upstream electrode, does not pass over the downstream one, or the turbulence characteristics change entirely while an eddy is transported to the downstream electrode by the bulk flow. Thus the optimal distance between electrodes depends on the spectrum of scales of eddies and on the speed of decay of eddies in liquid phase. Considering these effects, several kinds of probes that have different micro-electrode distance dimensions were tested. The 6-mm distance was decided to be most suitable.

Conclusions

Velocity and direction was measured with the aid of a newly developed probe, and complicated flow patterns were manifested in contrast with previous investigations that postulate simple and fixed flow patterns.

The liquid flow observed in batch operations and continuous operations at low liquid superficial velocities has such features as: (1) liquid phase is mainly upward in the central core region; (2) in the vicinity of the wall both upward and downward flow is observed although nearer to the wall the ratio of the period of downflow to data-acquiring time is greater; (3) across the entire crosssection radial flow exists. These observations must be taken into account in the prediction of the performance of bubble-column reactors.

Nomenclature

$C_{AB}(\tau), C_{BC}(\tau), C_{CA}(\tau)$	cross-correlation function
D_T	bubble column diameter, cm
L	liquid height, cm
r	radial distance measured from the axis of column, cm
R	bubble column radius, cm
t	time, sec
u	liquid mean velocity, cm/sec
u_g	superficial gas velocity, cm/sec
u_l	superficial liquid velocity, cm/sec
z	distance from gas distributor, cm
$V_A(t), V_B(t)$	velocity fluctuation

Greek Letters

θ	angle (<i>see</i> Figure 4)
τ	time lag, sec

Literature Cited

1. Pavlov, V. P., *Khim. Prom.* (1965) **41**, 698.
2. Yoshitome, H., Shirai, T., *J. Chem. Eng. Japan* (1970) **3**, 29.
3. De Nevers, N., *AIChE J.* (1968) **14**, 222.
4. Kunugita, E., Ikura, M., Otake, T., *J. Chem. Eng. Japan* (1970) **3**, 24.
5. Freedman, W., Davidson, J. F., *Trans. Inst. Chem. Eng. (London)* (1969) **47**, T251.
6. Rietema, K., Ottengraf, S. P. P., *Trans. Inst. Chem. Eng. (London)* (1970) **48**, T54.
7. Miyauchi, T., Shyu, C., *Kagaku Kogaku* (1970) **34**, 958.
8. Kojima, E., Ph.D. Dissertation, Tokyo Institute of Technology, 1973.

RECEIVED January 2, 1974.

Liquid Dispersion, Mass Transport, and Chemical Reaction in Supported Liquid Phase Catalysts for SO₂ Oxidation

HANS LIVBJERG, BENNY SORENSEN, and JOHN VILLADSEN

Instituttet for Kemiteknik, Danmarks tekniske Højskole, Lyngby, Denmark

A mathematical model for liquid dispersion, diffusive mass transport restrictions, and chemical reaction in supported liquid phase catalysts is presented. The liquid phase is assumed to be dispersed by capillary forces, and the length of the liquid phase diffusion path can be obtained from pore structure data for the support. Both liquid phase and gas phase pore diffusion restrictions are important in preparing supported liquid phase catalysts that exhibit the largest possible overall conversion per catalyst volume. Activity was calculated for industrial SO₂ oxidation catalysts. A good estimate of catalyst activity can be obtained from pure liquid catalyst properties.

Supported liquid phase systems (SLP systems) are gas/liquid contact systems where the liquid phase is dispersed in a porous support material. Such systems are effective contactors in mass transfer operation with high diffusion resistance in the liquid phase since the liquid must be highly dispersed to reduce the length of liquid phase diffusion paths. Rony has studied SLP catalysts (1, 2) and proposed a mathematical model to simulate the interior liquid dispersion and diffusion kinetics. He extended Thiele's original single pore model to include the liquid catalyst inside the porous support. The liquid forms a layer at the pore wall or a plug at the bottom of the long single pore. However, the liquid distribution cannot be determined independently, and thus the model cannot be used to predict *a priori* catalyst activity for a given liquid loading and given pore structure.

Recently Abed and Rinker (3) proposed a different model for SLP systems. They consider the liquid phase to be evenly distributed throughout the pellet, and they determined diffusion fluxes through the pellet for different liquid loadings by steady-state counterdiffusion experiments. The diffusion mechanism was analogous to ordinary pore diffusion with an effective diffusivity which was proportional to the square of the residual porosity. The most important feature of their model is that the liquid is assumed to be so finely distributed that local diffusion resistance into the liquid phase from a pore at a given position in the pellet can be neglected. They also allow for enhancement of the effective

diffusivity through liquid diffusion, assumed to be proportional to the square of the liquid loading. Their model and Rony's, with a distinction between liquid in plugs and pore wall adhering liquid, predict an optimal liquid loading.

This paper analyzes industrially important SLP systems where liquid phase diffusion is small enough to invalidate the assumption that local activity is proportional to liquid loading. This system requires a more detailed knowledge of liquid phase distribution to compute the local diffusion path length from the gas phase into the liquid phase. We show that liquid pore size distribution can be estimated if the catalyst pore structure is known; then the influence of liquid loading can be studied. Calculations are presented for an industrial SO_2 oxidation catalyst with a severe liquid phase diffusion restriction.

The catalytic oxidation of SO_2 with a V_2O_5/K_2O catalyst is the most important industrial application of an SLP catalyst. This homogeneous reaction occurs in a melt containing the active catalyst species. The melt is distributed in the pore structure of an inactive support which is usually SiO_2 based (4, 5, 6).

This system was investigated by Kenney and co-workers (5, 6) who studied non-steady-state absorption kinetics of reactants into non-supported catalyst melts of large volume. Boreskov *et al.* (7, 8) measured SO_2 oxidation rates for catalyst melts on porous and non-porous supports. Using catalyst films of different thickness they extended the measurements from the purely kinetic region into the region with severe liquid phase diffusion restriction. They showed that the reaction zone in the pure liquid phase is thin; liquid phase diffusion becomes important in liquid layers > 2000 Å at $485^\circ C$. Thus, a gradientless liquid phase reaction cannot be obtained by macrostirring in a large catalyst volume. The pure kinetics of the homogeneous reaction can only be obtained with experiments on thin liquid films. Gas phase pore diffusion restrictions at industrial reaction conditions are important (9, 10, 11, 12). Kadlec *et al.* (9, 10) calculated optimum catalyst loadings, assuming negligible liquid phase diffusion resistance. Thus the activity of a SO_2 oxidation catalyst is a result of a complicated interaction between homogeneous liquid phase kinetics, liquid phase diffusion, and gas phase pore diffusion that is characteristic for an SLP catalyst.

Distribution of the Liquid Phase in the Pores

Because the pore system used for liquid support in SLP systems (*e.g.*, the SLP catalyst for SO_2 oxidation) is finely dispersed, the forces governing the liquid distribution in the pore system will be surface forces acting at the solid-liquid and gas-liquid interfaces—*i.e.*, capillary, surface tension, and adsorption forces. The influence of gravity on the geometry of the liquid surfaces is negligible. Under the influence of the surface forces the liquid will be distributed so that the thermodynamic free energy of the system attains a minimum. For liquids with contact angle $< 90^\circ$ (*i.e.*, with positive affinity to the solid surface), this implies a tendency to minimize the area of the high energy gas/liquid surface and at the same time maximize the area of the low energy liquid/solid surface. Thus, the liquid is drawn into the smaller pores, and if the liquid loading in the SLP system is increased, larger and larger pores will be filled with liquid. This phenomenon is extensively used to analyze pore structures by measuring capillary condensation of vapors (13). The mobility of the non-volatile liquid phase in an SLP catalyst, which is necessary for redistributing



Figure 1. Liquid contained in smaller pores of support pore system

the liquid in the pores, has been proved by Topsøe and Nielsen (4). They showed that a catalyst melt initially non-uniformly distributed in a support pellet would be uniformly distributed after some time at reaction conditions.

The resulting liquid distribution is shown schematically in Figure 1. The SLP system is divided into two regions. One is the pore system of larger gas-filled pores which will be called the residual pore system. The other is a two-phase area consisting of a solid phase permeated by a pore system of liquid-filled smaller pores—*i.e.*, liquid-filled region (LFR). The geometry of the residual pore system—*i.e.*, pore size distribution and porosity—is important for the rate at which reaction components diffuse through it. The geometry of the liquid-filled region is important in determining the lengths of the liquid phase diffusion paths from the residual pores and into the liquid-filled pores. These geometrical characteristics can be derived from the pore volume distribution of the support.

The pore radius of the largest pores completely filled with liquid is r_f . Thus the total liquid volume equals the pore volume with radii $\leq r_f$ or

$$w_L/\rho_L = \int_0^{r_f} v(r)dr \quad (1)$$

where w_L/ρ_L is the volume of liquid per unit weight support, and $v(r)$ is the density function of the pore volume distribution. For a given liquid loading w_L/ρ_L Equation 1 can be solved iteratively for the corresponding value of r_f . The residual pore system is formed by all pores $> r_f$. Therefore the residual pore volume distribution is defined by:

$$v_{res}(r) = \begin{cases} 0; & r \leq r_f \\ v(r); & r > r_f \end{cases} \quad (2)$$

Figure 2 shows a support pore distribution curve (A) and a corresponding residual pore distribution curve (B) for a given liquid loading.

For Equations 1 and 2 the liquid phase is assumed to be uniformly distributed in the LFR—*i.e.*, the probability for a point in LFR at a given distance l from a residual pore to be in the liquid phase is independent of l . Under certain circumstances, much of the liquid may be concentrated in areas in immediate contact with the residual pores. This is true in general for very low liquid loadings when the liquid presumably is kept in short micropores along

the surface of the residual pore system and for liquid molecules kept in an adsorbed state at the solid surface. Such distribution variations can be accounted for by assuming the existence of a liquid layer of thickness t at the pore walls of all residual pores as a model perturbation to Equations 1 and 2.

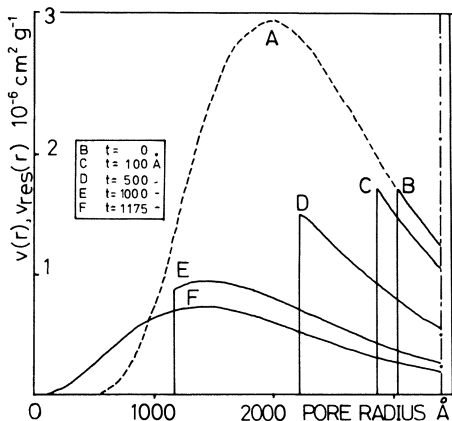


Figure 2. Support pore distribution (curve A) (with mean pore radius $r_m = 2500$ Å and variance $\beta_r = 0.3$ for $\ln r$) and residual pore distributions for 75% liquid loading. Curve B corresponds to Equations 1 and 2, curves C–F correspond to Equations 3 and 4.

If part of the liquid is enclosed in pores with radii $\leq r_t$ and the rest is in a layer of thickness t at the walls of pores with radii $> r_t$, the formula corresponding to Equation 1 becomes

$$w_L/\rho_L = \int_0^{r_t} v(r)dr + \int_{r_t}^{\infty} \left[1 - \left(\frac{r-t}{r} \right)^2 \right] v(r)dr \quad (3)$$

assuming non-intersecting cylindrical pores. For a given liquid loading and liquid layer thickness t , Equation 3 can be solved iteratively for r_t . The corresponding residual pore distribution is defined by:

$$v_{res}(r) = \begin{cases} 0; & r \leq r_t - t \\ \left(\frac{r}{r+t} \right)^2 v(r+t); & r > r_t - t \end{cases} \quad (4)$$

Figure 2 shows a family of residual pore distribution curves generated by Equations 3 and 4 for different values of t . Curve F corresponds to the highest t that is possible for the given liquid loading. This curve is constructed by substituting $r_t = t$ in Equations 3 and 4. The corresponding liquid distribution represents an extreme type compared with that defined by Equations 1 and 2 in that as much as possible of the liquid is distributed as a homogeneous layer at the pore walls of the residual pore system. When r_t has been computed by Equations 1 or 3, the following geometrical properties of the LFR become available. The pore volume of the LFR—*i.e.*, the total volume of liquid filled pores, is

$$V_{pt} = \int_0^{r_t} v(r)dr \quad (5)$$

and the total volume of the LFR per unit weight support:

$$V_t = \frac{1}{\rho_s} + V_{pt} \quad (6)$$

where ρ_s is the true density of the solid phase. The porosity of the LFR is defined by:

$$\theta_t = \frac{V_{pf}}{V_t} \quad (7)$$

The "external" surface area of the LFR S_t —i.e., the area exposed by the LFR to the residual pores (or a liquid layer, if any)—equals the surface area of support pores $> r_t$. Thus for non-intersecting cylindrical pores:

$$S_t = \int_{r_t}^{\infty} \frac{2}{r} v(r) dr \quad (8)$$

where $2/r$ is the surface to volume ratio for infinitely long cylinders. If S_t and V_t are known, one can compute the average diffusion length δ_t in the LFR which equals the volume to surface ratio:

$$\delta_t = \frac{V_t}{S_t} \quad (9)$$

Further geometrical characteristics for the LFR are developed below.

Catalytic Reaction and Diffusion in the Liquid Phase

The liquid-filled region of the catalyst is considered a homogeneous phase. Diffusion occurs in all directions, and reaction occurs at every point. The reaction rate and diffusivity are, of course, smaller than in a pure liquid phase since part of the total volume of the region is taken up by the solid. This is our basic assumption of a uniformly distributed liquid phase in the LFR, and it agrees with generally accepted pseudo-homogeneous models for diffusion and chemical reaction in porous bodies (e.g., Ref. 14, chap. 4 for further details).

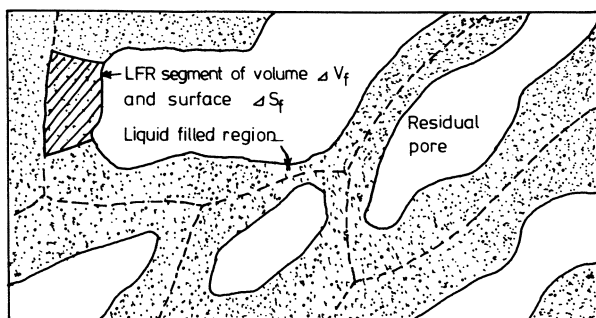


Figure 3. Homogeneous model of the liquid-filled region

The effective diffusivity in the LFR is derived from the pure liquid phase diffusivity D_{iL} by

$$D_{iL} = \frac{D_{iL} \theta_t}{\tau_t} \quad (10)$$

where τ_t is the tortuosity factor for the LFR.

Figure 3 is an enlarged view of the pore structure in which the heterogeneity of the LFR is neglected. Because of the high gas phase diffusion rate,

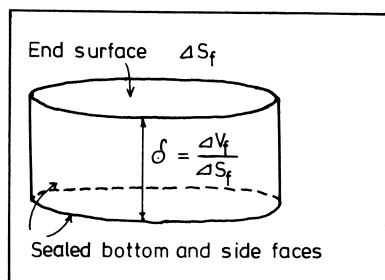


Figure 4. Idealized geometrical model of LFR segment of Figure 3 for calculating η

the gas phase concentration is constant for the small pore structure section shown. Thus, the liquid phase concentration at the gas/liquid interface is also constant. Inside the LFR the concentration of reactants decreases to a minimum at positions farthest away from neighboring residual pores. The main direction for diffusion of reactants in the LFR is from the residual pore walls towards the imaginary dividing lines between neighboring pores (broken lines in Figure 3). Therefore it is possible to divide the LFR into imaginary segments for which the mass transport is essentially one dimensional—*i.e.*, with no transport across the side and bottom faces (Figures 3 and 4). For each segment the continuity equation for diffusion and reaction can be solved for the simple boundary conditions of the idealized segment geometry shown in Figure 4. Each segment is characterized by its volume ΔV_f , its surface to residual pores ΔS_f , and the corresponding equivalent segment thickness $\delta = \Delta V_f / \Delta S_f$.

For a real SLP system, δ varies within a certain range. This variation is accounted for by a distribution density function $\Omega(\delta)$. Ω is defined so that $\Omega d(\delta)$ is the total surface area exposed to residual pores per unit weight support by segments with thickness between δ and $\delta + d(\delta)$. Further properties of Ω are given in Equations 24–26.

The contribution to the local reaction rate per unit volume of support of such segments is equal to

$$dv = \rho_p \theta_l v' \eta \delta \Omega d(\delta) \quad (11)$$

where v' is the reaction rate in the absence of liquid phase diffusion restriction in a unit volume of pure liquid, η is the effectiveness factor for a segment with thickness δ and exposed to the gas phase at the unsealed surface. The observed local reaction rate in the LFR per unit volume of support is obtained by integrating Equation 11:

$$v = \rho_p \theta_l v' \int_0^{\infty} \eta \delta \Omega d(\delta) \quad (12)$$

With few exceptions all currently used rate equations for SO_2 oxidation on a vanadium catalyst are of the form of Equation 13. We will use this form for the pure liquid phase kinetics with the rate constant k of Equation 15 from rate measurements unaffected by diffusion.

$$v'_B = \kappa (P_B - \zeta) \quad (13)$$

with

$$\zeta = \left[\frac{P_C}{K_p P_A} \right]^2 \quad (14)$$

and

$$\kappa = \kappa(P_A, P_C, T) \quad (12).$$

P_A , P_B , and P_C are partial pressures of SO_2 , O_2 , and SO_3 ; K_p is the gas phase equilibrium constant for the reaction $\text{SO}_2 + \frac{1}{2}\text{O}_2 \rightleftharpoons \text{SO}_3$; v'_B is the oxygen rate of consumption in the absence of transport resistance.

Here the rate equation of Boreskov (15) will be used:

$$\kappa = k \frac{P_A}{P_A + 0.8 P_C} \quad (15)$$

For SO_2 oxidation in deep catalyst melts it has been suggested that the reaction rate is controlled by liquid phase diffusion of oxygen because of extremely low oxygen solubility in the salt melt (7, 8). In that case the liquid concentration of SO_2 and SO_3 can be considered constant for constant gas phase concentration. Hence the local liquid phase reaction rate as a function of the liquid phase oxygen concentration C_B is

$$v'_B = \kappa (h_B C_B - \zeta) \quad (16)$$

where h_B is a Henry's law constant for dissolved oxygen in the catalyst melt.

The one-dimensional continuity equation for diffusion and chemical reaction in the segment in Figure 4 is thus:

$$D_{BL} \frac{d^2 C_B}{dl^2} = \theta_l \kappa (h_B C_B - \zeta) \quad (17)$$

with boundary conditions:

$$C_B = P_B/h_B \quad \text{for } l = 0$$

and

$$dC_B/dl = 0 \quad \text{for } l = \delta$$

θ_l = volume liquid/volume LFR = LFR porosity.

Solution of Equations 17 and 18 yield, in terms of the liquid phase effectiveness factor η :

$$\eta = \frac{\tanh \Phi_0}{\Phi_0} \quad (19)$$

The Thiele modulus Φ_0 is

$$\Phi_0 = \delta \sqrt{\frac{\theta_l \kappa h_B}{D_{BL}}} = \delta \sqrt{\frac{\kappa}{\Delta_B}} \quad (20)$$

with

$$\Delta_B = \frac{D_{BL}}{h_B \tau_l} \quad (21)$$

in which Equation 10 has been substituted for the effective oxygen diffusivity in the LFR.

The only data available to estimate the pure liquid kinetics and transport parameters of Equations 19, 20, and 21 seem to be the measurements by Boreskov and co-workers (7, 8). They used a potassium promoted catalyst

with potassium/vanadium mole ratio of 3.5. From their data at 485°C one can extract the following:

$$k = 4.3 \times 10^{-4} \text{ mole/atm/sec/cm}^3 \quad (22)$$

for the rate constant of Equation 15 and

$$\frac{D_{BL}}{h_B} = 2 \times 10^{-13} \text{ mole/atm/sec/cm} \quad (23)$$

An independent estimation of D_{BL} and h_B is not possible from Refs. 7 and 8, but the ratio between these quantities is sufficient in Equation 21.

The main parameters of the distribution function Ω for the LFR thickness δ can be derived in terms of previously calculated properties of the support structure. From the definition of Ω the zero'th moment of Ω is equal to the total surface of residual pores:

$$\int_0^\infty \Omega d(\delta) = S_f \text{ (of Equation 8)} \quad (24)$$

The first moment is equal to the LFR volume:

$$\int_0^\infty \delta \Omega d(\delta) = V_f \text{ (of Equation 6)} \quad (25)$$

Hence from Equation 9 the median of Ω is δ_r . If Ω is assumed to be a Dirac delta function, all segments are of thickness δ_r . That is identical to using the particle shape factor of Aris (16) to compensate for the geometrical irregularity of the LFR in computing η . The model can be refined further by using finite Ω functions. In this work a log normal distribution (Ref. 17, Chap. 2) was arbitrarily assumed—*i.e.*

$$\Omega = \frac{S_f}{\sqrt{2\pi} \beta \delta} \exp \left[- \frac{\left(\ln \left(\frac{\delta}{\delta_r} \right) + \frac{\beta^2}{2} \right)^2}{2\beta^2} \right] \quad (26)$$

β^2 is the variance of $\ln(\delta)$, and at present it must be arbitrarily assumed. However, within reasonable limits, its value is not of decisive importance (*see* Figure 10).

Finally one important consequence of a pseudo-homogeneous model approximation for the LFR must be noted. The pore size of the liquid-filled pores in the LFR cannot generally be assumed to be small compared with δ . This gives rise to an uncertainty by assigning a value to τ_f in Equations 10 and 21. We used a value of 2 which is between the theoretical value of 3 for random diffusion in small pores and 1 for diffusion directly into larger pools of liquid. τ_f can therefore be expected to change with pore structure and liquid loading. However, the variation of δ which follows from changes in pore structure and liquid loading is much larger than the limited variation of τ_f (Figure 11). Furthermore, changes in τ_f only affect the activity through the square-root dependence of Equations 19, 20, and 21.

Macroscopic Continuity Equations

The liquid phase diffusion resistance was assumed to be significant for at least one of the reactants even on the microscopic scale shown in Figure 3. For such species it is reasonable to assume that diffusion through the residual

pore system will be similar to diffusion in ordinary porous solids without embedded liquid. Hence one can use ordinary pore diffusion models. This assumption is supported by experimental evidence for the industrial SO_2 oxidation catalysts (11, 12).

For any single reaction scheme

$$\sum_{i=1}^s \nu_i A_i = 0 \quad (27)$$

the continuity equation for component A_i in a porous catalyst yields (14):

$$D_i C_T \nabla^2 Y_i = - \nu_i v \quad (28)$$

where D_i is the effective diffusion coefficient for component A_i , Y_i is the mole fraction of A_i in the residual pores, and $-\nu_i v$ is the production rate of A_i per unit pellet volume.

Substituting Equation 12 into the right hand side of Equation 28, the corresponding continuity equation for an SLP catalyst is obtained:

$$D_i C_T \nabla^2 Y_i = - \nu_i \rho_p \theta_l v' \int_0^\infty \eta \delta \Omega d(\delta); \quad i = 1, \dots, s \quad (29)$$

with boundary conditions:

$$Y_i = Y_{i0} \text{ at the external pellet surface.}$$

Note that v' is the liquid phase reaction rate without diffusion restriction for the gas phase concentration Y_i .

The assumption of a small liquid phase diffusivity for at least one component used in deriving Equation 12 leads to a decoupling of the microscopic liquid phase diffusion and the macroscopic pore diffusion and results in the simple form of Equation 29 for the macroscopic continuity equation. The decoupling is not necessarily violated even in the unlikely situation where liquid phase diffusion for some components contributes significantly to the macroscopic diffusion rate. However, for such components the effective diffusivity cannot be estimated from ordinary pore diffusion models.

To characterize the mass transport efficiency of SLP catalysts three different effectiveness factors are defined besides the effectiveness factor $\eta(\delta)$ for diffusion in an LFR segment used in Equation 29.

(Normal) Pore Diffusion Effectiveness Factor η_n . η_n is defined in the usual way for porous catalysts as the ratio of the observed reaction rate to the rate which would have been observed in the absence of pore diffusion resistance:

$$\eta_n = \frac{\iiint_{\text{pellet volume}} [\rho_p \theta_l v' \int_0^\infty \eta \delta \Omega d(\delta)] dV_s}{V_s \rho_p \theta_l v_o' \left[\int_0^\infty \eta \delta \Omega d(\delta) \right]_o} \quad (30)$$

where V_s is the support pellet volume and subscript o refers to conditions at the external support pellet surface.

Local Average Liquid Effectiveness Factor η_l . η_l is the ratio of the actual local reaction rate to the rate that would have been observed with negligible liquid phase diffusion restriction. The volumetric average of η at a given

position in the pellet is obtained using Equation 25:

$$\eta_i = \frac{1}{V_f} \int_0^\infty \eta \delta \Omega d(\delta) \quad (31)$$

Overall Effectiveness Factor η_0 . η_0 is the ratio of the observed reaction rate to the rate that would have been observed if the whole pellet volume were replaced by a pure liquid phase with negligible diffusion resistance. η_0 is most conveniently computed by

$$\eta_0 = \eta_a \eta_{i0} \theta_f (1 - \theta_{res}) \quad (32)$$

where η_{i0} is η_i at the external pellet surface. η_0 is a convenient measure of the effect of changes in pore structure, liquid loading, pellet size, etc. for a liquid catalyst with constant activity.

Results for SO_2 Oxidation

If the liquid phase reaction rate for SO_2 oxidation derived in Equations 13–21 is substituted into Equation 29 with SO_2 as the key component, one obtains (after manipulation):

$$D_A C_T \nabla^2 Y_A = 2 \rho_p \theta_f \Delta_B^{1/2} \kappa^{1/2} P_T (Y_B - \zeta/P_T) \int_0^\infty \tanh \left[\delta \sqrt{\frac{\kappa}{\Delta_B}} \right] \Omega d(\delta) \quad (33)$$

Concentrations of O_2 (Y_B) and SO_3 (Y_C) are obtainable (14) as linear functions of the SO_2 concentration Y_A . κ , ζ , and Y_B of Equation 33 can thereby be transformed into functions of the single variable Y_A .

For a spherical support pellet with radius R_0 a dimensionless form of Equation 33 is finally obtained:

$$\frac{1}{x^2} \frac{d}{dx} \left(x^2 \frac{dy}{dx} \right) - \Psi v u \int_0^\infty \tanh (v \Phi z) \omega dz = 0 \quad (34)$$

with

$$y = 1 \text{ for } x = 1 \text{ and } y' = 0 \text{ for } x = 0$$

The dimensionless variables x , y , and z , the dimensionless parameters Ψ and Φ , and the dimensionless functions $v(y)$, $u(y)$, and $\omega(z)$ are defined in Table I.

For the effectiveness factors η_a and η_i Equations 30 and 31 yield

$$\eta_a = \frac{3 \int_0^1 [x^2 v u \int_0^\infty \tanh (v \Phi z) \omega dz] dx}{v_0 u_0 \int_0^\infty \tanh (v_0 \Phi z) \omega dz} \quad (35)$$

and

$$\eta_i = \frac{1}{\Phi v} \int_0^\infty \tanh (v \Phi z) \omega dz \quad (36)$$

The effective diffusion coefficients for SO_2 , O_2 , and SO_3 , D_A , D_B , and D_C were calculated by the pore diffusion model of Johnson and Stewart (18). For diluted diffusing species or equimolar diffusion one obtains:

$$D_i = \frac{1}{\tau_r} \int_0^\infty (D_{iG}^{-1} + D_{iK}^{-1})^{-1} \rho_p v_{res} dr \quad (37)$$

\mathcal{D}_{iG} is the bulk gas phase diffusion coefficient of i , \mathcal{D}_{iK} the Knudsen diffusion coefficient for pore size r . τ_r is the tortuosity factor for which a value of 3 has been assumed (12, 18). The data used for this system are described in more detail in Ref. 12.

The physical parameters required to solve Equation 34 are divided into four groups:

(1) Support properties include pellet radius R_o , apparent density ρ_p , and pore volume distribution $v(r)$ for unimpregnated support. For a narrow pore size distribution, porosity and mean pore size may be sufficient to define $v(r)$. Commercial SO_2 catalysts are often well described by a log-normal distribution which is completely defined by mean pore radius r_m , support porosity θ_p , and variance β_r for $\ln r$ (cf. Figure 2, curve A).

(2) Liquid distribution properties δ_f , θ_f , S_f , and $v_{res}(r)$ are obtained from Equations 1-9 using the support properties and liquid loading w_L/ρ_L . In our calculations the distribution model (Equations 1 and 2) has been used with no liquid layer at the pore walls. The log-normal Ω distribution Equation 26 (given in a dimensionless form ω in Equation 34) contains one arbitrary parameter β —the variance of the distribution—but numerical calculations with $0 \leq \beta \leq 1$ show that this parameter has only a small influence on the results even for broad liquid distributions ($\beta = 1$).

Table I. Dimensionless Variables, Parameters, and Functions of Equations 34-36

Variables

$$x = R/R_o; y = Y_A/Y_{AO}; z = \delta/\delta_f$$

Parameters

$$\Phi = \delta_f \sqrt{\frac{k}{\Delta_B}}$$

$$\Psi^* = \frac{2R_o^2 \rho_p \theta_f \sqrt{k \Delta_B} S_f R_g T}{D_A} = \frac{2R_o^2 \rho_p \theta_f k P_T S_f \delta_f}{C_T D_A \Phi}$$

Functions

$$u = \left\{ \frac{Y_B}{Y_{AO}} - \left[\frac{Y_C}{K_p Y_A} \right]^2 \times \frac{1}{P_T Y_{AO}} \right\}$$

$$= \alpha_1 + \alpha_2 y - \alpha_3 (v(y))^2$$

with

$$v(y) = \frac{Y_C}{Y_A} = -\alpha_4 + \alpha_5 y^{-1}$$

$$\alpha_1 = \frac{Y_{B0}}{Y_{AO}} - \alpha_2; \alpha_2 = \frac{1}{2} \frac{D_A}{D_B}; \alpha_3 = \frac{1}{K_p^2 P_T Y_{AO}}$$

$$\alpha_4 = \frac{D_A}{D_C}; \alpha_5 = \frac{Y_{C0}}{Y_{AO}} + \alpha_4$$

$$v = \sqrt{\frac{\kappa}{k}} = (1 + 0.8 v(y))^{-1/2}$$

$$\omega = \frac{\delta_f}{S_f} \Omega = \frac{1}{\sqrt{2\pi\beta z}} \exp \left\{ \frac{-\left[\ln z + \frac{\beta^2}{2} \right]^2}{2\beta^2} \right\}$$

(3) Liquid catalyst properties include liquid phase rate constant k and diffusivity D_{BL}/h_B which must be determined from independent measurements. We have used Boreskov's data for Equations 22–23. The dimensionless rate functions u and v of Equation 34 and Table I are derived from liquid phase kinetics (in our case from Equations 13–15).

(4) Effective gas phase diffusivities D_A , D_B , D_C are taken from Equation 37.

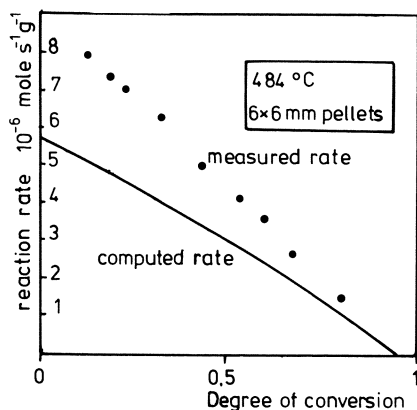


Figure 5. Simulation of experimental data from Ref. 12. Reactor inlet: 11% O₂, 7% SO₂. Support pore structure: $r_m = 2500 \text{ \AA}$, $\beta_r = 0.4$, $\beta = 0.3$, liquid loading = 50% of pore volume.

Equation 34 can now be solved numerically. We used orthogonal collocation (19, 20): The integral in Equation 34 contains the dependent variable y in the non-linear function v , and at each of N collocation point x_i the integral is expressed by quadrature as a weighted sum of $v(y_j)$. Finally u is taken as $u(y_i)$ in each collocation equation, and the total set of N non-linear algebraic equations is solved by Newton-Raphsons method.

As a primary test of the model, experimental rate data from Ref. 12 were simulated. The measurements were obtained with a Haldor Topsøe VK38A catalyst as 6.6-mm cylindrical pellets, and the temperature was the same as in the pure liquid measurements of Boreskov *et al.* The support pore distribution was not available but was estimated from a knowledge of catalyst composition and residual pore data obtained at room temperature of Ref. 12.

The results in Figure 5 show reasonably good agreement between predicted and measured reaction rate. The agreement is better than expected in view of the difference in the catalyst compositions used in Refs. 8 and 12 and the experimental uncertainty involved in determining pure catalyst data for the extremely thin catalyst films used in Ref. 8.

Figure 6 shows some predictions of the effect of changing support pore size and liquid loading. All computations are for reaction conditions identical to those of Ref. 8—*i.e.*, 485°C and a conversion 20% below equilibrium for a reactor inlet of 11% oxygen and 7.5% sulfur dioxide. Hence the overall effectiveness factor η_0 in Equation 32 used as the ordinate in Figure 6 is a direct measure of the catalytic activity for an SLP catalyst at these conditions.

The existence of an optimal liquid loading for given pore structure on Figure 6 is similar to the effect studied by Rony (2) and is explained by the gradual disappearance of the residual pore system at high liquid loading.

The existence of an optimal pore size in Figure 6 is an important consequence of the liquid distribution model. Poor liquid dispersion (large δ) and

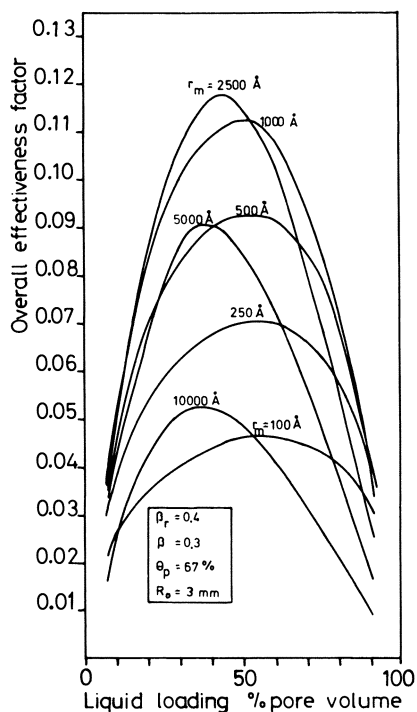


Figure 6. Catalyst activity for different support pore sizes and liquid loadings

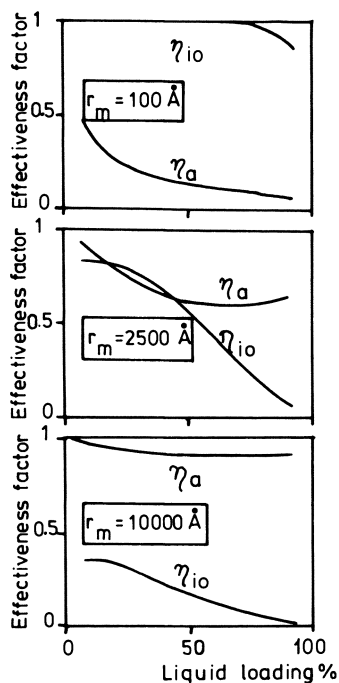


Figure 7. Pore diffusion controlled reaction for small support pores of Figure 6

Figure 8. Reaction controlled by both liquid phase- and gas phase diffusion for intermediate support pores of Figure 6

Figure 9. Liquid phase diffusion controlled reaction for large support pores of Figure 6

low catalyst activity result from a large mean pore size. Below a given pore size, however, any further reduction of pore size to increase the local liquid effectiveness factor is overcompensated by increasing Knudsen pore diffusion restriction. Hence activity should be lower for very large and very small pore sizes. In Figures 7–9 with three mean pore sizes from Figure 6 the shift from pore diffusion controlled reaction to liquid phase diffusion controlled reaction is illustrated by the variation of the pore diffusion effectiveness factor η_a and the local liquid effectiveness factor at the pellet surface η_{i0} .

For the “optimal” liquid loading and pore size (Figure 8) the diffusion resistance is almost evenly divided between liquid phase diffusion and pore diffusion. Hence the necessity of including both factors in the SLP model is accentuated. Also the “optimal” pore size of 2500 Å and liquid loading of

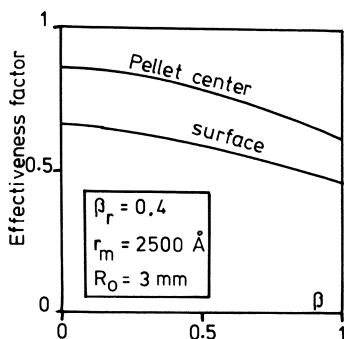


Figure 10. Local liquid effectiveness factor as a function of β

$\sim 50\%$ for a support porosity of 66% closely resembles a typical industrial catalyst with 7–9 wt % vanadium, a potassium/vanadium mole ratio of 2.5–4, and a mean pore size of 1000–4000 Å.

Figure 10 shows the effect of using different values of β in the density function Ω Equation 26 for a liquid loading of 0.3 and an average support pore size of 2500 Å. Increasing β decreases the local liquid effectiveness factor η_i since the broader distribution of δ contains more liquid volume in ineffective large δ segments even though δ_r is the same. The difference between surface η_i (η_{i0}) and center η_i is the result of the non-linear form of the rate expression (Equation 15).

Figure 11 shows the variation of δ_r for some of the liquid distributions used in the computation of Figure 6. The figure clearly illustrates the pronounced effect of pore structure and liquid loading on the liquid diffusion path lengths.

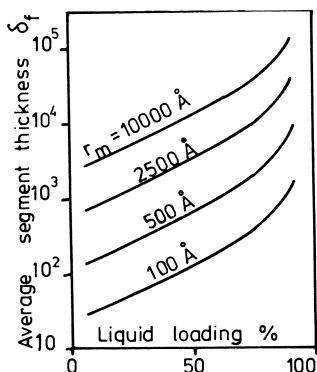


Figure 11. Variation of liquid diffusion path length with mean pore size and liquid loading for the support pore size distributions used in Figure 6

Conclusion

Liquid and gas phase diffusivity are important factors in manufacturing high activity SLP catalysts, and they are both determined by the support material properties. Thus, the search for optimal support pore structure must be done in parallel with basic research on the active catalyst components to obtain the best catalyst formulation. The model presented here is qualitatively correct, and it allows one to predict liquid distribution and catalyst pellet performance using fundamental, measurable properties such as the support pore structure, liquid diffusivities, and the true kinetics of the homogeneous liquid phase reaction.

Interesting results are obtained even at this stage. The catalyst pellet activity has a pronounced maximum for a certain liquid loading and for a certain mean pore size. The overall maximum for SO_2 oxidation is found for a mean pore size ($\sim 3000 \text{ \AA}$) and catalyst load ($\sim 30\%$ of pellet volume) which corresponds to values for commercial catalyst pellets.

Although this correspondence reinforces the credibility of the model, much experimental research remains before SLP catalyst formulation is as sophisticated as is the case for typical solid-gas catalysts.

Liquid diffusivity combined with chemical reaction for very thin catalyst films is the principal object for investigation. This is being done at our institute using measurements of the heat of reaction for 100–50,000 \AA films in a micro-calorimeter to obtain the detailed kinetics of the SO_2 oxidation.

Nomenclature

A_i	reaction component
C_B	liquid phase concentration of oxygen, moles/cm ³
C_T	total concentration in residual pores, moles/cm ³
D_i, D_A, D_B, D_C	effective pore diffusion coefficients, cm ² /sec
D_{iL}, \bar{D}_{BL}	effective diffusion coefficients in the liquid filled region, cm ² /sec
D_{iL}, \bar{D}_{BL}	pure liquid phase diffusivity, cm ² /sec
D_{iG}	gas phase bulk diffusivity, cm ² /sec
D_{iK}	Knudsen pore diffusivity, cm ² /sec
h_B	Henry's law constant for oxygen, atm cm ³ /mole
k	rate constant, <i>see</i> Equation 22
K_p	gas phase equilibrium constant, atm ^{-1/2}
l	distance from surface of LFR segment, cm
P_A, P_B, P_C	partial pressures, atm
P_T	total pressure, atm
r	pore radius, cm
r_f	largest support pores filled with liquid, cm
r_m	mean pore size for support, cm
R, R_0	radial coordinate in a sphere, cm
s	number of reaction components
S_f	surface area of LFR per gram support, cm ² /gram
T	temperature, °K
t	liquid layer thickness, cm
u	dimensionless function of Table I
$v(r)$	density function of support pore distribution, cm ² /(grams support)
$v_{\text{res}}(r)$	density function of residual pore distribution, cm ² /(grams support)
v	dimensionless function of Table I

v	reaction rate per unit support volume, moles/cm ³ /sec
v', v'_B	reaction rate per unit liquid volume, moles/sec/cm ³
V_f	volume of LFR per gram support, cm ³ /gram
V_{pf}	pore volume of LFR per gram support, cm ³ /gram
V_s	support pellet volume, cm ³
w_L	weight of liquid per gram support
x	dimensionless variable of Table I
y	dimensionless variable of Table I
Y_A, Y_B, Y_C	mole fraction for SO ₂ , O ₂ , and SO ₃
Y_{AO}, Y_{BO}, Y_{CO}	mole fraction at external pellet surface
z	dimensionless variable of Table I

Greek Letters

β	parameter of distribution function Ω (Equation 26)
β_r	square root of variance of $\ln r$ for support pore distribution
δ	LFR segment thickness, cm
δ_f	average segment thickness, cm
Δ_B	diffusion parameter defined by Equation 21, mole/atm/sec/cm
ζ	reaction rate function defined in Equation 14, atm
η	effectiveness factor for LFR segment
η_a, η_i, η_o	effectiveness factors defined in Equations 30, 31, 32
θ_{res}	residual porosity
θ_p	support porosity
θ_f	porosity of LFR
κ	rate function defined in Equation 15, moles/atm/sec/cm ³
ν_i	stoichiometric coefficient
ρ_L	density of liquid phase, grams/cm ³
ρ_s	density of solid phase, grams/cm ³
ρ_p	apparent density of support, grams/cm ³
τ_f	tortuosity factor for the LFR
τ_r	tortuosity factor for pore diffusion
Φ_o	Thiele modulus defined in Equation 20
Φ	Thiele modulus defined in Table I
Ψ	dimensionless parameter defined in Table I
Ω	density function for distribution of LFR segment surfaces defined in Equation 26, cm/gram
ω	dimensionless Ω function defined in Table I

Literature Cited

1. Rony, P. R., *Chem. Eng. Sci.* (1968) **23**, 1021.
2. Rony, P. R., *J. Catalysis* (1969) **14**, 142.
3. Abed, R., Rinker, R. G., *J. Catalysis* (1973) **31**, 119.
4. Topsøe, H., Nielsen, A., *Trans. Danish Acad. Tech. Sci.* (1948) **1**, 1.
5. Glueck, A. R., Kenney, C. N., *Chem. Eng. Sci.* (1968) **23**, 1257.
6. Holroyd, F. P. B., Kenney, C. N., *Chem. Eng. Sci.* (1971) **26**, 1963.
7. Polyakova, G. M., Borekov, G. K., Ivanov, A. A., Davydova, L. P., Marochkina, G. A., *Kinet. Katal. (USSR)* (1971) **12** (3) 666 (Eng. transl.).
8. Borekov, G. K., Dzis'ko, V. A., Tarasova, D. V., Balaganskaya, G. P., *Kinet. Katal. (USSR)* (1970) **11** (1) 181 (Eng. transl.).
9. Kadlec, B., Hudgins, R. R., Silveston, P. L., *Chem. Eng. Sci.* (1973) **28**, 935.
10. Kadlec, B., *IV CHISA Congr., Prague, 1972*, Paper No. J 2.2.
11. Kadlec, B., Michalek, J., Šimeček, A., *Chem. Eng. Sci.* (1970) **25**, 319.
12. Livbjerg, H., Villadsen, J., *Chem. Eng. Sci.* (1972) **27**, 21.
13. Gregg, S. J., Sing, K. S. W., "Adsorption, Surface Area and Porosity," Academic, New York, 1967.
14. Petersen, E. E., "Chemical Reaction Analysis," Prentice-Hall, Englewood Cliffs,

- 1965.
15. Ivanov, A. A., Boreskov, G. K., Buyanov, R. A., Polyakova, G. P., Davydova, L. P., Kochkina, L. D., *Kinet. Katal. (USSR)* (1968) **9** (3) 463 (Eng. transl.).
 16. Aris, R., *Chem. Eng. Sci.* (1957) **6**, 262.
 17. Himmelblau, D. M., "Process Analysis by Statistical Methods," Wiley, New York, 1970.
 18. Johnson, M. F. L., Stewart, W. E., *J. Catalysis* (1965) **4**, 248.
 19. Villadsen, J., Stewart, W. E., *Chem. Eng. Sci.* (1967) **22**, 1483.
 20. Villadsen, J., "Selected Approximation Methods for Chemical Engineering Problems," Danmarks Tekniske Højskole, 1970.

RECEIVED January 2, 1974.

Mass Transfer Characteristics of Stacked Metal Screens

MAROOF A. SHAH¹ and DONALD ROBERTS

Department of Chemical Engineering, University of Birmingham,
Birmingham B15 2TT, England

The continuous heterogeneous decomposition of hydrogen peroxide vapor on a variety of stacked platinum or silver wire screens was studied at 190°–340°C using nitrogen as a diluent gas. The 40-fold range of Reynolds numbers used encompassed those of interest in commercial high pressure NH₃ oxidation. The existence of mass transfer control enabled mass transfer coefficients to be determined. The wire diameter and fractional opening or porosity of a typical screen were the most significant screen properties affecting mass transfer behavior; the data were correlated accordingly and agreed well with most of that obtained for mass transfer to screens by other workers. The data also agreed with the accepted heat transfer correlation for a single cylinder. Satisfactory agreement with published work on the rate of NH₃ oxidation was demonstrated.

The heat or mass transfer from fluids to woven metal screens has been studied over a wide range of flow velocities and screen characteristics. Direct measurements of mass transfer rates with gases, suitable for use in estimating the platinum catalyst screen requirement of an ammonia oxidation reactor, have until recently been inadequate. A study by Satterfield and Cortez (1), at low Reynolds numbers, and the present study, at higher Reynolds numbers, satisfied this need.

Unlike flow through simple geometries, flow through stacked screens does not lend itself to thorough mathematical analysis—a difficulty which is reflected in the varying correlation methods used by different workers resulting from differing conceptual models of the system: a porous bed or an array of cylinders. This inevitably has led to differing definitions of dimensionless parameters used in the correlations, especially Reynolds numbers. Anomalies in correlating transfer characteristics of geometrically dissimilar screens have been reported, but more seriously, differences in the magnitudes of transfer coefficients and their variation with flow velocity for similar screen geometries also exist in earlier work. These problems have been discussed extensively by Satterfield and Cortez (1).

¹ Present address: Gases Engineering, British Oxygen Co. Ltd., Deer Park Road, London S.W.19, England.

The reported anomalies and differences arise from an unsuitable choice of dimensionless parameters or from difficulties inherent in the techniques used by previous investigators. Gay and Maughan (2) pointed out that discrepancies between their mass transfer measurements and the heat transfer data of Coppage and London (3) might arise from the neglected effect of longitudinal heat conduction in the latter work. Satterfield and Cortez (1) confirmed that the heat transfer data were especially susceptible to the effect of longitudinal heat conduction at low flow velocities. Doubts exist about the effects of back-diffusion and axial dispersion in earlier work, particularly at low flow rates. Satterfield and Cortez attempted to reconcile differences in the earlier data. The aims of our work were two-fold:

(1) To report mass transfer coefficients for stacked screens at Reynolds numbers similar to those used in the ammonia burners of high pressure nitric acid plants.

(2) To select a flow model and correlation method which would reconcile the transfer coefficients of geometrically different screens and the results of earlier work.

Selection of System

Satterfield and Cortez (1) studied the heterogeneous oxidation of hexene and toluene in the mass transfer limited regime in their measurement of mass transfer to screens. Independently, we derived measurements from observations of a mass transfer limited heterogeneous reaction using the heterogeneous decomposition of hydrogen peroxide. This decomposition had been shown (4) to be strongly diffusionaly limited when carried out on nonporous catalyst surfaces.

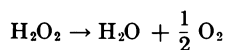


Table I. Measured Screen Characteristics for This Work

Gauze Characteristic	80-mesh Pt	60-mesh Ag	48-mesh Ag	48-mesh Pt	24-mesh Pt	24-mesh Ag
Mesh size, (inch ⁻¹)	80	60	48	48	24	24
Wire diameter (inch)	.00307	.0065	.00707	.0059	.00945	.01415
Fractional opening, γ	0.559	0.34	0.453	0.522	0.613	0.437
Porosity, ϵ	.86	.725	.767	.825	.825	.785

Advantages of this system for our purpose were:

- (1) The reaction is highly irreversible.
- (2) There are no side reactions, the only product being oxygen and water vapor.
- (3) The homogeneous decomposition is slow, but the heterogeneous reaction is readily catalyzed by many metals.

Since instrumental techniques of analysis were not available, the ease of analyzing such a simple system was attractive. The exothermic nature of the reaction was a disadvantage as was the difficulty of finding construction materials which did not catalyze the reaction.

Operating pressure was atmospheric; nitrogen was the diluent, carrying 0.3–2.0% $\text{M H}_2\text{O}_2$, ensuring a temperature rise through the reactor which was

commonly around 10°–25°C and did not exceed 45°C. The measured temperature rise provided a useful check on measured conversion. The operating temperature, mostly *ca.* 250°C, ranged between 190° and 340°C, which was high enough to ensure mass transfer control but low enough to avoid excessive loss of reactant by decomposition ahead of the catalyst screens. Both platinum and silver catalyst screens were studied, in sizes ranging from 24 to 80 meshes per linear inch. The characteristics of screens used in the present work are given in Table I.

Demonstration of Mass Transfer Control

Under mass transfer controlled conditions, the rate of reaction may be equated to the rate of mass transfer to the catalyst surface, the driving force being taken as the difference between concentration or partial pressure of the reacting species in the bulk and an assumed concentration, effectively zero at the catalyst surface. Thus, for uniform velocity distribution across the screens, ignoring axial dispersion and back-diffusion:

$$- \frac{d}{dA_T} \left[F_m \frac{p_A}{P} \right] = k_o p_A$$

For low concentrations of the reactant, F_m is effectively constant; at constant temperature and pressure this equation may be integrated to:

$$X = \frac{p_{A1} - p_{A2}}{p_{A1}} = 1 - \exp \left(- \frac{Pk_o A_T}{F_m} \right) \quad (1)$$

Equation 1 applies equally to a situation where a first-order surface reaction is controlling or to any intermediate state between this and mass transfer limitation if k_o is regarded as the overall first-order rate constant. Thus, the applicability of Equation 1 does not constitute proof of mass transfer control.

Demonstration of mass transfer control for this system is treated in detail by Shah (5) and will be the subject of a separate publication. In summary, the evidence falls into two categories:

- (1) Evidence for a limiting first-order mechanism:
 - (a) Conversion X was independent of inlet partial pressure of H_2O_2
 - (b) Overall reaction rate was directly proportional to the log mean of inlet and outlet partial pressures of H_2O_2
 - (c) Plots of $\log_e(1/(1-X))$ against A_T were straight lines through the origin

These observations are consistent with the applicability of Equation 1.

- (2) Evidence that mass transfer is the limiting first-order mechanism:
 - (a) Overall reaction rate and rate constant showed no significant variation with temperature
 - (b) Overall reaction rate and rate constant were markedly flow dependent, *i.e.*, at constant contact time represented by A_T/F_m , conversion increased with increasing gas velocity
 - (c) There was no detectable difference between results obtained with platinum or silver catalyst beyond that which could be attributed to the slight variation in geometric screen characteristics

Equipment and Experimental Procedure

The flow system for measuring the continuous heterogeneous decomposition of hydrogen peroxide consisted essentially of a hydrogen peroxide vapor generator, preheating furnace, reactor, condenser, and scrubber. The high

purity nitrogen carrier gas was passed through silica gel and soda lime before being metered through a Rotameter. The temperature and pressure of the dried gas stream were determined. The nitrogen stream passed on to the vapor generator, where it was bubbled through an 86 wt % aqueous solution of hydrogen peroxide maintained at a constant temperature. The issuing gas was 80–90% saturated, depending on gas velocity; the partial pressure of hydrogen peroxide vapor was controlled within the range 0.003–0.02 atm by adjusting the operating temperature of the vapor generator within the range 40°–70°C. Any entrained liquid was removed before the gas stream entered the preheating furnace.

The gas stream passed through a 1-m long, 1.1-cm diameter tube inside a cylindrical preheating furnace which was heated by individually controlled sectional heaters.

The reactor, constructed entirely of quartz, was an outer tube 50 cm long and 1.4 cm inside diameter with an elbow at the bottom. A precision bore quartz tube 37.6 cm long with 1.1 cm inside, and 1.4 cm outside, diameters was matched to the outer tube to form a sliding fit inside it, which was effectively gas tight at the pressures used. This tube occupied the lower part of the reactor, serving as a calming section. Its upper end was finely ground to serve as a seat for the stacked screens. Another 7.7-cm length of the same tubing slid firmly in from above to hold the stacked screens securely in place. Thin-walled quartz thermocouple wells extended axially into the inner reactor tube from either end; thermocouples in these wells measured gas inlet and outlet temperatures. Four additional thermocouples were placed along the length of the reactor tube to aid in reactor temperature control. The main body of the reactor was wound with four individually-controlled electrical heaters and was heavily insulated.

Samples were taken through heated tubes at the preheater inlet and at the reactor inlet and outlet. The hydrogen peroxide in the sample was absorbed in acidified water, extreme care being taken to ensure that all hydrogen peroxide was recovered. The hydrogen peroxide recovered from a measured gas sample was determined by titration with ceric sulfate. Total water content was also determined by dissociating the hydrogen peroxide in another sample over silver chippings at 180°C, the total water vapor in the resulting sample being determined by adsorption on silica gel. This enabled a mass balance to be completed. During operation, repeated samples were taken after stable operation had been achieved and maintained for more than an hour.

Before use, catalyst screens were washed in acetone and rinsed in distilled water. Then, the silver screens were pickled in 1% nitric acid solution for a few minutes, the platinum screens were pickled in concentrated hydrochloric acid for a few hours. After pickling, the screens were washed in distilled water and vacuum dried. A series of four to six runs always ended with a repeat of the first run of the series to determine if catalytic activity of the screens had changed. Only rarely was any significant change observed, in which case the whole series was discarded, and the catalyst was retreated.

A little hydrogen peroxide decomposed between the reactor inlet and outlet sampling points even in the absence of catalyst screens. An allowance was made for this by carrying out regular blank runs with no catalyst over the full range of operating conditions and referring all experimental runs to these blanks. The extent of this adjustment to measured reaction rates was normally 5–7% and never exceeded 15%, even at the highest temperature and lowest gas velocity.

Evaluation of Mass Transfer Coefficients

Assuming plug flow, the concentration distribution through the screen stacking is given by integration of the equation:

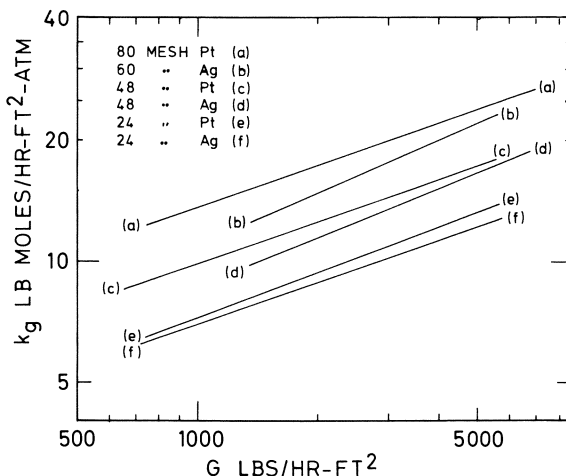


Figure 1. Mass transfer coefficients for different screens

$$\frac{d}{dx}(uc_A) + \frac{d^2c_A}{dx^2}(D + DE) = -k_cac_A$$

allowing for axial diffusion and axial dispersion. Practical demonstration earlier of the applicability of Equation 1 argues that axial diffusion and dispersion are unimportant in our work and that mass transfer coefficients can be defined in terms of a log mean driving force. The correlation lines obtained by least-squares fit for mass transfer coefficients obtained with each type of screen used are shown in Figure 1. The transport coefficients clearly depend on screen characteristics.

A problem arose in the estimation of the effective area for transfer. The structure of our equipment, in which the screens filled the full cross-section of the reactor tube, guaranteed the absence of by-passing of reactant, as reported in Ref. 1. Nevertheless, the gas flow occupied a smaller area. We were reluctant to use gasket materials in our reactor because of the high reactivity of hydrogen peroxide and the desire to avoid separating the screens at all. We hoped to simulate the type of stacking arrangement obtained in ammonia burners. However, this meant that the unexposed peripheral area of the screens was in theory partly accessible to the gas; in practice, however, if the stacking is sufficiently thin, this effect is negligible. Shah (5) made extensive calculations on potential flow analogs of geometrically similar systems and estimated the total transfer area available in such a potential flow situation. For the flow conditions prevailing in our work, we would expect the flow of gas into the peripheral area to be much less than that estimate. As a conservative measure, we used as effective area, the mean of the directly exposed area and the estimate of available area from the potential flow calculations. The resultant range of uncertainty in A_T was estimated to be less than $\pm 2.5\%$ for the various 80-mesh stackings, $\pm 4.5\%$ for most of the others, but ranging as high as $\pm 9\%$ for the 3-layer 24-mesh stacking. Any error in A_T , because of a compensating error in mean gas velocity, causes a much smaller error in j_D . The values of k_g based on log mean driving force were converted into j_D factors using gas properties evaluated at the mean film temperature. Over our experimental range N_{sc} varied from 0.96 to 1.01.

Axial Diffusion. Axial concentration gradients established in gas phase mass transfer experiments with screens are certainly steep, and diffusion in the direction of flow, particularly at low Reynolds number, may be significant, thus invalidating mass transfer coefficients derived from a log mean driving force. However, D/u in our work never exceeded 0.0042 cm, which is much smaller than the depth of screen stackings used; thus, very little modification by axial diffusion of the assumed concentration profile would be expected. This effect may have been more significant in the lower Reynolds number work of Satterfield and Cortez (1) and Gay and Maughan (2), but would have been absent from the liquid-phase work of Vogtlander and Bakker (6).

Axial Dispersion. Axial dispersion results in a similar modification of the concentration profile. Dispersion coefficients for screens do not appear to be available, and previous studies of mass transfer have not attempted to account for it.

We attempted to analyze our results on the basis of a perfect-mixer model, and somewhat more realistically, by regarding stacked screens as a sequence of perfect-mixing stages. Both attempts failed, but conversely, our measured mass transfer rates correlated well with log mean concentration. Axial dispersion does not seem to exert a significant influence under our operation conditions.

Correlation of Mass Transfer Coefficients

Dimensional considerations suggest that a correlation of the form:

$$N_{Sh} = f(N_{Re}, N_{Sc}, \text{geometry}) \quad (2)$$

be sought, although the introduction of a Chilton-Colburn type j -factor offers the alternative

$$j_D = N_{Sh}/N_{Re}N_{Sc}^n = f(N_{Re}, \text{geometry}) \quad (3)$$

With the notable exception of Vogtlander and Bakker (6), most studies of transfer coefficients to screens have used the latter approach, omitting the "geometry" term by selecting a single dimension, used in definition of Reynolds number, as characteristic of the geometry of a screen stacking. The exponent n is commonly assumed to be 2/3 for fluid-solid systems, although in comparing transfer coefficients obtained with similar fluids, its precise value is irrelevant. In comparing gas-solid transfer coefficients with the liquid-solid coefficients of Vogtlander and Bakker, however, its value becomes important.

Correlations in terms of Sherwood number avoid the inclusion of gas velocity on both sides of the correlating equation, but for the sake of conformity, we too present our data in terms of j -factors. We are left with the selection of a suitable characteristic dimension for stacked screens.

Regarding the screen stacking as a packed bed or porous solid, Coppage and London (3) correlated their heat transfer data for stacked screens with respect to a Reynolds number defined in terms of mean interstitial gas velocity and hydraulic diameter of a single screen. Gay and Maughan (2) correlated their data on mass transfer coefficients to a single screen in a similar manner. In both studies satisfactory correlations of the type shown in Equation 3 were obtainable for each screen type, but it was not possible to correlate satisfactorily the data for different screens by a single equation; there remained a strong, unaccounted for, functional dependence on screen porosity.

Attempts to correlate our mass transfer coefficients in this way were similarly unsuccessful. Clearly, the hydraulic diameter does not adequately characterize the screen geometry. It seems that it is incorrect to model such an open structure as woven screens, stacked or single, as a packed bed or porous solid. For multiple screen matrices, screen separation has been reported to have no effect on transfer coefficients. Screens are certainly not isotropic as regards flow characteristics, presenting markedly differing resistance in radial and axial directions. The concept of hydraulic radius is applicable to internal flow configurations whereas the correct flow model for this system is essentially one of external fluid flow around a wire.

Modelling the system as an array of stacked cylinders with transverse flow suggests wire diameter as the characteristic dimension, but it would be unreasonable to expect screens of low porosity or fractional opening to have the same transport properties as more open screens. The use of mean interstitial fluid velocity immediately suggests itself as a characteristic velocity. Multiple screen matrices have lower porosities than single screens and therefore higher interstitial velocities, suggesting that they should have higher transfer coefficients. The little available evidence suggests the opposite. Satterfield and Cortez (1) noted that their mass transfer coefficients for multiple screen matrices were slightly lower than those for single screens, but the difference was not significant. We could not detect any significant difference in our work between mass transfer coefficients for one, three, or five screens. Evidence that the heat transfer rate to the first row of a tube bank (7) is lower than that to the remaining tubes and the similar observations of London *et al.* (8) for crossed-rod matrices generally relate to much higher Reynolds numbers than those used in the present work; the effect is explained in terms of turbulence generated in the wake of the leading rod. This effect would be less important at lower Reynolds numbers.

Satterfield and Cortez (1) correlated their mass transfer coefficients by an equation of the form:

$$j_{D,\varepsilon} = CN_{Re,\varepsilon}^{-m} \quad (4)$$

defining Reynolds number in terms of the mean velocity through a single screen, *i.e.*:

$$N_{Re,\varepsilon} = \frac{Gd}{\mu\varepsilon}$$

Such a definition avoids the problem just discussed, and the difficulty of reproducing and measuring the porosity of stacked screens; however, when applied to multiple screen matrices, G/ε loses its significance as the mean interstitial mass velocity. However, ε remains a convenient measure of the degree of openness of a screen.

A more direct alternative measure of the openness of a screen, is its fractional projected frontal free area, γ . G/γ approximates the maximum velocity through a single screen, and is probably still representative of the maximum velocity through stacked screens. For the screens used in our work γ was determined from photographs of single screens, but may be estimated for a square weave from the expression:

$$\gamma = (1 - Nd)^2 \quad (5)$$

Thus, ε and γ are related approximately by:

$$1 - \epsilon = \frac{\pi}{4} (1 - \sqrt{\gamma}) \sqrt{1 + (1 - \sqrt{\gamma})^2} \quad (6)$$

Values of ϵ for screens of different manufacture but the same mesh size and wire diameter could be influenced by the degree of flattening of the wire in the weaving process, yet it is doubtful if such a change would markedly affect mass transfer characteristics; γ is less susceptible to such ambiguity. Vogtlander and Bakker (6) correlated their single-screen liquid-solid mass transfer coefficients in terms of Reynolds number based on wire diameter and superficial velocity but noted that the correlation was improved by the use of maximum velocity through the screen.

While acknowledging that there is no reason to expect a linear relation between $\log j_D$ and $\log N_{Re}$, we recommend the following alternative correlations of our data for mass transfer to stacks of one to five screens:

$$j_{D,\epsilon} = 0.751 N_{Re,\epsilon}^{-0.56} \quad 3 < N_{Re,\epsilon} < 135 \quad (7)$$

$$\text{mean deviation} = \pm 14.3\%$$

$$j_{D,\gamma} = 0.644 N_{Re,\gamma}^{-0.57} \quad 5 < N_{Re,\gamma} < 245 \quad (8)$$

$$\text{mean deviation} = \pm 10.2\%$$

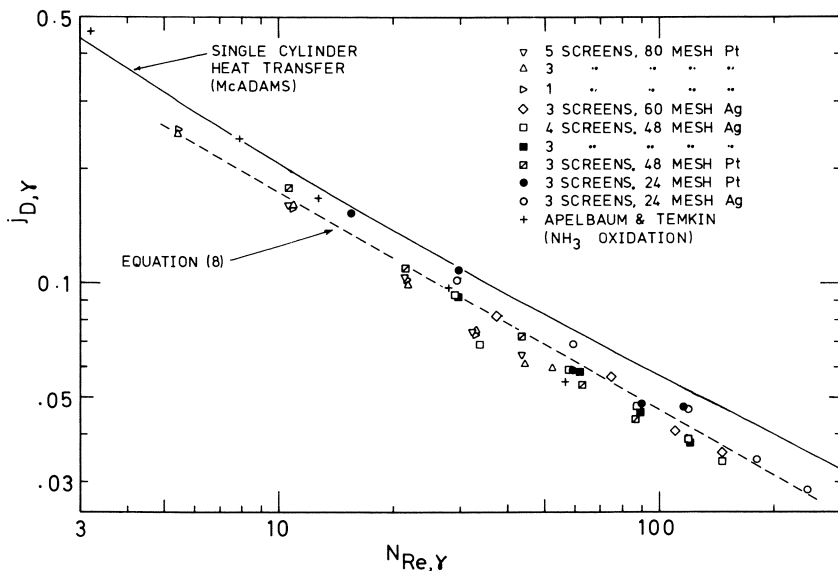


Figure 2. Correlation of the present work in terms of $N_{Re,\gamma}$

Both correlations refer to Reynolds number based on wire diameter; the latter equation, using γ as an additional parameter, gives a significantly better correlation. Our data are plotted in Figures 2 and 3 in these alternative ways.

Comparison with Previous Work

Mass Transfer. In Figure 3 the values of $j_{D,\epsilon}$ obtained here are compared with the data of Satterfield and Cortez (1), Vogtlander and Bakker (6), and Gay and Maughan (2). The data of Vogtlander and Bakker are as recorrelated

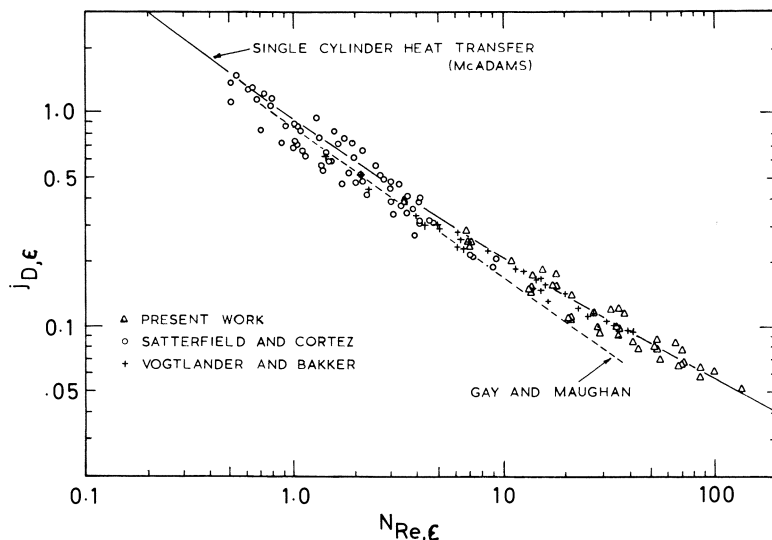


Figure 3. Comparison of mass transfer data with previous results in terms of $N_{Re,\epsilon}$

by Satterfield and Cortez, introducing the parameter ϵ ; only their correlation line for Gay and Maughan's work is plotted, not the data points. There is excellent agreement of our work with that of Vogtlander and Bakker on this basis and with the work of Satterfield and Cortez over the range of overlap. The correlation of:

$$j_{D,\epsilon} = 0.773 N_{Rc,\epsilon}^{-0.585} \quad (9)$$

proposed by Satterfield and Cortez for the data of Vogtlander and Bakker is very similar to Equation 7 for our work.

The data of these three studies, presented in this way agree well with the heat transfer correlation of McAdams (7) for a single cylinder, even imitating the curvature of the latter correlation. This is to be expected if a single cylinder can be regarded as a screen of nearly 100% voidage.

The fact that the data of Vogtlander and Bakker for mass transfer in liquids, where N_{Sc} ranged from 1300 to 2000, can be successfully correlated with the data of the other two studies, where N_{Sc} was around 1.6 or 1, by a $j_{D,\epsilon}$ correlation involving $N_{Sc}^{2/3}$ testifies strongly in favor of the validity of the $2/3$ exponent in this case.

The only flaw in this comparison is the departure of the Satterfield and Cortez correlation of Gay and Maughan's work from the other data at their higher Reynolds numbers. Agreement at lower Reynolds numbers is satisfactory. The possibility that at high Reynolds numbers, Gay and Maughan's data are too low may be argued on the following grounds:

(1) Their data agree with Vogtlander and Bakker at low Reynolds number, confirming the comparability of the two studies, both using single screens. There is little cause to doubt the validity of the latter's data, especially since they were not forced by high transfer rates to base their coefficients on log mean driving forces as were other workers in this field. For similar reasons, their work is not susceptible to the effects of axial diffusion. Vogtlander and Bakker's results are confirmed by our work.

(2) Gay and Maughan's data are the only mass transfer data which do not follow the McAdams correlation curve for heat transfer to a single cylinder and therefore are alone in not confirming the model of external flow around the wires as the principal characteristic of flow through screens.

(3) Correlations for individual screens in Gay and Maughan's work exhibit an unusually low dependence of mass transfer coefficient on gas velocity, as low as $C^{0.15}$ in one instance.

The only suggestion we can offer is that perhaps at high Reynolds numbers, the mercury vaporization technique used by Gay and Maughan might have suffered from localized depletion of the mercury coating on the wires.

Ammonia Oxidation. Ammonia oxidation is regarded as a mass transfer-controlled process. Since determination of mass transfer coefficients suitable for use in ammonia burner design was one of the objectives of the present study, it is relevant to demonstrate the validity of our measured transfer coefficients for this purpose.

The ammonia oxidation data of Dixon and Longfield (9) was compared by Satterfield and Cortez (1) with their measured values of $j_{D,\epsilon}$. The degree of conversion of ammonia varied from 95 to 99.9% so that j -factors derived using a log mean driving force are subject to considerable error. Although the Reynolds number range was well below the range of Satterfield and Cortez' work, the ammonia oxidation data was consistent with their correlation of $j_{D,\epsilon}$. Since our Reynolds number range is higher than that of Satterfield and Cortez, it is pointless comparing this ammonia oxidation data with our measured j -factors, in view of the apparent curvature of the $\log j_{D,\epsilon}$ vs. $\log N_{Re,\epsilon}$ correlation.

Apelbaum and Temkin (10) studied ammonia oxidation at four Reynolds numbers within our range of interest, analyzing the exit gases leaving the catalyst pad and interpreting their results in terms of mass transfer. The term, $j_{D,\gamma}$, based on mass transfer coefficients derived assuming a log mean driving force with ammonia diffusion limiting, is compared in Figure 2 with our mass transfer data. The agreement is satisfactory.

Heat Transfer. The satisfactory agreement between our results when based on mean interstitial velocity and McAdams' single cylinder heat transfer correlation, has already been mentioned. The agreement is somewhat less when Reynolds number based on G/γ is used.

The data of Coppage and London (3) for heat transfer to stacked screens has been widely criticized for ignoring the effect of longitudinal conduction through the metal. To reconcile these results with the mass transfer coefficients of Gay and Maughan (2), Satterfield and Cortez (1) had to make sometimes large, in part arbitrary, adjustments to them.

Using the numerical analysis of Pucci *et al.* (11) of the type of experiment conducted by Coppage and London, Shah (5) also argued that criticism of their data is valid at low gas velocities corresponding to the range of Satterfield and Cortez' work but that the effect of longitudinal conduction was much less significant over our present range of interest. Our mass transfer data agree very well with selected unadjusted data of Coppage and London obtained at high gas velocities.

Conclusions

There is now sufficient mass transfer data for screens to confirm that $j_{D,\epsilon}$ or $j_{D,\gamma}$ correlates well with Reynolds number based on wire diameter and

mean or maximum interstitial velocity. The log-log correlation of literature data exhibits a curvature similar to that displayed by the similar correlation for heat transfer to a single cylinder and agrees satisfactorily with that correlation. The $2/3$ exponent on Schmidt number appears to be correct. The correlation is well enough defined to allow its use in designing catalyst loading for ammonia burners.

Nomenclature

a	area density of screen (ft^{-1})
A_T	total transfer area (ft^2)
c_A	concentration of diffusing component ($\text{lb moles}/\text{ft}^3$)
C	constant in Equation 4
d	wire diameter (ft)
D	diffusivity (ft^2/hr)
D_E	eddy diffusivity (ft^2/hr)
F_m	molar flow rate ($\text{lb moles}/\text{hr}$)
G	superficial mass velocity ($\text{lbs}/\text{hr}\text{-ft}^2$)
j_D	j -factor for mass transfer, $= (k_g MP/G) N_{Sc}^{2/3}$
$j_{D,\gamma}$	j -factor for mass transfer based on maximum velocity, $= (\gamma k_g MP/G) N_{Sc}^{2/3}$
$j_{D,\epsilon}$	j -factor for mass transfer based on interstitial velocity $= (\epsilon k_g MP/G) N_{Sc}^{2/3}$
k_c	mass transfer coefficient (ft/hr)
k_g	mass transfer coefficient ($\text{lb moles}/\text{hr}\text{-ft}^2\text{-atm}$)
k_0	overall first-order rate constant ($\text{lb moles}/\text{hr}\text{-ft}^2\text{-atm}$)
m	exponent in Equation 4
M	mean molecular weight of gas
N	meshes per linear foot (ft^{-1})
N_{Re}	Reynolds number
$N_{Re,\gamma}$	Reynolds number based on maximum velocity, $= dG/\gamma\mu$
$N_{Re,\epsilon}$	Reynolds number based on interstitial velocity, $= dG/\epsilon\mu$
N_{Sc}	Schmidt number, $= \mu/\rho D$
N_{Sh}	Sherwood number
p_A	partial pressure of diffusing species (atm)
p_{A1}	partial pressure p_A at inlet (atm)
p_{A2}	partial pressure p_A at outlet (atm)
P	atmospheric pressure (atm)
u	gas velocity (ft/hr)
x	distance in direction of flow (ft)

Greek Letters

γ	minimum fractional opening of single screen
ϵ	porosity of single screen
ρ	density of gas (lb/ft^3)
μ	viscosity of gas (ft^2/hr)

Literature Cited

1. Satterfield, C. N., Cortez, D. H., *Ind. Eng. Chem., Fundamentals* (1970) **9**, 613.
2. Gay, B., Maughan, R., *Int. J. Heat Mass Transfer* (1963) **6**, 277.
3. Coppage, J. E., London, A. L., *Chem. Eng. Progr.* (1956) **52** (2), 57F.
4. Satterfield, C. N., Resnick, H., Wentworth, L. R., *Chem. Eng. Progr.* (1954) **50**, 504.
5. Shah, M. A., Ph.D. thesis, University of Birmingham, England (1970).
6. Vogtlander, P. H., Bakker, C. A. P., *Chem. Eng. Sci.* (1963) **18**, 583.
7. McAdams, W. H., "Heat Transmission," 3rd ed., pp. 258-275, McGraw-Hill, New York, 1954.
8. London, A. L., Mitchell, J. W., Sutherland, W. A., *J. Heat Transfer* (1960) **82**, 199.

9. Dixon, J. K., Longfield, J. E., "Catalysis," Vol. 7, P. H. Emmett, Ed., pp. 281-304, Reinhold, New York, 1960.
10. Apelbaum, L., Temkin, M., *J. Phys. Chem. (USSR)* (1948) **22**, 179.
11. Pucci, P. F., Howard, C. P., Piersall, C. H., Jr., *A.S.M.E. Trans., J. Eng. Power* (1967) **A89**, 29.

RECEIVED January 2, 1974.

Fluid Flow Model for a Packed-Fluidized Bed

KUNIO KATO, HIRO ARAI, and UTARO ITO

Chemical Engineering Department, Gunma University,
Kiryu, Gunma, Japan 376

To establish a fluid flow model in a packed-fluidized bed, mesityl oxide was synthesized by the catalytic aldol condensation of acetone in a fixed and a packed-fluidized bed. Reaction kinetics were determined in the fixed bed. Reactant conversion in a packed-fluidized bed was analyzed by a two-phase model with a known reaction rate. This two-phase model has two parameters: the gas interchange coefficient between the bubble and emulsion phases and the fraction of catalyst in the bubble phase. Using the known gas interchange coefficient, the fraction of catalyst in the bubble phase in a packed-fluidized bed was experimentally determined to be about 0.2.

A packed-fluidized bed is one in which particles are fluidized with gas in a column suitably packed with spheres, open-ended cylindrical screens, and the like. Since such packings prevent the growth of gas bubbles in the bed, particles (catalyst) and gas contact each other well. Gas and particle flow patterns are standardized by the packing, and scale-up of this reactor is simplified.

To simulate the reaction characteristics or particle-gas transport phenomena in a packed-fluidized bed, a fluid flow model is the most important factor. Two methods are used to investigate the fluid flow pattern in such a bed. In one, tracer gas is put into the reactor, the response curve of this gas is analyzed by suitable model, and the model parameter is calculated. In the other method, the reactant conversion in the bed is analyzed by a suitable model with known reaction kinetics, and the model parameter is calculated from it. The gas interchange coefficient between the bubble and emulsion phase in packed-fluidized bed was obtained (1) by analyzing the residence time curve of step response of tracer gas with a two-phase model.

Ishii and Osberg (2) isomerized cyclopropane on a silica-alumina catalyst in fixed and packed-fluidized bed packed with open-ended screen packing. The reaction kinetics were studied in a fixed bed. Conversion in the packed bed was smaller than that calculated by the plug flow model and larger than that calculated by the perfect mixing model. Thus, the reactant conversion in packed-fluidized bed was analyzed by the diffusion model. Kato *et al.* (3) hydrogenated ethylene in fixed and packed-fluidized bed packed with spheres and open-ended screen packing. The decrease of reactant conversion in packed-fluidized bed from fixed bed under the same contact time was explained by catalyst contact efficiency.

In this work, mesityl oxide was synthesized by the catalytic aldol condensation of acetone in a fixed and a packed-fluidized bed with open-ended screen packing. Reaction kinetics were studied in a fixed bed, and the reactant conversion in a packed-fluidized bed was analyzed by a two-phase model with known reaction kinetics. The fraction of catalyst particles in the bubble phase was obtained.

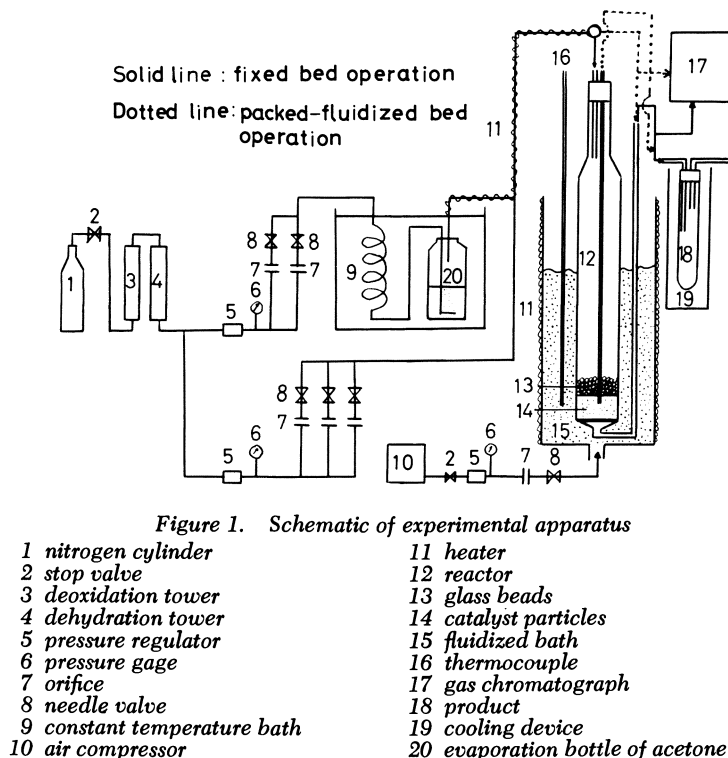


Figure 1. Schematic of experimental apparatus

- | | |
|-----------------------------|----------------------------------|
| 1 nitrogen cylinder | 11 heater |
| 2 stop valve | 12 reactor |
| 3 deoxidation tower | 13 glass beads |
| 4 dehydration tower | 14 catalyst particles |
| 5 pressure regulator | 15 fluidized bath |
| 6 pressure gage | 16 thermocouple |
| 7 orifice | 17 gas chromatograph |
| 8 needle valve | 18 product |
| 9 constant temperature bath | 19 cooling device |
| 10 air compressor | 20 evaporation bottle of acetone |

Experimental

A schematic of the experimental apparatus is shown in Figure 1. Since oxygen gas hinders this reaction, nitrogen was used as carrier gas. Taken from a cylinder it was passed through a deoxidation tower and divided into two streams. One stream entered the orifice for metering the flow rate and was fed to an acetone bottle submerged in a constant-temperature bath heated to 25°C. Nitrogen was saturated with acetone gas in this bath. The flow rate of another stream of nitrogen gas was measured with orifice meter, and both streams were combined. The concentration of acetone and the flow rate of the feed gas to the reactor were determined by measuring the flow rate in both streams. Acetone concentration in the feed gas was usually 5 and 10 vol %. Gas chromatography was used to analyze acetone and mesityl oxide. Polyethylene glycol 1000 was packed in the chromatograph column, and hydrogen was the carrier gas. To prevent condensation of acetone vapor between the exit point of the constant temperature bath and the entrance point of the reactor, the tube was heated to 40°C. The reactor used for this experiment (Figure 2) was a borosilicate glass cylinder, 5.2 cm id and 40 cm high. To

Solid line : fixed bed operation

Dotted line : packed-fluidized bed operation

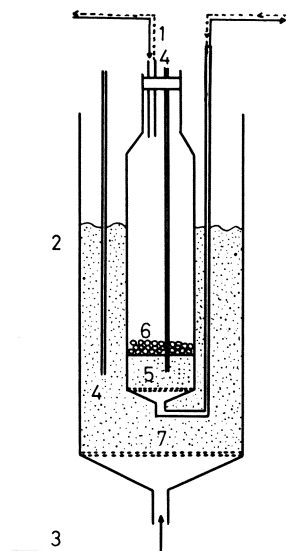


Figure 2. Details of the reactor

- 1 reactant gas
- 2 heater
- 3 air
- 4 thermocouple
- 5 catalyst particles
- 6 glass beads
- 7 fluidized bath

control the reaction temperature, the reactor was put into the fluidized bath, 10 cm id and 50 cm high as shown in Figure 1. Catalyst particles used in this experiment were 80–100 mesh alumina (Tekkosha Co., Ltd.). Packing used for a packed-fluidized bed was 1 cm id and 1 cm long 16 mesh open-ended screen packing.

To eliminate water in catalyst particles, the reactor was heated for 1 hr at 450°C in nitrogen and cooled to reaction temperature with flowing nitrogen gas (100 cc/min). After the reaction temperature was reached, acetone of constant concentration was fed to the reactor, and the reaction was started. After catalyst activity was constant, experimental data were taken. In the fixed bed operation, reactant flowed upward in the reactor. Since the porous plate of this reactor is a good gas distributor in a packed-fluidized bed operation, only catalyst particles are put into reactor and are fluidized among packings with reactant gas.

Results

Fixed Bed. Mesityl oxide is synthesized from acetone according to Reaction 1:



When the reaction temperature was 280°–370°C, most of the product gas was mesityl oxide. A small amount of mesitylene and polymer were detected.

The fluid flow pattern in the fixed bed is approximately plug flow, and the fixed bed is operated at constant temperature. From material balance of reactant gas in the small increment of the bed, the following equation is obtained.

$$-U \frac{dC}{dZ} = r \quad (2)$$

If the reaction rate of the aldol condensation of acetone is expressed to be proportional to the concentration difference between the concentration of acetone in reaction and equilibrium concentration of acetone defined in Reaction 1, Equation 3 results:

$$r = K(C - C_{eq}) \quad (3)$$

From Equations 2 and 3,

$$-\log(1 - X/X_{eq}) = KL/U \quad (4)$$

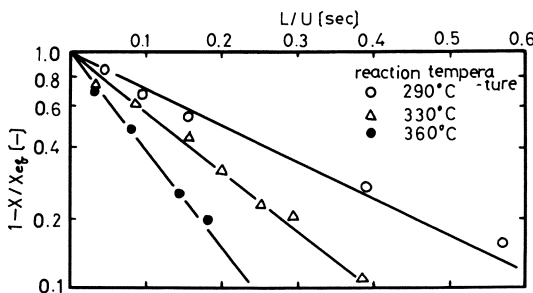


Figure 3. Relationship between $1-x/x_{eq}$ and L/U in fixed bed

Figure 3 shows the relationship between reactant conversion and L/U at different reaction temperatures. From Figure 3 the reaction rate of this reaction is expressed as Equation 3. The reaction rate constant at 290°, 330°, and 360°C per unit volume of bed is 3.66, 5.85, and 9.1 (liters/sec), respectively. The effect of temperature upon the reaction rate constant in this temperature range is:

$$K = 1.75 \times 10^4 \exp(-9500/RT) \quad (5)$$

Packed-Fluidized Bed. There are bubble and emulsion phases in a packed-fluidized bed; the size of gas bubbles is restricted by the packing. When the gas flow rate is increased, the number of gas bubbles per unit bed volume and the bubble raising velocity are increased, but the size of the gas bubbles is almost constant. Therefore, the fluid flow model based on the bubble size in the bed seems unsuited to fluid flow model in a packed-fluidized bed, it is better to use the same kind of model as shown in Mathis and Watson (4) and Lewis *et al.* (5). The following assumption are made to calculate the reactant conversion.

(1) The bed consists of bubble and emulsion phases. The bubble phase consists of bubbles and particles around the bubble. The fraction of catalyst in the bubble phase is a .

(2) The total volume of gas bubbles in the bed may be expressed as $S(L-L_{mf})$.

(3) Gas interchange occurs between two phases. According to Kato *et al.* (1), the gas interchange coefficient per unit volume of bubble is

$$F_o = 4.2 \left[\frac{U - U_{mf}}{U_{mf}} \right]^{-0.06} \quad (6)$$

(4) The gas flow rate in the emulsion phase is the same as the minimum fluidized gas velocity of particles.

(5) The gas in the bubble phase and emulsion phase flows through the bed as plug flow.

(6) Since the effective thermal conductivity in a packed-fluidized bed is considerably large and the heat of reaction of this reaction is small, the bed is assumed to be operating under constant temperature.

Using these assumptions, from material balance of reactant in the small increment of each phase, the following equations are derived.

Bubble phase:

$$\frac{dC_b}{dZ} + \frac{F_o(R_b-1)}{R_b(U-U_{mf})} (C_b-C_e) + \frac{a r_b}{R_b(U-U_{mf})} = 0 \quad (7)$$

Emulsion phase:

$$\frac{dC_e}{dZ} - \frac{F_o(R_b-1)}{R_b U_{mf}} (C_b-C_e) + \frac{(1-a) r_e}{R_b U_{mf}} = 0 \quad (8)$$

where:

$$R_b = \frac{L}{L_{mf}}$$

Boundary condition:

$$Z = 0$$

$$C_b = C_e = C_o$$

In Equations 7 and 8, the relationship between the bed expansion ratio and operating conditions is obtained from Kato *et al.* (6). Therefore, if the reaction kinetics of reactant are known, concentrations of reactant at the exit of bubble phase and emulsion phase are calculated from Equations 7 and 8 with fraction of catalyst in bubble phase, a , as parameter. From this value, the concentration of reactant at the exit of packed-fluidized bed becomes:

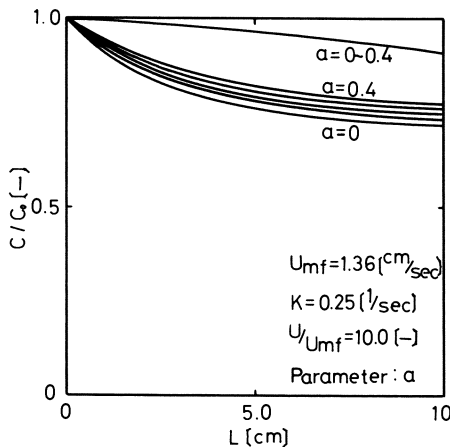


Figure 4. Relationship between reactant concentrations in the bubble and emulsion phases and bed height when the reaction rate constant is small

$$C_{out} = \frac{U_{mf}}{U} C_{eo} + \frac{(U-U_{mf})}{U} C_{bo} \quad (9)$$

The Runge-Kutta method is used to calculate Equations 7 and 8. Before comparing the experimental results with calculated ones, to investigate the reaction characteristics of this model, the reactant conversion in packed-fluidized bed in the first-order reaction is calculated with the fraction of particle in

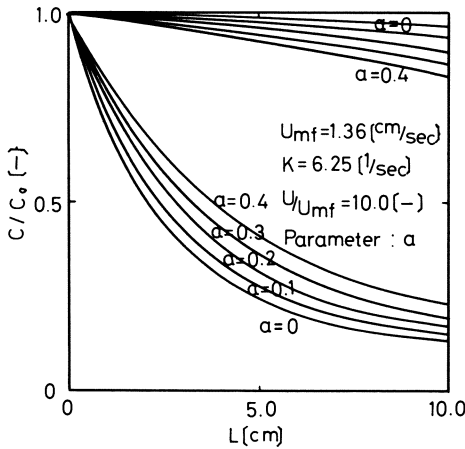


Figure 5. Relationship between reactant concentrations in the bubble and emulsion phases and bed height for intermediate reaction rate constant

bubble phase as a parameter. Figures 4, 5, and 6 show the relation between the reactant concentration in bubble and emulsion phase and bed height with fraction of the particles in the bubble phase as a parameter where the reaction rate constant is 0.1, 6.25, and 12.5 (liters/sec) respectively. From these figures, the larger the reaction rate constant, the larger the concentration difference between two phases. When a is increased, the reactant conversion in bubble phase is increased. The reactant concentrations in bubble and emulsion

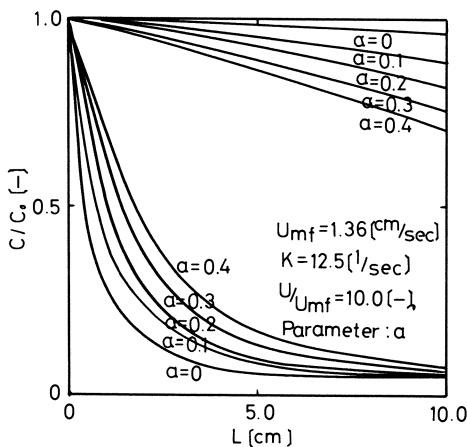


Figure 6. Relationship between reactant concentrations in the bubble and emulsion phases and bed height for large reaction rate

phases are quite sensitive to a when the reaction rate constant is large. Figure 7 shows the relationship between the reactant conversion and KL_{mf}/U with the reaction rate constant and fraction of particles in bubble phase as parameters. From Figure 7, when the reaction rate constant is small and a is large, the reactant conversion calculated from this model is almost the same as that in plug flow reactor. However, when the reaction rate constant is large and a is small, the reactant conversion calculated from this model is smaller than that in perfect mixing flow reactor. From Figure 7, the reactant conversion in

packed-fluidized bed is also sensitive to a when the reaction rate constant is large. Therefore, to obtain a numerically from this kind of test reaction, the reaction rate constant for the test reaction must be large.

Figures 8 and 9 show the relation between the reactant conversion and L/U when the reaction temperature is 290° and 330°C, respectively. The dotted lines in Figures 8 and 9 show the conversion vs. L/U calculated from

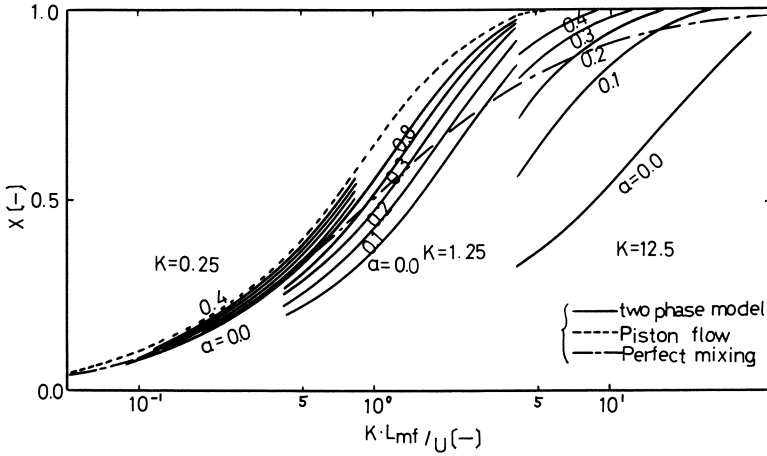


Figure 7. Relation between conversion and KL_{mf}/U

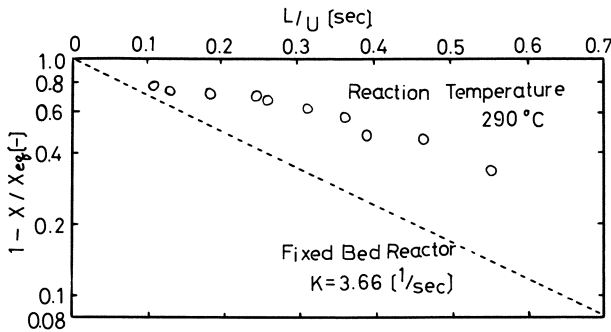


Figure 8. Conversion in packed-fluidized bed reactor vs. that in fixed bed reactor

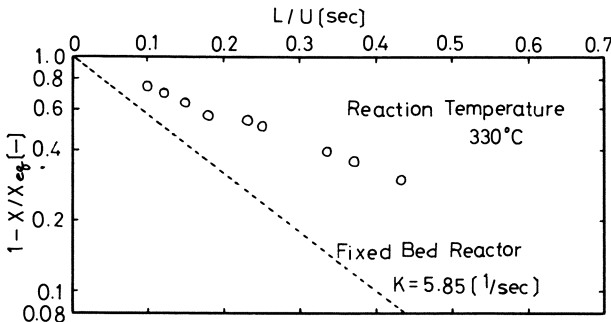


Figure 9. Conversion in packed-fluidized bed reactor vs. that in fixed bed reactor

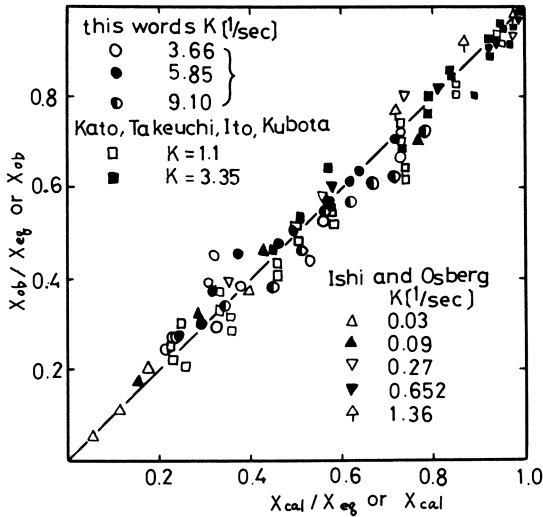


Figure 10. Experimental vs. calculated conversion

plug flow model under the same reaction rate constant. Figure 10 compares the experimental results with calculated ones in this model. From Figure 10, both the reactant conversion of this experiment and that of Ishii and Osberg (2) and Kato *et al.* (3) agree well with the value calculated from this model when the fraction of catalyst in bubble phase is 0.2. From Figure 10, the reactant conversion in a packed-fluidized bed with almost the same size of packing as that in this experiment is calculated from this model when the fraction of catalyst in bubble phase is 0.2.

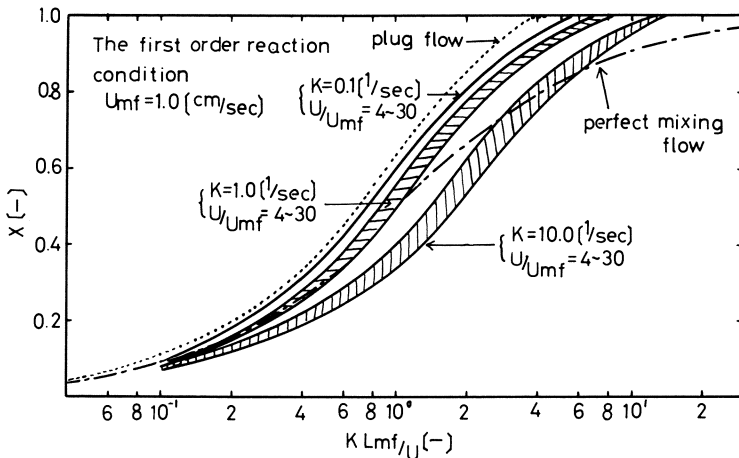


Figure 11. Conversion calculated from this model vs. that in plug flow and perfect mixing reactors for first-order reaction rate

Discussion

In a packed-fluidized bed, the size of the gas bubble is restricted by the packing. No matter how the bed diameter and bed height are changed, the fluid flow pattern in the bed is almost the same as that in this kind of experimental apparatus. The fluid flow model and the fraction of catalyst particle obtained in this experiment may be applied to the packed-fluidized bed with almost the same type and the same size packing ($D_p = 1.0\text{--}3\text{ cm}$) as these of this experiment. Figure 11 shows the relationship between KL_{mf}/U and reactant conversion calculated from this model for a first-order reaction with reaction rate a constant parameter when the minimum fluidized gas velocity is 1.0 cm/sec. From Figure 11, when the reaction rate constant is small (0.1 liter/sec), the reactant conversion in packed-fluidized bed is almost the same as that in the plug flow reactor. When the reaction rate constant is intermediate (1.0 liter/sec), the reactant conversion calculated from this model is smaller than that in plug flow reactor but usually larger than that in perfect mixing flow reactor. When the reaction rate constant is large (10.0 liters/sec), most of the reactant conversion calculated from this model is smaller than that in perfect mixing flow reactor. When the reaction rate constant is large, the reactant conversion in a packed-fluidized bed is affected by U/U_{mf} at the same value of KL_{mf}/U .

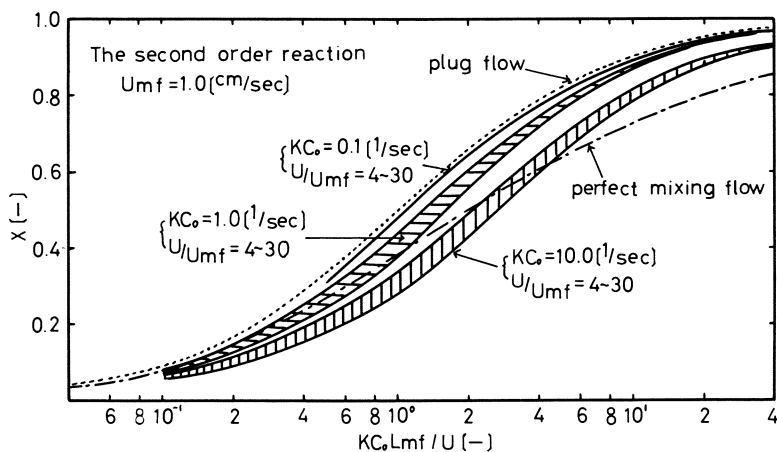


Figure 12. Conversion calculated from this model vs. that in plug flow and perfect mixing reactors for second-order reaction rate

Figure 12 shows the relationship between $KC_o L_{mf}/U$ and reactant conversion calculated from this model for the second-order reaction with KC_o as parameter. The same results as those described above are found in Figure 12. Generally, the reactant conversion in a packed-fluidized bed may be larger than that in fluidized bed reactor under the same reaction condition as shown in Figures 11 and 12.

Conclusions

A fluid flow model in packed-fluidized bed is proposed. Comparing the reactant conversion in packed-fluidized bed with that in fixed bed, the fraction

of catalyst in bubble phase is obtained. The fraction of catalyst in bubble phase is about 0.2 for 1.0–3.0 cm open-ended screen packing.

Nomenclature

- a = fraction of particles in bubble phase
 C = concentration of reactant (gram-mole/cc)
 C_b = concentration of reactant in bubble phase (gram-mole/cc)
 C_{bo} = concentration of reactant at the outlet of bubble phase (gram-mole/cc)
 C_e = concentration of reactant in emulsion phase (gram-mole/cc)
 C_{eo} = concentration of reactant at the outlet of emulsion phase (gram-mole/cc)
 C_{ea} = equilibrium concentration of reactant (gram-mole/cc)
 C_o = concentration of reactant in feed gas (gram-mole/cc)
 C_{out} = concentration of reactant at the outlet of packed-fluidized bed (gram-mole/cc)
 F_o = gas interchange coefficient between bubble and emulsion phase (liters/sec)
 K = chemical reaction rate constant (liters/sec)
 L = bed height (cm)
 L_{mf} = bed height at the minimum fluidized gas velocity (cm)
 R_b = bed expansion ratio
 r = reaction rate per unit volume of bed (gram-mole/cc sec)
 r_b = reaction rate in bubble phase (gram-mole/cc sec)
 r_e = reaction rate in emulsion phase (gram-mole/cc)
 S = cross sectional rate (cm²)
 T = absolute temperature (°K)
 U = superficial gas velocity (cm/sec)
 U_{mf} = the minimum fluidized gas velocity (cm/sec)
 X = conversion of reactant gas
 X_{ea} = equilibrium conversion of reactant gas
 Z = axial length (cm)

Literature Cited

1. Kato, K., Imafuku, K., Kubota, H., *Chem. Eng. Japan.* (1967) **31**, 967.
2. Ishii, T., Osberg, G. L., *A.I.Ch.E. J.* (1965) **11**, 279.
3. Kato, K., Takeuchi, N., Ito, U., Kubota, H., *J. Chem. Eng. Japan* (1969) **2**, 8, 204.
4. Mathis, J. F., Watson, C. C., *A.I.Ch.E. J.* (1956) **2**, 518.
5. Lewis, W. K., Gilliland, E. R., Glass, W., *A.I.Ch.E. J.* (1959) **5**, 419.
6. Kato, K., Imafuku, K., Hattori, K., Kubota, H., *Chem. Eng. Japan.* (1966) **30**, 8, 748.

RECEIVED January 2, 1974.

Pore Structure and Diffusion

N. WAKAO

Department of Chemical Engineering, Yokohama National University,
Minami-Ku, Yokohama, Japan

Unsteady state diffusion experiments were done to determine effective diffusivity values for inert systems. There was no difference between the diffusivity values at unsteady state and those at steady state. A two-dimensional network of macro and micro passageways was assumed as a pore model. The effective diffusivity values for inert systems were estimated on the model, and they did not depend on steady or unsteady state conditions. The effective diffusivity for a reacting system was also computed on the pore model, and the value for a reacting system was predicted to be smaller than that for an inert system if there were many macropores all the way through the pellet. If there are deadends of macropores, however, the two diffusivity values tend to be the same.

Diffusion experiments under inert conditions either at steady state or at unsteady state have been done to determine effective diffusivity values of porous catalyst pellets for reacting systems. Steisel and Butt (1), using the computational model for pore structure of Foster and Butt (2), suggested that the effective diffusivity for inert systems (D_e^D) is considered to be identical with that for reacting systems (D_e^R). A similar conclusion has been reached experimentally by Balder and Petersen (3) and Toei *et al.* (4).

The purposes of this investigation are to examine, first, if D_e^D values measured from unsteady state diffusion experiments are the same as those at steady state, and, second, if there is any difference in value between D_e^D and D_e^R .

Experimental Measurements of D_e^D

As shown in Figure 1, hydrogen is kept flowing in the two chambers to replace air in the porous solid with hydrogen; then hydrogen flowing into one chamber (pulse-side chamber) is changed to nitrogen for a certain period, and again back to hydrogen. Hydrogen is kept flowing in the hydrogen-side chamber. The gas in either chamber is at atmospheric pressure.

The nitrogen concentration in the hydrogen-side chamber is measured as a function of time by intermittent sampling of the outgoing gas and determination of the concentration by gas chromatography. For the unsteady state experiments each chamber is designed to have a small volume.

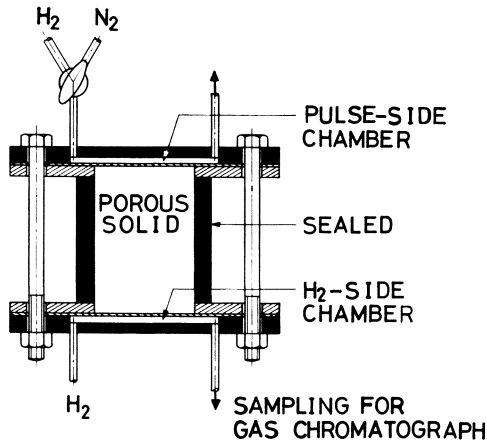


Figure 1. Experimental apparatus

If we assume that D_e^D is constant in each run, the material balance for nitrogen is

$$\epsilon_p \frac{\partial c}{\partial t} = D_e^D \frac{\partial^2 c}{\partial z^2} \quad (1)$$

with

$$c = 0, \text{ at } t = 0 \quad (2)$$

$$\left. \begin{array}{l} c = c_0, \text{ at } 0 < t < t_0 \\ c = 0, \text{ at } t > t_0 \end{array} \right\} z = 0 \quad (3)$$

$$c = 0, \text{ at } z = L \quad (4)$$

The solution in the Laplace domain is

$$\begin{aligned} \bar{c} &= \int_0^\infty c e^{-st} dt \\ &= c_0 \frac{1 - e^{-st_0}}{s} \frac{\sinh \lambda \left(1 - \frac{z}{L}\right)}{\sinh \lambda} \end{aligned} \quad (5)$$

where

$$\lambda = L \sqrt{\frac{\epsilon_p s}{D_e^D}}$$

The rate of nitrogen diffused through the solid to the hydrogen-side chamber is

$$N_L = -A D_e^D \left(\frac{\partial c}{\partial z} \right)_L \quad (6)$$

In the Laplace domain

$$\bar{N}_L = \int_0^\infty N_L e^{-st} dt = -A D_e^D \left(\frac{d\bar{c}}{dz} \right)_L \quad (7)$$

Substituting Equation 5 into Equation 7 and setting $s = 0$, one obtains

$$\int_0^{\infty} N_L dt = \frac{A}{L} D_e^D c_0 \phi_0 \quad (8)$$

The transient rate (N_L) is calculated from the nitrogen concentration-time curve and flow rate in the hydrogen-side chamber. The nitrogen concentrations are so small (less than 2%) that they are assumed to be zero (*i.e.*, boundary condition 4) in solving Equation 1.

The concentration-time curves together with the D_e^D values determined from Equation 8 are illustrated in Figure 2. The D_e^D values in the unsteady-state period are not different from the steady-state values.

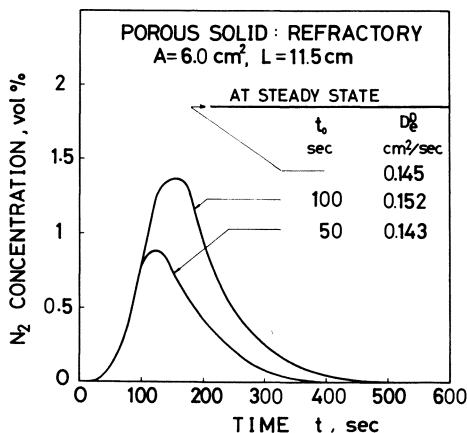


Figure 2. Response of nitrogen in hydrogen-side chamber and D_e^D values calculated

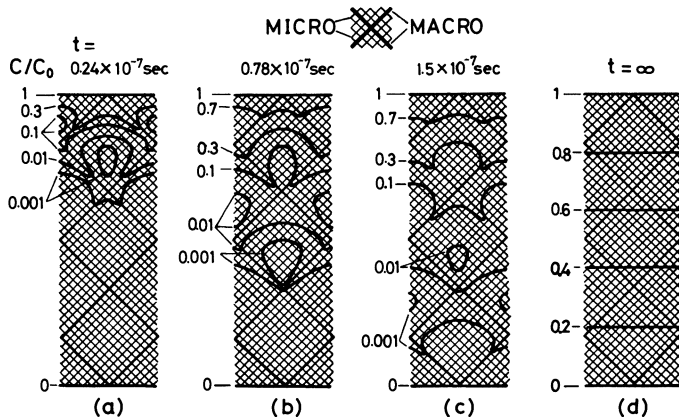


Figure 3. Concentration profiles in grid under inert conditions as a function of time. Ten 100-A micro per 1000-A macro passageway, $b = 2000$ -A, $L = 102,000$ -A, $D_a = 0.640$ cm²/sec, and $D_i = 0.0588$ cm²/sec.

Effective Diffusivities for Network Model with No Deadend Pores

Figure 3 is a grid model made up of two-dimensional macro and micro passageways (slit-shaped pores). The gridrods are assumed to be arranged in the staggered form with square pitch. The network geometry and the rod

Table I. Grid Characteristics and Computed Data of Effective Diffusivity

System	Width of Path, A ^a		No. ^b of Micro Paths per Macro Path	Computed Steady State Data					
	Macro r _a	Micro r _i		No Deadend			8% Deadend		
				D _e ^D , cm ² /sec	D _e ^R , cm ² /sec	D _e ^D /D _e ^R	D _e ^D , cm ² /sec	D _e ^R , cm ² /sec	D _e ^D /D _e ^R
1	10,000	10	4	0.128	0.0461	2.78	0.0290 ^c	0.0241	1.20
2	10,000	10	10	0.0582	0.00982	5.93	0.00981 ^d	0.00450	2.18
3	10,000	10	20	0.0304	0.00321	9.47			
4	10,000	100	4	0.128	0.101	1.27			
5	10,000	100	20	0.0307	0.0116	2.65			

^a Conductance of macro passageway subrod per unit grid depth = $r_a D_a/b$, where D_a is assumed as 0.640 cm²/sec. Conductance of micro passageway subrod per unit grid depth = $r_i D_i/b$, where D_i is 0.00588 cm²/sec for $r_i = 10$ Å and $D_i = 0.0588$ cm²/sec for $r_i = 100$ Å. Incidentally the D_a and D_i values are, respectively, equal to the bulk diffusivity in hydrogen-nitrogen system and the Knudsen diffusivity of hydrogen, both at 21°C.

^b Length of subrod is assumed as $b = 10,000$ Å.

^c Different locations of deadend.

^d Same deadend locations as in Figure 6.

conductances for a diffusing component under constant total pressure are illustrated in Table I.

Under Inert Conditions. The numerical computation is carried out (as outlined in the Appendix) in a digital computer with the following conditions:

$$(1) \text{ at } t=0, c=0 \quad (9)$$

$$(2) \text{ at upper face } (z=0), c=c_0 \quad (10)$$

$$(3) \text{ at bottom face } (z=L), c=0 \quad (11)$$

Figure 3 shows how the step change of concentration penetrates into the grid in time. As expected, the diffusion first takes place in macro passageways and then into micro. Finally, however, the concentration profiles become linear at $t = \infty$, as shown in Figure 3d. The date of diffusion into the grid (N_0) is easily computed from concentration gradients and conductances at $z = 0$.

On the other hand, the solution to Equation 1 under the conditions listed above is

$$\frac{c}{c_0} = 1 - \frac{z}{L} - \frac{2}{\pi} \sum_{n=1}^{\infty} \frac{1}{n} \sin\left(\frac{n\pi z}{L}\right) e^{-\left(\frac{n\pi}{L}\right)^2 \left(\frac{D_e^D t}{\epsilon_p}\right)} \quad (12)$$

Therefore, N_0 evaluated for the network grid is to be equal to

$$\begin{aligned} N_0 &= -A D_e^D \left(\frac{\partial c}{\partial z}\right)_0 \\ &= \frac{A}{L} D_e^D c_0 \left[1 + 2 \sum_{n=1}^{\infty} e^{-\left(\frac{n\pi}{L}\right)^2 \left(\frac{D_e^D t}{\epsilon_p}\right)} \right] \end{aligned} \quad (13)$$

from which D_e^D values are determined as shown in Figure 4. It indicates that D_e^D values are low at first and increase rapidly to a constant value. The time when D_e^D is lower than the steady-state value is so short that D_e^D values determined from unsteady-state experiments, such as chromatographic methods, will be steady-state values themselves. The steady-state values for some pore models are given in Table I.

Under Reaction Conditions. A similar computation is carried out by Wakao and Naruse (5) for steady-state concentrations in the grid under the following conditions (Appendix):

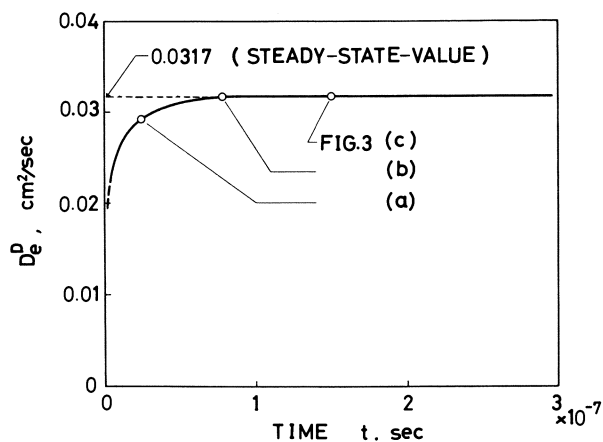


Figure 4. Time vs. D_e^D for network pore model

(1) chemical reaction with first-order kinetics (rate constant k) at passageway walls (14)

(2) at upper face ($z = 0$), $c = c_0$ (15)

(3) at bottom face ($z = L$), $dc/dz = 0$ (16)

The total reaction rate (R) is evaluated as the diffusion rate at $z = 0$.

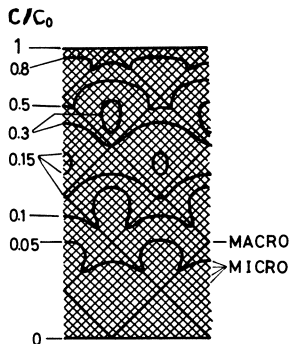


Figure 5. Concentration profiles in grid under reaction conditions; $k = 3.0$ cm/sec, same grid as in Figure 3

If the following equation expressed in terms of D_e^R :

$$D_e^R \frac{d^2c}{dz^2} = kac \quad (17)$$

is solved under the same conditions, the rate is

$$\begin{aligned} R &= -AD_e^R \left(\frac{dc}{dz} \right)_{z=0} \\ &= ALkac_0 \frac{\tanh\phi}{\phi} \end{aligned} \quad (18)$$

where

$$\phi = L \sqrt{\frac{ka}{D_e^R}}$$

and a is the specific surface area (Appendix). From Equation 18 and R evaluated for the grid, D_e^R values are determined as shown in Table I. They vary with the assumed value of k unless L is sufficiently long, but the D_e^R data listed in Table I are the limiting values which are independent of k and L (L is long enough) as they are reasonably expected for actual catalyst pellets. Table I shows that D_e^D is larger than D_e^R .

The concentration profiles in Figure 5 are those computed on conditions 14, 15, and $c_{z=L} = 0$ instead of 16, using the same grid parameters as Figure 3 and $k = 3.0$ cm/sec. In this case the reaction rate is

$$R = ALkac_0 \frac{\cosh\phi - 1}{\phi \sinh\phi} \quad (19)$$

and again it is shown that D_e^D is larger than D_e^R ; $D_e^R = 0.0260$ cm²/sec, while $D_e^D = 0.0317$ cm²/sec (Figure 4).

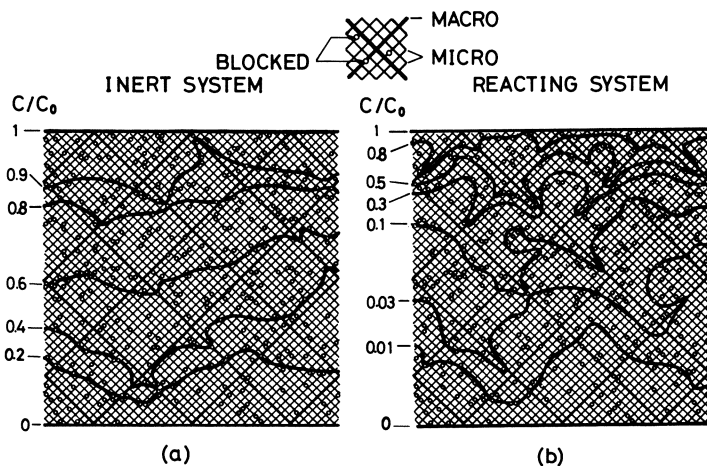


Figure 6. Concentration profiles in grid with 8% deadend subrods. Same grid as in Figure 3 except deadends. (a) Inert system—from the profiles $D_e^D = 0.0160$ cm²/sec. (b) Reacting system with $k = 3.0$ cm/sec—from the profiles $D_e^R = 0.0158$ cm²/sec.

Network Model with Deadend Pores

If we assume that some of the subrods (rods between two adjacent nodal points) are interrupted in the middle and that the area of passageway walls remains unchanged, the numerical computation is carried out (Appendix). Figure 6 illustrates 8% of the total subrods (8% macro as well as 8% micro subrods) interrupted. A table of random numbers is used to select the interrupted (or deadend) locations.

Table I of Wakao and Naruse (5) indicates that the deadends cause considerable decreases in D_e^D and D_e^R values. D_e^D values decrease so much more than D_e^R values that the ratio D_e^D/D_e^R tends to unity. Only the case with 8% deadends is illustrated in Table I, but it is apparent that the differ-

ence between D_e^D and D_e^R becomes less if there are more deadends. The larger decrease in D_e^D value is caused by the fact that deadend macro passageways form detours through micro passageways.

It is true that the difference depends on frequency of occurrence of deadends, particularly of macro passageways, as well as their locations. Some of the deadends of macro passageways are expected to result in the so-called ink-bottle pores. In actual catalyst pellets the deadend frequency of macropores will probably be high, as suggested from hysteresis loop in measurement of pore size distribution or ink-bottle pores, and in fact there will be not much difference in value between D_e^D and D_e^R .

Discussion

The evaluation of D_e^D and D_e^R values from the pore size distribution is outside the scope of this work. However, if the porous solid may be assumed to be a bundle of capillary tubes of uniform size, D_e^D and D_e^R will be expressed in terms of the diffusivity in the capillary tube, the number of tubes, and the tortuosity factor. If there are no deadends of macropores originally in the solid, then the defined capillary tubes or average pores must be macropores in the inert system and micropores in the reacting system. If some of the macropores are deadend, however, the average pore under inert conditions will change toward the detours or original micropores because of their controlling diffusion step while the average pores under reaction conditions are still micropores because of their large amount of internal surface area where chemical reaction takes place.

Actual pore structure is far more complicated. In determining pore size distribution, the ink-bottle macropores are measured as many micropores. If such a solid sample is broken into fine pieces, some of the ink-bottle macropores will become ordinary macro- and micropores. We measured the macropore size distribution of a commercial silica-alumina catalyst pellet in a mercury porosimeter and found that the volume occupied by mercury at equilibrium at each pressure increased somewhat (a few percent) with a decrease of sample size from 12 mm to a few millimeters. For further fine particles, however, we have failed in measuring macropore volume; the mercury penetration-pressure relations were considerably different from those for particles of a few millimeters. Probably this is a result of the fact that there is a kind of packed bed of fine particles formed in the dilatometer, and the extraparticle void behaves like macropores. More work seems necessary to interpret measured pore size distribution and to examine actual pore structure.

Conclusions

The D_e^D values determined from unsteady-state measurements are verified to be the same as the steady-state values. The D_e^R values are expected to be lower than D_e^D values if there are many macropores all through the whole pellet. The difference between D_e^D and D_e^R values decreases considerably by deadend of macropores. The latter will probably be the case for many actual catalyst pellets.

Appendix

Numerical Calculation for Pore Model. Figure 7 is the two-dimensional network of passageways. The steady-state concentration at each nodal point is computed as outlined below:

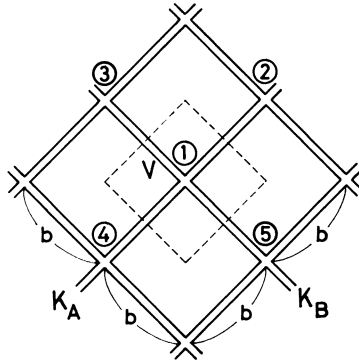


Figure 7. Sketch illustrating nomenclature for numerical calculation

(1) UNSTEADY state with no chemical preaction. From a mass balance on a point such as 1 (for symbols also see Figure 7),

$$K_A(c_2 + c_4 - 2c_1) + K_B(c_3 + c_5 - 2c_1) = \frac{V}{\Delta t} (c'_1 - c_1) \quad (\text{A1})$$

where $K_A, K_B = r_i D_i / b$ for micro passageway
 $= r_a D_a / b$ for macro passageway
 $V = 2r_i b + r_i^2$ for micro-micro intersection
 $= (r_i + r_a)b + r_i r_a$ for macro-micro intersection
 $= 2r_a b + r_a^2$ for macro-macro intersection
 $c_j =$ concentration at node j at time t
 $c'_1 =$ concentration at node 1 at $t + \Delta t$

(2) STEADY state with no chemical reaction.

$$K_A (c_2 + c_4 - 2c_1) + K_B (c_3 + c_5 - 2c_1) = 0 \quad (\text{A2})$$

(3) STEADY state with chemical reaction (first-order).

$$K_A (c_2 + c_4 - 2c_1) + K_B (c_3 + c_5 - 2c_1) = 4bkc_1 \quad (\text{A3})$$

where $4b =$ wall area of passageways and is related to a (Equation 17).

$$a = \frac{4b}{(b + r_i)^2} \quad \text{for micro-micro passageways}$$

$$= \frac{4b}{(b + r_i)(b + r_a)} \quad \text{for macro-micro passageways}$$

$$= \frac{4b}{(b + r_a)^2} \quad \text{for macro-macro passageways}$$

(4) DEADEND PORES. If there is a deadend midway between nodes 1 and 2, for example, Equations A2 and A3 become, respectively

$$K_A (c_4 - c_1) + K_B (c_3 + c_5 - 2c_1) = 0 \quad (\text{A4})$$

$$K_A (c_4 - c_1) + K_B (c_3 + c_5 - 2c_1) = 4bkc_1 \quad (\text{A5})$$

Nomenclature

A	external surface area, cm^2
a	internal surface area per unit volume, cm^{-1}
b	length of subrod, cm
c	concentration of diffusing gas, mole/cc
c_0	concentration of diffusing gas at $z = 0$ (nitrogen in experiments), mole/cc
D_a	diffusivity in macropore, cm^2/sec
D_i	diffusivity in micropore, cm^2/sec
D_e^D	effective diffusivity for inert system, cm^2/sec
D_e^R	effective diffusivity for reacting system, cm^2/sec
k	chemical reaction rate constant, cm/sec
L	height of solid or grid, cm
N_0	diffusion rate at $z = 0$, mole/sec
N_L	diffusion rate at $z = L$, mole/sec
R	total reaction rate, mole/sec
r_a	width of macropore, cm
r_i	width of micropore, cm
t	time, sec
t_0	time of pulse, sec
z	distance variable, cm
ϵ_p	void fraction
λ	$L \sqrt{\frac{\epsilon_p s}{D_e^D}}$
ϕ	$L \sqrt{\frac{ka}{D_e^R}}$

Literature Cited

- Steisel, N., Butt, J. B., *Chem. Eng. Sci.* (1967) **22**, 469.
- Foster, R. N., Butt, J. B., *AIChE J.* (1966) **12**, 180-185.
- Balder, J. R., Petersen, E. E., *J. Catal.* (1968) **11**, 195-210.
- Toei, R., Okazaki, M., Nakanishi, K., Kondo, Y., Hayashi, M., Shiozaki, Y., *J. Chem. Eng. Japan* (1973) **6**, 50-58.
- Wakao, N., Naruse, Y., *Chem. Eng. Sci.* (1974) **29**, in press.

RECEIVED January 2, 1974.

Gas Mixing in Fluidized Beds as a Function of the Adsorbency of the Solids for the Gas

H. V. NGUYEN and O. E. POTTER

Department of Chemical Engineering, Monash University, Wellington Road, Victoria 3168, Australia

Backmixing studies of gas mixing were done with non-adsorptive helium and adsorptive Freon-12 as tracers in a 12-inch id fluidized bed, charged with two average sizes (145 and 258 μ) of a porous adsorbent solid. Tracer is injected across a plane in the upper section of the bed, is sampled below the injection plane both radially and axially, and the radial values are averaged. The results are interpreted in terms of the countercurrent backmixing model, modified by terms involving gas transport from the cloud-wake region to the dense phase region caused by exchange of solids bearing adsorbed gas. Backmixing is enhanced by adsorption. The bed approaches a well-mixed state when the adsorptivity coefficient, $m \geq 5$ and $U/U_{mf} \geq 7$.

Reactor models for fluidized bed reactors, proposed by Davidson and Harrison (1), Partridge and Rowe (2), Van Deemter (3), Van Swaay and Zuideweg (4) have not—except for Chiba and Kobayashi (5)—included the terms for transport of reactants in the adsorbed state. The present study was done to determine the importance of adsorptive mixing in reactor models. Measurements of backmixing by Miyauchi *et al.* (6) using tracers of varying adsorbency confirmed that the greater the adsorptivity the greater the axial mixing (apparent diffusion) coefficient. The simple one-phase diffusional model used by Miyauchi *et al.* (6) does not successfully correlate the data (7). Yoshida, Kunii, and Levenspiel (8) investigated the response of a bed to a step disturbance using tracers of different adsorptivity.

Potter and co-workers used a backmixing technique for mixing studies with non-adsorbent solids (9, 10, 11). Tracer injected uniformly across a plane in the top of the bed was measured upstream—*i.e.*, at different depths below the plane of injection. The countercurrent backmixing model (9, 10, 11, 12) was used to determine f_w , the ratio of the volume of the wake to the volume of the bubble, and the overall gas exchange coefficients between bubble and dense phase. Here, a porous adsorptive solid is used with helium—which is not adsorbed—and Freon-12—which is adsorbed—to evaluate the influence of adsorption on the solids mixing.

Countercurrent Backmixing Model Modified for Adsorptive Transfer

Gas Exchange. The basis for the gas exchange rate is the same as that used by Kunii and Levenspiel (13)—*viz.*, that transfer between bubble and cloud wake follows the suggestion of Davidson and Harrison (1):

$$K_{BC} = 4.5 \frac{U_{mf}}{D_e} + 5.85 \frac{D^{1/2} U_{mf}^{1/4}}{D_e^{5/4}} \quad (1)$$

while transfer between the cloud-wake and the dense phase is given by a Higbie-type relation calculated (13) to be:

$$K_{CP} = 6.78 \left(\frac{\epsilon_{mf} D U_A}{D_e^3} \right)^{1/2} \quad (2)$$

Solids Exchange. Solids (not including associated gas in the solid phase) are assumed to be exchanged between the cloud-wake and the dense phase at a volumetric rate:

$$K_B' = \frac{U_b K_o f_w (U - U_{mf})(1 - \epsilon_{mf})}{D_e U_A} \quad (3)$$

as suggested by Potter (7) who used measurements with single bubbles to arrive at $K_o = 1 \pm 0.5$. An alternative expression would be that proposed by Kunii and Levenspiel (13):

$$K_o = \frac{3 U_{mf}}{(1 - \epsilon_b) \epsilon_{mf} U_b f_w} \quad (4)$$

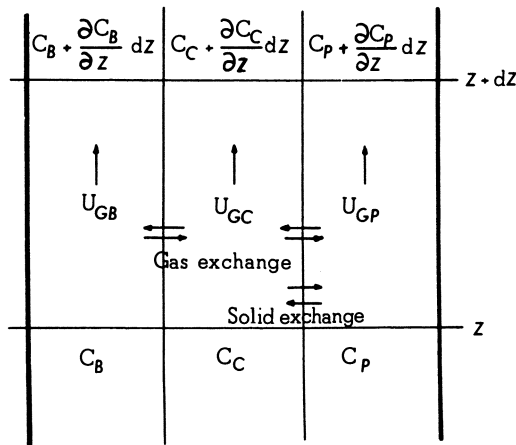


Figure 1. Three-phase representation of an ag-gregatively fluidized bed

Ratio of Cloud-Wake Volume to Bubble Volume. The ratio of cloud-wake volume to bubble volume f_w can be determined from the critical velocity for backmixing (see Figure 6); this is the intercept velocity for zero axial diffusion coefficient. At velocities greater than critical for backmixing, the axial diffusion coefficient rises above zero while at velocities below critical, there is no back-

mixing. The critical velocity for backmixing in non-adsorptive cases was calculated by Stephens *et al.* (12) as:

$$\text{Non-adsorptive: } \frac{U_{crit}}{U_{mf}} = 1 + \frac{1}{\epsilon_{mf} f_w} \tag{5}$$

For the adsorptive case Potter (7) modified Equation 5 as:

$$\text{Adsorptive: } \frac{U_{crit}}{U_{mf}} = 1 + \frac{1}{\epsilon_{mf} f_w + m(1 - \epsilon_{mf}) f_w} \tag{6}$$

$$\text{where bubble gas flow: } U_{GB} = U - U_{mf} \tag{7}$$

Table I. Solid Properties

Solid Size, μ	Apparent (Bulk) Density, lb/ft ³	Absolute Density, lb/ft ³	Pore Volume, %	Coefficient of adsorption m with Freon-12
145	75.5	142.6	20.6	2.5 ± 0.2
258	76.0	143.3	21.0	2.4 ± 0.2

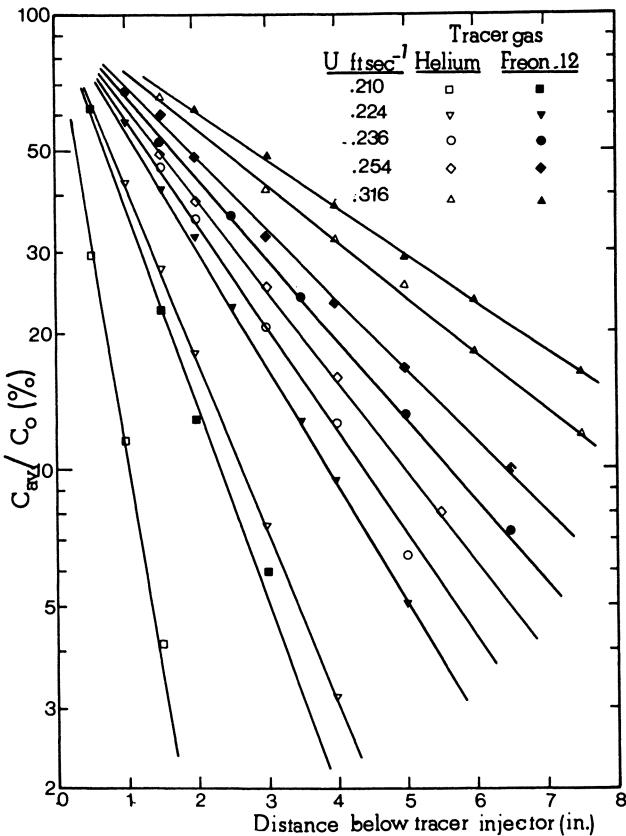


Figure 2. Axial backmixing profiles of concentration (averaged over the section). Particle size 145 μ m, $U_{mf} = 0.083$ ft/sec. Distributor contains 100 bubble caps.

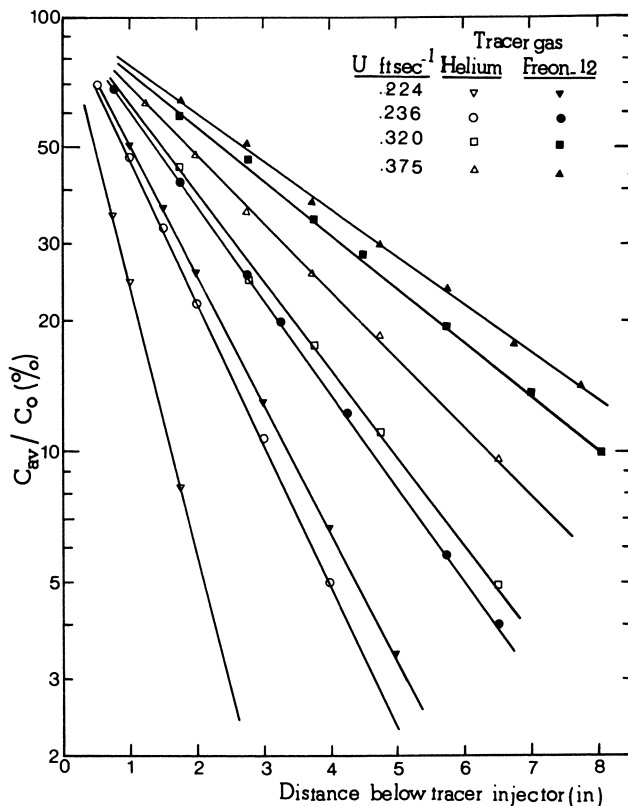


Figure 3. Axial backmixing profiles of concentration (averaged over the section). Particle size $145 \mu\text{m}$, $U_{mf} = 0.083 \text{ ft/sec}$. Distributor contains seven tuyeres.

Here an allowance for the cross-sectional area taken up by bubbles and wakes is neglected (13, 14).

$$\text{Cloud-wake gas flow: } U_{GC} = \epsilon_{mf} f_w U_{GB} \quad (8)$$

$$\text{Dense phase gas flow: } U_{G2} = U - (U_{GB} + U_{GC}) \quad (9)$$

$$\begin{aligned} \text{Solids set in motion by the bubble} &= (1 - \epsilon_{mf}) f_w U_{GB} \quad (10) \\ &= \frac{U_{GC}}{\epsilon_{mf}} (1 - \epsilon_{mf}) \end{aligned}$$

Material Balances

The flows and exchanges are shown in Figure 1. Material balances are as follows:

Bubble phase:

$$U_{GB} \frac{dC_B}{dz} + K_{BC} \epsilon_B (C_B - C_C) + \frac{\epsilon_{B0}}{1 - \epsilon_{B0}} m U_{GB} \frac{dC_B}{dz} = 0 \quad (11)$$

Cloud-wake phase:

$$U_{GC} \frac{dC_C}{dz} + K_{BC} \epsilon_B (C_C - C_B) - K_{CP} \epsilon_B (C_P - C_C) + K_S' m (C_C - C_P) \quad (12)$$

$$+ \frac{1 - \epsilon_{mf}}{\epsilon_{mf}} m U_{GC} \frac{dC_C}{dz} = 0$$

Dense phase:

$$U_{GP} \frac{dC_P}{dz} + K_{CP} \epsilon_B (C_P - C_C) + K_S' m (C_P - C_C) \quad (13)$$

$$- \frac{(1 - \epsilon_{mf})}{\epsilon_{mf}} m U_{GC} \frac{dC_P}{dz} = 0$$

If C_P and C_C are eliminated, a third-order differential equation in C_B is

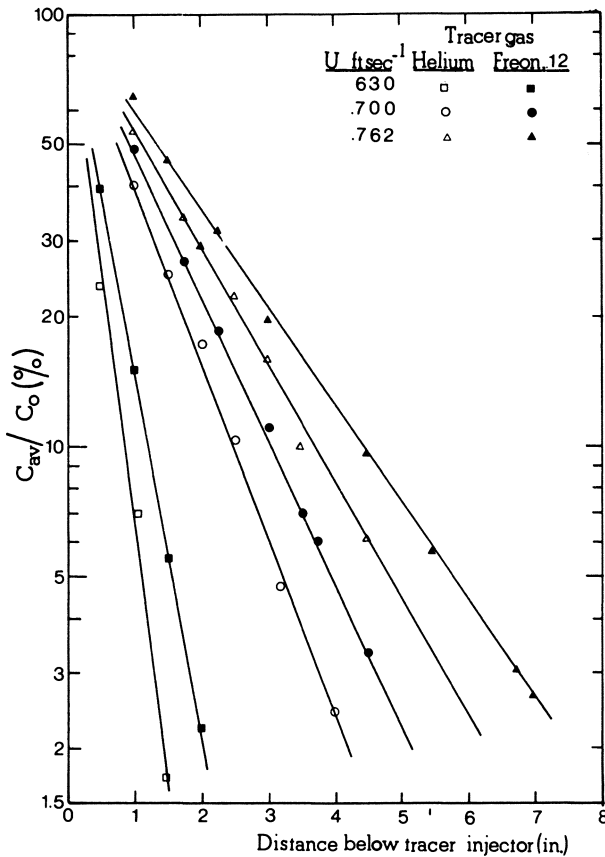


Figure 4. Axial backmixing profiles of concentration (averaged over the section). Particle size 258 μm , $U_{mf} = 0.218$ ft/sec. Distributor contains 100 bubble caps.

obtained:

$$A \frac{d^3 C_B}{dz^3} + B \frac{d^2 C_B}{dz^2} + C \frac{dC_B}{dz} = 0 \quad (14)$$

with boundary conditions:

$$z = 0, \quad C_B = C_{B0} \quad (15)$$

$$z = -\infty, \quad C_B = 0, \quad \text{and} \quad \frac{dC_B}{dz} = 0$$

The solution is given in the Appendix:

$$C_B = C_{B0} e^{\lambda_1 z} \quad (16)$$

where λ_1 is the positive root of the characteristic equation:

$$A\lambda^2 + B\lambda + C = 0 \quad (17)$$

Hence a graph of $\ln(C_B/C_{B0})$ vs. $(-z)$ yields a straight line of slope $(-\lambda_1)$. Since this slope is the same for each phase, sampling is not a serious problem.

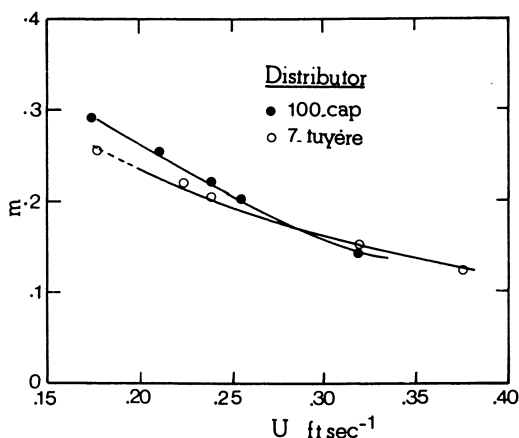


Figure 6. Axial diffusivity as measured by back-mixing as a function of gas velocity U , tracer gas, and distributor

Experimental

The column was 12 inches in diameter and 2 ft 6 inches high. A de-entrainment section of equal dimensions was fitted on top. Solid used was pre-fired clay, obtained from grinding unglazed pottery pieces. Each load was closely sized, and particle properties are listed in Table I. Air was the fluidizing medium with helium and Freon-12 as tracers. The tracers injector consisted of 32 $\frac{1}{4}$ -inch MS pipes, each with three horizontally drilled No. 64 holes as injecting ports. In operation, only the tips of these pipes with injecting holes were submerged in the column to minimize interference to the bed. Gas was sampled by a probe with a $\frac{1}{2}$ inch tip, equipped with a sintered glass filter.

The probe could travel both radially and axially and was held rigidly at each sampling position. On-stream analysis of tracer gas concentration was done by thermoconductivity cells. The pressure in the cells was kept constant, and a thermostated housing provided constant temperature surrounding for the cells. Two distributors were used, one with 100 $\frac{3}{8}$ -inch bubble caps and one with seven 3-inch tuyeres of type B used and described by Whitehead (15). Bubble frequency at any height was determined by filling the bed with different solid charges and filming, at high film speeds, the bubbles that burst at the surface. The average experimental radial concentration at any axial point was computed by integrating the radial profiles. The adsorption coefficient m was measured in a 1-inch diameter bed, packed with solids to a depth of 6 inches.

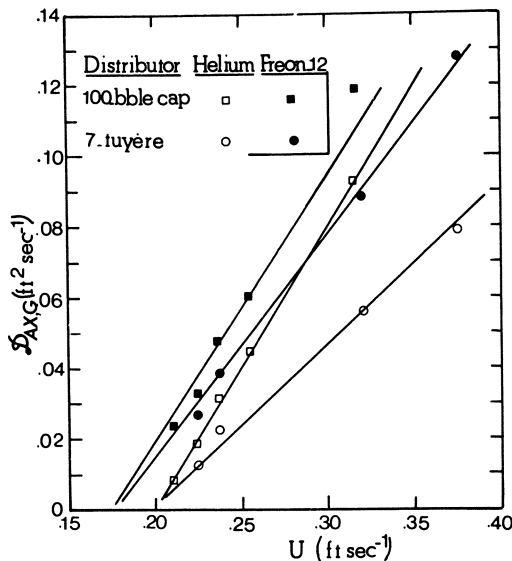


Figure 5. Variation in the apparent adsorption coefficient with gas velocity U . Compare with $m = 2.5$ at equilibrium.

The mass transfer coefficients were determined from non-adsorptive runs first; these coefficients were corrected for the difference in diffusivity of tracer gases, and then fitted to the adsorption coefficients m . Since no independent evaluation of each transfer coefficient was available from experimental data, the predicting Equations 1 and 2 were used for comparison with the experimental values. In all cases, the experimental values were about three times the predicted values. The reasons for this are not known.

Results and Discussion

Results are shown as axial tracer concentration profiles in Figures 2, 3, and 4. Because of imperfect mixing and disturbances around the injecting ports, the tracer concentration at the plane of injection could not be accounted for with reliability. Therefore, it was necessary to extrapolate experimental data from lower depths to determine the average concentration at zero level and thus determine the ratio of C_{av}/C_0 at any level.

In each case, the tracer concentration was markedly increased by adsorption. Two major points emerged from the runs with adsorbable Freon-12:

(1) The adsorption was not in equilibrium. As the fluidizing velocity was increased, the value of m that fitted the experimental data decreased. This conclusion was also reached by Kunii and Levenspiel. Solids were constantly mixed, and little time was provided for equilibrium.

(2) There appeared to be a limiting value of m which corresponded to the critical fluidizing velocity. At this point, backmixing commenced, and for a given solid, the bubbles then were smallest at any given height because of the lower gas volume passing through the bed as bubbles. The low rising velocity therefore gave more opportunity for adsorption to occur. The value of $f_w = 1.50$ was determined from non-adsorptive runs using Equation 3; use of this value in Equation 4 yielded $m = 0.29$, corresponding with $U_{crit}/U_{mf} = 2.05$. Extrapolation of m at various fluidizing velocities showed this trend (Figure 5).

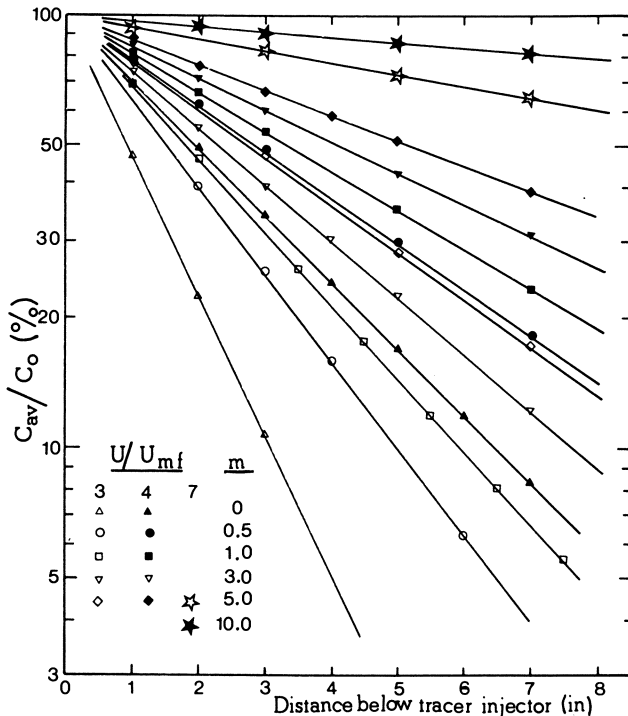


Figure 7. Axial concentration profiles predicted by the model. Gradients are small for $m \geq 5$ and $U/U_{mf} \geq 7$.

The enhancement of backmixing by adsorption is also evident in Figure 6 where results in terms of the apparent axial diffusivity for the tracer gas are plotted. $D_{AX,G}$ increases rapidly between the non-adsorptive and the adsorptive runs with the same distributor configuration.

The equations describing the model were also used to predict the backmixing concentration profile of a tracer as a function of the adsorptivity of the solid (Figure 7). It is evident from Figure 7 that the concentration of a tracer

injected at the top of the bed was almost uniform throughout the bed, when $m > 5$, $U/U_{mf} > 7$.

Conclusion

Adsorption enhances the rate of backmixing and thereby promotes a more uniform concentration in the bed. This effect must be taken into account in models of fluid bed reactors. However, the model used here is based on adsorptive equilibrium, and the results suggest that this does not apply. However, when so many parameters are required it is possible that equilibrium does exist but that other parameters vary. Also, under diffusion-limited conditions, adsorptive transport will increase the net reaction rate.

A fundamental difficulty in including adsorption in fluid bed reactor models is the more or less complete lack of required information on the catalytic chemisorptive or adsorptive behavior. We scarcely have rate equations that represent the data, let alone tell us how much of each species is adsorbed on the surface. This comment applies to the steady state. The position is worse when we consider the unsteady-state behavior of a reaction occurring on a particle moving from the wake to the dense phase. A careful reactor study by Fryer and Potter (14) showed fairly good agreement between experiment and the countercurrent backmixing model without adsorptive transport. That study, however, used nonporous particles.

Nomenclature

A, B, C	coefficients in Equations 14 and 17
C_B	concentration of tracer in bubbles, lb/ft ³
C_{B_o}	concentration of tracer in bubbles at injection plane, lb/ft ³
C_C	concentration of tracer in cloud wake, lb/ft ³
C_D	concentration of tracer in dense phase, lb/ft ³
C_{av}	average concentration of tracer, lb/ft ³
C_o	average concentration of tracer at injection plane, lb/ft ³
D	column diameter, ft
D_e	bubble diameter, ft
D	diffusivity coefficient, ft ² /sec
$D_{AX, G}$	apparent axial diffusivity of gas component, ft ² /sec
f_w	wake-to-bubble ratio
g	gravitational acceleration, ft/sec ²
H	height of bed, ft
K_o	constant in Equation 3
K_{BC}	gas transfer coefficient from bubble to cloud wake, sec ⁻¹
K_{CP}	gas transfer coefficient from cloud-wake to dense phase, sec ⁻¹
K_S'	solid exchange coefficient, sec ⁻¹
m	adsorption coefficient (gram mole/cm ³ solid)/(gram mole/cm ³ gas)
U	superficial fluidizing velocity, ft/sec
U_A	rise velocity of bubbles in a swarm, ft/sec
U_b	rise velocity of a single bubble, ft/sec
U_{crit}	critical velocity at which backmixing starts
U_{GB}	bubble gas velocity, ft/sec
U_{GC}	cloud-wake gas velocity, ft/sec
U_{GP}	dense phase gas velocity, ft/sec
U_{mf}	incipient fluidizing velocity, ft/sec

Greek Letters

ϵ_{BO}	fraction of solids in bubble
ϵ_B	fraction of bed made up by bubbles
ϵ_{mf}	incipient voidage
λ_1, λ_2	roots of the characteristic Equation 17

Appendix

Solution for Equation 14:

$$A \frac{d^3 C_B}{dz^3} + B \frac{d^2 C_B}{dz^2} + C \frac{dC_B}{dz} = 0 \quad (14)$$

If

$$A_1 = \frac{U_{GB}}{K_B C \epsilon_B}$$

$$A_2 = K_{CP} \epsilon_B + K_B' m$$

$$A_3 = A_1 \left[1 + \frac{K_B C \epsilon_B}{A_2} \right] + \frac{U_{GC}}{A_2} \left[1 - \frac{1 - \epsilon_{mf}}{\epsilon_{mf}} m \right]$$

$$A_4 = U_{GC} \frac{A_1}{A_2} \left[1 + \frac{1 - \epsilon_{mf}}{\epsilon_{mf}} m \right]$$

$$A_5 = U_{GP} \left[1 - \frac{1 - \epsilon_{mf}}{\epsilon_{mf}} m \frac{U_{GC}}{U_{GP}} \right]$$

Then

$$A = A_4 A_5$$

$$B = A_3 A_5 + A_2 A_4$$

$$C = A_5 + A_2 (A_3 - A_1) = U > 0$$

When backmixing takes place in the fluidized bed, $U_{GP} < 0$; thus $A < 0$.
Solution to Equation 14 is:

$$\frac{dC_B}{dz} = C_1 e^{\lambda_1 z} + C_2 e^{\lambda_2 z} + C_3$$

and

$$C_B = \frac{C_1}{\lambda_1} e^{\lambda_1 z} + \frac{C_2}{\lambda_2} e^{\lambda_2 z} + C_3 z + C_4$$

where $\lambda_2 < 0 < \lambda_1$ are roots of the characteristic equation

$$\text{At } z = -\infty, \quad \left. \frac{dC_B}{dz} \right|_{-\infty} = 0 = 0 + C_2 e^{-\lambda_2 \infty} + C_3$$

The only solution is:

$$C_2 = C_3 = 0$$

Therefore

$$C_B = \frac{C_1}{\lambda_1} e^{\lambda_1 z} + C_4$$

At $z = -\infty$

$$C_B \Big|_{-\infty} = 0 = 0 + C_4$$

Thus, $C_A = 0$

At $z = 0$

$$C_B \Big|_0 = C_{B_0} = \frac{C_1}{\lambda_1}$$

Therefore, in general

$$C_B = C_{B_0} e^{\lambda_1 z}$$

Literature Cited

1. Davidson, J. F., Harrison, D., "Fluidised Particles," Cambridge University Press, 1963.
2. Partridge, B. A., Rowe, P. N., *Trans. Inst. Chem. Eng.* (1966) **44**, T335.
3. Van Deemter, J. J., *Chem. Eng. Sci.* (1961) **13**, 143.
4. Van Swaay, W. P. M., Zuideweg, F. J., *Preprint, Int. Congr. Fluidization Its Applications, 1973, Toulouse, France.*
5. Chiba, T., Kobayashi, K., *Preprint, Int. Congr. Fluidization Its Applications, 1973, Toulouse, France.*
6. Miyachi, T., Kaji, H., Saito, K., *J. Chem. Eng. Japan* (1968) **1**, 72.
7. Potter, O. E., in "Fluidization," J. F. Davidson, D. Harrison, Eds., Academic, London, 1971.
8. Yoshida, K., Kunii, D., Levenspiel, O., *Ind. Eng. Chem., Fundamentals* (1969) **8**, 402.
9. Latham, R. L., Hamilton, C. J., Potter, O. E., *Brit. Chem. Eng.* (1968) **13**, 666.
10. Latham, R. L., Potter, O. E., *Chem. Eng. J.* (1970) **1**, 152.
11. Hamilton, C. J., Fryer, C., Potter, O. E., *Chemeca '70 Conf., Acad. Sci., Inst. Chem. Eng., Australia* (Butterworth) (1970).
12. Stephens, G. K., Sinclair, R. J., Potter, O. E., *Powder Technol.* (1967) **1**, 157.
13. Kunii, D., Levenspiel, O., "Fluidization Engineering," Wiley, New York, 1969.
14. Fryer, C., Potter, O. E., *Preprint, Int. Congr. Fluidization Its Applications, 1973, Toulouse, France.*
15. Whitehead, A. B., Dent, D. C., *Proc. Int. Symp. Fluidization, Eindhoven, Netherlands, 1967*, 802.

RECEIVED January 2, 1974.

Mathematical Modeling of the Sorption of Volatile Components in Newtonian, High-Viscous Liquids with the Aid of Bubbling

JOHANNES P. ROOS

Corporate Research Department, Akzo Research Laboratories,
Arnhem, The Netherlands

With the aid of capillaries gas is bubbled through a viscous liquid contained in a vessel to add or extract some volatile components to or from the viscous liquid. A general mathematical model is presented for this sorption. Theoretical and experimental literature data on bubble formation, velocity of rise, and mass transfer, especially with regard to viscous liquids are discussed. The results of lab-scale experiments for bubble behavior in polyisobutene (viscosity: 15–50 kgrams/msec) agree well with theoretical predictions. The mathematical model was used to calculate the desorption rates of water and lactam from a nylon 6 melt, and these results agree well with data from pilot-plant measurements.

This paper deals with a general steady-state sorption process. A diagram of a continuously operating, gas-liquid contacting reactor is shown in Figure 1. Liquid is fed at a volumetric flow rate V ; gas is injected through n capillaries at a total volumetric gas flow rate G ; and the temperature is constant throughout the reactor. The total amount of mass absorbed into or desorbed from the liquid is small compared with the liquid mass. Thus, the liquid density and the liquid flow rate can be assumed to be constant.

Consider a number of I components indicated as $i = 1, 2, \dots, I$. The concentrations in the liquid are c^i . The liquid is described as an ideal mixer because in the lab-scale experiments (discussed below) liquid circulations induced by the rising bubbles were visible. The circulation time (about 1 min) is shorter than the liquid residence time (about 1 hr). If necessary, other types of flow patterns can easily be incorporated into the model.

Let c_{in}^i be the concentration of component i in the liquid feed, and let $Q^i(0)$ and $Q^i(H)$ be the molar flow rates of component i in the bubble phase entering and leaving the liquid, respectively. The overall mass balances can be written as:

$$c^i V + Q^i(H) = c_{in}^i V + Q^i(0) \quad (1)$$

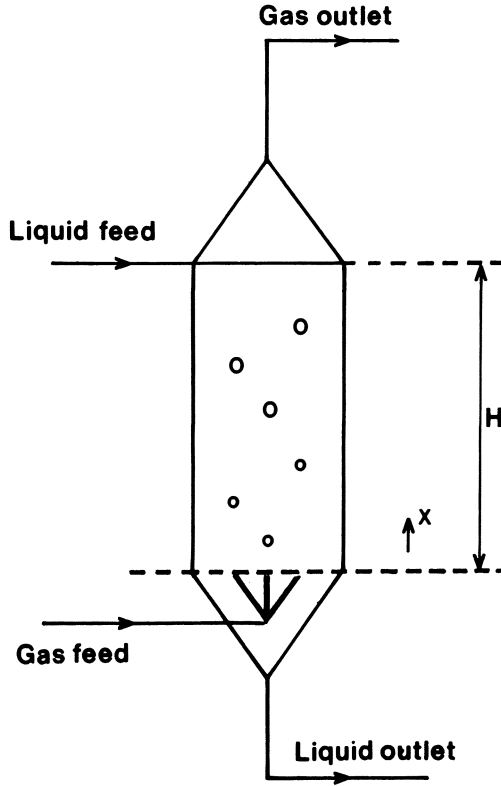


Figure 1. Continuous gas-liquid reactor

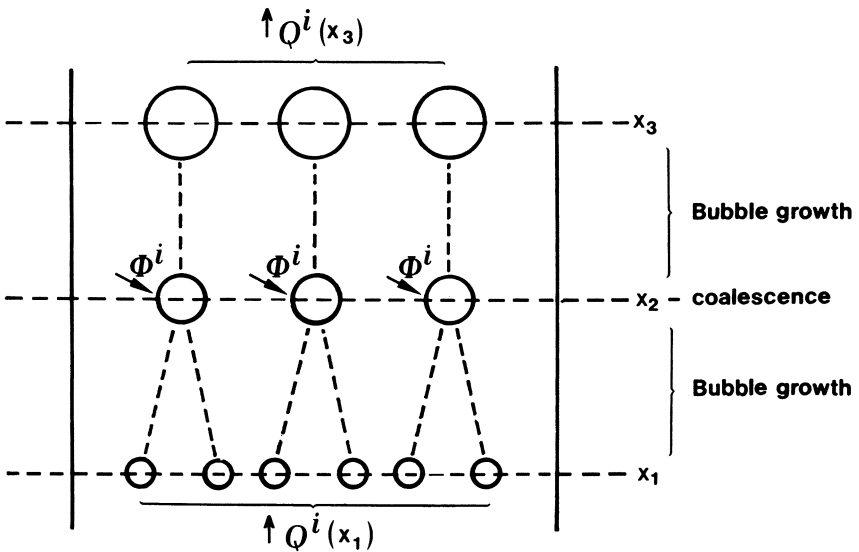


Figure 2. Rising bubbles with growth and horizontal coalescence

Mass Balances in the Bubble Phase

At the orifices \dot{N}_0 bubbles are formed per unit time. As a bubble rises, its volume changes because of hydrostatic pressure, mass exchange with the liquid, and coalescence with a neighboring bubble. Because of coalescence the number of bubbles $\dot{N}(x)$ passing through a horizontal plane per unit time varies with the height x (see Figure 2); $\dot{N}(0) = \dot{N}_0$. Since coalescence between two bubbles is fast, we assume that it occurs instantaneously—*i.e.*, at particular heights. Thus, both $\dot{N}(x)$ and the molar mass M^i of component i in a bubble are discontinuous functions of x . However, the molar flow rate Q^i of component i in the bubble phase, which satisfies

$$Q^i = \dot{N}(x) M^i \quad (2)$$

is continuous.

Let v be the velocity of rise of a bubble; the number of bubbles per unit length then equals $\dot{N}(x)/v(x)$. Further, let $\Phi^i(x)$ be the molar flow rate of component i passing from the liquid into one bubble having its center at height x . The amount of component i transferred per unit time from the liquid into the bubbles between the heights x_1 and x_2 is given by

$$\int_{x_1}^{x_2} \Phi^i(x) \dot{N}(x) \frac{dx}{v(x)}$$

The mass balance for component i in the bubble phase now reads:

$$Q^i(x_2) - Q^i(x_1) = \int_{x_1}^{x_2} \Phi^i(x) \frac{\dot{N}(x)}{v(x)} dx$$

or, as a differential equation:

$$\frac{dQ^i}{dx} = \Phi^i \frac{\dot{N}}{v} \quad (3)$$

We define the coalescence function $f_c(x)$:

$$f_c(x) = \frac{\dot{N}(x)}{\dot{N}_0} \quad (4)$$

This function is discussed in detail under Coalescence. It can be assumed that the physical mass transfer between liquid and bubbles is determined by its resistance in the liquid phase (1). Let c_{int}^i be the concentration of component i in the liquid at the bubble interface, d be bubble diameter, and k^i be the coefficient of mass transfer; then

$$\Phi^i = k^i \pi d^2 (c^i - c_{\text{int}}^i) \quad (5)$$

It is assumed that at the interface between bubble and liquid the concentration in the gas phase (c_{gas}^i) is proportional to that in the liquid phase (c_{int}^i):

$$c_{\text{int}}^i = m^i c_{\text{gas}}^i = m^i \frac{6M^i}{\pi d^3} \quad (6)$$

This equation defines the distribution coefficient m^i . Its relationship to the saturated vapor pressure P^i of the pure component i can easily be derived from the ideal gas law and Henry's law:

$$p^i = \gamma^i P^i x^i \quad (7)$$

where p^i is the partial vapor pressure, γ^i is the activity coefficient of component i in the liquid, and x^i is the mole fraction of component i in the liquid. Thus,

$$m^i = \frac{\rho RT}{M \gamma^i P^i} \quad (8)$$

where ρ is the liquid density, M is the molecular weight of the liquid, R is the gas constant, and T is the absolute temperature. Let Q be the total molar flow rate in the bubble phase—*i.e.*, $Q(x) = \Sigma Q^i(x)$ (sum over all gases and vapors); the following equation relates bubble diameter d and total gas flow rate Q :

$$Q = \dot{N} \rho_b \frac{\pi}{6} d^3 \quad (9)$$

where ρ_b is the molar gas density.

Using Equations 2, 4, 5, 6, and 9, Equation 3 can be written as:

$$\frac{dQ^i}{dx} = f_c \dot{N}_o k^i \pi \frac{d^2}{v} \left(c^i - m^i \rho_b \frac{Q^i}{\Sigma Q^i} \right) \quad (10)$$

The molar gas density ρ_b depends on position x ; from the ideal gas law and the hydrostatic pressure (*see* Figure 1) it follows that

$$\rho_b = \frac{B + \rho g(H-x)}{RT} \quad (11)$$

where B is the pressure above the liquid, ρ is the liquid density, g is the acceleration from gravity, and H is the distance between the orifices and the liquid level. The amount of component i fed through the orifices per unit time is known. The initial conditions for the system of differential equations (*see* Equation 10) therefore read:

$$x = 0 \quad Q^i = Q^i(0) = \text{known} \quad (12a)$$

Comparing Equations 9 and 12a, we note that

$$Q(0) = \Sigma Q^i(0) = G \rho_b = \dot{N}_o \rho_b \frac{\pi}{6} d_o^3 \quad (12b)$$

where d_o is diameter of the bubble formed at an orifice. Since we wish to describe sorption especially in high-viscous liquids, our discussion on bubble behavior is directed to viscous liquids.

Bubble Formation

Since narrow capillaries are used, the gas flow rate in a capillary does not vary with time because of the large pressure drop in the capillary [constant-flow conditions according to Davidson and Schüler (2)]. There are three main physical models that describe bubble formation at an orifice. They have been developed by Van Krevelen and Hoftyzer (3), Davidson and Schüler (2), and Kumar, Kuloor, and co-workers (4, 5, 6).

Kumar and Kuloor's model gives a good description of bubble formation under widely varying conditions (4, 5, 6). It leads to the following equation

for the diameter d_o of a bubble formed at an orifice in a liquid with a viscosity higher than 0.5 kg/msec:

$$d_o = 2.36 \left(\frac{\nu G}{gn} \right)^{1/4} \quad (13)$$

where G/n is the volumetric gas flow rate per orifice and ν the kinematic liquid viscosity. The coefficient 2.36 in Equation 13 has the value of 2.42 according to Van Krevelen and Hoftyzer (3) and 2.31 according to Davidson and Schüler (2).

For high-viscous liquids no literature data are available. Table I gives some experimental data on bubble behavior in molten polyisobutene. Some experimental details are given in the Appendix. The fifth column of Table I gives a value of 2.3 for the coefficient in Equation 13, which is in good agreement with the theoretical one. The diameter of a bubble formed at an orifice in a high-viscous liquid such as polyisobutene is two to four times larger than that of a bubble formed in a low-viscous liquid at the same gas flow rate. In other words, the production at a sufficiently high rate of small bubbles in high-viscous liquids, which is desirable from the point of view of mass transfer, is not possible with the use of a simple capillary.

Table I. Experimental Data on Bubble Behavior in Polyisobutene
(see Appendix)

Experiment	μ (kg/ msec)	G/n (cm ³ / sec)	d_o (cm)	Con- stant ^a	\bar{v}^b (cm/ sec)	Ratio ^c	\bar{f}_c
2B	40.0	2.18	2.26	2.27	1.61	1.07	0.39
3	47.5	2.32	2.37	2.24	1.43	1.04	0.36
4	24.0	2.37	1.99	2.22	2.30	1.19	0.46
5	25.3	2.37	2.05	2.26	2.30	1.19	0.46
6	31.0	2.35	2.15	2.26	2.01	1.15	0.44
7	30.5	4.58	2.54	2.26	2.72	1.10	0.36
8	15.5	2.40	1.85	2.30	3.12	1.21	0.50
9	16.5	1.12	1.65	2.44	1.87	0.97	0.50
10	31.2	2.35	2.16	2.26	2.06	1.18	0.46
11	31.1	8.01	2.91	2.25	3.91	1.23	0.35
12	31.0	11.30	3.19	2.26	4.97	1.29	0.39
13	31.0	13.75	3.21	2.16	4.77	1.23	0.32
14	28.0	0.92	1.73	2.35	1.35	1.08	0.49
15	45.0	0.94	2.05	2.47	0.73	0.67	0.48

^a Constant in Equation 13, calculated.

^b Velocity of rise after one coalescence.

^c Ratio between the measured velocity of rise and the velocity calculated with the aid of Hadamard's Equation 18b.

Bubble Behavior during Rising

Since we are dealing with high-viscous liquids, we restrict ourselves to laminar flow. This means that the Reynolds number (Re) defined by

$$Re = \frac{vd}{\nu} \quad (14)$$

is less than about 2. In low-viscous liquids bubbles behave like solid spheres: velocity of rise and mass transfer are described by the corresponding equations derived for solid spheres (see Equation 18a and 19a); these bubbles are called rigid interface bubbles. The same holds for sufficiently small bubbles in a high-

viscous liquid (7, 8, 9). Larger bubbles in a high-viscous liquid, however, are internally mobile. They are still spherical, but the gas inside them circulates (9); they are called free interface bubbles.

Bond and Newton (7) have established a critical diameter d^* :

$$d^* = 2 \sqrt{\frac{\sigma}{\rho g}} \quad (15)$$

where ρ is the liquid density and σ is the surface tension; they suggested that bubbles with a larger diameter ($d > d^*$) have a free interface, and those with a smaller diameter have a rigid interface. Note that d^* is about 0.1–0.5 cm for any liquid. Experimental data of Garner and Hammerton (9), however, show that Equation 15 can only be used as a first approximation. The Reynolds number corresponding to the critical diameter d^* must be less than 2 so that the transition from rigid to free interface can take place under laminar flow conditions. This means that the fluidity number M satisfies:

$$M = \frac{g\mu^4}{\rho\sigma^3} > 10^{-2} \quad (16)$$

where μ is the dynamic viscosity; this corresponds to a viscosity of 0.1 kg/msec or higher. The interface mobility of bubbles in laminar flow can thus be characterized as:

$$\begin{aligned} M < 10^{-2}: & \text{ rigid interface} \\ M > 10^{-2}, d < d^*: & \text{ rigid interface} \\ M > 10^{-2}, d > d^*: & \text{ free interface} \end{aligned} \quad (17)$$

In the application discussed below the bubbles have a free interface, M being about 10^8 and the bubble diameter exceeding 1 cm.

Velocity of Rise

The velocity of rise v of a rigid interface bubble satisfies the Stokes' equation:

$$v = \frac{gd^2}{18\nu} \quad (18a)$$

The gas density has been neglected because it is small compared with the liquid density. Details on the derivation of Equation 18a are given by Schlichting (10). For a free interface bubble (Hadamard-Rybczynski) the velocity of rise satisfies (11):

$$v = \frac{gd^2}{12\nu} \quad (18b)$$

There is enough experimental evidence to show that Equation 18a holds for low-viscous liquids. For liquids with viscosities of 0.1 kg/msec or higher, however, Equation 18b applies as shown in Table II.

Table I gives some experimental data for molten polyisobutene. Column seven shows the ratio between the measured velocities and those calculated by Equation 18b. The measured velocity is too high, perhaps because of liquid circulations induced by the rising bubbles. This effect of liquid circulations on the velocity of rise of bubbles (12, 13) is not taken into consideration.

Table II. Experimental Data on the Relation between Velocity of Rise and Diameter for Bubbles Rising in a Liquid with a Viscosity of 0.1 kg/msec or higher

<i>Liquid</i>	v (cm ² /sec)	d_0 (cm)	v (cm/sec)	<i>Ratio</i> ^a	<i>Reference</i>
Sugar syrup	122	0.4	0.11	1	(7)
	122	1.2	0.97	1	
Oil (unspecified)	8.81	0.059	0.027	0.83	(14)
	9.95	0.088	0.048	0.75	
	8.87	0.119	0.102	0.79	
Glycerol	10.0	0.42	1.1	0.77	(9)
	12.1	0.36	0.87	1.00	
	12.1	0.48	1.45	0.94	
	12.1	0.24	0.37	0.99	
Dextrose/water	10.5	0.64	3.25	1	(15)
	21.6	0.37	1.41	1	
	21.6	1.04	4.13	1	
	23.0	0.54	1.05	1	
	23.0	1.09	4.22	1	
Glycerol/water	1.46	0.21	2.5	1	(16)
	1.46	0.38	8	1	
	6.17	0.61	5	1	
	6.17	0.87	10	1	

^a Ratio between the measured velocity of rise and the velocity calculated with the aid of Hadamard's Equation 18b.

Mass Transfer

Levich (11) has derived the following relations for mass transfer between bubbles and liquids in laminar flow. For rigid interface bubbles (Stokes' regime):

$$\text{Sh} = 0.65 \text{ Pe}^{1/3} \quad (19a)$$

For free interface bubbles (Hadamard's regime):

$$\text{Sh} = 1.01 \text{ Pe}^{1/2} \quad (19b)$$

where Sh is the Sherwood number (kd/D), Pe is the Peclet number (vd/D), and D is the diffusivity. Other workers have derived similar equations with slightly different values for the coefficients (17, 18). The mobility of the bubble interface is characterized by Equation 17. Generally, Pe is large (1000 or higher), so that mass transfer at a free interface is five times higher than that at a rigid interface. Recent experiments (15, 16) show that mass transfer between bubbles and liquids with viscosities of 0.1 kg/msec or higher does satisfy Hadamard's relation (Equation 19b).

Coalescence

Some studies of coalescence in liquids with viscosities up to 0.1 kgram/msec have been reported (19, 20). As far as we know, however, they have not yet resulted in a description of coalescence which can be extrapolated to a viscous melt.

Although it has been assumed that at any height the bubbles have the same diameter and velocity of rise, these quantities vary in practice. One

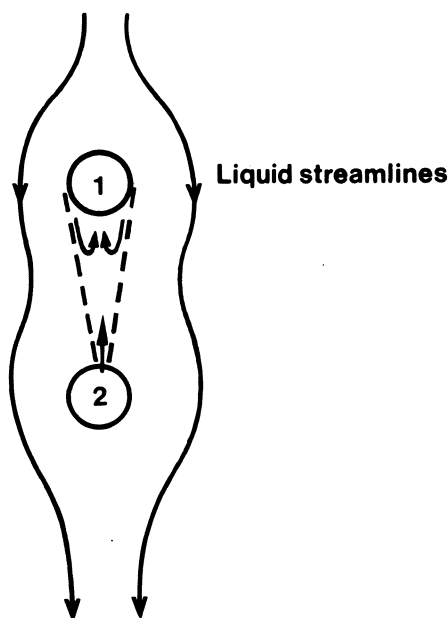


Figure 3. Initiation of vertical coalescence

cause of coalescence is that the rise of a bubble is accelerated by the wake of a neighboring bubble (see Figure 3). The rise of bubble 2, which is attracted by the wake of bubble 1, is accelerated, and after some time the two bubbles coalesce. Lab-scale experiments with polyisobutene have shown that the first coalescence occurs at about 5–10 cm from the orifices, the second coalescence at about 70–80 cm from the orifices, followed by a third, a fourth and sometimes a fifth coalescence. Figure 4 shows the relation between residence time and height of rise. The dots, where the velocity shows a jump, represent coalescence. These experiments show that coalescence is influenced by the gas flow rate and the viscosity.

Since coalescence is complex and since the total rate of sorption is important, it seems reasonable to take coalescence into account by using an average value of the function $f_c(x)$, defined in Equation 4. Let x_1, x_2, \dots, x_c be the heights x at which the 1st, 2nd, \dots , c^{th} coalescence occurs, and let $x_0 = 0, x_{c+1} = H$, then

$$\begin{aligned}
 f_c(x) &= 1 & x_0 < x < x_1 \\
 &= \frac{1}{2} & x_1 < x < x_2 \\
 &\vdots \\
 &= 2^{-c} & x_c < x < x_{c+1}
 \end{aligned} \tag{20}$$

The main effect of coalescence on the desorption is expected to be caused by an average value of $f_c(x)$, which is called the coalescence factor \bar{f}_c , defined as:

$$\bar{f}_c = \frac{1}{H} \int_0^H f_c(x) dx \quad (21)$$

From Equations 20 and 21:

$$\bar{f}_c = \sum_{i=0}^c \frac{x_{i+1} - x_i}{2^i H} \quad (22)$$

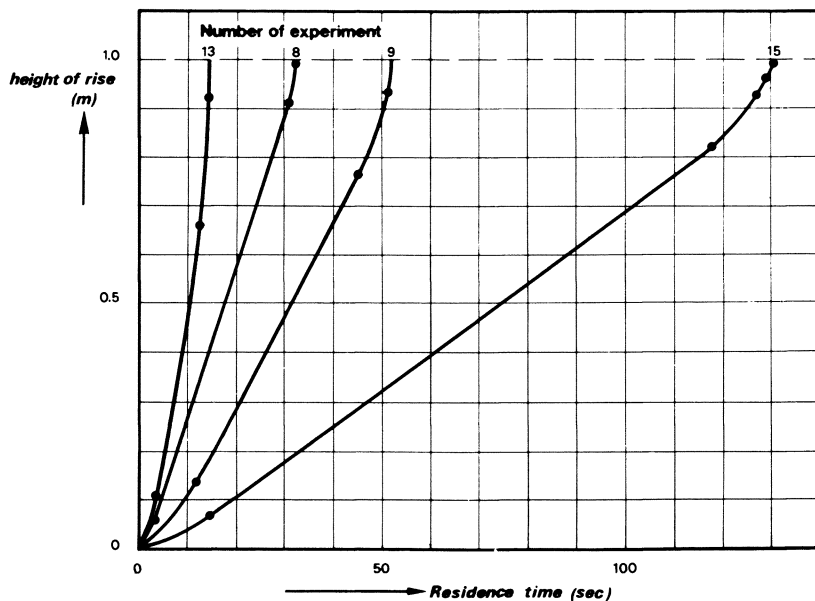


Figure 4. Height of rise of a bubble vs. residence time for some experiments reported in Table I. A jump in the slope (i.e., velocity of rise) corresponds to coalescence.

The coalescence factor calculated from lab-scale experiments with polyisobutene is given in Table I. For these experiments \bar{f}_c lies between 0.3 and 0.5. We assume that the overall effect of the coalescences can be described by a single coalescence immediately at the orifices:

$$\bar{f}_c = 0.5 \quad (23)$$

Coalescence considerably influences the desorption rate. In fact, if coalescence is neglected, with $\bar{f}_c = 1$, the desorption rates predicted for the application discussed in the following section would be 80% higher than in the case of $\bar{f}_c = 0.5$.

The pilot-plant scale application to be discussed was run under process conditions similar to those of the lab-scale experiments (similar dimensions, the same capillaries, similar liquid viscosity). For this application the use of Equation 23 is therefore justified, but it is not known how accurately this equation describes coalescence for other process conditions.

Application

Our model was applied to the extraction of water and caprolactam from a nylon 6 melt by N_2 . Details about N_2 injection are given in the Belgian patent

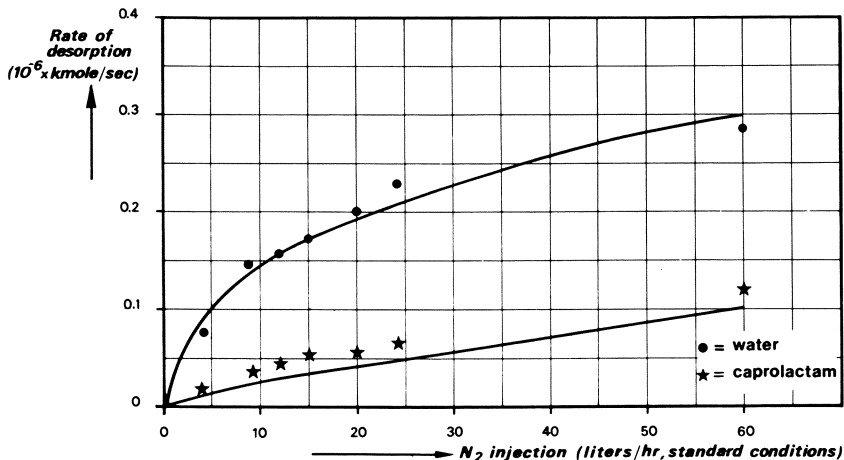


Figure 5. Influence of N_2 injection on water and caprolactam desorption: measured and calculated results

596,903 and in the British patents 987,963 and 1,004,558. We compare the extraction rates measured in pilot plant experiments with those calculated by the model which comprises Equations 1, 10, 11, 12, 13, 18b, 19b, and 23. Diffusivity, vapor pressure, and activity coefficients (Equations 24–29) were taken from other sources (literature, lab-scale experiments); these parameters were not adjusted on the basis of the results of pilot plant experiments carried out in a continuous reactor, which is shown in Figure 1.

The process conditions (constant in each experiment) chosen were:

pressure	atmospheric
throughput	690 kg/day (about 8 cm ³ /sec)
residence time	0.8–3.2 hrs
capillaries	see Figure 7, the same as in the lab-scale experiments
melt temperature	245°–280°C
polymer level	0.4–1.0 m
N_2 injection	4–90 liters/hr (standard pressure and temperature)
water content	0.06–0.24 moles/kg
caprolactam content	0.8–1.3 moles/kg
viscosity	ca. 40 kg/msec

Since the melt viscosity is about 40 kg/msec, the relations describing the bubble behavior for high-viscous liquids can be used. We also used the following parameters:

$$\text{water diffusivity } D^w = 5 \times 10^{-10} \text{ m}^2/\text{sec} \quad (24)$$

$$\text{caprolactam diffusivity } D^l = 10^{-8} \text{ m}^2/\text{sec (rough estimate)} \quad (25)$$

$$\text{vapor pressure of pure water } P^w = 10^5 \exp\left(12.53 - \frac{4628}{T}\right) \text{ N/m}^2 \quad (26)$$

$$\text{vapor pressure of pure caprolactam } P^l = 10^5 \exp\left(12.445 - \frac{6671}{T}\right) \text{ N/m}^2 \quad (27)$$

$$\text{activity coefficient of water } \gamma^w = 1.2 \quad (28)$$

$$\text{activity coefficient of lactam } \gamma^l = 1.5 \quad (29)$$

Viscosity. When Equations 13, 18b, and 19b are substituted into Equation 10, the total desorption rate is proportionate to $\nu^{-1/8}$; this leads to the unexpected conclusion that with high-viscous liquids the viscosity has only a minor influence on the desorption rate.

Diffusivity of Lactam. Because of the hydrophilic character of nylon 6, Van Krevelen (21) D^w was estimated to be about 5×10^{-10} m²/sec.

Diffusivity of Lactam. Because of the hydrophilic character of nylon 6, D^l is expected to be larger than D^w . Model calculations show that in this case caprolactam desorption is determined by vapor-liquid equilibrium and does not depend on the diffusivity of caprolactam. We do not quite agree with Nagasubramanian and Reimschuessel (22) who recently reported $D^w = 2.5 \times$

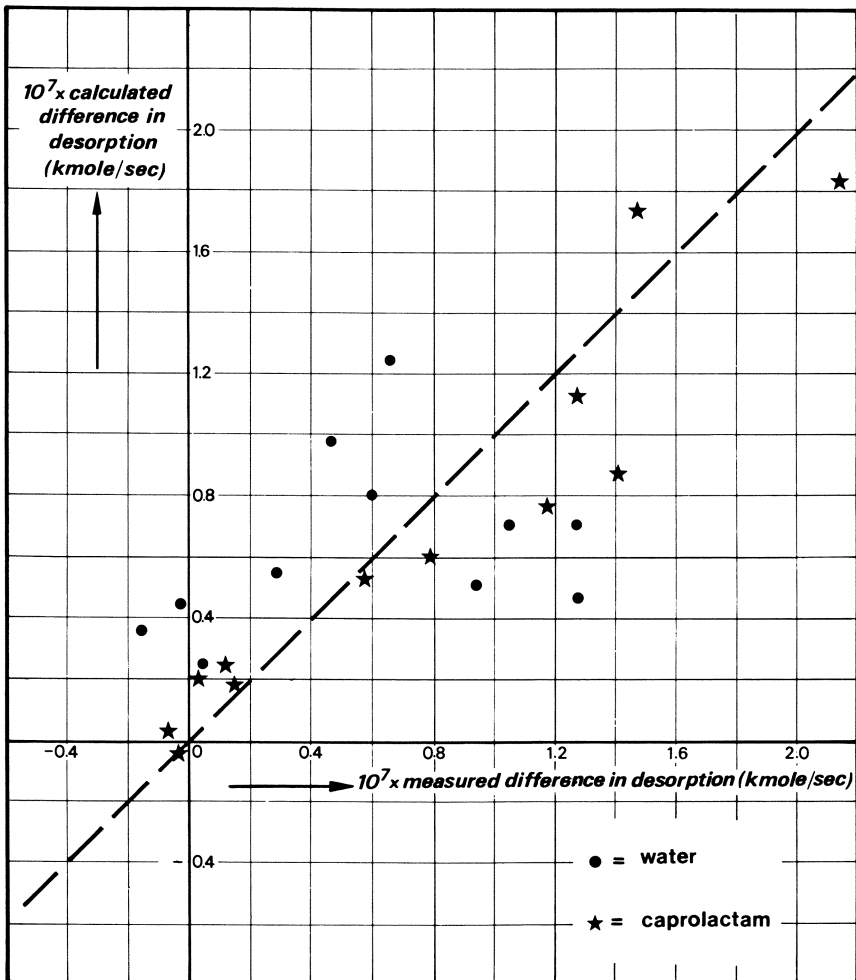


Figure 6. Measured and calculated differences in the water/caprolactam desorption for pilot plant experiments

10^{-8} m²/sec and $D^1 = 8 \times 10^{-12}$ m²/sec. Especially suspect, in our opinion, is their finding that caprolactam diffuses more slowly than water.

Vapor Pressure of Water. Equation 26 is based on well-known data (steam tables) for the temperature range considered.

Vapor Pressure of Lactam. Equation 27 is based on experimental data from others (23, 24 25).

Activity Coefficient of Water in a Nylon 6 Melt. Equation 28 is based on data of others (24, 26, 27).

Activity Coefficient of Caprolactam in a Nylon 6 Melt. Equation 29 is based on experimental data of others (24, 28).

The mathematical model for the desorption of caprolactam and water consists mainly of two differential equations which have been integrated numerically. Figure 5 shows the results of experiments in which all the process variables were kept constant, except the amount of N₂ injected; it also shows the calculated desorption rates. Figure 6 shows the results of many experiments; in these experiments, one process variable (polymer level or N₂ injection), was changed. The calculated and measured differences in the desorption rates are shown in Figure 6. Generally, the calculated results of the mathematical model developed agree well with the experimental data obtained in the pilot plant experiments.

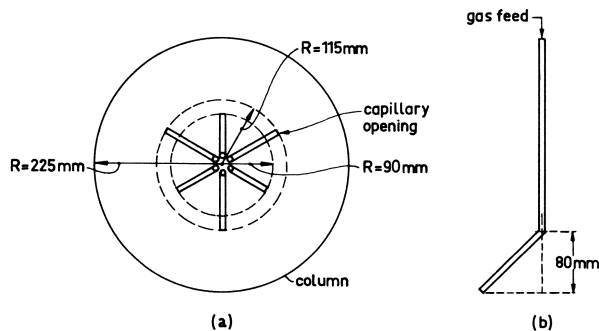


Figure 7. Position of the capillaries

Appendix

Table I gives data from measurements done under the following conditions. Dry air was injected into a Plexiglass column (height 1.5 m, inner diameter 45 cm) through 6 capillaries (outer diameter 6 mm, wall thickness 2 mm) with orifices positioned as shown in Figure 7. The column was filled with polyisobutene (density 900 kg/m³); its temperature was set and controlled; the settings varied between 16° and 32°C. The total gas flow rate was set by a pilot valve and measured by a Rotameter combined with a pressure gage. The flow rates of the partial streams to each capillary were controlled by needle valves in a distributing box. These rates were not measured individually; while counting the number of bubbles at each capillary, the needle valves can be set sufficiently accurately. The data of Table I were obtained from streams of bubbles widely spaced (about 5 to 10 cm). Vertically attached to the column is a graduated rod for measuring the bubble diameter.

Acknowledgment

Thanks are due to B. L. A. van der Schee and G. Plat who carried out the lab-scale experiments reported in Table I, and to B. Zoetbrood, P. G. M. Vermeulen and co-workers who guided the pilot-plant experiments. We thank the referees J. Bridgwater and W. Strieder for their valuable comments.

Literature Cited

1. Calderbank, P. H., in "Mixing, Theory and Practice," V. W. Uhl, J. B. Gray, Eds., Vol. II, Chap. XI, p. 88, Academic Press, New York, 1967.
2. Davidson, J. F., Schüler, B. O. G., *Trans. Inst. Chem. Engrs.* (1960) **38**, 144-54, 335-42.
3. Van Krevelen, D. W., Hoftyzer, P. J., *Chem. Eng. Progr.* (1950) **46**, 29-35.
4. Kumar, R., Kuloor, N. R., *Adv. Chem. Eng.* (1970) **8**, 255-368.
5. Krishnamurti, S., Kumar, R., Kuloor, N. R., *Chem. Process Engr.* (1968) 91-97, 100.
6. Ramakrishnan, S., Kumar, R., Kuloor, N. R., *Chem. Eng. Sci.* (1969) **24**, 731-47.
7. Bond, W. N., Newton, D. A., *Phil. Mag.* (1928) **5**, 794-80.
8. Haberman, W. L., Morton, R. K., *Am. Soc. Civil Engrs., Trans.* (1954) **121**, 227-50.
9. Garner, F. H., Hammerton, D., *Chem. Eng. Sci.* (1954) **3**, 1-11.
10. Schlichting, H., "Boundary Layer Theory," McGraw-Hill, New York, 1960.
11. Levich, V. G., "Physico-chemical Hydrodynamics," Prentice-Hall, New Jersey, 1962.
12. Crabtree, J. R., Bridgwater, J., *Chem. Eng. Sci.* (1969) **24**, 1755-68.
13. Happel, J., Brenner, H., "Low Reynolds Number Hydrodynamics," Prentice-Hall, New Jersey, 1965.
14. Robinson, J. V., *J. Phys. Colloid Chem.* (1947) **51**, 431-7.
15. Redfield, J. A., Houghton, G., *Chem. Eng. Sci.* (1965) **20**, 131-9.
16. Calderbank, P. H., Johnson, D. S. L., Loudon, L., *Chem. Eng. Sci.* (1970) **25**, 235-56.
17. Lochiel, A. C., Calderbank, P. H., *Chem. Eng. Sci.* (1964) **19**, 471-84.
18. Lindt, J. T., Ph.D. Thesis, Technological University of Delft, Holland (1971).
19. Crabtree, J. R., Bridgwater, J., *Chem. Eng. Sci.* (1971) **26**, 839-51.
20. De Nevers, N., Wu, J. L., *AIChE J.* (1971) **17**, 182-6.
21. Van Krevelen, D. W., "Properties of Polymers," North-Holland, Amsterdam, 1972.
22. Nagasubramanian, K., Reimschuessel, H. K., *J. Appl. Polymer Sci.* (1973) **17**, 1663-77.
23. Mizerovskij, L. N., Pajkacev, Ju. S., *Sovj. Beiträge Faserforsch. Textil.* (1969) **6**, 449-52.
24. Fukumoto, O., *Konunski Kagaku* (1961) **18**, 19-21.
25. Hodgeman, C. D., "Handbook of Chemistry and Physics," Chemical Rubber Co., Cleveland, 1965.
26. Van Velden, P. F., van der Want, G. M., Heikens, D., Kruissink, Ch. A., Hermans, P. H., Staverman, A. J., *Rec. Trav. Chim.* (1955) **74**, 1376-94.
27. Wiloth, F., Dietrich, W., *Makromol. Chem.* (1956) **21**, 50-8.
28. Čefelin, P., Stehliček, J., Wichterle, O., *Collections Czechoslov. Chem. Commun.* (1959) **24**, 516-21.

RECEIVED January 2, 1974.

A Numerical Investigation of Model Reforming Reactions Using Porous Bifunctional Catalysts

R. A. AL-SAMADI, P. R. LUCKETT, and W. J. THOMAS

Department of Chemical Engineering, University of Bath,
Clavertown Down, Bath BA2 7AY, England

The chemical kinetics of a reforming action were modeled for reaction in the presence of a bifunctional catalyst as compounded pellets containing both catalyst components and as a discrete mixture of separate pellets each containing only one component. Intraparticle and interparticle mass and heat transfer were considered. For both models, no temperature gradients exist within the catalyst particles, and the major resistance to heat transfer is from fluid to catalyst particle. Reactors with a compounded catalyst were compared with those containing a mixture of discrete pellets. Highest yields occur for an optimally compounded catalyst with a constant composition in a single zone or as two different compositions in two successive zones. A compounded catalyst operating under non-isothermal conditions is relatively insensitive to catalyst composition.

Catalysts used to reform petroleum naphthas often consist of two active components—one promotes hydrogenation–dehydrogenation, and the other promotes isomerization. A highly dispersed noble metal such as platinum on porous silica-alumina is such a catalyst and is called bifunctional. The fact that an optimum catalyst formulation might be desirable was first suggested by Gunn and Thomas (1) following experiments of Weisz and Swegler (2) and Weisz (3). Further theoretical work (4, 5, 6) showed that an optimum profile, in which the catalyst composition varied from one component at the reactor inlet through a mixed composition to the second component near the reactor exit, further enhances throughputs. If the product is further degraded or if the reaction stoichiometry is described by two consecutive reactions (the first reversible and the second irreversible), then a bang-bang profile (consisting of one catalyst component filling one portion of the reactor and the second component packed in the remaining reactor length or a second reactor) proves to be the optimal policy. The more pragmatic and easily prepared constant composition profile is a sub-optimal alternative which gives relatively high throughputs.

When the two catalyst components are contained within a compounded catalyst rather than packed in the reactor as a discrete mixture of particles, higher throughputs and yields are predicted, except for those situations demanding a bang-bang solution when discrete particles are necessary. Jenkins and Thomas (7) determined the kinetics of reactions involved in the aromatization of methylcyclopentane; they computed the optimal composition profile for a mixture of discrete particles and compared this with work where the optimal policy was deduced by a hill climbing Simplex procedure. The experimental optimal profile agreed remarkably well with the computed optimal profile; hence it is not unreasonable that the theory, formulated for conditions where the reactor is isothermal and intraparticle mass transfer resistance negligible, can predict an optimal catalyst composition profile for certain reactions within an isothermally operated reactor. Mendiratta *et al.* (8) and Glasser and King (9) have since extended the theory to include kinetics other than pseudo-first order.

We investigated the effect of non-isothermal conditions and resistance to transport on reactors packed with bifunctional catalysts to establish those circumstances for which optimum policy decisions lead to substantially improved throughputs.

Transport and Reaction in Bifunctional Catalyst Pellets

The two catalyst components can be present as a discrete physical mixture of separate particles or as composite particles, each particle containing both active components. Since the latter arrangement is the way bifunctional catalysts are normally used, we first consider typical reforming reactions (*e.g.*, those which occur during the aromatization of methylcyclopentane) in contact with composite catalyst pellets containing an active hydrogenation-dehydrogenation agent and an active isomerization agent.

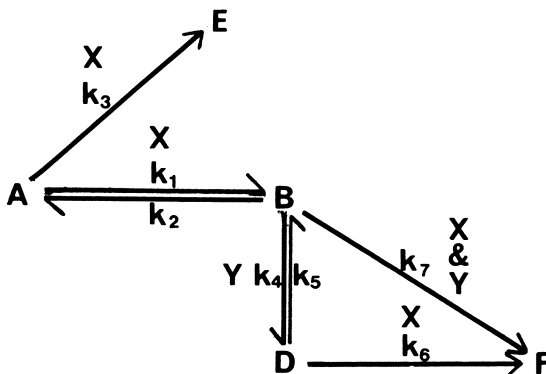


Figure 1. Kinetic model for a compounded catalyst

Composite Pellets. Chemical kinetic and infrared studies (10, 11) established that reforming reactions can be represented in terms of stoichiometric steps, each described by a pseudo-first-order rate constant. The route which is followed on a composite catalyst such as highly dispersed platinum supported on fluorinated alumina differs somewhat from that reported (7) for discrete pellets, probably because of cooperative effects between the two

catalyst components. For such composite catalysts the chemical kinetics may be described by the model in Figure 1 where A, B, D, F, and E refer to methylcyclopentane, methylcyclopentene, cyclo-1-hexene, benzene, and cracked products, mainly C₄ paraffins. The active catalyst component which promotes each step is either platinum (X) or fluorinated silica-alumina (Y). The final product F can be formed directly from the intermediate B because of a cooperative effect between the two catalyst components acting collaterally, or it can come indirectly from D by isomerization of B.

If we define the specific rate constant for a given stoichiometric reaction step on the basis of unit surface area of the component catalyzing the step, then if that reaction occurred in a catalyst pellet compounded from two such catalyst components, the rate constant is necessarily modified by a factor equal to the ratio of the surface area of the active component to the total active surface area. We define ϵ as the ratio of the specific surface area of X to the sum of the surface areas of X and Y. Hence, referring to the kinetic model (Figure 1), the specific rate constant for A \rightarrow B in a compounded catalyst would be ϵk_1 , and for B \rightarrow D it would be $(1 - \epsilon)k_4$. The cooperative effect apparently implicit in B \rightarrow F would best be represented by the kinetic constant $\epsilon(1 - \epsilon)k_7$ since the total effect (11) appears to be greater than the sum of its parts. Other kinetic constants can be written from the model.

We can now write the differential equations describing the mass and heat dispersion within a spherical porous composite catalyst pellet. For a fully distributed parameter model of the pellet the differential mass balances for components A, B, D, and F are:

$$\frac{D_e}{R^2} \frac{\partial}{\partial R} \left(R^2 \frac{\partial C_A}{\partial R} \right) - \epsilon(k_1 + k_2) \cdot C_A + \epsilon \cdot k_2 C_B = 0 \quad (1)$$

$$\frac{D_e}{R^2} \frac{\partial}{\partial R} \left(R^2 \frac{\partial C_B}{\partial R} \right) + \epsilon k_1 C_A - \{ \epsilon k_2 + (1 - \epsilon)k_4 + \epsilon(1 - \epsilon)k_7 \} C_B + (1 - \epsilon)k_5 C_D = 0 \quad (2)$$

$$\frac{D_e}{R^2} \frac{\partial}{\partial R} \left(R^2 \frac{\partial C_D}{\partial R} \right) + (1 - \epsilon)k_4 C_B - \{ (1 - \epsilon)k_5 + \epsilon k_6 \} C_D = 0 \quad (3)$$

$$\frac{D_e}{R^2} \frac{\partial}{\partial R} \left(R^2 \frac{\partial C_F}{\partial R} \right) + \epsilon(1 - \epsilon)k_7 C_B + \epsilon k_6 C_D = 0 \quad (4)$$

$$\frac{D_e}{R^2} \frac{\partial}{\partial R} \left(R^2 \frac{\partial T}{\partial R} \right) + \epsilon \{ (-\Delta H_3)k_3 C_A + (-\Delta H_{12})(k_1 C_A - k_2 C_B) + (-\Delta H_6)k_6 C_D \} \\ + (1 - \epsilon) \{ (-\Delta H_{45})(k_4 C_B - k_5 C_D) + \epsilon(1 - \epsilon)(-\Delta H_7)k_7 C_B \} = 0 \quad (5)$$

$$k_i = A_i \cdot \exp \left(\frac{-\Delta E_i}{R_g \cdot T} \right) \quad (6)$$

Boundary conditions which are applicable and which account for interparticle transport effects are:

$$\frac{\partial C_i}{\partial R} = \frac{\partial T}{\partial R} = 0 \text{ at } R = 0; i = A, B, D, \text{ and } F \quad (7)$$

$$\left. \begin{aligned} D_e \frac{\partial C_i}{\partial R} &= h_D (C_{if} - C_i) \\ k_e \frac{\partial T}{\partial R} &= h (T_t - T) \end{aligned} \right\} \text{ at } R = R_s; i = A, B, D, \text{ and } F \quad (8)$$

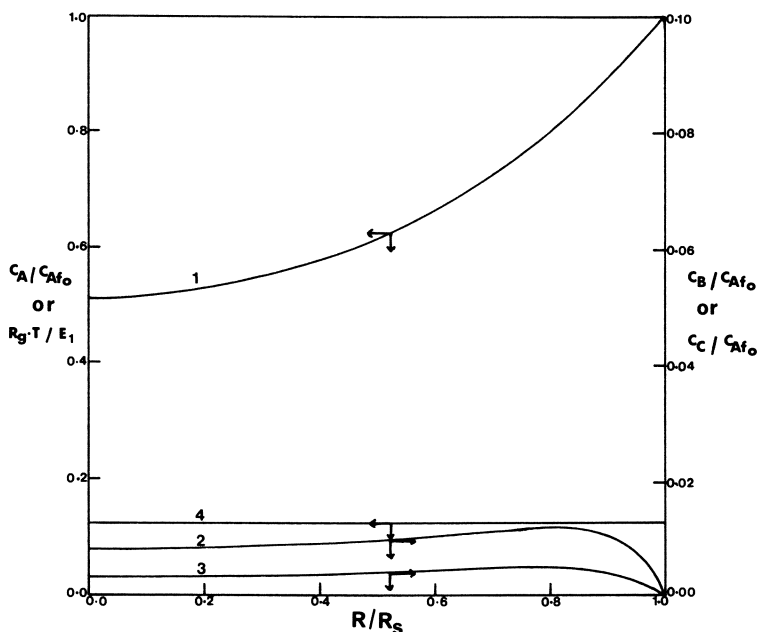


Figure 2. Composition and temperature profiles within a compounded catalyst pellet. Curve 1, concentration profile of A; curve 2, of B; curve 3, of D. Curve 4, temperature profile.

By solving the above equations, effectiveness factors for the pellet can be computed by comparing the rate of formation of a given component of the reaction mixture in the presence of transport effects with the corresponding rate in the complete absence of transport effects. In terms of the initial reactant A, the effectiveness factor of A is

$$\eta = \frac{3 h_D (C_{Af} - C_{As})}{R_S \{ \epsilon (k_1 + k_3) C_{Af} - \epsilon k_2 C_{Bf} \}} \quad (9)$$

where subscript S refers to conditions at the exterior surface ($R = R_S$). Highly non-linear two-point boundary value problems similar to that represented by Equations 1-8 can be solved efficiently by an iterative implicit finite difference method using a well established algorithm to effect a decomposition and subsequent solution of the tridiagonal matrix resulting from the central difference approximation to the problem (12, 13). In solving the problems posed here we found that convergence was not possible without the use of double precision arithmetic, undoubtedly because of the extremely interactive nature of Equations 1-8.

Typical computed concentration and temperature profiles within the pellet are given in Figure 2. The most striking result is that temperature gradients are virtually absent within the pellet. In view of the overall endothermicity of the conversion of methylcyclopentane to benzene and cracked C_4 paraffins, this is not surprising. Nevertheless, the step in which cracking occurs ($A \rightarrow E$) is sufficiently exothermic to cause appreciable heat release within the pellet. However, the pellet behaves isothermally, and any resistance to heat transfer does not reside within the pellet. This result, for a particular system, agrees

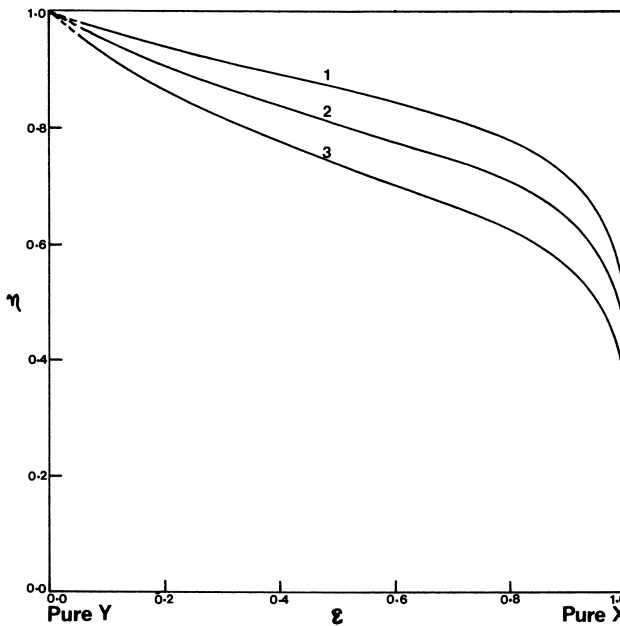


Figure 3. Effectiveness factor as a function of catalyst composition (compounded pellets). Curve 1, fluid temperature 720°K; curve 2, 770°K; curve 3, 820°K.

well with the general thesis of Beek (14) and Irving and Butt (15) which states that except for the most extreme operating conditions and the most exothermic reactions, the major resistance to heat transfer is from particle to fluid.

Thus, we can replace Equation 5 with an appropriate algebraic heat balance over the fluid film surrounding the apparently isothermal particle, considerably reducing the computational effort. The uniform temperature T_s of the catalyst particle, which will differ from the fluid temperature T_f , must satisfy the heat balance equation..

$$T_s = T_f + \frac{h_D}{h} \{ \alpha_1 + (\alpha_2 + \alpha_3) \alpha_4 (C_{Af} - C_{As}) + (\alpha_1 + \alpha_2 + \alpha_3) (C_{Bf} - C_{Bs} + C_{Df} - C_{Ds}) + (\alpha_1 + \alpha_2 + \alpha_3 \alpha_5) (C_{Ff} - C_{Fs}) \} \quad (10)$$

where

$$\alpha_1 = \frac{(-\Delta H_{12})k_1 + (-\Delta H_3)k_3}{k_3} \quad (11)$$

$$\alpha_2 = \frac{(k_1 + k_3) \{ \epsilon(1 - \epsilon)(-\Delta H_7)k_7 + (1 - \epsilon)(-\Delta H_{45})k_4 - \epsilon(-\Delta H_{12})k_2 \}}{\epsilon k_2 k_3} \quad (12)$$

$$\alpha_3 = \frac{k_7(k_1 + k_3) \{ (1 - \epsilon)(-\Delta H_{45})k_5 - \epsilon(-\Delta H_6)k_6 \}}{\epsilon^2 k_2 k_3 k_6} \quad (13)$$

$$\alpha_4 = \frac{k_1}{k_1 + k_3} \quad (14)$$

$$\alpha_5 = \frac{\epsilon(1 - \epsilon)k_7(k_1 + k_3) + \epsilon k_2 k_3}{\epsilon(1 - \epsilon)k_7(k_1 + k_3)} \quad (15)$$

Solution of the set of simultaneous differential mass balance Equations 1-4 together with the algebraic heat balance given by Equation 10 therefore solves the problem of estimating concentration profiles within the pellet and thereby allows the effect of catalyst composition to be expressed in terms of the ϵ . Because the pellet is regarded as isothermal and the differential equations are linear, Equations 1-4 can now be solved analytically (tedious), or eigenvalues can be sought numerically. Double precision arithmetic was used for all computer programs. Pellet temperature can be found by iterating Equation 10. Figure 3 shows the effect of catalyst composition on the pellet effectiveness factor η for three fluid temperatures. No reaction is possible if only component Y is present in the composite particle; thus η is indeterminate for $\epsilon = 0$. The decrease in effectiveness factor with increasing amount of catalyst component X is explained by the corresponding increase in reaction rate and the concomitant increasing influence of molecular diffusion which eventually becomes limiting. This point is made clearer by the curve in Figure 4 which shows the influence of temperature on the effectiveness factor. As expected, the effectiveness of the pellet is reduced as the temperature increases because of the greater importance of intraparticle transport. The first flat portion of the curve represents a region of chemical control whereas the portion of the curve at fluid temperatures greater than *ca.* 1100°K signifies rate control from molecular diffusion. Clearly it is desirable for a pellet to lie somewhere between these values of the reaction rate and the effectiveness factor.

Discrete Pellet Mixtures. To compare the performance of a reactor containing composite catalyst pellets with one containing a mixture of discrete

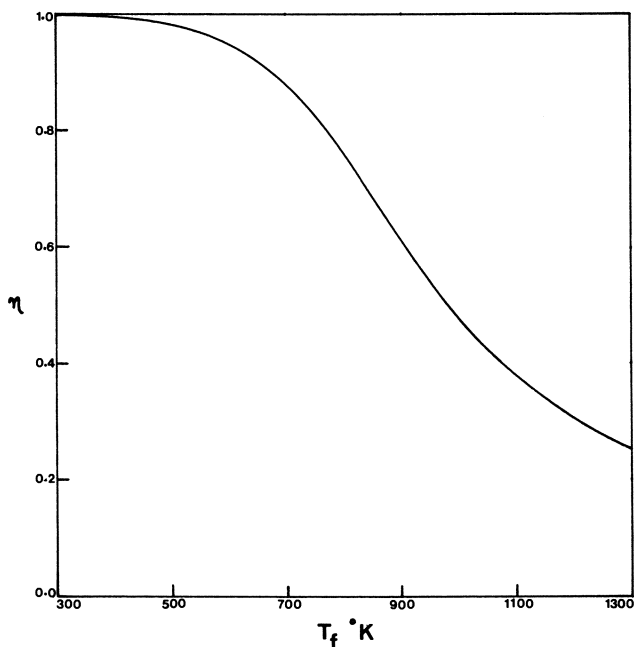


Figure 4. Effectiveness factor as a function of fluid temperature for compounded pellets of composition $\epsilon = 0.5$

catalyst pellets, we briefly consider the form of the pellet equations for the same reforming reaction, but we use components X and Y in separate porous particles. Thus the platinum might be dispersed, for example, within inert porous carbon on silica particles whereas the fluorinated silica-alumina would exist as distinct discrete particles without platinum. For a mixture of the two components the overall composition is expressed as the volume fraction of reactor space occupied by type X particles. The differential mass balance equations and the algebraic heat balance can be written by similar considerations to that for the compounded catalyst except that, for a discrete mixture of particles, balances must be written for both X and Y type particles and the kinetic terms would not contain a fraction describing the catalyst composition. The effective diffusivities for both types of particle are taken as identical. The kinetics differ mainly because there is no possibility for any cooperative effect between the two types of catalyst sites now present in different particles rather than the same particle. With these differences the particle differential mass balance equations can easily be written for the kinetic scheme postulated by Jenkins and Thomas (7) for discrete mixtures of pellets. We consider the scheme (Figure 5) in terms of their kinetic model where the side product C is methylcyclopentadiene not formed in any significant quantities if composite pellets are used. The differential mass balance equations for particles containing component X are:

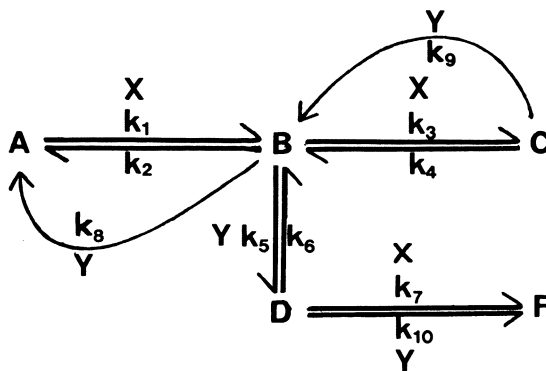


Figure 5. Kinetic model for discrete mixture of catalyst pellets

$$\frac{D_e}{R^2} \frac{\partial}{\partial R} \left(R^2 \frac{\partial C_A}{\partial R} \right) - k_1 C_A + k_2 C_B = 0 \quad (16)$$

$$\frac{D_e}{R^2} \frac{\partial}{\partial R} \left(R^2 \frac{\partial C_B}{\partial R} \right) + k_1 C_A - (k_2 + k_3) C_B + k_4 C_C = 0 \quad (17)$$

$$\frac{D_e}{R^2} \frac{\partial}{\partial R} \left(R^2 \frac{\partial C_C}{\partial R} \right) + k_3 C_B - k_4 C_C = 0 \quad (18)$$

$$\frac{D_e}{R^2} \frac{\partial}{\partial R} \left(R^2 \frac{\partial C_D}{\partial R} \right) - k_7 C_D = 0 \quad (19)$$

$$\frac{D_e}{R^2} \frac{\partial}{\partial R} \left(R^2 \frac{\partial C_F}{\partial R} \right) + k_7 C_D = 0 \quad (20)$$

$$\text{At } R = 0, \frac{\partial C_i}{\partial R} = 0; i = A, B, C, D, \text{ and } F. \quad (21)$$

$$\text{At } R = R_s, D_e \frac{\partial C_i}{\partial R} = h_D(C_{if} - C_i); i = A, B, C, D, \text{ and } F \quad (22)$$

For type X particles, assuming no temperature gradients within the pellet, the particle temperature T_X is given by the heat balance

$$T_X = T_f + \frac{h_D}{h} \{(-\Delta H_{12})(C_{Af} - C_{AS}) - (-\Delta H_{34})(C_{Cf} - C_{CS}) + (-\Delta H_7)(C_{Df} - C_{DS})\} \quad (23)$$

The differential mass balance equations for particles of type Y is:

$$\frac{D_e}{R^2} \frac{\partial}{\partial R} \left(R^2 \frac{\partial C_A}{\partial R} \right) + k_8 C_B = 0 \quad (24)$$

$$\frac{D_e}{R^2} \frac{\partial}{\partial R} \left(R^2 \frac{\partial C_B}{\partial R} \right) - (k_5 + k_8) C_B + k_9 C_C + k_6 C_D = 0 \quad (25)$$

$$\frac{D_e}{R^2} \frac{\partial}{\partial R} \left(R^2 \frac{\partial C_C}{\partial R} \right) - k_9 C_C = 0 \quad (26)$$

$$\frac{D_e}{R^2} \frac{\partial}{\partial R} \left(R^2 \frac{\partial C_D}{\partial R} \right) + k_5 C_B - (k_6 + k_{10}) C_D = 0 \quad (27)$$

$$\frac{D_e}{R^2} \frac{\partial}{\partial R} \left(R^2 \frac{\partial C_F}{\partial R} \right) + k_{10} C_D = 0 \quad (28)$$

subject to the boundary conditions

$$R = 0, \frac{\partial C_i}{\partial R} = 0; i = A, B, C, D, \text{ and } F \quad (29)$$

$$R = R_s, D_4 \frac{\partial C_i}{\partial R} = h_D(C_{if} - C_i); i = A, B, C, D, \text{ and } F \quad (30)$$

while the heat balance for type Y particles is:

$$T_Y = T_f + \frac{h_D}{h} \{ \alpha_6(C_{Bf} - C_{BS}) + \alpha_7(C_{Cf} - C_{CS}) + \alpha_8(C_{Df} - C_{DS}) \} \quad (31)$$

where

$$\alpha_6 = \{ (\Delta H_{12})(k_6 k_8 + k_8 k_{10}) + [(-\Delta H_{56}) + (-\Delta H_7)] \cdot k_5 k_{10} \} / \alpha_9 \quad (32)$$

$$\alpha_7 = \{ (\Delta H_{12})(k_6 k_8 + k_8 k_{10}) + \alpha_9 (\Delta H_{34}) + [(-\Delta H_{56}) + (-\Delta H_7)] k_5 k_{10} \} / \alpha_9 \quad (33)$$

$$\alpha_8 = \{ (\Delta H_{12}) - (-\Delta H_{56}) \} \frac{k_6 k_8}{\alpha_9} + (-\Delta H_7) \alpha_{10} \quad (34)$$

$$\alpha_9 = k_6 k_8 + k_5 k_{10} + k_8 k_{10} \quad (35)$$

$$\alpha_{10} = \frac{k_5 k_6 k_{10} + k_6 k_8 k_{10} + k_5 k_{10}^2 + k_8 k_{10}^2}{k_6^2 k_8 + k_5 k_6 k_{10} + 2k_6 k_8 k_{10} + k_5 k_{10}^2 + k_8 k_{10}^2} \quad (36)$$

Solution of Equations 16–36 gives the concentration profiles and temperature within each type of catalyst pellet. We do not present the solution separately but utilize the equations in conjunction with the reactor equations below.

Performance of a Reactor Containing Bifunctional Catalyst Pellets

We consider a single reactor, of tube diameter d_t , packed with catalyst pellets and make the usual simplifying assumptions that plug type flow obtains, that the length L of the reactor is considerably greater than 100 particle diameters, that there is no radial or longitudinal mass or heat dispersion, and that the resistance to heat transfer from reactor to heating fluid is only near the tube wall and can be described by a lumped parameter modified heat transfer coefficient h'_w . With these assumptions the general mass and heat balance equations for the system are:

$$eu \frac{\partial c_{jt}}{z} = -N_j, \quad j = A, B, \dots \quad (37)$$

$$eu\rho\bar{c}_p \frac{\partial T_t}{\partial z} = -N_h + \frac{4h'_w}{d_t} (T_h - T_t) \quad (38)$$

in which e is the bed porosity, T_h is the constant heating fluid temperature and where, for a reactor packed with composite pellets,

$$N_j = \frac{3(1-e)D_e}{R_s} \left(\frac{\partial C_j}{\partial R} \right)_{R_s} \quad (39)$$

while for a discrete mixture of pellets it is:

$$N_j = N_{jX} + N_{jY} = \frac{3(1-e)D_e}{R_s} \left\{ \epsilon \left(\frac{\partial C_j}{\partial R} \right)_{R_s, X} + (1-\epsilon) \left(\frac{\partial C_j}{\partial R} \right)_{R_s, Y} \right\} \quad (40)$$

assuming the particle radii to be identical. The heat flux N_h in Equation 38 is defined as

$$N_h = \frac{3(1-e)h}{R_s} (T_t - T) \quad (41)$$

for a compounded pellet, but for a discrete mixture of pellets it is:

$$N_h = \frac{3(1-e)h}{R_s} \{T_t - \epsilon T_X - (1-\epsilon)T_Y\} \quad (42)$$

The initial conditions apposite to Equations 37 and 38 are those corresponding to the entrance to the reactor—*viz.*,

$$z = 0, C_{jt} = C_{jto}, T_t = T_{to} \quad (43)$$

Table I. Kinetic Data for Compounded Catalyst

Reaction Step	Catalyst Component	Numerical Index	$A,^{-1} \text{ sec}$	$E, \text{ kcal/mole}$	$\Delta H \text{ kcal/mole}$
A → B	X	1	5.848×10^{10}	39.88	
B → A	X	2	63.38	8.99	
A ⇌ B	X	12			25.28
A → E	X	3	1.85×10^{12}	49.03	-11.82
B → D	Y	4	5.73	8.66	
D → B	Y	5	1.52×10^2	9.81	
B ⇌ D	Y	45			1.12
D → F	X	6	1.386×10^{10}	34.32	22.79
B → F	X + Y	7	2.25×10^{13}	47.72	23.91

To solve the two non-linear simultaneous Equations 37 and 38 over the entire reactor length, an initial value method was used. The Runge-Kutta-Merson algorithm was satisfactory. Double precision arithmetic for computer programs was essential to produce a convergent solution. Data used in computing reactor performance when the reactor is packed with a composite catalyst are given in Tables I and II. Kinetic data corresponding to a discrete mixture of catalysts are given in a previous publication by Jenkins and Thomas (7). Fluid conditions, voidage, effective diffusivity, and particle size were assumed the same for both sets of computations.

Table II. Parameters Used in Computations

<i>Symbol</i>	<i>Magnitude</i>	<i>Symbol</i>	<i>Magnitude</i>
C_{Afo}	0.000149 gram mole/cm ³	h_w	0.0005 cal/cm ² /sec/°K
\bar{c}_p	0.35	L	360 cm
D_e	0.004 cm ² /sec	R_s	0.20 cm
d_t	15.0 cm	T_h	2200°K
h	0.001 cal/cm ² /sec/°K	u	40 cm/sec
h_D	4.0 cm/sec	ρ	0.014 gram/cm ³

Typical concentration and temperature profiles in the reactor are illustrated for one packed with a compounded catalyst (Figure 6) and one packed with discrete separate particles of each catalyst component (Figure 7). For compounded catalysts the most significant kinetic step is that which displays a cooperative catalytic effect. This has also been confirmed experimentally. Similar curves computed in the absence of mass and heat transfer effects

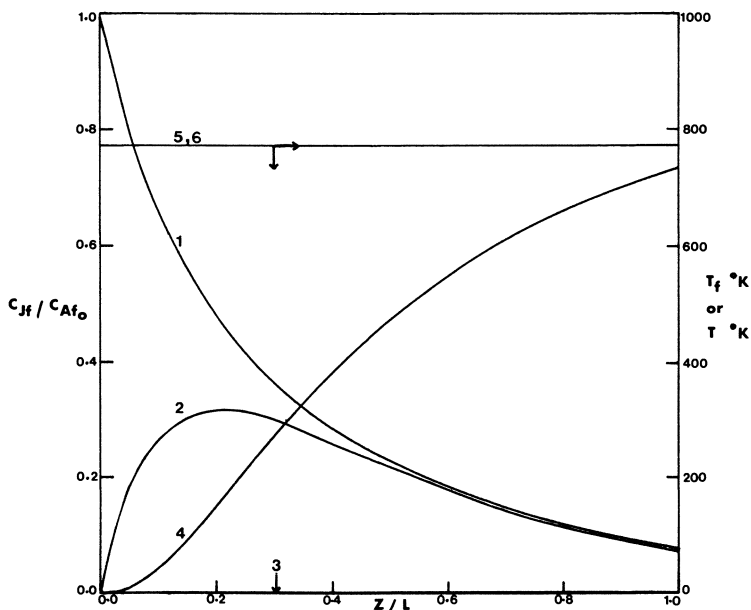


Figure 6(a). Profiles of fluid concentration and temperature along an isothermal reactor (compounded catalyst, no mass and heat transfer effects). Curve 1, concentration of A; curve 2, of B; curve 3, of D; curve 4, of F. Curves 5 and 6, temperature of fluid and solid.

indicate that the rate of benzene (F) production using a compounded catalyst is less than that using separate discrete particles and is reflected in the kinetic data (Table I and Ref. 7). The explanation of this fact appears to be that the formation of methylcyclopentane (B) is considerably enhanced on separate particles where there is no second constituent diluting or interacting with the component responsible for catalyzing its formation.

For non-isothermal reactors the minimum in the temperature profile is less for composite pellets than for discrete mixtures of pellets because for all positive values of the catalyst composition ϵ , the compounded catalyst pellets remain at a higher temperature than discrete mixtures of pellets. This difference in pellet temperatures arises because the overall heat transfer resistance is less for compounded pellets than for discrete mixtures of pellets, and the overall endothermicity is less.

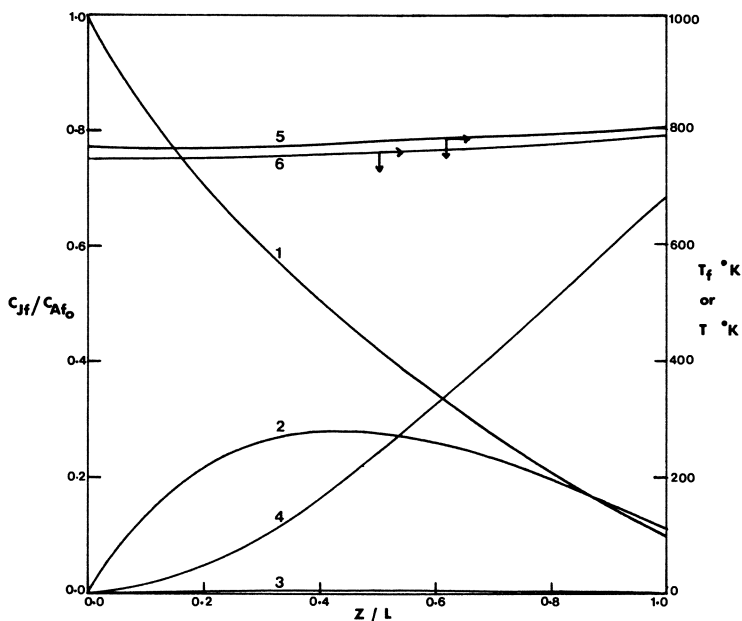


Figure 6(b). Profiles of fluid concentration and temperature along a non-isothermal reactor (compounded catalyst). Curve 1, concentration of A; curve 2, of B; curve 3, of D; curve 4, of F. Curve 5, temperature of fluid; curve 6, temperature of solid.

The closer the catalyst composition approaches $\epsilon = 1$, the more likely temperature runaway is. In the limit, because heat is supplied to the reactor and the chemical steps producing cracked products generate more heat than is absorbed by methylcyclopentene (B) formation, the catalyst pellets become excessively hot with no possibility of heat removal in the absence of reactions catalyzed by the second component. Benzene yield as a function of catalyst composition shows that for composite pellets the maximum benzene (F) yield is obtained when $\epsilon = 0.5-0.6$; we regard this as an optimum constant composition for a non-isothermal reactor containing composite pellets.

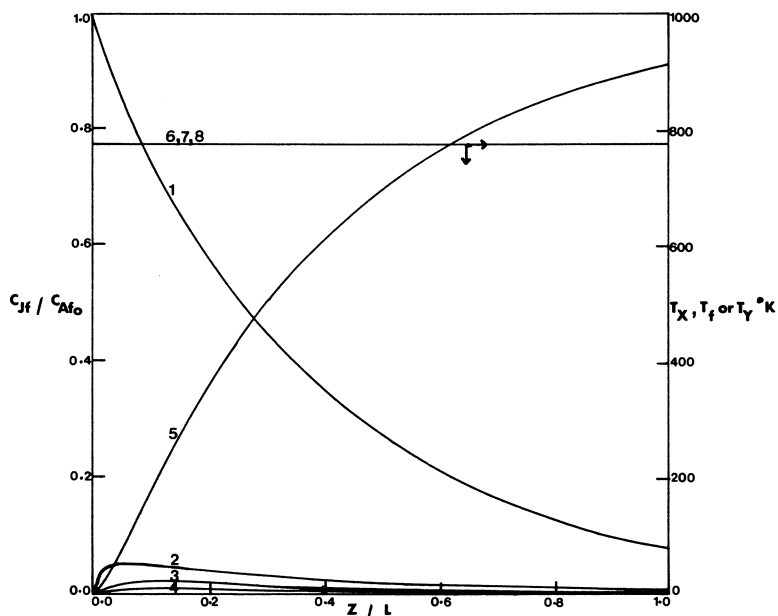


Figure 7(a). Profiles of fluid concentration and temperature along an isothermal reactor (discrete mixture of catalyst pellets, no mass or heat transfer effects). Curve 1, concentration of A; curve 2, of B; curve 3, of C; curve 4, of D; curve 5, of F. Curves 6, 7, and 8: temperature of pellets X, fluid, and pellets Y.

Comparison of performance for various classes of reactors packed either with the optimum composite pellet composition (Figure 8) or with the optimum mixture of discrete pellets (Figure 9) indicates that the lowest yields are obtained with an adiabatic reactor (curve 1), and the highest with an isothermal reactor. This of course is the result of the overall endothermicity of the reforming process. When interparticle and intraparticle mass transfer are unimportant and isothermal conditions prevail (curve 5), the highest yields are predicted for discrete mixtures of particles. The difference in yield is so striking that it is probably worth the inconvenience of arranging the reactor packing to conform with the optimum catalyst composition for a discrete mixture of particles. The larger yield can only be the result of the different kinetics between the two systems; if the kinetic models were identical, greater yields would be obtained if the two catalyst components were in compounded form; then the overall effect of interparticle resistances would be less because intermediate products would not have to be transported from one type of particle to another. This has been demonstrated (1). The reverse is true for an isothermal reactor operating where there is appreciable intraparticle diffusion (curves 3 and 4). There, resistance to mass transfer in a mixture of discrete particles is much greater than for a system of composite particles. Thus, despite the kinetics favoring a higher yield for a reactor packed with discrete particles, if mass transfer effects are liable to be important, the optimum composite catalyst preparation will be superior. This superiority is exaggerated further if heat is supplied to sustain the reaction (curve 2).

Optimum Composition Profiles

While solution of the particle and reactor equations for given values of the catalyst composition enables one to compute an optimum composition, such a maximum is constrained in the sense that ϵ is fixed and constant over the entire reactor length. In principle an unconstrained optimum profile can be computed by solving the particle and reactor equations coupled with the objective function

$$\text{Max } C_F(\theta) = \text{Max } \int_0^{\theta} \sum_j \left(-\frac{dC_j}{dt} \right) dt; j = A, B \dots E \quad (44)$$

subject only to the constraint that $0 \leq \epsilon \leq 1$.

Such a problem, as defined above, requires an inordinately lengthy computation, and with the computing equipment available (ICL 450) it was an uneconomical exercise. The problem was therefore reduced to one which would demand no more than about 30 minutes of the central processor's time. Thus it was only possible to seek optimum catalyst composition profiles where the overall reaction rate is controlled by chemical reaction. Nevertheless, useful comparisons can be made between isothermal, adiabatic, and non-isothermal conditions in reforming units packed with a composite catalyst of moderate activity and for which the rate is limited by the chemical kinetics rather than mass and heat transfer effects.

A quasi-homogeneous reactor model was adopted for computing catalyst composition profiles. This implies that, apart from the assumptions concerning

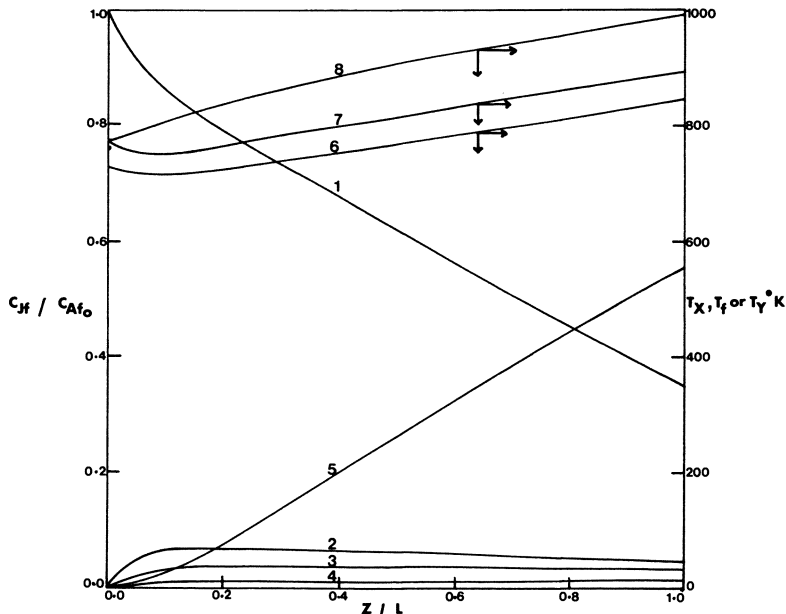


Figure 7(b). Profiles of fluid concentration and temperature along a non-isothermal reactor (discrete mixture of catalyst pellets). Curve 1, concentration of A; curve 2, of B; curve 3, of C; curve 4, of D; curve 5, of F. Curve 6, temperature of pellets X; curve 7, of fluid; curve 8, of pellets Y.

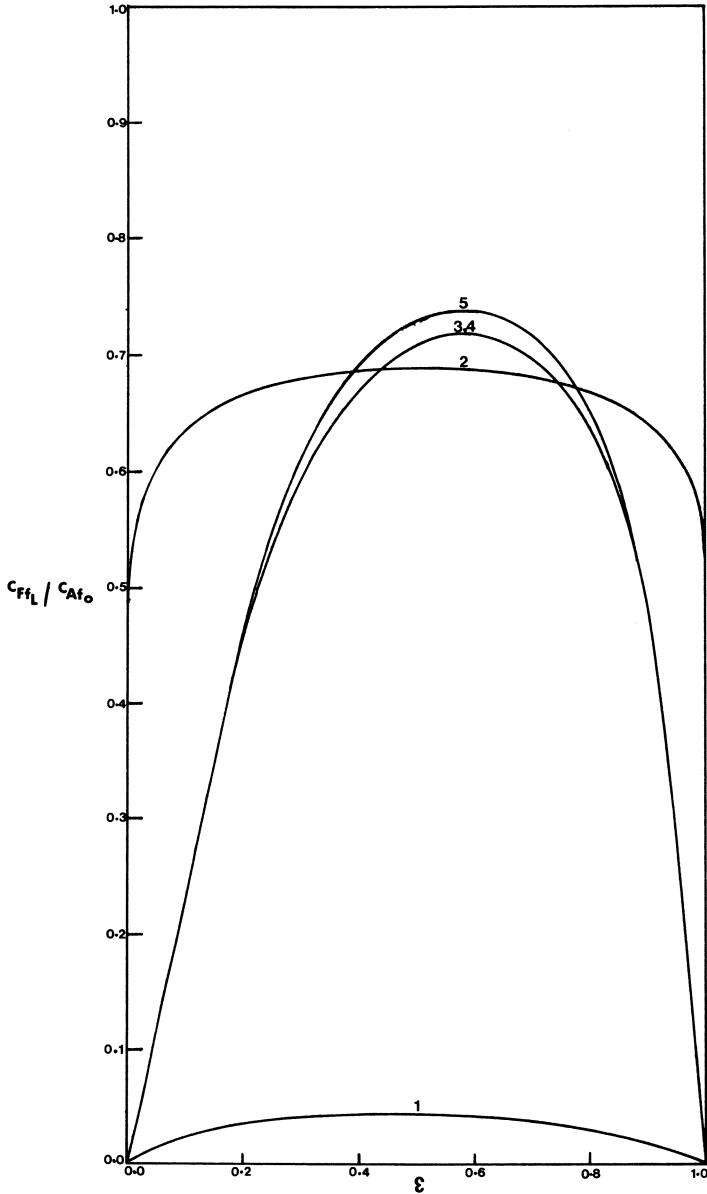


Figure 8. Yield of benzene as a function of catalyst composition (compounded catalyst). Curve 1, adiabatic; curve 2, non-isothermal; curves 3 and 4, isothermal, no film mass transfer resistance; curve 5, isothermal, chemical control.

the neglect of radial and longitudinal dispersion terms, particle effectiveness factors are unity and that the state equations for the optimization can be written by replacing the flux derivatives in Equations 1-5 with the appropriate

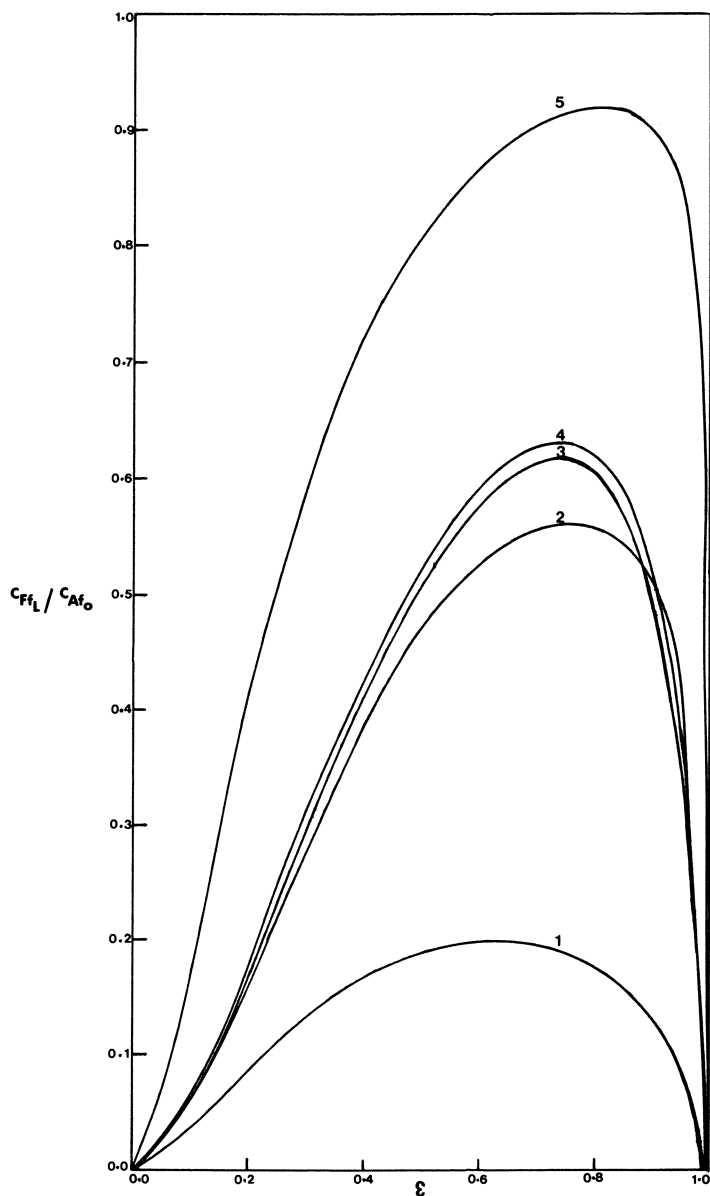


Figure 9. Yield of benzene as function of catalyst composition (discrete mixture of pellets). Curve 1, adiabatic; curve 2, non-isothermal; curve 3, isothermal, intra- and inter particle mass transfer resistances finite; curve 4, isothermal, no film mass transfer resistance; curve 5, isothermal, chemical control.

concentration or temperature derivatives with respect to contact time. These state equations are:

$$\frac{dc_j}{dt} = f_j; j = A, B, D, E, \text{ and } i = 1, 2, 3, 4.$$

$$\frac{dT}{dt} = f_5$$

where the f_i are the kinetic terms in Equations 1–4 and f_5 corresponds to the product of kinetic and heat of reaction terms as defined in Equation 5. The optimum seeking procedure used in this work is the Maximum principle of Pontryagin. Thus a system of adjoint equations is defined by

$$\frac{d\lambda_i}{dt} = - \sum_{n=1}^5 \lambda_n \left(\frac{\partial f_n}{\partial x_i} \right)$$

where x_i and the c_j or T correspond to $i = 1, 2, 3, 4$ or 5. The Hamiltonian function

$$H[\varepsilon(t)] = \sum_{i=1}^5 \lambda_i f_i$$

must then be a maximum and constant value over the range $0 \leq t \leq \theta$ to satisfy the maximum principle and $\varepsilon(t)$ chosen so that this condition is satisfied. The computational procedure has been documented (16) and is applied to

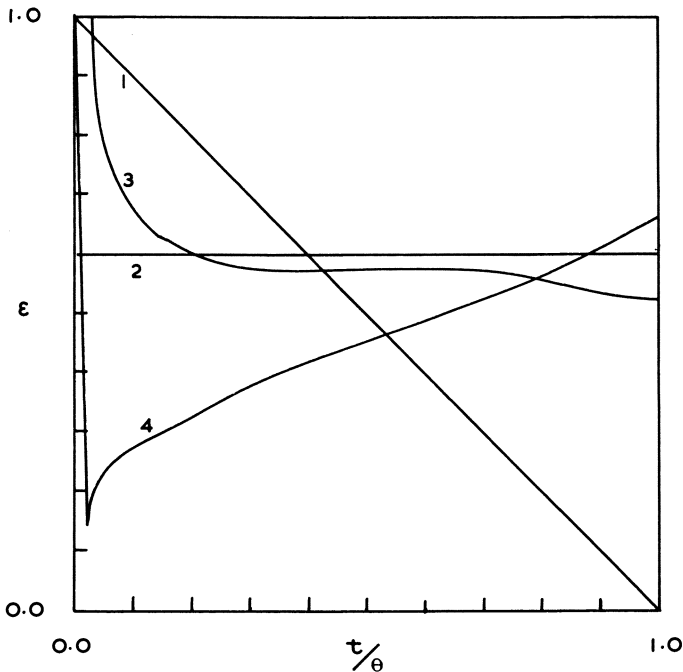


Figure 10. Optimum catalyst composition profiles (compounded catalyst, kinetic control). Curve 1, initially assumed ramp profile; curve 2, initially assumed constant profile; curve 3, optimum profile for isothermal reactor; curve 4, optimum profile for adiabatic reactor.

this problem. It entails the assumption of an initial profile which is updated at each iteration cycle by adding the term $K\delta H/\delta \epsilon$ (where K is an arbitrary constant whose magnitude will ensure convergence) to the most recently computed profile.

Figure 10 illustrates the computed optimal compounded catalyst composition profile for an adiabatically and an isothermally operated reactor in which chemical kinetic control dominates the conditions. Essentially the same optimum profile was reached in five iterations whether the initial profile was constant or a ramp function. Since the maximum yield in the adiabatic case only amounts to 1.4% even when the optimum is unconstrained, clearly an adiabatic reforming reactor should never constitute a design choice. The character of the optimal profile is quite different for an isothermally operated reactor as is clear from curves 3 and 4 in Figure 10. An isothermal optimum profile could be emulated in practice by operating two beds in series; one would be short and contain only the platinum component while the second would contain a compounded catalyst of constant composition (with $\epsilon \approx 0.55$ for the parameters pertaining to this example). For such an isothermally operated reactor the desired yield is as high as 73.5%.

Perhaps the most revealing result is that obtained for a non-isothermal reactor. Figure 8 shows that the maximum constant composition (curve 2) is ill defined; this is also reflected in the results obtained when seeking the optimum composition profile along the reactor length. Whether one begins the computation with a constant or ramp profile, the final yield computed after as many as 30 iterations hardly differs from that obtained using the initially assumed profile. We thus conclude that a reforming reactor operated non-isothermally in the chemically controlled region and which contains a compounded catalyst preparation is insensitive to the catalyst composition for a fairly wide range of ϵ .

Nomenclature

A	methylcyclopentane
A_i	Arrhenius factor for species i , T^{-1}
B	methylcyclopentene
C	methylcyclopentadiene
\bar{c}_p	average specific heat of fluid in reactor
c_j	concentration of chemical component j , ML^{-3}
D	cyclo-1-hexene
D_e	effective diffusivity, L^2T^{-1}
d_t	tube diameter, L
E	C_4 paraffins
E_i	activation energy for species i , L^2T^{-2}
e	void fraction of bed
F	benzene
h	fluid to solid heat transfer coefficient, $ML^{-2}T^{-1}$
h_D	fluid to solid mass transfer coefficient, LT^{-1}
h_w	wall heat transfer coefficient, $ML^{-2}T^{-1}$
h'_w	modified wall heat transfer coefficient, $ML^{-2}T^{-1}$
	$= \frac{4h_w}{4 + Nu_w}$
K	arbitrary constant used to seek the optimum
K_e	effective thermal conductivity of solid, $ML^{-1}T^{-1}$
K_r	radial thermal conductivity of fluid, $ML^{-1}T^{-1}$

k_i	kinetic rate constant for chemical component i , T^{-1}
L	reactor length, L
N_j	molar rate for component j , $ML^{-3}T^{-1}$
N_h	heat transfer rate, $ML^{-1}T^{-3}$
Nu_w	($= d_t h_w / K_t$) wall Nusselt number
R	pellet radius variable, L
R_g	universal gas constant, $L^2T^{-2} (^\circ K)^{-1}$
R_s	pellet radius, L
T	particle temperature, $^\circ K$
T_h	heating fluid temperature, $^\circ K$
T_f	fluid temperature, $^\circ K$
T_s	temperature of compounded pellets, $^\circ K$
T_x	temperature of pellets of type X, $^\circ K$
T_Y	temperature of pellets of type Y, $^\circ K$
u	velocity of fluid in tube, LT^{-1}
X	platinum catalyst component
Y	fluorinated silica-alumina catalyst component
z	reactor length variable, L
$(-\Delta H)$	heat of reaction, L^2T^{-2}

Subscripts

f	conditions in the fluid
fo	conditions in the fluid at reactor inlet
fL	conditions in the fluid at reactor outlet
i, j	indices used to identify chemical components and kinetic constants
S	conditions in the solid
X	pertaining to platinum catalyst
Y	pertaining to fluorinated silica-alumina catalyst

Greek Symbols

α	constant defined in text
ϵ	surface area fraction (for compounded pellets) or volume fraction (for discrete pellets) of catalyst component X
η	effectiveness factor
θ	reactor holding time, T
ρ	fluid density, ML^{-3}

Literature Cited

- Gunn, D. J., Thomas, W. J., *Chem. Eng. Sci.* (1965) **20**, 89.
- Weisz, P. B., Swegler, E. W., *J. Phys. Chem.* (1955) **59**, 823.
- Weisz, P. B., *Intern. Conf. Catalysis, 2nd* (1961) **1**, 937.
- Gunn, D. J., *Chem. Eng. Sci.* (1967) **22**, 963.
- Thomas, W. J., Wood, R. M., *Chem. Eng. Sci.* (1967) **22**, 1607.
- Jackson, R., *J. Optim. Theory Appl.* (1968) **2**, 1.
- Jenkins, B. G. M., Thomas, W. J., *Can. J. Chem. Eng.* (1970) **48**, 179.
- Mendiratta, A. K., Prabhu, A. V., Davidson, B., *Chem. Eng. Sci.* (1971) **26**, 885.
- Glasser, D., King, E. P., *Chem. Eng. Sci.* (1973) **28**, 1685.
- Wade, S. W., M.Sc. dissertation, Bath University (1972).
- Hall, F., Ph.D. thesis, Bath University (1974).
- McGreavy, C., Cresswell, D. L., *European Symp. Chem. Reaction Eng., 4th, Brussels, 1968*.
- McGreavy, C., Thornton, J. M., *Can. J. Chem. Eng.* (1970) **48**, 187.
- Beek, J., *A.I.Ch.E. J.* (1961) **7**, 350.
- Irving, J. P., Butt, J. B., *Chem. Eng. Sci.* (1967) **22**, 1859.
- Rosenbrock, H. H., Storey, C., "Computational Techniques for Chemical Engineers," Pergamon, New York, 1966.

RECEIVED January 2, 1974.

Dispersed Flow Reactors with Sections of Different Properties

WOLF-DIETER DECKWER and ENNO A. MAEHLMANN

Institut für Technische Chemie, Technische Universität Berlin,
Strasse des 17. Juni 135, 1 Berlin 12, Germany

A liquid phase reactor divided into three sections with different properties was studied. When applying the axial dispersed plug flow model and the Wehner-Wilhelm boundary conditions at section boundaries, the measured conversion properties deviated remarkably from those calculated for the model. However, when the model equations were integrated with the Danckwerts boundary conditions, which admit the occurrence of concentration jumps at section boundaries, the calculated conversions agreed with the experimental values.

Commercially important chemical reactors are frequently divided into sections with different properties, such as reaction rates, flow velocities, or dispersion coefficients. Sections are used so that reactor volume as well as installment costs can be minimized. Since heating and cooling equipment can cause different cross sectional areas of the reactor, the flow velocities and the dispersion coefficients may be changed. Particularly in catalytic reactors, the amount of catalyst used and the manner in which the catalyst is packed can be varied with reactor length.

To describe those reactors with zones of different properties, Langemann and Kölbel (1) proposed a model which can be regarded as an extension of the treatment of the boundary conditions of the axial dispersed plug flow model of Wehner and Wilhelm (2).

Boundary Conditions of Axial Dispersed Reactors

Wehner and Wilhelm (2) presented a profound analysis of the boundary conditions of flow reactors with dispersion, which Danckwerts (3) suggested originally. Danckwerts derived the boundary conditions by assuming that the mass flow must be continuous at reactor boundaries. Wehner and Wilhelm included in their analysis a semi-infinite fore and aft section as well as the reaction zone—a concept which had been applied by Damköhler (4, 5). Each zone was characterized by different dispersion coefficients. The mass balance equations of the three zones were simultaneously solved with a first-order reaction taking place in the reaction zone. The equations were solved by applying the condition of continuity of mass flow at the boundaries between the zones and by assuming that the concentrations would be continuous near

any point. By introducing this assumption, it was possible to avoid concentration jumps at the entrance boundary of the reaction zone. Wehner and Wilhelm showed that the concentration profile in the fore section depended on the parameters of the reaction section. This back effect is discussed later.

The Wehner-Wilhelm treatment was adopted by van der Laan (6) to derive moments of the one-dimensional dispersion model, and this model was examined by van Cauwenberghe (7) for the unsteady state. Using theoretical considerations, Bischoff (8) showed that the conclusion of Wehner and Wilhelm was correct for reactions of any order. In subsequent publications, Levenspiel and Bischoff (9, 10) extensively used the Wehner-Wilhelm boundary conditions which had been denoted to be "true in general" (8). Standart (11) critically discussed the boundary conditions of dispersed flow reactors from the point of irreversible thermodynamics. He concluded that it was not necessary for the concentration to be continuous at the boundary surface, in general.

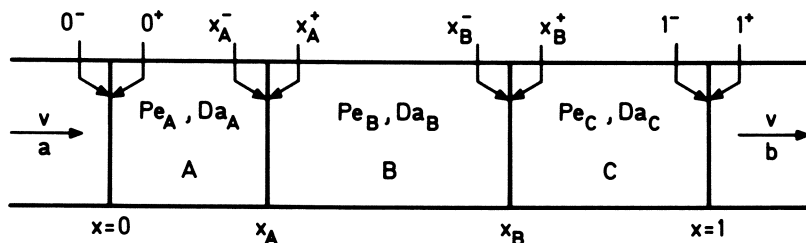


Figure 1. Tubular flow reactor subdivided into sections with different properties

Model for Reactors Subdivided in Sections

Returning to reactors with different properties from section to section, Langemann and Kölbel (1) divided the reaction zone into three parts, each having different dispersion characteristics, flow velocities, and reaction rates. Their concept is illustrated in Figure 1, where A, B, and C are the reaction sections. No dispersion exists in the entrance and exit section; the properties of each section are assumed to be constant. For further convenience, each section is isothermal, and no volume changes are considered. The mass balance equations for component i are in dimensionless form:

$$\frac{x_A}{Pe_A} \frac{d^2 C_i}{dx^2} - \frac{dC_i}{dx} - \frac{Da_A}{x_A} f_A(C) = 0 \quad 0 \leq x \leq x_A \quad (1)$$

$$\frac{x_B - x_A}{Pe_B} \frac{d^2 C_i}{dx^2} - \frac{dC_i}{dx} - \frac{Da_B}{x_B - x_A} f_B(C) = 0 \quad x_A \leq x \leq x_B \quad (2)$$

$$\frac{1 - x_B}{Pe_C} \frac{d^2 C_i}{dx^2} - \frac{dC_i}{dx} - \frac{Da_C}{1 - x_B} f_C(C) = 0 \quad x_B \leq x \leq 1 \quad (3)$$

The concentrations are reduced to the entrance concentration $c_{i,a}$, $C_i = c_i/c_{i,a}$. The Peclet number and the Damköhler group relate to the sections. The term, $f(C)$, designates functions of the concentrations which depend on the rate laws of the particular reaction. The boundary conditions are:

$$C_i(0^+) = C^* + \frac{x_A}{Pe_A} \frac{dC_i(0^+)}{dx} \quad (4)$$

$$C_i(x_A^-) - \frac{x_A}{Pe_A} \frac{dC_i(x_A^-)}{dx} = C_i(x_A^+) - \frac{x_B - x_A}{Pe_B} \frac{dC_i(x_A^+)}{dx} \quad (5)$$

$$C_i(x_A^-) = C_i(x_A^+) \quad (6)$$

$$C_i(x_B^-) - \frac{x_B - x_A}{Pe_B} \frac{dC_i(x_B^-)}{dx} = C_i(x_B^+) - \frac{1 - x_B}{Pe_C} \frac{dC_i(x_B^+)}{dx} \quad (7)$$

$$C_i(x_B^-) = C_i(x_B^+) \quad (8)$$

$$\frac{dC_i(1^-)}{dx} = 0 \quad (9)$$

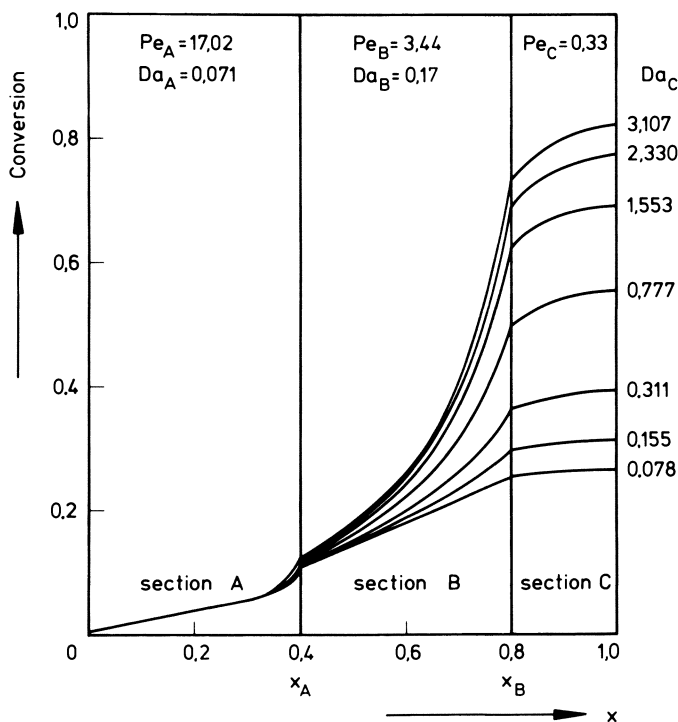


Figure 2. Concentration profiles for a first-order reaction, $Pe_B = 3.44$. Parameter: Da_c .

If component i is consumed, $C^* = 1$; otherwise $C^* = 0$. Equations 4 and 9 resemble the Danckwerts conditions of a closed vessel while Equations 5–8 correspond to the Wehner-Wilhelm boundary conditions. Langemann and Kölbl succeeded in analytically solving the boundary value problem (Equations 1–9) for a first-order reaction in each zone. Their solution clearly indicates that the concentration profile of a distinct reactor section is determined by the properties of all sections. If, for example, the reaction rate in the last section is altered, a back effect alters the concentration profiles in the sections before. Figures 2 and 3 show conversion profiles calculated from the closed solution for first-order reactions. The properties of the first two sections remain unchanged, and the Damköhler number of the third section is only increased, as indicated on the right side of Figures 2 and 3. This increased reaction rate in zone C increases the conversion in zone B and, to a smaller extent, in zone A,

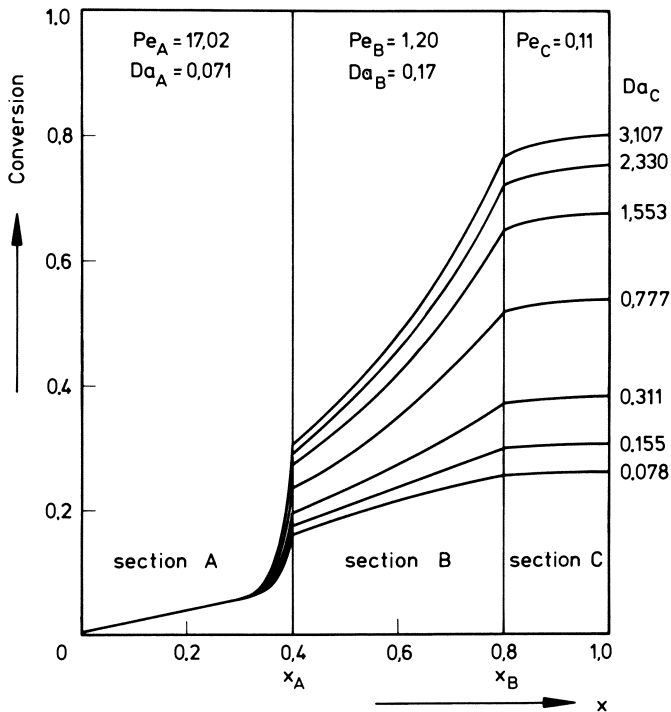


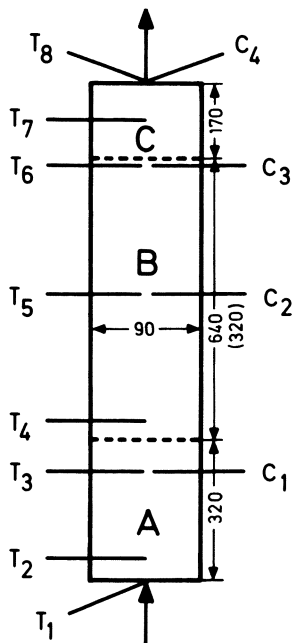
Figure 3. Concentration profiles for a first-order reaction, $Pe_B = 1.20$. Parameter: Da_C .

although the reaction parameters in A and B remain constant. Figures 2 and 3 also show that the back effect caused by the increased reaction rate in the last section depends strongly on the dispersion in the previous sections. In Figure 3, the dispersion is increased in section B; this strongly influences the location of the conversion profiles in sections B and A *vs.* Figure 2.

This experimental study of a laboratory scale chemical reactor divided in sections with different properties tested the validity of the boundary conditions of Wehner and Wilhelm. No direct experimental proof of these boundary conditions has been published.

Experimental Setup

Because this study was based on a strictly deterministic model, it was necessary to know all parameters of the model and to avoid fitting experimental results to model predictions. Therefore, a simple liquid phase tube reactor with a second-order reaction was used. The progress of the reaction was easily analyzed by conductivity measurements. The reactor was a Plexiglass tube with an internal diameter of 90 mm. The first section of the reactor was a bed of glass spheres (diameter 10 mm); the second section was only the empty tube. Their lengths were 320 mm and 640 mm, respectively. A stirred vessel was used as a third section. The vessel was equipped with a bifilar coiled heat-exchanger which allowed the temperature to be changed in this section. The experimental arrangement is shown in Figure 4.



T : thermometer
C : conductivity cell

Figure 4. Experimental setup

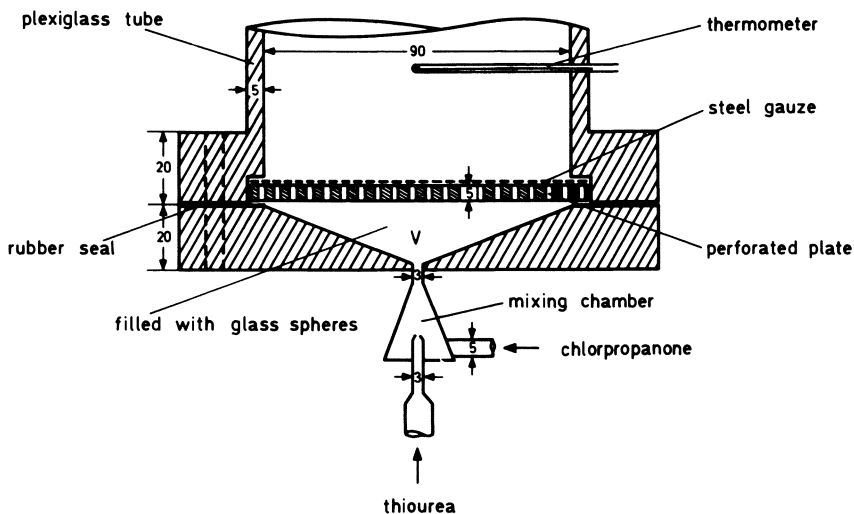


Figure 5. Details of reactor entrance

Conductivity cells were introduced to the reactor axis by side connections near the boundaries between two sections. Total conversion was calculated from the measured conductivity at the reactor exit. Temperatures were also measured at different points along the tube. Details of the reactor entrance and the third section are shown in Figures 5 and 6. The mixing chamber ensured intimate mixing of the feed streams of the two reaction components. The reaction mixture entered through a perforated plate which provided uniform distribution of the stream. Volume V was filled with glass spheres of 3-mm diameter to minimize its size

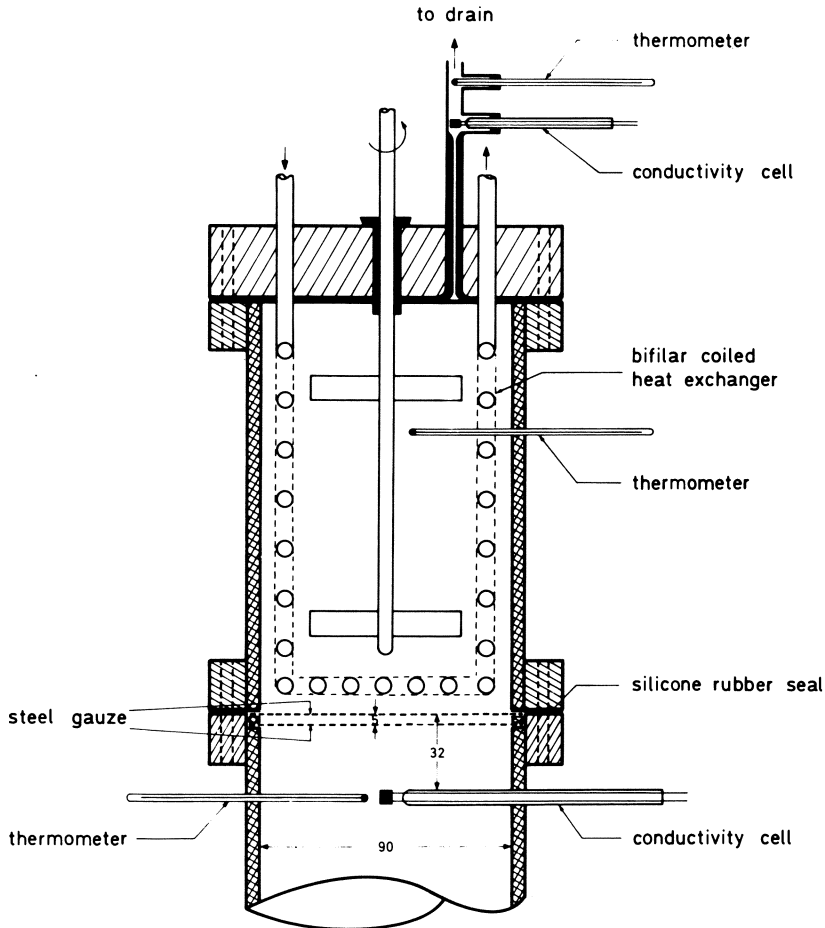


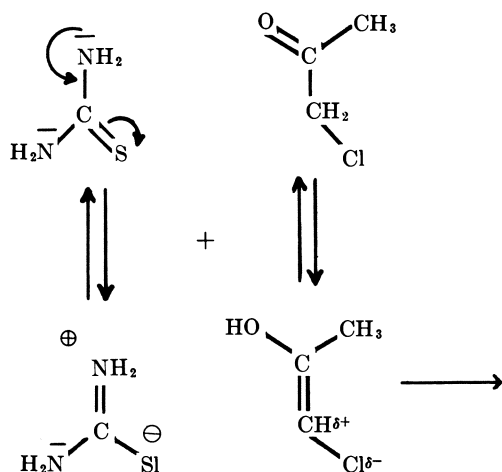
Figure 6. Section C of reactor

Each section was distinguished by different dispersion and different linear velocities; the ratio $v_A : v_B : v_C$ was 1 : 0.391 : 0.424. In the third zone, the reaction rate could be increased by raising the temperature. To ensure that the model assumptions were verified at section boundaries, any rigid separation of the different sections was avoided. Two steel gauzes were introduced to prevent large irregular fluctuations at the boundary surface between the second and the stirred section. The steel gauzes were 5 mm apart, each gauze having a free surface area of 60% of the total.

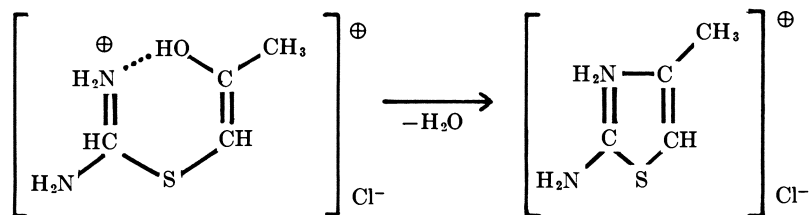
All measurements were done at temperatures in section C at least 3°C higher than in the previous section. This difference caused a density difference in the reaction mixture between the second and the third reactor sections. This difference, along with the effect of the steel gauzes, yielded a schlieren layer, whose position depended on the stirrer speed in the third section. Thus, the schlieren layer could be moved from about 5 to 30 mm upstream from the gauzes by increasing the stirrer speed from 50 to 300 rpm. During the measurement the location of the layer remained constant, with a fluctuation of less than 5 mm. This schlieren layer was taken as the boundary surface between the second and third reactor sections.

Determination of Parameters

Kinetic Data. The reaction used was the conversion of chloropropanone (A) and thiourea (B) in aqueous solution. This second-order reaction was previously applied in (12) for flow studies in stirred vessels:



2-amino-4-methylthiazolium chloride



Since the reacting components have negligible conductivity, the formation of the reaction product can be determined easily by measuring the conductivity. Kinetic data were determined batchwise at temperatures between 20° and 80°C. Thiourea concentration was varied from 0.05 to 0.5 gram-mole/liter; the initial concentration of chloropropanone was maintained at 0.05 gram-

mole/liter. Merck chemicals of 99% purity were used. The rate data did not depend on the value and the ratio of the concentrations applied. The following rate expression was obtained:

$$r = 1.125 \times 10^{11} \exp\left(-\frac{16\,950}{RT}\right) c_A c_B \quad (10)$$

Chloropropanone is difficult to purify, and although was always freshly distilled, different yields of it gave frequency factors with up to 10% deviation.

Dispersion Coefficients. The dispersion coefficients of each reactor section were determined separately. A δ -injection of KCl tracer was generated at the zone entry, and the dispersion coefficients were calculated from the variance of the response curve at the exit by applying the relation given by van der Laan (6) for the closed vessel system.

The dispersion coefficients obtained are plotted vs. the Reynolds number in Figure 7. The values measured in the packed bed of glass spheres agreed with the results of Schümmer (13). The dispersion coefficients of the empty tube and the stirred zone are scattered around the regression line. However, numerical simulations indicated that the conversion is not very sensitive to variations in the dispersion coefficients.

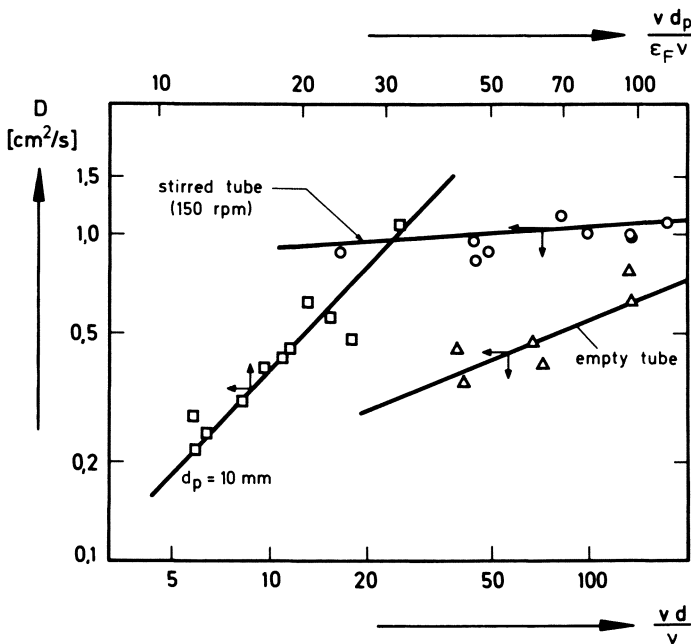


Figure 7. Dispersion coefficients of different reactor sections

Performance of Measurements

Every series of experimental runs was performed with fresh solutions of the reaction components in deionized water. Chloropropanone was the key component, and its concentration was varied from 0.01–0.045 gram-mole/liter. Thiourea was used in excess up to fivefold. The solutions were fed continuously from storage tanks through coiled heat-exchangers into the mixing chamber by piston pumps with less than 1% oscillation.

Table I. Conditions and Conversions for a Typical Series of Runs^a

Run	Pe_C	Da_C	X_{exp}	X_1	X_2	X_{1,C_3}
B.1	0.77	0.030	0.252	0.246	0.247	0.230
B.2	0.76	0.055	0.286	0.272	0.273	0.243
B.3	0.75	0.077	0.304	0.296	0.297	0.257
B.4	0.75	0.105	0.335	0.326	0.328	0.277
B.5	0.75	0.140	0.365	0.359	0.361	0.296
B.6	0.75	0.198	0.407	0.405	0.408	0.324
B.7	0.74	0.231	0.420	0.427	0.429	0.337
B.8	0.73	0.601	0.583	0.599	0.602	0.444

^a ($Q = 9.86$ l/h, $c_{A,a} = 0.0408$ gram-mole/liter, $\xi = 2.19$; dimensionless groups in section A and B are constant: $Pe_A = 15.2$, $Da_A = 0.02$, $Pe_B = 7.9$, $Da_B = 0.09$.)

During the first run of each series the temperature in section C was raised at least 3°C higher than in the section B. At a stirrer speed of 150 rpm the schlieren layer was located at about 1 cm below the gauze. Thus, the conductivity at the exit of section B could be measured with conductivity cell C_3 . The temperatures in each section did not differ more than 0.1°C.

When steady state was established, conductivities were measured. Thereafter, the temperature in section C was increased in 5°–10°C increments. At each the conductivities were measured when steady state was reached.

The higher temperature in section C caused an increase of reaction rate and dispersion there while the properties of section A and B were not changed. As shown in Figure 7, the increase of the dispersion coefficient in section C is small. Table I gives experimental conditions for a typical series of runs. The conversion at the reactor exit was calculated from the measured conductivity in cell C_4 . Up to 0.06 gram-mole/liter the conductivity depended linearly on the concentration of the salt formed by the reaction. The temperature dependence of the conductivity is given by:

$$\kappa_{21} = \frac{\kappa_t}{1 + 0.0242(t - 21)} \quad (11)$$

The conversions X_1 and X_2 in Table I refer to computed values from model 1 and model 2, respectively, which are discussed later.

Numerical Computations

The differential equations of the model were formulated for the reaction product P. Since the reaction is second order in each section, the function $f(C)$ in Equations 1–3 is:

$$f(C) = -(1 - C_p)(\xi - C_p) \quad (12)$$

with $C_p = c_p/c_{A,a}$ and $\xi = c_{B,a}/c_{A,a}$. The measured kinetic data and dispersion coefficients were used in the numerical calculations.

The set of the nonlinear differential equations was solved numerically by applying the quasi-linearization technique and the implicit difference method (14). At the boundary surface x_A we used Equations 5 and 6 which yield, in difference form:

$$\frac{x_A}{Pe_A \Delta x} [C_p(N_A - 1) - C_p(N_A)] = \frac{x_B - x_A}{Pe_B \Delta x} [C_p(N_A) - C_p(N_A + 1)] \quad (13)$$

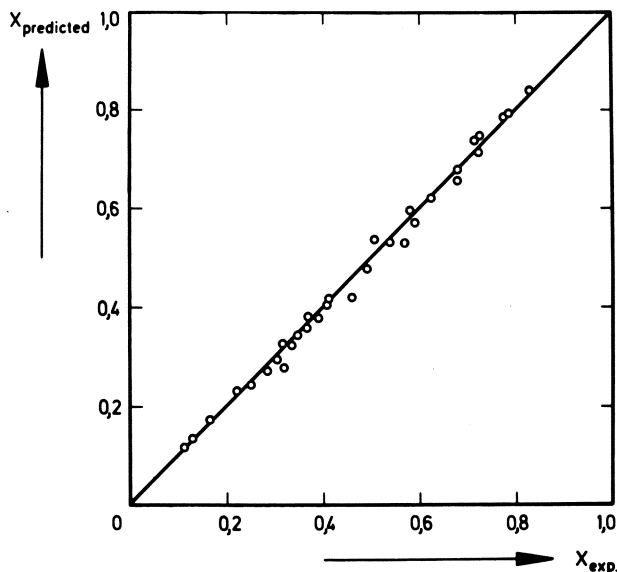


Figure 8. Experimental results vs. predictions from model 1 (boundary conditions of Wehner and Wilhelm)

where the point N_A refers to x_A . An equivalent expression is obtained for the boundary at x_B . Conversions calculated for a first-order reaction by the numerical method using Equation 13 agreed with those obtained from the analytical solution. This fact indicates that Equation 13 does represent the Wehner-Wilhelm boundary conditions.

Experimental Results and Model Predictions

The conversions computed from the model described above were compared with the experimental results in Figure 8. The predicted values agree with experimental ones, but the points scatter strongly around the straight line. As described above, this model (model 1) applies to the Wehner-Wilhelm boundary conditions which are distinguished from those of Dankwerts by the additional assumption that concentrations are continuous at boundary surfaces. The Wehner-Wilhelm boundary conditions cause a characteristic back effect. In the measurements carried out, this back effect could not be observed. When the temperature in the last section was raised, the conductivity measured with cells C_1 , C_2 , and C_3 remained constant. Thus, the back effect predicted from model 1 and illustrated in Figures 2 and 3 seems to be nonexistent in our experiments.

Since we found no back effect, the condition of continuity of concentrations was dropped. If these conditions (Equations 6 and 8) are not used, only four boundary conditions are available to integrate the differential Equations 1-3. Using the argument of Dankwerts, two further conditions may be obtained from a discussion of the mass balances at the boundary surfaces (Equations 5 and 7). Since the component considered is produced by the reaction, the gradients are positive or zero (when no reaction takes place). Now, when:

$$\frac{x_A}{Pe_A} \frac{dC_p(x_A^-)}{dx} > \frac{x_B - x_A}{Pe_B} \frac{dC_p(x_A^+)}{dx} \quad (14)$$

it follows from Equation 5:

$$C_p(x_A^-) > C_p(x_A^+) \quad (15)$$

This conclusion is also obtained from the limiting cases, $Pe_B \rightarrow \infty$ and $Pe_B \rightarrow 0$. Equation 15 is clearly absurd since it means that the conversion at the end of section A is higher than the conversion behind the boundary surface at x_A . This contradiction is resolved when the gradients are assumed to be zero at the ends of each section; thus, for x_A :

$$\frac{dC_p(x_A^-)}{dx} = 0 \quad (16)$$

This variation is model 2. Explicitly written, the set of boundary conditions used to integrate the differential equations of the different sections is, in model 2:

for section A:

$$C_p(0^+) = \frac{1}{Pe_A} \frac{dC_p(0^+)}{d\bar{x}} \quad (17)$$

$$\frac{dC_p(x_A^-)}{d\bar{x}} = 0 \quad (18)$$

for section B:

$$C_p(x_A^+) = C_p(x_A^-) + \frac{1}{Pe_B} \frac{dC_p(x_A^-)}{d\bar{x}} \quad (19)$$

$$\frac{dC_p(x_B^-)}{d\bar{x}} = 0 \quad (20)$$

and for section C:

$$C_p(x_B^+) = C_p(x_B^-) + \frac{1}{Pe_C} \frac{dC_p(x_B^-)}{d\bar{x}} \quad (21)$$

$$\frac{dC_p(1^-)}{d\bar{x}} = 0 \quad (22)$$

Here \bar{x} is the reduced length: $\bar{x} = z/l$, where l is the appropriate section length. When Equations 18–21 are applied, concentration jumps are allowed at the section boundaries x_A and x_B .

The conversions at the reactor exit calculated from model 2 deviate little from those calculated from model 1. Data of X_1 and X_2 are given for a typical series of runs in Table I. At reactor exit the difference between the predictions of both models is smaller than the experimental error. However, the conversion profiles of model 1 and model 2 are quite different near section boundaries, as shown in Figure 9. In Figure 10 the predictions of model 1 and model 2 are compared with those experimentally obtained from conductivity cell C_3 . While the experimental values as well as those predicted from model 2 remain constant, the conversions calculated from model 1 increase at the position of measuring cell C_3 when the temperature and, thus, the reaction rate, is increased in the last reactor section. Therefore, the conversions predicted from model 1 deviate more and more from the measured value. This is demonstrated further by the data in Table I. There the measured conversion at reactor exit along with those predicted from model 1 and model 2 are shown. The last column in

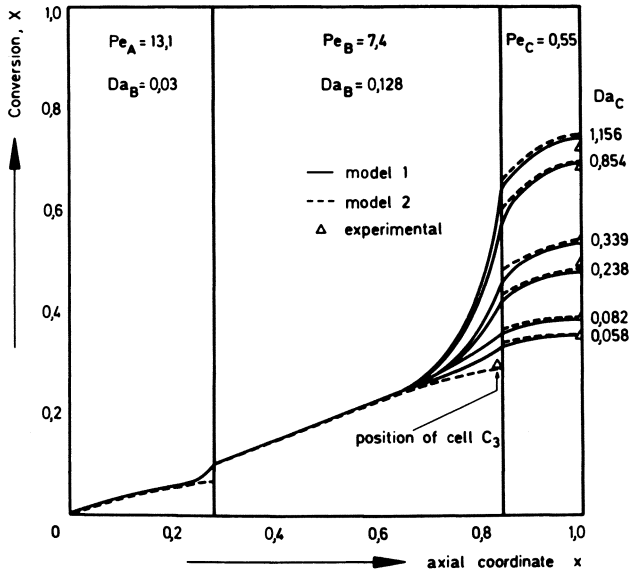


Figure 9. Experimental results and predicted profiles from model 1 and model 2

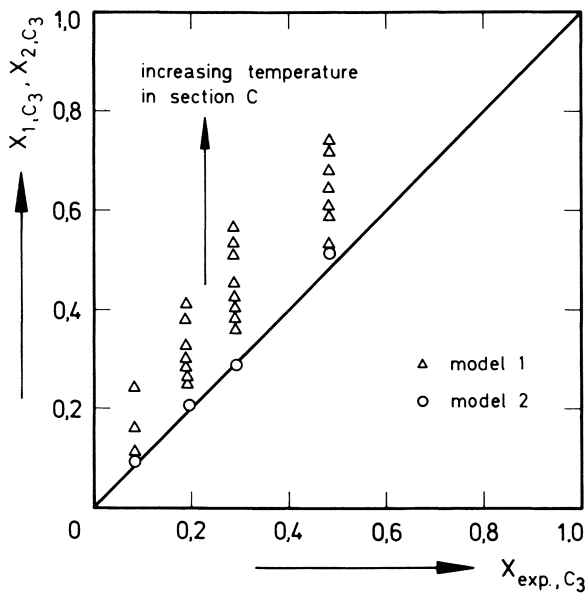


Figure 10. Measured conversions and predicted conversions from model 1 and model 2 at the end of section B (conductivity cell C_3)

Table I contains conversions calculated from model 1 at the position of the conductivity cell C_3 . Compare these values with the appropriate experimental conversion and with that computed from model 2:

$$X_{\text{exp.}, C_3} = 0.194 \text{ and } X_{2, C_3} = 0.196$$

Discussion and Conclusions

Since the assumption of continuity of concentrations as applied in model 1 is well established in the literature, it is surprising that the conversions resulting from our experimental arrangement do not confirm this assumption. Moreover, a satisfactory agreement is obtained if each section is treated separately and alternating effects are ignored. This agreement is attained when constant mass flow is assumed and the concentration gradients are assumed to be zero at the end of each section. Thus, concentration jumps are permitted at the boundary surfaces between the reactor sections.

To prevent hasty conclusions concerning the validity of the Wehner-Wilhelm conditions, remember that the boundary surface between sections B and C strongly influences our experiments since the increase in temperature in the last section should give the predicted back effect. This boundary consisted of a schlieren layer resulting from density differences of the reaction medium in sections B and C. Although density effects are negligible in the model equations as long as the properties are constant in each section, the boundary between section B and C seems to behave like a phase transition which prevents any feedback. Further studies in different experimental arrangements and other reacting systems may yield a more severe formulation of the generally accepted Wehner-Wilhelm boundary conditions.

It is questionable whether the experimental setup agrees with the conditions of the dispersion model's applicability. First, the dispersion model requires plug flow of the reaction mass. Since the liquid velocities are in the range 0.02–0.1 cm/sec, this condition is not satisfied. Since the reaction tube is short and of large diameter, a laminar flow profile is not established. This fact was confirmed by tracer injections with dye where a flat profile was observed. Secondly the dispersion mechanism is usually explained by stochastic fluctuations of fluid elements, whose dimensions are small compared with reactor dimensions. This condition cannot be fulfilled in the stirred reactor section where the Peclet numbers are less than 1. When these objections are considered, agreement of the experimental results with the predictions of the dispersion model applying the Danckwerts boundary conditions for each section is surprising. If the results prove to be correct in a more general sense, reactors divided into sections with different properties will be mathematically easy to handle since each section can be treated independently.

The Wehner-Wilhelm conditions are sensible from the physical point of view. On the other hand, applying the principles of irreversible thermodynamics, Standart (11) pointed out that there are no *a priori* reasons why properties must be continuous at boundary surfaces. It may be argued that the Wehner-Wilhelm conditions are not applicable to experimental setups which consist of three reaction zones since Wehner and Wilhelm considered only one section with reaction. However, the Wehner-Wilhelm condition that the concentration is continuous around any point does not depend on a reaction taking place on both sides of the boundary surface.

The concentration is continuous from a microscopic point of view. However, it is still not known whether the transport mechanisms which prevail in

the bulk of a reaction section also exist at boundaries. Since the transition regions can be small, discontinuities are possible from a macroscopic point of view. Thus, the mathematical formulation of boundary conditions idealizes the real situation from this macroscopic point of view.

Nomenclature

c	concentration
C	dimensionless concentration, $C = c/c_a$
d_p	diameter of particle
d_t	diameter of tube
D	dispersion coefficient
Da	Damköhler number of section, $klc_{A,a}^{n-1}/v$
k	reaction rate constant
l	length of section
L	total length of reactor
Pe	Peclet number of section, vl/D
Q	volume flow rate
r	reaction rate
R	gas constant
t	temperature, °C
T	temperature, °K
x	dimensionless axial coordinate, z/L
\bar{x}	dimensionless axial coordinate, z/l
X	conversion, $(c_{A,a} - c_A)/c_{A,a}$
z	axial coordinate
ν	kinematic viscosity
ξ	excess, $c_{B,a}/c_{A,a}$
κ	electrical conductivity

Subscripts

1	model 1
2	model 2
a	reactor entry
A	section A or key component
B	section B or excess component
C	section C
i	component i
p	reaction product

Literature Cited

- Langemann, H., Kölbl, H., *Verfahrenstechnik* (1967) **1**, 1.
- Dahner, J. F., Wilhelm, R. H., *Chem. Eng. Sci.* (1956) **6**, 89.
- Dankwerts, P. V., *Chem. Eng. Sci.* (1953) **2**, 1.
- Damköhler, G., in "Der Chemie-Ingenieur," A. Eucken and M. Jakob, Eds., III/1, p. 359, 1937.
- Damköhler, G., *Zeitschr. Elektrochemie* (1937) **43**, 1.
- van der Laan, E. T., *Chem. Eng. Sci.* (1958) **7**, 187.
- van Cauwenberghe, A. R., *Chem. Eng. Sci.* (1966) **21**, 203.
- Bischoff, K. G., *Chem. Eng. Sci.* (1961) **16**, 131.
- Bischoff, K. B., Levenspiel, O., *Chem. Eng. Sci.* (1962) **17**, 245, 257.
- Levenspiel, O., Bischoff, K. B., *Adv. Chem. Eng.* (1963) **4**, 95.
- Standart, G., *Chem. Eng. Sci.* (1968) **23**, 645.
- Kerber, R., Gestrich, W., *Chem. Ing. Tech.* (1966) **41**, 1222.
- Schümmer, P., Doctoral thesis, TH Aachen, Germany, 1963.
- Lee, E. S., "Quasilinearization and Invariant Imbedding," Academic Press, New York, London, 1968.

RECEIVED January 2, 1974.

Influence of Chemical Parameters on Micromixing in a Continuous Stirred Tank Reactor

ANDRÉ ZOULALIAN and JACQUES VILLERMAUX

Département de Génie Chimique, Ecole Nationale Supérieure des Industries Chimique, 1, rue Grandville, 54042 Nancy, France

The state of micromixing in a CSTR was experimentally investigated through its (marked) influence on the selectivity of consecutive competitive reactions $A + B = R$, $R + B = S$ in the liquid phase. An experimental segregation index was defined. The influence of the following parameters was investigated: stirring, space time, viscosity, ultrasounds, concentrations, temperature, nature of the reaction, and contacting of reactants. Segregation becomes more important as $k_1 C_0 \exp(E/RT)$ increases; C_0 = total concentration, and E = experimental activation energy. Micromixing results from a combination of reaction and molecular diffusion in the ultimate fluid aggregates having a size below the turbulence concentration microscale, which can be estimated by this method. Thus, the usual assumption of maximum mixedness in the design and use of the CSTR for complex reactions may be quite erroneous. The CSTR is not well suited to kinetic studies of complex reactions unless experimental conditions ensuring a perfect micromixing are determined.

The question of the influence of micromixing on the extent of chemical reactions in continuous reactors has been the subject of many investigations. Most of the studies are theoretical and rather academic ones (1, 2, 3, 4, 5, 6, 7, 8, 9, 10, 11, 12, 13, 14). Several authors have attempted however to study this problem in an experimental way (15, 16, 17, 18, 19, 20, 21, 22, 23, 24, 25, 26, 27, 28, 29, 30, 31).

In a previous work (29), we demonstrated experimentally that if the residence time distribution (RTD) and the batch kinetics are accurately known, it is possible to deduce the state of mixing of the fluid from chemical conversion measurements. For moderately dispersed RTD and single reactions, segregation effects are usually very small (a few per cent) and consequently of little practical importance; this is a fortunate result for the designer.

The sensitivity to mixing effects can become much more important if we use a reactor having a broad RTD and use another chemical characteristic: the product distribution (selectivity) in a system of multiple reactions. This led us to study the selectivity of consecutive competitive reactions of the type

$A + B = R$, $R + B = S$ in a continuous stirred tank reactor (CSTR). In this case, an elementary calculation shows that at total conversion of B—initially in defect—the selectivity in the production of R strongly depends on the micromixing state and may vary in a range of 100% between the maximum mixedness limit and the total segregation limit (batch reactor selectivity). In particular, we were asking the following questions:

- (1) Are micromixing and macromixing tied together in a CSTR?
- (2) Is it possible to influence only the first one, and if so, in varying which physicochemical parameters?
- (3) Is a CSTR a well suited tool for the determination of the kinetics of complex reactions in the liquid phase?
- (4) Does the chemical study of segregation effects allow the estimation of a micromixing scale?

In addition to the answers to those questions, the surprising results we obtained eventually led us to a new appraisal of micromixing phenomena, discussed below.

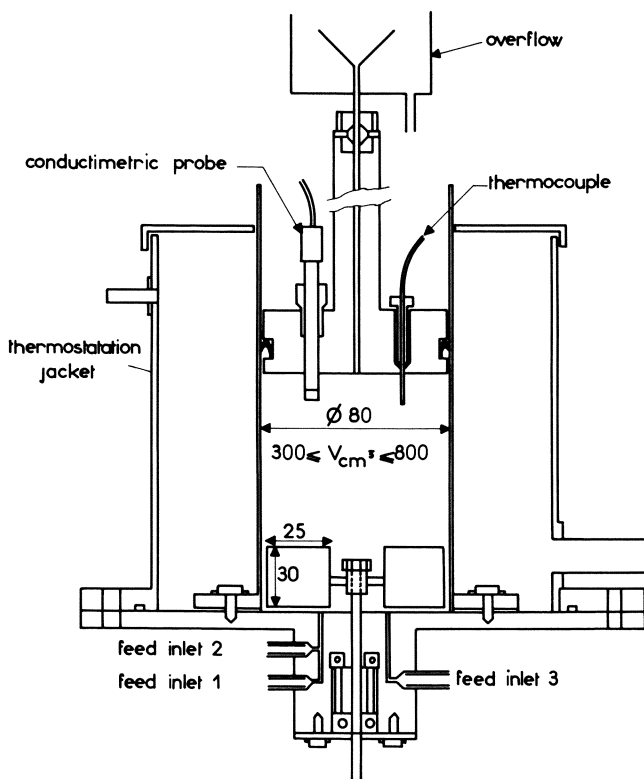


Figure 1. Experimental reactor (linear dimensions in mm)

The Experimental Reactor

The reactor is a vertical cylindrical tube fixed on its base to a strap including the various feed inlets and the mechanical agitation device (Figure 1). The upper side of the reactor is a piston through which the fluid flows out.

The displacement of the piston allows the geometric reacting volume to be varied. When ionic reactants are used, their outlet concentration is measured by an electrical conductivity probe. The temperature of the fluid can be controlled and measured by a thermocouple.

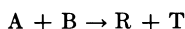
Residence Time Distribution

Except at the lower stirring speeds ($N < 60$ rpm) for which the mixing time is clearly perceptible, the experimental RTD is undistinguishable from a pure exponential decay (Figure 2). The mean residence time and the space time (calculated from the volume and the flow rate) agree within 2%. Because of accuracy limitations in the measurements of volumes, flow rates, and slopes, such an uncertainty has no systematic character and is usual in experimental RTD determinations. We thus consider below that the reactor behaves as a perfect macromixer.

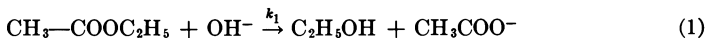
Choice of the Chemical Reactions—Definition of an Experimental Micromixing Index

To investigate the influence of micromixing on the reactor performance, three liquid phase reactions have been selected:

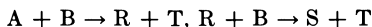
- (1) A single second-order reaction:



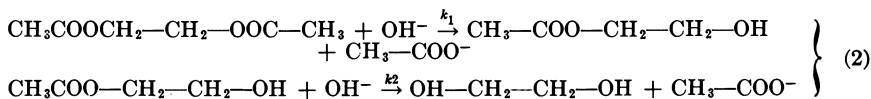
The well known alkaline hydrolysis of ethyl acetate:



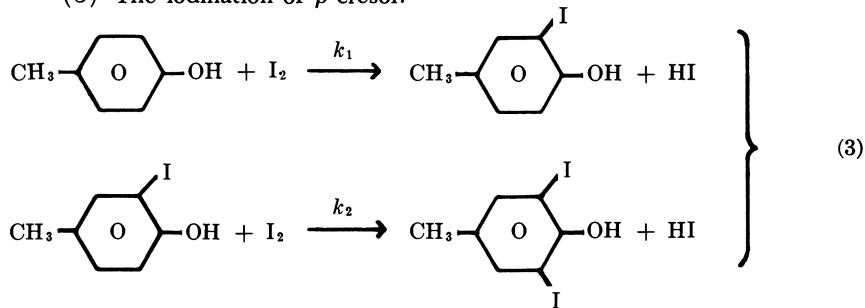
- (2) Two consecutive competitive second-order reactions



The alkaline hydrolysis of glycol diacetate:



- (3) The iodination of *p*-cresol:



The products were analyzed by conductimetry (OH^-), chromatography (glycol acetate) and/or spectrophotometry (iodoparacresols). The initial reactant concentrations were in the range of 0.1 to 0.4M (Reactions 1 and 2) and 10^{-4} to 5×10^{-4} M (Reaction 3). Experimental details are given else-

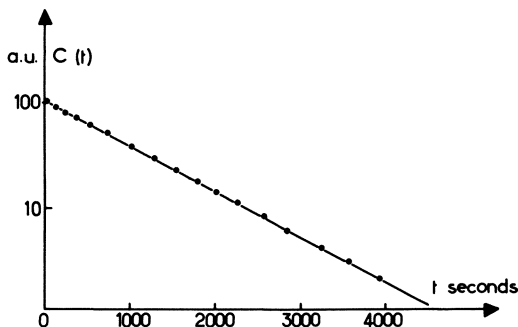


Figure 2. An example of RTD—experimental conditions: $N = 1400$ rpm; $V = 492$ cm³; $Q = 0.495$ cm³/sec; $\tau = V/Q = 994$ sec; $\bar{t} = 982$ sec; deviation: 1.2%.

where (32).

Before continuous processing, careful batch experiments were done to determine the kinetic constants. The best results are summarized below:

$$\text{Reaction 1: } k_1 = 2.635 \times 10^7 \exp \left[-\frac{11400 \pm 200}{RT} \right] \text{ l/mole/sec}$$

$$\text{Reaction 2: } k_1 = 1.1 \times 10^7 \exp \left[-\frac{10000 \pm 1000}{RT} \right] \text{ l/mole/sec}$$

$$k_2 = 1.4 \times 10^8 \exp \left[-\frac{12000 \pm 1000}{RT} \right] \text{ l/mole/sec}$$

Reaction 3: in fact, the mechanism is more complex than written above, so that both the Γ concentration (0.03M) and the pH must be specified. In a buffer solution of pH 9.08 at 20°C

$$k_1 = 2.3 \times 10^{11} \exp \left[-\frac{13000 \pm 500}{RT} \right] \text{ l/mole/sec}$$

$$k_2 = 1.27 \times 10^{14} \exp \left[-\frac{17000 \pm 500}{RT} \right] \text{ l/mole/sec}$$

In a buffer solution of pH 11.0 at 20°C

$$\left. \begin{array}{l} k_1 = 3.25 \times 10^3 \text{ l/mole/sec} \\ k_2 = 1.28 \times 10^3 \text{ l/mole/sec} \end{array} \right\} \text{ at } 24.2^\circ\text{C}$$

These constants enable the calculation of the yield in R , at the two limiting assumptions of maximum and minimum mixedness. Let P_0 and P_1 be the corresponding representative points on the conversion diagrams (Figure 3) and let P be an experimental point obtained in the same conditions. We define an experimental segregation index X as the ratio:

$$X = \frac{\overline{PP_0}}{P_1 P_0} \quad (4)$$

X is an empirical characterization of the reactor behavior. $X = 0$ corresponds

to maximum mixedness and $X = 1$ to minimum mixedness (total segregation).

The first and rather surprising result is that under typical conditions, apparently providing excellent fluid mixing, the segregation index X may be quite different from 0. We found $X = 0.232$ in our first experiments with Reaction 2.

$C_{AO} = 0.197$ mole/liter, $C_{BO} = 0.194$ mole/liter
 space time = 272.7 sec
 temperature = 22.1°C
 stirring velocity = 300 rpm
 C_R/C_{AO} : maximum mixedness = 0.365
 total segregation = 0.526
 observed = 0.403
 $X = 0.232$

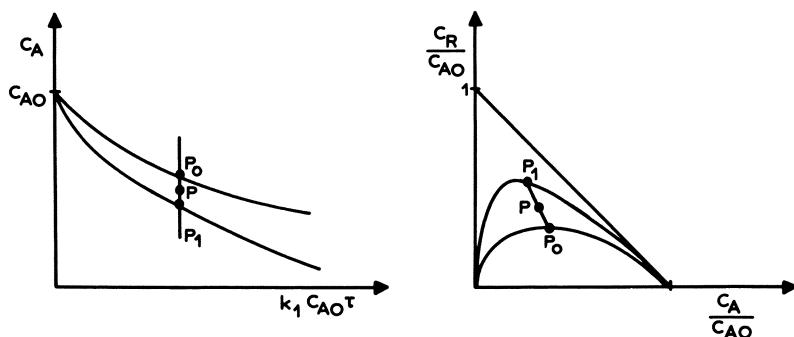


Figure 3. Conversion diagrams

Table I. Influence of Total Concentration C_0 and Stoichiometric Ratio M . Alkaline Hydrolysis of Glycol Diacetate (Reaction 2)

Exp.	C_0	M	t°, C	C_A/C_{AO}			C_R/C_{AO}			$\frac{(C_R)_{seg.}}{(C_R)_{min.}}$ $\frac{(C_R)_{min.}}{(C_R)_{min.}}$	X
				Calculated		Exptl.	Calculated		Exptl.		
				Max. Mix.	Seg.		Max. Mix.	Seg.			
102	0.1535	1.117	21.0	0.311	0.217	0.301	0.356	0.533	0.372	49.7	0.090
100	0.1488	1.050	21.0	0.326	0.236	0.316	0.360	0.532	0.379	47.8	0.108
77	0.2464	1.037	20.3	0.356	0.271	0.345	0.366	0.529	0.388	44.5	0.131
76	0.3206	1.626	20.6	0.186	0.091	0.170	0.287	0.473	0.316	64.8	0.158
66	0.2844	0.555	22.0	0.562	0.519	0.554	0.329	0.413	0.344	25.5	0.158
117	0.3880	0.980	19.6	0.343	0.246	0.321	0.365	0.532	0.405	45.8	0.235
119	0.3950	1.026	20.2	0.341	0.255	0.320	0.365	0.532	0.407	45.8	0.250
111	0.4361	1.247	19.7	0.239	0.141	0.216	0.328	0.517	0.371	57.6	0.230
75	0.4461	0.853	20.6	0.413	0.339	0.393	0.367	0.509	0.405	38.7	0.267
67	0.5041	1.634	22.0	0.115	0.055	0.091	0.207	0.359	0.250	73.4	0.293
81	0.7630	1.272	20.9	0.217	0.121	0.180	0.311	0.500	0.384	60.8	0.392
68	0.8043	0.941	21.6	0.351	0.267	0.308	0.365	0.529	0.448	44.9	0.511

To explain this observation, we studied the influence of various experimental parameters on X . Most of the experiments were done with Reaction 2. Typical results obtained are reported in Table I. The difference in conversion calculated by the segregated flow and the maximum mixedness model is noticeable since it ranges, for this particular example, between 25 and 74% of the perfectly micromixed CSTR conversion—well beyond the uncertainty of experimental errors. The direct gas chromatographic determination of the

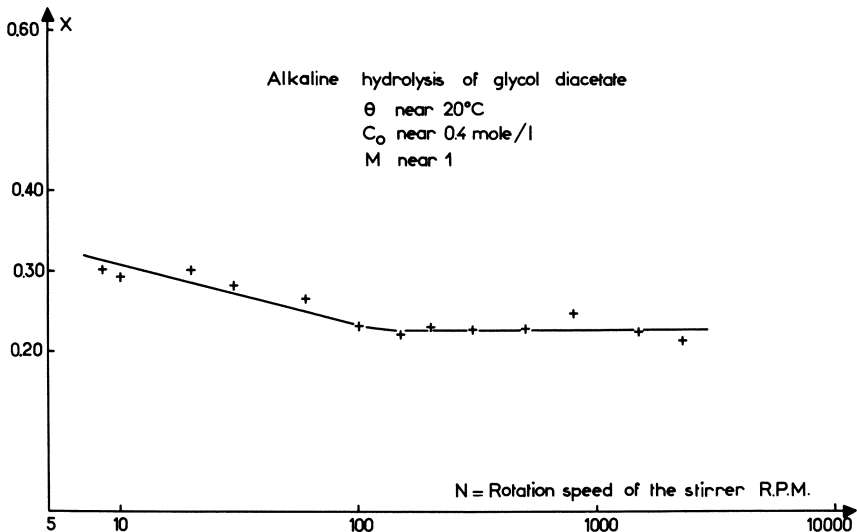


Figure 4. Variation of the segregation index X as a function of the rotation speed of the stirring device

C_R/C_A ratio, joined to C_B titration and material balances, allows the concentrations to be known to better than a few percent. We thus estimated the uncertainty on the segregation index X to about 10%.

Parameters

Influence of Stirring. Six different stirrers were used, differing in their shapes and number of paddles. Shear and turbulence were increased by baffles or a suspension of glass microbeads. X was independent of the stirring device. The stirring velocity was then varied between 8 and 2300 rpm. Above about 100 rpm, X remains constant. Below 60-100 rpm, a slight but significant increase of X can be noticed (Figure 4). The little deviation to perfect macro-mixing at low stirring speed can be taken into account and does not alter this conclusion.

Influence of Ultrasounds. Okada *et al.* (33) have already noted the possible effect of ultrasounds on the micromixing intensity. To test this, a 22-KHz ultrasonic transducer was immersed in the reactor. In the presence of an ultrasonic field, the X value was decreased by a factor 2 but did not go to zero.

Influence of the Viscosity of the Solution. The viscosity of the mixture was increased from 1 to 12 cp by adding sodium polyacrylate. The RTD and the kinetic constants were not altered. X increased slightly with viscosity but far less than expected (Figure 5).

Influence of Space Time. The space time τ was varied between 51 and 1674 sec, and the sodium hydroxide conversion remained higher than 85%. No variation of X could be observed.

Influence of Initial Concentrations and Temperature. The second surprising result was that X varied with the initial concentration of reactants when all other aspects, especially the hydrodynamic parameters, were kept constant. In fact X does not depend on the stoichiometric ratio $M = C_{B0}/C_{A0}$

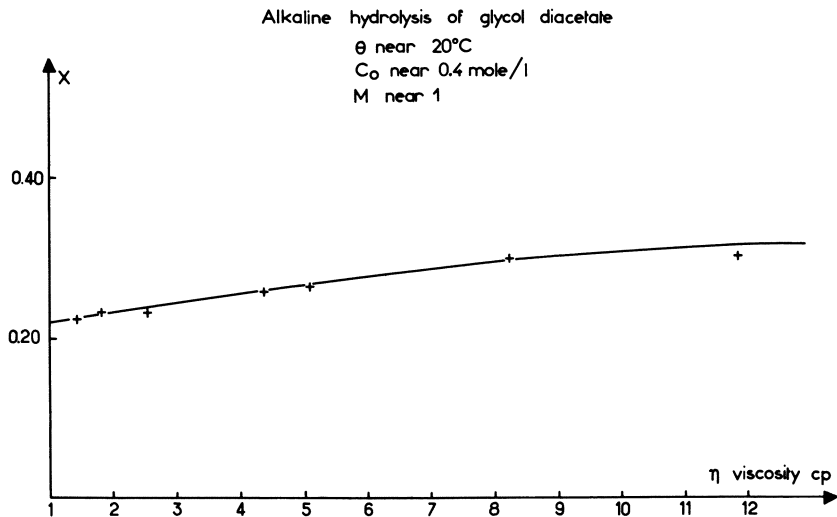


Figure 5. Variation of the segregation index X as a function of viscosity

but only on the total concentration $C_0 = C_{A0} + C_{B0}$. Experimental evidence for this is in Table I (compare experiments no. 76 and 66). Two different values of M (1.626 and 0.555) yield the same X (0.158) because C_0 is nearly the same (about 0.3 mole liter). Figure 5 shows a regular increase of X as a function of C_0 . Experimentally, the state of maximum mixedness ($X = 0$) is found by extrapolation as $C_0 \rightarrow 0$. Besides, X increases as a function of temperature (Figure 6). The X value is the same whether A and B are premixed or fed separately.

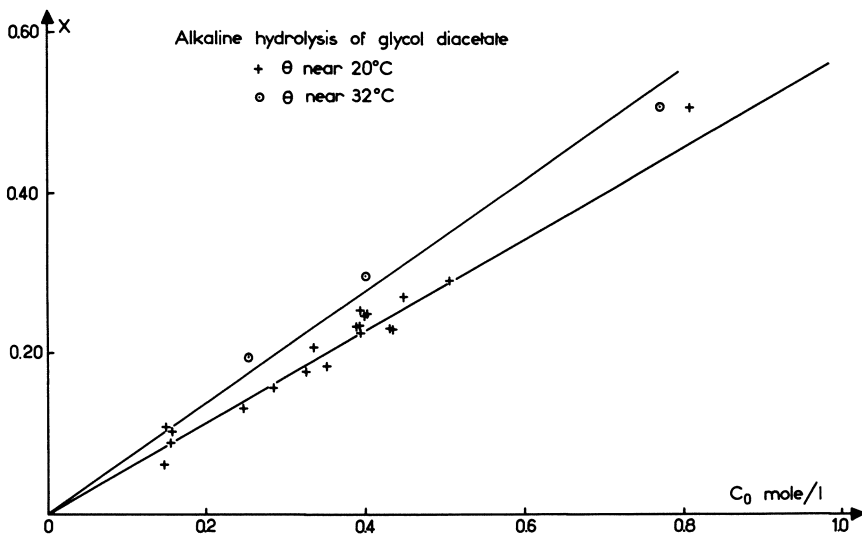


Figure 6. Variation of the segregation index as a function of the total concentration of reactants at the inlet of the reactor

Correlation of Experimental Results

The parameters acting on the state of micromixing in the reactor are: the total concentration of reactants, the viscosity and temperature of the fluid, the stirring velocity below 60 rpm, the presence of ultrasounds, and the nature of the reaction, which influences the magnitude of the above mentioned effects. In a given fluid, X mainly increases with C_0 and with temperature in a way which depends on the nature of the reaction. This last influence is included in the rate constant k_1 , but experience shows that the k_1 temperature dependence is too steep and must be corrected by an empirical factor $\exp(E/RT)$, where E is an experimental activation energy. Finally, after a thorough inspection of experimental results, we established a tentative correlation between X and a

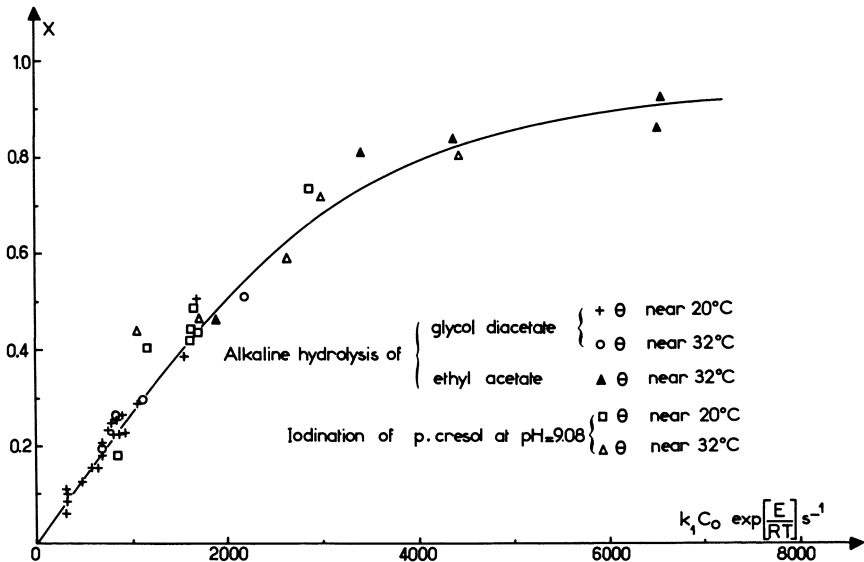


Figure 7. Variation of the segregation index X as a function of the $k_1 C_0 \exp [E/RT]$ group for three chemical systems

purely empirical parameter

$$Y = k_1 C_0 \exp [E/RT]$$

E has to be determined from experience in order to ensure a reasonable groupment of all experimental points around a unique curve. Figure 7 shows this plot of X vs. Y , which corresponds to the following values of E :

Reaction 1: $E \approx 6.6$ kcal/mole (estimated)

Reaction 2: $E = 5.0 \pm 0.2$ kcal/mole

Reaction 3: $E = 6.5 \pm 0.3$ kcal/mole

Discussion

By inspection, the simplest equation which can be suggested to fit the experimental curve is:

$$X = 1 - \exp[-BY] \quad (5)$$

where B is a constant. A logarithmic plot shows that Equation 5 is acceptable and yields $B = 3.37 \times 10^{-4}$ sec. How can these results be explained? Before proposing any interpretation, we emphasize that our first aim is to report experimental results to suggest a new appraisal of micromixing phenomena. Definitive conclusions would need further study. On the other hand, existing theories relating micromixing to turbulence have been developed with simple hypotheses such as isotropic turbulence. The hydrodynamic pattern in a real mixer is probably more complex, involving a highly turbulent core near the turbine surrounded by a quieter fluid. At this point, the search for a refined theoretical explanation of our results seems to be unrealistic. Nevertheless, a semiquantitative and suggestive explanation can be sought from the description given by Beek and Miller (34) as already pointed out by Paul (35). Beek and Miller distinguish three stages in mixing:

(1) Distribution of one fluid through the other and uniformization of average composition without decreasing local concentration variations. This is brought about by ordinary eddy diffusion.

(2) Reduction of size of the regions of uniform composition and correlative increase of the areas of contact between regions of different composition.

(3) Mixing by molecular diffusion.

The relative independence of the segregation index X upon the stirring velocity clearly proves that the first two stages do not play an essential role in determining the micromixing state, except perhaps below 60 rpm. The controlling step would then be the molecular diffusion of reactants into the segregated clumps having a size well below the turbulence concentration microscale, and thus it is unaffected by a modification of the turbulence intensity. Let λ be a characteristic dimension of these segregated regions and D the molecular diffusivity. In the above assumption, the intensity of micromixing will depend on the ratio of a diffusion time to a reaction time—that is, something like $m = k_1 C_0 \lambda^2 / D$, which is analog to the square of a Thiele modulus. The reaction thus appears to be diffusion controlled in the small fluid aggregates, as it might be in a catalyst pellet.

If this explanation holds, then $X \rightarrow 0$ as $m \rightarrow 0$ and $X \rightarrow 1$ as $m \rightarrow \infty$. On a purely phenomenological basis, a function exhibiting such a behavior is:

$$X = 1 - \exp[-m/m_0] \quad (6)$$

It is reasonable to suppose that X takes intermediate values between 0 and 1 when the diffusion time equals the reaction time ($m = 1$). We shall thus make the additional assumption that $m_0 \approx 1$. From Equation 5 we are led to identify m to BY :

$$m = k_1 C_0 \lambda^2 / D = BY = Bk_1 C_0 \exp[E/RT] \quad (7)$$

In this case, we should verify that λ^2/D (1) varies as $\exp[E/RT]$, $E \approx 5-6$ kcal/mole; (2) only undergoes a slight increase as a function of the viscosity; (3) decreases in the presence of ultrasounds.

The E value is of the order of magnitude of the activation energy of the diffusivity of solutes in aqueous solutions, and this might account for point (1). On the other hand, one might expect that $1/D$ is proportional to the viscosity of the solution. The addition of sodium polyacrylate increases the shear viscosity but may lead to the formation of a microphase through which small molecules can diffuse as in the pure solvent. This has been proved by Huizenga

et al. (36, 37) for sodium ions and might account for point (2). This statement is still speculative and should be checked experimentally.

The following expression has been proposed by Corrsin (38) in the case of liquids:

$$\frac{l^2}{D} = 18 \left[\frac{1}{k_0^{2/3} \epsilon^{1/3}} + \frac{1}{3} \left(\frac{\nu}{\epsilon} \right)^{1/2} \log Sc \right] \quad (8)$$

where l is the concentration fluctuations microscale.

The influence of the viscosity ν is weak since it figures in the second term which only amounts for a few percent of the first one (*see* below). The role of ultrasounds (point 3) can be understood if we imagine that they produce an increase of ϵ , which represents the kinetic energy dissipation per unit mass. Of course, these crude arguments need to be refined, and we can imagine the actual processes occurring in the segregated regions to be far more complex, depending on the nonuniform turbulence pattern in the reactor. On the whole, we can consider that the above interpretation is not inconsistent with our experimental observations. If we accept it, we can estimate an order of magnitude of λ . From Equation 7 it results that:

$$\lambda^2 = BD \exp(E/RT) \quad (9)$$

Taking $D = 7.2 \times 10^{-6}$ cm²/sec (aqueous diffusivity of glycol diacetate calculated from the Wilke and Chang (39) formula) and $E = 5$ kcal/mole, we obtain at room temperature:

$$\lambda = 3.3 \times 10^{-3} \text{ cm}$$

This value is not unrealistic but is difficult to compare with the microscale l given by Equation 8 because the energy dissipation term ϵ is not known. In this respect, it would be interesting to carry out direct measurements of the concentration fluctuations in the reacting fluid. Conversely, if we assume that λ and l are of the same order of magnitude, we can estimate ϵ .

We shall use the Corrsin formulas, as reported by Brodkey (40). The wave number k_0 can be expressed by the approximate relation:

$$k_0 = (\pi/5) L_s^{-1}$$

where L_s is the segregation macroscale. Then:

$$\frac{l^2}{D} \approx \frac{\lambda^2}{D} = 18 \left[\left(\frac{5}{\pi} \right)^{2/3} \left(\frac{L_s^2}{\epsilon} \right)^{1/3} + \frac{1}{3} \left(\frac{\nu}{\epsilon} \right)^{1/2} \log Sc \right] \quad (10)$$

Taking $L_s \approx 2$ cm (1/3–1 times the blade width according to Ref. 41), $\nu = 10^{-2}$ cm²/sec, $\lambda = 3.3 \times 10^{-3}$ cm, $D = 7.2 \times 10^{-6}$ cm²/sec, one obtains $Sc = 1388$ and

$$\epsilon = 23000 \text{ cm}^2/\text{sec}^3$$

The second term in Equation 10 represents only 2% of the sum, justifying the fact that the dependence of λ^2 on the viscosity is weak.

A typical value of ϵ is reported by Evangelista *et al.* (42) in a commercial application as $\epsilon = 20000$ cm²/sec³, in excellent agreement with the above estimation.

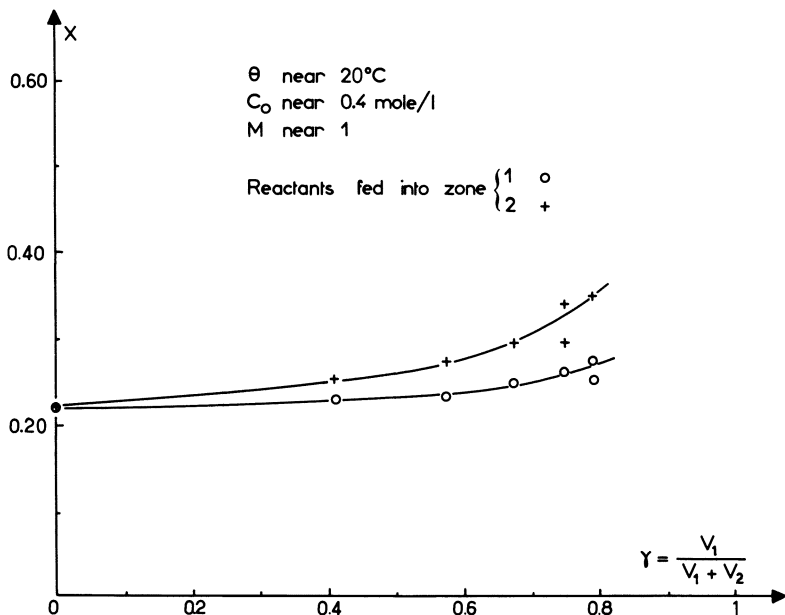


Figure 8. Variation of the segregation index X as a function of the volume ratio $\gamma = V_1/(V_1 + V_2)$. Zone 1: containing the stirrer; Zone 2: free of mechanical stirring. The reactants are fed alternately into the two zones.

For a reactor volume, $V = 450 \text{ cm}^3$, the total dissipation of kinetic energy amounts to

$$V\rho\varepsilon = 450 \times 2.3 \times 10^4 \times 10^{-7} \approx 1 \text{ watt}$$

It is interesting to compare this value with the energy consumption (43):

$$P = \Phi\rho N^3 D_a^5 \quad (11)$$

Under typical conditions, $N = 10 \text{ rps}$, D_a , agitator diameter = 6 cm. $Re = D_a^2 N/\nu = 36000$ so that Φ is nearly constant and can be estimated to $\Phi \approx 6$ for a two-blade turbine in the turbulent domain (44). With these values, one obtains:

$$P = 4.7 \text{ watts}$$

The efficiency of the turbulent production is thus:

$$\eta = V\rho\varepsilon/P \approx 0.2$$

a reasonable value (Corrsin cites $\eta = 0.5$ from work in pipe flows, as reported in Ref. 42). Of course, because of the crudeness of our assumptions, such estimations can only yield an order of magnitude.

Two Micromixing Zones Reactor

We now present the results of experiments which prove that the micromixing state in the inner volume of the reactor can be made locally variable. The reactor volume was divided into two zones by a metallic screen or a layer

of glass beads, allowing a perfect global macromixing of the fluid, as checked by the RTD. The first zone (1) (volume V_1) contained the stirrer whereas the second one (2) (volume V_2), was free of mechanical stirring. Figure 8 reports the variation of the segregation index X at the outlet of the reactor as a function of the ratio: $\gamma = V_2/(V_1 + V_2)$, the reactants being alternately fed into the first or the second zone of the reactor. The results clearly show that the second zone (no mechanical stirring) is more segregated than the first one, as could be expected.

Conclusion

(1) Micromixing is not only the result of hydrodynamic phenomena. It must not be considered (as many authors have done) as a physical framework in which chemical reactions take place. On the contrary, it can exist as irreducible coupling between reaction and diffusion, which gives rise to the segregation phenomenon. The intensity of segregation is then a function of concentration and depends on the size of the ultimate clumps of fluid. Chemical performance measurements thus appear to be a possible tool for studying turbulence phenomena.

(2) Thus, the usual and implicit assumption of perfect micromixing in the design and use of the CSTR for complex reactions may be quite erroneous, especially in viscous media, even if the RTD seems to be ideal and if the mechanical stirring power is high. We emphasize that a strong dependence of selectivity on segregation effects may however arise even for moderately rapid reactions in low viscosity media as those used in the present investigation.

(3) The CSTR is not well suited to kinetic studies of such complex reactions in the liquid phase (especially if selectivity measurements are to be carried out), unless experimental conditions ensuring maximum mixedness are defined. Preliminary experiments and the use of the general correlation we have proposed may help find these conditions. Fortunately segregation effects are probably less severe in gases, so that the above restrictions do not seem to entirely apply to the widespread gas phase kinetic measurements using a CSTR. This point deserves special study.

Nomenclature

A	{ ethyl acetate glycol diacetate paracresol	(Reaction 1) (Reaction 2) (Reaction 3)
B	{ sodium hydroxide iodine	(Reactions 1 and 2) (Reaction 3)
R	{ ethanol glycol monoacetate monoiodoparacresol	(Reaction 1) (Reaction 2) (Reaction 3)
T	{ sodium acetate hydriodic acid	(Reactions 1 and 2) (Reaction 3)
B	constant, sec	
C_i	concentration of reactant i , mole/liter	
C_{i0}	initial concentration of reactant i	
C_{O0}	$C_{A0} + C_{B0}$	
D	molecular diffusivity, cm^2/sec	
D_a	agitator diameter, cm	
k_0	wave number (turbulence theory), cm^{-1}	
k_1, k_2	kinetic constants, liter/mole/sec	

l	Taylor turbulent concentration microscale, cm
L_s	segregation macroscale, cm
$m = k_1 C_O \lambda^2 / D$	dimensionless criterion
M	C_{BO} / C_{AO}
N	rotation speed of the stirrer, sec^{-1} or min^{-1}
P	power consumption of the stirrer, watts
Sc	Schmidt number
T	absolute temperature, $^\circ\text{K}$
V, V_1, V_2	volumes of reaction zones, cm^3
X	segregation index
$Y = k_1 C_O \exp(E/RT)$	correlation parameter, sec^{-1}

Greek Letters

γ	volume ratio
ϵ	turbulent kinetic energy dissipation rate per unit mass, cm^2/sec^3
η	dynamic viscosity, cp
λ	characteristic dimension of the microsegregated regions, cm
ν	kinematic viscosity, cm^2/sec
ρ	density, gram/cm^3
τ	space time, sec
Φ	power number

Literature Cited

- Chen, M. S. L., Fan, L. T., *Can. J. Chem. Eng.* (1971) **49**, 704.
- Costa, P., Trevissoi, C., *Chem. Eng. Sci.* (1972) **27**, 653.
- Curl, R. L., *A.I.Ch.E. J.* (1963) **9**, 175.
- Danckwerts, P. V., *Chem. Eng. Sci.* (1958) **8**, 93.
- Kattan, A., Adler, R. J., *Chem. Eng. Sci.* (1972) **27**, 1013.
- Ng, G. Y. C., Rippin, D. W. T., *3rd Europ. Symp. Chem. Reaction Eng.*, Pergamon Press, Oxford, p. 161, 1965.
- Nishimura, Y., Matsubara, M., *Chem. Eng. Sci.* (1970) **25**, 1785.
- Rietema, K., *Advan. Chem. Eng.* (1964) **5**, 237.
- Rippin, D. W. T., *Chem. Eng. Sci.* (1967) **22**, 247.
- Trealeaven, C. R., Tobgy, A. H., *Chem. Eng. Sci.* (1972) **27**, 1497.
- Villiermaux, J., Devillon, J. C., *5th Europ. 2nd Intern. Symp. Chem. Reaction Eng.*, B-1-13, May 1972.
- Villiermaux, J., Zoulalian, A., *Chem. Eng. Sci.* (1969) **24**, 1513.
- Weinstein, H., Adler, R. J., *Chem. Eng. Sci.* (1967) **22**, 65.
- Zwietering, T., *Chem. Eng. Sci.* (1959) **11**, 1.
- Aubry, C., Thesis, Université de Nancy, 1972.
- Constantinides, A., M.S. Thesis, Ohio State University, 1964.
- Devillon, J. C., Thesis, Université de Nancy, 1972.
- Geurden, J. M. G., Thoenes, D., *5th Europ. 2nd Intern. Symp. Chem. Reaction Eng.*, B-1-35, May 1972.
- Harada, M., *et al.*, *J. Chem. Eng. Japan* (1968) **1**, 148.
- Hatate, Y., *et al.*, *J. Chem. Eng. Japan* (1971) **4**, 348.
- Leitman, R. H., Ziegler, E. N., *Chem. Eng. J.* (1972) **3**, 245.
- McWharf, J. E., Ph.D. Thesis, University of Rochester, 1967.
- Methot, J. C., Roy, P. H., *Symp. Kinetics Catalysis, Reactor Design, 21st Can. Chem. Eng. Conf.*, 1971.
- Paul, E. L., Treybal, R. E., *A.I.Ch.E. J.* (1971) **17**, 718.
- Ross, J. M., O'Brien, G., Ph.D. Thesis, University of Pennsylvania, 1966.
- Treleaven, C. R., Tobgy, A. H., *Chem. Eng. Sci.* (1973) **28**, 413.
- Worrel, G. R., Eagleton, L. C., *Can. J. Chem. Eng.* (1964) **42**, 254.
- Zoulalian, A., Thesis, Université de Nancy, 1969.
- Zoulalian, A., Villiermaux, J., *Chim. Ind. Génie Chim.* (1970) **103**, 973.

30. Zoulalian, A., Villermaux, J., *Chem. Eng. J.* (1970) **1**, 76.
31. Hovorka, R. B., Ph.D. Thesis, Case Institute of Technology, Cleveland, Ohio, 1961.
32. Zoulalian, A., Ph.D. Thesis, Université de Nancy, 1973.
33. Okada, K., *et al.*, *Chem. Eng. Sci.* (1972) **27**, 259.
34. Beek, J., Jr., Miller, R. S., *Chem. Eng. Prog. Symp. Ser.* (1959) **55** (25), 23.
35. Paul, E. L., Ph.D. Thesis, New York University, 1968.
36. Huizenga, J. R., *et al.*, *J. Amer. Chem. Soc.* (1950) **72**, 2636.
37. Huizenga, J. R., *et al.*, *J. Amer. Chem. Soc.* (1950) **72**, 4228.
38. Corrsin, S., *A.I.Ch.E. J.* (1964) **10**, 870.
39. Wilke, C. R., Chang, P., in "The Properties of Gases and Liquids," 2nd ed., R. C. Reid and T. K. Sherwood, Eds., McGraw-Hill, New York, p. 549, 1966.
40. Brodkey, R. S., "The Phenomena of Fluid Motions," Addison Wesley, Reading, Mass., Chap. 14, 1967.
41. Rao, M. A., Brodkey, R. S., *Chem. Eng. Sci.* (1972) **27**, 137.
42. Evangelista, J. J., Katz, S., Shinnar, R., *A.I.Ch.E. J.* (1969) **15**, 843.
43. Uhl, V. W., Gray, J. B., "Mixing, Theory and Practice," Vol. 1, Academic Press, New York, p. 123, 1966.
44. Uhl, V. W., Gray, J. B., *Op. Cit.* p. 134.

RECEIVED January 2, 1974.

Optimization of a Non-Isothermal, Non-Adiabatic Fixed-Bed Catalytic Reactor Model

THOMAS GORDON SMITH and JAMES J. CARBERRY

Department of Chemical Engineering, University of Notre Dame,
Notre Dame, Ind. 46556

A mathematical model of a non-isothermal, non-adiabatic fixed bed catalytic reactor was optimized as a function of six variables using the Hooke-Jeeves algorithm. Two objective functions were used: yield and productivity. Productivity is more useful for preliminary design. High productivities can be obtained with little sacrifice in yield by using small catalyst particles, large tubes, low feed concentrations, and high gas velocities. Operating conditions for high productivity exhibit relatively low parametric sensitivity. Although long reactors are required for the highest productivity, optimization has established a goal against which the results of new strategies for improving reactor performance can be compared. A more active catalyst limits maximum productivity because of increased parametric sensitivity. Parametrically sensitive conditions can be discovered and thus avoided by this approach.

Although various aspects of fixed bed catalytic reactors have been studied during the past decade, specific guidelines are needed to design such reactors, as well as base conditions against which proposals for improving their performance can be measured. This information is particularly desirable for non-isothermal, non-adiabatic fixed bed catalytic reactors because of the many interdependent parameters which determine their local and overall behavior. This, together with the nonlinear nature of the system, renders intuitive design approaches suspect. This work discusses results which may be useful to both the plant engineer and the design specialist in this regard.

The oxidation of naphthalene to phthalic anhydride on a vanadium pentoxide (V_2O_5) catalyst was analyzed to determine the optimum combination of feed concentration, temperature, and flow rate, coolant temperature, tube diameter, and catalyst particle diameter. These negotiable parameters, together with the reaction kinetics, fix reactor performance. Industrially, it is

necessary to achieve 99% conversion of the naphthalene which in turn specifies reactor length. Although the production of phthalic anhydride is a well established commercial process, detailed operating conditions are not available in the literature. However, the following general articles are of interest.

Froment (1) investigated the stability of fixed bed catalytic reactors for phthalic anhydride production from *o*-xylene on a V_2O_5 catalyst, using the following parameters:

$$T'_o = 357^\circ\text{C}, c_o = .0092, \text{Re}^* = 120, T'_c = 357^\circ\text{C},$$

$$D_t = 2.5 \text{ cm}, d_p = .3 \text{ cm}.$$

Computations using a steady-state, two-dimensional model showed that the maximum phthalic anhydride concentration occurs at a reactor length of 3m for these conditions. However, this length did not achieve the desired *o*-xylene conversion. Furthermore, an increase in, say, inlet temperature, in an attempt to increase conversion, caused runaway—*i.e.*, complete reaction of the phthalic anhydride and large thermal excursions. Froment concludes that no one would risk running the reactor at the conditions chosen and asserts that the reactor performance could probably be improved by reducing the magnitude of the hot spot using some form of catalyst dilution (*see, e.g.*, Ref. 2). The question arises as to the basis on which the conditions were chosen and whether a different choice would lead to more desirable results.

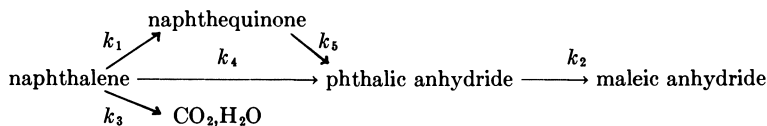
Along similar lines Carberry and White (3), using kinetic constants from a fluidized bed reactor, simulated the production of phthalic anhydride from naphthalene over V_2O_5 . They used as a base case $T'_o = 320^\circ\text{C}$, $c_o = .005$, $\text{Re}^* = 75$, $T'_c = 310^\circ\text{C}$, $D_t = 5 \text{ cm}$, and $d_p = 0.5 \text{ cm}$. The reactor length for this and other nearby conditions varied between 100 and 1000 cm. Their two-dimensional model was similar to Froment's but with the important inclusion of terms to account for inter-intraphase mass diffusion and interphase heat diffusion. Also, most of the calculations were based on 99% naphthalene conversion. While Froment looked at severe parametric sensitivity leading to reactor instability, Carberry and White illustrated milder forms of parametric sensitivity of conversion and yield with respect to Pe_h , Pe_m , T'_c , c_o , and activation energy. They also demonstrated that mass transfer limitations within the catalyst seriously limited the expected yield of phthalic anhydride for the operating conditions and kinetics chosen. As with Froment, these conditions were chosen arbitrarily. However, regardless of the conditions, it is unlikely that absolute results can ever be attained, and design techniques must thus rely on relative simulations.

Obviously a more detailed study is needed to determine if higher conversion and yield and decreased sensitivity can be obtained, and how it can be couched in terms of an approach useful to the design engineer. The results of such a study follow.

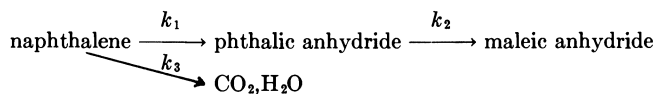
Kinetics

Our kinetics are based on the efforts of D'Alessandro and Farkas (4) and Drott (5). The former obtained experimental data for the naphthalene oxidation in a fixed bed reactor over pure V_2O_5 cylindrical pellets. Using their data and a computerized direct search algorithm, Drott "backed out" the five activation energies and the five frequency factors associated with the following

scheme



Since k_4 is relatively small and $k_5 \gg k_1$, this can be reduced to



with

$$k_1 = \exp\left(22.4 - \frac{28000}{RT'_k}\right)$$

$$k_2 = \exp\left(20.35 - \frac{30000}{RT'_k}\right)$$

$$k_3 = \exp\left(15.74 - \frac{23000}{RT'_k}\right)$$

These kinetics result in inlet operating temperatures of 400°–450°C which are those used industrially.

Reactor Model

The mathematical model is essentially the same as that used by Carberry and White with the following changes:

(1) The Peclet number for heat is computed as a function of reactor conditions using the Beek (6) modification of the Argo-Smith equation.

(2) Since appreciable axial temperature gradients exist, the gas density is calculated as a function of length. Any variables or properties (*e.g.*, u , Sc , Pe_h , K_g , h , etc.) which depend on density are similarly adjusted.

For reference, the equations solved on the digital computer are listed below:

$$\frac{\partial C}{\partial z} = \frac{1}{Pe_m} \left(\frac{\partial^2 C}{\partial r^2} + \frac{1}{r} \frac{\partial C}{\partial r} \right) - \frac{d_p \eta (k_1 + k_3) C}{u} \quad (4)$$

$$\frac{\partial T}{\partial z} = \frac{1}{Pe_h} \left(\frac{\partial^2 T}{\partial r^2} + \frac{1}{r} \frac{\partial T}{\partial r} \right) + \frac{d_p H}{\rho C_p u T'_o} \quad (5)$$

Equations 4 and 5 are dimensionless with respect to d_p , c_o , and T'_o . The point yield of the intermediate, phthalic anhydride, is calculated as

$$\frac{dC_{pa}}{dC} = \gamma \frac{m_1 \phi_2 \tanh \phi_2}{m_2 \phi_1 \tanh \phi_1} \left(\frac{C_{pa}}{C} + \frac{\beta}{\gamma \beta - 1} \right) - \gamma \left(\frac{\beta}{\gamma \beta - 1} \right) \quad (6)$$

where dC represents the amount of naphthalene converted to phthalic anhydride. The following boundary conditions were used:

$$\text{at } z = 0: T = 1, C = 1, C_{pa} = 0 \quad (7)$$

$$\text{at } r = 0: \frac{\partial T}{\partial r} = \frac{\partial C}{\partial r} = 0 \quad (8)$$

$$\text{at } r = D_t/2d_p: \frac{\partial C}{\partial r} = 0$$

$$\frac{dT}{dr} = -\frac{h_w d_p}{\rho C_p \lambda} (T - T_w) \quad (9)$$

where T_w is not a function of length. At the surface of the particle

$$\eta' (k_1 + k_3) C_s = \eta (k_1 + k_3) C = k_g a (C - C_s) \quad (10)$$

$$H = ha (T'_s - T') \quad (11)$$

In addition, the following equations were needed:

$$\lambda = \frac{\rho C_p \varepsilon u d_p}{Pe_m} + \frac{0.6 h d_p k_{sd}}{2k_{sd} + 0.7 h d_p} + 2 \left(\frac{e}{2-e} \right) \sigma d_p (T'_k)^3 \quad (12)$$

$$\frac{h}{\rho C_p u} (Pr)^{2/3} = \frac{k_g}{u} (Sc)^{2/3} = \frac{1.15}{\sqrt{Re}} \quad (13)$$

$$h_w = 0.18 \frac{K_g}{d_p} (Re^*)^{0.8} \quad (14)$$

For most conditions of industrial importance, the first term in Equation 12 dominates. Values assumed for the physical and chemical properties are given in Table I.

Table I. Property Values Assumed

$\Delta H_1 =$	380,000	cal/gram-mole (exothermic)
$\Delta H_2 =$	360,000	cal/gram-mole
$\Delta H_3 =$	1,110,000	cal/gram-mole
$C_p =$	7	cal/gram-mole °C
$K_g =$	1.1×10^{-4}	cal/sec cm °C
$k_{sd} =$	5×10^{-4}	cal/sec cm °C
$\mu =$	0.446×10^{-4}	gram/cm sec
$D =$	0.1	cm ² /sec
$\varepsilon =$	0.4	
$Pe_m =$	10	
$\gamma =$	1	
$e =$	0.9	

Numerical Procedures

Simulation. The Crank-Nicolson method was used to solve the finite difference versions of Equations 4 and 5. The density and all parameters depending on density were computed at each axial increment. In the more severe circumstances, this had an appreciable effect on the location and magnitude of the hot spot relative to that predicted by a constant density model.

At a given value of z , the dependent variables were calculated in the following order. First, the gas temperature at all radial locations was predicted using Equation 5 together with the value of the heat released by the chemical reaction determined at the previous increment. Since the solid temperature depends on the heat released, and in turn the rate constants depend on the solid temperature, Equation 11 was solved iteratively using the gas temperatures just calculated but gas concentrations calculated at the previous axial increment. Five iterations were adequate for convergence. The solid temperatures were then used with Equations 4, 6, and 10 to compute the radial gas concentrations. This completed the calculations at a given increment.

Verification that the combined mathematical model and numerical algorithm predict realistic results is desirable, but for catalytic packed bed reactors, it is difficult to achieve. Since no industrial data are available, we relied on the work of Drott as an indirect check. For the same system as considered here, Drott used a one-dimensional model and, after an appropriate modification of kinetic constants, favorably checked his results against the experimental concentration profile data of Volfson (7). We in turn assigned Pe_m and Pe_h a value of 0.1, rendering our model temporarily one-dimensional and matched Drott's results.

Aside from accuracy, the precision of the numerical model depends on the magnitude of the axial and radial step size, Δz and Δr . It is critical to determine a value of Δz which is large enough to render the model sufficiently fast to use in an optimization scheme yet small enough to compute changes near the hot spot accurately. Δz between 1 and 2 cm satisfies both criteria. Computation time for a long reactor, 6 m, using $\Delta z = 2$, is less than 1 minute, yet reducing Δz by a factor of 4 changes the results by only 1%. Tests show that $\Delta r = 0.3$ cm is similarly satisfactory. If the hot spot is severe, a smaller Δz is needed. However, besides the fact that certain assumptions in the model would no longer be valid near the hot spot, one would not run an actual reactor at such conditions because of yield deterioration. Therefore, a Δz between 1 and 2 cm should be adequate for most conditions of industrial importance.

Optimization. To optimize the reactor operating conditions, one must choose the objective function or functions, the particular operating conditions with respect to which the objective function will be optimized, and the optimization procedure itself. The basis for these choices is given below.

Inlet gas temperature T'_o , inlet gas concentration, c_o , inlet velocity in terms of Re , coolant temperature T'_c , tube diameter D_t , and particle diameter d_p were chosen as independent variables because they are negotiable in the initial stages of design. Several objective functions—*e.g.*, profit, yield of phthalic anhydride, space-time yield, and productivity (*i.e.*, amount of phthalic anhydride produced per tube per unit time)—were tested. However, not enough accurate cost information was available to render a profit objective function meaningful. Space-time yield was also unsuitable because it resulted in very short reactors with relatively low yields—an unlikely optimum. Yield and productivity used individually gave reasonable optimums, and their combined results generated a significant picture of the nature of the optimum.

Because of the high dimensionality of the optimization and the complexity of the simulation needed to determine the objective function, the pattern search method of Hooke and Jeeves (8) was used. The best step sizes for the independent variables were determined empirically to be approximately

$$\begin{array}{ll} \Delta T'_o = 2^\circ\text{C} & \Delta T'_c = 2^\circ\text{C} \\ \Delta c_o = .0002 \text{ mole fraction} & \Delta D_t = .05 \text{ cm} \\ \Delta Re = 5 & \Delta d_p = .01 \text{ cm} \end{array}$$

Thus, although the method starts cautiously with short excursions from the starting vector of operating conditions, the total change vector grows rapidly with repeated success. Subsequent failure reduces the amount of change. Step sizes smaller than those above increases computing time while larger step sizes, in the face of possible parametric sensitivity, can lead to spurious results. Further aspects of the optimization are best described in the context of the results obtained during its use.

Results

The optimization was first carried out using productivity as the objective function, allowing yield to vary and then vice-versa. The results for three different sets of starting operating conditions are shown in Figures 1 and 2. Operating conditions refer to conditions at the reactor inlet unless stated otherwise. Starting operating conditions are those used to initiate the optimization. Other starting operations were tried, and results were similar to those shown. Gaps between data points occur when the vector representing successful parameter perturbations doubles in accordance with the Hooke-Jeeves algorithm.

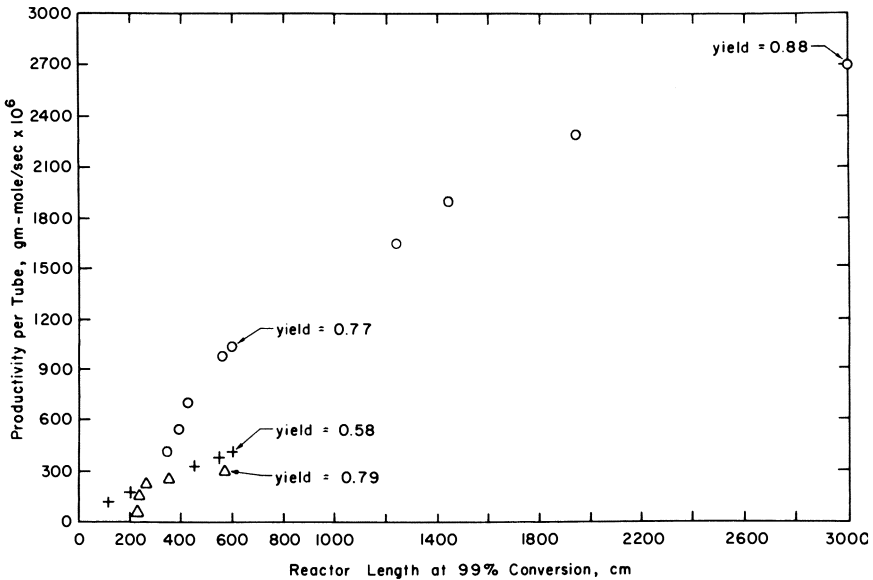


Figure 1. Optimization using productivity as the objective function

	Initial Operating Conditions			Operating Conditions at			
	Δ	O	+	L = 600 cm		L = 3000 cm	
	Δ	O	+	Δ	O	+	O
T_o'	460	480	440	465	468	442	456
c_o	.004	.005	.01	.0043	.0054	.0096	.0052
Re^*	120	440	440	140	460	450	500
T_o'	460	480	440	420	462	435	430
D_t	2.0	2.5	2.5	2.7	2.85	2.25	3.5
d_p	0.2	0.25	0.25	.1	.15	.275	.1

Each point in Figures 1 and 2 represents a different set of operating conditions as determined by the starting operating conditions and the subsequent search pattern. For a given set of conditions, the simulation is continued to the reactor length at which 99% conversion is obtained. The manner in which four of the individual operating conditions vary during one optimization is shown in Figure 3. The curves for a given parameter may or may not be monotonic, depending on the choice of starting operating conditions. This choice is arbitrary insofar as the optimization technique itself is

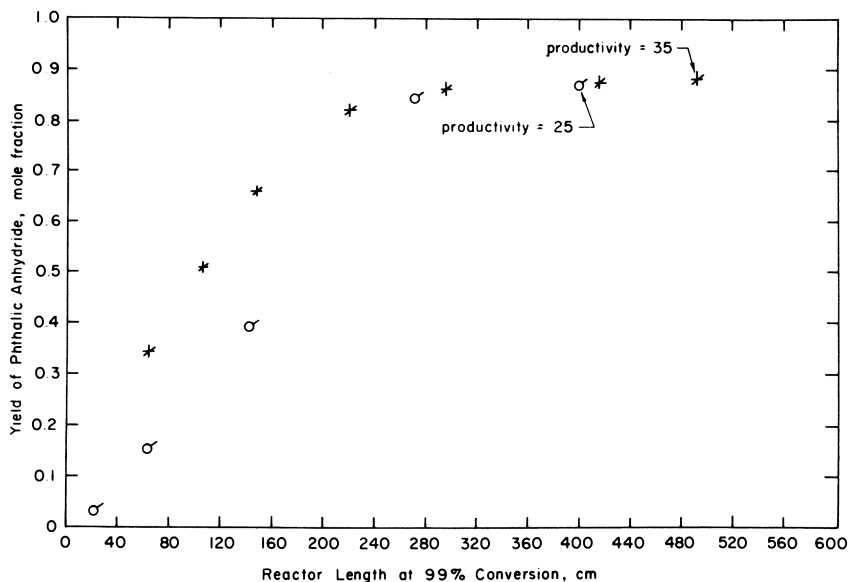


Figure 2. Optimization using yield as the objective function

	Initial Operating Conditions		Operating Conditions at $L = 400$ cm	
	*	σ	*	σ
T_o'	440	440	420	460
c_o	.005	.01	.004	.0082
Re^*	120	120	128	130
T_c'	440	440	420	420
D_t	2.5	2.5	1.5	1.
d_p	.25	.25	.25	.35

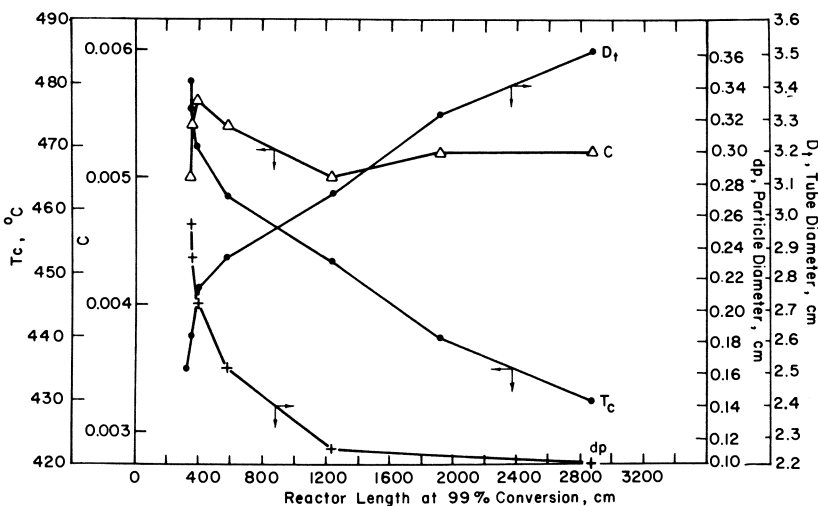


Figure 3. Variation of optimization parameters during an optimization. Same conditions as Figures 1 and 2.

concerned. By trial and error a set of starting conditions must be found which will result in 99% conversion (yield or productivity need not be high) in a length considerably less than the maximum tolerable during optimization. For Figure 1, this maximum length was chosen as 3000 cm; for Figure 2, it was 600 cm. The choice of maximum length is a function of the length at which the optimum is reached or, as is usually the case, the available computing time. Recall that a single simulation of a 600-cm reactor took about 1 minute of computing time. A typical optimization to a maximum length of 600 cm requires on the order of 40 separate simulations.

As shown in Figures 1 and 2, the starting operating conditions for the optimization have a considerable effect on the subsequent pattern leading to the optimum and the number of simulations needed to arrive there. Ideally, the optimization algorithm would operate on all starting conditions in such a way that the final optimum set of operating conditions would be identical. If yield is the objective function, the results of all optimization runs, regardless of starting conditions, arrived at an apparent plateau of between 0.85 and 0.88 at 600 cm, but the final "optimum" operating conditions were not the same. If a sufficiently long reactor were used, all optimization patterns would eventually result in an optimum yield approaching one and similar operating conditions (an isothermal reactor). The same reasoning holds when productivity is the objective function. However, a much greater length is now needed to even approach the (tilted) plateau.

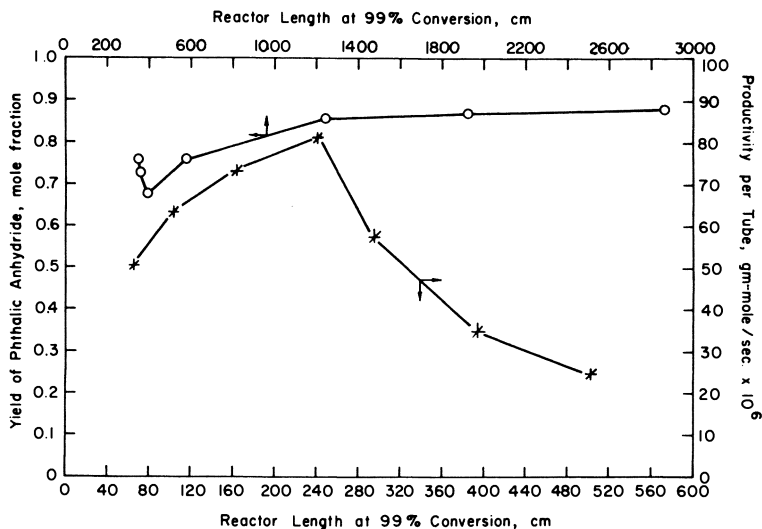


Figure 4. Variation of productivity and yield during an optimization. Same conditions as Figures 1 and 2.

Figure 4 shows the progress of yield when productivity is the objective function and vice-versa. When productivity is the objective function, the yield eventually increases to an acceptable value, but when yield is optimized, productivity drops as optimization proceeds (other results show that the productivity generally varies in a random manner). Also, the conditions which favor the highest yield invariably result in low productivity. Thus, if a single objective function had to be used, productivity would be better.

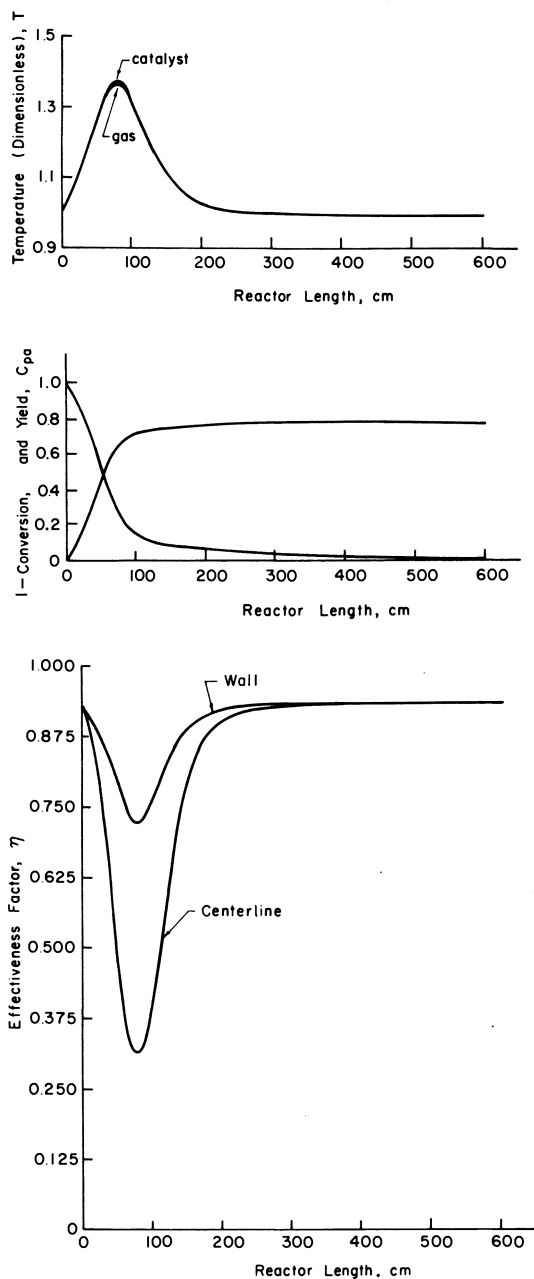


Figure 5. Base conditions: $T'_o = 468^\circ\text{C}$, $c_o = 0.0054$ mole fraction, $Re^* = 460$, $T'_c = T'_w = 462^\circ\text{C}$, $D_i = 2.85$ cm, $d_p = 0.15$ cm. Top: gas and catalyst temperature profiles; middle: conversion and yield profiles; bottom: effectiveness factor profiles.

Analysis of Figures 1 and 4 shows that high productivities can be obtained with only a modest sacrifice in yield; also long reactors are needed to approach the optimum if one insists on 99% conversion. If this constraint is relaxed, the reactor length at which the plateau is reached decreases dramatically. For example, if 98% conversion were tolerable, a reactor 25% shorter would be sufficient and would simultaneously result in a slightly higher yield. The precise conditions the design engineer would choose would be a function primarily of feed cost and pressure drop and would likely represent a compromise between optimum productivity and optimum yield. Assume that a 600-cm reactor is designed for maximum productivity and 99% conversion. For the upper curve in Figure 1, note the operating conditions at 600 cm. With these as inlet conditions to the reactor, Figure 5 shows the progress of some of the dependent variables with length. In essence, the optimization has manipulated the six independent variables so that the maximum temperature is not so high that further reaction of the phthalic anhydride can occur to a great extent, yet it is high enough that the desired conversion can be achieved in the given length. It seems evident that the model should take into account both catalytic effectiveness and radial influences even near the optimum. The calculated particle diameter is quite small (*see* caption, Figure 1). This prevents the catalyst from becoming totally ineffective around the hot spot (where most of the reaction is occurring). The optimization also favors high Reynolds numbers which correspondingly reduce the magnitude of the radial temperature gradient and permit larger tube diameters—a desirable feature. High Reynolds numbers also maintain the catalyst temperature near the fluid temperature

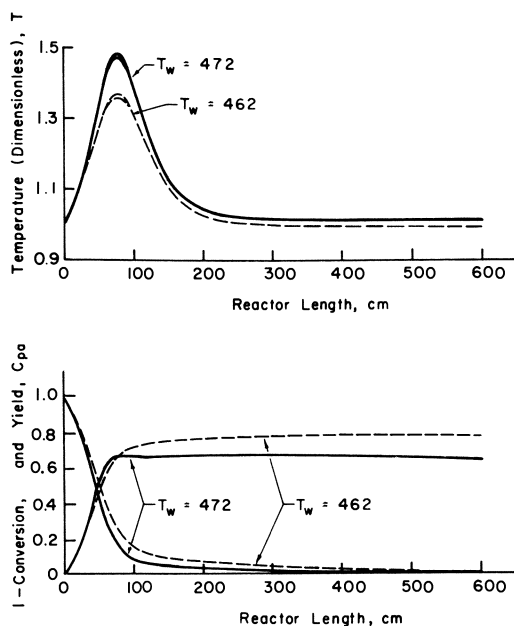


Figure 6. Effect of 10° increase in coolant temperature, T_w , on reactor temperature, conversion, and yield

as shown in Figure 5. Some industrial processes operate with low residence times which probably indicates high gas velocities and Reynolds numbers. Thus, it may be profitable to tolerate much higher pressure drops than are presently considered acceptable. Finally, the optimization recommends a low feed concentration. We found, in contrast to Froment but in agreement with Drott, that lower feed concentrations lead to operating conditions which exhibit less parametric sensitivity.

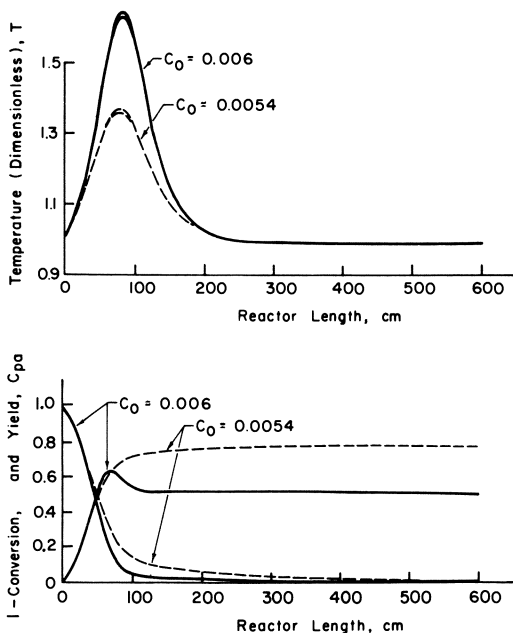


Figure 7. Effect of 10% increase in inlet feed concentration, c_0 , on reactor temperature, conversion, and yield

Some of these trends, such as those involving temperature, Reynolds number, or particle diameter may appear obvious on an individual basis (this is in fact how the various starting operating conditions for the optimization were chosen), but selecting the optimum set of six independent variables from the many possible combinations is another matter, particularly since the results change considerably (not necessarily in an unstable manner) for relatively small changes in the parameters in certain regions of the parameter space. Furthermore, a given parameter change may either increase or decrease the objective function depending on the state of the other five parameters, as illustrated in Figure 3 for the concentration. Thus, an unsystematic search, as might occur from random observations of plant data, could prove frustrating in locating the optimum operating conditions. Most important, Figures 1 and 2 show that the choice of the objective function itself requires care. For example, one could reasonably look only at yield; in that case the highest yields are obtained with smaller tube diameters together with larger particle diameters and lower inlet temperatures and Reynolds numbers. However, Figures 1 and 4 show that much higher productivities, with only a small sacrifice in yield,

can be secured by using larger tube diameters and smaller particles, in direct contrast to the trend indicated with yield as the objective function.

Immunity to parametric sensitivity is of course not guaranteed for the particular "optimum" conditions obtained. However, as Froment notes, this may be as critical a factor as any in selecting an operating strategy. Figures 6 and 7 show the sensitivity of the results of Figure 5 to a 10° perturbation in coolant temperature, and a 10% increase in naphthalene concentration, respectively, these representing the two most crucial operating conditions. The resulting temperature profiles are impressively stable. Note also the yield deterioration of approximately 10% which accompanies the enlarged hot spot. During some optimizations, with the kinetics we have used, we have noticed that there are combinations of the operating parameters which result in sensitive behavior. Higher feed concentration is one. Large catalyst particle diameters also exhibit increased parametric sensitivity. Thus, as a side benefit, the algorithm seems to lead to conditions which are not only in some sense optimum but also more stable. Indeed, this might indicate that parametric sensitivity, as it relates to design and simulation, is not as major a problem as suspected.

The effect of dealing with a more active catalyst particle—*i.e.*, a particle containing more actual catalytic material—can be studied by carrying out the simulation with pre-exponential factors increased by a factor of 5. Optimization with productivity as the objective function showed that the more vigorous kinetics enables the reactor to operate at a lower temperature for greater yield, in agreement with the results of Chomitz (9) and Drott (5). In fact, yields >90 mole % were possible with these kinetics. This advantage is secured at the price of greater parametric sensitivity which in turn reduces maximum productivity by restricting inlet concentration and tube diameter. In addition, reactor control would be more difficult.

Regardless of the kinetics, one might inquire as to the nature of the solutions at lengths preceding those of the plateau. Actually, in Figures 1 and 2, the points prior to the plateau are not necessarily optimal, and there seems to be no straightforward way of obtaining the optimum for these lengths. This is because if one proceeds from given starting operating conditions and perturbs each independent variable in turn, those successful perturbations invariably result in a reactor which requires additional length to achieve the desired 99% conversion. Since optimization involves changing the character of the hot spot, the above observation makes sense. However, as a result, there is no obvious method, short of superimposing an optimization of the starting operating conditions themselves, to ensure an absolute optimum for shorter reactors. The variety of starting operating conditions tried, although speculative, were guided by the parameter trends and ensure that the magnitude of the plateau itself is correct.

Conclusions

The major results of the optimization are as follows:

(a) Productivity is the most useful objective function for preliminary design work.

(b) Very high productivities can be obtained with little sacrifice in yield by using small catalyst particles, large tubes, low feed concentrations, and high Reynolds numbers (*i.e.*, high gas velocities). In contrast, optimization based on yield alone calls for large catalyst particles, small tubes, and lower temperatures and gas velocities and results in low productivities.

(c) The operating conditions for high productivity exhibit relatively low parametric sensitivity.

(d) Although long reactors are necessary to reach the highest productivity (not the case with yield), the optimization has established a goal against which the results of new strategies to improve reactor performance can be compared. Also a slight relaxation in the 99% conversion specification results in much shorter reactors.

(e) The design engineer, in light of previous plant experience, can suggest additional constraints (*e.g.*, pressure drop limitations) which will reduce the size and limits of the search space. He can also construct a more meaningful objective function in terms of total capital and operating costs rather than productivity per tube. This would settle the question of whether the higher pumping costs resulting from the small catalyst particles and high gas velocities are outweighed by the associated large increase in productivity.

(f) A more active catalyst limits maximum productivity because of increased parametric sensitivity.

(g) The question of parametric sensitivity as it relates to invalidating computer oriented design and simulation now appears academic. If a certain combination of operating conditions renders the reactor parametrically sensitive, then, as shown by the optimization, said conditions will also result in productivities and yields which are far from optimum. It is therefore sufficient that a simulation can alert one to the existence of parametrically sensitive conditions so they can be avoided.

Nomenclature

a	external surface-to-volume ratio of catalyst particle
Bi	Biot number for mass transfer, $k_g L/D$
c	naphthalene concentration in air, mole fraction
C	concentration, dimensionless with respect to c_0
C_p	heat capacity of gas, cal/gram-mole °C
d_p	catalyst particle diameter, cm
D_t	inside tube diameter, cm
D_{er}	effective mass diffusivity in radial direction, cm ² /sec
D	molecular diffusivity, cm ² /sec
e	emissivity
E_i	activation energy of i th reaction, cal/gram-mole
h	interphase heat transfer coefficient, cal/sec cm ² °C
h_w	wall heat transfer coefficient, cal/sec cm ² °C
ΔH_i	heat released by i th reaction, cal/gram-mole
H	total rate of heat release, $\sum_{i=1}^4 \Delta H_i R_i$, cal/cm ³ sec
k_i	reaction rate constant of i th reaction, sec ⁻¹
k_{0i}	frequency factor of i th reaction, sec ⁻¹
k_g	interphase mass transfer coefficient, cm/sec
k_{sd}	thermal conductivity of solid, cal/sec cm °C
K_g	thermal conductivity of gas, cal/sec cm °C
L	$1/a$
m_i	$1 + \frac{\phi_i \tanh \phi_i}{Bi}$
Pe_h	Peclet number for effective heat transfer in radial direction, $d_p u^* / \lambda$
Pe_m	Peclet number for effective mass transfer in radial direction, $d_p u / D_{er}$
Pr	Prandtl number, $c_p \mu / K_g$
r	radial coordinate, dimensionless with respect to d_p
R	ideal gas law constant, 1.987 cal/gram-mole °K
Re	Reynolds number, $d_p u / \nu$, at reactor inlet

Re^*	Reynolds number based on superficial velocity, $d_p u^* / \nu$, at reactor inlet
R_i	rate of i th reaction, gram-mole/cm ³ sec
Sc	Schmidt number, $\mu / \rho D$
T	temperature, dimensionless with respect to T'_o
T'	temperature, °C
T'_k	temperature, °K
u	interstitial gas velocity, cm/sec
u^*	superficial velocity, ϵu , cm/sec
z	axial coordinate, dimensionless with respect to d_p

Greek Letters

β	ratio of rate constants, k_1/k_2
γ	intrapphase diffusivity ratio, D_{na}/D_n
Δ	step change
ϵ	void fraction of catalyst bed
η'	catalytic effectiveness factor, $\tanh\phi/\phi$
η	modified catalytic effectiveness factor, $\phi \left(1 + \frac{\phi \tanh\phi}{Bi} \right)$, accounting for interphase mass transfer
λ	effective thermal conductivity in radial direction, cal/cm sec °C
λ'	$\lambda' / \rho C_p$, cm ² /sec
μ	viscosity, gram/cm sec
ν	kinematic viscosity, μ/ρ , cm ² /sec
ρ	gas density, gram-mole/cm ³
σ	Stefan-Boltzmann constant, cal/sec cm ² °K ⁴
ϕ_i	Thiele modulus for i th reaction, $L \sqrt{\frac{k_i}{D}}$

Subscripts

o	entrance of reactor, $z = 0$
c	coolant
n	naphthalene
pa	phthalic anhydride
s	surface
sd	solid
w	wall

Literature Cited

1. Froment, G. F., "Fixed Bed Catalytic Reactors," *Ind. Eng. Chem.* (Feb. 1967) **59**, 18-27.
2. Caldwell, A. D., Calderbank, P. H., "Catalyst Dilution—A Means of Temperature Control in Packed Tubular Reactors," *Brit. Chem. Eng.* (1969) **14**, 1199-1201.
3. Carberry, J. J., White, D., "On the Role of Transport Phenomena in Catalytic Reactor Behavior," *Ind. Eng. Chem.* (July 1969) **61**, 27-35.
4. D'Alessandro, A. F., Farkas, A., "The Kinetics of the Catalytic Oxidation of Naphthalene," *J. Colloid Sci.* (1956) **11**, 653-670.
5. Drott, D. W., "An Analysis of Catalytic Chemical Reactors," Ph.D. Thesis, University of Minnesota (1972).
6. Beek, J., "Design of Packed Bed Catalytic Reactors," *Advan. Chem. Eng.* (1962) **3**, 229-232.
7. Vol'fson, V. Ya. *et al.*, *Intern. Chem. Eng.* (1961) **1**, 31-36 (transl.).
8. Hooke, R., Jeeves, T. A., "'Direct Search' Solution of Numerical and Statistical Problems," *J. Assoc. Comp. Mach.* (April 1961) **8**, 212-229.
9. Chomitz, N., U.S. Patent **2,973,371** (Feb. 28, 1961).

RECEIVED January 2, 1974.

Mixing and Product Distribution with Series-Parallel Reactions in Stirred Tank and Distributed Feed Reactors

B. W. RITCHIE and A. H. TOBGY¹

Department of Chemical Engineering, University of Exeter, Devon, England

Micro- and macromixing models are presented which enable one to correlate the effects of the operating variables with the performance of multistage reactors. Comparison between the single parameter micromixing model and the single parameter models of Ng and Rippin and of Villermaux and Devillon indicate general agreement on micromixing effects for two isothermal series parallel reactions in a CSTR. For distributed feed reactors segregation improves performance for premixed feedstreams and reduces maximum yields for unpremixed feedstreams. Macromixing is characterized by the theoretical and experimental residence time frequency functions of a distributed feed reactor. Analysis of reactor performance shows that, although improvement in maximum yield obtained by using crossflow is small, it is possible to operate at high yields while reducing reactant conversion.

To analyze the importance of mixing on product yield in chemical reactors, many models have been developed. They have concentrated mainly on the effects of residence time and micromixing for single reactions with arbitrary kinetics. With more complex reactions (several products) where high conversion should be accompanied by high selectivity, mixing will probably be more important.

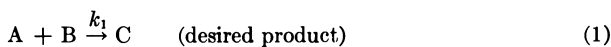
A qualitative analysis by Levenspiel (1) indicates the importance of mixing on product distribution for various complex reactions. For series-parallel reactions various contacting patterns are possible, leading to big differences in product distribution. To consider quantitatively these effects in reactors with distributed feeds such that the residence time distributions of the separate feedstreams are different, the deterministic flow, stochastic micromixing model of Treleaven and Tobgy (2) was invoked. This model was applied to a set of two series-parallel reactions which are assumed to have second-order kinetics

¹ On leave from the Department of Chemical Engineering, University of Cairo, Giza, Cairo, Egypt.

and to take place isothermally with no volume change. The importance of macromixing characterized by the residence time distributions and of micro-mixing characterized by the degree of segregation intermediate between the states of complete segregation and of maximum species and age mixedness (3), on the selectivity, yield, and conversion was determined.

General Considerations

Ideal States of Mixing. The reaction chosen is typical of many important industrial systems, such as the nitration and halogenation of hydrocarbons, the addition reactions of alkenes with proton donors, and the saponification of polyesters, where the intermediate product is desired. These processes are frequently bimolecular, irreversible, and, when occurring in the liquid phase, essentially constant density reactions. The reactions considered are:



where k_1 and k_2 are the reaction velocity constants; selectivity, σ , and yield, η , may be defined with reference to either A or B, such that,

$$\sigma_{CA} = \frac{c_C}{c_{AO} - c_A}; \quad \sigma_{CB} = \frac{c_C}{c_{BO} - c_B}; \quad \eta_{CA} = \frac{c_C}{c_{AO}} = \sigma_{CA}X_A; \quad \eta_{CB} = \frac{c_C}{c_{BO}} = \sigma_{CB}X_B$$

Reaction behavior in plug flow (or batch) reactors, in perfectly mixed continuous stirred tank reactors and in combinations of these reactors, has been considered (1, 4-10). To improve performance, recent publications have considered operating stirred reactors under semicontinuous conditions (11-13) while others have advocated the use of temperature programming (14).

With steady operating conditions in an isothermal reactor, product distribution at different conversions is determined by solving relevant material balances. The ratio of the rate equations of A and C eliminates the time variable so that,

for a plug flow (or batch) system:

$$\frac{\partial c_C}{\partial c_A} = K \left(\frac{c_C}{c_A} \right) - 1 \quad (3)$$

and for a single PCSTR:

$$\frac{c_C}{c_{AO}} = \frac{1 - \frac{c_A}{c_{AO}}}{1 + K \left(\frac{c_{AO}}{c_A} - 1 \right)} \quad (4)$$

Levenspiel (1) indicates product behavior at different conversions of A. For any value of K , selectivity and yield are higher in a PFR than in a single PCSTR. In both cases the yield of the intermediate can pass through a maximum, whose magnitude increases with decreasing K and occurs at increasing conversions. To determine the effects of reactor holding time and initial reactant concentrations, it is necessary to solve the relevant rate equations (6, 7, 8). Their solutions indicate that although any reaction path is determined

Table I. Conditions Necessary for Maximum Yield in Ideal Reactors

	PFR (or Batch)	1-PCSTR
Conversion of A	$X_A = 1 - K^{1/(1-K)}$; $K \neq 1$ $X_A = 0.632$; $K = 1$	$X_A = 1/(1 + K^{1/2})$
Damkohler number	Da_1 is a function of (X_A, K, β) ; the rate equations must be solved simultaneously.	$Da_1 = \frac{1}{K^{1/2} \left[\beta - \frac{2K^{1/2} + 1}{(K^{1/2} + 1)^2} \right]}$
Maximum yield	$\eta_{CA} = K^{K/(1-K)}$; $K \neq 1$ $\eta_{CA} = 0.368$; $K = 1$	$\eta_{CA} = 1/(1 + K^{1/2})^2$
Minimum stoichiometric ratio	$\beta = 2(1 - \frac{K^{1/(1-K)}}{K^{K/(1-K)}})$ - $\beta = 0.896$; $K \neq 1$; $K = 1$	$\beta = \frac{1}{1 + K^{1/2}} \left[2 - \frac{1}{1 + K^{1/2}} \right]$

by reactor type and the value of K , the position along the path at any holding time is a function of β and the Damköhler number (Da_1). Decreasing β at fixed Da_1 improves the selectivity. Table I summarizes the conditions necessary for maximum yield in a PFR and single PCSTR. The optimum combination of selectivity and yield at which a reactor operates depends largely on the value of the raw materials and products and the cost of subsequent separation.

Intermediate States of Mixing. If the hydrodynamic properties of the fluids, the reactor geometry, and agitation are such that mixing is not ideal, the relationships on which the reaction paths of a PFR or PCSTR are formulated become invalid. It then is necessary to develop a model which considers mixing effects. The most successful approach used to characterize intermediate states of mixing seems to be that involving the random coalescence model involving a single mixing history parameter, I , and simulated by Monte Carlo methods. Other approaches have been used to establish whether micromixing affects the outcome of various reactions by quantifying the difference between the extreme mixedness states of complete segregation and maximum mixedness (15). Tobgy (16) has reviewed this subject in great detail.

For I to be an essentially hydrodynamic parameter it should be independent of those parameters which characterize the chemical reactions; for isothermal homogeneous second-order reactions, these are the first Damköhler number and the stoichiometric ratio. The jet reactor mentioned below and described by Treleaven and Tobgy (17) was designed as a relatively severe experimental test of whether I is such a suitable hydrodynamic parameter, and this was shown to be the case. There is however no inherent reason in formulating random coalescence models for using a single value of I to characterize micromixing throughout a given reactor. In correlating the experimental data of Vassilatos and Toor (18) for an unpremixed feed tubular reactor, Kattan and Adler (19) found that the model that closely fitted the results involved a variation of I with axial position. On the other hand, others (20, 21, 22, 23) have correlated the same data using two different models, each based on single values of I , and I was independent of the chemical reaction parameters above. Evangelista *et al.* (24) showed that for a given working fluid in stirred tanks of similar geometric dimensions, the theory of homogeneous, isotropic turbulence leads to a value of I which agrees well with the experimental results for the overall mixing time determined by Van de Vusse (25). A similar approach was adopted by Otte *et al.* (26). Evangelista *et al.* (27) also used a single value of I and turbulence theory to analyze the effect

of imperfect mixing on stirred combustion reactors. Komasa *et al.* (28) and Villermaux and Devillon (29) studied second-order and complex reactions in two-phase continuous flow stirred tanks and obtained good agreement, within experimental error, between coalescence and redispersion rate as determined by chemical conversion and direct physical measurements. The foregoing seems to suggest that I does account for the fluid mixing patterns within the vessel and is independent of the reaction—providing the reacting fluids have the same hydrodynamic characteristics.

The Random Coalescence Model

Formulation. The flow process is simulated in a non-random manner by using deterministic forms of the residence time frequency functions (2). Each residence time and residual lifetime frequency function is expressed in K_λ discrete intervals of magnitude $\Delta\lambda$. Elements from the K_λ th residence time interval of each feedstream are entered into the K_λ th residual lifetime interval in the reactor, and on the basis of the value of I , a corresponding number of elements are selected at random, and instantaneous pairwise coalescence and redispersion simulate the micromixing. I is the average number of coalescences and redispersions experienced by each fluid element in the reactor. After these flow and micromixing steps, the batch kinetics are integrated over the residual lifetime interval, $\Delta\lambda$, for each fluid element. These three simulation steps are repeated for each decreasing residual lifetime interval until $\lambda = 0$, when all elements with zero residual lifetime exit the reactor. The selectivity and yield of the desired product and the conversions of the reactants are calculated from the population of leaving elements.

Integrating the Batch Kinetics. At the end of each flow and micromixing step in the simulation procedure, each fluid element is subjected to a batch reaction of duration $\Delta\lambda$. The number of reaction rate equations to be solved can be reduced from four to two by defining conversion parameters, v and w so that the concentrations of the reacting species are:

$$\bar{c}_A = \bar{c}_{A0} - \bar{v}; \bar{c}_B = \bar{c}_{B0} - \bar{v} - \bar{w}; \bar{c}_C = \bar{v} - \bar{w}; \text{ and } \bar{c}_D = \bar{w}.$$

Material balances on reactant A and product D then give:

$$\frac{d\bar{v}}{dt} = k_1 (\bar{c}_{A0} - \bar{v}) (\bar{c}_{B0} - \bar{v} - \bar{w}) \quad (5)$$

and,

$$\frac{d\bar{w}}{dt} = k_2 (\bar{v} - \bar{w}) (\bar{c}_{B0} - \bar{v} - \bar{w}) \quad (6)$$

where

$$\bar{c}_{A0} = \bar{c}_A + \bar{c}_C + \bar{c}_D \quad (7)$$

and,

$$\bar{c}_{B0} = \bar{c}_B + \bar{c}_C + 2\bar{c}_D \quad (8)$$

Further treatment of the parent rate equations reduces the number of differential equations to one:

$$\frac{d\bar{c}_A}{dt} = -k_1 \left[\left(\frac{1-2K}{1-K} \right) \bar{c}_A + \left(\frac{\bar{c}_{A0}^{1-K}}{1-K} \right) \bar{c}_A^K - \bar{c}_0 \right] \bar{c}_A; K \neq 1 \quad (9)$$

where

$$\bar{c}_0 = 2\bar{c}_{A0} - \bar{c}_{B0} \quad (10)$$

Solution of Equation 9 gives $c_A(t)$, and the concentration of B can be calculated from

$$\bar{c}_B = \left(\frac{1-2K}{1-K} \right) \bar{c}_A + \left(\frac{c_{AO}^{1-K}}{1-K} \right) \bar{c}_A^K - \bar{c}_O; K \neq 1 \quad (11)$$

The concentration of C and D follow from a material balance

$$\bar{c}_C = \bar{c}_B - 2\bar{c}_A + \bar{c}_O \quad (12)$$

$$\bar{c}_D = \bar{c}_A - \bar{c}_{AO} - \bar{c}_B + \bar{c}_{BO} \quad (13)$$

Here, the batch kinetics were integrated using a sixth-order Runge-Kutta procedure (30). The integration time step length is given by

$$Dt_{RK} = \Delta\lambda / \text{DENOM} \quad (14)$$

where DENOM is an integer input to the simulation procedure. With high values of Da_1 it was necessary to specify a large value for DENOM (e.g., with $Da_1 = 100$ and $\beta = 0.5$, Dt_{RK} was $\tau/800$). In attempting many simulations in this region it would help to use predictor-corrector techniques (31) to solve the differential equations. In solving the set of batch kinetic equations, generally no computer time was saved in reducing the differential equations to one.

Simulations. Simulations were done on an ICL 4/50 computer using a total feed population of $M = 200$ elements. The residence time and residual lifetime distributions were discretized into intervals of ca. $\tau/40$ sec. The number of elements representing the reactor population follows from $N_R = M\tau/\Delta\lambda$. In calculating Da_1 and the stoichiometric ratio, the flow weighted inlet concentrations were calculated from

$$c_{AO} = \frac{\sum_{j=1}^2 Q_j c_{Aj0}}{\sum_{j=1}^2 Q_j}, \quad c_{BO} = \frac{\sum_{j=1}^2 Q_j c_{Bj0}}{\sum_{j=1}^2 Q_j} \quad (15) \text{ and } (16)$$

where c_{Aj0} and c_{Bj0} are the inlet concentrations of A and B, respectively, in stream j .

Checking the Simulation Algorithms. To test the simulation procedure and the associated computer programs, initial trials were done using the residence time frequency function of a single CSTR to characterize macromixing. In these cases,

$$f_1(t) = f_2(t) = \left(\frac{1}{\tau} \right) e^{-t/\tau} \quad (17)$$

Both premixed and unpremixed feed stream situations were considered, and K , Da_1 , and β were selected to allow comparison between the predictions of the random coalescence model and those of the single parameter models of Villiermaux and Devillon (29) and of Ng and Rippin (32), as applied by Anand (33).

COMPARISON WITH THE MODEL OF VILLERMAUX AND DEVILLON. In quantifying the effects of micromixing in 1-CSTR, Villiermaux and Devillon (29) assumed a particular coalescence and redispersion mechanism and defined a transfer coefficient such that the concentration of an element within the reactor

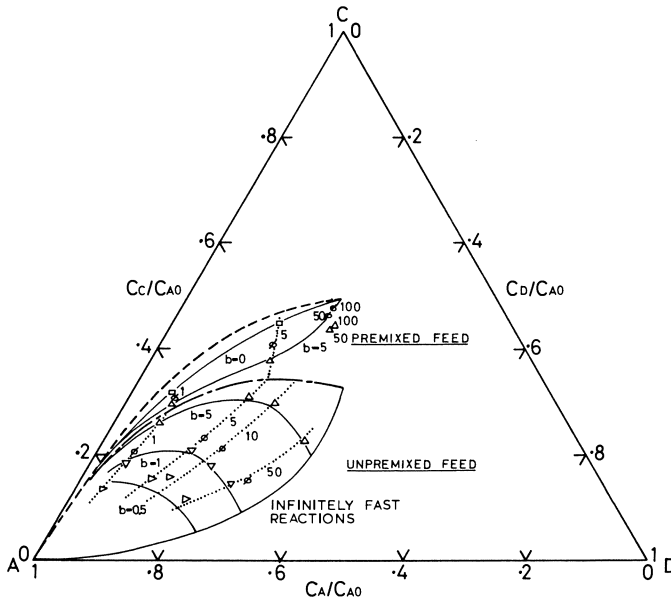


Figure 1. Comparison with the predictions of Villermaux and Devillon's model, when $K = 0.5$, $\beta = 1$. Random coalescence model: \square , $I = 0$; \triangleright , $I = 2$; ∇ , $I = 4$; ϕ , $I = 5$; \triangle , $I = 20$; ———, data of Villermaux and Devillon (29); - - - -, PFR; - - - -, 1-PCSTR;, lines of constant Damköhler number.

population evolves as a function of time:

$$\frac{dc_i}{dt} = h(\bar{c}_i - \bar{c}_i) - r_i, \quad i = A, B, C, D \tag{18}$$

where \bar{c}_i is the average concentration of coalescing elements. The fluid interaction mechanism is that postulated by others (34, 35, 36). Villermaux and Devillon related the transfer coefficient, h , to the frequency of coalescence, ω , by

$$h = \omega/4 \tag{19}$$

and introduced a dimensionless micromixing parameter $b (= h\tau)$ such that when $b = 0$, the reactor is completely segregated, and when $b = \infty$, the reactor is at maximum mixedness.

Figure 1 shows the results of simulations with $K = 0.5$, $\beta = 1$, and $1 \leq Da_1 \leq 100$. Maximum mixedness conversions are calculated from the material balance equations for a single PCSTR. Solid lines are predictions of reactor performance based on the Villermaux and Devillon model for premixed and unpremixed feedstreams; also shown are the predicted average exit concentrations based on the random coalescence model and premixed PFR. Two distinct regions are formed, depending on whether the feed is premixed or unpremixed. Serious quantitative comparison between the models is difficult for premixed feedstreams because micromixing effects are small; the models do however predict behavior within the same limits. Conversions calculated

with intermediate mixing are bounded by the completely segregated and maximum mixedness conversions. Segregation favors both selectivity and yield. With high Da_1 values and finite values of the micromixing parameters both models indicate that behavior is approaching that in a PFR; only in the maximum mixedness case does the reaction path terminate at the maximum mixedness conversion. This is understandable because since Da_1 is high, conversions are calculated with high values of k_1 and k_2 resulting in reactant B being almost entirely consumed in the fluid elements before the latter have had time to coalesce or to exit from the reactor.

With unpremixed feedstreams, conversion with intermediate mixing states fall between the maximum mixedness conversion and that calculated on the basis that the reactions are infinitely fast (*i.e.*, k_1 and k_2 are very large, but the ratio K remains constant). Here segregation is detrimental to performance. Although the two models are based on different mechanisms of fluid element interaction and thus do not compare exactly in their predictions, these predictions are not very different if $I = 4b$, at least where interaction is significant, $0 < I < 40$. Only when segregation is high and the concept of an average concentration influencing the rate of transfer becomes less than realistic do the models' predictions differ considerably ($I < 4$, $b < 1$). Under such conditions, the random coalescence model would be expected to represent local conditions better (37).

COMPARISON WITH THE MODEL OF NG AND RIPPIN. The micromixing model of Ng and Rippin (32) stipulates an entering environment which is in a state of complete segregation and a leaving environment which is in a state of maximum mixedness. The exit stream from the reactor is a mixture from both environments, and it is assumed that any fluid element in the entering environment has an equal probability of being transferred to the leaving environment. The rate of transfer between these two environments is

$$-\frac{dm}{dt} = mR \quad (20)$$

For second-order and autocatalytic reactions in a single CSTR, Tobgy (38) has shown that if a reduced yield, Y , is defined such that $Y = \text{actual yield}/\text{yield at maximum mixedness}$, a unique relationship exists between Y and the micromixing parameter, $R\tau$,

$$Y = \frac{R\tau}{R\tau + 1} \quad (21)$$

which is not a function of any reaction parameter excepting as they influence the maximum mixedness conversion. On analyzing the results of Anand (33). Equation 21 was found also to hold for series-parallel reactions (Figure 2).

The models are identical in their predictions for reactors at maximum mixedness; transfer between the entering and leaving environments is complete. Intermediate mixedness represented by the Ng and Rippin model is defined in terms of elements in the two extreme states only; this is not the case with the random coalescence model, and a reactor operating with an arbitrary state of micromixing may contain elements having a spectrum of mixing states. Nevertheless, both models indicate micromixing effects of the same order of magnitude, but with the random coalescence model the relationship between Y and I is not unique. The random coalescence model presented here, when applied to 1-CSTR, should give results identical to the model of Spielman and Levenspiel (39) and Kattan and Adler (40) since the micromixing mechanism

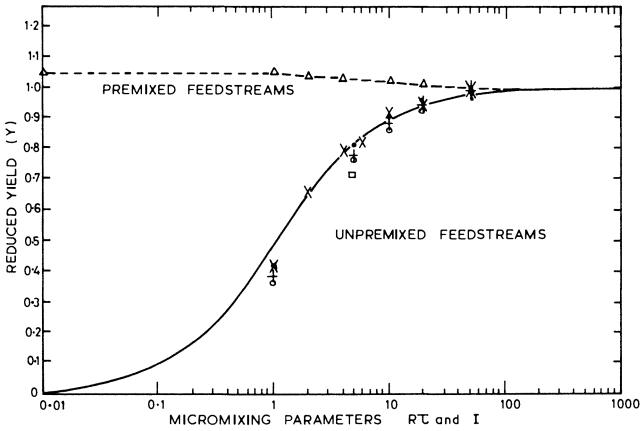


Figure 2. Comparison with the predictions of Ng and Rippin's model. Random coalescence model (Y vs. I).

	β	K	Da ₁
○	1	3	0.544
+	1	5	0.544
△	3	3	0.198
●	3	3	0.544
□	3	5	0.138
×	3	5	0.544

—, $R\tau/(R\tau + 1)$ vs. $R\tau$ and also Y vs. $R\tau$ based on the results of Anand (33).

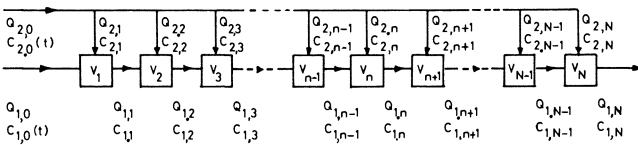


Figure 3. Multistage reactor with fresh feed introduction between stages

is the same. Rao and Edwards (41) have indicated general agreement between the Ng and Rippin model and that of Spielman and Levenspiel.

Performance in Reactors with Feed Distribution

To improve selectivity reactant A should react uniformly while reactant B should be introduced so that the concentration of A is kept high and that of B is kept low. To do this, one can operate stirred reactors semicontinuously by adding B gradually into a vessel which already contains all of feed A (11, 12). For continuous reactors a crossflow system such as that in Figure 3 can be used. In such a system each feedstream has its own residence time distribution.

Effects of Micromixing. To predict the effects of micromixing in reactors with distributed feed, one set of experimentally determined residence time distributions for the axisymmetric jet reactor (42) was used to characterize macromixing. Stream 2 is the jet stream, and stream 1 is the surrounding

secondary flow. The different residence time distributions for the streams were produced by using a relatively high U_2/U_1 , and turbulent entrainment was achieved by keeping the jet Reynolds' number above 1500. Figure 4 shows the values of the flow rates, mean residence times, and residual lifetime frequency functions. The residence time frequency functions are available (42). Analysis of these residual lifetime distributions indicates that only elements of stream 1 are available for micromixing at $\infty < \lambda < 11$. Population balances on the elements forming the reactor population show that this region accounts for 8% of the reactor volume. At $11 < \lambda < 4$, which accounts for 42% of the reactor volume, stream 1 is in excess volumetrically, and selectivity should be highest when the reactants are introduced separately and stream 2 contains reactant B.

Reactor performance has been simulated at $0.05 < K < 10$, for industrially important series-parallel reactions (4, 9). In particular, consideration is given to the effects of mixing intensity (I), Da_1 , and the method of introducing the feedstreams on the selectivity and yield of the intermediate product when the residual lifetime distributions of Figure 4 characterize the macromixing.

Three methods for introducing the reactants are considered. Two are for unpremixed feedstreams and arise when stream 2 contains only A and then only B; the third is for premixed feedstreams both containing A and B. Initial simulations were done with $\beta = 1$ and $K = 1$ at $0 < Da_1 \leq 10$, with two values of I :

(a) $I = 7.5$, a typical value found (17) on calibrating the reactor using a known second-order reaction

(b) $I = 100$ which would correspond to micromixing conditions in a distributed feed reactor operating at almost maximum mixedness.

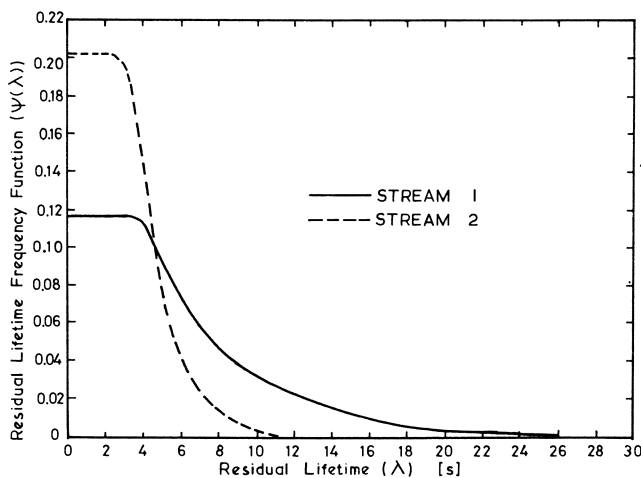


Figure 4. Residual lifetime frequency functions for the jet reactor. —, coaxial secondary stream; $Q_1 = 50 \text{ cm}^3 \text{ sec}^{-1}$; $\tau_1 = 8.52 \text{ sec}$. - - - - -, central jet stream; $Q_2 = 50 \text{ cm}^3 \text{ sec}^{-1}$; $\tau_2 = 4.94 \text{ sec}$.

The results in Figure 5 indicate that the method can be influenced largely by the degree of segregation in the reactor and that performance, even with low mixing intensities, is generally better than operation in 1-PCSTR. For the

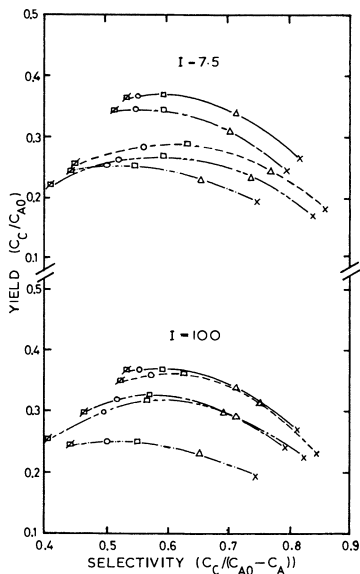


Figure 5. Yield vs. selectivity with jet reactor RTD's, at two values of I and three operating policies vs. a PFR and single PCSTR; $K = 1$; $\beta = 1$.

————, PFR; ————, 1-PCSTR;
 - - - -, jet reactor with stream 1 containing only B and stream 2 containing only A
 - · - · -, jet reactor with stream 1 containing only A and stream 2 containing only B
 · · · ·, jet reactor with both streams containing premixed A and B.
 ×, $Da_1 = 0.5$; Δ , $Da_1 = 1$; \square , $Da_1 = 2.43$;
 ○, $Da_1 = 4$; \diamond , $Da_1 = 10$.

jet reactor and $I = 7.5$, conditions are segregated, and the highest yields occur when the feedstreams are premixed; selectivities approach those obtainable with plug flow, although the yields are lower.

When the reactants are introduced separately, selectivity and yield (at the same Da_1) are higher when B is introduced in the stream with the shorter mean residence time—*i.e.*, stream 2. When Da_1 is less than the plug flow optimum of 2.43, selectivities with separate feeding are greater than those with plug flow, but the yield is reduced. With $I = 100$ and stream 2 containing only B, the reaction path closely matches that with plug flow, and selectivity is markedly improved for $Da_1 < 2.43$. Figure 5 also shows that the yield increases with Da_1 and passes through a maximum at or near the plug flow optimum. In each case, however, the maximum yield is lower.

Figure 6 shows the effect of changing I on the selectivity and yield for three values of K . With these reaction conditions, selectivities are relatively insensitive to micromixing; only at low K is increased mixing intensity accompanied by increased selectivity. In all cases, however, increased mixing intensity

is accompanied by an increased yield and conversion as more of the reactor volume becomes effective.

The dependence of the yield from the jet reactor on the reaction velocity constant ratio is shown in Figure 7. The yields for plug flow operation, and steady state processing in a single PCSTR are the maxima obtainable with these

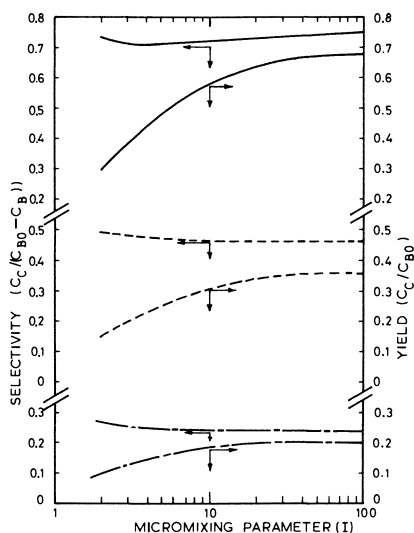


Figure 6. Effect of micromixing on selectivity and yield when jet reactor is operated with stream 1 containing only A, and stream 2 containing only B.

	K	β	Da_1
—————	0.1	1.127	11
- - - - -	1	1	2.43
- - - - -	8	0.443	2

K ratios. In each case β was chosen so that the PFR and PCSTR would operate with 95% conversion of B:

$$\beta = \frac{2X_A - \eta_{CA}}{0.95} \quad (22)$$

where X_A and η_{CA} are calculated from Table I, and Da_1 is calculated accordingly. The jet reactor was considered to operate with the same Da_1 and β as calculated for plug flow operation and with stream 2 containing only B. The highest yield at each K is that from plug flow operation, but with the segregated jet reactor ($I = 7.5$) the yield is greater than that from a single PCSTR when $K > 1.5$, and the selectivity is greater than that obtainable with plug flow. For example, when $K = 1$, the jet reactor yield is 3% less than that from the PCSTR, but selectivity is 29% greater; when $K = 8$, the jet reactor yield is 19% greater than the PCSTR's, and selectivity increases by 64%. Since the calculations are based on a PFR and single PCSTR operating at the same conversion of B, the volume requirement of the jet reactor would be considerably less than its PCSTR counterpart.

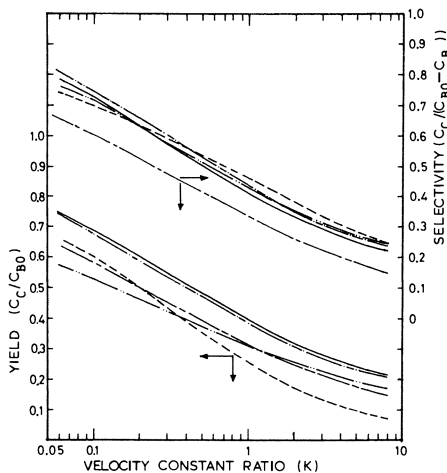


Figure 7. Selectivity and yield obtainable with jet RTD's vs. steady-state processing in a PFR, a single PCSTR, and with unsteady processing in a single PCSTR (13) as a function of the velocity constant ratio. — · — · —, jet reactor with $I = 100$; — · · — · —, jet reactor with $I = 7.5$; —, PFR; — — —, steady PCSTR; — — — —, pulsed PCSTR.

The selectivities and yields possible with periodic operation of a PCSTR (13) are included in Figure 7. They were calculated at the optimum period θ and with $\beta = 1$ at each K value. While the jet reactor is better than a PCSTR when $K > 1.5$, at the other end of the scale ($K < 0.2$) periodic operation offers a similar improvement, but the volume requirement of the reactor is not reduced.

Effects of Macromixing. In illustrating the effects of micromixing, consideration has been restricted to the effects of changing the intensity of mixing for a single macromixed state. One feature of series-parallel reactions is the variety of contacting patterns possible. To consider the effects of such changes on the maximum mixedness conversions, the authors have developed a model for the residence time distributions in general multistage systems with fresh feed introduction between stages (43).

A schematic of the system is shown in Figure 3, and the residence time frequency functions, when each stage is a perfect macromixer are:

$$f_1(t) = \sum_{j=1}^N \frac{\frac{N}{\pi} \left(\frac{1}{\tau_i}\right) e^{-t/\tau_j}}{\frac{N}{\pi} \left(\frac{1}{\tau_i} - \frac{1}{\tau_j}\right)} \quad (23)$$

$$f_2(t) = \left(\frac{1}{\tau_N Q_{2,0}}\right) \sum_{k=1}^N \sum_{j=N+1-k}^N \frac{Q_{2,N+1-k} \frac{N-1}{\pi} \left(\frac{1}{\tau_i}\right) e^{-t/\tau_j}}{\frac{N}{\pi} \left(\frac{1}{\tau_i} - \frac{1}{\tau^j}\right)} \quad (24)$$

where $\tau_j = \frac{V_j}{Q_{i,j}}$, $j = 1, 2 \dots N$, and all τ_j are different. (25)

To show the effects of changing the feed distribution, results are reported for a system where stream 2 is distributed so that the cross-flow forms an arithmetic progression, so that:

in general,

$$Q_{2,n} = Q_{2,n-1} + d_Q \quad (26)$$

and, in particular,

$$Q_{2,n} = \frac{Q_{2,n}}{N} - \frac{1}{2} (N + 1) d_Q + n d_Q \quad (27)$$

and

$$Q_{1,n} = Q_{1,0} + n \left[\frac{Q_{2,0}}{N} - \frac{1}{2} (N + 1) d_Q \right] + \frac{n(n+1)}{2} d_Q \quad (28)$$

When each stage in the cascade is a PCSTR, the conversion can be calculated by applying steady-state material balances across each stage in turn. Such a reactor is in the state of sequential mixedness (44). To illustrate the possible operating policies available for a series of equal volume PCSTR's, results are

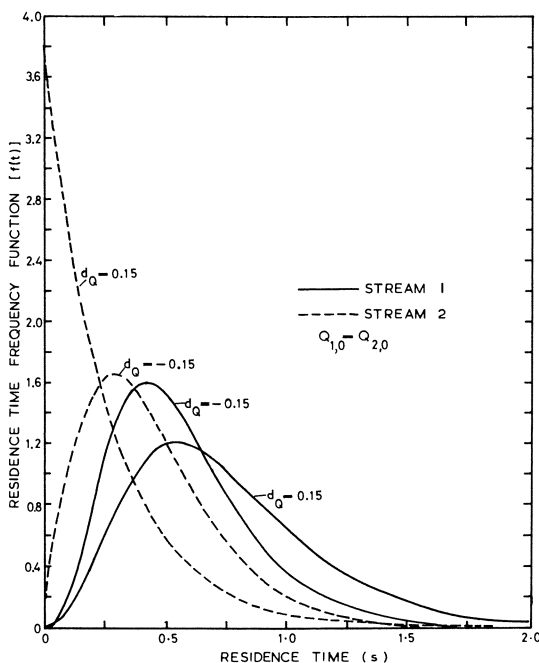


Figure 8. Residence time frequency functions of four PCSTR's in series with crossflow of stream 2 between stages. $V/(Q_{1,0} + Q_{2,0}) = 0.5$ sec.

reported for a four-stage cascade. In order that each $Q_{2,n}/Q_{2,0}$ is always greater than zero, the common difference d_Q must be:

$$-\frac{2}{N(N-1)} < \frac{d_Q}{Q_{2,0}} < \frac{2}{N(N-1)} \quad (29)$$

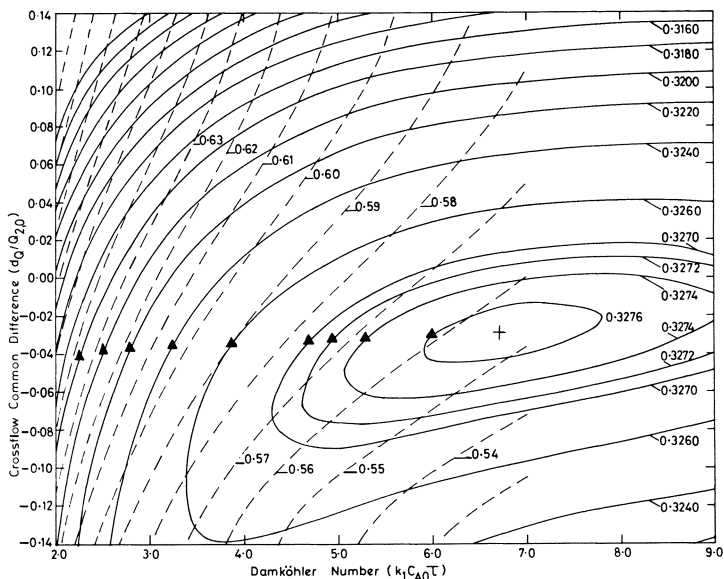


Figure 9. Yield and selectivity of an equal-volume, four-stage reactor in the state of sequential mixedness as a function of $d_Q/Q_{2,0}$ and Da_1 . \blacktriangle Conditions for high yield accompanied by high selectivity. — Yield of $C(C_c/C_{A0})$. - - - Selectivity $(C_c/C_{A0} - C_A)$.

Thus, in the case in question, $-0.1666 < d_Q/Q_{2,0} < 0.1666$.

Figure 8 shows the residence time frequency functions of the feedstreams when $d_Q = -0.15$ and $d_Q = 0.15$. Stream 2 has a smaller mean residence time than stream 1; as d_Q increases, the mean and variance of the residence time frequency function of stream 1 increases while the mean residence time of stream 2 decreases.

The response surfaces of yield and selectivity as a function of $d_Q/Q_{2,0}$ and Da_1 are shown in Figure 9 when B is the crossflow, stream 1 contains A , $K = 1$, and $\beta = 1$. The maximum yield $(\eta_{CA})_{\max} = 0.3276$ and occurs when $d_Q/Q_{2,0} = -0.029$ and $Da_1 = 6.724$. It represents a 1.7% increase *vs.* that from a four-stage, equal-volume, cascade with no crossflow. Since both reactions are of the same order with respect to B , the improvement in yield when B is distributed across the cascade is small and requires an increase in the total reactor volume for the same production rate. However, Figure 9 indicates that the crossflow cascade can be operated at the maximum yield of a four-stage, equal-volume cascade operated with no crossflow while reducing the conversion of A by about 6.8%.

Discussion

This study was done first to develop a method to predict the performance of multistage distributed feed reactors with fresh feed addition between stages.

Where the stage boundaries are not clearly defined, the conversion limits lie between those of complete segregation and maximum mixedness, based on the exit residence time distributions of each feedstream. Intermediate mixing states can be characterized by the random coalescence model. When the stage boundaries are well defined (—*e.g.*, in a series of stirred tanks with crossflow), sequential application of the random coalescence model can be used to determine performance.

The second objective was to determine whether deviations from ideal mixing are detrimental to reactors with series-parallel reactions. In the cases considered here a degree of segregation will improve performance if the feedstreams are premixed whereas with unpremixed feedstreams, segregation reduces possible maximum yields. An important stage in designing feed distribution systems will thus involve methods of improving micromixing by improving both the design of impellers and method of feed introduction. For example, multiple impellers with multiple feed entry points per impeller could increase micromixing without increasing energy consumption. This need for proper design will become increasingly important as the relative rates of reaction increase, to prevent oversubstitution in segregated regions adjacent to the feed entry points (11).

With the same total reactor volume and with distributed feeding the highest selectivity occurs when B is introduced with the shorter mean residence time. By progressively increasing the crossflow volumetric flow rate across the cascade, the ratio of the mean residence time of stream 2 to stream 1 is reduced; this improves selectivity further, and, with suitable choice of an operating Da_1 number, the sequential mixedness yield can exceed that for a staged reactor with no crossflow.

The best operating conditions for distributed feed reactors are difficult to select because the secondary stream volumetric flow rate and/or the stage volume distribution may be varied. The macromixing models presented here and elsewhere (43) allow direct search algorithms to be applied to optimization of suitably formulated objective functions. Application of the random coalescence micromixing model to these optimum cascades will then indicate quantitatively the micromixing effects and how rapidly performance might be expected to fall off if mixing conditions in the cascade deviate from the ideal.

Nomenclature

A, B, C, D	reactants
b	micromixing parameter of Villermaux and Devillon
c	concentration, moles/vol
CSTR	continuous stirred tank reactor
d_Q	common difference in the crossflow volumetric flow rate, vol/time
Da_1	Damköhler number ($k_1 c_{A0} \tau$)
DENOM	integer input to simulation procedure (defined in text)
Dt_{RK}	integration time step length
f	residence time frequency function, time ⁻¹
h	transfer coefficient defined by Equation 18, time ⁻¹
I	micromixing parameter of random coalescence model
k	second-order reaction velocity constant, vol/mole/time
K	ratio of reaction velocity constants, (k_2/k_1)
K_λ	residual lifetime and residence time intervals
m	mass of material in the entering environment of the Ng and Rippin model

M	number of elements representing total feedstream population, dimensionless
n	number of a general stage in multistage reactor
N	total number of stages in multistage reactor
N_R	total number of elements representing reactor population
PCSTR	perfectly mixed continuous stirred tank reactor
PFR	plug flow reactor
Q	volumetric flow rate, vol/time
r	rate of reaction, moles/vol/time
R	mixing transfer coefficient, defined by Equation 20, time ⁻¹
RTD	residence time distribution
t	time, or residence time
U	velocity, length/time
v	conversion parameter, moles/vol
V	reactor volume
w	conversion parameter, moles/vol
X	fractional molar conversion $[(c_0 - c)/c_0]$
Y	reduced yield (actual yield/maximum mixedness yield)

Greek symbols

β	stoichiometric ratio (c_{B0}/c_{A0})
η	yield
θ	duration of pulse, defined by Renken (13)
λ	residual lifetime
σ	selectivity
τ	mean residence time
ψ	residual lifetime frequency function, time
ω	frequency of coalescence, time ⁻¹

Subscripts

o	initial value
1, 2	streams 1 or 2 or Reaction 1 or 2
A, B, C, D	reactant A, B, C, or D
i, j	i th or j th stream or species for the multistage system. For volumetric flowrates and concentrations, i , is feedstream. For stream 2 flows and concentrations, j is the stage into which the material flows. For stream 1 flows and concentrations j is the stage from which the material originates.
n	a general stage
N	the final stage
overbar	fluid element local mean value
double overbar	ensemble average of coalescing fluid elements

Literature Cited

- Levenspiel, O., "Chemical Reaction Engineering," 2nd ed., Chap. 7, Wiley, New York, 1972.
- Treleaven, C. R., Tobgy, A. H., *Chem. Eng. Sci.* (1972) **27**, 1497, 1756.
- Treleaven, C. R., Tobgy, A. H., *Chem. Eng. Sci.* (1971) **26**, 1259
- Russell, T. W. F., Buzzelli, D. T., *Ind. Eng. Chem., Process Design Develop.* (1969) **8**, 2.
- Kramers, H., Westerterp, K. R., "Elements of Chemical Reactor Design and Operation," pp. 36-52, Chapman Hall, London, 1963.
- Kerber, R., Gestrich, W., *Chem. Ing. Tech.* (1966) **38**, 536.

7. Kerber, R., Gestrich, W., *Chem. Ing. Tech.* (1967) **39**, 458.
8. Kerber, R., Gestrich, W., *Chem. Ing. Tech.* (1968) **40**, 129.
9. Friedman, M. H., White, R. R., *AIChE J.* (1962) **8**, 581.
10. Trambouze, P. T., Piret, E. L., *AIChE J.* (1959) **5**, 384.
11. Paul, E. L., Treybal, R. E., *AIChE J.* (1971) **17**, 718.
12. Saddy, M., Luchi, N. R., *Lat. Am. J. Chem. Eng. Appl. Chem.* (1972) **2**, 3.
13. Renken, A., *Chem. Eng. Sci.* (1972) **27**, 1925.
14. Newberger, M., Kadlec, R. H., *AIChE J.* (1971) **17**, 1381.
15. Ritchie, B. W., Tobgy, A. H., *Chem. Eng. Sci.* (1974) **29**, 533.
16. Tobgy, A. H., Ph.D. Thesis, University of Exeter (1974).
17. Treleaven, C. R., Tobgy, A. H., *Chem. Eng. Sci.* (1973) **28**, 413.
18. Vassilatas, G., Toor, H. L., *AIChE J.* (1965) **11**, 666.
19. Kattan, A., Adler, R. J., *AIChE J.* (1967) **13**, 580.
20. Harris, I. J., Srivastava, R. D., *Can. J. Chem. Eng.* (1968) **46**, 66.
21. Rao, D. P., Dunn, I. J., *Chem. Eng. Sci.* (1970) **25**, 1275.
22. Rao, D. P., Edwards, L. L., *Ind. Eng. Chem., Fundamentals* (1971) **17**, 398.
23. Rao, D. P., Edwards, L. L., *AIChE J.* (1971) **17**, 1264.
24. Evangelista, J. J., Katz, S., Shinnar, R., *AIChE J.* (1969) **15**, 843.
25. Van de Vusse, J. G., *Chem. Eng. Sci.* (1955) **4**, 178, 209.
26. Otte, L. L., *et al.*, *AIChE Ann. Meetg., 64th, San Francisco, Nov. 28, 1971*.
27. Evangelista, J. J., Shinnar, R., Katz, S., *Proc. Symp. (Int.) Combust., 12th*, p. 901, The Combustion Institute (1969).
28. Komazawa, I., Sasakura, T., Otake, T., *Chem. Eng. Japan* (1969) **2**, 208.
29. Villermaux, J., Devillon, J.-C., *Fifth European/Second Intern. Symp. Chem. Reaction Eng., Amsterdam, May 2-4, 1972*, pp. B1-13, Elsevier, Amsterdam (1972).
30. Butcher, J. C., *Austr. Math. Soc. J.* (1964) **4**, 179.
31. Lapidus, L., Seinfeld, J. H., "Numerical Solution of Ordinary Differential Equations," Academic, New York, 1971.
32. Ng, D. Y. C., Rippin, D. W. T., *Proc. European Symp. Chem. Reaction Eng., 3rd, Amsterdam, 1964*, pp. 161, Pergamon, Oxford (1965).
33. Anand, U. S., Ph.D. Thesis, University of London (1967).
34. Harada, M. *et al.*, *Mem. Fac. Eng. Kyoto Univ.* (1962) **24**, 431.
35. Yamazaki, H., Ichikawa, A., *Int. Chem. Eng.* (1970) **10**, 471.
36. Costa, P., Trevissoi, C., *Chem. Eng. Sci.* (1972) **27**, 2041.
37. Ritchie, B. W., Tobgy, A. H., written comment on paper B1-13, *Fifth European/Second Int. Symp. Chem. Reaction Eng., Amsterdam, May 2-4, 1972*.
38. Tobgy, A. H., University of Exeter, *Chem. Eng. Dept. Tech. Rept. No. CRE 5* (1973).
39. Spielman, L. A., Levenspiel, O., *Chem. Eng. Sci.* (1965) **20**, 247.
40. Kattan, A., Adler, R. J., *Chem. Eng. Sci.* (1972) **27**, 1013.
41. Rao, D. P., Edwards, L. L., *Chem. Eng. Sci.* (1973) **28**, 1179.
42. Treleaven, C. R., Tobgy, A. H., *Chem. Eng. Sci.* (1972) **27**, 1653.
43. Ritchie, B. W., Tobgy, A. H., University of Exeter, *Chem. Eng. Dept. Tech. Rept. No. CRE 6* (1973).
44. Novosad, Z., Thyn, J., *Collection Czech. Chem. Commun.* (1966) **31**, 3710.

RECEIVED January 2, 1974.

Kinetics and Mechanism of the Oxidation of Ethylene over Silver Catalysts

HAGEN T. SPATH and KLAUS D. HANDEL

Institut für Physikalische und Theoretische Chemie,
Technische Hochschule Graz, Austria

A study was made of the kinetics and the mechanisms governing the oxidation of ethylene over a silver catalyst using mechanistic model building. Initial rates obtained for different sets of the independent variables (feed composition, temperature) were tested against model equations which were derived from available information on the chemisorption and desorption characteristics of the gases involved. The best fit to the data was obtained with dual site mechanisms at an oxidized silver surface; ethylene oxide is formed most likely from a molecular oxygen species whereas there is a distinct preference of atomic oxygen to be involved in the full oxidation of ethylene.

The kinetics of ethylene oxidation over silver catalysts have been studied in both industrial and university laboratories. A literature survey up to 1966 is given in Ref. 1, and more recent material is collected in Refs. 2, 3, and 4. The reported kinetic data extend from empirical correlations to complicated rate equations, mostly Hougen-Watson type, and in some cases they account for the inhibiting action of the reaction products. Differences in the reported mechanisms and kinetic equations arise primarily from the question of the type of chemisorbed oxygen present at the catalyst surface (3, 4, 5, 6, 7, 8, 9) as well as from opposing opinions as to the role played by ethylene chemisorption on silver under reaction conditions (10, 11). Both single- and dual-site mechanisms involving atomic and/or molecular oxygen for EO and $\text{CO}_2 + \text{H}_2\text{O}$ formation have been discussed (12, 13, 14, 15, 16, 17). However, none of the kinetic equations proposed has found a general acceptance. This is also true for reaction mechanisms derived solely from kinetic equations. Some reasons for these contradicting results are considered below.

The supported or unsupported silver catalysts studied in different laboratories had varying composition (on a microscopic scale) and varying configuration (even not always properly defined); thus, the attempts of the individual studies with respect to kinetic equations were too divergent to result in equations of general validity. The type of reactor and experimental conditions (feed composition, feed rate, temperature) must be selected to guarantee the absence of external and internal mass transport processes and temperature gradients along the reaction zone which could distort the proper chemical reaction rates.

Temperature gradients are not easy to exclude owing to the high exothermicity of the reactions ($\Delta H = -27$ and -316 kcal/mole for the oxidation of E to EO and $\text{CO}_2 + \text{H}_2\text{O}$, respectively). Correlations of catalyst activity and selectivity with respect to different catalysts depend strongly on the physical and chemical configuration of the catalyst and its surface. The surface properties of silver depend strongly upon the composition of the feed gas and the temperature during raw catalyst conditioning, usually in a stream of E/air (18, 19). This should be considered for kinetic studies where a wide range of process variables must be covered and the studies may extend over a long time. Therefore, it is necessary continuously to control slow changes in activity and selectivity on varying the experimental variables using a suitable standard feed at standardized conditions. The individual rate data then should be properly corrected with respect to the chosen standard (normalization). There are examples in the literature where these slow changes in activity and selectivity have been taken into account (12, 13, 16).

Derivation of kinetic equations should involve the full spectrum of available additional information on the adsorption and desorption characteristics of the gases as well as on the structure of the catalyst surface and the surface interactions between the individual species under realistic experimental conditions. Furthermore, reliable considerations as to the rate-controlling step in the sequence of reactions are necessary.

However, certain arguments should be stressed in this context. Information obtained under extreme conditions (*e.g.*, ultrahigh vacuum) should be transferred carefully to realistic catalytic conditions. Only information obtained from a catalyst surface with composition similar to that under reaction conditions is of value in deriving plausible model equations. This is essential with metal catalysts which, during catalysis, most often do not exhibit their true metallic properties but rather properties dominated by the existence of a thin nonstoichiometric binary layer composed of the metal on the one hand and one of the gaseous species on the other, on top of the actual metal phase (4). The catalytic active centers thus are no longer metal atoms but sites on top of the binary film which is not necessarily present as a separate phase. With silver catalysts reaction occurs on a more or less oxidized silver surface. This surface determines the actual catalytic properties as compared with an idealized pure silver surface present under ultrahigh vacuum conditions. An example is the chemisorption of E on an oxidized silver surface which is absent with "pure" silver.

Model Building

Reactor Design. A flow-type integral reactor of special geometry was used. The reaction section consists of a set of 13 rectangular sheets of silver ($7 \times 3 \times 0.05$ cm) held at two sides in a frame of parallel grooves 0.15 cm apart. A suspension of the raw catalyst (AgO) in acetone is sprayed as a thin homogeneous layer (< 0.01 -cm thick) over both sides of the sheets. By standardized conditions in a stream of air/E at 300°C AgO is reduced to metallic silver forming a spongy, nonporous network, closely adhering to the sheets. Because of the excellent heat conductivity of silver only negligible temperature gradients occurred across the reacting zone. For experimental details *see* Refs. 18, 19, 20, 21.

Owing to the relatively large free reactor volume and laminar flow characteristics, both transversal and longitudinal dispersion caused by diffusion like fluxes may alter the measured rates. Therefore, a relation between the reactor

dimensions, reaction rate, and the volumetric feed rate F_v^0 was derived to provide safe criteria for measuring the actual chemical rates free from physical transfer terms (21). If these criteria are met, the reaction can be thought to proceed quasi-homogeneously. For the actual situation these calculations showed that the volumetric flow rate must exceed a critical value $F_{v, \text{crit}}^0 \geq 10 \text{ cm}^3 \text{ NTP/sec}$. Actually, the rate measurements were done at flows from 10–30 $\text{cm}^3 \text{ NTP/sec}$. Above the critical flow rate mass transfer problems to the catalyst surface do not arise.

Selection of Independent Variable Sets and Rate Measurements. Two series of independent variable sets $\{x_i^0, T\}$ were selected. One series at constant temperature ($T = 533^\circ\text{K}$) covers increasing x_E^0 at constant $x_{O_2}^0$ and vice-versa. A second series, partly selected according to a statistic design procedure, was set up to study both the temperature dependence and the influence of reaction products on the rates. The data sets are compiled in Tables I and

Table I. Series I Data^a Sets and Normalized Initial Rates \hat{r}_j^0

No.	Sets of Independent Variables		$\hat{r}_{E^0}^0$	$\hat{r}_{CO_2^0}^0$	S
	$x_{O_2}^0$	x_E^0			
1	.117	.026	.0665	.0905	42.0
2	.120	.039	.0708	.1166	48.0
3	.124	.063	.0914	.1304	41.0
4	.115	.083	.0946	.1816	34.0
5	.113	.109	.0997	.1683	37.0
6	.212	.018	.0711	.0695	50.0
7	.212	.036	.0644	.0831	43.0
8	.213	.058	.0928	.1139	45.0
9	.216	.083	.1250	.1293	49.0
10	.207	.100	.1597	.2213	42.0
11	.227	.030	.1272	.1118	53.0
12	.249	.048	.1449	.1573	48.0
13	.239	.070	.1418	.1755	45.0
14	.279	.091	.1678	.2091	44.0
15	.257	.111	.1731	.2100	45.0
16	.400	.020	.0861	.0782	52.5
17	.400	.039	.1376	.1328	51.0
18	.400	.076	.2253	.2059	52.0
19	.400	.097	.2396	.2273	51.0
20	.400	.121	.2236	.2453	48.0
21	.479	.027	.1277	.1126	53.0
22	.488	.042	.1413	.1309	52.0
23	.456	.062	.1806	.1707	51.0
24	.465	.087	.2051	.2240	48.0
25	.460	.111	.2165	.2633	45.0
26	.800	.029	.1643	.1113	60.0
27	.800	.050	.2601	.1611	62.0
28	.800	.067	.2600	.2156	55.0
29	.800	.090	.3279	.2432	57.0
30	.800	.114	.3335	.2869	54.0
31	.971	.029	.1362	.1213	52.0
32	.951	.049	.1816	.1518	54.5
33	.935	.065	.2316	.1859	56.0
34	.914	.086	.2786	.2246	55.0
35	.891	.108	.3225	.2902	53.0

Table I. Continued

No.	Sets of Independent Variables		$\hat{r}_{E^{\circ}}$	$\hat{r}_{CO_2^{\circ}}$	S
	$x_{O_2^{\circ}}$	$x_{E^{\circ}}$			
36	.084	.048	.0818	.1169	41.0
37	.126	.045	.0953	.1173	45.0
38	.161	.046	.0806	.0815	50.0
39	.415	.046	.1602	.1297	55.0
40	.843	.044	.1700	.1509	53.0
41	.023	.076	.0338	.0775	30.0
42	.042	.076	.0526	.0896	37.0
43	.063	.078	.0723	.1153	38.5
44	.091	.078	.0895	.1298	41.0
45	.101	.080	.0881	.1211	42.0
46	.117	.078	.1027	.1614	39.0
47	.170	.077	.1220	.1476	45.0
48	.219	.073	.1440	.1646	47.0
49	.487	.070	.2278	.2178	51.0
50	.690	.070	.2459	.1995	55.0
51	.106	.107	.1043	.1501	41.0
52	.146	.115	.1195	.1281	48.0
53	.186	.114	.1335	.1594	46.0
54	.488	.115	.2690	.2799	49.0
55	.670	.111	.2640	.2295	53.5

* S is calculated from $S = \hat{r}_E^{\circ}/(\hat{r}_E^{\circ} + \hat{r}_{CO_2}^{\circ})$, $T = 533^{\circ}\text{K}$.

II; the inert diluent was N_2 or He. Initial rates were determined at atmospheric pressure from ξ_j vs. $(1/F_v^{\circ})$ data points (obtained at both rising and falling F_v° to control stationarity) according to

$$r_j^{\circ} = x_{E^{\circ}} \{d\xi_j/d(1/F_v^{\circ})\}_{\xi_i \rightarrow 0} \text{ (cm}^3 \text{ NTP } E \rightarrow j\text{)}/\text{sec} \quad (1)$$

The data points were fitted either by an exponential function (two fitting parameters) or by a third degree polynomial (three fitting parameters) using least-squares techniques. Recording of the ξ_j vs. $(1/F_v^{\circ})$ data points within each set was preceded by 12 hrs of catalyst pretreatment with the respective feed of the set. A new set was preceded by 48 hrs catalyst pretreatment with a standard feed ($x_{E^{\circ}} = 0.05$, $x_{O_2^{\circ}} = 0.19$, balance N_2) at standard conditions ($T = 533^{\circ}\text{K}$, $F_v^{\circ} = 10 \text{ cm}^3 \text{ NTP}/\text{sec}$).

Normalization of Rate Data. Slow variations of activity, selectivity, and conversion within the time of study were controlled by test runs after each rate measurement. The standard feed was passed over the catalyst at the given standard conditions. The individual rates $r_{j,k}^{\circ}$ were corrected using a multiplication factor $f_{j,k}$ to give the normalized rates $\hat{r}_{j,k}^{\circ}$, with

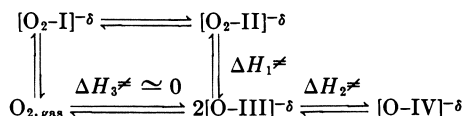
$$f_{j,k} = \frac{1}{n} \left\{ \sum_{k=1}^n C_{s,j,k} \right\} / \{C_{s,j,k}\} \quad (2)$$

($C_{s,j,k}$ is the conversion of E to j for standard feed at standard conditions (subscript s) following the k-th kinetic run). Summation in Equation 2 extends over the $C_{s,j}$ data bracketing all n kinetic runs.

The contribution of the silver foil beneath the active silver layer to the overall activity is negligible. Therefore, possible changes in the catalytic sur-

face area of the carrier sheets cannot be responsible for the time dependence of the overall catalytic properties. Catalytic activity can change because of variation in the number of active sites on varying the feed composition; the nature of the active sites, however, remains unaffected. These variations, of course, must be distinguished from the formal kinetic behavior. This normalization was justified by plots of $\ln(k_{\text{eff},j})$ vs. $1/T$ determined after different catalyst pretreatments; only the preexponential factors varied: the slopes remained unchanged. The corrected rates are given in Tables I and II. Since the two series of data were recorded at different catalyst masses, there is no 1:1 relationship between the rates. This, however, is insignificant with respect to the data analysis.

Kinetic Model Equations. From contact potential measurements at varying temperature and pressure the following scheme for oxygen chemisorption on silver was obtained (4, 21)



With additional information from the literature the O_2/Ag system can be characterized as follows. O_2 is chemisorbed very strongly and rapidly below 10^{-4} torr, forming at least a monolayer of O atoms. Further chemisorption takes place *via* a loosely bound form $[\text{O}_2\text{-I}]$ on top of the oxidized silver involving both a molecular ($[\text{O}_2\text{-II}]$) and an atomic species ($[\text{O-III}]$). Dissociative adsorption is bound to specific centers which are accessible to the molecular species at elevated temperatures (activated chemisorption, enthalpy of activation $\Delta H_1 \neq$). Formally, this results in an overall endothermic heat of adsorption in agreement with experiments. At higher p_{O_2} and T oxygen is taken up by silver layers adjacent to the surface, resulting in a $[\text{O-IV}]$ species. This process again is activated ($\Delta H_2 \neq$) and reversible only at very high T . The negative charges $-\delta$ at the chemisorbed species (not necessarily integer) increase from $[\text{O}_2\text{-I}]$ to $[\text{O-IV}]$. Desorption spectra indicated at least two distinct oxygen peaks, ascribed to molecular $[\text{O}_2\text{-II}]$ and atomic $[\text{O-III}]$ (4, 21). The existence of different oxygen species probably accounts for the unique properties of silver with respect to the oxidation of E. This chemisorption O_2 model implies that

(a) At constant p_{O_2} the ratio $[\text{O}_2\text{-II}]/[\text{O-III}]$ decreases with increasing T

(b) At constant T the ratio $[\text{O}_2\text{-II}]/[\text{O-III}]$ increases with increasing p_{O_2}

(c) Increasing T and p_{O_2} results in the formation of a nonstoichiometric layer of Ag_xO_y (involving $[\text{O-IV}]$) with altered catalytic properties.

E as well as the reaction products are definitely chemisorbed at the oxygenated surface. These gases are chemisorbed with ΔH_{ad} negative, the free energy of chemisorption, ΔG_{ad} , following the sequence:

$$|-\Delta G_{\text{ad,E O}}| > |-\Delta G_{\text{ad,E}}| > |-\Delta G_{\text{ad,C O}_2}|$$

Fast heating of a catalyst surface after simultaneous adsorption of E and O_2 resulted in three distinct desorption peaks, one definitely ascribed to EO formed from chemisorbed E and the molecular $[\text{O}_2\text{-II}]$ species in a dual-site step (4,

Table II. Series II Data^a Sets

No.	Sets of Independent Variables					T = 560°K		
	x _{O₂} ^o	x _E ^o	x _{CO₂} ^o	x _{EO} ^o	x _{H₂O} ^o	ŷ _{EO} ^o	ŷ _{CO₂} ^o	S
1	.1900	.0400	.0003	.0000	.0000	.0445	.0358	59.
2	.9584	.0316	.0000	.0000	.0000	.1122	.0550	68.
3	.9789	.0102	.0000	.0000	.0000	.0255	.0192	60.
4	.2590	.0414	.7000	.0000	.0000	.0210	.0082	71.
5	.2000	.0526	.2320	.0000	.0000	.0360	.0156	70.
6	.8112	.1505	.0183	.0000	.0000	.3325	.1615	67.
7	.0712	.0499	.0002	.0000	.0000	.0345	.0343	60.
8	.7414	.0223	.0000	.0263	.0000	.0360	.0222	60.
9	.0414	.2040	.0000	.0000	.0000	.0484	.0748	44.
10	.0346	.0387	.9026	.0241	.0000	.0059	.0025	70.
11	.2854	.0644	.2862	.0153	.0000	.0270	.0136	68.
12	.1900	.0369	.0003	.0000	.0420	.0211	.0114	66.
13	.1162	.0977	.0000	.0230	.0000	.0391	.0261	63.
14	.1112	.0933	.0000	.0220	.0430	.0108	.0108	60.
15	.0371	.9629	.0002	.0000	.0000	.0760	.1143	47.
16	.0354	.9196	.0002	.0000	.0450	.0423	.0513	48.

^a Selectivity *S* obtained experimentally. Data taken from Ref. 24.

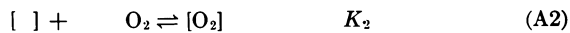
21). In the absence of [O₂-II], however, no EO is formed. Convincing evidence for the formation of EO from a molecular oxygen species has been obtained from IR data (3).

At reaction temperature the equilibria between the various oxygen species are fully established. Owing to the surface heterogeneity these equilibria as well as adsorption of E, EO, and CO₂ do not obey Langmuir-type isotherms. However, assuming that the actual fraction of reactive centers is small and that this fraction behaves almost homogeneously (average adsorption sites) Langmuir-Hinshelwood mechanisms are felt to be realistic approximations of the true situation. Indeed, the results of the kinetic study justify this assumption. On the other hand, the rate equations were developed on the basis of steady-state hypothesis, with the surface reaction rate controlling. The latter assumption is verified from the \hat{r}_j vs. x_E^o (or $x_{O_2}^o$) characteristics (*cf.* Table I). When analysis of the data is associated with initial rates, the oxidation kinetics of E can be described in terms of two independent reactions—*i.e.*, without considering consecutive oxidation of EO. From the principles discussed above, alternative mechanisms will essentially differ in the type of catalyst surface and adsorption centers assumed. The most likely reaction schemes should be derived from a more or less oxidized silver surface and involve dual-site steps between chemisorbed reactants. The rate equations developed for dual-site mechanisms are summarized in Table III. They account for the formation of EO and CO₂ + H₂O from either [O₂-II] (DSO2) or [O-III] (DSO). For completeness, the corresponding single site (SS) equations (not given in Table III) with E impinging from the gas phase were included into the data analysis. The different types of catalyst surfaces assumed are characterized as shown below.

TYPE A (PARTLY OXIDIZED SILVER SURFACE). Dissociative and molecular adsorption of oxygen associated with silver atoms or groups of silver atoms acting as adsorption centers. Adsorption of E, EO, CO₂, and H₂O involves [O] as adsorption sites resulting in charged adsorption complexes [O.Y_i]. [O] is acting both adsorptive and reactive:

and Normalized Initial Rates \hat{r}_j°

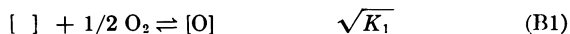
T = 529°K			T = 498°K		
$\hat{r}_{\text{EO}}^\circ$	$\hat{r}_{\text{CO}_2}^\circ$	S	$\hat{r}_{\text{EO}}^\circ$	$\hat{r}_{\text{CO}_2}^\circ$	S
.0170	.0231	56.	.0061	.0054	58.
.0856	.0308	73.	.0451	.0135	78.
.0161	.0090	67.	.0156	.0046	79.
.0104	.0026	80.	.0025	.0007	80.
.0161	.0060	73.	.0046	.0014	76.
.1434	.0674	68.	.0467	.0200	70.
.0180	.0230	45.	.0097	.0109	48.
.0196	.0120	62.	.0096	.0045	68.
.0331	.0335	49.	.0102	.0071	59.
.0020	.0007	75.	—	—	—
.0103	.0045	70.	—	—	—
.0091	.0040	70.	.0034	.0013	72.
.0174	.0067	72.	.0081	.0027	75.
.0089	.0034	72.	.0028	.0010	74.
.0297	.0310	49.	.0072	.0058	62.
.0119	.0139	47.	.0039	.0031	61.



Type A1. Only that portion of [O] not covered by other species is in equilibrium with p_{O_2} of the gas phase.

Type A2. The total portion of [O] is in equilibrium with p_{O_2} of the gas phase (*cf.* Ref. 16).

TYPE B (PARTLY OXIDIZED SILVER SURFACE). Dissociative adsorption of oxygen at silver atoms or groups of silver atoms ([]) to form the actual adsorptive sites [O]. Dissociative and molecular chemisorption of oxygen at [O] sites acting only adsorptive, whereas [O.O], [O.O₂] as well as [O.E] are reactive:



B1, B2. Alternatives corresponding to A1 and A2.

TYPE C (TOTALLY OXIDIZED SILVER SURFACE). Dissociative and molecular adsorption of oxygen associated with [O] or groups of [O] centers acting adsorptive:



TYPE D (TOTALLY OXIDIZED SILVER SURFACE). Silver surface fully covered with [O] acting adsorptive as well as reactive. Molecular [O₂] and chemisorption complexes formed according to (D1) and (D2):



TYPE E (PARTLY OXIDIZED SILVER SURFACE). Basically the same as type B but without dissociative adsorption of O_2 according to step B3. $[O]$ is acting both adsorptive and reactive. E1/E2 like A1/A2.

Table III. Rate Equations for Dual-Site Mechanisms According to Models A1-F^a

Type of Surface	DSO2 Mechanisms $\hat{r}_i^\circ =$	DSO Mechanisms $\hat{r}_i^\circ =$
A1	$\{k_j K_E \sqrt{K_1} K_2 x_{E^\circ} (x_{O_2^\circ})^{3/2}\} / \{N_{A1}^2\}$	$\{k_j K_E K_1 x_{E^\circ} x_{O_2^\circ}\} / \{N_{A1}^2\}$
A2	$\{k_j K_E \sqrt{K_1} K_2 x_{E^\circ} (x_{O_2^\circ})^{3/2}\} / \{N_{A2}^2 M_{A2}\}$	$\{k_j K_E K_1 x_{E^\circ} x_{O_2^\circ}\} / \{N_{A2}^2 M_{A2}\}$
	$N_{A1} = \{1 + \sqrt{K_1} (x_{O_2^\circ})^{1/2} + K_2 x_{O_2^\circ} + \sqrt{K_1} (x_{O_2^\circ})^{1/2} \sum_i K_i x_i^\circ\}$ $N_{A2} = \{1 + \sqrt{K_1} (x_{O_2^\circ})^{1/2} + K_2 x_{O_2^\circ}\}$ $M_{A2} = \{1 + K_E x_{E^\circ}\}$	
B1	$\{k_j K_E K_1 K_2 x_{E^\circ} (x_{O_2^\circ})^2\} / \{N_{B1}^2\}$	$\{k_j K_E K_1 \sqrt{K_3} x_{E^\circ} (x_{O_2^\circ})^{3/2}\} / \{N_{B1}^2\}$
B2	$\{k_j K_E K_1 K_2 x_{E^\circ} (x_{O_2^\circ})^2\} / \{N_{B2}^2 M_{B2}^2\}$	$\{k_j K_E K_1 \sqrt{K_3} x_{E^\circ} (x_{O_2^\circ})^{3/2}\} / \{N_{B2}^2 M_{B2}^2\}$
	$N_{B1} = \{1 + \sqrt{K_1} (x_{O_2^\circ})^{1/2} + \sqrt{K_1} \sqrt{K_3} x_{O_2^\circ} + \sqrt{K_1} K_2 (x_{O_2^\circ})^{3/2} + \sqrt{K_1} (x_{O_2^\circ})^{1/2} \sum_i K_i x_i^\circ\}$ $N_{B2} = \{1 + \sqrt{K_3} (x_{O_2^\circ})^{1/2} + K_2 x_{O_2^\circ} + K_E x_{E^\circ}\}$ $M_{B2} = \{1 + \sqrt{K_1} (x_{O_2^\circ})^{1/2}\}$	
C	$\{k_j K_E K_2 x_{E^\circ} x_{O_2^\circ}\} / \{N_C^2\}$	$\{k_j K_E \sqrt{K_3} x_{E^\circ} (x_{O_2^\circ})^{1/2}\} / \{N_C^2\}$
	$N_C = \{1 + \sqrt{K_3} (x_{O_2^\circ})^{1/2} + K_2 x_{O_2^\circ} + \sum_i K_i x_i^\circ\}$	
D	$\{k_j K_E \sqrt{K_2} x_{E^\circ} (x_{O_2^\circ})^{1/2}\} / \{N_D^2\}$	$\{k_j K_E x_{E^\circ}\} / \{N_D^2\}$
	$N_D = \{1 + \sqrt{K_2} (x_{O_2^\circ})^{1/2} + \sum_i K_i x_i^\circ\}$	
E1	$\{k_j K_E K_1 K_2 x_{E^\circ} (x_{O_2^\circ})^2\} / \{N_{E1}^2\}$	$\{k_j K_E K_1 x_{E^\circ} x_{O_2^\circ}\} / \{N_{E1}^2\}$
E2	$\{k_j K_E K_1 K_2 x_{E^\circ} (x_{O_2^\circ})^2\} / \{N_{E2}^2 M_{E2}^2\}$	$\{k_j K_E K_1 x_{E^\circ} x_{O_2^\circ}\} / \{N_{E2}^2 M_{E2}^2\}$
	$N_{E1} = \{1 + \sqrt{K_1} (x_{O_2^\circ})^{1/2} + K_2 \sqrt{K_1} (x_{O_2^\circ})^{3/2} + \sqrt{K_1} (x_{O_2^\circ})^{1/2} \sum_i K_i x_i^\circ\}$ $N_{E2} = \{1 + K_2 x_{O_2^\circ} + K_E x_{E^\circ}\}$ $M_{E2} = \{1 + \sqrt{K_1} (x_{O_2^\circ})^{1/2}\}$	
F	$\{k_j K_E K_2 x_{E^\circ} x_{O_2^\circ}\} / \{N_F^2\}$	$\{k_j K_E x_{E^\circ}\} / \{N_F^2\}$
	$N_F = \{1 + K_2 x_{O_2^\circ} + \sum_i K_i x_i^\circ\}$	

^a i . . . E, EO, CO₂, H₂O in summation terms.

TYPE F (TOTALLY OXIDIZED SILVER SURFACE). Basically the same as type D, step D1 being modified:



For types A, B, and E the number of adsorption centers $[\text{O}]$ increases with increasing $x_{\text{O}_2}^{\circ}$. Reaction rates are formulated according to the following example (type E):

$$j/\text{E1}/\text{SSO} : r_j^{\circ} = k_j [\text{O}] x_{\text{E}}^{\circ} \quad j/\text{E1}/\text{SSO2} : r_j^{\circ} = k_j [\text{O.O}_2] x_{\text{E}}^{\circ} \quad (3)$$

$$j/\text{E1}/\text{DSO} : r_j^{\circ} = k_j [\text{O}] [\text{O.E}] \quad j/\text{E1}/\text{DSO2} : r_j^{\circ} = k_j [\text{O.O}_2] [\text{O.E}] \quad (4)$$

with

$$[\text{O}] = \{K_1(x_{\text{O}_2}^{\circ})^{1/2}\} / \{N_{\text{E1}}\}; [\text{O.O}_2] = K_2[\text{O}]x_{\text{O}_2}^{\circ}; [\text{O.E}] = K_{\text{E}}[\text{O}]x_{\text{E}}^{\circ} \quad (5)$$

$$N_{\text{E1}} = \{1 + \sqrt{K_1}(x_{\text{O}_2}^{\circ})^{1/2} + K_2\sqrt{K_1}(x_{\text{O}_2}^{\circ})^{3/2} + K_{\text{E}}\sqrt{K_1}(x_{\text{O}_2}^{\circ})^{1/2}x_{\text{E}}^{\circ}\} \quad (6)$$

DSO and DSO2 are dual-site mechanisms involving adsorbed $[\text{O}]$ or $[\text{O.O}_2]$ and $[\text{O.E}]$. SSO and SSO2 are single site mechanisms associated with adsorbed $[\text{O}]$ and $[\text{O.O}_2]$, E impinging from the gas phase.

Data Analysis. The rate data with respect to the model equations of Table III were analyzed on a specification stage. Conclusive calculations were done by a nonlinear least-squares technique using a modified Gauss-Newton algorithm. Initial estimates of the parameters were obtained from unweighted and/or weighted linear regression. This requires linearization of the models and the assumption of either a constant error variance $\sigma^2\{f(r_j^{\circ})\}$ of the transformed quantities $f(r_j^{\circ})$ (unweighted) or a constant error variance σ_r^2 of the rates themselves where the coefficients $\sigma_k^2\{f(r_j^{\circ})\}$ of the weighting matrix are obtained from

$$\sigma_k^2\{f(r_j^{\circ})\} = \{\partial f(r_j^{\circ})/\partial r_j^{\circ}\}^2_k \sigma_r^2 \quad (7)$$

The latter assumption is closer to the nonlinear case and is even more realistic for discrimination among rival models. The statistical techniques involved in the data analysis are summarized in two excellent reviews (22, 23).

Final acceptance or rejection of a model equation was based on the following statistical and physical criteria:

(a) The parameters of the weighted linear models must be statistically significant. This is tested by a partial F test on a 90% probability level. Insignificant parameters are removed from the model. A model is rejected if there is more than one insignificant parameter (series II data).

(b) The parameters of the nonlinear analysis must be significantly positive—*i.e.*, a positive parameter value must be conceivable statistically within reliable confidence regions. This is derived from a partial F value and the parameter variance $\sigma_{r_j}^2$. No model with a significantly negative parameter was accepted.

(c) From the nonlinear versions of the models remaining after criteria a and b were applied, only those have been accepted for which the error mean square Q (*i.e.*, the normalized residual sum of squares) was smaller or equal to a critical value calculated from Q_{min} on a $\alpha = 95\%$ probability F level (25) (P and N are the number of parameters and rate data):

$$Q_{\text{crit}} = Q_{\text{min}} \left\{ 1 + \frac{P}{N - P} F(P, N - P, \alpha) \right\} \quad (8)$$

(d) The absolute magnitude of the parameters and their ratios as well as their temperature dependence must be physically reasonable—*i.e.*, the heats and entropies of adsorption, in general, should be negative.

In any case, the models derived should be estimated as statistical statements having been verified within certain ranges of the independent variables.

Results and Discussion

The two series of rate data summarized in Tables I and II show qualitatively that:

(a) The initial rates r_0 increase with both increasing $x_{\text{O}_2}^0$ and x_{E}^0 in a hyperbolic manner

(b) The initial rates r_0 decrease on addition of the reaction products EO, CO₂, H₂O

(c) S increases on increasing the ratio $x_{\text{O}_2}^0/x_{\text{E}}^0$

(d) Addition of the reaction products increases S

(e) S decreases with increasing temperature

(f) Increase of the total oxidation rate ($r_{\text{O}_1}^0 + r_{\text{O}_2}^0$)—*i.e.*, increase of A—always is accompanied by a decrease in S.

Mathematical analysis of the series I data showed that only DS mechanisms satisfactorily describe the rate data sets.

From the total of the mechanisms of Table III the adequate alternatives describing the initial rates r_0 within the criteria claimed above are summarized in Table IV, including the parameters (K_i , k_j), their standard deviations σ_i , and the residual mean squares Q obtained from nonlinear regression. With a single exception, mechanisms involving interaction of adjacently chemisorbed [E] and [O₂-II] are most likely for EO formation; however, there is a distinct preference for the atomic oxygen species [O-III] to be involved in the full oxidation of E to CO₂ + H₂O although this is less obvious than the DSO₂-models for formation of EO. No further discrimination among mechanisms based upon either a partly (A1/A2, E1/E2) or a fully (C,D,F) oxidized silver surface could be derived from the data. Mechanism C could be interpreted equally well in terms of a bare silver surface. However, from chemisorption studies (*cf.* above) a bare silver surface is unlikely to exist at reaction conditions. Arguing that the two independent oxidation reactions must take place on the same type of catalyst surface, mechanisms A1, C, D, and F are the most likely ($\sqrt{K_1} \simeq 10^{16}$ for EO/E2/DSO₂ means that this mechanism transforms into EO/F/DSO₂).

Table IV shows that because of the large K_{E} , E is strongly adsorbed on an oxygenated silver surface. This also was evident from an experiment first done by Belousov and Rubanik (26). Repetition of this experiment proved that on simultaneously passing E and propylene over a silver catalyst the oxidation rate of E decreased by a factor 20. Along with the chemisorption studies, this clearly accounts for the strong chemisorption of E. Since K_{O_2} ($= K_2$) is small, molecular oxygen must be present only to a small extent on the catalyst surface at reaction temperatures. These results, again, are in good agreement with chemisorption studies. Similar kinetic results have been discussed in Refs. 11 and 17.

The series II data were analyzed isothermally and nonisothermally; the temperature was one of the independent variables in the nonlinear least-squares procedure where all data were treated simultaneously. Series II primarily pro-

Table IV. Adequate Mechanisms for $E \rightarrow EO$ and $E \rightarrow CO_2 + H_2O$ Allowed within the Selection Criteria for Series I Data^a

	$\sqrt{K_1}(\sqrt{K_3})^*$ (σ)	K_2 (σ)	K_E (σ)	k_j (σ)	$Q \times 10^3$
EO/A1/DSO2	2.07 (3.06)	2.94 (0.54)	14.86 (14.34)	2.77 (1.47)	0.89
EO/C/DSO2	1.32* (1.87)	1.14 (0.60)	13.68 (6.09)	4.65 (4.17)	0.75
EO/D/DSO2	—	0.05 (0.09)	5.40 (0.98)	27.7 (44.9)	0.93
EO/E2/DSO2	10^{16} —	1.50 (0.22)	9.83 (1.76)	2.49 (0.30)	0.77
EO/F/DSO2	—	1.50 (0.22)	9.83 (1.74)	2.49 (0.29)	0.75
EO/A2/DSO	0.53 (0.81)	0.57 (0.41)	5.33 (0.81)	20.6 (54)	0.89
$Q_{crit} = 0.95 \times 10^{-3}$					
CO ₂ /A1/DSO	2.85 (2.35)	0.36 (0.96)	8.37 (4.35)	1.56 (0.71)	0.98
CO ₂ /A2/DSO	5.05 (3.03)	0.15 (1.01)	5.10 (0.80)	1.70 (0.85)	0.88
CO ₂ /C/DSO	0.42* (0.76)	0.37 (0.46)	7.53 (1.88)	5.14 (8.43)	0.78
CO ₂ /E1/DSO	2.70 (0.50)	0.14	8.53 (1.57)	1.57 (0.14)	0.97
CO ₂ /E2/DSO	3.03 (1.28)	0.27 (0.22)	5.94 (1.11)	2.48 (0.96)	0.85
CO ₂ /D/DSO2	—	1.03 (0.21)	8.61 (1.64)	2.41 (2.40)	0.77
CO ₂ /F/DSO2	—	3.44 (0.51)	12.6 (2.71)	1.77 (0.19)	0.88
$Q_{crit} = 0.98 \times 10^{-3}$					

^a Parameters K_i and k_j and their standard deviation σ are given.

vides information about the temperature dependence of the E oxidation as well as a control of the adequacy of the basic mechanisms derived from the series I data if, in addition, reaction products are present in the feed. The latter fact increases the number of terms in the denominator of the rate equations and parameters to be determined. However, the data sets having been selected, within given ranges, according to statistical techniques, a small number of initial rates were sufficient for an adequate analysis. Application of the selection criteria discussed above to the analysis resulted in the following adequate mechanisms:

EO : D/DSO2*, F/DSO2

CO₂ : A1/DSO*, D/DSO*, E1/DSO*, F/DSO*, D/DSO2, F/DSO2

(Owing to the lack of initial parameter estimates for models A2, B2, and E2, these were not included in the calculations). Analysis of the series II data showed that for most of the mechanisms the coefficient for chemisorption of a molecular oxygen species (K_2 , $\sqrt{K_2}$) was small (occasionally even negative) and statistically insignificant (statistical F below a 90% probability). If in a stepwise regression, this coefficient were eliminated first, it was excluded from the following nonlinear analysis. In this case, the coefficients in the nominator

were combined into a single constant k_j . Rate equations not including K_2 or not including K_2 or $\sqrt{K_2}$ are marked with an asterisk.

For the series II data, again, DSO2 mechanisms are the most likely for EO formation, and, less obviously, DSO mechanisms are the best to describe the full oxidation of E. For the nonisothermal nonlinear analysis the coefficients K_1 and k_j were put in the form:

$$K_i = \exp(\Delta S_{ad,i}/R) \exp(-\Delta H_{ad,i}/RT)$$

$$k_j = \exp(\Delta S_j^\ddagger/R) \exp(-\Delta H_j^\ddagger/RT) \quad (9)$$

and the parameters $\Delta S_{ad,i}/R$, $\Delta H_{ad,i}/R$, $\Delta S_j^\ddagger/R$, and $\Delta H_j^\ddagger/R$ were calculated directly. The adequate mechanisms exhibit the correct sign as well as a reasonable magnitude of the ΔS and ΔH -parameters; the only exception was K_2 , accounting for the unusual chemisorption characteristics of oxygen. The data for three mechanisms are in Table V. Values for k_j marked with an asterisk result from "truncated" rate equations (*see above*).

Table V. Kinetic Parameters for Series II Data Using Non-Isothermal Nonlinear Least-Squares Techniques for Three Selected Mechanisms

Mechanism		K_2	K_E	K_{EO}	K_{CO_2}	K_{H_2O}	k_j	$Q \times 10^4$
EO/D/ DSO2:	$\Delta S_{ad}/R(\Delta S^\ddagger/R)$ (σ)	-9.41 (3.1)	1.0 (7.6)	-12.5 (9.7)	-3.5 (12.4)	8.1 ^a (2.1)		
	$-\Delta H_{ad}/R(\Delta H^\ddagger/R)$ $\times 10^{-3}$ (σ)	5.7 (1.7)	1.3 (4.2)	7.2 (5.3)	2.0 (6.9)	3.75 ^a (1.1)	1.1	
	$K_{i,529}$	3.72	31.1	3.34	29.2			
EO/F/ DSO2:	$\Delta S_{ad}/R(\Delta S^\ddagger/R)$ (σ)	5.36 (3.8)	-7.9 (2.56)	-0.4 (7.76)	-21.2 (4.4)	-3.75 (13.0)	14.9	
	$-\Delta H_{ad}/R(\Delta H^\ddagger/R)$ $\times 10^{-3}$ (σ)	-3.19 (2.1)	4.5 (1.4)	1.9 (4.2)	12.7 (2.4)	3.6 (7.2)	7.0 (0.12)	0.8
	$K_{ii,529}$	1.13	3.7	40.1	5.0	26.5		
CO ₂ /D/ DSO:	$\Delta S_{ad}/R(\Delta S^\ddagger/R)$ (σ)	-9.6 (6.52)	-5.4 (21.4)	-9.0 (22.4)	-2.9 (24.6)	7.75 ^a (6.1)		
	$-\Delta H_{ad}/R(\Delta H^\ddagger/R)$ $\times 10^{-3}$ (σ)	5.9 (3.6)	5.1 (11.9)	5.4 (12.3)	3.6 (13.7)	3.8 ^a (3.4)	9.0	
	$K_{i,529}$	4.5	73.3	3.6	52.6			

^a Values from truncated rate equations (*see text*). For comparison, the adsorption equilibrium constants K_i are given for 529° K.

The data of Table V basically reflect the results of the chemisorption studies: H₂O, EO, E, and CO₂ are strongly chemisorbed on an oxygenated silver surface. The low values for $\Delta H_{ad,i}$ may account for the strong interaction of the negatively polarized surface and the negatively charged adsorption complexes. Positive values for $\Delta S_{ad,i}$ are not impossible for complex adsorption structures like $[Ag_x-O_y-EO]^{-\delta}$. The adsorption/desorption characteristics are

essentially governed by the Gibbs free energy of adsorption. Following the relationship $\Delta G_{ad,1} = -RT \ln (K_1)$, Table V shows that (at 529°K *e.g.*)

$$| -\Delta G_{ad,H_2O} | \simeq | -\Delta G_{ad,EO} | > | -\Delta G_{ad,E} | \simeq | -\Delta G_{ad,CO_2} |$$

in excellent agreement to the chemisorption studies. Thus, the following conclusions can be drawn:

(a) The rates r_j^o increase hyperbolically with $x_{O_2}^o$ and x_E^o according to the rate equations of Table III (some DSO models are exceptional for CO₂ formation).

(b) Because of the strong chemisorption of the reaction products they decrease the rates in a defined order.

(c) The rate equations imply that *S* increases proportional to $(x_{O_2}^o)^{1/2}$ if one assumes a DSO₂ and a DSO mechanism for the formation of EO and CO₂ + H₂O. In addition, the ratio [O-II]/[O-III] increases with $x_{O_2}^o$, thus favoring *S*.

(d) Since the reaction products are strongly adsorbed at [O-III] sites, they are blocked for the full oxidation of E, again enhancing *S*. This, however, strictly is only true for a fully oxidized silver surface where [O-III] is simultaneously adsorptive and reactive (type A, D, E, and F surfaces).

(e) From the ratio of the apparent enthalpies of activation, $\Delta H_{j,eff}^\ddagger$, calculated from $k_{eff,j}$ data (obtained from $r_j^o = k_{eff,j}(x_E^o, x_{O_2}^o)$) it follows that *S* should decrease with increasing *T*. Using a standard feed ($x_E^o = 0.05$, $x_{O_2}^o = 0.19$) the following values are obtained for mechanism D:

EO/D/DSO₂ : $\Delta H^\ddagger = 10.6$ kcal/mole ; CO₂/D/DSO : $\Delta H^\ddagger = 11.5$ kcal/mole

Therefore, full oxidation of E is favored with increasing *T*. On the other hand, with increasing *T* the ratio [O₂-II]/[O-III] decreases and so does *S*.

As to the intrinsic mechanism of the two independent modes of the oxidation of E the following model could apply. Addition of oxygen to E from a molecularly chemisorbed species results in an adsorption complex [O.EO] also formed from the reverse reaction—*i.e.*, chemisorption of EO. This has been shown experimentally; on passing EO over a silver catalyst E was found in the exit gas stream, clearly demonstrating that EO must have been chemisorbed on the catalyst surface. The (rate-controlling) step in the full oxidation of E probably is the rupture of the C=C bond by the atomic oxygen species [O-III]. The intermediate formed—*i.e.*, [CH₂O.O] is rapidly oxidized to CO₂ + H₂O. The latter step is supported by oxygen of the [O-IV] type. The oxygen equilibria are rapidly reestablished. Traces of formaldehyde have been detected in the exit stream (27).

Conclusions

The general kinetic and mechanistic features of the oxidation of E over silver have been shown. Even if the true mechanism is far from being understood, the assumptions of this present study are felt to be reasonable approximations. This essentially concerns the understanding of the basic characteristics of the oxidation of E—*e.g.*, the dependence of r_j^o , *A*, and *S* on the process variables as well as the agreement between the kinetic and chemisorption studies. However, it is likely that the rate equations and mechanisms discussed should be applied to more narrow ranges of the independent variables. This becomes obvious if one recalls that a large oxygen content in the feed modifies

the catalytic active surface by forming a nonstoichiometric Ag_xO_y layer of varying thickness on top of the metal (4, 28). This, clearly, must be accounted for by admitting different mechanisms and kinetic equations in different regions of the independent variables. This, perhaps, is a specific situation for model building activities: statistically designed experiments are not the only clue for discriminating among rival models (such as those in Tables IV and V); much more intrinsic knowledge of the basic catalytic mechanism is required.

Nomenclature

E	ethylene
EO	ethylene oxide
A	integral activity; $A = \{(\text{volume E oxidized to EO, CO}_2 + \text{H}_2\text{O})\} / \{(\text{volume E in feed})\} \times 100 (\%)$
C_j	integral conversion; $C_j = \{(\text{volume of E oxidized to } j)\} / \{(\text{volume of E in feed})\} \times 100\%$
S	selectivity; $S = C_1/C_2 \times 100\%$
$[i]$	adsorbed species i; fractional concentration of adsorbed species i
$[\quad], [O]$	adsorption center; fractional concentration of adsorption center
$x_i^0, (p_i^0)$	mole fraction (partial pressure) of component i in feed gas
$r_i^0, (\hat{r}_i^0)$	uncorrected (corrected) initial rate ($\text{cm}^3 \text{ NTP E} \rightarrow j$)/sec
$k_j, (k_{\text{eff. } j})$	rate constant (effective rate constant) ($\text{cm}^3 \text{ NTP E} \rightarrow j$)/sec
K_i	adsorption equilibrium constant of component i
Q	residual mean square (sum of squares/degrees of freedom)
ξ_j	fractional conversion $\text{E} \rightarrow j$
j	subscript for $\text{E} \rightarrow \text{EO}$ ($j = 1$) and $\text{E} \rightarrow \text{CO}_2 + \text{H}_2\text{O}$ ($j = 2$)
°	superscript for initial conditions (reactor entrance)

Acknowledgment

This study was financially supported by the Fonds zur Förderung der wissenschaftlichen Forschung, Wien, Austria. The authors thank A. Taeb for assistance with part of the experimental work.

Literature Cited

- Voge, H. H., Adams, Ch. R., *Advan. Catalysis* (1967) **17**, 151.
- Hofmann, H., *Proc. European (2nd Intern.) Symp. Chem. Reaction Eng., 5th, Amsterdam, 1972*, Elsevier (1972), A 2-1.
- Kilty, P. A., Rol, N. C., Sachtler, W. M. H., *Proc. Intern. Congr. Catalysis, 5th, Miami Beach, 1972*, North-Holland (1973), 929.
- Spath, H. T., *Proc. Intern. Congr. Catalysis, 5th, Miami Beach, 1972*, North-Holland (1973), 945.
- Smeltzer, W. W., Tollefson, E. F., Cambron, A., *Can. J. Chem.* (1956) **34**, 1046.
- Czanderna, A. W., *J. Phys. Chem.* (1964) **68**, 2765.
- Sandler, Y. L., Hickam, W. M., *Proc. Intern. Congr. Catalysis, 3rd, Amsterdam, 1964*, North-Holland (1965) **1**, 227.
- Sandler, Y. L., Durigon, D. D., *J. Phys. Chem.* (1965) **69**, 4201.
- Sandler, Y. L., Beer, S. Z., Durigon, D. D., *J. Phys. Chem.* (1966) **70**, 3881.
- Twigg, G. H., *Proc. Roy. Soc.* (1946) **A 188**, 92, 105, 123.
- Nault, L. G., Bolme, D. W., Johanson, L. N., *Ind. Eng. Chem., Process Design Develop.* (1962) **1**, 285.
- Orzechowski, A., McCormack, K. E., *Can. J. Chem.* (1954) **32**, 388, 415, 432, 443.

13. Kurilenko, A. I., Kul'kova, N. V., Baranova, L. P., Temkin, M. I., *Kinet. Katal.* (1962) **3**, 208.
14. Imre, L., *Ber. Bunsenges. Phys. Chem.* (1970) **74**, 220.
15. Herzog, W., *Ber. Bunsenges. Phys. Chem.* (1970) **74**, 216.
16. Klugherz, P. D., Harriott, P., *AIChE J.* (1971) **17**, 856.
17. Verma, A., Kaliaguine, S., *J. Catal.* (1973) **30**, 430.
18. Spath, H. T., Tomazic, G. S., Wurm, H., Torkar, K., *J. Catal.* (1972) **26**, 18.
19. Spath, H. T., *Ber. Direktabb. Oberflächen* (1972) **5**, in press.
20. Spath, H. T., Torkar, K., *J. Catal.* (1972) **26**, 163.
21. Spath, H. T., Habilitationsschrift, Technische Hochschule, Graz, Austria, 1971.
22. Kittrell, J. R., *Advan. Chem. Eng.* (1971) **8**, 98.
23. Hofmann, H., *ADVAN. CHEM. SER.* (1972) **109**, 8-516.
24. Frank, B., Thesis, Technische Hochschule, Graz, Austria (1971).
25. Beale, E. M. L., *J. Roy. Stat. Soc.* (1960) **B 22**, 41.
26. Belousov, V. M., Rubanik, M. Y., *Kinet. Katal.* (1963) **4**, 892.
27. McDonald, R. W., Hayes, K. E., *J. Catal.* (1969) **15**, 301.
28. Feller-Kniepmeier, M., Feller, H. G., Titzenthaler, E., *Ber. Bunsenges. Phys. Chem.* (1967) **71**, 606.

RECEIVED January 2, 1974.

Analysis of Chemical Reaction Networks

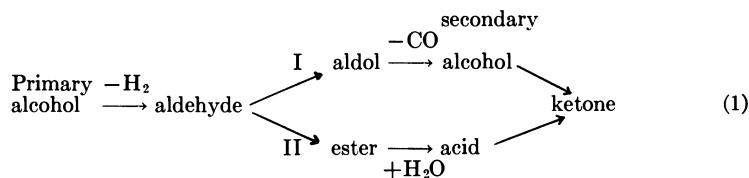
The Dehydrogenation of 1-Propanol on NaOH-Doped γ -Alumina

E. KIKUCHI, S. E. WANKE, and I. G. DALLA LANA

Department of Chemical Engineering, University of Alberta,
Edmonton, Alberta, Canada

The rate behavior of multiple-step reaction systems is difficult to model realistically because of uncertainties in the correctness of the network, its stoichiometry, and the form of appropriate rate expressions. The kinetics of dehydrogenation of 1-propanol raised four alternative networks. The isothermal conversion-space time data were smoothed, differentiated, and decomposed algebraically into differential rate data for each step. Rate constants and reaction orders for power-law rate expressions were fitted to each step. A kinetic model was constructed directly, integrated, and compared with experimental results. The models were sorted according to their predictive abilities and agreement with chemical evidence. More statistically significant parameters were then computed for the most acceptable network kinetic model.

In 1936 Ipatieff described (1) the gas-phase heterogeneous catalytic reaction of ethanol to acetone and isopropyl alcohol. Later, Komarewsky *et al.* (2) presented yields from ethanol and other primary alcohols, including 1-propanol, over chromic oxide catalyst. Dalla Lana *et al.* (3) found diethyl ketone as the main product from when 1-propanol reacted over a NaOH-doped Alundum support containing chromic oxide. Since they encountered all of the species in Reaction 1 but the acid, they interpreted the reaction scheme using Ipatieff's view—*i.e.*, catalytic conversion of primary alcohols to ketones involves two condensation routes from the aldehyde (here propionaldehyde):



Route II was used by Kagan (4, 5) to interpret the formation of acetone from ethanol in the presence of γ -alumina and Al_2O_3 -FeO-MgO catalysts. In their view, the ester may also react directly to the corresponding ketone, even in the absence of water vapor.

Further work by Komarewsky *et al.* (6), in which 1-octanol deuterated in the α -position was dehydrogenated over chromic oxide, suggested that the

ratio of atomic deuterium to gaseous hydrogen corresponded to route II. More recently, Minachev *et al.* (7) observed appreciable 4-heptanol during the formation of dipropyl ketone from 1-butanol over neodymium oxide, corresponding to route I. The relative importance of routes I and II in the dehydrogenation of a primary alcohol is probably determined by the specificity of the catalyst. Although most studies, excepting Ipatieff's, produced only small amounts of the aldol and secondary alcohol intermediates, route I cannot be discounted since small concentrations of these could arise from rapid conversion of these forms to the ketone.

Reaction 1 illustrates the complex stoichiometry of a multiple reaction system involving at least six significant species. Until recently, the literature has offered no general basis for interpreting the kinetics of such irreversible systems except when first-order kinetics applies to all steps (8). Thus, quantitative predictions from empirical rate measurements would probably be restricted. Further, at higher conversions the 1-propanol system generates (3) many other "unaccountable" high molecular weight products, presumably from the reactive carbonyl compounds. Here, we examine the kinetic behavior of 1-propanol over an NaOH-doped γ -alumina catalyst. The global reaction rates measured for each species should then relate to the overall reaction steps comprising a known or postulated network. To formulate a kinetic model, the observed global integral rate data were first differentiated and then decomposed into single-step rates. These rates were used to model each reaction step by a procedure recently described (9). Lacking a mechanistic basis for developing appropriate rate expressions, power-law rate expressions were used to correlate each set of single step reaction rates. This article develops this approach and describes its usefulness.

Experimental Basis

Materials. 1-Propanol (Fisher Scientific Co.) was of C.P. grade; GC separation revealed only trace impurities. 1-Propanol vapor was diluted with 99.998% argon (Canadian Liquid Air, Ltd.) and used as purchased. The catalyst was prepared by impregnating previously crushed -12+24 mesh Houdry γ -alumina (HS-100S) with an aqueous solution of 3.5N NaOH, allowing the mixture to drain and then to dry overnight at 110°C.

Apparatus and Procedures. Global reaction rates for the species in Reaction 1 were measured by a fixed-bed integral reactor of 96% silica glass, 17 mm id. These species had been previously separated and identified (3). Bed temperatures were recorded by a traveling axial thermocouple within a 96% silica glass well. Liquid 1-propanol was quantitatively fed to a preheater by a syringe feeder at $0.1033\text{--}1.233 \pm 1.0\%$ moles/hr. A regulated argon flow was preheated separately and then mixed with 1-propanol vapor in a final preheating section before entering the reactor. The reactor was immersed in a temperature-controlled electrically heated eutectic salt bath. Argon minimized volume changes and was also used as an internal standard in the GC product analysis.

A portion of the reaction effluent was condensed in a cold trap at -60°C until at least 2 ml was obtained, usually within 5 to 20 min. The combined flow rate of argon plus non-condensed gases, such as H_2 and CO, was then measured using a soap-bubble meter. To determine the concentrations of components in the condensed phase a Carbowax 400 column was used. 1-Butanol was used as an internal standard to obtain production rates of individual components. Calibrations to obtain response factors for the major components were carried out.

At the maximum feed rate, over 98% 1-propanol could be recovered in a single cold trap during a blank run. Carbon dioxide was determined by volumetric absorption in a 30% aqueous KOH. Other gaseous products were collected over acidified saturated brine, and samples from this were injected directly into Poropak S or activated charcoal columns *via* a gas sampling valve. Peak areas were quantitatively related to the argon peak area by previously calibrated concentration peak area relationships. Their production rates could be determined from these analyses and the total gas flow. Although CO and CH₄ could be analyzed, only minor amounts were detected in the gaseous products. The presence of water was checked and was always negligible.

Material Balance Calculations. Since the ratio of 1-propanol to argon in both feed and product streams was known, we could calculate the total moles of 1-propanol reacted, independently of product analyses. The individual products were obtained separately because of the molar correction factors used along with the 1-butanol internal standard. Their stoichiometric equivalents of 1-propanol were then calculated, summed, and compared with the reacted 1-propanol previously calculated. The following notations were adopted:

$$\begin{aligned} A_1 &= \text{1-propanol} = \text{PrOH} \\ A_2 &= \text{propionaldehyde} = \text{PrH} \\ A_3 &= \text{3-pentanol} = \text{PN} \\ A_4 &= \textit{n}\text{-propyl propionate} = \text{PP} \\ A_5 &= \text{diethyl ketone} = \text{DEK} \end{aligned}$$

The yield, Q_i , of component, A_i , was defined by Equation 2,

$$Q_i = \frac{\text{moles of } A_i \text{ in product}}{\text{moles of } A_i \text{ in feed}} \quad (2)$$

The fractional conversion of A_1 is given by Equation 3,

$$x = 1 - Q_1 \quad (3)$$

The reaction time was expressed using the reciprocal space velocity for an integral reactor, $\tau = W/F$, where W and F are weight of catalyst (grams) and feed rate of 1-propanol (moles/hr).

Carbon balances were calculated from Equation 4:

$$\text{Carbon accountability (\%)} = \frac{100}{3} \frac{\sum (n_i Q_i)}{\text{All analyzed products}} \quad (4)$$

where, n_i = number of carbon atoms in component A_i . Hydrogen and oxygen accountabilities were established by similar relationships.

Results

Experimental Studies. Initial studies with 1-propanol over pure γ -alumina showed this catalyst to promote dehydration to dipropyl ether or propylene. When γ -alumina was doped to NaOH content above 8.62 wt %, it catalyzed dehydrogenation but did not promote dehydration of 1-propanol (10). This catalyst was used throughout. The empty reactor showed no catalytic wall influences or homogeneous decomposition of 1-propanol.

Isothermal steady-state conversions were obtained at 400°C and 705.1 mm Hg for various 1-propanol feed rates. A catalyst charge of 10.08 grams was pretreated by heating overnight at 450°C in an argon stream. The results from seven experiments are reported in Table I. Since some catalyst discoloration occurred, run 1 was repeated (run 7); both runs showed that catalyst activity

Table I. Isothermal Kinetic Results

Run	7	1	2	3	4	5	6
τ_1 (gm catalyst) (hr) (mole)	97.6	97.6	65.3	48.8	32.6	16.3	8.2
x_1 Fractional conversion of 1-propanol	0.2064	0.1902	0.1393	0.1002	0.0865	0.0689	0.0484
	Yield, Q_i						
1-Propanol	0.7936	0.8098	0.8607	0.8998	0.9135	0.9311	0.9516
Propionaldehyde	0.0531	0.0513	0.0472	0.0494	0.0498	0.0306	0.0203
3-Pentanol	0.0006	0.0006	traces	traces	traces	traces	traces
<i>n</i> -Propyl propionate	0.0060	0.0060	0.0056	0.0052	0.0051	0.0042	0.0023
Diethyl ketone	0.0251	0.0221	0.0185	0.0120	0.0083	0.0039	0.0007
Hydrogen	0.210	0.207	0.185	0.143	0.122	0.056	0.036
Propylene	0.003	0.003	0.002	0.001	traces	traces	traces
Carbon dioxide	0.025	0.021	0.021	0.015	0.009	0.005	0.001
Material Balances, %							
carbon	91.3	92.0	95.9	98.6	99.0	97.8	97.8
hydrogen	93.2	94.1	97.5	99.6	99.9	97.9	98.0
oxygen	92.8	93.9	98.0	100.2	100.0	98.4	97.9

had not changed appreciably. Under our conditions the reactions are essentially irreversible.

Table I lists only those products which were previously (3) separated and identified with high certainty. When the Carbowax column was heated to 170°C, the corresponding chromatograms showed many small unidentified peaks at elution times greater than for propyl propionate. With increasing conversions of 1-propanol, these peaks also increased. The material balances in Table I show this increasing discrepancy at fractional conversions greater than 0.1. The unknown products probably formed in side reactions involving highly reactive aldehydes or ketones.

With the integral kinetic data from runs 1-6, we postulated a network of apparent reaction steps which could interrelate the compounds and (here) explain the formation of diethyl ketone. Since a network such as Reaction 1 is not generally available from previous studies, alternatives may be validly postulated. The approach of Dalla Lana *et al.* (9) to such a problem was used to evaluate reaction sequences.

Analysis of Experimental Data. The effect of space time on the composition of the product stream is illustrated in Figure 1. Since these plots give integral conversion data, to obtain reaction rates for each species, the Q_i - τ points were first smoothed and then differentiated. Analytical functions were used to obtain a smooth Q_i - τ function subject to: (1) at $\tau = 0$, the compositions were zero for all products and unity for 1-propanol; (2) the smoothing functions for products could not contain more than one maximum; and (3) the smoothing function had to decrease monotonically for 1-propanol. For each compound, several arbitrary functions were tested; the one which met the above conditions and generated the minimum variance, S^2 (as defined by Equation 5), was taken to be the best,

$$S^2 = \frac{\sum_{k=1}^N [(Q_i)_{\text{Exp}} - (Q_i)_{\text{Pred}}]^2}{N - P} \quad (5)$$

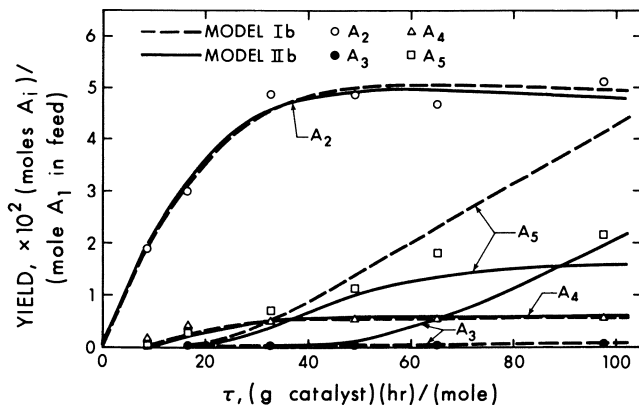


Figure 1. Comparison of experimental results with predictions of models Ib and IIb

where N = number of experimental points

P = number of parameters in the smoothing function.

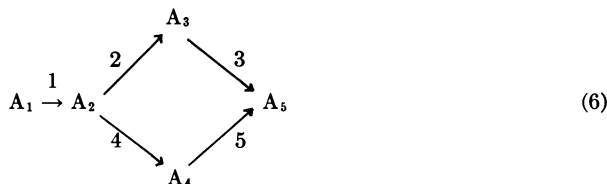
The functions in Table II generated minimum variances when applied to the data from runs 1–6. (Run 7 was done after data smoothing was completed.) A linear smoothing function was used to describe the 3-pentanol yield since Q_3 appeared to be directly proportional to τ even at higher conversions (II).

Table II. Smoothing of Experimental Data

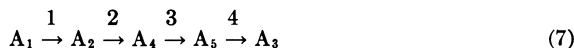
Component	$Q_i = \text{Function Fitted}$	Variance
A_1 (PrOH)	$\exp(-0.00230 \tau)$	$0.378 (10^{-3})$
A_2 (PrH)	$0.0503 \tanh(0.0488 \tau)$	$0.605 (10^{-5})$
A_3 (PN)	0.00000594τ	$0.568 (10^{-7})$
A_4 (PP)	$0.00556 \tanh(0.0564 \tau)$	$0.690 (10^{-7})$
A_5 (DEK)	$0.0308 (\arctan(0.001 \tau))^{1,13}$	$0.122 (10^{-5})$

Model Discrimination. Considering the reaction step shown by Network 1 and the possibility that 3-pentanol may have been formed by diethyl ketone hydrogenation, the following two networks seemed feasible,

Model I



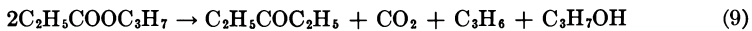
Model II



Numbers on the arrows refer to each reaction step. These networks relate the species observed but not the unknowns. Although 3-pentanol (A_3) was present in small quantities, model I is not negated since A_3 may have been very reactive.

The reaction rate of any chemical species, A_i , is r_i which will *always* mean a point value for the rate. Since A_i may take part in several independent steps, the characteristic rates for each j th step will be defined as R_j . Thus, r_i will include contributions from all R_j which affect the amount of A_i present.

To evaluate the contribution from each step to the global rate of production for a given species, the stoichiometry of each step must be evaluated. Except for the formation of diethyl ketone from n -propyl propionate (steps 5 or 3 in models I or II) the network stoichiometry is well defined. Two alternative stoichiometries have been proposed:



Since Reaction 8 requires water, which is absent from the feed and the products, this possibility is eliminated. Reaction 9 is possible, but little propylene was detected and thus did not correspond to the larger amounts of diethyl ketone or CO_2 observed. Since propylene may have reacted further, the possibility of either Reaction 9 or 10 was considered for models I and II,



On this basis, four alternative networks must be tested with the smoothed rate data:

Model Ia: step 5 described by Equation 9

Model Ib: step 5 described by Equation 10

Model IIa: step 3 described by Equation 9

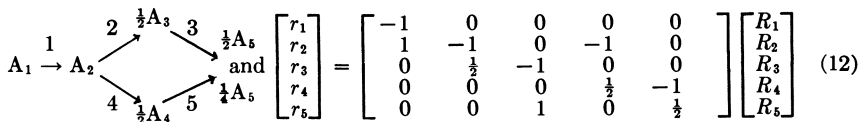
Model IIb: step 3 described by Equation 10

The procedure used to decompose the global rates into characteristic reaction rates for single steps—*i.e.*, (r_1, r_2, \dots) transformed to (R_1, R_2, \dots) —will be illustrated for model Ia. Differential material balances for model Ia within an isothermal volume element are:

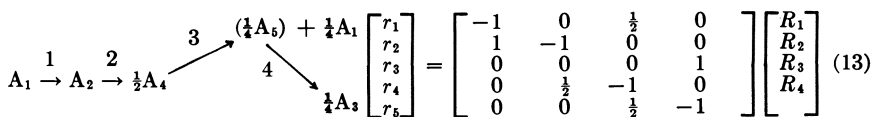
$$\begin{bmatrix} r_1 \\ r_2 \\ r_3 \\ r_4 \\ r_5 \end{bmatrix} = \begin{bmatrix} -1 & 0 & 0 & 0 & \frac{1}{2} \\ 1 & -1 & 0 & -1 & 0 \\ 0 & \frac{1}{2} & -1 & 0 & 0 \\ 0 & 0 & 0 & \frac{1}{2} & -1 \\ 0 & 0 & 1 & 0 & \frac{1}{2} \end{bmatrix} \begin{bmatrix} R_1 \\ R_2 \\ R_3 \\ R_4 \\ R_5 \end{bmatrix} \quad (11)$$

which must be solved for $[R_j]$ using the known values of $[r_i]$. Thus, models Ib, IIa, and IIb lead to:

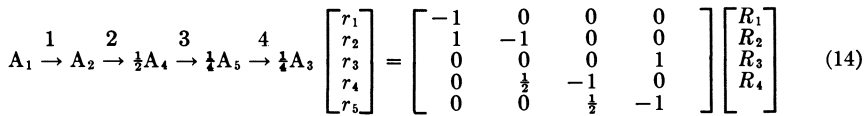
Model Ib



Model IIa



Model IIb



Each contains one linearly dependent equation. Eliminating one of the r_i equations arbitrarily from each set removes this degeneracy.

We eliminated r_5 from Equations 11 and 12 and r_3 from Equations 13 and 14. In the latter two cases, one may then readily solve for the unknown R_j in terms of r_i . In the former two cases, a solution is still not possible because the reduced coefficient matrix is only of rank 3, but four R_j are unknown. This difficulty can be overcome by introducing another independent condition. This was achieved by independently estimating the parameters for a kinetic model postulated for one (or more) of the unknown R_j . We restricted the choice of rate functions to simple power-law relationships. Using this approach for model Ia, the following combination of steps provided a convenient additional independent condition for solving Equations 11,

$$r_1 + r_2 + \frac{1}{2}r_4 = -R_2 - \frac{3}{4}R_4 = -k_2C_2^{n_{22}} - \frac{3}{4}k_3C_2^{n_{23}} \quad (15)$$

To solve Equations 12, the condition used was,

$$r_1 + r_2 = -R_2 - R_4 = -k_2C_2^{n_{22}} - k_4C_2^{n_{24}} \quad (16)$$

Using the smoothed differentiable functions for Q_i , and the corresponding,

$$C_i = 8.44 (10^{-3}) Q_i, \text{ moles/liter} \quad (17)$$

where $8.44 (10^{-3})$ is the concentration of A_1 in the feed, numerical values of their derivatives were calculated for values of τ to obtain

$$r_i = \frac{dQ_i}{d\tau} \quad (18)$$

Equation 17 approximates C_i closely since the volume changes from reaction were small because of low fractional conversions and dilution of 1-propanol with argon. Using smoothed points (C_i, τ, r_i) , the parameters, k_j and n_{ij} , were determined by a nonlinear parameter estimation based upon a steepest descent technique. Equations 15 and 16 were estimated:

$$r_1 + r_2 + \frac{1}{4}r_4 = 8.65(10^{-3})C_2^{0.336} - 2.79(10^3)C_2^{1.78} \quad (19)$$

and,

$$r_1 + r_2 = -17.7C_2^{1.40} - 2.21(10^3)C_2^{1.82} \quad (20)$$

Equations 19 and 20, in principle, can then be used to generate values of R_2 and/or R_4 and thus solve matrix Equations 11 and 12. At this stage, smoothed characteristic rate data are available for each step in any of the four networks. A power-law rate expression may be fitted

$$R_j = k_j C_i^{n_{ij}} \quad (21)$$

to each reaction step. The appropriate fitted R_j can be substituted into the

Table III. Estimates of Kinetic Parameters for Model Ib

R_j	k_j	n_{ij}
R_1	0.273	$n_{11} = 1.00$
R_2	17.7	$n_{22} = 1.40$
R_3	$1.72 (10^3)$	$n_{34} = 1.22$
R_4	$2.21 (10^3)$	$n_{23} = 1.82$
R_5	$9.19 (10^{10})$	$n_{45} = 3.25$

differential material balance equations, such as Equation 11, allowing simultaneous integration. The experimental points may be compared with these predictions from the integrated network power-law kinetic model. Since none of the above models included step(s) for formation of unknowns, R_j values were calculated using smoothed data at $\tau = 0-45$, the region of good material balances. Normally, 19 points were used at equidistant $\Delta\tau$ of 2.5.

Model Ia was rejected because k_2 was negative. Table III summarizes the parameters estimates for model Ib, and Table IV for models IIa and IIb. Model Ia predicted that n_{11} should be negative, -1.21 . Since this step follows monomolecular stoichiometry, a negative exponent predicts an anomalous rate behavior, and model IIa was also rejected. Models Ia and IIa were rejected because of inconsistencies between estimated parameters and implied chemical behavior. While this reasoning is valid, error in the manipulated and smoothed data cannot be discounted.

Figure 1 compares the predictions with results for components A_2 , A_3 , A_4 , and A_5 using the network power-law rate expressions for models Ib and IIb. The agreement is satisfactory up to $\tau = 45$; at higher τ , and thus higher con-

Table IV. Estimates of Kinetic Parameters for Models IIa and IIb

R_j :	R_1		R_2		R_3		R_4	
	k_1	n_{11}	k_2	n_{23}	k_3	n_{43}	k_4	n_{54}
Model								
IIa		-1.21		2.10		1.89		2.08
	$7.15(10^{-6})$		$3.18(10^4)$		$1.74(10^5)$		$9.55(10^4)$	
IIb		1.00		2.11		1.91		2.31
	0.273		$2.70(10^4)$		$1.58(10^5)$		$4.38(10^5)$	

versions of 1-propanol, model Ib does not correlate the yields for A_5 , and model IIb fails for A_3 and A_5 . 1-Propanol yields are not shown since both models predict satisfactory but identical results.

The addition of reaction steps to these networks to account for unknowns should result in better agreement at $\tau > 45$. Examination of Figure 1 suggests that a reaction of the type,



should force model Ib to predict a smaller yield of A_5 , and model IIb to predict a smaller yield of A_3 . When Ib is adjusted by adding step 6, we obtain model Ic, in which all the characteristic rates except R_6 , are identical to those in Ib. R_6 was calculated from the material balance for A_5 —i.e.,

$$R_6 = R_3 + \frac{1}{2}R_5 - r_5 \quad (23)$$

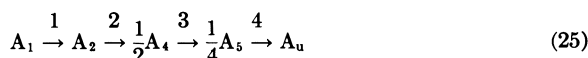
The values of r_5 were obtained from the smoothed data for $\tau \leq 100$. Fitting a power-law function to R_6 yields

$$R_6 = k_6 C_5^{n_{56}} = 158.8 C_5^{1.43} \quad (24)$$

Model Ic was numerically integrated, and the predicted Q_5 - τ plot was compared with the experimentally determined points. Before commenting on the results, the modification to model Iib, leading to model Iic, is developed.

To improve model Iib, the production of unknowns from A_5 should be considered. This leads to

Model Iic:



which now includes the formation of A_3 within the unknown products, A_u . Since Q_3 was always small, especially relative to the total unknowns at $\tau > 45$, this simplification is justified. The essential differences between Ic and Iic remain: formation of A_3 from A_2 as a parallel route to A_5 or formation of A_3 from A_5 via a network involving only consecutive reaction steps. Model Iic is identical to Iib if A_3 is replaced by A_u (Equation 14). Values of R_4 were calculated using

$$R_4 = \frac{1}{2} R_3 - r_5 \quad (26)$$

r_5 being evaluated from the smoothed function for A_5 for $\tau \leq 100$. The resulting power-law equation for R_4 is:

$$R_4 = 14.6 C_5^{1.25} \quad (27)$$

Model Iic was also numerically integrated, and the predictions were compared with experimental values.

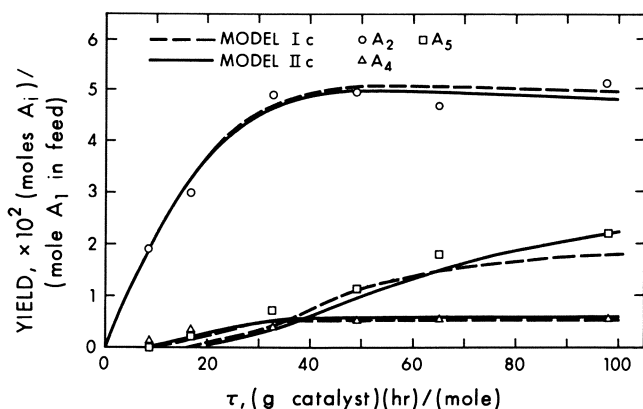


Figure 2. Comparison of experimental results with predictions of models Ic and Iic

Figures 2 and 3 compare experimental and predicted plots of Q_i vs. τ . Models Ic and Iic agree well with experimental yields for diethyl ketone. The deficiency of model Iib for predicting 3-pentanol has been eliminated but not

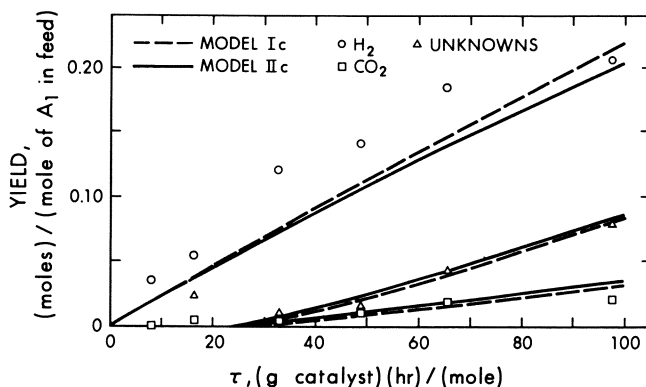


Figure 3. Comparison of experimental results with predictions of models Ic and Iic

explicitly since A_3 is now regarded as an “unknown.” Earlier studies (3) indicated qualitatively that A_3 was formed in a route parallel to that involving A_4 , as shown in model I. We observed very little A_3 , and thus, it was included, realizing that questions pertaining to the origin of A_3 were unlikely to be resolved. The increased temperatures necessary to promote A_3 formation would create an even more difficult experimental problem.

The rates of gaseous product formation (H_2 and CO_2) were not used to check model predictions. Assuming H_2 is formed from steps 1 and 3 in model Ic and in step 1 in model Iic, the network models predict:

$$r_{H_2} = R_1 + R_3 = 0.273 C_1 + 1.72(10^3) C_3^{1.22} \quad (28)$$

and

$$r_{H_2} = R_1 = 0.273 C_1 \quad (29)$$

The differential material balance equations were integrated for models Ic and Iic; Figure 3 compares the results with the experimental H_2 yields. Both model plots are close but lie generally below experimental values. Since alcohol dehydrogenation is promoted by the NaOH-doped alumina, further reactions of this type are expected with unknown molecules containing hydroxyl groups.

If CO_2 is formed from step 5 in model Ic and in step 3 of model Iic, the network models predict:

$$r_{CO_2} = \frac{1}{2}R_5 = 4.59 (10^{10}) C_4^{3.25} \quad (30)$$

and

$$r_{CO_2} = \frac{1}{2}R_3 = 0.79 (10^5) C_4^{1.91} \quad (31)$$

The results from the integrated models (Figure 3) agree closely with experimental values. The difference between the H_2 plots corresponds to the H_2 produced in model Ic from 3-pentanol. Model Iic predicts a higher yield of CO_2 since all of the diethyl ketone was formed from step 3 whereas in model Ic, some diethyl ketone was formed from 3-pentanol *via* step 3. Rates of unknown formation, expressed in 1-propanol equivalents, predicted are

$$r_u = \frac{5}{3}R_6 + R_5 = 265 C_5^{1.43} + 9.19 (10^{10})C_4^{3.25} \quad (32)$$

for model Ic, and

$$r_u = R_3 + \frac{5}{3}R_4 = 1.58(10^5)C_4^{1.91} + 24.3C_5^{1.25} \quad (33)$$

for model IIc. The integrated results for both models agree closely with experimental data (Figure 3). The experimental data for unknown formation were obtained from carbon balances (Table I).

Discussion

This study of the dehydrogenation of 1-propanol illustrates the difficulty in proceeding with detailed analyses of multiple chemical reaction step systems without first obtaining good experimental data in sufficient quantities and without prior clarification of the underlying stoichiometry. The decomposition technique and power-law rate expressions for the apparent chemical steps revealed the superiority of models Ib and IIb for predicting conversions at $\tau \leq 45$. Extension of models Ib and IIb into models Ic and IIc, by incorporating formation of unknowns, required additional chemical insight for postulating suitable reaction steps. These extensions for predictions at $\tau > 45$ may be questioned on the basis that the material accountabilities in this range of τ are inaccurate. The accountabilities at lower τ values are good since it was shown experimentally that the condensation efficiency in the product collection cold trap increased from $\sim 98\%$ to almost 100% when τ went from 8.2 to 48.8. This explains the $< 100\%$ accountabilities obtained where formation of unknowns is small. At $\tau > 45$, the condensation efficiency is $\sim 100\%$, and thus, the decreasing accountabilities relate to the increasing extent of unknown products being formed, not to the lack of reliability of chemical analyses for known products.

Models Ic and IIc agree with the experimental results equally well. While model Ic is more general in that 3-pentanol formation is treated more realistically; being a closed network it required additional independent information (*via* nonlinear parameter estimation) with consequent computational difficulties before the network rates could be decomposed into single-step rates. On the other hand, model IIc provided a simpler basis for calculating single-step rates but subject to negligible formation of 3-pentanol. In addition, the orders of reaction obtained for each step in model IIc approximate those expected from the law of mass action—*i.e.*, 1.0 and 2—whereas the order of reaction for step 5 in model Ic was more suspect, being 3.25.

The agreement between observed and measured yields demonstrates the adequacy of the smoothing technique since the rate of formation of unknowns, r_u , was obtained from material balances. Further experimental validation was tried with *n*-propyl propionate as feed. The results were nullified because the formation of many unknowns (probably polymeric) caused the catalyst to deactivate rapidly. These experiments presumably failed to duplicate the microscopic reaction conditions at the catalyst surface. Other experiments at higher conversions and with mixed feeds should be used to test (or extend) the models for extrapolated predictions.

In estimating values of multiple parameters for nonlinear models, others may prefer a statistical basis for multiresponse analysis (12). For example, model IIc could be examined by simultaneously estimating all of the power-law parameters (eight) in the differential equations for network 25, from the original experimental data (seven sets of integral responses). This is difficult,

Table V. Comparison of Rate Constants Obtained by Various Parameter Estimation Methods for Model IIc

Method of estimating rate constants	Rate Constants			
	k_1	k_2	k_3	k_4
Network decomposition	0.273	2.70(10 ⁴)	1.58(10 ⁵)	14.6
Simultaneous, using experimental concentrations	0.274	2.51(10 ⁴)	1.56(10 ⁵)	11.4
Simultaneous, using smoothed concentrations	0.273	2.67(10 ⁴)	1.58(10 ⁵)	11.5

and attempts proved to be computationally indecisive. As a compromise, rate constants were calculated for model IIc by simultaneous parameter estimation, assuming the orders of reaction to be those in Table IV. Table V gives rate constants from experimental and smoothed data (seven and 12 points) and contrasts them with those from the decomposition approach.

The computational difficulties and the comparison in Table V vindicate our view that the decomposition method and the use of single-step power-law rate expressions provide a direct route for kinetic modeling. The simultaneous estimation of rate constants and orders of reactions for networks containing more than eight steps may be possible but certainly not easier. Also, one can interject physical and chemical insights into the modeling—*e.g.*, selecting smoothing functions, testing different forms of global or intrinsic rate expressions. The statistically sound methods for simultaneous parameter estimation are limited when integral rate data cannot be treated easily or when few experimental data are available. With the decomposition method, however, valid models may be rejected prematurely. The combination of using the simple decomposition method and power-law expressions to relate the observed physicochemical data to a valid chemical network and its kinetic model and then obtaining statistically sound parameter estimates should provide an adequate basis for network modeling.

Literature Cited

1. Ipatieff, V. N., "Catalytic Reactions at High Pressures and Temperatures," pp. 411-451, MacMillan, New York, 1936.
2. Komarewsky, V. I., Coley, J. R., *J. Amer. Chem. Soc.* (1941) **63**, 700, 3269.
3. Dalla Lana, I. G., Vasudeva, K., Robinson, D. B., *J. Catalysis* (1966) **6**, 100.
4. Kagan, M. J., Rossinskaya, Y., Chertsov, S. M., *Zh. Obshch. Khim.* (1932) **3**, 244.
5. Kagan, M. J., Sobolew, I. A., Lubarsky, G. D., *Chem. Ber.* (1935) **68**, 1140.
6. Komarewsky, V. I., Coley, J. R., *Advan. Catalysis* (1956) **8**, 207.
7. Minachev, M., Loginov, G. A., Markov, M. A., *Kin. i Kat.* (1966) **7**, 904.
8. Wei, J., Prater, D. C., *Advan. Catalysis* (1962) **8**, 581.
9. Dalla Lana, I. G., Myint, A., Wanke, S. E., *Can. J. Chem. Eng.* (1973) **51**, 578.
10. Chuang, T., Dalla Lana, I. G., *J. Chem. Soc., Far. Trans. I.* (1972) **68**, 773.
11. Wanke, S. E., M.Sc. Thesis, University of Alberta, 1966.
12. Box, G. E. P., Draper, N. R., *Biometrika* (1965) **52**, 355.

RECEIVED January 2, 1974.

Coke and Deactivation in Catalytic Cracking

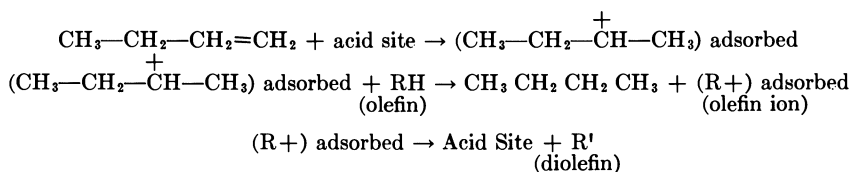
THOMAS M. JOHN, ROMAN A. PACHOVSKY, and
BOHDAN W. WOJCIECHOWSKI

Department of Chemical Engineering, Queen's University,
Kingston, Ontario, Canada

Catalyst decay and the mode of coke formation in the catalytic cracking of extracted neutral distillates were studied. Feedstocks differed only in wax content and ranged from ~0 to ~27 mole % wax. This study unequivocally shows that coke is the product of secondary cracking reactions. Coke is suspected to be produced by the olefin reactions which arise in the primary cracking step. This view is supported by the total lack of high boiling condensed products in the cycle stock. We have also shown that the catalyst decays purely as a function of the time-on-stream whereas coke is not such a function. We thus conclude that in this case the relationship between coke-on-catalyst and catalyst activity is at best not a simple one and in fact may not exist.

The loss of catalytic activity during cracking reactions has long been attributed entirely to the formation of "coke" on the catalyst. Although no clear definition of coke exists, the term usually embraces all hydrogen-deficient carbonaceous materials remaining on the catalyst after post reaction stripping. X-ray diffraction studies by Appleby *et al.* (1) and infrared work by Eberly *et al.* (2) indicated that coke deposits are at least partly composed of condensed aromatic structures of low hydrogen content. The existence of such putative aromatic structures in coke deposits arising from the cracking of pure aliphatic hydrocarbons has led to much speculation on the mechanism of formation of coke deposits.

In these considerations, attention has centered on mechanisms of coke formation which involve aromatics and olefins as the principal coke-forming fractions. One such mechanism arises from the consideration of olefin saturation by successive hydrogen transfers (2, 3, 4):



where RH is the donor species which eventually becomes coke.

Thomas (3), Greensfelder and Voge (4), and Blue and Engle (5) have presented data which show that naphthenes are a valuable source of hydrogen for olefin saturation and can thus be considered as donor species. This observation has led to a mechanism involving the formation of aromatics *via* the successive transfer of hydride ions, followed by the loss of a proton from the resulting carbonium ion. In this way, depending on the structure of the naphthene, hydrogen-transfer reactions could lead to the production of highly unsaturated or aromatic species, which finally result in coke. On the other hand, Thomas (3) and Petrov and Frost (6) obtained high coke yields and considerable product saturation when pure octene was passed over an acidic catalyst at 375°C. They concluded that hydrogen transfer from one olefin to another and polymerization or aromatization of the alkyl carbonium ion were responsible for coke formation. This postulate represents the other proposed mechanism of coke formation—*viz.*, polymerization on the catalyst surface.

To determine the role of aromatics in coke formation, Appleby *et al.* (1) compared the product yields from cracking recycle oil with a high concentration of polyaromatic compounds and the yields from cracking the same stock after it had undergone hydrogenation. The results show that at 50% feed conversion, coke yield was 13 wt % in the first case and only 4 wt % for the second. The high activity of polycyclic and heterocyclic aromatics in coke formation identified these compounds as one of the main coke-forming species. What was not shown is whether coke is formed directly from the feed constituents or whether it is the product of secondary reactions.

In this investigation, feeds from which virtually all polycyclic and heterocyclic aromatic materials had been removed by solvent extraction were cracked over La-Y at three reaction temperatures in a fixed-bed reactor. The ranges of the properties and molecular compositions of the two feedstocks obtained from the solvent extraction processes are summarized in Table I. [The catalyst was prepared by repeated exchanges of Linde SK40 sieves with a 0.1M solution of LaCl₃. The exchanges were interspersed with 4-hr calcination at 200°C and continued until no further exchange was occurring as determined by atomic adsorption spectrophotometry of the exchange medium.]

Table I. Properties and Composition of the Wax-Bearing (A0W1) and Wax-Free (A1W0) Feedstocks^a

	A1W0	A0W1
Average molecular weight	387	400
Sulfur, wt %	0.5	0.17
Conradson carbon, wt %	0.01	0.018
Aniline point, °F	210.0	118.0
Bromine number	0.0	0.0
Pour point, °F	+5	+87
<i>Mass Spectrometry</i>		
Paraffins, wt %	15	26
Naphthenes, wt %	69.6	65.1
Aromatics, wt %	14.6	8.4

^a A2W1 is a blend of 70% A1W0 and 30% A0W1. A1W2 is a blend of 70% A0W1 and 30% A1W0. Both are on a volume basis.

In each experimental run coke yield was determined quantitatively, and the effects of various parameters on the coke yield and catalyst decay were observed. The results on conversion, selectivity, and others are discussed elsewhere; we confine our discussion to the relationship between coke and catalyst activity.

Treatment of Experimental Results

Catalytic cracking occurs at temperatures which make thermal cracking reactions unavoidable. In this study coke is one product of these thermal reactions. This fact was deduced from the results obtained in the absence of any catalyst when the reactor was packed with crushed glass. Thus the overall coke formed, and in general the overall catalytic yield of any product, consists of two components: thermal and catalytic. Our experiments were done in a packed bed reactor preceded by a heater-vaporizer, and the catalyst was purged and then regenerated *in situ*. Thus, to obtain purely catalytic yields, the thermal yields obtained in blank runs using no catalyst were subtracted from the results of runs of similar time-on-stream where catalyst was used. The assumption that the thermal conversion during a blank run was approximately the same as that during catalytic reaction was satisfactory within the limits of our conditions, and its validity is improved under conditions important in this study—*viz.*, at low times-on-stream (short space time).

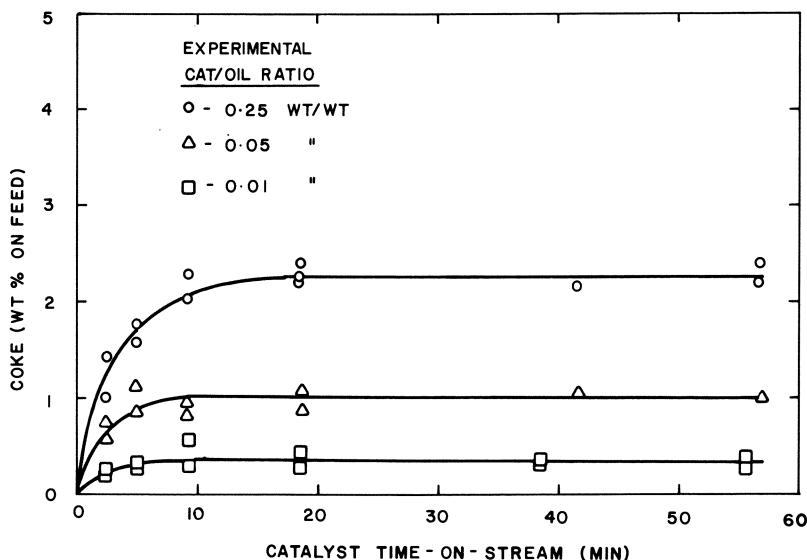


Figure 1. Coke-on-feed vs. catalyst time-on-stream at 937°F for AlW0. Similar plots at 900°F and 975°F produce morphologically identical results.

Discussion

A discussion on coke formation is difficult because the "coke" is poorly defined. The most common definition is "the material which remains on the catalyst after a post reaction stripping purge with an inert gas for a specific period of time and at the reaction temperature." This definition is inadequate because the above conditions represent important, flexible parameters. We used nitrogen gas for purging the 300-cc reactor at the reaction temperature and at a flow rate of 200 cc/min for 30 minutes.

Since some question may arise concerning the validity of separating the total coke yield into catalytic and thermal fractions, we offer the following observation. Most of the thermal coke produced during a blank run was

formed in the preheater-vaporizer zone of the reactor and not on the inert packing replacing the catalyst. Thus, it seems reasonable to assume that the additional coke formed thermally does not plug or coat the catalyst particles to any significant degree.

Our data are consistent in their morphological behavior with those of Eberly *et al.* (2). Figure 2 shows that as the cat/oil ratio is increased at a constant time-on-stream, the weight percent coke on catalyst decreases. Since data were not collected at a sufficiently low cat/oil ratio, we did not observe the maximum in coke on catalyst yield for a constant time-on-stream observed by Eberly *et al.* However, the fact that the difference between our lower two cat/oil ratios is less than the difference between the highest and middle ratios suggests that the trend may be toward a maximum.

Relationship of Coke to Catalyst Decay. Figures 1 and 2 show weight percent catalytic coke based on feed and on catalyst as a function of time-on-stream for AlW0 at one reaction temperature. These figures are representative of the results for all temperatures and feeds studied. Figure 3 shows the thermal coke yield for the same stock and at the same temperature. The dashed lines are the thermal coke yields at the two other temperatures we studied. A suitable summation of the values from Figures 2 and 3 will produce composite curves for total coke yield that behave in some n^{th} order fashion. On the other hand Figure 2 shows that the catalytic coke-on-catalyst curves at all catalyst to oil ratios reach an early maximum and remain there for all longer times-on-stream. At the same time the catalyst activity (Figure 4), as measured by θ , continues to decline (7). Pachovsky and Wojciechowski (8) showed that catalyst decay with this particular stock follows an exponential decay function

$$\theta = e^{-k_d t}$$

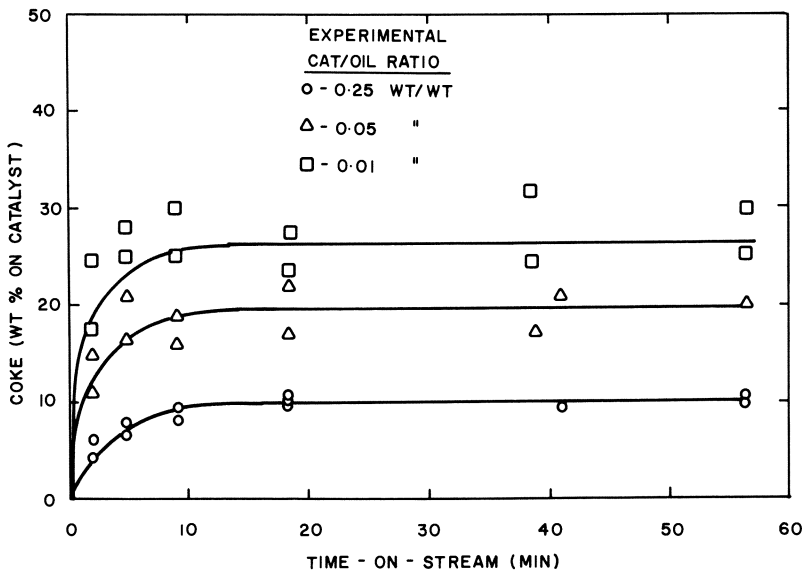


Figure 2. Coke-on-catalyst vs. catalyst time-on-stream at 937°F for AlW0. More coke is produced per unit weight of catalyst as the absolute amount of catalyst is decreased (that is, cat/oil ratio is decreased). Similar plots result at 900°F and 975°F.

with time-on-stream (t). It is clear from the above that catalyst decay is not a function of catalyst-to-oil ratio whereas coke-on-catalyst is. In view of these fundamental disagreements in the behavior of θ and of coke we must say that coke-on-catalyst is not a measure of catalyst decay.

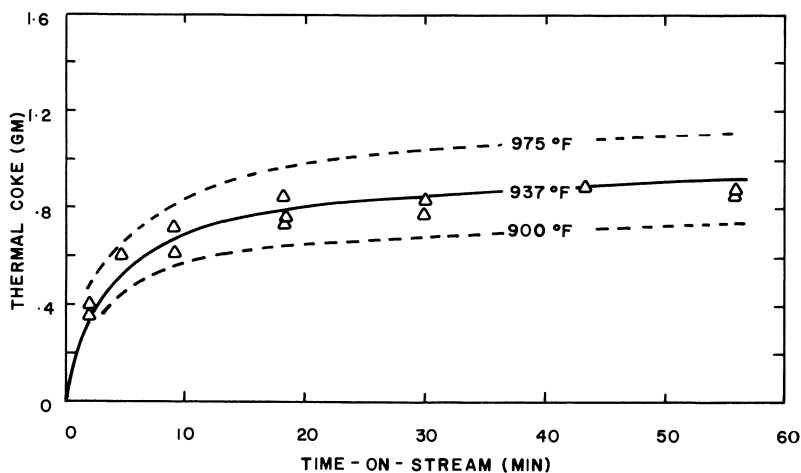


Figure 3. Thermal coke vs. run time for the three temperatures studied. Solid and dashed lines are least-squares fittings, and experimental points obtained at 937°F are shown.

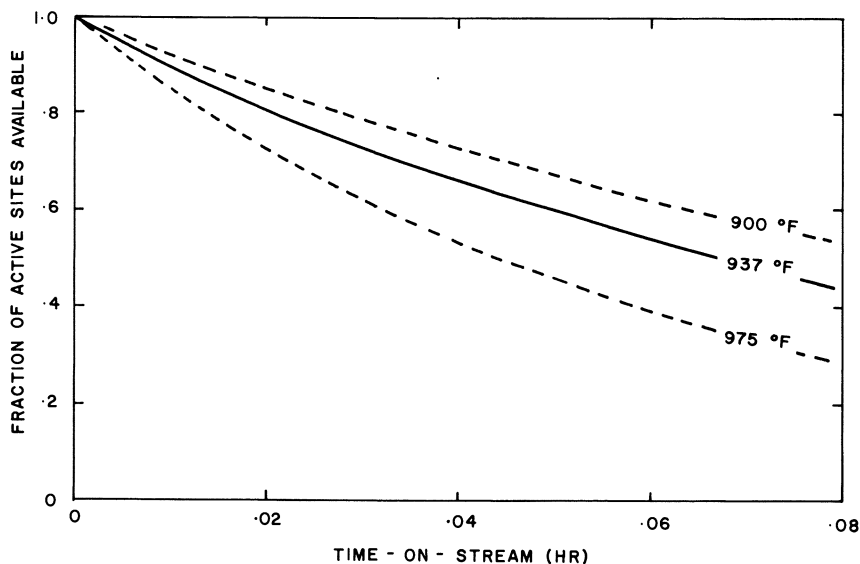


Figure 4. Effect of temperature on the catalyst decay as calculated from conversion data

Froment and Bischoff (9, 10) have postulated that the fraction of unpoisoned active sites remaining on a catalyst is a function of the coke-on-catalyst

$$\theta = e^{-\alpha C_c}$$

where α is a constant and C_c is a coke-on-catalyst. To reconcile this concept with the time-on-stream approach we would have to accept that coke on catalyst is related to time-on-stream by a linear relationship. Figure 2 shows that this would only be approximately true at low times-on-stream.

It should not, however, be immediately assumed that our results contradict Froment and Bischoff (9, 10) or Ruderhausen and Watson (11) since they based their correlations on total coke yield (thermal plus catalytic). There is little doubt that total coke yield which is an n^{th} order function of time-on-stream can be correlated with catalyst deactivation in some systems over certain conditions. However, the use of total coke rather than catalytic coke, we feel, leads to erroneous conclusions and certainly does not give a realistic picture of the relationship between coke and catalyst decay. From our treatment of the data, we conclude that coke is not directly responsible for decay but should be treated merely as an undesirable side product.

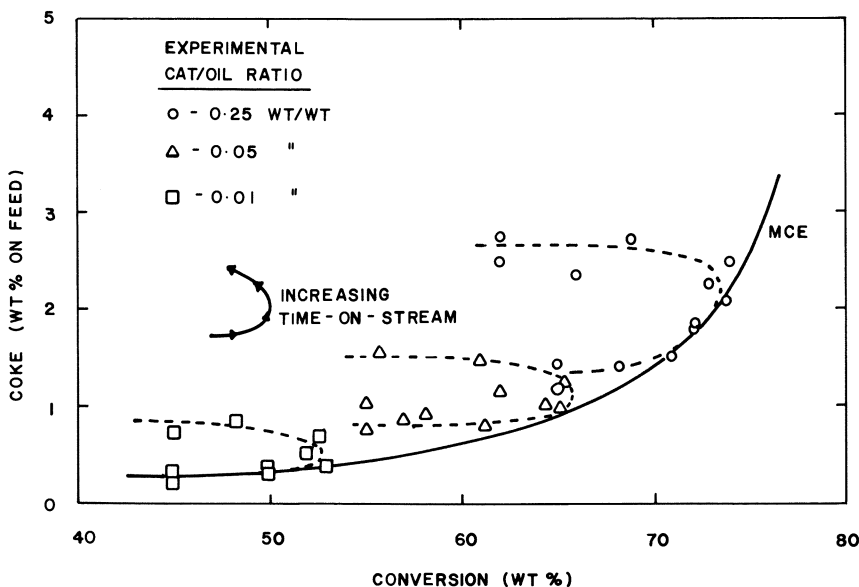


Figure 5. Coke selectivity plot. MCE is the minimum coke envelope and represents the results that would be observable in a moving or fluidized bed reactor.

Sources of Coke in Catalytic Cracking. Figures 5 and 6 show the relationship between percent coke based on feed and percent conversion for the different feedstocks used. Feeds A2W1 and A1W2 are prepared from blends of A1W0 and A0W1. In Figure 5 the actual cat/oil loops are shown, and the minimum coke envelope is inferred from these. In Figure 6, however, only the four minimum coke envelopes have been shown.

The slopes of the coke curves at the origin are all zero. This is important and shows that whereas at initial conditions the cracking reaction is proceeding

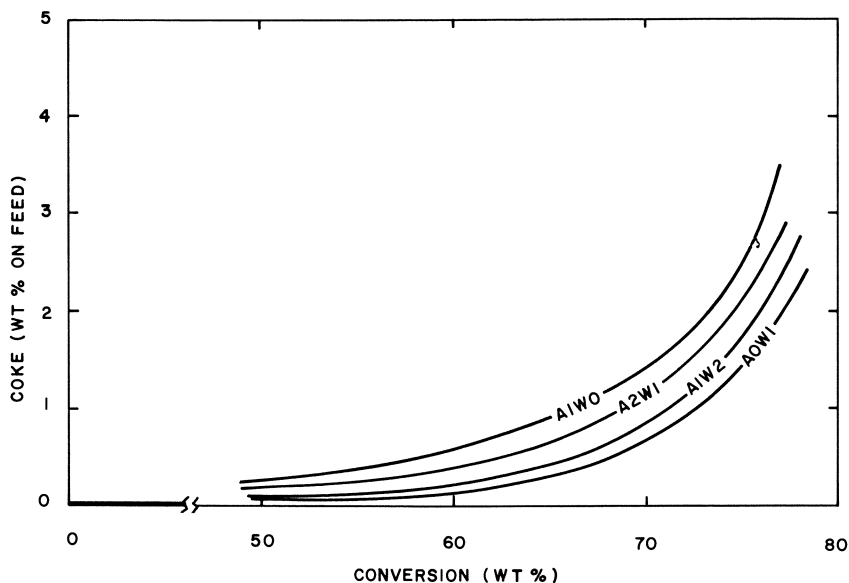


Figure 6. Coke selectivities for the four charge stocks studied. The MCE decreases as the wax content is increased; all MCE's have zero slope at the origin.

at a finite rate, the rate of catalytic coke production is zero. At the same time the catalyst is decaying at a finite rate (Figure 4). This result underlines our main point—*i.e.*, coking is not directly responsible for catalyst decay. Furthermore, Figures 5 and 6 show that coke is most certainly not produced in primary cracking reactions but is solely a product of the secondary reactions of primary products. Since the only primary products which are qualitatively different from the feed are olefins, we ascribe coke formation in this case to the reactions of olefins.

The curves in Figures 5 and 6 are not those for a constant time-on-stream. They are those which we call the minimum coke envelopes, and it has been shown elsewhere (12) that these would be the results observed if data were obtained for catalytic coke in moving or fluid bed reactors. Such curves can be obtained from static bed reactor data by tracing an optimum envelope as shown in Figure 5. Figure 7 is a theoretical case and shows that interpreting coke results at various cat/oil ratios but at a constant time-on-stream is likely to lead to erroneous results. The dashed curve is the locus of runs at constant time-on-stream and various cat/oil ratios. Such data could lead to the erroneous conclusion that the coke-*vs.*-conversion curve has a finite initial slope and hence that coke is a result of primary cracking reactions. Using such considerations, we see that the data reported by Plank *et al.* (13) and Eberly *et al.* (2) for cracking of methylcyclohexane and *n*-hexadecane respectively all show the absence of coke formation in the primary reaction step. For methylcyclohexane and *n*-hexadecane cracking, accounting for thermal coke was unnecessary since these pure, low molecular weight, saturated hydrocarbons do not yield any significant amount of thermal coke. On the other hand, without accounting for thermal coke, the data at constant time-on-stream reported by Plank and

Rosinski (14) for cracking gas oil leads to the potentially wrong conclusion that coke is a primary reaction product.

Plank *et al.* (13) and more recently Butt (15) have speculated that polymerization and hydrogen transfer reactions might be involved in coke formation. The cycle stock obtained in this study did not reveal any compound with either a higher carbon number or higher boiling point than the feed (*see* Figures 8 and 9). Any polymerization which might occur would have to involve substances adsorbed on the catalyst surface which do not subsequently desorb.

We are not denying the suggestion that coke can be produced from aromatics. In fact, Appleby *et al.* (1) and White (16) have shown that aromatics, especially polynuclear aromatics, produce a large amount of coke for a particular degree of conversion. However, their runs were not corrected for thermal conversion; this leaves two possibilities: (1) that the complex aromatics may adsorb readily, leading to high "coke" values, or (2) that the high coke values are the result of thermal conversion. In either case the coke resulting from complex aromatics would represent a material present in the feed and should not be seen in the same light as coke which is a product of the catalytic cracking reaction. Unfortunately their definition of coke does not allow this distinction at this time.

Since we were interested in studying coke formation during reaction, we chose a feed that was very low in polynuclear aromatics (0.6–3.0%). In the absence of large quantities of polynuclear aromatics, coke was formed strictly through secondary reactions. Since these involve olefins, which were not present in our original feed, it must be argued that olefins are the source of coke formation.

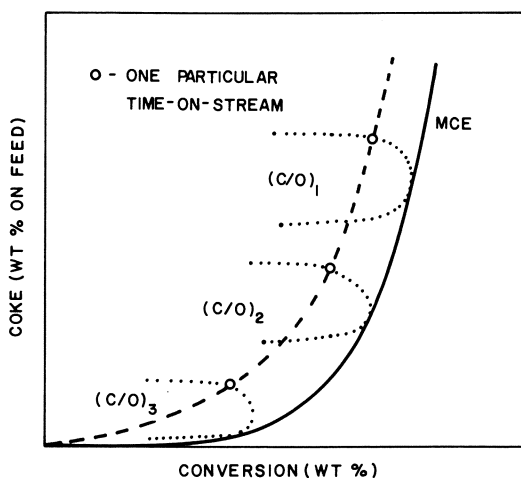


Figure 7. Theoretical coke selectivity plot, illustrating the danger of trying to obtain results from constant time-on-stream data. The locus of points at a fixed time-on-stream will show a finite slope at the origin whereas the true behavior of coke as derived from the MCE indicates zero slope at the origin and hence zero rate of coke production under initial conditions.

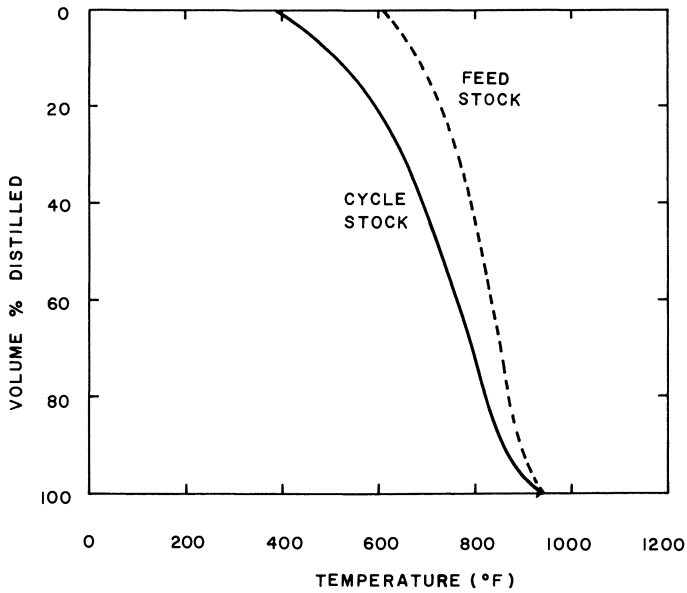


Figure 8. Distillation curves for AOW1 feedstock and cycle stock at $\sim 65\%$ conversion

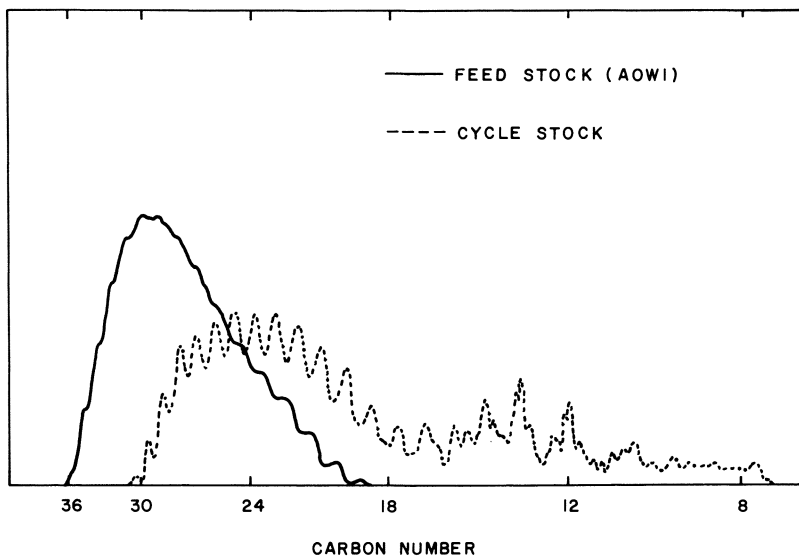


Figure 9. Gas chromatogram for AOW1 feedstock and cycle stock. Cycle stock shows no species higher in molecular weight than the feed.

Conclusions

On the basis of the success of the time-on-stream theory in describing catalyst activity as a monotonically decreasing function of time-on-stream and on the basis of the observed behavior of coke-on-catalyst we conclude that the relationship between coke-on-catalyst and activity is not direct. We also conclude that coke in catalytic cracking of extracted neutral distillate arises solely from secondary reactions and not directly from the feed. Furthermore, we infer that coke in this system arises from the reactions of product olefins but not from their polymerization to a range beyond the final boiling point of the feed.

Nomenclature

- α = empirical constant
 C_c = coke on catalyst
 k_d = first-order decay rate constant
 t = time-on-stream
 θ = fraction of active sites remaining unpoisoned

Acknowledgment

We thank Imperial Oil for the chargestocks and for assistance with some of the analytical work.

Literature Cited

1. Appleby, W. G., Gibson, J. W., Good, G. M., *Ind. Eng. Chem., Process Design Develop.* (1962) **1**, 102.
2. Eberly, P. E., Kimberlie, C. N., Miller, W. H., Drushel, H. V., *Ind. Eng. Chem., Process Design Develop.* (1956) **5**, 193.
3. Thomas, C. L., *J. Amer. Chem. Soc.* (1944) **66**, 1586.
4. Greensfelder, B. S., Voge, H. H., *Ind. Eng. Chem.* (1945) **37**, 1038.
5. Blue, R. W., Engle, C. J., *Ind. Eng. Chem.* (1951) **43**, 494.
6. Petrov, A. A., Frost, A. V., *Dokl. Akad. Nauk SSSR* (1949) **65**, 851.
7. Wojciechowski, B. W., *Can. J. Chem. Eng.* (1968) **46**, 48.
8. Pachovsky, R. A., Wojciechowski, B. W., in press.
9. Froment, G. F., Bischoff, R. B., *Chem. Eng. Sci.* (1961) **16**, 189.
10. *Ibid.*, (1962) **17**, 105.
11. Ruderhausen, C. G., Watson, C. C., *Chem. Eng. Sci.* (1954) **3**, 110.
12. Campbell, D. R., Wojciechowski, B. W., *Can. J. Chem. Eng.* (1971) **48**, 224.
13. Plank, C. J., Sibbett, D. J., Smith, R. B., *Ind. Eng. Chem.* (1957) **49**, 742.
14. Plank, C. J., Rosinski, E. J., *Chem. Eng. Progr., Symp. Ser.* (1967) **63**, 26.
15. Butt, J. B., *ADVAN. CHEM. SER.* (1972) **109**, 259.
16. White, P. J., *Petrol. Refiner* (1968) **47**, 103.

RECEIVED January 2, 1974.

Practical Model of the Benzoic Acid Oxidation Step as a Means towards Optimization of the Phenol Process

L. VAN DIERENDONCK, P. DE JONG, J. VON DEN HOFF,
and H. VONKEN

Central Laboratory, DSM, P.O. Box 18, Geleen, The Netherlands

R. VERMIJS

CIR, P.O. Box 1021, Rozenburg, Rotterdam, The Netherlands

In the preparation of phenol from toluene by the toluene-benzoic acid route, the economics of the process largely depend on the process conditions used in the benzoic acid oxidation step. It is possible to describe the chemical and physical phenomena in the reactor by a mathematical model. The information needed to develop this model was taken from plant test runs and from additional laboratory research on the kinetics in the process step. Study of the model has furnished more insight into what occurs in the process, thus permitting the settings to be better adapted to the process conditions.

Toluene is oxidized to phenol in two independently operated units (Figure 1). The process starts with partial conversion of toluene to benzoic acid in a gas-stirred oxidation reactor. The resulting mixture is fractionated in several successive operations, yielding purified benzoic acid. In the reactor of the second oxidation section this benzoic acid stream is converted to phenol by a homogeneous catalyst consisting of copper and magnesium benzoates. The air needed enters the reactor base *via* a gas distributor together with steam. The steam causes the phenylbenzoate initially formed as an intermediate product to hydrolyze to phenol, which is stripped from the reaction medium by the effluent gas. This effluent is fed to a column separator to recover crude phenol and unconverted benzoic acid; the latter is then recycled *via* evaporators.

Byproducts formed in the oxidation predominantly consist of low volatile components, *i.e.*, tar. The tar concentration in the reactor is controlled by discharging reactor liquid to the extraction unit where the byproducts are removed, and the benzoic acid, copper, and magnesium are recycled to the oxidation reactor. The residual streams from the first and second oxidation section are burned together.

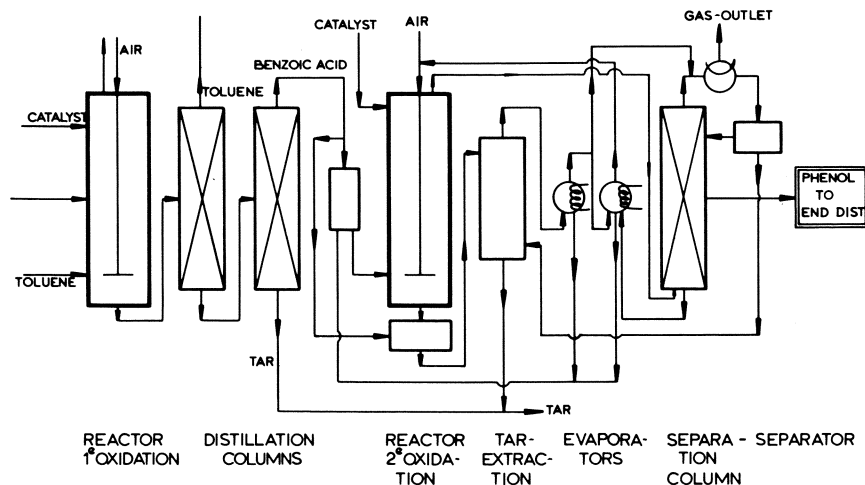


Figure 1. Flowsheet

Points of Investigation

To improve the economics of phenol production, the efficiency output and onstream times of the process had to be increased. Our study was directed at several aspects, such as the development of a model for the second oxidation stage. The required information was derived partly from plant measurements. The kinetics of each step, for example, were determined in a reactor of *ca.* 1 liter. Some other aspects were not as well suited to laboratory investigation because of scale-up problems. These include:

(a) The relation between rate of mass transfer ($K_L S$) and superficial gas velocity (V_s). In view of the process conditions, laboratory research would call for a superficial gas velocity so low that production rates comparable with those realized in practice could be attained only under conditions of mechanical stirring.

(b) The relation between reaction conditions and tar formation. The long residence times obtained in the industrial reactor, in combination with recycling light tar components, would make it impossible for a semitechnical reactor to be scaled down to the point where the costs are no longer prohibitive.

(c) The influence of the oxidation temperature above the boiling point of benzoic acid. Studying this point on a laboratory scale would involve large experimental problems of evaporation rate, benzoic acid recycle, and sealing the equipment.

Partly for these reasons, the data needed in our model study were taken from test runs done in the plant reactor. As far as possible, the kinetic and physico-technological information obtained from these test runs has been used for the ultimate model. Only in some cases did we use equations derived from a regression analysis of measuring data.

Research during model building was done by workers from the plant staff and from several departments of the DSM Central Laboratory. The team included specialists from organic chemistry, technology, and systems engineer-

ing who worked closely with the production division. This guaranteed assembling of the relevant information and offered the possibility of regularly checking the validity of the model.

Basis of the Model

Reaction Scheme and Stoichiometry. The preparation of phenol from benzoic acid (second oxidation) is done by oxidative decarboxylation with air in the presence of copper and magnesium (1, 2, 3, 4, 5, 6, 7, 8, 9, 10). Normally, phenylbenzoate is regarded as an intermediate product. The hydrolysis of phenylbenzoate—the actual phenol formation—is effected in the oxidation reactor by steam; magnesium is the catalyst.

Practice has shown that phenol production along this route invariably entails several consecutive and side reactions in which, *e.g.*, tar is formed. The formation of tar *via* a consecutive reaction appeared from the fact that in an experiment using radioactive phenol, phenol was incorporated in the tar. Also, part of the tar forms directly from benzoic acid or cupric benzoate.

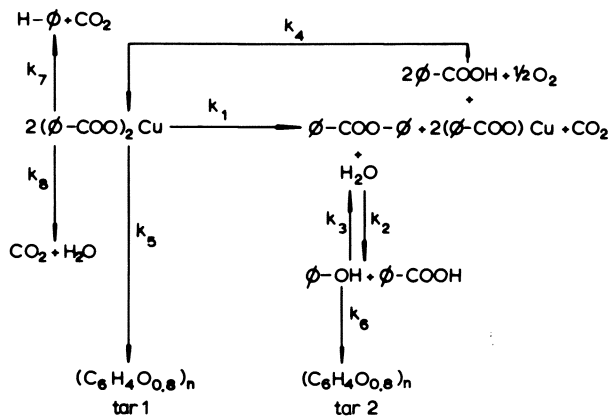


Figure 2. Reaction scheme

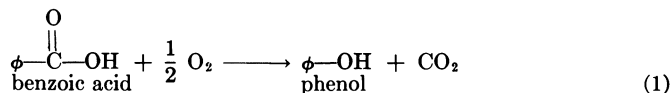
Other experiments have disclosed that benzoic acid conversion is invariably accompanied by tar formation, independently of the phenol concentration. In drawing up a reaction scheme it has been assumed, therefore, that tar is formed *via* two different reactions: One, the side reaction in the conversion of benzoic acid to phenol, is called the tar 1 reaction, and the other, the consecutive reaction of phenol, the tar 2 reaction. In principle, both tars can be regarded as precursors leading to tar structures in which the aromatic rings may or may not be connected by oxygen bridges; all of these can be represented by the gross formula $(\text{C}_6\text{H}_4\text{O}_z)_n$. Although plant measurements disclose a spread of the z values, we decided to take z equal to 0.8 as an average value. The possible consequences of this assumption are discussed below under Ring Degradation.

Another important side reaction is benzene formation, which proceeds only at a temperature-dependent rate. This benzene is recovered as a useful product.

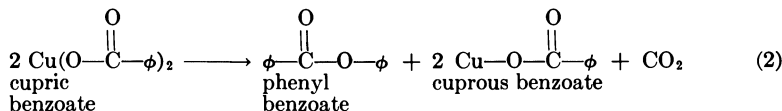
Finally, ring degradation also occurs; however, it is difficult to follow, because the reaction products are practically indistinguishable from those forming in the reactions mentioned above.

The above reactions can be represented by the following general equations, which have been included in the model:

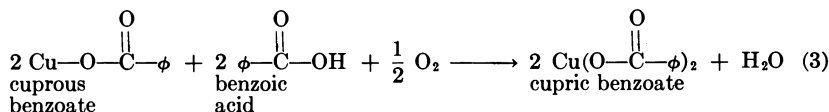
1. The gross oxidation reaction



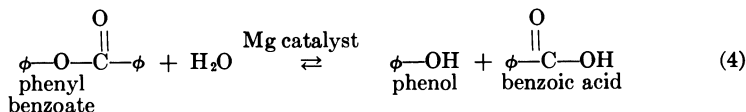
the partial reactions (a) decomposition of cupric benzoate



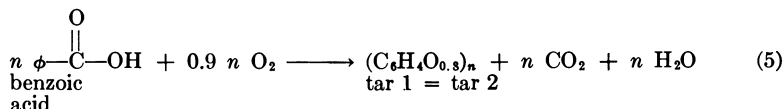
(b) reoxidation of cuprous benzoate to cupric benzoate



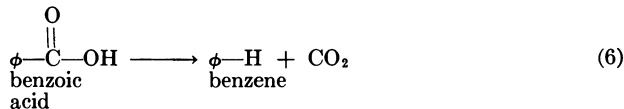
(c) hydrolysis of phenol benzoate



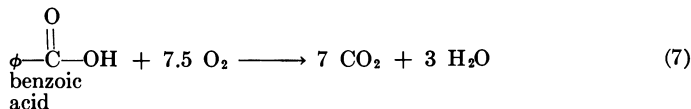
2. Formation of tar (1 + 2), which proceeds in agreement with the gross equation



3. Formation of benzene by decarboxylation of benzoic acid



4. Ring degradation



These reactions have been incorporated in the reaction scheme, which served as a basis for the model (Figure 2).

Kinetics. The kinetics of the partial steps in the reaction scheme were studied in bench-scale experiments. The reactor—a glass, stirred, gas-liquid

contactor—was normally operated on the batch principle, and was provided with the necessary feeding, measuring, and analytical equipment. The majority of the components were analyzed by gas-liquid chromatography. The amount of tar formed was determined after fractionation of the reactor contents.

The amounts of phenol, tar, and benzene were measured as functions of several variables, such as temperature, pressure, copper and magnesium content, gas load, and residence time (independent variables), and phenol concentration, degree of hydrolysis, cupric-cuprous ratio, oxygen partial pressure, *etc.* (dependent variables). The results of these experiments were used to derive the order of the various reactions as well as the reaction rate constants and their temperature dependencies.

Similar measurements were done under plant conditions to assemble supplementary information and to check the validity of the model. These measurements were done in many strictly defined test runs in which the production of phenol, the consumption of toluene, the temperature, the pressure, the liquid level, and the air and steam loads were varied. The test runs also yielded information on specific aspects such as ring degradation, oxygen content of the tar, gas holdup, and tar viscosity. All this information was used to describe the individual reactions which are discussed below.

OXIDATION OF CUPROUS TO CUPRIC BENZOATE. The oxidation of cuprous to cupric benzoate under the process conditions proceeds at a fast rate; the reduction of cupric benzoate, on the other hand, is a much slower reaction. Hence, the equilibrium lies entirely on the side of the cupric compound. This implies that during the oxidation the cupric benzoate concentration is fairly constant and high with respect to the amount of copper present. Thus, a given $[Cu^{2+}]/[Cu^+]$ is a function of the reaction conditions. The reaction rate equation

$$r_{Cu^{2+}} = k_4 \cdot C_{Cu^+} \cdot C_{O_2} \quad (8)$$

was derived from measurements of the rate of oxygen consumption as a function of the temperature, the oxygen partial pressure, and the $[Cu^{2+}]/[Cu^+]$ ratio. This problem is analyzed below, under Oxygen Absorption.

FORMATION OF PHENOL AND HYDROLYSIS OF PHENYL BENZOATE. Phenyl benzoate (phb), which forms from the cupric benzoate, has a distinctly lower vapor pressure than benzoic acid (BZO) and thus accumulates in the reaction liquid. It is removed by hydrolysis with water; Mg benzoate is the catalyst. Phenol (ph) is stripped from the reaction medium by the offgas stream.

The rate of the homogeneous hydrolysis as a function of temperature, water concentration, phenyl benzoate concentration, and magnesium content was measured in a separate pressure assembly. At a sufficiently high water:phenyl benzoate mole ratio the reaction is zero-order with respect to water and first order with respect to phenyl benzoate. When the magnesium concentration exceeds a given minimum, its influence on the hydrolysis is nil. Since the equilibrium of the reaction phenyl benzoate + H₂O $k_2 \rightleftharpoons k_3$ phenol + benzoic acid lies far enough to the right ($k_2 \gg k_3$), at the phenyl benzoate and water concentrations used under plant conditions the forward reaction ($k_2 C_{phb}$) will predominate. The rate of hydrolysis was derived from data assembled from laboratory and plant measurements (*see* Figure 3):

$$r_{ph} = k_2 \cdot C_{phb} \quad (9)$$

$$\text{where } k_2 = k_{2_0} \times e^{-E/RT} \quad (10)$$

E (activation energy) = 80 kJ/mole.

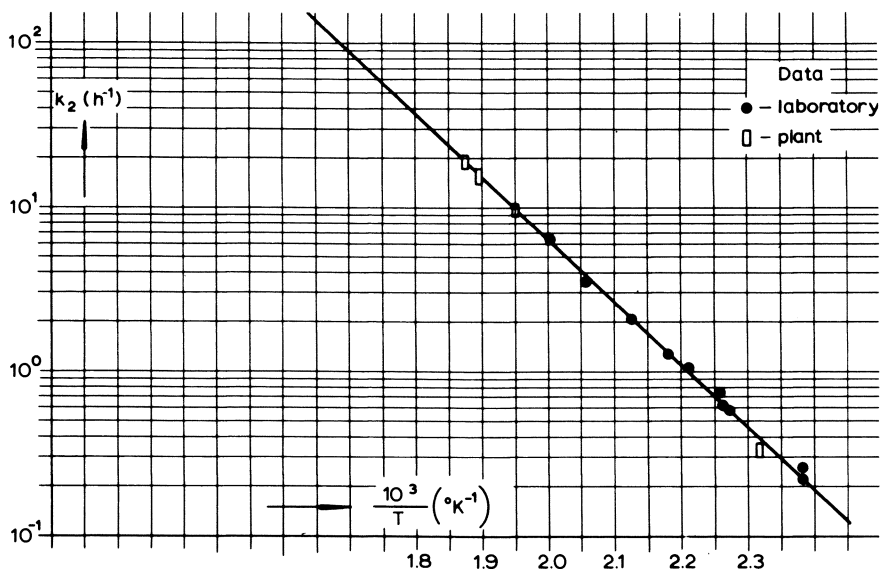


Figure 3. Reaction rate constant for the hydrolysis of phenyl benzoate as a function of temperature

BENZENE FORMATION. Oxidative decarboxylation of benzoic acid to phenol also yields benzene, under the action of the copper component in the catalyst system. The amount of benzene formed can be easily measured in laboratory experiments. The results are described by the zero-order reaction rate equation:

$$r_{\text{benzene}} = k_7 = k_{7_0} \times e^{-E/RT} \quad (11)$$

where $E = 147$ kJ/mole, which implies that the rate of formation is independent of the copper concentration.

FORMATION OF TAR 1. As shown in the reaction scheme (Figure 2), phenol formation is attended by a side reaction in which tar is formed. In bench-scale experiments (9) the phenol concentration can be kept extremely low (little formation of tar 2), with the result that the rate of tar 1 formation can be measured. The rate of tar 1 formation appears to depend on the benzoic acid consumption, the temperature, and the oxygen partial pressure. Test runs in the plant have proved the correctness of the above relations. In interpreting the experimental results, z in $(\text{C}_6\text{H}_4\text{O}_z)_n$ was taken equal to the average value of 0.8.

To calculate the production of tar 1, the following relation was used in the model:

$$\text{tar 1 production} = a_0 + a_1 \times \text{BZOH consumption} + a_2 \times T + a_3 \cdot \bar{p}_{\text{O}_2} \quad (12)$$

One mole of tar in the above relation means 1 mole of $\text{C}_6\text{H}_4\text{O}_{0.8}$ (aromatics) incorporated in the tar.

FORMATION OF TAR 2. The formation of tar in the consecutive reaction (tar 2) can be followed if the phenol concentration is increased by passing additional phenol through the reaction mixture. The kinetics of this reaction are represented by:

$$-\frac{dC_{ph}}{dt} = \frac{dC_{tar2}}{dt} = k_6 \times C_{ph} \quad (13)$$

The activation energy of the reaction amounts to approximately 77.5 kJ/mole.

RING DEGRADATION. Analysis of byproducts formed both in industrial installations and in the laboratory equipment (*i.e.*, carbon monoxide and diacetyl) clearly shows that aromatic rings are degraded. Since the various products could not be determined exactly, we assumed that the degradation goes as far as CO₂ and H₂O (*see* Equation 7). The data on ring degradation were obtained by separately quantifying the amounts of tar 1 and degradation products by oxygen and benzoic acid balances, starting from the test run values. As stated above, we used a fixed value for z (0.8) in these calculations. However, another value for z will yield a different distribution of the amounts of tar 1 and ring degradation products in the mass balance. The sensitivity of the reaction system to this change has not been satisfactorily established; however, the consequences for the total model seem to be of secondary importance.

The amount of degradation products has been correlated with the oxygen consumption and the temperature by the following equation:

$$\text{ring degradation} = a_0 + a_1 \times O_2 \text{ consumption} + a_2 \times T \quad (14)$$

Losses. As in most processes, losses occur, and here they have been taken into account in drawing up the balances. The principal losses occur in the following sections: (1) primary oxidation (losses assumed to be constant); (2) extraction; (3) distillation (phenol). On the basis of plant experience, all these losses were determined with a fair degree of accuracy and are expressed as a fixed percentage of the phenol production.

Balances. BENZOIC ACID BALANCE. Making allowance for the above mentioned reactions leading to benzoic acid consumption, as well as for the principal losses, we set up the following benzoic acid balance:

$$\text{BZOH consumption} = \text{phenol production} + \text{production of (tar 1 + tar 2)} + \text{benzene production} + \text{ring degradation} + \text{losses} \quad (15)$$

OXYGEN BALANCE. Summation of the amounts of oxygen consumed in the various reactions (including the amount lost with the phenol losses) yields the following oxygen balance:

$$\begin{aligned} \text{oxygen consumption} &= 0.5 \text{ phenol production} + 0.9 (\text{tar 1} + \text{tar 2}) \\ &+ 7.5 \text{ ring degradation} + 0.5 \text{ phenol distillation losses} \end{aligned} \quad (16)$$

It will be evident that the effect of ring degradation manifests itself particularly in this oxygen balance.

TOLUENE CONSUMPTION PER TON OF PHENOL. A practical quantity for expressing the total efficiency of the first and second oxidation steps is the toluene consumption per ton of phenol produced. This is, in fact, the reciprocal of the overall yield or the yield of the first oxidation step multiplied by that of the second. The former yield is measured; the latter is calculated from the model.

Physical Aspects of the Oxidation Reactor

The chemical aspects of the process as discussed in the previous section are now considered as they relate to the physical aspects of the reactor. Inside the reactor the contacting gas and liquid flows exchange oxygen, water, phenol,

and benzoic acid. These mass transfer processes depend partly on physical factors, partly on the chemical reaction rate. Coupling such physicochemical relations, including those for the solubility, the vapor pressure, and the residence time distributions of the gas and liquid phases, to the kinetic model yields a computer program whereby the situation in the plant reactors can be simulated.

Oxygen Absorption. An important transfer relation in the process is the absorption of oxygen in the oxidation medium. The oxygen is used mainly to oxidize cuprous to cupric benzoate and must be transferred from the gas to the liquid phase. This process can be described by:

$$r_{O_2} = K_{ov} S \Delta C \quad (17)$$

Information on this transfer process has been obtained from laboratory experiments in which the oxygen absorption was studied in a stirred reactor (1 liter volume). The results are given below:

$$(a) r_{O_2} = K_{ov} S p_{O_2, out}/R T \text{ He (at constant } V_s, T, \text{ and } V_{L,o}) \quad (18)$$

$$(b) r_{O_2} = a V_{L,o} \text{ (at constant } p_{O_2}, V_s, \text{ and } T), \quad (19)$$

where

$$V_{L,o} \left[= (N - N_o) \frac{d_n^2}{d_r} \right]$$

$$(c) K_{ov} = k_o C_{Cu^{+1/2}} e^{-E/RT} \text{ (at constant } S \text{ and } V_s) \quad (20)$$

From these data it can be concluded that: (1) the resistance to mass transfer is controlled by the liquid phase ($K_L^{-1} \gg K_g^{-1}$); (2) mass transfer is chemically enhanced because $K_{ov}(\cdot) C_{Cu^{+1/2}}$ and $E_{(K_{ov})} = 50.4$ kJ/mole. It appears therefore that the oxidation reaction is in fact a film reaction in which the bulk concentration is extremely low. For such a case the value of the mass transfer coefficient can be derived from the Hatta number, which is defined as:

$$Ha = K_{eff}/K_L = \frac{1}{K_L} \left(\frac{2}{n+1} k C_{O_2,i}^{n-1} C_{Cu^{+m}} D_{O_2} \right)^{1/2}, \text{ where } K_{ov} = K_{eff} \quad (21)$$

The chemical enhancement factor (ϕ) shows how much the mass transfer coefficient K_L is increased. It also gives the ratio between actual consumption and maximum physical mass transport:

$$\phi = \frac{r_{O_2, act}}{r_{O_2, phys. max.}} = \frac{r_{O_2, act}}{K_L S C_{O_2,i}} \quad (22)$$

If $Ha > 2$, then

$$Ha = \phi \text{ since } \frac{C_{Cu^{+}}}{C_{O_2,i}} \gg 10 \quad (23)$$

The absorption of oxygen then satisfies the equation:

$$r_{O_2} = \phi K_L S C_{O_2,i} = K_{eff} S p_{O_2,i}/R T \text{ He} \quad (24)$$

The effective mass transfer coefficient is proportional to the root of the copper concentration and independent of the oxygen concentration. This leads to the conclusion that in our case m and n in the Hatta number are equal to unity, so that

$$K_{eff} = (k_4 C_{Cu} + D_{O_2})^{1/2} \quad (25)$$

and

$$k_4 = k_{4o} e^{-E/RT}, \text{ where } E_{(k_4)} = 2 E_{(K_{ov})}$$

It follows, therefore, that the oxidation of cuprous benzoate mentioned above is first order with respect to copper and oxygen. Since the solubility of oxygen in benzoic acid is unknown, k_4 can be calculated only after the Henry coefficient (He) is estimated in similar system. However, in calculations regarding the plant reactor, it is enough to use the value of K_{eff}/He , and this can be derived experimentally.

To calculate the O_2 transfer in the plant reactor, both K_{eff} and the specific interfacial area S must be known. The size of S depends mainly on the superficial gas velocity V_s (no mechanical stirring). The relation between S and V_s is known from the literature (10, 11):

$$S = a_o V_s^\alpha \quad (26)$$

where $\alpha = 1$, if the gas holdup $\epsilon < 0.3$ and $\alpha \leq 1$ if $\epsilon > 0.3$.

Further, the temperature dependence of S over a limited range is small. The interdependence of oxygen absorption and reactor variables can therefore be derived from a mass balance taken over a very small part of the reactor volume, dV ($dV = FdH$), on the assumption that plug flow occurs in the gas phase:

$$\frac{\Phi_k}{RT} dp_{\text{O}_2} = -K_{\text{eff}} S \frac{p_{\text{O}_2}}{\text{He}RT} FdH \quad (27)$$

Further $\Phi_g/F = V_s$ and $H =$ height of the gas-liquid dispersion.

After integrating over the height H , it follows from Equations 26 and 27 that

$$\ln \frac{p_{\text{O}_2, \text{ in}}}{p_{\text{O}_2, \text{ out}}} = a_o \frac{K_{\text{eff}} V_s^{\alpha-1}}{\text{He}} H \quad (28)$$

We can assume that V_s remains approximately constant when the height is varied and that the gas holdup changes only slightly with variations in V_s if $V_s > 0.3$ m/sec. A good approximation of Equation 28, obtained by a regression analysis, reads:

$$\ln(1 - X) = (a_o + a_1 T + a_2 V_s) H_{\text{eff}} \quad (29)$$

where $X = 1 - (p_{\text{O}_2, \text{ out}})/(p_{\text{O}_2, \text{ in}})$ and $H_{\text{eff}} =$ the effective absorption height. The sum of the terms in brackets is negative in sign.

This relation enables the total oxygen consumption to be calculated within the entire range of operating conditions. It is also the basic equation needed to calculate the phenol production, which is one of the terms in the oxygen and benzoic acid balances.

Phenol Stripping. The required yield is one of the factors determining the phenyl benzoate and phenol concentrations to be maintained in the reaction liquid. In adjusting the phenol concentration, the rate of transfer from the liquid to the gas phase is important. In view of the consecutive reaction which leads from phenol to tar, the bulk concentration of phenol must be kept as low as possible.

The transfer process is described by:

$$r_{\text{ph}} = k_2 C_{\text{phb}} = K_L S (C_{\text{Lph}} - C_{\text{iph}}) \quad (30)$$

Under the conditions prevailing in our reactor, the transfer rate $K_L S$ is of the order one (sec^{-1}) (11, 12, 13). At the production rate of 0.3–1 kmole/m³ hr

reached in our bench-scale experiments, the driving force equals

$$\Delta C = C_i - C_L = (0.9 \longrightarrow 3) \times 10^{-4} \text{ kmole/m}^3$$

The difference between the concentrations in the bulk and at the interface is related to the bulk concentration by

$$\frac{\Delta C}{C_L} \approx \frac{10^{-4}}{10^{-1}} \approx 10^{-3}$$

which shows that the bulk concentration may be taken approximately equal to the concentration at the interface. This also holds under the conditions in the plant reactor. Hence, the bulk concentration is related to the partial pressure as:

$$p_{\text{ph}} = a C_{\text{ph}} \quad (31)$$

The magnitude of the proportionality constant for phenol-benzoic acid can be derived by Raoult's law, whose validity has also been demonstrated in bench-scale experiments.

Hence,

$$p_{\text{ph}} = y P_t \quad (32)$$

and

$$p_{\text{ph}} = x P_{\text{ph}} \quad (33)$$

where x , y denote the mole fractions of phenol in the liquid and gas phases, respectively, and P_{ph} is the vapor pressure of pure phenol.

Since part of the phenol dissolves in the condensing benzoic acid, it is recycled with the latter to the evaporators and subsequently resupplied to the reactor. Thus, the phenol partial pressure is increased by a given factor (recycle parameter), which adversely affects the yield. However, the consecutive reaction of phenol can be suppressed by leading inert gases through the reactor to lower the phenol partial pressure. Application of this principle enabled laboratory yields to be raised to *ca.* 90% (*see* Figure 4). Under plant conditions efficiency could also be improved in this way (passage of additional steam).

Water Solubility. As stated above, the rate of the phenyl benzoate hydrolysis is a function of the water concentration. Like the phenol concentration, the concentration of water in the liquid is defined by the direct relation between partial pressure and bulk concentration. Therefore:

$$C_{\text{H}_2\text{O}} = a x_{\text{H}_2\text{O}} = a p_{\text{H}_2\text{O}}/P_{\text{H}_2\text{O}} \quad (34)$$

$$p_{\text{H}_2\text{O}} = 1/a C_{\text{H}_2\text{O}} P_{\text{H}_2\text{O}} \text{ (Raoult's law)} \quad (35)$$

where $P_{\text{H}_2\text{O}}$ = vapor pressure of pure water.

Bench-scale experiments proved the validity of these relations. Thus, to achieve the required water concentration in the liquid, the partial pressure of the steam in the reactor must not be allowed to drop below a given minimum.

Benzoic Acid Evaporation. Compared with the other reactants, benzoic acid is always present in excess, even if the amount bound to copper and magnesium (in benzoate form) is disregarded. The excess benzoic acid partly comes from the first and partly from the recycle streams of the second oxidation step. Because of the smooth exchange between the gas and liquid phases, it takes little time for gas-liquid equilibrium to be established. The ultimate vapor pressure again conforms to Raoult's law provided the copper and magnesium salts, as well as the heavy tar products, are not regarded as volatile constituents.

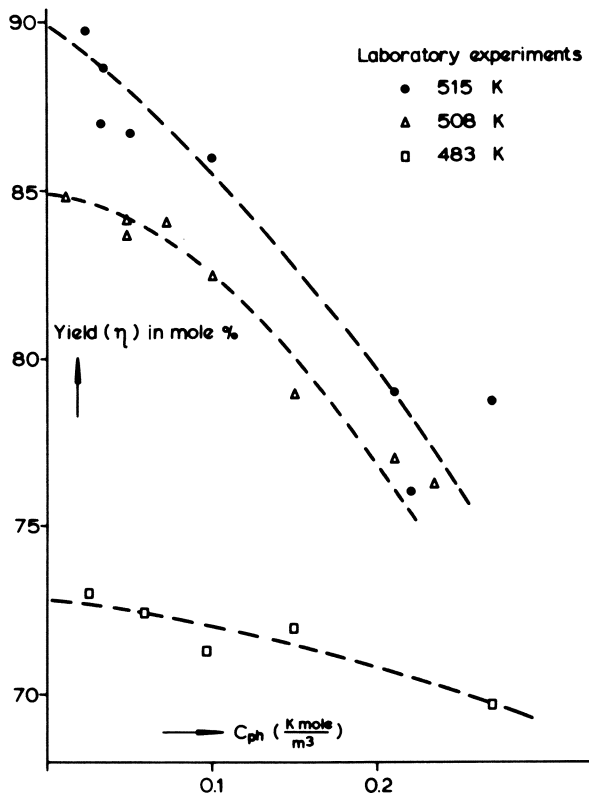


Figure 4. Chemical yield vs. phenol concentration

Hence

$$p_{BZO\dot{H}} = x P_{BZO\dot{H}} \quad (36)$$

where $P_{BZO\dot{H}}$ = vapor pressure of pure benzoic acid.

Gas Holdup. The passage of large quantities of benzoic acid vapor, air, and steam results in a high superficial gas velocity ($V = \Phi_{\text{gas tot.}}/F$), limited by the entrainment factors in the condensation column and the reactor. The superficial gas velocity (V_s) determines the magnitude of the gas holdup (ϵ), and thus the specific interfacial area and the effective reactor volume. According to the literature, ϵ and V_s are related as follows

$$\epsilon = 1.2 \left(\frac{\eta V_s}{\sigma} \right)^{1/4} \left(\frac{V_s}{4 \sqrt{\frac{\sigma g}{\rho_L}}} \right)^{1/2} \quad (37)$$

If we allow for the reaction conditions, this relation can be simplified to

$$\epsilon = a_0 V_s^{3/4} \quad \text{provided } \epsilon < 0.3 \quad (38)$$

The surface tension and viscosity of this system are difficult to determine under the reaction conditions, so the magnitude of the constant in Equation 38 was calculated from measurements in the plant reactor. From the value of the gas holdup thus found, the specific interfacial area S can be estimated

$$S = 6 \epsilon / d_b \quad (39)$$

Equation 38 can be substituted in Equation 39. Since $d_b \sim V_s^{-1/4}$ (10), $S \sim V_s^{1.0}$ (see Equations 26 and 27) provided that $\epsilon < 0.3$. The holdup relation is also used in the model to calculate the effective reactor volume (V_L):

$$V_L = (1 - \epsilon) V_r = (1 - \epsilon) F H \quad (40)$$

where H is the height of the gas-liquid dispersion.

Residence Time Distribution of the Gas and Liquid Phases. Besides knowledge of kinetics and mass transfer, information is needed about the degree to which production rate and yield are influenced by the residence time distribution of the gas and liquid phases. Some data on the mixing times can be found in the literature (11, 12, 14). The mixing time in the liquid phase (11) is given by

$$t_m = 4.7 H + 1 \quad \text{provided } V_s > 0.03 \text{ m/sec} \quad (41)$$

Applied to the liquid heights and gas velocities used in practice, Equation 41 yields a t_m value of 25-40 sec. Considering the mixing time in its relation to certain important reaction times in the model, the reaction time/mixing time ratio (t_r/t_m) is around 5-100. These values are large enough to allow calculations for a perfectly mixed liquid phase. The mixing pattern in the gas phase must be derived from data on backmixing the gas bubbles. This backmixing is accounted for by the Péclet number—*i.e.*, $Pe = (V_s H) / (\epsilon D_{mg}) = \text{transport by the gas flow} / \text{transport by axial mixing}$. As to the magnitude of the axial mixing coefficient in the gas phase in industrial reactors, little information is available. The assumption regarding plug flow in the gas phase, which forms the basis of Equation 29, is not refuted by the outcome of the test runs done at various liquid levels in the reactor. On the other hand, under these conditions the Péclet number would have to be larger than 3, which implies that the mixing coefficient derived from it for the system discussed will have to be of

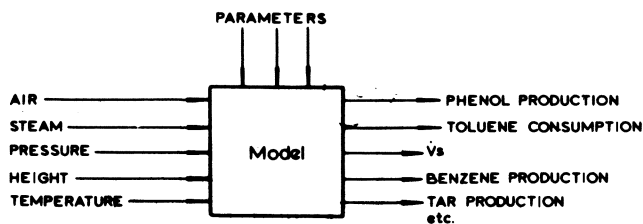


Figure 5. The model

the order of 3 m²/sec. Considering the observations by Towell and others (12) and the results of gas mixing experiments in fluid beds (15), this is a likely value.

Model and Results

General. The mathematical model comprises all the previous relations combined into a system of algebraic nonlinear equations (Figure 5). Beside the numerous dependent variables in the system, five independent variables, or

degrees of freedom, can be distinguished; they are all related to operationally controlled factors and are: reactor temperature, reactor pressure, height of the gas-liquid dispersion in the reactor, air load, and steam load. In addition to these, other parameters exist which, under certain conditions, may deviate and thus must be accounted for in the computer program—*e.g.*, the reactor diameter and the recycle characteristics.

The calculation procedure comprises two iteration loops, which do not present any convergence problems. Besides the essential model equations, the program also includes several derived equations which ensure comprehensive results (*e.g.*, partial pressures and superficial gas velocity). This brings the number of equations used in the model to approximately 50 (Fortran V; terminal Univac 1108; calculation time: a few msec).

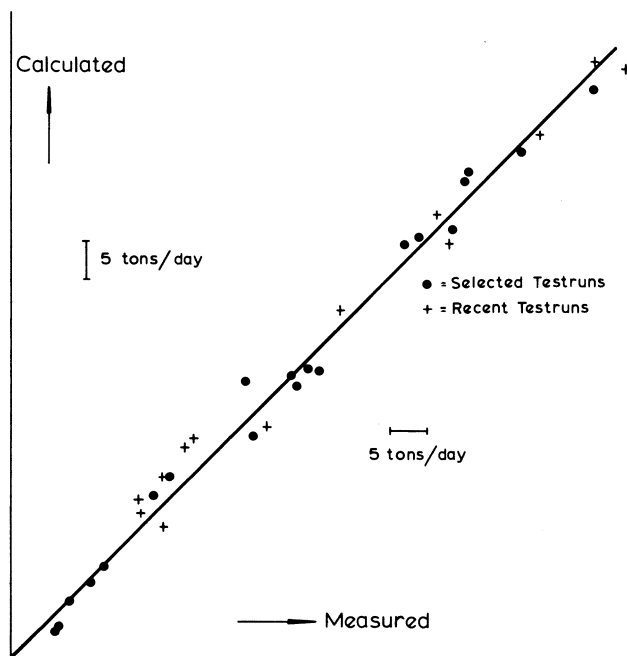


Figure 6. Phenol production in tons/day. Plant test runs performed under various conditions.

Reliability and Accuracy. In estimating the reliability of the model, two points should be taken into account: (a) the fundamental physical, technological, and chemical relations; (b) the incorporation in the model of a few regression equations based on some 20 plant measurements. Whereas point (a) affords certainty as to the reliability of the interpolations in most cases, the regression approach in (b) calls for some limitation of the range over which the extrapolations are carried out.

The two most essential quantities in the process and, hence, in the model are the phenol production (tons/day) and the consumption of toluene per ton of phenol produced (kg/ton). To illustrate the accuracy obtained in the model-building stage, we have plotted the measured *vs.* the calculated values of the two quantities. The data were obtained from 20 selected runs and are

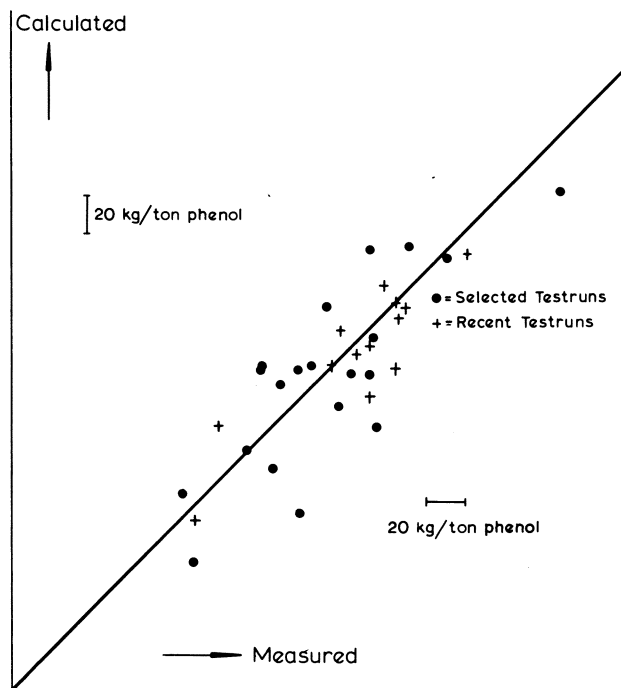


Figure 7. Toluene consumption in kg/ton phenol. Plant test runs performed under various conditions.

the same as those used in the model building. Beside the graphical representation in Figures 6 and 7, characteristic values are compiled in Table I. These indicate the accuracy of the model, both in an absolute sense and its relation

Table I. Absolute and Relative Accuracy of the Model Related to the 20 Test Runs

Description	Phenol Production, Tons/Day	Toluene Consumption per Ton Phenol, kg
Range of data actually occurring in the plant (Δm)	70	200
Mean error of prediction ($\bar{\epsilon}$)	0.1	-2
Standard deviation of error ϵ (σ_{ϵ}) (square root of variance)	2.5	30.7
Relative error of prediction $\left(\frac{\sigma_{\epsilon}}{\Delta m} \times 100\%\right)$	3.6%	15.4%

to the intervals between the maxima and minima in production and consumption. Recent test runs, done under more widely varied conditions, confirm the predictive quality of the model (see Figures 6 and 7; symbols +).

Results. Implemented with a cost function, the model can be used as a tool in economic optimization efforts where technological, marketing, or other constraints must be observed (efficiency optimization *vs.* production optimization).

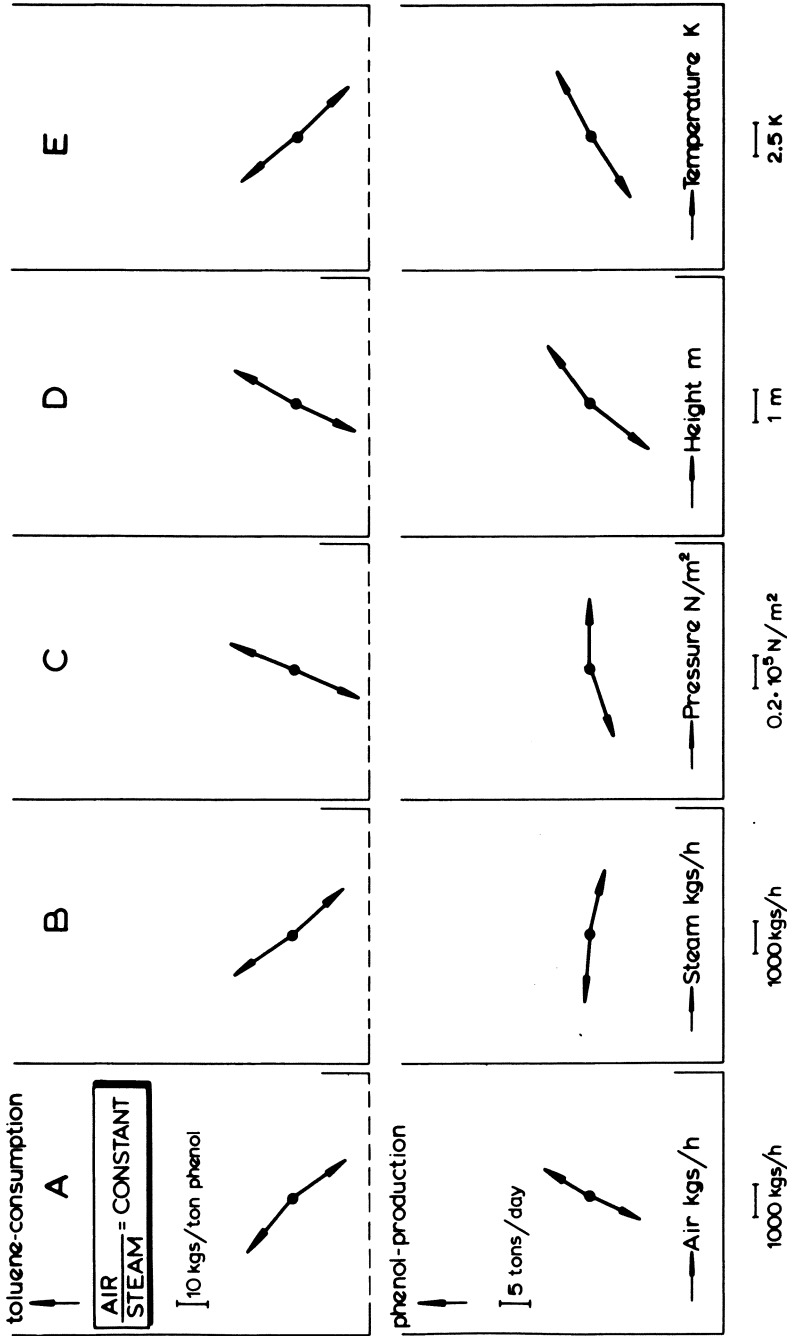


Figure 8. Sensitivity of the model

We examined the sensitivity of the model to changes in air or steam feed, pressure, liquid level, and temperature. An illustration of these sensitivities regarding phenol production and toluene consumption under a given operational condition is shown in Figure 8A-E. It is seen here that, *e.g.*, the consequences of a pressure rise can be largely offset by increasing the steam feed. The model has also been used to calculate process adjustments required by operational troubles (*e.g.*, one reactor out of service) or unpredictable circumstances (*e.g.*, toluene shortage).

Finally, the model has been very helpful in designing a reactor extension where the reactor diameter was used as the main parameter. However, in calculations involving a change in such an essential dimension of the process equipment, extrapolations cannot be carried too far. We obviated this hazard by fixing temperature-dependent maxima with regard to the specific oxygen consumption (kmole/m³ sec). These were derived from the maximum values measured in the current plant reactor.

Weighing the costs of this investigation against the profits, we see that cost of the research for developing the model is returned within one year. In summary, this intensive research work has made it possible for the phenol production per reactor to be increased to 300% of the 1964 design capacity, thereby enabling the original phenol process to hold its own against the competition from alternative technologies, next to other cost price decreasing means.

Nomenclature

$a_{0, 1, 2, \dots, n}$	general constant
C	concentration, kmole/m ³ sec
C_i	concentration at interface, kmole/m ³ sec
C_L	bulk concentration, kmole/m ³ sec
D	diffusion coefficient, m ² /sec
d_b	bubble diameter, m
D_{mg}	mixing coefficient in the gas phase, m ² /sec
d_r	reactor diameter, m
d_s	stirrer diameter, m
E	activation energy, kJ/mole
F	cross-sectional area of the reactor, m ²
g	acceleration of gravity, m/sec ²
H	height, m
Ha	Hatta-number = $\left(\frac{1}{n+1} \cdot k \cdot C_i^{n-1} \cdot C_{L,B} \cdot D \right)^{1/2}$
He	Henry coefficient = $p/R \cdot T \cdot C$
$H_{eff.}$	effective height of the gas-liquid dispersion, m
k	reaction rate constant, kmole ⁽¹⁻ⁿ⁾ /m ³⁽¹⁻ⁿ⁾ sec
$K_{eff.}$	effective mass transfer coefficient, m/sec
K_g	mass transfer coefficient in gas phase, m/sec
K_L	mass transfer coefficient in liquid phase, m/sec
K_{ov}	overall mass transfer coefficient, m/sec
m, n	reaction order
n	coefficient
N	revolution number, 1/sec
N_0	minimum revolution number required for bubble dispersion, 1/sec
p	partial pressure, kg/m ²
P	pressure of pure component, kg/m ²
P_t	total pressure, kg/m ²
Pe	Péclet number
r	reaction rate, kmole/m ³ sec

R	gas constant, kJ/ mole °K
S	specific interfacial area, m^2/m^3
t	time, sec
T	temperature, °K
t_m	mixing time, sec
t_r	reaction time, sec
V_L	volume of the liquid in the reactor, m^3
V_{L_0}	effective stirrer speed, m/sec
V_r	volume of the gas-liquid dispersion in the reactor, m^3
V_s	superficial gas velocity, m/sec
x	mole fraction in the liquid phase
y	mole fraction in the gas phase
z	oxygen content in the tar

Greek Letters

α	exponent
Δ	difference
ϵ	gas holdup
η	viscosity, $N = \text{Newton}$, Nsec/ m^2
ρ	density, kg/m^3
σ	surface tension, N/m
φ	chemical enhancement factor
Φ_g	gas flow rate, m^3/sec

Subscripts

B	component
b	bubble
disp	dispersion
eff	effective
g	gas
i	interface
in	inlet
L	liquid
out	outlet
s	stirrer
r	reactor
t	total

Literature Cited

1. Keading, W. W., Lindblom, R. O., Temple, R. G., *Ind. Eng. Chem.* (1961) **53**, 805.
2. Keading, W. W., *J. Org. Chem.* (1961) **26**, 3144.
3. Keading, W. W., *J. Org. Chem.* (1962) **27**, 3551.
4. Keading, W. W., *J. Org. Chem.* (1963) **28**, 1063.
5. Keading, W. W., *J. Org. Chem.* (1964) **29**, 2556.
6. Keading, W. W., *J. Org. Chem.* (1965) **30**, 3750.
7. Keading, W. W., *J. Org. Chem.* (1965) **30**, 3754.
8. Schoo, W., *et al.*, *Rec. Trav. Chem.* (1961) **80**, 134.
9. Schoo, W., *et al.*, *Rec. Trav. Chem.* (1963) **82**, 172, 954, 959.
10. van Dierendonck, L. L., Fortuin, J. M. H., Venderbos, D., *4th Europ. Symp. Chem. Reaction Eng.*, 1968.
11. van Dierendonck, L. L., Thesis Technical Highschool Twente, 1970.
12. Towell, G. D., Ackerman, G. H., *5th Europ. 2nd Intern. Symp. Chem. Reaction Eng.*, 1972.
13. van Dierendonck, L. L., *4th Chisa Congr.*, 1972.
14. Reith, T., Thesis Technical Highschool Delft, 1968.
15. Kunii, D., Levenspiel, O., "Fluidization Engineering," Wiley, New York, 1969.

RECEIVED January 2, 1974.

Temperature and Concentration Gradients In a Catalytic Packed Bed Reactor

N. G. KARANTH and R. HUGHES

Department of Chemical Engineering, University of Salford, England

Temperatures and concentrations were measured during the exothermic catalytic reaction between hydrogen and toluene in an experimental packed bed reactor. A nickel catalyst was used as cylindrical pellets 6 mm in diameter. Transient and steady-state measurements were made of both intraparticle and bed temperatures. The intraparticle temperature measurements showed that the assumption of an isothermal pellet was valid for most of the experimental range investigated but that large interphase temperature rises could occur. Attempts were made to model the system using standard procedures, but these predicted higher temperatures than were observed experimentally. Good agreement with the experimental results was obtained when the limiting non-key component effect was incorporated into the model.

Packed bed catalytic reactors are used extensively in the chemical and process industries, and prediction of their behavior has resulted in many modeling studies. Because of the complicated interaction between diffusion, heat transport, and chemical reaction, coupled with the system hydrodynamics, the models must be complex if realistic predictions are to be obtained.

It is also important to have experimental verification of theoretical models. Although studies on heterogeneous catalysis in packed bed reactors have been reported (1, 2, 3, 4), they have been few and have not generally kept up with theoretical developments. Therefore, there seemed to be a real need for experimental measurements of temperature and concentration in packed bed reactors. In the present work temperature measurements were made both within the catalyst particles and in the external field of the bed for the nickel-catalyzed hydrogenation of toluene; bed concentration profiles were also determined.

Models for a Packed Bed Reactor

The transient behavior of the packed bed reactor was modeled in two ways. In the first, pseudo-first order kinetics were assumed for the reaction, no account being taken of the low fractional order in toluene found experimentally (5). The second method used the limiting non-key component concept. This has been described in detail for single particles, and with certain simplifying assumptions it can be extended to packed beds.

The complete set of equations for a non-adiabatic reactor with pseudo-first-order kinetics can be written in dimensionless form as:

For the single particle

$$\nabla^2 C_p^* - \phi^2 C_p^* \exp \left[\gamma \left(1 - \frac{1}{T_p^*} \right) \right] = N_1 \frac{\partial C_p^*}{\partial t^*} \quad (1)$$

$$\nabla^2 T_p^* + \phi^2 \beta C_p^* \exp \left[\gamma \left(1 - \frac{1}{T_p^*} \right) \right] = N_2 \frac{\partial T_p^*}{\partial t^*} \quad (2)$$

where

$$N_1 = \frac{\epsilon_1 u d_p^2}{4 D_e L} \quad N_2 = \frac{\rho_s c_s u d_p^2}{4 K_e L}$$

with the boundary conditions

$$\begin{aligned} \frac{\partial C_p^*}{\partial y} \Big|_{y=0} &= \frac{\partial T_p^*}{\partial y} \Big|_{y=0} = 0 \\ -\frac{\partial T_p^*}{\partial y} \Big|_{y=1} &= \text{Nu}^* \left[T_p^* \Big|_{y=1} - T^* \right] \\ -\frac{\partial C_p^*}{\partial y} \Big|_{y=1} &= \text{Sh}^* \left[C_p^* \Big|_{y=1} - C^* \right] \end{aligned}$$

and for the external field

$$\frac{1}{\text{Pe}_M} \frac{d_p}{L} \frac{\partial^2 C^*}{\partial x^2} - \frac{\partial C^*}{\partial x} - \alpha \left(C^* - C_p^* \Big|_{y=1} \right) = \frac{\partial C^*}{\partial t^*} \quad (3)$$

$$\frac{1}{\text{Pe}_H} \frac{d_p}{L} \frac{\partial^2 T^*}{\partial x^2} - \frac{\partial T^*}{\partial x} - \alpha' \left(T^* - T_p^* \Big|_{y=1} \right) + W_F (T_w^* - T^*) = \frac{\partial T^*}{\partial t^*} \quad (4)$$

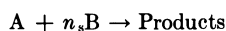
where

$$\alpha = \frac{a_v k_m L}{\epsilon_2 u} \quad \alpha' = \frac{a_v h L}{\epsilon_2 u \rho_g c_g} \quad W_F = \frac{2h_w L}{R_1 \epsilon_2 u \rho_g c_g}$$

with the boundary conditions

$$\begin{aligned} \frac{\partial C^*}{\partial x} \Big|_{x=1} &= \frac{\partial T^*}{\partial x} \Big|_{x=1} = 0 \\ x = 0, \quad -\frac{\partial C^*}{\partial x} &= \text{Pe}_M \frac{L}{d_p} \left(C^* \Big|_{x=0^-} - C^* \right) \\ -\frac{\partial T^*}{\partial x} &= \text{Pe}_H \frac{L}{d_p} \left(T^* \Big|_{x=0^-} - T^* \right) \end{aligned}$$

The limiting non-key component effect is described in detail elsewhere (6, 7); only the salient features are presented below. Consider the reaction



If component B is much less than the stoichiometric ratio and its diffusivity is also less than that for A, this limiting component would be expected to be exhausted before reaching the center of the catalyst pellet. Such a situation occurs in many hydrogenation reactions including the work described here. Using this concept, the dimensionless material and energy balances for a single

particle many be combined, utilizing the modified Prater relation which includes finite film effects (8) to give:

$$\frac{d^2 T_p^*}{dy^2} + \frac{2}{y} \frac{dT_p^*}{dy} = -\beta\phi^2 \exp \left[\gamma \left(1 - \frac{1}{T^*} \right) \right] \left\{ 1 + \frac{Nu^*}{\beta Sh^*} + \frac{T_s^*}{\beta} \left(1 - \frac{Nu^*}{Sh^*} \right) - \frac{T_p^*}{\beta} \right\} \quad (5)$$

with the boundary conditions

$$\left. \frac{dT_p^*}{dy} \right|_{y=\lambda} = 0 \quad \left. \frac{dT_p^*}{dy} \right|_{y=1} = Nu^*(1 - T_s^*) \quad (6)$$

Now, redefining a radial coordinate

$$\xi = \frac{y - \lambda}{1 - \lambda} \quad (7)$$

where λ is the radius of the unreacted core. Equations 5 and 6 are transformed as

$$\frac{1}{(1 - \lambda)^2} \frac{d^2 T_p^*}{d\xi^2} + \frac{2}{(\lambda + (1 - \lambda)\xi)} \frac{1}{(1 - \lambda)} \frac{dT_p^*}{d\xi} = -\beta\phi^2 \exp \left[\gamma \left(1 - \frac{1}{T^*} \right) \right] \left\{ 1 + \frac{Nu^*}{\beta Sh^*} + \frac{T_s^*}{\beta} \left(1 - \frac{Nu^*}{Sh^*} \right) - \frac{T_p^*}{\beta} \right\} \quad (8)$$

$$\left. \frac{dT_p^*}{d\xi} \right|_{\xi=0} = 0, \quad \left. \frac{dT_p^*}{d\xi} \right|_{\xi=1} = Nu^*(1 - \lambda)(1 - T_s^*) \quad (9)$$

The limiting non-key component effect is accounted for by the parameter ψ where

$$\psi = 1 - \frac{C_{B_0}}{C_{A_0}} \frac{1}{n_s} \frac{D_{eB}}{D_{eA}}$$

Thus, as C_{B_0} (the limiting component) increases, the value of ψ decreases and approaches zero as C_{B_0} approaches $C_{A_0} n_s D_{eA} / D_{eB}$. The temperature at the junction of the reactive outer shell and the inert inner core is then given by the dimensionless form of the modified Prater relation

$$\xi = 0, T^* = \left(\beta + \frac{Nu^*}{Sh^*} \right) + \left(1 - \frac{Nu^*}{Sh^*} \right) T_s^* - \beta\psi \quad (10)$$

The limiting non-key effect as described above applies only to single particles. Effectiveness factor values are reduced almost 20 times when $\psi = 0.81$. The most obvious way to take this factor into account is to apply a suitable correction factor in the reaction rate term in the mass and energy balance equations of the packed bed reactor. This factor is based on the limiting non-key component effect on the first particles at the entrance with an average reactor temperature and is equal to the factor of reduction of the effectiveness factor at this point. This uniform average correction factor is assumed to apply throughout the length of the bed. Both models were solved using the orthogonal collocation method as described by Villadsen and Stewart (9).

Experimental

Kinetics. Kinetic data were obtained in a small differential reactor using powdered catalyst material (coprecipitated nickel (55%) on silica), diluted

with an equal part of inert silica carrier. The results are reported in detail elsewhere (7); briefly they conformed to the following expressions

$$\text{Below } 170^{\circ}\text{C } R^* = 0.1815 e^{-13.9/RT} p_H p_T^{0.24}$$

$$\text{Above } 170^{\circ}\text{C } R^* = 6.49 \times 10^{-9} e^{1.28/RT} p_H p_T^{0.24}$$

Packed Bed Reactor. The reactor was a preheater section packed with stainless steel turnings and raschig rings mounted above a catalyst bed. The latter was 300 mm long, 41 mm diameter and was packed with 4.8 mm equant cylindrical silica-supported nickel catalyst pellets. Two instrumented pellets containing embedded thermocouples were positioned at dimensionless bed depths of 0.17 and 0.31 respectively. These pellets were as dense as normal ones but were slightly larger (6 mm \times 6 mm). Unfortunately, during reactor packing the small diameter thermocouple wires (0.025 mm) in the pellet at the lower position ($x = 0.31$) were broken so that intraparticle temperature measurements were available only for the upper position. A movable capillary sampling probe was situated on the axis of the reactor, and gas samples were analyzed using an MS10 mass spectrometer. Bed thermocouples were located

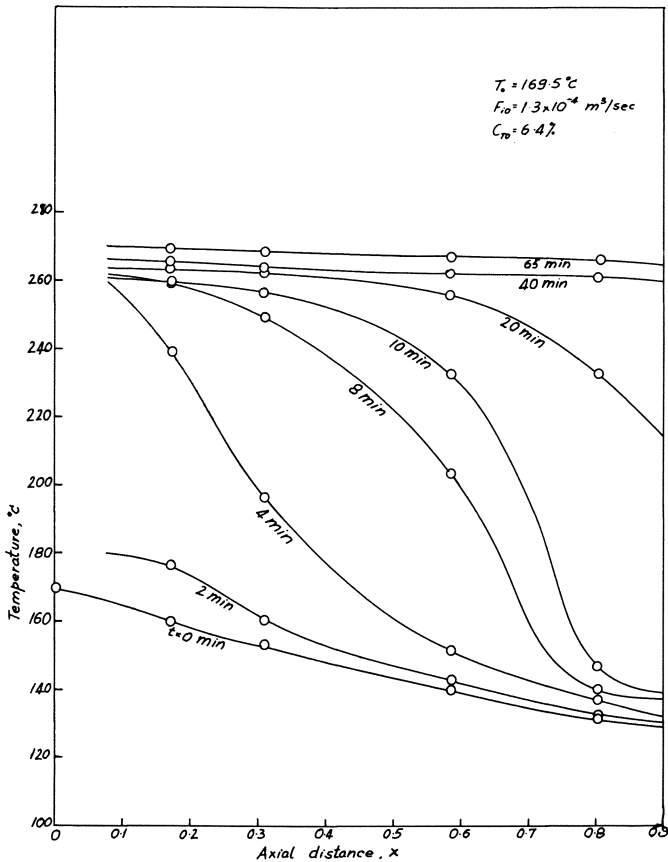


Figure 1. Transient axial bed temperature profiles. High reactivity—effect of toluene introduction.

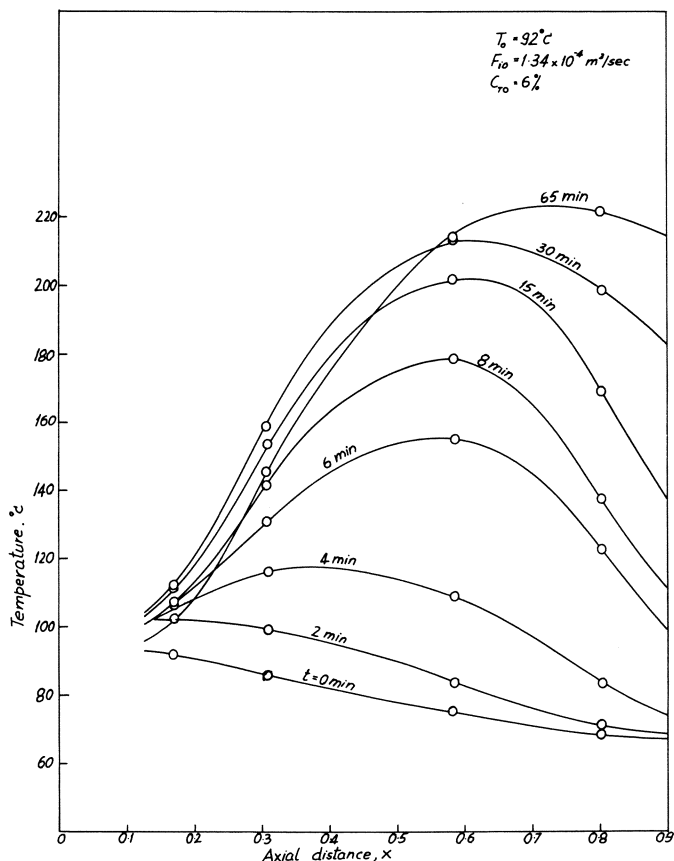


Figure 2. Transient axial bed temperature profiles. Lower reactivity—effect of toluene introduction.

at five positions close to the central axis including the entrance, and radial temperatures were measured at the two planes $x = 0.17$ and $x = 0.31$, with three thermocouples in each plane. The estimated maximum error of the chromel-alumel bed thermocouples was $\pm 1^\circ\text{C}$. That of the intraparticle thermocouples was also within this range since conduction losses were minimized by the use of 0.025-mm wire.

Originally the reactor was intended to be operated adiabatically so that heating was placed around the preheater only, the bed section having lagging only. Initial experiments showed that this ideal was not achieved, and small radial heat losses were occurring. This accounts for the gradual drop in axial temperature obtained in the bed under non-reactive conditions.

Results

Transient Bed Temperature Profiles. HIGH REACTIVITY, HIGH INLET TEMPERATURE. Figure 1 shows the transient temperature profiles in the axial direction in the external field when the vaporized toluene is introduced into

the entering hydrogen stream at a time $t = 0$ min. In the first two minutes the profile moved relatively slowly, but then the temperature buildup at all points in the reactor was swift. Initially ($t < 8$ min) the temperature at the reactor entrance (shown by the thermocouple at $x = 0.17$) attained a high value first, and the section further down the bed responded more slowly. However, at a later time ($t > 8$ min) the temperatures in the region closer to the exit responded much faster, and those in the entrance section climbed only

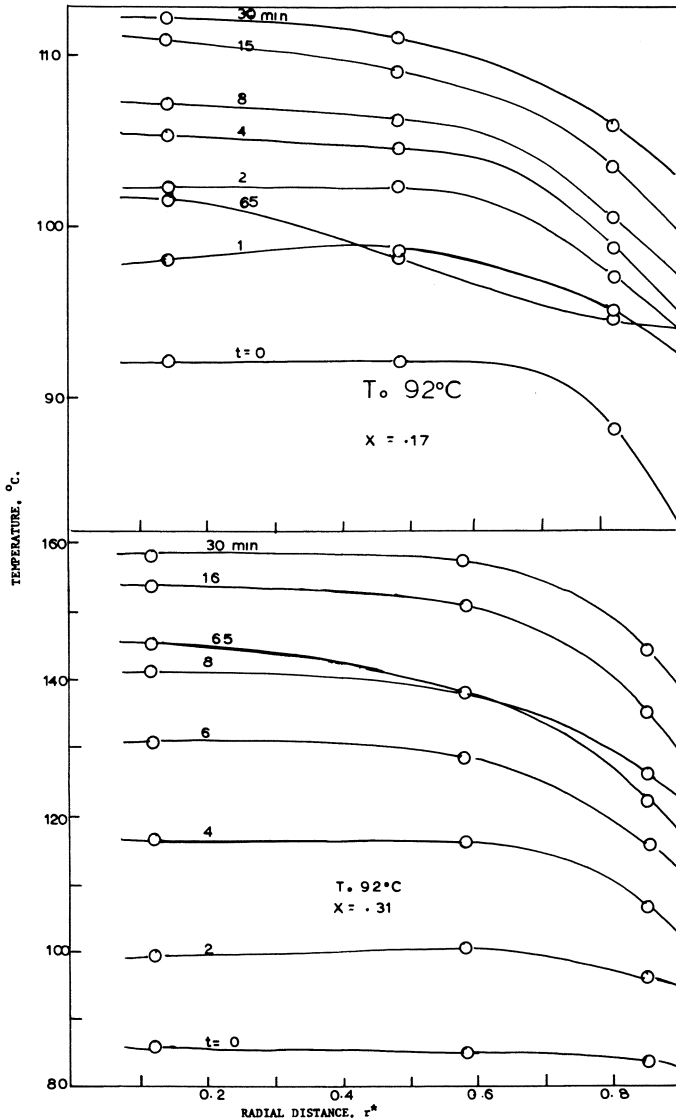


Figure 3. Transient radial bed temperature profiles at $x = 0.17$ and $x = 0.31$ (corresponding to axial profiles of Figure 2)

slowly. After 40 minutes the profile was virtually equal to the steady-state values, and the maximum temperature was stationary at the reactor entrance whereas the exit temperature slowly approached the entrance temperature level. At the steady state, the total temperature drop from entrance to exit was only about 5°C.

The radial temperature profiles corresponding to the axial profile of Figure 1 were determined at dimensionless bed depths of 0.17 and 0.31 at radial positions r^* of 0.12, 0.59, and 0.86. At steady state the central two thermocouples recorded identical temperatures while the junction at $r^* = 0.86$ was only 6°C lower, thus justifying the lumped wall heat transfer assumption.

LOW INLET TEMPERATURE. Figure 2 shows the transient response of the system when toluene is admitted, the entrance temperature now being lower than earlier (92°C). In this case the temperature maximum was developed at a point inside the reactor and moved towards the exit. Initially ($t \leq 2$ min) the temperatures started rising more slowly compared with the high entrance temperature case, the largest increases being registered in the entrance section. At $t = 2$ min, the temperature continuously decreased from the entrance to the exit. However, at $t = 4$ min, a temperature maximum had developed at about $x = 0.4$. This maximum moved gradually towards the reactor exit. The temperatures at all reactor positions increased continuously with time except for the final steady state) but with different speeds. In the initial period the rate of temperature rise at $x = 0.7$ was the highest. This zone of highest rate of increase gradually moves towards the exit with time. After $t = 30$ min, the temperatures in the entrance regions started declining slowly, probably because of the decrease in the inlet temperature. At the steady state the temperature profile increased steeply from entrance to exit.

The radial temperature transients corresponding to the above case (Figure 3) show that the temperature rise at $x = 0.17$ is quite small and occurs in the initial period whereas at $x = 0.31$ the temperature rise is larger and spread over a longer time interval. At both positions the character of the radial temperature profiles remained unchanged through the transients.

Intraparticle Temperature Measurements. The pellet in which 0.025 mm Pt-13% Rh-Pt thermocouples were embedded was positioned at the same axial distance as the first set of external thermocouples ($x = 0.17$). The cylindrical pellet was placed upright, and the center of the pellet was approximately 8 mm from the center of the bed. The thermocouples in the pellet were situated at dimensionless radial distances (r/R) of 0.25, 0.73, and 0.98. The last thermocouple was situated so close to the surface of the pellet that readings there can be regarded as surface temperatures.

For the high inlet temperature corresponding to the axial profiles of Figure 1 there was virtually no temperature gradient within the particle, all three thermocouples recording the same temperature. This was achieved rapidly (in about 8 minutes). The interphase gradient was appreciable however, reaching a peak of 41°C before decreasing slightly at the steady state.

The intraparticle temperature profiles at a lower entrance temperature of the reactor are shown in Figure 4. The toluene composition was the same as in the last case. In this case temperature gradients developed within the particle. Within one minute the temperature close to the center had risen by about 14.5°C and that close to the surface by about 11°C, establishing intraparticle gradients. This gradient increased slightly in the later stages, and the

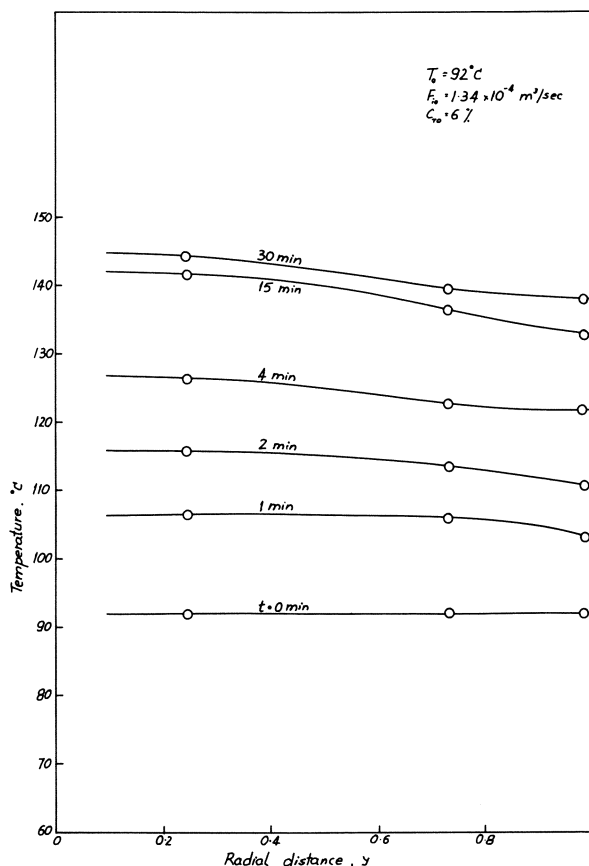


Figure 4. Transient intraparticle temperature profiles

final temperature difference between the center and the surface was about 9°C . The character of the profile changed little with time.

Interphase and Intraparticle Temperature Rises. The transient variations of the intraparticle and interphase temperature rises are plotted in the upper part of Figure 5 for the high reactivity case. There was a rapid interphase temperature rise in the beginning, which peaked and then slowly dropped. The intraparticle temperature rise, however, was slightly negative in the beginning but quickly (within 20 min) settled down to a negligible value, showing the isothermal nature of the particle. Figure 5 also shows the transient response when the feed is at a lower temperature level and toluene is introduced into the feed stream. Here again, the interphase temperature rise increased rapidly in the beginning, reached a maximum, and then slowly decreased. The intraparticle temperature rise on the other hand, rose more slowly and to a much lower maximum and then decreased slightly to settle at a lower level. On the whole, the steady-state temperature within the particle is attained much faster than the interphase steady state. The latter is more gradual but higher in magnitude.

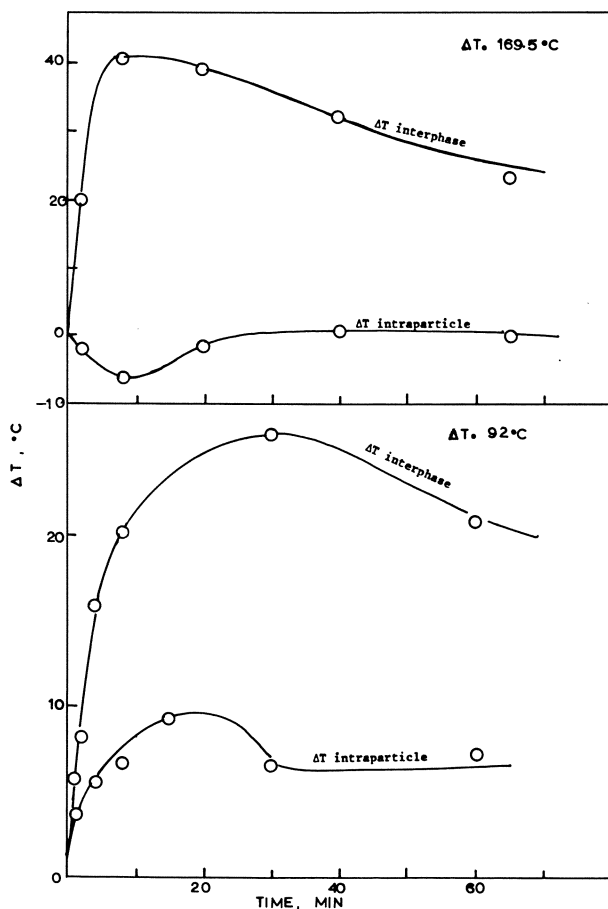


Figure 5. Interphase and intraparticle temperature rises corresponding to inlet temperatures of 169.5° and 92°C

Steady-State Concentration Profiles. Concentration profiles were measured by moving the tip of the capillary sampling probe along the axis of the reactor. For convenience, the concentrations were measured at every 25-mm length. Only steady-state profiles were measured because of the lengthy operation in moving the capillary to different axial positions.

Figure 6 shows the effect of a change in the toluene concentration of the feed from 6 to 10%. At 6% a large part of the reaction takes place in the early part of the bed and remains almost constant in the later sections. At the higher concentration, the reaction takes place at a greater distance from the entrance, indicating that the reaction zone has moved towards the exit. The conversion in the latter case is slightly more than in the first case.

Discussion

Figures 1 and 2 show the effect of bed reactivity on the axial temperature profiles. For the high inlet temperatures of Figure 1 the reaction was so fast

that the zone of highest temperature was located near the reactor entrance throughout the whole run. The temperature increases in the inlet region were very fast initially whereas those at the outlet responded more slowly. This is because of the finite time required to heat up the particles along the length of the bed so that for positions further down the bed a correspondingly larger time is required.

The expected hot spot in the reactor appeared when the entrance temperature of the feed was lowered to 92°C (Figure 2). The temperature rise was now faster in the entrance section and later in the section near the outlet.

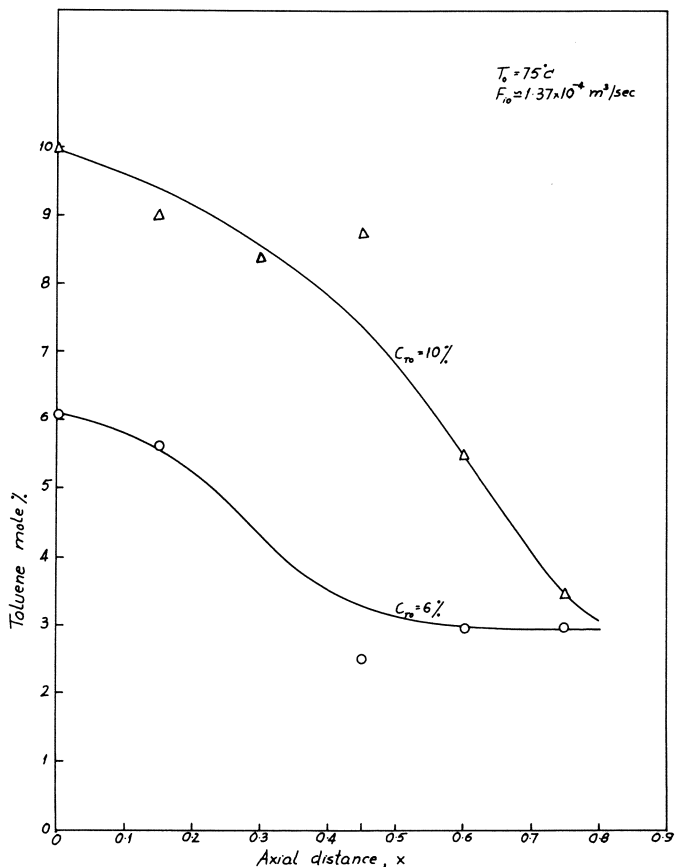


Figure 6. Steady-state axial concentration profiles. Effect of feed composition.

This similarity to the profile shape in an adiabatic reactor is the result of the small amount of wall heat transfer present. The radial temperature profiles confirm these effects.

For the high inlet temperature the particle temperature profiles were flat. Under these conditions the chemical reaction resistance is negligible; thus, the external transport resistances predominate, causing the pellet to be isothermal, even in the transient state. Intraparticle gradients appeared only at lower feed

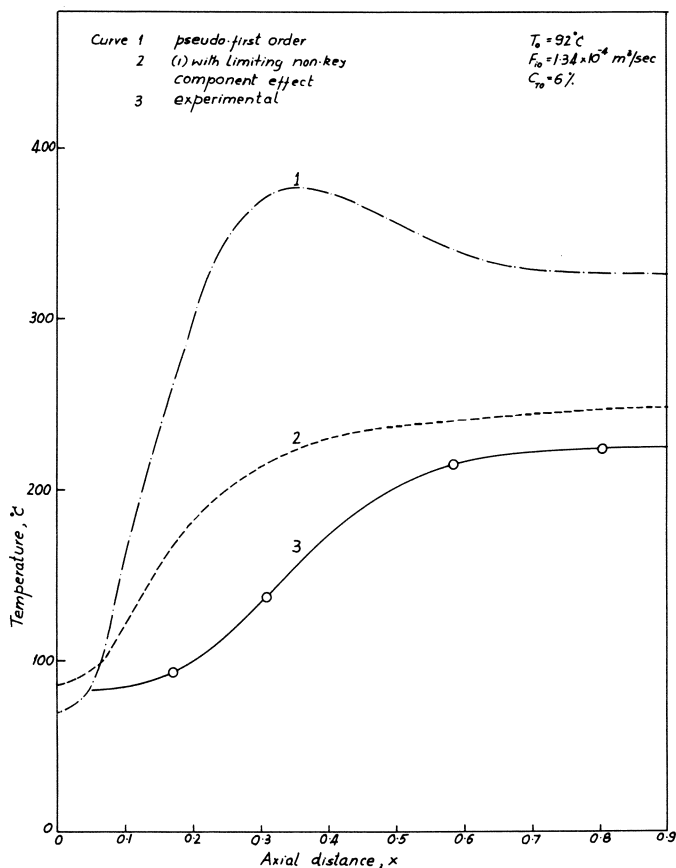


Figure 7. Comparison of theoretical and experimental axial bed temperature profiles at steady state

temperatures, but these were much smaller than the interphase gradients. Figure 5 shows that although the interphase temperature rise was greater than the intraparticle, the latter occurred more quickly. This is probably caused by the higher thermal conductivity of the particle.

Experimental vs. Simulated Results. Transient and steady-state temperature and concentration profiles were calculated for some experimental runs using the non-adiabatic model with pseudo-first-order kinetics and the approximate method based on the limiting non-key component concept. The parameters required for the theoretical model were determined experimentally where possible (pore volume, pore size distribution, effective thermal conductivity, etc.); otherwise they were estimated using standard formulas available in the literature. For the kinetic rate expression, a single activation energy and frequency factor could not be used because an inversion temperature existed for the reaction. Therefore two different sets of frequency factors and activation energies for the two temperature ranges ($T \leq 170^\circ\text{C}$ and $T > 170^\circ\text{C}$) were used.

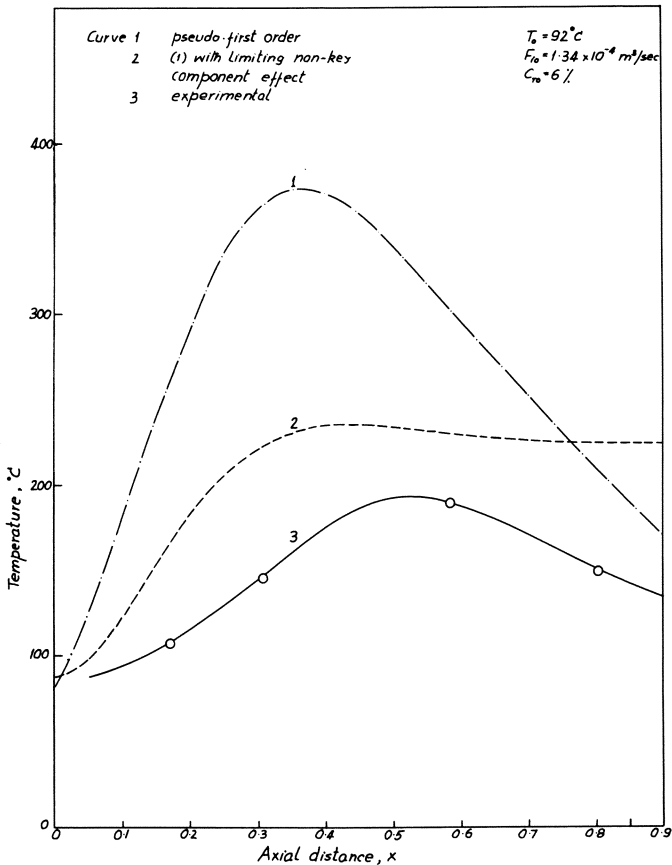


Figure 8. Comparison of theoretical and experimental axial bed temperature profiles at $t = 10 \text{ min}$

The computed steady-state axial temperature profiles, with and without the limiting non-key component effect, are compared with the experimental axial profiles for an inlet temperature of 92°C in Figure 7. The simulated profile based on the non-adiabatic model with pseudo-first-order kinetics gives a high temperature peak at $x = 0.3$, which is not obtained experimentally. This peak is also about 200°C higher than the experimental value at this point. The temperature profile based on a limiting non-key component gives much better agreement with the experimental values. A similar result is also found when the transient profiles are compared for the same initial conditions (Figure 8). Thus a closer approach to the measured profiles can be obtained using this model.

For the computations seven collocation points in the external field and three in the pellet (including the boundary points) were used. More collocation points would no doubt refine the calculations and possibly give less deviation between curves 2 and 3 in Figures 7 and 8. Nevertheless the marked disparity between the pseudo-first-order kinetic model and the experimental curve would

still exist. Closer agreement between the experimental and limiting non-key component model would probably be obtained if the latter effect was incorporated directly into the reactor equations instead of using the effect to modify the particle effectiveness factors as was done here.

Nomenclature

a_v	surface area of catalyst per unit volume of bed
c_g	average specific heat of gas
c_s	specific heat of solid
$C^*(C_p^*)$	dimensionless concentration in bulk fluid, C/C_o (particulate phase, C_{ps}/C_o)
d_p	diameter of catalyst particle
D_e	effective diffusivity of catalyst particle
h	heat transfer coefficient, bulk phase to particle surface
h_w	wall heat transfer coefficient
k_m	mass transfer coefficient
K_e	effective thermal conductivity of catalyst particle
L	reactor length
N_1, N_2	defined by Equation 2
Nu^*	modified Nusselt number, hR/K_e
p_H, p_T	partial pressure of hydrogen, toluene
$Pe_M(Pe_H)$	longitudinal Peclet number for mass (heat) dispersion
R^*	reaction rate
Sh^*	modified Sherwood number, $k_m R/D_e$
t^*	dimensionless time, tu/L
$T^*(T_p^*)$	dimensionless temperature in external field, T/T_o (particulate phase, T_p/T_o)
T_s	temperature at particle surface
u	interstitial gas velocity
x	dimensionless axial distance, z/L
y	dimensionless radius in particle, r/R

Greek Letters

α, α'	defined in Equation 4
β	thermicity factor, $(-\Delta H)D_e C_o/K_e T_o$
γ	activation energy parameter, $E/R_g T_o$
$\epsilon_1(\epsilon_2)$	void fraction of particle (bed)
$\rho_g(\rho_s)$	average gas (bulk-solid) density
ξ	modified radial coordinate in the pellet, $(y - \lambda)/(1 - \lambda)$
λ	radius of unreacted core

Subscripts

A, B	components A and B in binary mixture (specifically B = toluene)
o	conditions in the bulk fluid for single particle; conditions at entrance for packed bed reactor
p	particle
ps	particle surface
T	toluene

Literature Cited

1. Maymo, J. A., Smith, J. M., *AIChE J.* (1966) **12**, 845.
2. Hawthorn, R. D., Ackerman, G. H., Nixon, A. C., *AIChE J.* (1968) **14**, 69.

3. Richarz, V. W., Lattmann, M. A. S., *Symp. Chem. Reaction Eng., 4th, Brussels*, 1968.
4. Yamazaki, T., Noguchi, Y., Akazuka, T., Iwamura, T., Otani, S., *Kagaku Kogaku* (1970) **34**, 402.
5. Karanth, N. G., Koh, H-P., Hughes, R., *Chem. Eng. Sci.* (1974) **29**, 451.
6. Gioia, F., Greco, G., Gibilaro, L. G., *Chem. Eng. Sci.* (1970) **25**, 969.
7. Karanth, N. G., Ph.D. thesis, Salford University (1973).
8. McCreavy, C., Cresswell, D. L., *Can. J. Chem. Eng.* (1969) **49**, 583.
9. Villadsen, J. V., Stewart, J. M., *Chem. Eng. Sci.* (1967) **22**, 1483.

RECEIVED January 2, 1974.

Epitaxial Deposition of Silicon in a Barrel Reactor

FRANK W. DITTMAN

Department of Chemical and Biochemical Engineering, Rutgers University,
New Brunswick, N. J. 08903

Data from a rotating-barrel reactor for epitaxial deposition, on sapphire, of Si from SiH₄, and n-type arsenic dopant from AsH₃, both in H₂ carrier gas, are analyzed using transport equations for a similar but simpler apparatus. The mass transfer data for silicon are represented by: $j_D = 0.73 (LG/\mu)^{-1/2}$. This is close to previous data for cylinders and indicates that Si deposition is mass-transfer controlled. Apparent mass-transfer coefficients for As deposition are orders of magnitude below those for Si, indicating revaporization of As from the solid deposit. The apparent activity coefficient for n-type As dopant in epitaxial silicon is calculated as 1×10^{-5} .

All our chemical vapor deposition experiments were done in a vertical cylindrical quartz chamber.

Equipment and Process

The gas-tight chamber (ampoule) was about 6 inches id, 12 inches high (see Figure 1). The stationary ampoule with transparent water cooling jacket was supported on a water-cooled aluminum base plate. The ampoule was surrounded outside the water jacket by a helical induction coil of water-cooled copper tubing, connected to an rf power supply. A horizontal, circular aluminum support plate for graphite susceptors was supported by an aluminum rod projecting vertically up from the base plate. The plate, rod, and susceptor (or barrel) were concentric with the ampoule and were rotated by a variable-speed motor at 5 to 40 rpm.

The susceptor was heated inductively to 1000°C while rotating and supporting circular or oval sapphire wafers, 1 to 1.5 inches diameter, 0.010–0.025 inch thick, also at 1000°C. The position of a typical wafer on the susceptor is shown in Figure 1.

The reactants, SiH₄ and AsH₃, were conveyed at constant flow rate by H₂ gas into the reaction zone. Sapphire wafers to be coated epitaxially with Si and an n-type As dopant, were placed on the susceptor before each batch and removed afterward. One could not admit and remove wafers continuously be-

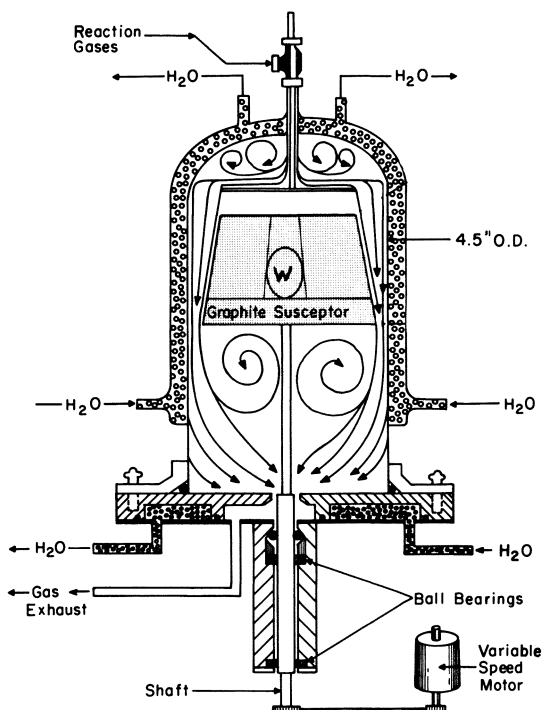


Figure 1. Barrel reactor, quartz ampoule, and auxiliaries ($W = \text{wafer}$)

cause of the system tightness required; no oxygen or water vapor could be tolerated inside the apparatus. Gas flow rates and compositions were continuous and constant during any one batch.

Channel Geometry. The channel formed by the susceptor and ampoule is a tapering annulus, with inside wall rotating at constant speed; this wall has several flat sides. An exact solution of momentum, heat, and mass transfer equations for this shape is difficult. Therefore laminar-flow solutions for flow channels of related shapes were used, as follows:

(a) Non-tapering annulus, with equivalent diameter $D_{eq} = D_2 - D_1$, and Reynolds number equal to $D_{eq}u_b\rho/\mu$ (dimensionless).

where $D_2 =$ inside diameter of ampoule
 $D_1 =$ outside diameter of susceptor
 $u_b =$ bulk average velocity of fluid
 $\rho =$ density of fluid
 $\mu =$ viscosity of fluid

(b) Single flat plate of length L , with parallel flow of fluid medium extending to infinite distance perpendicularly. This is applicable only in the entrance region; the Reynolds number for this case $= Lu_b\rho/\mu = LG/\mu$ where $G = u_b\rho =$ mass velocity of fluid.

(c) Two parallel flat plates of infinite width and finite length L . Reynolds number $= Lu_b\rho/\mu = LG/\mu$.

None of these is exact for the barrel reactor, but the approximation should be close. Figures 2 and 3 show flow cross sections and equivalent radii of the ampoule-susceptor combinations used here.

Control and Measurement. Gas flow was measured and controlled by Rotameters, valves, and tubing. Gas flow could be established at any steady-state flow rate using pure H_2 only; then, at a known time, using a quick-operating three-way valve, the reactant streams (pure H_2 , H_2 containing SiH_4 , and H_2 containing AsH_3) could be turned on or off and the stopwatch started or stopped simultaneously, without disturbing the established velocity and temperature pattern.

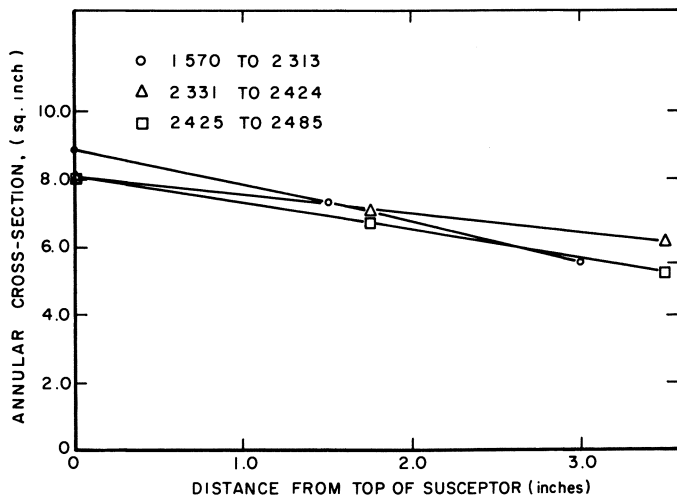


Figure 2. Barrel reactor, runs 1570-2485, cross sectional area for gas flow

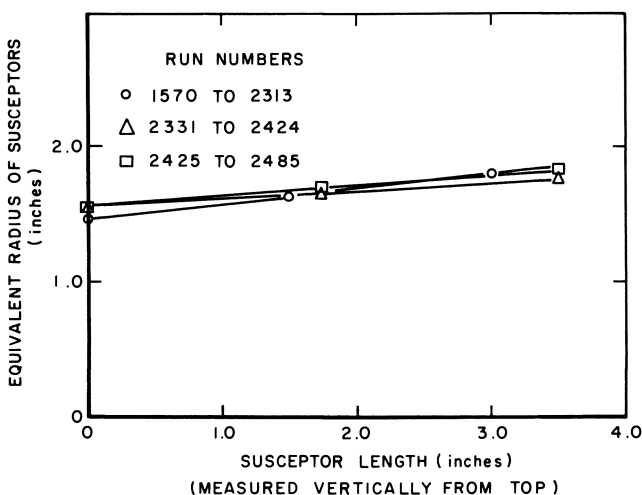


Figure 3. Barrel reactor, runs 1570-2485, equivalent radii of susceptors

Si thickness was measured by the Talysurf method and by interference fringes since both wafers and deposits are transparent. Arsenic concentration is measured by measuring point-probe resistivity and then using a correlation between resistivity and As concentration.

Operating Problems. The tubing, valves, and flowmeters, after assembly, were pressurized with H₂ to 25 psig and held overnight to check for leaks. Leaks were located with an electronic detector. A more sensitive method was the helium leak detector (mass spectrographic type). The ultimate test was poor quality in the deposited Si films; this was particularly helpful in finding leaks in connections to the quartz ampoule, which could not be pressure tested.

Safety Hazards. Hydrogen, silane, and arsine are highly reactive with oxygen; thorough preliminary purging of the system with nitrogen is essential. Spent process gas must be vented safely, preferably to an oxidizing process to convert the components to harmless forms. The acute local toxic hazard rating of silane for skin irritation, ingestion, or inhalation is *High*, according to N. I. Sax ("Dangerous Properties of Industrial Materials," 3rd ed., Reinhold). The acute local, acute systemic, and chronic systemic toxic hazard ratings for arsine by inhalation are all *High*. A rating of *High* means: "May cause death or permanent injury after very short exposure to small quantities."

Results

Thickness and Resistivity. Fractional standard deviations of thickness and resistivity of As-doped silicon epitaxial layers are listed for each set of conditions in Table I.

Table I. Data for As-Doped Silicon Epitaxial Layers

Total runs	43
Total gas flow rates, ml/min at 20°C, 1 atm	15,530 to 42,225
Deposited silicon film thickness, microns	0.8395 to 1.3428
Standard deviations of silicon film thickness, microns	0.0141 to 0.1530
Film resistivities, ohm-cm	0.069 to 235.0
Standard deviations of film resistivities, ohm-cm	0.0074 to 182.0

SiH₄ and AsH₃. Using data from the vaporization of naphthalene to air under steady laminar flow parallel to the axis of a cylinder, Christian and Kezios (1) obtained the following mass transfer solutions:

Local Coefficient:

$$\text{Local Sherwood number} = (\text{Sh})_x = \frac{k_p^\circ x}{D_{AB}} = 0.339 \left(\frac{xG}{\mu} \right)^{1/2} \left[\frac{\mu}{\rho D_{AB}} \right]^{1/3} \quad (1)$$

where k_p° = local mass transfer coefficient at any distance x downstream from leading edge of mass transfer surface, cc/cm², sec, or cm/sec (with bulk flow in direction of diffusion negligible)

x = distance; varies from 0 to L , cm.

D_{AB} = diffusivity of A in non-diffusing gas B, cm²/sec

G = mean mass velocity of gas, gm/sec, cm²

μ = gas viscosity, gm-cm/sec

ρ = mass density of gas mixture gm/cc

The mean mass transfer coefficient for their whole cylinder, and the corresponding Sherwood number, are given by Christian and Kezios as:

Overall Mean Mass Transfer Coefficient:

$$(\text{Sh})_m = \frac{k_p^\circ mL}{D_{AB}} = 0.678 \left(\frac{LG}{\mu} \right)^{1/2} \left[\frac{\mu}{\rho D_{AB}} \right]^{1/3} \quad (2)$$

This equation is obtained by integrating $k_p(b)(dx)/bL$ from 0 to L , where b is the width of the mass transfer surface and k_p° is obtained from Equation 1. Details are given in Reference 2, p. 476.

Let μ_A = the viscosity of pure silane and ρ_A = the density of pure silane. Now, in Equation 2, let $k_p^\circ = K_m p_{gt} M / \rho_A$. Then multiply both sides by $(\mu_A / \rho_A D_{AB})^{2/3}$ and divide both sides by LG . The result is the Chilton-Colburn (3) equation for mass transfer along a plane surface of length L .

$$\frac{K_m p_{gt} M}{G} \left(\frac{\mu}{\rho D_{AB}} \right)^{2/3} = 0.678 \left(\frac{LG}{\mu} \right)^{-1/2} = j_D \quad (3)$$

In Equation 3,

j_D = mass transfer or diffusion factor

= friction factor $\times 1/2$

K_m = mass transfer coefficient in gram-moles/cm², sec, atm

p_{gt} = mean partial pressure of inert gas, atm (= 1 atm in this work)

M = molecular weight of diffusing gas, gram/gram-mole

Subscripts may be removed within a given dimension group. Viscosities of Si and SiH₄ are assumed to be equal.

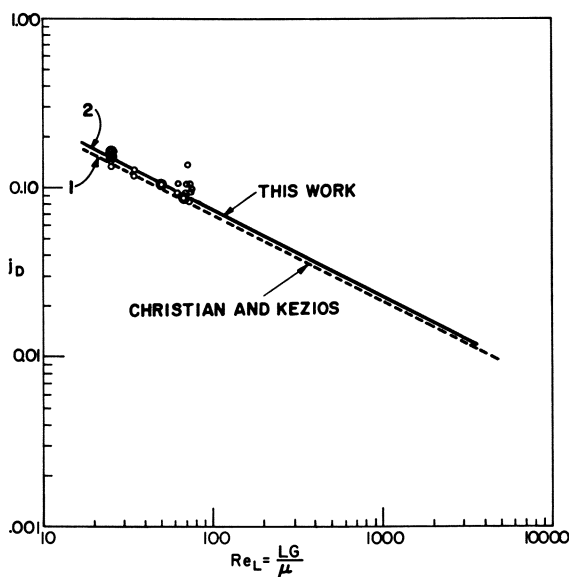


Figure 4. Correlation of overall mass transfer data for SOS process, barrel reactor, runs 1570-2485

From our silane mass transfer data, values of j_D are plotted vs. LG/μ in Figure 4. Our resulting equation is

$$j_D = 0.73 (LG/\mu)^{-1/2} \quad (4)$$

while the data of Christian and Kezios for the cylinder are represented by:

$$j_D = 0.678 (LG/\mu)^{-1/2} \quad (5)$$

Both of these equations are plotted in Figure 4.

Since our coefficient in the overall mass transfer equation is 0.73, we may assume that our local mass transfer coefficient is given by

$$\frac{K_x p_{gt} M}{G} (\mu/\rho D_{AB})^{2/3} = 0.365 (xG/\mu)^{-1/2} \quad (6)$$

Apparent mass transfer coefficients for the deposition of arsenic, calculated from known inlet concentrations of AsH_3 and the deposited As concentrations based on film resistivity, are many orders of magnitude smaller than expected. This is attributed to the high vapor pressure of As at 1000°C (see later text). Until we have sensitive methods for analyzing the outlet gas for As_4 and AsH_3 or until we have activity coefficients for As in the epitaxial layer, the proper inlet concentration of AsH_3 to achieve a desired resistivity must be based on experience. The activity coefficient of As in Si is estimated below.

Table II. Entrance Lengths in Barrel Reactor

Total Gas Flow Rate		Entrance Length	
cc/min	lb/hr, ft ²	K & E Method inches	Langhaar Method inches
42,200	9.17	13.3	3.32
15,600	3.69	4.19	1.31

Barrel Reactor. Calculations of momentum boundary layer thickness were originally made using a correlation presented by Schlichting (4) for flow between parallel plates. Calculations by that method showed that the momentum boundary layers expanded to fill the flow cross section within 0.1 to 0.2 inch downstream from the top of the susceptor (total length 3 to 3.5 inches). The Blasius solution (Ref. 2, p. 113) gave similar results. These results seemed incompatible with the experimental fact that the mass transfer coefficient in the barrel reactor is a function of overall susceptor length L . Prandtl and Schmidt numbers are close to unity, so that momentum, heat, and mass transfer entrance lengths should be similar. Therefore other sources supported by experimental data were sought.

Table III. Vapor Pressure vs. Temperature for Si and As (7)

Temp., °C	Equilibrium Vapor Pressures, mm Hg	
	$\text{Si}(s) \rightleftharpoons \text{Si}(v)$	$\text{As}(s) \rightleftharpoons \text{As}_4(v)$
200		8.5×10^{-5}
300		1.0×10^{-1}
400		3.1×10^0
500		5.4×10^1
600		6.2×10^2
700		4.0×10^3
800	1.0×10^{-8}	2.2×10^4
900	3.5×10^{-7}	1.0×10^5
1000	8.5×10^{-6}	4.1×10^5

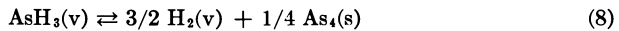
Two methods were found in the literature, one by Kreith and Eisenstadt (5) and the other by Langhaar (6). Results are in Table II. Thus, in the barrel reactor the entrance region probably extends the full length of the susceptor. This result is consistent with the work of Mickley *et al.* (summarized in Ref. 2, p. 539). When Prandtl and Schmidt numbers are close to unity

(as in this work), the velocity, temperature, and concentration profiles in laminar entrance regions cannot be very different from each other.

Chemical Kinetics

According to Nesmeyanov (7), solid silicon vaporizes as the monomer, Si, while solid arsenic vaporizes as As_4 . These facts agree with the formulas used in the reaction equilibrium constants (see Table III).

Reaction Equilibria. The reactions involved in the chemical vapor deposition work here are:



while the reactions for which reaction equilibrium constants are available are slightly different:



Values of K_p for the silane Reaction 9 (from Ref. 8) and for the arsine Reaction 10 (calculated from an equation furnished by Kirwan (8)) are compared in Table IV. A plot of K_p vs. temperature for SiH_4 - H_2 is shown in Figure 5.

Table IV. Reaction Equilibria for SiH_4 -Si and AsH_3 - As_4 Reactions

Temperature		$\log_{10} K_p$ where: $K_p = \frac{p_{\text{SiH}_4(\text{v})}}{p_{\text{Si}(\text{v})} [p_{\text{H}_2}]^2}$ (<i>p</i> in atm)	$\log_{10} K_p$ $K_p = \frac{p_{\text{AsH}_3(\text{v})}}{d_{\text{As}_4(\text{v})} [p_{\text{H}_2}]^{3/2}}$ (<i>p</i> in atm)
°C	°K		
20	293	-9.77	-27.53
100	373	-8.61	-22.24
300	573	-7.17	-15.50
500	773	-6.61	-12.28
700	973	-6.34	-10.39
900	1173	-6.13	- 9.12
1000	1273	-6.07	- 8.64

Since the gas phase in our experiments was over 99 vol % H_2 at 1 atm total pressure, it is evident that in the above equilibrium constants

$$[p_{\text{H}_2}]^2 \cong [p_{\text{H}_2}]^{3/2} \cong 1.00$$

Also, $p_{\text{Si}(\text{v})}$ and $p_{\text{As}_4(\text{v})}$ cannot exceed the corresponding vapor pressures of Si and As_4 ; excess Si and As_4 in the vapor phase would result in nucleation of the solids. This is much more likely to happen for Si than As because of their widely different vapor pressures and different concentrations.

Therefore, between 20° and 1000°C, the equilibrium concentrations of SiH_4 and AsH_3 are extremely small. Both compounds must be considered unstable or metastable over that temperature range, requiring only energies of activation to decompose quantitatively.

At 1000°C, 1 atm, for the system Si-SiH₄-H₂,

$$\log_{10} K_p = -6.07 = 3.93 - 10$$

$$K_p = 9.68 \times (10^{-7}) = \frac{(p_{\text{SiH}_4})_v^*}{(p_{\text{Si}})_v \times 1.00} \quad (11)$$

But

$$(p_{\text{Si}})_v \leq (p_{\text{Si}})_v^* = \text{equilibrium vapor pressure at } 1000^\circ\text{C} \\ = 8.50 \times 10^{-6} \text{ atm.}$$

Therefore, at equilibrium,

$$(p_{\text{SiH}_4})_v \leq 9.68 \times (10^{-7}) \times 8.50 \times (10^{-6}) = 80 \times 10^{-13} \text{ atm.}$$

Eversteijn (9, 10) observed gas-phase nucleation of Si from SiH₄ in H₂ at 1 atm only when $T > 1050^\circ\text{C}$ and $C_{\text{SiH}_4} \geq 0.12$ to 0.14 vol %. This was confirmed in our work; in fact, silicon smoke was created at that temperature purposely to permit the study of flow patterns in the barrel reactor. (We observed smooth laminar flow with an absence of turbulence or thermal convection.) Our Reynolds numbers (LG/μ) were 25 to 70.

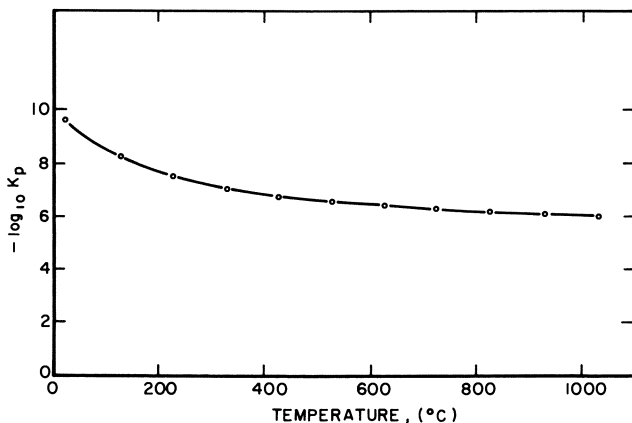


Figure 5. Equilibrium constant for reaction of silicon (g) and H₂ vs. temperature

Thus, even though SiH₄ is unstable or metastable from 20° to 1000°C and beyond, the required activation energy for gas-phase decomposition of SiH₄ is not furnished unless Eversteijn's above-mentioned threshold conditions are equaled or exceeded. It appears that below those conditions silane decomposes only at the hot surface, which serves as a catalyst. Vapor-phase nucleation of As₄(s) has not been observed in our work. At these very low concentrations the solid could be present but undetectable in the gas phase.

Overall Reaction Mechanism. Since the reaction



takes place and goes to completion at the hot surface only (*see above*), the

rate of reaction of component A (SiH_4 here) at the hot surface must equal the observed rate of mass transfer:

$$\begin{array}{ccccccc} \text{(Flow rates} & = & \text{Chemical} & = & \text{Mass transfer} & = & \text{Combination} \\ \text{(in minus out)} & & \text{reaction} & & \text{rate} & & \text{of chemical} \\ & & \text{rate} & & & & \text{mass-transfer} \\ & & & & & & \text{rates} \end{array} \quad (13)$$

$$(N_A)_{\text{obs}} = \frac{M}{S} (C_{A1} - C_{A2})_m = k'_{RA} (C_{AS})_m = + k_G (C_{Ab} - C_{AS})_m = k_{ov} [C_{Ab}]_m - 0 \quad (14)$$

where $(N_A)_{\text{obs}}$ = observed deposition rate of A—i.e., silicon.
= moles of A transported to hot surface and converted, per unit area and unit time.

M = total gas flow rate, moles/unit time

C_{A1} = inlet concentration of A in total gas flow

C_{A2} = outlet concentration of A in total gas flow

S = area of hot surface

k'_{RA} = surface reaction rate constant, moles/time, area, unit concentration

k'_{pA} = surface reaction rate constant based on partial pressures

C_{AS} = concentration of A, moles per unit volume, in gas layer adjacent to surface (A may be SiH_4 or AsH_3)

k_{GA} = gas-phase mass transfer coefficient of A, moles/time, area, unit concentration = $k^\circ \rho_m$ in Equation 2

$$C_{Abm} = \text{average bulk concentration} = \frac{C_{A1} + C_{A2}}{2}$$

Since $(C_{Ab})_m - 0 = (C_{Ab})_m - C_{As} + C_{As}$ (concentrations in mole fractions)

(or) $(p_{Ab}) - 0 = [(p_{Ab})_m - (p_{As})] + (p_{As})$ (partial pressures, atm)

or
$$\frac{(N_A)}{k_{ov}} = \frac{(N_A)}{k_G} + \frac{N_A}{k'_{RA}} \quad (15)$$

If $k'_{RA} \cong \infty$ at 1000°C vs. k_G , then $k_{ov} = k_G$.

Since our mass transfer data correlation is close to the results of others for similar processes, and since we assumed a partial pressure of $\text{SiH}_4 = 0$ at the hot surface, the following conclusions may be drawn:

(a) $k'_{RA} \cong \infty$ for decomposition of SiH_4 at 1000°C when catalyzed by a solid surface

(b) the vapor pressure of Si at 1000°C (see Table III) is too low for reevaporation to cause any appreciable loss. Therefore the overall Si deposition rate = $\bar{N}_A = k_{GA} C_{Abm}$.

For the reaction



the situation is somewhat different. There is an opposite process—viz., vaporization of solid As at the hot surface:



The net observed deposition rate of As (s), in gram-moles/hr, cm^2 or similar units is the difference between the rates of these two opposite mass transfer processes.

$$\bar{N}_A = k_{GA} [(C_{Ab})_m - C_{As}] - 4k_{GA}' [C_{As}' - (C_{Ab}')_m] \quad (19)$$

If the mass transfer coefficients for AsH_3 and As_4 in H_2 gas are the same (both equal to k_A), the net deposition rate of As is

$$\bar{N}_A = k_A \{[(C_{Ab})_m - C_{As}] - 4[C_{As'} - (C_{Ab'})_m]\} \quad (20)$$

where C_{As} is that concentration of AsH_3 in the vapor phase at the surface in chemical equilibrium with the actual partial pressure of As_4 (component A'). Let (C/p) be the unit conversion term from atmospheres to mole fraction. $C/p = 1.00$ when total pressure = 1 atm. Therefore, for arsenic

$$\bar{N}_A = k_A \{[p_{Ab})_m - p_{As}] - 4[p_{As'} - (p_{Ab'})_m]\} \quad (21)$$

P'_{As} is not the vapor pressure of pure arsenic at the hot surface; it is the partial pressure of $(\text{As})_4$ vapor over a solid phase consisting of Si plus a very small concentration of solid As. At the hot surface, the partial pressure of arsenic vapor must be

$$p_{As'} = \alpha_{A'} x_{A'} p_{A'}^* \quad (22)$$

where $\alpha_{A'}$ = activity coefficient of As in solid phase
 $x_{A'}$ = mole fraction of As in solid phase
 $p_{A'}^*$ = vapor pressure of pure arsenic at 1000°C.

Activity Coefficient of As. To estimate the activity of As in a tetrahedral lattice of Si, the following assumptions were made:

(a) Mass transfer coefficients for SiH_4 , AsH_3 , and As (or As_4) vapor in hydrogen are all identical.

(b) AsH_3 diffusing toward hot surface decomposes almost completely to As_4 and H_2 (see previous equilibrium constant).

(c) As_4 vaporizes from the hot surface in accordance with its vapor pressure at 1000°C and its concentration in the solid.

Several data are known accurately: (i) total inlet gas rate, (ii) concentration of AsH_3 in inlet gas, (iii) concentration of As in solid Si, (iv) vapor pressure of pure As at 1000°C.

Based on (b), (c), (i), (ii), and (iii), we can calculate the mean partial pressure of As_4 in the outlet gas. We can then calculate $(P_{As_4})_s$, the partial pressure of As_4 vapor at the hot surface, from the known values of mass transfer rate and mass transfer coefficient. Defining the activity coefficient as:

$$\gamma_{As_4} = \frac{(P_{As_4})_s}{(P_{As_4})_s^* X_{As}} \quad (23)$$

where $(P_{As_4})_s^*$ = vapor pressure of pure arsenic at 1000°C.
 $X_{As} = 0.539 \times 10^3$ atm.

X_{As} = mole fraction As in epitaxial silicon layer.

For a typical experimental run, $X_{As} = 0.929 \times 10^{-7}$, and $(P_{As_4})_s = 0.502 \times 10^{-9}$ atm. Therefore, $\gamma_{As_4} = 1 \times 10^{-5}$. This very low activity coefficient is additional evidence of the stability and bond strength of the epitaxial As-Si structure.

Acknowledgment

Data analyzed in this report were developed by Glenn W. Cullen and J. F. Corboy at David Sarnoff Laboratories, RCA, Princeton, N. J. 08540. The mathematical work was supported by RCA.

Literature Cited

1. Christian, W. J., Kezios, S. P., *AIChE J.* (1959) **5**, 61.
2. Bennett, C. O., Myers, J. E., "Momentum, Heat, and Mass Transfer," McGraw-Hill, New York, 1962.
3. Chilton, T. H., Colburn, A. P., *Ind. Eng. Chem.* (Nov. 1934) **26**, 1183.
4. Schlichting, H., "Boundary Layer Theory," 4th ed., McGraw-Hill, New York, 1960.
5. Kreith, F., Eisenstadt, R., *Trans. ASME* (1957) **79**, 1070; Perry's Chemical Engineering Handbook, 4th ed., pp. 5-31.
6. Langhaar, H. L., *J. Appl. Mech. (Trans. ASME)* (1942) **64**, A55-A58; Perry's Chemical Engineering Handbook, 4th ed., pp. 5-31.
7. Nesmeyanov, A. N., "Vapor Pressure of the Chemical Elements," Elsevier, New York, 1963.
8. Kirwan, D. J., *Solid State Sci.* (Dec. 1970) 1572.
9. Eversteijn, F. C. *et al.*, *J. Electrochem. Soc.* (1970) **117**, 925.
10. Eversteijn, F. C., *Philips Res. Repts.* (1971) **26**, 134-144.

RECEIVED January 2, 1974. Work sponsored by the David Sarnoff Laboratories, RCA, Princeton, N. J.

Influence of the Wall on the Dynamic Behavior of Homogeneous Tubular Reactors with a Highly Exothermic Reaction

GERHART EIGENBERGER¹

Institut fuer Systemdynamik und Regelungstechnik,
Universitaet Stuttgart, West Germany

The influence of the tube wall on the behavior of tubular reactors with a highly exothermic reaction was studied. The effect of heat accumulation in the wall has a considerable influence upon the transient behavior of the reactor. Because of this influence excess temperatures can occur if the feed temperature is lowered or the flow velocity is raised. For a gas phase reaction the transient behavior is determined almost completely by the heat capacity of the wall. An example of multiple steady states caused by axial heat conduction in the wall is given, and the influence of heat conduction in the wall is compared with that in the reaction mixture.

Homogeneous tubular reactors are usually described in terms of a plug flow or diffusion model. The temperature of the reactor wall is assumed constant with time of operation. However, only the coolant temperature can be held constant while the wall temperature will be between that of the coolant and the reaction mixture. Thus, the wall temperature is influenced by changes in the reaction temperature, and the wall temperature in turn influences the behavior of the reaction. This wall influence is studied below. A highly exothermic first-order reaction ($A \rightarrow$ products) is considered. The simple reaction mechanism does not restrict the general validity of the results since the important dynamic effects are the result of exothermic acceleration of the reaction.

Tubular Reactor with Liquid Phase Reaction

Homogeneous liquid phase reactions in tubular reactors are often described by the plug flow model, Equations 1–3:

$$\frac{\partial c}{\partial t} + v \frac{\partial c}{\partial z} = -r_{(c,T)} \quad (1)$$

$$\frac{\partial T}{\partial t} + v \frac{\partial T}{\partial z} = \frac{2\alpha_1}{r_1 \rho c_p} (T_w - T) + \frac{(-\Delta H_R)}{\rho c_p} r_{(c,T)} \quad (2)$$

$$\text{with } r_{(c,T)} = k_0 c e^{-E/RT} \quad (3)$$

¹ Present address: Department of Chemical Engineering, Northwestern University, Evanston, Ill. 60201.

Table I. Constants of the Liquid Phase Reaction

Reaction:	frequency factor, $k_o = 10^{13}$ liters/sec activation energy, $E = 22000$ kcal/kmole reaction enthalpy, $(-\Delta H_R) = 76000$ kcal/kmole feed concentration, $c_o = 1.2$ kmoles/m ³
Reactor:	length, $l = 10$ m inner tube radius, $r_1 = 0.01$ m outer tube radius, $r_2 = 0.02$ m flow velocity, $v = 0.4$ m/sec heat capacity: of reaction mixture, $\rho c_p = 1000$ kcal/m ³ grad of the reactor wall, $\rho_w c_w = 864$ kcal/m ³ grad heat transfer coefficient fluid-wall, $\alpha_1 = 2000$ kcal/m ² hr grad wall-coolant, $\alpha_2 = 1000$ kcal/m ² hr grad coolant temperature, $T_c = 50^\circ\text{C}$

To account for the wall influence, an energy balance for the wall must be added. Consider the radial mean temperature of the wall. If the axial heat conduction in the wall is neglected, the wall has only a cumulative effect, and its energy balance is:

$$\frac{\partial T_w}{\partial t} = \frac{2\alpha_1 r_1}{\rho_w c_w (r_2^2 - r_1^2)} (T - T_w) + \frac{2\alpha_2 r_2}{\rho_w c_w (r_2^2 - r_1^2)} (T_c - T_w) \quad (4)$$

with initial and boundary conditions:

$$\begin{aligned} c(o, z) &= c_o(z); T(o, z) = T_s(z); T_w(o, z) = T_{ws}(z) \\ c(t, o) &= c_o; T(t, o) = T_o \end{aligned} \quad (5)$$

The values of the constants in Equation 1-4 are given in Table I.

Figure 1 shows the transient of the system caused by a step increase in feed temperature (time t as parameter). The front of the disturbance moves with flow velocity v through the reactor. For a plug flow reactor without wall influence, temperature and concentration would jump from their old steady-state value to the new one, and the transient would be finished within one residence time. However, since the heat transfer to the wall is limited, establishment of the new steady state is delayed. Here the transient takes more than two residence times.

A step decrease of feed temperature shows an unexpected result. As shown in Figure 2, a decrease in feed temperature temporarily increases the maximum temperature. Similar behavior is observed if the flow velocity is suddenly increased (Figure 3). The reverse behavior occurs if the flow velocity is lowered (Figure 4). This phenomenon is caused by the heat capacity of the wall. If the temperature maximum is moved downstream by a sudden change of operating conditions, the wall will first retain its high temperature where the former maximum was located (*see e.g.*, Figure 3, $t = 5$ sec). To remove this surplus heat, heat fluxes from the wall to the reaction mixture. If the temperature maximum moves upstream, the wall at the front of the reactor must be heated. The required amount of heat will be taken from the reaction mixture so that the maximum temperature during this transient is lower than its steady-state value.

This phenomenon can be observed experimentally (1). The upper part of Figure 5 shows measured temperatures at different locations in a 10-m long tubular reactor. Temperature profiles at discrete times are shown in the lower section. The reaction is the homogeneous liquid phase oxidation of ethanol with the overall stoichiometry:

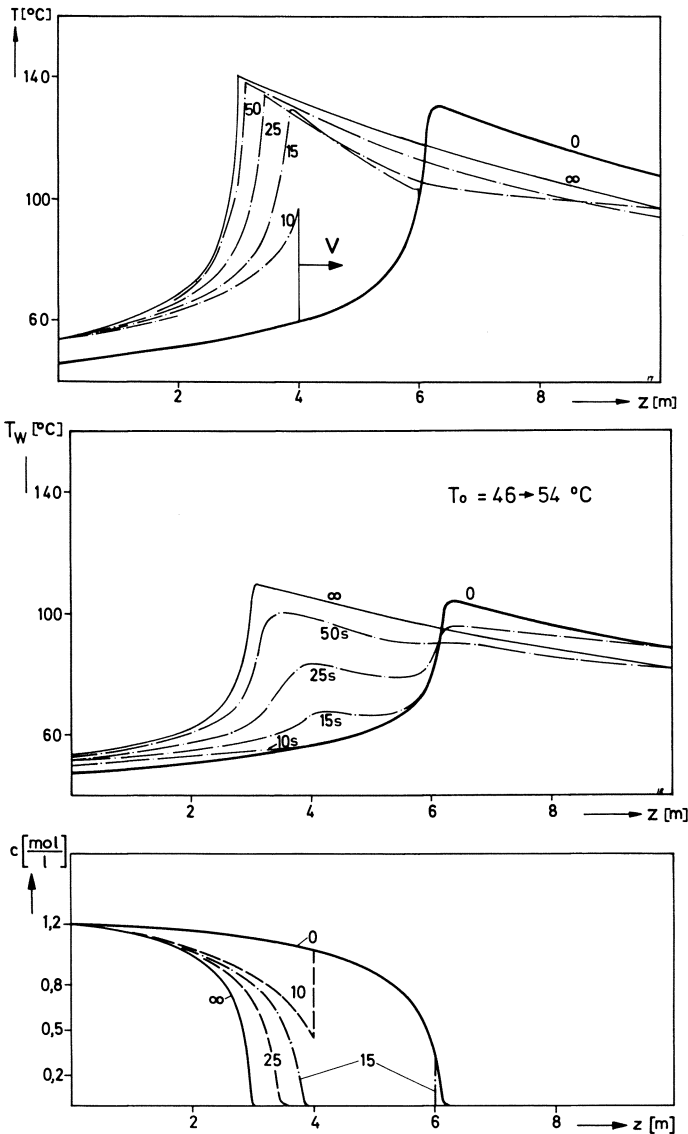


Figure 1. Transient profiles of the liquid phase reactor upon a step increase in feed temperature

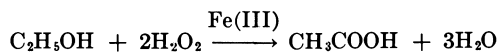


Figure 5 shows the transient temperatures measured when flow velocity was doubled (flow velocity was increased rampwise over 8 sec).

This effect has a counterpart in the behavior of creeping profiles in fixed bed reactors. Wicke *et al.* (2, 3, 4) showed that the maximum temperature of

a creeping profile lies beyond or below its steady-state value, depending on the direction of the creeping velocity. The maximum temperature varies for reasons similar to those above, and the fixed bed can provide an even higher heat capacity than the reactor wall.

So far the effect of axial heat conduction in the reactor wall has been neglected. This is permissible since the convective heat flow is much higher

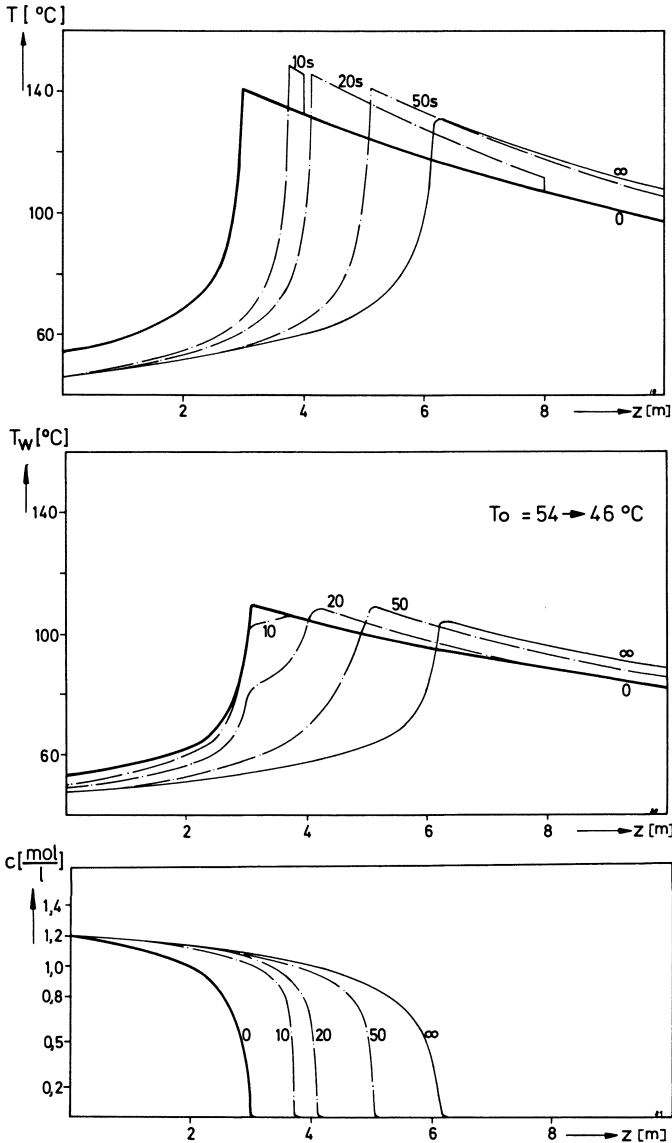


Figure 2. Transient profiles of the liquid phase reactor upon a step decrease in feed temperature

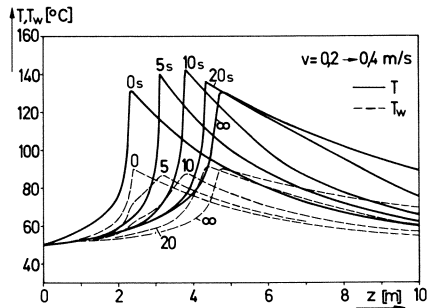


Figure 3. Transient profiles of the liquid phase reactor upon a step increase in the flow velocity

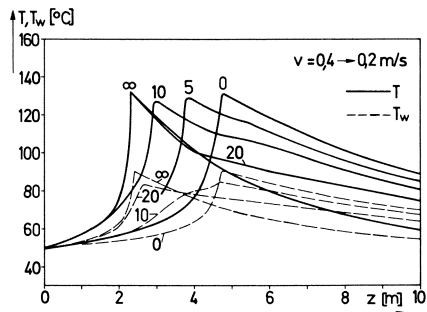


Figure 4. Transient profiles of the liquid phase reactor upon a step decrease in the flow velocity

than the heat conduction in the wall because of the high heat capacity of the liquid reaction mixture. For a gaseous reaction mixture this is not necessarily the case.

Tubular Reactor with Gas Phase Reaction

Because a gaseous reaction mixture is compressible, it is useful to consider a mass-dependent concentration measure. Using the weight fraction g instead of the molar concentration c , Equations 1-3 yield:

$$\frac{\partial g}{\partial t} + v \frac{\partial g}{\partial z} = -r^*(g, T) \quad (6)$$

$$\frac{\partial T}{\partial t} + v \frac{\partial T}{\partial z} = \frac{\alpha_1}{\rho c_p} \frac{2}{r_1} (T_w - T) + \frac{(-\Delta H_R)}{M_A c_p} r^*(g, T) \quad (7)$$

$$r^*(g, T) = k_\infty g_A e^{-E/RT} \quad (8)$$

Now the influence of axial heat conduction in the reactor wall will be included in the wall heat balance. Therefore Equation 4 must be extended by a heat conduction term.

$$\frac{\partial T_w}{\partial t} = \frac{2\alpha_1 r_1}{\rho_w c_w (r_2^2 - r_1^2)} (T - T_w) + \frac{2\alpha_2 r_2}{\rho_w c_w (r_2^2 - r_1^2)} (T_c - T_w) + \frac{\lambda_w}{\rho_w c_w} \frac{\partial^2 T_w}{\partial z^2} \tag{9}$$

with new boundary conditions:

$$g(0,t) = g_0; T(0,t) = T_0; \left. \frac{\partial T_w}{\partial z} \right|_{(0,t)} = \left. \frac{\partial T_w}{\partial z} \right|_{(L,t)} = 0 \tag{10}$$

If one assumes constant pressure over the length of the reactor, only the following continuity equation must be added to the above model:

$$\frac{\partial \rho}{\partial t} = - \frac{\partial(\rho v)}{\partial z} = \left\{ \rho \frac{\partial v}{\partial z} + v \frac{\partial \rho}{\partial z} \right\} \tag{11}$$

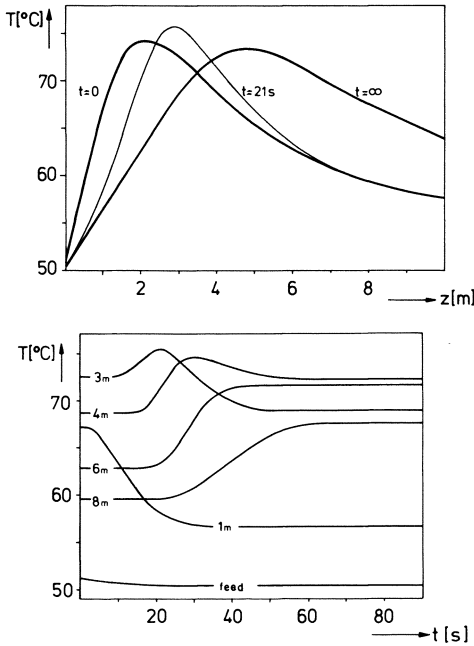


Figure 5. Measured transient temperatures of a laboratory reactor after doubling the flow velocity. Upper part: measured temperatures at different axial positions; lower part: transient profiles.

It is further assumed that the density rapidly establishes its quasi-steady-state value. With $\partial \rho / \partial t = 0$, Equation 11 can be integrated, leading to the criterion for constant mass flux:

$$\rho(z,t) v(z,t) = \rho_0 v_0 = \text{constant} \tag{12}$$

These assumptions are justified later.

If the reaction: $A \rightarrow nB$, takes place in a mixture of ideal gases, density can be derived by:

$$\rho(z,t) = \rho_o \frac{T_o}{T(z,t)} \frac{M_A}{M_o} \frac{1}{\left\{ g(z,t) + n(g_o - g(z,t)) + \frac{M_A}{M_o} - g_o \right\}} \quad (13)$$

ρ and v are now functions of $T(z,t)$ and $g(z,t)$, and the coefficients of the model equations are no longer constants. The behavior of the above model is discussed below. Values for the parameters are in Table II.

Table II. Constants for the Gas Phase Reaction

Reaction:	A \rightarrow n B frequency factor, $k_\infty = 1.6 \times 10^{14}$ 1/sec activation energy, $E = 55000$ kcal/kmole reaction enthalpy, $(-\Delta H_R) = 15,000$ kcal/kmole molecular weight of A, $M_A = 65$ kg/kmole decomposition No, $n = 2$
Reactor:	length, $l = 10$ m inner tube radius, $r_1 = 0.025$ m outer tube radius, $r_2 = 0.035$ m heat capacity: of the fluid, $c_p = 0.3$ kcal/kg grad of the wall, $\rho_w c_w = 864$ kcal/m ³ grad heat transfer coefficient: fluid-wall, $\alpha_1 = 75$ kcal/m ² hr grad wall-coolant, $\alpha_2 = 10$ kcal/m ² hr grad coolant temperature, $T_c = 100^\circ\text{C}$ axial heat conductivity: in the wall, $\lambda_w = 30$ kcal/m hr grad in the fluid, $\lambda = 0.05$ kcal/m hr grad
Feed:	weight fraction of A, $g_o = 0.5$ kg A/kg density, $\rho_o = 10$ kg/m ³ mean molecular weight, $M_o = 40$ kg/kmole flow velocity, $v_o = 2.0$ m/sec temperature, $T_o = 520^\circ\text{C}$

Figure 6 shows the steady-state profiles of the adiabatic reactor for the complete model (Equations 6–10, 12, 13) and for a reduced model ($\rho(z) = \rho_o$, $v(z) = v_o$, $\lambda_w = 0$). The differences are not large. Figures 7 and 8 show the dynamics of the reactor as feed temperature and flow velocity change. The effect of excess maximum temperatures, caused by feed temperature decrease or flow velocity increase, is even more pronounced than for a liquid reaction, and the transient lasts longer. It consists of two periods. During the first which takes one residence time the disturbance spreads over the whole reactor length. Because of the high heat capacity of the wall (*vs.* the reaction mixture) the wall temperature does not change. The second period lasts several orders of magnitude longer. It is determined by the change in wall temperature while all the other variables are in quasi-steady state. This fact justifies the assumptions of quasi-steady density and constant pressure. Schuchmann (5) showed that dynamic changes in density and pressure in a gas phase reactor usually fade within fractions of the residence time, so they can influence only the short, first period. However, under certain conditions self-excited pressure and density oscillations can occur, causing the reactor to behave as an acoustic generator (6). These effects are not covered in our model.

Influence of Axial Heat Conduction

Comparisons of the calculations with and without a heat conduction term show that the influence of axial heat conduction is not very significant in the above examples ($v \geq 1$ m/sec). However, axial heat conduction provides a

feedback mechanism which can cause instabilities and multiple steady states. This problem, first considered by van Heerden (7) has often been discussed, but the discussions have always been based on the diffusion model (without wall influence). Figure 9 shows that multiple steady states can also arise because of the back conduction of heat in the reactor wall. Note the temperature profiles of an upper and a lower stable steady state. The unstable state between the two stable states has not been calculated. Compared with the above examples the flow velocity in the area of multiple steady states was much smaller, and even with $v = 0.1$ m/sec the hysteresis in feed temperature between ignition and extinction was only a few tenths of a °C.

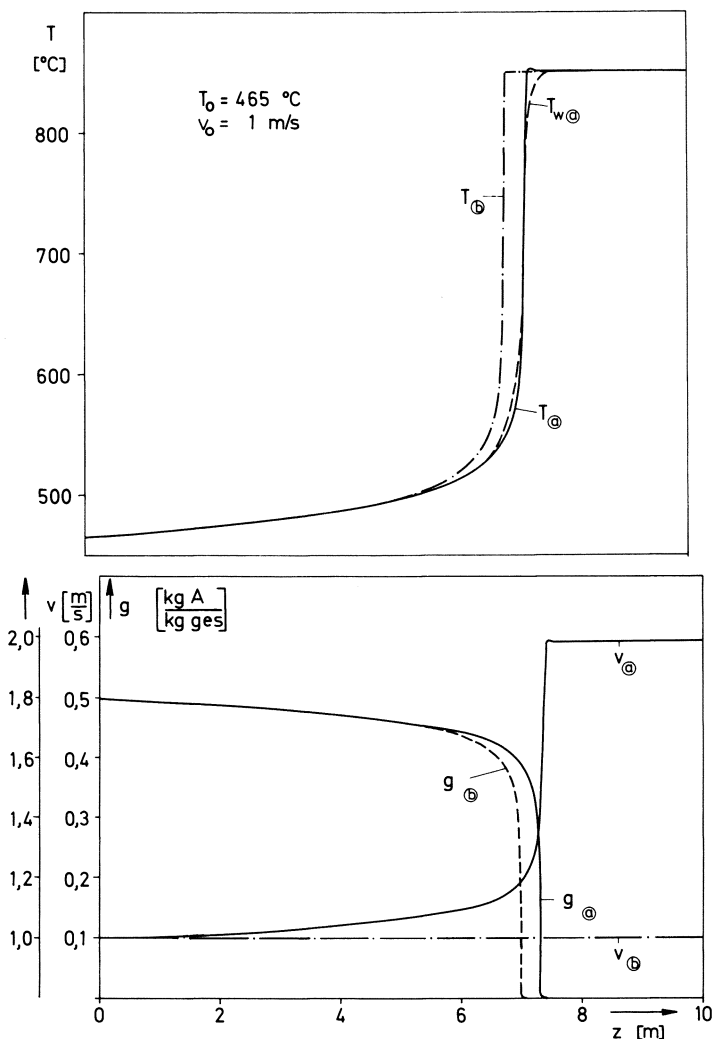


Figure 6. Steady-state profiles of the adiabatic gas phase reactor. (a) Complete model, (b) reduced model ($\rho(z) = \rho_0$, $v(z) = v_0$, $\lambda_w = 0$).

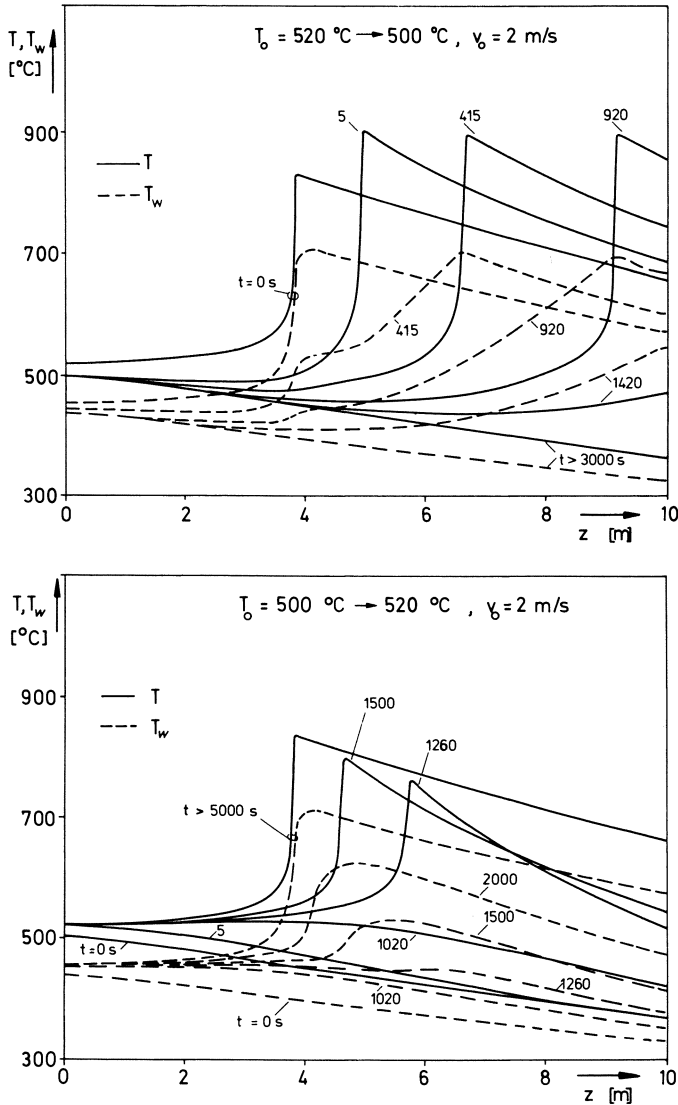


Figure 7. Transient profiles of the non-adiabatic gas phase reactor upon step changes in feed temperature

The distinct temperature peak in the ignited profile 2 is caused by the back conduction of heat into the main reaction zone. Thus, in addition to the heat of reaction released the fluid is heated by conductive heat backflow. In Figures 6 and 8 the peak is much smaller because of the larger influence of convective heat transport. (A similar temperature peak can also occur in calculating the diffusion model if $D_{\text{eff}} < \lambda_{\text{eff}}/\rho C_p$.)

To decide whether the influence of the back conduction of heat in reactor wall or mixture is the major cause of multiple steady states, the following estimate is given. Only an adiabatic reactor is considered. The backward

conducted heat Q in the lower steady state is decisive for the reaction ignition (and thus for the occurrence of multiple steady states). One portion of Q is the heat conducted back in the wall:

$$Q_w = (r_2^2 - r_1^2) \pi \lambda_w \frac{dT_w}{dz}$$

Since the wall is isolated adiabatically and the wall temperature in the front of the reactor is almost equal to the fluid temperature (Figure 9), all Q_w is transferred to the reaction mixture. The second portion of Q is the heat conducted back in the reaction mixture:

$$Q_R = r_1^2 \pi \lambda_{\text{eff}} \frac{dT}{dz}$$

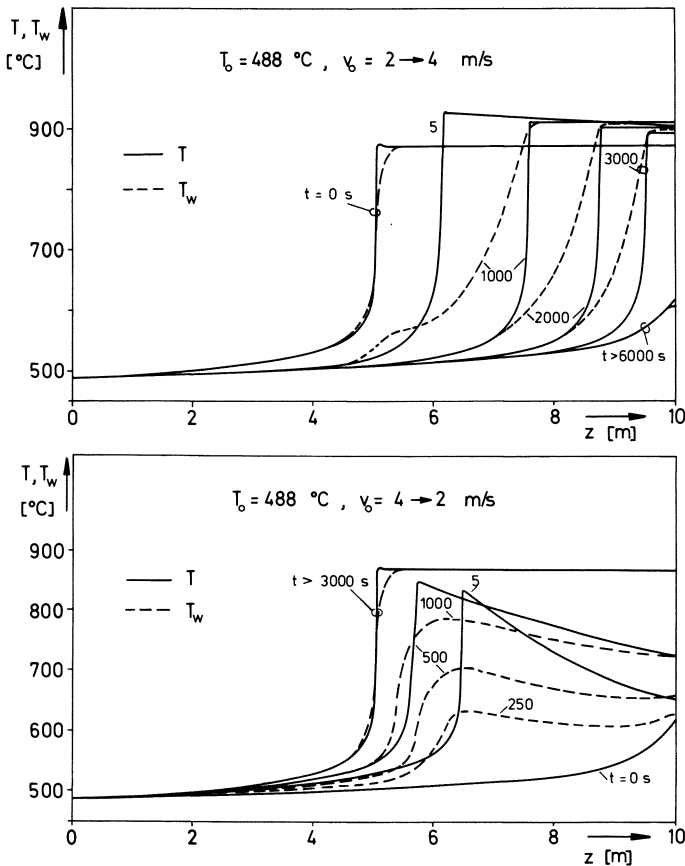


Figure 8. Transient profiles of adiabatic gas phase reactor upon step changes in flow velocity

Profile 1 in Figure 9 shows a steady state immediately before reaction ignition. T_w and T coincide almost over the whole length of the reactor. As an approximation assume $dT_w/dz \approx dT/dz$. Then only the ratio $Q_w/Q_R = (r_2^2 - r_1^2)\lambda_w/r_1^2\lambda_{\text{eff}}$ has to be considered to decide whether the influence of the wall heat conduction or the influence of the heat conduction in the reaction mixture is

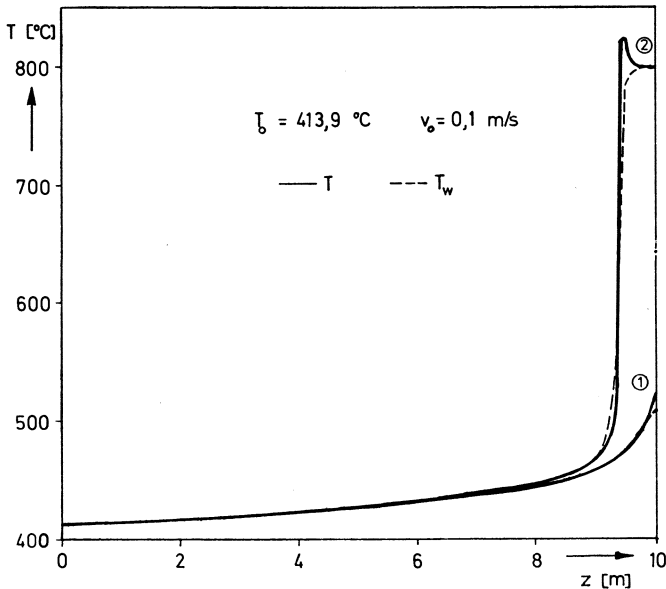


Figure 9. Temperature profiles of an upper and a lower stable steady state caused by heat conduction in the wall

dominant. First, however, the concept of effective heat conduction in empty tubular reactors must be discussed. The effective heat conduction is the sum of the molecular heat conduction and the contributions from Taylor diffusion and eddy diffusion. The molecular heat conduction provides a feedback mechanism in a temperature ascent, but it is usually very small compared with other contributions. However, neither the contributions from Taylor diffusion nor those from eddy diffusion are real feedbacks since they account only for the spread in residence time distribution caused by non-plug flow. (There is no continuous backstream of fluid particles but only a retardation in forward movement.) Therefore, the values for effective heat conduction and effective diffusion should be reduced to those molecular effects if the diffusional model is used with a highly exothermic reaction in an empty tubular reactor. Otherwise the model will predict too high a backflow of heat.

Therefore in the ratio of the conductive heat flow in wall and fluid, only the molecular heat conductivity λ is considered for the fluid. Using the values in Table II, the conductive heat flux in the wall exceeds the conductive heat flux in the fluid about 500 times. It can be assumed that in all cases where axial heat conduction can influence homogeneous tubular reactors, the amount of heat conduction in the wall may be significant.

Conclusions

Heat accumulation in the wall influences the dynamic behavior of a homogeneous tubular reactor with a highly exothermic reaction. The possibility of excess temperatures caused by decreased feed temperature or increased flow velocity can be important for operating and controlling such reactors. In case of an emergency shut off, a decrease of the feed temperature or an increase of the flow velocity to blow out the reaction should be avoided. An increase in the cooling rate and a decrease of feed concentrations seems to be advised instead.

A very large stepwise decrease in feed temperature or increase in flow velocity leads to an immediate extinction of the reaction (*e.g.*, in Figure 8 the flow velocity has to be raised above 15 m/sec). However, the danger of additional excess temperatures still exists since large changes in operating conditions usually cannot be realized stepwise.

The influence of axial heat conduction is small and is negligible in liquid phase reactions. In gas phase reactions backward heat conduction in the wall can lead to multiple steady states if the flow rate is very low. The amount of backward conducted heat in the wall can be considerably higher than the back-flow of heat from conduction in the reaction mixture.

Nomenclature

c	molar concentration of reacting component A
c_p	specific heat of reaction mixture
c_w	specific heat of reactor wall
g	mass fraction of reacting component A
k_0	frequency factor of liquid phase reaction
k_∞	frequency factor of gas phase reaction
l	reactor length
n	decomposition number ($A \rightarrow n B$)
r	reaction rate of liquid phase reaction, kmoles/m ³ /sec
r^*	reaction rate of gas phase reaction, l/sec
r_1	inner tube radius
r_2	outer tube radius
t	time coordinate
v	flow velocity
z	space coordinate
E	activation energy
M_A	molecular weight of component A
M_0	mean molecular weight of feed
R	gas constant
T	reaction temperature
T_w	wall temperature
T_c	coolant temperature
α_1	heat transfer coefficient fluid-wall
α_2	heat transfer coefficient coolant-wall
ΔH_R	reaction enthalpy
λ	axial heat conductivity in the fluid
λ_w	axial heat conductivity in the wall
ρ	density of reaction mixture
ρ_w	density of wall

Subscripts

s	steady state
o	reactor inlet

Literature Cited

1. Widmaier, H., unpublished data.
2. Wicke, E., Vortmeyer, D., *Ber. Bunsenges.* (1959) **63**, 145-52.
3. Padberg, G., Wicke, E., *Chem. Eng. Sci.* (1967) **22**, 1035-51.
4. Wicke, E., Padberg, G., Arens, H., *Proc. European Symp. Chem. Reaction Eng., 4th, Bruxelles, 1968*, 425-37.
5. Schuchmann, H., *Chem. Ing. Tech.* (1969) **47**, 868-77.
6. Gilles, E. D., *Chem. Eng. Sci.* (1967) **22**, 745-758.
7. van Heerden, C., *Chem. Eng. Sci.* (1958) **8**, 133-145.

RECEIVED January 2, 1974.

Dynamic Behavior of an Adiabatic Fixed-Bed Methanator

H. VAN DOESBURG and W. A. DE JONG

Laboratory of Chemical Technology, Delft University of Technology,
Julianalaan 136, Delft, The Netherlands

The hydrogenation of small amounts of CO and CO₂ to methane—a purification step in hydrogen synthesis—is used as the test reaction to study the transient behavior of an adiabatic fixed-bed reactor containing Ni/Al₂O₃ catalyst. The response of a 0.5-liter methanator to step changes in inlet conditions was measured in the parameter space: 0.6–2.5 vol % CO or CO₂ in hydrogen, 180°–250°C inlet temperature, and space velocity 5,000–32,000 hr⁻¹. A quasi-homogeneous plug flow model was selected to compare the experimental results with calculations, integrating the partial differential equations with a finite difference approximation containing the Crank-Nicholson algorithm. The results show that the model gives a good description of the measurements.

Knowledge of the non-stationary behavior of chemical reactors is important to predict responses to changes in feed conditions, for control purposes, and so forth. Much progress has been made in this field during the last decade, particularly with catalytic fixed-bed reactors; detailed mathematical models have been developed and solved by computers. However, the results of such calculations are often not checked with experimental data, and it is not always clear whether the complex models developed by some authors are really required in practical applications (1, 2, 3). In the present work we have tried to use as simple a model as possible by:

- (a) Defining the problem by choosing a test reaction, limiting ourselves to heterogeneous solid/gas catalytic reactions.
- (b) Writing down the requisite model equations.
- (c) Performing experiments and calculations to establish which of the theoretically possible terms of the equations are significant.
- (d) Performing experiments in a pilot reactor to compare the results of our calculations with actual data.

Selection of Model Reaction

The model reaction should preferably have the following properties:

- (1) The equation describing its chemical kinetics should apply to a wide temperature range.

(2) A commercial catalyst with high activity and stability should be available.

(3) Reactants should be gases of high purity and low price.

(4) Consecutive or side reactions should not occur.

(5) The heat of reaction must be large.

Furthermore, the test reaction should be industrially important; the same should apply, if possible, to the dynamic behavior of the reactor.

The above requirements are met by the methanation of carbon oxides, a step in the process for manufacturing hydrogen and ammonia synthesis gas by steam reforming or partial oxidation of hydrocarbons. The stoichiometric equations involved are:



The dynamic behavior of a methanator can be important when, for example, the inlet concentration of CO_2 increases suddenly because of misoperation or failure of the CO_2 absorber, a previous process step. When the concentration of carbon dioxide in hydrogen increases by 1% (here concentration in % refers to vol %) the adiabatic temperature rise increases by as much as 56°C in seconds when the feed temperature exceeds 250°C . It is thus important to obtain a better knowledge of the response to such sudden changes in feed conditions.

Model Development

Method. The mathematical model for an adiabatic methanator was developed according to the level scheme of Figure 1. This scheme is similar to those set up by Slin'ko (4), Matros *et al.* (5), and Beskov *et al.* (6). It can be used for stationary and dynamic reactor models. Each level is treated separately below.

Level I	Separate stages of chemical change adsorption/reaction/desorption	
Level II	Transfer processes inside catalyst pellet	
	Heat	Mass
Level III	Transfer processes in a film layer	
	Heat	Mass
Level IV	Transfer processes in a layer of catalyst	
	Heat	Mass
Level V	Interaction with the environment	
	adiabatic	non-adiabatic

Figure 1. Level scheme for model development

Level I. We began this investigation by studying the kinetics of CO and CO_2 hydrogenation at atmospheric pressure; the results are published elsewhere (7). Care was taken to exclude transport resistances in the kinetic measurements. The following equations describe the reaction rates with good precision in the concentration ranges 0.1–2.5% CO or CO_2 in H_2 and at 170° – 210°C and 200° – 230°C for CO and CO_2 , respectively:

$$r_{\text{co}} = \frac{2.09 \times 10^5 \exp(-10.1/RT) P_{\text{co}}}{(1 + 4.56 \times 10^{-4} \exp(12.4/RT) P_{\text{co}})^2} \text{ moles}_{\text{co}}/\text{hr}/\text{gram} \quad (1)$$

$$r_{\text{co}_2} = \frac{1.36 \times 10^{12} \exp(-25.3/RT) P_{\text{co}_2}}{(1 + 1270 P_{\text{co}_2})} \text{ moles}/\text{hr}/\text{gram} \quad (2)$$

The equations were tested at temperatures up to 280°C and described the rates at those temperatures quite satisfactorily. Therefore, they were applied throughout this work.

Level II. Table I contains data on the supported nickel catalyst used which were required to establish whether heat and mass transport resistances occur inside the catalyst particles. These data allow the calculation of effectiveness factors under methanation conditions; we found that the effectiveness factor is invariably higher than 0.9 at reaction temperatures below 320°C. Thus, pore diffusion does not influence the overall rate. Furthermore, it was established using Anderson's criterion (8) that the particles are isothermal up to that temperature.

Table I. Properties of Catalyst

Girdler G-65 Catalyst

composition	: 25 wt % Ni on γ - Al_2O_3
crushed particles: d_p	= 0.42 - 0.60 mm
particle density	: 2750 kg/m ³
particle porosity	: 0.46
bed density	: 1175 kg/m ³
bed porosity	: 0.57
S_{bet}	: 42.4 m ² /gram
S_{Ni}	: 6.6 m ² /gram
average pore diameter:	25 Å

Level III. The formulas of Chu *et al.* (9) and Petrovic and Thodos (10) for mass transfer resistance and the graph of Nu vs. Re_p given by Kunii and Smith (11) for heat transfer were applied to show that concentrations and temperatures in the two phases (gas and catalyst particles) do not differ significantly. The result for heat transfer was confirmed experimentally by placing a 0.5-mm thermocouple in a 5 × 5 mm catalyst pellet and another in the surrounding gas phase. A temperature difference could not be detected even at conditions known to give 100% carbon oxide conversion. This also confirms that the catalyst pellet is isothermal, as was concluded at Level II. Therefore, a quasi-homogeneous reactor model can be used to describe the methanator.

Level IV. The questions to be answered at this level are (1) whether dispersion contributes to mass transport in the catalyst bed, and (2) whether conduction, radiation, and dispersion should be taken into account when considering heat transport in the reactor.

In general, axial dispersion of mass and heat can be neglected whenever the bed is longer than 50 particle diameters (12); alternatively, the criterion of Marek and Hlavacek (13) can be applied:

$$Pe_1 \frac{L}{d_p} > 100$$

Since $L/d_p = 600$ and $D/d_p = 92$ for the pilot reactor used in this work and because $Pe_{1(\text{mass})} = 0.5-2.0$ (14, 15, 16) in the range of Re_p values encountered here (1.5-10), a plug flow description for mass transport applies. Fur-

thermore, results of Vortmeyer and Jahnel (17, 18) indicate that much higher reactor temperatures would be required for radiation to contribute significantly to heat flow in the catalyst bed. Radial heat transport can be neglected because the methanator is adiabatic. To confirm the above calculations the axial heat conductivity was also determined experimentally because data for systems containing relatively good heat conductors like the Ni/Al₂O₃ methanation catalyst and hydrogen could not be found in the literature. We applied the method of Yagi *et al.* (19), which was also used in recent work by Votruba *et al.*; the results show that axial heat conduction can be described quite well by Votruba's equation (20) for Pe_H and that it is not important in our methanator.

Level V. In the heat balance of a non-stationary adiabatic reactor it is necessary to take into account the heat capacity of the reactor wall as well as that of the catalyst bed. The two contributions to the time-dependent heat capacity term in the enthalpy balance of our pilot reactor are of the same order of magnitude. If the heat losses to the surroundings and heat conduction along the reactor wall are small and heat transfer from the catalyst bed to the wall is fast compared with the temperature changes in the reactor, the temperature profile along the reactor wall is invariably almost the same as the axial profile in the bed. Under such conditions the wall can be considered as part of the quasi-homogeneous catalyst medium relative to the temperature. The experiments were designed to comply with the above requirements, generating temperature profiles in catalyst bed and reactor wall which change synchronously.

Final Model Equations. Based on the above, the mass balance of a small volume element of the reactor can be written as:

$$uS \frac{\partial c}{\partial t} dl + \varepsilon S \frac{\partial c}{\partial t} dl = \rho_{\text{bed}} S r dl$$

This balance was applied to CO as well as CO₂; the concentration of all the other components of the reaction mixture can be calculated directly from the carbon oxide concentrations and the reaction stoichiometry. The heat balance reads as follows:

$$u c_{\text{tot}} C_{p_g} S \frac{\partial T}{\partial t} dl + \varepsilon c_{\text{tot}} C_{p_g} S \frac{\partial T}{\partial t} dl + \rho_{\text{bed}} C_{p_{\text{cat}}} S \frac{\partial T}{\partial t} dl \\ + \pi dl (R^2_{\text{out}} - R^2_{\text{in}}) \rho_{\text{wall}} C_{p_{\text{wall}}} \frac{\partial T}{\partial t} = - \rho_{\text{bed}} S r \Delta H^\circ r dl$$

It can be modified to

$$u c_{\text{tot}} C_{p_g} \frac{\partial T}{\partial t} + C_{p_m} \frac{\partial T}{\partial t} = - \rho_{\text{bed}} \Delta H^\circ r \quad (6)$$

where C_{p_m} stands for the heat capacity of the quasi-homogeneous system comprising gas phase, catalyst bed, and reactor wall:

$$C_{p_m} = \varepsilon c_{\text{tot}} C_{p_g} + \rho_{\text{bed}} C_{p_{\text{cat}}} + \frac{R^2_{\text{out}} - R^2_{\text{in}}}{R^2_{\text{in}}} \rho_{\text{wall}} C_{p_{\text{wall}}} \quad (7)$$

The equations are handled best in the dimensionless form—*i.e.*, by substituting:

$$C = \frac{c}{c_{\text{in}}}, T' = \frac{T}{T_{\text{in}}}, \lambda = \frac{l}{L}, \tau = \frac{tu}{\varepsilon L}$$

The final result is:

$$\frac{\partial C}{\partial \lambda} + \frac{\partial C}{\partial \tau} = A_1 r \quad (8)$$

$$\frac{\partial T'}{\partial \lambda} + B^* \frac{\partial T'}{\partial \tau} = B_1 r \quad (9)$$

$$r_{\text{CO}_2} = \frac{\exp(A_2 c_{\text{CO}_2}/T') C_{\text{CO}_2}}{(1 + A_3 c_{\text{CO}_2} \times C_{\text{CO}_2})} \quad (10)$$

$$r_{\text{CO}} = \frac{\exp(A_2 c_{\text{CO}}/T') \times C_{\text{CO}}}{(1 + A_3 c_{\text{CO}} \times \exp(A_4 c_{\text{CO}}/T') \times C_{\text{CO}})^2} \quad (11)$$

$$A_1 = \frac{-\rho_{\text{bed}} k_{\infty} L}{u} \quad (12)$$

$$A_2 = \frac{-Ea}{R T_{\text{in}}} \quad (13)$$

$$A_3 = K_{\infty} c_{\text{in}} \quad (14)$$

$$A_4 = \frac{\Delta H_{\text{ads}}}{R T_{\text{in}}} \quad (15)$$

$$B_1 = \frac{-\rho_{\text{bed}} k_{\infty} \Delta H^{\circ} r_{\text{CO}} c_{\text{in}} L}{u c_{\text{tot}} C_{p_g} T_{\text{in}}} \quad (16)$$

$$B^* = \frac{C_{p_m}}{\varepsilon c_{\text{tot}} C_{p_g}} \quad (17)$$

Table II. Data Used to Calculate Reactor Response

$k_{\infty \text{CO}}$	$= 1.039 \times 10^3$	$\text{m}^3/\text{kg}/\text{sec}$
Ea_{CO}	$= 10.1$	kcal/mole
$k_{\infty \text{CO}_2}$	$= 6.76 \times 10^9$	$\text{m}^3/\text{kg}/\text{sec}$
Ea_{CO_2}	$= 25.3$	kcal/mole
$\Delta H^{\circ}_{r_{\text{CO}}}$	$= -49.3$	kcal/mole
$\Delta H^{\circ}_{r_{\text{CO}_2}}$	$= -39.4$	kcal/mole
K_{CO_2}	$= 28.5$	m^3/mole
$K_{\infty \text{CO}}$	$= 10.2 \times 10^{-6}$	m^3/mole
ΔH_{adsCO}	$= 12.4$	kcal/mole
L	$= 0.3$	m
R_{in}	$= 2.3 \times 10^{-2}$	m
R_{out}	$= 2.7 \times 10^{-2}$	m
ρ_{bed}	$= 1175$	kg/m^3
ε	$= 0.57$	—
ρ_{wall}	$= 2900$	kg/m^3
$C_{p_{\text{wall}}}$	$= 0.19$	$\text{kcal}/\text{kg}/^{\circ}\text{K}$
$C_{p_{\text{gas}}}$	$= 7 \times 10^{-3}$	$\text{kcal}/\text{mole}/^{\circ}\text{K}$
c_{tot}	$= 44.7$	mole/m^3
$C_{p_{\text{cat}}}$	$= 0.211$	$\text{kcal}/\text{kg}_{\text{cat}}/^{\circ}\text{K}$

Since the boundary conditions depend on the type of disturbance at the reactor inlet and the initial profiles of temperature and concentrations in the reactor, they are discussed together with the results.

Solution Method. Because the Equations 8 and 9 are non-linear, an analytical solution is not possible, and a finite difference approximation was applied containing the Crank-Nicholson algorithm. The calculation requires expansion of the reaction rate equations in a Taylor series. The resulting set of linear equations can be solved easily by inversion of the linear band matrix, similar to the method for partial parabolic differential equations described by Valstar (21). The values of the physical and chemical parameters used in the calculations are given in Table II. The kinetic parameters were obtained by non-linear regression analysis of data obtained in a microreactor using Equations 1 and 2. For further details we refer to our earlier paper (7).

Experimental

Equipment. The response of a 0.5-liter methanator to step changes in feed temperature and reactant concentration was studied with the equipment shown in Figure 3. Two gas dosage systems can be connected in turn to reactor 4 *via* valves 2. One of the feed gas streams enters the reactor by way of preheater 3 equipped with by-pass 7. The flow rate of the reactor product is measured with Rotameter 6, and the compositions of feed and product gases are analyzed by on-line gas chromatograph 9.

The reactor (Figure 2) was insulated by a vacuum mantle and placed in a metal cylinder to protect it. At the outlet (bottom), glass and metal are connected by a Quick-Fit joint; at the top, glass and metal can expand independently. Twenty 0.5-mm thermocouples are inserted in the bed—*viz.*, 16 in the center and four near the wall as a check on the occurrence of radial temperature profiles. Since the previous discussion on model reduction has shown that the temperature of the catalyst particles is the same as that of the gas phase, it is immaterial whether the thermocouples are in contact with the catalyst or not. The thermocouples are connected to a 20-channel data logging system which can register a complete axial temperature profile on a tape puncher at certain intervals; the shortest possible interval is 3 sec.

Materials. A commercial nickel on alumina catalyst, G-65 from Girdler Südchemie (Munich, West Germany) was used; Table I contains the relevant data on this catalyst. Measurements of stationary temperature profiles indicated that the catalyst sample had a lower activity than the material with which the kinetic study (7) was done; it was possible to account for this by lowering the frequency factor by 20%. The fact that the second batch of catalyst is less active than the previous one was confirmed by kinetic measurements in a microreactor. The feed gases were commercially available, chemically pure; they were dried separately over molecular sieves, 3A.

Procedures. The reactor is brought to a stationary state with the feed of one of the two dosage systems; the flow of the product gases is first measured with Rotameter 6 and then diverted to "vent" by switching valves 5. Simultaneously, valve system 5 directs the flow from the second feed unit to the Rotameter *via* by-pass 8; this feed stream differs from the other in reactant concentration. By switching valve system 2, a step change in feed concentration can be obtained. A temperature disturbance is created by feeding gas to the reactor through the preheater as well as by-pass 7 to give a steady state with a known inlet temperature. The temperature disturbance is produced by closing the valve in the by-pass.

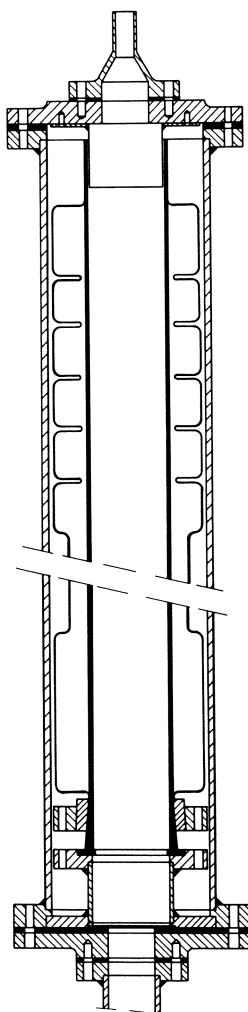


Figure 2. Reactor

Safety Precautions. Since the hydrogen consumption of the experimental unit is high by laboratory standards (*viz.*, 3–16 nm^3/hr), the unit was built in the open air. Valves, heaters, etc. could be operated from a control panel in the laboratory; the registration and data logging equipment was also placed indoors to separate it from the reactor system. The usual safety measures, such as automatic shutdown in case of power failures, a central switch to shut down the unit in case of emergency, and other precautions were taken.

Results

Table III lists the ranges of flow, temperature, and concentration in which the experiments with mixtures of CO_2 or CO in hydrogen were done. For comparison, the conditions for industrial methanators are also given.

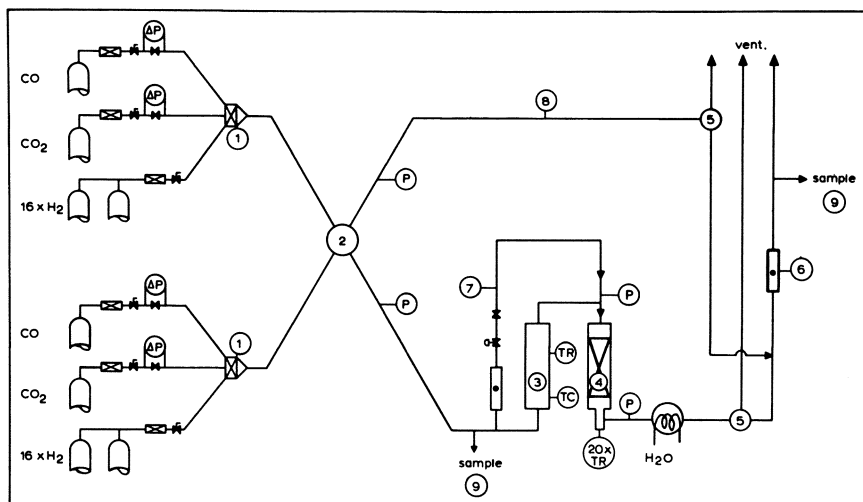


Figure 3. Simplified flow sheet of equipment

Table III. Experimental Conditions

	$S.V. \text{ hr}^{-1}$	$T_{in}, ^\circ\text{C}$	$C_{in}, \text{ vol } \%$	Pressure, atm
CO_2 hydrogenation	5000–32000	190–250	0.6–2.2	1
CO hydrogenation	5000–32000	190–250	0.6–2.0	1
Industrial methanator	4000–5000	300–310	0.3–0.5	10–40

The temperature at the wall and at the same axial position in the center of the catalyst bed were equal within experimental error. Therefore, radial temperature profiles were not taken into account in experiments under the conditions listed in Table III.

Three types of disturbances in a feed of CO_2 and CO in hydrogen are considered separately:

Type 1: step increase in concentration in the feed to an isothermal reactor.

Type 2: a similar concentration step in the feed to a reactor with a temperature profile.

Type 3: a temperature disturbance.

Hydrogenation of CO_2 . TYPE 1. Computer simulation with the model shows that the concentration profile in the reactor changes appreciably within 1–2 residence times after a step increase in concentration. This phenomenon, the fast concentration response (FCR), is followed by the formation of a temperature profile, which develops much more slowly than the FCR. We refer to this as the slow temperature response, STR, which is accompanied by an equally slow further change in the concentration profile. Typical results of such calculated profiles are shown in Figure 4. Hansen made a similar approach to this problem (22, 23, 24). An FCR calculation requires a very small time step whereas an STR can be computed using 1000-fold longer time step. To minimize the computing time required, the FCR calculation, which takes about 10 min on an IBM 360/65, can be replaced by a simple 4th-order Runge Kutta integration of the isothermal stationary mass balance which requires

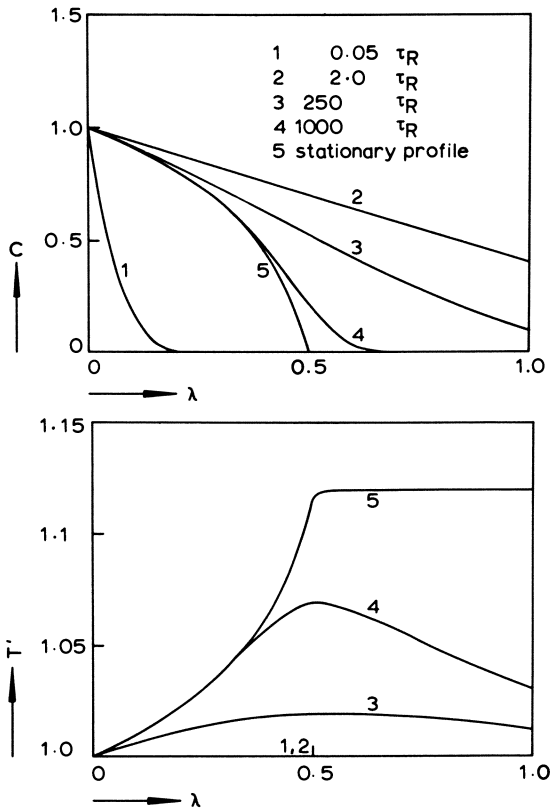


Figure 4. Sample response to a type 1 disturbance (calculated)

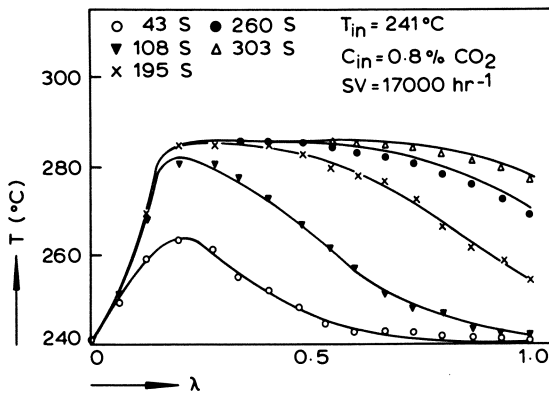


Figure 5. Axial temperature profile at various times after a type 1 disturbance (lines: calculated; points: measured)

only a few seconds. The result is then used as the boundary condition for the STR calculation. About 20 experiments were done within the range of conditions in Table III, concerning a type 1 disturbance. In all cases examined the agreement between measured and calculated temperatures and their changes in time is quite satisfactory; a representative example is shown in Figure 5.

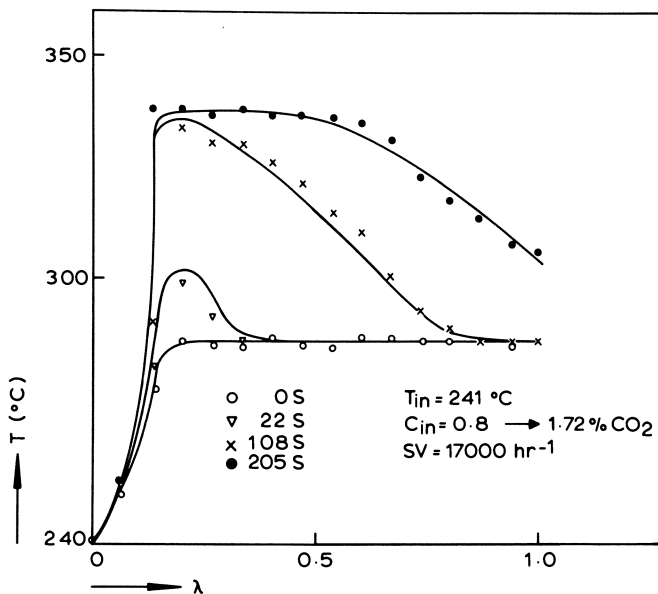


Figure 6. Axial temperature profile at various times after a type 2 disturbance (lines: calculated; points: measured)

TYPE 2. Here the FCR develops in a different manner because the reactor is not isothermal but contains an axial temperature profile at the time of the step change in concentration. It appeared that, here too, the concentration profile after the FCR could be found by Runge-Kutta integration of the mass balance, but by substituting after each axial step the temperature at the corresponding position in the reactor obtained from the initial stationary temperature profile. Agreement between measured and calculated temperature profiles was very good for all experiments in which a feed concentration step was applied to a reactor containing an axial temperature profile; an example is shown in Figure 6.

TYPE 3. With type 3 disturbances a distinction between FCR and STR cannot be made. Initial concentration and temperature profiles are first calculated from stationary mass and heat balances by Runge-Kutta integration, and a temperature disturbance is then imposed on the reactor inlet conditions. A sharp step increase or decrease of the feed temperature was impossible with the equipment used because of the large heat capacity of the piping between the cold and hot gas mixer and the reactor inlet. The resulting smooth inlet temperature/time curve could, however, be described adequately by two or three straight lines. A typical result of a type 3 disturbance is shown in Figure 7.

Interestingly, the temperature in the second part of the bed decreases when the entrance temperature is raised; conversely, the temperature in the

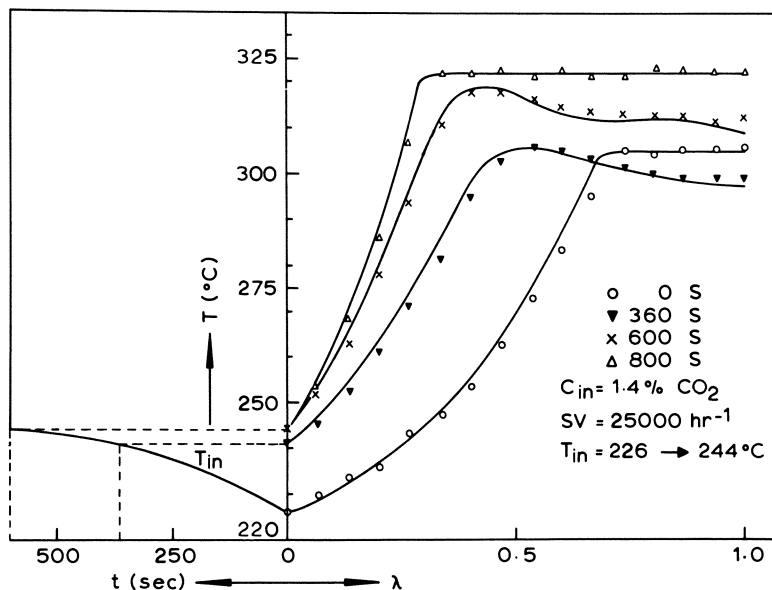


Figure 7. Inlet temperature and axial temperature profile for a type 3 disturbance (lines: calculated; points: measured)

second part of the bed increases with decreasing feed temperature. This can be explained by considering that less CO_2 is converted in the first part of the bed when the entrance temperature is lowered. Thus, more CO_2 reaches the second part. This condition persists until the second part is cooled enough so that the exponential influence of the decrease in temperature overshadows the competitive effect of the increased concentration on the reaction rate. A

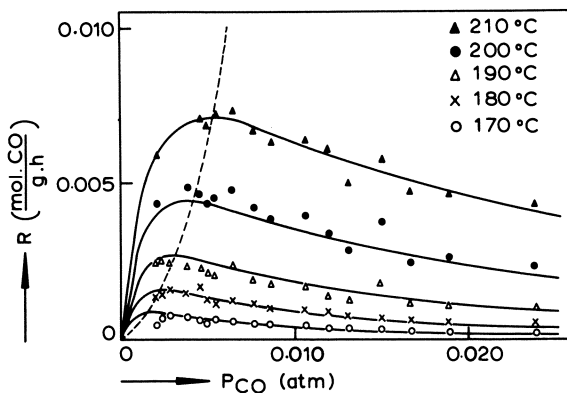


Figure 8. Initial rate of CO hydrogenation (lines calculated from Equation 1; points: measured)

similar explanation applies to an increased feed temperature. Similar conclusions were drawn for a packed tubular reactor by Crider and Foss (26) on the basis of calculations; the effects were determined experimentally by Hoiberg

et al. (25) for a fixed-bed catalytic reactor. According to Eigenberger (27) it occurs even in a homogeneous tubular reactor when the influence of the reactor wall is taken into account.

Hydrogenation of CO. Figure 8 shows a maximum in the rate of CO hydrogenation as a function of CO content in the feed. Thus, the response of the reactor to a step change in CO concentration should differ from the response to a step change in the CO₂ content of the feed; an increase of CO concentration causes the rate of hydrogenation to decrease when the partial pressure of CO is above p_{\max} . The maximum in the CO hydrogenation rate found by Van Herwijnen *et al.* (7) is confirmed by the pilot plant experiments, as follows from the stationary temperature profiles in Figure 9 at various inlet

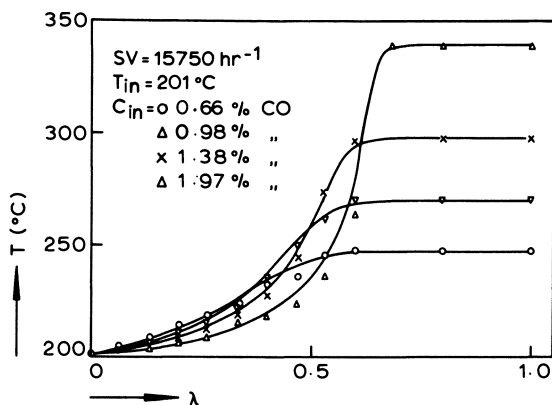


Figure 9. Stationary axial temperature profiles for CO hydrogenation (lines: calculated; points: measured)

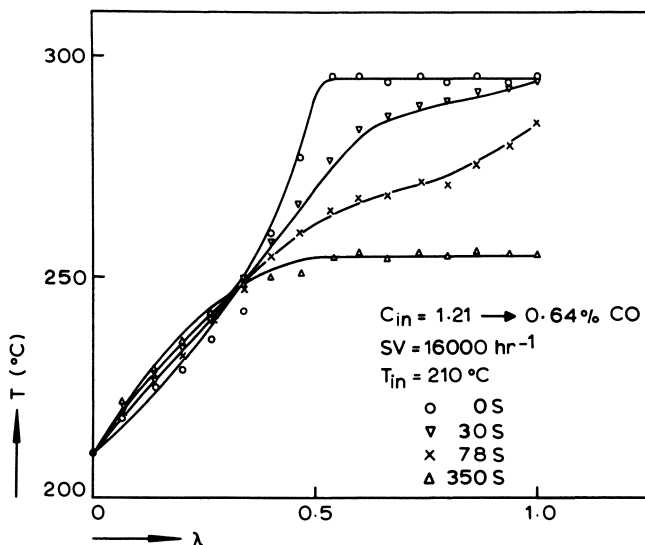


Figure 10. Axial temperature profile after a type 3 disturbance (CO hydrogenation; lines: calculated; points: measured)

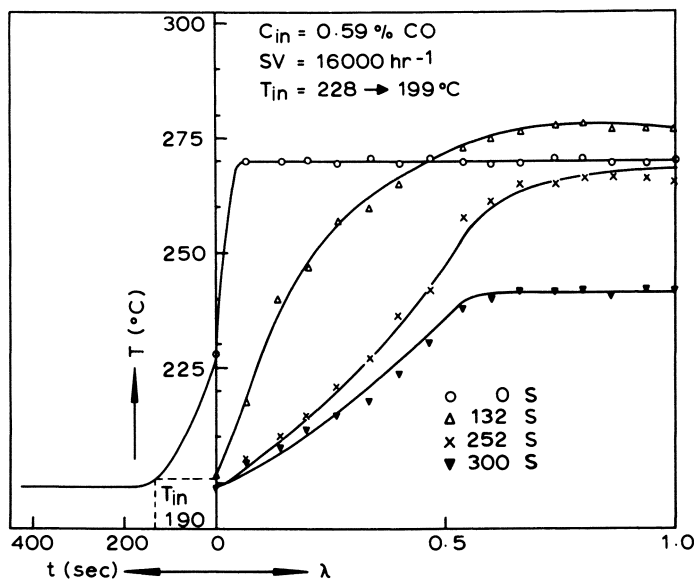


Figure 11. Inlet temperature and axial temperature profile for CO hydrogenation observed after a type 3 disturbance (lines: calculated; points: measured)

concentrations of CO. The typical behavior of the rate of CO methanation is also reflected in the response to a type 2 disturbance. When the CO concentration in the feed is lowered from 1.21 to 0.65%, the temperature in the front end of the catalyst bed increases because the reaction rate increases (Figure 10). Note also that the temperature in the second part of the bed then becomes lower. The agreement between theory and experiment is also satisfactory for type 1 disturbances. For type 3 disturbances, it is difficult to predict reactor behavior because the exit temperature change is a composite of, *e.g.*, decreasing inlet temperature, increasing concentration, and decreasing rate of hydrogenation. A typical example is shown in Figure 11.

Discussion

The good agreement between calculated and measured temperature profiles shows that non-linear effects other than the dependence of concentration and temperature on the methanation rate need not be taken into account in the parameter space investigated. The question can now be answered as to how soon after a sudden increase of the CO₂ concentration in the feed the temperature of an industrial methanator reaches a maximum. The experiments and calculations for methanation at atmospheric pressure show that the new stationary state of the reactor is reached within a few seconds when the reactor inlet temperature exceeds 250°C. In practical applications, however, the pressure is usually much higher than atmospheric (*cf.*, Table II). The effect of pressure on the rate of CO₂ hydrogenation can be estimated from laboratory experiments which show that the reaction rate of 1% CO₂ in H₂ at 208°C increases by a factor of 1.7 when the pressure is raised from 1 to 10 atm. Thus, response times of 1–2 sec must be expected in industrial methanators.

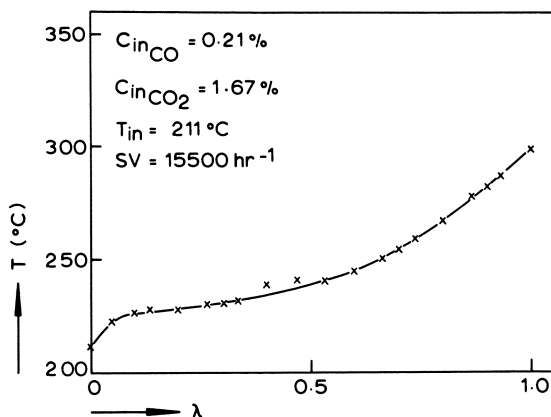


Figure 12. Measured stationary axial temperature profile for the hydrogenation of a mixture of carbon oxides in hydrogen

There are, however, two important differences between our experiments and industrial methanation. First, the effect of the heat capacity of the reactor wall is much smaller industrially than with our pilot methanator. In the latter case the thermal capacity of the reactor wall is almost equal to the capacity of the catalyst bed; this means that the small reactor responds more slowly than an industrial reactor. Secondly, feeds to industrial reactors used in making ammonia synthesis gas or hydrogen invariably contain both CO and CO₂. Since previous work has shown (7) that CO inhibits the hydrogenation of CO₂ until the CO concentration has decreased to about 200 ppm, the response to an increase in CO₂ concentration is noticeable only in the second part of the reactor—*i.e.*, after CO has been hydrogenated. This causes the response time to step change in CO₂ concentration to be much shorter when the feed also contains CO. The reactor behaves as if the first part of the bed in which CO is hydrogenated does not contribute to the changes; in other words, the response of the second part is similar to that of a reactor with an inlet temperature equal to the temperature of a CO₂/H₂ feed plus the adiabatic temperature rise caused by the conversion of CO. An example of a measured stationary profile is given in Figure 12.

At the time of writing only a few experimental results with feed consisting of CO, CO₂, and H₂ were available. These data confirm that with CO present the response of CO₂ is faster than in the absence of CO. Further work with mixed feeds is in progress.

Nomenclature

A_1, A_2, A_3, A_4	dimensionless constants
B_1, B^*	dimensionless constants
c	concentration, moles/m ³
C	dimensionless concentration
c_{tot}	total concentration, moles/m ³
C_{p_g}	specific heat of gas, kcal/mole/°K

$C_{p\text{cat}}$	specific heat of catalyst, kcal/kg _{cat} /°K
$C_{p\text{wall}}$	specific heat of wall, kcal/kg/°K
$C_{p\text{m}}$	specific heat pseudo-homogeneous medium, kcal/m ³ /°K
d_p	particle diameter, m
Ea	activation energy, kcal/mole
k_∞	frequency factor, m ³ /kg _{cat} /sec
K_∞	adsorption equilibrium constant, m ³ /mole
ΔH_{ads}	heat of adsorption, kcal/mole
ΔH°_r	heat of reaction, kcal/mole
l	running variable in reactor length, m
L	reactor length, m
Pe_1	axial Péclet number
Pe_H	axial Péclet number for heat transport = $\frac{uc_{\text{tot}}C_{p\text{g}}d_p}{\lambda_{\text{eff}}}$
R	gas constant, kcal/mole/°K
R_{in}	inner tube diameter, m
R_{out}	outer tube diameter, m
r	reaction rate, moles/kg _{cat} /sec
Re_p	Reynolds particle number
S	cross-sectional area of cylindrical reactor, m ²
T	temperature, °K or °C
T_{in}	inlet temperature, °K or °C
T'	dimensionless temperature
t	time, seconds
u	superficial gas velocity, m ³ /m ² /sec

Greek Symbols

η	viscosity of gas, kg/m/sec
ε	porosity of catalyst bed
ρ_{bed}	density of catalyst bed, kg _{cat} /m ³
ρ_{wall}	density of wall material, kg/m ³
τ	dimensionless time variable
λ	dimensionless reactor length

Literature Cited

1. Beek, W. J., *Symp. Chem. React. Eng., 5th, Amsterdam 1972*, review section 4.
2. Froment, G. F., *Symp. Chem. React. Eng., 5th, Amsterdam 1972*, review section 5.
3. Ray, W. H., *Symp. Chem. React. Eng., 5th, Amsterdam 1972*, review section 8.
4. Slin'ko, M. G., *Brit. Chem. Eng.* (1971) **16** (4/5) 363.
5. Matros, Yu. Sh., Kirillov, V. A., Slin'ko, M. G., *Proc. IFAC Symp. DISCOP, Győr, Hungary, Sept. 1971*, paper M3.
6. Beskov, V. S., Vyatkin, Yu. L., *Proc. IFAC Symp. DISCOP, Győr, Hungary, Sept. 1971*, paper B6.
7. Van Herwijnen, T., Van Doesburg, H., De Jong, W. A., *J. Cat.* (1973) **28**, 391-402.
8. Anderson, J. B., *Chem. Eng. Sci.* (1963) **18**, 147.
9. Chu, C. J., Kalil, J., Wetteroth, W. A., *Chem. Eng. Progr.* (1953) **49**, 141.
10. Petrovic, L. J., Thodos, G., *Ind. Eng. Chem., Fundamentals* (1968) **7**, 274.
11. Kunii, D., Smith, J. M., *A.I.Ch.E. J.* (1961) **7** (1) 29.
12. Carberry, J. C., Wendel, M. M., *A.I.Ch.E. J.* (1963) **9** (1) 129.

13. Marek, M., Hlavacek, V., *Chem. Eng. Sci.* (1966) **21**, 493.
14. Gunn, D. J., Pryce, C., *Trans. Inst. Chem. Engrs.* (1969) **47**, T341.
15. Gunn, D. J., *Trans. Inst. Chem. Engrs.* (1969) **47**, T351.
16. Edwards, M. F., Richardson, J. F., *Chem. Eng. Sci.* (1968) **23**, 109.
17. Vortmeyer, D., Jahnelt, W., *Chem. Eng. Sci.* (1972) **27**, 1485.
18. Vortmeyer, D., Jahnelt, W., *Chem. Ing. Tech.* (1971) **43** (7) 461.
19. Yagi, S., Kunii, D., Wakao, N., *A.I.Ch.E. J.* (1960) **6** (4) 543.
20. Votruba, J., Hlaváček, V., Marek, M., *Chem. Eng. Sci.* (1972) **27** 1845.
21. Valstar, J. M., Thesis, Delft, 1969.
22. Hansen, K. W., Livbjerg, H., Villadsen, J., *Proc. IFAC Symp. DISCOP, Győr, Hungary, Sept. 1971*, paper W1.
23. Hansen, K. W., *Chem. Eng. Sci.* (1971) **26**, 1555-1569.
24. Hansen, K. W., *Chem. Eng. Sci.* (1973) **28**, 723.
25. Hoiberg, J. A., Lyche, B. C., Foss, A. S., *A.I.Ch.E. J.* (1971) **17** (6) 1434.
26. Crider, J. E., Foss, A. S., *A.I.Ch.E. J.* (1966) **12** (3) 514.
27. Eigenberger, G., *Chem. Ing. Tech.* (1974) **46** (1) 11.

RECEIVED January 2, 1974.

Experimental Investigation of the Dynamics of a Catalytic Fixed Bed Reactor

KNUD WAEDE HANSEN and STEN BAY JORGENSEN

Instituttet for Kemiteknik, Technical University of Denmark,
2800 Lyngby, Denmark

A pilot plant fixed bed reactor for dynamic experiments was specially designed to emphasize the dispersion effects of the packed bed itself. Peclet numbers of about 0.8 (based on particle diameter) are found from inlet temperature disturbances in the bed without reaction. A homogeneous model for the reactor is suggested. The heat transport parameters and the reaction kinetic parameters are found from independent experiments. The reactor dynamic experiments consist of startup experiments and step and periodic changes in the inlet temperature. The agreement between experiments and simulations are qualitatively good. The discrepancies in the last part of the reactor are believed to be caused by inaccurate determination of the reaction kinetic parameters or an inaccurate kinetic model.

The dynamic behavior of many gas phase catalytic fixed bed reactors is dominated by the heat transport processes. The small heat capacity of the gas compared with that of the catalyst pellets gives a thermal residence time which is several hundred times greater than the gas residence time. Heat diffusion and dispersion phenomena which normally do not influence stationary profiles are very important for propagating inlet disturbances (1).

In practical systems several heat diffusion processes contribute to the overall dispersion. Depending on the relative importance of these phenomena one might formulate different model types, accentuating the most important contributions to the total dispersion. These different models correspond to those reviewed by Froment (steady state) (2) and Ray (dynamic state) (3). Their reviews also contain a comprehensive list of previous work in the area, and their main conclusion is that the theoretical level is far beyond what has been verified experimentally.

The classical paper of Padberg and Wicke (4) gives interesting experimental results in the multiple steady-state regime. These results can be explained by several quite different physical phenomena, e.g., as shown through the simulation studies (5, 6). This multitude of possible interpretations indicates a need for experiments on less complicated systems where the physical phenomena can be investigated more independently. Hoiberg *et al.* (7, 8) have studied the relatively simple oxygen-hydrogen system. They obtained

fine agreement between experiments and model simulations by using frequency response techniques. However—as is often the case in heat transfer experiments—the wall dynamics overshadow the dynamics of the packed bed itself. To suppress this and other secondary effects not characteristic for the packed bed, we built a large-scale reactor pilot plant. Construction of this equipment was based on the simulations described in Ref. 9. The present paper describes the first series of experiments performed. The experimental results consist of startup experiments and step and periodic disturbances in inlet temperature. The results are compared with model simulations where the parameters are determined by independent experiments.

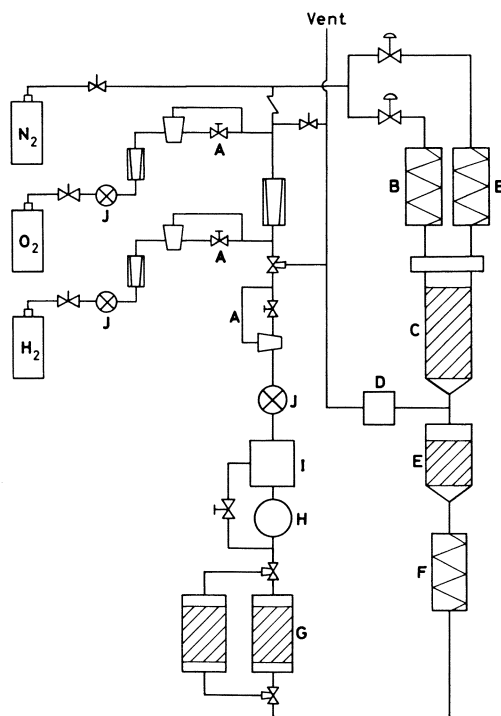


Figure 1. Simplified sketch of experimental system

- | | |
|---------------------------|----------------------|
| A Flowcontroller | F Cooler |
| B Heat exchangers | G Drying towers |
| C Reactor | H Compressor |
| D Back-pressure regulator | I Expansion tank |
| E After converter | J Pressure regulator |

Apparatus and Experimental Conditions

The reaction between oxygen (about 1%) and hydrogen (99%) was chosen as a characteristic reaction system. Figure 1 shows a sketch of the apparatus, and some characteristics of the system are summarized in Table I. Because of the high flow rate (about 180 liters/min), the product stream is regenerated, and the purified hydrogen returned to the inlet by a diaphragm compressor. The unused oxygen is converted in a reactor with a catalyst of high activity, and the water formed is adsorbed in one of two drying towers con-

nected in parallel. Each drying tower has a capacity corresponding to about 10 hrs operation. The regeneration of the drying towers takes place *in situ* by direct heating in a nitrogen stream. The three supply streams to the hydrogen loop are nitrogen for washing, the reactant oxygen, and makeup hydrogen. The reactor outlet pressure is held constant by a back-pressure regulator.

The inlet concentration of oxygen can be changed rapidly by varying the oxygen flow rate almost without changing the total flow rate. The inlet temperature can also be changed rapidly by varying the ratio between the flows of two parallel inlet streams, each heated to constant but different temperatures in the inlet heat exchangers. The heating medium is oil.

The reactor itself is a cylindrical (9.6×50 cm) vessel insulated with 15 cm of glass wool. The inlet section is made of low heat conductivity Gafion, preventing any heat interaction between the two inlet streams. The reactor wall is very thin steel plate (0.01 cm), which reduces the wall heat capacity to about 2% of the total heat capacity. Temperature is measured by iron-constantan thermocouples (0.2-mm diameter) in 11 axial positions and in three radial points at the middle of the reactor. The thermocouple leads are collected at the center and taken out in the top section. The oxygen content of the gas is measured by a paramagnetic analyzer with two channels from six different axial positions. Small sample streams are taken to the top section through thin steel tubes (1-mm diameter).

Table I. Properties of Reactor and Catalyst

<i>Parameter</i>	<i>Value</i>
Reactor length (L)	50 cm
Reactor diameter (D)	9.6 cm
Reactor porosity (ϵ_1)	0.41
Thickness of reactor wall	0.01 cm
Catalyst density (ρ_k)	1.24 gram/cm ³
Pore volume (V)	0.54 cm ³ /gram
Catalyst porosity ($\rho_k V$)	0.67
Surface area (S), BET	24×10^4 cm ² /gram
Av. pore radius ($2V/S$)	450A
Catalyst diameter (d)	0.37 cm
Specific heat capacity of catalyst (calorimetric measurement)	0.23 cal/gram

The catalyst is platinum supported by alumina pellets (Pechiney, type A). The platinum content had to be very low, about 6 ppm, to ensure suitable reaction rate. Platinum was distributed on the alumina pellets by wet impregnation technique with a solution of hydrochloroplatinic acid and nitric acid. Before impregnation the alumina pellets were sintered at 1100°C to destroy the micropores, giving a low area material which is convenient for this study. Activation was done in a hydrogen stream at 350°C for 15 hrs.

The performance of the reactor system is good. Measurements of the stationary temperature profiles in the center indicate nearly adiabatic behavior. However we sometimes observed that the radial profile shows a parabolic shape with the maximum temperature away from the center. We believe this is caused by the thermocouple arrangement because the velocity of the gas near the thermocouple leads at the center is higher than the mean velocity. This phenomenon might disturb the temperature measurements.

The normal procedure for the experiments at one specific flow rate included the following steps:

(a) Without addition of oxygen to the hydrogen stream the system is allowed to stabilize at a given flow and inlet temperature.

(b) The reactor bed is used as heat regenerator. The heat transfer parameters are found by studying the response on step and pulse disturbances in inlet temperature at otherwise constant operating conditions.

(c) Startup process. When the packed bed again is heated to a constant temperature, oxygen is added to the inlet stream, and the transient is followed until a steady-state profile is reached. The period after the first rapid changes might sometimes take several hours.

(d) Periodic changes in inlet conditions. In this study pulse disturbances in inlet temperature are considered. The reactor is then again allowed to stabilize at the earlier inlet temperature to check the stationary profiles.

(e) Some small step changes in inlet temperature are performed—*e.g.*, giving the static gain profile.

Two characteristic series of experiments of this kind are presented here. The parameters are shown in Table II.

Table II. Experimental Conditions

<i>Exp. No.</i>	<i>g, gram/cm² sec</i>	<i>Y_o, mole %</i>	<i>T_o, °K</i>	<i>P_{tot}, atm</i>	<i>ΔP, atm</i>	<i>Reynolds No. (Inlet)</i>
F22	0.00437	0.70	371.3	1.072	0.066	15.5
F31	0.00298	0.80	371.8	1.000	0.033	10.6

Reactor Model

The following assumptions are introduced into the reactor model:

(a) The reaction rate is described by an overall rate expression of the Arrhenius type

$$Re = k_t P e^{-(E/R_g T)}$$

The first-order dependence of oxygen pressure on reaction rate is found through experiments in a recirculation reactor. This is in close agreement with other investigators who found reaction orders between 0.8 and 1 (7, 10). Recirculation reactor experiments at temperatures between 100° and 230°C indicate that the apparent activation energy is nearly independent of the temperature.

(b) A homogeneous model is used. The justification of this assumption involves discussion of the following points. First, the temperature difference between catalyst and gas must be so small that the reaction rate is not changed significantly by using the gas temperature instead of the catalyst temperature. The simulations mentioned earlier (9) show that this temperature difference is less than 2°C, which might lead to an error of 5% in the reaction rate. Second, all the relevant heat dispersion phenomena (finite heat transfer rate between gas and particle, finite heat transfer rate inside the catalyst particle, axial dispersion in the gas phase, and possible secondary phenomena) must be combined into one overall dispersion mechanism. By equating the second moment of the impulse responses of a heterogeneous and homogeneous model for heat transfer in a packed bed one can derive:

$$\frac{1}{Pe_{tot}} = \frac{1}{Pe_g} + \frac{1 + \nu/5}{H_g} \quad (1)$$

Pe_{tot} is the total Peclet number in the homogeneous model, and Pe_g is the Peclet number in the gas phase in the heterogeneous model. H_g is the number of heat transfer units, and ν is the modified Nusselt number of the catalyst

particle. Hansen and Jørgensen (11) investigated the accuracy of this formula for heat transfer in packed beds and found that it can be used in a wide parameter range even for high frequency disturbances. Calculations have shown that it is much more difficult to give exact criteria for the validity in the case with reaction. However, for the system parameters in Tables I and II our calculations have shown that the homogeneous model is very good when the normalized disturbance frequency is below 3–4 (residence times)⁻¹.

(c) The concentration profile behaves quasi-stationarily. The validity of this assumption is evident from the simulations with the fast model and slow model (9).

(d) The reactor is assumed to be adiabatic (*see* the section on Apparatus and Experimental Conditions).

(e) The total pressure is assumed to be constant since the pressure drop is small even at high flow rates (*see* Table II).

Assumptions (a)–(e) give the following model:

$$\frac{\partial y}{\partial t} + \frac{\partial y}{\partial z} = \frac{1}{\text{Pe}_h} \frac{\partial^2 y}{\partial z^2} + D_h \cdot x \cdot e^{\gamma(1-y)} \quad (2)$$

$$\frac{\partial x}{\partial z} = \frac{1}{\text{Pe}_m} \frac{\partial^2 x}{\partial z^2} - D_m \cdot x \cdot e^{\gamma(1-y)} \quad (3)$$

Boundary conditions:

$$y(0) = y_1 \quad (4)$$

$$x(0) = x_1 \quad (5)$$

$$\frac{\partial y}{\partial z}(1) = \frac{\partial x}{\partial z}(1) = 0 \quad (6, 7)$$

$$y = \frac{T}{T_o}, \quad x = \frac{P}{P_o}, \quad z = \frac{l}{L}, \quad t = \frac{t'}{\tau}, \quad \gamma = \frac{E}{R_g T_o}$$

$$D_h = \frac{(-\Delta H)L k_f e^{-\gamma} P_o(1-\varepsilon)}{g_o C_{pR} T_o} \quad (8)$$

$$D_m = \frac{L k_f e^{-\gamma} P_{tot} M(1-\varepsilon_1)}{g_o} \quad (9)$$

This model is used for three different purposes:

(a) Derivation of the transfer function for the bed used as heat regenerator. Letting $k_f = 0$, Equations 2, 4, and 6 are solved to give the transfer function:

$$\frac{y}{y_1} = \exp \left[-\frac{\text{Pe}_h}{2} (1 - \sqrt{1 + 4s\tau/\text{Pe}_h}) \right] \quad (10)$$

(b) Calculation of the frequency response. Following a procedure described by Michelsen *et al.* (12), the equations are locally linearized around a stationary state and discretized in space by orthogonal collocation. The transfer function is found by diagonalization of the system matrix. Fourteen internal collocation points are used in most cases.

(c) Calculation of the nonlinear time response. Again a global collocation method is used for discretization of the space derivative. The resulting ordinary differential equations are solved from the given initial state by a fourth-order Runge Kutta method with variable step size. This method has been used by

several authors to solve partial differential equations of this kind and is described by Hansen (13). Villadsen and Sørensen (14) used a double collocation method, and Ferguson and Finlayson (15) compared various integration methods in the time direction.

Determination of Parameters

Heat Transport Parameters. The parameters Pe_h and τ in the transfer function (Equation 10) are determined by fitting the model response to the experimental response following a pulse disturbance in inlet temperature. Experimentally the inlet temperature is changed from about 108° to about 86°C and then changed back again after about one-half thermal residence time. The central temperatures are registered at discrete time intervals.

The estimation method is based on minimalization of the least-square error in the time domain. Michelsen (16) has tried the method on several flow model examples and found it very efficient. The results of the estimation for the two experiments is shown in Table III. Each data series includes 64 points but is prolonged with the stationary value by a factor of 8 to ensure good interpolation of the transfer function. The estimated values are all based on the measured inlet temperature disturbance as reference time series.

Table III. Estimation of Heat Transfer Parameters; Data Series of 64 Points Prolonged to 512 Points

<i>Exp. No.</i>	T_a , <i>min</i>	<i>z</i>	Pe_h	τ , <i>min</i>	<i>Av. Values</i>
F22	168	0.393	121.5 ($\pm 10\%$)	10.17 ($\pm 0.8\%$)	$\tau = 10.4$ min
F22	168	0.496	121 ($\pm 8\%$)	10.00 ($\pm 0.5\%$)	$Pe_h = 118$
F22	168	0.790	117 ($\pm 7\%$)	10.75 ($\pm 0.4\%$)	$Pe_h \times d/L = 0.87$
F22	168	0.890	111.5 ($\pm 4\%$)	10.59 ($\pm 0.2\%$)	
F31	196	0.393	112 ($\pm 4\%$)	16.17 ($\pm 0.3\%$)	$\tau = 16.1$ min
F31	196	0.496	110.5 ($\pm 5\%$)	15.74 ($\pm 0.4\%$)	$Pe_h = 103.5$
F31	196	0.790	98 ($\pm 8\%$)	16.33 ($\pm 0.4\%$)	$Pe_h \times d/L = 0.77$
F31	196	0.890	93.5 ($\pm 11\%$)	16.00 ($\pm 0.6\%$)	

Table III shows that the parameter estimates are fairly independent of the measuring position even though small systematic errors seem to be present. An average value of the estimates will give the thermal residence time within 2% accuracy and the Peclet number within 5–10%. Using the average parameter values of Table III, the regenerator pulse response is simulated with the reactor time response program (point (c), above). Figure 2 shows regenerator profiles for F22 at different times together with the experimental temperature measurements. The agreement is good, and it seems reasonable to use the average parameter values for the whole reactor. The values of the estimated Peclet numbers clearly indicate that the heat dispersion of the reactor bed is close to the expected heat dispersion from Equation 1. The number of heat transfer units based on reactor length is about 300 and the modified Nusselt number is 2.5. Mass transfer experiments (e.g., Ref. 17) have given values for the Peclet number in the gas phase of about $2L/D = 270$. When inserted in Equation 1, this gives, $Pe_{tot} = 115$, $Pe_{tot} \cdot d/L = 0.85$. This result is somewhat in contrast to the results of Votruba *et al.* (18) who determined Peclet numbers by a stationary method and obtained considerably lower values.

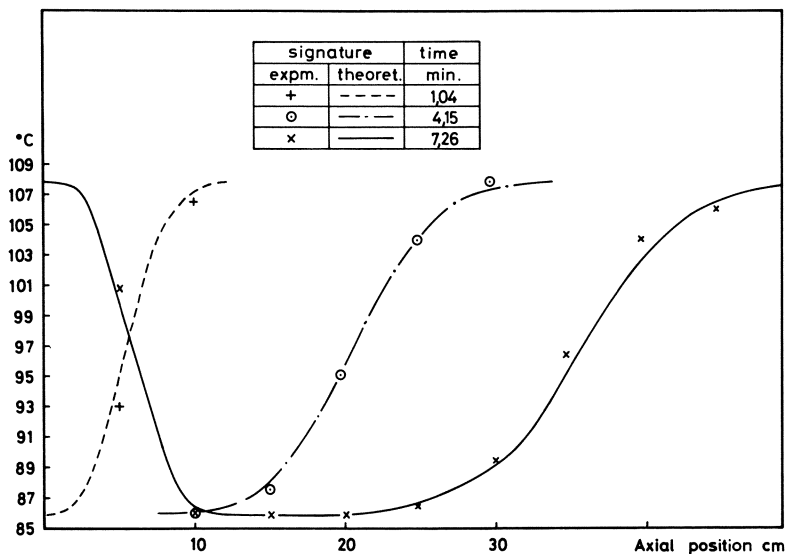


Figure 2. F22 Regenerator response after pulse disturbance in inlet temperature. Inlet pulse height 22°C, width 6.0 min; estimated model parameters shown in Table III.

Reaction Kinetic Parameters. The reaction rate was measured as a function of oxygen partial pressure and temperature in a recirculation reactor connected to the integral reactor system. The reaction rate was determined within an accuracy of 4 to 10%. The reaction was close to first-order in oxygen partial pressure, and no influence from the water vapor was found at temperatures above 90°C. Also the temperature had a greater influence on reaction rate (activation energy ≈ 10 kcal/mole) than is normally found for alumina catalysts. Maymo and Smith (10) found $E \approx 5.2$ kcal/mole for a Boehmite carrier.

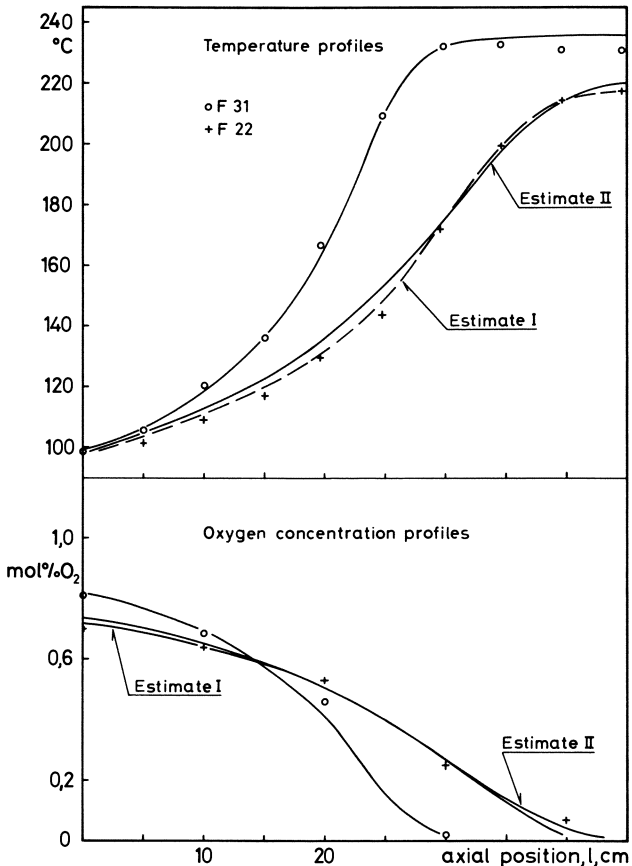
However, catalyst activity depended on pretreatment. The activity was 10–30% greater for high temperature pretreatment than for low temperature pretreatment. Precise determination of the kinetic parameters based on measurements in the recirculation reactor is therefore not possible, and we decided to estimate the kinetic parameters from each set of steady state temperature profile and oxygen partial pressure profile in the fixed bed reactor. This approach has the advantage of partially compensating for the inaccuracies introduced through the assumption of negligible temperature difference between pellet and gas. The weighted least-squares estimates of the inlet concentration, frequency factor, and activation energy were found by using Marquardt's (19) method. This algorithm starts with a steepest descent and slowly changes to the Newton-Raphson method as the minimum is approached. Support plane confidence limits are evaluated by the method of Box (20) to estimate the reliability of the best estimates.

The result of the estimation is shown in Table IV, and the experimental points are plotted together with the estimated profiles in Figure 3. The concentration measurements have only one-third weight compared with the temperature measurements in agreement with the expected measurement accuracy. Since the temperature measurements especially in the first part of the reactor

Table IV. Estimates of Reaction Kinetic Parameters

Linear 95% Support Plane Limits in Parentheses

Exp. No.	Weights		$k_1 e^{-(E/R_g T_o)}$ mole/ (cm ³ cat·sec) ·10 ⁴	$E,$ kcal/mole	Y_{o_2} mole %
	Temp. Profile	Concn Profile			
F22	1, all z	1/3, all z	0.268 ($\pm 15\%$)	11.8 ($\pm 14\%$)	0.720 ($\pm 7\%$)
F22	(0, $z \leq 0.5$) (1, $z > 0.5$)	1/3, all z	0.305 ($\pm 22\%$)	10.2 ($\pm 21\%$)	0.732 ($\pm 9\%$)
F31	1, all z	1/3, all z	0.246 ($\pm 15\%$)	11.1 ($\pm 14\%$)	0.816 ($\pm 6\%$)

**Figure 3. Steady state profiles; estimated model parameters shown in Table IV**

might include small systematic errors resulting from the thermocouple arrangement (*cf.*, above), the F22 parameters are re-estimated without including the temperature measurements from 5 to 25 cm. This alters the estimates somewhat inside the confidence limits of the first estimate. Because of the shape of the profiles in F31, there is no basis for doing the same here. The following simulations are performed using the estimates for each experimental run itself (estimate 2 for F22).

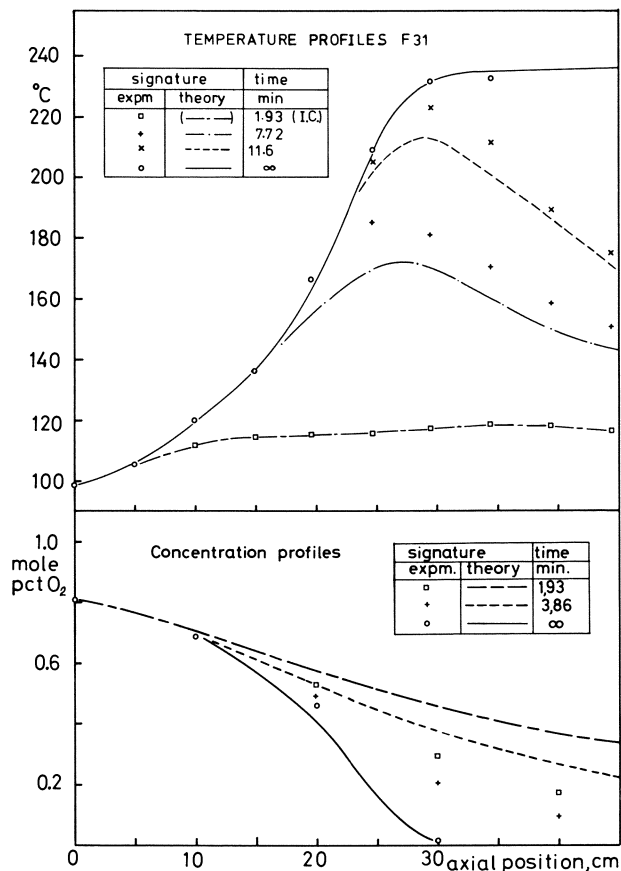


Figure 4. Startup profiles for F31. Measured temperature profile at 1.93 min is used as initial condition for simulation.

Mass Transport Parameter. Calculations have shown that even if the Peclet number for mass transport is of the order of 2–300, the mass dispersion has some influence on the reactor dynamics. Here we have used (17)

$$Pe_m = 2 \frac{L}{d} = 270$$

Results

Results from dynamic experiments on the reactor are shown in Figures 4–8. Figure 4 shows a startup experiment for F31. Oxygen is suddenly added to the inlet stream after the bed has been heated to the inlet temperature. The oxygen concentration profile changes very fast in the beginning. Later the dynamic behavior is characterized by the slowly changing temperature profile. However, there is no quantitative agreement in this slow dynamic period between the concentration profile and the temperature profile in the last part of the reactor. This discrepancy appears clearly from the comparison between the

simulated profiles and the experimental points. To eliminate possible irregularities in the oxygen feed just after the start of the experiment, the measured temperature profile after 1.9 min has been inserted as initial condition in the simulation. The startup experiment with F22 shows the same lack of quantitative agreement with simulation. No obvious reason for this behavior has been found.

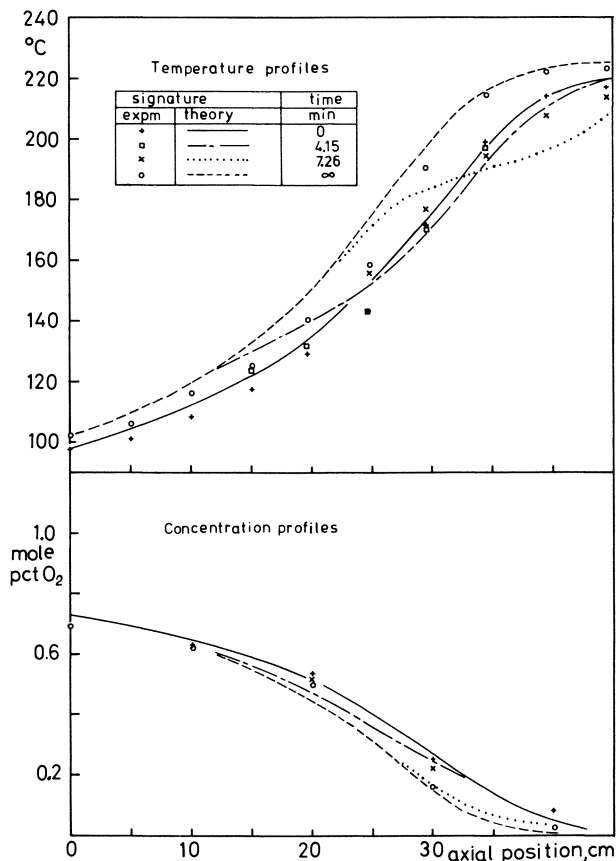


Figure 5. F22 response profiles to a step increase in inlet temperature of 4.3°C. Estimate II in Table IV was used as model parameters.

The reactor response following a step change in inlet temperature for F22 is shown in Figure 5 together with the simulated results. The “wrong way behavior” of the temperature profile in the last part of the reactor is evident for both the experiments and the simulations. The quantitative agreement is rather good when the discrepancies originating from differences in the measured and estimated stationary profiles are taken into account. To illustrate the dynamic deviation the time response at an axial position in the latter part of the reactor is shown in Figure 6.

Profiles of amplitude and phase of the primary temperature wave following pulse disturbances in inlet temperature at given frequencies have been plotted

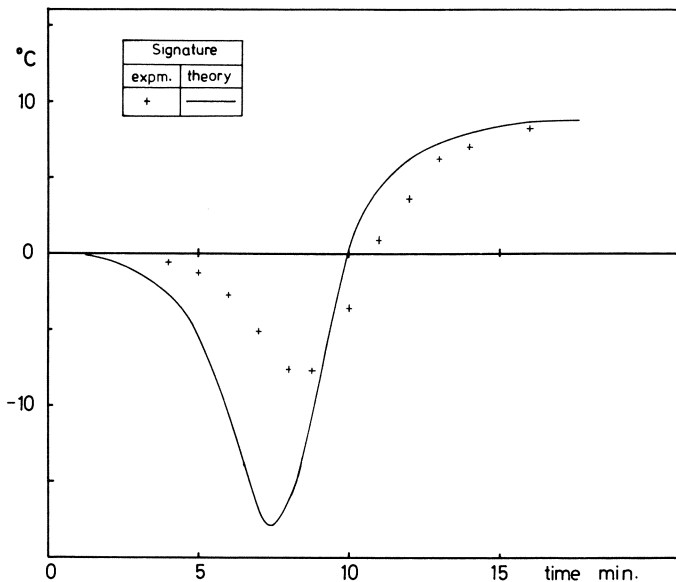


Figure 6. F22 time response at axial position 39.5 cm to same disturbance as in Figure 5

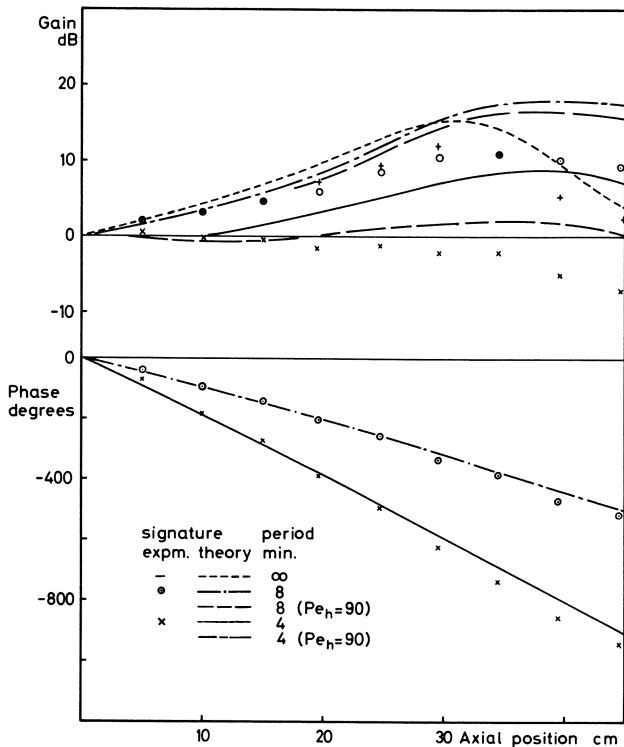


Figure 7. Temperature amplitude ratio and phase angle profiles for F22 at discrete disturbance frequencies of inlet temperature. Estimate 2 in Table IV was used as model parameters. In one set of theoretical profiles Pe_h is reduced to 90.

in Figures 7 and 8. For the phase curves, which in the first part of the reactor essentially exhibit the time lag from the thermal residence time, the agreement between experiment and theory is good. But the theoretical amplitude profiles all show higher gain than has been found experimentally, especially in the reaction zone. The discrepancy is not believed to be caused by nonlinear effects even if the experimental pulse response has pronounced nonlinear character—such as wave distortion and movement of the mean value at a given position to a higher average than the stationary level (*cf.* Ref. 9, Figures 9–12). Inaccurate determination of the kinetic parameters or an inadequate kinetic model might be better explanations of the high theoretical amplification of the inlet temperature in the reaction zone.

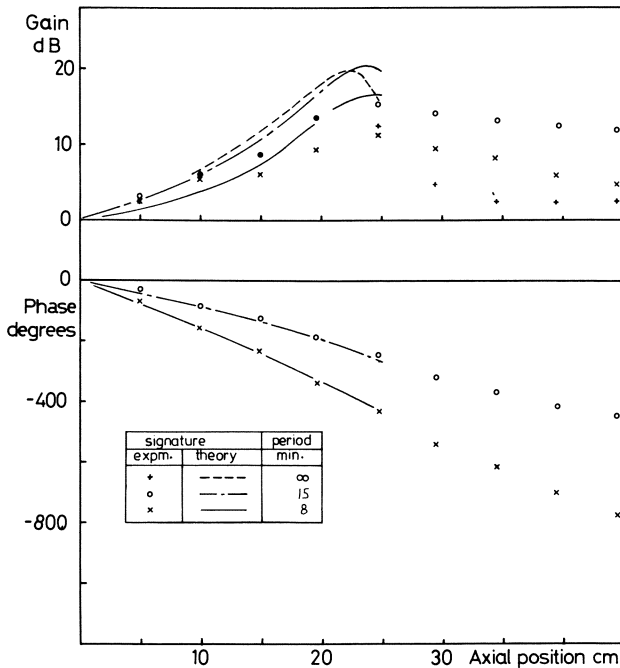


Figure 8. Temperature amplitude ratio and phase angle profiles for F31 at discrete disturbance frequencies of inlet temperature. Theoretical profiles were only calculated for first half of reactor.

On Figure 7 the influence of the value of the Peclet number is illustrated. A relatively small decrease of $Pe = 115$ to 90 changes the theoretical amplitude ratio only mildly at the lower frequency (period = 8 min). At the higher frequency (period = 4 min) the effect is much more pronounced. Thus the estimated Peclet number seems to be the right order of magnitude.

Summary and Conclusion

The experimental reactor has an almost ideal behavior since secondary dispersion effects (*e.g.*, large wall heat capacities) are suppressed to a high

degree. The Peclet number for heat transport based on particle diameter is determined by regenerator experiments to about 0.8. Experiments in a differential reactor showed that the catalyst activity depends on pretreatment. The kinetic parameters in a simple model are therefore determined by curve fitting to stationary profiles in the integral reactor. The parameters determined in this way are inserted in a homogeneous type model, and the dynamic experiments are compared with simulations. Qualitative agreement is found for all types of experiments, but some discrepancies are found, especially in the most reactive part of the reactor. This lack of agreement is believed to be caused by inaccurate determination of the reaction kinetics. On the other hand the Peclet number seems to be correctly determined from heat regenerator experiments.

Acknowledgment

The authors thank H. Livbjerg for helpful advice in planning the apparatus and M. L. Michelsen for preparing the frequency analysis program and for helpful discussions.

Nomenclature

a	external catalyst surface/reactor volume, cm^{-1}
C_p	specific heat capacity, $\text{cal}/(\text{gram } ^\circ\text{C})$
D	reactor diameter, cm
D_h	defined, Equation 8
D_m	defined, Equation 9
d	catalyst diameter, cm
E	activation energy, cal/mole
g	mass flow rate (empty tube), $\text{gram}/(\text{cm}^2 \text{ sec})$
$-\Delta H$	heat of reaction = 116,300 cal/mole
H_g	$ahL/(gC_{pg})$
h	heat transfer coefficient, $\text{cal}/(\text{cm}^2 \text{ sec } ^\circ\text{C})$
k_e	effective heat conductivity of catalyst, $\text{cal}/(\text{cm sec } ^\circ\text{C})$
k_f	frequency factor, $\text{mole}/(\text{cm}^3 \text{ sec atm})$
L	reactor length, cm
l	axial coordinate, cm
M	molecular weight, gram/mole
P	partial pressure of oxygen, atm
P_{tot}	average pressure in reactor, atm
ΔP	pressure drop in reactor, atm
Pe_h	Peclet number for heat transport
Pe_m	Peclet number for mass transport
R_g	gas constant, $\text{cal}/(\text{mole } ^\circ\text{K})$
Re	reaction rate, $\text{mole}/(\text{cm}^3 \text{ sec})$
S	internal catalyst surface area, cm^2/gram
s	La Place parameter, sec^{-1} or min^{-1}
T	temperature, $^\circ\text{C}$ or $^\circ\text{K}$
t	dimensionless time, t'/τ
t'	time, sec or min
V	catalyst pore volume, cm^3/gram
x	P/P_0
Y	mole fraction of oxygen
y	T/T_0 (T in $^\circ\text{K}$)
z	l/L

Greek Letters

γ	$E/(R_g T_0)$
ϵ_1	reactor porosity
ϵ_2	catalyst porosity
ρ	density, gram/cm ³
ν	$hd/(2k_e)$
τ	thermal residence time, min or sec

Subscripts

g	gas
I	inlet condition
k	catalyst
0	stationary inlet condition

Literature Cited

1. Hansen, K. W., Livbjerg, H., Villadsen, J. V., *IFAC Symp. DISCOP*, Győr, Hungary, 1971, paper W1.
2. Froment, G. F., *5th Europ. Symp. Chem. Reaction Eng.*, Amsterdam, 1972, section 5.
3. Ray, W. H., *5th Europ. Symp. Chem. Reaction Eng.*, Amsterdam, 1972, section 8.
4. Padberg, G., Wicke, E., *Chem. Eng. Sci.* (1967) **22**, 1035.
5. Eigenberger, G., *Chem. Eng. Sci.* (1972) **27**, 1909.
6. Vanderveen, J. W., Luss, D., Amundson, N. R., *AIChE J.* (1968) **14**, 636.
7. Hoiberg, J. A., Ph.D. Thesis, University of California, Berkeley, 1969.
8. Hoiberg, J. A., Lyche, B. C., Foss, A. S., *AIChE J.* (1971) **17**, 1434.
9. Hansen, K. W., *Chem. Eng. Sci.* (1973) **28**, 723.
10. Maymo, J. A., Smith, J. M., *AIChE J.* (1966) **12**, 845.
11. Hansen, K. W., Jørgensen, S. B., *4th CHISA Congr.*, Prague, 1972, section J3.
12. Michelsen, M. L., Vakil, H. B., Foss, A. S., *Ind. Eng. Chem., Fundamentals* (1973) **12**, 323.
13. Hansen, K. W., Ph.D. Thesis, The Technical University of Denmark, 1970.
14. Villadsen, J. V., Sørensen, J. P., *Chem. Eng. Sci.* (1969) **24**, 1337.
15. Ferguson, N. B., Finlayson, B. A., *Chem. Eng. J.* (1970) **1**, 327.
16. Michelsen, M. L., *Chem. Eng. J.* (1972) **4**, 171.
17. Paris, J. R., Stevens, W. F., *Can. J. Chem. Eng.* (1970) **48**, 100.
18. Votruba, J., Hlavacek, V., Marek, M., *Chem. Eng. Sci.* (1972) **27**, 1845.
19. Marquardt, D. W., *J. Soc. Ind. Appl. Math.* (1963) **11**, 431.
20. Box, G. E. P., *Ann. N.Y. Acad. Sci.* (1960) **86**, 792.

RECEIVED January 2, 1974.

Parametric Sensitivity and Temperature Runaway in Heterogeneous Fixed Bed Reactors

COLIN MCGREAVY and COLIN I. ADDERLEY

Department of Chemical Engineering, The University of Leeds,
Leeds, LS2 9JT, England

A criterion for parametric sensitivity and temperature runaway in heterogeneous reactors is presented, and its relationship to the multiple steady states and the significant operating variables is demonstrated. Application to reactor design and control is discussed. We show how the practical range of operating conditions of the reactor may be rapidly established for any system so that design information relating the size of the reactor to "safe" operating conditions can be presented in a simple manner. This provides considerable insight into the behavior of the system for both the reactor designer and the control engineer since it is possible to establish a definitive relationship between local and global reactor stability and operating variables.

Instability in the operation of fixed bed reactors may arise from various causes; most attention has been focussed on that from multiple steady states caused by either the catalyst pellets or axial diffusion of heat and mass within the bed. However, as Froment (1) has shown, the latter is unlikely to occur in most reactors of industrial interest, and Thornton (2) and Adderley (3) have shown that even when regions of multiple steady states of the catalyst pellets are avoided considerable operational difficulties can arise because of parametric sensitivity near these regions. Whether instability occurs from multiple steady states or parametric sensitivity, the consequences are much the same: a tendency for high temperatures to develop causing catalyst and equipment damage, or "blowout" occurs resulting in poor reactant conversions. It is essential that such regions of instability be predicted for a given system so that reactor operation within these regions can be avoided; if this is not possible because of constraints (such as a maximum reactor size for a specific reactant conversion), appropriate control action can be applied in the event of system disturbances which would tend to cause temperature runaway or reaction "blowout."

Previous analyses of parametric sensitivity outside of regions of multiple solutions have dealt with quasi-homogeneous systems (4, 5) and are therefore

generally only applicable in the limiting case of non-porous catalyst pellets. Quasi-homogeneous and heterogeneous systems must be distinguished since the source of parametric sensitivity in each is quite different. In the former, it is caused by the exponential dependence of the reaction rate on temperature; in the latter it arises because of the mass and heat transport resistances both within and around the catalyst pellets (*i.e.* from the heterogeneity of the system). Consequently parametric sensitivity criteria derived for one system are not usually applicable to the other, and in particular, quasi-homogeneous criteria lead to conservative operating conditions for heterogeneous systems.

This paper discusses the application of a temperature runaway criterion to both the design and control of a heterogeneous reactor and shows how the relationship between local and global stability and the operating variables for a particular system can be established.

The Temperature Runaway Criterion

A criterion for the onset of temperature runaway and parametric sensitivity has been fully described by McGreavy and Adderley (6) who showed that for a single first-order irreversible reaction, the onset of temperature runaway can be characterized by a specific catalyst pellet temperature, t_s , which is a function of the interphase temperature difference, $(t - T)$. This followed from an examination of the heat balance of the isothermal pellet model (2) given in Equation 1.

$$t - T = \frac{B \text{Sh}_A (r - g)}{(sg + r)} \quad (1)$$

where:

$$r = \theta \exp\left(-\frac{1}{2t}\right)$$

$$g = \tanh(r)$$

$$s = \frac{\text{Sh}_A}{2} - 1$$

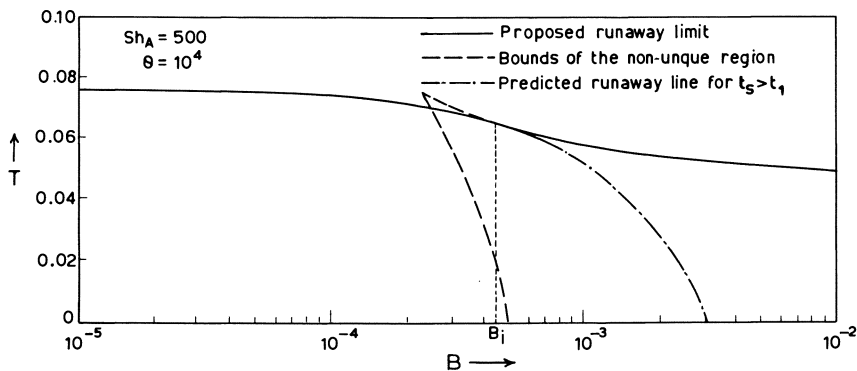


Figure 1. The runaway limit on the T vs. B phase diagram for a typical set of parameters

It was shown (6) that by setting $t = t_s$ in Equation 1, the coordinates of the locus of the temperature runaway line on the T vs. B phase diagram can be obtained. Figure 1 shows both the runaway line and the region of non-

unique solutions (7) on the T vs. B diagram for typical values of Sh_A and θ . The runaway line intersects the upper bound of the non-unique region (at $B = B_1$) which becomes the runaway line for $B > B_1$ since in this region $t_s > t_1$ (the pellet temperature on the upper bound of the non-unique region) and this has no meaning. In general, the desirable operating domain will be below the runaway line and to the left of the non-unique region.

The Use of the Runaway Criteria

General Considerations. By solving the equations describing the heterogeneous reactor, it is possible to plot longitudinal trajectories along various radii on the T vs. B phase diagram. The runaway line, together with the region of multiple solutions of the catalyst pellet, are drawn on the same diagram; if any of the trajectories cross the runaway line, then temperature runaway would tend to occur in the bed, and the reactor may be described as unstable. Even when a particular trajectory crosses the runaway line but does not go far past it, this still indicates potential instability and problems of control because the trajectory passes into a region of parametric sensitivity; high temperatures may develop during perturbations from this state. It is in indicating trajectories of this nature that the runaway criterion is particularly useful since, although high fluid temperatures are not apparent, the potential instability of the state is easily observed (3).

Figure 2 shows longitudinal reactor trajectories at various radial positions for a typical set of data. This graph shows that it may often be necessary to use the axial temperatures rather than, for example, the radial mean values, when attempting to choose operating conditions which avoid temperature runaway. Only radial mean temperatures are considered below. By using appropriate reactor models such as those developed by Thornton (2) and Turner (8), the analysis can be applied to the axial temperature profiles.

The reactor designer is usually confronted with a fixed set of parameters, and he must produce the best design within the freedom available. The fixed conditions are the reaction rate parameters and thermodynamic properties, the type of catalyst to be used, and the maximum allowable pressure drop across the bed. Thus, the degrees of freedom which remain are the inlet conditions, including the coolant temperature, and the dimensions of the reactor tube. However, total freedom in the choice of values for these parameters is never the case. With exothermic reactions the choice of gas flow rate is confined to a very narrow range. The upper constraint being that which produces the maximum allowable pressure drop, which is related to the tube and catalyst particle dimensions; the lower constraint is determined by the minimum allowable gas-to-tube wall heat transfer coefficient and gas-to-pellet mass transfer coefficient. Generally, since heat removal from the bed to the coolant is the most important process, the design will be based on the maximum available gas flow rate. In most situations the choice of tube diameter is restricted to a few sizes because of cost and availability, and is, therefore, not a true design variable. Thus, for a given system most parameters are fixed at the outset, or at best they are confined to very narrow limits, and only the inlet conditions and the tube length, below a certain maximum, remain as true design variables. Values of these parameters must then be chosen which give an economically satisfactory, safe design, avoiding temperature runaway or regions of instability.

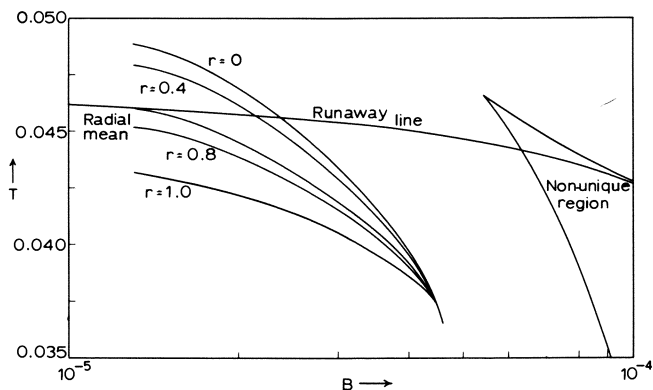


Figure 2. Reactor trajectories at various radial positions ($T_0 = 0.03655$, $T_c = 0.03742$, other data as given in Table I)

In the discussion below attention is mainly confined to the case of equal coolant and gas inlet temperatures since this is the situation commonly encountered in practice. It probably represents the worst case for exothermic reactions since heat removal is the greatest problem with these reactions, and therefore it would not be realistic to use a coolant temperature higher than the gas inlet value. Nevertheless, the methods may easily be extended to the case of differing coolant and inlet temperatures and even adiabatic operation.

Calculation of Values of Parameters Leading to Parametric Sensitivity and Runaway. Rigorous determination of critical reactor operating conditions, *i.e.* conditions which cause the reactor trajectory on the T vs. B phase diagram to reach the runaway line but not cross it, obviously requires numerical integration of the reactor equations. It is useful to map out the range of operating conditions to be considered to summarize the relationship between the significant variables.

A trivial, but necessarily stated upper limit to the inlet temperature of the gas at any inlet concentration is provided by the runaway line on the T vs. B diagram. However, the lower limit of the inlet temperature, and the coolant temperature often depend on the length of the reactor as well as the inlet concentration, although a value can be determined. For any given inlet and coolant temperature the range of inlet concentration which need be considered is easily determined. This range is more conveniently expressed in terms of the inlet value of the thermal load factor, B_1 , which is directly proportional to reactant concentration.

INLET CONCENTRATION. The upper limit on B_1 ($B_0 \times C_0$) is based on the assumption that the designer will wish to avoid reactor operation in the non-unique as well as the runaway region. Consider the point where the runaway line crosses the lower bound of the non-unique region on the T vs. B diagram. If the adiabatic trajectory through this point meets the line $T = T_0$ at a value of B outside of the non-unique region, then this value of B represents the maximum permissible inlet value to avoid operation in the non-unique region under adiabatic conditions. Normally this will be so because the slope of the adiabatic trajectory is much greater than that of the lower bound of the non-unique region. If this value of B lies inside the non-unique region, the maximum value of B_1 is given by the value of B where the line $T = T_0$ crosses the lower

bound of the non-unique region. Let the value of B in either case be B_{iu} . Since reactor trajectories on the T vs. B diagram start with an adiabatic slope for $T_o = T_c$ and then bend under this line because of heat exchange between the bed and the coolant, then B_{iu} represents an approximate upper limit on B_1 to avoid the non-unique region under non-adiabatic conditions. Clearly it will be less than the actual upper limit for non-adiabatic operation, but it thus guarantees that if temperature runaway is avoided then, for $B_1 < B_{iu}$, operation in the non-unique region is also avoided. It is therefore the best obtainable upper limit on B_1 at any inlet temperature without extensive computation. B_{iu} may be easily determined either graphically or computationally using the equations for the non-unique region and the runaway line.

The lower limit on B_1 , B_{il} , to be considered is also easily determined. Using the one-dimensional heterogeneous reactor model developed by Thornton (2) for the $A \rightarrow B$ reaction scheme, the heat and mass balances can be written in dimensionless form as:

$$\frac{dC_A}{dZ} = -G_2 \eta k_1 C_A \quad (2)$$

$$\frac{dT}{dZ} = G_4 (t - T) - \frac{2Nu_w^*}{G_3} (T - T_c) \quad (3)$$

with appropriate boundary conditions:

where: $k_1 = \theta^2 \exp(-1/t)$

and using the isothermal catalyst pellet model:

$$t = T + B \text{Sh}_A(r - g)/(sg + r)$$

$$\eta = 1.5 \text{Sh}_A(r - g)/(k_1(sg + r))$$

From Equations 2 and 3, the reactor trajectory on the T vs. B diagram is given by:

$$\frac{dT}{dB} = -\frac{G_4(t - T)}{G_2 \eta k_1 B} + \frac{2Nu_w^*(T - T_c)}{G_2 G_3 \eta k_1 B} \quad (4)$$

When the trajectory passes through a maximum, $dT/dB = 0$. (A maximum on the phase trajectory corresponds to a maximum in the axial temperature profile). Hence, the locus of this maximum is given by:

$$G_4(t_m - T_m) = \frac{2Nu_w^*}{G_3} (T_m - T_c) \quad (5)$$

Subscript m denotes the value at the maximum. The pellet temperature, t_m , is given by Equation 1, with $B = B_m$.

The only operating variable in Equation 5 is the coolant temperature, T_c . The loci given by Equation 5 on the T vs. B diagram are shown in Figure 3 for various values of T_c . Thus for a given value of coolant temperature the locus of the maximum of the reactor trajectories may be plotted. One of the criteria for temperature runaway given by Van Welsenaere and Froment (5) for quasi-homogeneous reactors is based on the fact that the locus of the reactor trajectory maxima passes through a maximum and appears to have been derived empirically by observation of computed reactor trajectories. Examination of the equations of the quasi-homogeneous system shows a fundamental reason why this criterion applies for that system (3). The results for quasi-homogeneous systems may not be applied to a heterogeneous reactor because of

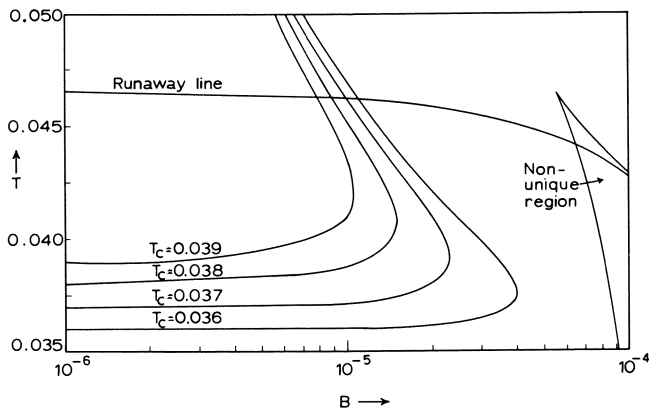


Figure 3. Maxima curves for various coolant temperatures (data as given in Table I)

their conservatism (6). The actual position of the maximum on this locus depends on the inlet reactant concentration and temperature when $T_o \neq T_c$. A critical trajectory will be one where the maximum occurs at the runaway line, that is, the locus of the maximum given by Equation 5 which crosses the runaway line since increasing the value of B_1 from the critical value will cause the maximum of the trajectory to occur above the runaway line; decreasing B_1 will ensure that the maximum occurs below this line. At the maximum of the critical trajectory, co-ordinate (B_{cr}, T_{cr}) on the T vs. B diagram, the pellet temperature is given by t_s . Thus substituting $t_m = t_s$ in Equation 5 and solving this equation simultaneously with Equation 1 gives B_{cr} and T_{cr} for any values of T_c .

The slope of the adiabatic line on the phase diagram is given by:

$$\frac{dT}{dB} = - \frac{G_4}{1.5G_2} \quad (6)$$

Therefore the value of B_1 , B_{11} , for the adiabatic line through the maximum of the critical trajectory is given by:

$$B_{11} = B_{cr} + 1.5G_2(T_{cr} - T_o)/G_4 \quad (7)$$

Since the adiabatic trajectory on the T vs. B diagram has the steepest slope, B_{11} is the minimum value of B_1 which need be considered for a given inlet and coolant temperature. For $B_1 < B_{11}$ at $T_o = T_c$ the maximum temperature in the reactor will always occur below the runaway line. This lower limit on B_1 tends to be slightly conservative—the actual value is a little larger. A method of extrapolation proposed by Van Welsenaere and Froment (5) for quasi-homogeneous reactors cannot be used to obtain a less conservative estimate in the heterogeneous case because of the difference of the shape of the reactor trajectories in this case. Nevertheless, B_{11} represents a very useful limit since safe operation for $B_1 < B_{11}$, at a given coolant and inlet temperature, can be guaranteed. At low values of inlet and coolant temperature the situation which is illustrated schematically in Figure 4 may arise. Clearly, the value of B_{11} determined by the above method and shown in Figure 4, will be very conservative in such situations. A better estimate of B_{11} may be obtained by

drawing the adiabatic trajectory through the maximum value of B on the curve giving the locus of the trajectory maxima, *i.e.* through the point marked X in Figure 4. This requires finding the coordinates of point X on the T vs. B diagram. From Equations 1 and 5 the locus of the trajectory maxima may be expressed as:

$$B_m = 2Nu_w^*(T_m - T_c)(sg_m + r_m)/G_sG_4Sh_A(r_m - g_m) \quad (8)$$

The point X may then be found by differentiating Equation 8 at the point where $(dB/dT)_m = 0$. Let the coordinates of the point X , evaluated in this way be (B_a, T_a) . If B_{il} determined from the adiabatic line through the point where the locus of the trajectory maxima crosses the runaway line, as described above, is less than B_a , then a better estimate of B_{il} may be obtained by replacing B_{cr} and T_{cr} in Equation 7 by B_a and T_a .

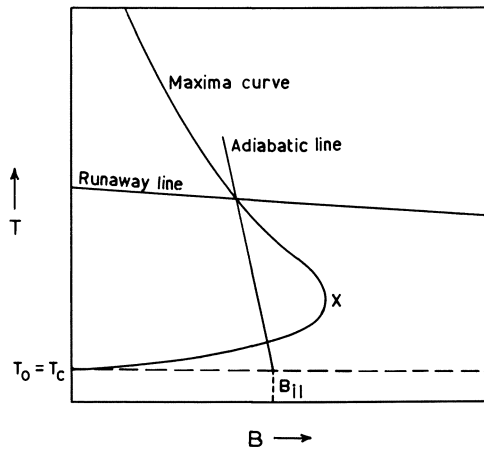


Figure 4. Schematic showing the location of B_{ii} on the T vs. B phase diagram

COOLANT AND INLET TEMPERATURE. From Figure 3 it can be seen that as T_c is decreased, B_a increases and approaches the non-unique region as does B_{cr} . This may be used to calculate the theoretical minimum coolant and inlet temperature which need be considered for any system if operation in the non-unique region is to be avoided. B_{iu} is the maximum value of B_i which avoids operation in the non-unique region at a given coolant and inlet temperature as discussed previously. Since B_{il} (from Equation 7), B_a and B_{iu} may be expressed as functions of T_c , the minimum value of T_c and T_0 for $T_0 = T_c$ which need be considered is that for which:

$$B_i \geq B_{iu} \text{ if } B_{il} > B_a$$

or

$$B_a \geq B_{iu} \text{ if } B_{il} < B_a$$

This minimum value of T_0 , for $T_0 = T_c$, is easily determined computationally; graphically the task may be somewhat arduous. This minimum value of T_0 applies only for $T_0 = T_c$ and for operation outside of the non-unique region. For any value of T_0 less than that determined in this way, safe operation is guaranteed for $B_i < B_{iu}$. In most cases this value of T_0 results in virtually

no reaction occurring within the bed because of the very low initial reaction rates. However, its evaluation is useful in cases where no information exists on the sort of temperature which must be used for a particular system. When this is the case, it precludes the necessity of trial and error integration of the reactor equations to find a minimum working value.

Thus, for any inlet and coolant temperature the range of inlet concentration, or thermal load factor, which will produce temperature runaway depending on the length of the reactor may be rapidly determined. For a given inlet and coolant temperature, the range of inlet concentration described by B_{il} and B_{iu} for any system is a working range. Temperature runaway may occur at any value of B_i within this range, and the remaining parameter which determines this is the reactor length. The calculation of this range is simply a means of saving unnecessary work in, for example, the solution of the bed equations. The upper limit on B , B_{iu} , is somewhat different in nature from the lower limit, B_{il} . At a given inlet and coolant temperature with the inlet value of B less than B_{iu} , the steady-state reactor trajectory will not pass through the non-unique region provided that the length of the reactor is such that it does not cross the runaway line. The lower limit on the inlet value of B , B_{il} , is, however, a global limit for the given inlet and coolant temperature. For all inlet values of B less than B_{il} at the inlet and coolant temperature for which B_{il} is determined, the reactor trajectory will never cross the runaway line whatever the length of the reactor. This could be used as an upper limit on the value of B_i so that safe operation is always guaranteed for any reactor length. However, it tends to lead to rather conservative reactor designs because of the low reaction rates at low values of B_i ; very long reactors would be necessary to achieve a given conversion. In some circumstances using B_{il} as an upper limit may be acceptable, particularly when the pressure drops in the bed and, therefore, the length of the reactor is not a serious constraint or when there is very great uncertainty in, for example, the heat transfer parameters. Figure 5 shows schematically the two limits on B_i and their relation to other regions on the T vs. B phase diagram.

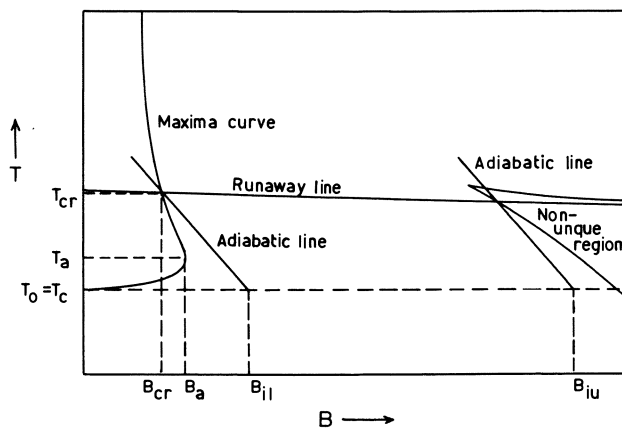


Figure 5. Schematic showing the location of the operating region for a particular coolant and inlet temperature

REACTOR LENGTH. Once the range of B_1 has been determined at a chosen inlet and coolant temperature, some value of B_1 within that range must be found for which temperature runaway will not occur for a particular reactor length. If the reactor length is chosen first, then trial and error solution of the bed equations is necessary to find a suitable value of B_1 at each value of the inlet and coolant temperatures. This can be wasteful and time consuming. This method would also fail to give a total picture of the situation since information about only a single reactor length would be obtained. A better approach is to integrate the bed equations for various values of B_1 in the range of B_{11} to B_{1u} for different values of inlet (and coolant) temperature and determine the critical length of the reactor in each case. This is not a particularly time consuming process with a one-dimensional model of the reactor, especially since the runaway line in the form of the pellet temperature at runaway, t_{rs} , can be used to stop the integration at each value of B_1 as soon as the reactor trajectory reaches the runaway limit. The range of coolant temperature which need be considered may often be further limited by the nature of the cooling medium; for highly exothermic reactions a molten salt coolant is usually employed, and so the minimum coolant temperature is determined by the viscosity decrease with temperature. This can result in a minimum value greater than that determined by the previously described method. The upper limit on the coolant temperature may be less than that described by the runaway line, for $T_o = T_c$, since above a certain temperature, charring and decomposition of the salt or an unacceptable increase in corrosion rate on the reactor tube may occur.

Table I. Data Used for Case Study

B_0	4.602×10^{-6}
E	$26.6 \times 10^{-3}(\text{cal/gram mole})$
G_2	0.0949
G_3	0.84
G_4	76.85
Nu_w	2.0
Nu_w^*	1.33
Sh_A	500.0
θ	10^6

The length of the reactor determined in this way at each set of inlet conditions is then the critical or maximum value for which temperature runaway can be avoided in the steady state at those conditions. By this method, charts of critical length *vs.* inlet concentration, or thermal load factor, at various inlet and coolant temperatures, may be drawn for the system. Figure 6 shows such a chart for the data given in Table I. The critical length in Figure 6 is expressed as a dimensionless value for convenience, although this is not essential and actual length could be used.

Adderley (3) has shown the effect of the parameters θ , Nu_w and Sh_A on such a chart. Only one chart is usually required for a particular system since these parameters are constant for previously stated reasons.

The advantage of this approach is that the chart conveys at a glance the critical inlet conditions for any reactor length or conversely the critical length for any inlet conditions; thus the task of the designer is simplified. A scale of pressure drop can be added to the charts, and during their preparation similar graphs of reactor outlet conditions or reactant conversion at various lengths may also be drawn.

Application to Reactor Control. Perhaps the greatest advantage of this approach to the design problem is the information which these charts give

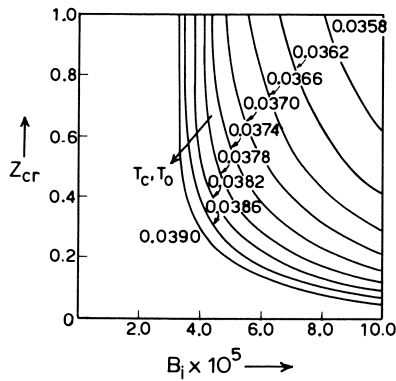


Figure 6. Effect of the inlet conditions on maximum reactor length to avoid temperature runaway (data as given in Table I)

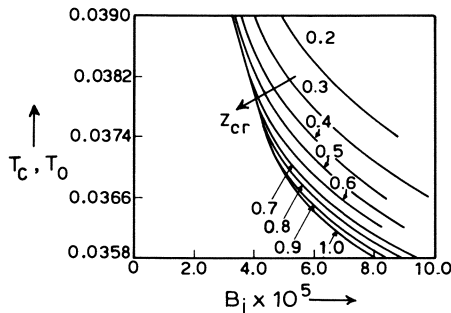


Figure 7. Inlet conditions to avoid temperature runaway for various reactor lengths

concerning the control of the reactor and the way this may be used to design control systems. For example, using Figure 6, graphs like Figure 7 can be constructed which show a plot of critical inlet temperature against critical inlet thermal load factor as a function of reactor length. Thus, for a particular reactor length, this graph shows how, if one of the inlet conditions is varied, the other should be adjusted to prevent the temperature runaway in the new steady state. This information has to be related to the dynamic changes but can be easily included in a computer control algorithm for a particular reactor. When a reactor is operating in the steady state at critical or subcritical conditions and a perturbation of one of the inlet variables occurs, a control algorithm indicates the adjustment on the other inlet conditions to compensate for this perturbation. It is essential that this adjustment does not lead to temperature runaway in the new steady state; thus, some form of check or constraint on the control action is required. One method of checking is to integrate the bed equations at the new values of the inlet conditions. Unfortunately, this would be a lengthy process for a control algorithm, and undesirable behavior could occur before the control action takes place, especially when the reactor is operating close to the critical conditions. What is required, therefore, is a much more rapid check on the proposed control action; this can be provided

by graphs like Figure 7. For a particular reactor length, the plot of critical inlet temperature against critical inlet thermal load factor, or concentration, can be fitted to a simple algebraic function. For example, the line for the reactor length corresponding to $z = 1.0$ in Figure 7 may be fitted to a function of the form:

$$T_o = P \exp(-B_i) (1 + B_i)/B_i^2 + Q \quad (9)$$

where P and Q are constants which may be determined by a simple regression analysis. Clearly, since the curves of Figure 7 form a family, a similar relationship between T_o and B_i may be used for other reactor lengths by appropriate adjustment of P and Q . This functional relationship between the critical inlet conditions for the reactor may be included in the control algorithm. Thus, once the new values of the inlet variables have been selected by the controller, Equation 9 may be used to rapidly check whether or not they will lead to a safe operating state. For example, if at the new value of inlet concentration the value of T_o computed by Equation 9 is less than the selected value of inlet temperature, then the new steady state will lead to temperature runaway, so a smaller value of inlet temperature is required.

This procedure will be much quicker than any attempt at solving the bed equations and by providing more insight into the general behavior will lead to far better and more effective reactor control. Since the global stability of the reactor is essentially expressed by Equation 9 as a function of the inlet conditions, it may not be necessary to monitor the conditions in other parts of the reactor; this will depend on the tightness of the control and the type of perturbations which are likely to occur.

Conclusion

A method of identifying regions of temperature runaway in fixed bed catalytic reactors was described which is expressed in terms of the intrinsic properties of heterogeneous systems. Use of this method in design and control of reactors was discussed. The results can be summarized in simple charts which give information about those inlet conditions and reactor dimensions which would lead to critical situations, thus enabling a full evaluation of the various reactor operating conditions. These charts may also be used in the development and implementation of computer control strategies for the reactor. This method can also be applied when other system constraints exist (*e.g.* a maximum reactor outlet temperature) even when these constraints do not coincide with the runaway criterion. Although the proposed criterion for temperature runaway has been developed for the steady state operation of the reactor, it may be used to give an insight into the dynamic behavior since it defines a region of parametric sensitivity in state variable space.

Nomenclature

A_o	Pre-exponential factor in Arrhenius rate expression
b	Pellet radius
C_o	Reference concentration (reactor inlet concentration)
C_A'	Concentration of reactant A in the fluid
c_p	Heat capacity of the fluid
D_p	Effective radial diffusivity of the reactant in the pellet

D_r	Effective interstitial radial diffusivity in the bed
e	Bed voidage
E	Activation energy
h	Heat transfer coefficient at the pellet surface
$(-\Delta H)$	Heat of reaction
k_g	Mass transfer coefficient at the pellet surface
K_r	Effective radial conductivity of the fluid in the bed
L	Reactor length
R_g	Gas constant
R	Reactor radius
r'	Distance from reactor center line
T_c'	Coolant temperature
T_f'	Fluid temperature
T_p'	Pellet temperature
U	Overall tube-wall heat transfer coefficient
u	Interstitial fluid velocity
Z'	Distance from reactor entrance
θ	$b \sqrt{\frac{A_o}{D_p}}$
ρ	Density of the fluid
η	Effectiveness factor

Dimensionless Variables and Parameter Groups

B_o	$\frac{(-\Delta H) D_p C_o R_g}{2bhE}$
B	Dimensionless thermal load factor = $B_o \times C_A$
B_i	Inlet value of B
C_A	Dimensionless fluid concentration = $\frac{C_A'}{C_o}$
G_2	$\frac{(1-e)LD_p}{b^2ue}$
G_3	$\frac{R^2 u \rho c_p}{K_r L}$
G_4	$\frac{3hL(1-e)}{bu\rho c_p e}$
Nu_w	Wall Nusselt number = $\frac{RU}{K_r e}$
Nu_w^*	Effective overall wall Nusselt number = $\frac{4 Nu_w}{(4 + Nu_w)}$
r_R	Dimensionless radial coordinate in the reactor = r'/R
Sh_A	Sherwood number = $\frac{2bk_g}{D_p}$
t	Dimensionless pellet temperature = $\frac{R_g T_p'}{E}$
T	Dimensionless fluid temperature = $\frac{R_g T_f'}{E}$
T_o	Inlet value of T
T_c	Dimensionless coolant temperature = $\frac{R_g T_c'}{E}$
Z	Dimensionless axial coordinate in the reactor = $\frac{Z'}{L}$

Literature Cited

1. Froment, G. F., *Proc. 5th European/2nd Intern. Symp. Chem. Reaction Eng., Amsterdam*, 1972.
2. Thornton, J. M., Ph.D. Dissertation, University of Leeds (1970).
3. Adderley, C. I., Ph.D. Dissertation, University of Leeds (1973).
4. Barkeley, C. R., *Chem. Eng. Progr., Symp. Ser.* (1959) **55**, 25.
5. Van Welsenaere, R. J., Froment, G. F., *Chem. Eng. Sci.* (1970) **25**, 1503.
6. McGreavy, C., Adderley, C. I., *Chem. Eng. Sci.* (1973) **28**, 577.
7. McGreavy, C., Thornton, J. M., *Can. J. Chem. Eng.* (1970) **48**, 187.
8. Turner, K., Ph.D. Dissertation, University of Leeds (1970).

RECEIVED January 2, 1974. The Science Research Council provided financial support for one of the authors (C. I. Adderley) during this work.

Investigation of the Multiplicity of Steady States with the Generalized Recycle Reactor Model

TAI-CHENG YANG and HERBERT WEINSTEIN

Department of Chemical Engineering, Illinois Institute of Technology,
Chicago, Ill. 60616

BARRY BERNSTEIN

Department of Mathematics, Illinois Institute of Technology, Chicago, Ill. 60616

The effect of incomplete mixing on the multiplicity of steady states and reactor stability is studied with the generalized recycle reactor model. This model represents an infinite number of states of micromixing at any given level of macromixing. The concept of segregation of mass is extended to include that of temperature. Two extreme cases in energy segregation are studied. The high thermal conductivity model behaves as an isothermal reactor. The low thermal conductivity model represents complete segregation of energy. The method of invariant imbedding is used to solve the equations. Conversion curves show that for a given residence time distribution, multiple solutions can exist at some states of micromixing whereas only a single solution exists at other states. Stable optimal conditions can be found for each mixing pattern by varying the adjustable inlet conditions.

The multiplicity of steady-state operating points of chemical reactors has been studied for both varying reactor models and varying reaction models [see for example, Bilous and Amundson (1), Aris (2), and an excellent review of this work by Perlmutter (3)]. Almost all the analyses reported in the literature used the "ideal" plug flow tubular (PFTR) and backmix (or CSTR) reactors, the PFTR with recycle, and the PFTR with axial and/or radial dispersion. The limitation of all these models is that when using them to calculate chemical conversion, one usually can only couple a single description of the small-scale mixing, called micromixing, with each description of the gross mixing patterns which determine the distribution of holding or residence times of the reacting fluid. This latter type is called macromixing and is essentially a linear description of a nonlinear mixing process.

The operation of a reactor is not, however, limited to the discrete state of micromixing usually attached by a particular model to the state of macro-

mixing measured for that reactor. There are, in fact, an infinite number of micromixing states possible for any reactor which is described only by its residence time distribution (RTD), except for the PFTR. Because the state of micromixing is not necessarily that described by a single parameter model, instabilities may not be discovered in reactor design with these models. It is important, therefore, to be able to search through a spectrum of possible micromixing states for a given RTD to determine if multiple steady states can exist.

In this paper a model is formulated for the behavior of an adiabatic reactor system in which macro- and micromixing states can be varied independently. This model is then used to investigate the effects of variable micromixing on the number of steady-state operating points of a reactor system defined by its macromixing level or residence time distribution. The kinetic rate expressions used are limited to the n th-order type, and heat transfer across the boundary of the reactor system is not considered.

Method

Generalized Recycle Reactor Model for Micromixing. The RTD for n equal-sized CSTR's in series with recycle has been developed by Fu *et al.* (4). The RTD

$$E(t) = \frac{1}{R} \sum_{m=1}^{\infty} \left(\frac{R}{R+1} \right)^m \frac{(R+1)^{mn} n^{mn} t^{mn-1}}{\bar{t}^{mn} (mn-1)!} e^{-\frac{n(R+1)t}{\bar{t}}} \quad (1)$$

has first moment $\bar{t} = V/q$ and dimensionless variance

$$\bar{\sigma}^2 = \frac{1+nR}{n(1+R)} \quad (2)$$

where R is the recycle ratio. Both $E(t)$ and σ^2 have, as parameters, R and n . The dimensionless variance, $\bar{\sigma}^2$, or the first and second moments are usually taken to be enough information to describe the RTD because higher moments of experimental RTD curves are greatly affected by measurement error. Dohan and Weinstein (5) imposed two assumptions to this n stirred tanks in series with recycle model—*viz.*, (a) allow for perfect mixing at the junction between the recycle stream and fresh feed stream, (b) operate the reactor internal to the recycle loop under a completely segregated flow condition. Thus, they separated the effects of micromixing and macromixing with a fixed $\bar{\sigma}^2$. They showed that a negligible error is introduced because moments of the RTD higher than the second are not held constant. Holding $\bar{\sigma}^2$ constant, one can vary n and R simultaneously to describe different levels of micromixing for a fixed state of macromixing. For the special case of $\bar{\sigma}^2 = 1$, a single-stirred tank with variable recycle can be used to describe any level of micromixing.

Addition of the Energy Balance Equation. To study the multiplicity of steady states of a nonisothermal reacting system, we must add an energy balance equation to the generalized recycle reactor model. To do this we must model the heat transfer within the reactor in a manner analogous to the modeling of the mass transfer. The state of micromixing corresponds to this mass transfer modeling.

When the thermal conductivity is very high, heat transfers swiftly through the reacting fluid. In the limiting case of infinite thermal conductivity, temperature is uniform throughout the reacting fluid down to the molecular scale.

This statement defines our high thermal conductivity model. In this case there is no segregation of energy. On the other hand, when the thermal conductivity is very low, heat transfer through the reacting fluid is very slow. In the limiting case of zero thermal conductivity, energy is completely segregated. This is our low thermal conductivity model. For an exothermic reaction, a "point" of fluid [defined by Danckwerts (6)] is, according to the low conductivity model, exposed to low temperature when the concentration of reactant is high and to high temperature when the concentration of reactant is low. According to the high conductivity model, however, a point of fluid sees only a single temperature during its passage through the reactor.

We limit ourselves here to these two limiting cases to describe the mode of heat transfer within the reactor. The model based on the generalized recycle reactor model with the temperatures is shown in Figure 1. At point A, we allow perfect mixing. Inside the reactor, reacting fluid is completely segregated. Temperature is either completely segregated or uniform.

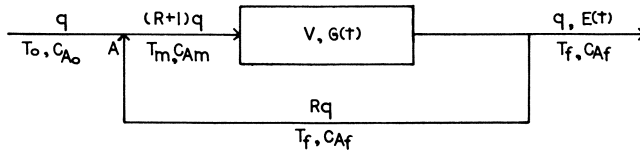


Figure 1. Recycle flow system

High Thermal Conductivity Model for One-Stirred Tank with Recycle ($\bar{\sigma}^2 = 1$). For a system with the dimensionless variance of the RTD, $\bar{\sigma}^2$, equal to 1, the degree of segregation is uniquely represented by the recycle ratio. When $R = 0$, $J = 1$, the system is completely segregated. When $R \rightarrow \infty$, $J \rightarrow 0$, the system is completely mixed. Varying R from zero to infinity, we have a spectrum of intermediate degrees of segregation or micromixing.

A mass balance at point A gives

$$C_{Am} = \frac{1}{1+R} C_{Ao} + \frac{R}{1+R} C_{Af} \quad (3)$$

where C_{Af} is given by

$$C_{Af} = \int_0^{\infty} (C_A)_{\text{batch}} G(t) dt \quad (4)$$

The first passage time distribution of a single-stirred tank is given by

$$G(t) = \frac{1}{\tau} e^{-\frac{t}{\tau}} \quad (5)$$

where $\tau = V/(1+R)q$.

For an n th-order reaction

$$\frac{d(C_A)_{\text{batch}}}{dt} = -k (C_A)^n_{\text{batch}}, \quad (6)$$

with initial condition $C_A(0) = C_{Am}$.

We have for a 1/2-order reaction, noting that reactant A will go to complete conversion at time equal to $(2/k)C_{Am}^{1/2}$ in a batch reactor,

$$C_{Af} = C_{Am} - C_{Am}^{1/2} k\tau + 1/2 K^2\tau^2 \left[1 - \exp\left(-\frac{2 C_{Am}^{1/2}}{k\tau}\right) \right] \quad (7)$$

For a first-order reaction, we have

$$C_{Af} = \frac{C_{Ao}}{1 + k\left(\frac{V}{q}\right)} \quad (8)$$

Finally, for a second-order reaction, we have

$$C_{Af} = C_{Am} \alpha e^\alpha E_i(\alpha) \quad (9)$$

where $\alpha = 1/C_{Am}k\tau$, and $E_i(\alpha)$ is the exponential integral.

An energy balance at point A gives

$$T_m = \frac{1}{1+R} T_o + \frac{R}{1+R} T_f \quad (10)$$

and an energy balance over the internal reactor gives

$$T_f = T_o + \frac{(1+R)(-\Delta H_R)}{\rho C_p} (C_{Am} - C_{Af}) \quad (11)$$

Substituting Equation 3 into Equation 11, we obtain

$$T_f = T_o + \frac{C_{Ao}(-\Delta H_R)}{\rho C_p} x_A \quad (12)$$

This gives a straight line for conversion *vs.* exit temperature. The intersection(s) of this (these) line(s) with the curve of the solution of mass balance equation is (are) the operating point(s) of this system. Calculations are straightforward. For a first-order reaction, Equation 8 is independent of recycle ratio. For the second-order reaction, the exponential integral can be evaluated by numerical integration or by a polynomial approximation.

In the limiting case $R \rightarrow \infty$ it can be shown that the asymptotic solution is given by (7):

$$T = -\frac{E/R_\alpha}{\ln \frac{1-x_m}{Dx_m^n}} \quad (13)$$

where n is reaction order and $D = k_o C_{Ao}^{n-1} V/q$. We also note that $x_m = x_f$ in the limit.

Low Thermal Conductivity Model for One-Stirred Tank with Recycle ($\bar{\sigma}^2 = 1$). In the low thermal conductivity model, batch reactor information on concentration and temperature are coupled. Mass and energy balances around point A give

$$x_m = \frac{1}{1+R} + \frac{R}{1+R} x_f \quad (14)$$

$$y_m = \frac{1}{1+R} + \frac{R}{1+R} y_f \quad (15)$$

At the exit of the system,

$$x_f = \int_0^\infty x_{\text{batch}} G(\theta) d\theta \quad (16)$$

$$\text{and} \quad y_t = \int_0^\infty y_{\text{batch}} G(\theta) d\theta \quad (17)$$

where $G(\theta) = \exp(-\theta)$ for a single stirred tank.

For an n th-order reaction, the batch reactor information is given by the equations

$$\frac{dx}{d\theta} = -K e^{-A/\nu} x^n \quad (18)$$

$$\text{and} \quad \frac{dy}{d\theta} = B \frac{dx}{d\theta} \quad (19)$$

with initial conditions $x(0) = x_m$, $y(0) = y_m$, and where $K = k_0 C_{A_0}^{n-1} \tau$, $A = E/R_g T_0$, and $B = \frac{\Delta H_R C_{A_0}}{\rho C_p T_0}$. Equation 19 can be integrated for a given system with fixed physical properties to give

$$y = Bx + (1 - B) \quad (20)$$

This integration of one of the differential equations in the batch reactor description still does not make the solution straightforward. Because of the non-linearity, Equations 18 and 19 cannot be solved analytically in terms of the initial conditions. An imbedding technique is used to obtain the numerical solutions and is presented below.

for the limiting case $R \rightarrow \infty$, the asymptotic solution is given by (7):

$$T_0 = Px_m - P - \frac{E/R_g}{\ln \frac{1 - x_m}{Dx_m^n}} \quad (21)$$

where $P = -BT_0$, a positive number for exothermic reactions, and $D = k_0 C_{A_0}^{n-1} V/q$. We note again that in the asymptotic case, $x_t = x_m$.

High Thermal Conductivity Model for n Stirred Tanks in Series with Recycle ($\bar{\sigma}^2 < 1$). For the model of n equal-sized stirred tanks in series with recycle, $\bar{\sigma}^2 = 1/n_{\min}$, where n_{\min} is the number of tanks with $R = 0$. This case of n_{\min} , $R = 0$, corresponds to segregated flow. As n increases from n_{\min} to infinity, R increases from zero to R_{\max} , and the degree of segregation falls from one to its minimum value corresponding to the maximum mixedness state for that $\bar{\sigma}^2$. We consider second-order reactions only.

It is shown [Fu *et al.* (4)] that the first passage time distribution in this case with total volume of reactors equal to V is given by

$$G(t) = \frac{n^n t^{n-1}}{\tau^n (n-1)!} e^{-\frac{nt}{\tau}} \quad (22)$$

Defining the dimensionless time as $\theta = nt/\tau$, we have

$$G(\theta) = \frac{\theta^{n-1}}{(n-1)!} e^{-\theta} \quad (23)$$

Thus for a second-order reaction with uniform reactor temperature

$$C_{A_t} = C_{A_m} \int_0^\infty \frac{\theta^{n-1} e^{-\theta}}{(n-1)! \left(1 + \frac{C_{A_m} k \tau}{n} \theta\right)} d\theta \quad (24)$$

where C_{Am} is given by Equation 3. The energy balance is given by Equation 12. Equation 24 is integrated numerically, and the intersections of the integral with Equation 12 represent the solutions for this case.

Low Thermal Conductivity Model of n Stirred Tanks in Series with Recycle ($\bar{\sigma}^2 < 1$). We consider this case with second-order kinetics only. The batch reactor behavior then takes the form,

$$\frac{dx}{d\theta} = -K e^{-A/y} x^2 \quad (25)$$

with initial condition, $x(0) = x_m$, and where $y = Bx + (1 - B)$, $K = k_0 C_{Ao} \tau/n$

Thus

$$x_t = \int_0^\infty [x(\theta)]_{\text{batch}} \frac{\theta^{n-1} e^{-\theta}}{(n-1)!} d\theta \quad (26)$$

Again, Equations 14, 25, and 26 are solved by the method of invariant imbedding.

Solution by the Method of Invariant Imbedding. The solution of integral and differential equations can be reduced to solving a family of initial-value problems by combining invariant imbedding techniques (8). We demonstrate the technique here with the solution of the low conductivity model in a single-stirred tank for second-order reactions.

Equation 25 has the initial condition, $x(0) = X_m$; X_m is one of the parameters of this equation. Let us differentiate Equation 25 for $n = 2$ with respect to x_m , holding R fixed. We get

$$\frac{\partial}{\partial \theta} \frac{\partial x}{\partial x_m} = p \frac{\partial x}{\partial x_m} + q \quad (27)$$

where

$$p = -Kx \left(\frac{ABx}{y^2} + 2 \right) \exp(-A/y)$$

$$q = -\frac{KAx^2}{yT_o} \left(1 + \frac{B}{y} - \frac{Bx}{y} \right) \exp(-A/y) \frac{dT_o}{dx_m}$$

$$y = Bx + (1 - B).$$

For a given $x(\theta)$, Equation 27 is a differential equation for $\partial x/\partial x_m$. Let $\phi(x_m, \theta)$ be the solution of

$$\frac{\partial \phi}{\partial \theta} = p\phi, \quad \phi(x_m, 0) = 1 \quad (28)$$

By variation of parameters we seek u such that $\partial x/\partial x_m = \phi u$ satisfies the inhomogeneous Equation 27. We have

$$\frac{\partial x}{\partial x_m} = \phi(x_m, \theta) \left[\int_0^\theta \phi^{-1}(x_m, \xi) q(x_m, \xi) d\xi + 1 \right] \quad (29)$$

ϕ can be solved from Equations 25 and 28,

$$\phi = \frac{x^2}{x_m^2} \exp(A/y_m - A/y) \quad (30)$$

where

$$y_m = Bx_m + (1 - B)$$

Substituting Equation 16 into Equation 14 and differentiating with respect to x_m , we have

$$\frac{dT_o}{dx_m} = \frac{R \int_0^\infty \phi e^{-\theta} d\theta - (1 + R)}{R \int_0^\infty \phi(\theta) \left[\int_0^\theta \phi^{-1}(\xi) \frac{KAx^2}{yT_o} \left(1 + \frac{B}{y} - \frac{Bx}{y} \right) \exp(-A/y) d\xi \right] e^{-\theta} d\theta} \quad (31)$$

Equations 20, 30, 31, and 29 must be solved. We take n equally spaced mesh points $0 = \theta_1 < \theta_2 < \dots < \theta_n$, $\theta_{k+1} = k\theta_2$, $k = 1, \dots, n - 1$ along the θ axis. For each mesh point θ_i there is a corresponding $x(\theta_i)$. After expressing the integrations in terms of the mesh points by a numerical integration formula, we obtain from Equation 29 a set of n simultaneous ordinary differential equations. To start the solution we must first seek a set of $x(\theta_i)$, $i = 1, \dots, n$ at a particular R and T_o which is to be used as the initial conditions in Equation 29. Using Equations 29 and 30, these equations are readily solved to the desired accuracy by the invariant imbedding technique. To suppress errors which build up after many steps, we correct our solution from time to time by Newton's iteration.

Results and Discussion

To illustrate the effects of micromixing, calculations were made with all models discussed above with an arbitrarily chosen but reasonable set of physical constants: $E = 3 \times 10^4$, $R_g = 1.987$, $k_o = 1 \times 10^{11}$, $C_{A0} = 1$, $V/q = 100$, and $\Delta H_R \cdot C_{A0} / \rho C_p = 150$, each with a consistent set of units.

The results are presented in Figures 2-5. The high conductivity model cases are shown as plots of conversion *vs.* exit temperature with recycle ratio (degree of segregation) as parameter. The energy balance line is also shown. The low conductivity model results are given as plots of conversion *vs.* feed temperature with recycle ratio as parameter.

Single-Stirred Tank. The results for the single-stirred tank are presented for both $\frac{1}{2}$ - and second-order reactions. Figure 2 shows the $\frac{1}{2}$ -order kinetics for high and low conductivity cases. Consider first the high conductivity case. The interval of the T_f axis contained between the two parallel straight (energy balance) lines represents the range of exit (or inlet) temperatures for which multiple steady states are possible. For given inlet temperature and recycle ratio, multiple steady states are possible if the corresponding energy balance line has more than one intersection with the curve of constant recycle ratio. There is no unusual behavior visible because the maximum conversion occurs at the maximum mixedness condition. The region of multiple steady states is not really a function of the particular model of micromixing used. However, the low conductivity case in this figure exhibits some unusual behavior. Multiple steady states which are shown by multiple conversion values for a given inlet temperature exist only for about $R \geq 0.5$. For $R < 0.5$, there is only a single operating point for each inlet temperature. In both high and low conductivity cases, multiple steady-state operating points can be avoided by operating at inlet temperatures above about 181°C while the lower limit on inlet temperature is not the same for both cases. One might be tempted to explore further the possibility of operating at low inlet temperatures, $\sim 120^\circ$ -140°C, and almost complete conversion indicated by this figure.

The results for the high and low conductivity cases for the single-stirred tank and second-order kinetics are shown in Figure 3. These results differ

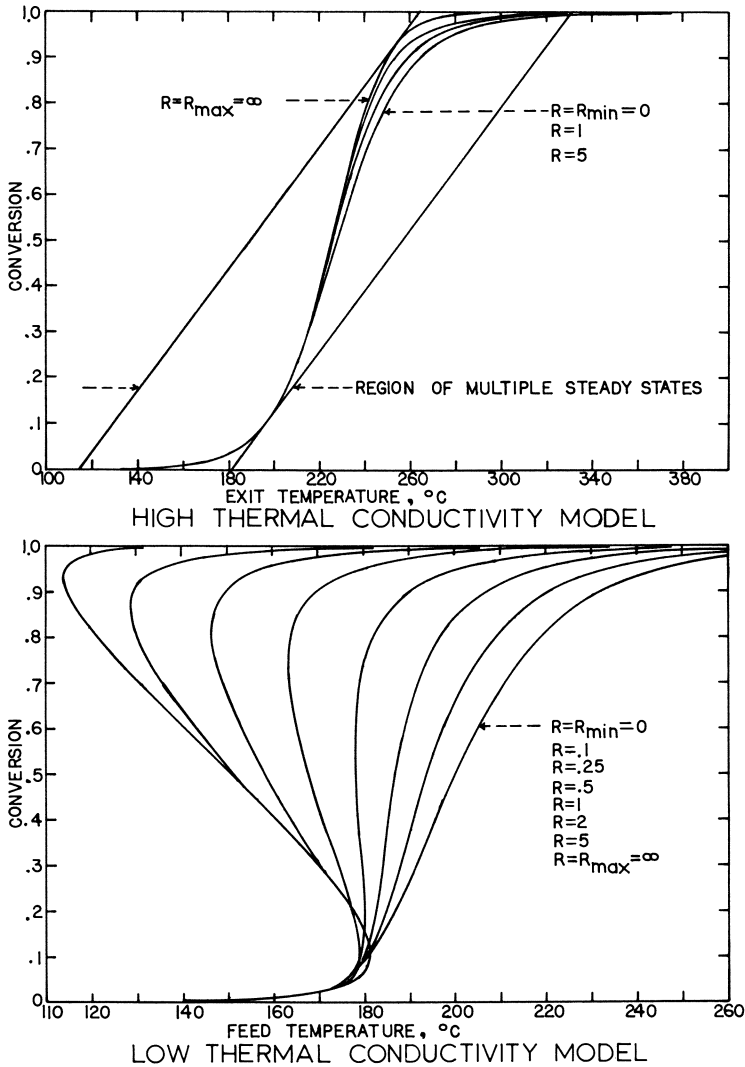


Figure 2. Conversion as a function of temperature for RTD variance, $\bar{\sigma}^2 = 1$, $\frac{1}{2}$ -order reaction (physical constants given in text)

from the previous cases in only two respects: (a) the segregated flow, $R = 0$, yields the maximum conversions for the high conductivity model; (b) the degree of the effects is different. The minimum inlet for which high conversion can be obtained without a multiplicity of steady states is still about the same. The lower bound on the inlet temperature for the multiple steady-state region is, however, higher than for the $\frac{1}{2}$ -order case, about 160°C .

It is interesting to extend the criterion for stability to the model of one-stirred tank with recycle, low conductivity case. One can show from the asymptotic solution, *e.g.*, for the second-order reaction (7),

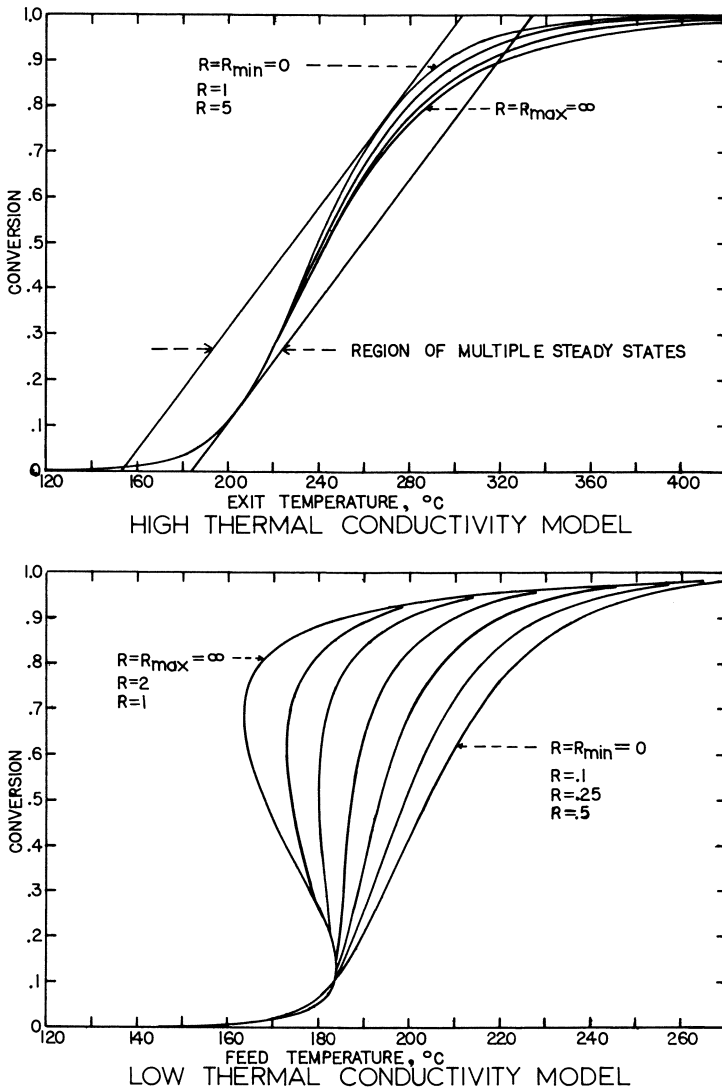


Figure 3. Conversion as a function of temperature for RTD variance, $\sigma^2 = 1$, second-order reaction (physical constants given in text)

$$\frac{dT_o}{dX_m} = \frac{-\frac{(E/R_g)X_m}{1-X_m} - 2(E/R_g) + PX_m \left(\ln \frac{1-X_m}{DX_m^2} \right)^2}{X_m \left(\ln \frac{1-X_m}{DX_m^2} \right)^2} \quad (32)$$

For endothermic reactions, $P < 0$, and we always have $dT_o/dX_m < 0$, which means the system is stable. For moderate exothermic reactions, $P > 0$, and we still have $dT_o/dX_m < 0$ and a stable system. Only for highly exothermic reactions, $P \gg 0$, is $dT_o/dX_m > 0$, indicating that the system has a region of instability.

n -Stirred Tanks in Series with Recycle, $\bar{\sigma}^2 < 1$. Calculations were made on the model of n stirred tanks in series with recycle, with both high and low conductivity cases and with second-order kinetics. The results for $\bar{\sigma}^2 = 0.5$ are shown in Figure 4, and those for $\bar{\sigma}^2 = 0.2$ are shown in Figure 5. Both figures indicate there is essentially no micromixing effect for the high conductivity model. The band of conversions caused by variation in micromixing, $R = 0$ to R_{\max} , is essentially a line. In these two figures the effects of micromixing are more apparent in the results for the low conductivity model. The trends are the same as in Figure 3. As $\bar{\sigma}^2$ becomes smaller, the permissible

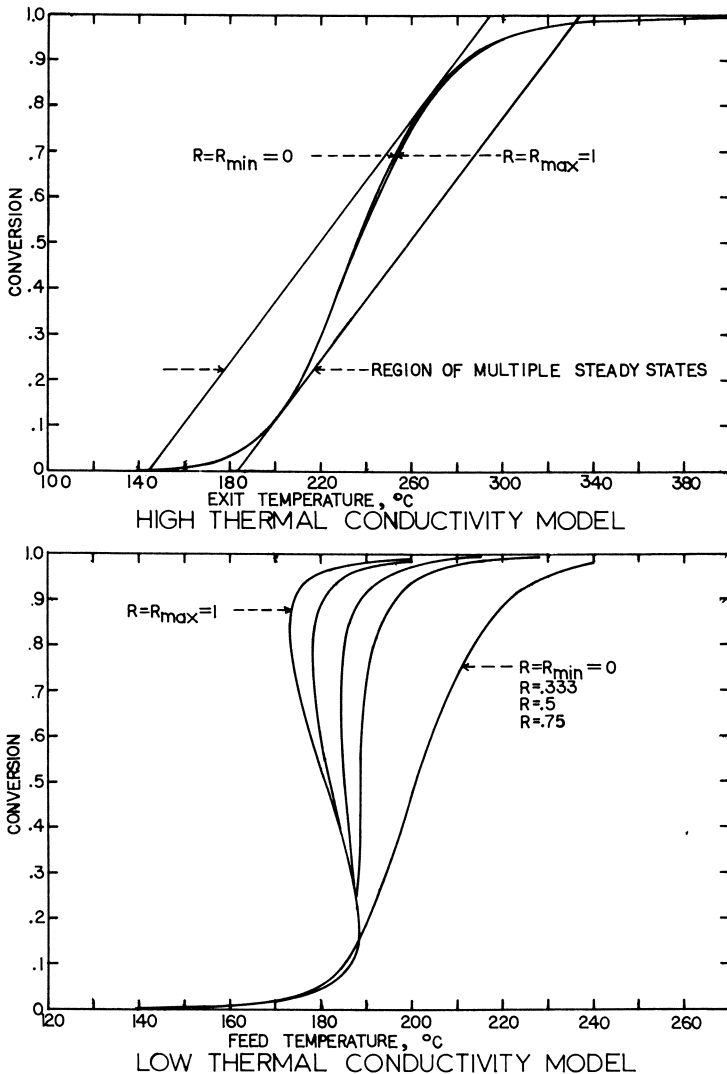


Figure 4. Conversion as a function of temperature for RTD variance, $\bar{\sigma}^2 = 0.5$, second-order reaction (physical constants given in text)

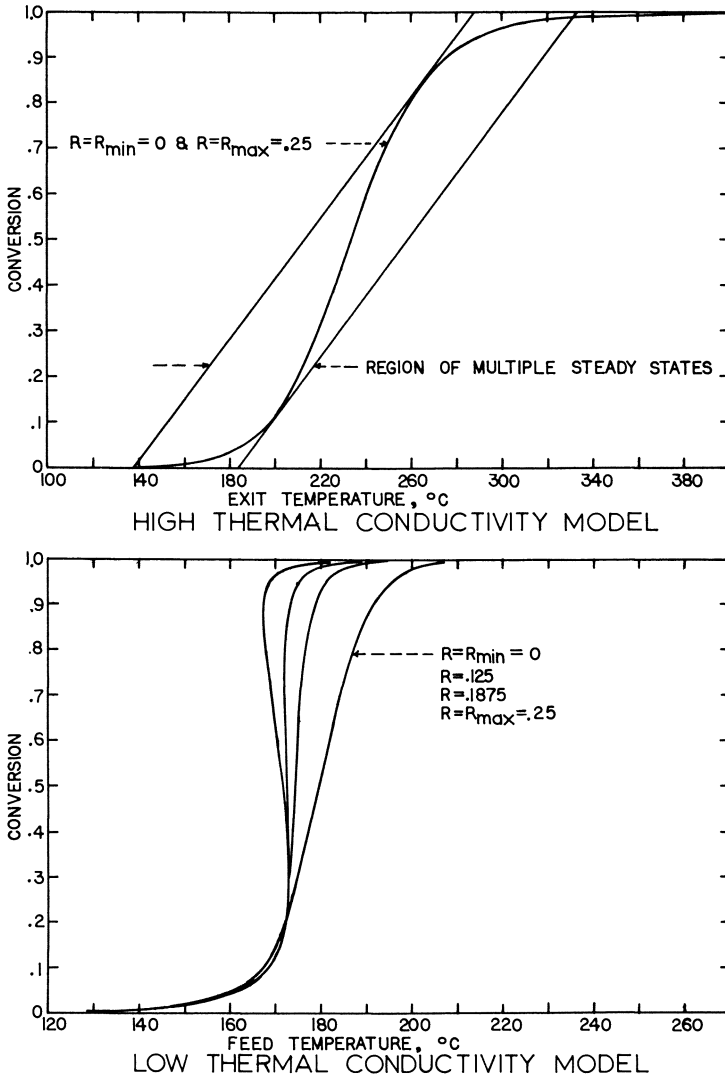


Figure 5. Conversion as a function of temperature for RTD variance, $\sigma^2 = 0.2$, second-order reaction (physical constants given in text)

amount of micromixing becomes smaller, and the effects of varying the micromixing level must diminish (*cf.* the low conductivity case of Figure 4 with those of Figure 5). The band of inlet temperatures which covers the range of large conversion change is much narrower for $\sigma^2 = 0.2$ than for $\sigma^2 = 0.5$.

These latter two figures also indicate that calculations made for a reactor model which allows for a single value for the degree of segregation can give misleading results on the existence of multiple steady states. However, at least in these figures if the inlet temperature is chosen high enough either to avoid multiple states where the simple reactor model indicates their presence, or high

enough to obtain close to complete conversion in the case where the simple model does not indicate the presence of multiple steady states, then high conversion and a single steady-state operating point are ensured. Intermediate conversion cases cannot be discussed in detail here because the single set of physical constants chosen provides for a very large gradient in conversion over a short temperature range.

Nomenclature

A	$E/R_g T_o$, dimensionless
B	$\Delta H_R C_{A_o} / \rho C_p T_o$, dimensionless
C_A	Concentration of A, gram-mole/liter
C_p	Specific heat, cal/gram-mole, °K
D	$k_o C_{A_o}^{n-1} V / q$, dimensionless
E	Activation energy, cal/gram-mole
$E(t)$	Residence time distribution of a system
$G(t)$	First passage time distribution of internal reactors
$G(\theta)$	Dimensionless first passage time distribution of internal reactors
ΔH_R	Heat of reaction, cal/gram-mole of reactant
J	Degree of segregation
k	Reaction rate constant, (mole/liter) ¹⁻ⁿ /hr
k_o	Frequency factor
K	$k_o C_{A_o}^{n-1} \tau / n$, dimensionless
n	Order of reaction or number of tanks
p	Group of variables given by Equation 27
P	$\Delta H_R C_{A_o} / \rho C_p$, °K
q	Volumetric flow rate, liters/hr, or group of variables given by Equation 27
R	Recycle ratio
R_g	Ideal gas law constant, 1.987 cal/gram-mole, °K
t	Time, hr
\bar{t}	V / q , hr
T	Temperature, °K
V	Total volume of reactor(s), liters
x	Dimensionless concentration, C_A / C_{A_o}
y	Dimensionless temperature, T / T_o

Greek Symbols

θ	t / τ or nt / τ , dimensionless time
ξ	A dummy variable
ρ	Molar density, gram-mole/liter
σ^2	Dimensionless variance of residence time distribution
τ	$V / (1 + R) q$, hr
ϕ	A parameter

Subscripts

f	Leaving or final conditions
m	Inlet condition to internal reactor(s)
o	Inlet or fresh feed conditions to a system

Literature Cited

1. Bilous, O., Amundson, N. R., *A.I.Ch.E. J.* (1955) **1**, 513.
2. Aris, R., *Chem. Eng. Sci.* (1969) **24**, 149.

3. Perlmutter, D. D., "Stability of Chemical Reactors," Prentice-Hall, Englewood Cliffs, N. J., 1972.
4. Fu, B. J., Weinstein, H., Bernstein, B., Shaffer, A. B., *Ind. Eng. Chem. Proc. Design Dev.* (1971) **10**, 501.
5. Dohan, L. A., Weinstein, H., *Ind. Eng. Chem., Fundamentals* (1973) **12**, 64.
6. Danckwerts, P. V., *Chem. Eng. Sci.* (1958) **8**, 93.
7. Yang, T. C., Ph.D. Thesis, Illinois Institute of Technology, Chicago (1974).
8. Kalaba, R., Ruspini, E. H., *J. Computat. Phys.* (1971) **8**, 489.

RECEIVED January 2, 1974.

Experimental Study of Multiple Steady States in Adiabatic Catalytic Systems

VLADIMÍR HLAVÁČEK and JAROSLAV VOTRUBA

Department of Chemical Engineering, Institute of Chemical Technology, Prague 6, Suchbátarova 1903, Czechoslovakia

Experimental results which can be used to model the behavior of a strongly exothermic reaction (carbon monoxide oxidation) in catalytic tubular systems is reported. Both one-phase and two-phase models (plug flow, axial dispersion, cell model) were used. Theoretical results are compared with the experimental observation of regions of multiplicity. The effect of inlet temperature, CO concentration, gas velocity, and length of the system on the region of multiplicity were studied experimentally. In an adiabatic tubular system, three distinct steady state profiles were observed. Experimental results on multiple steady states are presented for both tubular packed bed and honeycomb structures. The applicability of various models is discussed.

Simultaneous heat and mass transfer and exothermic chemical reaction in packed catalytic systems have been of great interest in designing and operating tubular catalytic reactors. Generally, for a strong exothermic reaction, multiple steady states can be expected. While ignition-extinction phenomena can be easily observed, quantitative data are not available.

This paper presents extensive experimental data on hysteresis phenomena in heterogeneous reaction systems for the oxidation of carbon monoxide over various catalysts. On various catalysts this reaction proceeds by different mechanisms which are described by different rate expressions (1, 2, 3). Numerous models of packed beds were tested. The study of packed beds is an area in which future development depends strongly on critical experimental (4, 5, 6, 7, 8) as well as theoretical evaluation (9, 10, 11, 12).

Experimental

To analyze the behavior of the CO oxidation reactor three types of catalyst were used: Pd on alumina cylinders (5.6×4 mm), Pt on alumina spheres ($d_p = 3.4$ mm), and CuO on alumina spheres ($d_p = 3.4$ mm). The honeycomb-structure catalyst was prepared from porous block alumina ($L = 6$ cm, $d_p = 3$ mm, $\epsilon = 23$) and was activated by CuO or Pt.

The Pd catalyst was a commercial product (0.2% Pd) while the unsupported cupric oxide catalyst was prepared by alkaline precipitation of cupric

nitrate according to the procedure devised by Ken Nobe (13). The Pt catalyst (0.4% Pt) was obtained by impregnating the catalyst carrier with a solution of Na_2PtCl_6 , followed by reduction with sodium formate. After washing and drying, the catalysts were activated *in situ* at 220°–250°C for ~ 48 hrs in pure oxygen. The catalyst maintained its full activity during an experimental run.

Oxidation of CO was studied in an adiabatic tubular reactor provided with an evacuated jacket covered by silver coating. A schematic of the reactor setup and a flow diagram of the apparatus are in Figures 1a and 1b. In each run the axial temperature profile was measured, and the composition of the exit gas was analyzed by the thermal conductivity cell. Flow rates of CO and oxygen were measured by variable-area flowmeters. Additional details concerning the experimental apparatus and procedure are available (14).

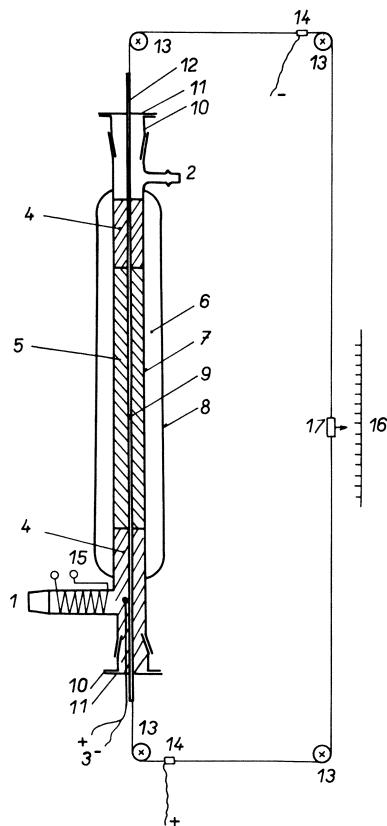


Figure 1a. Laboratory tubular adiabatic reactor

- 1 inlet for reacting gas
- 2 gas exit
- 3 auxiliary thermocouple
- 4 glass beads
- 5 catalyst
- 6 evacuated jacket with silver coating
- 7 internal tube
- 8 external tube
- 9 thermocouple
- 10 ground joints
- 11 silicon rubber packing gland
- 12 thermowell
- 13 rubber wheels
- 14 connection to temperature recorder
- 15 auxiliary preheater of inlet gas
- 16 scale
- 17 pointer

Results

The measurements on the adiabatic tubular reactor showed that exit conversion or temperature depend on certain parameters. The effects of initial temperature, inlet concentration, velocity, length of the bed, and reaction rate expression were studied.

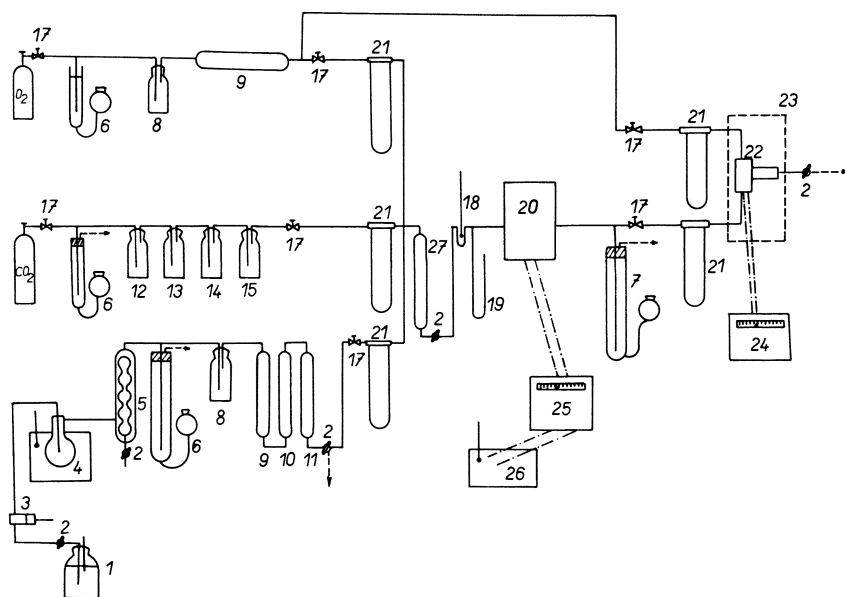


Figure 1b. Schematic of apparatus

- | | |
|--|----------------------------------|
| 1 storage tank with formic acid | 17 needle valve |
| 2 stopcocks | 18 thermometer |
| 3 micropump | 19 difference manometer |
| 4 heated flask with concentrated sulfuric acid | 20 reactor and thermostat |
| 5 cooler | 21 capillary flowmeter |
| 6, 7 manostats | 22 thermal conductivity detector |
| 9-11 drying apparatus | 23 thermostat |
| 12-15 sparging apparatus | 24, 25 recorders |
| | 26 reference thermocouple bath |

Effect of Inlet Temperature. The inlet temperature strongly affects the exit conversion because of the exponential dependence of the reaction rate constant on temperature. For a strong exothermic reaction in a tubular adiabatic system hysteresis phenomena can be observed. Figure 2 graphically compares the hysteresis loops measured for CuO, Pd, and Pt catalysts; the inlet CO concentration was 3%. The circles are the measured steady states, the arrows show the orientation of the hysteresis loop, and the dashed lines are the ignition and extinction transitions. The hysteresis loop for the CuO catalyst is short (15°–30°C) while the platinum catalysts are more apt to result in multiple steady states—*i.e.*, the hysteresis amounts to 30°–120°C. Figure 3 shows two steady-state profiles measured experimentally for a CuO catalyst in the region of the multiple steady states.

Effect of Inlet Concentration of Carbon Monoxide. In several experiments the exit conversion was followed as a function of inlet CO concentration. The results are shown in Figure 4 for Pd and CuO catalysts.

For a Pd catalyst, decreasing inlet CO concentration increases the reaction rate, resulting in a jump to the upper steady-state. Obviously the lower steady state disappears. On the other hand, for a CuO catalyst, for lower inlet CO concentration the upper steady state is extinguished, and a lower steady

state results. Obviously there are significant differences in reaction rate expressions for CO oxidation on both catalysts.

Effect of Inlet Gas Velocity. The gas velocity affects heat and mass transfer between the particles and flowing gas as well as the axial dispersion and heat conduction phenomena. Residence time influences exit conversion. For a reactor operating near the extinction boundary, increase of inlet velocity results in a sudden decrease of exit conversion. Sometimes this effect is called blowout (*cf.* Figure 5a). On the other hand, for a very active catalyst a decrease of inlet velocity leads to an ignited upper steady state (Figure 5b).

Figure 6 compares the shape of axial temperature profiles for different inlet velocities. The higher the inlet velocity, the more enlarged is the temperature profile.

Effect of Reactor Length. Recent theoretical studies (9, 10, 11, 12) have shown that for higher Peclet numbers—*i.e.* for longer beds—multiple solutions disappear. This conclusion was supported by our observations. For a bed packed with a CuO catalyst, multiple solutions disappeared with a bed length higher than 12 cm while for the Pt and Pd catalysts, multiple steady states were observed for a bed of 30 cm (*i.e.* for $Pe_M \sim 180$) (*cf.* Figure 7). Extrapolation of this observation indicates that multiple steady states occur also for high Peclet values. This agrees with our recent theoretical findings (11).

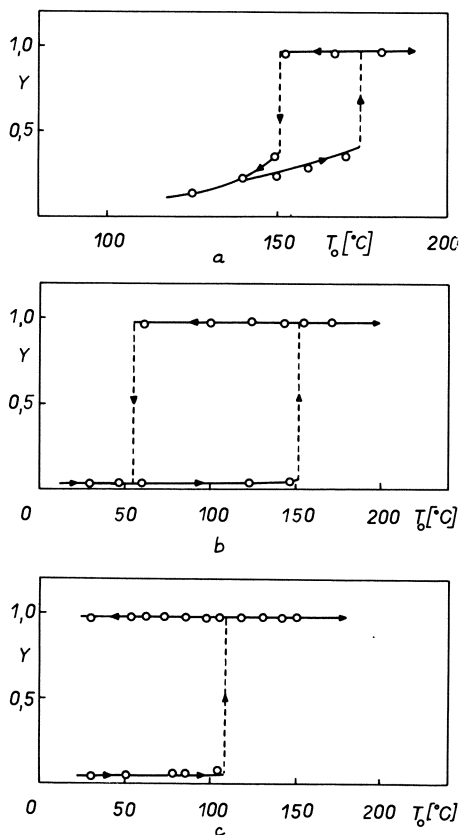


Figure 2. Dependence of exit conversion on inlet temperature: (a) CuO/Al₂O₃ (3% CO, L = 8.9 cm, Re = 40); (b) Pd/Al₂O₃ (3% CO, L = 6.8 cm, Re = 75); (c) Pt/Al₂O₃ (3% CO, L = 10.3 cm, Re = 58)

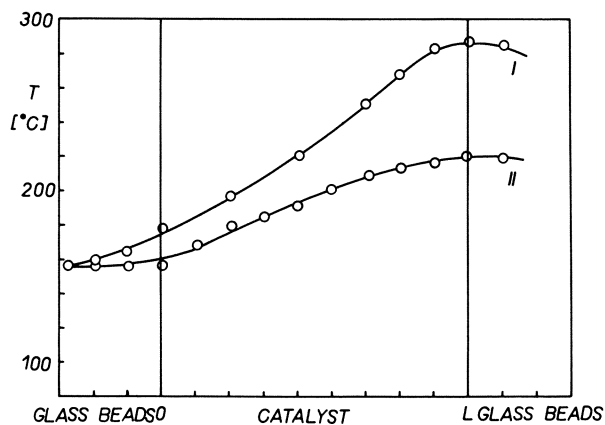


Figure 3. Typical temperature profiles in the bed. Region of multiplicity ($\text{CuO}/\text{Al}_2\text{O}_3$, 4% CO, $Re = 26$, $T_o = 166^\circ\text{C}$). I, $Y = 0.81$; II, $Y = 0.42$.

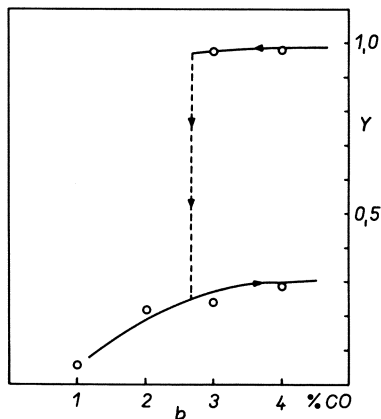
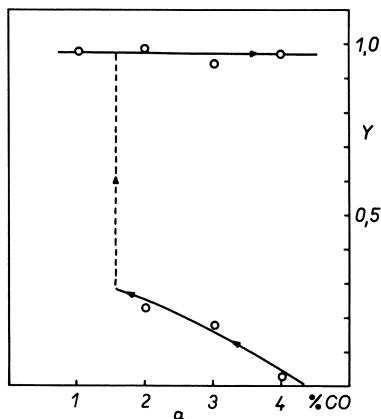


Figure 4. Dependence of exit conversion Y on CO inlet concentration: (a) $\text{Pd}/\text{Al}_2\text{O}_3$ ($Re = 100$, $L = 32$ cm, $T_o = 124^\circ\text{C}$); (b) $\text{CuO}/\text{Al}_2\text{O}_3$ ($Re = 34$, $L = 8.9$, $T_o = 148^\circ\text{C}$)

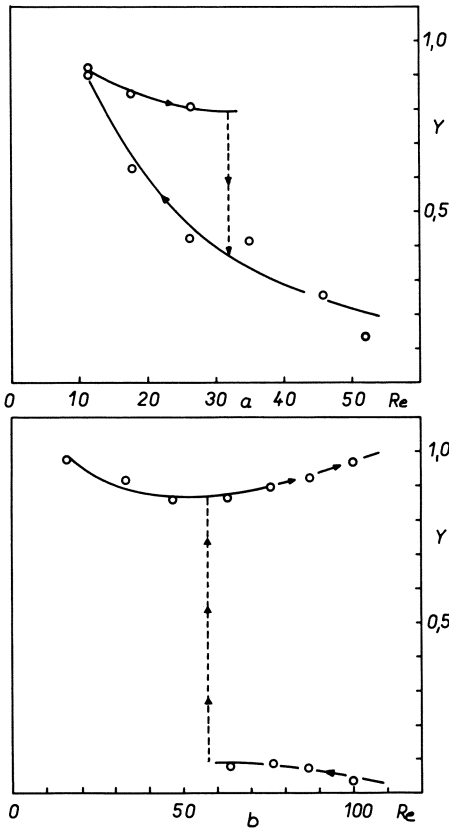


Figure 5. Dependence of exit conversion Y on Reynolds number (Re): (a) CuO/Al_2O_3 (4% CO, $L = 8.3$ cm, $T_o = 166^\circ C$); (b) Pd/Al_2O_3 (4% CO, $L = 6.8$ cm, $T_o = 145^\circ C$)

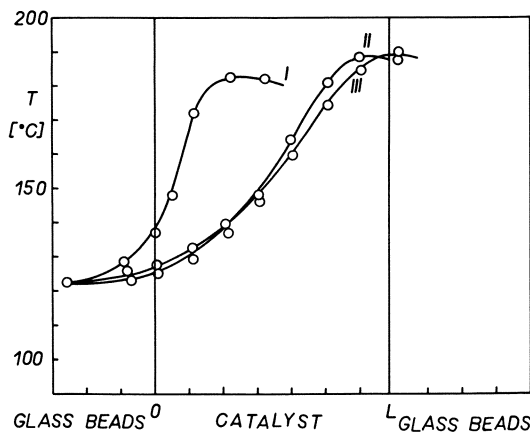


Figure 6. Effect of the inlet velocity on the shape of temperature profiles. CuO/Al_2O_3 ($L = 6.8$ cm, $T_o = 124^\circ C$, 1% CO). I, $Re = 75$, $Y = 0.99$; II, $Re = 150$, $Y = 0.98$; III, $Re = 218$, $Y = 0.99$.

Measurements on Honeycomb-Structure Catalyst. To compare the behavior of the packed catalytic bed with the honeycomb catalyst, CO oxidation was studied for identical inlet conditions. Figure 8 shows typical dependencies of inlet temperature (T) vs. exit conversion (Y) for Pd and CuO catalysts. Apparently the behavior of the honeycomb catalyst is similar to that of the packed bed; however, the domain of multiple steady states is wider. For a honeycomb-structure, the effect of axial heat transfer is more pronounced because of higher thermal conductivity. A detailed examination will be presented elsewhere (12).

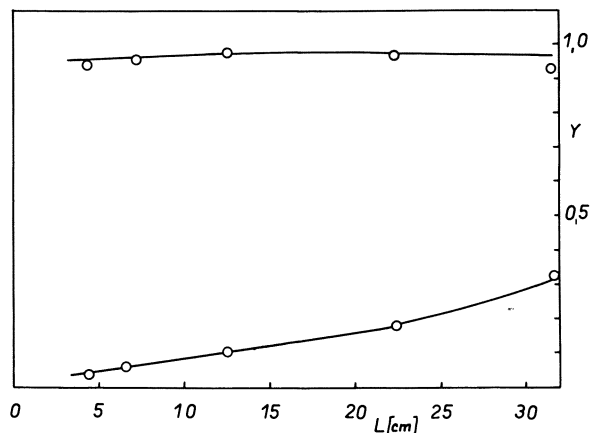


Figure 7. Dependence of exit conversion on reactor length. Pd/Al₂O₃ (3% CO, $Re = 63$, $T_0 = 124^\circ\text{C}$).

Occurrence of Three Steady States in Packed Bed. A detailed experimental exploration of temperature profiles in the reactor packed with the CuO catalyst showed near the extinction boundary three steady-state axial temperature profiles which were easily reproducible (Figure 9). Profile I was adjusted as follows: the reactor was heated to 148°C in the presence of pure oxygen only; after attaining the steady state, pure oxygen was replaced by 4% CO in oxygen at the same inlet velocity. The steady-state profile did not change in 8 hrs.

Profile II was obtained after a short temporary increase of initial temperature to 170°C . After returning the inlet temperature to the original value, a profile developed in 4 hrs. The shape of the profile did not change during 6 hrs.

Profile III was obtained after a short temporary increase of the inlet CO concentration to 15%. The steady state was attained after 3 hrs, and the reactor was run without any change in this steady state for 8 hrs. The experiment was repeated in the sequence I, II, and III with the same results.

Discussion

Measured temperature profiles and extinction and ignition phenomena can be used to discriminate between rival transport models for packed catalytic beds. While great effort has been devoted to problems of discriminating between kinetic models, a systematic study of transport models based on experimental data does not exist. Behavior of packed catalytic beds has been investi-

gated using a one-phase diffusional model. The study of other models remains theoretical. Hence, our primary objective was to compare directly eight different transport models under identical experimental conditions to see whether it was possible to fit the data by an appropriate model.

The reaction data were measured in a laboratory recycle reactor and after the discrimination procedure the "best" reaction rate expressions were chosen (Table I). Kinetic parameters were calculated with the modified version of Marquardt's method (15).

To determine the temperature profiles we had to use empirical correlations to evaluate the necessary parameters in transport equations. The effective axial thermal conductivity was calculated from our own results (16); axial mass dispersion was evaluated from Gunn's results (17). Coefficients of heat and mass transfer between the particle and the flowing gas were determined from equations recommended by Satterfield (18) and Aerov (19). These data are also reported in Table I.

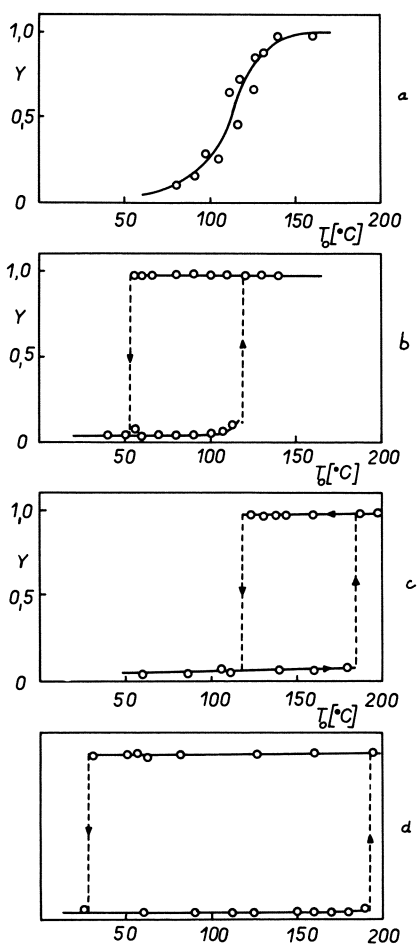


Figure 8. Dependence of exit conversion Y on inlet temperature T_0 . Honeycomb structure. (a) CuO (2% CO, $Re = 152$); (b) CuO (6% CO, $Re = 152$); (c) Pt (2% CO, $Re = 152$); (d) Pt (4% CO, $Re = 152$).

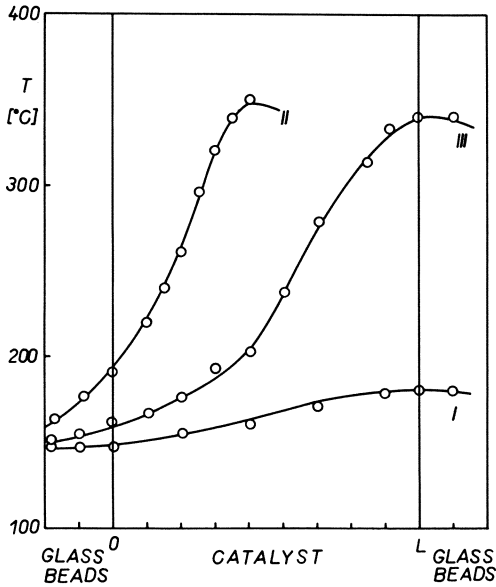


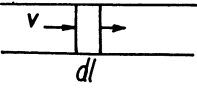
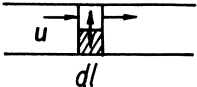
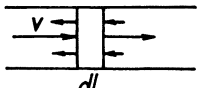
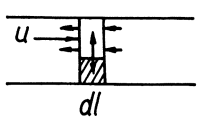
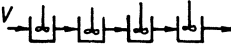
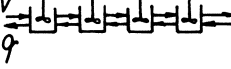
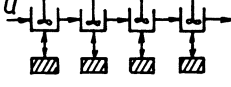
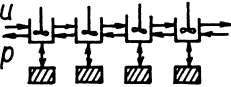
Figure 9. Three steady-state temperature profiles in packed bed. $\text{CuO}/\text{Al}_2\text{O}_3$ (4% CO , $L = 8.9$ cm, $Re = 52$, $T_0 = 148^\circ\text{C}$): I, $Y = 0.25$; II, $Y = 0.99$; III, $Y = 0.99$.

Table I. Reaction Rate Expressions of CO Oxidation on Different Catalysts and Experimental Values for Main Model Parameters

Catalyst	Kinetic Expression	E [Kcal/mole]	A	$K[\text{atm}^{-1}]$
$\text{Pt}/\text{Al}_2\text{O}_3$	$R = \frac{k p_{\text{CO}} p_{\text{O}_2}}{1 + K p_{\text{CO}}}$	12.5	1.98×10^6	$\frac{105.1}{(\text{at } 60^\circ\text{--}210^\circ\text{C})}$
$\text{Pd}/\text{Al}_2\text{O}_3$	$R = \frac{k p_{\text{CO}} p_{\text{O}_2}}{(1 + K p_{\text{CO}})^2}$	16.4	2.28×10^6	$\frac{206.2}{(\text{at } 55^\circ\text{--}210^\circ\text{C})}$
$\text{CuO}/\text{Al}_2\text{O}_3$	$R = k p_{\text{CO}}$	22.9	8.04×10^6	—

[R]	Gram-mole CO/min Grams Catalyst
void fraction	0.34 — 0.45
$\frac{v \rho d_p}{\mu}$	8.4 — 62.7
$\frac{v d_p}{D_e}$	2 — 3.2
$\frac{v \rho c_p d_p}{k_e}$	0.2 — 0.42
a	6.12 — 12.3 cm^2/cm^3
$\frac{q}{v}$	0 — 3.2
length of bed	3.5 — 30.2 cm
$\frac{\alpha}{v \rho c_p}$	0.01 — 0.05
$\frac{k_c}{v}$	0.01 — 0.05

Table II. Transport Models Describing Heat

Type of Model	Mass Balance
A	 $-v \frac{dc_i}{dl} + R(c_i, T) = 0$
B	 $-u \frac{dc_i}{dl} + k_c a (c_i - c_{i_s}) = 0$ $k_c a (c_i - c_{i_s}) - R(c_{i_s}, T_s) = 0$
C	 $De \frac{d^2 c_i}{dl^2} - v \frac{dc_i}{dl} + R(c_i, T) = 0$
D	 $De \frac{d^2 c_i}{dl^2} - u \frac{dc_i}{dl} + k_c a (c_i - c_{i_s}) = 0$ $k_c a (c_i - c_{i_s}) - R(c_{i_s}, T_s) = 0$
E	 $v S (c_i^k - c_i^{k-1}) + V R (c_i^k, T^k) = 0$
F	 $S[v(c_i^k - c_i^{k-1}) - q(c_i^{k+1} - c_i^k)] + V R(c_i^k, T^k) = 0$
G	 $u S (c_i^k - c_i^{k-1}) + V k_c a (c_i^k - c_i^{k-1}) = 0$ $k_c a (c_i^k - c_{i_s}^k) - R(c_{i_s}^k, T_s^k) = 0$
H	 $S[u(c_i^k - c_i^{k-1}) - q(c_i^{k+1} - c_i^k)] +$ $+ V k_c a (c_i^k - c_{i_s}^{k-1}) = 0$ $k_c a (c_i^k - c_{i_s}^k) - R(c_{i_s}^k, T_s^k) = 0$

To demonstrate the agreement between experimental data and theoretical descriptions, eight different models, reported in Table II were used. The first four descriptions are based on the quasi-continuum approach; the last four have discrete character. We assumed that the experimental laboratory reactor was completely adiabatic. Thus, radial heat and mass transport are not included.

Table II reports the models used along with heat and mass balance equations. For cell models with axial mixing, backmixing was calculated after comparing mixing characteristics of the cells with a diffusion model (*see Ref. 20*). Figures 10 and 11 show observed and calculated dependencies of inlet temperature T_0 vs. exit conversion (Y).

How well do the calculated and measured curves $Y = f(T_0)$ agree for different catalysts? Figure 10 shows the results for a Pd catalyst ($d_p = 5.6$ mm). The one-phase model describes the lower and upper branches quite well. Of course, there is no sudden discontinuous transition from one branch to the other; however, a steep increase in the exit conversion as a result of inlet tem-

and Mass Transfer in Packed Catalytic Reactors

<i>Heat Balance</i>	<i>Specification</i>
$-v\rho c_p \frac{dT}{dl} + (-\Delta H) R(c_i, T) = 0$	piston flow model
$-u\rho c_p \frac{dT}{dl} + \alpha a(T_s - T) = 0$	piston flow model with external transfer
$\alpha a(T_s - T) - (-\Delta H) R(c_{is}, T_s) = 0$	
$k_e \frac{d^2T}{dl^2} - v\rho c_p \frac{dT}{dl} + (-\Delta H) R(c_i, T) = 0$	dispersion model
$k_e \frac{d^2T}{dl^2} - u\rho c_p \frac{dT}{dl} + \alpha a(T_s - T) = 0$	dispersion model with external transfer
$\alpha a(T_s - T) - (-\Delta H) R(c_{is}, T_s) = 0$	
$v\rho c_p S(T^k - T^{k-1}) + V(-\Delta H) R(c_i^k, T^k) = 0$	cell model
$\rho c_p S[v(T^k - T^{k-1}) - q(T^{k+1} - T^k)] +$ $+ V(-\Delta H) R(c_i^k, T^k) = 0$	cell model with axial mixing
$u\rho c_p S(T^k - T^{k-1}) + \alpha aV(T_s^k - T^k) = 0$	two-phase cell model
$\alpha a(T_s^k - T^k) - (-\Delta H) R(c_{is}^k, T^k) = 0$	
$\rho c_p S[u(T^k - T^{k-1}) - q(T^{k+1} - T^k)] +$ $+ V\alpha a(T_s^k - T^k) = 0$	two-phase cell model with axial mixing
$\alpha a(T_s^k - T^k) - (-\Delta H) R(c_{is}^k, T_s^k) = 0$	

perature increase was calculated. The prediction of the jump from the low conversion to the upper conversion region is subject to an error of 10°C. The model cannot predict multiple steady states. The one-phase piston flow model may be sometimes used successfully to describe reactor behavior in the region of low parametric sensitivity. The two-phase piston flow model can describe the sudden transition from the low to the upper conversion region as well as predict the measured points on the upper branch. The model does not predict the extinction at 60°C. The other two-phase models—*i.e.* the one-phase dispersion model and the sequence of simple stirred tanks with and without back-mixing—are much better in predicting ignition temperature. As far as the upper branch is concerned, all models with feedback features are satisfactory, but they cannot predict the extinction point.

Agreement between the measured and calculated dependences $Y = f(T)$ for a Pt catalyst is similar to that for the Pd catalyst; however, the superiority of the two-phase models is not obvious. We could not evaluate experimentally the extinction point because, for the inlet temperature $T_0 = 30^\circ\text{C}$, the upper

state was still observed. Two models predict the extinction temperature which is in complete disagreement with the observations.

Interphase transport determines the ignition temperature. Apparently the intraparticle mass transfer must be incorporated in the transport equations to predict the extinction point also. It is a formidable task to handle simultaneously both external fields along with the interphase and intraparticle transport (21); however, work is in progress. Axial heat transfer strongly affects the size of the particular hysteresis loop. In the bed packed with small catalyst particles and in the honeycomb structures the extinction temperature is shifted toward lower values—*i.e.*, the axial heat transfer enlarges the region of multiplicity. This effect is, of course, compensated by intraparticle mass transfer. To fit the models we have adopted the dependence of the inlet temperature on the exit

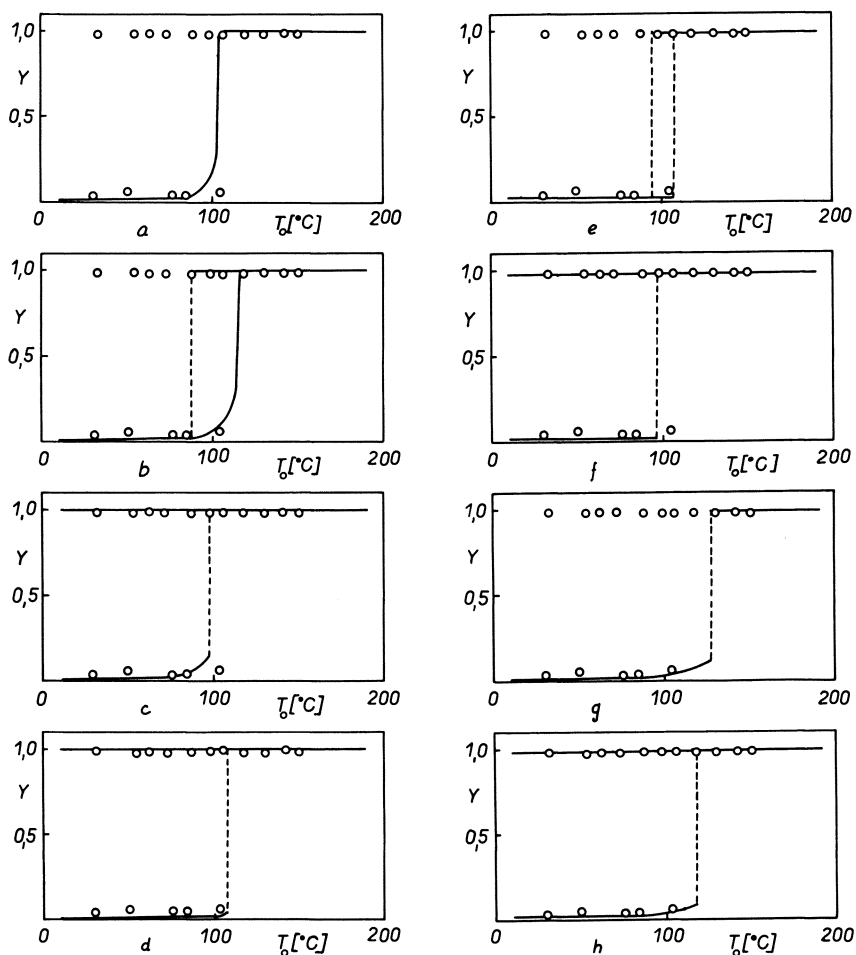


Figure 10. Measured vs. calculated dependencies of exit conversion and inlet temperature for Pt catalyst

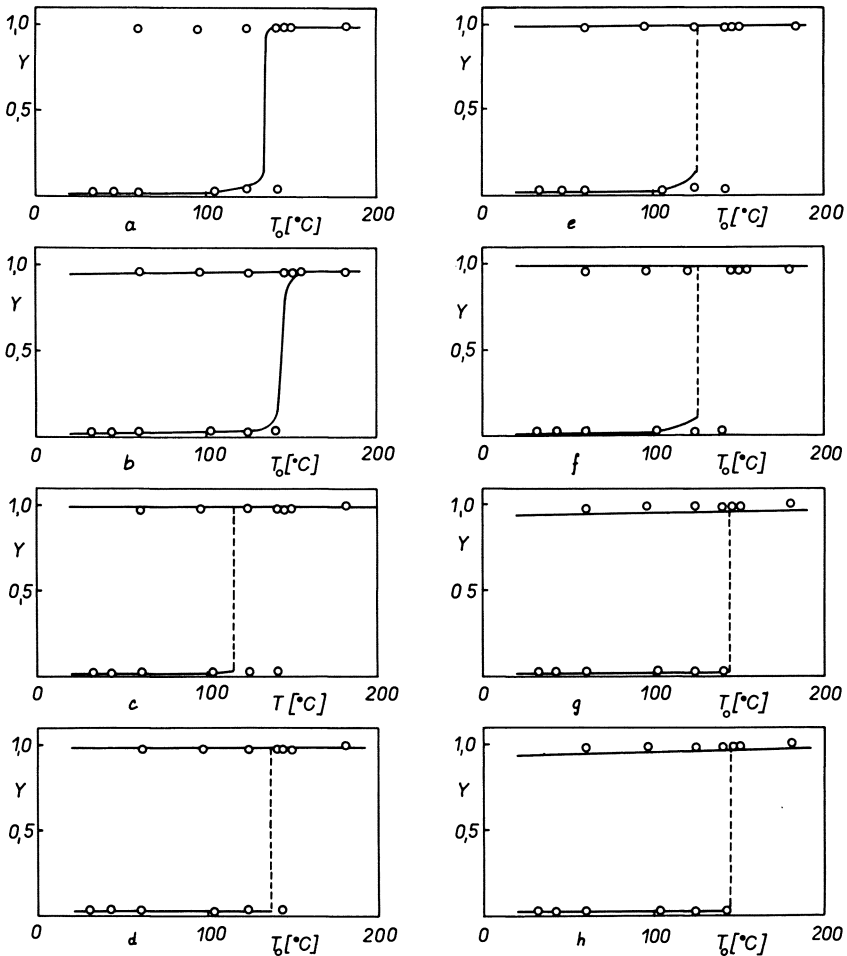


Figure 11. Measured vs. calculated dependencies of exit conversion and inlet temperature for Pd catalyst

conversion. The temperature profile measured in the bed is usually influenced by the thermocouple probe.

Conclusions

Experimental observations revealed the following:

For integer-power reaction rate expressions, the lower the formal order, the more prone the system is to multiplicity. With higher values of adiabatic temperature rise, the domain of multiple profiles is enlarged. A long packed bed suppresses the occurrence of multiple profiles. For strong axial heat conduction, the region of multiplicity is enlarged. To fit the experimental observations with a model description one must consider axial heat and mass dispersion along with the interphase and intraparticle effects. However, the resulting complex models give rise to very complicated computations. To predict the ignition boundary the intraparticle transfer can be neglected.

Nomenclature

a	external surface of catalyst, m^2/m^3
A	pre-exponential factor
c_i, c_{is}	concentration of component i in gas phase, on catalyst surface, $kmole\ i/m^3$
c_p	specific heat, $kcal/m^3$
D_e	effective diffusivity, m^2/sec
E	activation energy (<i>cf.</i> Table I), $kcal/kmole$
$(-\Delta H)$	heat of reaction, $kcal/kmole$
k, K	rate and equilibrium constants (<i>cf.</i> Table I)
k_c	mass transfer coefficient, $moles/sec$
k_e	effective axial thermal conductivity, $kcal/mole\ sec^\circ K$
l	axial coordinate, m
L	length of catalytic bed, m
p_{CO}, p_{O_2}	partial pressure of carbon monoxide, oxygen, atm
q	backflow velocity, m/sec
Re	Reynolds number based on mean interstitial velocity and particle diameter
S	cross sectional area, m^2
T, T_s, T_0	temperature of gas, solid phase, inlet gas, $^\circ K$
u	mean interstitial velocity, m/sec
v	gas velocity based on empty tube, m/sec
V	volume of mixer in cascade, m^3
Y	outlet conversion
α	heat transfer coefficient, $kcal/m^2\ sec\ ^\circ K$
ρ	gas density, kg/m^3

Literature Cited

1. Katz, M., *Advan. Catalysis* (1953) **V**, 177.
2. Dixon, J. K., Longfield, J. E., *Catalysis* (1960) **7**, 281.
3. Schwab, G. M., "Handbuch der Katalyse," *II*, Springer Verlag, Wien, 1957.
4. Wicke, E., Padberg, G., *Chem. Eng. Sci.* (1967) **22**, 1035.
5. Wicke, E., Padberg, G., Arens, H., *IV. European Symp. Reaction Eng., Brussels, 1968*.
6. Wicke, E., Fieguth, P., *Chem.-Ing.-Tech.* (1971) **43**, 604.
7. Wicke, E., Beusch, H., Fieguth, P., *Chem.-Ing.-Tech.* (1971) **43**, 475.
8. Wicke, E., *Memo. Soc. Roy. Sci. Liege, Ser. 6 Tome I*, (1971) **4**, 211.
9. Hlaváček, V., Hoffmann, H., *Chem. Eng. Sci.* (1970) **25**, 186.
10. Hlaváček, V., Hoffmann, H., *Chem. Eng. Sci.* (1970) **25**, 173.
11. Hlaváček, V., Hoffmann, H., Votruba, J., Kubíček, M., *Chem. Eng. Sci.* (1973) **28**, 1897.
12. Sinkule, J., Hlaváček, V., Votruba, J., *Chem. Eng. Sci.*, in press.
13. Accomazo, M. A., Ken Nobe, *CEP Symp. Ser.* (1963) **59** (45), 71.
14. Votruba, J., Ph.D. Thesis, Institute of Chemical Technology, Prague, 1973.
15. Marquardt, D. W., *J. SIAM* (1963) **11**, 431.
16. Votruba, J., Hlaváček, V., Marek, M., *Chem. Eng. Sci.* (1972) **27**, 1845.
17. Gunn, J., *Chem. Eng.* (1968) **219**, 153.
18. Satterfield, C. N., "Mass Transfer in Heterogeneous Catalysis," M.I.T. Press, 1970.
19. Aerov, M. E., Todes, O. M., "Hydrodynamics and Heat Transfer in Equipment with Fixed and Fluidized Bed," Publishing House Nauka, Leningrad, 1968 (in Russian).
20. Sinkule, J., Hlaváček, V., Votruba, J., *Chem. Eng. Sci.* (1974) **29**, 689.
21. McGuire, M. L., Lapidus, L., *AIChE J.* (1965) **11**, 85.

RECEIVED January 23, 1974.

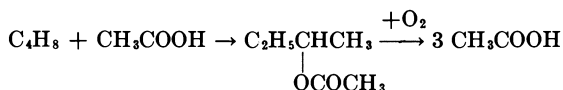
The Use of Mathematical Models in Developing an Acetic Acid Process

JOHANN GAUBE

Chemische Werke Hüls AG, 437 Marl, Postfach 1180, West Germany

Acetic acid is produced by oxidation of butene with air or oxygen over solid catalysts containing vanadium. An acetic acid process is developed as an example in which kinetic models and mathematical process models are used. The kinetic model describes the conversion rate of butene and the selectivity of acetic acid and byproducts as a function of reaction temperature, pressure, and composition of the reaction gas. Then, models for various preliminary process designs are developed which allow the calculation of the main stream of material and energy as a function of the process parameters. The cost of raw materials, utilities, and investment is calculated as a function of the process parameters. It is then possible to find the optimal process parameters for the various process designs.

In the last 10 years acetylene as a feedstock for acetic acid manufacture has been mainly replaced by olefins such as ethylene and butenes. The interest is chiefly on processes that are based on butene since to an increasing extent C₄ fractions are obtained as byproducts of ethylene production by way of hydrocarbon pyrolysis. First of all, butadiene and isobutene are separated from these C₄ fractions. The remaining mixture of *n*-butene and butane (approximately 10–20% butane) may then be used, for instance, by the two-stage Bayer process (1):



R. Brockhaus (Chemische Werke Hüls AG) has developed catalysts over which acetic acid can be obtained with a selectivity of about 50–60% by gas phase oxidation (2, 3, 4, 5, 6):



After the catalysts were developed and suitable reaction conditions were roughly defined, extensive tests were done to determine the functional relationships between the conversion and product selectivity and the reaction

parameters. At that time consideration was already given to the technical design of a new process, whereby various possibilities of technical feasibility were revealed. First the scope of reaction variables was defined, within which the above mentioned relationships had to be examined.

The catalysts developed by Brockhaus (3, 4, 5) are mixed oxides of vanadium with titanium, antimony, or tin. Over these catalysts butenes can be oxidized by air to acetic acid in the presence of steam at 170° to 250°C with selectivities up to 60% based on the carbon which is present in the butene. Reaction can be done at normal pressure and higher pressures. Intermediates such as acetaldehyde and acetone are obtained, which can easily be further oxidized to acetic acid. Carbon monoxide, carbon dioxide, and formic acid are undesired oxidation byproducts. The presence of water vapor is required to achieve sufficient selectivity of the acetic acid formation. Air or oxygen can be used as oxidation gas.

Various Processing Methods

The mode of operation should preferably be approximately isothermal since with rising temperature the reaction proceeds increasingly towards total oxidation to CO_2 . Heat removal from the highly exothermal reaction is very important. For a process with a fixed-bed catalyst, the only reactors to be used—analogue to the process for the oxidation of ethylene oxide—are tube-bundle reactors with catalyst-filled tubes of diameters less than 35 mm, which are cooled by a heat transfer agent or by boiling water. The temperature in the tube does not exceed that of the coolant by more than 20°C. The lengths of such reactors range between 3 and 10 m.

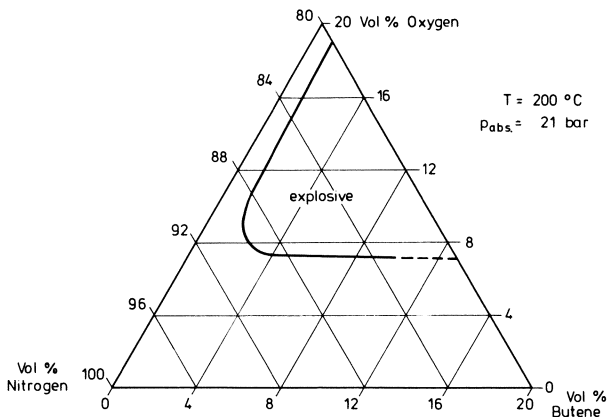


Figure 1. Explosion limit in the system $\text{C}_4\text{H}_8\text{-O}_2\text{-N}_2$.

The composition of the reaction gas is restricted by the explosion limit of the system butene–oxygen–inert gases because for a commercial process no explosive gas mixture may be present in any part of the plant. Figure 1 shows the explosion limit of the system (measurement done by Grosse-Wortmann, Chemische Werke Hüls AG).

When a mixture of air and butene is passed through the reactor once, the fraction of butene in the gas must not exceed 0.9 vol %. Higher fractions of

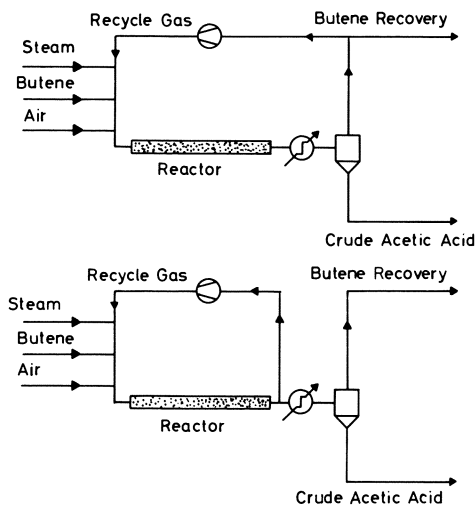


Figure 2. Recycling alternatives

butene are not admissible unless the fraction of oxygen is much lower (<7 vol %). Such levels of oxygen can easily be achieved by recycle gas operation. First estimates have shown that the recycle system results in lower costs than those of a process using a once-through gas passage. Two alternatives are shown in Figure 2 (7).

(1) The gas leaving the reactor is subjected to condensation, and the gas, which has been branched off from the waste gas stream and for the most part freed from acetic acid and water, is then fed into the reactor as recycle gas.

(2) Subsequent to the take-off of a quantity of gas corresponding to that of the waste gas, the gas leaving the reactor is recycled back to the reactor without cooling. The reaction product is condensed in the waste gas stream.

The second case is of interest because (a) the condenser is smaller, (b) a greater part of the reaction heat can be utilized as steam, (c) a more concentrated acetic acid can be obtained because no steam is added from outside. As a result of the recycle gas system, water vapor is also present at the reactor inlet; the water was formed by the side reactions leading to CO and CO_2 . The selectivity of the acetic acid formation slightly decreases since acetic acid accumulates in the reaction gas and is therefore oxidized to an increasing extent.

Pilot Plant and Evaluation

The pilot plant (Figure 3) permits experiments to be carried out in all reaction areas which correspond to the various processing methods mentioned before (6). In this way it is possible to recycle crude acid condensate to simulate the second recycle process. The test parameters used in the preliminary tests are temperature, pressure, butene feed, steam feed, recycle of condensate, and addition of air.

The reaction depends directly on the concentrations in the reaction space. Reactor calculations for any arrangements and dimensions of the reactor cannot be made unless the correlation between reaction rate, temperature, and concentration of the reaction components is known. For kinetic evaluation the material streams at the inlet and outlet of the reaction tube were calculated for each test by electronic data processing.

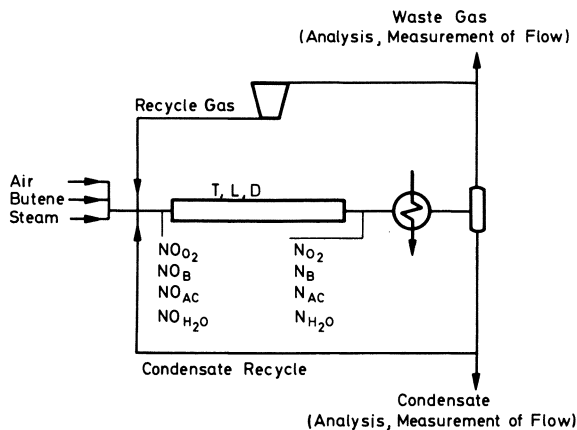
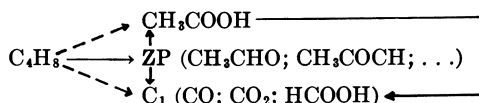


Figure 3. Oxidation of butene: testing plant

Kinetic Equations



$$\frac{dC_B}{dt} = - \frac{y_B}{1 + k_a y_B + k_b y_{AC}} k_{o1} \exp(-E_{A1}/RT) \quad (1)$$

$$\frac{dC_{ZP}}{dt} = \frac{4}{CZ_{ZP}} \frac{dC_B}{dt} - \frac{y_{ZP}}{1 + k_a y_B + k_b y_{AC}} k_{o2} \exp(-E_{A2}/RT) \quad (2)$$

$$\frac{dC_{C1}}{dt} = -f\left(\frac{y_{H_2O}}{y_{AC}}, y_B, T\right) \frac{dC_B}{dt} \quad (3)$$

$$\frac{dC_{AC}}{dt} = 2 \frac{dC_B}{dt} - \frac{CZ_{ZP}}{2} \frac{dC_{ZP}}{dt} - \frac{1}{2} \frac{dC_{C1}}{dt} \quad (4)$$

The system consists of three equations corresponding to the course of the reaction scheme with its full arrows. Equation 1 describes the conversion of butene. Equation 2 describes the formation and conversion of intermediates (acetaldehyde, acetone, and others). It is assumed that all products are formed *via* intermediates (ZP). Equation 3 describes the formation of C_1 compounds (CO, CO_2 , HCOOH). Acetic acid formation results from Equation 4. In all equations the total pressure does not influence the course of the reaction. The independence of the pressure strictly applies to higher pressures, starting from about 5 bars. At pressures below 5 bars the reaction rates decrease slightly. Selectivity however, is largely independent of total pressure. According to Brockhaus (6), the concentration of oxygen has very little influence on the reaction rate of acetic acid formation if the mole fraction $Y_{O_2} > 0.03$. In the range of $0.03 < Y_{O_2} < 0.08$ the influence of oxygen concentration on the selectivity of acetic acid formation is very small. Accordingly, Y_{O_2} is not included in the kinetic equations.

Equation 1: Conversion of Butene. The dependence of the reaction rate on the concentration of butene and acetic acid can be described by a term similar to an adsorption isotherm. As far as the surface coverage of the catalyst

is concerned, butene and acetic acid probably compete. However, no statements shall be made here on microkinetics since the kinetic term includes also the mass transfer in the catalyst pellet. Figure 4 shows the reaction rate *vs.* the butene and acetic acid concentrations. For low acetic acid concentrations the dependence of the reaction rate on the butene concentration is low whereas it is pronounced at higher concentrations of acetic acid.

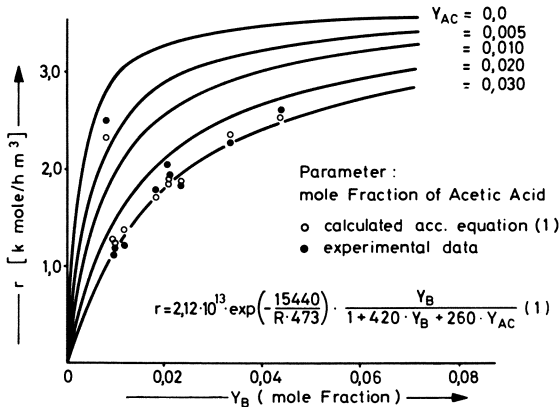


Figure 4. Reaction rate *vs.* mole fraction of butene

Equation 2. The second term of Equation 2 which describes the conversion of the intermediate is also formulated as an adsorption isotherm. This formulation reveals that the conversion rate of the intermediates decreases with the increase of the acetic acid or butene concentration. Thus the concentrations of the intermediates increase in the gas phase in these particular cases.

Equation 3: Formation of Byproducts CO₂, CO, and HCOOH. Because of the numerous possibilities of obtaining C₁ compounds, it was hardly possible to find a term commensurate with the physical-chemical processes. Therefore a formal term was chosen. The formation of C₁ byproducts can be described as function of the ratio y_{H_2O}/y_{AC} , of the mole fraction of butene y_B and of the temperature.

Equation 4: Formation of Acetic Acid. The formation of acetic acid is calculated by a balance equation for carbon. For a Ti,V catalyst, prepared according to Brockhaus (5), the constants of the set of equations are

$$k_{o1} = 2.12 \times 10^{13} \text{ kmole/m}^3 \text{ hr} \quad k_a = 420 \quad k_b = 260 \quad E_{A1} = 15,400 \text{ cal/mole}$$

$$k_{o2} = 2.72 \times 10^7 \text{ kmole/m}^3 \text{ hr} \quad E_{A2} = 6000 \text{ cal/mole} \quad CZ_{ZP} = 2.15$$

Different catalyst preparation charges may have different catalyst activities. This mainly affects the constants k_{o1} , k_{o2} , and k_{o3} . The influence on the other constants can be neglected. The dependences of formation of C₁ byproducts applying to reaction states with an acetic acid mole fraction of $y_{AC} > 0.02$ in the reaction gas, which is caused by the recycle process without cooling of recycle gas, are approximately given by the equation:

$$\left(\frac{dC_{C1}}{dt}\right) = -k_{o3} \left(\frac{y_{H2O}}{y_{AC}}\right)^{n1} y_{B(E)}^{n2} \exp\left(-\frac{E_{A3}}{RT}\right) \left(\frac{dc_B}{dt}\right) \quad (3a)$$

$\left(\frac{dC_{C_1}}{dt}\right)$, $\left(\frac{dC_B}{dt}\right)$, \bar{y}_{H_2O} , \bar{y}_{AC} are the mean values in the reactor, $y_{B(E)}$ is the mole fraction of butene at the reactor outlet $k_{o_3} = 17.2$, $n_1 = -0.12$, $n_2 = -0.24$, $E_{A_3} = 2240$ cal/mole.

The kinetic model can be applied to reaction states characterized by the following ranges of parameters.

temperature, 170°–230°C
 pressure, 10–30 bars
 total gas feed (per tube), 400–1200 mole/hr
 reactor diameter, 0.02–0.03 m
 reactor length, 3–10 m
 mole fraction of acetic acid, $y_{AC} > 0.02$
 pellet size of catalyst, 3–8 mm

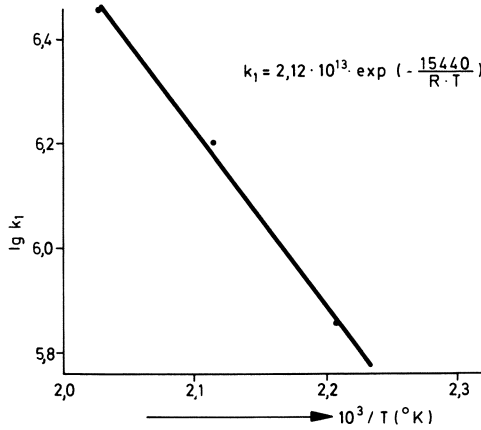


Figure 5. Oxidation of butene: Arrhenius diagram

For reaction states with an acetic acid mole fraction of $y_{AC} < 0.01$ in the reaction gas, caused by the recycle process with cooling of recycle gas the structure of Equation 3a is the same. The constants are different; n_2 decreases.

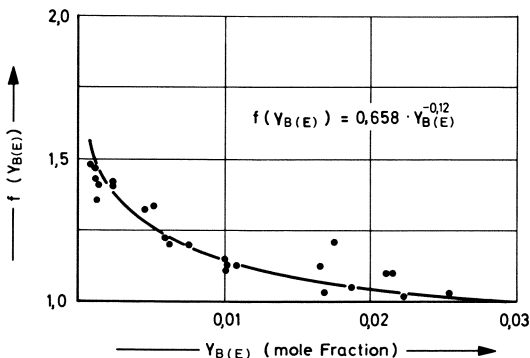


Figure 6. Total oxidation vs. butene content (reactor outlet)

Figure 4 shows the reaction rate as a function of mole fractions of butene and acetic acid for a special set of constants given above. For some experiments average reaction rates and those corresponding to Equation 1 are marked.

If the values obtained for k_1 are plotted for different temperatures according to Arrhenius, the points lie on a straight line (Figure 5); the formal energy of activation of about 15 kcal/mole can be derived from the slope.

Figure 6 is concerned with the influence of butene concentration. A decrease in butene concentration from $y_B = 0.03$ to 0.002 implies an increase in the formation of C_1 products by about 50%. The results of experiments marked in Figure 6 were obtained at temperatures of 200°C.

By means of further estimated equations of the form $y_i = a_i + b_i T$, the intermediate ZP and the C_1 compounds can be divided into the various components (CH_3CHO , CH_3COCH_3 , ; CO_2 , CO , HCOOH). The consumption of oxygen and the formation of water are then derived from balance equations for hydrogen and oxygen.

The kinetic model permits the calculation of material streams at the reactor outlet as a function of the streams at the inlet, the temperature in the reactor, the tube diameter, and tube length. The radial temperature profile in the reactor which should not be neglected is taken into account by a mean temperature according to

$$\bar{T} = -E_{A1}/R \ln \left(\frac{8}{D^2} \int_0^{D/2} r \exp \left(-\frac{E_{A1}}{RT(r)} \right) dr \right)$$

$T(r)$ is calculated by a simplified model including the energy balance. It is only the convective mass transfer which is considered in the reactor calculation. The flow rate is assumed to be constant along the reaction tube.

$$\frac{dN_i}{dx} = \frac{\pi D^2}{4} \frac{dC_i}{dt} \quad Ni(x=0) = NO_i$$

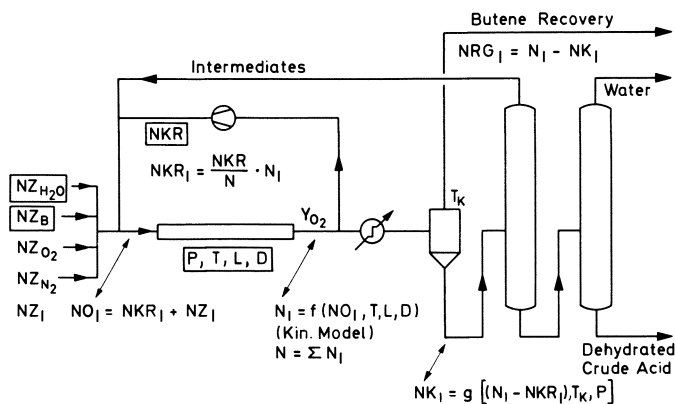


Figure 7. Oxidation of butene: process model

Process Model

A process model of the recycle process without cooling the recycle gas is illustrated in Figure 7. The stream leaving the condenser (temperature T_K) is divided into the dilute crude acetic acid and the waste gas. The recovery of butene from waste gas can be done by absorption. The dilute crude acid is dehydrated by azeotropic rectification.

Table I. Cost Items

<i>Raw Materials</i>	butene oxygen	
<i>Utilities</i>	electrical energy	air compression recycle gas revolution
	steam	azeotropic rectification of dilute acetic acid for dehydration rectification to regenerate the solvent for butene recovery recovered steam generated by cooling of reactor is subtracted
	cooling water	dehydration butene recovery
<i>Investments</i>	reactor catalyst rectification column for dehydration compressor (air) compressor (recycle gas)	

The formulas which form the mathematical process model are marked in Figure 7. The boxed-in parameters are the variables of the model. The material streams are calculated by iteration which is started on the basis of estimated input streams. The convergence of the calculation is satisfactory.

The process model permits the calculation of a complete material flow diagram. On this basis, the amount of heat to be removed from the reactors and to be exchanged in the heat exchangers can be calculated by an enthalpy balance. From these calculated material and energy streams, pressures and temperatures, butene, electrical energy, steam, and cooling water required by the various units for the manufacture of acetic acid can be calculated by a computer routine. Also the necessary investments as a function of the process variables could be calculated on the basis of the function of cost for the units that are variable in size. By adding all cost items which depend on the process variables, a cost factor for the particular operating conditions is obtained which is suitable for comparisons of various operating conditions and process concepts. All cost items which are taken into account are listed in Table I. The cost factor refers to the unit of quantity of acetic acid produced.

Process Studies

For the following process alternatives, optimal operating conditions were calculated by parameter studies.

- (1) Process where the cycle gas is branched off after condensation:

11—if air is used
12—if oxygen is used

- (2) Process where the cycle gas is branched off prior to condensation:

21—if air is used
22—if oxygen is used

The same model could be applied if oxygen were used instead of air. The nitrogen which is present in the system if air is used is partially substituted by

carbon dioxide and carbon monoxide. This substitution, however, does not affect the chemical reaction. The example of the parameter study in Figure 8 shows only the tendency of relationships. Commercial realities make it impossible to give complete information at this time.

For various butene feed streams, the cost factor as a function of the reaction temperature was calculated. The curves obtained showed a pronounced minimum. The increase in the range of lower temperatures is caused by the lower utilization of the relatively expensive reactor and by the higher costs for the recovery of butene while the increase in the range of higher temperatures is caused by the decreasing selectivity in the formation of acetic acid as a result of higher temperatures and lower butene concentrations. Optimal temperature and optimal butene feed values are thus obtained. The dotted curves indicate the range of reactor instability. Further studies concerning the remaining process variables lead to a set of optimal process variables for each process concept. The calculations show that the process concepts where the cycle gas is branched off prior to condensation are superior to systems where the cycle gas is branched off after condensation (7).

The savings that can be achieved by using smaller heat exchangers and better utilization of the reaction heat, through increased steam generation, lower energy consumption, and reduced investments in the dehydration of acetic acid outweigh the higher butene feed necessitated by the lower selectivity of the acetic acid formation. It is of crucial importance, however, that the butene concentration be kept at a sufficiently high level to counteract an increased total oxidation and to attain a sufficiently high reaction rate. To

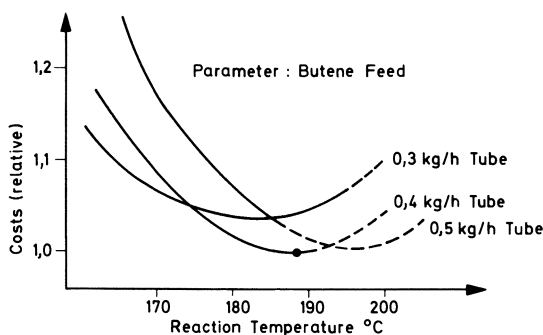


Figure 8. Costs vs. reaction temperature

ensure the best possible utilization of the expensive reactor, the possibilities for heat transfer from the reaction tube are exhausted to the greatest possible extent.

The question as to which oxidizing agent—air or oxygen—should be used, cannot generally be decided because the oxygen costs which depend on local conditions play an important role. The situation is similar to that with ethylene oxide processes where both oxygen and air are used as oxidizing agents.

Acknowledgment

The development of the process model and the optimization of the process are the teamwork of R. Brockhaus, U. Clauss, K. Hachmann, and the author.

Nomenclature

C	concentration, kmole/m ³
CZ_{ZP}	C-number of intermediates
D	reaction tube diameter, m
E_A	activation energy, cal/mole
k_{o1}, k_{o2}	reaction rate constants, kmole/m ³ hr
k_{o3}, k_a, k_b	constant values
L	reaction tube length, m
NZ_I	feed stream, component I, kmole/hr
NO_I	stream component I, reactor inlet, kmole/hr
N_I	stream component I, reactor outlet, kmole/hr
NKR_I	recycle stream, component I, kmole/hr
R	gas constant, cal/mole °K
T	reaction temperature
x	reaction tube length, m
y	mole fraction

Subscripts

AC	acetic acid
B	butene
ZP	intermediates
C_1	C_1 compounds: CO ₂ , CO, HCOOH

Literature Cited

1. Höfermann, *et al.*, *Chem. Ind.* (1969) **21**, 866.
2. Brockhaus, R., *Chemie-Ing. Tech.* (1966) **38**, 1039.
3. Brockhaus, R., Berger, E., German patent **DT-PS 1,271,104** (1965).
4. Brockhaus, R., German patent **DT-PS 1,269,119** (1965).
5. Brockhaus, R., German patent **DT-PS 1,279,011** (1966).
6. Brockhaus, R., *Erdöl Kohle* (1971) **24**, 397.
7. Hachmann, K., *et al.*, (German Offenlegungsschrift) DT-OS 2,059,945.

RECEIVED January 2, 1974.

Removal of SO₂ from Waste Gases by Reaction with MnO_x on Gamma-Alumina

P. J. W. M. VAN DEN BOSCH and W. A. DE JONG

Laboratory of Chemical Technology, Delft University of Technology,
Julianalaan 136, Delft, The Netherlands

Sulfur dioxide can be removed from oxygen-containing waste gases by reaction with MnO_x on γ -alumina between 300° and 600°C. Since reduction of the resulting Mn-sulfate with hydrogen is reasonably rapid at 475°C, isothermal swing operation with a fixed-bed reactor system is theoretically possible. This paper deals with the complex "pseudo-autocatalytic" reduction mechanism. Experiments in a thermobalance gave kinetic data which were used in calculations with a mixed homogeneous/heterogeneous fixed-bed reactor model. The results of the calculations agree semiquantitatively with experimental data obtained on a fixed bed containing Mn-sulfate on γ -alumina.

Waste gas desulfurization is one way to eliminate sulfur dioxide pollution in flue gases produced by burning sulfur-containing fuels and in stack gases of smelters and sulfuric acid plants.

Several methods for sulfur removal from stack gases are based on simultaneous reaction of SO₂ and O₂ with a solid sorbent consisting of or containing an oxide from which a stable sulfate can be produced. Since such processes should be regenerative to avoid secondary soil or water pollution, the sulfate must be decomposed thermally or chemically. If reductive regeneration can be done at about the same reactor inlet temperature as the sulfation, fixed-bed reactors can be used, thus avoiding attrition problems associated with pneumatic transport of the solid (1). Such a fixed-bed process is the Shell FGD, in which the reactive solid is copper oxide on alumina (2).

We expected that manganese oxide would also be a suitable agent for SO₂ removal because the literature indicates that simultaneous sorption of SO₂ and O₂ by Mn oxides is possible. Calculations suggest that the reduction of Mn sulfate with H₂ is thermodynamically possible at moderate temperatures. Since preliminary experiments indicated that sulfation and reduction with H₂ both proceed at acceptable rates with MnO_x on γ -Al₂O₃ at 475°C, a program was set up to establish whether the following cyclic regenerative process is feasible:

(1) Sorptive reaction of SO₂ and O₂ with MnO_x on a highly porous carrier which provides a large surface area as well as minimum diffusional resistance to the reaction;

(2) Reduction of the sulfate formed on the carrier with H_2 , giving regenerated solid and a gaseous product with a high sulfur content.

Literature Data on Process Chemistry

General. Many sorption/regeneration cycles can be done with MnO_x/Al_2O_3 . The active oxide from which the sulfate is formed is a complex mixture of Mn oxides containing Mn_2O_3 , formed by oxidation of initially formed MnO. A summary of a literature survey of the chemistry of sulfation and regeneration is given below.

Sorption of SO_2/O_2 . Three groups of papers on the sulfation of MnO and Mn_2O_3 by SO_2 and O_2 can be distinguished. In the first are the purely chemical studies—*e.g.*, Hammick (3) and Davis (4) reported complex solid intermediate products, irrespective of the starting material, and agreed that the final product was invariably $MnSO_4$ up to $800^\circ C$. Above $800^\circ C$ the sulfate decomposes thermally.

The second group contains kinetic studies of sulfation and oxidation of Mn oxides. Ingraham and Marier (5) studied sulfation in a thermobalance at partial pressures of SO_2 and O_2 much higher than those in stack gases—*viz.*, 0.33 and 0.66 atm. Unfortunately, their data cannot be used here.

In the third group are studies (6, 7) on the use of Mn oxides in stack gas desulfurization. One of these describes (6) the use of fixed-beds of Mn oxides for SO_2 removal between 130° and $330^\circ C$.

A coprecipitate of Mn and Al hydroxides is recommended by AVCO Corp. (8) as a sorbent in a regenerative system. However, their experimental data do not agree with thermodynamic calculations; these predict that MnS should be produced upon reduction of $MnSO_4$ by H_2 , but MnO and MnS are actually found, the MnO content being unexpectedly high. Uno *et al.* (9) describe the DAP-Mn process, in which SO_2 is sorbed by an uncommon Mn oxide of general formula $MnO_{1+i} \cdot nH_2O \cdot (O < i < 1 \text{ and } 0 < n < 1)$. This solid, which is formed in a regeneration step consisting of precipitation of Mn hydroxides with ammonia from $MnSO_4$ solution, filtration, and subsequent oxidation, is very reactive towards SO_2 as compared with various other Mn oxides. Graham (10) studied the performance of a fixed bed reactor for the reaction of SO_2 with MnO_2 to give $MnSO_4$. A recent patent to Kennecott Copper Corp. (11) describes the desulfurization of oxygen-containing stack gases with solids containing MnO. Results show high conversion of the solid (10–30%) between 100° and $400^\circ C$.

Reduction of Sulfate. Reduction of $MnSO_4$ with various agents has been studied by Fuller and Edlund (12), who found conversion to MnO and MnS which depend on temperature and amount of reducing agent. Their proposed mechanism involves reaction to $MnSO_3$ and two possible subsequent reactions—*viz.*, decomposition to SO_2 and MnO and disproportionation to MnS and $MnSO_4$. The theory fits well the data of Cola (13) who studied the reaction of $MnSO_3$ upon heating in a stream of N_2 and in an autoclave. In the autoclave MnS and $MnSO_4$ were formed, no solid desulfurization taking place, but in the flow experiment an increasing amount of oxide was formed when the temperature was higher. The above literature indicates a temperature of at least $600^\circ C$ for reasonably fast and complete sulfate reduction. Although this is high, regeneration is feasible because the sulfate is stable in an oxidizing atmosphere up to $800^\circ C$.

Oxidation of Acceptor. When oxygen-containing gases are passed over a regenerated $MnO_x/\gamma-Al_2O_3$ acceptor, the solid is oxidized and a large amount

of heat is generated. Consequently, deactivation and sintering can occur. Among the possible oxidation reactions are those of MnS and MnO produced by previous sulfate reduction. Bourgeois *et al.* (14) quantified such heat effects in a modeling study of a fixed-bed reactor containing Cu₂O on alumina. They found that a temperature peak as high as 100°C above the inlet temperature travels through the bed during oxidation to CuO. The oxidation of MnO has been studied by Moore *et al.* (15) and Pechkovskii *et al.* (16). The first group found Mn₂O₃ as the solid product whereas Pechkovskii detected also Mn₃O₄. Although MnO₂ is thermodynamically the most stable oxide at the conditions applied, the formation of this compound is not reported by anyone. Roasting of MnS was studied by Batsonov *et al.* (17) and Chagunava *et al.* (18). Appreciable desulfurization of the solid is observed if the temperature is kept below 980°C.

Conclusions from the Literature Study. Most studies deal with unsupported Mn compounds (except Ref. 8); we used a disperse system on γ -alumina, which may influence the course of some reactions. From the literature it appears that MnSO₄ is likely to be the main, if not sole, product of the reaction between MnO₂-containing acceptors, SO₂, and O₂. The reactions occurring during reduction with H₂ are probably very complex (*see* Table I).

Table I. Possible Reactions

I	Mn ₃ O ₄	+ 3SO ₂ + O ₂	→ 3MnSO ₄
II	2Mn ₂ O ₃	+ 4SO ₂ + O ₂	→ 4MnSO ₄
III	6MnO	+ O ₂	→ 2Mn ₃ O ₄
IV	4Mn ₃ O ₄	+ O ₂	→ 6Mn ₂ O ₃
V	MnS	+ 2O ₂	→ MnSO ₄
VI	2MnS	+ 3O ₂	→ 2MnO + 2SO ₂
VII	MnSO ₄	+ 4H ₂	→ MnS + 4H ₂ O
VIII	MnSO ₄	+ H ₂	→ MnO + SO ₂ + H ₂ O
IX	3MnSO ₄	+ MnS	⇌ 4MnO + 4SO ₂
X	MnS	+ H ₂ O	⇌ MnO + H ₂ S
XI a.	3MnSO ₄	+ H ₂ S	→ 3MnO + 4SO ₂ + H ₂ O
b.	3MnSO ₄	+ 4H ₂ S	→ 3MnS + 4SO ₂ + 4H ₂ O
XII	SO ₂	+ 3H ₂	→ H ₂ S + 2H ₂ O

Experimental

Materials. Acceptors containing Mn compounds were prepared from: (1) γ -alumina 000-1.5E 6 (crushed and sieved to 0.6-1.0 mm) obtained from Ketjen (AKZO) Amsterdam, surface area 241 m² gram⁻¹, pore volume 0.7 cc gram⁻¹, silica gel AT 23 (Gembo Chemie), surface area 470 m² gram⁻¹, pore volume 0.7 cc gram⁻¹, and (2) high purity MnSO₄ · 1H₂O (Merck, Darmstadt). The acceptors were prepared by impregnation methods; in most cases the procedure in Ref. 19 was used after modification for Mn compounds.

Equipment. A Cahn RG-HV thermobalance combined with a Perkin-Elmer microfurnace/programming unit, a modified high-temperature Guinier-Lamé x-ray camera, and an experimental unit containing a fixed-bed reactor were used. The x-ray camera showed changes in the solid during isothermal reaction.

Figure 1 is a flow sheet of the equipment containing two fixed-bed reactors, quartz tubes of 8 mm id and 300 mm long. Reactant gases were metered by a combination of Brooks ELF flow controllers (1) and Fisher-Porter Rotameters (2). Electromagnetic valves (3) were operated by a timing mechanism to control the complete cycle and feed gas composition for reactors R1 and R2. Water was fed by special motor buret (4) in combination with electromagnetic valves. The gases were preheated, and water was evaporated in preheaters

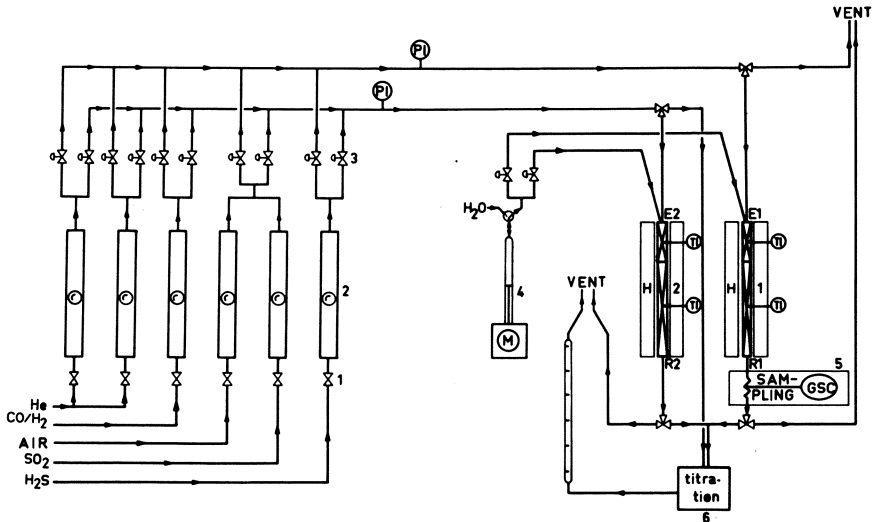


Figure 1. Twin-reactor flow equipment

E1 and E2. Samples of product gases were injected automatically into an on-line gas chromatograph (5); a fully automatic acidimetric titration (6) in 5% H_2O_2 solution was also used to monitor product gases. In the GSC system the components H_2 , H_2S , SO_2 , and H_2O were separated at 130°C over a 3-m Chromosorb 104 column (7) using He as the carrier gas.

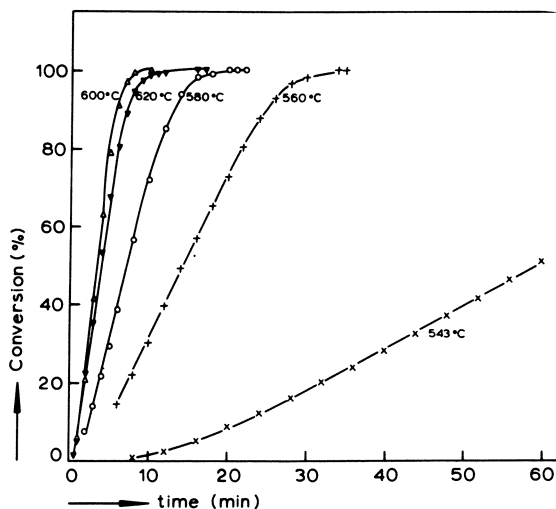


Figure 2. Influence of temperature on Reaction VII
($p_{\text{hydrogen}} = 0.73 \text{ atm}$)

Experimental Process Cycle. The reactor was filled with about 5 grams of acceptor. If the acceptor was in the sulfate form, it was heated to 475°C while passing through N_2 ; when this temperature had been reached, regeneration was started by introducing H_2 . After 50 min regeneration, the reactor was flushed with N_2 ; then a simulated flue gas was introduced which contained

known amounts of SO₂ (say 0.4%) and O₂. Sulfation was continued for 60 min, the reactor was again flushed with N₂, and a second cycle was started. Since almost all the sulfur is usually converted to SO₂ upon regeneration, continuous monitoring of the gases leaving the reactor indicated whether sulfur recovery was complete. The high degree of automation allows life testing of acceptors; more than 1000 cycles were run with a promising acceptor.

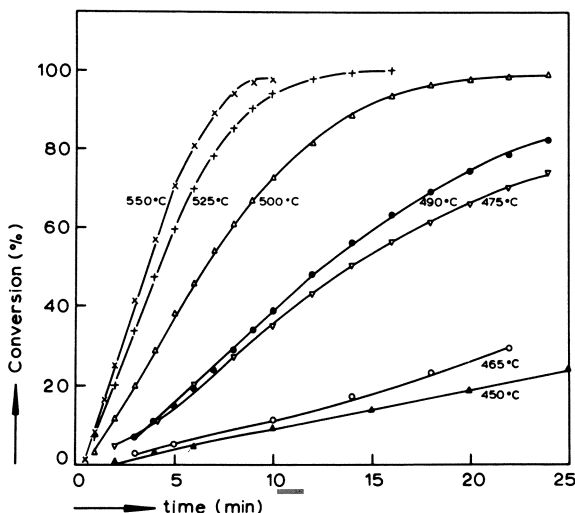
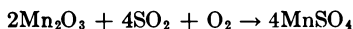


Figure 3. Effect of temperature on Reaction XI ($p_{\text{SO}_2} = 0.05 \text{ atm}$)

Results on Process Chemistry

Sorption of SO₂. Thermobalance experiments (Figures 2 and 3), x-ray data, and flow experiments prove that in the sorption phase of the cycle, sulfate is formed on the acceptor at 475°C according to:



On a basis of mass balances we established that Mn₂O₃ is the active oxide, but we are not sure about its exact crystalline form.

Examples of SO₂ breakthrough curves obtained in the flow equipment are given in Figure 4. The amount of Mn on the acceptor seems to have a marked influence on oxide conversion under dynamic conditions; presumably this results from diffusional retardation in the solid product layer, its density being smaller than that of the solid reactant. Similarly incomplete conversion was obtained when sulfating pure Mn₂O₃ and MnO_x on γ -alumina in the thermobalance. Calculations show that rate of sulfation of MnO_x on γ -alumina is also limited by pore diffusion, which necessitates an acceptor support of high porosity and surface area on which the MnO_x is very finely dispersed. It was also found that the temperature, space velocity, and water content of the simulated flue gas have very little influence on acceptor capacity.

Reductive Regeneration. The thermobalance experiments of Figure 2 indicate that the temperature should exceed 550°C when regenerating with H₂. The main product is expected to be MnS, indicating that desulfurization of the solid is incomplete. Thus, it is surprising that H₂ reduces MnSO₄ on

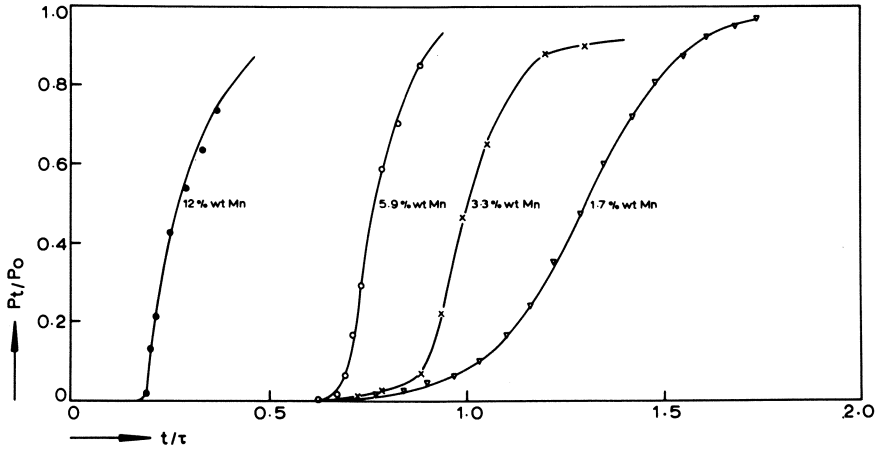


Figure 4. SO_2 breakthrough with various acceptors at 475°C ($p_{\text{SO}_2} = 0.004 \text{ atm}$; $p_{\text{O}_2} = 0.05 \text{ atm}$)

$\gamma\text{-Al}_2\text{O}_3$ rapidly even at 475°C , with fairly complete conversion of the solid sulfur compound into (mainly) SO_2 (Figures 5, 6, and 7). However, regeneration at 475°C is fast only when γ -alumina is used as the support for MnO_x ; neither unsupported MnSO_4 nor MnSO_4 on silica can be reduced with H_2 at acceptable rates at 475°C ; at least 600°C is required for this reaction. These facts as well as the negative effects of water on the rate of regeneration (Figure 6) are explained as follows: presumably the active species during regeneration with H_2 is H_2S , formed initially by hydrolysis of traces of MnS originating from the slow reduction of MnSO_4 with H_2 :

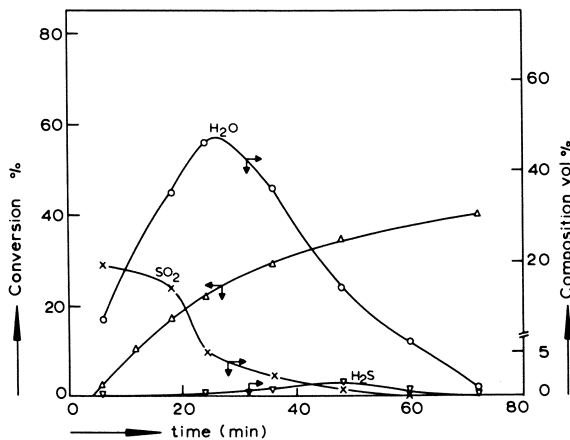
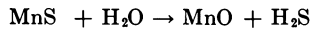
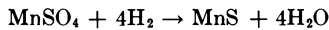


Figure 5. Conversion to SO_2 and product composition during acceptor regeneration ($T = 475^\circ\text{C}$, $\text{GHSV}_{\text{H}_2} = 120 \text{ hr}^{-1}$; previous sulfation with dry gas)

Reduction of MnSO_4 by H_2S is much faster than with H_2 . The product is SO_2 :



In the fixed-bed reactor, SO_2 is formed; further amounts of H_2S needed for rapid conversion are produced by hydrogenation of SO_2 with γ -alumina as the catalyst. Figure 8 shows that hydrogenation of SO_2 is possible over $\gamma\text{-Al}_2\text{O}_3$;

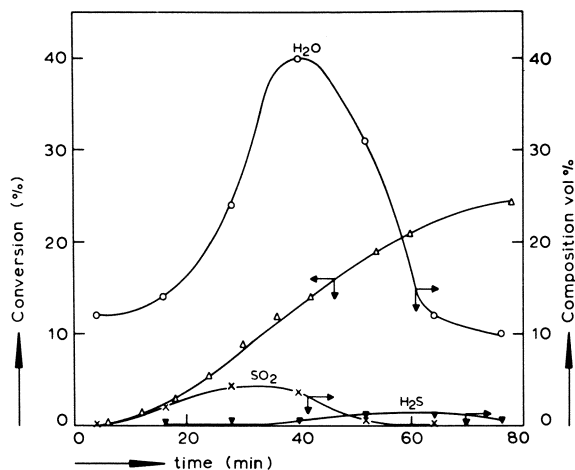


Figure 6. Conversion to SO_2 and product composition during acceptor regeneration (conditions similar to those of Figure 15 but previous sulfation with wet gas)

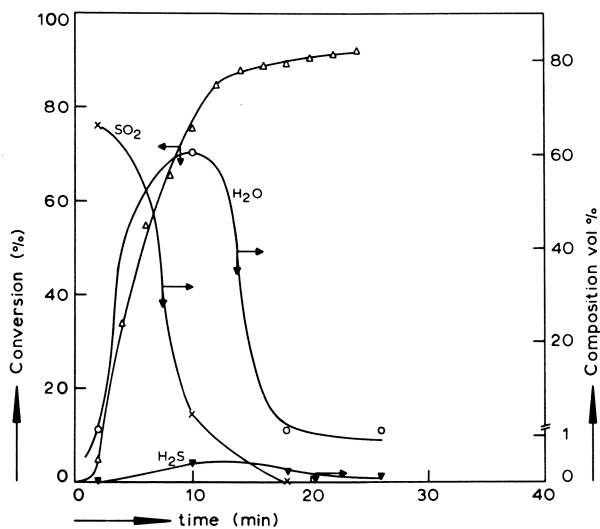


Figure 7. Conversion to SO_2 and product composition during acceptor regeneration ($T = 525^\circ\text{C}$; $\text{GHSV}_{\text{H}_2} = 120 \text{ hr}^{-1}$; previous sulfation with dry gas)

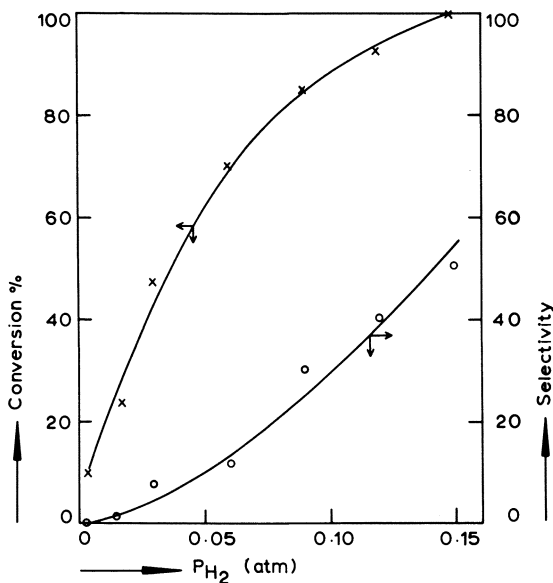


Figure 8. Hydrogenation of SO_2 over γ -alumina ($450^\circ C$, $GHSV = 6000$, $p_{SO_2} = 0.003$ atm)

silica activity is quite small or negligible under conditions where γ -alumina is an effective catalyst. Water supposedly retards the hydrogenation of SO_2 , a phenomenon also found with the Claus reaction (27). Thus, the reactions which occur during regeneration with H_2 show "pseudo-autocatalytic" behavior. The initial slow attack by H_2 on $MnSO_4$ is followed by a rapid conversion of the sulfate with H_2S , formed *in situ* from H_2 and SO_2 , the gaseous product of the reaction between $MnSO_4$ and H_2S . To strengthen this qualitative and intuitive picture of the regeneration, we set up a model of a non-stationary fixed-bed reactor to simulate the reduction of $MnSO_4$ on γ -alumina.

Modelling of Regeneration in a Fixed-Bed Reactor

Model Equations and Assumptions. A mixed homogeneous/heterogeneous reactor model was derived. We feel that Reaction XIa predominates over Reaction XIb when regenerating in a fixed bed. The two sets of rate equations included in the model are listed in Table II. The mathematical model contains six homogeneous mass balances: three for gases, three for solid compounds, and one heterogeneous mass balance for water. The contribution of the solid phase—*i.e.*, of adsorbed gases, to the mass balance for H_2 , H_2S , and SO_2 is negligible, but this is not true for water, which is adsorbed in appreciable amounts. Plug flow and isothermal operation are assumed, and transport resistances are considered absent.

The mass balance for H_2 , H_2S , and SO_2 is as follows:

$$\frac{\partial p_i}{\partial t} + \frac{\epsilon}{u} \left(\frac{\partial p_i}{\partial t} \right) = \frac{\rho_b \kappa}{u} \sum_j \nu_{ij} r_{i,j} \quad (1)$$

The mass balance for the solid components, $MnSO_4$, MnO , and MnS , is:

$$\frac{\partial C}{\partial t} = \sum_j v_{ij} r_{ij} \quad (2)$$

For water we have two mass balances:

$$\begin{aligned} \frac{\partial p_{H_2O}}{\partial t} + \frac{\epsilon}{u} \left(\frac{\partial p_{H_2O}}{\partial t} \right) &= \left(\frac{\rho_b \kappa}{u} \right) \left(\sum_j v_{ij} r_{H_2O,j} r_{H_2O,j} \right) + \left(\frac{K_{des} C_{max} \rho_b \kappa}{u} \right) \theta_{H_2O} \\ &- \left(\frac{C_{max} K_{ads} S \rho_b \kappa}{u} \right) (p_{H_2O}) (1 - \theta_{H_2O}) \end{aligned} \quad (3)$$

$$\frac{\partial \theta_{H_2O}}{\partial t} = K_{ads} p_{H_2O} (1 - \theta_{H_2O}) - (K_{des} \theta_{H_2O}) \quad (4)$$

for $l = 0$ and $t = 0$: $p_{H_2} = 0$, $p_{H_2O} = 0$, $p_{H_2S} = 0$, $p_{SO_2} = 0$

for $l = 0$ and $t > 0$: $p_{H_2} = 1$, $p_{H_2O} = 0$, $p_{H_2S} = 0$, $p_{SO_2} = 0$

for $l > 0$ and $t = 0$: $p_{H_2} = 0$, $p_{H_2O} = 0$, $p_{H_2S} = 0$, $p_{SO_2} = 0$,

$C_{MnSO_4} = 1$, $C_{MnO} = 0$, $C_{MnS} = 0$

These equations for the reduction are formulated as if the systems were homogeneous. This is permitted only when the reactive ingredient is so highly dispersed on the carrier that mass transfer limitations through the product layer can be neglected, when diffusion in the pores of the carrier does not limit the rate, and when the particles of the reactive ingredient of the acceptor react homogeneously. These conditions appear to be fulfilled for the reduction of $MnSO_4$ on $\gamma-Al_2O_3$. The above partial differential equations were solved by the method of characteristics described in Ref. 20.

Table II. Reactions and Rate Equations Used in Fixed-bed Simulation

Set 1

VII	$MnSO_4 + 4H_2 \rightarrow MnS + 4H_2O$	$r = k_1 p_{H_2} C_{MnSO_4}$
XII	$SO_2 + 3H_2 \rightarrow H_2S + 2H_2O$	$r = k_2 p_{H_2} p_{SO_2} (1 - \theta_{H_2O})$
XIa	$3MnSO_4 + H_2S \rightarrow 3MnO + 4SO_2 + H_2O$	$r = k_3 p_{H_2S} C_{MnSO_4}$
X	$MnO + H_2S \rightarrow MnS + H_2O$	$r = k_4 C_{MnO} p_{H_2S} - k_5 C_{MnS} p_{H_2O}$

Set 2 same as set 1 but Reaction XIa replaced by:

XIb	$3MnSO_4 + 4H_2S \rightleftharpoons 3MnS + 4SO_2 + 4H_2O$	$r = k_7 p_{H_2S} C_{MnSO_4}$
-----	---	-------------------------------

Kinetic Data from Thermobalance Experiments. GENERAL ASPECTS. Calculations with the above model require knowledge of the kinetic parameters of the relevant reduction reactions. It is impossible to obtain such data on the various Mn compounds on $\gamma-Al_2O_3$ from kinetic experiments in the thermobalance. Strong adsorption of reactants and products obscures the weight differences from chemical reactions so much that reliable conversion data cannot be determined. Another problem is the adsorption of water on the carrier which occurs under reaction conditions. This is more serious because water retards the hydrogenation of SO_2 to H_2S over $\gamma-Al_2O_3$, the key step which governs the overall rate of acceptor regeneration. Since the flow regime in the thermobalance differs markedly from that in the fixed bed and since this regime is one of the factors which determine the water concentration on the surface, the rate of acceptor reduction in the thermobalance also differs from the rate in the fixed bed.

The only way to overcome these difficulties is to determine the kinetics of the reduction reactions involved from thermobalance experiments on the unsupported Mn compounds. This poses the problem of converting the data on such model compounds into rate expressions valid for the disperse systems actually used in the process cycle because the dimensions of the reactive particles are vastly different in the two cases. The extent to which mass transfer limitations occur in thermobalance and fixed bed are expected to differ.

This problem can be tackled as follows. The rate of the elementary reaction between solid and gas is taken to be first-order in each of the two reactants. If the concentration of the gas is expressed by partial pressure p and that of the solid in moles/kg solid reactant, the rate equation becomes:

$$r_w = k_w p C_s \quad (5)$$

In the "shrinking core model" for gas/solid reactions the dependence of the rate on the concentration of the solid reactant is neglected; nevertheless, this model holds quite well for a number of gas/solid systems because the reaction proceeds in a relatively thin zone, whose thickness is small compared with the particle diameter. This zone does not change in thickness over a relatively wide range of solids conversion as it travels inwards. In terms of rate Equation 5 this implies that C_s is constant, and the rate equation simplifies to:

$$r_w = k_w p C_{s,0} \quad (5a)$$

in which $C_{s,0}$ is equivalent to the reciprocal of the molecular weight:

$$r_{w, \text{pure solids}} = k_w p M^{-1} \quad (5b)$$

However, with very small particles such as those in disperse systems like our acceptors, C_s can no longer be considered constant. The reaction zone then is of the same order of magnitude as the dimensions of the reactive particles, which, in other words, react more or less homogeneously (21). Therefore, Equation 5 should be used in the regeneration model.

Nevertheless, the basic kinetic parameter, k_w , can be found from experiments on solids which react according to the shrinking core model. Rate data for this model are usually expressed in terms of rates per unit surface area r_s :

$$r_s = k_s p \quad (6)$$

Rate r_s is related to the rate per unit weight, r_w , according to

$$r_w = r_s S_r \quad (7)$$

S_r being the surface area per unit weight in the reaction zone. Since this quantity is considered to be independent of the conversion over a wide range (*see above*), it should also apply to the initial reaction zone—*i.e.*, the outer surface S_0 , and it can, therefore, be calculated from the diameters of the particles used in the kinetic experiments.

The above approach is similar to that followed by Schwab (22) in a study of gas/solid reactions; it was also used by Mars (23) in his study of the CO shift reaction on iron oxide catalysts. Mars related the frequency factor to the number of collisions of gas molecules with the surface, assuming that each collision leads to reaction.

So far, diffusion effects have not been discussed, although in many cases diffusion resistances in the solid reactant and the product layer can affect the

overall rate of solid conversion. Models applicable to such cases have been developed by Shen and Smith (24) and by Szekely *et al.* (25, 26). These authors also give criteria for establishing the possible occurrence of diffusion limitations.

MODEL APPLIED TO ANALYZE THE THERMOBALANCE DATA. The criterion developed by Szekely (25, 26) was applied to show that intraparticle diffusion resistance affects the rates of the gas/solid reactions under the conditions prevailing in the thermobalance. A similar conclusion was reached from calculations based on the criteria of Shen and Smith (24): it appears that diffusion resistance cannot be neglected. Thus, we used one of the models of Shen and Smith (24)—*i.e.*, the model incorporating diffusion in the particle and chemical reaction but no film diffusion, to describe the experimental results obtained in the thermobalance. The relevant equation is:

$$\theta = \frac{b k_s C_{a_g} M_{MnSO_4} t}{\rho d_p} = \{1 - (1 - \xi)^{1/3}\} \left\{ 1 + \frac{k_s d_p}{6 D_e} (1 + (1 - \xi)^{1/3} - 2(1 - \xi)^{2/3}) \right\} \quad (8)$$

The effective diffusivity used in Equation 8 was obtained as described by Shen and Smith (24).

Nonlinear regression was applied to the thermobalance data using Equation 8; this proved to be possible only with Reactions VII and XI from Table I. The results of the sulfidation of MnO (Reaction X) could not be analyzed in this way because the reaction did not go to high conversion levels and was poorly reproducible.

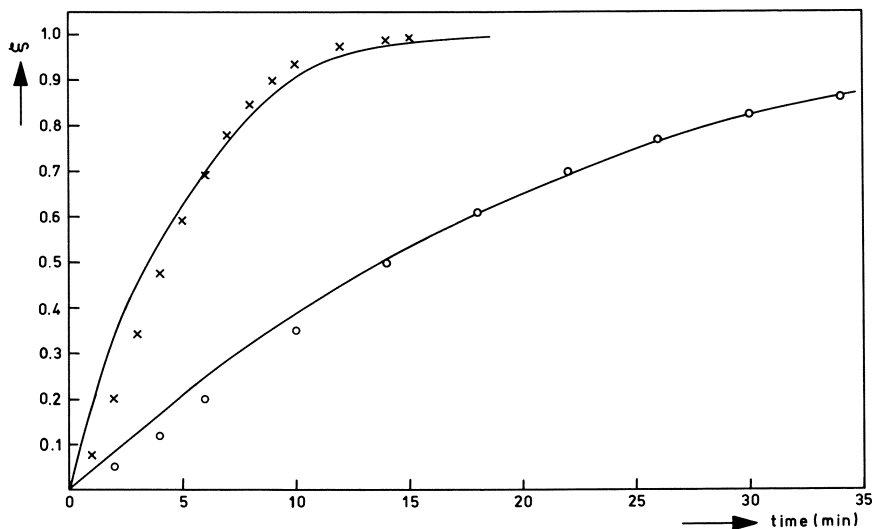


Figure 9. Measured conversions at 475°C (o) and 525°C (x) vs. those calculated with Equation 8 (Reaction XI; thermobalance experiments)

Two examples of the quality of the fit of Equation 8 to experimental data of conversion against time are given in Figure 9. The fit of Figure 9, in which the effect of intraparticle diffusion is taken into account, is decidedly better than that of Figure 10, where diffusion resistance is neglected. Figure 11

shows Arrhenius plots of the rate constants k_s of Reactions VII and XI. The final rate Equations VII and XI are given in Table III.

Kinetic Parameters used in Regeneration Simulations. Table II lists two sets of stoichiometric equations to which simulations with the fixed-bed reactor model were applied. There are two possible stoichiometries for Reaction XI; although accurate sulfur balance determinations of fixed-bed regenerations indicate that Reaction XIa is probably the correct one, independent evidence was sought from the simulation results that this tentative conclusion is correct. This aspect is also important because the sole solid product of reduction of MnSO_4 or $\text{MnSO}_4/\gamma\text{-Al}_2\text{O}_3$ with H_2 or H_2S is MnS when the reaction is done in the thermobalance whereas fixed-bed reductions of the sulfated acceptor with H_2 result in MnO and SO_2 as the main products.

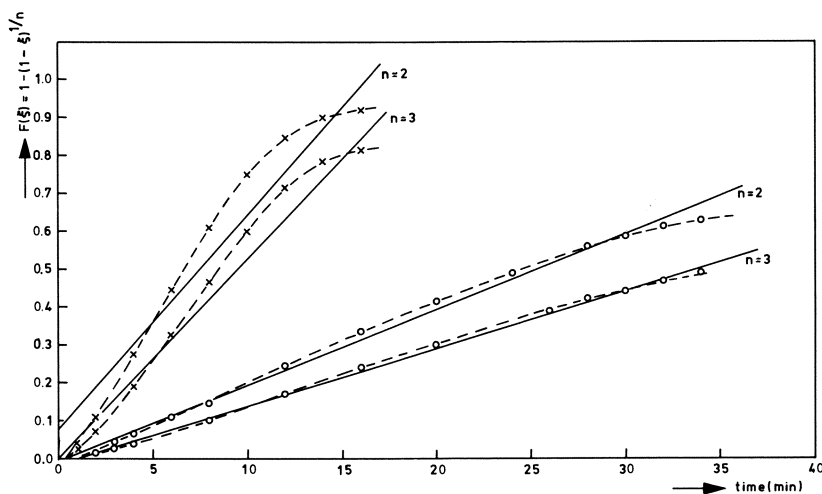


Figure 10. Measured and calculated conversions for Reaction XI at 475°C (o) and 525°C (x) with a model in which diffusion resistance was neglected (thermobalance experiments)

A typical set of kinetic parameters used in the simulations is shown in Table IV which also shows how the parameters were obtained. Rate constant k_3 was assigned to Reaction XIa and XIb. Parametric sensitivity analysis was applied by varying some of the rate constants because there was still some uncertainty about a few of their numerical values. Selected results are given in Table V. Table VI contains the numerical values of other chemical and physical properties substituted in the model. Results of some of the simulations are shown in Figures 12 and 13; the numbers of the curves correspond to those in Table V.

Discussion

Simulation results of Table V and Figure 12 show that reductive regeneration with H_2 is obtained only when Reaction XIa is included. Whenever Reaction XIb is assumed, regeneration is very slow or does not proceed at all. This supports our conclusion from mass balance determinations that XIa is the correct reaction.

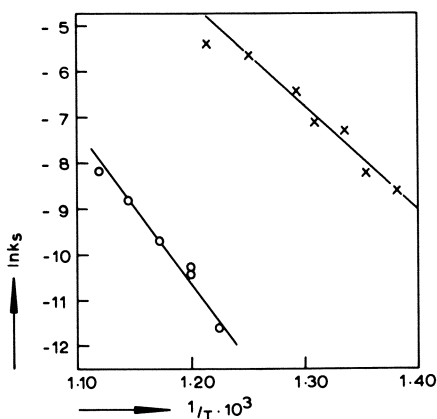


Figure 11. Arrhenius plot of Reaction VII (o) and Reaction XI (x)

Table III. Rate Equations Found for Reactions VII and XI

$$\tau_{w,VII} = 1.5 \times 10^{15} (\exp - (67000/RT)) p_{H_2} C_{MnSO_4}$$

$$\tau_{w,XI} = 9 \times 10^{11} (\exp - (44400/RT)) p_{H_2} C_{MnSO_4}$$

Table IV. Typical Set of Kinetic Parameters

Parameter	Value	Source
k_1	3×10^{-6}	thermobalance measurements
k_2	10^{-2}	extracted from Ref. #7
k_3	3×10^{-1}	thermobalance measurements
k_4	10^{-4}	estimated from thermobalance data
k_5	2×10^{-3}	estimated from thermobalance data
k_{ads}	varied	
k_{des}	varied	

We consider the agreement between calculated and measured concentration profiles of SO₂ in the exit gas to be satisfactory in a semiquantitative manner (*cf.*, Figure 7 and curve 11 of Figure 13). The agreement is not as good for water, presumably because incorrect values were assigned to the rate constants for water adsorption and desorption. Adsorption of water is probably much more complex kinetically than we assumed. Parametric sensitivity analysis shows that the system is insensitive towards changes in k_4 and k_5 . Changes in k_3 and those of water desorption and adsorption have, however, large effects in the overall rate of sulfur removal during regeneration.

Other calculations show that diffusional resistances are absent during regeneration of the sulfated acceptor. A modified Thiele modulus was used for this purpose; it is defined by:

$$\varphi = 1/2d_p \left(\frac{k_w C_s p_b K}{\epsilon D_e} \right)^{1/2} \quad (9)$$

Effectiveness factors found from this modulus were generally higher than 0.90, except for acceptors with very high sulfate concentrations.

Soon after H₂ is introduced, a reaction zone is established which travels through the acceptor bed as the regeneration proceeds. Ahead of the zone the

Table V. Results of Parameter Sensitivity Analysis of the Fixed-bed Model

Simulation ^a	k_1	k_2	k_3	k_4	k_5	k_3 for Reaction:	Results
1	4×10^{-6}	0	6×10^{-3}	10^{-4}	2×10^{-3}	XIa	no reaction
2	6×10^{-5}	0	2×10^{-2}	10^{-4}	2×10^{-3}	XIa	no reaction
3	3×10^{-6}	10^{-2}	6×10^{-3}	10^{-4}	2×10^{-3}	XIa	very low conversion to SO_2
4	3×10^{-6}	10^{-2}	18×10^{-3}	10^{-4}	2×10^{-3}	XIa	very low conversion to SO_2
5	3×10^{-6}	10^{-2}	3.6×10^{-3}	10^{-4}	2×10^{-3}	XIa	see Figure 12
6	3×10^{-6}	10^{-2}	3.6×10^{-3}	10^{-3}	1×10^{-4}	XIa	no conversion
7	3×10^{-6}	10^{-2}	1×10^{-1}	10^{-4}	2×10^{-3}	XIa	see Figure 12
8	3×10^{-6}	10^{-2}	1×10^{-1}	10^{-2}	2×10^{-3}	XIa	see Figure 12
9	3×10^{-8}	10^{-2}	2×10^{-1}	10^{-4}	2×10^{-3}	XIa	see Figure 12
10	3×10^{-6}	10^{-2}	2×10^{-1}	10^{-4}	2×10^{-3}	XIa	see Figure 12
11	3×10^{-6}	10^{-2}	3×10^{-1}	10^{-4}	2×10^{-3}	XIa	see Figures 12 and 13
12	3×10^{-6}	10^{-2}	3×10^{-1}	10^{-4}	2×10^{-3}	XIa	$K_{\text{des}} = 10^{-2}$; see Figure 13
13	4×10^{-6}	0	6×10^{-3}	10^{-4}	2×10^{-3}	XIb	no reaction
14	6×10^{-5}	0	2×10^{-2}	10^{-4}	2×10^{-3}	XIb	no reaction
15	3×10^{-6}	10^{-2}	6×10^{-3}	10^{-4}	2×10^{-3}	XIb	low conversion to MnS and H_2O
16	3×10^{-6}	10^{-2}	1.8×10^{-3}	10^{-4}	2×10^{-3}	XIb	same
17	3×10^{-6}	10^{-2}	3.6×10^{-3}	10^{-4}	2×10^{-3}	XIb	same
18	4×10^{-6}	10^{-2}	7×10^{-2}	10^{-4}	2×10^{-3}	XIb	same

^a Curves in Figures 12 and 13 have the same numbers.

Table VI. Physical and Chemical Parameters

C_{MnSO_4}	= 0.6	mole/kg _{solid}	
C_{max}	= 4×10^{-6}	mole/m ² _{cat}	
d_p	= 6×10^{-5}	m	(in thermobalance work)
d_p	= 10^{-3}	m	(in flow experiments)
K_{ads}	= 10^{-1}	atm ⁻¹ /sec	
K_{des}	= 10^{-1}	sec ⁻¹	
L	= 10^{-1}	m	
M_{MnSO_4}	= 0.151	kg/mole	
S	= 25×10^4	m ² /kg _{cat}	
S_r	= 79	m ² /kg	
u	= 3×10^{-3}	Nm ³ /m ² /s	
ϵ	= 5×10^{-1}	m ³ _{gas} /m ³ _{reactor}	
κ	= $0 \times .0224$	atm/m ³ _{gas} /mole	
ρ	= 3.25×10^3	kg/m ³	
ρ_b	= 1000	kg/m ³ _{reactor}	

solid consists of sulfated acceptor and the gas phase contains SO_2 and water formed by the reduction of MnSO_4 . During the first part of the regeneration, high concentrations of SO_2 and water are present in the product gas. (*cf.*, Figure 7). Behind the reaction zone the solid contains mainly $\text{MnO}/\gamma\text{-Al}_2\text{O}_3$; traces of MnS are also present. The gas phase in this region consists of H_2 and some water, which is retarded by adsorption relative to the SO_2 (*cf.*, Figure 7).

In the reaction zone three steps occur side by side: some SO_2 is hydrogenated to H_2S and water over γ -alumina; the H_2S thus formed reduces MnSO_4 to MnO and SO_2 ; the equilibrium $\text{MnO} + \text{H}_2\text{S} \rightleftharpoons \text{MnS} + \text{H}_2\text{O}$ shifts to the right in the front end of the zone, where the H_2S is relatively high; in the tail end of the reaction zone it shifts back to the left because water hydrolyzes the sulfide. Hydrogenation of SO_2 is slow in this region because fairly high water concentrations are present.

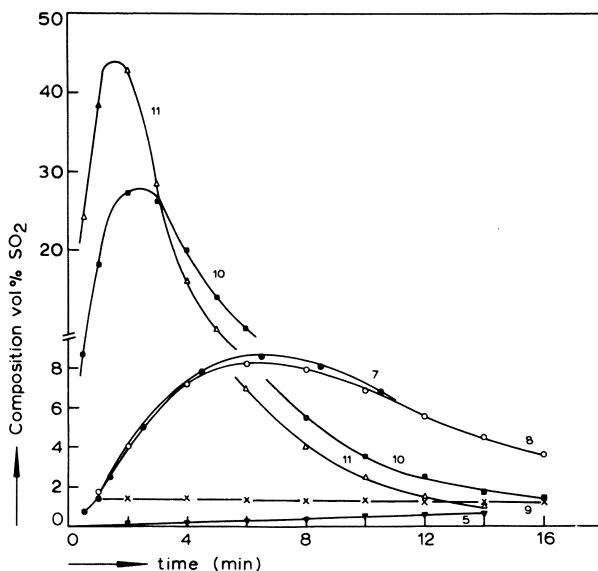


Figure 12. Examples of calculated product composition during regeneration

This explains why small amounts of H₂S emerge from the reactor toward the end of the regeneration (Figure 7). The above sequence of events is obviously impossible in the thermobalance, where a reaction zone cannot be established. A shortcoming of our model is that plug flow was assumed whereas with the relatively low flow rates used experimentally, a fair amount of back-mixing must be expected. Backmixing may explain our observation that the regeneration of a sulfated acceptor in a fixed bed is substantially complete, whereas the model predicts low regeneration efficiency in the front end of the bed. It is not certain what the effects of including mixing in our model would be: with a pseudo-autocatalytic reaction sequence of the type postulated here mixing may well lead to increased rates of acceptor regeneration. A finite-stage regeneration model is now being developed in which allowance is made for mixing effects in the bed.

Conclusions

(1) Fixed beds of MnO_x/γ-Al₂O₃ can be used in a cyclic regenerative operation consisting of sulfation with a simulated flue gas and regeneration with H₂ at the same reactor inlet temperature, *viz.*, 475°C.

(2) Reduction of the sulfated acceptor with H₂ in a fixed bed produces SO₂ and smaller quantities of H₂S.

(3) Reduction of MnSO₄/γ-Al₂O₃ in the fixed bed gives MnO/γ-Al₂O₃; small amounts of MnS are also formed on the carrier.

(4) When reducing MnSO₄ or MnSO₄/γ-Al₂O₃ in a thermobalance, MnS is the main Mn compound formed.

(5) Our experimental observations can be explained on the basis of a pseudo-autocatalytic reaction sequence in which H₂S is the active reduction agent; it is formed by hydrogenation of SO₂ over γ-alumina in a reaction zone which travels through the acceptor bed.

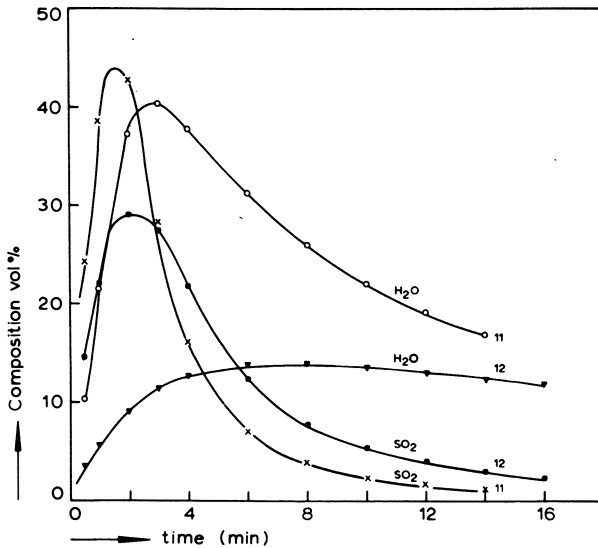


Figure 13. Examples of calculated product composition during regeneration

(6) Simulation with a simple reactor model has contributed to our knowledge of the reduction process.

(7) The use of rate Equation 5 gives very good results in the fixed-bed simulations and appears to be justified for reactions between gases and highly dispersed solids.

Nomenclature

b	stoichiometric coefficient
C_{a_g}	concentration of gaseous reactant a, mole/m ³
C_i	concentration of reactive solid i, mole/kg
C_{max}	maximum concentration of adsorbed water on γ -alumina, mole/m ² _{cat}
C_s	concentration of reactive solid, mole/kg
d_p	particle diameter, m
D_e	effective diffusivity, m ² /sec
E_A	activation energy, cal/mole
k_w	reaction rate constant defined by Equation 5, atm ⁻¹ /sec
k_s	reaction rate constant defined by Equation 6, mole/atm/m ² /sec
K_{ads}	adsorption rate constant, atm ⁻¹ /sec
K_{des}	desorption rate constant, sec ⁻¹
l	axial coordinate, m
M	molecular weight, kg/mole
p_i	partial pressure of component i, atm
p_t	outlet partial pressure of SO ₂ , atm
p_o	inlet partial pressure of SO ₂ , atm
r_{ij}	reaction rate of component i in reaction j, mole/kg/sec
r_s	reaction rate defined by Equation 5, mole/kg/sec
r_w	reaction rate defined by Equation 7, mole/m ² /sec
S	specific surface, m ² /kg _{cat}
S_o	specific outer surface of particles, m ² /kg

S_r	specific surface reaction zone, m^2/kg
t	time, sec
T	temperature, $^{\circ}C$ or $^{\circ}K$
u	superficial gas velocity, $Nm^3/m^2/sec$

Greek Letters

ϵ	bed porosity, $m^3_{gas}/m^3_{reactor}$
θ	coverage
κ	conversion factor, $atm\ m^3_{gas}/mole$
ρ	specific weight of solid, kg/m^3
ρ_b	specific weight of fixed bed, $kg/m^3_{reactor}$
ν_{ij}	stoichiometric coefficient of component i in reaction j
ξ	conversion
τ	theoretical time for complete sulfation of available Mn, sec
ϕ	Thiele modulus
Θ	reaction time defined by Equation 8, sec

Literature Cited

1. McCrea, D. H., Forney, A. J., Myers, J. G., *Ann. Meetg. A.P.C.A.*, 63rd, St. Louis, June 1970.
2. Dautzenberg, F., *et al.*, *Chem. Eng. Progr.* (1971) **67** (8), 86.
3. Hammick, D. L., *J. Chem. Soc.* (1971) **111**, 379-89.
4. Davis, C. W., *U.S. Bu. Mines Rept. Invest.* **3033** (1930).
5. Ingraham, T. R., Marier, P., *Trans. Met. Soc. AIME* (1968) **242**, 2039-43.
6. Bienstock, D., Field, F. J., *J. Air Pollut. Contr. Ass.* (1960) **10** (2), 121-5.
7. Kun, Li, *et al.*, *Environm. Sci. Technol.* (1968) **2** (8), 619-21.
8. AVCO Corp., Lowell, Mass., Final Report PB **185 190** (Feb. 1969).
9. Uno, T., *et al.*, *Proc. World Petrol. Congr.*, 7th (1967) **IX** (19), 289-95.
10. Graham, R. R., Ph.D. Thesis, Texas Technological College 1969, Univ. Microfilms Ann Arbor, Mich. 70-1472.
11. Kennecott Copper Corp., U.S. Patent **3,723,598** (1973).
12. Fuller, H. C., Edlund, V. E., *U.S. Bu. Mines Rept. Invest.* **6794** (1966).
13. Cola, M., Tarantino, S., *Gazz. Chim. Ital.* (1962) **92**, 174-88.
14. Bourgeois, S. V., *et al.*, *AIChE J.* (1974) **20** (1), 94-102.
15. Moore, T. E., *et al.*, *J. Amer. Chem. Soc.* (1950) **72**, 856-66.
16. Pechkovskii, V. V., *et al.*, *Zh. Fiz. Khim.* (1963) **37** (6), 1328-35; *Chem. Abstr.* **59**, 7152b.
17. Batsanov, S. S., *et al.*, *Zh. Neorg. Khim.* (1967) **12** (6), 1417-22; *Chem. Abstr.* **62**, 85386 m.
18. Chagunava, V. T., *et al.*, *Soobshch. Akad. Nauk. Gruz. SSR* (1964) **33** (2), 353-60; *Chem. Abstr.* **62**, 8725f.
19. British Patent, **1,220,105** (1971).
20. Acrivos, A., *Ind. Eng. Chem.* (1956) **48**, 703-10.
21. Ishida, M., Wen, C. Y., *Chem. Eng. Sci.* (1971) **26**, 1031-41.
22. Schwab, G. M., Philinis, J., *J. Amer. Chem. Soc.* (1947) **69**, 2588-96.
23. Mars, P., Gorgels, M. J., Zwietering, P., *Proc. Int. Congr. Catalysis*, 2nd, 1960, Paris, 2429-35.
24. Shen, J., Smith, J. M., *Ind. Eng. Chem., Fundamentals* (1965) **4** (3), 293-301.
25. Sohn, H. Y., Szekeley, J., *Chem. Eng. Sci.* (1972) **27**, 763-78.
26. Szekeley, J., Lin, C. I., Sohn, H. Y., *Chem. Eng. Sci.* (1973) **28**, 1975-89.
27. Dalla Lana, I. G., *et al.*, *Proc. European Symp. Chem. Reaction Eng.*, 5th, Amsterdam, 1972, B2 9-18.

RECEIVED January 2, 1974.

Comparison of One- and Two-Phase Model Predictions for Adiabatic Packed Bed Chemical Reactors

DIETER VORTMEYER, KLAUS J. DIETRICH, and KURT O. RING

Technische Universität München, 8 München 2, Arcisstrasse 21, West Germany

Mathematical models for packed bed chemical reactors can be divided into two groups: (1) homogeneous or one-phase models, and (2) heterogeneous or two-phase models. Although the models are based on different physical assumptions, both describe such important aspects of reactor behavior as multiplicity of reaction states, ignition and extinction, hysteresis, and migrating reaction zones. We demonstrate that both models are equivalent if the second derivatives of gas and solid temperature profiles are the same. Temperature dispersion by heat transfer in the two-phase model can be replaced by a dispersion coefficient in the one-phase model. The equivalence condition cannot be true in all parts of the profiles. Therefore, it is only approximately valid. Good agreement was found between the calculated results of both models concerning reaction states, ignition, hysteresis and moving reaction zones.

Many numerical solutions of equations for the fixed bed exothermic reactor have been obtained. Numerical solutions of the heterogeneous or two-phase model (1) and of the homogeneous or one-phase model (2, 3) led to results predicting ignition, multiplicity of reaction states, hysteresis, and moving reaction zones. Since there is no correlating formula between the heat transfer number h of the two-phase model (see Equations 1 and 2 and the flow-dependent part of the axial dispersion coefficient λ_{ax}^{eff} of the homogeneous model (see Equation 8), model results are difficult to compare directly. Our goals are to derive an expression relating these coefficients to each other and to compare the numerical solutions of the one- and two-phase models.

The idea of equivalence between homogeneous and heterogeneous models is not new. An analogous situation occurs with isothermal mass exchange between solid and fluid phase when the fluid is flowing through a packed column. Using the two-phase model analytical solution of Lapidus and Amundson (4), van Deemter, Zuideweg, and Klinkenberg (5) derived a dispersion term arising from mass transfer which can be added to other disperse mechanisms. Using a model different from ours, Green, Perry, and Bab-

cock (6) and Babcock *et al.* (7) considered the total dispersion of thermal energy in a packed bed to be the sum of the individual dispersive mechanisms occurring in the bed. In contrast to the above authors (5, 6, 7), who obtained their results essentially from the mathematical solution of their model, we obtain the one-phase model from the two-phase model, and the connecting relationship, directly *via* transformation of the differential equations for the two-phase model.

Conservation Equations

Energy Equations of the Two-phase Model. We consider an exothermic reaction catalyzed at the inner and outer surface of the catalyst particle. These particles are heated by the exothermic reaction, and heat is transferred from the particles to the gas. A realistic model is the two-phase model with separate energy balances for the solid and gas phases:

$$\text{Gas: } \epsilon \rho_G c_G \frac{\partial T}{\partial t} = - \dot{m} c_G \frac{\partial T}{\partial x} - ha (T - \theta) \quad (1)$$

$$\text{Solid: } (1 - \epsilon) \rho_S c_S \frac{\partial \theta}{\partial t} = \lambda_o^{\text{eff}} \frac{\partial^2 \theta}{\partial x^2} + ha (T - \theta) - r \Delta H \quad (2)$$

By a frequency response method Littman and Sliva (8) obtained Equations 1 and 2 without reaction as the best fixed bed model at low Reynolds numbers. All dispersion processes could be attributed to the solid phase, where λ_o^{eff} was approximately the heat conductivity of the quiescent bed. Dispersion terms for the gas phase were small and negligible. The gas phase capacity term in Equation 1 can be neglected as Nusselt (9) did.

The numerical solution of Equations 1 and 2 together with the material balance equation (*see* Equation 10) gives temperature profiles for the gas T and solid θ . Although the temperature of the gas is lower, both temperature profiles rise in a similar way as shown in Figure 1. The only major difference occurs near the end of the reaction.

An Equivalent One-phase Model. If one assumes the validity of the equivalence hypothesis that at each point the second derivatives of the temperature profiles are the same (or very close to one another),

$$\frac{\partial^2 T}{\partial x^2} = \frac{\partial^2 \theta}{\partial x^2} \quad (3)$$

then it is shown (10) that the two energy equations, Equations 1 and 2, can be replaced by a homogeneous equation which allows the computation of the solid temperature:

$$(1 - \epsilon) \rho_S c_S \frac{\partial \theta}{\partial t} = \left(\lambda_o^{\text{eff}} + \frac{\dot{m}^2 c_G^2}{ha} \right) \frac{\partial^2 \theta}{\partial x^2} - \dot{m} c_G \frac{\partial \theta}{\partial z} - r \Delta H \quad (4)$$

Since the derivation is easy, it can be repeated here. Adding Equations 1 and 2 gives:

$$(1 - \epsilon) \rho_S c_S \frac{\partial \theta}{\partial t} = - \dot{m} c_G \frac{\partial T}{\partial x} + \lambda_o^{\text{eff}} \frac{\partial^2 \theta}{\partial x^2} - r \Delta H \quad (5)$$

If the expression:

$$0 = \dot{m} c_G \left(\frac{\partial \theta}{\partial x} - \frac{\partial \theta}{\partial x} \right)$$

is added to Equation 5, we obtain:

$$(1 - \epsilon) \rho_S c_S \frac{\partial \theta}{\partial t} = - \dot{m} c_G \frac{\partial \theta}{\partial x} + \lambda_o^{\text{eff}} \frac{\partial^2 \theta}{\partial x^2} - \dot{m} c_G \frac{\partial (T - \theta)}{\partial x} - r \Delta H \quad (6)$$

It follows from Equation 1:

$$- \frac{\partial (T - \theta)}{\partial x} = \frac{\dot{m} c_G}{ha} \frac{\partial^2 T}{\partial x^2} \quad (7)$$

Inserting Equation 7 into Equation 6 and using the equivalence hypothesis, Equation 3, leads to Equation 4.

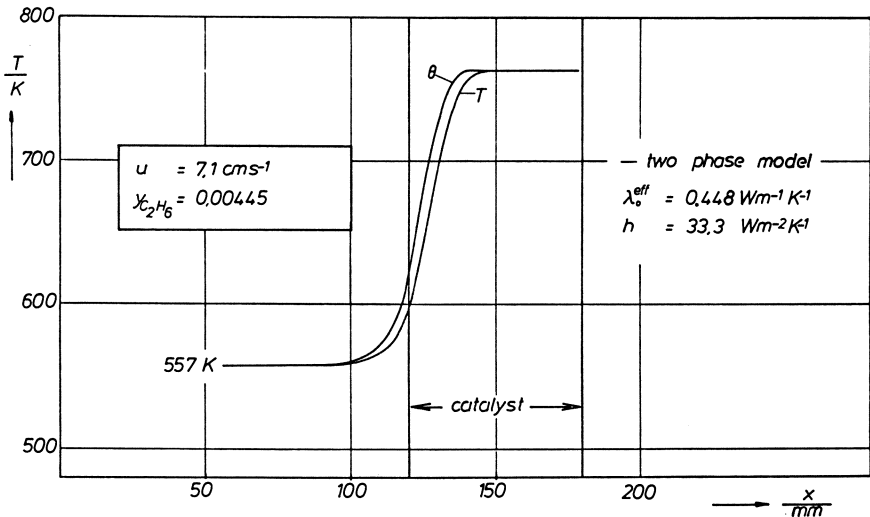


Figure 1. Solid and gas temperature profiles from the two-phase model for an upper reaction state at $u = 7.1$ cm/sec

The equivalence hypothesis provokes some questions. It is certainly not exactly valid at the low temperature point in Figure 1 where solid and gas temperatures start to rise separately, and it is incorrect near the end of the reaction zone where the solid temperature is greater than the adiabatic temperature. Nevertheless, it should hold reasonably well in large parts of the profiles. Since results for fixed beds without chemical reactions turned out well (10), it seemed worthwhile to extend those calculations to chemical reactors.

The postulated hypothesis, Equation 3, can only be fulfilled approximately. Assuming that Equation 3 is correct for most sections of the two profiles, then Equation 4 should give a correct temperature profile of the solid. From the way it was derived, Equation 4 is no energy conservation equation. Since for fixed beds with gas flow most of the energy is stored by the solid, Equation 4 can be regarded as a pseudo-energy balance. Thus, Equation 4 becomes comparable with the one-phase energy equation currently in use:

$$(1 - \epsilon) \rho_s c_s \frac{\partial \Theta}{\partial t} = - \dot{m} c_G \frac{\partial \Theta}{\partial x} + (\lambda_o^{\text{eff}} + 0.8 \text{ Re Pr } \lambda_G) \frac{\partial^2 \Theta}{\partial x^2} - r \Delta H \quad (8)$$

The temperature Θ is defined by Equation 8. Comparison of Equations 4 and 8 leads to the conclusion that if the equivalence condition is fulfilled satisfactorily, the following relation must hold:

$$\frac{\dot{m}^2 c_G^2}{h a} = 0.8 \text{ Re Pr } \lambda_G \quad (9)$$

The term on the right was measured at $\text{Re} < 40$ by Yagi *et al.* (11). The term on the left can be evaluated using the various experimental results for h . Ref. 10 shows that the postulated equality of the terms in Equation 9 is supported by experimental results. To compare calculated temperature profiles for the fixed bed exothermic reactor, the material balance equation must be set up.

The Material Balance. The two-phase or heterogeneous model for the concentration balance could be set up similar to Equations 1 and 2. Besides other effects, the model would have to contain mass transfer to and porous diffusion effects within the particles, effective axial diffusion processes, and the kinetics of the surface reaction. Such a model would require too much computing time, and the problem of measuring the kinetics without diffusion effects, particularly in high temperature ranges, would still exist.

A way out of these difficulties is to measure the overall reaction rate as a function of catalyst temperature and of gas concentration under conditions of fixed-bed operation for gas flow velocity and particle size. Then, in a first approximation the overall kinetic function accounts for the various diffusion processes. With this overall rate function the material balance for both models can be written for the case of negligible volume changes:

$$u c_{\text{total}} \frac{\partial y}{\partial x} = - r \quad (10)$$

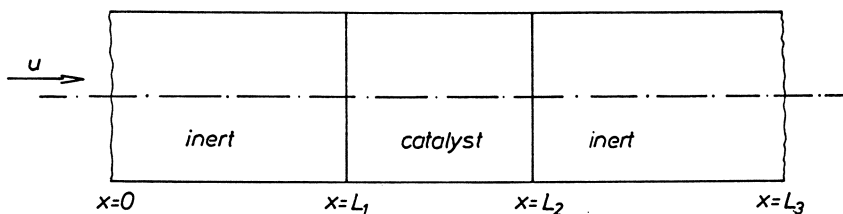


Figure 2. Schematic of the packed bed reactor

In Equation 10 the axial diffusion term is neglected because the author and Jahnle (3) discovered that for moving reaction zones the best agreement between computations and experiments was obtained if the dispersion coefficient was represented by (negligible) molecular diffusion. The time-dependent capacity term is neglected because the dynamic behavior of the fixed-bed reactor is governed mainly by the heat capacity term of the solid. The smallness of the term can be proved numerically (12).

Boundary Conditions. Calculations are performed for a catalytic reaction section which is imbedded between two extended layers of inactive particles with the same diameter. This situation is shown in Figure 2. If the inert entrance section is long enough, the inlet conditions for both models are at:

$$x = 0$$

$$T = T_0 = \theta \quad (11)$$

$$y = y_0 \quad (12)$$

For an adiabatic bed the exit conditions are at:

$$x = L_3$$

$$\frac{dT}{dx} = 0 = \frac{d\theta}{dx} \quad (13)$$

$$\frac{dy}{dx} = 0 \quad (14)$$

Initial conditions were chosen suitable for each problem. If there is no entrance section, the Danckwerts conditions apply for the homogeneous model. The equivalent boundary conditions for the two-phase model are presented in Ref. 10.

Data for the Numerical Calculations. The catalyst bed consists of 0.43-cm diameter particles which are covered with palladium to catalyze ethane oxidation in air. The overall reaction rate was measured by Dietrich (12) in a differential reactor; the measured conversion rates could be represented at temperatures $\theta < 820^\circ\text{K}$ for ethane mole fractions $0.03 < y < 0.05$ by three successive mathematical expressions (oxidation in humid air):

$$(1) \quad \theta < 599^\circ\text{K}$$

$$r = k e^{-E/R\theta} y_{\text{C}_2\text{H}_6}^{0.515} \left(\frac{575 + \Delta\theta}{575} \right)^4 \cdot 1.07 \text{ kmole m}^{-3}\text{sec}^{-1}$$

$$k = 585,370 \text{ kmole m}^{-3}\text{sec}^{-1}$$

$$E = 100,187,000 \text{ J kmole}^{-1} \text{ or } 24 \text{ kcal mole}^{-1}$$

$$\Delta\theta = (\theta - 575)^\circ\text{K}$$

$$(2) \quad 599 < \theta < 770^\circ\text{K}$$

$$r = 67.1 \left(0.001688 - \frac{1}{\theta} \right) y_{\text{C}_2\text{H}_6}^{0.515} 1.07$$

$$(3) \quad 770 < \theta < 820^\circ\text{K}$$

$$r = 0.0261 y_{\text{C}_2\text{H}_6}^{0.515} 1.07$$

The same reaction was used previously by Wicke *et al.* (13) for experimental work. The other fixed-bed data are:

$$d_p = 0.0043 \text{ m}$$

$$\epsilon = 0.4$$

$$\rho_G = 1.29 \text{ kg/m}^3 \text{ (at standard conditions)}$$

$$c_G = 1048 \text{ J/kg/}^\circ\text{K at } 573^\circ\text{K}$$

$$(1 - \epsilon) \rho_S = 750 \text{ kg/m}^3$$

$$c_S = 1052 \text{ J/kg/}^\circ\text{K at } 573^\circ\text{K}$$

$$\lambda_{\text{ax}}^{\text{eff}} = 10 \lambda_G + 0.8 \text{ Re Pr } \lambda_G$$

u = superficial velocity m/sec (at standard conditions)

$\lambda_G = 0.0448$ W/m/°K

$c_{\text{total}} = 1/22.414$ kmole/m³ (at standard conditions)

$-\Delta H = 1.425 \times 10^6$ J/kmole

Results

Upper and Lower Reaction States. In certain flow ranges the steady-state equations of the adiabatic exothermic fixed bed reactor are fulfilled by three solutions. This result was first predicted by van Heerden (14). A stability analysis of Amundson (15) showed that the upper and lower states are stable, and only these can be obtained by experimental work. This was demonstrated experimentally by Wicke *et al.* (13).

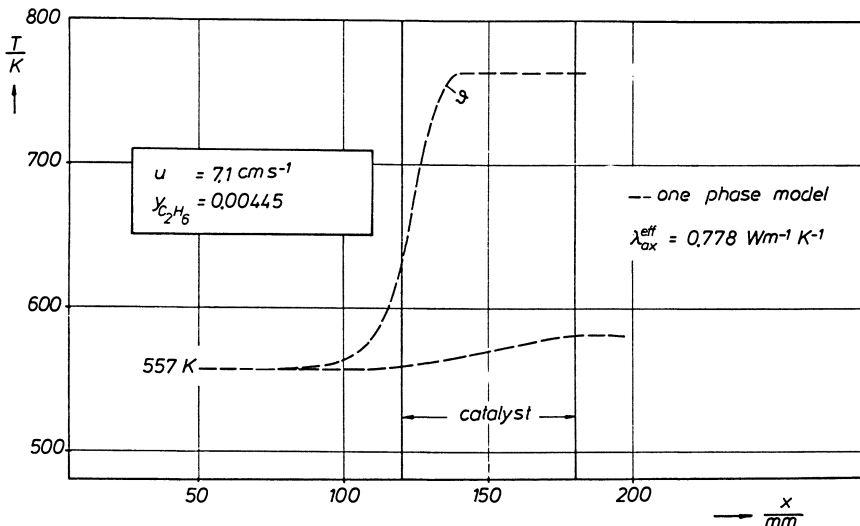


Figure 3. Lower and upper reaction state of the one-phase model at $u = 7.1$ cm/sec (standard conditions)

Since our equations are dynamic, the solution leads only to the upper and lower steady states as shown in Figure 3, where at a flow velocity of $u = 7.1$ cm/sec (at standard conditions), the two steady states of the homogeneous model are plotted. In Figure 4 the same solution is plotted together with the solutions of the equivalent two-phase model. The lower steady states predicted by both models overlap completely while there are slight differences between the solid temperature curve of the two-phase model and the one-phase model in the upper state. In Figure 5 similar results are plotted for the lower velocity of $u = 4$ cm/sec. Again the agreement is good and probably lies in the range of experimental error. The lower states agree perfectly.

Calculation of Ignition Profiles. If at a low constant flow rate and at constant inlet mole fraction the inlet temperature T_0 gradually is increased, there exists a critical value for T_0 where the lower solution no longer is possible and it jumps to an upper steady state. The last stable lower profile is

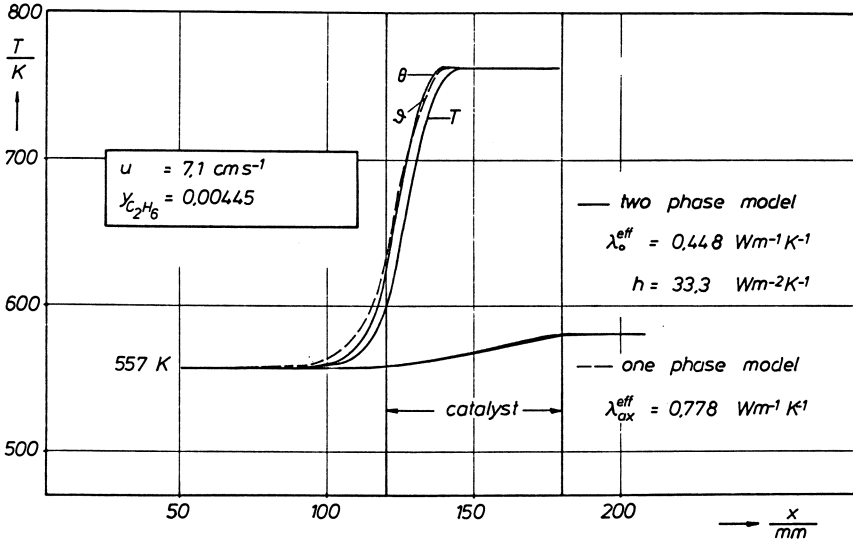


Figure 4. Comparison of lower and upper reaction states predicted by the one-phase and two-phase models at $u = 7.1$ cm/sec (standard conditions)

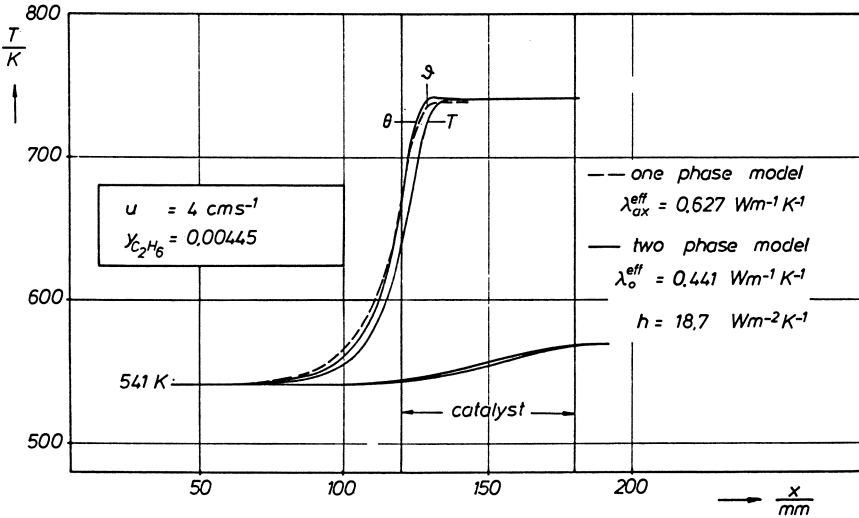


Figure 5. Comparison of lower and upper reaction states predicted by the one-phase and two-phase models at $u = 4$ cm/sec (standard conditions)

called the critical profile, and the corresponding temperature T_0 is called the ignition temperature since a very small temperature increase leads to ignition. Comparison of those critical profiles as they are predicted by both models is a highly critical test for the equivalence of both models. In Figures 6 and 7 critical profiles are evaluated for the two velocities of $u = 4$ and $u = 7.1$ cm/sec. In both cases the computed ignition temperatures differ only by 1°K. Again the temperature curve of the one-phase model lies very close to the solid

temperature θ of the two-phase model as expected if the equivalence hypothesis is fulfilled.

Since in both cases the ignition temperature of the two-phase model exceeds the one-phase model ignition temperature, this effect is increased by looking at the temperatures at the end of the reactor. The differences at this position are 3°K for the two-phase model and 2°K for the one-phase model. Predictions of both models are practically the same with regard to experimental confirmation.

The Hysteresis. Once a reactor is ignited, the upper steady state is reached. Decreasing the inlet temperature T_0 , the upper steady state eventually may be terminated and transformed again to a lower steady state. However, the reactor extinguishes at inlet temperatures much lower than the ignition temperature. The difference between ignition temperature and extinction temperature is called the hysteresis caused by feedback of the system.

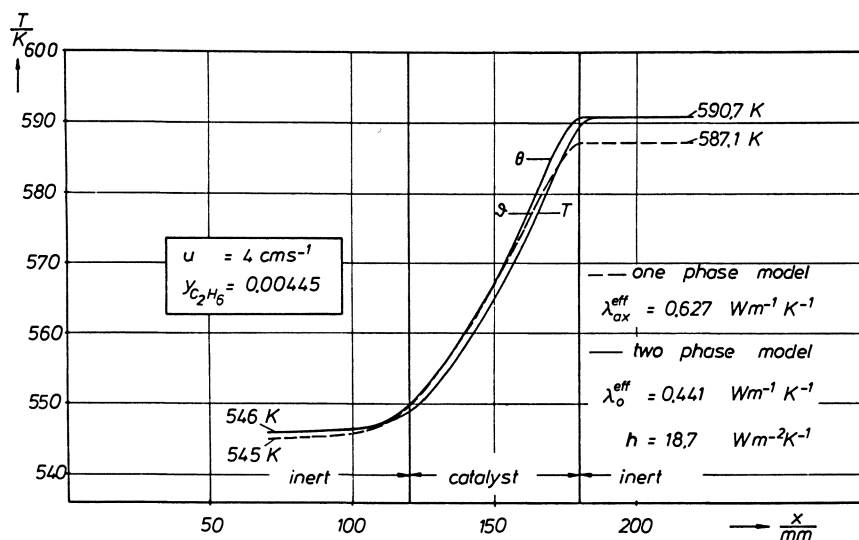


Figure 6. Ignition temperatures and critical profiles for the one-phase and two-phase models at $u = 4$ cm/sec (standard conditions)

The above experiments were simulated on the computer with both models using equivalent data for h and λ_{ax}^{eff} . These time-consuming computations were done only for a velocity of $u = 7.1$ cm/sec and an inlet concentration of $y = 0.00445$. Under these conditions, the ignition temperature is 562°K for the two-phase model and 561°K for the one-phase model (Figure 7). The corresponding extinction temperatures are calculated as 541°K for the two-phase model and 536°K for the other model. Taking the difference between the corresponding temperatures, the two-phase model predicts a hysteresis of $\Delta T_H = 21^\circ\text{K}$ and the one-phase model of $\Delta T_H = 25^\circ\text{K}$. Again this result lies within experimental uncertainty. Padberg and Wicke (16), Wicke *et al.* (13), and Fieguth and Wicke (17) have devoted much experimental work to hysteresis studies.

Moving Reaction Zones. Migrating reaction zones are a well understood phenomenon in fixed-bed reactor theory (3, 18). At low inlet flow velocities

the reaction zone may move against the incoming flow; at high flow rates it is blown out of the reactor. Since under equivalent conditions the model results agreed, nothing else is expected with regard to the moving velocity of the reaction zone. At an inlet temperature of $T_0 = 480^\circ\text{K}$, two inlet velocities were chosen so that at velocity $u = 5$ cm/sec the reaction zone was moving against the gas flow while at $u = 10$ cm/sec it was blown out of the catalyst bed. For $u = 5$ cm/sec the one-phase or homogeneous model gave a moving speed of $w = +1.74 \times 10^{-3}$ cm/sec, and the two-phase or heterogeneous model gave $w = +1.67 \times 10^{-3}$ cm/sec. For $u = 10$ cm/sec, we obtained $w = -3.21 \times 10^{-3}$ cm/sec for the one-phase and $w = -3.66 \times 10^{-3}$ cm/sec for the two-phase model. The agreement is very satisfactory; experiments did not distinguish the quality of the two models.

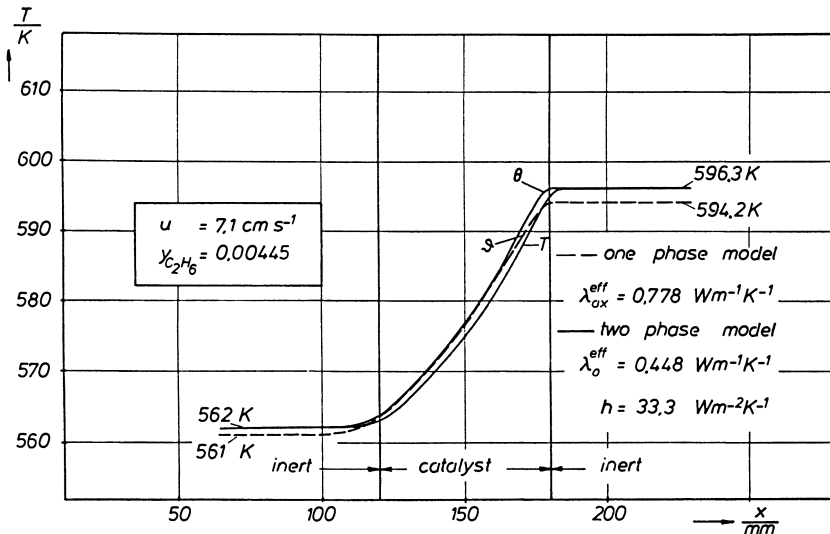


Figure 7. Ignition temperatures and critical profiles at $u = 7.1$ cm/sec (standard conditions) for one-phase and two-phase models

A Further Test of the Equivalence Condition $\partial^2 T / \partial x^2 = \partial^2 \theta / \partial x^2$. A result of this condition is that the total axial dispersion coefficient in Equation 4 was:

$$\lambda_o^{\text{eff}} + \dot{m}^2 c_G^2 / ha = \lambda_{\text{ax}}^{\text{eff}} \quad (15)$$

For each flow rate this coefficient has a value based on the heat conductivity λ_o^{eff} of the quiescent bed, m , c_G , and on h . To solve Equation 4, however, it does not matter whether λ_o^{eff} and h are physically meaningful values as long as $\lambda_{\text{ax}}^{\text{eff}}$ remains constant. In fact one can find an infinite number of pairs for λ_o^{eff} and h for a given mass flow rate m and c_G which fulfill the condition $\lambda_{\text{ax}}^{\text{eff}} = \text{constant}$.

In contrast to the one-phase model the two-phase model must be solved with different sets of parameters λ_o^{eff} and h . If the equivalence hypothesis is approximately fulfilled, this change of parameters should not affect the solution of the two-phase model either.

With the flow velocity $u = 7.1$ cm/sec such calculations were done for the upper and lower reaction state and were plotted in Figures 8 and 9. For both diagrams two sets of corresponding h and λ_o^{eff} were chosen. Both figures show that in all cases the solid temperature curves nearly overlap completely while there are minor differences in the gas temperature. This result again favors the equivalence condition.

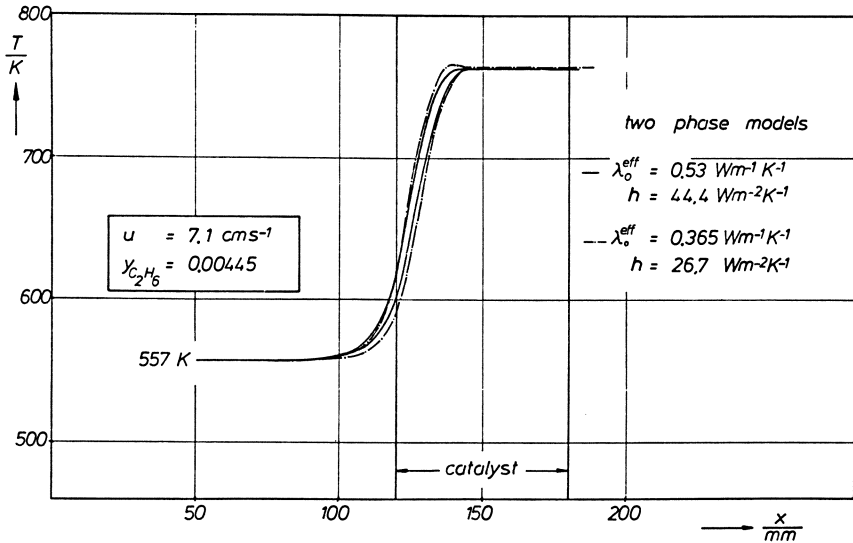


Figure 8. Solution of the two-phase model for different sets of λ_o^{eff} and h at the upper reaction state

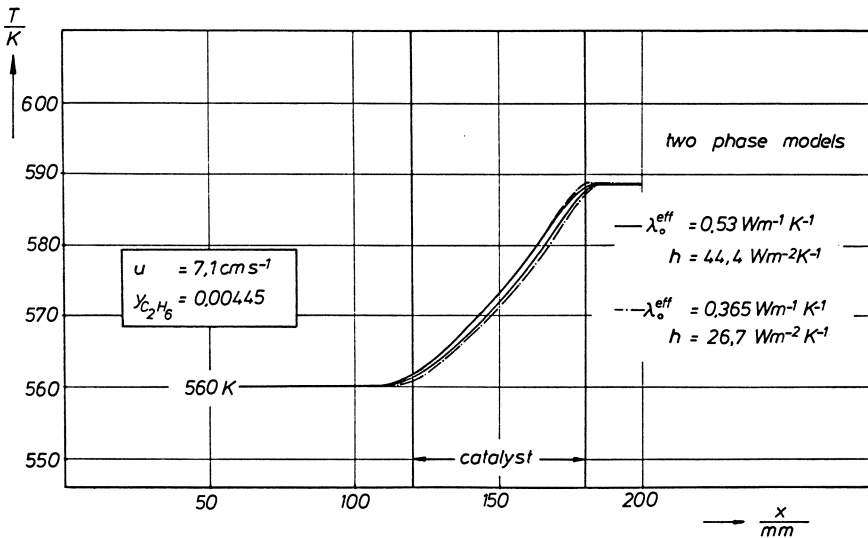


Figure 9. Solution of the two-phase model for different sets of λ_o^{eff} and h at the lower reaction state

Conclusions

Assuming the second derivatives of gas and solid temperatures to be equal:

$$\frac{\partial^2 T}{\partial x^2} = \frac{\partial^2 \theta}{\partial x^2}$$

a quantitative relation between the one-phase and two-phase model for a fixed bed chemical reactor can be established. A newly derived dispersion coefficient $m^2 c_G^2 / ha$ in the one-phase model accounts for the temperature dispersion caused by heat transfer in the two-phase model. To prove the above equivalence assumption, extensive calculations were done for an adiabatic exothermic fixed bed reactor. Upper and lower reaction states, ignition temperatures, lower critical profiles, hysteresis, and moving speeds of reaction zones were evaluated. The agreement between model predictions is very good and should be within experimental error. It is therefore possible to rewrite the results of one model type in terms of the other. The only notable difference can occur near the end of the reaction zone where the solid temperature can reach values higher than the adiabatic end temperature. This temperature maximum cannot be predicted by a one-phase model—a fact which is already known. Application of the equivalence hypothesis to concentrations in the field of absorption processes leads to an effective dispersion term caused by mass transfer as derived by van Deemter *et al.* (5).

Acknowledgment

The authors thank the Max-Buchner-Forschungsstiftung for financial support of one of the authors.

Nomenclature

a	surface area per unit bed volume, m^2/m^3
c_G	specific heat of the gas (constant pressure), $J/kg/^\circ K$
c_S	specific heat of the solid, $J/kg/^\circ K$
c_{total}	concentration of the gas mixture (at standard conditions), $kmole/m^3$
d_p	particle diameter, m
E	activation energy, $J/kmole$
ΔH	reaction enthalpy (positive for endothermic reactions), $J/kmole$
h	heat transfer coefficient, $W/m^2/^\circ K$
k	frequency factor, $kmole_{C_2H_6}/m^3/sec$
L_i	<i>see</i> Figure 2, m
m	mass velocity, $kg/m^2/sec$
n	reaction order
Pr	Prandtl number = $\frac{\rho_G v c_G}{\lambda_G}$
R	gas constant = $8314.3, J/kmole/^\circ K$
Re	Reynolds number = $\frac{u d_p}{\nu}$
r	reaction rate of a reactant (positive), $kmole/m^3/sec$
t	time, sec
ΔT_H	temperature hysteresis ignition-extinction, $^\circ K$
T	temperature of the gas, $^\circ K$
T_o	inlet temperature of the gas, $^\circ K$
u	superficial velocity at standard conditions, m/sec

- x axial distance, m
 y mole fraction of a reactant
 y_0 inlet mole fraction of a reactant

Greek Letters

- ε void fraction
 Θ temperature (one-phase model), °K
 θ temperature of the catalyst (solid), °K
 λ_{ax}^{eff} effective thermal conductivity for the one-phase model, W/m/°K
 λ_G thermal conductivity of the gas mixture, W/m/°K
 λ_0^{eff} thermal conductivity for the catalyst phase of the two-phase model, W/m/°K
 ν kinematic viscosity, m²/sec
 ρ_G density of the gas, kg/m³
 ρ_S density of the catalyst (solid), kg/m³

Literature Cited

1. Eigenberger, G., *Chem. Eng. Sci.* (1972) **27**, 1909-1915, 1917-1924.
2. Hlaváček, V., Hofmann, H., *Chem. Eng. Sci.* (1970) **25**, 173-185, 187-199.
3. Vortmeyer, D., Jahnel, W., *Chem. Eng. Sci.* (1972) **27**, 1485-1496.
4. Lapidus, L., Amundson, N. R., *J. Phys. Chem.* (1952) **56**, 984.
5. Van Deemter, J. J., Zuiderweg, F. J., Klinkenberg, A., *Chem. Eng. Sci.* (1956) **5**, 271.
6. Green, D. W., Perry, R. H., Babcock, R. E., *AIChE J.* (1964) **10**, 645.
7. Babcock, R. E., Green, D. W., Perry, R. H., *AIChE J.* (1966) **12**, 922.
8. Littman, H., Sliva, D. E., *4th Int. Heat Transfer Conf., Paris-Versailles, 1970*, **VII**.
9. Nusselt, W., *Z. Ver. Deut. Ing.* (1927) **71**, 85.
10. Vortmeyer, D., Schaefer, R. J., *Chem. Eng. Sci.* (1974) **29**, 485-497.
11. Yagi, S., Kunii, D., Wakao, N., *AIChE J.* (1960) **6**, 543-546.
12. Dietrich, K., Dissertation, Technische Universität München (1973).
13. Wicke, E., Padberg, G., Arens, H., *Proc. European Symp. Chem. Reaction Eng., 4th, Brussels, 1968*.
14. Van Heerden, C., *Chem. Eng. Sci.* (1958) **8**, 133-144.
15. Amundson, N. R., *Can. J. Chem. Eng.* (1965) 49-55.
16. Padberg, G., Wicke, E., *Chem. Eng. Sci.* (1967) **22**, 1035-1051.
17. Fieguth, P., Wicke, E., *Chem.-Ing.-Tech.* (1971) **43**, 604-608.
18. Wicke, E., Vortmeyer, D., *Ber. Bunsenges. Phys. Chem.* (1959) **63**, 145; (1961) **65**, 282.

RECEIVED January 2, 1974.

Estimation of Platinum Catalyst Requirement for Ammonia Oxidation

DONALD ROBERTS

Department of Chemical Engineering, University of Birmingham,
Birmingham B15 2TT, England

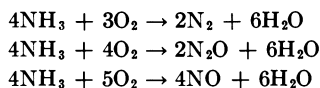
G. RICHARD GILLESPIE

Engelhard Industries, 430 Mountain Ave., Murray Hill, N. J. 07974

Despite the temperature gradients present in the Pt catalyst pad used in NH₃ oxidation and the usual surface rearrangement of the platinum, measured mass transfer coefficients for stacked metal screens can be used to estimate the amount of catalyst required for satisfactory operation of a commercial NH₃ burner. Burner design as a mass transfer operation using a transfer unit concept is recommended. Considerable reduction in platinum inventory, from previously accepted levels, seems possible. Calculations indicate that operation at a higher mass velocity or with closer mesh screens woven from finer wire would reduce catalyst requirement although other factors might be adversely affected.

It has long been argued that the catalytic oxidation of ammonia with air is a mass transfer controlled reaction. Under typical operating conditions of industrial ammonia burners, Oele (1) demonstrated that the kinetic stoichiometric O₂/NH₃ ratio is exceeded, ensuring an oxygen-rich atmosphere at the catalyst surface with ammonia diffusion as the limiting reaction step. Such a situation is probably necessary to conduct this reaction satisfactorily.

The stoichiometry (not intended to represent mechanism) of formation of the three alternative products can be represented as follows:



Equilibrium conditions are too far to the right to present any problem. The desired product is usually nitric oxide, and it is significant that this represents the highest oxidation state of the three alternatives. Its preferential formation will probably be encouraged by a high relative proportion of oxygen to ammonia at the catalyst surface.

Irrespective of the chemical mechanisms involved and considering nitric oxide as the desired product, yield losses can occur because of: (a) insufficient catalyst, and (b) poor selectivity; it is constructive to distinguish the two. By distinguishing the former it is possible to make more meaningful studies of

the effect of operating variables on selectivity. This, we contend, we are now able to do. This paper demonstrates that recent correlations of mass transfer coefficients enable one to estimate the amount of catalyst required for any specific duty.

The Catalyst System

The traditional catalyst for ammonia oxidation is a stack of woven wire screens, typically of 90Pt/10Rh alloy or occasionally of some other platinum alloy. A common standard for the screens is 80 meshes per linear inch, constructed of 0.003-inch diameter wire although other standards are in use. The number of screens constituting a catalyst pad varies from as few as three at near atmospheric pressure to as many as 20 or 30 at around 8 atm. An increase in mass velocity usually accompanies an increase in operating pressure.

During use, substantial catalyst is lost; despite this the leading wires in the pad thicken considerably because of cauliflower-like growths; these growths progressively weaken the structure of the screen, necessitating eventual replacement. Photographs published by Schmidt and Luss (2) represent the appearance of used catalyst.

Clearly the mechanical support of such flimsy catalyst structures requires careful consideration. A suitable support should have a fine structure able to spread the mechanical load evenly across the full width of the reactor. It should be deep enough to prevent bulkier elements of the reactor structure from interfering with flow through the catalyst pad, and the support system and catalyst pad together should present a sufficient and uniform resistance to flow to smooth out minor flow variations in the entering gas stream. If installed catalyst weight is to be critically designed, it would be a useful safety precaution if the support system could catalytically react with any residual ammonia, not necessarily to the desired product NO. Ammonia might otherwise escape to cooler parts of the plant and form potentially dangerous ammonium nitrite. Random Pack system has been recently introduced (3, 4) and seems to possess these properties. Claims (5) that its use enables satisfactory operation of an ammonia burner with as little as 40% of the normal catalyst charge appear to suggest that earlier designs relied upon excess catalyst as support. The high cost of installing an excess charge of a noble metal catalyst argues the need for a design procedure to estimate catalyst requirement in a system where the flow through the pad is uniformly distributed.

Mass Transfer Coefficients

Apelbaum and Temkin (6) and Oele (1) tried to compare the rate of ammonia oxidation on stacked screens with the rate of ammonia mass transfer, although they used a heat transfer correlation for flow perpendicular to a single cylinder as the source of their mass transfer coefficient. Nowak (7), in a similar comparison, had the advantage of heat transfer coefficients for stacked screens reported by London *et al.* (8) and the mass transfer coefficients for single screens reported by Gay and Maughan (9). All three studies suggested that the limiting mass transfer rate and the reaction rate were similar.

Since then, more relevant measurements of mass transfer coefficients to stacked metal screens were made by Satterfield and Cortez (10) and by Shah (11); independently both suggested Chilton-Colburn type correlations based upon wire diameter as the critical dimension. They both had to base

their correlations on mass velocities corrected for the reduction to flow area presented by the screen; Satterfield and Cortez chose G/ε the average mass velocity through a single screen, and Shah chose G/γ the maximum mass velocity. The correlations otherwise agree generally, although the higher Reynold's number range of Shah's work and the greater number of screens in the stack makes his measurements more relevant to high pressure ammonia oxidation conditions and possibly less affected by axial diffusion. The correlations can be summarized as follows in terms of Reynold's number based upon superficial velocity:

$$\text{Satterfield and Cortez: one to three screens; } \quad 0.4 < N_{Re} < 9 \\ \epsilon j_D = 0.865 (N_{Re}/\epsilon)^{-0.648} \quad (1)$$

$$\text{Shah: } \quad \text{one to five screens; } \quad 3 < N_{Re} < 107 \\ \gamma j_D = 0.644 (N_{Re}/\gamma)^{-0.67} \quad (2)$$

These two correlations cover the range of interest in ammonia oxidation.

Design for Mass Transfer in NH₃ Oxidation

To suggest that the surface rearrangement and high temperature gradients present in this system preclude accurate analysis is counterproductive, but it helps to establish the objective. Can conservative design equations be derived which, even after allowance for uncertainties, enable catalyst weight to be reduced? The answer is intended primarily for high pressure plants.

Treating the catalyst pad as a fixed-bed reactor which exists to transport ammonia to the catalyst surface where it rapidly reacts, we can draw up the following balance over an element of depth dL

$$-d[(G/M)(p/P)] = k_g a p dL$$

The omission of axial dispersion or diffusion terms is not serious, especially for high pressure plants, since the data for k_g were measured in a similar system assuming a log mean driving force—*i.e.*, ignoring axial dispersion or diffusion.

Although at the front of the pad ammonia flux to the catalyst surface is high, there is accompanying oxygen diffusion with counterdiffusion of products (steam, nitric oxide, nitrous oxide, and nitrogen). Since only a modest difference exists between the molar fluxes of reactants and products, there is little need for any major correction for net bulk flow to or from the catalyst.

The gas molar flow rate G/M increases by no more than 2½ % throughout the bed, and the relative change in total pressure P is slight, especially in high pressure plants; thus these parameters are essentially constant. Therefore,

$$-\frac{dp}{p} = (k_g M P / G) a dL \\ \text{or} \quad d[\log_e(p_I/p)] = j_D a N_{Sc}^{-2/3} dL$$

We now introduce the concept of a transfer unit which, at constant conditions, would cause unit change in $\log_e(p_I/p)$ —*i.e.*, decrease p by a factor e . The bed depth L required to reduce ammonia partial pressure in the gas from p_I to p_E is then:

$$L = \int_{p=p_I}^{p=p_E} [N_{Sc}^{2/3} / j_D a] d[\log_e(p_I/p)] = \int_0^{(NTU)} (HTU) d(NTU) \quad (3)$$

where the height of a transfer unit (HTU) is the local value of $N_{sc}^{2/3}/j_D a$, and the number of transfer units (NTU) is $\log_e(p_I/p_E)$.

Integration is required since (HTU) cannot be constant throughout the catalyst pad owing to temperature variations and the surface rearrangement of the leading screens, resulting in some variation in j_D and surface area a . Nevertheless, it would be more convenient to evaluate an average value ($\overline{\text{HTU}}$) for the height of a transfer unit to be applied to the whole pad and to estimate catalyst requirement by

$$L = (\overline{\text{HTU}})(\text{NTU}) \quad (4)$$

Since mass transfer control implies a roughly exponential decline in ammonia consumption throughout the pad, a catalyst pad designed to burn 99.5% of the ammonia fed would consume nearly 75% of it over the leading 25% of the catalyst. Thus 75% of the temperature rise in the gas would occur before the remaining 75% of the catalyst is contacted. Since this latter fraction of the pad is also relatively free from major catalyst surface rearrangement, little error will result from an averaged ($\overline{\text{HTU}}$) over this section. ($\overline{\text{HTU}}$) can conveniently be estimated from the Shah correlation, Equation 2, basing the calculation on the wire diameter of unaged screens.

Combining the Shah correlation with the definition of (HTU) yields

$$(\text{HTU}) = 1.55 N_{sc}^{2/3} N_{Re}^{0.57} \gamma^{0.43}/a \quad (5)$$

The units of (HTU) depend only on the units of a . For example, if a is $\text{ft}^2/\text{troy oz}$ of catalyst, (HTU) is given as $\text{troy oz}/\text{ft}^2$ of reactor cross section; if a is ft^2/ft^2 of single screen, (HTU) is given as number of screens. The problem of estimating (HTU) or ($\overline{\text{HTU}}$) over the leading section of the pad remains.

Estimation of $\overline{\text{HTU}}$

Temperature Variation. Bearing in mind the objective of a conservative, approximate design equation, use over the whole pad of ($\overline{\text{HTU}}$) estimated at the mean film temperature seems reasonable, and a suitable mean temperature \overline{T} is defined by

$$\overline{T} = T_S - 0.5 (T_S - T_B)_{\log \text{ mean}}$$

Oele (1) examined the temperature profiles expected through the metal structure of the catalyst pad and through the gas stream. Because of the nearly adiabatic nature of the reaction and mass transfer limitation, the wire temperature varies little from the inlet to the outlet of the catalyst pad, departing slightly from the adiabatic flame temperature of the gas by an amount which depends on N_{Pr}/N_{Sc} . The gas temperature rises exponentially throughout the pad to within $\sim 20^\circ\text{C}$ of the adiabatic flame temperature. Calculations based upon such temperature profiles indicate that \overline{T} is within 50°C of the exit gas temperature.

The Schmidt number is relatively insensitive to temperature, and at the temperatures of interest, $> 800^\circ\text{C}$, viscosity is proportional to $T^{0.5}$. Thus, even if the exit gas temperature is used instead of \overline{T} , the additional error in estimating ($\overline{\text{HTU}}$) will be only $\sim 2\%$. Since it is more convenient to estimate ($\overline{\text{HTU}}$) at the exit gas temperature, this might often be satisfactory. Nevertheless, the

large temperature difference existing between the gas and the catalyst at the front of the pad leaves considerable doubt over the relevance of (HTU) estimates to this part of the pad.

Surface Rearrangement. The cauliflower-like growths which develop on the leading wires have two results. One is an increase in the effective wire diameter with a corresponding increase in transfer area; the other is a roughening effect which, while invalidating the Shah correlation, should lead to enhanced mass transfer.

If we study the effect of increasing wire diameter from d_c to the diameter d_a of aged catalyst on the (HTU) value predicted by Equation 5, while holding mesh size n and mass velocity constant, we can estimate that:

$$\frac{(\text{HTU})_{\text{aged wire}}}{(\text{HTU})_{\text{clean wire}}} \leq \left[\frac{\left(\frac{1}{nd_c} - \frac{d_a}{d_c}\right)^2}{\left(\frac{1}{nd_c} - 1\right)^2 \frac{d_a}{d_c}} \right]^{0.43}$$

This shows that wire thickening leads to a marked reduction in (HTU). The inequality allows for the further unquantified reduction which is expected from the roughening effect although it could be removed if d_a is interpreted as the "effective" diameter of aged wire.

Thus the estimation of (HTU) from Equation 5 based upon the wire diameter of clean catalyst screens would be a conservative design practice; it leads to an under-estimate of the mass transfer capability of the leading screens, probably sufficiently conservative to dispel any remaining doubts about the effect of the severe temperature gradients in this region.

Estimation of Catalyst Requirement

We suggest that catalyst requirement can satisfactorily be estimated by using Equation 5 to evaluate $(\overline{\text{HTU}})$ at the average, or even exit, conditions of the bed, and multiplying by the required number of transfer units (NTU). The required (NTU) is a decision for the designer and probably should represent an economic balance between the value of increased ammonia converted to nitric oxide and the added cost of installing more catalyst.

80-Mesh Screens at 900°C. Simplified versions of Equation 5 are possible if one assumes that 80-mesh screens are used and that exit gas temperature will be around 900°C. By substituting typical values of 0.56 for γ , 1.56 for a , and an estimate of 0.56 for N_{sc} , we have

$$(\text{HTU}) \simeq 0.52 N_{Re}^{0.57} \text{ screens} \quad (6)$$

Since N_{sc} is relatively insensitive to temperature, this should be suitable for a range of temperatures. Nitric acid plant operations do not generally collect data on Reynold's number or number of screens; thus, introducing the parameters x = mole fraction of NH_3 in feed, and R_{NH_3} = loading in short tons NH_3 /day/ft² of reactor cross section, leads to:

$$(\text{HTU}) \simeq 0.34 (1.70/x - 0.70)^{0.57} / R_{\text{NH}_3}^{0.43} \quad (7)$$

in units of troy oz/ton of NH_3 /day, of 90Pt/10Rh catalyst. This version is restricted to temperatures $\sim 900^\circ\text{C}$.

EXAMPLE. For a typical value of $x = 0.095$ and $R_{\text{NH}_3} = 11$, and arbitrarily choosing (NTU) = 5.3 for 99.5% ammonia consumption within the catalyst

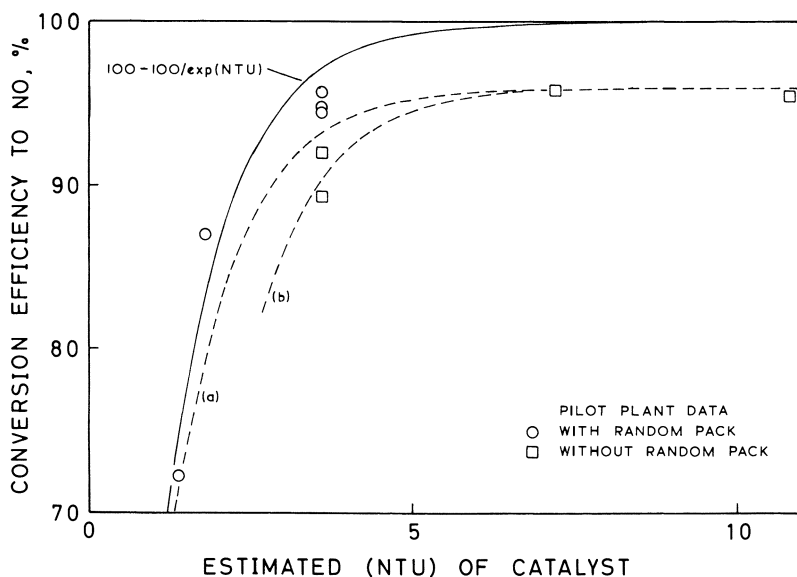


Figure 1. Effect of amount of installed catalyst on NH_3 conversion efficiency

pad, we estimate the requirement of 90Pt/10Rh catalyst to be 3.2 troy oz/ton NH_3 /day. Assuming an overall fixed nitrogen efficiency of 93% for a nitric acid plant, this figure corresponds to ~ 0.95 troy oz/ton HNO_3 /day.

One might suggest that a 99.5% consumption of ammonia is too low, but this estimate of < 1 troy oz/ton HNO_3 /day is much lower than the reputedly traditional catalyst loading of 2 troy oz/ton of HNO_3 /day in high pressure nitric acid plants. Thus we see how much catalyst can be saved if uniform flow conditions across the reactor can be ensured.

Practical Application

Short Term Validity. Pilot plant data are given in Figure 1 as conversion of ammonia to nitric oxide *vs.* our estimate (from Equation 5) of the number of transfer units represented by the catalyst pad used. Some of the data were obtained with a catalyst pad using a Random Pack catalyst-support system, and some were obtained without. The catalyst was aged between 150 and 600 hours. The solid line represents our theoretical estimate of the degree of ammonia consumption by the catalyst pad—*i.e.*, $100 - 100/\exp(\text{NTU})$.

Since even a fully adequate catalyst pad is not selective enough for 100% conversion, the data are mostly below the estimated ammonia consumption; however if a consistent yield loss of 4% from poor selectivity on the catalyst is assumed for all the data, one of the broken lines is obtained. These lines assume either (a) residual NH_3 reacts one to one with O_2 to produce waste products, or (b) residual NH_3 reacts one to one with NO or NO_2 to produce waste products. The data are limited, but the agreement is encouraging. Conversion efficiency obtained with the Random Pack system seems higher than that without it. This might result from either improved flow distribution or from the Random Pack support perhaps ensuring that residual ammonia reacts with oxygen rather than nitric oxide (probably the former).

Further support comes from our recent experience with two full-scale commercial nitric acid plants using the Random Pack system. Agreement in Table I between our estimated and measured conversion efficiency to NO is satisfactory.

Table I. Commercial Nitric Acid Plant Data

	Plant A		Plant B
	(i)	(ii)	(i)
N_{Re}	28	28	25
Estimated (NTU) of catalyst	3.7	5.3	3.5
Estimated NH_3 consumption by catalyst, %	97.6	99.5	97.1
Estimated conversion efficiency to NO, % (allowing 4% selectivity loss)	93.6	95.5	93.1
Measured conversion efficiency to NO, %	89-94	95-97	~94

Under conditions reported in columns (i) for either plant, surface rearrangement of the bottom screen in the catalyst pad clearly confirmed that insufficient catalyst was installed. The improved performance in column (ii) for plant A resulted from installation of a catalyst charge weight determined by the type of calculation proposed here. The result of a similar recommendation for plant B is not yet available.

Long Term Validity. Even if our calculations indicating a reduction in installed catalyst weight are accepted, nitric acid plant operators might argue that a catalyst charge of the size indicated, while initially adequate, would be reduced by platinum loss over a normal operating cycle to less than two-thirds of its original weight. Thus they would argue for excess catalyst as reserve.

To answer this argument, recall that the reaction occurs on the outer surface of the catalyst, and that despite platinum loss the catalyst wires thicken during use. As long as the catalyst wires retain their integrity as wires and retain their catalytic activity, their capacity to burn ammonia will increase. Doubts arise beyond the point where the wires disintegrate or clog the pore structure of the pad, but continued operation with such catalyst would probably be bad practice. Also, the addition of extra catalyst layers to the back of an already adequate and well-supported pad does not affect the amount of ammonia burned on the leading catalyst screen and thus cannot affect its longevity.

These arguments are well supported by the plant data in Figure 2. The installed catalyst charge for this 78-day production run was 0.82 troy oz./daily ton of nitric acid, representing less than 5 transfer units; this fell to 0.31 troy oz./daily ton by the end of the run, yet the ammonia conversion efficiency of the pad remained satisfactory. Catalyst loss rate at 0.0065 troy oz./ton of nitric acid was very satisfactory. Similar data were obtained on other runs with reduced weight pads using the Random Pack system; conversion efficiency was equivalent to comparative runs with catalyst loadings as high as 2.4 troy oz./daily ton of nitric acid.

Implications of the Shah Correlation

If the validity of Equation 5 for estimating catalyst requirement is accepted, certain conclusions can be drawn about the effect of screen characteristics and operating conditions.

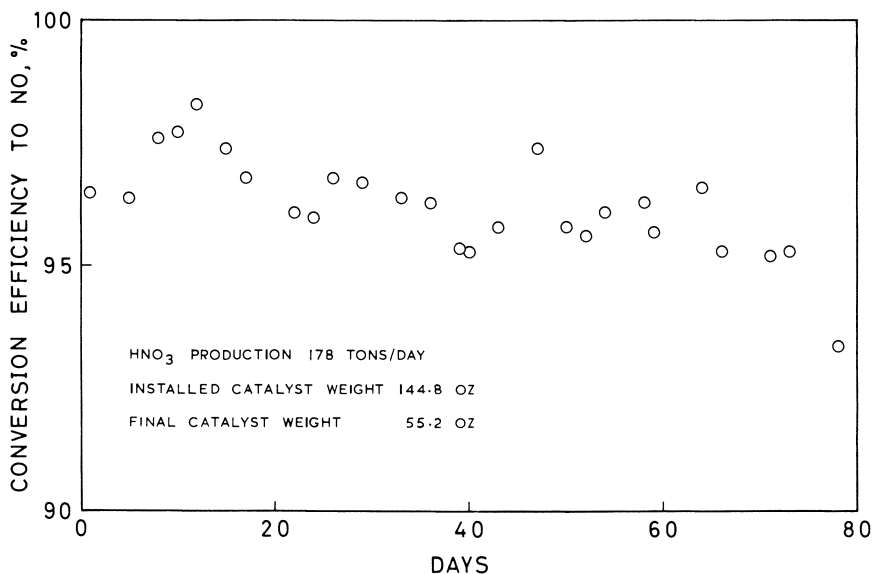


Figure 2. Nitric acid plant production run with reduced weight catalyst pad (with Random Pack and Degussa Getter)

Screen Characteristics. The only screen characteristics in Equation 5 are d , γ , and a ; to reduce catalyst requirement, it would seem necessary to decrease d and γ while increasing a , although these parameters are interdependent. Extracting superficial mass velocity and gas properties from the equation,

$$(\text{HTU}) \propto d^{0.57} \gamma^{0.43}/a$$

If a is $\text{ft}^2/\text{troy oz}$ of catalyst, $a \propto 1/d$, and since $\gamma \simeq (1 - nd)^2$, the catalyst requirement in troy oz $\propto d^{1.57} (1 - nd)^{0.86}$.

This function is plotted in Figure 3 for different mesh sizes. Although the curves pass through a maximum, it is at too high a wire diameter to be of practical interest. Obviously, the weight of catalyst required can be reduced significantly by moving towards a closer mesh screen woven from finer wire.

A similar analysis based on the Satterfield and Cortez correlation (Equation 1), leads to the approximate prediction:

$$\text{catalyst requirement in troy oz} \propto d^{1.648} \left(\frac{4}{\pi} - nd \sqrt{1 + n^2 d^2} \right)^{0.704}$$

a function which has a form similar to that in Figure 3, thus leading to the same qualitative conclusions.

The characteristics of screens used by Satterfield and Cortez (10) and by Shah (11) are plotted in Figure 3 as a guide to practical combinations.

Process Variables. PRESSURE. From Equation 5 we would expect changes in operating pressure to have little direct effect on catalyst requirement. However, higher pressures allow a higher mass velocity to be used with a consequent reduction in catalyst requirement.

EXIT GAS TEMPERATURE. The only property in Equation 5 which is significantly affected by temperature is the viscosity of the gas mixture. For minor variations around 900°C , therefore, $(\text{HTU}) \propto \bar{T}^{-0.28}$; that is, the effect is minor.

MASS VELOCITY OF GAS. Although Equation 5 indicates that $(HTU) \propto G^{0.57}$, a reduction in gauze requirement results from an increase in mass velocity; this is because for a specific reactor duty in terms of ammonia to be burned, the reactor cross sectional area can be reduced in inverse proportion to the mass velocity. Thus, the gauze requirement $\propto G^{-0.43}$.

A NOTE OF CAUTION. While it is tempting to suggest immediate modifications to ammonia oxidation catalysts and ammonia burner operating conditions in line with these observations, it would be wrong to do so. Many factors are involved, and the only one examined here is our estimate of the weight of catalyst required.

For example, one should not assume that catalyst requirement can be reduced by increasing mass transfer rates without possible detriment to selectivity. If at some point within the bed, bulk gas phase partial pressures of ammonia and oxygen are p_{NH_3} and p_{O_2} respectively and are diffusing toward the catalyst surface where the corresponding partial pressures are $p^*_{NH_3}$ and $p^*_{O_2}$, then the mass transfer rate of oxygen/unit area of catalyst surface is

$$k_{gO}(p_{O_2} - p^*_{O_2}) = 1.25 k_g (p_{NH_3} - p^*_{NH_3}) \simeq 1.25 k_g p_{NH_3}$$

since operating conditions are such that ammonia mass transport is limiting and assuming the yield is 100% (for simplicity).

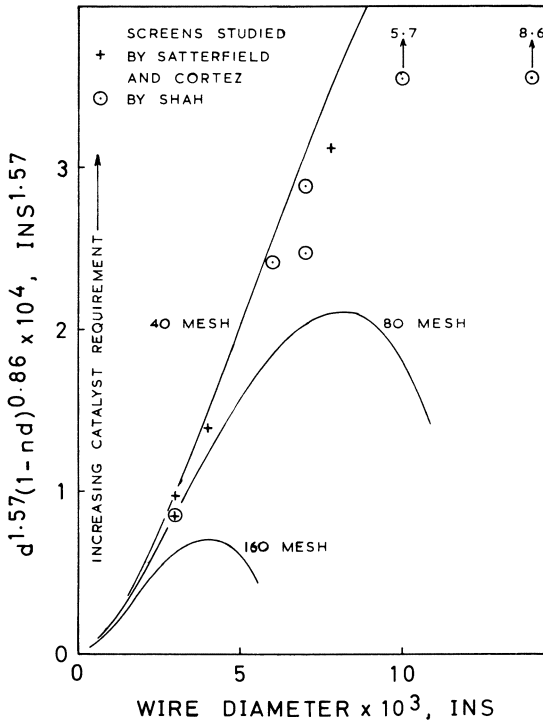


Figure 3. Effect of screen characteristics on mass transfer capacity of screens

$$\text{Thus } p^*_{\text{O}_2} \simeq p_{\text{O}_2} - 1.25 \frac{k_g}{k_{g0}} p_{\text{NH}_3}$$

If the mass transfer coefficients are doubled (*e.g.*, by increasing mass velocity), their ratio k_g/k_{g0} would be unchanged, and $p^*_{\text{O}_2}$ would effectively remain the same. The mass flux of both reactants to the surface however, is doubled, so that the reaction must proceed at twice the previous rate. This probably could not happen without a marked increase in $p^*_{\text{NH}_3}$, even though it may remain small relative to p_{NH_3} .

Thus, an increase in mass transfer coefficient results in a reduction in $p^*_{\text{O}_2}/p^*_{\text{NH}_3}$, representing probable deterioration in the reaction conditions at the catalyst surface and resulting from a modest move away from mass transfer control. Full implications of improvements in mass flux to the surface will become apparent only with better understanding of the complete chemical mechanism.

Catalyst Loss

No study of ammonia oxidation catalysts would be complete without some discussion of catalyst loss. Nowak (7) suggested that direct vaporization of PtO_2 is significant, but Schmidt and Luss (2) pointed out that Nowak's correlation differs from the observed loss rate by a factor of about four. Edwards *et al.* (12) explain the higher loss rate as a result of temperature fluctuations. Since precious metal loss rate is a convex function of temperature, higher losses occur with a fluctuating temperature than with the same average steady temperature. Gillespie and Kenson (5) claim that the Random Pack catalyst system, containing as much as 60% less Pt/Rh than a traditional catalyst pad, results in a platinum loss rate which is 25 to 30% less than normal. These reduced loss rates are accompanied by reports of reduced catalyst temperature fluctuations. A move towards thinner wire catalyst structures might accentuate these temperature fluctuations.

Diffusion of PtO_2 into the gas stream is one step in such a process, but it may be a limiting one. If PtO_2 diffuses more slowly than ammonia, then a catalyst pad correctly designed for ammonia consumption might contain insufficient surface for the platinum loss rate to reach its full potential. Additional catalyst would improve ammonia consumption very little but might add appreciably to PtO_2 vaporization. This argument is offered only tentatively. The catalyst loss mechanism is clearly a complex problem which deserves more thorough investigation.

Conclusions

The financial penalties incurred from excess platinum/rhodium catalyst in an ammonia burner are severe, comprising the servicing cost of the additional capital and apparently a higher platinum loss rate than necessary. The installed catalyst weight should be the minimum required for satisfactory operation.

The equations presented here can be used to estimate catalyst requirements for any high pressure installation; if reduced weight catalyst pads are used, uniform flow distribution and support must be ensured by installing a combined catalyst-support system such as Random Pack. Former methods of estimating catalyst requirement took little note of process variation between different installations.

While major doubts remain over the errors introduced by using isothermal mass transfer coefficients in the presence of large temperature gradients, such doubts are important only for the leading screens of the catalyst pad, where surface rearrangement of the metal should ensure that our equations otherwise underestimate the mass transfer capability of these screens.

Our calculations suggest that operation of an ammonia burner at higher mass velocity or use of closer mesh screens woven from finer wire would reduce catalyst requirement although other factors more important to nitric acid plant operations might be adversely affected. Apelbaum and Temkin (6) suggested thinner wires and higher gas velocities in 1948, but little progress has been made in this direction. Such developments have been restricted by high manufacturing costs and fears that such screens would have insufficient strength and poor aging properties.

Nomenclature

a	surface area of unit quantity of 1 ft ² of screen (units according to choice)
D	diffusivity, ft ² /hr
d	wire diameter, inches
d_a	aged wire diameter, inches
d_c	clean wire diameter, inches
G	superficial gas mass velocity, lbs/hr-ft ²
(HTU)	height of transfer unit, = $N_{sc}^{2/3}/j_D a$ (units according to choice)
($\overline{\text{HTU}}$)	value of (HTU) at mean conditions (units according to choice)
j_D	j factor for mass transfer, = $(k_g MP/G) N_{sc}^{2/3}$
k_g	mass transfer coefficient for NH ₃ , lb-moles/hr-ft ² -atm
k_{g0}	mass transfer coefficient for O ₂ , lb-moles/hr-ft ² -atm
L	depth of catalyst pad (units according to choice)
M	mean molecular weight of gas
N_{Re}	Reynolds number, = $d_c G/\mu$
N_{Sc}	Schmidt number, = ν/D
(NTU)	number of transfer units
n	mesh size, inches ⁻¹
P	total pressure, atm
p	partial pressure of NH ₃ , atm
p_{NH_3}	partial pressure of NH ₃ , atm
$p^*_{NH_3}$	partial pressure of NH ₃ at catalyst surface, atm
p_{O_2}	partial pressure of O ₂ , atm
$p^*_{O_2}$	partial pressure of O ₂ at catalyst surface, atm
p_E	partial pressure of NH ₃ exiting catalyst pad, atm
p_I	partial pressure of NH ₃ entering catalyst pad, atm
R_{NH_3}	NH ₃ loading of 1 ft ² of reactor cross section, short tons/day-ft ²
T	temperature, °C
\overline{T}	mean film temperature, °C
T_S	wire temperature, °C
T_B	gas temperature, °C
x	mole fraction of NH ₃ in feed

Greek

ϵ	porosity of single screen
γ	minimum fractional opening of single screen
μ	gas viscosity, lbs/ft-hr
ν	kinematic gas viscosity, ft ² /hr

Literature Cited

1. Oele, A. P., *Chem. Reaction Eng., Meeting Europ. Fed. Chem. Eng., 12th, Amsterdam* (1957) 146.
2. Schmidt, L. D., Luss, D., *J. Catalysis* (1971) **22**, 269.
3. U.S. Patent 3,660,024 (1972).
4. Canadian Patent 916,396 (1972).
5. Gillespie, G. R., Kenson, R. E., *Chem. Tech.* (1971) **1**, 627.
6. Apelbaum, L., Temkin, M., *J. Phys. Chem. (USSR)* (1948) **22**, 179.
7. Nowak, E. J., *Chem. Eng. Sci.* (1966) **21**, 19.
8. London, A. L., Mitchell, J. W., Sutherland, W. A., *J. Heat Transfer* (1960) **82**, 199.
9. Gay, B., Maughan, R., *Int. J. Heat Mass Transfer* (1963) **6**, 277.
10. Satterfield, C. N., Cortez, D. H., *Ind. Eng. Chem., Fundamentals* (1970) **9**, 613.
11. Shah, M. A., Ph.D. thesis, University of Birmingham, England (1970).
12. Edwards, W. M., Worley, F. L., Luss, D., *Chem. Eng. Sci.* (1973) **28**, 1479.

RECEIVED January 2, 1974.

The Catalytic Conversion of Sulfur Dioxide in Wet Stack Gases to Elemental Sulfur

M. F. MOHTADI and H. B. DINGLE¹

Department of Chemical Engineering, University of Calgary, Alberta Canada

The catalytic conversion of sulfur dioxide in wet stack gases to elemental sulfur, using carbon monoxide as reducing agent, was studied theoretically and experimentally. Computer models were developed to calculate equilibrium compositions for the reaction system. Experiments were done in a reactor designed to simulate equipment and operating conditions used in sulfur recovery plants. The method studied can remove up to 90% SO₂ in the wet stack gas. Complete conversion to elemental sulfur in the presence of water vapor, is, however, hampered by side reactions which produce carbonyl sulfide and hydrogen sulfide.

Conventional Claus-type sulfur recovery plants operate with overall efficiencies of 93–97% (1) although their potential efficiencies could be 99% (2). Thus, their tail gases contain much H₂S and SO₂ plus smaller amounts of COS and CS₂. The tail gas is fired with air and methane to oxidize all sulfur compounds to SO₂ and to elevate the gas temperature to the level required. Tightening controls on SO₂ emission have caused the sulfur gas plants to look for further means to desulfurize their effluent gas streams. This work studies the feasibility of CO as a reducing agent for SO₂ in wet stack gases. Specific objectives were:

- (1) To develop a suitable catalyst for this conversion.
- (2) To verify the conversion in a fixed bed reactor, under the same pressure, temperature, and space velocity used in conventional sulfur recovery plants.
- (3) To investigate the effect of large amounts of water vapor in the feed stream on the conversion reaction.

The literature reports at least five reducing agents suitable for converting SO₂ to elemental sulfur: hydrogen sulfide, carbon, hydrogen, methane, and carbon monoxide. Direct conversion by catalytic reduction with CO appeared to be the most applicable to sulfur recovery plants.

The catalytic conversion with CO was first studied in 1918 by Ferguson (3) who used ceramic chips as catalyst. Yushkevich and Karzhavin (4) noted later that the non-catalyzed reduction of SO₂ with CO was *ca.* 90% complete at 400–1200°C and that reaction velocity was enhanced by ferric/aluminum oxides as catalysts. Also, water vapor promoted H₂S formation. Ryason and Harkins (5) studied the simultaneous removal of SO₂ and NO_x from combus-

¹ Present address: Imperial Oil Ltd., Sarnia, Ontario, Canada.

tion gases. For a synthetic gas composed of SO_2 , CO , CO_2 , N_2 , and nitrogen oxides, they observed a maximum of 97% at 1000°F. Simultaneous catalytic reduction of NO and SO_2 by CO was also studied by Quinlan, Okay, and Kittrell (6). They showed that the maximum attainable removal of sulfur compounds is 75–85% in a single-bed reactor.

In a recent publication on SO_2 removal from stack gases using CO , Querido and Short (7) describe a process particularly suitable for treating of gases at typical power plant concentrations and temperatures. Their process removes 97% sulfur, using a dual copper-on-alumina catalyst reactor system and a $\text{CO}:\text{SO}_2$ ratio of 1.03. However, elemental sulfur and CO form COS —a harmful side reaction. Short and Okay (8) subsequently described the effect of water vapor on SO_2 reduction by CO and show that SO_2 reduction activity is adversely affected by water.

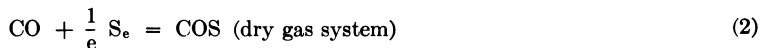
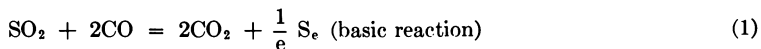
Our studies on sulfur removal were in two phases: (a) the theoretical phase (thermodynamic equilibrium studies), and (b) the experimental phase (conversion process under non-equilibrium conditions). The theoretical equilibrium studies delineated the absolute conversion limit. The experimental studies showed the overall conversion attainable under simulated plant conditions.

Theoretical Study

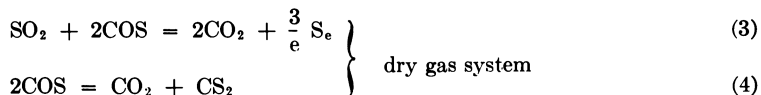
Suitable computer models were developed to: (1) calculate the equilibrium compositions for reaction systems and chemical species; (2) establish which reactions contributed significantly to the overall process; (3) evaluate the equilibrium compositions arising from changes in the feed gas compositions.

Two methods are available for calculating equilibrium gas compositions from thermodynamic principles. The first is based on successively correcting an initial, non-equilibrium composition by adjusting factors derived from the equilibrium expressions for each reaction—the simultaneous chemical equilibria (SCE) method. The second method relies on the minimization of the total free energy of the given system (9)—the free energy minimization (FEM) method. Details are given elsewhere (10). The two methods can be used in a complementary way.

Overall Reaction System. The principal reactions in the reduction of SO_2 with CO are:



Neglecting the presence of water vapor, the additional reactions which are thermodynamically dependent but which might be important kinetically are:



Water vapor in the feed allows three further reactions with the product sulfur, the by-product COS , and the reducing agent CO , respectively:

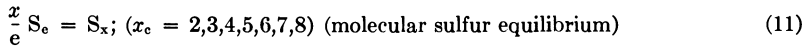


} wet gas system

Reaction 7, the water gas shift reaction, is important since the hydrogen produced will react with other system components:



In addition, sulfur vapor exists in a complicated equilibrium between S_2 , S_3 , S_4 , S_5 , S_6 , S_7 , and S_8 ; the distribution of these species is a function of temperature and the total sulfur partial pressure (11). Therefore, we must include in the overall reaction system:



Earlier workers (12, 13) considered only the equilibrium between S_2 , S_6 , and S_8 owing to the lack of accurate thermodynamic data for the remaining sulfur species. Data have become available recently for all the polymeric species of elemental sulfur (14). However, for convenience, the equilibrium between S_2 , S_6 , and S_8 are considered here.

Application of the Computer Programs. The SCE program was used to calculate the equilibrium gas compositions from the individual chemical reactions assumed to occur in the overall reaction system. These calculations were verified, where possible, with the FEM program. The feed compositions for each reaction are listed in Table I. A typical computation result is shown in Figure 1 (percent conversion (at equilibrium) of SO_2 to elemental sulfur as a function of temperature).

SCE and FEM programs were applied to the overall reaction system at 400°–1000°K. Pressure was assumed as 1 atm absolute. Although the programs were used to calculate equilibrium compositions for temperatures as low

Table I. Feed Compositions (vol %)

Specie	1	1	1	2	2	3	4	5
	(1)	(2)	(3)	(1)	(2)			
S^a	0.00	0.00	0.00	50.00	1.00	0.00	—	1.00
SO_2	33.33	7.69	1.00	—	—	1.00	—	0.00
CO	66.67	15.38	2.00	50.00	2.00	—	—	—
CO_2	0.00	76.93	10.00	—	—	10.00	10.00	—
COS	—	—	—	0.00	0.00	2.00	2.00	—
CS_2	—	—	—	—	—	—	0.00	—
H_2	—	—	—	—	—	—	—	—
H_2O	—	—	—	—	—	—	—	30.00
H_2S	—	—	—	—	—	—	—	0.00
N_2	—	—	87.00	—	97.00	87.00	88.00	69.00

^a $\text{S} = 2\text{S}_2 + 6\text{S}_6 + 8\text{S}_8$.

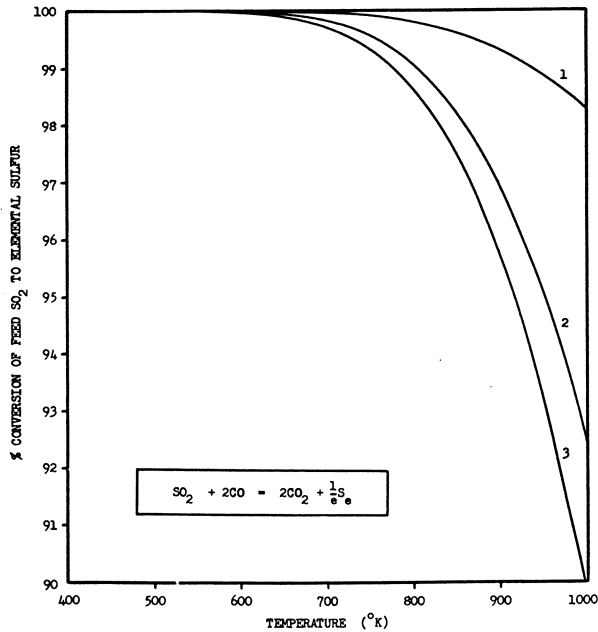


Figure 1. Theoretical equilibrium: $SO_2 + 2CO = 2CO_2 + \frac{1}{8}S_8$

as 400°K, the lower temperature limit for each case had to be corrected to correspond with the dew point of sulfur vapor in that system. Neither program was designed to treat a two-phase system. The dew points of sulfur vapor were taken from literature partial pressure/vapor pressure data.

Feed compositions used for the overall reaction system are given in Table II. Typical computed results are shown in Figures 2–6, where temperature is plotted vs. equilibrium conversion of feed sulfur dioxide to either elemental sulfur, H_2S , or COS at various $CO:SO_2$.

In all computer studies, equilibrium gas compositions were calculated at 25°K intervals. The thermodynamic data were obtained mainly from the paper by Gamson and Elkins (12).

for Individual Chemical Reactions

6	7	8	9	10	11
—	—	1.00	0.00	—	1.00
—	—	—	1.00	—	—
—	2.00	—	—	0.00	—
10.00	10.00	—	—	—	—
2.00	—	—	—	2.00	—
—	—	—	—	—	—
—	0.00	2.00	2.00	2.00	—
30.00	30.00	—	30.00	—	—
0.00	—	0.00	—	0.00	—
58.00	58.00	97.00	67.00	96.00	99.00

Table II. Feed Compositions

Species	Case Number							
	1	2	3	4	5	6	7	8
SO ₂	1.00	1.00	1.00	1.00	1.00	1.00	1.00	1.00
CO	2.00	2.50	3.00	3.50	4.00	2.00	2.00	2.00
CO ₂	10.00	10.00	10.00	10.00	10.00	10.00	10.00	10.00
H ₂ O	—	—	—	—	—	1.00	2.00	3.00
N ₂	87.00	86.50	86.00	85.50	85.00	86.00	85.00	84.00
2CO/SO ₂	1.00	1.25	1.50	1.75	2.00	1.00	1.00	1.00
% H ₂ O	0.00	0.00	0.00	0.00	0.00	1.00	2.00	3.00

* $P = 1.00$ atm; $T = 400^{\circ}$ - 1000° K.

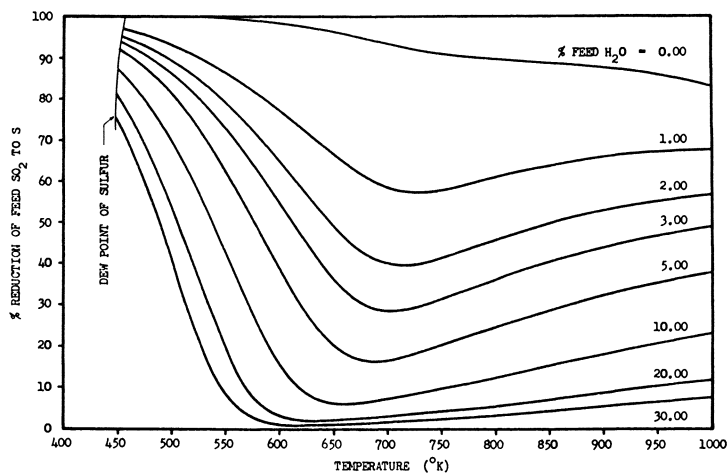


Figure 2. Percent feed sulfur dioxide reduced to elemental sulfur

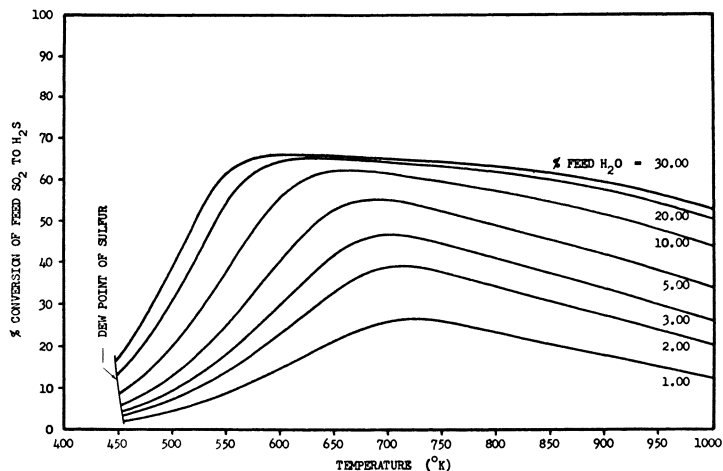


Figure 3. Percent feed sulfur dioxide converted to hydrogen sulfide

(vol %) for General System*

Case Number							
9	10	11	12	13	14	15	16
1.00	1.00	1.00	1.00	1.00	1.00	1.00	1.00
2.00	2.00	2.00	2.00	2.50	3.00	3.50	4.00
10.00	10.00	10.00	10.00	10.00	10.00	10.00	10.00
5.00	10.00	20.00	30.00	30.00	30.00	30.00	30.00
82.00	77.00	67.00	57.00	56.50	56.00	55.50	55.00
1.00	1.00	1.00	1.00	1.25	1.50	1.75	2.00
5.00	10.00	20.00	30.00	30.00	30.00	30.00	30.00

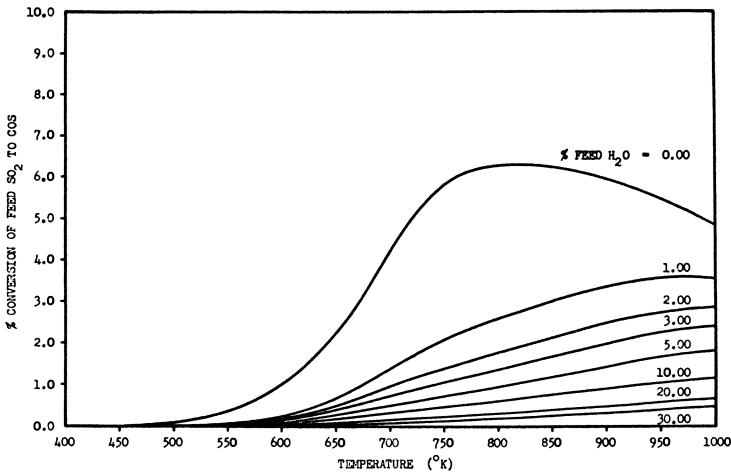


Figure 4. Percent feed sulfur dioxide converted to carbonyl sulfide

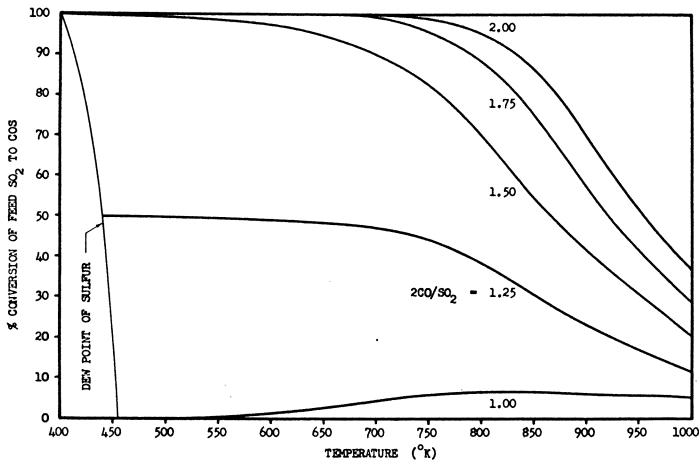


Figure 5. Percent feed sulfur dioxide converted to carbonyl sulfide as a function of feed CO:SO₂ ratio and temperature

Analyses of the Computer Studies. Equilibrium gas compositions computed for the individual reactions assumed showed the equilibrium performance of a single important species in the given reaction. No results were obtained for the reaction leading to CS_2 formation since the computer studies indicated virtually no conversion of COS to CS_2 under the prescribed conditions.

The results for the overall system (Figures 2–6) are those computed from the FEM program. The SCE program gave virtually identical results and was used for random point checks. Figure 5 shows the effect of increasing CO concentration on COS production in a dry gas system while Figure 6 indicates this effect on H_2S production for a wet gas. Water vapor in the feed gas is obviously significant. For example, Figure 2 shows that with 30.0% water

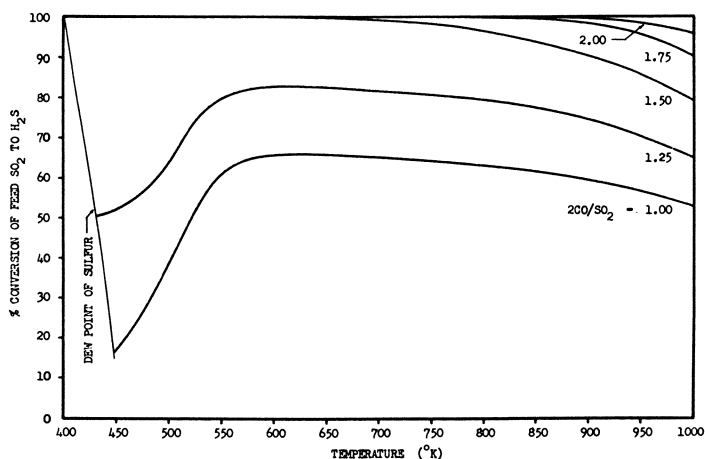


Figure 6. Percent feed sulfur dioxide converted to hydrogen sulfide as a function of feed $\text{CO}:\text{SO}_2$ ratio and temperature

vapor, elemental sulfur production approaches zero at $T > 550^\circ\text{K}$. The maximum adverse effect of water vapor is at $500^\circ\text{--}600^\circ\text{K}$.

In the dry reaction system excess CO reacts with product sulfur to form COS ; in the wet gas system, CO promotes H_2S production. The former observation agrees with Querido and Short (7). The latter can be attributed to the water–gas shift reaction where CO reacts with water vapor to produce hydrogen; the hydrogen then reacts with product sulfur to form H_2S . Thus, this process must operate at or below the dew point of sulfur vapor.

Experimental Study

The only published data on the kinetics of SO_2 reduction by CO is by Quinlan *et al.* and recent (6). However, it has been known for some time that reactions between CO and SO_2 proceed satisfactorily in a few tenths of a second.

Our experimental apparatus (Figure 7) was basically a fixed-bed reactor system, with flow control and gas analysis. It included a feed gas preheater, a fixed-bed catalytic reactor, and a sulfur/water recovery condenser. Details are given elsewhere (10).

All gas mixtures were analyzed on a Varian Aerograph dual column gas chromatograph (series 1700/model 20) with thermal conductivity detectors,

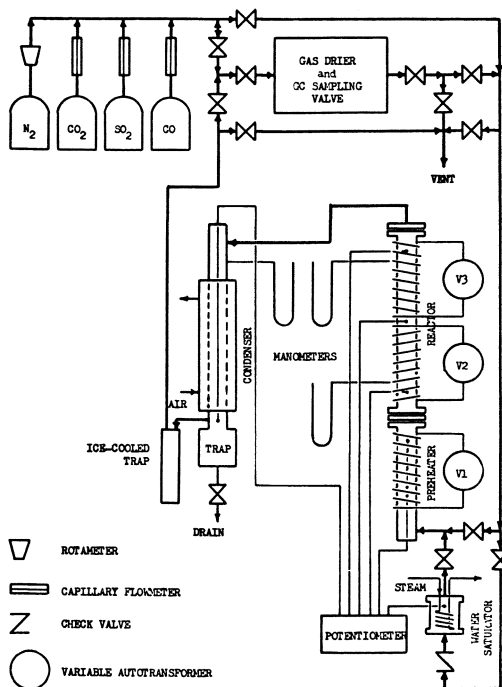


Figure 7. Reaction system schematic

a column switching valve, and a linear programmed oven. Two columns were necessary to analyze all the gas components since no single column packing was suitable for all. Nitrogen, hydrogen, and CO were analyzed on a 6-ft by $\frac{1}{8}$ -inch Teflon column packed with 80/100 mesh, 5A molecular sieve at 125°C. Water vapor, CO₂, H₂S, COS, and SO₂ were analyzed on a 6-ft by $\frac{1}{8}$ -inch Teflon column packed with 80/100 mesh, Porapak QS at 125°C. Typical responses are in Figure 8. All gas chromatographic analyses were recorded by a Varian Aerograph single-pen chart recorder (model 20) with a 1.0-mv response. A disc integrator was used to calculate peak area.

Catalysts. Two catalyst types were used: (1) 3/16-inch, cylindrical silica-alumina pellets (SMR 7-2423/grade 970: Davison Co.) with 0.3 wt % copper; (2) 8 to 14 mesh, hydrated alumina (T61: Canada Colours and Chemicals Ltd.) with 0.3 wt % copper. Hydrated alumina catalyst was also used by Rayson and Harkins and by Querido and Short. We used it as a comparison for the silica-alumina pellets which represent an industrial-sized catalyst with great resistance to attrition.

Elemental copper was deposited on the respective supports by soaking the support in cupric nitrate solution, drying in nitrogen, heating at 300°F to reduce the cupric nitrate to cupric oxide, and reducing the cupric oxide in hydrogen at 1000°F to give elemental copper. Final reduction was done just before each run.

Procedure. Seventeen separate experimental series were designed and conducted. The term series defines the collection of data points pertaining to various temperatures (500°–1100°K) for a single, fixed combination of the following variables:

(1) Catalyst: alumina, silica-alumina, copper on alumina, or copper on silica-alumina

- (2) Contact time: 0.1, 0.2, 0.4, or 3.35 sec.
 (3) Feed gas composition: vol % of N_2 , CO_2 , CO , H_2 , SO_2 , and water vapor.

The feed gas flow rate was fixed at $25 \text{ cm}^3/\text{sec}$ at standard temperature (0°C) and pressure (1.0 atm) for all experiments. For each series, a fresh charge of catalyst, sufficient to give the required contact time, was placed in the reactor unit. The reactor was heated, and the reactant gases were successively added in proportions to make the total volumetric flow rate $25 \text{ cm}^3/\text{sec}$.

Results. The first three series were done to determine the effect of catalyst support. The gas composition did not change on going through the reactor at reactor temperatures of 560° , 755° , and 975°K . Thus, the silica-alumina support was inert for the reaction between SO_2 and CO at contact times up to 3.5 sec.

Series 4, 5, 5a, 5b, and 6 involved dry gas mixtures and were designed to study the effectiveness of the catalyst supports for the active copper and the stability of the $Cu/Si-Al$ catalyst. These series were also done to see if the deactivated catalyst could be regenerated in a hydrogen atmosphere.

The effects of water vapor on the efficiency of SO_2 reduction with CO were studied in the remaining series. In series 7, 8, and 9 the water vapor in

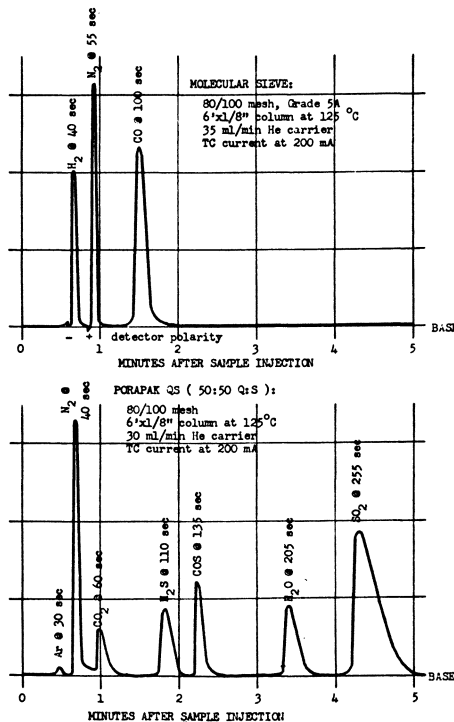


Figure 8. Chromatographic response times

the feed gas was kept at 2.0 vol % (i.e., the stoichiometric amount). Series 10, 11, and 12 determined the effect of water vapor (30 val %) in the reactant mixture. The effects of excess CO and the substitution of H_2 for CO were studied in the final series.

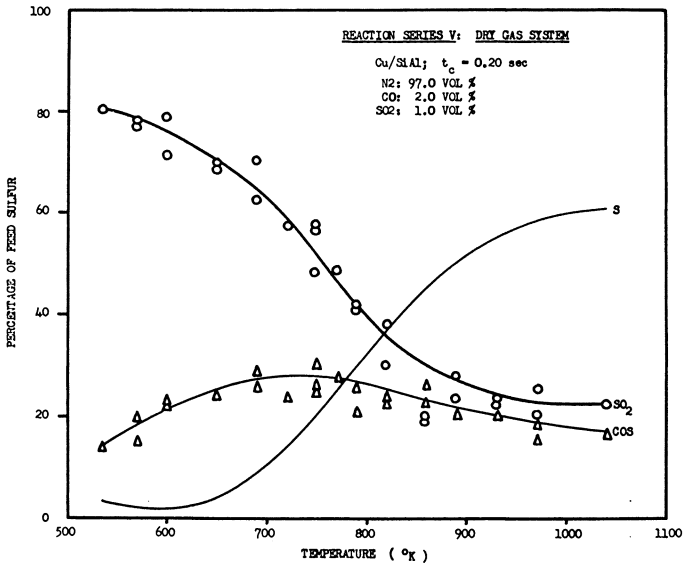


Figure 9. Series 5: dry gas system; $t_c = 0.2$ sec

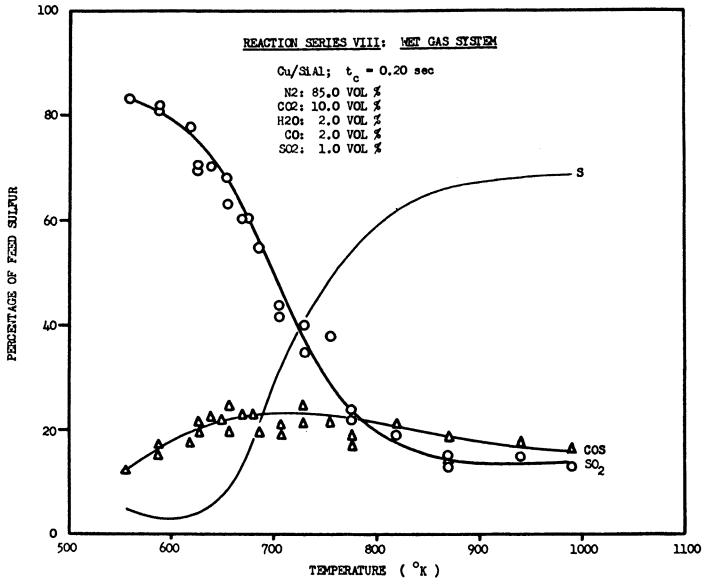


Figure 10. Series 7: wet gas system; $t_c = 0.2$ sec, $H_2O = 2.0\%$

Typical results are in Figures 9-14, where percent SO_2 feed converted to COS , H_2S , and elemental sulfur is plotted *vs.* reaction temperature for fixed contact times and $CO:SO_2$; copper on silica-alumina was the catalyst.

Figure 9 shows a typical result for SO_2 reduction in a dry gas system. Figures 10 and 11 show the results for wet-gas feeds with the same water

vapor (2.0 vol %) but different contact times. No H_2S is present in the product gases at a contact time of 0.2 sec, but H_2S does appear at 0.4 sec and above 750°K.

Figure 12 shows a typical result for the reduction of feed sulfur in a wet gas system containing 30 vol % water vapor (typical of sulfur recovery plant

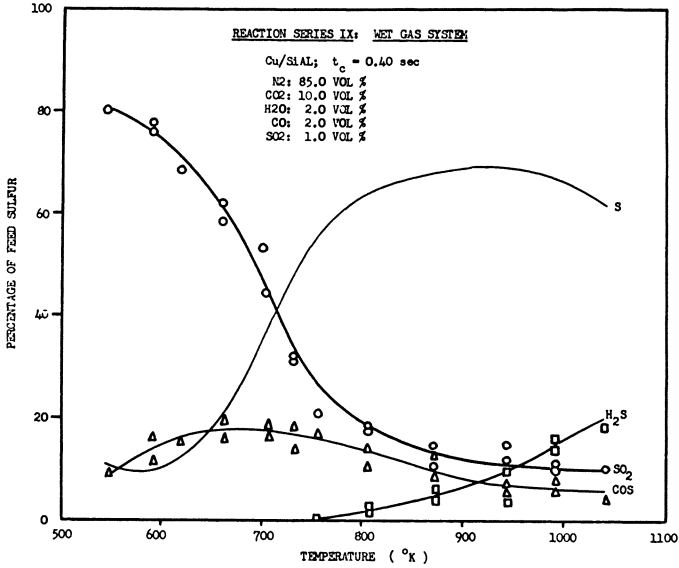


Figure 11. Series 9: wet gas system; $t_c = 0.4 \text{ sec}$, $\text{H}_2\text{O} = 2.0\%$

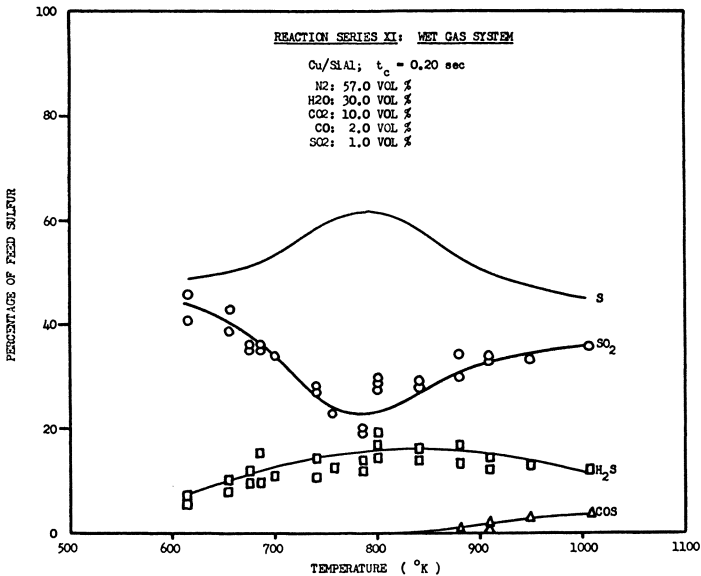


Figure 12. Series 11: wet gas system; $t_c = 0.2 \text{ sec}$, $\text{H}_2\text{O} = 3.0\%$

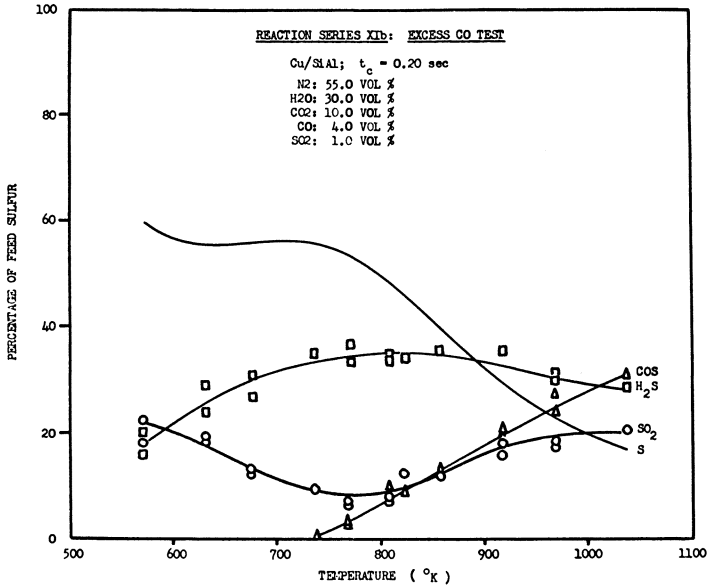


Figure 13. Series 11b: excess CO test

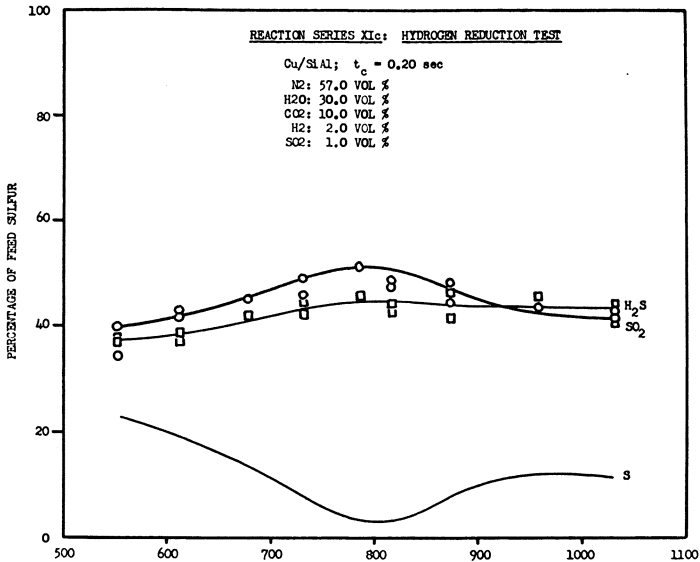


Figure 14. Series 11c: hydrogen reduction test

stack gas composition). It shows clearly the effect of water vapor on H₂S formation, and it confirms thermodynamic equilibrium predictions. Note that COS is absent below $\approx 850^\circ\text{K}$.

Figures 13 and 14 show, respectively, the effects of excess CO, and the substitution of H₂ for CO, on SO₂ reduction in a wet gas feed with 30 vol %

water. In both cases an appreciable amount of SO_2 appears to have been converted to H_2S . Similar plots using different reaction times, feed compositions, and catalysts are given elsewhere (10).

Discussion

In a dry gas system the only undesirable reaction is that between CO and elemental sulfur to produce COS. In a wet gas system CO can react with H_2O to produce H_2 (water-gas shift reaction). If this happens, other reactions could occur (*i.e.*, Reactions 5–10), leading to H_2S formation in the products. Thermodynamics of the wet gas system favor H_2S production, and the percent conversion of feed SO_2 to H_2S increases both with water vapor concentration (Figure 3) and with $\text{CO}:\text{SO}_2$ (Figure 6). Temperature also affects theoretical conversion but less simply (Figures 3 and 6). The theoretical equilibrium studies done here indicate, however, that even with large amounts of water vapor in the feed gas, up to 80% SO_2 can be converted to elemental sulfur with CO. The main adverse byproduct is H_2S , and the problem of minimizing its production hinges on two criteria: (1) operation of the process below 500°K , and (2) careful choice of catalyst and reaction time.

Let us compare the results of percent conversion of feed SO_2 to elemental sulfur, COS, and H_2S for feed gases containing 2.0% water (Figures 10 and 11) and 30% water (Figure 12). A small amount of water does not seem to lead to measureable quantities of H_2S , except at fairly high temperatures (*i.e.*, above 800°K) and long contact times (0.4 sec or more). This is in line with the results of Okay and Short (8), who concluded from their data that the water-shift reaction does not proceed for $T = 713^\circ\text{--}766^\circ\text{K}$, $\text{CO}:\text{SO}_2$ ratios of 1.35–1.51, space velocities of 29,300–38,700 hr^{-1} , and water concentrations of 9.6 vol % or less. However, 30 vol % water vapor drastically changes the product gas composition (Figure 12). COS production is now largely suppressed, decreasing to a unmeasurable amount below 850°K . Simultaneously, H_2S production is increased by almost the same magnitude as for COS in the dry gas system. The overall SO_2 reduction now is optimum at *ca.* 800°K and is a function of the contact time (10).

For dry gas systems (*see* Figure 9) SO_2 conversion is optimal at $> 900^\circ\text{K}$ with contact time 0.2 sec. Although conversion to elemental sulfur increases with contact time, the subsequent reaction of CO with the product sulfur is faster, and the net result is lower overall conversion. This again agrees with previous findings (7).

Conclusions

SO_2 can be removed from the stack gases of sulfur plants by catalytic reduction with CO over a specially prepared copper on silica-alumina catalyst. Up to 90% overall removal can be realized at optimum $\text{CO}:\text{SO}_2$ ratio and reaction time. Water in the system limits SO_2 conversion and gives rise to H_2S as a byproduct, in conformity with thermodynamic equilibrium predictions.

If CO is used at temperatures below the dew point of sulfur vapor, COS production is virtually zero and H_2S production diminishes. Subsequent work should, therefore, concentrate on low temperature reduction of SO_2 with CO in fluidized- or shower-bed reactors which provide cyclic catalysts regeneration and the removal of product sulfur.

Literature Cited

1. Klemm, R. F., "Environmental Effects of the Operation of Sulfur Extraction Gas Plants," *E.C.A. Rept.*, Alberta, 1972.
2. Rankine, R. P., Kerr, R. K., Pascall, H. G., "Potential Efficiencies of the Conventional Claus Sulfur Recovery Process," paper presented at the Alberta Sulfur Gas Research Workshop, Edmonton, Nov., 1973.
3. Ferguson, J. B., *J. Amer. Chem. Soc.* (1918) **40**, 1626.
4. Yushkevich, N. F., Karzhavin, V. A., *J. Chem. Ind. (Moscow)* (1931) **8** (1), 3; (2), 109; (14), 1; *Chem. Abstr.* **26**, 2016.
5. Ryason, P. R., Harkins, J., *J.A.P.C.A.* (1967) **17** (12), 796.
6. Quinlan, C. W., Okay, V. C., Kittrell, J. R., *Ind. Eng. Chem., Process Design Develop.* (1973) **12** (3), 359.
7. Querido, R., Short, W. L., *Ind. Eng. Chem., Process Design Develop.* (1973) **12** (1), 10.
8. Okay, V. C., Short, W. L., *Ind. Eng. Chem., Process Design Develop.* (1973) **12** (3), 291.
9. White, W. B., Johnson, S. M., Dantzig, G. B., *J. Chem. Phys.* (1958) **28** (5), 751.
10. Dingle, H. B., M.Sc. Thesis, University of Calgary, 1972.
11. Meyer, B., "Elemental Sulfur," p. 127, Interscience, New York, 1965.
12. Gamson, B. W., Elkins, R. H., *Chem. Eng. Progr.* (1953) **49**, 206.
13. Valdes, A. R., *Hydrocarbon Process. Petrol. Refiner* (1964) **43** (3), 104.
14. Dewart, J., Goldfinger, S., Dentry, W., *Z. Phys. Chem.* (1967) **55**, 314.

RECEIVED January 2, 1974. Work supported by the Canadian Natural Gas Processing Association and the National Research Council of Canada.

Mathematical Modeling of the Monolith Converter

LARRY C. YOUNG and BRUCE A. FINLAYSON

Department of Chemical Engineering, University of Washington,
Seattle, Wash. 98195

Mathematical models for the monolith converter are developed and applied to the oxidation of carbon monoxide in automobile exhausts. The converter consists of an array of ducts with catalyst coating the walls. The exhaust gas flows axially through the ducts in laminar flow. Two models for this type of converter are proposed and solved numerically. The simpler model uses heat and mass transfer coefficients for fully developed flow in ducts to account for the resistance to transfer between the fluid and the catalytic wall. The more complicated model accounts for the distribution of mass and energy in the duct cross-section, which is assumed to be circular. Both transient and steady-state calculations are performed for conditions which would be expected during vehicle operation. Mass and energy distribution in the duct cross-section is important. Transient calculations predict that the wall temperature can overshoot the steady-state adiabatic temperature and thus contribute to converter failure.

One of the contemporary challenges to technology is the control of automobile emissions. A promising method of meeting emission standards in the short term is to use catalytic converters. In this preliminary study the authors propose and solve two mathematical models for a particular type of converter, the monolith converter. Particular attention is given to the use of efficient computing techniques. Both transient and steady-state calculations are performed for conditions which could be expected in automobile operation, and the essential features of the problem are outlined.

Two types of catalytic converters, packed beds and monoliths, have been proposed for the oxidation of carbon monoxide and hydrocarbons in automobile exhausts. Mathematical models have been proposed and solved for packed bed converters (1, 2, 3, 4) while Kuo (5) has developed a model for the monolith converter which is similar to the simpler one solved here.

The monolith converter consists of an array of ducts or cells through which the exhaust gas flows axially. The internal surface area of the substrate material is relatively low; therefore, a wash coat of catalyst dispersed on activated alumina is deposited on the substrate. Because of a much smaller volumetric heat capacity, monolith converters warm up more quickly than

packed bed devices, giving the monolith an important advantage during cold starts of the engine. The monoliths have difficulties, however, caused by thermal expansion, and in certain driving modes the monolith substrate can melt, resulting in converter failure (6). The mathematical models developed below illustrate important features of the thermal behavior of the monolith converter.

Model Development

Available information on the reaction kinetics is reviewed in order to make realistic approximations to the kinetic parameters which might be expected for the monolith converter using either base metal oxide or platinum catalysts.

The base metal oxidation of carbon monoxide is a first-order reaction in carbon monoxide and independent of oxygen for oxygen concentrations greater than 2% (3). The base metal oxide rate expressions used in the calculations were estimated from those given by Kuo *et al.* (3), who used catalysts with base metal applied on the outer portion of alumina spheres. A rate expression was determined by assuming the reaction rate for the monolith converter would be the same based on the volume of active catalyst and by estimating the thickness of the catalytic layer on the monolith wall. Since the pre-exponential factor in the rate constant can vary according to catalyst deactivation, amount of active catalyst, *etc.*, we use the two rate expressions, B1 and B2, listed in Table I.

Table I. Reaction Rate Expressions

$$B1: -r_{co} = 7.8 \times 10^5 \frac{Y_{co}}{T} \exp(-16000 \text{ } ^\circ R/T) \frac{\text{lb-mole } ^\circ R}{\text{min ft}^2}$$

$$B2: -r_{co} = 3.9 \times 10^6 \frac{Y_{co}}{T} \exp(-16000 \text{ } ^\circ R/T) \frac{\text{lb-mole } ^\circ R}{\text{min ft}^2}$$

$$P1: -r_{co} = Y_{o_2} Y_{co} / (0.5 Y_{o_2} + 1.33 Y_{co}^2 \exp(11000 \text{ } ^\circ R/T)) \frac{\text{lb-mole}}{\text{min ft}^2}$$

The oxidation of carbon monoxide on platinum is generally agreed to be a first-order reaction in oxygen and inversely proportional to carbon monoxide (2, 7, 8). The rate expression is negative order in carbon monoxide because of the strong adsorption of carbon monoxide on platinum. As pointed out by Schlatter *et al.* (8) the rate expression would not apply at low carbon monoxide concentrations. For the oxidation of carbon monoxide on platinum wire, Sklyarov *et al.* (9) report a rate expression similar to the Langmuir-Hinshelwood type. For the conditions of the monolith converter, their rate expression can be accurately approximated by:

$$r_{co} = Y_{o_2} Y_{co} / (k_1 Y_{o_2} + k_2 Y_{co}^2) \quad (1)$$

The first term in the denominator is important only at high temperatures and low carbon monoxide concentrations. Under other conditions the reaction would appear to be inversely proportional to carbon monoxide. A rate expression of the form of Equation 1 is used in the calculations. The activation energy in the constant k_2 was taken from Harned (2), although Harned assumed k_1 was zero. Sklyarov *et al.* (9) report a zero activation energy for

k_1 , and this value is used here. The ratio of k_1 to k_2 was assumed to be the same as found by Sklyarov *et al.* (9) at 600°F. The magnitudes of the rate constants were estimated so that the platinum kinetics would give qualitatively the same comparison to the base metal kinetics as was observed by Schlatter *et al.* (8). The platinum rate expression, so determined, is designated P1 and listed in Table I.

Space limitations preclude a complete discussion of the justification of the assumptions. We therefore list the important assumptions and the available references.

1. The flow is laminar since $Re < 2000$ (10).
2. Except under conditions of very high flow rate, the velocity entry length is a small fraction of the converter length (11), and its effect on heat and mass transfer is small (12).
3. Axial diffusion in the fluid phase is negligible since $Pe > 50$ (13).
4. The transient response of the converter is controlled by the thermal response of the solid. All other time derivatives are set to zero (1).
5. Diffusion coupling can be neglected (14, 15).
6. The converter is adiabatic (6), and only a single cell is modeled. If the flow rate is different in adjacent cells, then a complete model must account for this flow distribution and repeat the single-cell calculations for each cell. This is beyond the scope of the present work.
7. The solid temperature at any axial position is uniform and equal to the fluid temperature at the fluid–solid interface.
8. Axial conduction in the solid is unimportant provided:

$$\left| r_h \frac{A^s}{A^f} k^s \frac{\partial^2 T^s}{\partial z^2} \right| \ll \left| \Delta H r_{co} \right|$$

9. Because the catalytic layer is very thin (16), internal diffusion effects in the catalytic layer are small and are included in the reaction rate expressions.

10. The concentration ratio of hydrogen to carbon monoxide is 1:3 everywhere in the reactor (3, 7).

11. The presence of hydrocarbons does not appreciably affect the conversion of carbon monoxide or the heat generated in the converter.

12. The mole fraction of oxygen is determined by stoichiometry.

Assumptions 9–12 are made because of a lack of sufficient information on the reaction kinetics. The calculations for which the inequality in assumption 8 does not hold are identified below. Although work is presently in progress to solve the problem relaxing assumptions 7 and 8 for typical irregular duct geometries, we solve the problem here for the case of a circular cross-section as an initial study. The governing equations are then:

$$\text{Model II: } 2r_h Pe_h (1 - r^2) \frac{\partial T^f}{\partial z} = \frac{1}{r} \frac{\partial}{\partial r} \left(r \frac{\partial T^f}{\partial r} \right) \quad (2a)$$

$$2r_h Pe_m (1 - r^2) \frac{\partial Y^f}{\partial z} = \frac{1}{r} \frac{\partial}{\partial r} \left(r \frac{\partial Y^f}{\partial r} \right) \quad (2b)$$

$$r_h \frac{A^s}{A^f} \frac{\rho^s C_p^s}{C_p^f} \frac{\partial T^s}{\partial t} = \frac{\Delta H}{C_p^f} r_{co} - \frac{2G}{Pe_h} \frac{\partial T^f}{\partial r} \Big|_{r=1} \quad (2c)$$

$$r_{co} = \frac{2G}{Pe_m} \frac{\partial Y^f}{\partial r} \Big|_{r=1} \quad (2d)$$

$$T^s = T^f \text{ at } r = 1; T^s = T_o^s(z) \text{ at } t = 0$$

$$T^f = T_o^f(t) \text{ and } Y^f = Y_o^f(t) \text{ at } z = 0$$

The resistance to heat and mass transfer is often modeled using heat and mass transfer coefficients. A model of this type can be derived by integrating Equation 2 across the cell cross-section and defining heat and mass transfer coefficients in the usual way. This approach results in the following governing equations:

$$\text{Model I: } r_h \text{ Pe}_h \frac{\partial T^m}{\partial z} = \text{Nu} (T^s - T^m) \quad (3a)$$

$$r_h \text{ Pe}_m \frac{\partial Y^m}{\partial z} = \text{Sh} (Y^s - Y^m) \quad (3b)$$

$$r_h \frac{A_s}{A^t} \frac{\rho^s C_p^s}{C_p^t} \frac{\partial T^s}{\partial t} = \frac{\Delta H}{C_p^t} r_{co} - \frac{G \text{Nu}}{\text{Pe}_h} (T^s - T^m) \quad (3c)$$

$$r_{co} = - \frac{G \text{Sh}}{\text{Pe}_m} (Y^m - Y^s) \quad (3d)$$

$$T^m = T_o^t(t) \text{ and } Y^m = Y_o^t(t) \text{ at } z = 0$$

$$T^s = T_o^s(z) \text{ at } t = 0$$

In the calculations, constant values of Nu and Sh are assumed while these quantities can be calculated from the solution of model II by:

$$\text{Nu} = 2 \left. \frac{\partial T^t}{\partial r} \right|_{r=1} / (T^s - T^m) \quad (4)$$

The Sherwood number is defined analogously. If the quantities Nu and Sh used in model I are calculated from the solution of model II by using Equation 4, the two models will give an exact correspondence.

Solution Method. The model I equations may be solved in a straightforward manner. We use the improved Euler method in time and either the improved Euler method or the trapezoidal rule in the axial direction. At a given time the equations are solved in the axial direction, and the right side of Equation 3c is determined. This information is then used to step forward in time. Equation 3d and Equation 3c for steady-state calculations are solved analytically when linear, and by using the Newton-Raphson method when they are nonlinear.

For model II the orthogonal collocation method (17) is used. Using this method the radial Laplacian operators in Equations 2a and 2b are replaced by matrix operators, and the equations are then reduced to a set of nonlinear first-order differential equations. Unfortunately, the resulting set of ordinary differential equations tend to be stiff, and a small step size would be required if an explicit integration scheme were to be used. An implicit scheme would allow a larger step size but would require the solution of a set of nonlinear algebraic equations at each position step. For these reasons an efficient solution algorithm was devised, which utilizes the results of two similar Graetz problems. The problems of flow with (1) specified wall temperature and (2) specified wall flux were solved as eigenvalue problems. The solution to the two eigenvalue problems can be expressed in terms of integrals involving the wall temperature and the wall flux, respectively (18). By using interpolating polynomials to approximate these quantities in model II, the equations could be solved very efficiently. Another advantage of this solution algorithm is that the same computer program can be used to solve the problem in different

geometries, provided assumption 7 above is justified. To solve the problem for other geometries all that is necessary is to solve the analogous eigenvalue problem appropriate to the geometry of interest.

By this method the problem reduces to one of solving (19):

$$Y^m(z, t) = Y_o^t(t) + \frac{1}{r_h G} \int_0^z r_{co} [Y^s(\tau, t), T^s(\tau, t)] d\tau \quad (5)$$

$$Y^s(z, t) = Y^m(z, t) + r_{co} [Y^s(z, t), T^s(z, t)] \text{Pe}_m / (2G A_{N+1, N+1}) \\ + \sum_{k=1}^{N-1} \left(\frac{Q_k}{4r_h G} \right) \int_0^z \exp \left[\frac{\lambda_k(z-\tau)}{2r_h \text{Pe}_m} \right] r_{co} [Y^s(\tau, t), T^s(\tau, t)] d\tau$$

$$T^m(z, t) = T_o^t(t) + \sum_{k=1}^N \left(\frac{Q'_k}{2r_h \text{Pe}_h} \right) \int_0^z \exp \left[\frac{\lambda'_k(z-\tau)}{2r_h \text{Pe}_h} \right] [T^s(\tau, t) - T_o^t(t)] d\tau \\ \frac{\partial T^t}{\partial r} \Big|_{r=1} = \frac{1}{2} r_h \text{Pe}_h \frac{\partial T^m}{\partial z} (z, t) \quad (6)$$

$$= \sum_{k=1}^N \left(\frac{Q'_k}{2r_h \text{Pe}_h} \right) \left(\frac{\lambda'_k}{2r_h \text{Pe}_h} \right) \int_0^z \exp \left[\frac{\lambda'_k(z-\tau)}{2r_h \text{Pe}_h} \right] [T^s(\tau, t) - T_o^t(t)] d\tau \\ + [T^s(z, t) - T_o^t(t)] \sum_{k=1}^N \frac{Q'_k}{2r_h \text{Pe}_h}$$

The Q_k and λ_k are the coefficients and eigenvalues from the flux specified problem, and Q'_k and λ'_k are the analogous quantities from the wall temperature specified problem. Equations 5 and 6 together with 2c constitute model II. For steady-state conditions, Equations 2a and 2c become analogous to 2b and 2d, and then an equation of the form of Equation 5 is used for temperature. The problems are discretized in the axial direction by the use of interpolating polynomials. For Equation 5 we use polynomials of the form:

$$r_{co}(z) \approx r_{co}(z_j, t) (1 - X^2) + \frac{\partial r_{co}}{\partial z} \Big|_{z_j, t} \Delta z (X - X^2) + r_{co}(z_{j+1}, t) X^2 \quad (7)$$

where $X = (z - z_j) / \Delta z$. For Equation 6 Lagrange interpolation is used. The interpolating polynomials are substituted into Equations 5 and 6, and the integration is performed. Since Equation 7 is implicit, this procedure resulted in one or two algebraic equations for transient and steady calculations, respectively, which must be solved at each axial step. This is accomplished analytically when the equations are linear or by Newton-Raphson iteration when they are nonlinear. For transient calculations the improved Euler method is used to integrate Equation 2.

Calculated Results

Calculations have been performed for the two models by using the rate expressions in Table I. The parameter values common to all of the calculations are listed after the appropriate symbol in the Nomenclature section.

The model I equations are the same as those studied by Lui and Amundson (20) and can exhibit multiple solutions for some parameter values. The

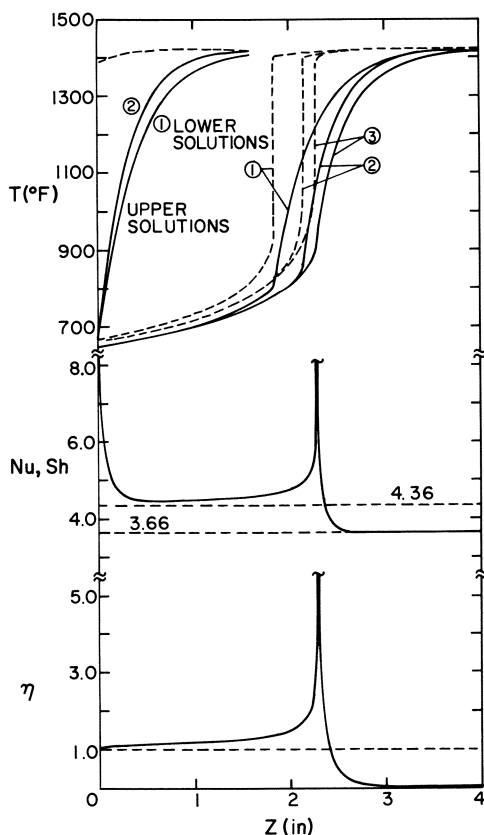


Figure 1. Typical steady-state calculation using Pt (platinum) catalyst: --- T_s ; — T_m ; $F = 28.5$ SCFM; $T_o' = 650^\circ\text{F}$; $Y_o' = 0.04$; 1: model I, $Nu = Sh = 3.5$; 2: model I, $Nu = Sh = 4.5$; 3: model II

analysis of Lui and Amundson can be applied directly to determine the parameter values for which multiple solutions can occur. Model I predicts multiple solutions to occur at high carbon monoxide concentrations with base metal catalyst, while with platinum catalyst they are predicted to occur over a wide range of conditions. Model II predicts that these multiple solutions cannot occur, and this result has been proved theoretically (19).

The calculations for typical cases using the two models and the three rate expressions are illustrated in Figures 1, 2, and 3. The asymptotic values of Nu and Sh , 3.66 for constant wall temperature and 4.36 for constant flux or linear wall temperature, are shown on the figures for reference. For cases when model I predicts multiple solutions the highest and lowest possible solutions are illustrated. The lower solution is typical of a situation when the converter is heated from an initial low temperature, while the higher solution results when the converter is cooled from some initial high temperature. For intermediate initial temperatures the final steady state may lie between those

shown. Such results are illustrated by Lui and Amundson (20) and have been confirmed for these kinetics by transient calculations using model I. Model II predicts only the one solution shown.

It is of particular interest that the solution for model II corresponds more closely to the lower solution of model I. Even if the lower solution of model I is chosen, model II predicts that the reaction will light off at a point further downstream than predicted by model I. Thus, model I always gives an optimistic prediction for the converter. These results can best be explained by observing the changes in the Nusselt number and effectiveness factor with position. The effectiveness factor is defined here as the reaction rate at the wall conditions divided by the reaction rate at the mixing cup fluid conditions. If mass and heat transfer were infinitely fast, then the effectiveness factor would always be unity. By observing the changes in these quantities, as illustrated in Figures 1, 2, 3, and 4, one can characterize the reactor in the following manner:

1. An initial entry length—In this region the Nusselt number decreases from an initial value of infinity in much the same manner as in a heat transfer problem.

2. A reaction limited region—In this region the effectiveness factor is near unity, and the conversion is limited by a low reaction rate.

3. A reaction zone—The reaction lights off, and the effectiveness factor and Nusselt number rise sharply.

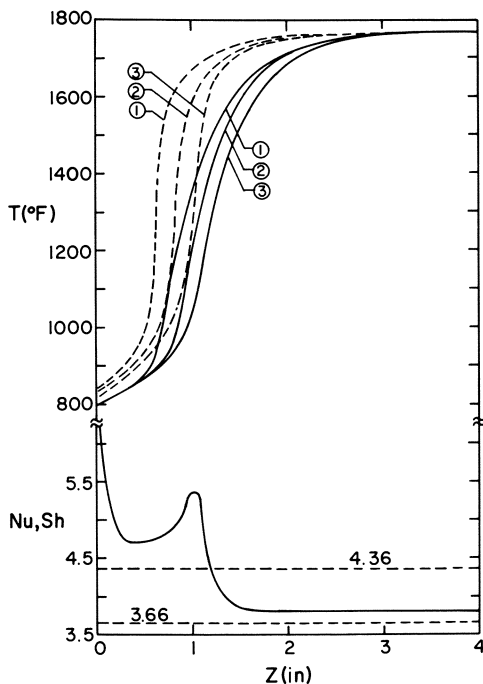


Figure 2. Typical steady-state calculation using B1 (base metal) catalyst: --- T' ; — T^m ; $F = 28.5$ SCFM; $T_o' = 800^\circ\text{F}$; $Y_o' = 0.05$; 1: model I, $Nu = Sh = 3.5$; 2: model I, $Nu = Sh = 4.2$; 3: model II

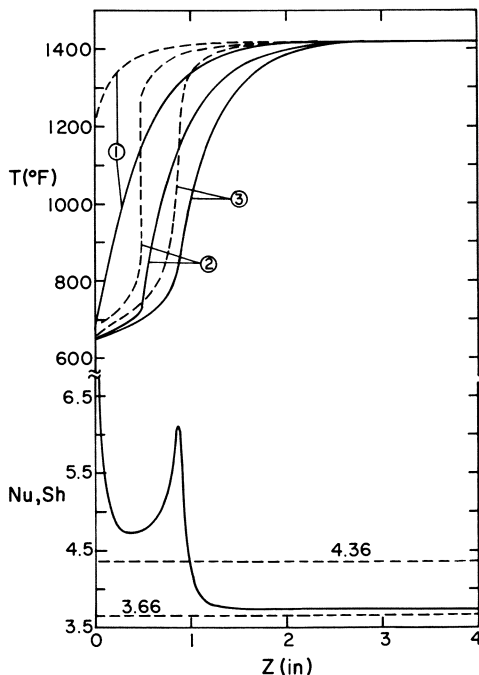


Figure 3. Typical steady-state calculation using B2 (base metal) catalyst: --- T' ; — T^m ; — T ; $F = 28.5$ SCFM; $T_0' = 650^\circ\text{F}$; $Y_0' = 0.04$; 1: model I, $Nu = Sh = 3.5$; upper solution; 2: lower solution of 1; 3: model II

4. A second entry length—After the reaction zone the Nusselt number goes through a second transition similar to the initial entry length.

5. A mass and heat transfer limited region—After the reaction zone the conversion is limited by the rate at which carbon monoxide can be transferred to the converter wall.

The discrepancy between model I and model II arises from the failure of model I to predict accurately the phenomena occurring in the reaction zone. In model I the Nusselt and Sherwood numbers are assumed to remain at their asymptotic values. Therefore, one must solve model II to accurately determine the transport rates in the converter.

Using the inequality in assumption 8, we determine the importance of axial conduction in the converter wall. For conditions when model I predicts multiple solutions there is a discontinuity in the wall temperature, so axial conduction would always be important in these cases. Indeed, Eigenberger (21) has shown that when axial conduction in the solid phase is included in model I, the infinite multiplicity of steady states reduces to two or three depending on the axial boundary conditions. Using model II, there is no discontinuity in wall temperature. In Figures 2 and 3 axial conduction is relatively unimportant, while in Figure 1 the ratio of axial conduction to reaction is 1.9 at $z = 2.28$ inches, using a value of $k^s = 0.83$ Btu/hr ft $^\circ\text{F}$. Since the reaction on platinum catalyst is strongly autocatalytic, the wall temperature rises rapidly in the reaction zone and axial conduction is important.

Morgan *et al.* (6) have discussed a phenomenon called emission breakthrough. Even though the reactor is fully warmed up some carbon monoxide can pass through the converter unreacted. This phenomenon can occur when there is insufficient oxygen for complete conversion, or when the flow rate through the converter is high. An example of this type of situation is shown in Figure 4. Under conditions when the reaction rate is large, the first four regions in the reactor, discussed above, combine into one, and the conversion is limited by mass transfer considerations. In Figure 4 the amount of carbon monoxide present at the outlet is 2.5% of that at the inlet even though the reaction lights off near the inlet of the converter. The discrepancy between model I and model II has particular significance for this situation, because model I always gives an optimistic prediction. As suggested by Morgan *et al.* (6), this problem can be reduced by increasing the converter length. Morgan *et al.* (6) also suggest that a converter geometry with good mass transfer be used. As stated above, in the limiting case of infinite transfer rates the effectiveness factor would be unity throughout the reactor. High mass transfer

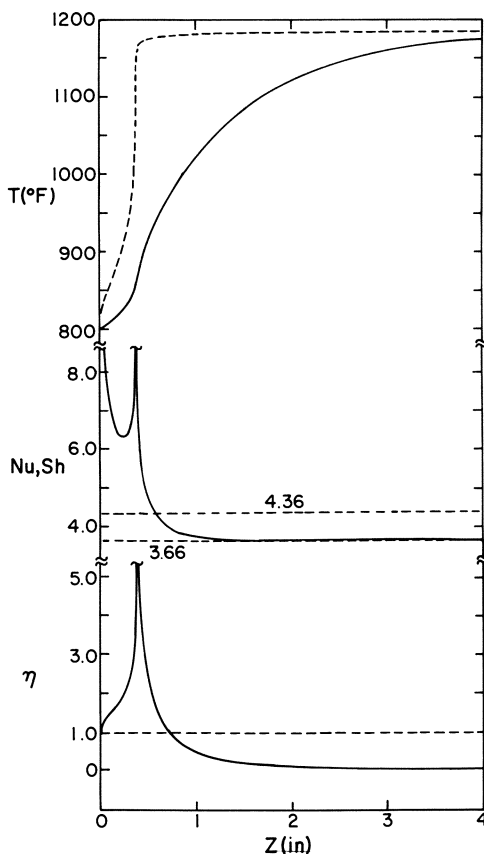


Figure 4. An example of emission breakthrough predicted by model II: --- T^* ; — T^m ; PI catalyst; $F = 80$ SCFM; $T_o' = 800^\circ F$; $Y_o' = 0.02$

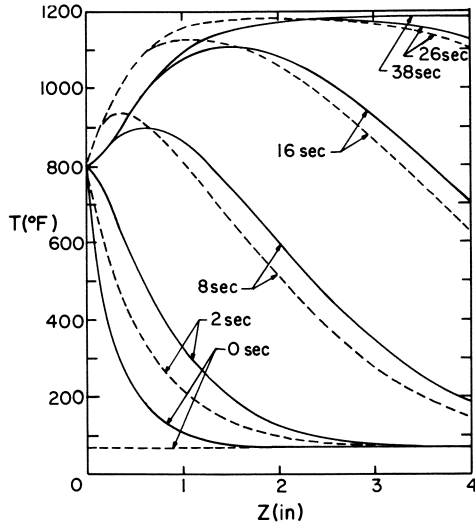


Figure 5. A warmup transient calculation using model II: --- T^w ; — T^m ; B2 catalyst; $F = 28.5$ SCFM; $T_o' = 800^\circ\text{F}$; $Y_o' = 0.02$; $T_s' = 70^\circ\text{F}$

rates are beneficial in the transfer limited region of the reactor, but detrimental in the reaction limited region. This effect is suggested, too, by the calculations using model I in Figures 1 and 2. A converter geometry with good transfer characteristics would probably be advantageous only in the case when the converter is purely mass and heat transfer limited.

Transient calculations have also been performed using the models. A calculation of converter warmup is illustrated in Figures 5 and 6. The transient response of the converter is indeed very fast. For this particular case, the conversion is essentially complete for all times greater than 15 sec. Model I gives a conservative prediction in this transient case because relatively low values of the Nusselt and Sherwood numbers were used. The variations of Sh and Nu in Figure 6 are interesting. When the mixing cup temperature and wall temperature intersect, the Nusselt number decreases to minus infinity and then jumps to plus infinity. At small times Sh decreases to low values caused by the rapidly decreasing reaction rate.

As stated above, during certain critical driving modes high temperatures can occur in the monolith converter. The following example is typical of what might happen when the automobile is cruising at highway speeds and then decelerates over some time interval to a lower speed. For this situation we use the following parameters:

$$F = 80 \text{ SCFM}, Y_o' = 0.01, t < 0$$

$$F = 28.5 \text{ SCFM}, Y_o' = 0.04, t > 0$$

The results using P1 catalyst are shown in Figure 7, and for B2 catalyst in Figure 8. The wall temperature during the transient exceeds the adiabatic temperature, which is the maximum wall temperature which can occur at the end of the transient. This phenomenon has been observed by Lui and Amund-

son (20) for model I; however, for these conditions model I does not exceed the adiabatic temperature while model II predicts that the adiabatic temperature is exceeded by 100°F. Although the temperatures here would not cause damage to the converter, if the inlet temperature or concentration had been higher, this overshoot phenomenon could cause damage to the converter. Figure 8 shows that with B2 catalyst the overshoot is less severe (25°F). These results would be affected by axial conduction. It will be very interesting to see if a similar phenomenon occurs when axial conduction is included in the converter model.

Accuracy and Computation Time

The validity of the results depend, of course, on the accuracy of the computation scheme. Other computations suggest that the results are accurate to within a few degrees. The order of approximation required depended strongly on the particular case studied. As stated above, model II can only have a single

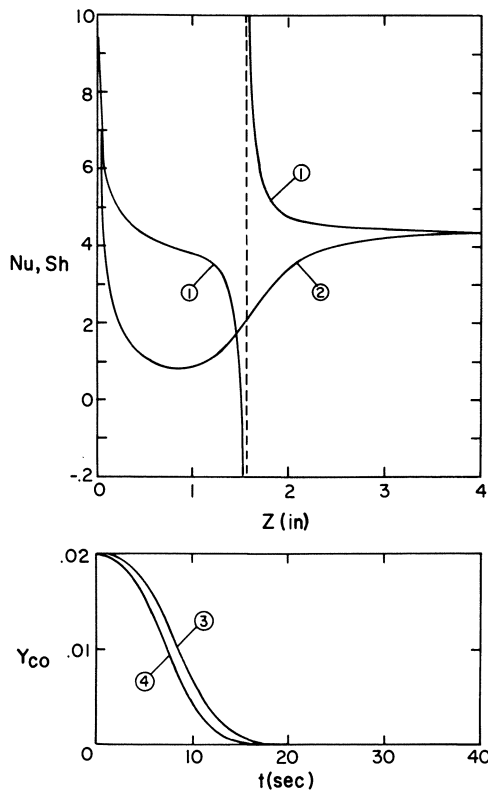


Figure 6. For the transient shown in Figure 5: Nu and Sh distributions during the transient; 1: Nu at $t = 16$ sec; 2: Sh at $t = 2$ sec; and outlet carbon monoxide mole fractions predicted by the two models; 3: outlet mole fraction, model I, $Nu = Sh = 3.5$; 4: outlet mole fraction, model II

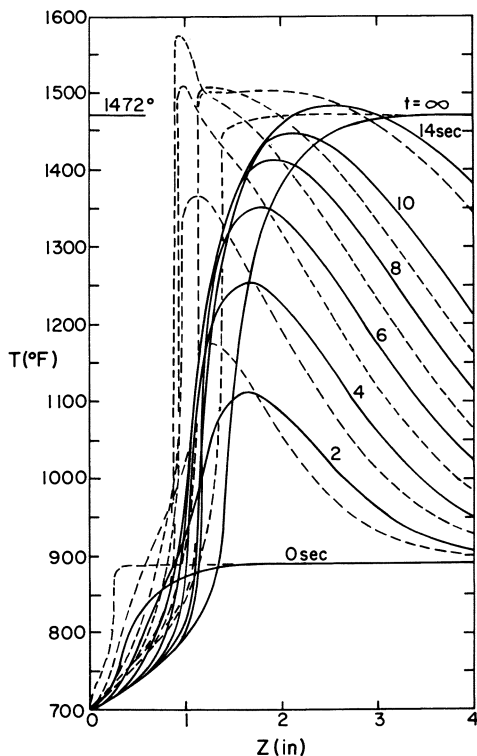


Figure 7. Transient resulting from vehicle deceleration from cruising speed using Pt (platinum) catalyst: --- T^s ; — T^m ; $F = 28.5$ SCFM; $T_o' = 700^\circ\text{F}$; $Y_o' = 0.04$; $T_o'(z)$ from steady state with $F = 80$ SCFM, $T_o' = 700^\circ\text{F}$, $Y_o' = 0.01$; model II - transient; $1472^\circ\text{F} =$ adiabatic temperature at $t = \infty$

steady state; however, the model equations were solved approximately, and it was sometimes necessary to use a very accurate approximation to obtain only a single solution. The results in Figure 1 required 2000 axial steps and five radial collocation points, resulting in a computation time of 10 sec. Computation times are for a CDC 6400 computer. Accurate results for the cases in Figures 2 and 3 could be obtained using three radial collocation points and 200 axial steps (0.4 sec).

During transient calculations a variable time step size was used, while in the axial direction the grid spacing was fixed. The step size was controlled by requiring the correction in the improved Euler method to remain within specified limits. This method of step size control worked well. The transient calculations in Figures 5 and 6 used 160 axial steps and four radial collocation points and required 50 sec of computation. The most extreme case, Figure 7, utilized 1000 axial grid points and four collocation points and required 900 sec of computer time. The strongly autocatalytic rate expression for platinum catalyst required accurate approximations and resulted in large computation times.

Conclusions

The distribution of mass and energy in the cross-section of the monolith cells is important and must be included in the converter model. Under conditions when the wall temperature rises sharply axial conduction in the converter wall must be included in the reactor model, although it was not included in this preliminary study. A solution algorithm which utilizes the results from the analogous eigenvalue problem allows one to solve the problem efficiently, and for different geometries. The orthogonal collocation method is an efficient method of solving the eigenvalue problems.

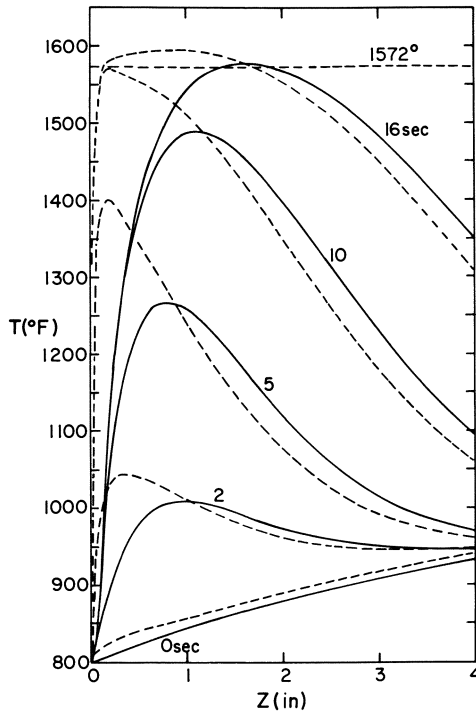


Figure 8. Transient resulting from vehicle deceleration from cruising speed using B2 (base metal) catalyst: --- T' ; — T'' ; $F = 28.5$ SCFM; $T_o' = 800^\circ\text{F}$; $Y_o' = 0.04$; $T_o''(z)$ from steady state with $F = 80$ SCFM, $T_o' = 800^\circ\text{F}$, $Y_o' = 0.01$; model II - transient; $1572^\circ\text{F} = \text{adiabatic temperature at } t = \infty$

Although axial conduction in the converter wall is important in some of the calculations, the calculations suggest that the wall temperature during some transients can significantly exceed the adiabatic temperature. The calculations also suggest that a converter cell geometry with very good mass and heat transfer characteristics may not always be preferable to a geometry with poor transfer characteristics.

Acknowledgment

The authors thank Engelhard Industries for supplying a noncatalytic PTX-4 converter for study. This research was supported by the National Science Foundation under Grant No. GK-12517 and by the donors of the Petroleum Research Fund, administered by the American Chemical Society under grant PRF 5965-AC7.

Nomenclature

A^f	frontal area of fluid, 5.54 inches ²
A^s	frontal area of solid, 2.77 inches ²
$A_{N+1,N+1}$	element of orthogonal collocation discretization matrix
C_p^f	molar heat capacity of fluid, 7.5 Btu/lb-mole °F
C_p^s	solid heat capacity, 0.2 Btu/lb °F
F	flow rate through converter, SCFM
G	molar velocity, 0.0704 F lb-mole/min ft ²
ΔH	heat of reaction, -145,000 Btu/(lb-mole CO + $\frac{1}{3}$ lb-mole H ₂)
k_1, k_2	rate constants
k^s	thermal conductivity of solid, 0.83 Btu/hr ft °F
N	number of interior collocation points
Nu	Nusselt number
Pe_h	Peclet number for heat, 0.7 Re
Pe_m	Peclet number for mass, 0.7 Re
Q_k	coefficients for flux specified eigenvalue problem
Q'_k	coefficients for wall temperature specified eigenvalue problem
r	radial coordinate
r_{co}	rate of carbon monoxide generation, lb-mole/min ft ²
r_h	hydraulic radius, duct area/duct perimeter, 0.012 inch
Re	Reynolds number, 5.62 F
Sh	Sherwood number
t	time, sec
T	temperature, °R
Y, Y_{co}	mole fraction of carbon monoxide
Y_{o_2}	mole fraction of oxygen, $\frac{2}{3}(0.03 + Y_{co})$
z	axial coordinate, inches
z_j	axial grid point, $j\Delta z$, inches
Δz	axial step size, inches

Greek Letters

η	effectiveness factor
λ_k	eigenvalues for flux specified eigenvalue problem
λ'_k	eigenvalues for wall temperature specified eigenvalue problem
ρ^s	solid density, 100 lb/ft ³

Subscripts and Superscripts

f	value for fluid
m	bulk mixed fluid value
o	inlet or initial value
s	value for solid

(The dimensionless quantities are nondimensionalized using the hydraulic diameter, $4 r_h$.)

Literature Cited

1. Ferguson, N. B., Finlayson, B. A., *AIChE, Nat. Meetg.*, Nov. 11-15, 1973, paper 40c.
2. Harned, J. L., *SAE, Meetg.*, 1972, paper 720520.
3. Kuo, J. C. W., Morgan, C. R., Lassen, H. G., *SAE, Meetg.*, 1971, paper 710289.
4. Wei, J., *Chem. Eng. Prog. Monograph Ser.* (1969) No. 6, **65**.
5. Kuo, J. C. W., private communication, 1973.
6. Morgan, C. R., Carlson, D. W., Voltz, S. E., *SAE, Meetg.*, 1973, paper 730569.
7. Langmuir, I., *Trans. Faraday Soc.* (1922) **17**, 621.
8. Schlatter, J. C., Klimisch, R. L., Taylor, K. C., *Science* (1973) **179**, 798.
9. Sklyarov, A. V., Tret'yakov, I. I., Shub, B. R., Roginskii, S. Z., *Doklady Akademii Nauk SSSR* (1969) **189**, 1302.
10. Knudsen, J. G., Katz, D. L., "Fluid Dynamics and Heat Transfer," McGraw-Hill, 1958, p. 105.
11. Fleming, D. P., Sparrow, E. M., *Trans. Amer. Soc. Mech. Eng. Ser. C* (1969) **91**, 345.
12. Monohar, R., *Int. J. Heat Mass Transfer* (1969) **12**, 15.
13. Hennecke, D. K., *Wärme-und Stoffübertragung* (1968) **1**, 177.
14. Bird, R. B., Stewart, W. E., Lightfoot, E. N., "Transport Phenomena," John Wiley & Sons, Inc., 1960, p. 571.
15. Soloman, R. L., Hudson, J. L., *AIChE J.* (1971) **17**, 371.
16. Harned, J. L., Montgomery, D. L., *SAE, Meetg.*, 1973, paper 730561.
17. Finlayson, B. A., "The Method of Weighted Residuals and Variational Principles," Academic Press, New York, 1972.
18. Franklin, J. N., "Matrix Theory," Prentice-Hall, Englewood Cliffs, 1968, p. 57.
19. Young, L. C., Ph.D. Thesis, University of Washington, Seattle, Wash., August, 1974 (est.).
20. Lui, S., Amundson, N. R., *Ind. Eng. Chem., Fund.* (1962) **1**, 200.
21. Eigenberger, G., *Chem. Eng. Sci.* (1972) **27**, 1909, 1917.

RECEIVED January 2, 1974.

Designing a Cyclohexane Oxidation Reactor

J. ALAGY, P. TRAMBOUZE, and H. VAN LANDEGHEM

Institut Francais du Pétrole, Centre d'études et de développement industriels
Solaize, B.P. 3, 69390 Vernaison, France

As part of the development of a liquid-phase cyclohexane oxidation process, various aspects of the reactor design were studied:

- (1) Fundamental research on the influence of mass transfer on reaction selectivity
- (2) Laboratory and development research on boric acid as coreagent
- (3) Hydrodynamic research to determine the optimum reactor configuration.

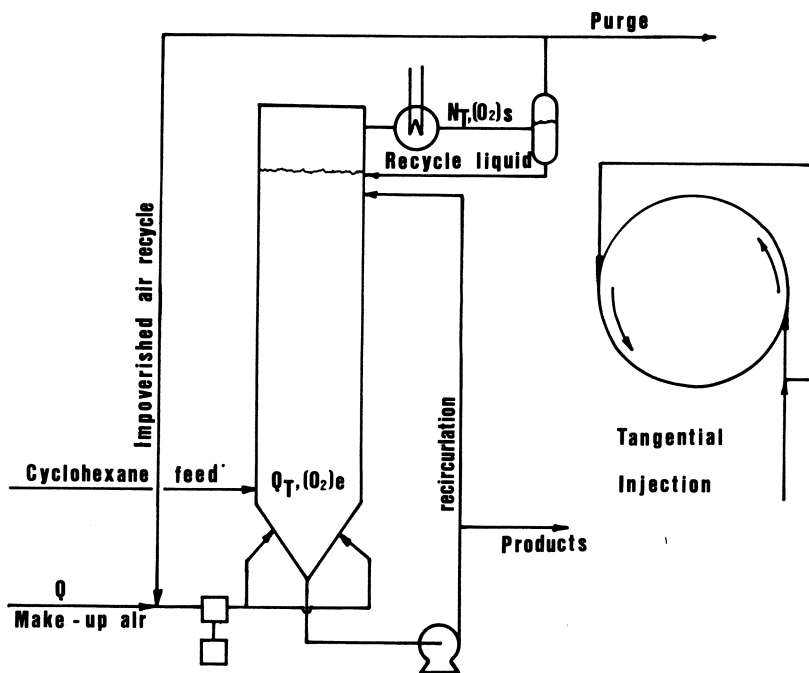


Figure 1. Pilot plant continuous reactor

A simplified reaction scheme was established which led to a mathematical model which was not too complex. This model was not available when the pilot plant began operating. Therefore, a simplified model was adopted, so that the results of a one-reactor stage pilot plant allowed design of a multistage industrial unit. These two approaches agreed well, and the industrial reactor confirmed predictions.

The conclusions from this study are:

(1) The reactor operates under kinetic conditions although mass transfer influences the transformation rate.

(2) As a result, stirring has no direct effect on selectivity.

(3) For the operating conditions chosen, conversion can be controlled by the fresh-air makeup in the reactor.

(4) The favorable influence of a high gas flow rate can be explained by the elimination of reaction water. This thus requires a sufficient gas-liquid transfer coefficient.

(5) The selectivity of the transformation can be appreciably increased by using perfectly-stirred reactors in series.

For the industrial construction of such a unit, we chose reactors of the type illustrated in Figure 1. This choice was motivated by the tendency, observed in the pilot plant, for heavy and sticky byproduct to accumulate on the reactor wall at the surface of the liquid. Tangential injections were performed to wash the wall at those points, but a poor design could result in the formation of a vortex inside the reactor; in this case the gas-liquid contact area would become very small; after gas is injected into the liquid, it is quickly sucked toward this axial channel created by the vortex. To prevent this, turbulence and non-systematic circulations caused by the gas flow must be relied upon. This phenomenon was analyzed in two scale models, 30 and 60 cm in diameter, and a design criterion was worked out. The mathematical models and this hydrodynamic criterion allowed the two industrial projects to be carried out with full success.

RECEIVED January 2, 1974.

Kinetics and Yields in the Catalytic Oxidation of *o*-Xylene to Phthalic Anhydride with V_2O_5 Catalysts

P. H. CALDERBANK

Department of Chemical Engineering, University of Edinburgh,
Edinburgh 3H9 3JL, Scotland

*The kinetics of phthalic anhydride formation in the air oxidation of *o*-xylene over a commercial vanadium catalyst were measured over a wide range of temperatures, using an isothermal spinning catalyst-basket reactor. The activation energy decreases as the reaction temperature is increased; thereby, runaway is avoided over the normal commercial operating range. The kinetics predict observed temperature profiles in large tubular reactors and the relatively poor selectivity to phthalic anhydride obtained on the back-mixing compared with the plug-flow mode. Some indications of possible reaction mechanisms are apparent.*

The problem of predicting the temperature and yield profiles in fixed-bed catalytic reactors for the air oxidation of *o*-xylene to phthalic anhydride has been discussed in previous papers (1, 2); these authors used kinetic data from the literature. Kinetic data and fixed-bed reactor performance for the same commercial catalyst are now presented which allow the problem to be re-examined with greater certainty.

Experimental

The spinning catalyst-basket reactor described by Brisk (3) was used for kinetic measurements. The basket and chamber were made of titanium because this was inert to phthalic anhydride below 420°C. The catalyst was a commercial sample of unpromoted V_2O_5 on silicon carbide as described previously (2). Air saturated by bubbling through reagent was fed to the CSTR reactor, and a sample of the product gas was analyzed by on-line gas-liquid chromatography with integrated peak printout. CO_2 , CO , and O_2 were sometimes analyzed on-line by infrared and paramagnetic analyzers. The products of the partial oxidation of *o*-xylene (OX) were *o*-tolualdehyde (TA), phthalide (PI), and phthalic anhydride (PA). These intermediates were found in relatively small amounts.

Kinetics

The disappearance kinetics of *o*-xylene were first-order up to nearly 1 mole % xylene concentration. At higher concentrations the catalyst was reversibly

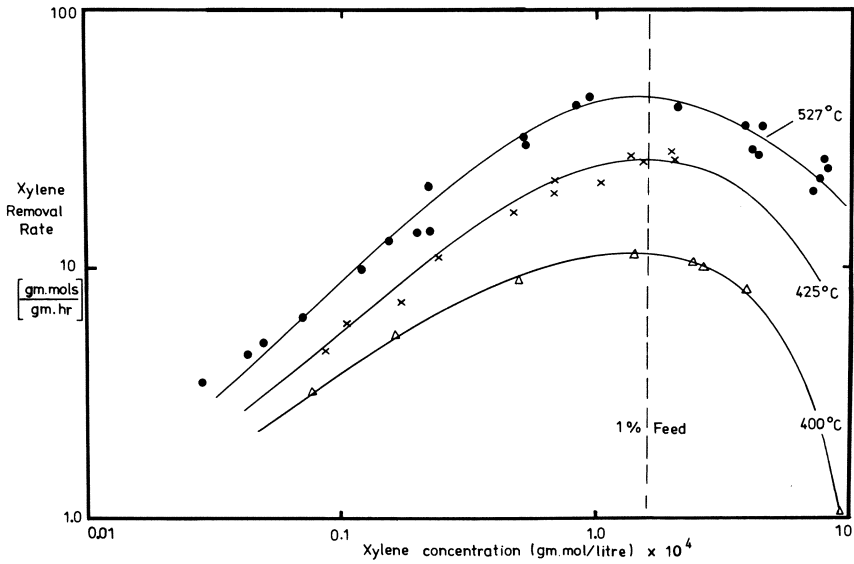


Figure 1. Oxidation rate of xylene with air in the CSTR

deactivated (see Figure 1). Possibly vanadium oxide is reduced to a lower valence state of less catalytic activity at high xylene concentrations. The amount of the lower oxide is evidently determined by the xylene/O₂ ratio because the portion of the curve which shows deactivation is multivalued; the steady states result from increasing oxygen concentration with decreasing xylene removal rate.

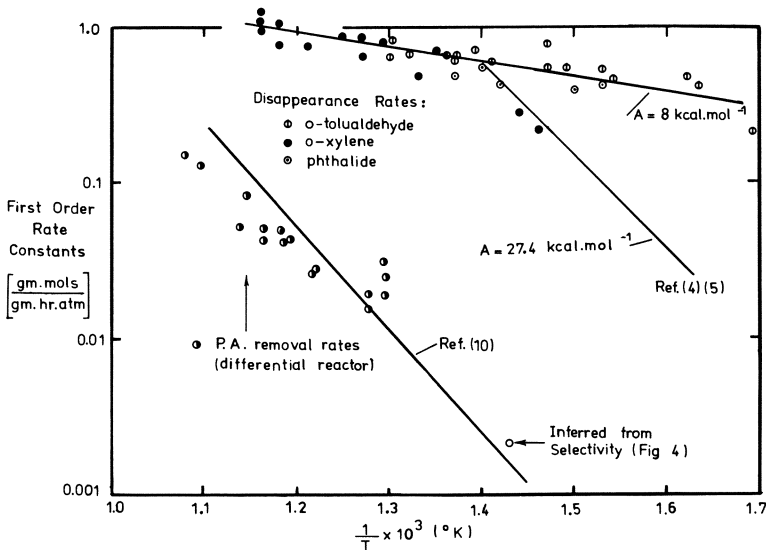


Figure 2. Kinetics of principal reactions

Figure 2 shows the first-order rate constants for the disappearance of *o*-xylene, TA, and PI, fed separately to the CSTR. These are the same for all three reactants above 440°C and the same for the latter two at all temperatures used. An important feature is the low activation energy (8 kcal/mole) for xylene disappearance above 440°C which, as will be seen, explains the absence of strong parametric sensitivity of the fixed-bed reactor. Below 440°C the xylene disappearance kinetics have an activation energy of about 27 kcal/mole and agree very well with those reported in this temperature range by Watt (4) and Froment (5) although the latter used another catalyst. This abrupt change in activation energy at high temperature has also been observed by Vaidyanathan (6) in the oxidation of benzene with a V₂O₅ catalyst. The phenomenon presumably results from a change from chemical reaction rate control to an undetermined step, perhaps surface diffusion of hydrocarbon. This process is apparently common to xylene, TA, and PI; the reaction step for TA and PI is relatively rapid down to 340°C. Mass transfer between the impermeable catalyst and the gas was calculated (3) to be relatively rapid compared with observed rates under all circumstances.

Derivation of Temperature Profiles in the Fixed-Bed Reactor

Above 440°C, to a first approximation, it may be assumed that the activation energy for xylene disappearance is zero and a one-dimensional model of the fixed bed reactor is appropriate. An analytical integration of the rate and conservation equations is thereby possible.

$$X = 1 - e^{-\alpha l}$$

$$T - T_w = \frac{\beta}{\gamma - \alpha} (e^{-\alpha l} - e^{-\gamma l}) \quad (1)$$

where

$$\alpha = \frac{\rho_B S \bar{M}}{G} \quad (2)$$

$$\beta = \frac{-\Delta H y_{o\alpha}}{C_p}$$

$$\gamma = \frac{2U}{R.G.C_p}$$

$$T = T_w \text{ and } X = 0 \text{ at } l = 0$$

Ellis (7) measured temperature and conversion profiles in 1- and 2-inch diameter fixed bed reactors containing the same catalyst as used here. He found that the excess temperatures were independent of jacket temperature over the range 430°–480°C in agreement with a negligible energy of activation for reaction in this range. He also found a constant selectivity to PA and precursors of 75%, showing that PA is strongly resistant to over-oxidation.

Figure 3 illustrates that Equation 2 can be fitted to Ellis's data using an unsophisticated numerical search which gives constrained and entirely acceptable values of the parameters U and S . The heat of reaction is calculated from the observed, almost constant overall selectivity to PA of 75%, assuming complete combustion of the remaining 25% (2).

We found that $S = 0.8$ and $U = 150$. The former value was obtained at 508°C (Figure 2), compared with a mean reaction temperature of 505°C,

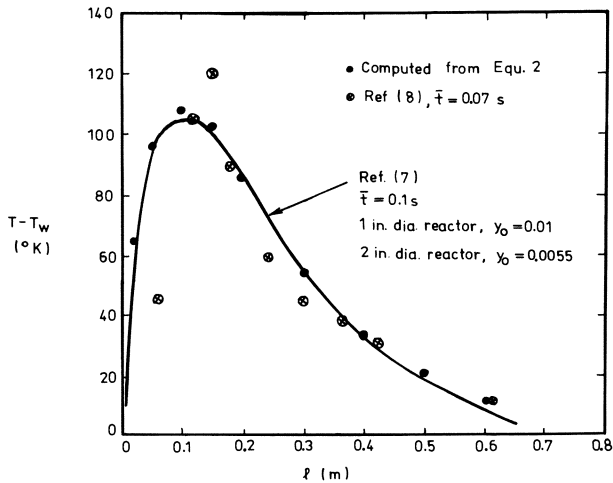


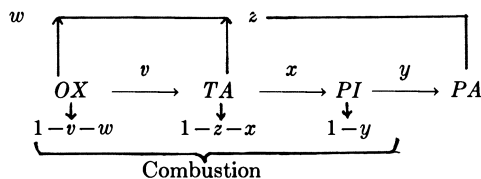
Figure 3. Temperature profiles in tubular reactors

and the latter value approaches reasonably well the value of 130 predicted from the correlation of Potter and Agnew (9). The model predicts the observation that when the reactor is scaled up from 1 to 2 inches in diameter, the feed concentration must be reduced from $y_0 = 0.01$ to $y_0 = 0.0055$ to maintain the same temperature profile. However the model fails to predict the hot-spot in the 2-inch diameter fixed bed reactor, probably because of its one-dimensionality. Figure 3 also illustrates that the model predicts reasonably well the results of Bernardini and Ramacci (8) who used a 19-mm diameter tube and another, although ostensibly similar, catalyst. Thus the kinetics explain the absence of parametric sensitivity under normal commercial operating conditions using packed tubes of small diameter and the catalyst described working outside the explosive limits.

It has been noted (2) that the reactor temperature can be appreciably reduced by recycling the tail gas; the same effect is observed when the feed concentration is increased above 1 mole % xylene (7). In both cases it would seem that the phenomenon results from a critical dependence of the reaction rate on oxygen concentration when this approaches the limit corresponding to the equilibrium partial pressure of a catalytically active oxide state. This reversible catalyst deactivation has been noted earlier (Figure 1).

The Reaction Scheme

It is convenient to investigate the reaction scheme and the factors which determine the selectivities with the CSTR. Writing



and noting that PA combustion is neglected (low conversions), w , v , x , y , and z represent the assumed constant selectivities at a constant temperature; the disappearance first-order rate constants of OX, TA, and PI are the same under these conditions (Figure 2). Thus with a xylene feed, calling $k_1 t = N$:

$$\begin{aligned} X_{OX} &= \frac{N}{1+N} \\ Y_{TA} &= v X_{OX} (1 - X_{OX}) \\ Y_{PI} &= x v X_{OX}^2 (1 - X_{OX}) \\ Y_{PA} &= xyv X_{OX}^3 + w X_{OX} + zv X_{OX}^2 \end{aligned} \quad (3)$$

With TA feed:

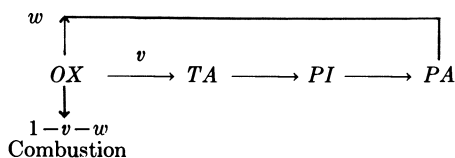
$$\begin{aligned} X_{TA} &= \frac{N}{1+N} \\ Y_{PI} &= x \left(\frac{X_{TA}}{1 - X_{TA}} \right) \\ Y_{PA} &= z X_{TA} + xy X_{TA}^2 \end{aligned} \quad (4)$$

With PI feed:

$$Y_{PA} = y X_{PI} \quad (5)$$

Experimental measurements of the yields of TA, PI, and PA with the three feeds can then be used to determine w , v , x , y , and z .

From Equation 5 it was typically found that $y = 1$ (no combustion of PI) and from Equation 4, $x = 0.09$ and $z = 0.55$ (36% combustion of TA). However from Equation 3, $x = 1$ and $z = 0$, showing that *o*-xylene completely inhibits the catalytic combustion of TA. A final reaction scheme is shown below:



where $v \approx 0.27$; $w \approx 0.43$ (30% combustion of *o*-xylene). The fact that 43% of the reaction to PA takes place directly simply means that it occurs without prior desorption of TA and PI. These results were obtained at low xylene conversions where PA combustion was negligible; however, such combustion was evident at higher conversions in the CSTR, mainly a result of the catalytic activity of the aluminum reactor as explained below.

Kinetics of Phthalic Anhydride Oxidation

Unlike the other oxidation reactions above, PA oxidizes unselectively on all surfaces; the least reactive found were titanium and very pure aluminum. However no purely homogeneous reactions took place in experiments in which the surface-to-volume ratio of the reactor was greatly altered.

The oxidation of PA on the 10 gram charge of vanadium catalyst was generally no more rapid than on the interior surfaces of aluminum and titanium

spinning basket reactors; both were used in this work so that a large and uncertain correction for metal activity was involved. However soft aluminum tubing of $\frac{3}{8}$ -inch bore retained a negligible activity for at least 50 hr operation; after that a strong activity was increasingly apparent. This fact made it possible to employ an easily renewable differential reactor of this tubing when approximate agreement was obtained with the few results of Hughes and Adams (10) at the same feed concentration of 1% PA using a similar catalyst. Results are shown as pseudo-first-order rate constants in Figure 2. It is immediately apparent that PA combustion on the catalyst is slow compared with the rate of PA formation from xylene between 400° and 550°C where fixed bed reactors using this type of catalyst operate. Moreover at the lower temperatures of fluid bed reactor operation (about 340°C), the catalytic combustion rate has the same activation energy as the PA formation rate and this produces a temperature-independent selectivity (*see below*). The order of reaction for PA combustion appeared to be first-order on V_2O_5 and zero-order on aluminum and titanium.

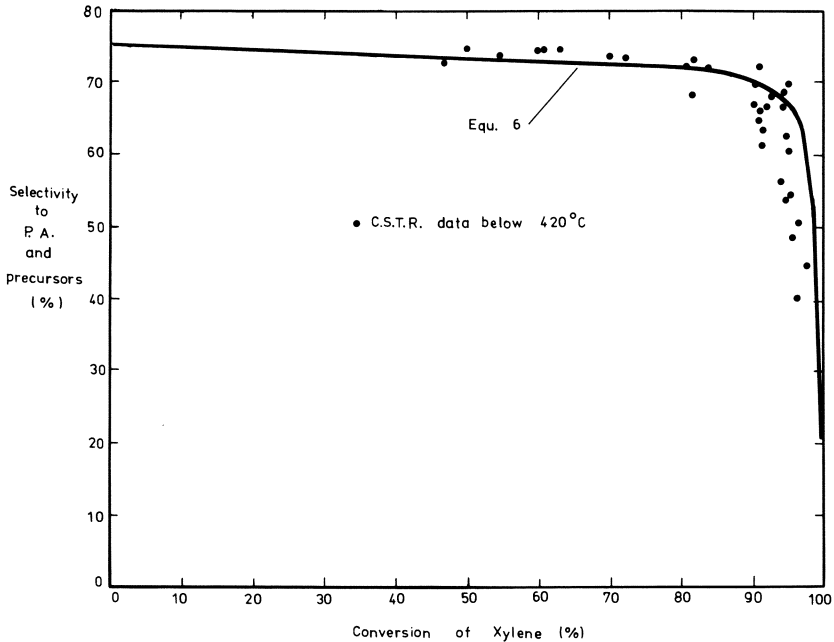
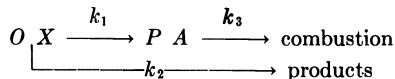


Figure 4. CSTR data below 420°C

Derivation of Selectivities

For the reaction scheme



it is easily shown for the CSTR that

$$\theta_{PA} = \frac{\frac{k_1}{k_1 + k_2}}{1 + \left(\frac{k_3}{k_1 + k_2}\right) \left(\frac{X}{1-X}\right)} \quad (6)$$

For temperatures below 440°C

$$\frac{k_1}{k_1 + k_2} = 0.75$$

and

$$\frac{k_3}{k_1 + k_2} = 5.64 \times 10^{-3}$$

both values are approximately constant, as seen from Figure 4, which shows data observed over a range of temperatures and concentrations.

The corresponding equation for isothermal plug-flow operation is

$$\theta_{PA} = \frac{\left(\frac{k_1}{k_1 + k_2}\right) \left(\frac{1-X}{X}\right)}{1 - \left(\frac{k_3}{k_1 + k_2}\right)} \left[\left(\frac{1}{1-X}\right)^{1 - \left(\frac{k_3}{k_1 + k_2}\right)} - 1 \right] \quad (7)$$

By substituting the above data into this equation it is found that PA combustion has a very small influence on selectivities in the plug-flow mode. For example, the selectivity falls from 75% at zero conversion to 72.5% at 99.9% conversion at all temperatures below 440°C. However, at higher bed temperatures, selectivities will diminish as found experimentally (7).

Nomenclature

A	energy of activation, kcal/gram-mole
C_0	concentration, gram-moles/liter
C_p	specific heat, kcal/gram-mole °K
G	superficial gas flow rate, kg/m ² hr
$-\Delta H$	heat evolved by reaction, kcal/gram-mole
$k_{1,2,3}$	first-order reaction velocity constants, gram-moles/gram hr atm
l	distance from inlet of fixed-bed reactor, m
\bar{M}	mean molecular weight of feed
N	dimensionless, = $k_1 t$
R	radius of tubular reactor, m
S	pre-exponential factor, gram-moles/hr kg
T	gas temperature, °K
T_w	wall temperature, °K
\bar{t}	mean residence time
U	overall heat-transfer coefficient, kcal/m ² hr °K
X	fractional conversion
y_0	mole fraction of hydrocarbon in feed
Y	yield
w, v, x, y, z	selectivities (as below)
θ	selectivity, moles product/moles reactant consumed
ρ_B	bulk density of catalyst bed, kg/m ³
α, β, γ	defined under Equation 2

Literature Cited

1. Calderbank, P. H., Caldwell, A. D., *ADVAN. CHEM. SER.* (1970) **109**, 38.
2. Calderbank, P. H., Watt, G. I., Ellis, S. N., "Chemical Reaction Engineering Symposium," Elsevier, Amsterdam, 1972.
3. Brisk, M. L., *et al.*, *Trans. Inst. Chem. Eng.* (1968) **46**, 3.
4. Watt, G. I., Ph.D. Thesis, University of Edinburgh, 1971.
5. Froment, G. F., *Ind. Eng. Chem.* (1967) **59**, 18.
6. Vaidyanathan, K., Doraiswamy, L. K., *Chem. Eng. Sci.* (1968) **23**, 537.
7. Ellis, S. N., Ph.D. Thesis, University of Edinburgh, 1972.
8. Bernardini, F., Ramacci, M., *Chim. Ind.* (1966) **48**, 9.
9. Agnew, J. B., Potter, O. E., *Trans. Inst. Chem. Eng.* (1970) **48**, T15.
10. Hughes, M. F., Adams, R. T., *J. Phys. Chem.* (1960) **64**, 781.

RECEIVED January 2, 1974.

Copper-Substituted Zirconium Phosphate— a New Oxidation Catalyst

THOMAS J. KALMAN¹ and MILORAD DUDUKOVIĆ

Chemical Engineering Department, Ohio University, Athens, Ohio 45701

ABRAHAM CLEARFIELD

Department of Chemistry, Ohio University, Athens, Ohio 45701

A novel catalytically active compound is obtained by substitution of copper cations into crystalline α -zirconium phosphate. Catalytic oxidation of carbon monoxide on crystalline copper-substituted zirconium phosphate was studied at different gas compositions, flow rates, and temperatures up to 400°C. A 1-ft long, tubular reactor with a preheater section is used for analysis. The rate of reaction is proportional to the square root of the carbon monoxide concentration. Oxygen, when present in large excess over its stoichiometric ratio, has no influence on the reaction rate. The apparent activation energy of 12.5 kcal/mole and the rate constant for the reaction are determined. Results indicate that copper-substituted α -zirconium phosphate is comparable in activity with a number of active catalysts for carbon monoxide oxidation.

The catalytic oxidation of carbon monoxide (CO) has been studied extensively with many catalysts. A complete literature review was compiled by Katz (1) and Dixon and Longfield (2). Most of this early work dealt primarily with predictions of catalytic activity of various metallic oxides, especially the transition group metallic oxides. Reaction mechanism and possible surface intermediates were thoroughly examined. Laidler (3) summarized a number of studies done on CO oxidation with different surfaces such as quartz glass, rock crystal, platinum, and copper oxide and tabulated the empirically found reaction rate orders which varied from -1 to 1 with respect to CO and from 0 to 1 with respect to oxygen. Schwab and Gossner (4) studied the oxidation of CO on silver, palladium, and silver-palladium alloys and found different rate expressions, which they qualitatively explained on the basis of the catalyst electron configuration and Langmuir adsorption theory. Parravano (5) reported the addition of foreign ions to nickel oxide and the subsequent use of the oxide in

¹ State of Ohio Environmental Protection Agency, Logan, Ohio.

CO oxidation. Tajbl *et al.* (6) studied the kinetics of CO oxidation by 0.5 wt % palladium on α -alumina pellets and found the rate to be proportional to oxygen to carbon monoxide ratio. Coekelbergs *et al.* (7) used x-ray irradiated alumina as catalyst and determined the reaction rate order to be 1 with respect to CO and 0.5 with respect to O₂.

The interest in catalytic CO oxidation was greatly renewed in the late 1960's when the increasing level of CO emissions forced the U.S. government to impose restrictions on the amount emitted from major sources (8). Automobile combustion of gasoline accounted for over 80% of the total U.S. CO emissions (9). At present, exhaust treatment devices, such as catalytic converters, show promise in reducing these emissions to the low levels required (10, 11). The catalysts to be used by auto manufacturers in the next few years contain noble metals, such as platinum, and do not represent an optimal choice for several reasons. Platinum is expensive and is easily poisoned by all types of impurities; it is even self-poisoned by excess CO, the oxidation rate is high at high temperatures but intolerably slow at low temperatures when most of the CO emissions occur. Thus, there still is a need for a cheaper catalyst with good performance.

This work evaluates the performance of an ion exchange compound, copper-substituted α -zirconium phosphate, ZrCu(PO₄)₂, in the catalytic oxidation of CO. This will initiate further studies into the possible use of transition metal-substituted zirconium phosphates as oxidation catalysts with potential applications for catalytic treatment of automobile exhaust. The present study was done when the preliminary tests presented in Table I showed the compound to be catalytically active. These results were obtained by injecting a small amount of air-carbon monoxide into a helium stream entering a pulse reactor filled with catalyst. The exit gas composition was monitored by a gas chromatograph.

Table I. Carbon Monoxide Oxidation on Copper-Substituted Zirconium Phosphate (Preliminary Results)

Reactor Temperature, °C	Carbon Monoxide: Air	Reactor Flow Rate (ml/min)	Products
60	3:2	60	CO
100	1:3	60	CO
150	1:4	8	Trace CO ₂
250	1:5	8	75% CO ₂ , 25% CO
300	1:10	8	100% CO ₂
300	1:1	12	70% CO ₂ , 30% CO

Catalyst Selection and Preparation

Selection of the Catalyst. The main effect of a catalyst is to lower the potential energy barrier which reactant gas molecules have to overcome in order for a chemical reaction to take place and thus allow a larger number of molecules to react per unit time. The activity of a solid surface in a particular reaction depends in general on its electron configuration, crystal structure, purity, and porosity. The studies reported in the literature indicate that besides noble metals such as palladium, platinum, and silver, many compounds containing transition metals are active catalysts for CO oxidation. On the other hand, certain crystal structures such as those of naturally occurring zeolites, are very conducive to catalytic activity.

In preparing new catalysts for CO oxidation reaction two novel approaches may be taken:

(a) substitution of transition metals into the zeolite framework with full preservation of the zeolite crystal configuration

(b) substitution of transition metals into an ion exchange compound with a defined crystal structure similar to zeolites.

In a recent effort one of the authors (12) managed to incorporate chromium(III), vanadium(V), and molybdenum(VI) into the zeolite framework. Nothing is known yet about the catalytic properties of these new zeolites. The second approach was taken in this work, and zirconium phosphate was selected as an ion exchange compound into which desired metal cations may be substituted for hydrogen.

The ion exchange properties of zirconium phosphate have been known for some time, and its high selectivity has been used to separate uranium and plutonium fission products (13) and to treat contaminated water in nuclear reactors (14). Practically all metallic cations can be exchanged for hydrogen in zirconium phosphate by a high temperature reaction between a metallic halide and zirconium phosphate (15). The substitution of transition metal ions will render compounds catalytically active, thus presenting an enormous amount of potential catalysts.

Zirconium phosphate has a layered structure (16). Each layer consists of a plane of zirconium atoms arranged in a hexagonal array. The phosphate groups are situated alternatively above and below the planes and have three of their oxygen atoms bonded to three different zirconium atoms. The fourth oxygen bears the hydrogen atom and points roughly perpendicular to the layers. The layers are staggered so that the phosphate groups in one layer are above zirconium atoms in the next layer. This arrangement forms zeolite type cages between the layers. The interlayer distance is 7.56 Å. The introduction of various cations tends to move the layers farther apart to accommodate a large ion. Copper-substituted zirconium phosphate was selected for this work since copper compounds are some of the most active catalysts for CO oxidation. As expected, the preliminary tests showed copper-substituted zirconium phosphate to be a more active oxidation catalyst (CO, methanol, SO₂ oxidation) than cobalt substituted zirconium phosphate (17). These preliminary qualitative results were obtained by passing the gas mixture through a U-tube filled with catalyst. The copper-containing catalyst readily converted methanol and CO to their ultimate oxidation products, CO₂ and water, at temperatures less than 300°C. It also showed promise for the oxidation of hydrocarbons and SO₂ at higher temperatures. The cobalt-containing catalyst was less effective for total oxidation, and it required higher temperatures for comparable performance. However, it showed promise as a catalyst for specific oxidations since it produced a 30% yield of butyraldehyde at 94% conversion of *n*-butyl alcohol, thus, yielding only a small amount of side products.

Catalyst Preparation. The preparation of the catalyst involved four major steps: (1) purification of zirconyl chloride, (2) preparation of α -zirconium phosphate, (3) cupric ion exchange for hydrogen in the α -zirconium phosphate, and (4) deposition of the catalyst on a support. The first two steps were presented in detail by Kalman (18) and to some extent by Clearfield and Stynes (19).

The cupric ion exchange reaction can be done by either a solid-solid (17) or wet method (18) using amorphous or crystalline zirconium phosphate. The

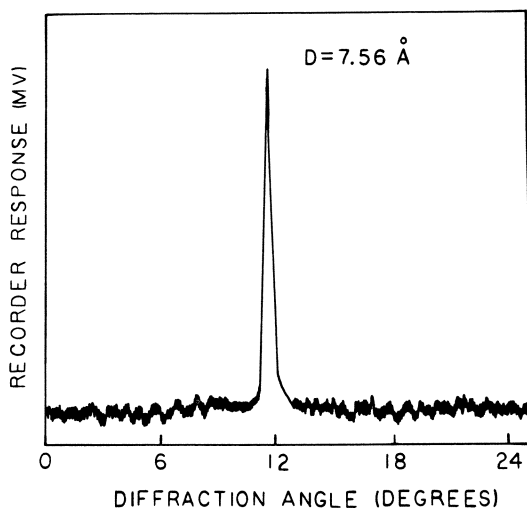


Figure 1. X-ray diffraction pattern of crystalline α -zirconium phosphate

starting material in this work was crystalline α -zirconium phosphate. An x-ray diffraction pattern (Figure 1) revealed that the starting material was crystalline, as indicated by the sharp peak at d spacing of 7.56Å. The solid-solid method, which consists in heating a finely ground mixture of zirconium phosphate and cupric chloride, was not convenient for making large amounts of catalyst. The wet method, developed in this work, involved refluxing α -zirconium phosphate

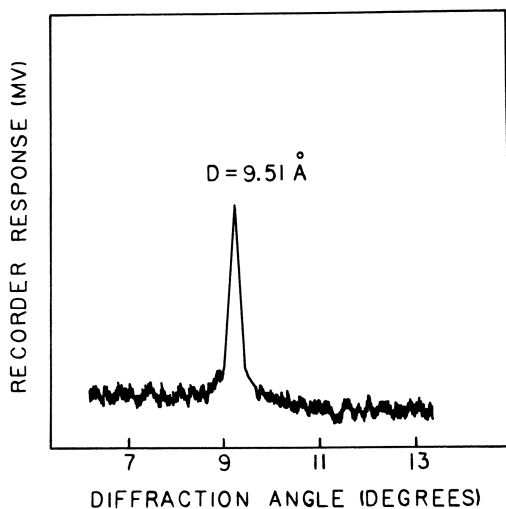


Figure 2. X-ray diffraction pattern of fully-substituted α -zirconium phosphate

with a cupric acetate solution until the supernatant became colorless. The reaction is:



X-ray powder patterns were taken during the reaction to determine the extent of the copper substitution. Copper-substituted α -zirconium phosphate has a characteristic d spacing of 9.51Å, as shown in Figure 2, and thus can be distinguished from α -zirconium phosphate ($d = 7.56\text{Å}$). The solid catalyst was filtered and dried, and the percentage of copper was determined analytically by an iodometric titration with sodium thiosulfate using the modified Fritz and Schenk (20) method. The percentage of copper substituted in every batch of catalyst made was greater than 90%. Thermal gravimetric analysis (TGA) gave the weight loss of catalyst with increasing temperature. A TGA of a 0.4015-gram sample of 93% copper-substituted zirconium phosphate is shown in Figure 3 with an explanation of the weight loss at certain temperature ranges. The catalyst has a density of 2.78 grams/cm³, and a BET area of 7.85 m²/gram was determined. This relatively low surface area can readily be improved by modifying the preparation procedure.

The last step in the preparation consisted of depositing the catalyst on a suitable support. A support was necessary since the catalyst consisted of micron-sized crystals. Although the catalyst adhered well to them, conventional supports such as alumina and clay were not used in this work because they

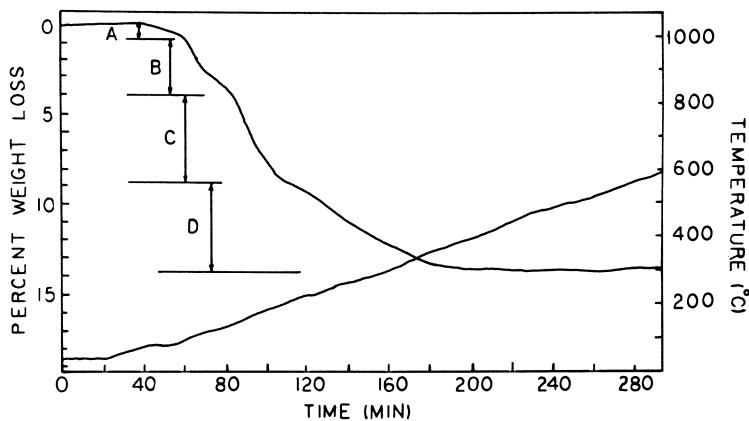


Figure 3. Thermogravimetric analysis of 93% copper-substituted α -zirconium phosphate. A, assumed to be surface moisture; B and C, weight loss from two moles of water; D, from incomplete substitution which results in condensation of phosphate groups.

masked the catalyst activity by being catalytically active themselves. Asbestos was used since it does not affect catalyst activity and adhere to it very well.

To deposit the catalyst on asbestos a slurry was first prepared with the desired amount of copper-substituted α -zirconium phosphate (4 grams) and benzene. Then, 8.0 grams of acid-washed, medium fiber purified asbestos was mixed in with the slurry. The benzene was next allowed to evaporate, and the

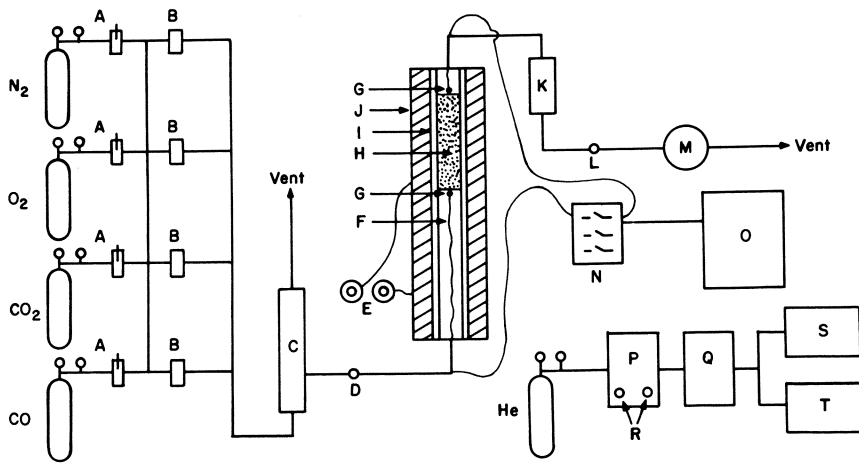


Figure 4. Apparatus for carbon monoxide oxidation. A—needle valve, B—flowmeter, C—manometer, D—feed sampling port, E—temperature controller, F—preheater, G—thermocouple, H—catalytic bed, I—heating tape, J—insulation, K—condenser, L—effluent sampling port, M—wet test meter, N—junction board, O—temperature recorder, P—gas chromatograph oven, Q—gas chromatograph control module, R—oven injection ports, S—strip chart recorder, T—digital integrator.

residual vapors were removed by heating the catalyst to 120°C for 12 hrs. The surface area of the catalyst on support was 10.91m²/grams as determined by the BET method.

Experimental

Apparatus. The experimental apparatus for CO oxidation on copper-substituted α -zirconium phosphate on asbestos is shown in Figure 4. The gas flow rate from each tank was controlled by a needle valve (A) and measured by a flowmeter (B). The flowmeters were calibrated with a wet test meter (M) and a 10-cc soap bubble meter. The gas pressure upstream from the reactor was measured by a mercury manometer (C), and the downstream line was vented to the atmosphere. The reactor consisted of 2.5 ft of 25 mm diameter borosilicate glass tubing, 1 ft of which was used for the catalytic bed (H) and 1.5 ft for the preheat section (F). Both sections were wrapped with heating tape (I), powered by variacs (E), and enclosed with fiberglass insulation (J). The catalytic bed was filled with 4 grams of catalyst (93% copper-substituted zirconium phosphate) on 8 grams of asbestos fibers as support. The temperature in the reactor was measured by two thermocouples (G), one at the entrance and the other at the exit of the catalytic bed. The temperature was continuously controlled within $\pm 3^\circ\text{C}$ and monitored by a strip chart potentiometric recorder (O). The blind probe with asbestos fibers indicated no CO conversion. The effluent gases from the reactor were cooled in a condenser (K) and expelled through an exhaust hood. Two sampling ports (D, L) were located before and after the reactor to withdraw feed and effluent samples for analysis. They contained a rubber septum through which a syringe needle could be inserted for sample removal.

The gas samples were analyzed by a Gow Mac thermal conductivity gas chromatograph (P, Q, R). The analysis required that N₂, O₂, CO and CO₂ be separated by the columns in the gas chromatograph in order to calculate the composition of the feed and effluent streams. A column containing molecular sieve 5A could separate N₂, O₂, and CO but adsorbed CO₂ (21, 22). A

second column containing silica gel, which separated CO_2 from the other gases, completed the analysis. The best separation was obtained with 16 ft of molecular sieve 5A and 4.5 ft of silica gel, using 0.25-inch copper tubing for columns at an oven temperature of 100°C and a carrier gas flow rate of 50 cc/min of helium. A digital integrator (T) was used during all experimental runs to evaluate composition. Since the volume percent of each gas found from the integrator did not exactly equal the actual volume percent of the gases, a calibration curve was determined for all ranges of composition.

The results obtained with two feed mixtures consisting of O_2 and CO are reported in this study. One contained a $\text{CO}:\text{O}_2$ ratio of 1:4, the other had a $\text{CO}:\text{O}_2$ ratio of 1:9. The flow rate through the reactor was varied from 27.5 to 312 cc/min, corresponding to the range of mean contact times of 0.214 to 1.77 gram hr/liter. In this flow range the pressure drop across the reactor was negligible. However, the runs performed with N_2/O_2 mixture, corresponding to the composition of air with the addition of a small percentage of CO , resulted in complete conversion of CO since large contact times had to be used to avoid large pressure drops.

Procedure. Each batch of catalyst on asbestos support was initially heated at 400°C in the reactor for 3 hrs, under N_2 purge to remove any residual moisture. The catalyst was then heated at the desired temperature with the required O_2 flow rate for 1 hr. The CO was next introduced and was allowed to flow for 15 min until a steady state was established. The temperature was kept constant to within 3°C during this time and throughout the run. A feed sample (0.5 cc) was taken with a syringe from the entrance port to the reactor and injected into the molecular sieve column, which separated O_2 and CO . Two effluent samples were taken from the exit port of the reactor. The first was injected in the molecular sieve column, which again separated CO and O_2 , but adsorbed CO_2 . The second sample was injected into the silica gel column, which separated CO_2 from the mixture. This procedure was repeated several times for every flow rate to assure that steady-state composition was being obtained. The data for the compositions were then averaged and corrected using the calibration curve.

Table II. Kinetic Data for Carbon Monoxide Oxidation ($\text{CO}:\text{O}_2$ ratio is 1:4)

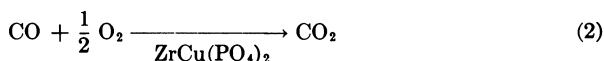
Run No.	Temperature ($^\circ\text{C}$)	Conversion x_{CO}	Feed Rate (cc/min)	Contact Time τ , (gram hr/liter)
1	325	1.00	37.5	1.77
2	325	1.00	43.3	1.54
3	325	1.00	56.5	1.18
4	325	0.866	75.1	0.889
5	325	0.608	112.5	0.592
6	325	0.471	156.0	0.427
7	300	0.921	37.5	1.77
8	300	0.842	43.3	1.54
9	300	0.729	56.5	1.18
10	300	0.649	75.1	0.889
11	300	0.405	112.5	0.592
12	300	0.294	156.0	0.427
13	275	0.689	37.5	1.77
14	275	0.574	43.3	1.54
15	275	0.469	56.5	1.18
16	275	0.413	75.1	0.889
17	275	0.276	112.5	0.592
18	275	0.152	156.0	0.427
19	250	0.433	37.5	1.77
20	250	0.376	43.3	1.54
21	250	0.289	56.5	1.18
22	250	0.232	75.1	0.889
23	250	0.0984	112.5	0.592
24	250	0.0919	156.0	0.427

Table III. Kinetic Data for Carbon Monoxide Oxidation (CO:O₂ ratio is 1:9)

Run No.	Temperature (°C)	Conversion x _{CO}	Feed Rate (cc/min)	Space Time τ, (gram hr/liter)
25	325	0.972	75.1	0.889
26	325	0.878	86.6	0.770
27	325	0.817	113.3	0.588
28	325	0.623	150.1	0.444
29	325	0.497	225.2	0.296
30	325	0.340	312.0	0.214
31	300	0.826	75.1	0.889
32	300	0.694	86.6	0.770
33	300	0.555	113.3	0.588
34	300	0.465	150.1	0.444
35	300	0.299	225.2	0.296
36	300	0.204	312.0	0.214
37	275	0.552	75.1	0.889
38	275	0.484	86.6	0.770
39	275	0.368	113.3	0.588
40	275	0.256	150.1	0.444
41	275	0.170	225.2	0.296
42	275	0.143	312.0	0.214
43	250	0.339	75.1	0.889
44	250	0.252	86.6	0.770
45	250	0.220	113.3	0.588
46	250	0.133	150.1	0.444
47	250	0.0530	225.2	0.296
48	250	0.0349	312.0	0.214

Discussion

In this study 48 experimental runs under varying conditions of temperature, flow rate, and composition were made. The weight of catalyst used in all of the runs was 4 grams (93% copper-substituted α -zirconium phosphate) on 8 grams asbestos support. CO oxidation proceeds according to the following stoichiometry:



Runs 1 through 24 were done with a volume ratio of CO:O₂ of 1:4 and runs 25 through 48 with a ratio of 1:9. No signs of catalyst deactivation were detected during several months of experimentation. The results are given in Tables II and III.

A material balance was done for each run by stoichiometrically balancing the number of moles of any two of the three gas species participating in Equation 2. The calculation involved the determination of the total number of moles of effluent per mole of feed by either of the three balances (CO and O₂, CO₂ and O₂, CO and CO₂) which ideally should give the same value if Reaction 2 were the only one taking place as assumed (18). The maximum difference between the three component balances was below 4% for all the runs presented here, which is a reasonably good agreement considering the type of apparatus used and possible experimental errors. To reduce the influence of this error in evaluating kinetic data, an average of the three values of the total moles of effluent per mole of feed was taken.

The porosity of the packed bed of asbestos fibers used was *ca.* 0.75, the apparent density of the fibers impregnated with the catalyst was less than the density of water. The fibers used were of different lengths, and radii and

formed irregular networks of high tortuosity factor. The mean fiber length and diameter were approximately 1 cm and 0.1 cm, respectively. Even for low Reynolds numbers, sufficient mixing occurred in the bed so that mass transfer was not rate controlling. For the flow rates and temperatures used, the Reynolds number was between 2 and 10. It is difficult to apply an empirical correlation for mass transfer coefficient predictions, such as the one obtained by Petrovic and Thodos (23) for beds packed with spheres to this irregular packed bed of fine fibers. However, it can be shown, following Satterfield (24), that if mass transfer were rate controlling, a 99% conversion of CO would be reached at a L/d_p ratio of 3.2 and 7.4 at Reynolds numbers of 1 and 10, respectively. The equivalent average particle diameter, d_p , is 0.38 cm at the most. A bed of over 30 cm in length, L , was used, and much lower conversions were obtained at the exit, which seems to indicate that the chemical reaction is rate controlling. This assumption was justified *a posteriori* by the magnitude of the evaluated activation energy. We assumed that axial dispersion may be neglected because of the large L/d_p ratio. This should be verified by a tracer experiment. Intuitively, the assumptions of good radial mixing and negligible axial dispersion are justified since it seems that the networks of asbestos fibers act like multiple screens to break repeatedly the velocity profile and create mixing.

The integral method of analysis was applied to all the data (24). A reaction rate expression was hypothesized, introduced into the plug flow reactor mass balance, and integrated. The integrated expression was plotted against contact time using the experimentally determined values. A plot of $\ln(1/1-x)$ vs. contact time, W/q , corresponding to the first-order reaction with respect to CO, failed to yield a straight line, exhibiting a definite convex curvature. A plot of conversion, x , vs. contact time, W/q , corresponding to a zero-order

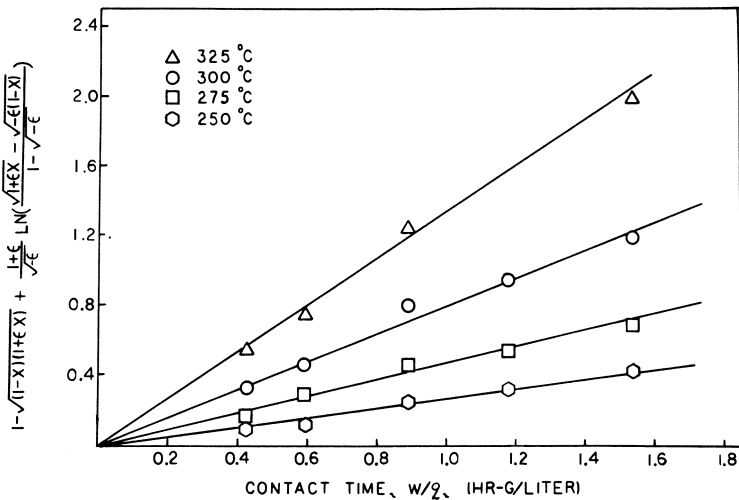


Figure 5. Carbon monoxide oxidation on copper-substituted zirconium phosphate at a CO:O₂ ratio of 1:4. Least-squares fit for: $-r_{CO} = kC_{CO}^{0.5}$.

reaction, resulted in a concave curve. This indicated that the order of reaction with respect to CO was between zero and one. The reaction rate of order 0.5 fitted the data very well.

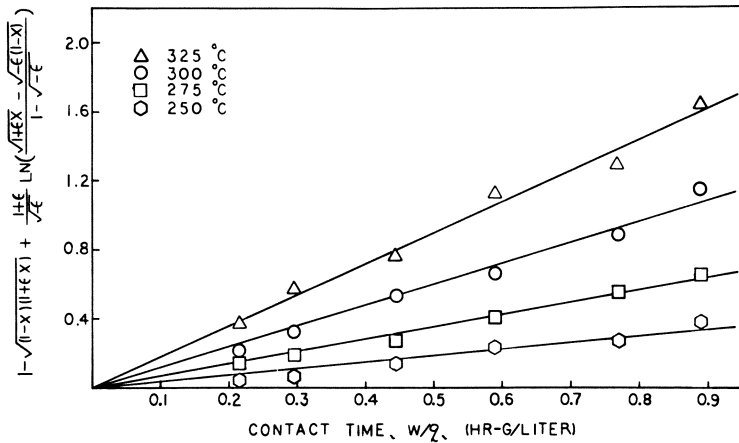


Figure 6. Carbon monoxide oxidation on copper-substituted zirconium phosphate at a $\text{CO}:\text{O}_2$ ratio of 1:9. Least-squares fit for: $-r_{\text{CO}} = kC_{\text{CO}}^{0.5}$.

$$-r_{\text{CO}} = k(C_{\text{CO}})^{0.5} \quad (3)$$

The integrated expression, taking into account the slight contraction of the reaction mixture caused by reaction, has the following form:

$$\frac{k W}{(C_{\text{CO}}^0)^{0.5} q} = 1 - \sqrt{(1-x)(1+\epsilon)} + \frac{(1+\epsilon)}{\sqrt{-\epsilon}} \ln \left[\frac{\sqrt{1+\epsilon x} - \sqrt{-\epsilon(1-x)}}{1 - \sqrt{-\epsilon}} \right] \quad (4)$$

By plotting the right side of Equation 4 vs. contact time, W/q , straight lines were obtained by a least-squares method for both $\text{CO}:\text{O}_2$ ratios. These results are presented in Figures 5 and 6. The reaction rate constant for each temperature was evaluated from the slope of the straight line fitted by the least-squares method.

The rate of CO oxidation probably depends in some manner on the O_2 concentration also. This dependence is difficult to establish from the results presented here since O_2 was used in large excess over the stoichiometric ratio and its concentration stayed well within 3% of its entrance value for both $\text{CO}:\text{O}_2$ feed ratios. Therefore, the O_2 concentration may be assumed to be constant and equal to its initial value at the reactor entrance. Increasing the initial O_2 concentration by 12.5% from the 1:4 to the 1:9 mixture did not have any effect, within experimental error, on the reaction rate constant; this indicates that the reaction rate is independent of O_2 concentration when large excess of it are present. At ratios of O_2 to CO larger than 8, the stoichiometric ratio the catalyst surface is always saturated with O_2 , and the steps in the reaction mechanisms involving O_2 are not rate limiting.

The reaction rate constants, evaluated in Figures 5 and 6 at different temperatures were used to prepare an Arrhenius plot of $\log k$ vs. $1/T$ as shown in Figure 7. A single straight line was obtained for both volume ratios $\text{CO}:\text{O}_2$. From the slope of the line an apparent activation energy of 12.5 kcal/mole

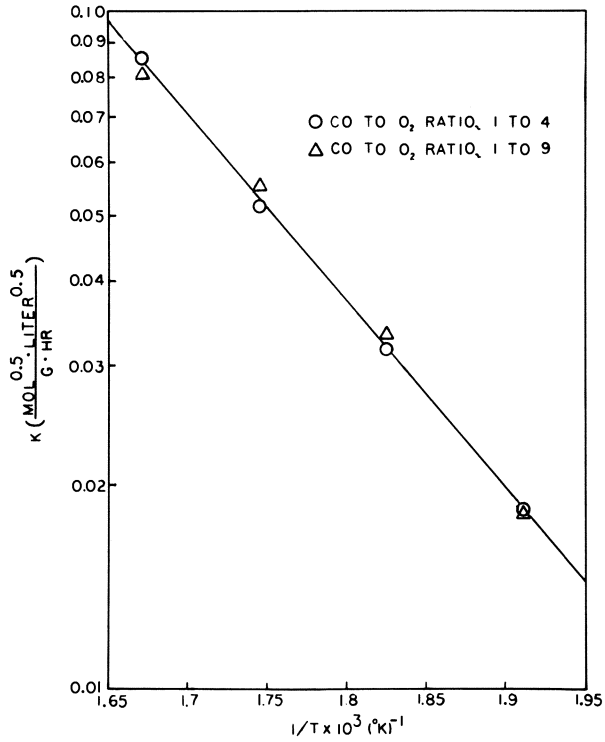


Figure 7. Arrhenius plot of the specific rate constant vs. temperature

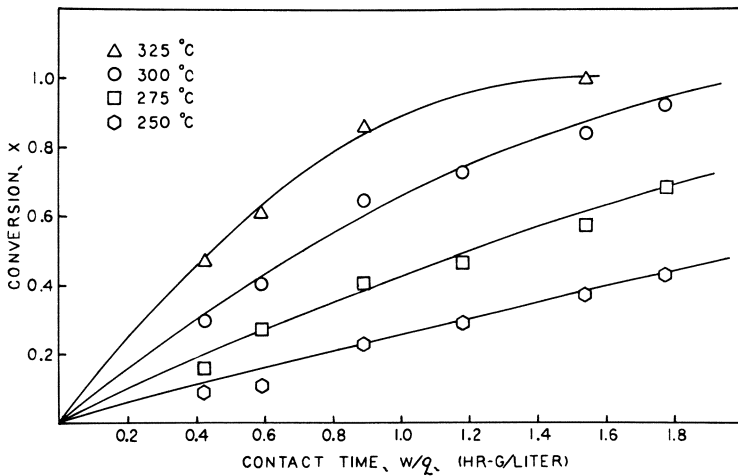


Figure 8. Conversion vs. contact time for a CO:O₂ feed ratio of 1:4

was calculated. The complete empirical rate expression for CO oxidation on copper-substituted zirconium phosphate at 250°–325°C and for CO:O₂ volume ratios smaller than 1:4, takes the following form:

$$-r_{\text{CO}} = 3.218 \times 10^3 e^{-\frac{12500}{RT}} C^{0.5}_{\text{CO}} \left(\frac{\text{moles CO}}{\text{gram hr}} \right) \quad (5)$$

The results obtained by using the rate expression given by Equation 5 are compared with the experimental values for both CO:O₂ volume ratios in Figures 8 and 9 and show good agreement.

It is difficult to compare the performance of this catalyst in CO oxidation with other catalysts used under similar conditions since literature data are scattered and the few reported rate expressions were determined under entirely different ranges of temperature and concentrations. Serious errors can arise in extrapolating empirical rate expressions to a different set of conditions since another step in a complex reaction mechanism may become rate determining. The reaction rate will also depend strongly on the intrinsic catalytic activity and on the availability of the catalyst surface. To estimate the performance of this new catalyst and others used in CO oxidation, Table IV lists known catalysts which are active in CO oxidation along with the operating conditions used

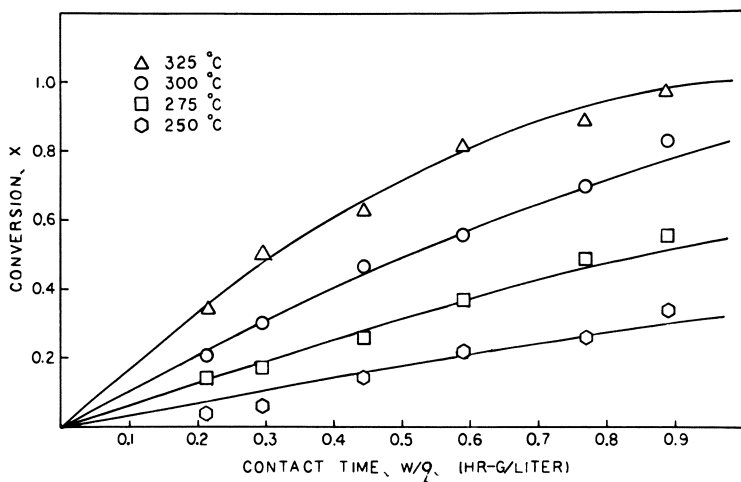


Figure 9. Conversion vs. contact time for a CO:O₂ feed ratio of 1:9

in those investigations. Rate constants were not given in some of these studies and were determined at 300°C whenever possible by extrapolating the available data. The catalysts are compared in the following ways: (a) the activation energies are listed, (b) the initial rates at 300°C for a 4% CO mixture are listed, (c) the contact times necessary to achieve 90% conversion of the above mixture in a plug flow reactor are calculated.

Table IV shows that copper-substituted α -zirconium phosphate is at least comparable with the other catalysts. The comparison is per gram of catalyst without considering some important parameters such as the surface area. The extreme values obtained for alumina and palladium on α -alumina (6) probably result from the fact that the data were extrapolated outside the region in which the determined rate expressions were valid and that the surface areas were different by a few orders of magnitude. Our catalyst seems to have a better

Table IV. Comparison of Different

<i>Investigator</i>	<i>Catalyst</i>	<i>Temperature Range (°C)</i>	<i>Rate Law</i>
Schwab (26)	CuO	310-430	$r = k[\text{CO}]$
Tajbl. <i>et al.</i> (6)	0.5 wt % Pd on α -alumina	200-234	$r = k \frac{[\text{O}_2]}{[\text{CO}]}$
Coekelbergs <i>et al.</i> (?)	alumina	210-360	$r = k[\text{CO}][\text{O}_2]^{0.2}$
	irradiated alumina	210-360	$r = k[\text{CO}][\text{O}_2]^{0.2}$
Parravano (5)	NiO	180-240	$r = k[\text{CO}][\text{O}_2]^{0.25}$
Hughes and Hill (27)	V ₂ O ₅	370-430	$r = k \frac{k_1[\text{CO}]}{1 + k_2[\text{CO}]}$
Schwab and Gossner (4)	Pd	250-320	$r = k \frac{[\text{O}_2]}{[\text{CO}]}$
	Ag	250-550	$r = k[\text{CO}][\text{O}_2]$
This work	ZrCu(PO ₄) ₂	250-325	$r = k[\text{CO}]^{0.5}$

performance than nickel oxide and vanadium oxide. The activation energy of 12.5 kcal/mole is well within the range of previously found values for CO oxidation on various surfaces. The effect of the reaction on the catalyst and the manner of deactivation is not known since conversions obtained could be reproduced after a long time with no sign of deactivation. There was no change in color or in the fine, powdery quality of the catalyst after prolonged use.

The evaluated reaction rate order of 0.5 indicates a complex reaction mechanism. A few experimental runs were performed at CO:O₂ feed ratios of 1:2 and 1:1. The results could still be interpreted on the basis of the previously evaluated rate expression of 0.5 order, and the reaction rate constant remained apparently independent of oxygen concentration. Several adsorption-desorption mechanisms could be devised to account for this behavior. However, the amount of experimental data available was insufficient to distinguish between various possible mechanisms. Further studies under different ranges of reactant concentrations are necessary to determine the correct mechanism.

Conclusions

Copper-substituted α -zirconium phosphate is comparable in activity with other active catalysts in CO oxidation and merits further investigation. The reaction rate was proportional to the square root of the CO concentration, indicating a complex reaction mechanism. Oxygen, when present in large excess over its stoichiometric ratio, did not influence the rate of reaction. The apparent activation energy is 12.5 kcal/mole.

Copper substitution into crystalline α -zirconium phosphate renders a catalytically active compound for CO oxidation. This catalyst does not exhibit any aging, and the rate expression indicates that it is not self-poisoned by CO. The potential for use in abatement in automobile pollution exists and should be explored further. The surface area of the catalyst and methods of deposition

Catalysts in Carbon Monoxide Oxidation

Activation Energy(kcal/mole)	Rate Constant at 300°C	Initial Rate (gram mole/hr gram)	Contact Time (gram hr/liter)
18.0			
28.5	0.0681 (mole/gram hr)	2.7×10^{-1}	0.001
18.0	0.026 (liter ^{1.2} /gram hr mole ^{0.2})	6.17×10^{-6}	317
18.0	0.068 (liter ^{1.2} /gram hr mole ^{0.2})	16.2×10^{-6}	121
13.0	3.98 (liter ^{1.25} /gram hr mole ^{0.25})	6.87×10^{-4}	2.9
	$k_1 = 0.045$ (liter/gram hr) $k_2 = 169.4$ (mole/liter) ⁻¹	3.34×10^{-5}	54.1
14.0			
22.0			
12.5	0.0531 (liter ^{0.5} mole ^{0.5} /gram hr)	1.55×10^{-3}	0.7

on various supports will be investigated as well as its activity in various oxidation reactions. Different transition metal cations can be exchanged for hydrogen into crystalline zirconium phosphate which has a structure with zeolite type cages. This produces an enormous amount of new catalysts. The catalytic activity of these substances should be further tested and compared.

Nomenclature

C_{CO}	carbon monoxide concentration, moles/liter
C_{O_2}	oxygen concentration, moles/liter
E	activation energy, cal
k	reaction rate constant (mole ^{0.5} liter ^{0.5} /gram hr)
N_i	number of moles of component i
N_T	total number of moles
N_i°	initial number of moles of component i
N_T°	initial total number of moles
q	volumetric flow rate of the gaseous mixture, liter/hr
R	universal gas constant, cal/mole °K
$-r_{CO}$	reaction rate based on disappearance of carbon monoxide, moles/gram hr
T	temperature, °K

$$x = \frac{N_i^\circ - N_i}{N_i} - \text{fractional conversion}$$

$$\varepsilon = \frac{N_T - N_T^\circ}{N_T^\circ} - \text{coefficient of expansion}$$

Literature Cited

1. Katz, M., *Advan. Catal.* (1953) **5**, 177-210.
2. Dixon, J. K., Longfield, J. E., *Catalysis* (1960) **7**, 303-322.
3. Laidler, K. J., *Catalysis* (1954) **1**, 161.

4. Schwab, G. M., Gossner, I., *A. Phys. Chem., N.F.* (1958) **16**, 39-63.
5. Parravano, G., *J. Amer. Chem. Soc.* (1953) **75**, 1448-1451.
6. Tajbl, D. B., Simons, J. B., Carberry, J. J., *Ind. Eng. Chem., Fundamentals* (1966) **5**(2), 171-175.
7. Coekelbergs, R., Collin, R., Cruz, A., Decot, J., Degols, L., Timmerman, L., *J. Catal.* (1967) **7**, 85-95.
8. Stern, A. C., "Air Pollution," Academic, New York, 1968.
9. Ross, R. D., "Atmospheric Pollution," Van Nostrand-Reinhold, New York, 1972.
10. Wei, J., *Chem. Eng. Process, Monograph Ser.* (1969) **65**(6), 1-17.
11. Patterson, D. J., Henein, N. A., "Emissions From Combustion Engines And Their Control," Ann Arbor Science Publishers, Ann Arbor, Mich., 1972.
12. Clearfield, A., Ohio University, unpublished results, 1973.
13. Amphlett, C. B., "Inorganic Ion Exchangers," Elsevier, Amsterdam, 1969.
14. Vesely, V., Pekarek, V., *Talanta* (1972) **19**, 237.
15. Clearfield, A., Troup, J. M., *J. Inorg. Nucl. Chem.*, in press.
16. Clearfield, A., Smith, G. D., *Inorg. Chem.* (1969) **8**, 431-436.
17. Troup, J., M.S. Thesis, Ohio University (1971).
18. Kalman, T. J., M.S. Thesis, Ohio University (1973).
19. Clearfield, A., Stynes, J. A., *J. Inorg. Nucl. Chem.* (1964) **26**, 117-129.
20. Fritz, J. S., Schenk, G. H., "Quantitative Analytical Chemistry," 2nd ed., Allyn and Bacon, Boston, 1966.
21. De Graph, A. C., *J. Chromatogr.* (1964) **2**, 357-363.
22. Leibrand, R. J., *J. Chromatogr.* (1967) **5**, 518-523.
23. Petrovic, L. J., Thodos, G., *Ind. Eng. Chem., Fundamentals* (1968) **7**, 274-280.
24. Satterfield, C. N., "Mass Transfer in Heterogeneous Catalysis," M.I.T. Press, Cambridge, 1970.
25. Levenspiel, O., "Chemical Reaction Engineering," 2nd ed., Wiley, New York, 1972.
26. Schwab, G. M., *J. Phys. Chem.* (1942) **52**, 234.
27. Hughes, M. F., Hill, G. R., *J. Phys. Chem.* (1955) **59**, 388-393.

RECEIVED January 2, 1974.

The Oxidation of *o*-Xylene in a Transported Bed Reactor

MARK S. WAINWRIGHT and TERRENCE W. HOFFMAN

Department of Chemical Engineering, McMaster University,
Hamilton, Ontario, Canada

o-Xylene was oxidized on a vanadia-on-silica catalyst in a bench-scale fixed bed reactor. Reaction products were analyzed at short on-stream times. These results indicated that reaction rates on freshly oxidized catalyst are much higher than those observed after steady state has been achieved; selectivity to organic oxidation products is also improved significantly. This reaction was also done in a pilot-scale transported bed reactor in which the catalyst was conveyed by the reactant/product gases. Stable operation was achieved at very high solid loadings (solid/gas ratios up to 250 and voidages from 0.60 to 0.86). The high reaction rates and selectivities can be exploited in such reactors, and suggestions for further research on such reactor systems are included.

O-Xylene was oxidized in a transported bed reactor where the finely divided catalyst (vanadia on a silica support) was conveyed upward in a tube by the reacting gas mixture. The advantages of a transported bed reactor are: (a) nearly plug flow behavior of the gas and solid and hence better control of residence time of the reacting and product gases, (b) essentially isothermal operation even at high reaction rates because of the good heat transfer rates from solid particles to gas and solid/gas slurry to wall and the heat sink provided by the mass of solid entrained in the gas, and (c) continuous use of reactivated catalyst since the solids are continually added and withdrawn (1). The main disadvantages are: (a) possibly the dilute concentrations of solids in pneumatically conveyed systems and hence the need for high specific reactivity of the catalyst, (b) possible high attrition of the catalyst and erosion of reactor internals, and (c) complicated equipment, especially the catalyst recovery system.

This study was done to evaluate the performance of this unique contacting reactor for oxidation reactions like *o*-xylene. In this reaction the rates are high enough and intermediate products are desired; moreover, it is highly exothermic.

Work with transported bed reactors has been limited because the reactions must be very fast. Most of the research has been done by industrial groups and is described in patents. Their use includes catalytic cracking, Fisher-Tropsch hydrocarbon synthesis, coal gasification, acetylene generation, and

nuclear reactors. Echigoya *et al.* (2) report a bench-scale reactor for cumene decomposition on an alumina-silicate catalyst, and recently deLasa and Gau (3) report the decomposition of ozone in a pilot-scale unit. Except for the latter, none of these studies reports on these units as chemical reactors.

The Oxidation Reaction

Reaction Steps. Definitive studies on *o*-xylene oxidation on vanadia catalysts have been done by Novella and Benloch (4), Herten and Froment (5), and Juusola (6). Although these workers used different vanadia catalysts, each with different amounts of vanadium pentoxide, with promoters of different concentration and with different catalyst supports, they detected essentially the same products; catalyst performance differed only in reaction rate and selectivity. In general, the reaction scheme can be represented by Figure 1.

Both Mann (7) and Juusola (6) indicate *p*-benzoquinone as a significant reaction product, but it is difficult to see how it can be part of the main reaction sequence. Moreover, usually *o*-toluic acid is present only in small quantities, indicating that its reaction rate to phthalide is quite fast. Oxidation rate studies of phthalide and phthalic anhydride to the carbon oxides and maleic anhydride suggest that these reactions are negligible below 400°C, indicating that these compounds are stabilized by the anhydride ring structure. Maleic anhydride concentration is usually small.

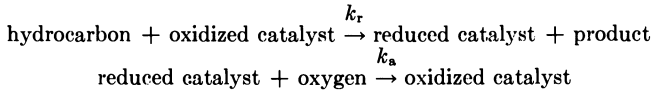
Oxidation Mechanism. The oxidation state of vanadium significantly affects product distributions. Simard *et al.* (8) showed that the oxidation state of vanadium in these catalysts is somewhere between 4 and 5 during reaction. In naphthalene oxidations the higher oxidation state favors formation of the organic oxides whereas the lower state favors the formation of carbon oxides (9).

The most significant systematic studies relating to catalyst properties have been done by the Japanese group (10, 11, 12, 13). They were concerned with the effect of support material, potassium sulfate (promoter) concentration, and sulfur trioxide addition on the catalyst activity and selectivity. It was shown that the optimal K_2SO_4 -to- V_2O_5 mole ratio depended on support material. From a phase diagram for this system, they concluded that with a silica-supported catalyst, most of the sulfate is associated with the support, and this, in turn, is important in determining catalyst performance. The importance of sulfur trioxide as a catalyst addition was determined by preparing catalysts treated with oleum; phthalic anhydride yield was dramatically affected. They concluded that the active catalyst component has a composition $V_2O_5 + 3V_2O_5 \cdot 2K_2SO_4 + nSO_3$ with perhaps the sulfate in the form of potassium pyrosulfate. All these studies have related more to measuring the effects of additions rather than defining their role or the mechanisms by which these components affect catalyst behavior.

Mars and van Krevelen (14) published a comprehensive study of oxidation reactions on vanadium pentoxide catalysts. The results were interpreted by a mechanism which has become known as the redox mechanism. In their model the oxygen for the organic oxidation is assumed to come from the vanadia; it is then assumed to be replaced by the catalyst reaction with gaseous oxygen. Steady-state behavior occurs when these two oxidation rates are equal. The model explains the much higher catalyst activity with fresh catalyst and the very fast catalyst decay that Wainwright and Hoffman (15) observed just after the reactor is put on stream.

Shelstad *et al.* (16) proposed a steady-state adsorption model to explain the behavior of these catalysts. Here the reaction is assumed to take place between the hydrocarbon molecule and chemisorbed oxygen. The resultant rate expressions are identical to those derived from the redox model, and therefore reaction kinetic experiments cannot discriminate between these models. However, the fast color change of the catalyst and the oxidation state of the vanadia suggest that the redox mechanism is the more likely, although the chemisorbed oxygen may be an important link in the catalyst reoxidation.

The essence of the model can be demonstrated by deriving the kinetic rate expression for the *o*-xylene to tolualdehyde reaction. Consider the following:



Assume, on the basis of experimental evidence, that both reactions are first order with respect to hydrocarbon and oxygen, respectively. The rate expressions for each step become:

$$r_r = k_r C_H \theta \quad (1)$$

and

$$r_a = k_a C_{O_2} (1 - \theta) \quad (2)$$

where θ is the fraction of oxygen sites available for hydrocarbon oxidation. In the steady state, these rates must be equal—*viz.*,

$$r_a = n r_r \quad (3)$$

where n is a stoichiometric coefficient for the number of oxygen molecules used per mole of hydrocarbon oxidized. Thus the fraction of active sites available becomes

$$\theta = \frac{k_a C_{O_2}}{k_a C_{O_2} + n k_r C_H} = \frac{1}{1 + \frac{n k_r C_H}{k_a C_{O_2}}} \quad (4)$$

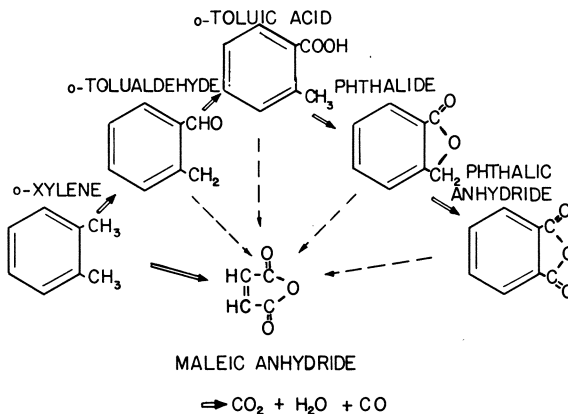


Figure 1. Reaction scheme

and the rate of overall hydrocarbon oxidation becomes:

$$r_r = \frac{k_a k_r C_{O_2} C_H}{k_a C_{O_2} + n k_r C_H} \quad (5)$$

Similar but somewhat more complicated expressions can be derived for the reaction scheme shown in Figure 1 involving parallel and series reaction steps.

Initially with a fully oxidized catalyst $\theta = 1$, and the reaction rate would be Equation 6, which is independent of oxygen concentration. This assumes that the reaction is not mass transfer controlled nor controlled by the rate of adsorption of the hydrocarbon molecules onto the reaction sites.

The ability of this model to describe the steady- and unsteady-state behavior of this reaction system is shown elsewhere (15). The model provides a reasonable description of a number of catalysts using different supports; the individual pre-exponential factors and activation energies for each catalyst are, however, quite different.

Here we review briefly some salient results for one catalyst used in the transported bed reactor so its performance in a fixed bed and a transported bed can be compared.

Packed Bed Studies

Apparatus. The packed bed apparatus was designed for all *o*-xylene conversions including 100%. The following effects were also taken into account:

(1) The reactor must be isothermal, and the temperature range must cover those encountered in industrial practice

(2) Catalyst dilution should be avoided, if possible, to avoid any catalytic effect of the diluent since anomolous effects of other materials have been reported (6, 7)

(3) Particle size should be small to avoid catalyst effectiveness effects and keep the particle essentially at the same temperature as the gas

(4) Reactor-to-catalyst diameter should be large to avoid short-circuiting effects

(5) Reactor length-to-diameter ratio should be large to avoid appreciable axial diffusion effects

(6) The reactor should operate at an appreciable velocity to ensure good heat and mass transfer from gas to particle

(7) The operating conditions relative to mass of catalyst-to-flow rate of reactant should be similar to those expected in the transported bed reactor.

The apparatus is shown in Figure 2. Oxygen and nitrogen are fed from high pressure cylinders and metered by capillary flowmeters. A back pressure valve maintained a constant pressure on the metering systems. This gas mixture was fed through an *o*-xylene saturator placed in a constant temperature bath, and the pressure in the saturator was measured. This mixture was heated to reaction temperature in a coil immersed in the salt bath surrounding the reactor and then fed to the top of the reactor. The reactor was a 14-cm length of 0.475-cm id stainless tubing, and a known amount of catalyst was charged to it (6 cm to 11-cm depth). The reactor was placed in a 12-inch id by 12-inch high molten salt bath (potassium nitrate-sodium nitrate-sodium nitrite eutectic). The exit gases passed through a Carle sampling valve. All lines and the valve were heated to *ca.* 200°C by hot air or electric heating tape to prevent condensation of products. Inlet gases flowed through the sampling valve and then to the reactor or were exhausted to the atmosphere. This allowed steady-state operation of the saturator to be achieved before the gases were passed to the reactor.

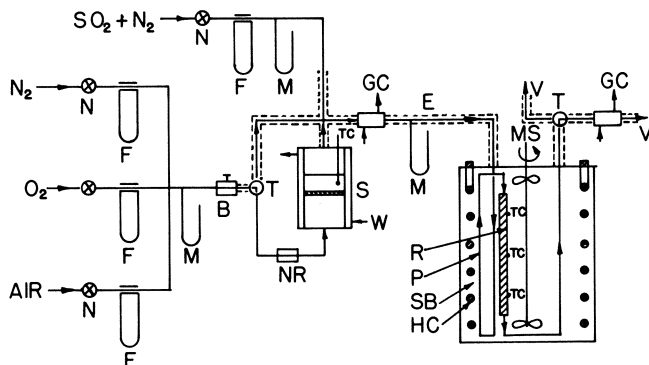


Figure 2. Flowsheet of packed bed apparatus

B	backpressure regulator	NR	non-return valve
E	electrical heating	P	preheating coil
F	capillary flow meter	R	reactor
Gc	gas sample valve to gas chromatograph	S	xylene saturator
Hc	heating elements	SB	molten salt bath
M	manometer	T	three-way valve
Ms	agitator	TC	thermocouple
N	needle valve	W	from constant temperature water bath
		V	vent

Table I. Approximate Composition (wt %) and Properties of Catalysts

	Silica Supported (No. 902)	Titania Supported
V ₂ O ₅	9	6
K ₂ SO ₄	29	—
K ₂ O	—	2
SO ₃	12	2
SiO ₂ or TiO ₂	50	84
Sb ₂ O ₃	—	6
Surface area, m ² /gram	40	5
Particle size (screened from original)	50/70 mesh	50/70 mesh
Bulk density, grams/cm ³	0.6	1.2
Average pore size	30 Å	—

The range of experimental conditions covered was:

reactor temperature	330°–390°C
catalyst	1.0 gram
<i>o</i> -xylene concentration	1–3%
<i>o</i> -xylene conversions	1–100%
oxygen concentration	10–30%

Initially the reactor was instrumented internally with thermocouples inserted at about 1-cm intervals over its length. Even at 100% conversion the observed maximum variation in temperature never exceeded 2°C. Blank reaction was negligible at all temperatures used. If silver solder was in contact with the reaction gases, considerable organic material oxidized so that only stainless steel was allowed to contact the gases. For this reason, the internal temperature of the reactor was not measured during the studies; three thermocouples on the reactor wall were used to monitor the reaction temperature.

To maintain constant catalyst activity, a small amount of sulfur dioxide gas was introduced with the incoming gas (0.01 vol %), consistent with industrial experience (17). In our experience, no appreciable long term catalyst decay could be attributed to this effect. The catalyst was always oxidized overnight with air and sulfur dioxide before any experiment to maintain its fully oxidized state. Gas samples of about 5 ml were analyzed by gas chromatography using a combination of columns containing Poropak Q, molecular sieves, and SE52 silicone gum rubber, with temperature programming and a complicated switching procedure described elsewhere (18). Peak areas were measured by a Hewlett-Packard 3370 B electronic integrator. Nitrogen was used as the tie component to allow direct comparison of inlet and outlet compositions. The accuracy of the analytical procedure was tested over *o*-xylene conversions from 1 to 100% and for selectivities of all other components from 0 to 85%. In general, all carbon balances were within 96–104%. Lower carbon balances were observed when considerable tar formation occurred. Problems associated with achieving this analytical accuracy are discussed elsewhere (18).

The reactants used were highest purity oxygen and nitrogen from Canadian Liquid Air, high purity *o*-xylene (Eastman), and a 0.502% mixture of SO₂ in nitrogen (Matheson).

Packed bed studies were done (19) with vanadia catalysts in industrial use. Their approximate composition and properties are shown in Table I, as supplied by W. R. Grace Co.

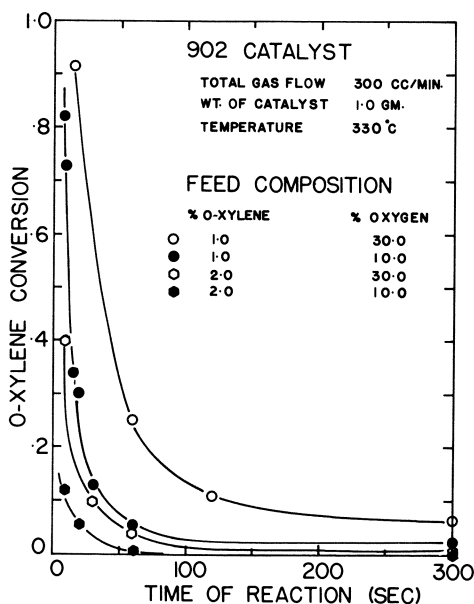


Figure 3. Approach to steady-state operation of packed bed

Effluent gases were analyzed at different times from the start of reactant flows to the reactor in order to monitor catalyst decay and performance with time. Because the analysis took approximately 35 minutes, the catalyst was generally reactivated for at least 1 hr at reaction temperature. This procedure gave reproducible results. At reaction times less than about 20 sec, a mass

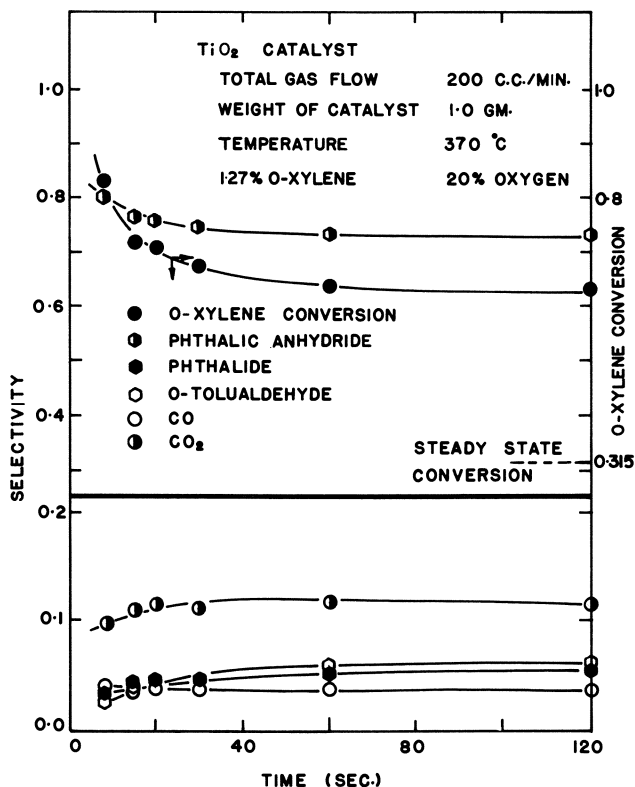


Figure 4. Initial rates and selectivities of TiO₂-supported catalyst

balance was often not achieved; the balance was poorer as reaction time decreased, probably because of adsorption and flow effects.

Results. Since the results of this program along with that with other catalysts are reported in great detail elsewhere (15), only those results salient to the transported bed are indicated here. A complete two-level factorial design was conducted on the 902 catalyst. In addition, eight center-point experiments were done between each experiment to monitor long term catalyst effects. Replication of four operating conditions provided variance estimates over a wide range of conversions.

Unsteady-State Performance. A typical plot of *o*-xylene conversion with time is shown in Figure 3 for this catalyst. Initial conversions of *o*-xylene, and hence reaction rates, are approximately 30 to 40 times those obtained after the catalyst achieves steady-state activity. Oxygen in the feed gas does affect the conversion, but this effect becomes less important at short reaction times. There is a suggestion that at zero time the effect of oxygen concentration disappears, thus suggesting that a model with $\theta = 1$ is reasonable. In addition, it has been shown here and by Herten and Froment (5) that selectivities to partial oxidation products improve with decreasing temperature. This is important since appreciable reaction rates can be achieved at temperatures much lower than those usually employed industrially.

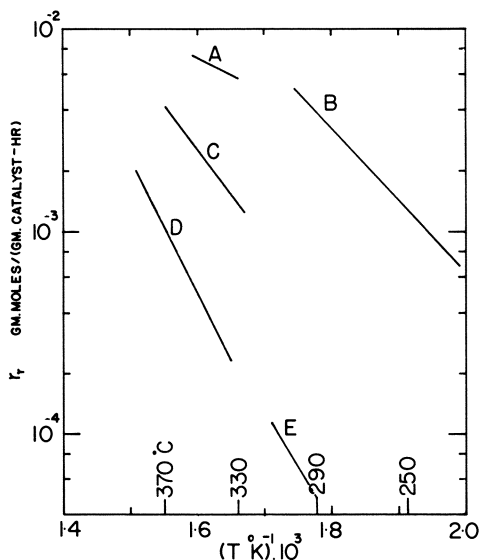


Figure 5. Rates of xylene conversion for different catalysts at .01 atm *o*-xylene and 0.21 atm oxygen pressures

- A after 10 sec contact on 902 catalyst in packed bed
 B transported bed data for 902 catalyst
 C steady-state packed bed data of Herten and Froment (5)
 D steady-state packed bed data on 902 catalyst
 E steady-state packed bed data of Juusola (6)

A highly oxidized catalyst also produces greater selectivity to partial oxidation products. Phthalic anhydride is more easily oxidized to maleic anhydride when oxygen lean mixtures are used (20). This is thought to be the result of the high ratio of V_2O_4/V_2O_5 existing in the catalyst. Thus, the initial selectivities should be higher than those obtained in the steady state; this effect is shown in Figure 4.

Steady-State Performance. Wainwright and Hoffman (15) show that the redox reaction model, with suitable parameter estimates, predicts the reaction product distribution quite well over the range of operating conditions used here and thus provides support for this mechanism. Figure 5 summarizes the steady-state reaction rate data for the 902 catalyst. The packed-bed experiments are an excellent base for discussing the performance of the transported bed reactor (below).

Transported Bed Studies

In a transported bed reactor, the reactant and product gases pneumatically convey the particles used to catalyze the reaction in a vertical pipe. The *o*-xylene oxidation, catalyzed by vanadia, was used to determine the operating characteristics and to evaluate such a reactor for oxidation reactions. Preliminary design consideration based on meager literature information suggested the following criteria for a pilot plant unit:

(a) To achieve smooth operation, characteristic of non-choking solids-gas flow, solid loadings would have to be low—*i.e.*, dilute phase transport would prevail and voidages would be greater than 97%. Thus, very little catalyst would be in contact with the reacting gases.

(b) Superficial gas velocities would have to be greater than 20 ft/sec to convey the particles. This, coupled with the low solids hold-up, suggested that the vertical pipe would have to be fairly long to achieve reasonable contact times.

(c) To achieve near turbulent conditions in the conveying system to provide some mixing of the gas, the conveying pipe diameter would have to be about $\frac{3}{4}$ inch.

(d) To achieve full control of the solids flow rate to the system, some form of forced solids feeding would be needed.

(e) Solids loading should be high enough to provide a good sink for the heat generated by the reaction and thus control the reaction temperature over the reactor length.

(f) Solids feed rate and solids hold-up measurements are necessary to evaluate reactor performance.

These criteria were used to design the apparatus used here.

Apparatus. The apparatus is shown in Figure 6. The solids circuit is a solids hold-tank, a solids feed-control tank, the entry section, the vertical reactor, a cyclone separator, and a solids receiver tank. The two upper tanks are 15 inches in diameter, and the solids feed control tank is 6 inches in diameter; all are heated to any desired temperature by low voltage, high current Kanthal strip heaters imbedded in Hiloset cement around the tanks. Air is supplied from the 100 psig mains, filtered, and passed through a sonic orifice whose upstream pressure is controlled by a controller/pneumatic valve. Some of the gas is split to provide the driving gas for the solids feed system; the remainder is heated in a steam heater and electrically heated system and then passed through a short horizontal section of pipe where the solids are dropped into the gas. They are conveyed about 8 inches and then transported around a 90° bend to a vertical ¾-inch od by 0.68-inch id stainless steel tube 27 ft long. During any run, the solids and gas temperatures were controlled to be at essentially the same temperature at the inlet. Electrical heaters on the reactor maintained isothermal operation. A 90° bend and an 8-inch horizontal section of tubing and expansion bellows connect the reactor to the cyclone separator. The gas leaving the cyclone is conveyed to another cyclone and a spray scrubbing section before it is discharged. The primary cyclone separated most of the solids so that solids loss was small. The solids receiver had a 2-inch ball valve on its bottom to collect solids. These were discharged back into the solids feed tank at the end of a run; thus, the system was operated batchwise. A solids inventory of approximately 300–350 lbs allowed at least a 10-min run at the highest solids feed rate. The solids receiver was connected to the solids feed tank by a 2-inch stainless steel bellows. The receiver is held by a yoke arrangement connected to a calibrated strain-gage weigh system so the receiver could be weighed continuously. A ½-inch diameter orifice was inserted on the bottom of the solids feed control tank. The solids level here was controlled by measuring it by a capacitance probe (Drexelbrook Eng. Co., Glenside, Pa.) which controlled the open-close operation of a 2-inch butterfly valve on the bottom of the tank. Air pressure in both tanks was controlled by pneumatic valves on the air lines. Upstream pressure on these valves was kept constant by restricting the main air flow by a manually controlled valve. The system provided excellent control as evidenced by the rate of weight increase of the solids receiver, and it allowed a fairly wide range of solids feed rates to be achieved.

o-Xylene was fed as liquid from a nitrogen pressurized feed tank; its flow rate was controlled by a needle valve and metered by a Rotameter. A steam-heated exchanger vaporized the *o*-xylene just prior to entering the reactor, and this vapor was fed through a ⅛-inch tube to mix with the air–solid mixture about 2 inches beyond the elbow. Originally, *o*-xylene was vaporized in a carburetor upstream of the solids addition point, but since appreciable reaction occurred in the horizontal section prior to the vertical reactor, the feed point location was changed. In one experiment *o*-xylene was admitted 7 ft above the elbow.

Three air-activated, quick shut-off ball valves were installed at 9, 158, and 281 inches from the reactor bottom. Gas samples were removed, and pressure was measured by mercury manometers near these valves. Gas samples were

collected through porous stainless steel filters into pre-evacuated bottles (*ca.* 1000 cc). The lines to these bottles were steam traced (100-psig) to prevent condensation. All lines and filters were flushed with helium just before sampling. Gas samples were drawn through the sampling valve and analyzed by the chromatographic technique described.

Sulfur dioxide was fed to maintain the same concentration level as in the packed bed experiments. Before a run, the solids were circulated through the system with air and SO₂ to ensure that the catalyst was fully regenerated. An orifice on the exit line indicated constant gas flow rate and provided a material balance check on the air flow rate. The catalyst used was No. 902 (W. R. Grace), the same as in the packed bed experiments. The mean particle size was 125 μ and its density was determined as 0.95 gram/cc.

The experimental conditions are shown in Table II. No significant homogeneous reaction occurred in the reactor at temperatures above 400°C or in the sample bottles at their operating temperature of *ca.* 200°C.

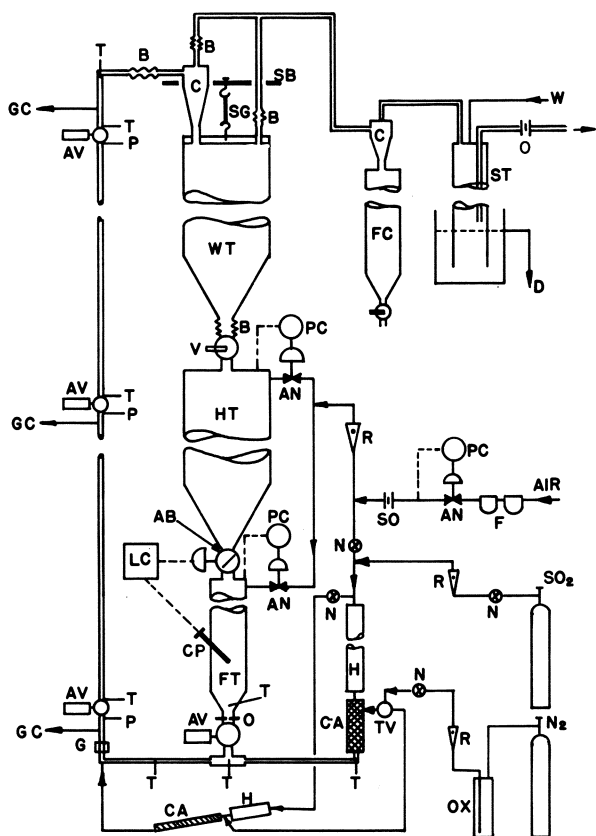


Figure 6. Flowsheet of transported bed apparatus

- AB air-operated butterfly valve
- AN air-operated needle valve
- AV air-operated ball valve
- B stainless steel bellows
- C cyclone
- CA carburetor
- CP capacitance probe
- D water overflow
- F filter
- FC catalyst fines
- FT feed tank
- G sight glass
- GC filtered sample to gas chromatograph
- H preheater
- HT catalyst hold tank
- LC on-off level controller
- N manually-operated needle valve
- O orifice
- OX xylene feed tank
- P pressure tap
- PC proportional pressure controller
- R Rotameter
- SB support beam
- SG strain gage weighing device
- SO sonic orifice
- ST scrubbing tower
- T thermocouple
- TV three-way valve
- V manually-operated ball valve
- WT high pressure water weighing tank

Table II. Experimental Conditions for the Transported Bed Reactor

Temperature	233°–342 °C
Solids flow rate	35 lb/min.
Air flow rate	2.0–3.5 SCFM
<i>o</i> -Xylene concentration	1–3 mole %
W/F_{a_0}	63–350 grams hr/gram mole

The problem of interpreting results from a chemical reactor resolves itself into two separate problems. First, the fluid mechanical behavior of the reactants and catalyst must be established and (perhaps) described mathematically. Second, some understanding of the chemical behavior and description of the chemical kinetics should be obtained. The packed bed study provided the chemical understanding and some indication of the modeling to describe the kinetics. Since there is little information on solids–gas flow, particularly at high solids loading, it was important to have experimental information relating to their fluid mechanical behavior under reactor conditions (*see below*).

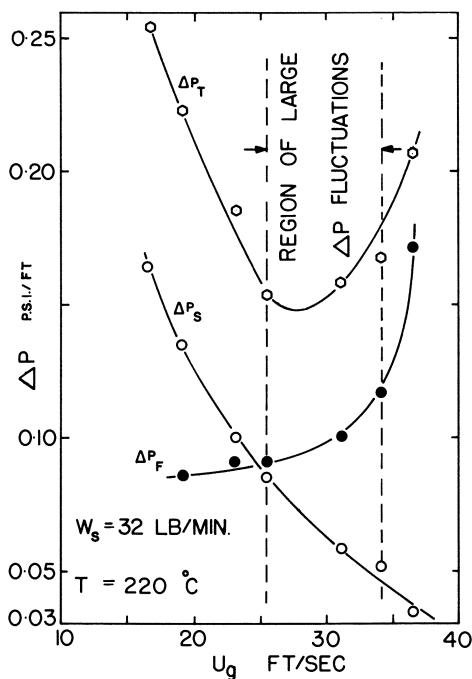


Figure 7. Pressure drop per unit length of reactor as a function of gas velocity at constant solids flow rate. V_s , superficial gas velocity. ΔP_T , total pressure drop. ΔP_S , pressure drop caused by solids. ΔP_F , frictional loss.

Solid–Gas Flow Experiments. Zenz and Othmer (21) suggest that the flow characteristics of a gas–solids conveying system can be interpreted from pressure drop observations as a function of solids and gas flow rate. We obtained this information at reaction temperatures, and a typical plot is shown in Figure 7 for the upper section of the reactor. Here, the solids flow rate was

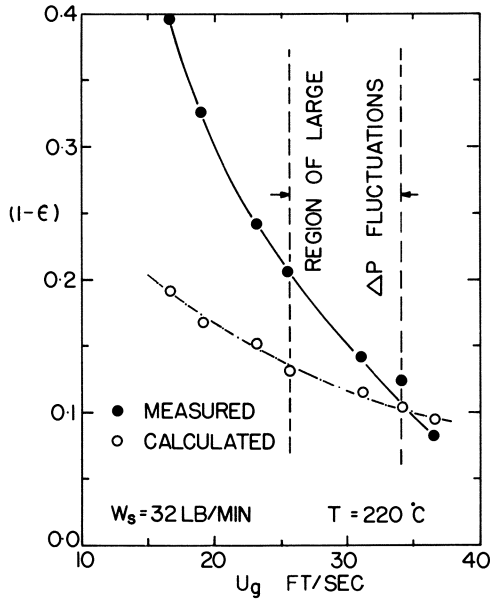


Figure 8. Solids loading as a function of superficial gas velocity at constant solids flow rate

held constant by judicious choice of air pressure in the feed tank, and the gas flow was varied. Since the solids hold-up in the 10-ft section of tubing was measured directly, the static pressure caused by the solids-gas mixture could be evaluated. The frictional pressure drop was obtained by difference. The pressure drop behavior in Figure 7 is similar to that reported by Zenz and Othmer (21), but the pressure drop fluctuations recorded over the range of gas flows are not. At gas flow rates below that where the minimum pressure drop is recorded, the system is expected to be in choked flow and exhibit characteristic large pressure fluctuations. These were observed in the region shown on Figure 7—*i.e.*, near the minimum pressure drop; however, at lower gas flow rates, these fluctuations became small, even less than those at the high gas flow rates, and the system was remarkably stable.

Figure 8 shows the fraction of solids in the tube corresponding to the experiments indicated in Figure 7. Those calculated voidages corresponding to homogeneous two-phase flow are also shown for comparison. The region of large pressure fluctuations is indicated. If we assume that the pressure fluctuations indicate slug flow, then for $W_s = 32$ lb/min and below a superficial gas velocity of about 28 ft/sec, the solid-gas suspension flows as a homogeneous mass similar to particulate fluidization but with a solids velocity much less than that of the gas. This flow phenomenon is difficult to explain; if the particles are freely suspended and in particulate flow, the drag coefficient on each particle would have to be reduced by orders of magnitude to achieve such high particle-gas slip velocities. At the same time, the voidages are so high that particles must be freely suspended and not moving through the bed (as a moving fixed bed) as might be expected if the exit line were restricting the flow of particles but not the gas. If, however, the particles formed concentrated clouds or agglomerates which can break and reform in the reactor *via* the wake

mechanism (21), then larger slip velocities are possible since this agglomerate has a terminal velocity determined by its diameter and apparent solids density. Another explanation might be the formation of an annular flow regime in which a slow moving concentrated particle mass flowed as an outer ring around a central core of gas-solid suspension in dilute phase transport. To our knowledge this is the first reporting of this solids-gas flow behavior with such high solids-to-gas loadings.

Operation of the transported bed reactor was restricted to the high solids fraction region below the onset of large pressure fluctuations. For lack of better information, we assumed that the gas and solids are in intimate contact throughout the reactor length; thus, by-passing of gas by bubble formation was assumed negligible. This is a weakness in our analysis, and the solid-gas fluid mechanics is now under study. Catalyst losses from attrition under these conditions were not excessive. Some fine material was lost initially from the catalyst as supplied. Likewise, erosion of the reactor tube did not occur.

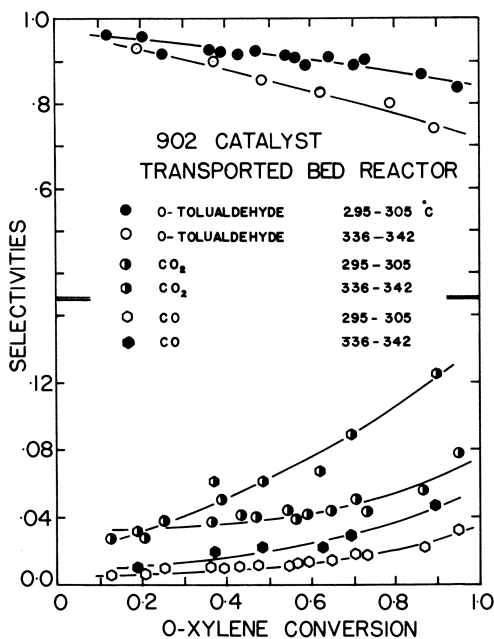


Figure 9. Selectivity data from transported bed reactor

Chemical Reaction. Figure 9 shows selectivities at *ca.* 300° and 340°C. Selectivity to the main partial oxidation product *o*-tolualdehyde is very high. Industrial reactors rarely exceed 70%. The low yields of phthalic anhydride are caused by the catalyst used. Wainwright and Hoffman (15) found that silica gel-supported catalysts have poor selectivity for phthalic anhydride production. This accounts for the lack of success in oxidizing *o*-xylene in fluidized beds. A silica-supported catalyst was used since no catalyst with the desired selectivity and fluidization characteristics is available in quantities sufficient for a pilot-plant study. Figure 9 also shows that the amounts of over-oxidation products—carbon dioxide and carbon monoxide—are doubled

by a 40°C temperature change. Therefore, the reactions should be done at low temperature for high yields of partial oxidation products. Selectivities for other reaction products—phthalic anhydride, phthalide, maleic anhydride, and *o*-toluic acid—are not included in Figure 9 since these were present in small amounts.

Analysis of Results. Because of the gas analysis and solids hold-up measurements, the reactor was analyzed in two sections. Gas analysis at the first sample port gave the feed composition for the lower section. The composition of the feed for the upper section was that obtained from mid-reactor samples. The data were analyzed as if they came from two separate reactors. Since no significant difference could be detected between the performance of these two reactors, the results are presented for the overall reactor.

The data were analyzed according to a simple parallel model in which *o*-xylene reacts to *o*-tolualdehyde and carbon oxides. This is reasonable since few other products were detected, consistent with the packed bed study with this catalyst.

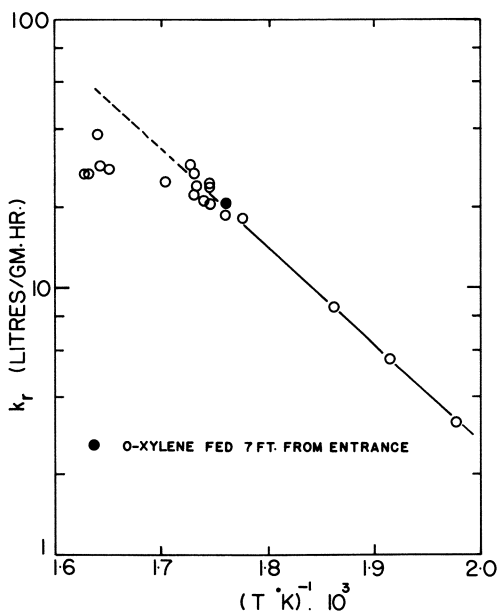


Figure 10. Arrhenius plot for k_r values obtained in transported bed reactor

The disappearance of *o*-xylene was modeled by a first-order reaction:

$$r_r = k_r C_H \quad (6)$$

that is, assuming $\theta = 1$ in all cases. Values of k_r are plotted vs. $1/T$ in Figure 10. An Arrhenius-type temperature dependence is obeyed below 300°C, with an activation energy of 16,700 cal/gram mole. Higher reaction temperatures produce only small increases in reaction rate (activation energies at least a third of that at lower temperatures), except for one experiment where the solids loading in the reactor was quite high. The following analysis attempts

to explain these observations and to indicate the various effects which must be considered in transported bed reactors.

MASS TRANSFER LIMITED REACTION. The mass transfer rate may be limiting the reaction rate at the higher temperatures. The calculated mass transfer rate is at least two orders of magnitude larger than the reaction rate; moreover, the measured conversions are almost the same for some of the lower temperature runs as those at the high temperature, thus indicating almost the same rate of reaction.

LOSS OF CATALYTIC ACTIVITY AT THE HIGHER TEMPERATURES. Perhaps catalyst activity is reduced at higher temperatures. The long term activity did not change since the experiments *ca.* 300°C ($1/T = 1.75 \times 10^{-3}$) were done after each experiment at other conditions to monitor catalyst activity. No significant or systematic variation is observed. Short-term activity relates to the assumption that $\theta = 1$. If the oxygen consumed per gram of catalyst was greater at higher temperatures than at lower ones, a decrease in activity might be suggested. Again there is no correlation of the deviation with this ratio.

Further, the reaction rate constants are essentially the same for both reactor sections. It might be argued that less of the catalyst contacts the reaction gases in the lower section because of the reactor length required to disperse the *o*-xylene over the entire reactor cross-section. It seems improbable that this effect would produce the same result for all the experiments considering the range of operating variables.

The extremely high reaction rates in the transported and packed bed reactors at short on-stream times suggest possible different types of active oxygen—*i.e.*, oxygen in the surface layers of the catalyst lattice and oxygen which is chemisorbed to the catalyst surface. Kakinoki *et al.* (11) have shown, by experiments in a BET apparatus at 400°C, that 2 cc of oxygen can be adsorbed on 1 gram of a similar catalyst. Even more oxygen is expected to be adsorbed at lower temperatures. The regeneration stage in the transported bed reactor not only reoxidizes the catalyst but replenishes the chemisorbed oxygen. The amount of chemisorbed oxygen will be reduced at the higher temperatures, and this could explain the reduced activity. This mechanism, however, should produce a gradual change of activity with temperature unless there are different types of chemisorbed oxygen above and below 300°C. Such differences have been detected in other catalyst systems.

ADSORPTION OF HYDROCARBON ON THE CATALYST. The model assumes that the rate of adsorption is instantaneous—*i.e.*, it reaches its equilibrium concentration on the catalyst surface within a short reactor length and hence does not influence the reaction rate. It is also assumed that the amount of reactant adsorbed is small relative to that in the gas phase. If this were an important effect, performance would correlate strongly with solids hold-up; this was not observed. Also, adsorption is assumed to be non-selective—*i.e.*, the ratio of concentrations of adsorbed species is the same as in the gas phase.

These adsorption effects could be important in transported bed reactors since they differ in this respect from normal reactors which contain a fixed catalyst charge which has time to equilibrate with the surrounding gas. However, this adsorption phenomena cannot explain the observed variation with temperature.

SOLIDS-GAS CONTACTING. Here the gas and solids are assumed to be intimately mixed. The fluid mechanical behavior is assumed to be the same under all operating conditions. On the other hand, as the reaction temperature

is increased, for the same mass flow rate of gases, the velocity must increase. Most of the runs at the higher temperatures were at about the same mass flow rates as those at the lower temperatures. If this increased gas velocity caused a change in flow behavior of the solids-gas mixture at just above 300°C, and this in turn caused part of the gas to bypass the catalyst, an apparent loss in reaction rate would be observed. Since operation is so close to the apparent slugging regime, this seems to be a logical explanation for the lower reaction rates. The one point which is much higher is at a much higher solids loading and lower gas velocity, and the flow regime under these conditions may be similar to that at the lower temperatures, thus somewhat substantiating this hypothesis. Thus, only when the flow regimes are properly mapped for this reactor, can reactor performance be analyzed adequately.

Overall Results. The transported bed is one way to obtain extremely high reaction rates for oxidations involving the catalytic mechanisms associated with *o*-xylene oxidation. Figure 5 shows that the reaction rates observed in this system are much higher than those observed by others for similar catalysts in fixed beds; they are even higher than those in the packed bed after it was on-stream for only 10 sec. These high rates can be exploited by doing hydrocarbon oxidations at temperatures lower than normally used. In this way, higher selectivities to partial oxidation products can be achieved. The industrial potential becomes an economic tradeoff between the savings in feedstocks and the additional costs of more complex equipment and possible catalyst losses.

The unsteady-state performance of another industrial catalyst used to produce phthalic anhydride from *o*-xylene is shown in Figure 4. Initial rates are only several times greater than steady-state rates. However, even this increase could result in the same yield as from a fixed bed at a 40°C lower reaction temperature, thereby improving selectivity to phthalic anhydride. A comparison between the two catalyst types is not necessary. Both show considerably increased activity in a highly oxidized state.

Conclusions

The advantages of conducting *o*-xylene oxidation on a highly oxidized vanadia catalyst have been described, particularly with respect to reaction rates and selectivities. The dense-phase conveying of a commercial fluidization catalyst is extremely stable where slugging would be expected. The oxidation of *o*-xylene in a transported bed is well described by assuming it to be first order with respect to *o*-xylene concentration and a fully oxidized catalyst ($\theta = 1$). This provides additional support for the redox and SSAM models.

Acknowledgments

This research program has been supported by grants from the National Research Council of Canada. Cyanamid of Canada provided catalyst for the initial studies, and W. R. Grace supplied catalyst samples. C. M. Crowe provided many useful suggestions in the early stages of the program.

Nomenclature

C_H, C_{O_2} concentration of hydrocarbon and oxygen, respectively,
gram-moles/liter

F_{A_0}	feed rate of <i>o</i> -xylene, gram-moles/hr
k_r	reaction rate constant for the hydrocarbon reaction, liters/(gram catalyst) (hr)
k_a	reaction rate constant for catalyst oxidation reaction, liters/(gram catalyst) (hr)
n	stoichiometric coefficient, gram-moles of oxygen consumed/gram-mole of hydrocarbon reacted
$\Delta P_T, \Delta P_S, \Delta P_F$	total pressure drop, hydrostatic pressure of solids, frictional pressure drop per ft of reactor, respectively, psi/ft
r_r	rate of reaction of hydrocarbon reactant, gram-moles/(gram catalyst) (hr)
r_a	rate of oxidation of catalyst, gram moles/(gram catalyst) (hr)
S_i	selectivity of component <i>i</i> , gram moles of component <i>i</i> produced per gram moles of <i>o</i> -xylene reacted
T	temperature, °K.
U_g	superficial velocity of gas, ft/sec
W	mass of catalyst in the reactor, gram
W_s	mass of catalyst fed to the reactor, lb/min

Greek Letters

θ	fraction of catalyst surface sites in fully oxidized state
ϵ	void fraction in the reactor

Literature Cited

1. Weekman, V. W., Jr., *Ind. Eng. Chem., Process Design Develop.* (1968) **7**, 90.
2. Echigoya, E., Yen, S., Morikawa, K., *Kagaku Kogaku* (1969) **32**, 1002-7.
3. de Losa, H., Gau, G., *Chem. Eng. Sci.* (1973) **28**, 1875-84.
4. Novella, E. C., Benllock, A. E., *An. Real Soc. Espan. Fis. Quim. Ser.* (1962) **783-802**.
5. Herten, J., Froment, G. F., *Ind. Eng. Chem., Process Design Develop.* (1968) **7**, 516-26.
6. Juusola, J. A., Ph.D. Thesis, Queen's University, Kingston, Canada (1971).
7. Mann, R. F., Ph.D. Thesis, Queen's University, Kingston, Canada (1966).
8. Simard, G. L., Steger, J. F., Arnott, R. J., Siegel, L. A., *Ind. Eng. Chem.* (1955) **47**, 1424-30.
9. Ushakova, V. P., Korneichuk, G. P., Zhigailo, Ya. V., *Ukrain, Khim. Zh.* (1957) **23**, 191.
10. Kakinoki, H., Sahara, N., Kamata, I., Aigami, Y., *Shokubar.* (1962) **4**, 113.
11. Kakinoki, H., Mizushina, F., Tanaka, T., Aigami, Y., Suzuki, H., *Sekiyu, Gakkai, Shi.* (1964) **7** (3), 164.
12. Mizushina, F., Tanaka, T., Aigami, Y., Kakinoki, H., Suzuki, H., *Sekiyu, Gakkai, Shi.* (1964) **7** (11), 30.
13. Suzuki, H., Kakinoki, H., Mizushina, F., Kamata, I., *Sekiyu, Gakkai, Shi.* (1964) **7** (1), 15.
14. Mars, P., Van Krevelen, D. W., *Chem. Eng. Sci. (Spec. Suppl.)* (1954) **3**, 41-59.
15. Wainwright, M. S., Hoffman, T. W., unpublished data.
16. Shelstad, K. A., Downie, J., Graydon, W. F., *Can. J. Chem. Eng.* (1960) **38**, 102.
17. Froment, G. F., personal communication (1971).
18. Wainwright, M. S., Hoffman, T. W., unpublished data.
19. Wainwright, M. S., Ph.D. Thesis, McMaster University, Hamilton, Canada (1974).
20. Hughes, M. F., Adams, R. T., *J. Phys. Chem.* (1960) **64**, 781-784.
21. Zenz, F. A., Othmer, D. F., "Fluidization and Fluid-Particle Systems," Reinhold, New York, 1960.

RECEIVED January 2, 1974.

INDEX

- A**
- Absorption, oxygen 439
- Acceptor, oxidation of 572
- Acetic acid manufacture 561, 565
- acetylene as a feedstock for . . . 561
- mathematical models for 561
- Acetone from ethanol 410
- Acetylene as a feedstock for acetic acid manufacture 561
- Activation energy for xylene disappearance 648
- Activity 398
- catalyst 399, 683
- coefficient 312
- of As 472
- of caprolactam in a nylon 6 melt 314
- of water on a nylon 6 melt . . . 314
- of a solid surface 655
- Adiabatic catalytic systems, multiple steady states in 545
- exothermic fixed bed reactor . . 598
- fixed-bed methanator 489
- mathematical model for 490
- packed bed chemical reactors . . 488
- trajectory 525
- tubular reactor 546
- Adsorbency of the solids for the gas Adsorption 200, 297
- of carbon monoxide on platinum coefficient 296
- equilibrium 191
- of hydrocarbons on catalyst . . . 683
- isotherms 185
- Langmuir type 210
- from liquids 183
- transfer 291
- of water 583
- Algorithm, Crank-Nicholson 489
- Algorithm, Gauss-Newton 403
- Algorithms, simulation 380
- Alkaline hydrolysis of glycol diacetate 352
- Alkenylbenzenes 137
- Alkyl carbonium ion 423
- Alumina
- copper on 619
- copper on silica- 619
- copper oxide on 571
- dehydrogenation of 1-propanol of NaOH-doped γ - 410
- hydrated 619
- hydrogenation of α -methylstyrene on palladium- 165
- nickel on 494
- particles 26
- pellets 507
- silica- 619
- reaction with MnO_x on γ - 571
- Aluminum 650
- Alundun, NaOH-doped 410
- Ammonia oxidation 268, 600
- Ampoule 463
- Analog closed-loop control 19
- Analysis of chemical reaction networks 410
- Analysis, molecular distribution . . 128
- Angle of contact 463
- Antimony 562
- Argon, diffusion of 210
- Aromatics
- in coke formation 423
- polynuclear 429
- Arrhenius type relationship 91
- Arsenic
- activity coefficient of 472
- deposition of 468
- dopant 464
- doped silicon epitaxial layers . . 466
- Arsine 466
- Asbestos 658
- AsH₃ 469
- Atomic oxygen 395
- Autocatalytic rate expression for platinum catalyst 640
- Automobile catalytic exhaust converters 34
- Automobile exhausts, oxidation of carbon monoxide in 629
- Average pores 287
- Axial
- backmixing profiles 292
- conduction 39, 641
- in the converter wall 636
- diffusion 264
- dispersed reactors 334
- dispersion 212, 264, 596
- model, trickle-bed 223
- heat conduction 483
- profile 455
- temperature profile 175, 497
- B**
- Backmixing model, countercurrent . 291
- Backmixing profiles, axial 292

- Backmixing, rate of 298
- Barrel reactor 468
- epitaxial deposition of silicon in 463
- Batch kinetics 379
- Bayer process, two-stage 561
- Bed
- burner, fluidized- 30, 32
- burning of graphite, fluidized- .. 25
- capillary rise in a packed 160
- chemical reactors, adiabatic
- packed 588
- countercurrent moving 191
- data, fixed- 592
- fluid flow model for packed-
- fluidized 271
- gas mixing in fluidized 290
- gas velocities in the fluidized .. 30
- height 276
- liquid holdup in packed 153
- methanator, adiabatic fixed- ... 489
- packed 629
- fluidized 274
- studies of 672
- three steady states in 551
- prewetted 153, 159
- reactor
- adiabatic exothermic fixed .. 598
- catalytic fixed 505
- catalytic trickle 164
- differential 82
- fixed 669
- heterogeneous 519
- mechanisms of the trickle ... 177
- performance, trickle 152
- schematic of the packed ... 591
- transported 679, 681
- of small particles 159
- studies, integral 90
- temperature profiles 453
- transported 669, 676
- wetting of 173
- Benzene 658
- formation 437
- Benzoic acid evaporation 441
- Benzoic acid oxidation step,
- model of 432
- Benzoic acid, phenol from 434
- BET surface areas 98
- Bifunctional catalyst pellets 324
- Bifunctional catalysts, porous 316
- "Blow out" 519
- Boehmite carrier 511
- Boundary conditions, Werner-
- Wilhelm 343
- Bubble
- behavior in polyisobutene 307
- behavior during rising 307
- columns, liquid phase in 231
- velocity and direction of 236
- formation 306
- frequency 296
- phase 275, 293, 305
- size of the gas 279
- volume 291
- Bubbling 303
- Butane 561
- Butene 91, 561, 567
- oxidation of 567
- oxygen-inert gases 562
- Butenes, high purity 80
- C**
- Capillary rise in a packed bed 160
- Caprolactam 311
- in a nylon 6 melt 314
- Carbon monoxide 547
- oxidation of 654
- in automobile exhausts 629
- on platinum, adsorption of 630
- Carbonium ion 423
- Catalyst(s)
- activity 683
- adsorption of hydrocarbons on .. 683
- autocatalytic rate expression for
- platinum 640
- basket reactor, isothermal
- spinning 646
- chromic oxide 410
- on coke 427
- compounded 324
- containing vanadium, solid 561
- decay 425
- effectiveness factors in supported
- liquid phase 250
- honeycomb-structure 551
- hydrogenation of α -methylsty-
- rene on palladium-alumina 165
- mass transport in supported
- liquid phase 250
- new oxidation 654
- nickel or alumina 494
- oxidation of ethylene over silver
- particles under trickle flow,
- wetting of 151
- pellet(s)
- isothermal 523
- reactor containing bifunctional
- temperature 520
- transport and reaction in
- bifunctional 317
- platinum 600
- porous bifunctional 316
- potential 656
- properties 99, 673
- requirement 604
- rhenium 96
- screens, platinum and silver .. 261
- support, monolithic 34
- supported liquid phase 242
- tungsten oxide-silica 80
- uranium dioxide 67
- utilization 218
- vanadia-on-silica 669
- vanadium 646
- pentoxide 362
- V₂O₅ 646
- o-xylene oxidation on vanadia .. 670

- Catalytic activity 399
 conversion of sulfur dioxide in wet stack gases 612
 converters 629
 cracking, coke and deactivation in exhaust converters, automobile .. 34
 fixed bed reactor 505
 packed bed reactor 449
 reaction, exothermic 449
 reactor, moving bed 191
 reactor, optimization of a non-isothermal, non-adiabatic fixed-bed 362
 reactors, heat and mass transfer in packed 555
 systems, multiple steady states in trickle bed reactor 164
 Chain reaction with chemical induction 137
 Characteristics, method of 122
 Chemical induction, chain reaction with 137
 Chemical reaction networks, analysis of 410
 Chemical reactors, non-stationary behavior of 489
 Chemisorption, hydrogen 99
 Chemisorption on silver, oxygen .. 399
 Chloropropanone and thiourea, conversion of 340
 Chromic oxide catalyst 410
 Chromium 656
 Chromatography, gas 205
 Chromatographic reactor 181
 optimum design studies for ... 189
 Chromatographic separation 191
 Claus-type sulfur recovery plants .. 612
 Clay, pre-fired 295
 Cloud-wake phase 294
 Cloud-wake volume 291
 Coalescence 309
 model, random 379
 Coefficients, activity 312
 Coefficients, mass transfer 262, 264
 CO 553, 613
 hydrogenation of 500
 oxidation of 553, 663
 CO₂, hydrogenation of 496
 Coke
 on catalyst 427
 deactivation in catalytic cracking 422
 definition of 422, 424
 formation, aromatics in 423
 Columns, liquid phase in bubble .. 231
 velocity and direction of 236
 Composite pellets 317
 Composition profiles 328
 Compounded catalyst 324
 Computer studies 618
 Concentration 353
 gradients, temperature and ... 449
 inlet 522, 547
 Concentration (*Continued*)
 profiles, steady-state 456
 temperature profiles 48
 Conduction
 axial 39, 641
 in the converter wall 636
 heat 483
 Conductivity model for one-stirred tank with recycle 534
 Conductivity model for a stirred tank in series with recycle ... 536
 Conjugate dehydrogenation of diethylbenzene 143
 Conjugate dehydrogenation of hydrocarbons 137
 Conjugate dehydrogenation of isopropylbenzene 142
 Conservation of population, principle of 123
 Contact, angle of 463
 Contaminated water 656
 Continuous steady states 193
 Continuous stirred gas-solid reactor 67
 Continuous stirred tank reactor .. 13
 micromixing in 348
 Control
 analog closed-loop 19
 direct digital 22
 reactor 527
 teaching reactor design and ... 13
 Conversion 188, 398
 of chloropropanone and thiourea 340
 isothermal 410
 isothermal steady-state 412
 model based on effective wetting 220
 model based on holdup 218
 reactant 271
 of sulfur dioxide in wet stack gases, catalytic 612
 Converters, catalytic 629
 Converter wall, axial conduction in 636
 Coolant 525
 Cooling, recycle process without .. 567
 Copper
 on alumina 619
 oxide on alumina 571
 on silica-alumina 619
 -substituted zirconium phosphate 654
 Countercurrent backmixing model 291
 Countercurrent moving bed 191
 Cracking, coke and deactivation in 422
 Cracking of methylcyclohexane and *n*-hexadecane 428
 Cracking, thermal 424
 Crank-Nicholson algorithm 489
 Crank-Nicholson method 365
 Critical flow rate 397
 Critical length of the reactor 527
 Crushed fuel 28
 Crushing studies on fuel spheres .. 29
 Crystal, zeolite 656

Crystallite size determinations . . .	103	Diffusivity (<i>Continued</i>)	
Cryosorption	48	of lactam	313
CSGSR experiments, combined		of water	313
plug flow and	68	Direct digital control	22
CSTR dynamics	14	Direction of liquid phase in bubble	
CSTR, "experimental simulation"		columns	236
of a	14	Discrete pellet mixtures	321
Cupric benzoate	436	Dispersed flow reactors	334
Cupric ion exchange reaction . . .	656	Dispersed reactors, axial	334
Cyclohexane oxidation reactor,		Dispersion	
designing a	644	axial	212, 264, 596
		effects	224
D		model, trickle-bed axial	223
Damkohler number	378	transversal and longitudinal . . .	396
Deactivation	109	Disproportionation of propylene,	
in catalytic cracking	422	kinetics of	80
reactors with immobilized en-		Dissipation per unit mass, kinetic	
zymes subject to	106	energy	357
Deadend pores	283	Distributed feed reactors	376
Decay, catalyst	425	multistage	389
Decomposition of hydrogen		Distribution	
peroxide	260	of liquids in supports	243
Definition of coke	422, 424	molecular	122
Dehydrogenation		reactors with feed	383
of diethylbenzene, conjugate . . .	143	residence time	443
of ethylbenzene to styrene	67	with series-parallel reactions,	
of hydrocarbons, conjugate	137	product	376
of isopropylbenzene, conjugate . .	142	Dual-site mechanism	87, 395, 402
kinetics, ethylbenzene	67	Dynamic response surfaces	122
of 1-propanol on NaOH-doped			
γ -alumina	410	E	
Dense phase	294	Effective diffusivities	283
Density, effects	346	for inert systems	281
Density population	346	for reactive system	281
Deposition of arsenic	468	Effectiveness factor	635
Deposition of silicon in a barrel		in supported liquid phase	
reactor, epitaxial	463	catalysts	250
Design and control, teaching reactor	13	Effective wetting	218
Design studies for chromatographic		conversion model based on	220
reactors, optimum	189	Eigenvalues	634
Designing a cyclohexane oxidation		Emission breakthrough	637
reactor	644	Emulsion phase	275
Desorption	200	Energy dissipation per unit mass,	
Desulfurization	571	kinetic	357
Devillon, model of Villerman and . .	380	Energy equations of the two-phase	
Diethylbenzene, conjugate dehy-		model	589
drogenation of	143	Enzymes subject to deactivation,	
Diffusion	212	reactors with immobilized . . .	106
Differential bed reactor	82	Epitaxial deposition of silicon in a	
Diffusion	212	barrel reactor	463
of argon	210	Equilibrium, adsorption	191
axial	264	Equilibrium gas compositions . . .	613
experiments, unsteady state	281	Equivalence between homogeneous	
in the fluid phase	203	and heterogeneous models . . .	588
interphase	84	Ethanol, acetone from	410
intraparticle	581	Ethylbenzene dehydrogenation	
mixing by molecular	356	kinetics	67
pore	84	Ethylene	80, 91, 561
structure and	281	over silver catalysts, oxidation of	395
in zeolites	205	Euler method	632
Diffusivity	312	Exit gas temperature	607
effective	283	Exothermic fixed bed reactor,	
for inert systems	281	adiabatic	598
for reactive system	281		

- Exothermic reactions 449, 477, 522
 "Experimental simulation" of a
 CSTR 14
- F**
- Feed distribution, reactors with . . 383
 Feed reactors, distributed 376
 multistage 389
 Feedstock for acetic acid manufac-
 ture, acetylene as a 561
 Fixed bed
 catalytic reactor, optimization of
 a non-isothermal, non-adia-
 batic 362
 data 592
 methanator, adiabatic 489
 process 571
 reactor 423, 578, 669
 adiabatic exothermic 598
 catalytic 505
 parametric sensitivity and tem-
 perature runaway in het-
 erogeneous 519
 temperature profiles in the . . 648
 Flow
 experiments, solid-gas 679
 model for packed-fluidized bed,
 fluid 271
 rate, critical 397
 reactors, dispersed 334
 type integral reactor 396
 Fluid flow model for packed-
 fluidized bed 271
 Fluid flow pattern 279
 Fluidized-bed
 burner 30
 burning of graphite 25
 fluid flow model for packed-
 gas velocities in the 30
 gas mixing in 290
 packed- 274
 reactor 363
 Fluidizing velocity 297
 Fluid phase, diffusion in the 203
 Formation
 benzene 437
 rates of styrene 141
 of tar 437
 Free energy minimization method . 613
 Free radical polymerizations 130
 Freon-12 295
 Fuel reprocessing, reactor 25
 Fuel spheres, crushing studies on . . 29
 Function, objective 366
- G**
- Gas
 adsorbency of the solids for the
 chromatography 205
 compositions, equilibrium 613
 exchange rate 291
 flow experiments, solid- 679
 holdup 442
- Gas (*Continued*)
 interchange coefficient 271
 -liquid contacting reactor 303
 mass velocity of 608
 mixing in fluidized beds 290
 -phase nucleation of Si 470
 -phase oxidation 561
 -phase reaction 481
 -solid catalyzed reactions 3
 -solid reactor, continuous stirred
 temperature, exit 607
 velocities in the fluidized bed . . 30
 velocity, inlet 548
- Gases
 butene-oxygen-inert 562
 removal of SO₂ from waste 571
- Gauss-Legendre quadrature
 formula 208
 Gauss-Newton algorithm 403
 Generalized recycle reactor model . 532
 Glycol diacetate, alkaline hydroly-
 sis of 352
 Gradients, radial 39
 Gradients, temperature and
 concentration 449
 Graphite
 fluidized-bed burning of 25
- H**
- Heat
 conduction, axial 483
 and mass transfer 18, 632
 in packed catalytic reactors . . . 555
 transfer 268
 transport 221, 505, 510
 Height, bed 276
 Helium 295
 4-Heptanol 411
 Heterogeneous fixed bed reactors . . 519
 Heterogeneous models 43, 588
 equivalence between homoge-
 neous and 588
 homogeneous- 578
 N-Hexadecane, cracking of methyl-
 cyclohexane and 428
 Highly exothermic reaction 477
 High purity butenes 80
 High-temperature gas-cooled
 reactors (HGTR'S) 25
 High thermal conductivity model
 for one stirred tank with re-
 cycle 534
 High thermal conductivity model
 for stirred tanks in series with
 recycle 536
 Holdup, conversion model based on . 218
 Holdup, gas 442
 Holdup, liquid 218
 Homogeneous model 42, 588
 equivalence between hetero-
 geneous and 588
 heterogeneous- 578
 Homogeneous tubular reactors . . . 477

Honeycomb-structure catalyst	551		
Hot spot	373		
H ₂ S	585		
Hydrated alumina	619		
Hydrocarbon pyrolysis	561		
Hydrocarbons, conjugate dehydrogenation of	137		
Hydrogen	454, 466, 619		
chemisorption	99, 102		
peroxide, decomposition of	260		
peroxide as an oxidant	137		
reaction between oxygen and	506		
transfer	423, 429		
Hydrogenation	423		
of CO	500		
of CO ₂	496		
of α -methylstyrene on palladium-alumina catalyst	165		
of α -methylstyrene in vapor phase	176		
Hydrolysis of glycol diacetate, alkaline	352		
Hydrolysis of methyl formate	181		
Hydrolysis of phenyl benzoate	436		
Hydroprocessing	218		
Hysteresis	595		
			I
Ideal states of mixing	377		
Ignition profiles	593		
Imbedding, method of invariant	537		
Index, micromixing	350		
Induction, chain reaction with chemical	137		
Inert systems, effective diffusivity for	281		
Influence of reactor wall	477		
Inhibition	109		
Inlet concentration	522, 547		
Inlet gas velocity	548		
Inlet temperature	525, 547		
Instability	519		
Integral bed studies	90		
Interparticle transport effects	318		
Interphase diffusion	84		
Interphase and intraparticle temperature rises	456		
Interphase transport	556		
Intraparticle diffusion	581		
Intraparticle temperature measurement	449, 455		
Invariant imbedding, method of	537		
Ion, alkyl carbonium	423		
Isopropyl alcohol	410		
Isopropylbenzene, conjugate dehydrogenation of	142		
Isothermal catalyst pellet	523		
Isothermal conversion	410		
steady-state	412		
Isothermal spinning catalyst-basket reactor	646		
Isotherms, adsorption	185		
			J
Jets, subsonic	60		
Jets, supersonic	62		
free	46		
			K
Kinetic energy dissipation per unit mass	357		
Kinetic model	410		
Kinetics			
batch	379		
of the disproportionation of propylene	80		
ethylbenzene dehydrogenation	67		
of phthalic anhydride	650		
polymerization	124		
			L
Lactam, diffusivity of	313		
Lactam, vapor pressure of	314		
Lagrangian interpolating polynomial	214		
Langmuir-Hinshelwood type mechanism	82		
Langmuir type adsorption	210		
Length, reactor	527, 548		
Limiting non-key component	449		
Liquid			
contacting reactor, gas-	303		
holdup	218		
Newtonian, high viscous	303		
in packed beds	153		
-phase in bubble columns	231		
velocity and direction of	236		
-phase catalysts	242, 250		
-phase reaction	477		
in supports, distribution of	243		
Longitudinal dispersion, transversal and	396		
Lower reaction states, upper and	593		
Low thermal conductivity model	535		
			M
Macro-micro pore model	214		
Macromixing	387		
characteristics of the reactor	7, 9		
Macropores	287		
Manganese oxide	571		
Mass			
kinetic energy dissipation per unit transfer	357, 8, 212, 259, 266, 309, 600, 632, 662		
coefficients	262, 264, 296, 468		
control	261		
in NH ₃ oxidation	601		
transport	513		
in supported liquid-phase catalysts	250		
velocity of gas	608		
Mathematical model	364		
for an acetic acid process	561		
for an adiabatic methanator	490		
of the monolith converter	629		

- Mathematical modeling 303
- Maximum mixedness 352
- Mean film temperature 602
- Mechanism
- dual-site 87
 - Langmuir-Hinshelwood type ... 82
 - oxidation 670
 - Rideal single-site 87
 - of the trickle bed reactor 177
- Mesityl oxide 273
- Methanator, adiabatic fixed-bed .. 489
- mathematical model for 490
- Method of characteristics 122
- Method of invariant imbedding .. 537
- Methylcyclohexane, cracking of .. 428
- Methyl formate, hydrolysis of 181
- α -Methylstyrene on palladium-alu-
mina catalyst, hydrogenation of 165
- α -Methylstyrene in vapor phase,
hydrogenation of 176
- Micromixing 383, 533
- in a continuous stirred tank
reactor 348
 - index 350
 - scale 349
 - to turbulence, relating 356
- Microscale, l 357
- Mixed oxides of vanadium 562
- Mixedness, maximum 352
- Mixing
- effects 348
 - ideal states of 377
 - by molecular diffusion 356
 - and product distribution with
series-parallel reactions ... 376
 - in stirred gas-solid reactors ... 70
- MnO₂ on gamma-alumina, reaction
with 571
- Model
- for an acetic acid process,
mathematical 561
 - for an adiabatic methanator,
mathematical 490
 - based on effective wetting,
conversion 220
 - based on holdup, conversion .. 218
 - of benzoic acid oxidation step .. 432
 - countercurrent backmixing 291
 - energy equation of the two-phase 589
 - equivalence between homo-
geneous and heterogeneous .. 588
 - generalized recycle reactor ... 532
 - heterogeneous 43, 588
 - homogeneous 42, 588
 - homogeneous/heterogeneous
reactor 578
 - kinetic 410
 - low thermal conductivity 535
 - macro-micro pore 214
 - mathematical 364
 - of the monolith converter 629
 - one-dimensional 527
 - one-phase 588
- Model (*Continued*)
- for one stirred tank with recycle,
high thermal conductivity .. 534
 - for a packed bed reactor 449
 - for packed-fluidized bed, fluid
flow 271
 - random coalescence 379
 - reactor 364
 - for reactors subdivided in
sections 335
 - reforming reactions 316
 - for stirred tanks in series with re-
cycle, thermal conductivity 536
 - trickle-bed axial dispersion 223
 - two-phase 588
 - of Villerman and Devillon ... 380
- Molecular diffusion, mixing by ... 356
- Molecular distribution 122
- analysis 128
- Molecular sieves 210
- Molybdenum 656
- Monolith converter, model of ... 629
- Monolithic catalyst support 34
- Monoliths, properties of 36
- Moving bed catalytic reactor 191
- countercurrent 191
- Moving reaction zones 595
- Multiple steady states 484
- in adiabatic catalytic systems .. 545
- Multiple-step reaction systems ... 410
- Multiplicity of steady states ... 532, 636
- Multistage distributed feed reactors 389
- N**
- NaOH-doped γ -alumina, dehydro-
genation of 1-propanol in ... 410
- NaOH-doped Alundum 410
- Naphthalene 373
- oxidation of 362
 - vaporization of 466
- Naphthenes 423
- Neodymium oxide 411
- Networks, analysis of chemical
reaction 410
- New oxidation catalyst 654
- Newtonian high-viscous liquids .. 303
- Newton-Raphson method 511
- NH₃ oxidation, mass transfer in .. 601
- Nickel 666
- on alumina catalyst 494
 - on silica 451
- Nitric acid 606
- plant production run 607
- Nitrogen 619
- cumene system 155
- Non-isothermal, non-adiabatic fixed-
bed catalytic reactor 362
- Nonlinear regression 581
- Non-stationary behavior of
chemical reactors 489
- Normalization of rate data 398
- Nozzle reactor, novel 46
- Nozzle reactors, supersonic 62

Nucleation	469	Palladium-alumina catalyst, hydro-	
of Si, gas-phase	470	genation of α -methylstyrene on	165
Nusselt number	34, 42	Parametric sensitivity	519, 522
Nylon 6 melt	311, 314	Peclet number	508, 516
O			
Objective function	366	Pellet(s)	
1-Octanol	410	alumina	507
One-dimensional model	527	composite	317
One-phase model	588	isothermal catalyst	523
Optimization	366	mixtures, discrete	321
of a non-isothermal, non-adia-		silica-alumina	619
batic fixed-bed catalytic re-		temperature, catalyst	520
actor	362	V ₂ O ₅ cylindrical	363
of the phenol process	432	Phthalic anhydride	362
Optimum design studies for		kinetics of	650
chromatographic reactors	189	oxidation of <i>o</i> -xylene to	646
Optimum productivity and yield ..	371	Phenol	436
Orthogonal collocation	632	from benzoic acid	434
Oxidant, hydrogen peroxide	137	process, optimization of	432
Oxidation		stripping	440
of acceptor	572	Phenyl benzoate, hydrolysis of ..	436
ammonia	268, 600	Pilot plant measurements	303
in automobile exhausts	629	Platinum	507
butene	567	adsorption of carbon monoxide on	630
carbon monoxide	654	catalyst	600
catalyst, new	654	autocatalytic rate expression for	640
CO	553	on porous silica-alumina	316
of ethylene over silver catalysts	395	and silver catalyst screens	261
gas phase	561	Plug flow and CSGSR experiments,	
mass transfer in NH ₃	601	combined	68
mechanism	670	Plug flow reactor	478
model of the benzoic acid	432	Polyisobutene, bubble behavior in	307
of naphthalene	362	Polymerization	429
rate of CO	663	free radical	130
reactions	46	grade ethylene	80
reactor	438	kinetics	124
designing a cyclohexane	644	Polynuclear aromatics	429
SO ₂	242, 251	Polyvinylidene chloride dynamics ..	132
on vanadia catalysts, <i>o</i> -xylene ..	670	Population density	122
of <i>o</i> -xylene	9, 646, 669	Population, principle of conserva-	
Oxidized silver surface	395	tion of	123
Oxygen		Pore(s)	
absorption	439	average	287
atomic	395	deadend	283
chemisorption on silver	399	diffusion	84
and hydrogen, reaction between	506	structure and diffusion	281
-inert gases, butene-	562	Porous bifunctional catalysts	316
sorption of SO ₂	572	Potential catalysts	656
P			
Packed bed(s)	629	Prater relation	451
fluidized	274	Prefired clay	295
reactors, adiabatic	588	Pressure	607
catalytic	449	of the fluidized-bed burner	32
heat and mass transfer in ..	555	vapor	312
fluid flow model for	271	Prewetted beds	153, 159
models for a	449	Product distribution with series-	
schematic of	591	parallel reactions	376
studies	672	Productivity	366
three steady states in	551	optimum	371
		Profile, axial	455
		temperature	497
		backmixing	292
		Profiles	
		concentration and temperature ..	48
		ignition	593

- Profit ratio 107
- 1-Propanol on NaOH-doped γ -alumina, dehydrogenation of ... 410
- 2-Propanol reactions, selectivity in 96
- Properties, catalyst 99, 673
- Properties of monoliths 36
- Propylene 91
- disproportionation kinetics 80
- Pyrolysis, hydrocarbon 561
- Q**
- Quasi-linearization technique 342
- R**
- Radial gradients 39
- Radiant displacement reaction 137
- Random coalescence model 379
- Random Pack 600
- Rate
- of backmixing 298
- of CO oxidation 663
- critical flow 397
- data, normalization 398
- gas exchange 291
- solids exchange 291
- of styrene formation 141
- Reactant conversion 271
- Reaction
- in bifunctional catalyst pellets .. 317
- cupric ion exchange 656
- exothermic 449, 477, 552
- gas phase 481
- gas-solid catalyzed 3
- hydrogen-transfer 423
- liquid phase 477
- mixing and product distribution
- with series-parallel 376
- with MnO_2 on gamma-alumina .. 571
- model reforming 316
- networks, analysis of chemical .. 410
- between oxygen and hydrogen .. 506
- radiant displacement 137
- states, upper and lower 593
- system, effective diffusivity 283
- systems, multiple-step 410
- vapor phase 221
- zones, moving 595
- Reactor(s)
- adiabatic exothermic fixed bed .. 598
- adiabatic packed bed chemical 588
- adiabatic tubular 546
- axial dispersed 334
- barrel 468
- behavior 196
- catalytic 164, 449, 505
- chromatographic 181
- containing bifunctional catalyst pellets 324
- continuous stirred gas-solid 67
- continuous stirred tank 13, 348
- control 527
- critical length of 527
- designing a cyclohexane oxidation 644
- design and control, teaching 13
- differential bed 82
- distributed feed 376, 383
- epitaxial deposition of silicon in
- a barrel 463
- fixed bed 423, 578, 598, 669
- catalytic 505
- temperature profiles in 648
- flow-type integral 396
- fluidized bed 363
- fuel reprocessing 25
- gas-liquid contacting 303
- high-temperature gas-cooled ... 25
- with immobilized enzymes sub-
- ject to deactivation 106
- isothermal spinning catalyst-
- basket 646
- length 527, 548
- macromixing characteristics of .. 7, 9
- mixing in stirred gas-solid 70
- model 364
- generalized recycle 532
- homogeneous/heterogeneous .. 578
- for a packed bed 449
- moving bed catalytic 191
- multistage distributed feed 389
- non-stationary behavior of
- chemical 489
- novel nozzle 46
- optimization of a non-isothermal,
- non-adiabatic fixed-bed catalytic 362
- optimum design studies for
- chromatographic 189
- oxidation 438
- packed bed 591
- heat and mass transfer in ... 555
- parametric sensitivity in heterogeneous fixed bed 519
- plug flow 478
- subdivided in sections, model for supersonic nozzle 62
- transported bed 669, 679, 681
- trickle-bed 152, 177, 218
- catalytic 164
- tubular 334, 477
- trajectories 521
- vibration mixed 3, 5
- wall influence 477, 480
- Recycle without cooling 567
- Recycle, high thermal conductivity model for one stirred tank with 534
- Recycle reactor model 532
- Recycle, thermal conductivity model for stirred tanks in series with 536
- Reduction of SO_2 with CO 613
- Reduction of sulfate 572
- Reductive regeneration 571, 575
- Reforming reactions, model 316
- Regeneration cycles, sorption/ 572

- Regeneration, reductive571, 575
 Removal of SO₂ from waste gases 571
 Residence time distribution 443
 Rhenium catalysts 96
 Rideal single-site mechanism 87
 Rise, velocity of 308
 Rising, bubble behavior during .. 307
 Runaway, temperature 522
 Runge-Kutta integration 498
 Runge-Kutta method111, 275
- S**
- Sapphire wafers 463
 Scaleup 218
 Schematic of the packed bed reactor 591
 Schlieren layer 346
 Screens, stacked259, 265, 600
 characteristics of 607
 platinum and silver catalyst ... 261
 Segregation effects 349
 Selectivity348, 398, 564, 650, 681
 in 2-propanol reactions 96
 studies 100
 Sensitivity, parametric 522
 Shah correlation 606
 Shell FGD process 571
 Shock wave formation 58
 Short space time 424
 Sieves, molecular 210
 Si, gas-phase nucleation of 470
 SiH₄ 469
 Silane 466
 Silica-alumina
 copper on 619
 pellets 619
 platinum on porous 316
 Silica catalyst, tungsten oxide- ... 80
 Silica catalyst, vanadia-on- 669
 Silica, nickel on 451
 Silicon in a barrel reactor, epitaxial
 deposition of 463
 Silicon epitaxial layers, As-doped .. 446
 Silver
 catalysts, oxidation of ethylene
 over 395
 catalyst screens, platinum and .. 261
 oxygen chemisorption 399
 surface, oxidized 395
 Simulation 365
 algorithms 380
 of a CSTR, experimental 14
 Simultaneous chemical equilibria
 method 613
 Single-stirred tank 538
 Size of the gas bubble 279
 SO₂ with CO, reduction of 613
 Solid
 catalysts containing vanadium .. 561
 catalyzed reactions, gas/ 3
 exchange rate 291
 for the gas, adsorbency of the .. 290
 -gas flow experiments 679
 Solid (*Continued*)
 surface, activity of 655
 Solubility, water 441
 SO₂ oxidation242, 251
 SO₂ removal from waste gases ... 571
 SO₂/O₂, sorption of 572
 Sorption
 regeneration cycles 572
 of SO₂/O₂ 572
 steady-state 303
 of volatile components 303
 Space time353, 410
 short 424
 Stability 539
 Stacked screens259, 265, 600
 Stack gases, conversion of sulfur
 dioxide in wet 612
 Stack gases, sulfur removal from .. 571
 Steady state(s)
 in adiabatic catalytic systems,
 multiple 545
 behavior 18
 concentration profiles 456
 continuous 193
 conversion, isothermal 412
 multiple 484
 multiplicity of532, 636
 performance 676
 sorption 303
 Step sizes 366
 Stirred tanks 376
 in series 541
 with recycle, thermal conduc-
 tivity model for a 536
 Stirring 353
 Stop-flow experiments 43
 Studies, packed bed 672
 Studies, transported bed 676
 Styrene, dehydrogenation of
 ethylbenzene to 67
 Subsonic jets 62
 Supersonic jets46, 62
 Supersonic nozzle reactors 62
 Sulfate, reduction of 572
 Sulfur
 dioxide 678
 in wet stack gases, catalytic
 conversion of 612
 recovery plants, Claus-type ... 612
 removal from stack gases 571
 vapor 614
 Surface, activity of a solid 655
 Surface, oxidized silver 395
 Surfaces, dynamic response 122
 Supported liquid-phase catalysts .. 242
 effectiveness factors in 250
 mass transport in 250
 Supports, distribution of liquid in 243
 System constraints 529
 Systems, multiple steady states in
 adiabatic catalytic 545

- T**
- Tank, stirred 376, 534
 Tar, formation of 437
 Teaching reactor design and control 13
 Temperature 353
 behavior, transient 34
 catalyst pellet 520
 and concentration gradients 449
 exit gas 607
 gradients 396
 inlet 525, 547
 mean film 602
 measurement, intraparticle 449, 455
 profile, axial 175, 497
 profiles, bed 453
 profiles, concentration and 48
 profiles in the fixed-bed reactor 648
 profiles, transversal 60
 rises, interphase and intraparticle 456
 runaway criterion 520
 wall 641
 Thermal conductivity model for one stirred tank with recycle, high 534
 Thermal conductivity model for stirred tanks in series with recycle, high 536
 Thermal cracking 424
 Thermal load factor 527
 Thiourea, conversion of chloropropanone and 340
 Time, space 410, 424
 Tin 562
 Titanium 562, 650
o-Tolualdehyde 682
 Toluene 432
 Transfer
 adsorptive 291
 heat 268
 mass 259, 266, 309
 coefficients 262, 264
 control 261
 Transient calculations 638
 Transient temperature behavior 34
 Transport
 interparticle 318
 interphase 556
 processes, heat 505
 and reaction in bifunctional catalyst pellets 317
 in supported liquid phase catalysts, mass 250
 Transported bed reactor 669, 679, 681
 Transported bed studies 676
 Transversal and longitudinal dispersion 396
 Transversal temperature profiles 60
 Trickle bed axial dispersion model 223
 Trickle bed reactor 152, 177, 218
 Trickle flow, wetting of catalyst particles under 151
 Tubular reactor
 adiabatic 546
 with exothermic reaction 477
- Tubular reactor (Continued)**
- flow 335
 homogeneous 477
 Tungsten oxide-silica catalyst 80
 Turbulence, relating micromixing to 356
 Two-micromixing zones reactor 358
 Two-phase model 588
 energy equation of 589
 Two-stage Bayer process 561
- U**
- Ultrasounds 353
 Unsaturated hydrocarbons 137
 Unsteady-state diffusion experiments 281
 Upper and lower reaction states 593
 Uranium dioxide catalyst 67
- V**
- Vanadia catalysts, *o*-xylene oxidation on 670
 Vanadia-on-silica catalyst 669
 Vanadium 656
 catalyst 646
 mixed oxides of 562
 oxide 666
 pentoxide catalyst 362
 solid catalysts containing 561
 Vapor
 -phase hydrogenation of α -methylstyrene 176
 -phase reaction 221
 pressure 312
 of lactam 314
 of water 314
 Vaporization of naphthalene 466
 Velocities in the fluidized bed, gas 30
 Velocity
 and direction of liquid phase in bubble columns 236
 fluidizing 297
 of gas, mass 608
 inlet gas 548
 of rise 308
 Vibration mixed reactor 3, 5
 Villerman and Devillon, model of 380
 Vinyl ethylbenzene, conjugate dehydrogenation of 143
 Viscosity 313, 353
 Viscous liquids, Newtonian high- 303
 V_2O_5 catalysts 646
 V_2O_5 cylindrical pellets 363
 Volatile components, sorption of 303
 Volume, bubble 291
 Volume, cloud-wake 291
- W**
- Wall influence, reactor 480
 Wall temperature 641
 Warm-up 34
 Waste gases, removal of SO_2 from 571

Water			
adsorption of	583		
contaminated	656		
diffusivity of	313		
in a nylon 6 melt, activity			
coefficient of	314		
solubility	441		
vapor	620		
vapor pressure of	314		
Wax-bearing feedstocks	423		
Wax-free feedstock	423		
Werner-Wilhelm boundary			
conditions	343		
Wetting			
of bed	173		
of catalyst particles under			
trickle flow	151		
effective	218		
conversion model based on ..	220		
		Wetting (Continued)	
		of packings	157
		X	
		Xylene disappearance, activation	
		energy for	648
		<i>o</i> -Xylene oxidation	9, 669
		on vanadia catalysts	670
		to phthalic anhydride	646
		Y	
		Yield	
		optimum	371
		Z	
		Zeolite crystal	656
		Zeolites, diffusion in	205
		Zirconium phosphate	656
		copper-substituted	654